USGS
science for a changing world

Integrated Geoscience Studies in the Greater Yellowstone Area—

Volcanic, Tectonic, and Hydrothermal Processes in the Yellowstone Geoecosystem

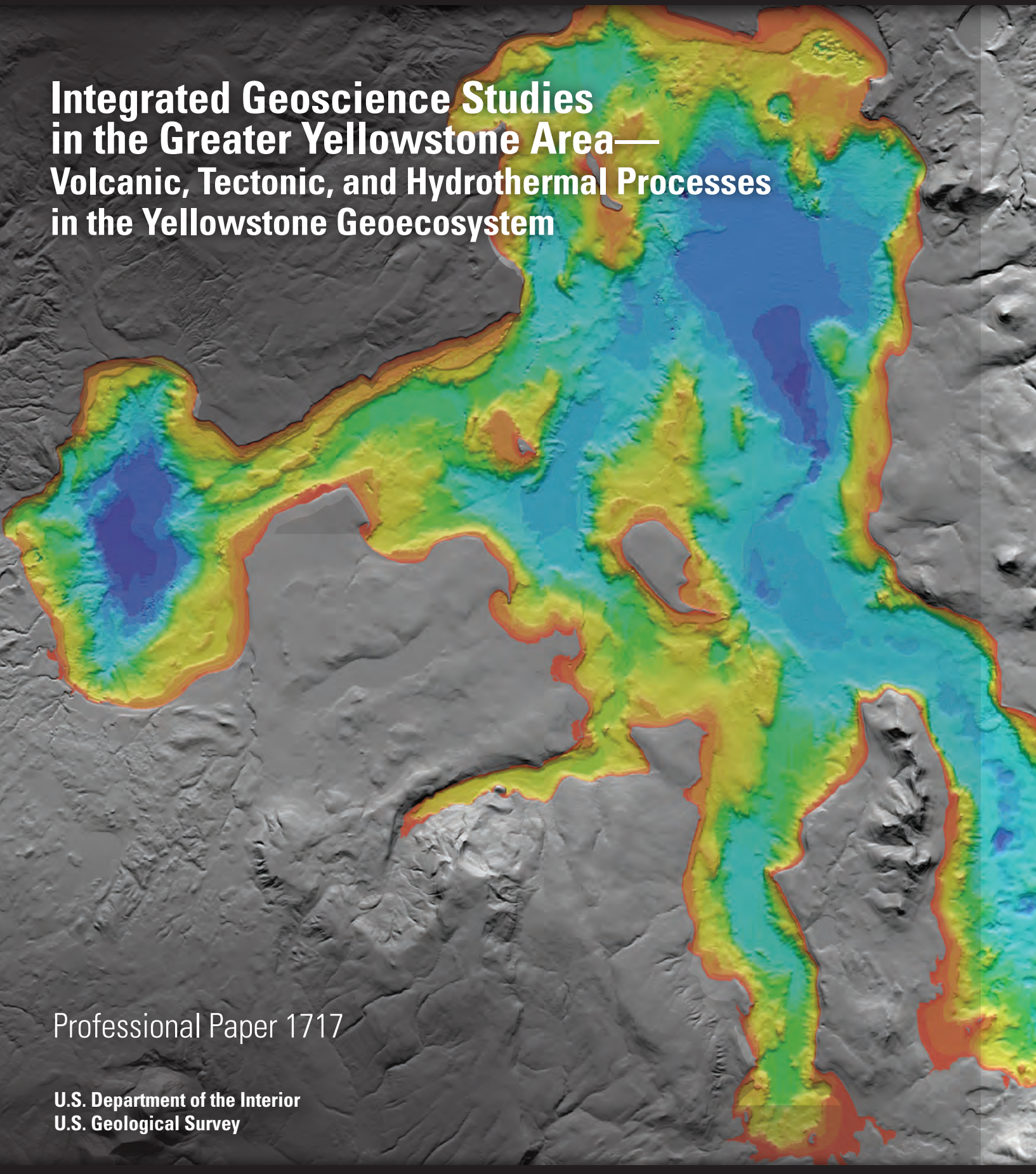

Professional Paper 1717

U.S. Department of the Interior
U.S. Geological Survey

Integrated Geoscience Studies in the Greater Yellowstone Area—Volcanic, Tectonic, and Hydrothermal Processes in the Yellowstone Geoecosystem

Edited by Lisa A. Morgan

Professional Paper 1717

U.S. Department of the Interior
U.S. Geological Survey

U.S. Department of the Interior
DIRK KEMPTHORNE, Secretary

U.S. Geological Survey
Mark D. Myers, Director

U.S. Geological Survey, Reston, Virginia: 2007

For sale by U.S. Geological Survey, Information Services
Box 25286, Denver Federal Center
Denver, CO 80225

For more information about the USGS and its products:
Telephone: 1-888-ASK-USGS
World Wide Web: http://www.usgs.gov/

Any use of trade, product, or firm names in this publication is for descriptive purposes only and does not imply endorsement by the U.S. Government.

Although this report is in the public domain, permission must be secured from the individual copyright owners to reproduce any copyrighted materials contained within this report.

Suggested citation:
Morgan, L.A., ed., 2007, Integrated geoscience studies in the greater Yellowstone area—Volcanic, tectonic, and hydrothermal processes in the Yellowstone geoecosystem: U.S. Geological Survey Professional Paper 1717, 532 p.

Volume Contents

Geologic Studies

A. The Yellowstone Hotspot, Greater Yellowstone Ecosystem, and Human Geography.....1
By Kenneth L. Pierce, Don G. Despain, Lisa A. Morgan, and John M. Good

B. Movement of a Large Landslide Block Dated by Tree-Ring Analysis, Tower Falls Area, Yellowstone National Park, Wyoming 41
By Paul E. Carrara

Yellowstone Lake Studies

C. Reconnaissance Study of Pleistocene Lake and Fluvial Deposits In and Near Ancestral Yellowstone Lake, Wyoming 53
By John D. Love, John M. Good, and D.G. Browne

D. The Floor of Yellowstone Lake is Anything but Quiet—New Discoveries from High-Resolution Sonar Imaging, Seismic-Reflection Profiling, and Submersible Studies.....91
By Lisa A. Morgan, Wayne C. Shanks, III, Kenneth L. Pierce, David A. Lovalvo, Gregory K. Lee, Michael W. Webring, William J. Stephenson, Samuel Y. Johnson, Stephen S. Harlan, Boris Schulze, and Carol A. Finn

E. Postglacial Inflation-Deflation Cycles, Tilting, and Faulting in the Yellowstone Caldera Based on Yellowstone Lake Shorelines 127
By Kenneth L. Pierce, Kenneth P. Cannon, Grant A. Meyer, Matthew J. Trebesch, and Raymond D. Watts

F. The Influence of Sublacustrine Hydrothermal Vent Fluids on the Geochemistry of Yellowstone Lake.....169
By Laurie S. Balistrieri, Wayne C. Shanks, III, Russell L. Cuhel, Carmen Aguilar, and J. Val Klump

G. Geochemistry of Sublacustrine Hydrothermal Deposits in Yellowstone Lake—Hydrothermal Reactions, Stable-Isotope Systematics, Sinter Deposition, and Spire Formation.....201
By Wayne C. Shanks, III, Jeffrey C. Alt, and Lisa A. Morgan

Geochemical Studies

H. The Question of Recharge to the Deep Thermal Reservoir Underlying the Geysers and Hot Springs of Yellowstone National Park.....235
By Robert O. Rye and Alfred H. Truesdell

I. Is Yellowstone Losing Its Steam?—Chloride Flux Out of Yellowstone National Park.....271
By Irving Friedman and Daniel R. Norton

J. Applications of Trace-Element and Stable-Isotope Geochemistry to Wildlife Issues, Yellowstone National Park and Vicinity.....299
By Maurice A. Chaffee, Wayne C. Shanks, III, Robert O. Rye, Charles C. Schwartz, Monique G. Adams, Robert R. Carlson, James G. Crock, Pamela A. Gemery-Hill, Kerry A. Gunther, Cynthia L. Kester, Harley D. King, and Shannon R. Podruzny

K. Environmental Geochemistry in Yellowstone National Park—Natural and Anthropogenic Anomalies and Their Potential Impact on the Environment....335
By Maurice A. Chaffee, Robert R. Carlson, and Harley D. King

L. Geochemical Data for Selected Rivers, Lake Waters, Hydrothermal Vents, and Subaerial Geysers in Yellowstone National Park, Wyoming and Vicinity, 1996–2004 365
By Pamela A. Gemery-Hill, Wayne C. Shanks, III, Laurie S. Balistrieri, and Gregory K. Lee

M. The Life Cycle of Gold Deposits Near the Northeast Corner of Yellowstone National Park—Geology, Mining History, and Fate 427
By Bradley S. Van Gosen

Geophysical Studies

N. Spectral Analysis of Absorption Features for Mapping Vegetation Cover and Microbial Communities in Yellowstone National Park Using AVIRIS Data 459
By Raymond F. Kokaly, Don G. Despain, Roger N. Clark, and K. Eric Livo

O. Hydrothermally Altered Rock and Hot-Spring Deposits at Yellowstone National Park—Characterized Using Airborne Visible- and Infrared-Spectroscopy Data 491
By K. Eric Livo, Fred A. Kruse , Roger N. Clark, Raymond F. Kokaly, and W.C. Shanks, III

P. Monitoring Changes in Geothermal Activity at Norris Geyser Basin by Satellite Telemetry, Yellowstone National Park, Wyoming....509
By Irving Friedman

ISBN 978-141132181-6

Printed on recycled paper

The Yellowstone Hotspot, Greater Yellowstone Ecosystem, and Human Geography

A

By Kenneth L. Pierce, Don G. Despain, Lisa A. Morgan, and John M. Good

Chapter A *of*

Integrated Geoscience Studies in the Greater Yellowstone Area—Volcanic, Tectonic, and Hydrothermal Processes in the Yellowstone Geoecosystem

Edited by Lisa A. Morgan

Professional Paper 1717

U.S. Department of the Interior
U.S. Geological Survey

Contents

Abstract 5
Introduction 6
Definition of the Greater Yellowstone Ecosystem (GYE) 6
Influence of the Yellowstone Hotspot on Landscape Formation 6
Ecological Effects of the Yellowstone Hotspot 13
    Rhyolite, Hotspot, and Lodgepole Pine 13
    Thermal Features and Associated Ecosystems 18
    Fault Valleys and Adjacent Mountains Associated with Hotspot Faulting 18
    Cold, Snowy Climate and Rugged Mountains Enhanced by Hotspot Uplift 19
    Modern and Pleistocene Snows Greatly Enhanced by Yellowstone Hotspot Geography 23
    Pleistocene Glaciation and Its Effects Enhanced by the Yellowstone Hotspot 24
Human Experience and Human Geography of the GYE as Influenced by the Yellowstone Hotspot 27
References Cited 36

Figures

1. Shaded-relief map of the greater Yellowstone ecosystem 7
2. Diagram of the main thesis of this report showing the cascade of effects from the geology of the Yellowstone hotspot, to ecology and human geography, to human experience. 8
3. Map of the Western United States showing track of the Yellowstone hotspot 9
4. Map showing track of the Yellowstone hotspot over the last 10 million years from the eastern Snake River Plain to the greater Yellowstone ecosystem 10
5. Illustration showing the hypothesis that a deep-seated mantle plume originating from excess heat at the core-mantle boundary drives the Yellowstone hotspot 12
6. Map showing rhyolite area that forms the Yellowstone Plateau in the core of the greater Yellowstone ecosystem 13
7. Photographs showing landscapes with forests of lodgepole pine developed on hotspot-generated rhyolite of the Yellowstone Plateau and showing contrasting vegetation in non-rhyolite areas 14
8. Photographs of hot springs, geysers, and other thermal features driven by hotspot heat 16
9. Photographs showing that active faulting associated with the Yellowstone hotspot created basins and ranges 20
10. Photographs showing that high, eroding mountains of the Yellowstone crescent of high terrain are related to hotspot uplift. 22
11. Diagram illustrating tilting of Wind River terraces away from the Yellowstone hotspot 24
12. Map showing that the major geoid anomaly in the Western United States centers on the present Yellowstone hotspot 25
13. Map showing average annual precipitation in Yellowstone National Park

and the nearby drainage areas. 26
14. Profile illustrating orographic snowfall across Yellowstone....27
15. Plot of snowpack from the Pacific Ocean through Yellowstone to the Big Horn Mountains 28
16. Map showing glacial cover of the Yellowstone area about 17,000 years ago 29
17. Photographs showing effect of glacial erosion and deposition on the landscape and soil of the greater Yellowstone ecosystem....30
18. Photographs showing the human experience in the greater Yellowstone ecosystem related to the Yellowstone hotspot. 32
19. Sketch map showing radial pattern of major rivers of the greater Yellowstone ecosystem....34
20. Cartoon showing central highland and idealized radial drainage pattern....35

Tables

1. Characteristics of the three main types of volcanic rocks found in the greater Yellowstone ecosystem....17
2. Rivers and other large drainages that head in the greater Yellowstone ecosystem....21
3. Governmental jurisdictions in the greater Yellowstone ecosystem....34

The Yellowstone Hotspot, Greater Yellowstone Ecosystem, and Human Geography

By Kenneth L. Pierce,[1] Don G. Despain,[1] Lisa A. Morgan,[2] and John M. Good[3]

Abstract

Active geologic processes associated with the Yellowstone hotspot are fundamental in shaping the landscapes of the greater Yellowstone ecosystem (GYE), a high volcanic plateau flanked by a crescent of still higher mountainous terrain. The processes associated with the Yellowstone hotspot are volcanism, faulting, and uplift and are observed in the geology at the surface. We attribute the driving forces responsible for the northeastward progression of these processes to a thermal plume rising through the Earth's mantle into the base of the southwest-moving North American plate. This progression began 16 million years ago (Ma) near the Nevada-Oregon border and arrived at Yellowstone about 2 Ma. Before arrival of the hotspot, an older landscape existed, particularly mountains created during the Laramide orogeny about 70–50 Ma and volcanic terrain formed by Absaroka andesitic volcanism mostly between 50–45 Ma. These landscapes were more muted than the present, hotspot-modified landscape because the Laramide-age mountains had worn down and an erosion surface of low relief had developed on the Absaroka volcanic terrain.

The Yellowstone Plateau was built by hotspot volcanism of rhyolitic lavas and caldera-forming rhyolite tuffs (ignimbrites). Streams eroding back into the edges of this plateau have created scenic waterfalls and canyons such as the Grand Canyon of the Yellowstone and Lewis Canyon. Rhyolite is poor in plant nutrients and forms sandy, well-drained soils that support the monotonous, fire-adapted lodgepole pine forests of the Yellowstone Plateau. Non-rhyolitic rocks surround this plateau and sustain more varied vegetation, including spruce, fir, and whitebark pine forests broken by grassy meadows. Heat from the hotspot rises upward and drives Yellowstone's famed geysers, hot springs, and mudpots. These thermal waters are home to specialized, primitive ecosystems, rich in algae and bacteria. The rock alteration associated with hydrothermal systems creates the bright colors of Yellowstone's Grand Canyon.

Basin-and-range-style faulting has accompanied migration of the hotspot to Yellowstone and formed the linear mountains and valleys that occur north and south of the hotspot track, which is the present-day eastern Snake River Plain. High rates of basin-and-range faulting occurred adjacent to the migrating Yellowstone hotspot, creating distinctive landscapes within the GYE such as the Teton Range/Jackson Hole, with characteristic rugged, forested ranges and adjacent flat-floored grassy valleys. The difference in altitude between the mountains and valleys provides a topographic gradient in which vegetation maturation advances with altitude; animal-migration patterns also follow this trend. The valleys provide natural meadows, agricultural land, town sites, and corridors for roads.

Uplift of the GYE by as much as 1 km (3,000 ft) during the last 5 million years has resulted in ongoing erosion of deep, steep-walled valleys. Many prominent ecological characteristics of Yellowstone derive from this hotspot-induced uplift, including the moderate- to high-altitude terrain and associated cool temperatures and deep snowfall.

Modern and Pleistocene climate and associated vegetation patterns strongly relate to the topography created by the hotspot and its track along the eastern Snake River Plain. Winter air masses from the moist northern Pacific Ocean traverse the topographic low of the Snake River Plain to where orographic rise onto the Yellowstone Plateau and adjacent mountains produces deep snow. A winter precipitation shadow forms on the lee (eastern) sides of the GYE. During Pleistocene glacial times, this moisture conduit provided by the hotspot-track-produced ice-age glaciers that covered the core of the present GYE. These glaciers sculpted bedrock and produced glacial moraines that are both forested and unforested, sand and gravel of ice-marginal streams and outwash gravels that are commonly covered with sagebrush-grassland, and silty lake sediments that are commonly covered by lush grassland such as Hayden Valley.

The effects of the Yellowstone hotspot also profoundly shaped the human history in the GYE. Uplift associated with the hotspot elevates the GYE to form the Continental Divide, and streams drain radially outward like spokes from a hub. Inhabitants of the GYE 12,000–10,000 years ago, as well as more recent inhabitants, followed the seasonal green-up of plants and migrating animals up into the mountain areas. During European immigration, people settled around Yellowstone in the lower parts of the drainages and established roads, irrigation systems, and cultural associations. The core Yellowstone highland is too harsh for agriculture and inhospitable to people in the winter. Beyond this core, urban and rural communities exist in valleys and are separated by upland areas. The partitioning inhibits any physical connection of communities, which in turn complicates pursuit of common interests across the whole GYE. Settlements thus geographically isolated evolved as diverse, independent communities.

[1] U.S. Geological Survey, Northern Rocky Mountain Science Center, Box 173492, Montana State Univ., Bozeman, MT 59717.

[2] U.S. Geological Survey, MS 973, Box 25046, Federal Center, Denver, CO 80225.

[3] U.S. Geological Survey volunteer, P.O. Box 4743, Jackson, WY 83001.

Introduction

Studies of the geology of Yellowstone National Park (the Park) began in the early 1870s with the Hayden Survey followed by the Hague Surveys. The Hayden Survey provided documentation by scientific studies, photography, and paintings of Yellowstone's wonders that were critical to its establishment in 1872 as the world's first national park. More than 125 years after these pioneering geologic studies, we have relied on the foundation of their work and incorporated more recent concepts such as plate tectonics, hotspot tracks, and possible mantle plumes to explain the geologic phenomena that influence the climate and distribution of plant and animal communities and human geography in the Yellowstone region today.

Overviews of the geology in the greater Yellowstone ecosystem (GYE) are found in Good and Pierce (1996), Smith and Siegel (2000), and Love and others (2003). Don Despain (1990) described vegetation of Yellowstone and many relations to the geology. Eversman and Carr (1992) composed a road guide to the ecology of the greater Yellowstone area. Pierce and others (2003) described a week-long field trip to the Quaternary geology and ecology of the GYE. For a mountainous area immediately northwest of Yellowstone, Duncan Patten (1963) made a pioneering study of the relation between geology and vegetation and determined that grassland and sagebrush are associated with claystones, siltstones, and alluvium.

Our central theme is that active geologic processes associated with the track of the Yellowstone hotspot have a profound effect on the geography, topography, climate, soils, and biota of the GYE (figs. 1 and 2). In fact, the hotspot and its associated processes may explain much of the character of the GYE. The salient geologic processes associated with the track of the Yellowstone hotspot (Pierce and Morgan, 1992) include (1) volcanism that produces such features as the Yellowstone rhyolite plateau and the eastern Snake River Plain, (2) faulting that created such features as the Teton Range/Jackson Hole and the Madison Range/Madison Valley, and particularly important, (3) uplift that resulted in the generally high altitude of the GYE and incision to form deep valleys, commonly in highly erodible rocks. The geothermal features of Yellowstone attest to deep-seated hotspot heat. Of course, prior to the hotspot's arrival in the last few million years, older landscapes existed, particularly those formed by Laramide mountain building about 70–50 million years ago (Ma) and by extensive Absaroka andesitic volcanism mostly about 50–45 Ma. These ancient landscapes were more muted than the present, hotspot-modified landscape because by about 20–10 Ma, the Laramide-age mountains had worn down and an erosion surface of moderate to low relief characterized the Absaroka volcanic basin and the old Laramide uplifts.

This shaping of the geography by hotspot processes has, in turn, influenced human settlement and use (fig. 2). Much of the ecosystem consists of an arc of mountains that wrap around the Yellowstone Plateau and include (clockwise from west) Centennial Mountains, Madison Range, Gallatin Range, Beartooth Mountains, Absaroka Range, Wind River Range, Gros Ventre Range, Wyoming Range, Salt River Range, and Teton Range, as well as a number of smaller mountain ranges in adjacent parts of Wyoming, Idaho, and Montana.

The location of the GYE in a hotspot-uplifted highland along the Continental Divide resulted in boundaries of Federal, State, and county jurisdictions being established within the GYE. Such Federal, State, and county jurisdictions with their attendant laws, regulations, and agencies often have conflicting goals. Two national parks (Yellowstone and Grand Teton) and seven national forests (Beaverhead, Gallatin, Custer, Shoshone, Bridger-Teton, Caribou, and Targhee) including three national forest regions compose the political core of the GYE (fig. 1). The States of Wyoming, Montana, and Idaho have responsibilities in the GYE, as do 21 counties. Thus, political decision-making in the GYE is cumbersome and complex.

Definition of the Greater Yellowstone Ecosystem (GYE)

The GYE extends outward from Yellowstone to include contiguous mountain ranges, foothills, and included valleys (fig. 1). The boundary of the GYE shown in figure 1 is based on ecological land units delineated as part of the Greater Yellowstone Cooperative Regional Transportation Study (U.S. National Park Service and U.S. Forest Service, 1979). The central and perhaps defining feature of the greater Yellowstone ecosystem is a group of about 24 conterminous mountain ranges extending from southwestern Montana to most of the western third of Wyoming and adjacent southeastern Idaho. The ecosystem considered here (fig. 1) includes all terrain from the foothills life zone (Daubenmire, 1943) and above. Where foothills do not exist at the base of the montane slopes, the GYE boundary is drawn on the basal plain 10 km (6 mi) from the base of the montane slopes. Locally, some mountain areas contiguous to the GYE are not included, such as the Owl Creek Mountains and the Bridger Range. These ranges form bridges to other mountain ecosystems. Our boundary is quite similar to that of others who have delineated this ecosystem (Glick and others, 1991; Marston and Anderson, 1991).

Influence of the Yellowstone Hotspot on Landscape Formation

The Yellowstone hotspot exerts a major influence on the ecology and human geography of the GYE (fig. 2) by shaping the larger scale features of the landscape. By human geography, we mean how humans and their works are organized on the landscape. Four types of geologic processes important to landscape formation are associated with the Yellowstone hotspot: (1) volcanism, (2) hot springs and associated thermal features, (3) active faulting, and (4) uplift followed by subsidence. Over

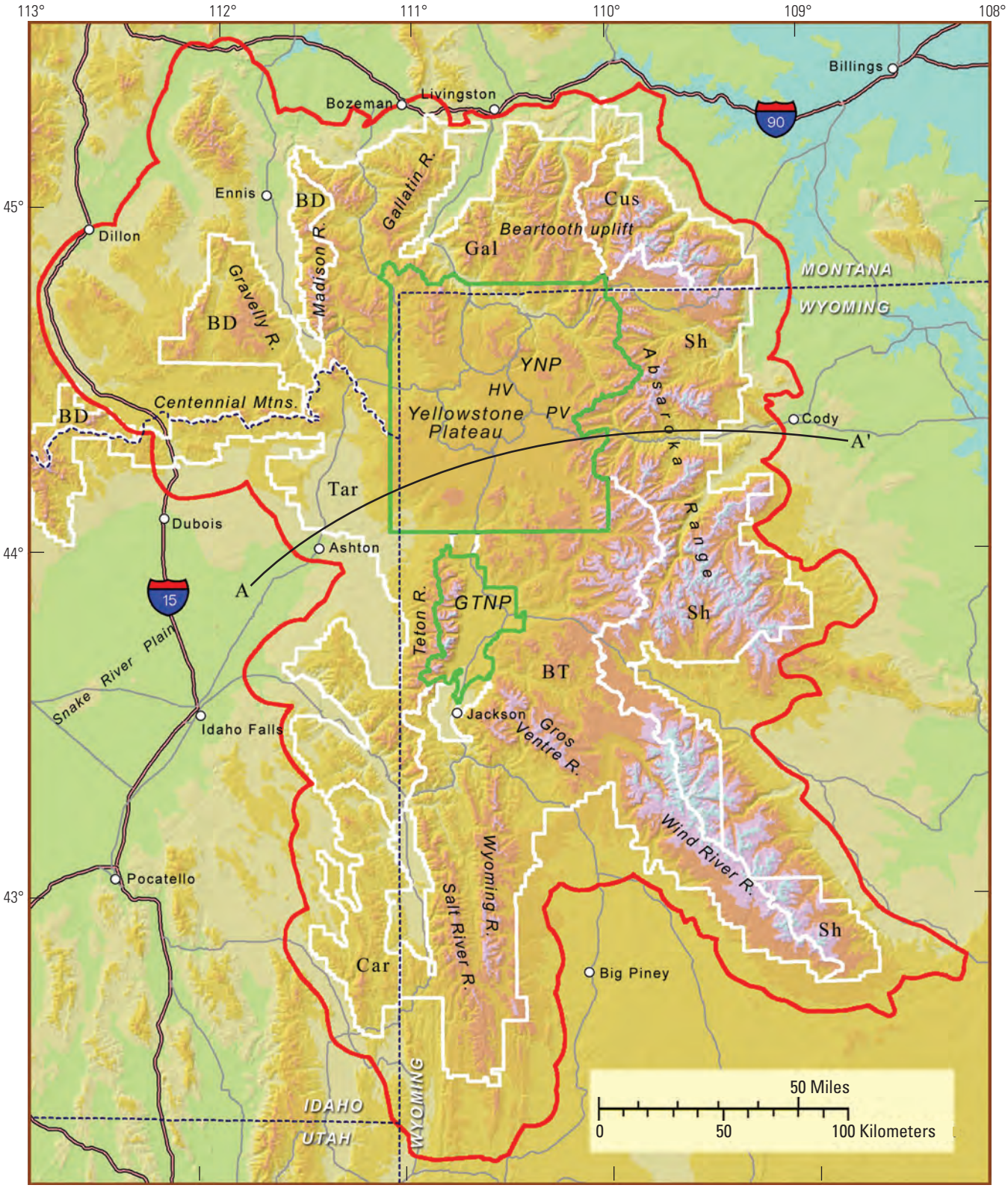

Figure 1. Shaded-relief map of the greater Yellowstone ecosystem (GYE, red line). The GYE incorporates Yellowstone and Grand Teton National Parks (YNP, GTNP outlined by green lines), 7 national forests (outlined in white), 3 States, and 21 counties (not shown). Roads are shown as thin gray lines. Designations of seven national forests: BD, Beaverhead-Deerlodge; Gal, Gallatin; Cus, Custer; Sh, Shoshone; BT, Bridger-Teton; Car, Caribou; and Tar, Targhee. Also designated, HV, Hayden Valley; PV, Pelican Valley. Map from Lisa Landenburger (written commun., 2004). A–A' line of section for figure 14.

the last 10 million years, Yellowstone hotspot activity has progressed northeastward at a rate of about 2.5 cm (1 in) per year[1] and has left in its wake the eastern Snake River Plain (figs. 3 and 4). The hotspot is a relatively fixed thermal disturbance in the Earth's mantle that is below the southwest-moving North American plate; thus, the associated geologic activity appears to be progressing northeastward.

From a geologist's perspective, the best way to understand the Yellowstone hotspot is to look at its influence through time. We think that the hotspot track originated about 16 Ma as a mantle "plume head" (Richards and others, 1989) centered near the McDermitt volcanic caldera complex on the Nevada-Oregon border (fig. 3) (Malde, 1991; Draper, 1991; Pierce and Morgan, 1992; Smith and Braile, 1993; Parsons and others, 1994; Pierce and others, 2000, 2003). From 17–14 Ma, the inferred plume head produced widespread volcanism, including the Columbia River and Oregon Plateau flood basalts (Hooper, 1997; Coffin and Eldholm, 1994; Camp, 1995; Camp and Ross, 2004) as well as widely dispersed rhyolitic fields (fig. 3) and the Nevada-Oregon rift zone (Zoback and Thompson, 1978). About 10 Ma, voluminous rhyolitic volcanism contributed to the Twin Falls and Picabo volcanic fields, an east-west belt 200 km (125 mi) long (Morgan and others, 1999; Morgan and McIntosh, 2005). From about 10 Ma to present, the leading edge of the hotspot volcanism defined a linear track and produced a sequence of three volcanic fields each containing overlapping or nested calderas. Each field started with a large caldera eruption (fig. 4)—the Picabo volcanic field at 10.23 Ma (Morgan and others, 1997), the Heise volcanic field at 6.65 Ma (Morgan and others, 1999; Morgan and McIntosh, 2005), and the Yellowstone Plateau volcanic field at 2.1 Ma (Christiansen, 2001). This sequence left in its wake the eastern Snake River Plain (fig. 4).

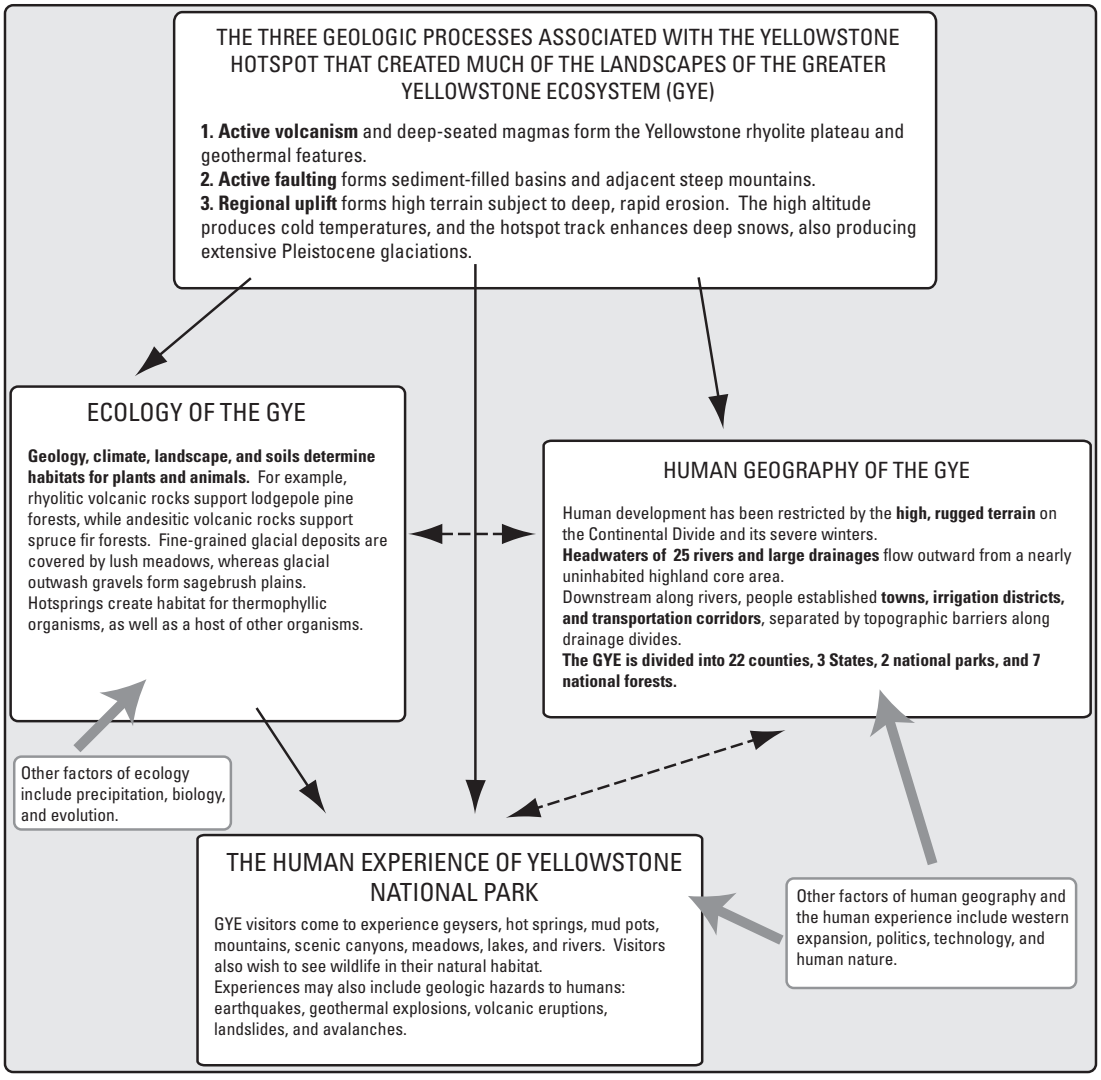

Figure 2. Diagram of the main thesis of this report showing the cascade of effects from the geology of the Yellowstone hotspot, to ecology and human geography, to human experience.

[1]For the hotspot track and motion of the North American plate during the last 10 million years, several approaches yield results of between about 2.2 and 2.9 cm/yr to the SSW. For the inferred motion of the North American plate: (1) a plate motion of about 2.5 cm/year S. 55° W. using the global solution of plate motion in the hotspot reference frame but with the Yellowstone hotspot track deleted (Alice Gripp, *in* Pierce and Morgan, 1992), (2) a track progression (opposite to plate motion) of about 2.9 cm/year to the N. 55° E. based on volcanic progression but not subtracting out post-volcanic extension (Rodgers and others, 1990; Pierce and Morgan, 1992; Smith and Braile, 1993), and (3) a track-associated fault progression of about 2.2 cm/yr to the NE. based on the migration of most active faulting associated with the hotspot and also subtracting the effect of post-volcanic extension (Anders, 1994).

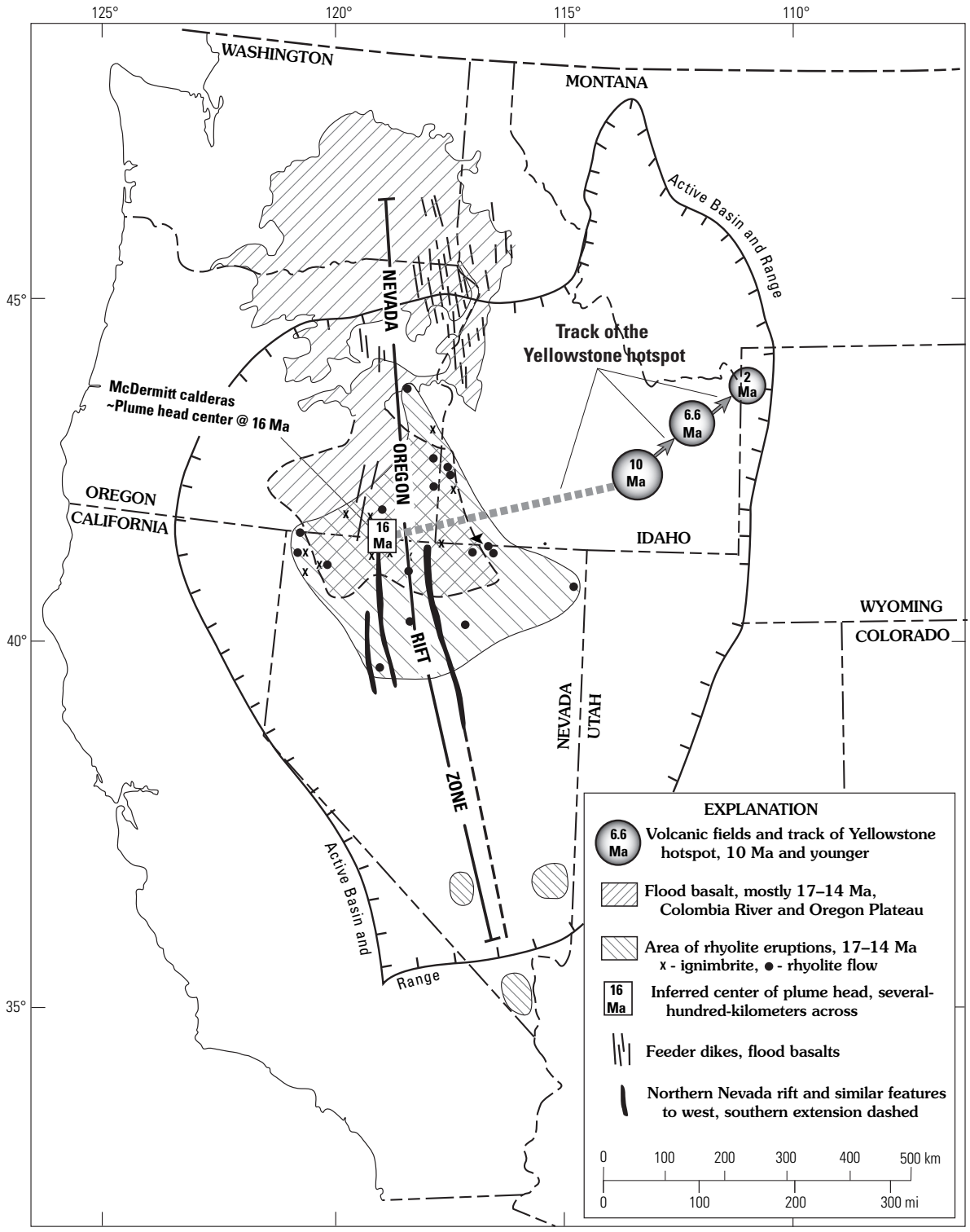

Figure 3. Map of the Western United States showing the track of the Yellowstone hotspot. Geologic evidence suggests that the hotspot originated about 16 million years ago when a postulated hot mantle-plume head about 400 km (250 mi) in diameter, pushed into the base of the North American plate. This plume head centered on the symbol labeled 16 Ma near the Nevada-Oregon border and produced both the flood basalts and rhyolite eruptions (indicated by the two directions of cross-hatching). From 10 to 2 million years ago, the hotspot track became more systematic and left in its wake the trench of the eastern Snake River Plain. The hotspot arrived in the greater Yellowstone area about 2 million years ago. The ages shown for individual volcanic fields refer to time of inception of volcanism.

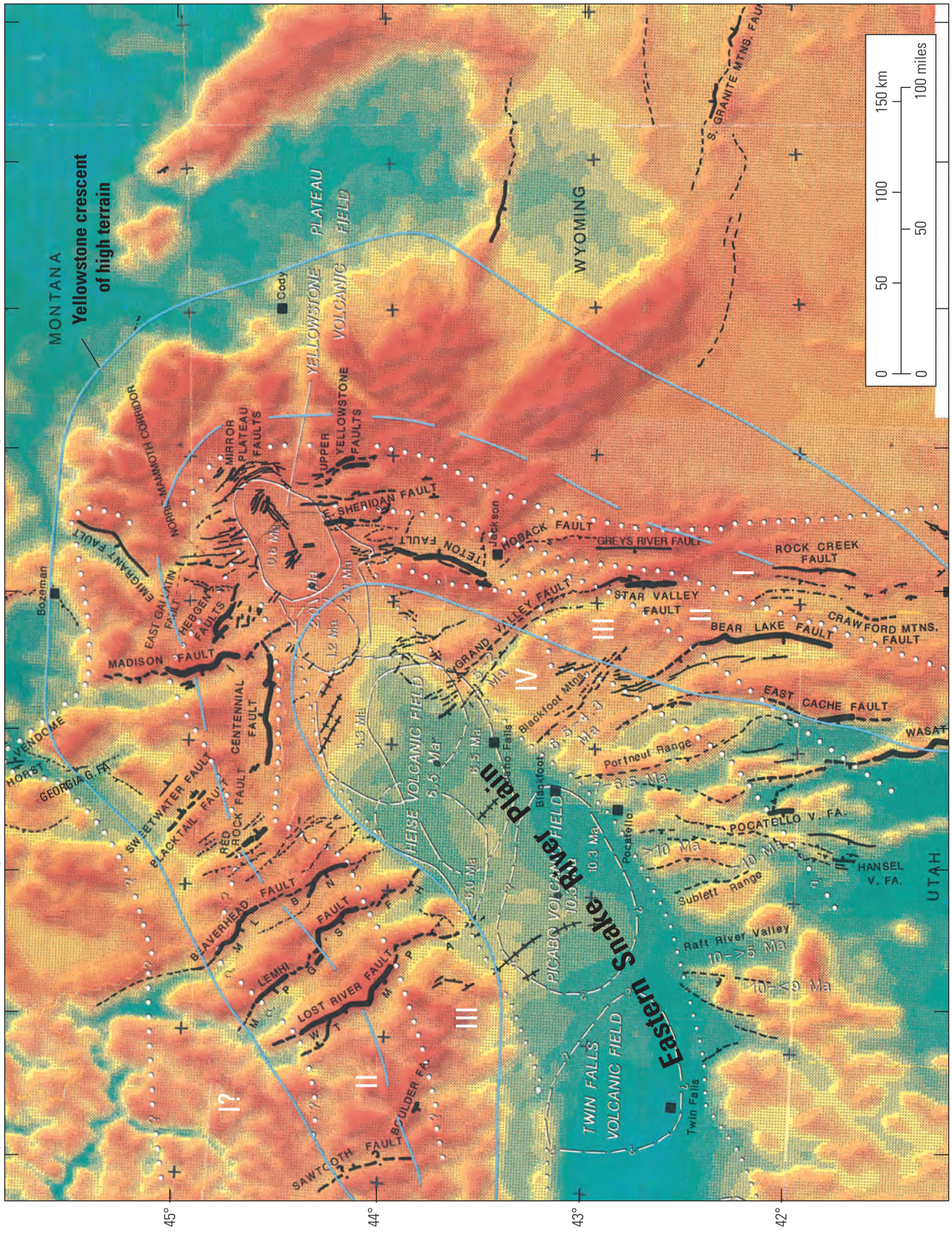
MONTANA
Yellowstone crescent of high terrain
WYOMING
UTAH
Eastern Snake River Plain
YELLOWSTONE VOLCANIC FIELD
PLATEAU
HEISE VOLCANIC FIELD
PICABO VOLCANIC FIELD
TWIN FALLS VOLCANIC FIELD
NORTHERN MAMMOTH CORRIDOR
MIRROR PLATEAU FAULTS
UPPER YELLOWSTONE FAULTS
SHERIDAN FAULT
TETON FAULT
HOBACK FAULT
GREYS RIVER FAULT
ROCK CREEK FAULT
STAR VALLEY FAULT
BEAR LAKE FAULT
CRAWFORD MTNS. FAULT
EAST CACHE FAULT
WASATCH
GRAND VALLEY FAULT
MADISON FAULT
EMIGRANT FAULT
EAST GALLATIN FAULT
HEBGEN FAULTS
CENTENNIAL FAULT
VENDOME
HORST
GEORGIA G. FA.
SWETWATER FAULT
BLACKTAIL FAULT
RED ROCK FAULT
BEAVERHEAD FAULT
LEMHI FAULT
LOST RIVER FAULT
BOULDER FA.
SAWTOOTH FAULT
POCATELLO V. FA.
HANSEL V. FA.
Porineut Range
Sublett Range
Raft River Valley
S. GRANITE MTNS. FAULT
Cody
Bozeman
Jackson
Idaho Falls
Blackfoot
Pocatello
Twin Falls
Blackfoot Mtns.
0.6 Ma
1.2 Ma
2.0 Ma
4.3 Ma
6.5 Ma
8.5 Ma
8.0 Ma
10.3 Ma
>10 Ma
10–>5 Ma
10–>9 Ma
I
II
III
IV
I?
II?
III?
0 50 100 150 km
0 50 100 miles
107°
108°
109°
110°
111°
112°
113°
114°
115°
45°
44°
43°
42°

We attribute this linear sequence to a thermal-plume tail (or chimney) phase of the Yellowstone hotspot, which is currently beneath Yellowstone (Pierce and Morgan, 1992).

We use *hotspot* and *hotspot track* to refer to observed features on the surface of the Earth, in particular such Earth-surface features as the volcanic progression, associated fault activity, and young uplift. Driving of such Earth-surface processes by a thermal mantle plume is only one interpretation. However, we prefer the explanation that the hotspot and its track are products of a hot mantle plume rising from perhaps the core-mantle boundary to the base of the overriding North American plate (fig. 5). Two geophysical studies conclude that a thermal mantle plume rises from a depth of 500 km and intercepts the crust beneath Yellowstone (Yean and Dueker, 2005; Waite and others, 2006). This plume rises to the southeast at an angle of~70°, and at a depth 500 km it is under the town of Dillon, Mont.[2] Other geoscientists consider the hotspot and the hotspot track to be the result of "… feedback between upper-mantle convection and regional lithospheric tectonics …" (Christiansen and others, 2002) and mantle upwelling forced by lithospheric extension of the Western U.S. (Humphreys and others, 2000). Whether deep or shallow origin, rising mantle material has generated hot magma.[3]

Figure 4. Track of the Yellowstone hotspot over the last 10 million years from the eastern Snake River Plain to the greater Yellowstone ecosystem. The Yellowstone crescent of high terrain is outlined in blue with a dashed blue line along the crest. The warmer colors indicate higher altitudes. Active faults are shown in black with the heaviest lines for more active faults on major mountain fronts. Dotted white lines denote four belts (I–IV) of faulting with belt II the most prominent. Volcanic fields and their ages are shown in white. Small black letters denote segments of faults described in Pierce and Morgan (1992).

Flared out from the hotspot track like the wake of a boat are two belts of active faulting that extend south and west from Yellowstone National Park and appear to have migrated northeastward with the hotspot (fig. 4) (Anders and others, 1989; Pierce and Morgan, 1992; Anders, 1994). This faulting has created the ecologically important landscape features of linear grassland basins and adjacent forested ranges.

Culminating a little farther to the northeast (or outward) of the active fault belts is the Yellowstone crescent of high terrain (fig. 4). This area appears to be rising and then subsiding like a large bow wave on the leading margin of the track of the Yellowstone hotspot. Pierce and Morgan (1992) estimate about 500–1,000 m (1,500–3,000 ft) of uplift; Smith and Braile (1993) estimate about 600 m (2,000 ft). Humphreys and others (2000) suggest that mantle buoyancy holds the Yellowstone crescent of high terrain (hotspot swell) about 1 km (3,300 ft) higher than would normal mantle. The highest geoid anomaly in the conterminous United States, which coincides with the current position of the Yellowstone hotspot, also suggests ongoing uplift (Milbert, 1991; Smith and Milbert, 1999; Pierce and others, 1992; Smith and Braile, 1993) (see fig. 10 later in this report). The geoid is an imaginary (mathematical) surface that coincides with the mean sea level in the ocean and its extension through the continents. The major United States geoid anomaly that centers on Yellowstone also indicates a deep-seated process beneath the North American plate.

Perhaps the most noteworthy aspect of the volcanism, faulting, and uplift in the GYE is the enormous scale of these processes, as expressed in the following measures. The three cycles of caldera-forming volcanism during the past 2.1 m.y. in the Yellowstone Plateau volcanic field have produced more than 6,500 km^3 (1,500 mi^3) of volcanic material (Christiansen, 1984, 2001). The large calderas formed during these eruptions are large depressions and do not have the conical or shield shape most people associate with volcanoes. The last major caldera formed 640,000 years ago and is a 40- by 65-km (25- by 40-mi) depression flanked by sheets of ash-flow tuff and is largely filled by younger rhyolite lava flows. The level of seismicity in the GYE area is one of the highest in North America, resulting in dozens of moderate to large earthquakes (magnitudes between 5.5 and 7.5) since 1900 (Smith and Arabasz, 1991). Heat flow from the Yellowstone caldera is about 50 times the continental mean. The geologically active Yellowstone Plateau stands more than 1,000 m (3,000 ft) higher than the older hotspot track of the eastern Snake River Plain. Finally, in the Yellowstone area, the crescent of high terrain, which largely coincides with the positive geoid anomaly, is about 400 km (250 mi) across in a northwest-southeast direction (fig. 4) and is quite similar to the dimensions of the GYE. The sheer magnitude of individual processes, as well as their cumulative effect on the

[2]The following arguments support a deep mantle origin of the Yellowstone hotspot, perhaps from the core-mantle boundary (fig. 5): (1) the broad scale (400 km, 250 mi) of faulting and uplift associated with the hotspot track, (2) $^3He/^4He$ values of 16 from both Yellowstone's thermal waters and rocks along the hotspot track that require a deep mantle source, whereas ratios of 8 are associated with the asthenosphere (soft upper mantle) at plate-spreading centers (Kennedy and others, 1987; Craig, 1990, 1997; Farley and Neroda, 1998), (3) a track defined by migrating volcanism and faulting closely matching motion of the North American plate in both rate and direction, (4) a major positive geoid anomaly that centers on Yellowstone and extends about 200 km (125 mi) "ahead" of Yellowstone, and is about 800 km (500 mi) across at Yellowstone (Smith and Milbert, 1999), reflecting an origin deeper than the crustal processes centered on Yellowstone (see fig. 10), (5) a pattern where uplift occurs well in advance of volcanism, indicating that upwelling is caused by deep-seated processes and is not in response to plate-interaction processes such as faulting, and (6) the start of the hotspot track with an inferred large diameter plume head that implies a deep vertical dimension.

[3]As mantle material (density ~3.3 g/cm^3) rises towards the surface, decompression melting (White and McKenzie, 1989) yields 10 percent or so basaltic magma (density ~3.0 g/cm^3) that ascends into the base of the crust (density <3.0 g/cm^3). As the basaltic magma pushes into the lower crust, heat from the molten basalt melts crustal material to form siliceous magmas, which have a lower melting temperature and density than basaltic magma. Meanwhile, down in the mantle, the material remaining (restite) after the basaltic partial-melt has risen upward also becomes lighter (density also roughly ~3.0 g/cm^3). The resultant hotspot uplift has three possible origins: (1) the higher temperatures, and therefore lower density, of the plume material and the heated crust, (2) the formation of two lower density materials (basalt and restite) from the higher density mantle source, and (3) possible thermal erosion of high-density mantle lithosphere (density ~3.3 g/cm^3) by hotter, lower density mantle material.

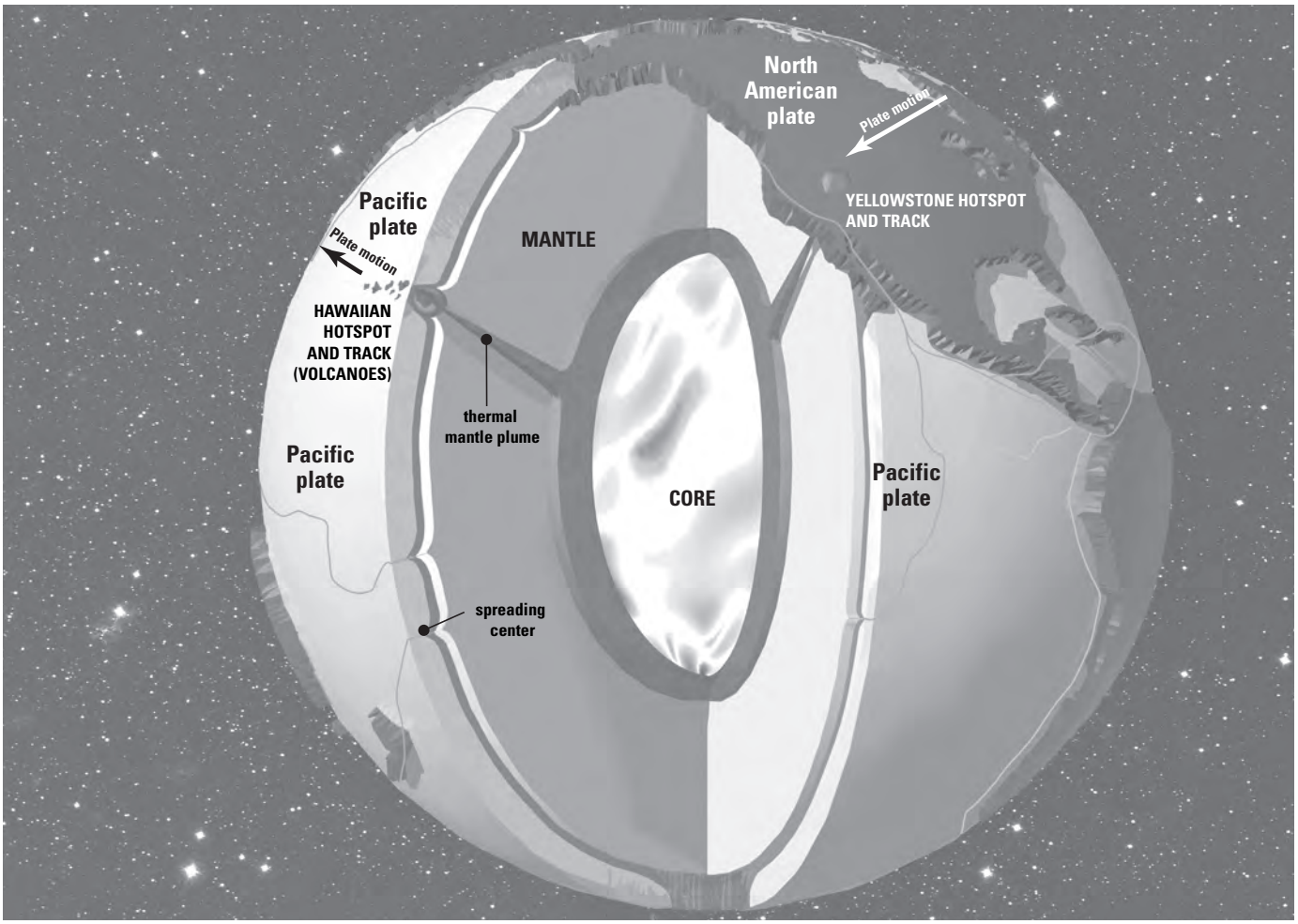

Figure 5. Illustration showing the hypothesis that a deep-seated mantle plume originating from excess heat at the core-mantle boundary drives the Yellowstone hotspot. Some researchers suggest a shallower mantle source with upwelling of the plume from a depth of near 600 km (400 mi) to produce the hotspot track. (From Good and Pierce, 1996.)

scale of hotspot-related geologic features, is an essential argument that a deep-seated geologic process is at work.

The Yellowstone Plateau, at about 2,450 m (8,000 ft) altitude, resulted from hotspot volcanism and probably also hotspot uplift (fig. 4). Key geologic features of the plateau are its rhyolitic lava flows, rhyolite tuffs (ignimbrites), and its famous geysers and hot springs. Both the plateau and surrounding mountains are snow covered much of the year and are too cold for profitable agriculture. For example, at an altitude of 2,750 m (9,000 ft), snow cover lasts three-fourths of the year (Despain, 1990, p. 127).

Some geologists favor shallower processes in the upper mantle to explain the origin and maintenance of the hotspot (see Christiansen, 2002; Humphreys and others, 2000). Although figure 5 is helpful in visualizing the idea of a thermal plume, we do not think that the depth of the thermal upwelling (deep plume, shallow upwelling) driving the hotspot is critical to the topic of this paper. What is important is that Yellowstone hotspot processes, whatever their depths of origin in the mantle, are responsible for the *Earth-surface processes* of volcanism, geothermal activity, faulting, and uplift[4].

[4]Hotspots, and particularly what drives them, are controversial and actively under investigation. The hotspot idea was introduced by J.T. Wilson (1963) for the Hawaiian Island chain, for which he suggested that the Pacific plate was moving across a stationary heat source in the mantle, later termed a mantle plume. Hotspot tracks define the hotspot reference frame for global plate motions. For the numerous moving plates, this hotspot reference frame has proven quite successful for solving the absolute motion of each plate. This suggests that, to a first approximation, hotspots have a source fixed in the relatively stationary mantle. Duncan and Richards (1991) give a comprehensive overview of hotspots around the world, their origin by mantle plumes, and relationship to flood-basalt volcanism. In his 1997 presidential address to the Geological Society of America, George Thompson (1998) emphasized the importance of hotspots and mantle plumes in the geologic record, including their need to be integrated with the modern plate-tectonic scheme. Norm Sleep (1990, 1997, 2002) concluded that hotspots are driven by deep mantle plumes, and with Thompson and Gibson (1991) noted that the thinner the lithosphere, the higher the rise of plume material and the more decompression melting and magma production occurs. Two recent volumes (Davies, 1999; Jackson, 2000) develop attributes and concepts of deep-mantle plumes.

In the anti-plume camp, Don Anderson (see 1998 and references therein)

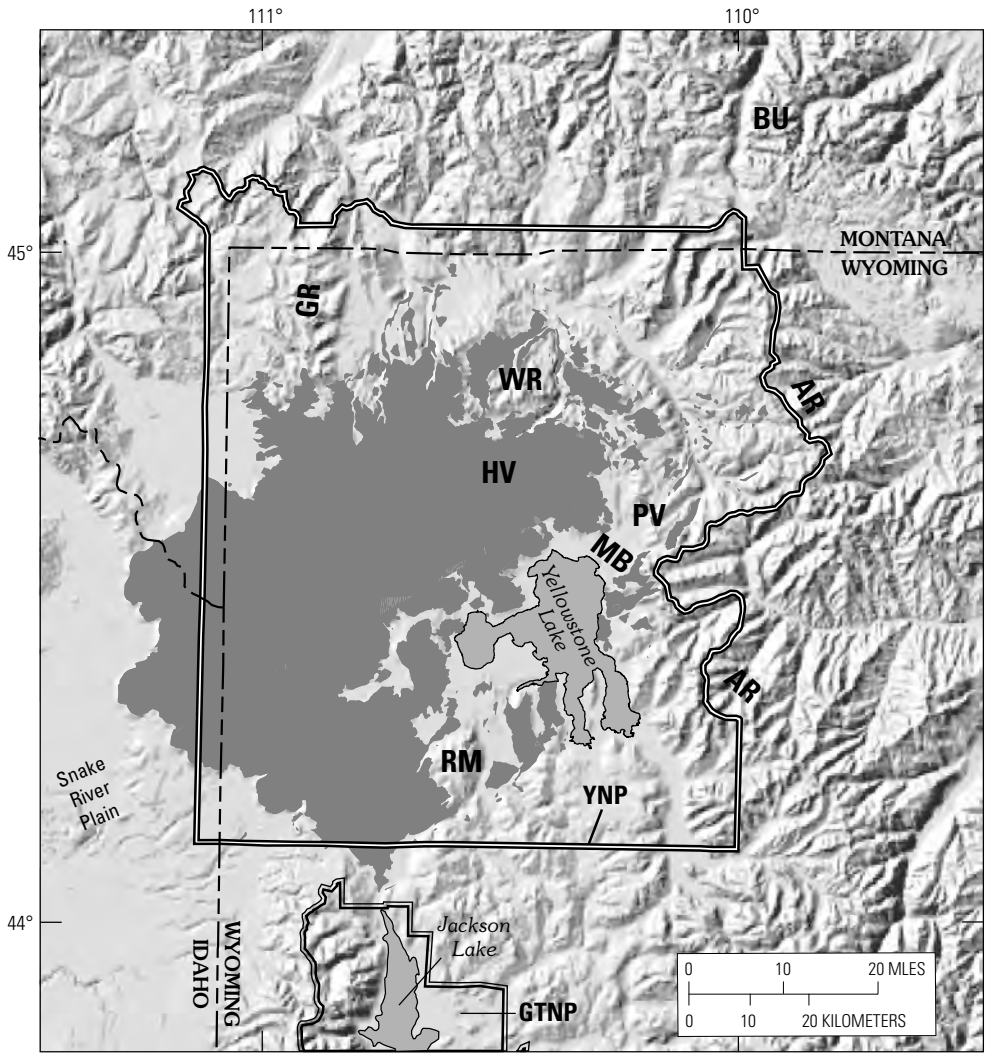

Figure 6. Rhyolite area (darkest shade) that forms the Yellowstone Plateau in the core of the greater Yellowstone ecosystem. Rhyolite has only one-fourth the nutrients of andesite—a volcanic rock intermediate between rhyolite and basalt. Rhyolite forms well-drained sandy soils with snowmelt infiltrating down to several meters. Lodgepole pine is well adapted to grow on the rhyolite soils, whereas spruce fir forests grow on other bedrock types such as (1) andesite in the Washburn Range (WR) and Absaroka Range (AR), (2) mixtures of sedimentary rocks (shale, sandstone, and limestone) in the Gallatin Range (GR) and Red Mountains (RM), (3) a variety of Precambrian rocks in the Beartooth Mountains uplift (BU), and (4) surficial materials from all of the previously mentioned rock types. Other locations on map are Hayden Valley (HV, where lake sediments overlie the rhyolite), Pelican Valley (PV), Mary Bay (MB), Yellowstone National Park (YNP), and Grand Teton National Park (GTNP).

Ecological Effects of the Yellowstone Hotspot

The Yellowstone hotspot theory provides a unifying concept for an understanding of how Earth processes have influenced ecology, human history, and cultural patterns of the greater Yellowstone ecosystem. In the following sections, we discuss how salient aspects of the GYE are related to the hotspot-associated processes of volcanism, active faulting, and uplift. Although we discuss uplift last, it has had the most profound effect on the ecosystem and has been the controlling factor determining human geography.

Rhyolite, Hotspot, and Lodgepole Pine

At an altitude of about 2,500 m (8,000 ft), the Yellowstone Plateau forms the core area of Yellowstone National Park. The plateau was built up by extrusion of rhyolitic volcanic rocks produced by hotspot volcanism (figs. 6 and 7) (Christiansen, 1984, 2001; U.S. Geological Survey, 1972b). Two distinct types of rhyolite are present: (1) relatively viscous lava flows originally emplaced with an irregular upper surface and steep flow margins 100 m or more high (hundreds of feet) (figs. 7*A*, 7*B*, 7*C*, 7*E*, and 7*F*), and (2) ash-flow tuffs (ignimbrites) emplaced by hot, incandescent, gas-rich, very fluidized pyroclastic flows that came to rest with nearly planar original upper surfaces.

and Warren Hamilton (2003) have argued strongly against the mantle-plume explanation of hotspots and particularly the idea of deep-seated mantle plumes. Foulger and Natland (2003) question deep mantle plumes and with Don Anderson convened a conference in 2003 looking for non-plume explanations for hotspots (see www.mantleplumes.org).

Recent papers supporting plumes include Courtillot and others (2003), who present evidence for three types and depths of mantle plumes. Using seismological analysis involving new wave-front techniques, Montelli and others (2004) identified more than thirty mantle plumes, about one-third of which are identified as originating at the core-mantle boundary.

Two seismic tomography studies conclude that a thermal mantle plume is inferred inclined to the northwest from Yellowstone at ~20° from vertical and extends to a depth of about 500 km (Yuan and Dueker, 2005; Waite and others, 2006). A relation may exist between the inferred plume and the asymmetric pattern of faulting and uplift. Faulting and uplift associated with the Yellowstone hotspot track flares outward ~1.6 times farther to the south than to the north of the volcanic track (Pierce and Morgan, 2005). Both this asymmetry and the southeast upward rise of the Yellowstone plume might be explained by upper mantle flow (mantle winds) as modeled to the east by Steinberger (2000) or most concordantly to the southeast (Bernhard Steinberger, written commun., 2005, Berkeley model).

Figure 7. RHYOLITE. Suite of six photographs (figs. 7A–7F) showing landscapes with forests of lodgepole pine developed on hotspot-generated rhyolite of the Yellowstone Plateau and two photographs (figs. 7G and 7H) showing contrasting vegetation in non-rhyolite areas. The rhyolite/lodgepole landscape of the Yellowstone Plateau relates directly to hotspot volcanism. The lodgepole pine forest and its sparse understory are practically an ecological desert that forms most of the central part of Yellowstone. The rhyolite bedrock favors a lodgepole forest because rhyolite is both poor in nutrients and has well-drained sandy soil and sub-soil so that much of the snowmelt infiltrates deeper than 30–50 cm (1–2 ft) and probably much of the snowmelt percolates below root depth.

A, View across the Yellowstone rhyolite plateau built up to an altitude of 2,500 m (8,000 ft) and forested with lodgepole pine.

B, Lodgepole pine forest on rhyolite—an ecologically challenged landscape.

C, Obsidian Cliff. Native Americans extensively quarried this rhyolite flow for obsidian.

D, Lodgepole pine forest that was burned in 1988 on the Obsidian Cliff rhyolite flow.

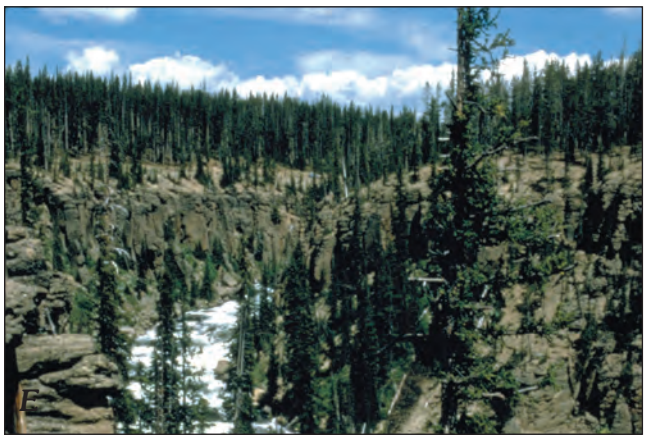

E, Lewis River incising the hotspot-built constructional Yellowstone rhyolite plateau.

F, Grand Canyon where Yellowstone's largest river has cut deepest into the constructional rhyolite plateau.

The rhyolite plateau is remarkably gently sloping (fig. 7A) except for steep flow fronts and incised scenic canyons. The plateau was built up by volcanic tuffs and lava flows emplaced on top of the original landscape. Streams developed steep gradients where they flowed off the edge of the plateau and cut canyons deep into its edge. The main rivers of Yellowstone have incised canyons deep into the margins of the plateau, creating part of the scenic grandeur of Yellowstone (figs. 7E and 7F). The largest and most powerful river, the Yellowstone, has cut the farthest back into the plateau (30 km, 18 mi) to form Yellowstone's Grand Canyon.

The Yellowstone rhyolite plateau is covered by vast expanses of lodgepole pine forest, which are commonly difficult to walk through because of crisscrossed down timber (figs. 7B and 7D). The lodgepole forests on the nearly flat rhyolitic plateau are considered by many to be the least scenic features of the GYE. The lodgepole forests might be considered ecologically challenged because of their monotonous appearance, low biodiversity, and limited wildlife habitat. C.C. Parry (1874, p. 179), a botanist on the William Jones expedition to northwestern Wyoming in 1873, commented that lodgepole pine forests covered vast expanses of the park and would forever be associated with the monotony of the Yellowstone Plateau:

"Not less than ninety-nine per cent of the pine growth of this district is made up of the single species, *Pinus contorta*…. Mile after mile of continuous forest may be traversed without seeing any other arborescent species, and their tall, straight, uniform trunks and scattering foliage will be always associated with the monotonous and disagreeable features of the park scenery. Only where the blazing campfire sends forth its grateful warmth to relieve the ordinary chill of a night temperature, where the thermometer in August ranges between 36°F. and 14°F., do we realize a manifest utility in this widespread forest production."

In contrast, adjacent areas on basaltic or andesitic volcanic rocks, sedimentary rocks, and Precambrian crystalline rocks have an entirely different vegetation composition and distribution pattern. Such non-rhyolitic rocks support a combination of forest and grassland. Forests are typically of Engleman spruce, subalpine fir, whitebark pine, or Douglas fir and patches of lodgepole pine. Highly productive grasslands, sagebrush steppes, or meadows typically occur on glacial and other fine-grained surficial deposits and form important habitat for elk, bison, deer, and bears. Talus accumulations below cliffs—essential habitat for marmots and pikas, lichen communities, and local congregations of moths eaten by grizzly bears—are also common on the steeply sloped andesite, sandstone, and Precambrian rock areas.

Why does the geologic substrate so markedly delineate species distributions? Soils developed on rhyolite are sandy and contain little clay or nutrients (Trettin, 1986; Rodman and others, 1996). Despain (1990, p. 141) estimates that, overall, soils on rhyolite have only one-fourth the plant nutrients of soils on andesitic volcanic rocks. Lodgepole is well adapted to the very limited nutrients available from rhyolite. It is not, however, very shade tolerant and is easily out-competed by more shade tolerant trees where soil moisture and nutrients are adequate for their growth. Compared to nearly all other bedrock types, soils derived from rhyolite are better drained and retain less water, favoring the growth of lodgepole over other conifers. Because rhyolite soils drain so rapidly, the large amount of water released by melting the thick snowpack on the Yellowstone rhyolite plateau rapidly percolates downward through thin, sandy soil into permeable rhyolite bedrock in which high permeability was developed from fracturing during initial cooling and thermal contraction. For example, the Pitchstone Plateau receives approximately 1.8 m (70 in) of annual precipitation (Farnes, 1977), mostly as snowfall. In spite of this high precipitation, few permanent streams or lakes are present, and a considerable portion of the surface water enters the deep ground-water system and thus becomes unavailable to plants. However, hundreds of feet lower at the base of the rhyolite flows, ground water emerges to form a nearly continuous band of swamps and springs (Benjamin, 2000).

Table 1 shows the three main types of volcanic rocks and their salient attributes including their typical vegetation at the altitude of the Yellowstone Plateau.

G, Hayden Valley—a meadowy enclave on fine-grained lake sediments surrounded by lodgepole forests on rhyolite.

H, Non-rhyolitic area in southern Teton Range with soils that hold moisture well and support lush vegetation.

Figure 8. THERMAL FEATURES. Photographs of hot springs, geysers, and other thermal features driven by hotspot heat, whose abundance, character, and uniqueness were the primary reasons for the establishment of Yellowstone as the world's first national park. Yellowstone is the world's largest and most energetic geothermal field. In photograph credits, NPS is for National Park Service photographs in collection at Yellowstone National Park.

A, Steamboat Geyser in full eruption to a height of about 100 m (300 ft) in Norris Geyser Basin. Photograph from NPS.

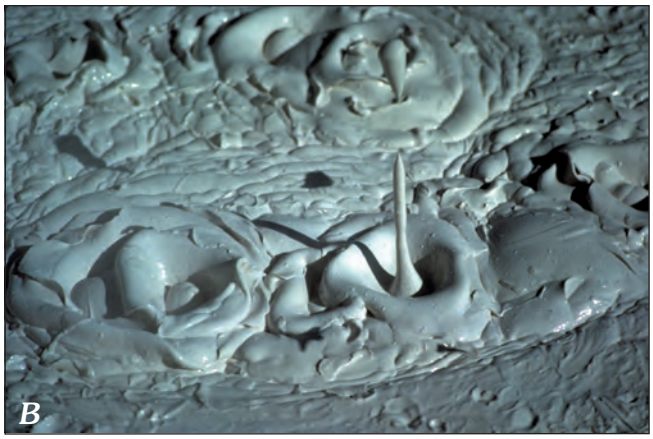

B, Mud Pots. Mud is formed by acid alteration of rhyolite. Photograph from NPS

C, Castle Geyser in Upper Geyser Basin. Photograph from NPS.

D, Excelsior Pool in Middle Geyser Basin. Painting by Thomas Moran.

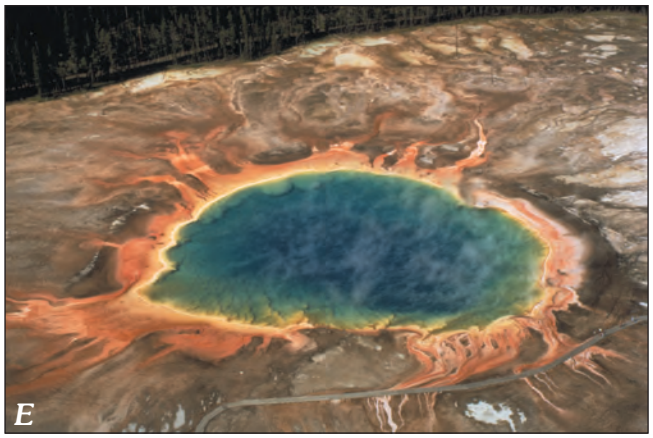

E, Grand Prismatic Spring in Middle Geyser Basin. Note boardwalk for scale. Photograph from NPS.

F, Mary Bay of Yellowstone Lake, formed by hydrothermal explosion(s). W.H. Jackson photograph (1871).

Table 1. Characteristics of the three main types of volcanic rocks found in the greater Yellowstone ecosystem.

Attribute	Rhyolite	Andesite	Basalt
Color	Light colored, pastels; local black obsidian	Medium colors; weathers brown	Dark gray, weathers reddish brown
Chemistry	Rich in silica; nutrient poor	Intermediate; nutrient rich	Rich in iron and magnesium; nutrient rich
Vegetation	Lodgepole forest, sparse understory	Mixed conifer forest and meadows	Mixed conifer forest and meadows
Geological setting	Melting of crust; hotspots(?)	Above subduction zones	Derived from partial melting of mantle

As the summer progresses, the upland rhyolite areas and their lodgepole forests become generally dry earlier than adjacent areas on non-rhyolite substrates where soils are deeper and contain more fine-grained materials (silt, clay, and organic matter). However, because lodgepole forests on rhyolite have little or no understory of spruce and fir, the return interval for fires in lodgepole is 350–400 years, longer than for lodgepole on andesite (Despain, 1990). Only an unusual combination of conditions leads to spectacular, crown-transmitted forest fires. Conditions necessary for extensive crown fires in lodgepole forests on the rhyolite plateau include (1) mature lodgepole forests, (2) development of local understory, (3) an extended period of drought, (4) ignition by lightening or human, and (5) perhaps most important, strong, persistent winds. This combination of conditions occurred in 1988 when fires burned a third of the Park during a hot, dry summer with strong, persistent winds (fig. 7D). The main difference between fires in lodgepole on rhyolite and other forest fires is this long return interval.

Hayden and Pelican Valleys are highly productive meadow communities, yet they lie within the Yellowstone rhyolite plateau (fig. 6). Even though these two valleys are flanked by rhyolite flows, the floors of the valleys consist of a thick blanket of fine-grained glacial lake and other sediments (U.S. Geological Survey, 1972a) that have sufficient water-holding capacity and nutrients so to favor herbaceous meadowlands. During Pleistocene glacial buildup and recession, damming by glaciers created lakes in which fine sediment relatively rich in nutrients was deposited. Bison, elk, grizzly bears, and trumpeter swans inhabit these valleys and thrive on this diverse and productive plant community. Whereas on the surrounding rhyolite bedrock, abundant wildlife cannot be sustained by the lodgepole pine forest growing in the sandy, well-drained and nutrient-poor rhyolite. But red squirrels, pine martins, and chickadees may be present.

Although limited in vegetative diversity, the rhyolite plateau was important to Native Americans because it provided high quality obsidian for tool making. Located between Mammoth and Norris Junction, Wyo., the Obsidian Cliff and nearby Spring Creek rhyolite flows supplied an essentially inexhaustible supply of high-quality obsidian to Native Americans (fig. 7C) (Davis and others, 1995). Locally the top of this flow is blanketed with a layer of obsidian chips produced centuries ago as Native American craftsmen prepared chunks of obsidian called bifaces for transport and trade out of the area. This obsidian was traded across North America; 15-cm (6-in) ceremonial blades from Obsidian Cliff have been identified in the mound builder culture in the State of Ohio (Griffin and others, 1969).

G, Mammoth Hot Springs with "terraces" of travertine (calcium carbonate). W.H. Jackson photograph (1871).

H, Site of geothermal well, across Yellowstone River from La Duke Hot Spring (in foreground).

[5]Some of the thermal waters of Yellowstone have exceptionally high values of $^{3}He/^{4}He$, commonly expressed as multiples compared to this ratio in the atmosphere. Values of about 16 times the atmospheric ratio have been obtained from thermal springs in Yellowstone (Kennedy and others, 1987; Craig, 1997). These high values contrast with maximum values of about 8 that are typical of mid-ocean spreading centers between tectonic plates where the helium source is in the upper mantle (Craig, 1990; Farley and Neroda, 1998) and support a deep-mantle-plume origin of the Yellowstone hotspot.

Thermal Features and Associated Ecosystems

The most dramatic and directly observable manifestations of the Yellowstone hotspot are Yellowstone's hot springs and geysers (fig. 8) (Fournier, 1989), whose attractiveness and uniqueness were the primary reasons for the establishment of Yellowstone as the world's first national park. Helium isotope studies suggest these geothermal features are driven from a heat source deep in the Earth's mantle.[5]

Almost all the active thermal areas lie within or near the margin of the 640,000-year-old Yellowstone caldera, which is 70 by 45 km (45 by 25 mi) in area (fig. 4, white ellipse at NE. end) (Christiansen, 1984, p. 92; Christiansen, 2001; Fournier, 1989). The main exception is the Norris-Mammoth corridor (White and others, 1988), which extends from the northern caldera margin near Norris 27 km (17 mi) north to Mammoth Hot Springs (fig. 8G) and perhaps 10 km (6 mi) farther north to La Duke Hot Springs along the Yellowstone River (fig. 8H).

The heat flow from the area underlain by the Yellowstone caldera is about 50 times greater than the continental mean.[6] Heat from deep magma, associated hot fluids, and hot rock drives the many geothermal features of Yellowstone, the world's largest and most energetic geothermal field.

Heat is also an essential component of hydrothermal explosions that have left craters surrounded by aprons of ejected material. Along the north shore of Yellowstone Lake (fig. 6), Mary Bay is a depression 3.5-km (2-mi) across formed by one or more large hydrothermal explosions with a main one erupting about 13,000 years ago (fig. 8F) (Pierce and others, 2002, this volume; Morgan and others, 1998). Smaller hydrothermal explosions are common in the geyser basins. In 1989, an explosion of Pork Chop Geyser blew out the upper part of the geyser system and hurled blocks of hydrothermal material (siliceous sinter) 60 m (200 ft). Such explosions probably formed deep, funnel-shaped pools such as Morning Glory Pool in Upper Geyser Basin (see fig. 18I later in this report) and Excelsior in the Middle Geyser Basin (fig. 8D). The hydrothermal-explosion craters now commonly form lakes or wetlands in steep-sided, protected basins that create warm niches for waterfowl and other organisms.

Yellowstone's thermal features provide habitat for a group of amazing organisms that were relatively unappreciated until life was discovered in thermal vents along the mid-ocean ridges, and a closer look at thermal microorganisms was undertaken (see Varley, 1993). This led to discovery of bacteria from Yellowstone hot springs that made possible the polymerase chain reaction (PCR)—the process used to identify DNA material. PCR subsequently revolutionized the study of biology, because it makes possible the rapid multiplication of genetic material so it can be analyzed. PCR also made possible a new look at the molecular level of living organisms, and thereby helped to restructure what is known about the Earth's earliest life and subsequent evolution. Significantly, many of the species that inhabit the thermal waters of the Park are close relatives of those first living organisms (Woese and others, 1990; Pace, 1991).

A thermal zonation follows the temperature gradient downflow from the thermal springs and pools, creating much of the vivid sequence of colors that enliven the outflow channels. The extreme thermophiles, including white bacteria, are nearest the vent at temperatures that are at or near the boiling point of water at this altitude. As the water cools, the white bacteria give way to yellow or orange microorganisms that, in turn, yield to green algal-bacterial mats. Whole miniature ecosystems occur along these channels. Mats of algae and bacteria form organic mats that are fed on by other organisms, including fly larvae. Spiders, predatory flies, and other predators feed on the larvae and adult flies (Brock and Brock, 1971). Nutrient-rich runoff from hot springs keeps some streams, such as the Madison River, warmer year-round and enhances the fishery. In addition to the algae and bacteria, large animals such as elk and bison inhabit the thermal areas in winter where the snowpack is thin or absent. Massive bison skulls in remote thermal areas mark the winterkill of some bison.

Fault Valleys and Adjacent Mountains Associated with Hotspot Faulting

Basin-and-range faulting has accompanied migration of the hotspot to Yellowstone and has formed the linear mountains and valleys that flank the north and east sides of the hotspot track delimited by the eastern Snake River Plain (figs. 1 and 4). The most active faults generally form the most prominent ranges and valleys; they define belt II that extends both southward and westward from Yellowstone (fig. 4, belt II). During the last 10 million years, as the hotspot migrated to the northeast, the most active faults were immediately adjacent to the caldera-forming hotspot volcanism. As the hotspot activity migrated farther northeast, the locus of faulting migrated in a bow-wave fashion farther outward from the hotspot track to form the present two belts that extend south and west from Yellowstone (Anders and others, 1989; Pierce and Morgan, 1992; Smith and Braile, 1993; Anders, 1994). The GYE includes only a small part of the basin-and-range, but along the hotspot track, high rates of basin-and-range faulting accompany the northeast migration of hotspot volcanism to its present position (Anders and others, 1989; Pierce and Morgan, 1992; Anders, 1994).

The western band of faulting (fig. 4) includes the 1959 Hebgen Lake earthquake (fig. 9B, magnitude 7.5) and the 1983 Borah Peak earthquake (fig. 9G, magnitude 7.3). Repeated such earthquakes and associated offsets have resulted in lowering the valleys and uplifting the adjacent ranges to form, respectively, the West Yellowstone Basin

[6]Irving Friedman (oral commun., 1999, and this volume) concluded that convective heat flow from Yellowstone to be 4.9×10^{16} cal/yr, as determined by the chloride content of rivers flowing from Yellowstone. This value is 22 percent higher than the 4.0×10^{16} cal/yr previously estimated (Fournier, 1989). Friedman's value converts to a heat flow of about 2,900 mW/m^2 for the 2,500-km^2 area of the Yellowstone caldera. The Yellowstone caldera's heat flow of 2,900 mW/m^2 is 51.2 times the continental mean of 56.6 mW/m^2 (Turcotte and Schubert, 1982).

and Madison Range, and the Thousand Springs Valley and the adjacent Lost River Range. The southern band of faulting extends south from Yellowstone toward the Wasatch fault near Salt Lake City, Utah, and includes the coupled basin-and-range faulting of Jackson Hole-Teton Range just south of Yellowstone (fig. 9A). Within Yellowstone National Park, this southern band includes the basin-and-range faulting between Heart Lake and Red Mountains (fig. 9E and 9F), where postglacial fault scarps are 25-m (90-ft) high (Pierce, 1979; structure number 766 in Machette and others, 2001). At any position along faults in the most active parts of these two belts, major offsets and associated earthquakes occur about every several thousand years.

In summary, basin-and-range faulting associated spatially and temporally with the Yellowstone hotspot forms distinctive landscapes within the GYE, with characteristic linear, rugged, forested ranges and adjacent flat-floored, grassy valleys. The valleys are the sites of accumulation of sediment, including glacial outwash gravels and alluvial fans. The adjacent mountains are characterized by steep slopes that are eroding by slope wash and mass wasting. To the west from Yellowstone are the following basins and ranges in the GYE: southern Madison Range/West Yellowstone basin (fig. 9B), Madison Range/Madison Valley (fig. 9D), Centennial Range/Centennial Valley (fig. 9C), and Lemhi Range/Little Lost River valley (fig. 9G). To the south are Mount Sheridan/Heart Lake (figs. 9E and 9F), Teton Range/Jackson Hole (fig. 9A), and Snake-Salt River Ranges/Star and Grand Valleys. The large difference of altitudes present in the basins and adjacent ranges is integral to the subsequent ecosystem that developed here providing a year-round environment for elk, bison, and other animals through annual migrations. The valleys provide nearly snow-free winter ranges with dried grasses in winter and lush green grass in spring, whereas the ranges provide lush grass all summer.

Cold, Snowy Climate and Rugged Mountains Enhanced by Hotspot Uplift

The most important effect of the Yellowstone hotspot on the GYE has been the consequence of uplift on altitude, climate, topography, ecology, and human geography. Deep winter snows, steep mountain slopes, lush mountain meadows, cool trout streams, and shady coniferous forests are characteristic of the GYE (fig. 10).

Uplift is a difficult geologic process to prove. The idea of geologic uplift in various parts of the world in the last few millions or tens of millions of years has been challenged by Molnar and England (1990) on the basis that such rapid changes in the isostatic balance of the lithospheric plate (crust plus mantle lithosphere) are geophysically unreasonable unless there is a clear driver for such lithospheric modification. They argue that evidence for uplift such as valley incision may be caused by accelerated stream erosion produced by Pleistocene glacial and climatic conditions. While this may hold true for many young mountains and plateaus elsewhere in the world, numerous indicators suggest that geologic uplift in Yellowstone is a very recent phenomenon, is ongoing, and is driven by a deep-seated process of probable mantle origin.

Pierce and Morgan (1992, p. 19–30) discuss in detail the following factors that support the argument for uplift of the GYE:

1. The present Yellowstone crescent of high terrain (fig. 4).
2. Evidence for uplift in swells associated with other hotspots, particularly oceanic ones where anomalies in sea-floor altitude can be estimated.
3. The present altitude of rhyolite tuffs (ignimbrites) from the Yellowstone Group in the crescent of high terrain a thousand meters (thousands of feet) above the altitude of their source calderas.
4. Historic uplift measured along level lines across the Yellowstone crescent of high terrain.
5. High, rugged mountains formed from easily erodible rocks such as the Absaroka Volcanic Group and Mesozoic sandstones and shales (figs. 10B and 10D).
6. Basalt flows dated at 3 Ma on high upland erosion surfaces incised by young, steep-sided stream valleys 1,000-m (3,000-ft) deep (fig. 10C).
7. Ratios of the lengths of glaciers during the last glaciation compared to those of the next-to-last glaciation suggesting uplift on the leading margin of the Yellowstone crescent of high terrain, and subsidence on the trailing margin during the last 140,000 years.
8. Tilting of stream terraces away from Yellowstone (fig. 11, after Jaworowski, 1994).
9. Lateral migration of stream courses away from Yellowstone.
10. On the leading margin of the Yellowstone hotspot, migration of inflection points between convergent/divergent terraces at a rate similar to the hotspot migration rate.
11. Calcic soils apparently uplifted above their present altitude of formation.
12. Perhaps most important, the major positive North America geoid anomaly that centers on Yellowstone (fig. 12) (Milbert, 1991; Smith and Milbert, 1999) indicates that a deep-seated process beneath the GYE is responsible for the scale, amplitude, and uplift of the Yellowstone crescent of high terrain.[7]

[7]This geoid anomaly is comparable to that of oceanic hotspots in amplitude and breadth (Pierce and Morgan, 1992; Pierce and others, 1992; Smith and Braille, 1993). The compensation depth for the geoid is deeper than that for the regional topography or the associated Bouguer gravity (geoid, approximately 100(?) km; Bouguer gravity and regional topography, approximately 30–40 km).

Figure 9. FAULTING. Active faulting associated with the Yellowstone hotspot created basins and ranges. The ranges have high mountains with steep valley walls, and are covered by a mosaic of forests, meadows, and sparsely vegetated talus below rocky cliffs. The basins have flat floors underlain mostly by gravel and other surficial deposits and form grasslands.

A, Teton fault scarp near foot of Teton Range. Postglacial offset is 18 m (60 ft).

B, Hebgen Lake fault scarp partly formed during the 1959 earthquake.

C, Oversteepened slopes on the Centennial fault that created the Centennial Range and Centennial Valley.

D, The Madison Valley (foreground) and Madison Range (distance) were formed by offset on the range-front fault.

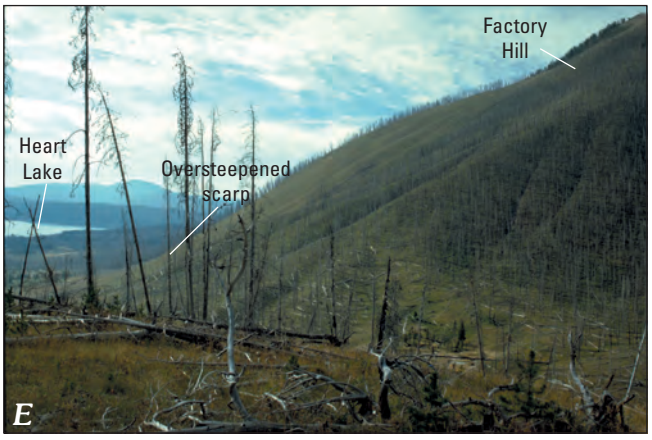

E, Faulting on the East Sheridan fault has oversteepened the lower part of Factory Hill and formed the Heart Lake basin.

F, Fissure Group hot springs are aligned along the East Sheridan fault that offsets postglacial deposits 9.6 m (32 ft).

The GYE forms the headwaters of 25 rivers and large drainages, and the Continental Divide traverses the GYE. This topography gives further support to the idea that the GYE is a topographic culmination (see fig. 19 later in this report; table 2). Studies of leaf morphology of a 45-million-year-old site (Eocene) within the GYE indicate the area has been uplifted by about 900 m (3,000 ft) since Eocene time (Wolf and others, 1998). Based on identification of white mangrove (*Terminalia*) and red mangrove (*Rizopora*) pollen or leaves in Eocene rocks (Fritz, 1980; Bill Fritz, written commun., 1999), the lowest parts of the Yellowstone area 45 million years ago *may* have been in salty water at sea level after the Laramide orogeny affected the area.[8] If so, uplift to the present altitude of more than 2,500 m (8,000 ft) has occurred since 45 million years ago, with perhaps about 900 m (3,000 ft) of this uplift associated with the Yellowstone hotspot.

Many salient ecological characteristics of the GYE relate to and are enhanced by this hotspot-induced uplift. Uplift of lower, more subdued pre-hotspot terrain has produced the moderate to high altitudes and associated cool temperatures, deep snowfall, and cool summers. The projection of a large mountain mass into the atmosphere intercepts moisture and creates cooler air temperatures and a markedly snowier climate. If this uplift had not occurred, mountains such as the present Beartooth uplift might look more like the Black Hills do today; the present Absaroka Range might look more like a dry, short-grass prairie like eastern Montana and Wyoming. Instead, the Yellowstone Plateau and the surrounding mountains are covered with forests of Douglas fir, lodgepole pine, Engleman spruce, subalpine fir, and whitebark pine, adapted to higher and wetter environments. Interspersed in the forests are mountain meadows of Idaho fescue, bearded wheatgrass and other grasses, and wildflowers (Despain, 1990). This

Table 2. Rivers and other large drainages that head in the greater Yellowstone ecosystem, listed clockwise from the Yellowstone River (fig. 19).

River	Towns associated with drainage
Yellowstone River	Gardiner, Livingston, Big Timber, Columbus, Laurel, Billings
Lamar River	–
Boulder River	Big Timber
Stillwater River	Nye, Columbus
Rosebud Creek	Absarokee
Rock Creek	Red Lodge
Clarks Fork	Clark, Bridger, Laurel
Shoshone River	Cody, Powell, Lovell
Greybull River	Meeteetse, Greybull
Wind River-Bighorn River	Dubois, Riverton, Thermopolis,
Owl Creek	Thermopolis
Green River	Big Piney, Green River (south of fig. 19)
Gros Ventre River	Kelly, Jackson (near)
Buffalo Fork	–
Snake River	Moran, Wilson, Idaho Falls
Hoback River	Bondurant
Greys River	–
Salt River	Afton
Teton River	Driggs, Rexburg (near)
Falls River	Ashton (near)
Henrys Fork	Macks Inn, Ashton (near), St. Anthony
Camas Creek	Kilgore
Red Rock River	Lakeview (near)
Madison River	West Yellowstone (near), Ennis, Three Forks
Gallatin River	Gallatin Gateway, Bozeman (near), Three Forks

G, Scarp formed by 1983 Borah Peak earthquake (magnitude 7.3). Such faulting eventually created a basin (left) and range (right).

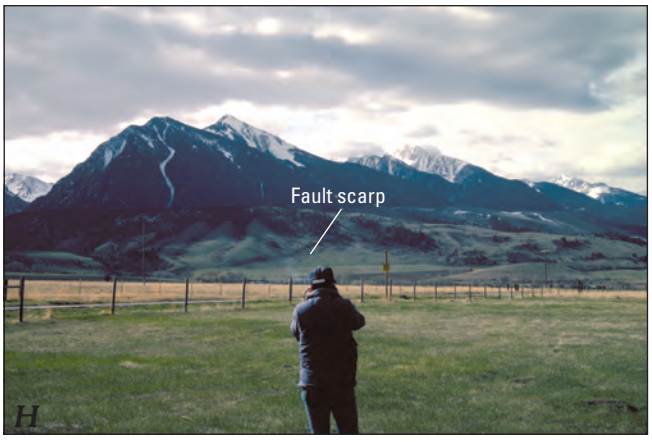

H, Range-front fault downdropping the Paradise Valley (foreground) and uplifting the Beartooth uplift (distance).

[8]Such uplift would have occurred after the Laramide orogeny, which climaxed about 70–50 million years ago, had produced uplifts such as the Beartooth Mountains and Wind River Range, and these uplifts had been eroded to more subdued mountains. Locally in the GYE, these Eocene Absaroka Volcanic Supergroup rocks were deposited across these Laramide thrusts and not subsequently offset by faulting. The possibility of mangrove trees in this region needs further study. For example, Scott Wing (written commun., 1999) has reservations about both the mangrove identification and consequently the sea-level altitudes in the Yellowstone area.

Figure 10. UPLIFT. High, eroding mountains of the Yellowstone crescent of high terrain are related to hotspot uplift. Uplift accompanied by erosion has carved deep valleys with steep valley walls. These steep slopes are subject to high rates of erosion, especially in readily erodible rocks such as the volcanic rocks of the Absaroka Volcanic Supergroup along the eastern Yellowstone boundary and in Mesozoic sandstones and shales south of the eastern part of Yellowstone.

A, Deep snows in the greater Yellowstone area along the Beartooth highway. Photograph from NPS.

B, High mountains formed by readily erodible rocks of the Absaroka Volcanic Supergroup along Yellowstone's eastern boundary.

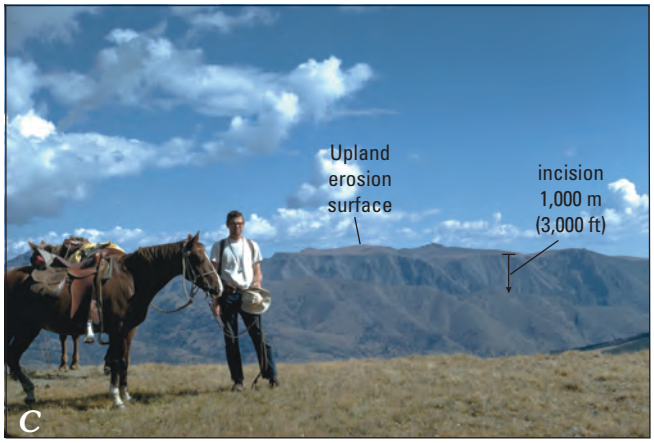

C, Upland erosion surface (foreground and distance) incised by valleys 1,000 m (3,000 ft) deep in the volcanic rocks of the Absaroka Volcanic Supergroup.

D, Soft, easily erodible Cretaceous shale and sandstone uplifted to form high terrain (3,000 m; 10,000 ft) in southern Yellowstone.

E, High, steep valley walls in the southern Gallatin Range. Spruce fir forest broken by meadows and avalanche chutes.

F, Prickly pear cactus flower near Gardiner, Mont., in deep, dry valley eroded by glacial and stream processes.

vegetation mix provides summer pasture for herds of ungulates and their young that thrive on the grasses flourishing in the cool, moist meadows. The winter snows feed clear, cold streams where abundant algae feed numerous species of insect larvae that feed large populations of trout. These animals and numerous smaller mammal species provide food for grizzly bears, black bears, coyotes, wolves, mountain lions, bald eagles, golden eagles, osprey, and a host of other predators and scavengers.

Without the hotspot-related uplift and the lowland hotspot track of the eastern Snake River Plain, the GYE would be drier, lower, and warmer, but many of the species noted above might well be present but in lesser numbers and on a lower, drier landscape. Yellowstone was designated a national park because of its hotspot-related thermal features. As a result, its ecosystem has been protected and has remained largely intact, and the public now values Yellowstone's wildlife as much as its geothermal features.

Ongoing uplift followed by erosion has created valleys 1 km deep (thousands of feet) (fig. 10C). Pleistocene glaciations have modified these valleys to form the characteristic U-shaped glacial form. Stream and glacial processes have deepened valleys to produce high, steep valley walls, a landscape feature common over much of the GYE. These steep valleys generate debris flows, particularly after forest fires, that move sediment out of the mountains to the valley floors of the GYE (Meyer and others, 1995) (fig. 10H).

Modern and Pleistocene Snows Greatly Enhanced by Yellowstone Hotspot Geography

Figure 13 shows contours on annual precipitation for Yellowstone National Park. The important topographic features enhancing snowfall in the GYE are the hotspot track of the topographically low eastern Snake River Plain, the Yellowstone Plateau, and the Yellowstone crescent of high terrain (fig. 4). Geophysical surveys of the eastern Snake River Plain show a significant thickening of dense material at mid-crustal depths—that together with the massive volume of material erupted, the large size of calderas, and cooling following passage of the hotspot—all contribute to the present-day topographic low of the plain.

Topography shaped by the Yellowstone hotspot (fig. 4) creates a mountain-induced (orographic) weather pattern as moisture-laden air rises up across mountain barriers and then descends into basins (figs. 13 and 14).

1. Winter moisture from the northern Pacific Ocean moves eastward and becomes channeled well inland by the eastern Snake River Plain, a trough created by the hotspot track.

2. The upper end of the Snake River Plain is a cul-de-sac, and the moist air mass then must rise above orographic (mountain) barriers including the Yellowstone Plateau (altitude about 2,500 m; 8,000 ft) where the resulting orographic rise produces deep snowfall.

3. Storms continue moving east and rise up and over the Yellowstone crescent of high terrain, between 2,700- and 3,300-m (9,000- and 11,000-ft) altitude, extracting additional orographic snowfall.

4. The eastward-moving storms descend and warm as they traverse the east side of the crescent of high terrain, causing the air to become dryer and leading to a snow shadow (precipitation shadow) along the east side of the GYE in the Cody, Wyo., area.

Figure 15 shows the snowpack (April 1) at a constant altitude of 2,450 m (8,000 ft) along latitude 44.5°N. from the Pacific Ocean, through the Oregon Cascades, through the mountains of central Idaho, then across Yellowstone and to the Bighorn Mountains. The eastern Snake River Plain is just south of this transect. The overall pattern shows decreasing snowpack inland, but at Yellowstone a major reversal occurs—Yellowstone has more snowpack at 2,440 m (8,000 ft) than the central Idaho area, even though central Idaho is nearer to the

G, Landslide west of Gardiner, Mont., in incompetent, muddy sediments beneath slopes oversteepened by glacial erosion.

H, Debris flow into the Gibbon River resulting from rain on steep slopes burned in the 1988 fires.

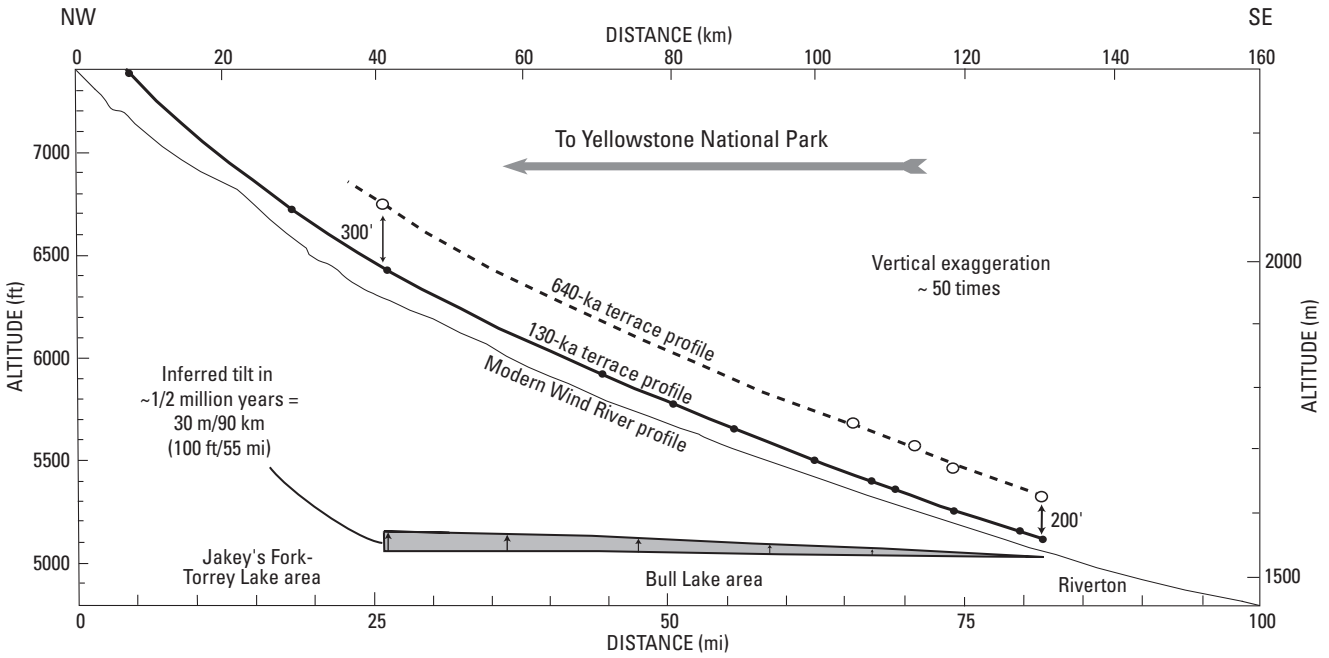

Figure 11. Diagram illustrating tilting of Wind River terraces away from the Yellowstone hotspot (modified from Jaworowski, 1994). The difference in terrace profiles suggests that in the 500,000 years between deposition of the upper terrace and the lower terrace, the upper terrace has been tilted away from the Yellowstone area about 30 m over a distance of 90 km (100 ft over 55 mi). Extrapolation of this inferred tilting over a distance of 200 km (125 mi) and to a time interval of 8 million years would yield uplift at the hotspot center of about 1,056 m (3,500 ft). This amount is somewhat larger than the uplift estimated to be associated with the Yellowstone hotspot of 0.5–1 km (1,600–3,300 ft) suggested by Pierce and Morgan (1992), and 600 m (2,000 ft) suggested by Smith and Braile (1993).

Pacific Ocean moisture source. East of Yellowstone, near Cody, Wyo., and farther east in the Bighorn Mountains, water in the snowpack at 2,440 m is 5 to 10 times less than it is on western Yellowstone Plateau.

The vegetation and ecology of the GYE is strongly influenced by this altitude and dry-wet-dry precipitation progression that results from hotspot-related topographic features. The increase in altitude at the upper end of the Snake River Plain produces deep snows that recharge the soil moisture in the vegetation root zone, and, consequently, this area supports lush vegetation (fig. 7H). A notable exception is the Yellowstone rhyolite plateau where low water-holding capacity, high permeability, and low nutrients in the soil produce a lodgepole forest with little understory (discussed earlier; figs. 6 and 7). Eastward from the crest of the Absaroka Range, annual precipitation decreases rapidly down the altitudinal gradient; Douglas-fir-dominated forests grow higher up the mountain sides, limber pine is a more common forest component, and lower timberline is about 450–600 m (1,500–2,000 ft) higher than on the western slope of the GYE. In addition, this precipitation shadow helps to produce vegetation adapted to arid conditions in much of the Big Horn Basin that is more like the vegetation in the Great Basin deserts than the Great Plains semiarid grasslands just 150 km (100 mi) to the north.

Another effect of increased altitude is the expression of different seasonal precipitation maximums (Despain, 1987, 1990; Porter and others, 1983; Whitlock and Bartlein, 1993). Mountain barriers intercept winter moisture (storm tracks) from the Pacific Ocean to the west and have a precipitation peak from November through March with annual snow accumulations of 100–150 cm (40–60 in) of water equivalent. Lower altitude areas, such as the Lamar Valley and the Mammoth, Wyo. and Gardiner, Mont. areas, receive a much lower total annual precipitation (fig. 13). Their basin topography prevents extraction of winter snows by orographic rise, and their main moisture is received during the more regional patterns of spring precipitation similar to that in the basal plains both east and north of the GYE, such as the Bighorn Basin and Gallatin Valley (Despain, 1990).

Pleistocene Glaciation and Its Effects Enhanced by the Yellowstone Hotspot

During the Pleistocene, both deep snowfall facilitated by the lowland hotspot track and cold temperatures resulting from hotspot uplift combined to generate glaciers that covered essentially all of Yellowstone National Park and much of the GYE (fig. 16). The glaciation of Yellowstone had two modes (Pierce, 1979; Sturchio and others, 1994; Pierce and Good, 1998): (1) a mode during both the early and late part of a glacial cycle when glaciers formed and flowed down valleys from the mountains surrounding the Yellowstone Plateau, and (2) a climax mode when a large ice cap built up on the Yellowstone Plateau to a thickness of more than 1,000 m (3,000 ft) and dominated the glacial flow from the surrounding mountains. With buildup of glacial ice on the plateau, either by glaciers flowing from the adjacent mountains or ice

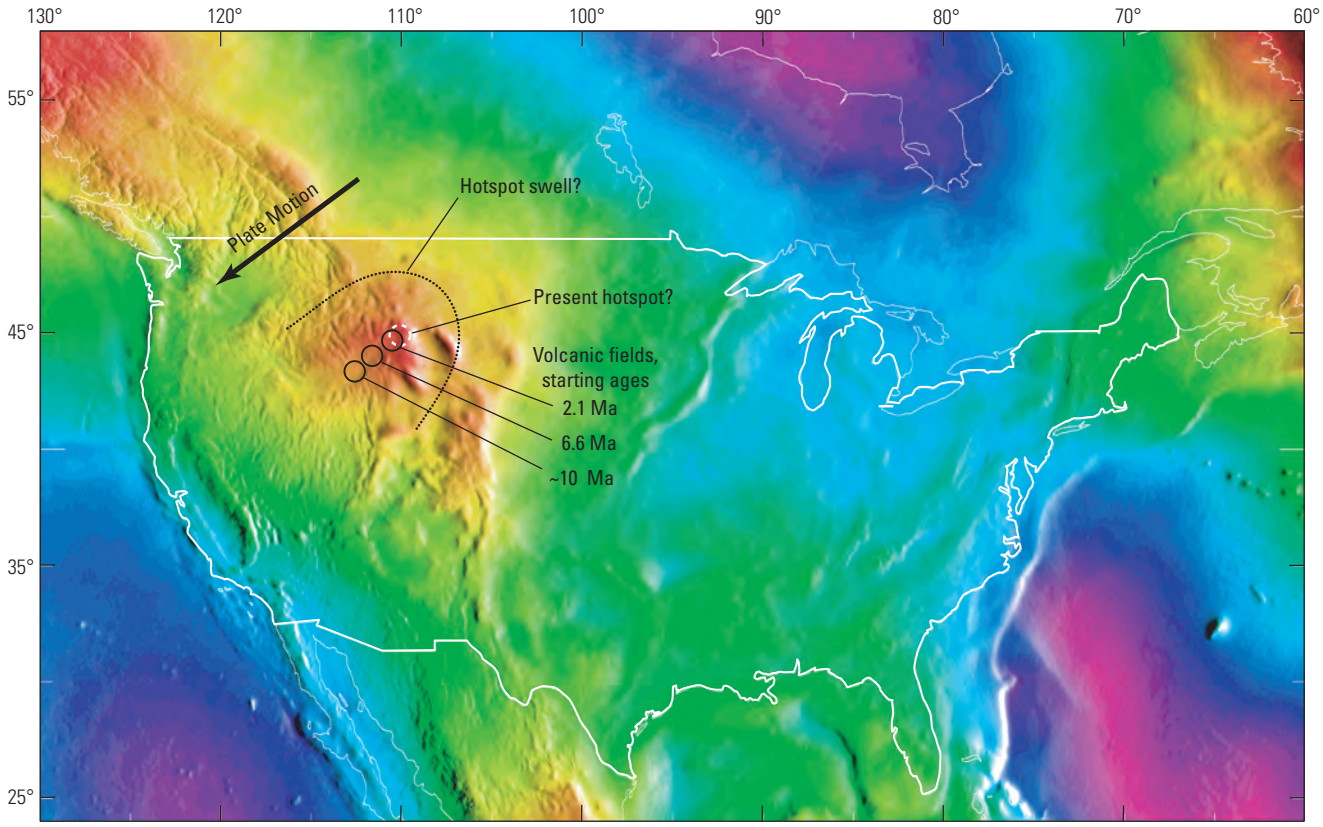

Figure 12. Map showing that the major geoid anomaly in the Western United States centers on the present Yellowstone hotspot. The warmer colors indicate higher altitude anomalies on the geoid, including the culmination in red at Yellowstone. Volcanic fields (circles) along the hotspot track are shown along with their starting ages. The dashed white circle shows the inferred position of the present hotspot based on a rate of plate movement of 25 km/m.y. The dotted line shows the inferred margin of the Yellowstone-hotspot swell, which is comparable in size to swells associated with oceanic hotspots. This major geoid anomaly suggests that the greater Yellowstone ecosystem stands high due to processes in the mantle.

formation on the plateau itself, the altitude of the plateau's surface increased so that orographic extraction of snow from storms channeled by the eastern Snake River Plain became self-amplifying. This positive-feedback loop resulted in an even more pronounced accumulation of snow and glacial ice on the plateau. Such unusual two-mode glacial behavior conforms elegantly to the hotspot-produced geography beyond the eastern end of the eastern Snake River Plain. Early and late in a cycle, glacial snows accumulated only on the Yellowstone crescent of high terrain; whereas, during full-glacial (climax) conditions, the rise of more than 1,500 m (5,000 ft) from the Snake River Plain (altitude 1,800 m, 6,000 ft) to the ice-cap crest (altitude 3,350 m, 11,000 ft) produced deep orographic snows on the Yellowstone Plateau itself (Pierce, 1979; Pierce and Good, 1998).

Glaciation sculpted the landscape of the GYE and older soils were scraped away. Deposits of glacial moraines, outwash gravels and sands, lake sediments, and thin glacial tills have greatly influenced soil and landscape development (fig. 17) (Rodman and others, 1996; Trettin, 1986). Soils on both glacially eroded areas as well as on glacial deposits formed in originally unweathered material in the relatively short interval of about 15,000–12,000 years since glaciation (fig. 17H). Many of the meadow areas of Yellowstone are fine-textured glacial deposits (figs. 17C and 7G). In northern Yellowstone near Gardiner, Mont., thick glacial ice converged to form a large outlet glacier that flowed north 65 km (40 mi) down the Yellowstone Valley to where it deposited extensive end moraines—beyond which a large, glacial-meltwater river deposited thick outwash gravels (figs.17A and 17B). Glacial flow was northward across the Washburn Range, where it overrode the highest peaks in the range (fig. 17D) and rounded the range into a smoothed form (fig. 17E) that is dramatically different from the rock pillars (hoodoos) and cliffs formed by similar bedrock in the unglaciated and drier terrain west of Cody, Wyo.

Jackson Lake and Jenny Lake in Grand Teton National Park were formed by Pleistocene glaciations (figs. 16, 17F, and 17G), as was the accumulation of lake sediments in Hayden and Pelican Valleys (located on fig. 6). Many of the topographic elements on a scale of 0.5 to 30 m (1 to 100 ft) in the GYE within the area covered by Pleistocene glaciations (fig. 16) are the result of glacial erosion and deposition. The topographic surface left by this glacial erosion and deposition is the "canvas" upon which the GYE vegetation was "painted" using a palette of vegetation types that provided the plant diversity upon which a broad range of biotic communities have developed.

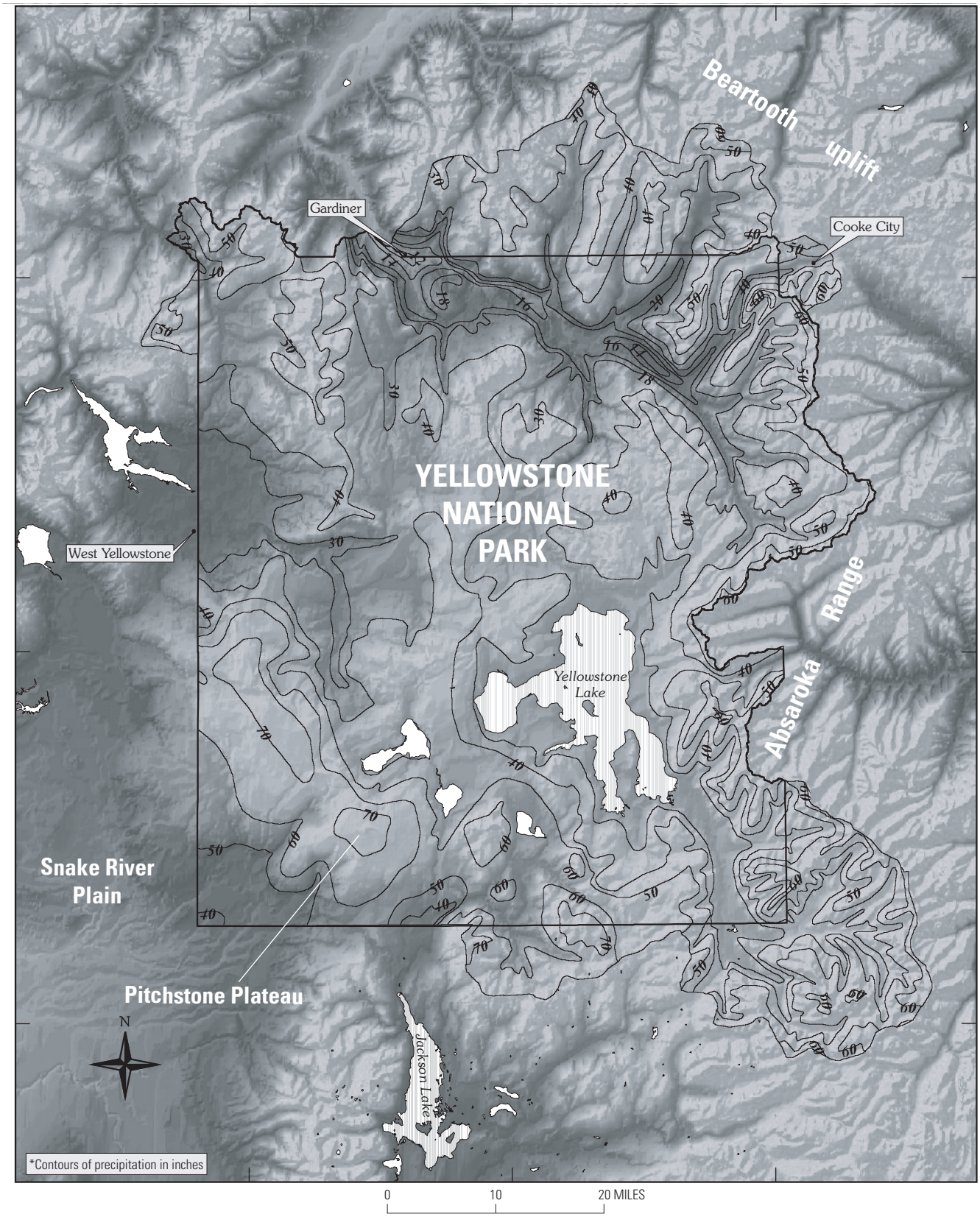

Figure 13. Map showing average annual precipitation (in inches) in Yellowstone National Park and the nearby drainage areas (modified from Farnes, 1997). Note that the precipitation shows a maximum of more than 180 cm (70 in) on the west side of the Yellowstone Plateau, where the altitudes reach only about 2,600 m (8,500 ft), and high but lesser values in the Absaroka Range along the east side of Yellowstone, where altitudes are about 1,000 m (2,000–3,000 ft) higher.

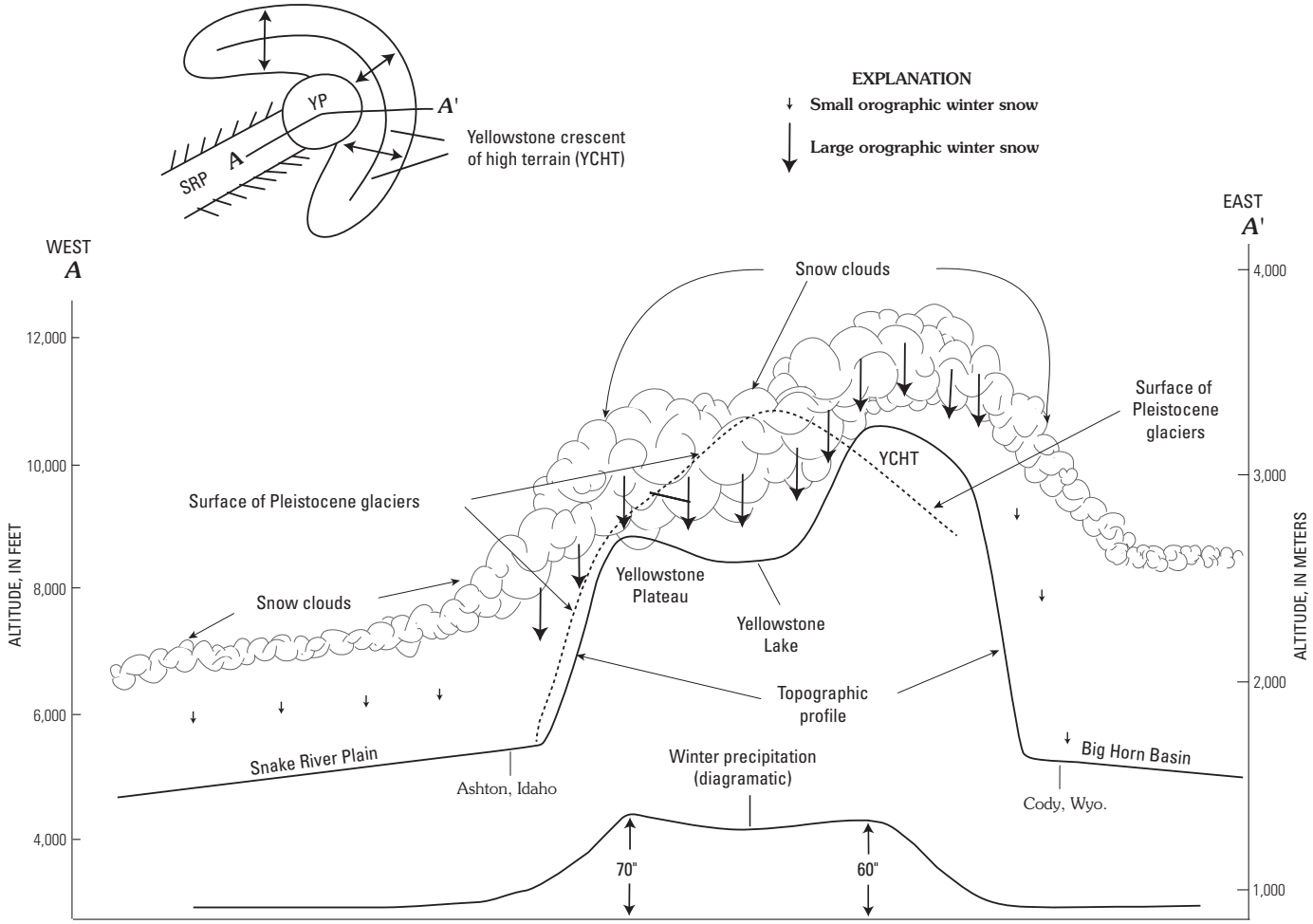

Figure 14. Profile illustrating orographic snowfall across Yellowstone. Storms first rise up from the Snake River Plain onto the Yellowstone Plateau, then ascend higher across the Absaroka Range crest, and then descend towards Cody, Wyo. Inset is schematic diagram of major topographic elements showing location of topographic section A–A′ (fig. 1). Abbreviations are SRP, Snake River Plain; YP, Yellowstone Plateau; and YCHT, axis of the Yellowstone crescent of high terrain. Length of vertical arrows diagrammatically indicates the relative amount of winter snow extracted from the west-to-east moving air mass. The increasing amount of snow clouds diagrammatically shows increasing amounts of orographic snowfall.

Human Experience and Human Geography of the GYE as Influenced by the Yellowstone Hotspot

> *The geographic environment is a mould into which the human race has been poured and the history of the race has been shaped by that mould (A.E. Parkins, 1934, p. 224).*

This paper concerns the relation between geology and ecology, and this final section concerns geology as applied to human geography or human ecology. The distinctive attributes of the landscapes of the GYE are critical to how people have experienced and used the GYE. In this section, we first portray the human experience in the GYE and then show how some salient aspects of human geography relate to hotspot-related processes.

Several Native-American origin myths are thought to refer to Yellowstone Lake and its outlet at Fishing Bridge (Reeve, 1989; Nabokov and Loendorf, 2002). Kiowa (Mooney 1979), Appachean (Gunnerson and Gunnerson, 1971; Perry, 1980), and Shoshonean (Dominick, 1964) myths and ethnohistories refer to Yellowstone Lake and its outlet at Fishing Bridge. Native Americans entered the GYE apparently not long after they entered North America, as indicated by early Paleoindian Clovis and Folsom projectile points dating from about 13,500–12,800 years ago (ages given here are in corrected radiocarbon ages). Sites on the shores of Yellowstone and Jackson Lake have abundant Cody Complex points indicating occupation there by 10,600–9,800 years ago. Native Americans were present in the GYE much of the time from then up to historic times, although probably only at times and in places where snows were not too deep. Although Native Americans regarded Yellowstone and its thermal features as sacred, Euro-Americans are responsible for

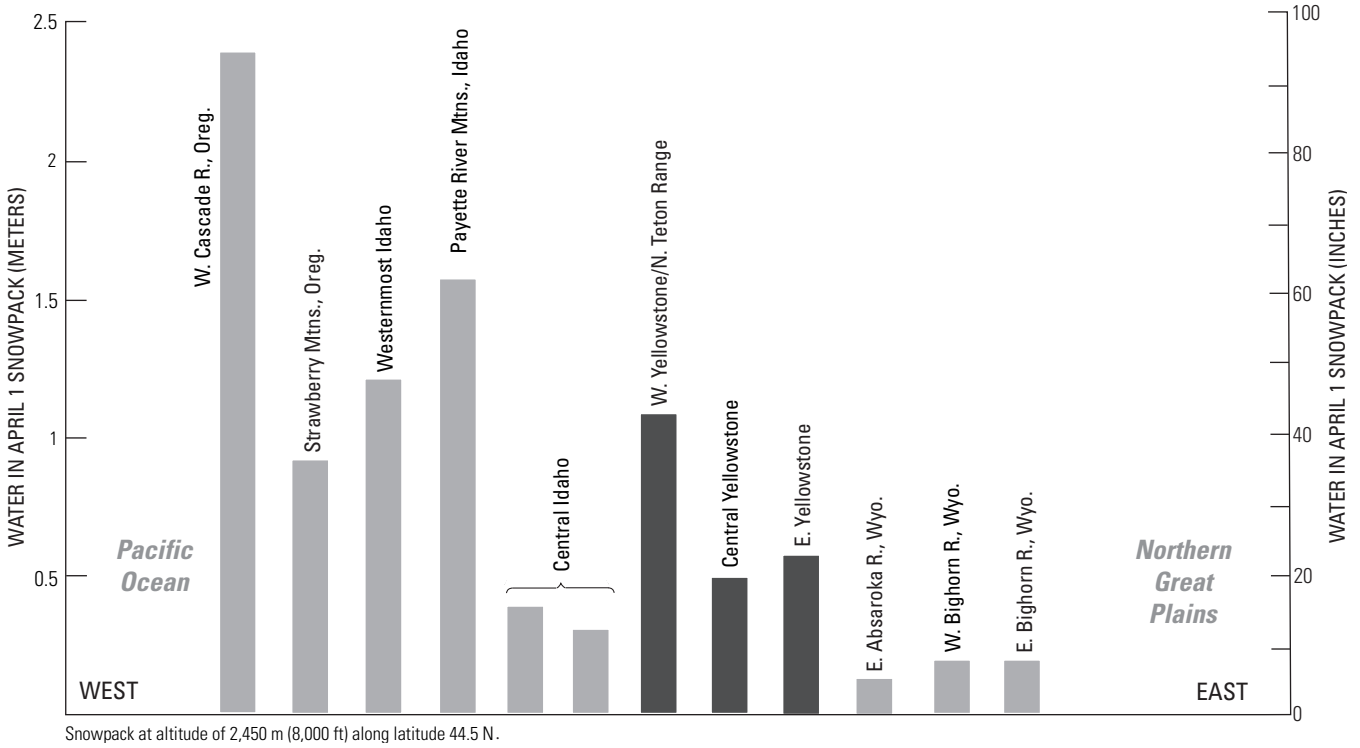

Figure 15. Plot of snowpack from the Pacific Ocean through Yellowstone to the Big Horn Mountains. The plot is along a latitudinal transect and normalized to 2,450-m (8,000-ft) altitude to isolate snowpack anomalies. Note major increase from central Idaho eastward to the Yellowstone Plateau. Storms moving northeast along the Snake River Plain are intercepted by mountains around the cul-de-sac at upper end of the plain; here moisture-laden air rises first up onto the Yellowstone Plateau resulting in a large orographic extraction of snow, and rise subsequently higher across the Yellowstone crescent of high terrain where additional snow is extracted. Farther east to the Cody, Wyo., area, the descending air becomes drying and snowfall decreases dramatically.

the myth that Native Americans were afraid of Yellowstone (Weixelman, 2001).

Ever since French and American fur trappers reported the amazing features of Yellowstone (fig. 18) in the early 1800s, the GYE has assumed almost mythical properties. Its geysers and hot springs suggest powers deep in the Earth. The human experience in the GYE is strongly related to the landscape, vegetation patterns, and climate that, in turn, are direct or indirect results of hotspot processes (fig. 18). Yellowstone is the best-known natural thermal feature in the world and, as such, attracts millions of visitors each year. It is the subject of many TV broadcasts and is the topic of many environmental concerns. Despite more than 3 million visitors annually from throughout the world, Yellowstone and vicinity remain the largest intact ecosystem in temperate North America (Reese, 1984).

The mountainous areas of the ecosystem have been a significant factor in human use of the region for the last 10,000 years or more. As the lower elevations dried out and game animals migrated to higher elevations for their summer range, hunter-gatherer groups also went to the moister, cooler mountains and gathered plant materials as they ripened or became ready for harvest (Wright, 1984). Seasonal plant maturation also migrated upslope reaching the proper growth or ripening (phenological) stage later than those lower down in the valleys. This hunter-gatherer culture lasted until the last vestiges of Native Americans were moved from Yellowstone National Park to a reservation in central Wyoming shortly after the Park was established in 1872.

Patterns of human settlement and political organization are elements in the study of human geography and are often governed by major landscape features. In the historical geography of Europe, the high Alps acted as a sparsely populated highland barrier, partitioning the human history, political associations, and commerce on the different sides of the mountains (Pounds, 1990). Similarly, the mountainous, snowy GYE remained a highland of mystery in the heart of expanding western development. Wagon roads were established to supply the gold camps of Montana, and settlements evolved to provide a closer supply. These wagon roads skirted the GYE uplands, avoiding steep grades. Native Americans attempted to protect their prairie hunting grounds from this encroachment on the north and east side of the GYE. Forts were constructed to guard incoming settlers. This state of affairs in American history provided many of the plots for the "westerns" that dominated the movie and TV industry for decades. Fort Ellis, established in 1867 near Bozeman, Mont. (established in 1864), was the jumping-off place for Yellowstone's early explorers. As the Native Americans were removed and the

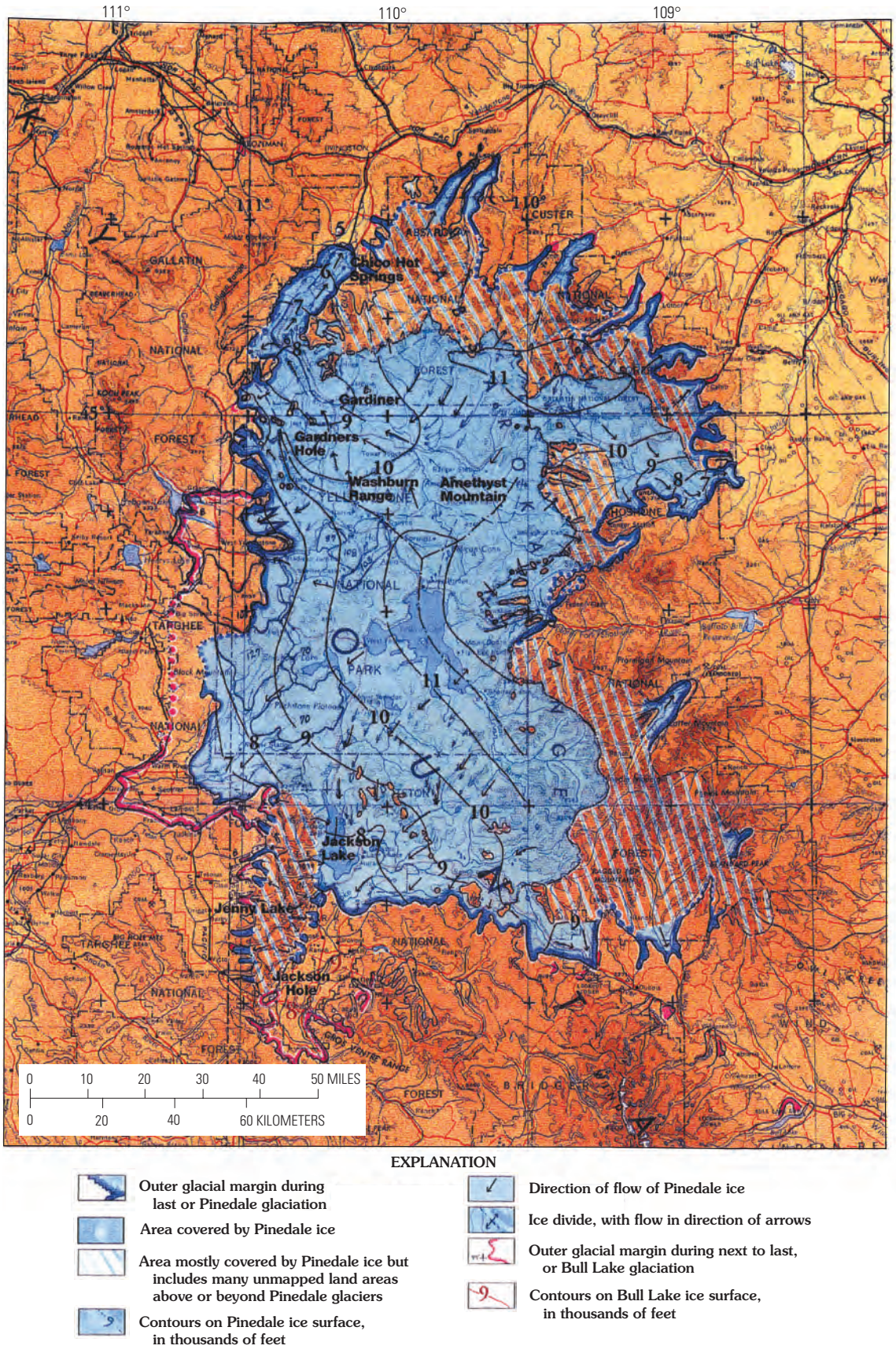

Figure 16. Map showing extensive glacial cover of the Yellowstone area about 17,000 years ago. Only the glaciers that were contiguous with those in Yellowstone are shown. Nearly all of Yellowstone Park was covered with glacial ice that was enhanced by three hotspot-related features: (1) the storm conduit of the eastern Snake River Plain, (2) the buildup of rhyolite to form Yellowstone Plateau, and (3) uplift to form the Yellowstone crescent of high terrain.

Figure 17. GLACIATION. Glacial erosion and deposition have greatly modified the landscape and soil of the greater Yellowstone ecosystem (GYE). Most of the soil in which GYE vegetation grows has formed only since the last glaciation and is weakly developed. Soils commonly are formed either in different-textured glacial deposits (till, gravel, and lake sediment) or on bedrock scraped clean during glaciation and, consequently, are very thin.

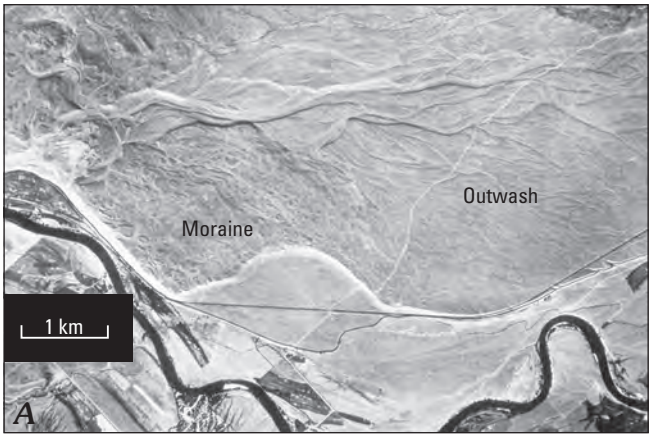

A, Glacial outwash plain (channel patterns) and moraines (left side of photograph) of the northern Yellowstone outlet glacier.

B, Glacial molding of landscape by right-to-left glacial flow 1,100 m (3,300 ft) thick above Gardiner, Mont.

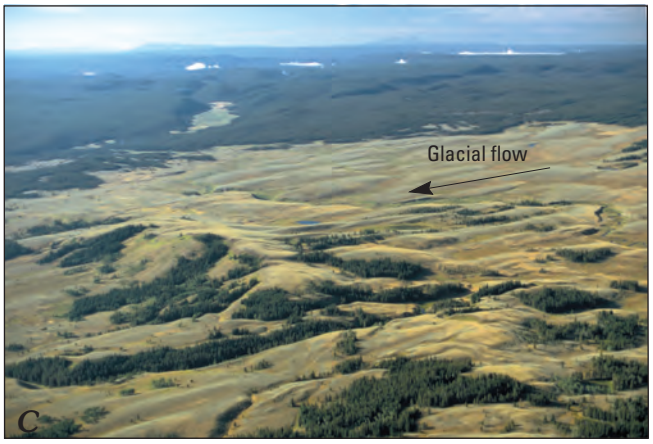

C, Gardners Hole consists of glacial deposits molded by glacial flow (fig. 16). Meadow is on glacial deposits; lodgepole forest is on rhyolite.

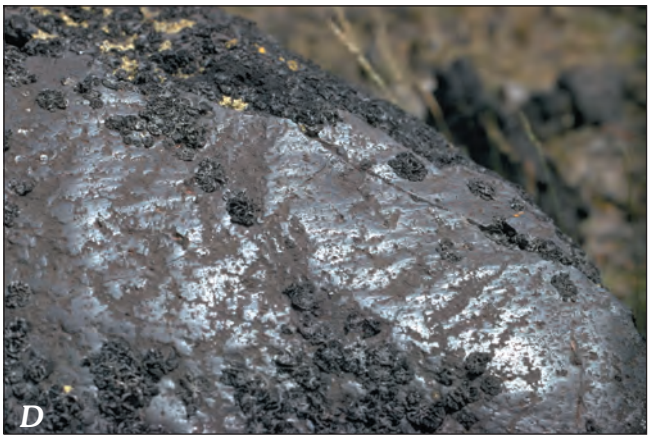

D, Glacial striations on the crest of the Washburn Range.

E, Washburn Range was smoothed and rounded by overriding ice.

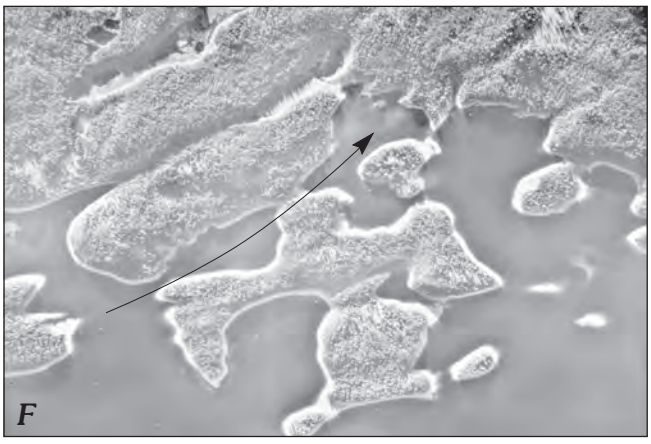

F, Glacial sculpting along east side of Jackson Lake by a thick glacier flowing south from Yellowstone.

railroads expanded from the east through Bozeman in 1883 and from the south into the Snake River Plain, the settlements rapidly expanded. Fingers of settlement reached into the GYE as pioneering ranchers settled the isolated lower valleys along major streams. Following construction of the railroad spur from Livingston, Mont., to Yellowstone National Park in the late 1800s, railroads brought ever-increasing numbers of tourists to the heart of the GYE, and the patterns of use that exist today were solidified. People visited Yellowstone during the summer but few could negotiate the deep snows of winter.

A similar "in-and-out" pattern of use by many animals was underway by about 15,000 years ago when Yellowstone was emerging from the most recent ice age. Then, vegetation was in a state of flux as stream valleys and snow-free mountain ridges opened dynamic ecological niches as climate warmed. From studies of pollen in cores from lakes, Whitlock (1993) documented the following vegetation changes. As the ice retreated, plants adapted to tundra conditions occupied the newly exposed ground. From about 13,200 to 12,200 years ago (carbon-14 ages are corrected to calendar years), climate continued to ameliorate, enabling whitebark pine, Englemann spruce, and subalpine fir to colonize the richer soils on the non-rhyolitic areas. The central rhyolite plateau with its infertile, well-drained soils, remained treeless about 1,000 years longer—until about 11,200 years ago when it became covered with lodgepole pine. Continued warming first brought the vegetation similar to today's, but warming culminated about 8,000 years ago with Douglas fir growing higher up the mountains than it does today. Subsequent cooling about 5,000 years ago led to several glacial oscillations, the youngest of which was the Little Ice Age that culminated in about A.D. 1850, or perhaps as recently as 1920. Subsequently, the climate has been warming and vegetation readjusting (Meagher and Houston, 1998).

Elk, bison, and deer moved into Yellowstone with spring green-up and were driven out by winter snows. Wolves and coyote movements mirrored migration patterns of the ungulates. Native Americans hunted in Yellowstone's plateaus, mountains, and valleys for thousands of years and mined obsidian for trade; trappers harvested beaver, and all left with autumnal storms.

The core of the GYE is a mountainous area along the Continental Divide that is the headwaters of 25 rivers and other large drainages that flow radially outward (fig. 19). The map pattern might be idealized as shown in figure 20 to that of a domal highland. The results of human activities—such as towns, roads, irrigation systems, ranches, and farms—are concentrated along the river valleys (table 2), and most commerce occurred within these valleys or across lower divides; however very little commerce was conducted across the rugged, mountainous core of the GYE.

The downstream parts of drainages shown in figure 19 became corridors for settlement and transportation by European settlers with the building of irrigation canals, roads, towns, and railroads. Each drainage has its key towns (table 2). The GYE includes 21 counties. This central highland "vacant hub" with its radially flowing streams helps explain a geographic political segmentation of the GYE—each river valley had its own associations and was separated from other valleys by barriers ranging from rugged, forested mountains across the upper parts of drainages to more open and arid divides farther down these drainages. More recently, with enhanced communication, media coverage, transportation, and organization of interest groups, strong differences and polarities for the management of the GYE are manifest from competing interest groups within the valleys, within the GYE, and within the Nation.

Because of its remote highland setting centering on the Continental Divide, the GYE contains the boundaries of many National, State, and local governmental jurisdictions (fig. 1; table 3). In large part because of its location at drainage headwaters, the GYE contains the boundaries of (1) Yellowstone and Grand Teton National Parks, (2) three National Forest regions and seven National Forests (Gallatin, Custer, Shoshone, Bridger-Teton, Caribou, Targhee, and Beaverhead), (3) the States of Wyoming, Montana, and Idaho, and (4) 21 counties (table 3). Collaborative decision-making within the GYE is hampered because of its many jurisdictions.

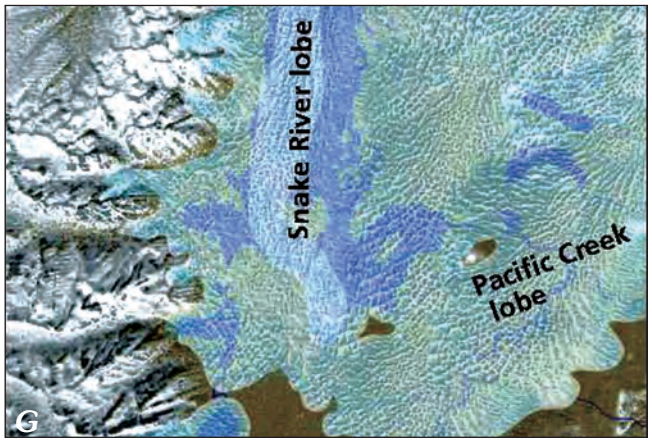

G, Reconstruction showing the glacier that flowed south from the Yellowstone Plateau and excavated Jackson Lake.

H, Glaciation of the GYE left fresh stony soils such as these on top of Amethyst Mountain.

Figure 18. HUMAN EXPERIENCE. Human experience in the greater Yellowstone ecosystem (GYE) related to the Yellowstone hotspot. The Yellowstone hotspot has created or enhanced the main features that attract people to the GYE: its thermal features, wildlife, mountain character, and scenic vistas. (YNP, Yellowstone National Park.)

A, Shoshone Native-American family in Yellowstone area. Photograph by W.H. Jackson in 1871.

B, Fire pits on Jackson Lake paleobeach. Surface hearth above deeper, buried hearth—both are about 2,000 years old.

C, Trapper painted in 1837. Photograph from YNP collection (no. 2901).

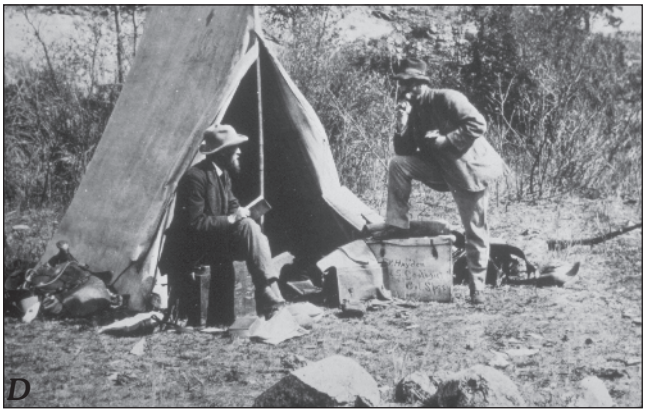

D, Geologist F.V. Hayden in camp. Photograph by W.H. Jackson in 1871.

E, Tower Falls as painted by Thomas Moran. Photograph from YNP collection (no. 3096).

F, Old tour bus at West Thumb in 1917. Photograph from YNP collection (no. 10,518).

H, Tourists at Mammoth Hot Springs. Photograph from YNP collection (no. 2863).

J, Teton Range as viewed across Jackson Lake. Photograph from YNP collection (no. 4519).

L, Grizzly bears dining at Trout Creek dump in 1970. Photograph from YNP collection (no.11,678).

G, Fishing Bridge in the early 1900s. Photograph from YNP collection (number not known).

I, Morning Glory Pool in Upper Geyser Basin. Photograph from YNP collection (no. 5710).

K, Old Faithful. Photograph from YNP collection (no. 5205).

Table 3. Governmental jurisdictions in the greater Yellowstone ecosystem (GYE).

Federal		
National Parks (2): Grand Teton Yellowstone	National Forests (7): Region 1: Custer, Gallatin, and Deer Lodge Region 2: Shoshone Region 4: Bridge-Teton, Caribou, and Targhee	Bureau of Land Management (many districts)
States (3) and counties (21)		
Montana (7): Beaverhead, Carbon, Gallatin, Sweet Grass, Madison, Park, and Stillwater	Wyoming (6): Fremont, Hot Springs, Lincoln, Park, Sublette, and Teton	Idaho (8): Bear, Bingham, Bonneville, Caribou, Clark, Fremont, Madison, and Teton
Indian reservations		
Wind River Indian Reservation Just beyond GYE (fig. 1) are the Fort Hall (Idaho) and Crow (Montana) Indian Reservations		

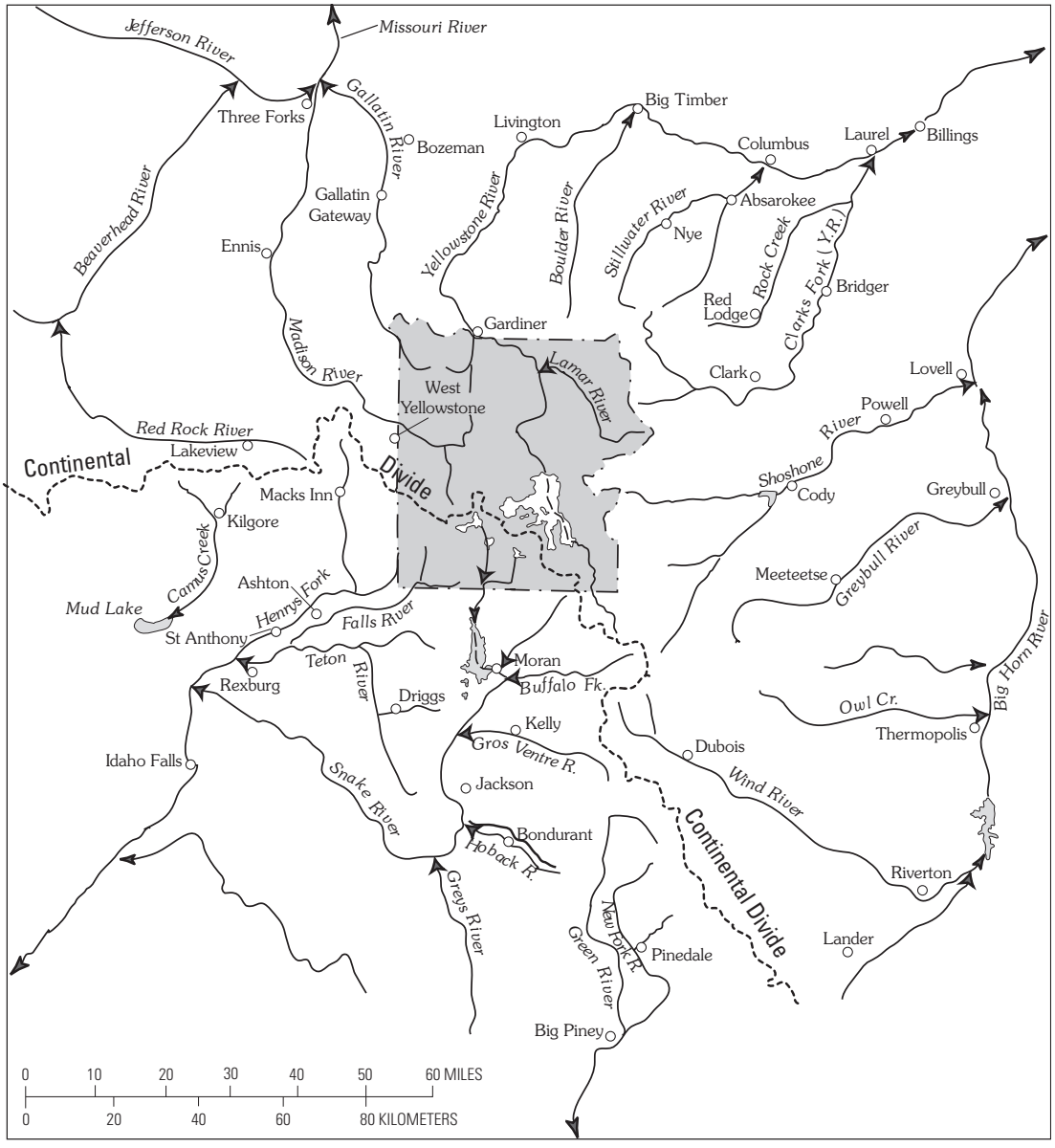

Figure 19. Sketch map showing radial pattern of major rivers of the greater Yellowstone ecosystem (GYE). The GYE is a mountainous area along the Continental Divide. From the central highland "hub" of the GYE, the headwaters of about 25 drainages (table 2) flow radially outward. This high, "mother of waters," location explains why Yellowstone was relatively late to be explored by Euro-Americans and even now is difficult to traverse in winter. This central highland "hub" also helps explain the political segmentation of the GYE; each river valley has its own human association and is separated from adjacent rivers by mountainous divides.

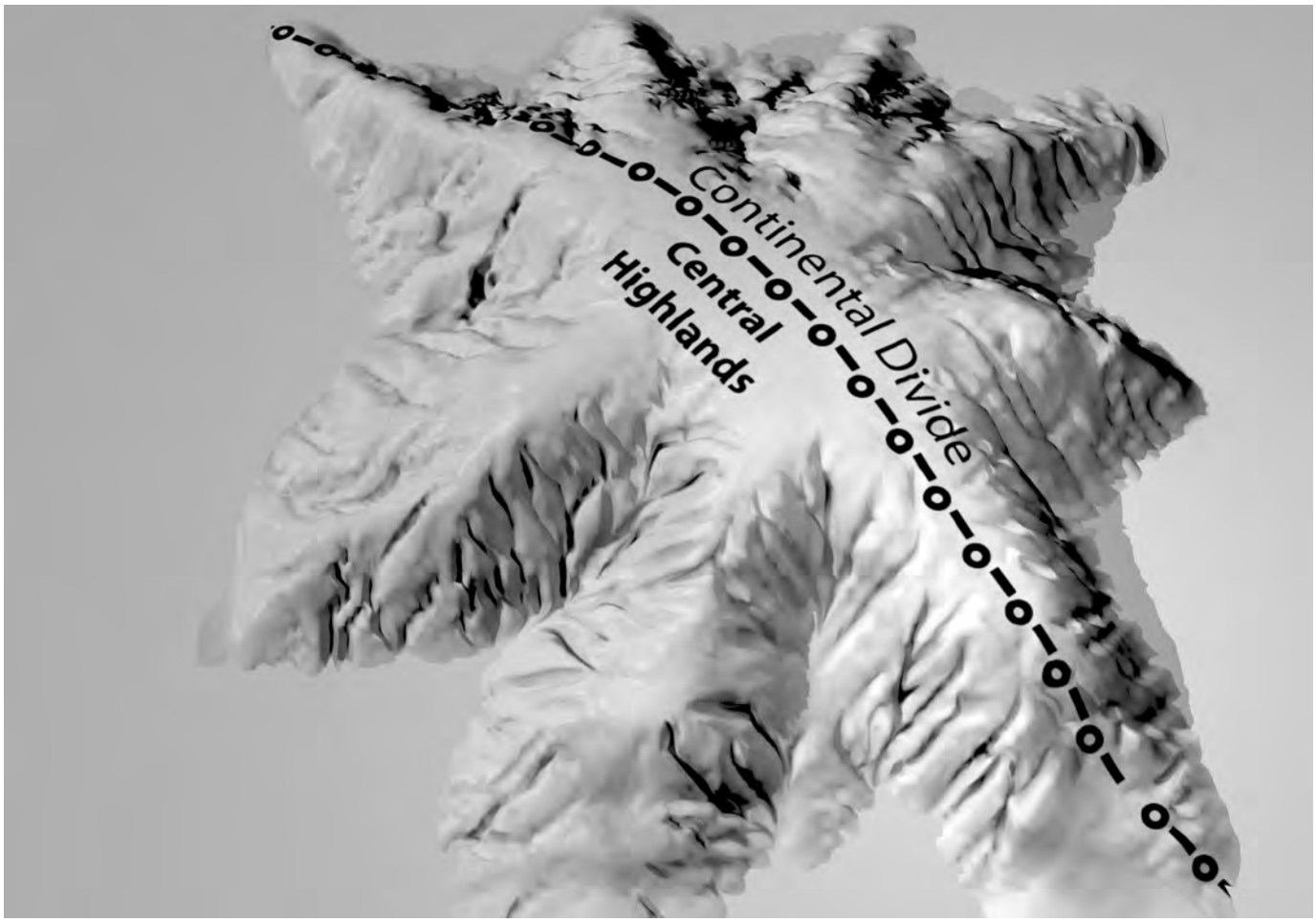

Figure 20. Cartoon showing central highland and idealized radial drainage pattern. Nature is more complicated than this simplified pattern, and the greater Yellowstone ecosystem has a geologic heritage older than the 2-million-year-old Yellowstone Plateau volcanic field, such as the topography produced by Laramide-age uplifts about 60 million years ago. In addition, rather than a dome, which would suggest static plate motion, the uplift appears to have a crescent pattern associated with the relatively stationary Yellowstone hotspot interacting with the southwest-moving North American plate.

Today, the historic "in-and-out" annual use pattern characteristic of Yellowstone National Park is blurred, but it truly extends over larger parts of the GYE. Air transport moves people quickly from anywhere in the world to communities near the GYE, and over-snow vehicles carry them swiftly to Old Faithful itself. Where ranchers once toughed out winters in near isolation, second homes and subdivisions dot the landscape. Human-use patterns have expanded; ungulate-use patterns have been truncated (which has also circumscribed predator migration patterns). Major ski resorts occupy snowy mountains once considered barriers to development. Improved transportation, affluence, and winter sports are increasing winter use in parts of the GYE, but Yellowstone, and its surrounding mountains and villages, is still visited by far more people during the summer months.

We have shown how the Yellowstone hotspot and associated geologic processes of volcanism, faulting, and uplift have shaped patterns of habitation and land-use in the GYE, even though many visitors to Yellowstone are unaware of the connection. The skier busting through powder snow above Teton Village in Jackson Hole, Wyo., or Big Sky, Mont., the photographer too close to a grizzly in the Park's Gallatin Range, or the summer resident enjoying her sunset from her new home above the Madison River may never ask, "Why these mountains, these animals, or these geysers and hot springs?" They could be surprised to learn that the driving force behind these scenic landscapes lies deep beneath their feet and that this long-lived source of energy has raised the mountains and high plateaus of Yellowstone; it has powered Yellowstone's famous thermal features; and it has been active for the last 16 million years. Without the hotspot, much of Yellowstone would resemble the dusty, dry landscape that surrounds it. Although there would have still been mountains, they would have been lower and drier than the present landscape. Precipitation would be much less than it is today, and grasslands would be less luxuriant. Without the hotspot, rivers would be smaller and there would be no geysers—the Yellowstone that we know today would have been very different indeed.

References Cited

Anders, M.H., 1994, Constraints on North American plate velocity from Yellowstone hotspot deformation field: Nature, v. 369, p. 53–55.

Anders, M.H., Geissman, J.W., Piety, L.A., and Sullivan, J.T., 1989, Parabolic distribution of circum-eastern Snake River Plain seismicity and latest Quaternary faulting—Migratory pattern and association with the Yellowstone hot spot: Journal of Geophysical Research, v. 94, no. B2, p. 1,589–1,621.

Anderson, D.L., 1998, The edges of the mantle, *in* Gurnis, Michael, Wysession, M.E., Kittle, Elise, and Buffett, B.A., eds., The core-mantle boundary region: American Geophysical Union, Geodynamics Series, v. 28, p. 255–271.

Benjamin, Lyn, 2000, Groundwater hydrology of the Henry's Fork springs: Intermountain Journal of Sciences, v. 6, no. 3, p. 119–142.

Brock, T.D., and Brock, M.L., 1971, Life in the geyser basins—Yellowstone National Park: Yellowstone Library and Museum Association, 32 p.

Camp, V.E., 1995, Mid-Miocene propagation of the Yellowstone mantle plume head beneath the Columbia River Basalt source region: Geology, v. 23, no. 5, p. 435–438.

Camp, V.E., and Ross, M.E., 2004, Mantle dynamics and genesis of mafic magmatism in the intermontane Pacific Northwest: Journal of Geophysical Research, v. 109, B08204, 14 p.

Christiansen, R.L., 1984, Yellowstone magmatic evolution—Its bearing on understanding large-volume explosive volcanism, *in* Explosive volcanism—Inception, evolution, and hazards; studies in geophysics: Washington, D.C., National Academy Press, p. 84–95.

Christiansen, R.L., 2001, The Quaternary and Pliocene Yellowstone Plateau volcanic field of Wyoming, Idaho, and Montana: U.S. Geological Survey Professional Paper 729-G, 145 p.

Christiansen, R.L., Foulger, G.A., and Evans, J.R., 2002, Upper mantle origin of the Yellowstone hotspot: Geological Society of America Bulletin, v. 2004, p. 1,245–1,526.

Coffin, M.F., and Eldholm, Olav, 1994, Large igneous provinces: Crustal structure, dimensions, and external consequences: Reviews of Geophysics, v. 32, p. 1–36.

Courtillot, Vincent, Davaille, Anne, Besse, Jean, and Stock, Joann, 2003, Three distinct types of hotspots in the Earth's mantle: Earth and Planetary Science Letters, v. 205, p. 295–308.

Craig, Harmon, 1990, Helium isotope distribution in mantle hotspots: EOS, Transactions of the American Geophysical Union , v. 71, p. 1,669.

Craig, Harmon, 1997, Helium isotope ratios in Yellowstone Park and along the Snake River Plain: Backtracking the Yellowstone hotspot: EOS, Transactions of the American Geophysical Union, v. 78, p. F801.

Daubenmire, Rexford, 1943, Vegetational zonation in the Rocky Mountains: Botanical Review, v. 9, p. 325–393.

Davies, G.F., 1999, Dynamic Earth—Plates, plumes, and mantle convection: Cambridge, England, Cambridge University Press, 470 p.

Davis, L.B., Aaberg, S.A., Schmitt, J.G., and Johnson, A.M., 1995, The Obsidian Cliff plateau prehistoric lithic source, Yellowstone National Park, Wyoming: Selections from the Division of Cultural Resources, Rocky Mountain Region, National Park Service, no. 6, 164 p.

Despain, D.G., 1987, The two climates of Yellowstone National Park: Proceedings of Montana Academy of Science, v. 47, p. 11–19.

Despain, Don G., 1990, Yellowstone vegetation—Consequences of environment and history in a natural setting: Boulder, Colo., Roberts Rinehart Publishers, 239 p.

Dominick, D., 1964, The Sheepeater: Annals of Wyoming, v. 36, p. 131–168.

Draper, D.S., 1991, Late Cenozoic bimodal magmatism in the northern Basin and Range Province of southeastern Oregon: Journal of Volcanology and Geothermal Research, v. 47, p. 299–328.

Duncan, R.A., and Richards, M.A., 1991, Hotspots, mantle plumes, flood basalts, and true polar wander: Reviews in Geophysics, v. 29, p. 31–50.

Eversman, Sharon, and Carr, Mary, 1992, Yellowstone ecology—A road guide: Missoula, Montana Press Publishing Company, 242 p.

Farley, K.A., and Neroda, E., 1998, Noble gases in the Earth's mantle: Annual Review of Earth and Planetary Sciences, v. 26, p. 189–218.

Farnes, Phil, 1997, The snows of Yellowstone: Yellowstone Science, v. 5, no. 2, p. 8–11.

Fee, David, and Dueker, Ken, 2004, Thermal structure of the transition zone beneath Yellowstone as revealed by receiver function imaging [abs.]: Geological Society of America Abstracts with Programs, v. 36, no. 4, p. 94.

Foulger, G.R., and Natland, J.H., 2003, Is "hotspot" volcanism a consequence of plate tectonics?: Science, v. 300, p. 921-922.

Fournier, R.O., 1989, Geochemistry and dynamics of the Yellowstone National Park hydrothermal system: Annual Reviews of the Earth and Planetary Sciences, v. 17, p. 13–53.

Fritz, W.J., 1980, Reinterpretation of the depositional environment of the Yellowstone "fossil forests": Geology, v. 8, p. 309–313.

Good, J.M., and Pierce, K.L., 1996, Interpreting the landscapes of Grand Teton and Yellowstone National Parks, recent and ongoing geology: Grand Teton National History Association, 58 p.

Griffin, J.B., Gordus, A.A., and Wright, G.A., 1969, Identification and sources of Hopewellian obsidian in the middle west: American Antiquity, v. 34, p. 1–13.

Glick, Dennis, Carr, Mary, Harting, Bert, and others, 1991, An environmental profile of the greater Yellowstone ecosystem: Bozeman, Mont., Greater Yellowstone Coalition, map.

Hamilton, W.B., 2003, An alternative Earth: GSA Today, v. 13, no. 11, p. 4–12.

Hooper, P.R., 1997, The Columbia River flood basalt province—Current status, *in* Mahoney, J.J., and Coffin, M.F., eds., Large igneous provinces—Continental, oceanic, and planetary flood volcanism: American Geophysical Union Monograph 100, p. 1–27.

Humphreys, E.D., Dueker, K.G., Schutt, D.L., and Smith, R.B., 2000, Beneath Yellowstone—Evaluating plume and nonplume models using teleseismic images of the upper mantle: GSA Today, v. 10., no. 12, p. 1–7.

Jackson, Ian, ed., 2000, The Earth's mantle—Composition, structure, and evolution: Cambridge, England, Cambridge University Press, 592 p.

Jaworowski, Sheryl, 1994, Geologic implications of Quaternary tephra localities in the western Wind River Basin, Wyoming: Friends of the Pleistocene, Rocky Mountain Field Trip, August 13–14, 1994.

Kennedy, B.M., Reynolds, J.H., Smith, S.P., and Truesdell, A.H., 1987, Helium isotopes—Lower Geyser Basin, Yellowstone National Park: Journal of Geophysical Research, v. 92, p. 12,477–12,489.

Lanphere, M.A., Champion, D.E., Christiansen, R.L., Izett, G.A., and Obradovich, J.D., 2002, Revised ages for tuffs of the Yellowstone Plateau volcanic field—Assignment of the Huckleberry Ridge Tuff to a new geomagnetic polarity event: Geological Society of America Bulletin, v. 114, p. 559–568.

Li, Xueqing, Kind, Ranier, Yuan, Xiaohui, Wolbern, Ingo, and Hanka, Winfried, 2004, Rejuvenation of the lithosphere by the Hawaiian plume: Nature, v. 427, p. 827–829.

Love, J.D., Reed, J.C., Jr., and Pierce, K.L., 2003, Creation of the Teton landscape—A geological chronicle of Jackson Hole and the Teton Range: Moose, Wyo., Grand Teton Natural History Association, 132 p.

Machette, M.N., Pierce, K.L., McCalpin, J.P., Haller, K.M., and Dart, R.L., 2001, Map and data for Quaternary faults and folds in Wyoming: U.S. Geological Survey Open-File Report 01-461, scale 1:500,000, 155 p.

Malde, H.E., 1991, Quaternary geology and structural history of the Snake River Plain, Idaho and Oregon, *in* Morrison, R.B., ed., Quaternary nonglacial history of the conterminous U.S.: Geological Society of America, The Geology of North America, v. K-2, ch. 4, p. 251–282.

Marston, R.A., and Anderson, J.E., 1991, Watersheds and vegetation of the greater Yellowstone ecosystem: Conservation Biology, v. 5, no. 3, p. 338–346.

Meagher, Mary, and Houston, Doug, 1998, Yellowstone and the biology of time: Norman, University of Oklahoma Press, 287 p.

Meyer, G.A., Wells, S.G., and Jull, A.J.T., 1995, Fire and alluvial chronology in Yellowstone National Park—Climatic and intrinsic controls on Holocene geomorphic processes: Geological Society of America Bulletin, v. 107, p. 1,211–1,230.

Milbert, D.G., 1991, GEOID90—A high-resolution geoid for the United States: EOS, Transactions of the American Geophysical Union, v. 72, p. 545–554.

Molnar, Peter, and England, Philip, 1990, Late Cenozoic uplift of mountain ranges and global climate change—Chicken or egg?: Nature, v. 346, p. 29–34.

Montelli, Raffaella, Nolet, Guust, Dahlen, F.A., Masters, Guy, Engdahl, G.E., and Hung, Shu-Huei, 2004, Finite-frequency tomography reveals a variety of plumes in the mantle: Science, v. 303, p. 338—343.

Mooney, J., 1979, Calender history of the Kiowa Indians: Washington, D.C., Smithsonian University Press.

Morgan, J.P., Morgan, W.J., and Price, Evelyn, 1995, Hotspot melting generates both hotspot volcanism and a hotspot swell?: Journal of Geophysical Research, v. 100, p. 8,045–8,062.

Morgan, L.A., and McIntosh, W.C., 2005, Timing and development of the Heise volcanic field, Snake River Plain, Idaho, Western U.S.A., Geological Society of America Bulletin, v. 117, p. 288–306.

Morgan, L.A., McIntosh, W.C., and Pierce, K.L., 1997, Inferences for changes in plume dynamics from stratigraphic framework studies of ignimbrites, central Snake River Plain, Idaho [abs.]: Geological Society of America Abstracts with Programs, v. 29, no. 6, p. A-299.

Morgan, L.A., Pierce, K.L., and McIntosh, W.C., 1999, $^{40}Ar/^{39}Ar$ ages of silicic volcanic rocks in the Snake River Plain—Timing of volcanism and tectonism along the track of the Yellowstone hotspot [abs.]: Geological Society of America, Abstracts with Programs, v. 31, no. 4, p. A-49.

Morgan, L.A., Shanks, W.C., Pierce, K.L., Rye, R., and Meeker, G.P., 1998, Hydrothermal explosion deposits in Yellowstone National Park—Links to hydrothermal processes: EOS, Transactions of the American Geophysical Union, v. 79, no. 45, p. F964.

Nabokov, Peter, and Loendorf, Lawrence, 2002, American Indians and Yellowstone National Park—A documentary overview, Yellowstone National Park, Wyo.: National Park Service, Yellowstone Center for Resources, 367 p.

Pace, N.R., 1991, Origin of life—Facing up to the physical setting: Cell, v. 65, p. 531–533.

Parkins, A.E., 1934, The geography of American geographers: Journal of Geography, v. 33, p. 221–230.

Parry, C.C., 1874, Botanical observations in western Wyoming: American Naturalist, v. 8, no. 3, p. 175–180.

Parsons, Tom, Thompson, G.A., and Sleep, N.H., 1994, Mantle plume influence on the Neogene uplift and extension of the U.S. western Cordillera?: Geology, v. 22, p. 83–86.

Patton, D.T., 1963, Vegetational pattern in relation to environments in the Madison Range, Montana: Ecological Monographs, v. 33, p. 375–406.

Perry, R.J., 1980, The Appachean transition from the subarctic to the southwest: Plains Anthropologist, v. 25(90), p. 79–296.

Pierce, K.L., 1979, History and dynamics of glaciation in the northern Yellowstone National Park area: U.S. Geological Survey Professional Paper 729-F, 91 p., 4 pl.

Pierce, K.L., Despain, D.G., Whitlock, Cathy, Cannon, K.P., Meyer, Grant, Morgan, Lisa, and Licciardi, J.M., 2003, Quaternary geology and ecology of the greater Yellowstone area, *in* Easterbrook, D.J., ed., Quaternary Geology of the United States, INQUA 2003 Field Guide Volume: Reno, Nev., Desert Research Institute, p. 313–344.

Pierce, K.L., and Good, J.M., 1998, Pleistocene glaciations of the greater Yellowstone geo-ecosystem: Yellowstone Science, v. 6, no. 2, Spring Supplement, p. 44.

Pierce, K.L., Milbert, D.G, and Saltus, R.W., 1992, Geoid dome culminates on Yellowstone: Yellowstone hotspot fed by a thermal mantle plume?: EOS, Transactions of the American Geophysical Union, v. 73, p. 284.

Pierce, K.L., and Morgan, L.A., 1992, The track of the Yellowstone hot spot—Volcanism, faulting, and uplift, *in* Link, P.K., Kuntz, M.A., and Platt, L.B., eds., Regional geology of eastern Idaho and western Wyoming: Geological Society of America Memoir 179, p. 1–53.

Pierce, K.L., and Morgan, L.A., 2005, Asymmetrical features across the Yellowstone hotspot track and the northwest inclination of the Yellowstone plume [abs.]: Geological Society of America Abstracts with Programs, v. 37, no. 7, p. 127.

Pierce, K.L., Morgan, L.A., and Saltus, R.N., 2000, Yellowstone plume head—Postulated tectonic relations to the Vancouver slab, continental boundaries, and climate: U.S. Geological Survey Open-File Report 00-498, 39 p.

Pierce, K.L., Morgan, L.A., and Saltus, R.N., 2003, Yellowstone plume head—Postulated tectonic relations to the Vancouver slab, continental boundaries, and climate, *in* Bonnichsen, Bill, White, C.M., and McCurry, Michael, eds., Tectonic and magmatic evolution of the Snake River Plain volcanic province: Idaho Geological Survey Bulletin 30, p. 5–33.

Porter, S.C., Pierce, K.L., and Hamilton, T.D., 1983, Late Pleistocene glaciation in the Western United States, *in* Porter, S.C., ed., The late Pleistocene, v.1, of Wright, H.E., Jr., ed., Late Quaternary environments of the United States: Minneapolis, Minn., University of Minnesota Press, p. 71–111.

Pounds, N.J. 1990, An historical geography of Europe: Cambridge, England, Cambridge University Press, 484 p.

Reese, Rick, 1984, Greater Yellowstone—The national park and adjacent wildlands: Helena, Mont., Montana Magazine, Inc., 104 p.

Richards, M.A., Duncan, R.A., and Courtillot, V.E., 1989, Flood basalts and hot spot tracks—Plume heads and tails: Science, v. 246, p. 103–107.

Rodgers, D.W., Hackett, W.R., and Ore, H.T., 1990, Extension of the Yellowstone Plateau, eastern Snake River Plain, and Owyhee Plateau: Geology, v. 18, p. 1,138–1,141.

Rodman, Ann, Schovic, H.F., and Thomas, David, 1996, Soils of Yellowstone National Park: Yellowstone Center for Resources, Yellowstone National Park, Wyoming, YCR-NRSR-96-2, 324 p.

Sleep, N.H., 1990, Hotspots and mantle plumes—Some phenomenology: Journal of Geophysical Research, v. 95, no. B5, p. 6,715–6,736.

Sleep, N.H., 1997, Lateral flow and ponding of starting plume material: Journal of Geophysical Research, v. 102, no. B5, p. 10,001–10,012.

Sleep, N.H., 2002, Ridge-crossing mantle plumes and gaps in tracks: Geochemistry, Geophysics, Geosystems (G^3), v. 3, (2001GC000290), 33 p.

Smith, D.A., and Milbert, D.G., 1999, The GEOID96 high-resolution geoid height model for the United States: Journal of Geodesy, v. 73, no. 5, p. 219–236.

Smith, R.B., and Arabasz, W.J., 1991, Seismicity of the intermountain seismic belt, *in* Slemmons, D.B., Engdahl, E.R., Zoback, M.M., and Blackwell, D.D., eds., Neotectonics of North America: Boulder, Colo., Geological Society of America, Decade Map, v. 1, p. 185–228.

Smith, R.B., and Braile, L.W., 1993, Topographic signature, space-time evolution, and physical properties of the Yellowstone-Snake River Plain volcanic system——The Yellowstone hotspot, *in* Snoke, A.W., Steidtmann, J.R., and Roberts, S.M., eds., Geology of Wyoming: Geological Survey of Wyoming Memoir No. 5, p. 694–754.

Smith, R.B., and Siegel, L.J., 2000, Windows into the Earth—The geologic story of Yellowstone and Grand Teton National Parks: Oxford, Oxford University Press, 242 p.

Steinberger, B., 2000, Plumes in a convecting mantle: Models and observations for individual hotspots: Journal of Geophysical Research, v. 105, no. B5, p. 11,127–11,152.

Sturchio, N.C., Pierce, K.L., Morrell, M.T., and Sorey, M.L., 1994, Uranium-series ages of travertines and timing of the last glaciation in the northern Yellowstone area, Wyoming-Montana: Quaternary Research, v. 41, p. 265–277.

Thompson, G.A., 1998, Deep mantle plumes and geoscience vision, Geological Society of America, and presidential address: GSA Today, April 1996, p. 17–25.

Thompson, R.N., and Gibson, S.A., 1991, Subcontinental mantle plumes, hotspots, and pre-existing thinspots: London, Journal of the Geological Society, v. 148, p. 973–977.

Trettin, C.C., 1986, Characterization of soils in Yellowstone National Park—Final project report: Contract no. CX-1200-1-B027, L'Anse, Michigan, Michigan Technological University, Ford Forestry Center, 33 p. and appendixes, 153 p.

Turcotte, D.L., and Schubert, G., 1982, Geodynamics applications of continuum physics to geological problems: New York, Wiley, 450 p.

U.S. National Park Service and U.S. Forest Service, 1979, Greater Yellowstone cooperative regional transportation study—Regional assessment environmental report: Denver, Colo., National Park Service, many pages with maps.

U.S. Geological Survey, 1972a, Surficial geologic map of Yellowstone National Park: U.S. Geological Survey Miscellaneous Investigations Series Map I-710, scale 1:125,000.

U.S. Geological Survey, 1972b, Bedrock geologic map of Yellowstone National Park: U.S. Geological Survey Miscellaneous Geologic Investigations Series Map I-711, scale 1:125,000.

Varley, John, 1993, Saving the parts: Yellowstone Science, v. 1, no. 4, p. 13–16.

Waite, G.P., Smith, R.L., and Allen, R.L., 2006, VP and VS structure of the Yellowstone hotspot upper mantle from teleseismic tomography: Evidence for an upper mantle plume: Journal of Geophysical Research, v. 111, B04303, doi: 1029/2005JB003867.

White, D.E., Hutchinson, R.A., and Keith, T.E.C., 1988, The geology and remarkable thermal activity of Norris Geyser Basin, Yellowstone National Park, Wyoming: U.S. Geological Survey Professional Paper 1456, 84 p.

White, R.S., and McKenzie, D.P., 1989, Magmatism at rift zones—The generation of volcanic continental margins and flood basalts: Journal of Geophysical Research, v. 94, no. B6, p. 7,685–7,729.

Whitlock, Cathy, 1993, Postglacial vegetation and climate of Grand Teton and southern Yellowstone National Parks: Ecological Monographs, v. 63, no. 2, p. 173–198.

Whitlock, Cathy, and Bartlein, P.J., 1993, Spatial variations of Holocene climatic change in the Yellowstone region: Quaternary Research, v. 39, p. 231–238.

Wilson, J.T., 1963, A possible origin for the Hawaiian Islands: Canadian Journal of Physics, v. 41, p. 863–870.

Woese, C.R., Kandler, Otto, and Wheelis, M.L., 1990, Towards a natural system of organisms—Proposal for the domains Archaea, Bacteria, and Eucarya: Proceedings of the National Academy of Science, v. 87, p. 4,576–4,579.

Wolfe, J.A., Forest, C.E., and Molnar, Peter, 1998, Paleobotanical evidence on Eocene and Oligocene paleoaltitudes in mid-latitude western North America: Geological Society of America Bulletin, v. 110, p. 664–678.

Wright, G.A., 1984, People of the high country, Jackson Hole before the settlers: American University Studies, ser. XI, Anthropology/Sociology, v. 7, 181 p.

Yuan, H., and Dueker, K., 2005, Teleseismic P-wave tomogram of the Yellowstone plume: Geophysical Research Letters, v. 32, doi: 10.1029/2004GL022056.

Zoback, M.L., and Thompson, G.A., 1978, Basin and range rifting in northern Nevada—Clues from mid-Miocene rift and its subsequent offsets: Geology, v. 6, p. 111–116.

Movement of a Large Landslide Block Dated by Tree-Ring Analysis, Tower Falls Area, Yellowstone National Park, Wyoming

B

By Paul E. Carrara

Chapter B *of*
Integrated Geoscience Studies in the Greater Yellowstone Area—Volcanic, Tectonic, and Hydrothermal Processes in the Yellowstone Geoecosystem
Edited by Lisa A. Morgan

U.S. Geological Survey Professional Paper 1717

U.S. Department of the Interior
U.S. Geological Survey

Contents

Abstract 43
Introduction 43
Previous Work 44
Methods 45
Types of Disturbance in the Tower Falls Tree-Ring Record 47
The Tower Falls Tree-Ring Record 47
Was the Landslide Movement Triggered by an Earthquake? 50
Limitations of Tree-Ring Analyses 50
Conclusions 50
Acknowledgments 51
References Cited 51

Figures

1. Aerial photograph of the Tower Falls area 44
2. Photograph of a group of tilted Douglas fir trees at site 1 44
3. Photograph of tilted Douglas fir trees at the Calcite Springs overlook (site 3) 45
4. Types of tree-ring reactions to physical damage 45
5. Photograph of core from tree 6, showing an abrupt reduction in annual-ring width beginning in 1694 A.D. 47
6. Plots of tree-ring widths from 1650 to 1750 A.D. from trees at:
   6A. Site 1 48
   6B. Site 2 48
   6C. The Calcite Springs overlook (site 3) 49
7. Plot of tree-ring indices of Douglas fir near Gardner, Mont., and tree-ring widths from 1650 to 1750 A.D. at the Rainy Lake site 49

Table

1. Response in tree-ring record of Douglas fir trees in the Tower Falls area of Yellowstone National Park to the proposed 1693 or 1694 A.D. landslide event 46

Movement of a Large Landslide Block Dated by Tree-Ring Analysis, Tower Falls Area, Yellowstone National Park, Wyoming

By Paul E. Carrara[1]

Abstract

Tree-ring analysis can be a valuable tool to date geomorphic events in regions lacking long historical records. In this study, the latest detectable movement of a section of a large landslide block in the Tower Falls area of Yellowstone National Park, Wyoming, is dated by tree-ring analysis of Douglas fir trees (*Pseudotsuga menziesii* var. *glauca*) damaged by the event. The movement tilted many of the trees and damaged their root systems. Thirteen old, tilted Douglas fir trees, at three sites, were sampled within the section of the landslide block that moved during the life of these trees. In addition, 10 young, upright, undisturbed Douglas firs were also sampled at the sites in order to establish a minimum age for the movement. The oldest of the 10 young, upright trees had an age of about 135 years, indicating that the latest movement of the landslide block occurred prior to 1865 A.D. The youngest of the 13 old, tilted trees dated to the early 1600s, providing a maximum age for this latest landslide movement. Analysis of the tree-ring record of the older, tilted Douglas firs revealed an abrupt reduction in annual-ring width beginning in 1694 A.D. As no other period in the tree-ring record between 1865 and 1600 A.D. revealed such an abrupt reduction in annual-ring width, the landslide movement is thought to have occurred sometime between the end of the 1693 A.D. growing season and before the end of the 1694 A.D. growing season. Because Yellowstone National Park is within the Intermountain seismic belt, a zone of pronounced seismic activity, movement of the landslide block may have been caused by an earthquake at that time.

Introduction

Because many tree species can live for several centuries or more (Brown, 1996), tree-ring analysis can be a valuable tool to date various geomorphic events, such as landslides, earthquakes, floods, and avalanches in regions lacking long historical records. For example, during a landslide a tree may suffer damage—such as topping, tilting, impact, or root breakage—from ground shaking, breakage, or movement. This damage is recorded in the annual-ring record, commonly as an abrupt reduction in tree-ring width. In addition, tree-ring analysis can date such an event to within a year, whereas radiocarbon ages within the last few centuries have relatively large error limits. The purpose of this study is to date, by tree-ring analysis, the latest movement of a section of a large landslide block near the Tower Falls area of Yellowstone National Park.

The small, seasonal community of Tower Falls is located in north-central Yellowstone National Park at an elevation of 1,960 m (fig. 1). A large landslide block is present immediately north of Tower Falls. This landslide block, about 5 km^2, is bounded on the northeast by the Yellowstone River, on the southeast by Tower Creek, on the northwest by Lost Creek, and on the southwest by an unnamed stream. Elevations range from about 1,830 m along the Yellowstone River to about 2,150 m at the highest point on the landslide block. Steep, step-like features on the block appear to be old scarps that separate individual blocks within the larger block. One prominent step is 20 to 30 m in height and dips 25°.

The landslide block is mantled by a thin covering of glacial deposits about 20,000 to 30,000 years old (Pierce, 1974). The glacial deposits are underlain by about 200 m of Lava Creek Tuff (Prostka and others, 1975) dated, by the $^{40}Ar/^{39}Ar$ method, at about 639,000 years old (Lanphere and others, 2002). Exposed along the Yellowstone River is a sequence of Pleistocene sediments underlying the Lava Creek Tuff (Pierce, 1974) that may contain the slip plane on which the landslide block moved. The initial age of the landslide block is presently unknown, but it may have initially formed in the late Pleistocene soon after deglaciation and has experienced recurrent movements since that time. A section of the road from Tower Falls north for about 0.5 km is presently subsiding (C.S. Dewey, oral commun., 2001). Understanding the history of this landslide block is important because Yellowstone National Park receives millions of

[1] U.S. Geological Survey, Mail Stop 980, Denver Federal Center, Denver, CO 80225.

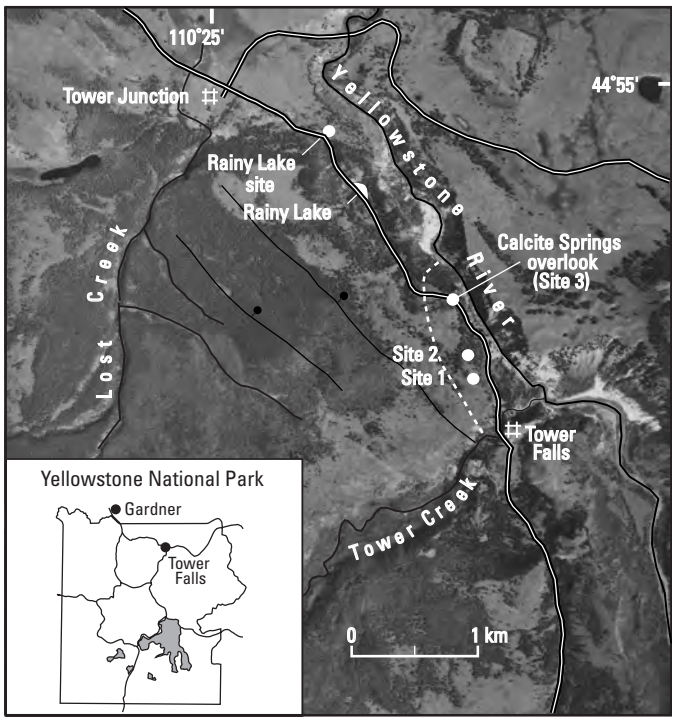

Figure 1. Aerial photograph of the Tower Falls area showing landslide block. Dashed white line shows area of trees affected by latest movement. Lines with black circles represent down-to-the-northeast faults on the geologic map of Prostka and others (1975) and are interpreted in this report as landslide scarps.

visitors each year, and its roads are heavily used. It is the area near this section of subsiding road and to the west that is the focus of this study.

In the study area, Douglas fir (*Pseudotsuga menziesii* var. *glauca*) is the dominant tree species. The trees can be divided into three age groups. The first group consists of smaller, younger, upright Douglas firs, established after the latest movement of the landslide block. These trees range between 15 and 50 cm in diameter, and 5 to 20 m in height. The second group consists of large, older Douglas firs that are tilted (fig. 2) as a consequence of the latest landslide movement. The trunks of these trees are tilted for a height of 5 to 10 m, whereas the upper parts of many of these trees are vertical. These tilted trees range between 60 and 130 cm in diameter, and about 15 to 30 m in height; angles of tilt ranged from 8° to 47°. The third group consists of standing dead trees that are tilted throughout their entire length as a result of the landslide movement. These trees range between 60 and 110 cm in diameter, and about 15 to 30 m in height; angles of tilt range from 10° to 27°. An excellent example of these large, tilted trees (groups 2 and 3) can be seen at the Calcite Springs overlook (fig. 3). These large, old, tilted Douglas firs, both alive and dead, contrast markedly with the smaller, younger, upright trees.

Figure 2. Photograph of a group of tilted Douglas fir trees, at site 1, on the Tower Falls landslide block. Tree on left is approximately 28 m in height.

Previous Work

Tree-ring analysis has been used to date various geomorphic events, such as landslides, earthquakes, and snow avalanches, in several ways. On the simplest level, the ages of the trees themselves supply important information. For instance, the oldest undisturbed tree on a landslide provides a minimum age of landslide movement (McGee, 1893; Fuller, 1912; Jibson and Keefer, 1988; Logan and Schuster, 1991).

One of the first investigators to use tree-ring analysis to date landslides was McGee (1893). On landslides near Reelfoot Lake, Tennessee, caused by the New Madrid earthquakes of 1811 and 1812, McGee (1893) noted trees "...frequently thrown out of the vertical." McGee (1893) observed that the trunks of trees 200 or more years old were inclined from base to top. The trunks of trees 100 to 150 years old were inclined, and the upper parts of the trees were vertical. Finally, undisturbed, vertical trees, 70 or 75 years in age, established a minimum age for the landslide movement. In 1904, Fuller (1912) studied the ages of upright and tilted trees on landslides caused by the New Madrid earthquakes along the bluffs of the Mississippi River. He determined that "...the greater part of the upright growth on the disturbed surfaces [landslides] is fairly uniform and a little less than 100 years of age, trees of greater age being in general tilted and partly overthrown."

A more complex analysis of landslide movement involves the interpretation of the tree rings in disturbed trees. Shroder (1978) was able to use tree-ring analysis to date recurrent movement on a rock-glacier-like deposit on the Table Cliffs Plateau in Utah. Reeder (1979) used tree-ring analysis to date movement of landslides in the Anchorage, Alaska, area and was able to correlate these movements with earthquakes in the region. Jensen (1983) was able to date episodic landslide movement in the upper Gros Ventre landslide of Wyoming

by tree-ring analysis. Hupp and others (1987) used tree-ring analysis to determine the magnitude and frequency of debris flows in many of the drainages of Mount Shasta, California. Williams and others (1992) investigated four landslides in the Seattle area—using tree-ring analysis, they were able to demonstrate that the four landslides were probably of the same age and, hence, were seismically induced. Fleming and Johnson (1994) used the tree-ring record of several trees on a landslide in the Cincinnati, Ohio, area to date movement to 1958, following near-record precipitation in 1957.

In the above-cited studies, several kinds of tree-ring anomalies were observed. The most common anomaly observed was an abrupt reduction in annual-ring width either for several years or an extended period (fig. 4). Other anomalies include, (1) discontinuous or missing rings due to severe damage, (2) the formation of reaction wood on the underside of tilted conifers, (3) scars, formed by the impact of the tree by an object, such as a dislodged boulder or falling tree, and (4) an abrupt increase in annual-ring width due to an improvement in environment, such as an increase in sunlight because surrounding trees were felled by landslide movement.

Methods

Thirteen live, tilted Douglas fir trees were sampled at three sites near Tower Falls at the southeastern end of the landslide block (fig. 1) near the section of road known to be subsiding (C.S. Dewey, oral commun., 2001). Sites 1 and 2 are in the area above the "Overhanging Cliff," site 3 is at the Calcite Springs overlook. Because all these trees are tilted, landslide movement likely occurred within the lifetime of the trees. In addition, attempts were made to sample several of the standing, tilted dead trees at the sites with the goal of obtaining a longer record. However, the interiors of these trees were rotten, and no cores were recovered. In order to establish a minimum age for the landslide movement, 10 young, upright, undisturbed Douglas fir trees were also sampled near sites 1 and 2. Finally, three Douglas firs were sampled northwest of Rainy Lake, about 2 km northwest of the section of subsiding road and that section of the landslide near Tower Falls thought to have been subjected to the latest movement (fig. 1).

Many of the Douglas firs were sampled in July 1999, with a 40-cm-long, 5-mm-diameter increment borer (an increment borer is a hand tool with a hollow drill bit that is screwed into a tree and allows the removal of a thin cylinder of wood from the tree with minimal damage). Because of the large diameters of some of the trees, the 40-cm bit did not penetrate the tree deep enough to include the pith. Therefore, several trees were cored again in August 2000 with a 50-cm-long increment borer. For the larger tilted trees, two cores were taken, one on the upper side of the tree, the other on the lower side. For smaller, younger, upright Douglas firs, two opposing radii were collected.

Figure 3. Photograph of tilted Douglas fir trees at the Calcite Springs overlook (site 3). Tree on right is about 16 m in height.

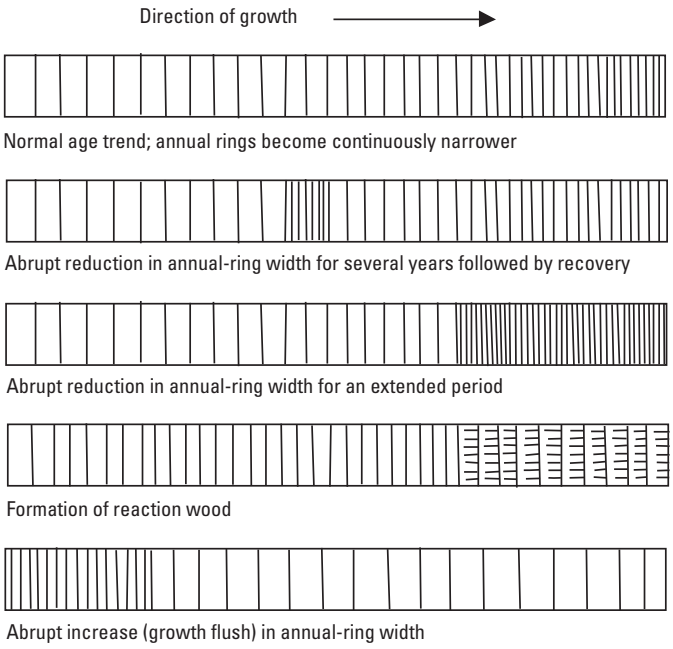

Figure 4. Drawing showing the type of reactions in the tree-ring record to physical damage (after Kienast and Schweingruber, 1986).

Table 1. Response in tree-ring record of Douglas fir trees in the Tower Falls area of Yellowstone National Park to the proposed 1693 or 1694 A.D. landslide event.

[M, missing ring; NR, narrow ring(s), less than 50 percent the width of the 1693 A.D. annual ring; --- , tree-ring sequence in core does not extend back to 1694 A.D.]

	Tree no./ core / year collected	Innermost ring in core (A.D.)	Estimated year (A.D.) tree germinated	Diameter (cm)	Angle of tilt (degrees)	Response to 1693 or 1694 A.D. event
Site 1	1/A/99	1799	1500	130	8	---
	1/B/99	1732				---
	1/A/00	1717				---
	1/B/00	1648				NR 1694-1700
	2/A/99	1800?	1620	72	32	---
	2/B/99	1692				M 1694, NR 1695-1701
	2/N/00	1641				M 1694, NR 1695-1709
	3/A/99	1612	1590	89	47	M 1694, NR 1695-1701
	3/B/99	1760				---
	3/B/00	1684				M 1694, NR 1695-98
	4/N/99*	1875	?	81	25	---
Site 2	6/A/99	1663	1620	86	20	NR 1694-98
	6/B/99	1667				NR 1694-95
	7/A/99	1669	1630	95	20	NR 1694-97
	7/B/99	1676				NR 1694-97
	8/A/99	1776	1620	69	18	---
	8/B/99	1650				NR 1694-98
	8/N/00	1653				NR 1694-96
	9/A/99	1646	1610	84	14	NR 1694-97
	9/N/00	1663				NR 1694-98
Site 3	16/A/99	1641	1610	60	32	NR 1694-97
	16/B/99	1652				NR1694-98
	17/A/99	1636	1590	62	32	NR 1694-98
	17/B/99	1610				NR 1694-98
	24/N/00*	1780	?	61	25	---
	25/B/00	1696	1570	73	10	---
	25/E/00	1615				NR 1694-1701
	27/A/00	1625	1590	103	21	NR 1694-97
	27/B/00	1664				NR 1694-97
	27/S/00	1630				NR 1694-97

* Cores from trees 4 and 24 are only partial cores because these trees had heart rot.

The cores were prepared using standard procedures as discussed in Stokes and Smiley (1968). In the field, the cores were placed in soda straws. Upon return to the laboratory the cores were placed in grooved, redwood drying boxes that allow the cores to dry with minimal twisting and curling. The cores were left in these boxes for several weeks to dry completely. The cores were then glued into a semicircular groove in a small board and sanded with progressively finer grits to a fine finish (600 grit). Finally, the cores were rubbed to a high polish with fine steel wool.

The polished cores were then inspected under a binocular microscope (6, 12, and 25×) for signs of disturbance in their tree-ring records. One year was assigned to each ring counted. In temperate regions a tree will add (grow) one ring every year. The annual ring consists of two parts, earlywood and latewood. Earlywood is produced in the early part of the growing season and is characterized by large, porous, thin-walled cells. Latewood is produced in the latter part of the growing season and is characterized by small, thick-walled cells that commonly have a darker color than earlywood cells (Panshin and de Zeeuw, 1970). It is the sharp contrast between the last-formed latewood cells of one year and the first-formed earlywood cells of the following season that distinguishes the boundary of the annual ring.

False annual rings were also noted in several cores and result from a cold period during a growing season. False annual rings can be distinguished from true annual rings because cells composing the latewood in false annual rings grade to the inside and outside into more porous tissue. In true annual rings the transition from the latewood of one year to the earlywood of the next year is abrupt (Panshin and de Zeeuw, 1970).

Types of Disturbance in the Tower Falls Tree-Ring Record

In this study, two signs of disturbance in the tree-ring record were detected in the tilted trees that were sampled. Most commonly the trees displayed an abrupt reduction in annual-ring width for several years (fig. 4). In addition, at the time when the tree-ring record of most trees began an abrupt reduction in annual-ring width, two trees did not form an annual ring (missing ring). Reaction wood (commonly formed on the underside of tilted conifers) and scars (formed by the impact of an object, such as a dislodged boulder) are readily recognizable in cross sections, they are difficult to identify in cores. I looked for evidence of reaction wood and scars in the cores collected for this study, but none were detected. This is due in part because the core samples show only a very small part of each annual ring, as compared to cross sections, which display the entire circumference of each ring.

A reduction in annual-ring width for several years or more can be the result of injury due to a geomorphic event, such as a landslide or earthquake (Shroder, 1978; Meisling and Sieh, 1980). Damage to the root system, loss of a major limb, or topping can all result in an abrupt reduction in annual-ring width. Therefore, at the study sites, the initial year of decreased growth (table 1) provides an estimate of the date of landslide movement. Movement could have taken place between the end of the previous growing season and during the growing season of the year in which the first narrow ring is produced.

Missing annual rings can result when a tree is severely damaged by landslide movement (Shroder, 1978). These damaged trees may not form annual rings in a given year or period of years (Panshin and de Zeeuw, 1970). In this study, the presence of missing annual rings (table 1) was detected by cross-dating (recognition of commonly shared distinctive annual rings of known age) with nearby trees. Particularly distinctive narrow annual rings that were useful for cross-dating are: 1646, 1656, 1678, 1708, 1712, 1717–18, 1721–22, 1748, 1752, 1800, 1834, 1846, 1848, 1865, 1872, 1891, 1901, 1919, 1934, and 1936 A.D.

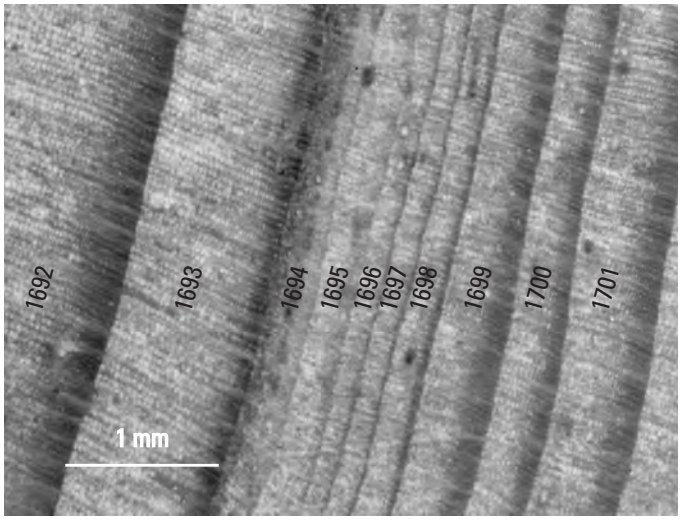

Figure 5. Photograph of core from tree 6 showing an abrupt reduction in annual-ring width beginning in 1694 A.D.

The Tower Falls Tree-Ring Record

Of the 10, upright, undisturbed trees cored in this study, the oldest had 120 annual rings and the pith was present in the core. Because the tree was cored at chest height (about 125 cm), an additional 15 years was added to the ring count to account for the years it took the tree to grow to this height. Thus, the age of the tree is estimated to be about 135 years. This age provides a minimum date for the latest movement of this section of the landslide, indicating that the movement occurred prior to 135 years ago (1865 A.D.). However, this age is probably a minimum by a number of years. The younger, upright, undisturbed trees were found in forested areas that are subject to occasional forest fires, such as those that swept through much of Yellowstone National Park during the summer of 1988. In contrast, the older, tilted trees were in more open areas with greater distances between trees and, hence, were less susceptible to forest fires.

The youngest of the 13 old, tilted trees is estimated to have germinated in the early 1600s (table 1). The years of germination of the tilted trees presented in table 1 are estimates for two reasons. First, because the pith was not present in the majority of cores collected, the number of missing annual rings between the end of the core and pith was estimated based on the curvature of the annual rings near the end of the core (Applequist, 1958). Secondly, because the trees were cored at chest height (about 125 cm), an additional 15 years was added to account for those years the tree took to grow to the sampling height. The youngest of the older, tilted trees date from the early 1600s—this establishes a maximum age for the landslide movement.

Inspection of the tree-ring record of the larger, older, tilted Douglas firs (13 trees) between 1600 and 1865 A.D. for which the recovered core included the late 1600s (11

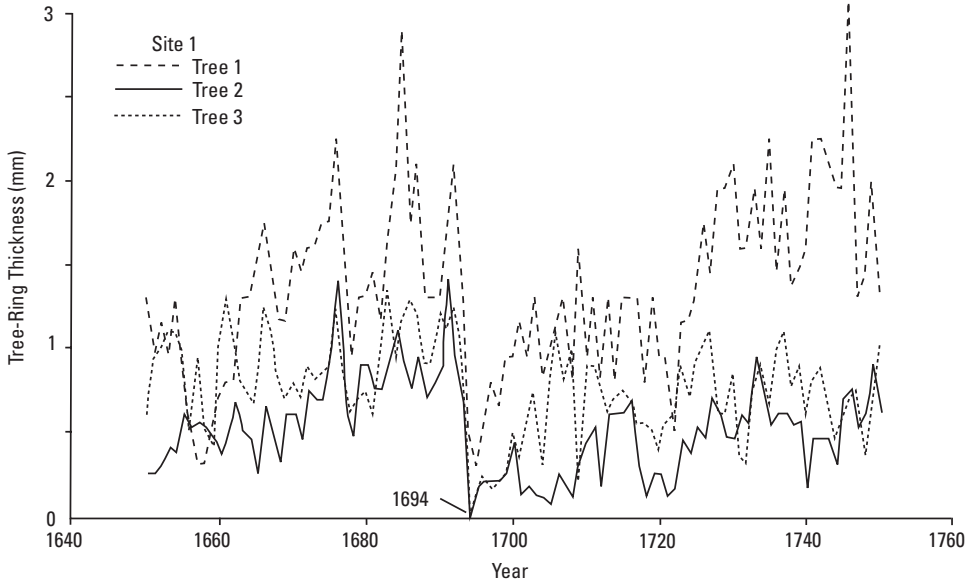

Figure 6*A*. Plot of tree-ring widths from 1650 to 1750 A.D. from trees at site 1, showing abrupt reduction in annual-ring width beginning in 1694 A.D.

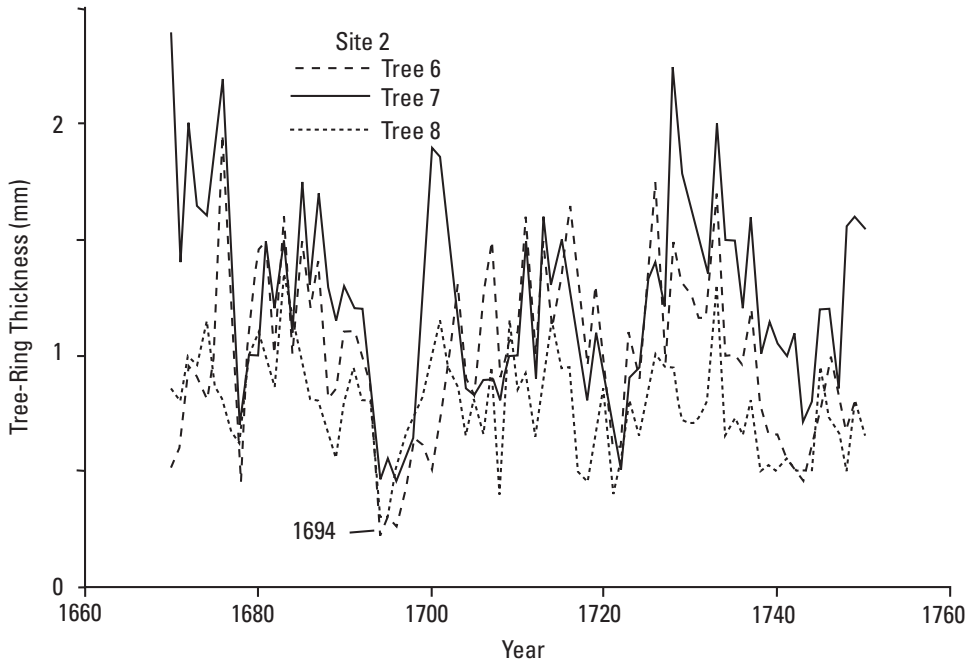

Figure 6*B*. Plot of tree-ring widths from 1650 to 1750 A.D. from trees at site 2, showing abrupt reduction in annual-ring width beginning in 1694 A.D.

trees), revealed an abrupt reduction (greater than 50 percent) in annual-ring width beginning in 1694 A.D (figs. 5, 6*A*, 6*B* and 6*C*; table 1). Because no other period in the tree-ring record revealed such a dramatic reduction in annual-ring width, the landslide movement is thought to have occurred after the growing season in 1693 or during the growing season of 1694 A.D.

The tree-ring response in nine of the sampled trees to the 1693 or 1694 A.D. event consisted of the formation of narrow annual rings beginning in 1694 A.D. and continuing for 2 to 8 years (table 1). However, the response of the trees was not necessarily uniform along opposing radii. Tree 6 produced narrow annual rings from 1694 to 1695 A.D. along one radius and narrow annual rings from 1694 to 1698 A.D. along the opposing radius.

Missing annual rings were noted in two trees (2 and 3) in which the 1694 A.D. annual ring was not formed (table 1). These trees began to form narrow annual rings in 1695 A.D. and continued to produce narrow annual rings for several years to as many as 15 years. For instance, in tree 2, two radii, whose record included the late 1690s, are missing the 1694 A.D. annual ring. Beginning in 1695, one radius formed a series of narrow annual rings until 1701 A.D., whereas the other radius produced a series of narrow annual rings until 1709 A.D. (table 1).

The abrupt reduction in annual-ring width in 1694 A.D. is thought to have been caused by landslide movement and not by climatic variations for several reasons. The reduction in annual-ring width beginning in 1694 A.D. displayed by the tilted Douglas firs sampled in this study is not reflected in a

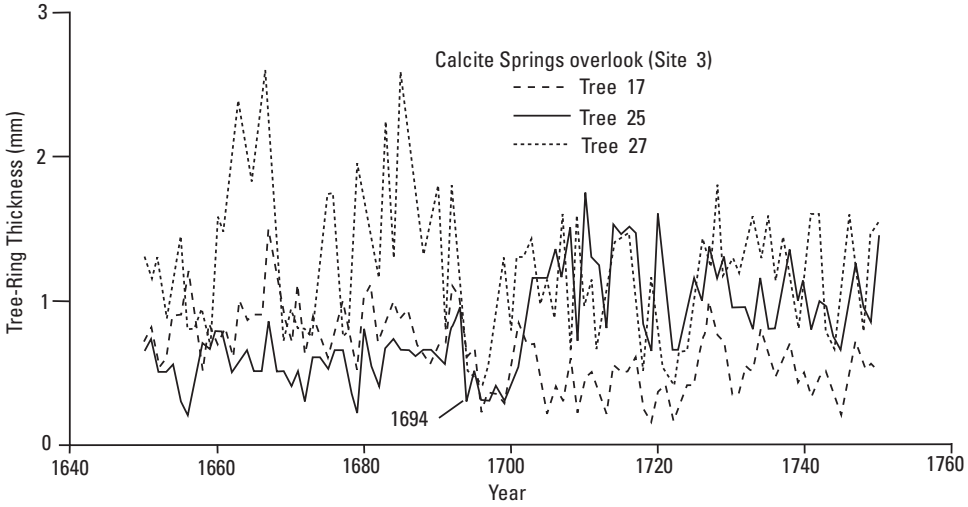

Figure 6*C*. Plot of tree-ring widths from 1650 to 1750 A.D. from trees at the Calcite Springs overlook (site 3), showing abrupt reduction in annual-ring width beginning in 1694 A.D.

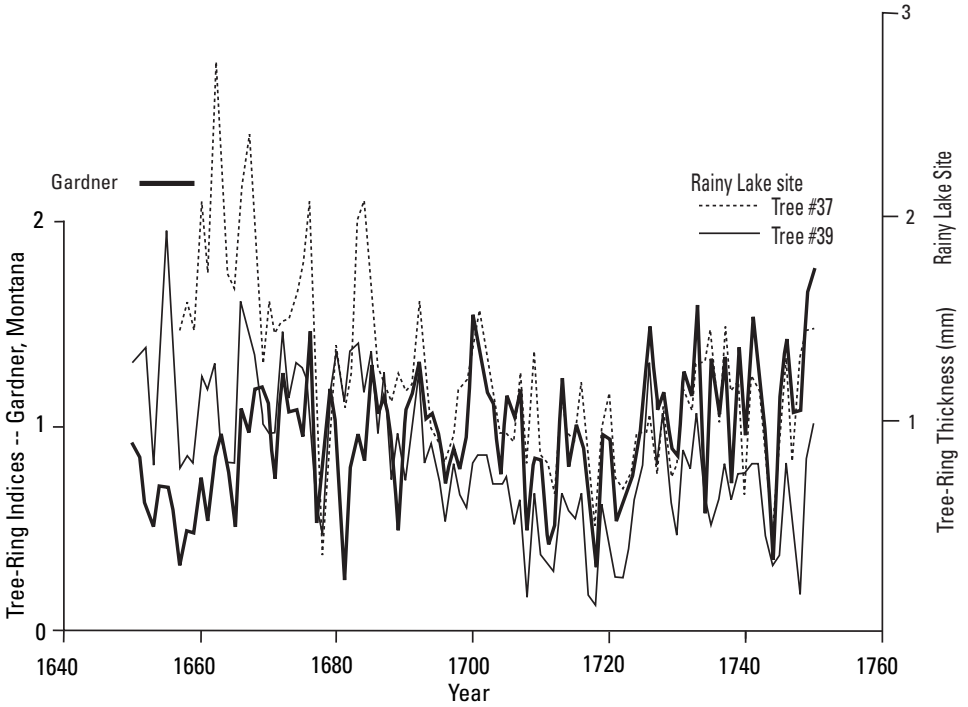

Figure 7. Plot of tree-ring indices of Douglas fir near Gardner, Mont. (after Drew, 1975), and plot of tree-ring widths from 1650 to 1750 A.D. from trees at the Rainy Lake site. Note the absence of narrow rings at 1694 A.D., as would be expected in trees unaffected by the landslide movement of 1693 or 1694 A.D.

500-year tree-ring chronology of Douglas firs at a site near Gardner, Mont. (fig. 7) (Drew, 1975), about 30 km northwest of the Tower Falls area, or in the ring widths of trees sampled at the Rainy Lake site (fig. 7), about 2 km north of the Calcite Springs overlook, or in whitebark pines (*Pinus albicaulis*) at a site near Dunraven Pass, approximately 10 km to the south of the study sites (John King, oral commun., 1999). If the 1694 A.D. response in the tree-ring record were climatically induced, it should be present over a broad area, including these other sites.

In addition, the response of the trees to the 1693 or 1694 A.D. event is typical of trees subject to physical damage and is not a typical climatic signature. Trees in a given area that exhibit a reduction in annual-ring widths caused by climatic factors have a more uniform response; hence, they generally recover at about the same year, and the climatic response is present over a broad region (Jacoby and others, 1988)—in this case, away from the landslide. Growth-rate reductions caused by physical damage may last from as little as 1 year to more than 20 years and may contain many missing rings (Shroder, 1978; Carrara, 1979). In this study, the tree-ring response to the 1693 or 1694 A.D. event lasted from as little as 2 years to as many as 16 years. In addition, prolonged growth suppression usually cannot be attributed to drought, which generally causes acute, diminished annual-ring growth for a single year (Jacoby and others, 1988).

The abrupt reduction in annual-ring width in 1694 A.D. could be caused by other factors, such as insect infestation or fire, but this seems unlikely. The sampled trees are clearly tilted, an effect not associated with either insect infestation or

fire. Furthermore, the Douglas firs at the nearby Rainy Lake site do not display the marked reduction in annual-ring width beginning in 1694 A.D. (fig. 7). If the 1694 A.D. response in the tree-ring record were caused by an insect infestation, it should be present over a broader region, similar to a climatic effect and would include the Rainy Lake site. In addition, no evidence of charred wood or fire scars was found in the sampled trees. Finally, the fact that the tilted trees are growing on a landslide block is also strong evidence for landslide-induced damage.

Was the Landslide Movement Triggered by an Earthquake?

The Yellowstone region is within the Intermountain seismic belt, a zone of pronounced seismic activity, that extends north from southern Nevada through northwestern Arizona, Utah, eastern Idaho, western Wyoming, and northwestern Montana (Smith and Sbar, 1974; Stickney and Bartholomew, 1987). The largest historic earthquake (magnitude 7.5) ever recorded in the Intermountain seismic belt occurred in the Yellowstone region during the night of August 17, 1959 (Doser, 1985). This earthquake, centered in the Hebgen Lake area of southwestern Montana, about 70 km west of the study area, was felt throughout an area of 1,500,000 km^2 (Witkind and Stickney, 1987) and caused considerable damage. Near Hebgen Lake, it released a large rockslide that overran a campground and killed 26 people, burying them under 21 million m^3 of debris (Witkind and Stickney, 1987). Other landslides in the Yellowstone region could have been caused by large prehistoric earthquakes. Was initial failure of the large landslide block triggered by an earthquake, and was latest movement of the section in the Tower Falls area in 1693 or 1694 A.D. earthquake induced? Because of the pronounced seismic activity in this region one or both hypotheses are possible.

Limitations of Tree-Ring Analyses

Several limitations of the detection of landslide events by tree-ring analyses became apparent in this study. First, in order for the event to be recorded in the tree-ring record, the event must be large enough to damage the trees, such as by topping, tilting, impact, or root breakage.

Secondly, the age of the trees themselves may be a limitation. Although ages of Douglas firs can exceed 1,000 years (Brown, 1996), the oldest tree in this study (tree 17) had an innermost ring date of 1610, and only four trees had records extending back prior to 1640 (table 1). Hence, information concerning landslide movements could only be extended back to about 1650 A.D. However, it should be noted that no significant disturbance other than that of the 1693 or 1694 A.D. event is recorded in the tree-ring record of the Tower Falls Douglas firs at the three sites investigated in this study.

In addition, damage to trees by landslides and other events, such as earthquakes and snow avalanches, may cause an additional limitation on the age of the trees. Damaged trees may not recover at all or be so slow to recover that they may be at a competitive disadvantage with other nearby trees that sustained little or no damage. This disadvantage may in time lead to an earlier-than-normal death. Thus, several decades after an event, those trees that suffered the most damage—and hence have the best evidence of the event in their tree-ring record—are no longer alive.

At a site in the Gravelly Range, about 100 km west of the study area, 11 Douglas firs, including one standing dead tree, were sampled for information concerning the relation between landslide movement and earthquake events (O'Neill and others, 1994; Carrara and O'Neill, 2003). Only the dead tree showed significant tree-ring evidence of a 1926 landslide movement believed to be related to the 1925 Clarkson, Mont., earthquake (magnitude 6.75), about 175 km northwest of Tower Falls. None of the live trees showed any evidence of this event. The dead tree was heavily damaged and tilted by landslide movement and formed wide annual rings of reaction wood for several years before entering a period of reduced growth rate (narrow annual rings). The tree died in 1932 A.D., yet it remained standing for 60+ years before it was cross-sectioned for analysis. Hence, it may be worthwhile to sample dead trees at a given site and cross-date them with live trees at the same site.

Finally, another limitation of tree-ring analysis is that, while a tree is recovering from damage sustained by one landslide event and forming very narrow annual rings, it may be hard to detect a subsequent landslide event. For example, in this study, the response of tree 2 along one radius lasted from 1694 to 1709 A.D.; this tree is missing the annual ring for 1694 A.D. and shows a marked reduction in annual-ring width from 1695 to 1709 A.D. (table 1). Subsequent landslide events, if they had occurred during the 1694 to 1709 A.D. period, would not have been detectable in this tree-ring sequence because this tree was already forming very narrow annual rings.

Conclusions

The majority of the large, tilted Douglas fir sampled in this study on the section of landslide block near Tower Falls recorded an abrupt reduction in annual-ring width that began in 1694 A.D and lasted for 2 to 16 years. This reduction in annual-ring width is interpreted to indicate the latest movement of the landslide sometime between the end of the 1693 A.D. growing season and during the 1694 A.D. growing season. This interpretation is based on several factors. (1) The age of the oldest upright, undisturbed tree indicates

that the latest landslide movement occurred prior to 1865 A.D. (2) The age of the youngest, tilted, disturbed tree indicates that this landslide movement occurred after the early 1600s. (3) The most severe and long-lasting reduction in annual-ring width between 1600 and 1865 A.D. began in 1694 A.D. (4) A tree-ring chronology of Douglas fir at a site near Gardner, Mont. (Drew, 1975), about 30 km northwest of the Tower Falls area, as well as trees at two other nearby sites, do not display any significant climate-related reduction in annual-ring width during the 1690s A.D. Because the Yellowstone region is in a seismically active zone, it is possible that an earthquake triggered this landslide movement.

Although the use of tree-ring analysis to date various geologic events or processes has its limitations, the method can be a valuable tool to date events in regions lacking long historical records. In this study, ages of the trees sampled provided information concerning possible landslide movement back to about 1650 A.D. No disturbance other than that of the 1693 or 1694 A.D. event is recorded in the tree-ring record of the Tower Falls Douglas firs. These results suggest that the approach used in this study could be applied to paleolandslide and paleoseismological investigations in forested regions throughout the Rocky Mountain region.

Acknowledgments

The author thanks K.M. Haller, L.A. Morgan, and S.F. Personius (U.S. Geological Survey, Denver), K.L. Pierce (U.S. Geological Survey, Bozeman), and E. Williams Clark (U.S. Park Service, Yellowstone) whose knowledge and ideas contributed to this paper. This manuscript benefited substantially from reviews by F.C. Brunstein, D.R. Muhs, and R.R. Shroba (U.S. Geological Survey, Denver).

References Cited

Applequist, M.B., 1958, A simple pith locator for use with off-center increment cores: Journal of Forestry, v. 56, p. 141.

Brown, P.M., 1996, Oldlist: A database of maximum tree ages, *in* Dean, J.S., Meko, D.M., and Swetnam, T.W., eds., Tree rings, environment, and humanity: Radiocarbon, p. 727–731.

Carrara, P.E., 1979, The determination of snow avalanche frequency through tree-ring analysis and historical records at Ophir, Colorado: Geological Society of America Bulletin, v. 90, p. 773–780.

Carrara, P.E., and O'Neill, J.M., 2003, Tree-ring dated landslide movements and their relationship to seismic events in southwestern Montana: Quaternary Research, v. 59, p. 25–35.

Doser, D.I., 1985, Source parameters and faulting processes of the 1959 Hebgen Lake, Montana, earthquake sequence: Journal of Geophysical Research, v. 90, p. 4,537–4,555.

Drew, L.G., ed., 1975, Tree-ring chronologies of western America, Washington, Oregon, Idaho, Montana, and Wyoming: Tucson, Laboratory of Tree-Ring Research, University of Arizona, v. 5, 45 p.

Fleming, R.W., and Johnson, A.M., 1994, Landslides in colluvium: U.S. Geological Survey Bulletin 2059-B, 24 p.

Fuller, M.L., 1912, The New Madrid earthquake: U.S. Geological Survey Bulletin 494, 119 p.

Hupp, C.R., Osterkamp, W.R., and Thornton, J.L., 1987, Dendrogeomorphic evidence and dating of recent debris flows on Mount Shasta, Northern California: U.S. Geological Survey Professional Paper 1396-B, 39 p.

Jacoby, G.C., Jr., Sheppard, P.R., and Sieh, K.E., 1988, Irregular reoccurrence of large earthquakes along the San Andreas fault: Evidence from trees: Science, v. 241, p. 196–199.

Jensen, J.M., 1983, The Upper Gros Ventre landslide of Wyoming: A dendrochronology of landslide events and possible mechanics of failure: Geological Society of America Abstracts with Programs, v. 15, no. 5, p. 387.

Jibson, R.W., and Keefer, D.K., 1988, Landslides triggered by earthquakes in the central Mississippi Valley, Tennessee, and Kentucky: U.S. Geological Survey Professional Paper 1336-C, p. 1–24.

Kienast, F., and Schweingruber, F.H., 1986, Dendroecological studies in the Front Range, Colorado, U.S.A.: Arctic and Alpine Research, v. 18, p. 277–288.

Lanphere, M.A., Champion, D.E., Christiansen, R.L., Izett, G.A., and Obradovich, J.D., 2002, Revised ages for tuffs of the Yellowstone Plateau volcanic field: Assignment of the Huckleberry Ridge Tuff to a new geomagnetic polarity event: Geological Society of America Bulletin, v. 114, no. 5, p. 559–568.

Logan, R.L., and Schuster, R.L., 1991, Lakes divided: The origin of Lake Crescent and Lake Sutherland, Clallam County, Washington: Washington Division of Geology and Earth Resources, Washington Geology, v. 19, p. 38–42.

McGee, W.J., 1893, A fossil earthquake: Geological Society of America Bulletin, v. 4, p. 411–414.

Meisling, K.E., and Sieh, K.E., 1980, Disturbance of trees by the 1857 Fort Tejon earthquake, California: Journal of Geophysical Research, v. 85, no. B6, p. 3,225–3,238.

O'Neill, J.M., LeRoy, T.H., and Carrara, P.E., 1994, Preliminary map showing Quaternary faults and landslides in the Cliff Lake quadrangle, Madison County, Montana: U.S. Geological Survey Open-File Report 94-198, scale 1:24,000.

Panshin, A.J., and de Zeeuw, C., 1970, Textbook of wood technology (3d ed., v. 1): New York, McGraw-Hill, 705 p.

Pierce, K.L., 1974, Surficial geologic map of the Tower Falls quadrangle and part of the Mount Wallace quadrangle, Yellowstone National Park, Wyoming and Montana: U.S. Geological Survey Miscellaneous Geologic Investigations Map I-647, scale 1:62,500.

Prostka, H.J., Blank, H.R., Jr., Christiansen, R.L., and Ruppel, E.T., 1975, Geologic map of the Tower Junction quadrangle, Yellowstone National Park, Wyoming and Montana: U.S. Geological Survey Geologic Quadrangle Map GQ-1247, scale 1:62,500.

Reeder, J.W., 1979, The dating of landslides in Anchorage, Alaska—A case for earthquake-triggered movements: Geological Society of America Abstracts with Programs, v. 11, no. 7, p. 501.

Shroder, J.F., Jr., 1978, Dendrogeomorphological analysis of mass movement on Table Cliffs Plateau, Utah: Quaternary Research, v. 9, p. 168–185.

Smith, R.B., and Sbar, M.L., 1974, Contemporary tectonics and seismicity of the Western United States with emphasis on the Intermountain seismic belt: Geological Society of America Bulletin, v. 85, p. 1,205–1,218.

Stickney, M.C., and Bartholomew, M.J., 1987, Seismicity and late Quaternary faulting of the northern Basin and Range Province, Montana and Idaho: Seismological Society of America Bulletin, v. 77, p. 1,602–1,625.

Stokes, M.A., and Smiley, T.L., 1968, An introduction to tree-ring dating: Chicago, University of Chicago Press, 73 p.

Williams, P.L., Jacoby, G.C., and Buckley, B., 1992, Coincident ages of large landslides in Seattle's Lake Washington: Geological Society of America Abstract with Programs, v. 24, no. 5, p. 90.

Witkind, I.J., and Stickney, M.C., 1987, The Hebgen Lake earthquake area, *in* Beus, S.S., ed., Centennial Field Guide: Boulder, Colorado, Rocky Mountain Section, Geological Society of America, v. 2, p. 89–94.

Reconnaissance Study of Pleistocene Lake and Fluvial Deposits In and Near Ancestral Yellowstone Lake, Wyoming

C

By J.D. Love, John M. Good, and D.G. Browne

Chapter C *of*
Integrated Geoscience Studies in the Greater Yellowstone Area—Volcanic, Tectonic, and Hydrothermal Processes in the Yellowstone Geoecosystem
Edited by Lisa A. Morgan

Professional Paper 1717

U.S. Department of the Interior
U.S. Geological Survey

Foreword

This reconnaissance study of the Pleistocene lake and fluvial sediments in and near the ancestral Yellowstone Lake in Yellowstone National Park (the Park) was begun in 1956 by J.D. Love, joined by John M. Good, Chief Park Naturalist-Geologist of the Park, in a cooperative project in 1963, and completed in 1967. It then went through technical review by G.M. Richmond, K.L. Pierce, and H.E. Malde of the U. S. Geological Survey (USGS).

At the time the original report was completed, no modern topographic maps were available for this area so key localities were only approximately located. Coincidentally, near the end of the field work, the National Aeronautics and Space Administration (NASA) proposed and financed a major program that included (1) constructing modern topographic maps on which new geologic mapping was completed and (2) making related and adequately financed geological studies in the Park, with helicopter support and a staff of experienced field geologists. It seemed likely that our reconnaissance studies would be duplicated and (or) replaced by more sophisticated studies—so this report was withdrawn in 1968.

During the subsequent 30 years, seven chapters in the USGS/NASA Professional Paper 729 volume (Baker, 1976; Christiansen, 2001; Christiansen and Blank, 1972; Love and Keefer, 1975; Pierce, 1979; Ruppel, 1972; Smedes and Prostka, 1972), many 15-minute geologic quadrangle maps (Blank, 1974; Christiansen, 1974, 1975; Christiansen and Blank, 1974a, 1974b, 1975; Christiansen and others, 1978; Prostka, Ruppel, and Christiansen, 1975; Prostka, Smedes, and Christiansen, 1975; Prostka and others, 1975; Smedes and others, 1989) (fig. 1), one general geologic map of the Park (U. S. Geological Survey, 1972), and one general geologic map of the Park and surrounding areas (Christiansen, 2001, pl. 1) were published. However, none of these reports attempted to duplicate or expand on data on the Pleistocene lake deposits—so the authors have, for the present report, resurrected the stratigraphic, lithologic, and paleontologic data with little alteration. A modern study of the glacial history of the region was published by Pierce (1979) and his colleagues in the USGS, and the tectonic history was summarized in Pierce and Morgan (1992) and references cited by them and Christiansen (2001). Therefore, the original discussion of these topics has been deleted.

This manuscript might still have remained dormant, except for the fact that colleagues within the USGS and other institutions recently discovered a siliceous-spire field on the floor of Yellowstone Lake in Bridge Bay less than three miles south of our study area. These spires consist mainly of bacterial mats and diatoms bound into a hard rock by silica cement (Morgan and others, 2003; Shanks and others, this volume). Individual spires rise as much as 25 feet and most are located in hydrothermal craters (see Morgan and others, this volume). Even more interesting to us, these spires contain about the same assemblage of some trace elements as those in some of the lacustrine and fluvial strata in our study area (Krajick, 2001). Therefore, data on nearby diatom assemblages as well as our data on the geochemical and spectrographic composition of the sediments have been included.

In addition, the authors were faced with the problem of how to reconcile 35-year-old scientific observations and interpretations with more modern work (including that presented in the remainder of this volume). In most cases, the original stratigraphic descriptions and lists of biota have been retained.

Lisa A. Morgan

About the Author

In 1956, J. David Love began his reconnaissance studies of the Yellowstone Lake area and continued them through the late 1960s when he began collaborating with John Good, writing the first version of *Reconnaissance study of Pleistocene lake and fluvial deposits in and near ancestral Yellowstone Lake, Wyoming*. At the time, no modern topographic base map of the area was available to record their detailed observations. In anticipation of possible new mapping in concert with the National Aeronautics and Space Administration's efforts in Yellowstone National Park and perhaps new interest in Yellowstone Lake, Love and Good withdrew their manuscript from publication in 1968 thinking it would be incorporated in a renewed effort. Love's interest in Yellowstone Lake never languished, and efforts by the U.S. Geological Survey to complete a high-resolution bathymetric survey of Yellowstone Lake proceeded, and included many stimulating and helpful discussions with Dave.

We have included the following chapter, *Reconnaissance study of Pleistocene lake and fluvial deposits in and near ancestral Yellowstone Lake, Wyoming*, by J.D. Love, John M. Good, and D.G. Browne, originally written in the 1960s, in the current Professional Paper as a companion and historical paper to the chapters on Yellowstone Lake. It has been modified slightly since, but the main parts of the manuscript have not been changed. Hydrothermal explosions and their associated breccia deposits were not understood in the 1950s and 1960s. In this chapter, hydrothermal-explosion breccia deposits were identified as distinct units but were referred to as "beach rock." This term has been retained in the manuscript. Today, we understand the "beach rock" units to be products of hydrothermal explosions.

Reconnaissance study of Pleistocene lake and fluvial deposits in and near ancestral Yellowstone Lake, Wyoming, by J.D. Love, John M. Good, and D.G. Browne is a marvelous example of the detailed and solid work performed by geologists 50 years ago. While technology in the geological sciences has advanced remarkably over this same time frame allowing us to "see" images never previously imagined, the observations made in the field and the never-ending attention to fine detail were trademarks of David Love. This is obvious in his ancestral Yellowstone Lake work. We include this historical manuscript for clues into Yellowstone Lake's past and as an example of work few have ever replicated.

Lisa A. Morgan

Contents

Abstract 59
Introduction and Acknowledgments 59
Previous Work 60
Chemical and Spectrographic Analyses 60
Stratigraphy 60
- Pleistocene(?) Strata Possibly Underlying Turbid Lake Sequence 65
- Turbid Lake Sequence 65
- Yellowstone Falls Sequence 65
- Hayden Valley Sequence 69
- Alum Creek Sequence 78
- Mudkettle Sequence 79
  - Measured Section of Mudkettle Sequence 79
- Astringent Creek Sand 81
- Pelican Valley Sequence 82
  - Section of Pelican Valley Sequence Along Astringent Creek 83
  - Section of Pelican Valley Sequence at Locality 14 83
- Other Deposits 86
  - Gibbon Canyon Deposits 86
  - Bannock Ford Deposits 87
  - "Beach Rock" 87
  - Glacial Deposits 87

Tectonic Significance of Pleistocene Strata 87
Spires and Craters in Yellowstone Lake 88
Conclusions 88
References Cited 88

Figures

1. Index map showing 15' quadrangles within Yellowstone National Park 60
2. Index map and physiography of the Yellowstone National Park region 61
3. Geologic map of central Yellowstone National Park 62
4. Graph of spectrographic analysis of Pleistocene lake deposits 67
5. Photographs across Bear Creek 67
6. Turbid Lake sequence 68
7. Air oblique view of Upper and Lower Falls of Yellowstone River 69
8. Pollen distribution in Yellowstone Falls sequence 76
9. Air oblique view of Hayden Valley sequence 77
10. Hayden Valley(?) sequence, north shore of Yellowstone Lake 77
11. Wave-cut cliff, Yellowstone Lake 78

12. Photograph of varved clay, Yellowstone Lake 78
13. Silt beds in Hayden Valley(?) sequence 78
14. Alum Creek sequence 78
15. Astringent Creek Sand and Mudkettle sequence, Wrong Creek 81
16. Unconformity in Mudkettle sequence 82
17. Type Astringent Creek Sand 82
18. Phototheodolite view of Pelican Valley 82
19. Bluff of Pelican Valley sequence on Pelican Creek 84
20. Detail of silt laminae in Pelican Valley sequence 84
21. Pelican Valley section on Astringent Creek 84
22. Pumice conglomerate in upper part of Pelican Valley sequence 85
23. "Beach rock" along Mary Bay 85
24. Relation of Pelican Valley sequence to till and rhyolite 86

Tables

1. Rock analyses of Pleistocene lake deposits 66
2. Diatoms in Pleistocene strata 70

Reconnaissance Study of Pleistocene Lake and Fluvial Deposits In and Near Ancestral Yellowstone Lake, Wyoming

By J.D. Love,[1] John M. Good,[2] and D.G. Browne[3]

Abstract

Seven sequences of Pleistocene strata, five of them predominantly lacustrine, are described from outcrops north of Yellowstone Lake. These are (1) Turbid Lake sequence, 30–50 feet of white pumiceous claystone and tuff with carbonaceous partings and a distinctive compositional pattern of excesses and deficiencies of many elements; (2) Yellowstone Falls sequence, 75 feet or more of varved white claystone and tuff containing pollen and diatoms, overlain by gray conglomerate and sandstone; (3) Hayden Valley sequence, 200 feet or more of gray and white silt and claystone containing sparse diatoms; (4) Alum Creek sequence, 30 feet or more of bedded sand and gravel with lesser amounts of clay; (5) Mudkettle sequence, 150 feet or more of light gray to white, soft clay and claystone with lesser amounts of sandstone and conglomerate, moderately lithified in part, and containing some pollen and diatoms; (6) Astringent Creek Sand (newly named), a gray, commonly unlithified sand as much as 300 feet thick and containing abundant volcanic debris; and (7) Pelican Valley sequence, 120 feet or more of light gray to white, soft clay, silt, sand, and some pumice pebble conglomerate and shard beds; finer grained beds contain diatoms, pollen, and carbonaceous debris that has a radiocarbon date of 7,550±350 years.

Other localized deposits with radiocarbon dates and abundant diatoms consist of white carbonaceous tuffaceous clay and sand with an age of 9,440±300 years, in Gibbon Canyon, and a gray and white carbonaceous clay, silt, and sand with an age of 3,750±300 years at Bannock Ford in Yellowstone Canyon.

Slight arching of the Upper Basin Member of the Plateau Rhyolite caused the Yellowstone River to develop an antecedent course across it. Uplift of the Pelican Valley area during the last 7,500 years averaged about one foot in 50 years.

[1]U.S. Geological Survey

[2]National Park Service

[3]University of California

Introduction and Acknowledgments

During the program of geologic mapping in Jackson Hole in 1956 (fig. 2), directly south of Yellowstone National Park, several Pleistocene lacustrine deposits were differentiated. Their present maximum altitude is about 7,000 feet, which is approximately the same as that of Yellowstone Lake (7,733 feet above sea level). The drainage divide (the Continental Divide) that separates the Yellowstone Lake drainage from that of the Snake River on the Jackson Hole side is lower than 8,000 feet. It seemed possible that one or more Pleistocene lakes may have extended northward continuously from Jackson Hole to ancestral Yellowstone Lake. This possibility prompted the present investigation. Preliminary data on a few localities were published by Love (1961).

Figure 2 shows the regional relations of mountains to basins and the distribution of present-day lakes. Figure 3 is a portion of the geologic map of Yellowstone National Park and vicinity by Christiansen (2001) showing localities discussed in the text. Data on the 19 numbered localities and adjacent areas consisted of reconnaissance mapping; measurement of stratigraphic sections; and sampling, chiefly for diatoms, pollen, radiocarbon determinations, and some chemical and spectrographic analyses. The writers wish to acknowledge the valuable contributions by Estella B. Leopold, who made field collections in 1958 and 1962 and identified the pollen. K.E. Lohman and G.W. Andrews identified the diatoms and R.W. Brown identified the fossil leaves. Robert S. Houston made a petrographic study of thin sections.

We are most grateful to Lisa Morgan, who reviewed our original manuscript and helped to formulate an up-to-date revision that would be compatible with the ongoing research in the adjacent Yellowstone Lake area. We also are grateful to her colleague, W.C. Pat Shanks, for sharing the discussion of the potential application of their work on Yellowstone Lake with our adjacent studies.

Previous Work

The existence of Pleistocene lake deposits in the vicinity of the present Yellowstone Lake was recorded by several pioneer explorers and scientists. The first was Lieutenant Gustavus C. Doane, U.S. Army, who noted on September 1, 1870, upon entering Hayden Valley:

> "Six miles above the falls we entered a wide valley of calcareous formation, open and branching among timbered ridges on either side of the river, which runs through its centre in a northeast [sic] course an old lake bed, as are all the grassy sections of the basin" (Doane, 1870, p. 15).

Another remarkably astute observation was made in 1875 by Theodore B. Comstock who stated:

> "The deposits of the Yellowstone Lake Basin and in the valley of the main river and its tributaries, which may be regarded as Pliocene, are mainly the sediments of an ancient lake, of which the present body of water is the representative on a much reduced scale. Beautiful and highly instructive sections of the old beach formations are exposed in the valleys of the streams, particularly in the lower valley of Pelican Creek, and far down the Yellowstone River, where they become more complicated, but on that account all the more interesting. An examination of these shows that the lake formerly extended over a much larger area, and that it has held its place amid changes of great importance" (Comstock, 1875, p. 130–131).

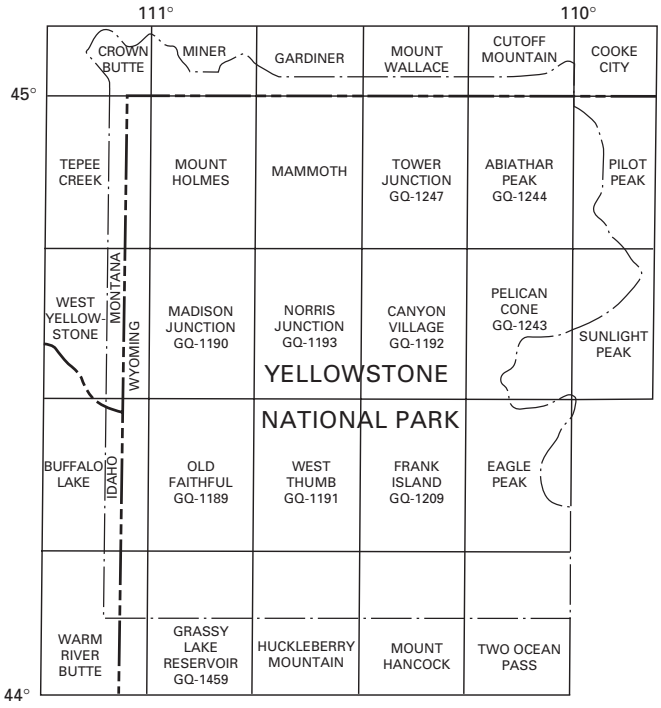

Figure 1. Index map showing 15′ quadrangles of Yellowstone National Park. Published USGS geologic quadrangle maps indicated by GQ numbers. From Christiansen (2001).

William Henry Holmes, in the final annual report of Ferdinand V. Hayden's Geological and Geographical Survey of the Territories, published a map of "Yellowstone Lake showing the dimensions of the ancient lake" (Holmes, 1883a, pl. 31). However, Arnold Hague, in his Yellowstone Park Folio (1896) and the Atlas accompanying USGS Monograph 32 (1904), apparently ignored these earlier descriptions and showed much of the area of lacustrine deposits as glacial drift or volcanic rocks on his folio maps. Howard (1937) made a superb study of the Grand Canyon of the Yellowstone River and included excellent descriptions of the associated fluvial and lacustrine sediments.

Chemical and Spectrographic Analyses

Rock analyses of selected samples were taken from measured sections of the Yellowstone Falls, Hayden Valley, Mudkettle, and Pelican Valley sequences (table 1). These indicate, in a general way, the variation in amount of common oxides within and between the sequences. The significance of these variations is not yet known, but they are probably not entirely random.

Figure 4 shows spectrographic analyses of selected groups of samples of strata from the Yellowstone Falls, Hayden Valley, Mudkettle, and Pelican Valley sequences and compares them with Pleistocene rhyolite from the Pitchstone Plateau in the southwestern part of the Park and with crustal abundance of these elements in the Earth (Mason, 1958, p. 44). The analyzed samples from the Yellowstone strata were, in general, well-sorted, highly tuffaceous sand and (or) clay. Each sample point on the graphs represents the average of five or more individual samples. These analyses represent an attempt to emphasize similarities and (or) contrasts in the composition of the stratigraphic sequence.

While the chemical and spectrographic data were collected and analyzed more than 30 years ago, we include this original data as a contribution that may provide leads to significant qualitative and quantitative associations of trace elements, not only in our exposed lacustrine and fluvial strata but also in some that may extend under Yellowstone Lake into the area of the spires and hydrothermal-explosion craters.

Stratigraphy

Seven sequences of Pleistocene lacustrine and fluvial strata are here discussed and given informal names. Formal names are undesirable until completion of detailed mapping and of paleontologic, geochemical, and petrographic studies and more age determinations. Such studies should demonstrate whether or not any of the sequences are lateral equivalents.

Figure 2. Index map and physiography of northwest Wyoming and adjacent areas showing the Yellowstone Plateau. From Christiansen (2001).

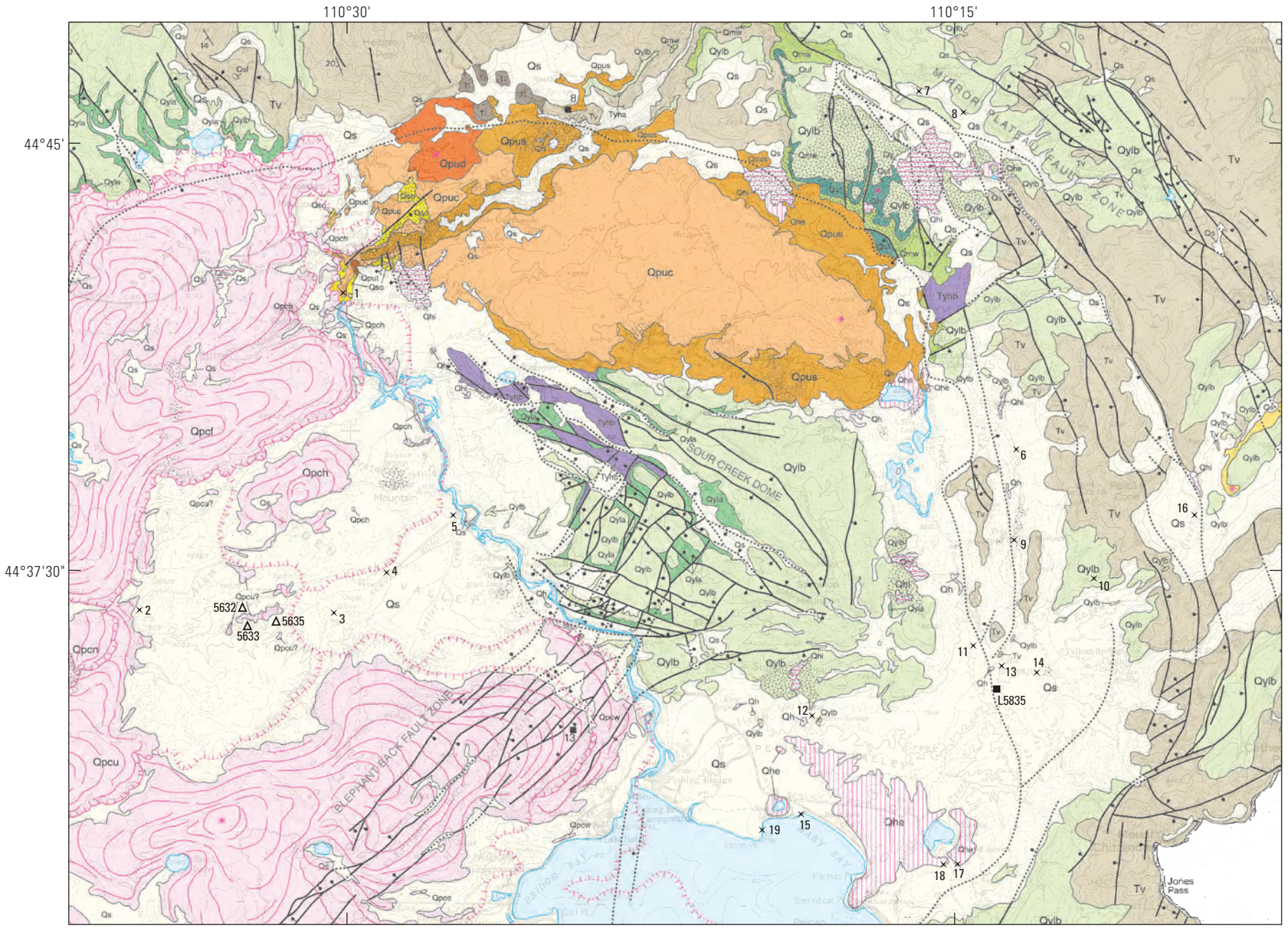

Figure 3. Geologic map of central Yellowstone National Park showing localities discussed in the text. After Christiansen (2001).

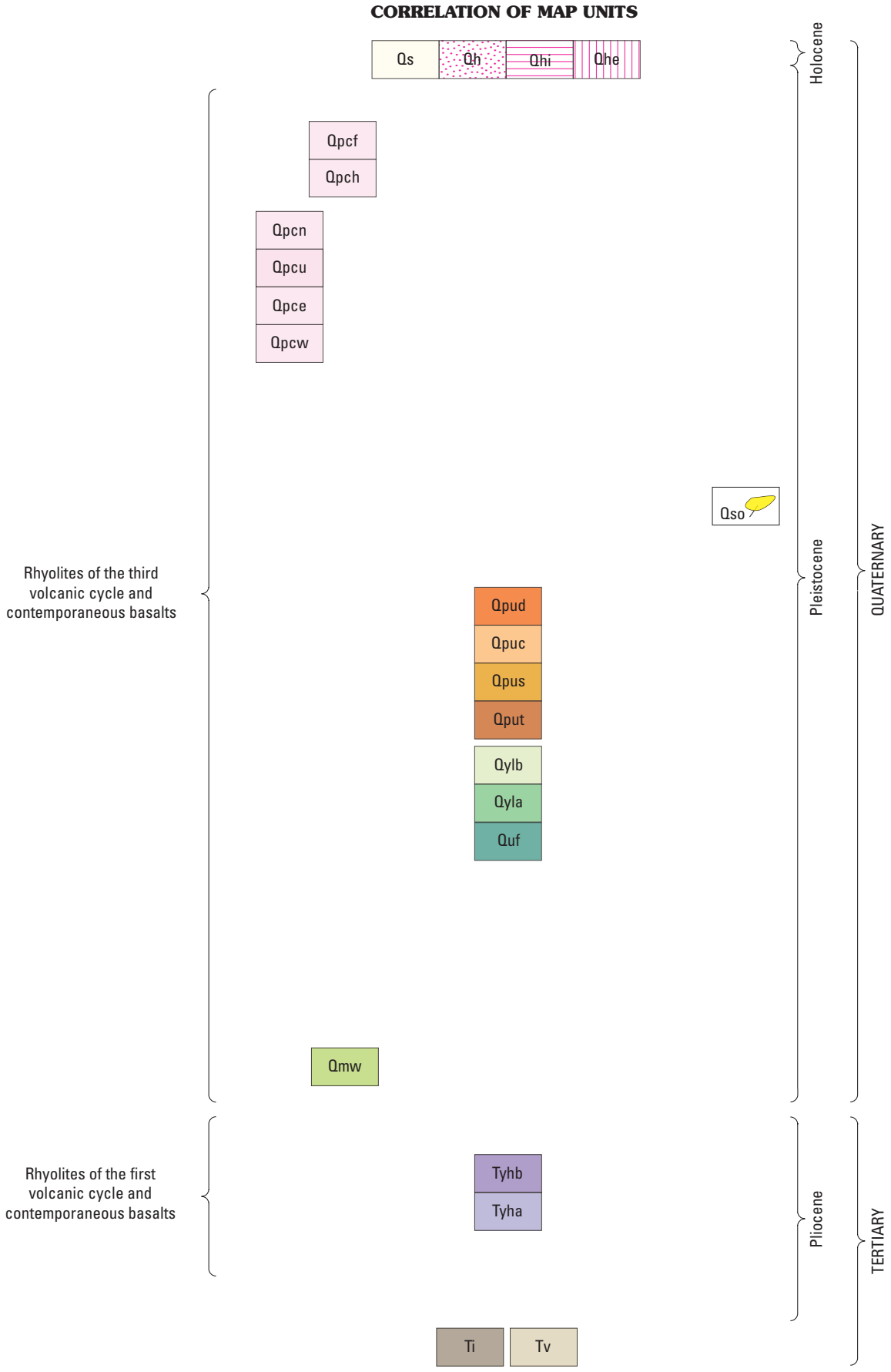
CORRELATION OF MAP UNITS
Qs
Qh
Qhi
Qhe
Holocene
Qpcf
Qpch
Qpcn
Qpcu
Qpce
Qpcw
Qso
Rhyolites of the third volcanic cycle and contemporaneous basalts
Qpud
Qpuc
Qpus
Qput
Qylb
Qyla
Quf
Pleistocene
QUATERNARY
Qmw
Rhyolites of the first volcanic cycle and contemporaneous basalts
Tyhb
Tyha
Pliocene
TERTIARY
Ti
Tv

LIST OF MAP UNITS

Surficial deposits (Holocene and Pleistocene)—Age ranges of individual units overlap

- Qs — **Detrital deposits**
- Qh — **Hot-spring deposits**
- Qhi — **Cemented ice-contact deposits localized by hot springs**
- Qhe — **Hydrothermal-explosion deposits**

Plateau Rhyolite (Pleistocene)

Central Plateau Member

- Qpcf — **Solfatara Plateau flow**
- Qpch — **Hayden Valley flow**
- Qpcn — **Nez Perce Creek flow**
- Qpcu — **Spruce Creek flow**
- Qpce — **Elephant Back flow**
- Qpcw — **West Thumb flow**

Upper Basin Member

- Qpud — **Dunraven Road flow**
- Qpuc — **Canyon flow**
- Qpus — **Tuff of Sulphur Creek**
- Qput — **Tuff of Uncle Tom's Trail**

Qso — **Sediments (Pleistocene)**—Interlayered with Plateau Rhyolite

Lava Creek Tuff (Pleistocene)

- Qylb — **Member B**
- Qyla — **Member A**

Quf — **Undine Falls Basalt (Pleistocene)**—Includes some gravel

Mount Jackson Rhyolite (Pleistocene)

Qmw — **Wapiti Lake flow**

Huckleberry Ridge Tuff (Pliocene)

- Tyhb — **Member B**
- Tyha — **Member A**

Ti — **Intrusive rocks (Tertiary)**

Tv — **Volcanic rocks (Tertiary)**

EXPLANATION

- **Contact**—Dotted where concealed
- **Lava-flow front**—Hachures on side of younger flow; dotted where concealed
- **Lava-flow form lines**
- **Normal fault**—Bar and ball on downthrown side; dotted where concealed
- **Area of hydrothermal acid alteration**
- × 4 — **Sample locality**
- **Volcanic vent**
- △ — **Diatom sample locality**
- ■ — **Pollen sample locality**

Pleistocene(?) Strata Possibly Underlying Turbid Lake Sequence

About 125 feet of poorly stratified detritus of uncertain age and correlation are exposed along Bear Creek, south of Turbid Lake (loc. 17 on fig. 3; fig. 5). The lower part of this deposit consists of 40 feet of chocolate brown to gray compact claystone and siltstone with sporadic sand grains and small pebbles of felsic volcanic rock. The base of this unit is below creek level at the section studied. Overlying the claystone and siltstone is about 85 feet of stratified, rusty brown sandstone and conglomerate. Pebbles in the conglomerate are highly rounded, as much as 3 inches in diameter, and are composed of rhyolite, felsic, and mafic porphyries, and gray chert of unknown origin. Some parts of the conglomerate are indurated enough to stand as pinnacles (lower left part of fig. 5*A*). The sandstone, some of which is indurated, is most abundant near the base and top. Overlying the sandstone is 20 feet of blue-green, coarse-grained, poorly cemented, stratified sand. This sand is unconformably overlain by as much as 15 feet of glacial or hydrothermal-explosion debris from nearby Turbid Lake. This debris contains a 2-inch layer of charcoal with a ^{14}C age of 8,310±300 years (Meyer Rubin, written commun., 1966, USGS Lab No. W-1944; Love, 1989, p. 52–53, his figs. 58 and 59). Overlying it is about 10 feet of possible hydrothermal-explosion debris.

No fossils were found in these strata. Their relation to the nearby Turbid Lake sequence is obscured, but field relations suggest that the Turbid Lake sequence is younger and that they are separated by an unconformity with an erosional relief of 100 feet in a horizontal distance of 300 feet. Both sequences are much less indurated than the nearby Tertiary volcaniclastic rocks so are tentatively considered to be Pleistocene.

Turbid Lake Sequence

The Turbid Lake sequence was studied at locality 18 (figs. 3 and 6) where it consists of 30–50 feet of white, bedded pumiceous claystone and tuff. Rounded grains and pebbles of white, fibrous pumice and granules of black obsidian are common. Several horizons contained flattened brown twigs, fragments of leaves, and other plant material. The strata are locally altered chemically by intrusion of active sulfurous vents.

Preliminary spectrographic analyses show that the Turbid Lake sequence contains conspicuously different amounts of trace elements from those of other Pleistocene sedimentary sequences thus far analyzed in the region (fig. 4). For example, it is lowest in Fe, Mg, Ca, V, Mn, Sr, Cr, Y, Sc, and Co, and highest in Ti, Zr, B, and Nb. The source of the volcanic debris has not yet been established.

The Turbid Lake sequence dips 5–10 degrees north, probably in response to local crustal tilting. This movement is suggested by a beheaded drainage on the north side of Turbid Lake, in line with Bear Creek on the south side, by the aggrading character of the valley of Sedge Creek before it enters the Turbid Lake, and by the entrenched course of the stream after it leaves the lake.

Yellowstone Falls Sequence

Howard (1937, p. 108) first recognized the presence of the strata here called the Yellowstone Falls sequence. He measured a stratigraphic section and discussed the age of the strata and their origin and significance. Additional data were given by Love (1961). The maximum thickness is less than 100 feet. The following section describes the general lithology and was measured by J. D. Love along the old Savage Trail (abandoned) on the east side of Yellowstone Canyon (fig. 7), about 600 feet downstream from Upper Falls (locality 1, fig. 3). Because of the steep slope, slumping, poor exposures, and lenticularity of some beds, the section is generalized. Some of Howard's observations on the lower part of the section are paraphrased here. Top of section coincides with flat on east side of canyon.

Unit	Lithology	Thickness (ft)
5	Tuff, white, slabby, grading up to reddish-brown conglomeratic sandstone and tuff with clayey matrix	6
4	Obsidian conglomerate, dark gray, evenly-bedded; upper half is hard and forms ledges; lower half is poorly cemented; consists of angular fragments, rarely more than 1 inch in diameter, of black obsidian, gray and white fibrous pumice and black, red, and white rhyolite; matrix of soft part is white, decrepitating, noncalcareous clay; matrix of ledge is a silica cement with little clay; this unit is the "Rim Conglomerate" of Howard (1937)	30
3	Claystone, diatomite, and shale, light gray to white, light weight, smooth-feeling, nondecrepitating in water, noncalcareous; some sandy layers and some clayey beds with sparse quartz and feldspar grains; lower part laminated to varved in part; contains carbonized leaves (for pollen and diatom collections, see figure 8 and table 2)	25
2	Sandstone and conglomerate, gray, hard in upper part and soft in lower part, composed of obsidian and rhyolite fragments	7
1	Claystone, white to light gray, thin-bedded, soft, light weight	5+
Thickness of measured part of Yellowstone Falls sequence		73+

Underlying units are rhyolitic volcanic rocks.

The strata here are much more completely lithified than any of the other Pleistocene sequences in this area. Thin sections of the hard part of the "rim conglomerate" show fragments of brown obsidian with diffused margin areas of alteration. Other fragments are of perlitic glass and welded rhyolite tuff with corroded quartz phenocrysts. Grains in the matrix include plagioclase, quartz, anorthoclase, biotite, and curved glass shards. The lower part

Table 1. Rock analyses of Pleistocene lake deposits north and northwest of Yellowstone Lake.

[All samples are arranged as nearly as possible in stratigraphic order. Rapid rock analyses are by P.L.D. Elmore, S.D. Botts, Gillison Chloe, Lowell Artis, and H. Smith, using methods similar to those described by Shapiro and Brannock (1956). Analyses are in percent]

Sequence	Locality on geologic map and unit in measured section described in text	Laboratory no.	SiO_2	Al_2O_3	Fe_2O_3	FeO	MgO	CaO	Na_2O	K_2O	TiO_2	P_2O_5	MnO	H_2O^-	H_2O^+	CO_2	Volatiles other than H_2O and CO_2
Pelican Valley	14, unit 2	D123124	70.5	13.2	1.0	1.0	0.91	1.7	2.7	4.6	0.28	0.07	0.00	0.64	3.1	<0.05	
Do--	11, unit 7	D123136	60.3	17.2	2.4	.28	.47	.28	.31	1.8	.74	.26	.33	2.8	8.1	< .05	4.6
Do--	11, unit 4	D123126	53.4	19.7	2.6	.76	.52	.36	.65	2.0	.89	.31	.02	2.5	8.7	< .05	7.5
Do--	11, unit 2	D123120	58.1	16.4	3.5	.88	1.2	1.7	1.5	2.2	.71	.33	.00	2.1	5.5	< .05	5.4
Do--	2,000 ft S. of 11	D123131	60.0	15.4	4.0	1.5	3.3	2.6	2.1	2.3	.65	.35	.07	4.3	3.4	< .05	
Do--	1,500 ft SW. of 12	D123132	62.6	16.3	4.5	.20	3.5	2.8	3.2	2.0	.56	.19	.08	.91	3.0	< .05	
Do--	13	D123127	62.9	15.9	2.4	1.6	2.9	4.8	2.9	2.3	.50	.18	.06	.95	1.8	< .05	
Do--	12	D123125	61.0	15.3	4.4	.64	2.8	3.2	2.7	2.3	.62	.23	.11	3.3	3.4	< .05	
Mudkettle	Fossil loc. 5907	D123135	71.5	12.4	1.0	.32	.49	.13	.50	1.5	.74	.13	.00	2.1	5.7	< .05	2.9
Do--	7	D123121	67.0	15.1	3.1	.60	1.2	1.2	2.0	3.5	.45	.11	.00	1.8	3.4	< .05	
Do--	7	D123118	66.4	14.2	4.0	.48	.99	.98	1.5	3.0	.45	.13	.05	2.4	4.0	< .05	1.2
Do--	6, unit 5	D123133	64.1	16.2	3.0	.24	.95	1.4	1.2	2.2	.46	.06	.03	3.1	5.6	< .05	1.0
Do--	6, unit 3, top	D123128	64.6	15.2	3.2	.60	1.0	1.4	1.2	3.1	.48	.11	.02	3.5	5.3	< .05	
Do--	6, unit 3, upper middle	D123123	67.8	12.5	5.0	.24	1.0	.68	.52	2.3	.43	.17	.00	4.2	4.6	< .05	
Do--	6, unit 3, lower middle	D123130 B	66.4	13.8	3.0		1.5	.93	.50	2.6	.48	.16	.04	5.5	3.7	< .05	
Do--	6, unit 3, base	D123115	66.0	13.6	3.5	.60 .20	1.6	1.0	.45	2.8	.48	.13	.04	5.4	4.7	< .05	
Hayden Valley	2	D123117	63.7	14.5	4.0	.60	2.4	2.2	2.1	2.8	.53	.21	.07	3.4	3.2	.05	
Do--	2,500 ft SW of 2	D123122	61.0	15.2	4.8	.48	2.5	2.4	2.1	2.7	.58	.20	.32	3.6	3.8	< .05	
Hayden Valley?	15	D123116	61.0	15.6	3.7	1.1	2.9	3.4	2.7	2.1	.62	.26	.00	2.9	2.9	< .05	
Yellow-stone Falls	1, unit 3, upper part	D123119	73.8	10.0	3.5	.12	.55	.41	.85	1.8	.30	.04	.05	2.8	3.7	< .05	1.3
Do--	1, unit 3, middle	D123134	66.6	14.9	3.1	.44	.84	1.5	1.9	2.9	.43	.14	.00	2.5	4.4	< .05	

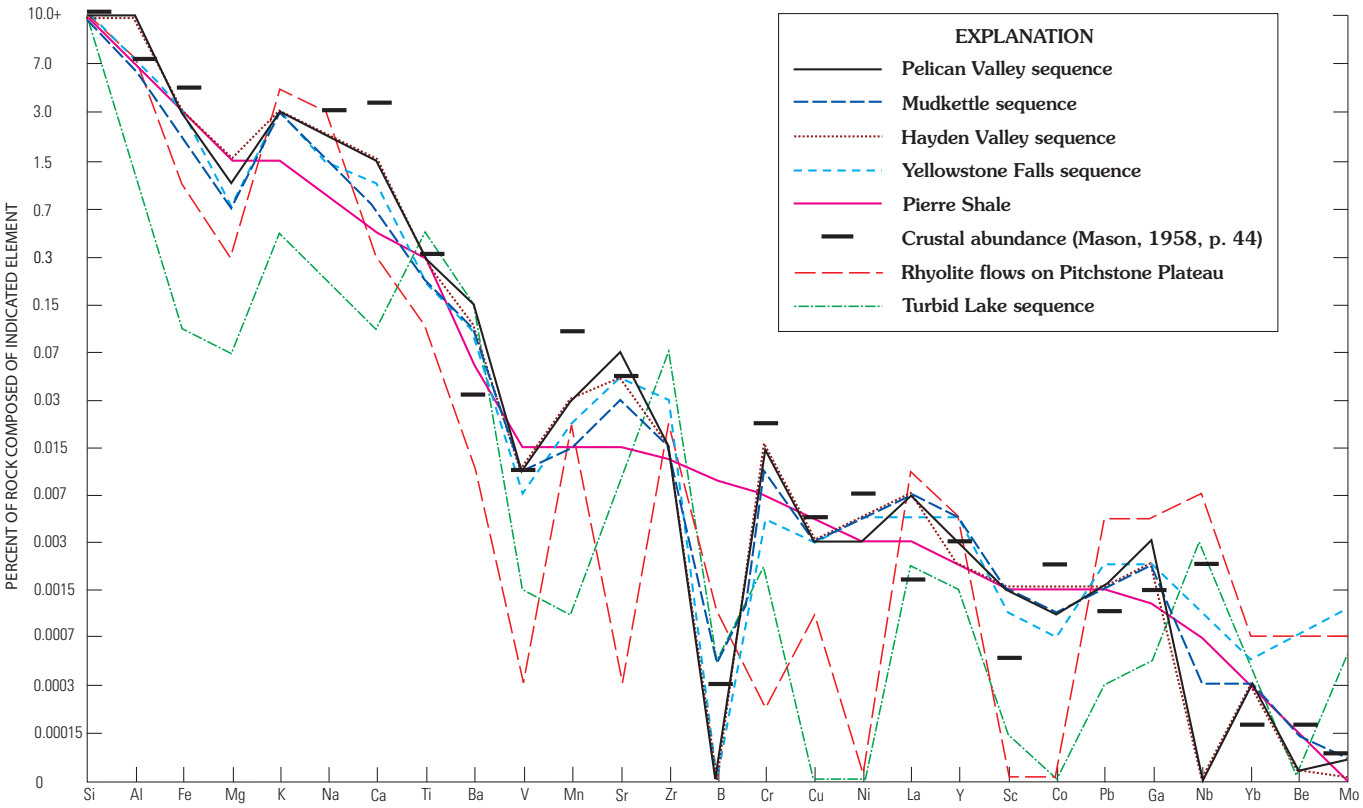

Figure 4. Semiquantitative spectrographic analyses of Pleistocene lake deposits north and northwest of Yellowstone Lake. Values of selected elements are graphed to show contrast in distribution with those in the Pierre Shale and other marine Cretaceous shales and with Pleistocene rhyolitic welded tuff on the Pitchstone Plateau. Quantities are reported in percent to the nearest number in the series (10 to 0:); at least 60 percent of results are expected to be in the correct range. Data on Cretaceous shales are by Tourtelot (1962). Numbers of samples: Pelican Valley sequence, 8; Mudkettle sequence, 8; Hayden Valley sequence, 3; Yellowstone Falls sequence, 3; rhyolite flows on Pitchstone Plateau, 6; and Turbid Lake sequence, 5.

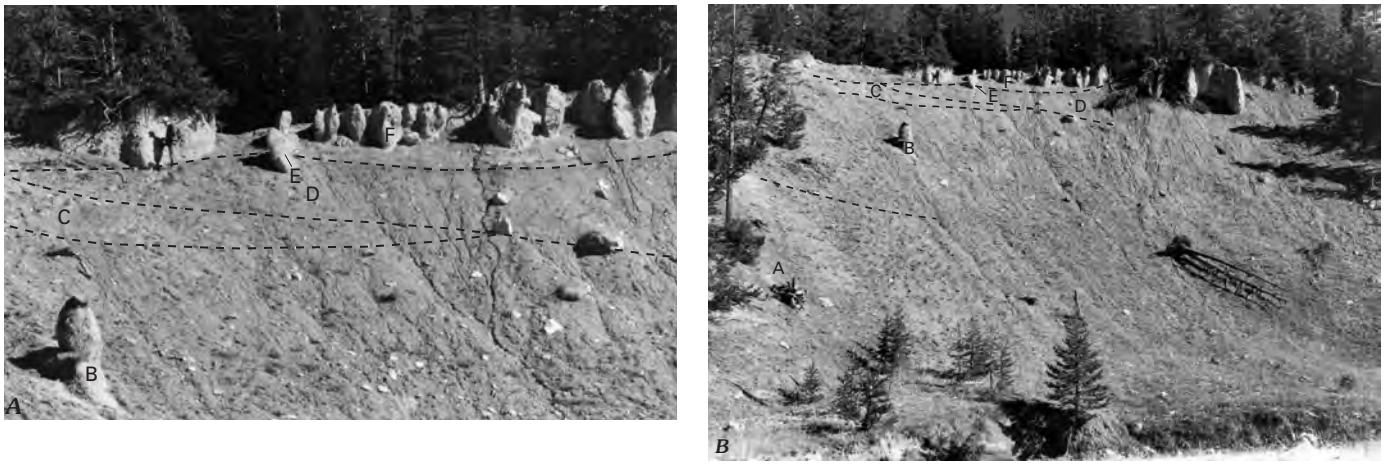

Figure 5. *A*, Telephoto view north across Bear Creek at locality 17. *B*, View north across Bear Creek at locality 17. Indicated are 40 feet of brown pebbly claystone (A); 85 feet of conglomerate and rust-brown sandstone (B); 20 feet of blue-green sand (C); lower till, 0–15+ feet (D); 2-inch charcoal horizon with 8,200 year ^{14}C date (E); and upper till, 10 feet (F).

of the unit contains rounded grains of welded rhyolite tuff, together with perlitic, spherulitic, brown, and clear glass. Crystals in the matrix include oligoclase(?), quartz, and sanidine-anorthoclase.

The strikingly laminated and varved clay in the lower part of unit 3 was determined by X-ray diffraction to contain about 75 percent montmorillonite or mixed-layer clay, 10 percent quartz, and 15 percent feldspar. Spectrographic analyses (fig. 4) show that the Yellowstone Falls sequence matches the average of the Pleistocene units, other than the Turbid Lake strata. Nevertheless, there are some variations in the general grouping. For example (again excluding the Turbid Lake sequence), the Yellowstone Falls sequence is the lowest in V, Cr, Sc, and Co and the highest in Zr, Pb, Nb, Yb, Be, and Mo. Among the scarcer trace elements, single samples show 0.015 percent Ce, 0.01 percent Nd, and 0.001 percent Sn. Although there are too few analyses of common oxides to be statistically valid, those available (table 1) suggest that the Yellowstone Falls sequence has a slightly higher content of SiO_2 and lower FeO, MgO, CaO, Na_2O, K_2O, TiO_2, and P_2O_5 than is present in the other sequences (none is available on the Turbid Lake sequence).

The Yellowstone Falls sequence was deposited on a rough topography developed on the Upper Basin Member of the Plateau Rhyolite of Christiansen and Blank (1972), and its lowest beds are therefore much more lenticular and less widespread than the upper. At locality 1, the strata are overlain by the Hayden Valley sequence and by till.

Howard found no diagnostic fossils in the Yellowstone Falls strata but considered them to be of Pleistocene age. A Pleistocene age is suggested by the discovery of abundant pollen and diatoms (table 2; Love, 1961) in unit 3. A series of pollen samples from bottom to top of unit 3 (fig. 8) shows a progressive change in vegetation types. In the lowest part, pine and spruce are dominant; in the middle is pine, spruce, and sage; in the upper part, sage dominates, with some greasewood, herbs, algae, and tree pollen. These data suggest that the local environment became drier and probably warmer during this interval of deposition, perhaps somewhat warmer than the present climate (E.B. Leopold, written commun., 1960). K.E. Lohman (written commun., 1960) discusses the diatoms from the upper part of unit 3 as follows:

"The following analysis of the assemblage indicates the percentage of the 64 species and varieties that also occur in several dated formations:

White marl associated with Pinedale glacial debris, Grand Teton National Park (Love, 1956) with a ^{14}C date of 9,580±350 yr B.P.	15%
Provo Formation, Utah, upper Pleistocene (11,650 to 13,000 yr B.P.)	27%
Hagerman [Glenns Ferry] Formation, Idaho, upper Pleistocene [upper Pliocene] (vertebrate fauna)	28%
Thousand Creek beds, middle Pliocene (vertebrate fauna)	15%
Esmeralda Formation, lower Pliocene (vertebrate fauna)	7.8%

Figure 6. Turbid Lake sequence composed of plant-bearing white pumiceous clay and tuff overlain by dark-colored till, with beveled upper surface; locality 18 on west bank of Bear Creek, south of Turbid Lake. Haze at left is stream from vents cutting through Turbid Lake sequence. Note beds dipping north (upper left to lower right) to left of man.

> "Two of the three extinct species (indicated by asterisks) in this assemblage were first described from the Provo Formation and one from the Hagerman [Glenns Ferry] Formation. These are not known from beds older than early Pleistocene [late Pliocene]. Based on the above analysis, the best estimate of age is somewhere in the Pleistocene. I say somewhere for the reason that statistically the correlation is about the same for the late Pleistocene (Provo) and the early Pleistocene [late Pliocene] Hagerman [Glenns Ferry], although the fact that it contains two extinct species from the Provo and only one from the Hagerman [Glenns Ferry] suggests upper Pleistocene rather than lower. The paleoecology indicated by this assemblage is that of a temperate, shallow lake of fresh to somewhat saline water."

The leaves are of the pondweeds *Myriophyllum* or *Proserpinaca* (R.W. Brown, written commun., 1956).

The Yellowstone Falls sequence apparently was deposited before the adjacent part of the present Yellowstone Canyon was cut. Likewise, prior to modern canyon development, the area was glaciated by ice that moved at least 35 miles southwestward from the Beartooth Mountains (fig. 2) and left huge granite erratics. Figure 7 shows the broad open valley along which the ice moved southwestward (the direction in which the camera was pointed). The ice also overrode the Hayden Valley sequence, which, in turn, overlies the Yellowstone Falls strata. Therefore, it seems likely that the Yellowstone Falls sequence is of early or middle Pleistocene age.

Figure 7. Air oblique view southwest showing Upper and Lower Falls of the Yellowstone River cut in Canyon Rhyolite. Fossiliferous strata of Yellowstone Falls sequence at locality 1 are exposed in white cut at left of Upper Falls. Treeless area at top of photo is underlain by Hayden Valley sequence. Photo by H.M. Cowling, 116th Photograph Section, Washington National Guard.

Hayden Valley Sequence

The presence of Pleistocene strata in Hayden Valley was first recognized by Hayden in reports for 1871 and 1872 (Hayden, 1872, 1873) but they were not described. Holmes (1883a, p. 56) gave a cursory mention of lake beds in Hayden Valley and presented two maps (Holmes, 1883a, pl. 31 and Holmes, 1883b) that included this area in ancestral Yellowstone Lake. On the latter map he used the name "Lake Hayden" for the ancestral Yellowstone Lake. Weed (1896) mapped the deposits as glacial drift and stated: "In Hayden and Pelican valleys extensive morainal deposits occur whose clays and loosely cemented sands closely resemble lake beds." Howard (1937) was the first to recognize and describe two sets of strata, the "divide sediments" and the "plains sediments," separated by an unconformity. He described the former as having abundant sand and gravel in the lower part, grading up to lacustrine deposits, and the latter as varved clay-rich silts. The "divide sediments" of Howard are here called the Hayden Valley sequence.

Figure 3 shows the described localities 2 and 3 of the Hayden Valley sequence, and figure 9 shows its characteristic treeless low rounded hills. The Hayden Valley sequence is at least 200 feet thick at several places.

Along Alum Creek at locality 2, the sequence consists of nearly 200 feet of soft, gray and white, noncalcareous, remarkably homogeneous silt and clay and some gravel beds. The latter contain abundant rounded granules of black obsidian, colorless angular crystals of quartz and feldspar, and conspicuous fresh shards. In the lower part of this exposure, laminae of silt alternate with clay, giving the strata a varved appearance. This laminated deposit lies between two knobs of obsidian nearly 100 feet high and 800 feet apart, thus indicating the amount of local relief on which the fine-grained strata were deposited.

At locality 3 is about 150 feet of well-exposed strata, chiefly light gray clay and silt in the lower part, interbedded with gravel of rounded rhyolite and obsidian fragments in the middle, and fine-grained silt and clay in the upper part. Elsewhere gravel and sand are common on the highest hills, but whether or not they are more closely related to the Hayden Valley sequence or to younger glacial debris remains to be determined.

Flooring the channel of Yellowstone River at the outlet of Yellowstone Lake and exposed farther east in a wave-cut scarp along the north edge of Mary Bay at localities 15 (fig. 10) and 19 are strata tentatively considered by us to be part of the Hayden Valley sequence. At locality 15, a composite section is 25–50 feet thick (fig. 11). The lowest beds are varved and laminated light-gray to brown (blue-gray when wet) clay (fig. 12), of which as much as 20 feet is exposed above lake level. The section at this locality was first described by Comstock (1875, p. 131). Overlying the varved unit, with a gradational contact, are light gray to rusty brown fine-grained sand beds alternating with thin silt and clay beds. At locality 19 (fig. 13), some one-fourth-inch laminae of silt and clay can be traced continuously for more than 25 feet along the outcrop. Local ripplemarks and cross-bedding are present in many layers. Coarser sands and pebble lenses contain abundant black obsidian. At locality 15, these strata are overlain by till (fig. 11). [*The "till" noted here is now interpreted as hydrothermal-explosion breccia, a concept not yet in the "working*

Table 2. Diatoms in Pleistocene strata north and northwest of Yellowstone Lake.

[YFs, Yellowstone Falls sequence; ACS, top of Astringent Creek(?) Sand; GCd, Gibbon Canyon deposit (this assemblage, although from beds from outside the map area, is included for comparison because it is dated by radiocarbon); BFd, Bannock Ford deposit. Sample localities are denoted by bold 4-digit number near top of columns—these localities are described at end of table. R, rare; F, frequent; C, common; A, abundant. Identified by K.E. Lohman and G.W. Andrews]

Genera and species	YFs	Hayden Valley sequence				Mudkettle sequence		ACS	Pelican Valley sequence			GCd	BFd
	4618	5632	5633	5635	5636	5589	5907	5637	5904	5905	5906	5596	5639
Achnanthes cf. *A. calcar* Cleve	R	--	--	--	--	--	--	--	--	--	--	--	--
flexella (Kützing) Brun	--	--	--	--	--	--	--	--	--	--	--	F	--
lanceolata (Brébisson) Grunow	--	--	--	--	--	--	--	--	--	R	R	--	R
lanceolata var. *rostrata* Hustedt	--	--	--	--	--	--	--	--	--	--	--	--	F
Amphora ovalis (Kützing) Kützing	F	--	--	--	--	--	--	--	R	--	R	--	R
ovalis var. *pediculus* Kutzing	--	--	--	--	--	--	--	--	--	--	--	--	R
Caloneis bacillum (Grunow) Mereschkowsky	F	--	--	--	--	--	--	--	--	--	--	--	--
schumanniana var. *biconstrica* Grunow	--	--	--	--	--	--	--	--	--	--	--	--	R
silicula (Ehrenberg) Cleve	F	--	--	--	--	--	--	F	--	--	--	--	--
trinodis (W. Smith) Boyer	--	--	--	--	--	--	--	--	R	--	--	--	--
cf. *C. trinodis* (W. Smith) Boyer	--	--	--	--	--	--	--	R	--	--	--	--	--
sp.	--	--	--	--	--	--	--	--	R	--	--	--	--
Campylodiscus sp.	F	--	--	--	--	--	--	--	--	--	--	--	--
Cocconeis pediculus Ehrenberg	--	--	--	--	--	--	--	--	R	--	--	--	--
placentula Ehrenberg	--	--	--	--	--	--	--	--	--	--	--	--	A
placentula var. *euglypta* (Ehrenberg) Grunow	F	--	--	--	--	--	--	--	--	--	--	--	A
Cyclotella americana (Ehrenberg) Kützing	C	--	--	--	--	--	--	--	--	--	--	--	--
comta (Ehrenberg) Kützing	--	F	R	F	F	F	R	--	F	--	R	--	F
kutzingiana var. *planetophora* Fricke	--	--	--	--	--	--	--	--	--	R	--	--	--
cf. *C. operculata* (Agardh) Kützing	--	--	--	--	--	F	--	--	--	--	--	--	F
sp.	--	--	--	--	--	F	--	--	--	--	--	--	F
Cymatopleura cf. *C. elliptica* (Brébisson) Wm. Smith	F	--	--	--	--	--	--	--	--	--	--	--	--
Cymbella affinis Kützing	F	--	--	--	--	--	--	--	--	--	--	--	F
arcus Gregory	R	--	--	--	--	--	--	--	--	--	--	--	--
cistula var. *maculata* (Kützing) Van Heurck	--	--	-- --	--	--	--	--	R	--	--	--	R	--
ehrenbergii Kützing	--	--	--	--	--	--	R	R	--	--	--	--	--
gracilis (Rabenhorst) Cleve	F	--	--	--	--	--	--	--	--	--	--	--	--
hybrida Grunow	--	--	--	--	--	--	--	--	--	--	--	--	F
mexicana (Ehrenberg) Cleve	--	--	--	--	--	--	--	--	--	--	--	--	R
naviculiformis Auerswald	F	--	--	--	--	--	--	--	F	F	R	--	--
cf. *C. sinuata* var. *antiqua* (Grunow) Cleve	R	--	--	--	--	--	--	--	--	--	--	--	--
turgida (Gregory) Cleve	F	--	--	--	--	--	R	F	--	R	--	--	F
cf. *C. turgida* (Gregory) Cleve	--	--	--	--	--	--	--	--	--	--	--	R	--

Table 2. Diatoms in Pleistocene strata north and northwest of Yellowstone Lake—*Continued.*

Genera and species	YFs	Hayden Valley sequence				Mudkettle sequence		ACS	Pelican Valley sequence			GCd	BFd
	4618	5632	5633	5635	5636	5589	5907	5637	5904	5905	5906	5596	5639
ventricosa Kützing	F	--	--	--	--	--	--	--	--	--	--	R	C
sp. A*	F	--	--	--	--	--	--	--	--	--	--	--	--
Denticula elegans Kützing	--	--	--	--	--	--	--	--	--	--	--	--	R
Diatoma anceps (Ehrenberg) Grunow	--	--	--	--	--	--	--	--	--	--	R	--	--
Diatomella balfouriana Greville	--	--	--	--	--	--	--	--	--	--	--	R	--
Diploneis elliptica (Kützing) Cleve	F	--	--	--	--	--	--	A	--	--	--	--	R
ovalis (Hilse) Cleve	--	--	--	--	--	--	--	--	R	R	F	--	--
Epithemia cf. *E. argus* (Ehrenberg) Kützing	F	--	--	--	--	--	--	--	--	--	--	--	--
sorex Kützing	--	--	--	--	--	--	--	--	--	--	--	--	F
turgida (Ehrenberg) Kützing	F	--	--	--	--	--	R	---	R	--	--	--	F
zebra var. *porcellus* (Kützing) Grunow	--	--	--	--	--	--	--	R	--	--	--	--	--
zebra var. *proboscidea* Grunow	--	--	--	--	--	--	--	--	R	--	--	--	--
zebra var. *saxonica* (Kützing) Grunow	--	--	--	--	--	--	--	R	--	--	R	R	--
sp. A*	F	--	--	--	--	--	--	--	--	--	--	--	--
sp.	R	--	--	R	--	--	--	--	--	--	--	--	R
Eunotia arcus Ehrenberg	--	--	--	--	--	--	--	--	--	--	--	--	C
lunaris (Ehrenberg) Grunow	R	--	--	--	--	--	--	--	--	--	--	--	--
monodon Ehrenberg	R	--	--	--	--	--	--	--	--	--	--	--	--
paludosa Grunow	--	--	--	--	--	--	F	--	R	F	F	--	--
cf. *E. parallela* Ehrenberg	--	--	--	--	--	--	--	--	--	--	--	--	R
praerupta Ehrenberg	--	--	--	--	--	--	R	R	--	--	--	--	--
praerupta var. *bidens* Grunow	--	--	--	--	--	--	--	F	--	--	--	--	--
praerupta var. *minor* (Kützing) Rabenhorst	--	--	--	--	--	--	--	--	--	--	--	R	--
sudetica (Müller) Hustedt	R	--	--	--	--	--	--	--	--	--	--	--	--
valida Hustedt	--	--	--	--	--	--	--	F	--	--	--	R	--
sp.	--	--	--	--	--	--	--	--	R	--	--	--	--
Fragilaria capucina Desmazieres	--	--	--	--	--	--	--	--	--	--	--	R	--
construens var. *subsalina* Hustedt	--	--	--	--	--	--	--	F	--	--	--	--	--
construens var. *binodis* (Ehrenberg) Grunow	--	--	--	--	--	--	--	--	--	--	--	--	F
leptostauron (Ehrenberg) Hustedt	--	--	--	--	--	--	--	--	--	R	--	R	F
leptostauron var. *rhomboides* Grunow	C	--	--	--	--	--	--	--	--	--	--	--	--
pinnata Ehrenberg	A	--	--	--	--	--	--	--	--	--	--	--	--
virescens Ralfs	A	--	--	--	--	--	--	--	--	--	--	--	--
sp.	F	--	--	--	--	--	--	--	--	--	--	--	--

Table 2. Diatoms in Pleistocene strata north and northwest of Yellowstone Lake—*Continued.*

Genera and species	YFs	Hayden Valley sequence				Mudkettle sequence		ACS	Pelican Valley sequence			GCd	BFd
	4618	5632	5633	5635	5636	5589	5907	5637	5904	5905	5906	5596	5639
Frustulia rhomboides (Ehrenberg) De Toni	--	--	--	--	--	--	--	--	--	--	--	--	F
rhomboides var. *saxonica* Rabenhorst) De Toni	--	--	--	--	--	--	R	--	--	--	--	--	--
sp.	R	--	--	--	--	--	--	--	--	--	--	--	--
Gomphoneis herculanea (Ehrenberg) Cleve	--	--	--	--	--	--	--	--	--	--	--	--	F
herculanea var. *clavata* Cleve	--	--	--	--	--	--	--	--	--	--	--	--	C
Gomphonema acuminatum var. *coronata* (Ehrenberg) W. Smith	--	--	--	--	--	--	--	--	--	--	R	--	--
cf. *G. acuminatum* Ehrenberg	--	--	--	--	--	--	--	--	--	--	--	--	R
intricatum Kützing	F	--	--	--	--	--	--	--	--	--	--	--	--
"*lanceolatum*" Cleve non Ehrenberg	--	--	--	--	--	--	--	--	--	--	R	--	--
lanceolatum var. *insignis* (Gregory) Cleve	C	--	--	--	--	--	--	--	--	--	--	--	F
longiceps var. *subclavata* Grunow	--	--	--	--	--	--	--	F	--	--	--	R	--
olivaceum (Lyngbye) Kützing	--	--	--	--	--	--	--	--	--	--	--	--	F
sphaerophorum Ehrenberg	--	--	--	--	--	--	--	--	--	--	--	--	F
subclavatum Grunow	R	--	--	--	--	--	--	--	--	--	--	--	--
ventricosum Gregory	--	--	--	--	--	--	--	--	--	--	--	--	F
sp.	R	--	--	--	--	--	--	R	--	--	--	--	--
Hannaea arcus (Ehrenberg) Patrick	--	--	--	--	--	--	--	--	--	--	--	--	C
Hantzschia amphioxys (Ehrenberg) Grunow	R	--	--	--	--	--	F	C	C	F	C	R	F
Melosira distans var. *lirata* (Ehrenberg) Bethge	R	--	--	--	--	--	--	--	--	--	--	--	--
cf. *M. distans* (Ehrenberg) Kützing													
italica (Ehrenberg) Kützing	C	R	R	R	R	--	--	A	F	F	F	--	C
cf. *M. italica* (Ehrenberg) Kützing	--	--	--	--	--	F	--	--	--	--	--	--	--
italica var. *tenuissima* (Grunow) O. Müller	--	--	--	--	--	--	--	--	--	F	--	--	--
sp.	--	--	--	--	--	R	R	--	--	--	--	R	F
Meridion constrictum Ralfs	--	--	--	--	--	--	R	F	R	--	R	F	R
Navicula amphibola Cleve	--	--	--	--	--	--	R	R	--	--	--	--	--
bacillum Ehrenberg	--	--	--	--	--	--	--	--	--	--	R	--	--
cincta (Ehrenberg) Kützing	--	--	--	--	--	--	--	--	--	--	--	--	R
cryptocephala Kützing	--	--	--	--	--	--	--	--	--	--	--	R	--
cuspidata Kützing	--	--	--	--	--	--	R	--	--	--	--	--	--

Table 2. Diatoms in Pleistocene strata north and northwest of Yellowstone Lake—*Continued.*

Genera and species	YFs	Hayden Valley sequence				Mudkettle sequence		ACS	Pelican Valley sequence			GCd	BFd
	4618	5632	5633	5635	5636	5589	5907	5637	5904	5905	5906	5596	5639
cuspidata var. *heribaudi* Peragallo and Héribaud	--	--	--	--	--	--	--	R	--	--	--	--	--
cf. *N. cuspidata* Kützing	--	--	--	--	--	--	--	--	--	--	R	--	--
dicephala (Ehrenberg) Wm. Smith	--	--	--	--	--	--	--	R	F	R	F	--	F
dicephala Ehrenberg var.	--	--	--	--	--	--	--	--	--	R	--	--	--
cf. *N. dicephala* (Ehrenberg) Wm. Smith	F	--	--	--	--	--	--	--	--	--	--	--	--
halophila (Grunow) Cleve	--	--	--	--	--	--	--	--	--	--	F	--	--
cf. *N. hassiaca* Krasske	--	--	--	--	--	--	--	--	--	--	--	--	R
mutica Kützing	--	--	--	--	--	--	--	C	--	--	--	--	--
mutica var. A	--	--	--	--	--	--	--	R	--	--	--	--	--
mutica Kützing var.	--	--	--	--	--	--	R	--	--	--	--	--	--
peregrina (Ehrenberg) Kützing	R	--	--	--	--	--	--	--	--	--	--	--	--
pseudoscutiformis Hustedt	F	--	--	--	--	--	--	--	--	--	--	--	--
pupula Kützing	F	--	--	--	--	--	--	--	--	--	--	--	--
pupula var. *capitata* Hustedt	--	--	--	--	--	--	--	--	--	--	--	--	F
pupula var. *rectangularis* (Gregory) Grunow	--	--	--	--	--	--	--	--	R	--	--	--	--
radiosa Kützing	F	--	--	--	--	--	--	--	--	R	--	--	--
aff. *N. reinhardtii* Grunow	F	--	--	--	--	--	--	--	--	--	--	--	--
scutiformis Grunow	F	--	--	--	--	--	--	--	--	--	--	--	--
semen Ehrenberg	--	--	--	--	--	--	--	R	--	--	--	--	--
cf. *N. verecunda* Hustedt	--	--	--	--	--	--	--	--	--	--	--	--	R
sp. A	--	--	--	--	--	--	--	F	--	--	--	--	--
sp. B	--	--	--	--	--	--	--	F	--	--	--	--	--
sp.	F	--	--	--	--	--	--	--	--	--	R	--	--
Neidium affine (Ehrenberg) Cleve	--	--	--	--	--	--	--	R	--	--	--	--	--
bisulcatum (Lagerstedt) Cleve	--	--	--	--	--	--	--	--	--	F	--	--	--
iridis (Ehrenberg) Cleve	F	--	--	--	--	--	--	R	--	--	--	--	--
iridis var. *vernalis* Reichelt	--	--	--	--	--	--	--	--	--	R	R	--	--
Nitzschia denticula Grunow	F	--	--	--	--	--	--	--	--	--	--	--	--
cf. *N. dissipata* (Kützing) Grunow	--	--	--	--	--	--	--	--	--	--	--	--	F
recta Hantzsch	--	--	--	--	--	--	--	--	--	--	R	--	--
sp. A	--	--	--	--	--	--	--	F	--	--	--	--	--
spp.	F	--	--	--	--	--	--	--	R	R	--	--	--
Pinnularia acrosphaeria Brébisson	--	--	--	--	--	--	--	R	--	--	--	--	--
appendiculata (Ehrenberg) Cleve	--	--	--	--	--	--	--	--	R	--	--	--	--
appendiculata (Agardh) Cleve	--	--	--	--	--	--	--	--	--	--	--	--	R
borealis Ehrenberg	--	--	--	--	--	--	F	--	C	F	F	F	R
brebissonii Kützing	--	--	--	--	--	--	--	R	--	--	--	--	--
cf. *P. brevicostata* Cleve	C	--	--	--	--	--	R	--	--	--	--	--	R

Table 2. Diatoms in Pleistocene strata north and northwest of Yellowstone Lake—*Continued.*

Genera and species	YFs	Hayden Valley sequence				Mudkettle sequence		ACS	Pelican Valley sequence			GCd	BFd
	4618	5632	5633	5635	5636	5589	5907	5637	5904	5905	5906	5596	5639
cf. *P. divergentissima* (Grunow) Cleve	--	--	--	--	--	--	--	--	--	--	--	R	--
gibba Ehrenberg	--	--	--	--	--	--	R	--	--	--	R	--	--
cf. *P. gibba* Ehrenberg	--	--	--	--	--	--	--	--	--	--	--	R	--
gibba var. *linearis* Hustedt	--	--	--	--	--	--	--	--	--	--	--	--	R
hemiptera (Kützing) Cleve	R	--	--	--	--	--	--	--	--	--	--	--	--
interrupta Wm Smith	-	--	--	--	--	C	--	--	F	F	A	--	--
interrupta var. *minutissima* Hustedt	--	--	--	--	--	--	--	--	--	--	F	--	--
aff. *P. interrupta* Wm. Smith	--	--	--	--	--	--	--	--	--	R	--	--	--
lata (Brébisson) Wm. Smith	--	--	--	--	--	--	--	C	--	--	--	--	--
major (Kützing) Cleve	--	--	--	--	--	--	--	--	--	R	--	--	--
mesolepta (Ehrenberg) Wm. Smith	C	--	--	--	--	--	--	--	R	R	--	--	--
mesolepta var. *angusta* Cleve	--	--	--	--	--	--	--	R	--	--	R	--	--
nodosa Ehrenberg	R	--	--	--	--	--	--	--	--	--	--	--	--
streptorapha Cleve	--	--	--	--	--	--	--	F	--	--	--	--	--
viridis (Nitzsch) Ehrenberg	--	--	--	--	--	--	--	R	R	R	R	--	--
cf. *P. viridis* var. *sudetica* (Hilse) Hustedt	R	--	--	--	--	--	--	--	--	--	--	--	--
sp. A*	R	--	--	--	--	--	--	--	--	--	--	--	--
spp.	F	--	--	--	--	--	R	R	--	R	R	--	--
Rhoicosphenia curvata (Kützing) Grunow	R	--	--	--	--	--	--	--	--	--	--	--	C
Rhopalodia gibba (Ehrenberg) Müller	C	--	--	--	--	R	--	--	--	R	R	R	R
gibba var. *ventricosa* (Kützing) Van Heurck	--	--	--	--	--	--	--	--	--	--	--	--	F
gibberula (Ehrenberg) Müller	--	--	--	--	--	--	R	--	F	F	F	R	F
parallela (Grunow) Müller	--	--	--	--	--	--	--	--	--	--	R	--	--
Stauroneis acuta Wm. Smith	--	--	--	--	--	--	--	F	--	--	--	--	--
anceps Ehrenberg	--	--	--	--	--	F	--	--	R	--	--	--	F
phoenicenteron Ehrenberg	F	--	--	--	--	--	--	--	R	R	R	--	--
sp. A	--	--	--	--	--	--	--	F	--	--	--	--	--
sp.	R	--	--	--	--	--	--	--	--	--	--	--	--
Stephanodiscus astraea (Ehrenberg) Grunow	--	R	R	R	F	F	--	--	--	--	--	--	C
astraea var. *minutula* (Kützing) Grunow	--	F	R	R	F	F	R	--	R	R	R	--	C
Surirella angustata Kützing	F	--	--	--	--	--	F	--	--	--	--	--	F
cf. *S. turgida* Wm. Smith	F	--	--	--	--	--	--	--	--	--	--	--	--
utahensis Grunow	--	--	--	--	--	--	--	--	--	--	--	--	R
Synedra ulna (Nitzsch) Ehrenberg	--	--	--	--	--	--	--	--	R	--	--	R	F
cf. *S. ulna* (Nitzsch) Ehrenberg	F	--	--	--	--	--	--	--	--	--	--	--	--

Table 2. Diatoms in Pleistocene strata north and northwest of Yellowstone Lake—*Continued*.

Genera and species	YFs	Hayden Valley sequence				Mudkettle sequence		ACS	Pelican Valley sequence			GCd	BFd
	4618	5632	5633	5635	5636	5589	5907	5637	5904	5905	5906	5596	5639
Tabellaria fenestrata (Lyngbye) Kützing	F	--	--	--	--	--	--	--	--	--	--	--	--
Tetracyclus emarginatus (Ehrenberg) Wm. Smith	R	--	--	--	--	--	--	--	--	--	--	--	--
cf. *I. emarginatus* (Ehrenberg) Wm. Smith	F	--	--	--	--	--	--	--	--	--	--	--	--
rupestris (A. Braun) Grunow	--	--	--	--	--	--	--	--	--	R	--	R	--

* Extinct species.

SAMPLE LOCALITIES

4618. Yellowstone Falls sequence at locality 1; varved tan claystone in upper part of unit 3 in measured section (see text) on east side of Yellowstone Canyon about 600 feet downstream from Upper Falls.
5632. Hayden Valley sequence at fossil locality 5632; thin-bedded dark-brown silt on top of hill 130 feet above contact with underlying rhyolite.
5633. Hayden Valley sequence at fossil locality 5633; brown structureless clay from south bank of creek 12 feet above contact with underlying rhyolite.
5635. Hayden Valley sequence at fossil locality 5635; thin-bedded ripple-marked silt and clay about 80 feet above contact with underlying rhyolite.
5636. Hayden Valley sequence at fossil locality 5635 but 20 feet stratigraphically below collection 5635; dense brown blocky clay.
5589. Mudkettle sequence at locality 8; white to blue-gray claystone and siltstone about 50 feet below top of sequence in big exposure 1,000 feet west of forks of Wrong Creek and on south side of creek.
5907. Mudkettle sequence at fossil locality 5907; chalky white tuffaceous soft claystone on east side of Pelican Creek, 5–10 feet above water level.
5637. Top of Astringent Creek? Sand at fossil locality 5637, 5,000 feet east-northeast of locality 16; gray structureless clay at about the same topographic elevation as the top of a 100-foot section of Astringent Creek Sand directly overlying basalt at locality 16. Faulting and poor exposures in the intervening area make stratigraphic relation of diatomaceous beds to the sand somewhat uncertain.
5904. Pelican Valley sequence at locality 11; gray to drab tough clay in unit 2 of measured section (see text). A radiocarbon age of 7,550 years was obtained from overlying bed.
5905. Pelican Valley sequence at locality 11; creamy gray dense clay in unit 4 of measured section (see text).
5906. Pelican Valley sequence at locality 11; creamy gray dense clay in unit 7 of measured section (see text).
5596. Gibbon Canyon deposits in highway cut 800 feet upstream from right angle bend in Gibbon Canyon and 7 miles west of geologic map area. Sample is split of carbonaceous white and black clay from which a radiocarbon age of 9,440 years was obtained.
5639. Bannock Ford deposits 3,000 feet east-northeast of Tower Falls, on east side of Yellowstone River, about 8 miles north of geologic map area. Sample is evenly bedded gray-green silty clay 12 feet above river level. Basal 3 feet of overlying sand bed contains carbonized wood from which a radiocarbon age of 3,750 years was obtained.

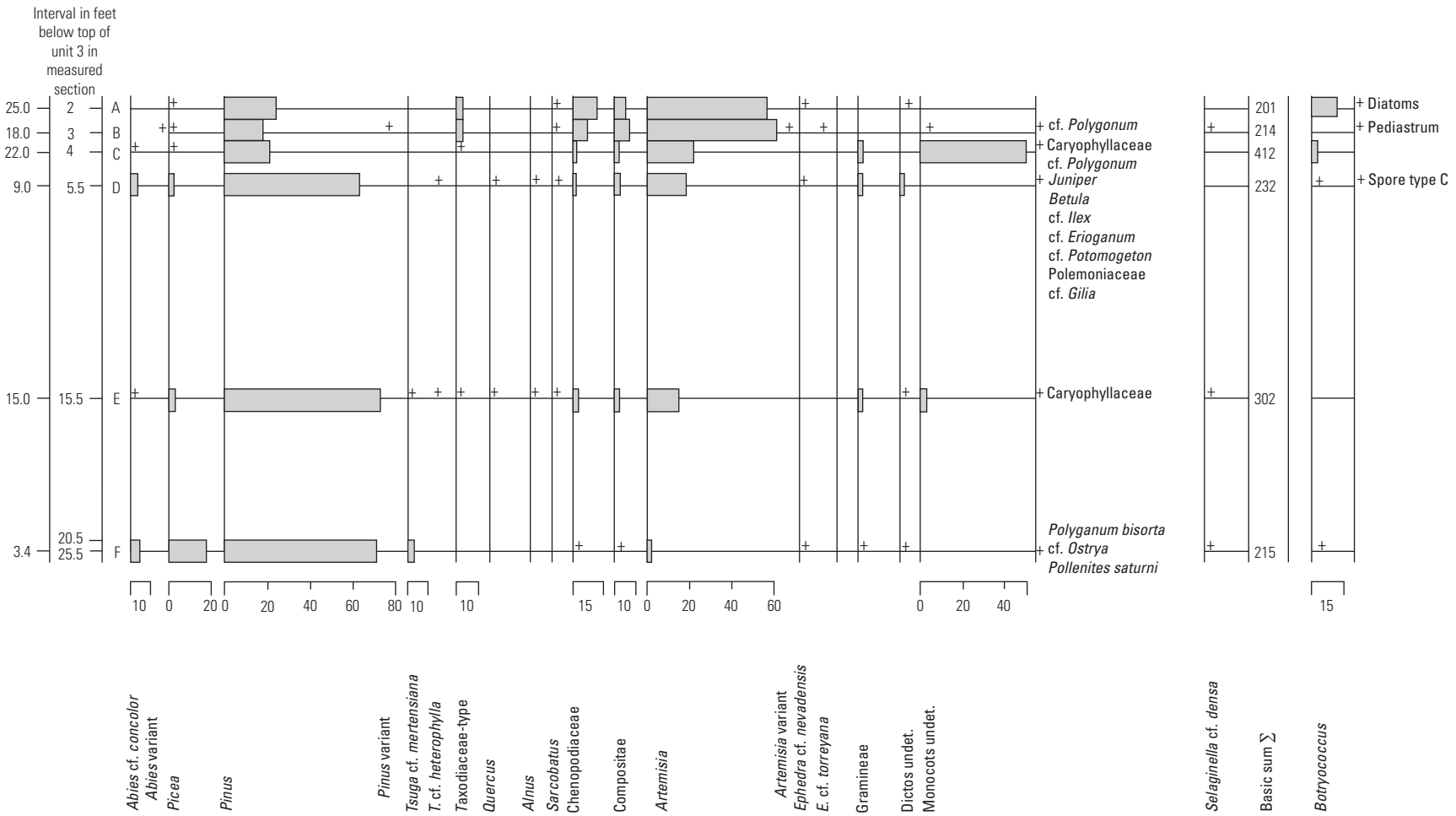

Figure 8. Pollen distribution in Yellowstone Falls sequence at locality 1. Identification and arrangement prepared by E.B. Leopold; samples from USGS paleobotany locality D1212, unit 3 of measured section (see text). Lithology: A, white light-weight clay with carbonized plant fragments; B, plant-bearing brown clay; C, white light-weight clay with brown plant fragments; D, brown clay; E, varved light-gray clay; F, laminated gray clay. Data are plotted in histogram form, showing percent composition of total pollen count. Spores and algae are not included in the basic sum, but are shown as number of specimens encountered per 100 pollen grains tallied. The basic sum Σ, which is entered on the right, represents a significant sample and is the basis for percentages. Pollen of tree forms are plotted on left, shrub and herbs in the middle, and spores and algae are plotted on the right of the basic sum column.

toolbox" of geologists in 1956; see Morgan and others, 1998; Pierce, Cannon and others, this volume—Editor.]

The rock floor on which the Hayden Valley strata were deposited is at an altitude of about 7,820 feet at locality 2 as well as along Trout Creek a mile west of locality 3. Farther north and east, the base is not exposed even though the altitude decreases to 7,680 feet at the Yellowstone River. This fact plus the distribution of the next younger sequence suggests that there was northeastward tilting after deposition of both sets of strata. The peculiar course of Alum Creek northeastward across Hayden Valley, all the way to the edge of the bounding volcanic rocks, likewise suggests tilting.

Howard recognized the high elevation of the youngest part of the Hayden Valley sequence and postulated that the lake in which it was deposited could not have been connected with Yellowstone Lake because southern outlets of the latter are much lower. He suggested, instead, that there may have been a high level "retreat lake" in Hayden Valley, between his "Lamar glacier" to the north and ice occupying Yellowstone Lake to the south. The presence of extensive Pleistocene faults and evidence of crustal warping as may be related with the active and ongoing deformation of the Yellowstone caldera (see Pierce, Cannon and others, this volume), however, suggests to us that there was only one lake at this time, as postulated by Holmes, and that the relation of elevation of sediments to lake outlets has not remained constant.

Spectrographic analyses of the Hayden Valley sequence in Hayden Valley show that it contains slightly more magnesium and cobalt and less yttrium and molybdenum than the Yellowstone Falls, Mudkettle, and Pelican Valley sequences. The varved clay at locality 15 is spectrographically almost identical to that of the Hayden Valley sequence in Hayden Valley. There is likewise a close similarity in amount of common oxides (compare, for example, D123116 with D123117 and D123122 in table 1). For these reasons, plus the lithologic similarity, the outcrops at localities 15 and 19 are tentatively correlated with the Hayden Valley sequence.

Diatoms were collected from four horizons in the Hayden Valley sequence (table 2). Concerning this assemblage (and those from the Mudkettle, Pelican Valley, and Bannock Ford deposits), K.E. Lohman and G.W. Andrews stated (written commun., 1966):

> "All of these species are still represented in living assemblages elsewhere, although some of them have geologic ranges extending back to the Miocene; a larger number do not go back beyond the Pliocene, and some, particularly the most abundant species in the assemblage, such as *Stephanodiscus astreaea* and its variety *minutula*, are not known from rocks earlier than Pleistocene. Thus the age of the beds from which these collections came cannot be older than Pleistocene, and probably not older than middle or late Pleistocene.
>
> "The environment in which these diatoms lived, was probably a cool to cold, fairly shallow, clear lake, very near neutral, as the rare species usually preferring slightly acidic water are balanced by those usually preferring slightly alkaline water, and many are indicative of water of low mineral content."

Figure 9. Air oblique view west-southwest up Alum Creek showing treeless exposures of Hayden Valley sequence in western part of Hayden Valley.

Figure 10. View east at locality 15 along cliff cut by storm waves; surface bevels till and underlying lake sediments of Hayden Valley(?) sequence, north edge of Mary Bay, Yellowstone Lake. Foreground is site of figs. 11 and 12. Indicated are varved clay (dark because it is wet) (A), sand and silt (B), till (C), and beach or dune sand (D). Units A and B are probably part of Hayden Valley sequence.

Figure 11. Wave-cut cliff at locality 15, north edge of Mary Bay, Yellowstone Lake.

Figure 12. Varved clay at base of exposure shown in figure 11, locality 15.

Alum Creek Sequence

The Alum Creek sequence is here described from exposures along Alum and Trout Creeks in Hayden Valley, and comprises the "plains sediments" of Howard (1937). It is present only in the topographically low parts of the valley. The maximum thickness is unknown, but a section, locally as much as 125 feet thick, is poorly exposed on broad treeless grassy slopes.

At locality 4 in a large gravel pit (fig.14), the basal 20 feet is dark-gray, sugary, fine-grained, remarkably homogenous sand with abundant tiny magnetite crystals, shards, pumice

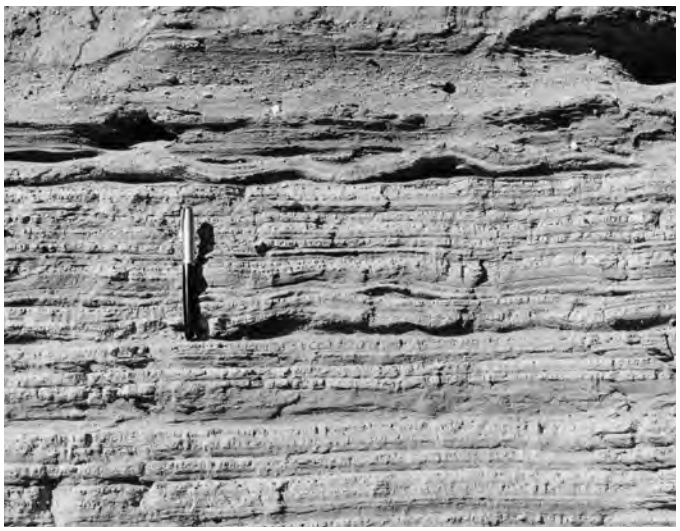

Figure 13. Silt beds in Hayden Valley(?) sequence at locality 19 on the northwest margin of Mary Bay, Yellowstone Lake. In nearby exposures, this unit overlies varved clay and underlies till.

Figure 14. Alum Creek sequence at locality 4. About 15 feet of strata can be seen; basal part is fine-grained gray sand; middle is dark gray obsidian sand and gravel interbedded with light gray sandy silt; upper part is dark brown soil. Origin of contorted zone has not been determined but may be due to frost wedges.

chunks, and black obsidian. The bed is overlain by 10 feet of dark-gray obsidian sand and loose gravel composed of rounded to angular fragments of rhyolite, obsidian, and basalt. Above this is 5 feet of sand, boulders, and weathered soil.

Along Trout Creek near the highway at locality 5 are broad natural exposures of the Alum Creek sequence. The basal 4 feet is a dark-gray, coarse-grained obsidian sand and gravel. Above this is 25 feet of gray, slightly clayey and silty sand. Some of it is crossbedded, but other parts have even layers as much as an inch thick with graded bedding from sand to thin clay laminae, which resemble coarse varves. The top 5 feet is a mixture of sand, gravel, and clay.

After retreat of the ice that overrode the Hayden Valley beds, broad northeast-trending valleys 100 to 200 feet deep were cut and in them the Alum Creek sequence was deposited. A few striated erratics, possibly reworked from the post-Hayden Valley till, are present in gravel pits, but no evidence of glacial debris with morainal form was found on the present surface.

The Alum Creek sequence has yielded no fossils as yet. A few tiny fragments of carbonized wood, not enough for a ^{14}C determination, were observed. The close coincidence of the down-valley part of these beds to the present level of the Yellowstone River suggests that they are of late Pleistocene age.

Mudkettle Sequence

The Mudkettle sequence is the oldest of the three lacustrine and fluvial sediment units recognized along and north of Pelican Valley, northeast of Yellowstone Lake. On Hayden's first trip through the area in 1871 (Hayden, 1872, p. 131), he not only recorded the presence of lake deposits but observed that they extended northward nearly to the head of the Pelican Creek drainage. These relations were not mentioned by subsequent workers. The strata are exposed in the bottoms of re-excavated stream valleys that separate hard ridges of Tertiary volcanic rocks. By far the best and most extensive exposures are near The Mudkettles, between localities 6 and 10 (fig. 3), along Pelican Creek. The Mudkettles, from which the name of the sequence is derived, are a series of hydrothermal vents that cut through these strata, and mud in the kettles is reworked from them.

The maximum thickness of the sequence is not known, although it appears the unit thickens from the north to the south. At locality 8, about 75 feet is visible in a continuous exposure (fig. 15), at locality 6 (fig. 16) about 85 feet, and farther south near The Mudkettles, 150 feet.

In the type area, east of The Mudkettles, the Mudkettle sequence consists of light-gray, soft claystone and siltstone with lesser amounts of sandstone and conglomerate that weather to rounded treeless badland hills. Vertical cuts show intricate depositional features (fig. 16 at locality 6) that are not readily apparent in more rounded exposures. The following section describes typical lithology:

Measured Section of Mudkettle Sequence

This section was measured by J.D. Love at locality 6 (fig. 16) on the east bank of Pelican Creek.

Unit	Lithology	Thickness (ft)
Top of section; younger beds eroded		
5	Claystone and siltstone, gray, with some pale-green spots, soft, crumbly, fine-grained, noncalcareous, highly tuffaceous	10+
4	Conglomerate and sandstone, gray, with green siliceous concretions, lenticular, cross-bedded; rock fragments are red and brown rhyolite ranging in size from cobbles to grit; sandstone is thin-bedded, with green fine-grained clay pellets and pumice chunks in limonitic hard siliceous matrix, noncalcareous, with sporadic angular grains of quartz and feldspar; forms prominent ledge at upper left in figure 16	15
3	Siltstone and sandstone with thin claystone partings, thin-bedded, moderately lithified. Upper part is noncalcareous, very tuffaceous, pale purplish-white, with texture of fine-grained bread; pink and clear sand grains are typical and very small; matrix contains enough clay to decrepitate rapidly in water. In the middle are beds of hard brittle, pale bluish-green to white noncalcareous, fine-grained, pure claystone. These are underlain by chalky, white colloidal, fine-grained blocky noncalcareous claystone. The basal beds are light gray mudstone interbedded with white, fine-grained, noncalcareous, hard to brittle claystone containing sporadic angular grains of quartz or sanidine; rock is limonite-stained along fractures; impregnated in places with a conspicuous blue stain of unknown composition.	40–50
Local unconformity		
2	Sandstone, greenish-gray to tan, chiefly a crystal tuff, pyritic, iron-stained, cross-bedded, moderately soft but sufficiently lithified to form conspicuous ledge (at lower right in fig. 16); middle part contains pumice breccia and conglomerate, dark gray, hard, a mass of altered pumice chunks and large shards in a silicified sandstone matrix; sporadic rounded pebbles of dense dark gray volcanic rock and quartz and feldspar grains; maximum dip of foreset beds is 25°N.	15–25
1	Conglomerate, mudstone, and claystone, pale green to brown, hard; forms ledge at water level of Pelican Creek; conglomerate is composed of coarse, rounded, rhyolite pebbles; claystone and mudstone are pale green, dense, hard, with layers of pumice chunks, shards, and angular quartz and feldspar grains	3
Thickness of measured part of Mudkettle sequence		73–93+

Underlying beds are not exposed here.

The north dip of foreset beds in unit 2 is of special interest. It suggests that this part of Pelican Valley may have been an outlet channel that drained northward from ancestral Yellowstone Lake at the time the Mudkettle sequence was being deposited.

The northernmost exposures of the Mudkettle sequence that have been examined are at localities 7 and 8, north of the present divide that separates southward drainage into Yellowstone Lake from northward drainage into Yellowstone River. About 75 feet of dull bluish-gray claystone and mudstone is exposed at locality 8 (fig. 15). It is blocky, soft, noncalcareous, limonite-stained, and interbedded with gray, fine- to medium-grained, poorly cemented volcanic sandstone containing abundant shards.

Perhaps the most unusual outcrop of any Pleistocene unit in the northern Yellowstone area is the Mudkettle sequence at locality 7. The rock here is impregnated with a volatile, extremely fluid, light-brown, paraffin-base oil, described and photographed elsewhere (Love and Good, 1970). The rock is a bright to dull, blue-gray claystone and mudstone. It is dense, hard, noncalcareous, blocky, and peppered with tiny black specks. Sporadic angular grains of clear quartz and feldspar are characteristic. Interbedded with the mudstone are partings of gray, fine-grained, homogeneous, "pepper and salt" volcanic sandstone that contains black magnetite grains, abundant tiny clear shards, and larger clear angular quartz and feldspar grains. The mudstone has a persistent acrid odor. Analysis of a representative sample shows 76 ppm arsenic, 0.5 ppm selenium, 0.10 percent fluorine, and 1.1 percent sulfur (determined by A.J. Bartel, G.T. Burrow, W.D. Goss, and I.C. Frost, respectively). In August 2004, a sample of similar description—a volatile, paraffin-base oil in a bright to dull, blue-gray claystone and mudstone that is dense, hard, noncalcareous, blocky, and peppered with tiny black pyrite crystals—was collected near active sublacustrine hydrothermal vents from the northern basin of Yellowstone Lake (L.A. Morgan and others, written commun., 2004).

Spectrographic analyses of the Mudkettle sequence shows that it contains less Fe, Ca, Mn, Sr, and Ni than the Yellowstone Falls, Hayden Valley, and Pelican Valley sequences (fig. 4) and no excessive amounts of any of the other elements listed in the figure. It is the highest of them all, however, in individual analyses (in percent) of yttrium (0.007), niobium (0.003), ytterbium (0.0007), cerium (0.02), neodymium (0.015), and tin (0.015). Common oxides in the Mudkettle sequence are given in table 1. They show no conspicuous excesses or deficiencies.

The Mudkettle sequence laps across Tertiary and pyroclastic rocks on the east and west sides of Pelican Valley and is correlated northward into areas that now drain directly into the lower part of Yellowstone Canyon. The presence of these lacustrine beds at localities 7 and 8 and the north-dipping foreset beds at locality 6 suggest that ancestral Yellowstone Lake extended around the east end of the Upper Basin Member of the Plateau Rhyolite. Perhaps this part of the Mudkettle sequence was deposited in sluggish outlet lagoons like those now present between Yellowstone Lake and the Upper Falls.

In some places the Mudkettle strata are overlain by moraines whose form has not been entirely destroyed; therefore, these moraines may be younger than the glacial debris overlying the Hayden Valley sequence. Elsewhere, glacial debris is missing and Astringent Creek Sand (a newly named unit described in the next section) rests directly on the Mudkettle sequence.

The Pleistocene age of the Mudkettle sequence is based on diatoms (table 2) and pollen. Only 3 of 30 species of diatoms are common to both the Mudkettle and Hayden Valley sequences, but, because of the paucity of collections, the significance of this difference is not known. The age and environmental interpretation by Lohman and Andrews is the same as for the Hayden Valley deposits.

Scant pollen assemblages from oil-saturated claystone at locality 8 consist of the following forms (identified by E. B. Leopold, written commun., 1964 and 1966):

	Rainbow Springs (pollen colln. D3310)	0.25 mi upstream from Rainbow Springs and stratigraphically a few feet higher (pollen colln. D3366)
Pinus	42	57
Artemisia	35	12
Picea	2	12
Ephedra and *Ephedra(?)*	1	1
Botryococcus	1	7
Quercus	—	1
Juniperus	—	1
cf. *Acer*	—	1
Erigonum	1	—
Polygonum cf. *bistortoides*	1	—
Sarcobatus vermiculatus	1	—
Gramineae	1	1
Compositae	2	—
Cyperaceae	1	2
Dicot, undet.	10	1
Chenipodiaceae, undet.	3	—
Total count	101	98

Essentially the same pollen assemblage as that at Rainbow Springs (locality 7) was found in a claystone directly above the unconformity shown in figure 16. Below the unconformity, 2 feet above creek level, another claystone yielded a similar flora except that the pine pollen count increased to 50 percent and spruce to 5 percent. These collections represent pollen rains that are nearly identical to local modern accumulations.

Astringent Creek Sand

The Astringent Creek Sand is here named for exposures on Astringent Creek at locality 9 (fig. 17). It has not been previously recognized or described. The sand was deposited along Pelican Valley and its tributaries and across drainage divides to the east (loc. 16) and north (loc. 8) (fig. 15). The thickness of eroded remnants is commonly about 100 feet; it is nearly 200 feet thick at the type locality and more than 300 feet at locality 10.

The basal beds at the type locality are very coarse gray sand with some pebble gravel but little or no silt or clay matrix. These beds grade up to coarse, loose, homogeneous, gray, unlithified sand. In the upper 100 feet, a few thin lenticular silt and impure clay beds are present. Highly rounded pebbles, up to 1 inch in diameter, of volcanic rocks become more numerous near the top. The sand throughout most of the section is gray-brown, coarse grained, and loose with rounded grains of black and gray obsidian, gray pumice, clear quartz and feldspar, red and black volcanic rocks, and sparse shards up to one-sixteenth-inch long. The more clay-rich beds contain yellow and brown clay balls that quickly disaggregate in water. At the top of the section are highly rounded pebbles and cobbles and sparse boulders of hard volcanic rocks of various types. No striations were found on them, and they apparently are part of a fluviatile deposit rather than morainal debris.

At locality 8, the Astringent Creek Sand is exposed in a continuous, 125-foot-thick section (fig. 15). The basal bed is a hard, rounded, pebble conglomerate. It is overlain by a sandstone that is sufficiently lithified to form a weak ledge about 15 feet thick. The remainder of the sequence is crudely stratified, uncemented, coarse- to fine-grained sand; much of the sand consists of clear shards and white pumice fragments. Black obsidian shards, clear angular quartz and feldspar grains, and some rounded granules of pink rhyolite are present also. The volcanic material is much more abundant and less waterworn than that at locality 9 and may be closer to a source vent. [*See Foreword and About the Author, this chapter.*]

The thickest section (more than 300 feet) is at locality 10 where the strata consist largely of brown-gray, coarse- to fine-grained, nonintegrated volcanic sand. The grains are chiefly shards, pumice, quartz, feldspar, black obsidian, and brown and red volcanic rocks. Magnetite is common as very small crystals.

The farthest eastern section measured, at locality 16 along Raven Creek (fig. 3), is composed of 100 feet of sand that overlies basalt. At the base is 5 feet of dark blue-gray cross-bedded sandstone, then 30 feet of ledge-forming sandstone with a brown iron cement. The remainder is brownish-gray unconsolidated "pepper and salt" sand. Shards are present but not abundant.

East of locality 16, the Astringent Creek Sand thins but apparently was deposited continuously across the drainage divide that separates Raven Creek (fig. 2) from Willow Creek, a tributary to Lamar River (figs. 2 and 3). The occurrence on the drainage divide is of special importance because at this site a distinctive collection of diatoms was obtained (colln. 5637, table 2).

As much as 150 feet of sand is exposed on the northeast side of Broad Creek, 1 mile west-southwest of Wapiti Lake (because of lack of field time, not mapped separately at this locality on fig. 3). Additional outcrops of the sand are present for several miles down Broad Creek.

One of the conspicuous features of the Astringent Creek Sand is that it supports a thick growth of trees, whereas the older and younger lacustrine beds are almost treeless.

The conditions of deposition of the Astringent Creek Sand are not fully understood. It is a well-sorted, water-lain sand with remarkably little clay, silt, or other bonding cement. It overlies the Mudkettle sequence and has buried the moraines that rest on those beds. It may represent an ice-marginal deposit that accumulated in valleys to the north and east of a static mass of ice occupying the Yellowstone Lake basin. If so, deposition of sand across the drainage divides to the north and east demands an explanation. On the other hand, if this is not an ice-marginal deposit, what happened to it in the vicinity of Yellowstone Lake?

The sand extends from Rainbow Springs at locality 7 down Wrong Creek toward Yellowstone Canyon. If it was deposited as far west as the present brink of the canyon, this would suggest that the canyon is younger than the sand.

The source of the abundant pumice and shards at localities 8 and 10 is not known but the angularity, freshness, and volume suggests that the source was one or more vents in the Yellowstone area. [*See Foreword and About the Author, this chapter.*]

No fossils have been found within the Astringent Creek Sand except at its probable top on the Raven Creek–Willow Creek

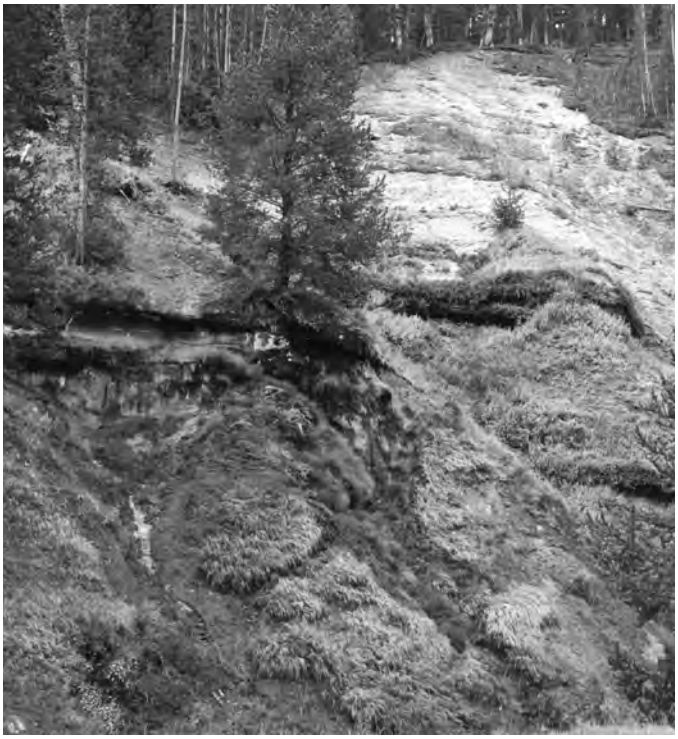

Figure 15. View south across Wrong Creek at locality 8, showing 200-foot scarp of Astringent Creek and Mudkettle sequences. About 75 feet of claystone in Mudkettle sequence is exposed in ravine below ledge at lower left. Ledge and overlying 125 feet of section is newly named Astringent Creek Sand.

Figure 16. Local unconformity in Mudkettle sequence at locality 6. View is east across Pelican Creek at cliff composed of 85 feet of strata, chiefly sandstone below unconformity and light greenish-gray claystone, siltstone, and sandstone above it. All ledges are highly tuffaceous sandstone.

Figure 17. Astringent Creek Sand (newly named) on east side of Astringent Creek, 2.5 miles north of Pelican Valley at locality 9. View is north at outcrop of nearly 200 feet of gray unconsolidated sand overlying white sulfurous thermal deposits that crop out in irregular areas.

drainage divide, 5,000 feet east-northeast of locality 16. Here abundant diatoms were found in a gray structureless clay (colln. 5637, table 2). This collection comprises an assemblage that is distinct from those in all the other sequences in the area. Concerning it, Lohman and Andrews stated (written commun., 1960):

> "The assemblage from locality No. 5637 suggests deposition in a cool, slightly saline, but fairly fresh water of low mineral content, and probably near the margin of a lake. This is indicated by a number of distinctly fluviatile species mixed with a larger number of species now living in lakes. All of the species in this assemblage are still represented in living assemblages elsewhere, so an age of Pleistocene (and probably late Pleistocene) is indicated. Although many of the species have long geologic ranges extending from Miocene to Recent, a few are not known from rocks earlier than Pleistocene in age."

Pelican Valley Sequence

The Pelican Valley sequence is named after Pelican Valley (fig. 18) where in the lower 10 miles it is exposed in broad treeless outcrops. These strata were recognized as representing a deposit in ancestral Yellowstone Lake by nearly all the earlier workers in the Park region, but they made no attempt to describe, measure, or date the beds.

The exposed thickness is commonly about 120 feet, but there is no information as to how much more underlies the valley floor. One of the best sections is in a bluff along Pelican Creek, one-half mile southwest of locality 12, where more than 100 feet can be seen (figs. 19 and 20). The lower part of this section is relatively massive, fine-grained, sparsely pebbly sandstone and siltstone; the middle is light-gray to white, thick-bedded siltstone with a velvety sheen; the upper 30 feet is finely layered white siltstone. At the top is 5 to 10 feet of hard, pale mustard-yellow, nodular porous sandstone and siltstone composed largely of tiny altered shards.

About halfway between localities 12 and 13, lenses of pebble gravel are interbedded with the siltstone. One rhyolite boulder three feet in diameter was observed in place in the siltstone. A thin but significant section is exposed at locality 11 (fig. 21).

Figure 18. Phototheodolite view southwest from Pelican Cone. White treeless area is Pelican Valley, underlain by the Pelican Valley sequence. Yellowstone Lake is gray expanse to right of upper center; Teton Range and Grand Teton Peak are on center skyline, 70 miles away.

Section of Pelican Valley Sequence Along Astringent Creek

The following section was measured on the east bank of Astringent Creek at locality 11:

Unit	Lithology	Thickness (ft)
Top of section		
8	Clay, rich rusty brown at base, gray and tan in middle, and greenish-brown at top, silty, crumbly; top of unit is horizon of soil at meadow surface	2.5
7	Clay and silt, light gray, with limonite stain in lower half; some grit and fine-grained sand partings; some creamy gray clay that is plastic when wet	4.0
6	Sand, gray, coarse-grained, loose with abundant shards	0.5
5	Clay, light gray, with rusty splotches, plastic massive, lenticular, sparse carbonized vegetal trash	2.0
4	Clay and silt, dull gray in lower part, becoming more carbonaceous near top, clay is creamy gray, fine-grained, noncalcareous, homogeneous; abundant twigs, rushes, blossoms, and seeds; sample collected for ^{14}C determination	2.3
3	Granule gravel, rusty brown, with 2 inches of clay in upper part, poorly cemented; abundant black obsidian, shards, and rhyolite fragments; brightly colored sand grains of many lithologies; pockets of carbonized trash, one of which contains a tree stump one foot in diameter dated as 7,550+350 yr B.P. (W-1684)	1.0
2	Clay and sand, deep indigo blue and green tinges when wet, dull gray to olive drab when dry; clay is massive, tough, dense, silty, noncalcareous; decrepitates in water after drying; contains abundant tiny white grains of pumice; sandy part is almost uncemented, with silty shard-bearing matrix; contains rounded pebbles up to one inch in diameter of gray previously silicified conglomerate, and pumice; highly carbonaceous, with abundant twigs, rushes, and tree branches as much as two inches in diameter; sample collected for ^{14}C determination	2.0
1	Conglomerate, blue gray, loose to moderately cemented, forms ledge at creek level; composed of highly rounded pea gravel to pebbles three inches in diameter in a shard-bearing matrix; most fragments are rhyolite but some are mafic rocks	3.0+
Total thickness of measured part of Pelican Valley sequence		17.3

Intermittent outcrops of velvety gray clay and silt are present along Astringent Creek between localities 11 and 14. Along the bank of Pelican Creek at locality 14 (fig. 22) is an exposure of the Pelican Valley sequence with a distinctive lithology.

Section of Pelican Valley Sequence at Locality 14

The following section was measured on the east bank of Pelican Creek about 100 yards downstream from the mouth of Astringent Creek.

Unit	Lithology	Thickness (ft)
Top of section		
7	Sand, dark gray, silty, loose	5
6	Sand, light gray, silty, pumiceous; forms slope back of creek bank	10
5	Conglomerate, dark brown, manganese-stained, hard, with striated boulders of volcanic rocks as much as 5 feet in diameter apparently reworked from a moraine to the south	5
4	Sandstone, gray, evenly bedded to cross bedded, slightly lithified (near top of right center in fig. 22)	8
3	Conglomerate, dark brown, with boulders of basalt and rhyolite in a course-grained ferruginous sand matrix; stratified in horizontal layers, in contrast with underlying unit	2
2	Pumice conglomerate composed of white fibrous, light-weight, rounded pumice pebbles up to 1-1/2 inches in diameter in a matrix of dark gray and clear shards, black obsidian, and clear angular quartz and feldspar grains; foreset beds strike N.40°E., dip N.25°W.	5
1	Sandstone, blue-gray, medium- to coarse-grained; grades up to overlying unit; base below creek levels	5+
Total thickness of measured part of Pelican Valley sequence		40+

Embedded in the glassy finer grained matrix of the pumice pebbles are numerous clear crystals of quartz and feldspar. The pebbles float in water; they are so abundant, yet so fragile that it is unlikely they could have survived transport over long distances.

At locality 13, about 300 feet upstream from the old Pelican Creek Service Road bridge, a bluish-gray shard-bearing claystone (Glacier Peak? ash) and siltstone 6 feet thick is

Figure 19. View southeast across Pelican Creek (not visible; between horses and cliff), 1,500 feet southwest of locality 12, showing 100 feet of white silt and lesser amount of sand in Pelican Valley sequence. Figure 20 shows detail in upper cliff at far left.

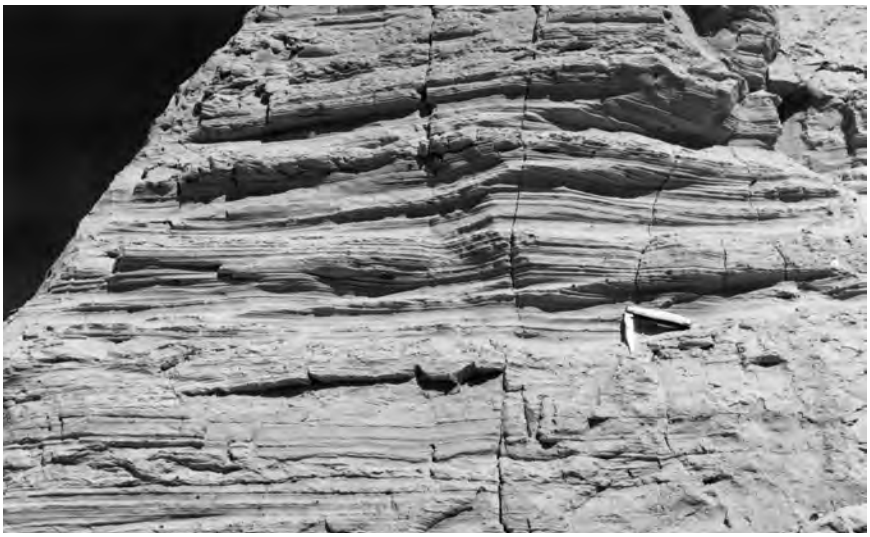

Figure 20. Bedding in white siltstone cliff of Pelican Valley sequence shown in Figure 19, 1,500 feet southwest of locality 12.

Figure 21. Upper part of Pelican Valley sequence at locality 11 on east side of Astringent Creek. This is site of detailed measured section and ^{14}C date of 7,500 years. Conspicuous units are shown by number used in section; horizons of wood collected for ^{14}C dating are indicated.

overlain by 2 feet of bluish-gray and brown, fine-grained, tuffaceous, soft sandstone. This locality is notable in three respects: the abundance of pollen, the unusual petrography of the rock, and the southwest dip of the beds. The rock is a pyroxene andesite tuff with abundant ortho- and clinopyroxene and andesine. This contrasts sharply with the felsic nature of the debris a mile upstream at the pumice pebble locality. The beds along a 50-foot outcrop strike N.60°W., and dip 9°SW. It is not known if this is an initial dip or the result of slumping or post-Pelican Valley warping. These beds are overlain by a brown hard conglomerate locally known as "beach rock" (fig. 23). [*For further discussion, see Foreword and About the Author, this volume.*]

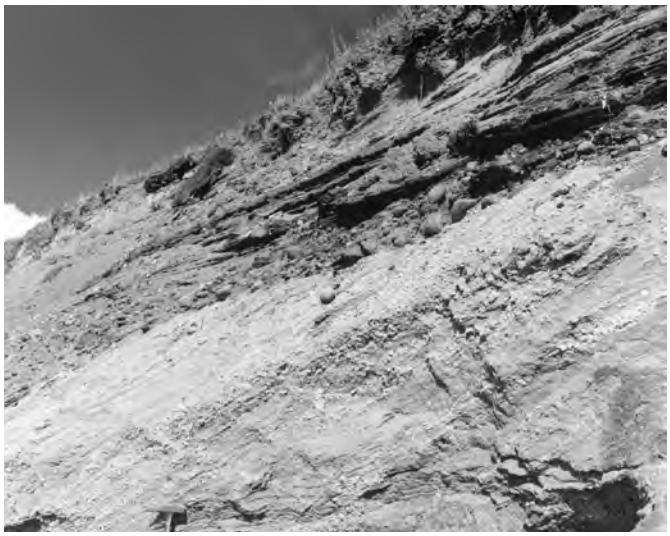

Figure 22. White pumice pebble conglomerate with steep foreset beds overlain by gravel and sand, all in upper part of Pelican Valley sequence at locality 14. Pumice pebbles will float on water.

Figure 23. Cliff of "beach rock" along north shore of Mary Bay, Yellowstone Lake. Rock is a conglomerate of silicified claystone, siltstone, sandstone, and volcanic rock fragments in a siliceous matrix. Black cap in foreground shows scale.

The Pelican Valley sequence laps across the lower part of the Astringent Creek Sand that forms the bordering hills to the north and northeast and buries part of the morainal deposits that lie between Pelican Valley and Yellowstone Lake. At locality 12 (fig. 24), the relations of rhyolite tuff, glacial deposits, and the Pelican Valley sequence are well exposed. At the base is 50 feet of white rhyolitic crystal tuff with abundant bipyramidal quartz crystals and obsidian fragments. This is overlain by 15 feet of till, chiefly of rounded to angular, striated erratics up to 3 feet in diameter, of rhyolite, basalt, and coarse porphyry with white euhedral phenocrysts. The top of the till has been reworked into the white velvety silt in the basal part of the Pelican Valley sequence. Above this contact is 50 feet or more of white silt. Sparse lag boulders of locally derived volcanic rocks are on the silt, but no evidence was found that these are of glacial origin.

Spectrographic analyses of the clays and silts in the Pelican Valley sequence are shown in figure 4. The composition is so similar to that of the older Hayden Valley sequence that it suggests the possibility of the younger deposit having been derived in part from the Hayden Valley or a lateral equivalent to the southwest. Transport would probably have been by wind. Of all the sedimentary units (excluding the Turbid Lake), the Pelican Valley sequence is highest in barium, strontium, and gallium, but does not have any record of low values in other trace elements. An especially interesting fact, the significance of which is not known, is that a spectrographic analysis of pumice pebbles in unit 2 of the measured section at locality 14 (fig. 22) shows almost the same composition as that of the silts and clays. A few elements in the pumice are at the top or bottom of the range for the silts and clays, but most fall within the span and none have excessively high or low concentrations. This composition pattern is in marked contrast with that of the similar-appearing pumiceous beds in the Turbid Lake sequence (fig. 4).

A rock analysis (D123124, table 1) of common oxides in the pumice pebbles in the Pelican Valley sequence shows slightly higher SiO_2 and K_2O and lower Al_2O_3, Fe_2O_3, and TiO_2 as compared with those for the clays and silts. With respect to clays and silts in other sequences, the Al_2O_3 content of those in the Pelican Valley sequence is high consistently, with values as high as 19.7 percent.

The age of the wood-bearing strata at locality 11 (fig. 21) has been determined by ^{14}C as 7,550±350 years B.P. (Meyer Rubin, written commun., 1965; USGS Lab No. W-1684). Diatom assemblages are listed in table 2. The quote of Lohman and Andrews regarding age and environment of deposition cited in connection with the Hayden Valley sequence applies equally well to the Pelican Valley.

Identification and evaluation of the following scant pollen collections (locations shown on fig. 3) were made by E.B. Leopold (written commun., 1960):

	L-5835	Loc. 13
Pinus		16
Populus	1	
Picea cf. *pungens*		3
Ephedra	1	
cf. *Tsuga*		1
cf. *Quercus*		1
Alnus	1	
cf. *Salix*	1	
Compositae undet.	14	6
Artemisia (primary)	62	89
Artemisia (secondary?)		2
Chenopodiaceae undet.	5	6
dicots undet.	15	6
monocots undet.	3	1
Umbelliferae		1
Selaginella cf. *densa*		13
Polypodiaceae(?) fern spores undet.	2	1
Redeposited:	4	
Foveotriletes	1	
Monosulcites	1	2
cf. *Quercus*	2	2
Total grains counted	111	111

"Both assemblages are primarily composed of *Artemisia* pollen and neither contains much tree pollen. Both contain small amounts of rebedded pollen which may be of Mesozoic origin (*Foveotriletes, Monosulcites*) and perhaps some reworked Upper [sic] Cenozoic material (dark brown grains of *Artemisia* and cf. *Quercus*). The virtual lack of trees among the primary pollen assemblage and the excellent representation of low growing forms leaves the question of environmental interpretation unanswered. We can suppose that extensive sagebrush in the absence of trees might be attributed to a drier-than-present environment, but whether the environment was cold and dry or warm and dry, cannot be inferred from the present assemblage."

The occurrence in unit 2, locality 14, of pumice pebble conglomerate (fig. 22) composed of very fragile unaltered fragments that could not have been transported far in addition to the presence of shard beds at the top of the section at the site of figures 19 and 20 (analysis D123132, table 1; spectrographic analysis incorporated in figure 4) may indicate a Holocene episode of felsic volcanism. As mentioned in connection with the Turbid Lake sequence, the composition of the volcanic debris is not the same as that on the Pitchstone Plateau.

Other Deposits

Deposits at two localities outside the map area (fig. 3) bear on the late Pleistocene history of the region because they (1) are dated by ^{14}C, (2) contain abundant diatoms, and (3) are at the bottoms of steep-sided canyons of major rivers.

Gibbon Canyon Deposits

A local accumulation of stratified white pumiceous clay and sand with black carbonaceous partings is present near the bottom of the narrow steep-walled Gibbon Canyon 7 miles west of the geologic map (at the "R" on Gibbon River, fig. 2). The locality is 800 feet upstream from a right-angle bend in the canyon and along the highway, 1.4 miles south of Beryl Spring and 2.3 miles north of Gibbon Falls. It is exposed in a 20-foot cut on the east side of the highway. The finer grained strata consist of several layers of white, thin-bedded clay, silt, and ash containing mats of white, partly silicified stems of rushes and other plants and abundant black carbonized twigs and stems. The coarse-grained beds are white to gray, soft sands and gravels composed of black and red, rounded to angular fragments of obsidian, rhyolite, quartz, and white, fibrous pumice and large and small, smoky gray, angular, fresh shards. The carbonaceous beds contain abundant diatoms (table 2) and have a ^{14}C age of 9,440±300 years B.P. (Meyer Rubin, written commun., 1964; USGS Lab No. W-1364).

Figure 24. View north across Pelican Creek one-fourth mile east of Vermilion Springs at locality 12. Indicated are 50 feet of white clayey rhyolite crystal tuff (A), 15 feet of till (B), 50 feet of light gray silt in Pelican Valley sequence (C).

Bannock Ford Deposits

A section of about 30 feet of beds is preserved in the bottom of Yellowstone Canyon, 3,000 feet east-northeast of Tower Falls, on the east side of the Yellowstone River, at Bannock Ford, Tower Junction quadrangle, about 8 miles north of the geologic map (fig. 3). They comprise a local sequence that is much younger than, and was deposited against the base of Howard's 400-foot section of Pleistocene deposits in Alden Valley (Howard, 1937, his fig. 27).

Extending up from the river level is 12 feet of bedded, silty, gray-green clay containing some pebbles and carbonaceous debris. Diatom collection 5639 (table 2), which yielded 58 forms, came from the upper part of this unit. Overlying it is 10 feet of bedded gray sand containing a vegetal trash and wood horizon 3 feet above the base. Some wood fragments are more than 1 inch thick and 1 foot long. They gave a ^{14}C age of 3,750±300 years (Meyer Rubin, written commun., 1964; USGS Lab No. W-1367). The sand is overlain by 8 feet of cobble conglomerate of volcanic rock fragments overlain by sand. The Bannock Ford deposits are especially significant because they record one of the latest events in the complex history of the Yellowstone Canyon.

"Beach Rock"

"Beach rock" is the name used locally to describe a brown, hard, ferruginous conglomerate that crops out in ledges along Pelican Creek and forms a widespread slope cover along the southern part of Pelican Valley. [*See Foreword and About the Author, this chapter.*] It also is present in many places along and near the shore of Yellowstone Lake (fig. 23). "Beach rock" is of several ages ranging from that which is older than the last glaciation to deposits now being formed near thermal areas. Much of it apparently accumulated along the ancient beaches of Yellowstone Lake as the water level rose and fell. This would account for its position extending from the present level of Pelican Creek near locality 13 to the top of the divide directly west of Turbid Lake and its presence at water level of Yellowstone Lake as well as on top of wave-cut cliffs 50 feet or more above the lake. It is one of the common rock types in local morainal debris.

Deposits of "beach rock" are commonly very irregular and 5–10 feet or more in thickness. They consist of rounded to angular poorly to well oriented fragments of volcanic rocks and silicified shale chips tightly cemented with silica and iron oxide. They are porous and contain little unaltered clayey matrix.

Glacial Deposits

Glacial deposits are present in many parts of the map area (fig. 3). Their relation to various Pleistocene sedimentary sequences is important to the present study but other aspects are beyond the scope of this paper. Pierce (1979) and Pierce and Morgan (1992) summarized the regional geologic history.

Tectonic Significance of Pleistocene Strata

The foregoing discussion of Pleistocene stratigraphic units demonstrates the complexity of depositional history involving the northern part of ancestral Yellowstone Lake during this epoch. Inasmuch as 5 of the 7 described sequences accumulated in or near the northern part of the ancestral lake basin, they give us some fragmentary clues as to the origin, extent, and tectonic history of this section of the Park, as well as to the age of its most conspicuous feature, the Grand Canyon of the Yellowstone River. Several suggestions regarding the relations of the stratigraphic sequences to cutting of the Yellowstone Canyon are presented here.

The Pelican Valley sequence apparently accumulated in the northeastern arm of Yellowstone Lake about 7,500 years ago and "drowned" older moraines. The lineations in the moraines, the relation of the Pelican Valley sequence to them, and the fine-grained nature and elevation of the westernmost, and topographically lowest part of the sediments make the possibility remote that they were deposited in a perched lake trapped against an ice cap in the Yellowstone Lake basin. These sediments have a close lithologic and chemical similarity to the Hayden Valley sequence. This suggests that some of the Pelican Valley deposits may have been derived by wind erosion from the uplifted and newly-exposed Hayden Valley sequence. Volcanism somewhere in the immediate vicinity contributed fresh felsic pumice pebbles and shard deposits.

The most recent event in the study area was the rapid rise of the land northeast of Yellowstone Lake, in and near the vicinity of Sour Creek Dome, one of two resurgent domes in the 0.640-Ma Yellowstone caldera. Deformation and faulting associated with the Yellowstone caldera (see Pierce, Cannon and others, this volume) have uplifted the lacustrine and fluvial sediments of the Mudkettle sequence along the abandoned postulated northern outlet channel of ancestral Yellowstone Lake, 10–15 miles north of the present lake and east of the Upper Basin Member of the Plateau Rhyolite, nearly 700 feet above the present lake level. The lacustrine strata of the Pelican Valley sequence at locality 12 radiometrically dated at 7,500 years old, in the Pelican arm of ancestral Yellowstone Lake, are now 150 feet above the lake. Inasmuch as no other such broad areas of recently emerged correlative sediments are known elsewhere along the shore of the lake, it is assumed that this emergence is not the result of lowering of the general lake level but that Pelican Valley was actually tectonically uplifted at a rate averaging 1 foot in 50 years.

The anomalous downstream terminal course of Pelican Creek likewise suggests uplift northeast of Yellowstone Lake. For several miles the creek flows westward along Pelican Valley and then, rather than continuing an unobstructed course west into the Yellowstone River, it makes an abrupt right-angle bend and flows south into the lake (fig. 3). The creek is incised in bedrock (fig. 24) upstream from the change in course and downstream is on a broad flood plain.

Spires and Craters in Yellowstone Lake

In 1997, David Lovalvo of Eastern Oceanics, Inc. discovered a siliceous-spire field in the northern basin of Yellowstone Lake. Subsequent high-resolution mapping of this area between 1999 and 2004 by the U. S. Geological Survey show 12–18 conical structures up to 26 feet tall in crater-like depressions (see discussion in Morgan and others, this volume; Shanks and others, this volume). The spires are hydrothermal in origin, occur in the shallow photic zone less than ~45 feet in depth, and are limited in their distribution in the lake, identified only in the Bridge Bay area. Subsequent examination and analyses of several samples reveal the spires are composed of nearly pure silica, much of it taken up by bacteria and diatoms (Morgan and others, 2003; Shanks and others, this volume). While they are present in the lake, they are not common, are geologically young (~11,000 years old), and are relatively fragile. These are discussed briefly here because they are or may be related to Pleistocene lakes.

It would be worthwhile to compare the diatom assemblages in the spires with the 180 forms listed by areas in table 2, especially in terms of climate and environment and trace element content.

Conclusions

Seven sequences of lacustrine and fluvial strata were deposited in shallow topographic depressions of tectonic, volcanic, and (or) glacial origin, west, north, and northeast of the northern part of Yellowstone Lake. Our study was limited in scope to a reconnaissance overview of the lithology, geochemistry, and microfossils in these strata. It became apparent that these sequences were complexly interrelated with several volcanic units, and that, if the study was expanded, it could help fill the gaps in the complex Quaternary history of lake development in the Yellowstone–Jackson Hole region. In addition, the topographic position of some of the lacustrine and fluvial strata had both tectonic and geomorphic significance relative to the time of cutting of the Yellowstone Canyon. The interpretations presented in our reconnaissance report must be considered simply as a guide to, and suggestions for, more detailed work on all aspects of this study of the lacustrine and fluvial strata.

Currently data are not available regarding the thickness of deposits in Hayden and Pelican Valleys, nor their extent under the adjacent part of Yellowstone Lake. Similarly, data are not available on how these deposits may be hydrothermally altered or what their relation might be to the spires and explosion craters on the lake floor. Future, more detailed investigations on the fluvial and lacustrine sediments in the areas now identified as ancestral Yellowstone Lake are warranted and hold great promise in further unraveling the complex Holocene tectonic and depositional history of the Yellowstone caldera.

References Cited

Baker, R.G., 1976, Late Quaternary vegetation history of the Yellowstone Lake Basin, Wyoming: U.S. Geological Survey Professional Paper 729-E, 48 p.

Blank, H.R., Jr., 1974, Geologic map of the Frank Island quadrangle, Yellowstone National Park, Wyoming: U.S. Geological Survey Geologic Quadrangle Map GQ-1209, scale 1:62,500.

Christiansen, R.L., 1974, Geologic map of the West Thumb quadrangle, Yellowstone National Park, Wyoming: U.S. Geological Survey Geologic Quadrangle Map GQ-1191, scale 1:62,500.

Christiansen, R.L., 1975, Geologic map of the Norris Junction quadrangle, Yellowstone National Park, Wyoming: U.S. Geological Survey Geologic Quadrangle Map GQ-1193, scale 1:62,500.

Christiansen, R.L., 2001, The Quaternary and Pliocene Yellowstone Plateau volcanic field of Wyoming, Idaho, and Montana: U.S. Geological Survey Professional Paper 729-G, 145 p.

Christiansen, R.L., and Blank, H.R., Jr., 1972, Volcanic stratigraphy of the Quaternary rhyolite plateau in Yellowstone National Park: U.S. Geological Survey Professional Paper 729-B, 18 p.

Christiansen, R.L., and Blank, H.R., Jr., 1974a, Geologic map of the Madison Junction quadrangle, Yellowstone National Park, Wyoming: U.S. Geological Survey Geologic Quadrangle Map GQ-1190, scale 1:62,500.

Christiansen, R.L., and Blank, H.R., Jr., 1974b, Geologic map of the Old Faithful quadrangle, Yellowstone National Park, Wyoming: U.S. Geological Survey Geologic Quadrangle Map GQ-1189, scale 1:62,500.

Christiansen, R.L., and Blank, H.R., Jr., 1975, Geologic map of the Canyon Village quadrangle, Yellowstone National Park, Wyoming: U.S. Geological Survey Geologic Quadrangle Map GQ-1192, scale 1:62,500.

Christiansen, R.L., Blank, H.R., Jr., Love, J.D., and Reed, J.C., Jr., 1978, Geologic map of the Grassy Lake Reservoir quadrangle, Yellowstone National Park and vicinity, Wyoming: U.S. Geological Survey Geologic Quadrangle Map GQ-1459, scale 1:62,500.

Comstock, T.B., 1875, Geological report, *in* Jones, W.A., Report on the reconnaissance of northwestern Wyoming, including Yellowstone National Park, made in the summer of 1873: Washington, D.C., Government Printing Office, p. 85–292.

Doane, G.C., 1870, The Yellowstone Expedition of 1870: Washington, D.C., 41st Congress, 3d Session, Senate Executive Document 51, 40 p. [Serial 1440].

Hague, Arnold, 1896, Yellowstone National Park sheets: U.S. Geological Survey Atlas, Folio 30, p. 1–4.

Hague, Arnold, 1904, Atlas to accompany U.S. Geological Survey Monograph 32.

Hayden, F.V., 1872, Preliminary report of the United States Geological Survey of Montana and portions of adjacent territories: U.S. Geological and Geographical Survey of the Territories 5th Annual Report, 538 p.

Hayden, F.V., 1873, Sixth annual report of the United States Geological Survey of the territories, embracing portions of Montana, Idaho, Wyoming, and Utah: U.S. Geological and Geographical Survey of the Territories 6th Annual Report, 844 p.

Holmes, W.H., 1883a, Report on the geology of the Yellowstone National Park, *in* Hayden, F.V., Twelfth annual report of the United States Geological and Geographical Survey of the Territories—A report of progress of the exploration in Wyoming and Idaho for the year 1878—Part II; Yellowstone National Park, Geology—Thermal Springs—Topography: Washington, D.C., Government Printing Office, p. 1–57.

Holmes, W.H., 1883b, Preliminary geological map of the Yellowstone National Park, plate 6, *in* [Portfolio of] Maps and Panoramas accompanying Twelfth annual report of the United States Geological and Geographical Survey of the Territories—A report of progress of the exploration in Wyoming and Montana for the year 1878—Part II; Yellowstone National Park, Geology—Thermal Springs—Topography: Washington, D.C., Government Printing Office.

Howard, A.D., 1937, History of the Grand Canyon of the Yellowstone: Geological Society of America Special Paper no. 6, 159 p.

Krajick, Kevin, 2001, Thermal features bubble in Yellowstone Lake: Science, v. 292, p. 1,479–1,480.

Love, J.D., 1956, Summary of geologic history of Teton County, Wyoming, during Late Cretaceous, Tertiary, and Quaternary times: Wyoming Geological Association, 11th Annual Field Conference, Guidebook, p. 140–150.

Love, J.D., 1961, Reconnaissance study of Quaternary faults in and south of Yellowstone National Park, Wyoming: Geological Society of America Bulletin, v. 72, p. 1,749–1,764.

Love, J.D., 1989, Yellowstone and Grand Teton National Parks and the middle Rocky Mountains: 28th International Geological Congress, Field Trip Guidebook T-328, 93 p.

Love J.D., and Good, J.M., 1970, Hydrocarbons in thermal areas, northwestern Wyoming: U.S. Geological Survey Professional Paper 644-B, 23 p.

Love, J D., and Keefer, W.R., 1975, Geology of sedimentary rocks in southern Yellowstone National Park, Wyoming: U.S. Geological Survey Professional Paper 729-D, 60 p.

Mason, B.H., 1958, Principles of geochemistry (2d ed): New York, Wiley, 310 p.

Morgan, L.A., Shanks, W.C., III, Pierce, K.L., Rye, R.O., and Meeker, G., 1998, Hydrothermal explosion deposits in Yellowstone National Park—Links to hydrothermal processes: Eos, American Geophysical Union, v. 79, no. 45, p. F964.

Morgan, L.A., Shanks, W.C., III, Lovalvo, D.A., Johnson, S.Y., Stephenson, W.J., Pierce, K.L., Harlan, S.S., Finn, C.A., Lee, G., Webring, M., Schulze, B., Dühn, J., Sweeney, R., and Balistrieri, L., 2003, Exploration and discovery in Yellowstone Lake—Results from high-resolution sonar imaging, seismic reflection profiling, and submersible studies: Journal of Volcanology and Geothermal Research, v. 122, p. 221–242.

Pierce, K.L., 1979, History and dynamics of glaciation in the northern Yellowstone National Park area: U.S. Geological Survey Professional Paper 729-F, 90 p.

Pierce, K.L., and Morgan, L.A., 1992, The track of the Yellowstone hotspot—Volcanism, faulting, and uplift, *in* Link, P.K., Kuntz, M.A., and Platt, L.B., eds., Regional geology of eastern Idaho and western Wyoming: Geological Society of America Memoir 179, p. 1–53.

Prostka, H.J., Blank, H.R., Jr., Christiansen, R.L., and Ruppel, E.T., 1975, Geologic map of the Tower Junction quadrangle, Yellowstone National Park, Wyoming: U.S. Geological Survey Geologic Quadrangle Map GQ-1247, scale 1:62,500.

Prostka, H.J., Ruppel, E.T., and Christiansen, R.L., 1975, Geologic map of the Abiathar Peak quadrangle, Yellowstone National Park, Wyoming: U.S. Geological Survey Geologic Quadrangle Map GQ-1244, scale 1:62,500.

Prostka, H.J., Smedes, H.W., and Christiansen, R.L., 1975, Geologic map of the Pelican Cone quadrangle, Yellowstone National Park, Wyoming: U.S. Geological Survey Geologic Quadrangle Map GQ-1243, scale 1:62,500.

Ruppel, E.T., 1972, Geology of pre-Tertiary rocks in the northern part of Yellowstone National Park, Wyoming: U.S. Geological Survey Professional Paper 729-A, 66 p.

Shapiro, Leonard, and Brannock, W.W., 1956, Rapid analysis of silicate rocks, *in* Contributions to geochemistry 1955–57: U.S. Geological Survey Bulletin 1036-C, p. 19–56.

Smedes, H.W., M'Gonigle, J.W., and Prostka, H.J., 1989, Geologic map of the Two Ocean Pass quadrangle, Yellowstone National Park and vicinity, Wyoming: U.S. Geological Survey Geologic Quadrangle Map GQ-1667, scale 1:62,500.

Smedes, H.W., and Prostka, H.J., 1972, Stratigraphic framework of the Absaroka Volcanic Supergroup in the Yellowstone National Park region: U.S. Geological Survey Professional Paper 729-C, 33 p.

Tourtelot, H.A., 1962, Preliminary investigation of the geologic setting and chemical composition of the Pierre Shale, Great Plains region: U.S. Geological Survey Professional Paper 390, 74 p.

Weed, W.H., 1896, Sedimentary rocks, *in* Yellowstone Park Folio: U.S. Geological Survey Geologic Atlas of the United States, Folio 30, p. 4–5.

U.S. Geological Survey, 1972, Geological map of Yellowstone National Park: U.S. Geological Survey Miscellaneous Geologic Investigations Map I-711, scale 1:125,000.

The Floor of Yellowstone Lake is Anything but Quiet—New Discoveries from High-Resolution Sonar Imaging, Seismic-Reflection Profiling, and Submersible Studies

D

By Lisa A. Morgan, Wayne C. Shanks III, Kenneth L. Pierce, David A. Lovalvo, Gregory K. Lee, Michael W. Webring, William J. Stephenson, Samuel Y. Johnson, Stephen S. Harlan, Boris Schulze, and Carol A. Finn

Chapter D *of*

Integrated Geoscience Studies in the Greater Yellowstone Area—Volcanic, Tectonic, and Hydrothermal Processes in the Yellowstone Geoecosystem

Edited by Lisa A. Morgan

Professional Paper 1717

U.S. Department of the Interior
U.S. Geological Survey

Contents

Abstract 95
Overview: History of Mapping Yellowstone Lake 95
Geologic Setting 97
Acknowledgments 97
Methods 97
Results and Discoveries of High-Resolution Mapping 99
    Topographic Margin of the Caldera 99
    Rhyolitic Lava Flows 103
    Large Hydrothermal-Explosion Craters 106
    Hydrothermal Vents and Domes on the Floor of Yellowstone Lake 107
    Siliceous Spires 112
    Fissures and Faults 112
    Landslide Deposits 116
    Submerged Shorelines 116
    Glacial Deposits and Features 117
Discussion 117
    Newly Discovered Features in Yellowstone Lake Pose Potential Geologic Hazards 117
    Do Rhyolitic Lava Flows Control Hydrothermal Activity? 118
Summary and Conclusions 120
References Cited 120

Plates

[In pocket]

1. Series of maps showing the evolution of mapping Yellowstone Lake over the past 130 years.
2. Bathymetric map of Yellowstone Lake.
3. High-resolution bathymetric images in the northern part of Yellowstone Lake.

Figures

1. Maps of Yellowstone National Park:
    A. Index map showing the Yellowstone caldera 98
    B. Geologic shaded-relief map of area surrounding Yellowstone Lake 98
    C. Color shaded-relief-image aeromagnetic map 98
2. High-resolution bathymetric maps of Yellowstone Lake:
    A. West Thumb basin 100
    B. Northern basin 100
    C. Central basin 101
    D. South, Southeast, and Flat Mountain Arms 102
3. Geologic map of Yellowstone Lake 104

4. High-resolution seismic-reflection images of:
   A. Northwestern West Thumb basin....107
   B. Elliott's explosion crater....107
5. Distribution of hydrothermal vents in Yellowstone Lake shown on blue-shaded bathymetric map....108
6. High-resolution images and simplified map of the "inflated plain" in northern basin of Yellowstone Lake:
   A. Blue-shaded-relief bathymetric map of the northern basin....109
   B. Aeromagnetic map of the northern basin....109
   C. Map showing deformation of the Yellowstone caldera from 1923–1975....109
   D. Gray-shaded-bathymetric close-up of the "inflated plain"....110
   E. Gray-scale-amplitude map of the "inflated plain"....110
   F. Two-dimensional color-bathymetric map of the "inflated plain"....110
   G. Three-dimensional color-shaded-relief image of the "inflated plain"....110
7. Annual lake-level variations in Yellowstone Lake....113
8. Siliceous spires in Bridge Bay in northern basin of Yellowstone Lake:
   A. Bathymetric image of spires....114
   B. Photographs of exterior and interior of a siliceous spire....114
   C. SEM image of diatoms, silicified filamentous bacteria, and amorphous silica from a spire sample....114
   D. Summary bar graph of chemical analyses of spire samples....114
9. Monument Geyser Basin:
   A. Photograph of Monument Geyser Basin....115
   B. Index map....115
   C. Photograph looking south into Monument Geyser Basin....115
   D. Photograph of spire-like structures, northern edge of Monument Geyser Basin....115
   E. Photograph of spire-like structure actively venting steam and H_2S....115
   F. Underwater photograph of large spire structure in Bridge Bay in northern basin of Yellowstone Lake....115
10. Flow model for hydrothermal vents and rhyolitic lava flows in Yellowstone Lake:
   A. Schematic diagram showing physical features of a rhyolitic lava flow....119
   B. Fluid-flow model with no caprock....119
   C. Fluid-flow model with caprock....119
   D. Map showing locations of hydrothermal vents on the northern Yellowstone Lake floor....119
   E. Fluid-flow model that includes a basal breccia zone beneath an impermeable lava flow....119

Appendix

D-1. Digital models and visualizations of bathymetry and topography in the Yellowstone Lake area, by Gregory K. Lee and Michael W. Webring....125

The Floor of Yellowstone Lake is Anything but Quiet—New Discoveries from High-Resolution Sonar Imaging, Seismic-Reflection Profiling, and Submersible Studies

By Lisa A. Morgan,[1] Wayne C. Shanks III,[1] Kenneth L. Pierce,[2] David A. Lovalvo,[3] Gregory K. Lee,[1] Michael W. Webring,[4] William J. Stephenson,[5] Samuel Y. Johnson,[6] Stephen S. Harlan,[7] Boris Schulze,[8] and Carol A. Finn[4]

> "…we arrived at the summit of the first ridge…It was a pretty steep climb to the top of it, over a volcanic sand composed of broken down obsidian which composed the only rocks around us." Albert Peale, mineralogist, U.S. Geological Survey, Hayden survey, August 6, 1871.

Abstract

Discoveries from multibeam sonar mapping and seismic-reflection surveys of Yellowstone Lake provide new insight into the recent geologic forces that have shaped a large lake at the active front of the Yellowstone hot spot, a region strongly affected by young (<2 m.y.), large-volume (>100–1,000s km^3) silicic volcanism, active tectonism, and accompanying uplift.

Specifically, our mapping has identified the extent of postcaldera-collapse volcanism and active hydrothermal processes occurring above a large magma chamber beneath the lake floor. Multiple advances and recessions of thick glacial ice have overlapped volcanic and hydrothermal activity leaving a lake basin that has been shaped predominantly by fire and ice. Yellowstone Lake has an irregular bottom covered with dozens of features directly related to hydrothermal, tectonic, volcanic, and sedimentary processes. Detailed bathymetric, seismic-reflection, and magnetic evidence reveals that rhyolitic lava flows underlie much of Yellowstone Lake and exert fundamental control on lake morphology and localization of hydrothermal activity in the northern, West Thumb, and central basins. Many previously unknown features have been identified and include more than 660 hydrothermal vents, several very large (>500-m diameter) hydrothermal-explosion craters, many small hydrothermal-vent craters (~1- to 200-m diameter), domed lacustrine sediments related to hydrothermal activity, elongate fissures cutting postglacial sediments, siliceous hydrothermal-spire structures, sublacustrine landslide deposits, submerged former shorelines, large glacial melting features, incipient faulting along the trace of the Eagle Bay fault zone, and a recently active graben. Sampling and observations with a submersible remotely operated vehicle confirm and extend our understanding of the identified features. Faults, fissures, hydrothermally inflated domal structures, hydrothermal-explosion craters, and sublacustrine landslides constitute potentially significant geologic hazards. Toxic elements derived from hydrothermal processes also may significantly affect the Yellowstone ecosystem.

Overview: History of Mapping Yellowstone Lake

Yellowstone Lake (fig. 1*A*) is the largest high-altitude lake in North America with an altitude of 2,357 m and a surface area of 341 km^2 (pl. 1). More than 141 rivers and streams flow into the lake. The Yellowstone River, which enters at the south end of the Southeast Arm, dominates the inflow of water and sediment. The only outlet from the lake is at Fishing Bridge (fig. 1*B*) where the Yellowstone River flows north and discharges 375–4,600 cfs (*http://nwis.waterdata.usgs.gov; accessed 3/30/2005)*.

The earliest attempt to produce a detailed map of the shoreline and bathymetry of Yellowstone Lake occurred during the 1871 U.S. Geological Survey (USGS) expedition.

[1]U.S. Geological Survey, Box 25046, MS 973, Federal Center, Denver, CO 80225, lmorgan@usgs.gov.

[2]U.S. Geological Survey, Northern Rocky Mountain Science Center, Box 173492, Montana State University, Bozeman, MT 59717.

[3]Eastern Oceanics, Inc., 25 Limekiln Rd., W. Redding, CT 06896.

[4]U.S. Geological Survey, Box 25046, MS 964, Federal Center, Denver, CO 80225.

[5]U.S. Geological Survey, Box 25046, MS 966, Federal Center, Denver, CO 80225.

[6]U.S. Geological Survey, 400 Natural Bridges Drive, Santa Cruz, CA 95060.

[7]George Mason University, Department of Geography and Earth Systems Science, 4400 University, MS 5F2, Fairfax, VA 22030-4444.

[8]L-3 Communication Elac Nautik GmbH Neufeldtstrasse, D-24118 Kiel, Germany.

Ferdinand V. Hayden led 28 scientists, scouts, and cooks in a survey of what is now known as Yellowstone National Park (Merrill, 1999). The sheer effort expended by this group in the most primitive of working conditions in tandem with the many accomplishments of the survey is impressive. A primary goal of the 1871 Hayden party was "***mak(ing) a most thorough survey of it [Yellowstone Lake]" (F.V. Hayden, letter of June 4, 1871, to Professor Spencer Fullerton Baird, *in* Merrill, 1999) and reflects Hayden's general interest in watersheds and river drainage basins (M.D. Merrill, written commun., 2002). A 4.5-ft by 11-ft (1.4-m by 3.4-m) oak boat with a woolen-blanket sail (A. Peale, July 28, 1871, *in* Merrill, 1999) was used to map Yellowstone Lake. Mapping took 24 days and included approximately 300 lead-sink soundings (pl. 1*B*). Navigation was carried out using a prismatic compass. As Albert Peale (Merrill, 1999) described in his journal, "a man stands on the shore with a compass and takes a bearing to the man in the Boat as he drops the lead, giving a signal at the time. Then the man in the Boat takes a bearing to the fixed point on the shore where the first man is located and thus the soundings will be located on the chart****[Elliott will] make a systematic sketch of the shore with all its indentations [from?] the banks down, indeed, making a complete topographical as well as a pictorial sketch of the shores as seen from the water, for a circuit of at least 130 mi (209 km). He will also make soundings, at various points" (A. Peale, July 1871, *in* Merrill, 1999). The survey mapped a shoreline of 130 mi (209 km); the most recently mapped shoreline shows the perimeter of Yellowstone Lake to be 227 km. More than 40 soundings were taken along the north and west shores in the Hayden survey, the deepest being around 300 ft (91 m). The survey estimated the deepest part of the lake would be farther east and no deeper than 500 ft (152 m) (Merrill, 1999). This depth range is comparable to what we know today; the deepest point in Yellowstone Lake is due east of Stevenson Island (pl. 2, pl. 3*B*) at 131 m deep (Kaplinski, 1991; this study). In addition, the Hayden survey identified the long northeast-trending trough crossing the central basin. Plate 1 shows the map of Yellowstone Lake as drawn by Henry Elliott of the Hayden survey (oral commun., Marlene Merrill, 2000). The map not only shows a detailed topographical sketch of the Yellowstone Lake shoreline, but many of the points where soundings were taken for the survey.

A second map of Yellowstone Lake incorporated elements of the original 1871 Elliott map from the Hayden expedition and was published in 1896. Even though no mention is made in the official U.S. Geological Survey report (Hague and others, 1896) of additional mapping or modifications made to the Elliott Yellowstone Lake map during the years of the Hague survey (1883–89, 1890–91, and 1893), clearly the lake was resurveyed and triangulated by H.S. Chase and others—this information is shown on maps in the Hague report (see plate 1*D*). The 1896 map built upon the Elliott map and refined areas on the shoreline, such as in the Delusion Lake area between Flat Mountain Arm and Breeze Point. Where the Elliott map of Yellowstone Lake shows Delusion Lake as an arm of the lake, the Hague map delineates the boundaries of Delusion Lake and identifies swampy areas nearby. The maps from the Hague survey of Yellowstone National Park also include a rather sophisticated geologic map of portions of the park around the lake.

The next significant attempts to map Yellowstone Lake came a hundred years later (Otis and others, 1977; Kaplinski, 1991). Kaplinski (1991) employed a single-channel echo sounder and a mini-ranger for navigation requiring interpolation between track lines. More than 1,475 km of sonar profiles were collected in 1987 using track lines spaced approximately 500 m apart and connected by cross lines spaced 1 to 2 km apart. An additional 1,150 km of sonar profiles were collected in 1988 to fill in data gaps from the 1987 survey. The map identified many thermal areas on the floor of the lake. The bathymetric map produced by Kaplinski (1991) (pl. 1*E*) has served as the most accurate lake map for Yellowstone National Park for more than a decade and has proven invaluable in addressing serious resource-management issues, specifically monitoring and catching the aggressive and piscivorous lake trout. The lake trout is estimated to consume as many as 60 native Yellowstone Lake cutthroat trout per year (Ruzycki and Beauchamp, 1997).

Ten years after the Kaplinski (1991) bathymetric map, development of global-positioning technology and high-resolution multibeam sonar imaging justified a new, high-resolution mapping effort of the lake. Mapping and sampling conducted in 1999 through 2002 as a collaborative effort between the U.S. Geological Survey, Eastern Oceanics, Inc., and the National Park Service (NPS) (Yellowstone National Park) utilized state-of-the-art bathymetric, seismic, and submersible remotely operated vehicle (ROV) equipment to collect data along 200-m track lines with later infill, where necessary. The 1999–2002 mapping effort of Yellowstone Lake took 62 days during a 4-year period—compared to Hayden's survey of 24 days in 1871—and began in 1999 with mapping the northern basin, continued in 2000 in West Thumb basin, in 2001 in the central basin, and in 2002 in the southern part of the lake including the Flat Mountain, South, and Southeast Arms (see inset in pl. 2). A small area, informally referred to as the "inflated plain," in the northern basin was resurveyed in 2002. In 2003, seismic-reflection profiles were collected in the South and Southeast Arms. Unlike any of the previous mapping efforts of Yellowstone Lake, the 1999–2002 swath, multibeam survey produced continuous overlapping coverage that collected more than 240 million soundings and produced high-resolution bathymetric images. Seismic-reflection records of the upper 25 m of the lake bottom were obtained along with the bathymetry of the entire lake. This effort has resulted in a map that is accurate to <1 m in most areas. The following report focuses on results of this mapping effort and the interpretation of newly discovered features.

Geologic Setting

Powerful geologic processes in Yellowstone National Park have contributed to the unusual shape of Yellowstone Lake, which straddles the southeast margin of the Yellowstone caldera (fig. 1), one of the world's largest active silicic volcanoes (Mason and others, 2004). Volcanic forces contributing to the lake's form include the explosive caldera-forming 2.05-Ma eruption of the Huckleberry Ridge Tuff followed by eruption of the 0.64-Ma Lava Creek Tuff to form the Yellowstone caldera (Christiansen, 1984, 2001; Hildreth and others, 1984; U.S. Geological Survey, 1972). Following explosive, pyroclastic-dominated activity, large-volume rhyolitic lava flows were emplaced along the caldera margin, infilling much of the caldera (figs. 1*A* and 1*B*). A smaller caldera-forming event about 200 ka (Morgan and Shanks, 2005), comparable in size to Crater Lake, Oreg., created the West Thumb basin (Christiansen, 1984; U.S. Geological Survey, 1972). Several significant glacial advances and recessions continued to shape the lake and overlapped the volcanic events (Pierce, 1974, 1979; Richmond, 1976, 1977). Glacial scour deepened the central basin of the lake and the faulted South and Southeast Arms (fig. 1*B*). More recent dynamic processes shaping Yellowstone Lake include currently active fault systems, development of a series of postglacial-shoreline terraces, and postglacial (<15–12 ka) hydrothermal-explosion events that created the Mary Bay hydrothermal-explosion crater complex and other craters.

Formation of hydrothermal features in Yellowstone Lake is related to convective-meteoric hydrothermal-fluid circulation, steam separation during fluid ascent, and possible CO_2 accumulation and release above an actively degassing magma chamber. Hydrothermal explosions result from accumulation and sudden release of steam and (or) CO_2, possibly reflecting changes in confining pressure that accompany, and may accelerate, failure and fragmentation of overlying lithologies. Sealing of surficial-discharge conduits due to hydrothermal-mineral precipitation contributes to overpressuring and catastrophic failure. Heat-flow maps show that both the northern and West Thumb basins of Yellowstone Lake have extremely high heat flux (1,650–15,600 mW/m^2) compared to other areas in the lake (Morgan and others, 1977). Earthquake epicenter locations indicate that the area north of the lake is seismically active (Smith, 1991), and ROV studies identify hydrothermally active areas within the lake (Balistrieri and others, this volume; Klump and others, 1988; Remsen and others, 1990; Shanks and others, this volume).

The objective of the present work is to understand the geologic processes that shape the lake floor. Our three-pronged approach to mapping the floor of Yellowstone Lake located, imaged, and sampled bottom features, such as sublacustrine hot-spring vents and fluids, hydrothermal deposits, hydrothermal-explosion craters, rock outcrops, glacial features, slump blocks, faults, fissures, and submerged shorelines.

Acknowledgments

We thank Kate Johnson, Ed duBray, Geoff Plumlee, Pat Leahy, Steve Bohlen, Tom Casadevall, Linda Gundersen, Denny Fenn, Elliott Spiker, Dick Jachowski, Mike Finley, John Varley, Tom Olliff, and Paul Doss for supporting this work. We gratefully acknowledge our collaboration and work with individuals from L-3 Communications, Jorg Duhn, Joerg Brockhoff, and Peter Gimpel. We thank Dan Reinhart, Lloyd Kortge, Paul Doss, Rick Fey, John Lonsbury, Ann Deutch, Jeff Alt, Julie Friedman, Brenda Beitler, Charles Ginsburg, Jim Bruckner, Pam Gemery, Rick Sanzolone, Dave Hill, Bree Burdick, Erica Thompson, Eric White, Bob Evanoff, Wes Miles, Rick Mossman, Gary Nelson, Christie Hendrix, Tim Morzel, and many others for assistance with field studies. We thank Marlene Merrill for use of the map by Henry Elliott of the 1871 Hayden survey. We thank Bob Christiansen, Karl Kellogg, Geoff Plumlee, Paul Carrara, Ian Ridley, and Tom Judkins for constructive reviews that substantially improved the manuscript. We are grateful to Coleen Chaney, Debi Dale, Joan Luce, Mary Miller, Vicky Stricker, Sandie Williamson, and Robert Valdez for their skillful assistance with project logistics. This research was supported by the U.S. Geological Survey, the National Park Service, and the Yellowstone Foundation.

Methods

Surveys of Yellowstone Lake (fig. 1*A*; pl. 2) between 1999–2002 (Morgan and others, 2003) utilized state-of-the-art bathymetric, seismic (except for the South, Southeast, and Flat Mountain Arms survey in 2002), and submersible remotely operated vehicle equipment. The multibeam swath-bathymetric surveys employed a SeaBeam 1180 (180 kHz) instrument with a depth resolution of ≤1 percent of the water depth. Water depth varied from ~4–133 m in the survey areas. The multibeam instrument uses 126 beams arrayed over a 150° ensonification angle to map a swath width of 7.4 times water depth. Sub-bottom seismic-reflection profiling utilized an EdgeTech SB-216S, which sweeps a frequency range from 2–10 kHz and has a beam angle of 15°–20°. Both the swath-unit transducer and the sub-bottom unit were rigidly mounted to the transom of an 8-m-long aluminum boat used for survey purposes. The new survey, which was navigated to an accuracy of ≤1 m using differential GPS, utilized more than 240 million soundings to produce high-resolution continuous overlapping coverage of the lake's bathymetry. In 1999, 2000, and 2001, we also surveyed more than 2,500 linear km with high-resolution seismic-reflection profiling that penetrated the upper ~25 m of the lake bottom. In 2003, additional seismic-reflection data was collected in the South, Southeast, and Flat Mountain Arms.

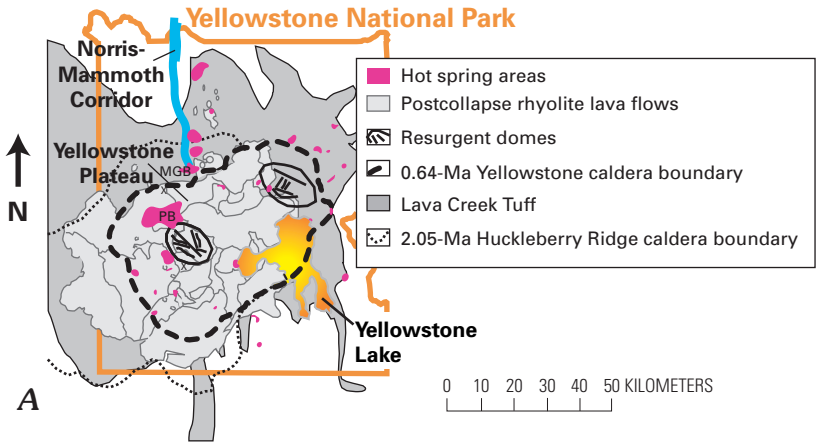

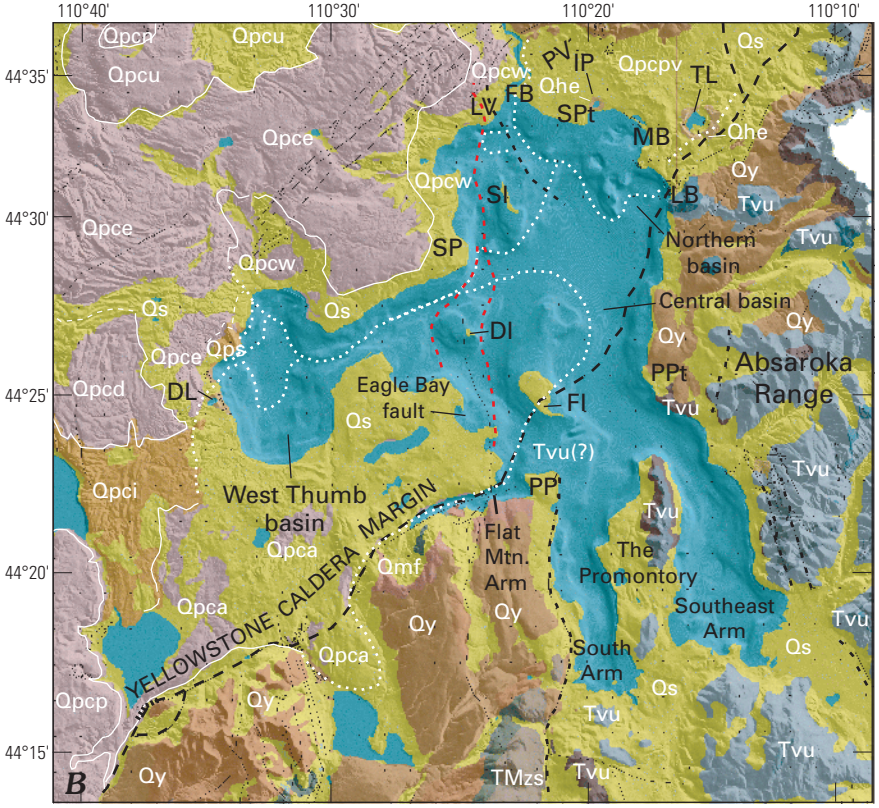

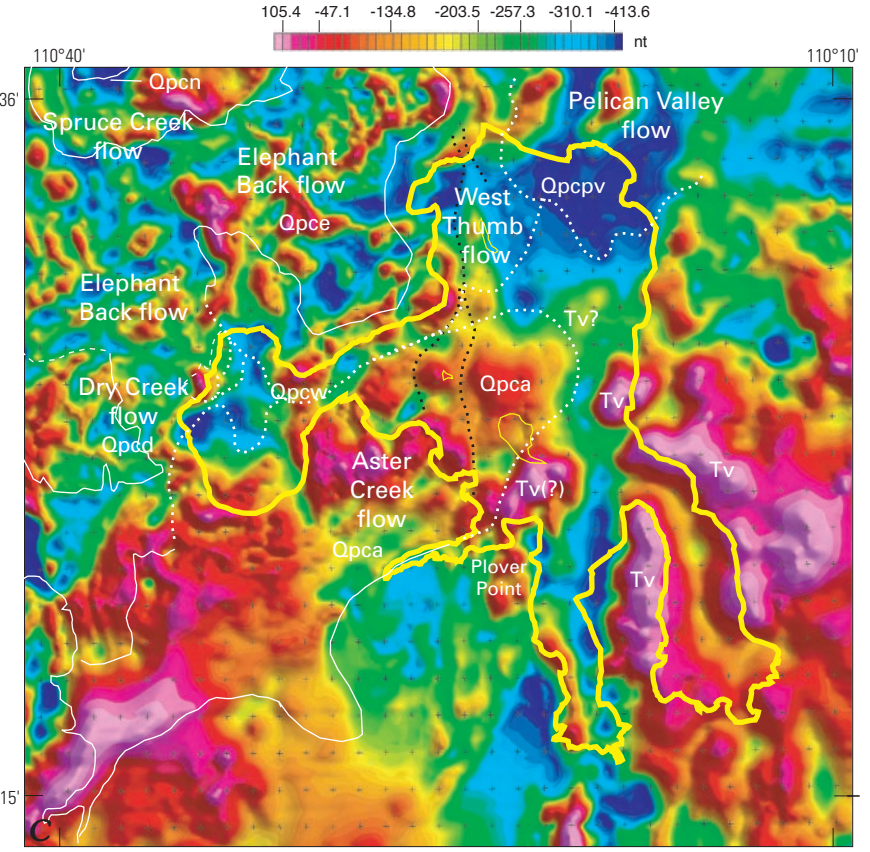

0 5 10 KILOMETER

The Eastern Oceanics submersible ROV is small (~1.5 m × 1 m × 1 m) and attached to the vessel with a 200-m tether. The ROV provides live video coverage and remote control of cameras and sampling equipment. The ROV has a full-depth rating of 300 m and is capable of measuring temperature, conductivity, depth, and retrieving hydrothermal-vent-water samples and rock samples as long as 40 cm.

Results and Discoveries of High-Resolution Mapping

Topographic Margin of the Caldera

Geologic maps (U.S. Geological Survey, 1972; Christiansen, 2001; Richmond, 1974) estimate the underwater topographic margin of the Yellowstone caldera in Yellowstone Lake to be between the western entrance to Flat Mountain Arm and north of Lake Butte (fig. 1*B*). Our mapping of the central basin of Yellowstone Lake in 2001 clearly identified the topographic margin of the 0.64-Ma Yellowstone caldera as a series of elongated troughs northeast from Frank Island across the deep basin of the lake. Based on our new data and high-resolution aeromagnetic data (Finn and Morgan, 2002), we infer the topographic margin of the Yellowstone caldera to pass through the southern part of Frank Island (pl. 2; figs. 1 and 3).

East and north of Frank Island, the topographic margin of the caldera follows a series of discontinuous moderate-amplitude magnetic lows in the reduced-to-the-pole magnetic map (Finn and Morgan, 2002) (fig. 1*C*). The anomalies coincide with bathymetric troughs (figs. 2*B,* 2*C,* and 2*D*) identified by the new mapping. The location of the caldera west of Frank Island continues through a series of subtle bathymetric lows toward the head of Flat Mountain Arm. Here, the caldera margin separates Tertiary andesitic rocks and pre-caldera and caldera-forming rhyolitic ignimbrites to the south from young, postcollapse rhyolitic lava flows to the north and northwest (U.S. Geological Survey, 1972; Christiansen, 2001).

Pronounced magnetic highs over much of the Absaroka Range along the eastern side of Yellowstone Lake (fig. 1*C*) are related to rugged topographic relief and highly magnetized Tertiary andesitic debris flows, dikes, and lava flows (Smedes and Prostka, 1972). Similar magnetic anomalies over The Promontory, which separates South Arm from Southeast Arm (figs. 1*B* and 2*D*), are associated with Tertiary andesitic lava and debris flows prominently exposed in cliffs several hundred meters thick. The same magnetic signature occurs along the eastern shore of the lake north and slightly west of Park Point, where a thin exposure of the Lava Creek Tuff overlies the magnetically dominant Tertiary volcanic rocks. North and east of Plover Point in southern Yellowstone Lake, the magnetic signature is similar to that of nearby Tertiary volcanic rocks; we suggest Tertiary volcanic rocks are present at depth and are overlain by younger Yellowstone Group volcanic rocks (figs. 1*C* and 2*D)*. These positive magnetic anomalies are caused by Tertiary volcanic rocks at

Figure 1. Maps of Yellowstone National Park. *A*, Index map showing the 0.64-Ma Yellowstone caldera, the distribution of its erupted ignimbrite (Lava Creek Tuff, medium gray), postcaldera rhyolitic lava flows (light gray), subaerial hydrothermal areas (red), and the two resurgent domes (shown as ovals with faults). The inferred margin of the 2.05-Ma Huckleberry Ridge caldera is also shown. Data are from (Christiansen, 2001). Locations of Monument Geyser Basin (MGB) and Pocket Basin (PB) are shown. *B*, Geologic shaded-relief map of the area surrounding Yellowstone Lake in Yellowstone National Park. Geologic mapping is from U.S. Geological Survey (1972), and Yellowstone Lake bathymetry is from Kaplinski (1991). The lithologic symbols are as follows: Qpci: tuff of Bluff Point; Qpcd: Dry Creek flow; Qpca: Aster Creek flow; Qpcw: West Thumb flow; Qpce: Elephant Back flow; Qpcu: Spruce Creek flow; Qpcn: Nez Perce flow; Qpcp: Pitchstone Plateau flow; Qpcpv: inferred "Pelican Valley flow"; Qs: Quaternary sediments (yellow); Qh: hydrothermal deposit; Qhe: hydrothermal explosion deposit; Qhi: cemented ice-contact deposits localized by hot springs; Qy: Quaternary Yellowstone Group ignimbrites (brown) (Christiansen, 2001; U.S.Geological Survey, 1972); Qyl: Lava Creek Tuff; Tyh: Huckleberry Ridge Tuff; Tvu: Tertiary volcanic rocks, undifferentiated; TMzs: Tertiary and Mesozoic sediments, undifferentiated. Location of Yellowstone caldera margin is from Christiansen (1984) with slight modifications from Finn and Morgan (2002). DI: Dot Island; DL: Duck Lake; FB: Fishing Bridge; FI: Frank Island; IP: Indian Pond; LB: Lake Butte; LV: Lake Village; MB: Mary Bay; PPt: Park Point; PV: Pelican Valley; PP: Plover Point; SI: Stevenson Island; SP: Sand Point; SPt: Storm Point; TL: Turbid Lake. Several postcaldera rhyolitic lava flows, outlined in white, shown in the lake are highlighted to emphasize their distribution in Yellowstone Lake. *C*, Color shaded-relief image of high-resolution, reduced-to-the-pole aeromagnetic map (Finn and Morgan, 2002). Sources of the magnetic anomalies are shallow and include the postcaldera rhyolite lava flows (some outlined in white) that have partly filled the Yellowstone caldera. Commonly, rhyolitic lava flow margins have low permeability glassy rinds that are not subject to hydrothermal alteration and produce distinctive positive magnetic anomalies. Extensive areas of negative magnetic anomalies in the West Thumb and northern basins and along the caldera margin northeast of the lake are areas of high heat flow and intense present and past hydrothermal alteration, as suggested by sublacustrine-vent locations (fig. 1B). Several postcaldera rhyolitic lava flows, outlined in white, shown in the lake are highlighted to emphasize their distribution in Yellowstone Lake. See figure 1B for descriptions of geologic units.

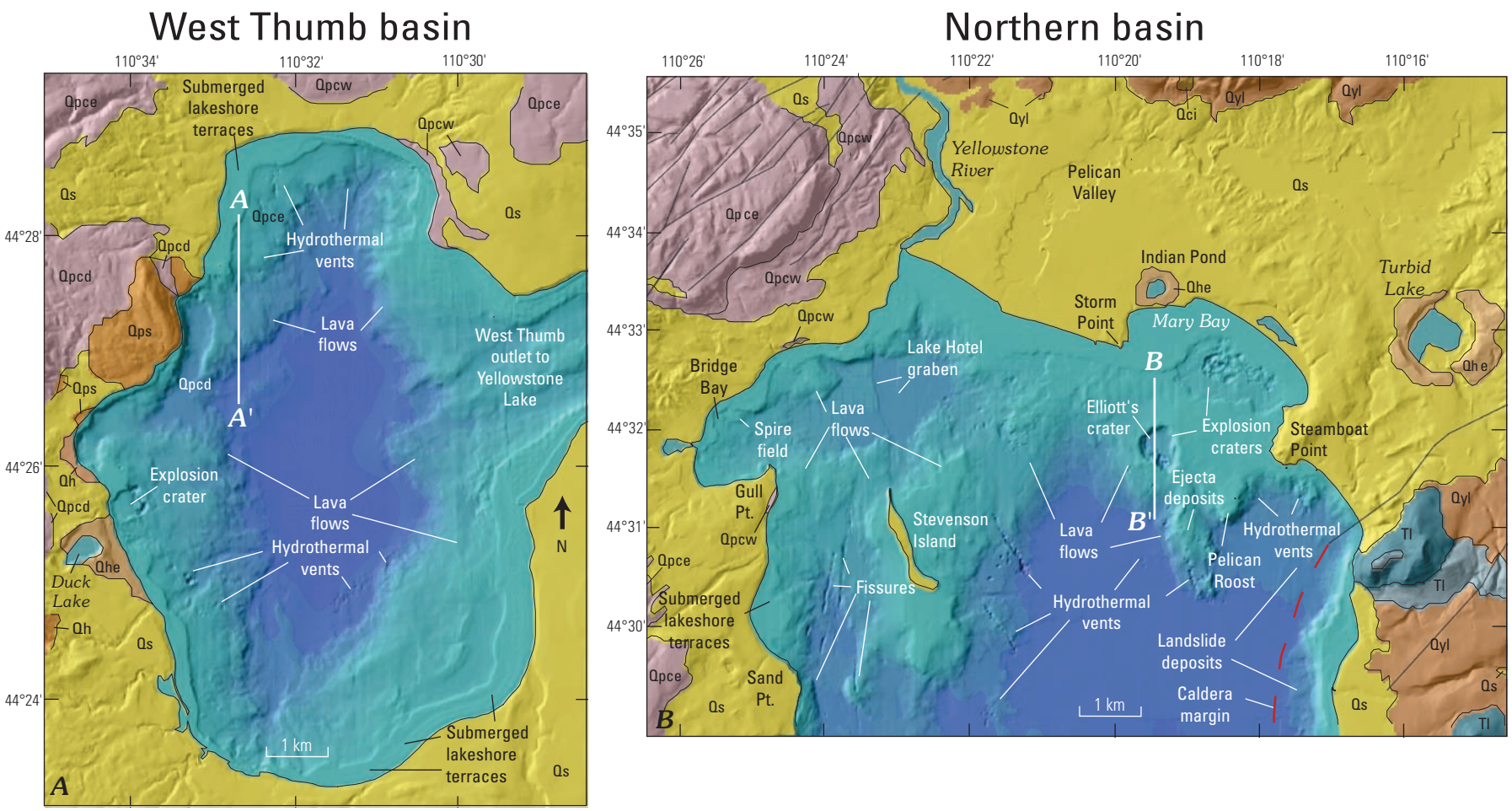

Figure 2. Close-up images of Yellowstone Lake bathymetric maps. *A,* New high-resolution bathymetric map of the West Thumb basin of Yellowstone Lake, acquired by multibeam-sonar imaging and seismic mapping in 2000, showing a previously unknown ~500-m-wide hydrothermal-explosion crater (east of Duck Lake), numerous hydrothermal vents, submerged lakeshore terraces, and rhyolitic lava flows that underlie 7–10 m of postglacial sediments. See figure 1B for descriptions of geologic units. *B,* High-resolution bathymetric map of the northern basin of Yellowstone Lake, acquired in 1999, showing large hydrothermal-explosion craters in Mary Bay and south–southeast of Storm Point, numerous smaller craters related to hydrothermal vents, and landslide deposits along the eastern margin of the lake near the caldera margin (fig. 1). Postcaldera rhyolitic lava flows underlie much of the northern basin. See fig. 1B for descriptions of geologic units. Fissures west of Stevenson Island and the graben north of it may be related to the young Eagle Bay fault (see fig. 1B). *C,* High-resolution bathymetric map of the central lake basin, acquired by multibeam-sonar imaging and seismic mapping in 2001, showing the Yellowstone caldera topographic margin, a large hydrothermal-explosion crater south of Frank Island, and numerous faults, fissures, and hydrothermal vents as indicated. See figure 1B for descriptions of geologic units.

Central basin

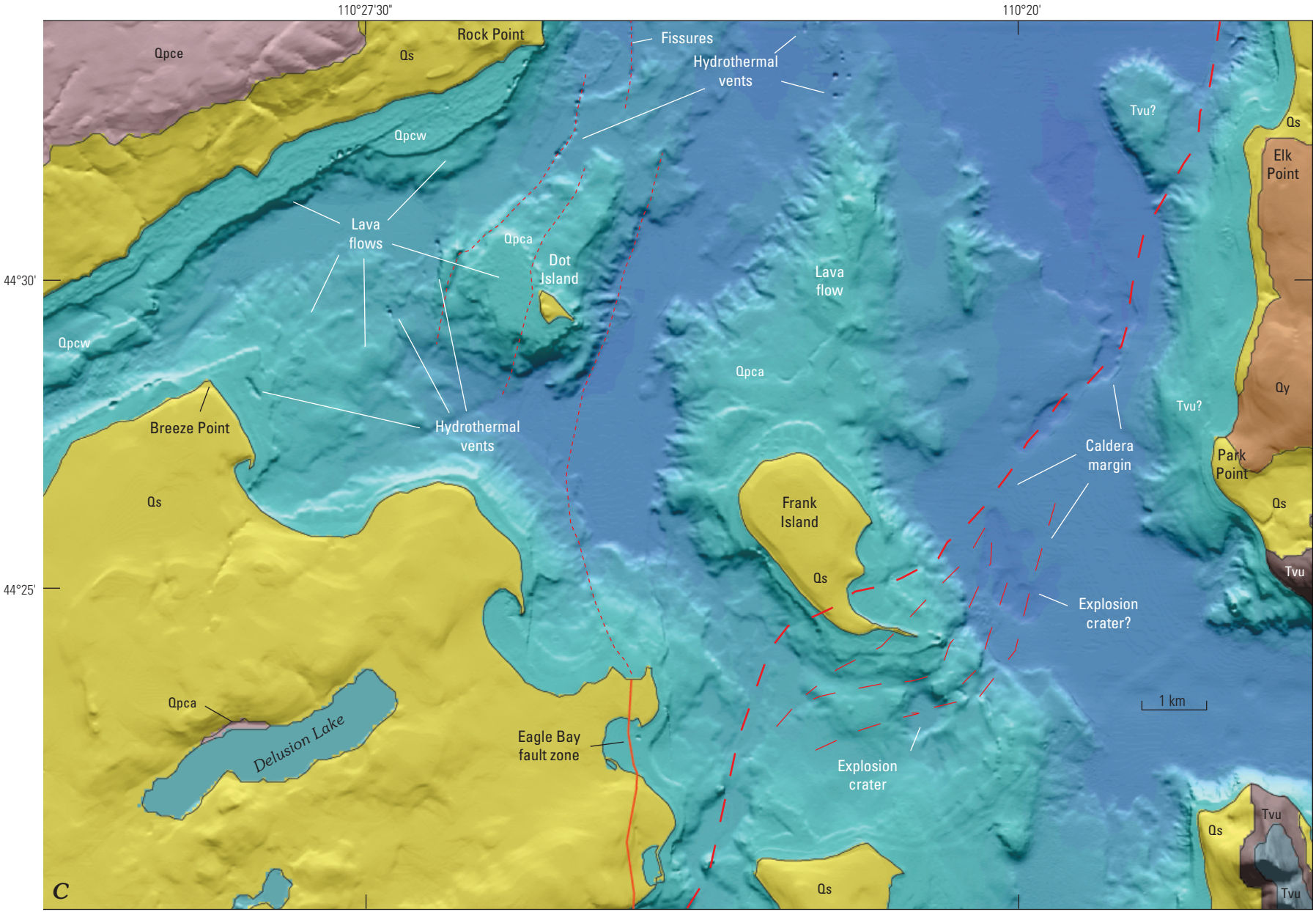

South, Southeast, and Flat Mountain Arms

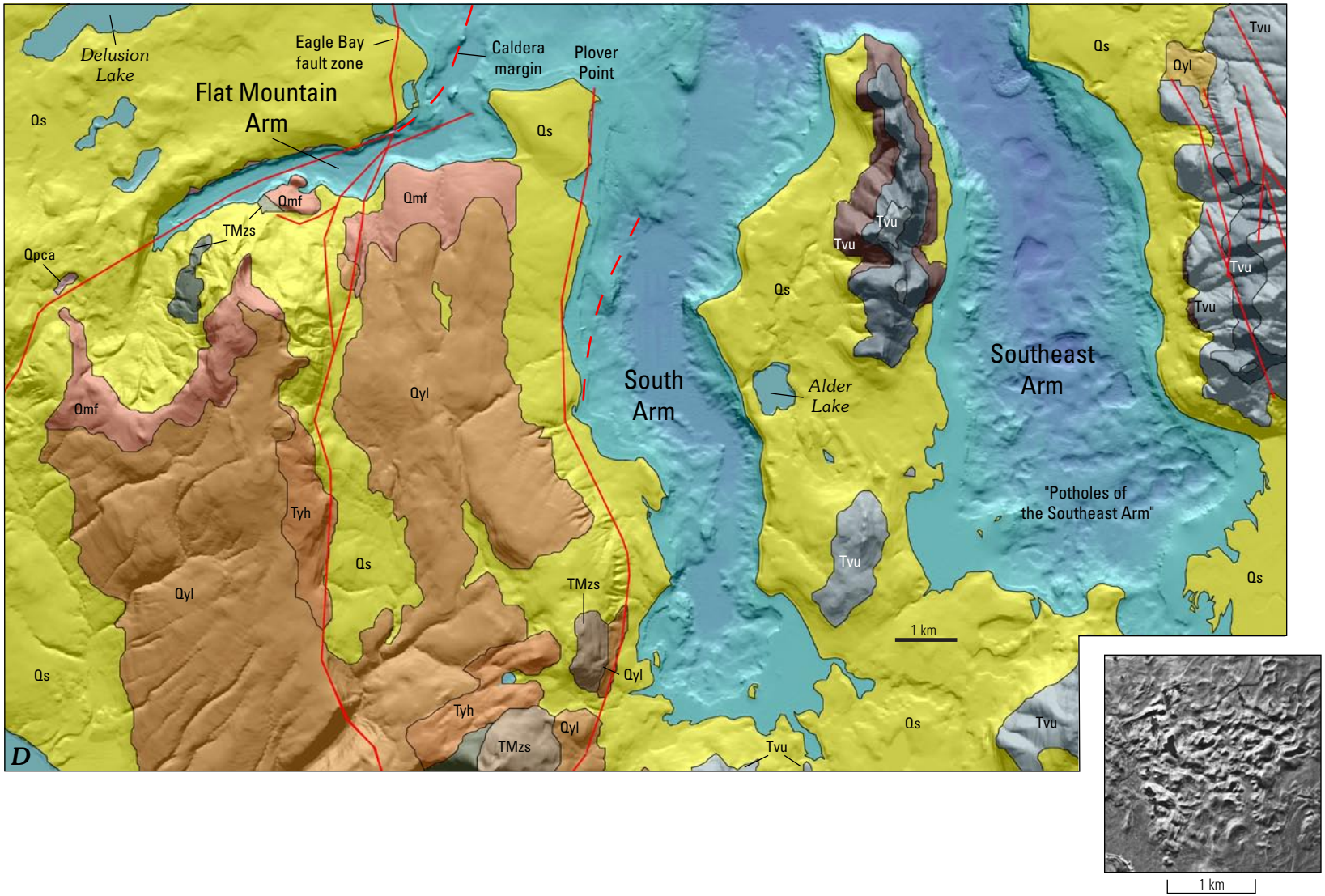

D, High-resolution bathymetric map of the South, Southeast, and Flat Mountain Arms, acquired by multibeam-sonar imaging in 2002, showing the glaciated landscape of the lake floor in the southernmost part of Yellowstone Lake and several faults. The bathymetry in the Southeast Arm contains many glacial-meltwater and stagnant-ice-block features; the area, informally referred to as the "Potholes of the Southeast Arm," resembles much of the kettle-dominated topography mapped by Ken Pierce and others in Jackson Hole, Wyo. See fig. 1B for descriptions of geologic units. The inset is a gray-shaded-relief map of "The Potholes" in Jackson Hole. Image from Good and Pierce (1996).

the surface, as exposed at The Promontory and in the Absaroka Range; alternatively, Tertiary volcanic rocks are buried at shallow depths in the lake, such as north of Plover Point extending northward into the southern third of Frank Island (Finn and Morgan, 2002). The high amplitude of the magnetic anomaly over the southern part of Frank Island is comparable to that present in the Absaroka Range, immediately to the east, or on The Promontory, suggesting a similar Tertiary source.

In contrast, the moderate amplitudes of positive magnetic anomalies in the reduced-to-the-pole map over the northern part of Frank Island are similar to those associated with postcollapse rhyolitic lava flows, such as seen in much of the West Thumb, Hayden Valley, and Aster Creek flows (figs. 1*B* and 1*C*) (Finn and Morgan, 2002). The topographic margin of the caldera immediately south of Frank Island may be represented by a series of concentric zones, possibly related to down-dropped (toward the north) blocks on the topographic margin of the caldera margin (fig. 2*C*). These areas may contain significant amounts of Tertiary volcanic rock as part of the slumped caldera wall, contributing to the magnetic signature seen in the reduced-to-the-pole aeromagnetic map of the southern third of Frank Island (fig. 1*C*).

Several blocks of slumped or detached material may be present along the eastern shore of Yellowstone Lake and may be associated with formation and development of the Yellowstone caldera or with sliding of detritus off the steep slopes of the highly altered terrain of the Absaroka Range, immediately to the east (pl. 2). A couple of these proposed slump blocks are located outside of, but close to, the southeastern caldera boundary. Another block lies slightly farther north and is just along and within the caldera boundary (fig. 3). We propose this block may be a slumped wall of the caldera or a detached block of material that slid off the adjacent steep-sloped Absaroka Range; it is due west of Elk Point (fig. 2*C*) where bathymetric mapping shows a slab-like structure rising 40 m from the lake floor. The reduced-to-the-pole magnetic map (Finn and Morgan, 2002) shows a moderate-amplitude anomaly associated with this structure, slightly different in magnetic signature than that described for the majority of Tertiary volcanic rocks in the area. Perhaps this structure is a rotated block of Tertiary volcanic material. Alternatively, this structure may be a northeastward extension of a thin section of the postcollapse-caldera Aster Creek rhyolite flow that appears separated from the main unit by glacial scouring. The thickest ice cap (>1 km) in the most recent glacial period resided in the central basin of Yellowstone Lake (Pierce, 1979). Additional areas of northeast-trending glacial scour can be seen immediately west of the deep central basin and continuing south onto land in the Delusion Lake area between West Thumb basin and Flat Mountain Arm (fig. 2*D*).

Rhyolitic Lava Flows

Large-volume subaerial rhyolitic lava flows (tens of cubic kilometers) on the Yellowstone Plateau control much of the local topography and hydrology. Characteristic lava-flow morphologies include near-vertical margins (some as high as 375 m, Christiansen, 2001), rubbly flow carapaces, hummocky or ridged tops, and strongly jointed interiors. Stream drainages tend to occur along flow boundaries, rather than within flow interiors (fig. 1*B*). Many flows have vitrophyric exterior rinds with shrinkage cracks and sheet-jointed crystallized interior zones. Spherulitic and lithophysal zones commonly include large cavities. Breccias occur locally.

A major discovery of the lake surveys is the presence of previously unrecognized rhyolitic lava flows underlying much of the lake floor. We believe the lava flows are key to controlling many morphologic and hydrothermal features in the lake.

Shelf areas of the lake bottom around the perimeter of the West Thumb, northern, and central basins (figs. 2*A,* 2*B*, 2*C,* and 3; pl. 2) have steep, nearly vertical margins, bulbous edges, and irregular hummocky surfaces, similar to postcollapse rhyolitic lava flows of the Yellowstone Plateau. Seismic-reflection profiles in the near-shore areas of West Thumb basin show high-amplitude reflectors beneath about 7–10 m of layered lacustrine sediments (fig. 4*A*). We interpret these sublacustrine features to be sediment-veneered rhyolitic lava flows that partly fill the interior of the 140-ka West Thumb caldera.

Based on air-gun seismic-reflection data, Otis and others (1977) recognized a high-amplitude reflector at various depths beneath glaciolacustrine sediments in the lake. Despite the hummocky top to the reflector and the extensive exposures of postcollapse rhyolitic lava flows nearby to the west and northwest of Yellowstone Lake, the reflector was misidentified as the Lava Creek Tuff. Whereas the Lava Creek Tuff and the postcollapse lava flows are both high-silica rhyolites, many of their physical properties differ, such as cooling-zonation patterns and magnetic characteristics; these differences have significant implications for localization of hydrothermal activity.

Unaltered, topographically high, postcollapse rhyolite flow deposits produce moderate-amplitude positive magnetic anomalies. Smaller areas within the flows show magnetic lows that are related to topographically low basins and faults as well as hydrothermally altered areas (Finn and Morgan, 2002). In contrast to the rhyolite flows whose vertical and vitric edges are easily discerned on the reduced-to-the-pole aeromagnetic map, the wide range of bulk-susceptibility values and the ignimbrite's tendency to have its vitrophyre as a horizontal basal layer rather than a vertical edge preclude clear identification of the Lava Creek Tuff as an individual geologic unit on the high-resolution aeromagnetic map. Positive anomalies are observed over the most magnetic and thickest (50–100 m) sections of the ignimbrite in elevated terrain (Finn and Morgan, 2002).

Areas such as the West Thumb and Potts Geyser Basins in West Thumb basin (pl. 1*F*) and Mary Bay in the northern basin, currently have extremely high heat-flow values (1,650–15,600 mW/m^2; Morgan and others, 1977), high

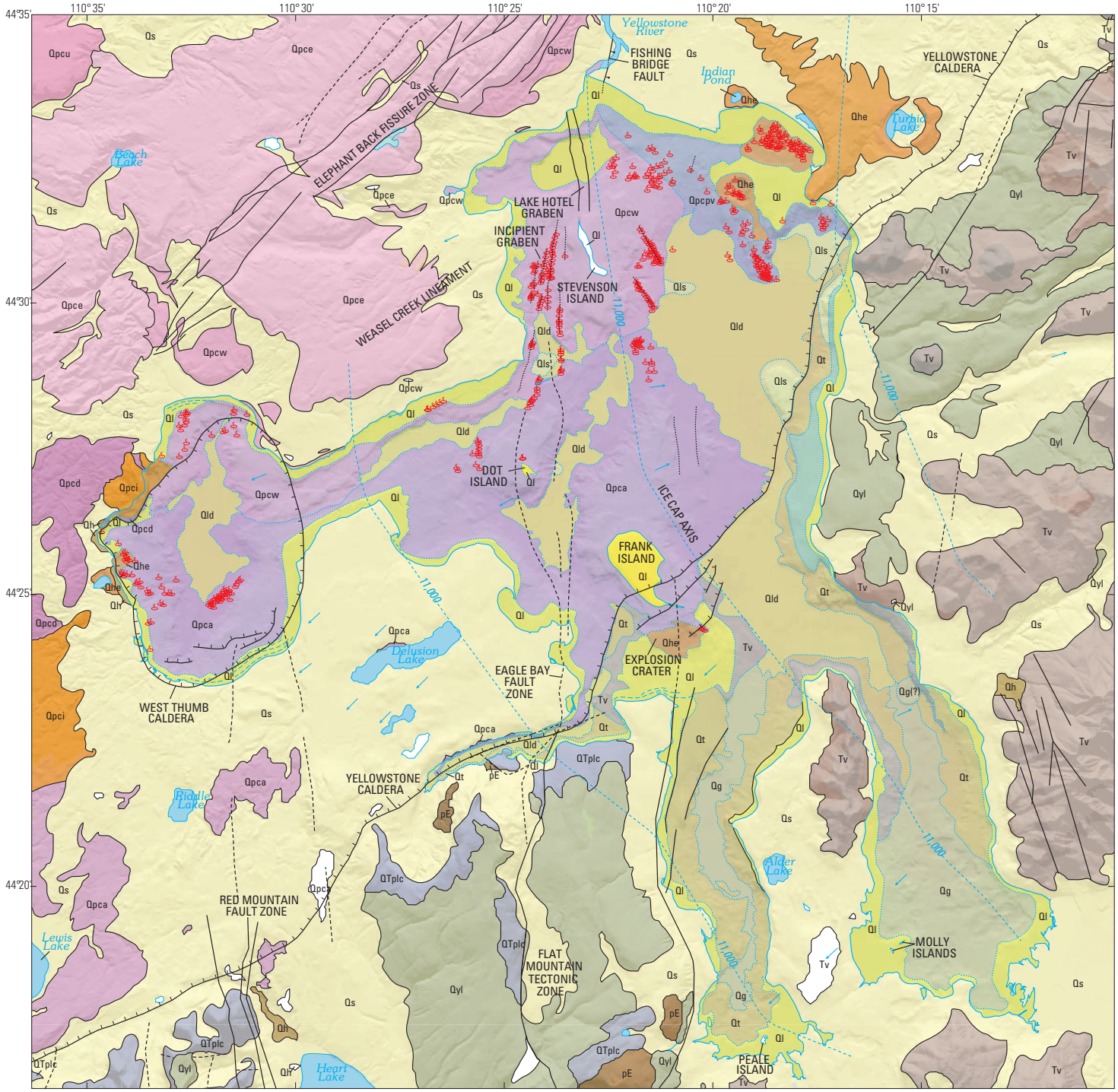

SCALE: 1:76,821

0 1 2 3 MILES

0 1 2 3 4 5 KILOMETERS

APPROXIMATE MEAN DECLINATION, 2007

EXPLANATION—Continued on facing page.

QUATERNARY UNITS

- Qs — Sediments
- Ql — Shallow-lake sediments—Shallow water deposits and submerged shoreline deposits
- Qld — Deep-lake sediments—Laminated deep-basin deposits
- Qhe — Hydrothermal-explosion deposits
- Qh — Hydrothermal deposits
- Qls — Landslide deposits
- Qt — Talus and slope deposits
- Qg — Glacial(?) deposits
- Qpcu — Spruce Creek rhyolite flow
- Qpce — Elephant Back rhyolite flow
- Qpcw — West Thumb rhyolite flow
- Qpca — Aster Creek rhyolite flow
- Qpci — Tuff of Bluff Point
- Qpcd — Dry Creek rhyolite flow
- Qpcpv — Pelican Creek rhyolite flow
- Qyl — Lava Creek Tuff

Figure 3. Geologic map of Yellowstone Lake.

enough to contribute significantly to the demagnetization of rocks by hydrothermal alteration. Current heat-flow values in Bridge Bay area (580 mW/m^2; Morgan and others, 1977) of the northern basin are relatively low compared to Mary Bay, yet the Bridge Bay area has low magnetic-intensity values in the reduced-to-the-pole magnetic map (Finn and Morgan, 2002); evidence for past hydrothermal activity is present as inactive hydrothermal vents and structures and may have been responsible for demagnetization of the rocks there (fig. 5, vents). Additionally, south of Bridge Bay and west of Stevenson Island, low magnetic-intensity values reflect active hydrothermal venting and relatively high heat-flow values (Morgan and others, 1977). Low magnetic-intensity values in the northern West Thumb basin also may be due to past hydrothermal activity, as evidenced by vent structures there (fig. 5). Field examination of rhyolite flows shows that many areas with low magnetic intensity values correspond to areas with hydrothermal activity or faulting or fracturing along which hydrothermal alteration has occurred. In contrast, the mapped extent of the Lava Creek Tuff is not revealed in the magnetic data. This difference may be due in part to the quenched vertical and thick (>100 m) flow margins common in many of the large-volume rhyolitic lava flows, whereas the Lava Creek Tuff is more tabular in extent, is generally thinner, and does not have quenched edges.

Because of the high-resolution, shallow-penetration seismic-reflection method we employed, rhyolitic-lava-flow tops are imaged as high-amplitude reflectors only in areas where sediment cover is thin. In other areas, high-resolution aeromagnetic data in conjunction with our recent bathymetric map provide critical evidence. Comparison of geologic maps (fig. 1*B*) (Blank, 1974; Christiansen, 1974; Christiansen and Blank, 1975; Richmond, 1973) with the high-resolution aeromagnetic maps (Finn and Morgan, 2002) shows a crude relation of magnetic anomalies to the mapped individual lava flows on land (fig. 1*C*). The magnetic signatures, combined with the high-resolution bathymetric and seismic-reflection data, allow identification and correlation of sediment-covered rhyolitic lava flows far out into the lake (figs. 1 and 2). For example, the Aster Creek flow (map unit Qpca, fig. 1*B*) southwest of the lake (figs. 1*C* and 3) is associated with a consistent moderately positive magnetic anomaly that extends over the lake in the southeast quadrant of West Thumb basin, along the southern half of the West Thumb channelway, and over the central basin of the lake well past Dot and Frank Islands (figs. 1 and 2*C*). The Aster Creek flow has few mapped faults and few areas that have been hydrothermally altered. Similarly, the West Thumb flow (map unit Qpcw, fig. 1*B*) can be traced into the lake in northeastern West Thumb basin, along the northern half of West Thumb channelway, and into the northern basin beneath Stevenson Island and Bridge Bay (figs. 2*B* and 3). In contrast, the Elephant Back flow contains a well-developed system of northeast-trending faults or fissures that has been extensively altered so that the magnetic signature of this unit is erratic, with a wide range of magnetic intensity values (figs. 1*C* and 3).

In the northern basin, rhyolitic lava flows are inferred mainly from the bathymetry. Interpretation of the magnetic data is somewhat more complicated owing to high temperatures and extensive hydrothermal alteration reflected in the low values of magnetic intensity. Extremely high heat flow in the Mary Bay area (1,650–15,600 mW/m^2) (Morgan and others, 1977) and abundant sublacustrine hydrothermal activity (fig. 1*B*; pl. 2) have resulted in hydrothermal alteration destroying or significantly reducing the magnetic susceptibility of minerals in rocks and sediments, producing the observed negative magnetic anomalies.

A rhyolitic body present at depth in the northern basin of Yellowstone Lake and in the lower Pelican Valley (figs. 2*B* and 3) is indicated from hydrothermally altered, quartz-bearing, felsite lithic clasts present in the hydrothermal-explosion breccia of Mary Bay and prevalent in the alluvium of the lower Pelican Valley (map unit Qpcpv, fig. 1*B*). This unit has not been described before and is not a mapped unit in Christiansen (2001). We suggest the felsite clasts are derived from either a buried volcanic or shallow intrusive unit beneath the lower Pelican Valley and the northern lake basin. This felsite produces a moderate positive magnetic anomaly in the lower Pelican Valley and a strong negative magnetic anomaly in the lake extending north as seen in the reduced-to-the-pole map (map unit Qpcpv, fig. 1*C*) in the lower Pelican Valley (Finn and Morgan, 2002).

Topographically low areas and hydrothermally altered areas cause magnetic lows over the Yellowstone Lake area. The altered portions of lava flows often produce characteristic high-amplitude (200–600 nT), circular or oval, magnetic lows that are particularly evident over the active geyser basins. Modeling of two of the characteristic anomalies within the caldera shows that the lows are caused by the magnetization contrast between ~200- to 500-m-thick non-magnetic altered zones and adjacent rhyolites with magnetizations between 3 and 6 A/m (Finn and Morgan, 2002). Hydrothermal-explosion craters, such as Mary Bay, Indian Pond, and Duck Lake, produce magnetic lows due to topography as well as hydrothermal alteration and high heat flow.

Field examination of subaerial rhyolitic lava flows indicates that negative magnetic anomalies, for the most part, are associated with extensive hydrothermal alteration or, in places, alteration due to emplacement of lava flows into water, such as ancestral Yellowstone Lake, or contact with ice. For example, the West Thumb rhyolite flow, due west of the Yellowstone

EXPLANATION—CONTINUED

OLDER UNITS

QTplc Quaternary and Tertiary pre-Lava Creek Yellowstone Group rhyolites, undifferentiated

Tv Tertiary volcanic rocks, undifferentiated

pE Pre-Eocene rocks, undifferentiated

Contact

Fracture, fault—Dashed where approximately located or inferred; dotted where concealed; bar and ball on downthrown side

Caldera margin and related structures

Hydrothermal vent

Direction of 16-ka ice flow

Underwater contact

11,000 Contour on upper surface of 16-ka ice cap

Yellowstone Lake shoreline

Submerged shoreline

Water

River (figs. 1*B,* 2*B*, and 3), is glassy, flow-banded, and fresh; the magnetic intensity values in this area generally are high (fig. 1*C*). In contrast, in areas where flows were emplaced into water, such as the West Thumb rhyolite flow exposed on the northeast shore of West Thumb basin (figs. 1*B* and 2*A*), magnetic-intensity values are low (fig. 1*C*). The low magnetic values of flows emplaced into water may be primarily carried by the fine-grained and altered matrix in the massive rhyolitic breccias, highly fractured perlitic vitrophyre, clastic dikes, and entrained stream, beach, and lake sediments in an altered matrix.

Large Hydrothermal-Explosion Craters

Subaerial hydrothermal explosions have occurred repeatedly during the past 14 k.y. in Yellowstone National Park (Muffler and others, 1971; Pierce and others, this volume; Morgan and others, 1998) and are confined primarily within the boundaries of the Yellowstone caldera (fig. 1). Large (>500 m) circular, steep-walled, flat-bottomed depressions are mapped at several sites in Yellowstone Lake in the West Thumb, central, and northern basins (figs. 2*A*, 2*B*, and 2*C*; pl. 2). These are interpreted as large composite hydrothermal-explosion craters similar in origin to those on land, such as Duck Lake, Pocket Basin in the Lower Geyser Basin (not in mapped area), the 8.3-ka Turbid Lake crater, and the 3.0-ka Indian Pond crater (figs. 1*B*, 2*A*, 2*B*, and 2*C*) (Morgan and others, 1998; Pierce and others, 2002; Muffler and others, 1971).

A newly discovered 500-m-diameter sublacustrine explosion crater, referred to informally as the Evil Twin explosion crater, in the western part of West Thumb basin near the currently active West Thumb Geyser Basin, is only 300 m northeast of Duck Lake (fig. 2*A*), a postglacial (<12 ka) hydrothermal-explosion crater (Muffler and others, 1971; Christiansen, 1974, 2001; Richmond, 1973; U.S. Geological Survey, 1972). In the western part of West Thumb basin, heat-flow values are as high as 1,500 mW/m^2 (Morgan and others, 1977), reflecting the hydrothermal activity that contributed to the formation of the offshore explosion crater. The 500-m-wide Evil Twin explosion crater is surrounded by 12- to 20-m-high, nearly vertical, walls and has several smaller nested craters along its eastern edge. These nested craters are as deep as 40 m and are younger than the main crater. Temperatures of hydrothermal fluids emanating from the smaller northeast nested crater have been measured at 72°C by ROV.

Another newly discovered, large, subaqueous hydrothermal-explosion crater is the >600-m-wide, elongate, steep-walled, flat-floored crater south of Frank Island (fig. 2*C*). Muted topography suggests that this explosion crater is one of the oldest still recognizable in Yellowstone Lake. Further, this crater occurs in an area where heat-flow values are, at present, relatively low. Submersible ROV investigations do not indicate hydrothermal activity within the crater.

In the northern basin of Yellowstone Lake, Mary Bay contains an approximately 2.4-km by 2.8-km area of coalesced explosion craters (Morgan and others, 1998; Wold and others, 1977) (fig. 2*B*), thus making it the world's largest known hydrothermal-explosion system (Browne and Lawless, 2001). Boiling temperature in the deep part of Mary Bay is about 160°C. Investigations using a submersible ROV show that fluids from a 35-m-deep hydrothermal vent in Mary Bay have temperatures near the 120°C limit of the temperature probes used, reflecting extremely high heat-flow values in this area (Morgan and others, 1977). Radiocarbon dates from charcoal in breccia deposits and underlying soils exposed in wave-cut cliffs along the shore of Mary Bay indicate that eruption of this crater occurred at 13.0 ka (Morgan and others, 1998; Pierce and others, 2002). Detailed stratigraphic measurements of the breccia deposits indicate that multiple explosions occurred during formation of this large and complex feature. A clean, planar-bedded sand overlying varved lake sediments occur as a sedimentary interbed between breccia deposits within the Mary Bay breccia deposit; the fine-sand unit may represent deposition from a wave-generated event associated with the development of the Mary Bay complex (Morgan and others, 1998; Morgan and others, 2002).

One kilometer southwest of the Mary Bay crater complex is another newly discovered, large (~800 m diameter) composite depression informally referred to as Elliott's crater (fig. 2*B;* pl. 3*A*), named after Henry Elliott, who helped map Yellowstone Lake in the 1871 Hayden survey (pl. 1*B*) (Merrill, 1999). Development of Elliott's hydrothermal-explosion crater is best illustrated in a north-south seismic-reflection profile (fig. 4*B*). Zones of nonreflectivity in the seismic profile on the floor and flanks of the large crater probably represent hydrothermally altered, and possibly heterolithic, explosion-breccia deposits, similar in character to those exposed on land and associated with subaerial explosion craters (Muffler and others, 1971). Seismic profiles in the hummocky area southeast of Elliott's crater also are nonreflective and may represent a layer of heterolithic and (or) hydrothermally altered material erupted from this crater. In contrast to the subaerial craters, which have radial aprons of explosion-breccia deposits that rim the crater (Hamilton, 1987; Muffler and others, 1971), many of the sublacustrine circular depressions lack an obvious apron. This may indicate more widespread dispersal of ejection deposits in the lake water or that some other process, such as catastrophic collapse of sealed caprock, created the depressions.

Following the initial major explosive event of Elliott's crater, lacustrine sediments, imaged as laminated reflective layers in the seismic profile (fig. 4*B*), accumulated in the floor of the crater and on its south flank. Posteruptive sediment thickness of ~8 m indicates the main hydrothermal explosion occurred between 13 and 8 ka, based on sedimentation rates in the lake. Opaque zones within the stratified sedimentary fill of the crater indicate the presence of hydrothermal fluids and (or) gases. The presence of two younger craters at the south end of the main crater floor and the presence of many smaller hydrothermal vents further indicates more recent hydrothermal activity and possibly younger explosions. Along the southeast rim of the main crater, more than 3 km south from shore, are rocks exposed above lake sediments on the lake floor of varying lithic compositions; these rocks may be the product of a more recent hydrothermal explosion. A north-south seismic profile across Elliott's explosion crater shows about 10 m of vertical difference in height between the rims. This difference may result from doming associated with hydrothermal activity prior to initial explosion.

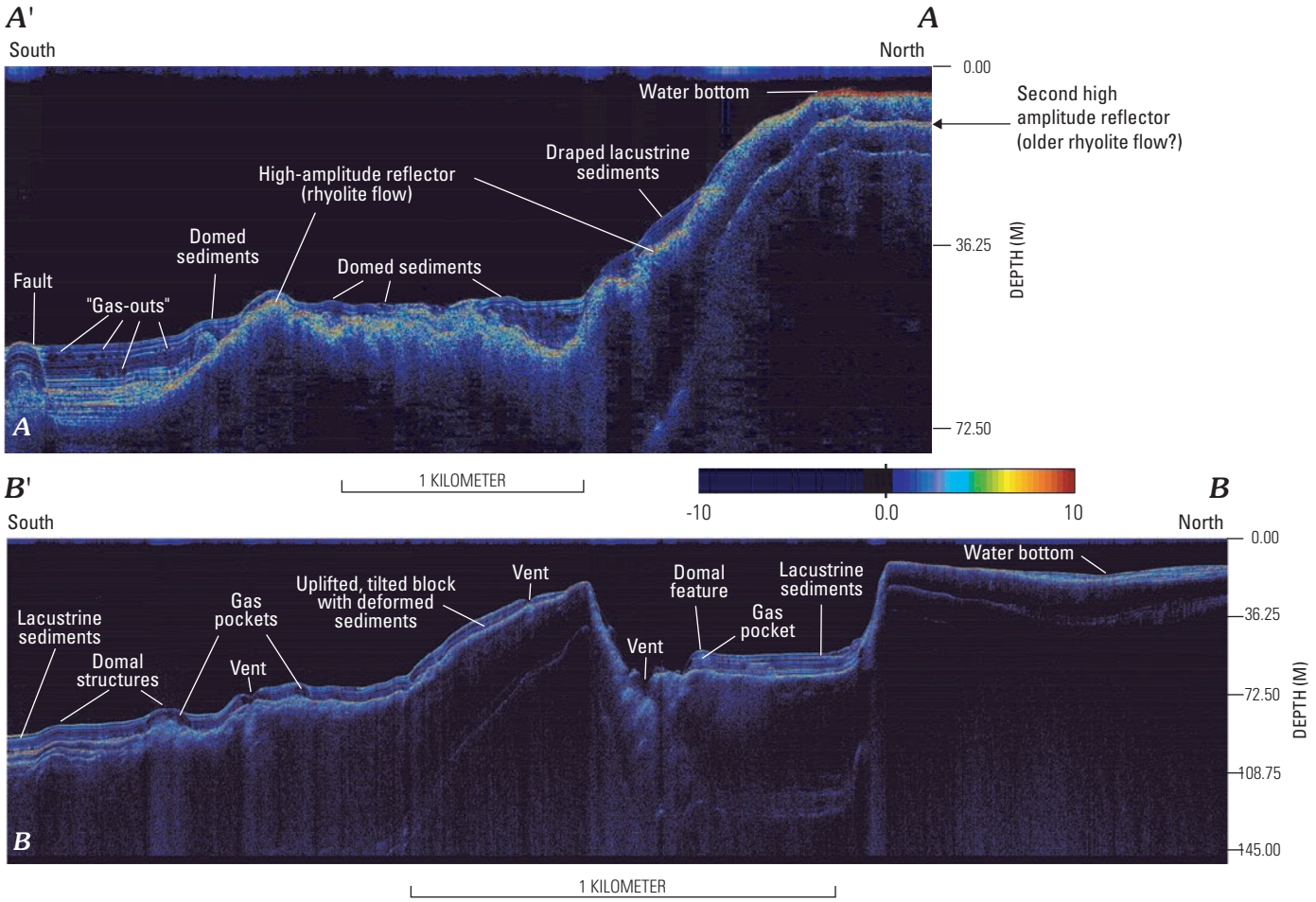

Figure 4. High-resolution seismic-reflection images. *A*, High-resolution seismic-reflection image from northwestern West Thumb basin showing high-amplitude (discontinuous red and yellow) reflector interpreted as a sub-bottom rhyolitic lava flow. Glacial and lacustrine sediments, marked in blue, overlie this unit. The data amplitudes have been debiased and spatially equalized only; no additional gain corrections or filtering were applied. *B*, High-resolution seismic-reflection image (line YL72) across part of Elliott's explosion crater showing small vents, gas pockets, and domed sediments in the lacustrine sediments that overlie the crater flank. Lacustrine-sediment thickness in the main crater indicates 5–7 thousand years of deposition since the main explosion. More recent explosions, in the southern part of the large crater, ejected postcrater lacustrine sediments and created new and smaller craters. Colors are the same as for figure 4A.

Hydrothermal Vents and Domes on the Floor of Yellowstone Lake

Seismic-reflection profiles of the surveyed areas in the northern, central, and West Thumb basins of Yellowstone Lake reveal a lake floor covered with laminated, diatomaceous, lacustrine muds, many of which are deformed, disturbed, and altered. High-resolution bathymetric mapping reveals that many areas contain small (<20 m) depressions pockmarking the lake bottom (pl. 1F and fig. 3).

Geochemical studies of the vents (fig. 5) indicate that ~10 percent of the total deep-thermal-water flux in Yellowstone National Park occurs on the lake bottom. Hydrothermal fluids containing potentially toxic elements (As, Sb, Hg, Mo, W, and Tl) significantly influence lake chemistry and possibly the lake ecosystem (Balistrieri and others, this volume). ROV observations indicate that shallow hydrothermal vents are home to abundant bacteria and amphipods that form the base of the food chain. This food chain includes indigenous cutthroat trout and piscivorous, exotic lake trout, as well as grizzly bears, bald eagles, and otters that feed on the potamodromous cutthroat trout during spawning in streams around the lake (Chaffee, Shanks, and others, this volume).

In seismic-reflection profiles (fig. 4*B*), hydrothermal-vent features typically are imaged as V-shaped structures associated with reflective layers that are deformed or have sediments draped across their edges. Areas of high opacity or no reflection occur directly beneath them and are interpreted as gas pockets containing steam or CO_2, gas-charged fluids, or hydrothermally altered zones. Evidence for lateral movement

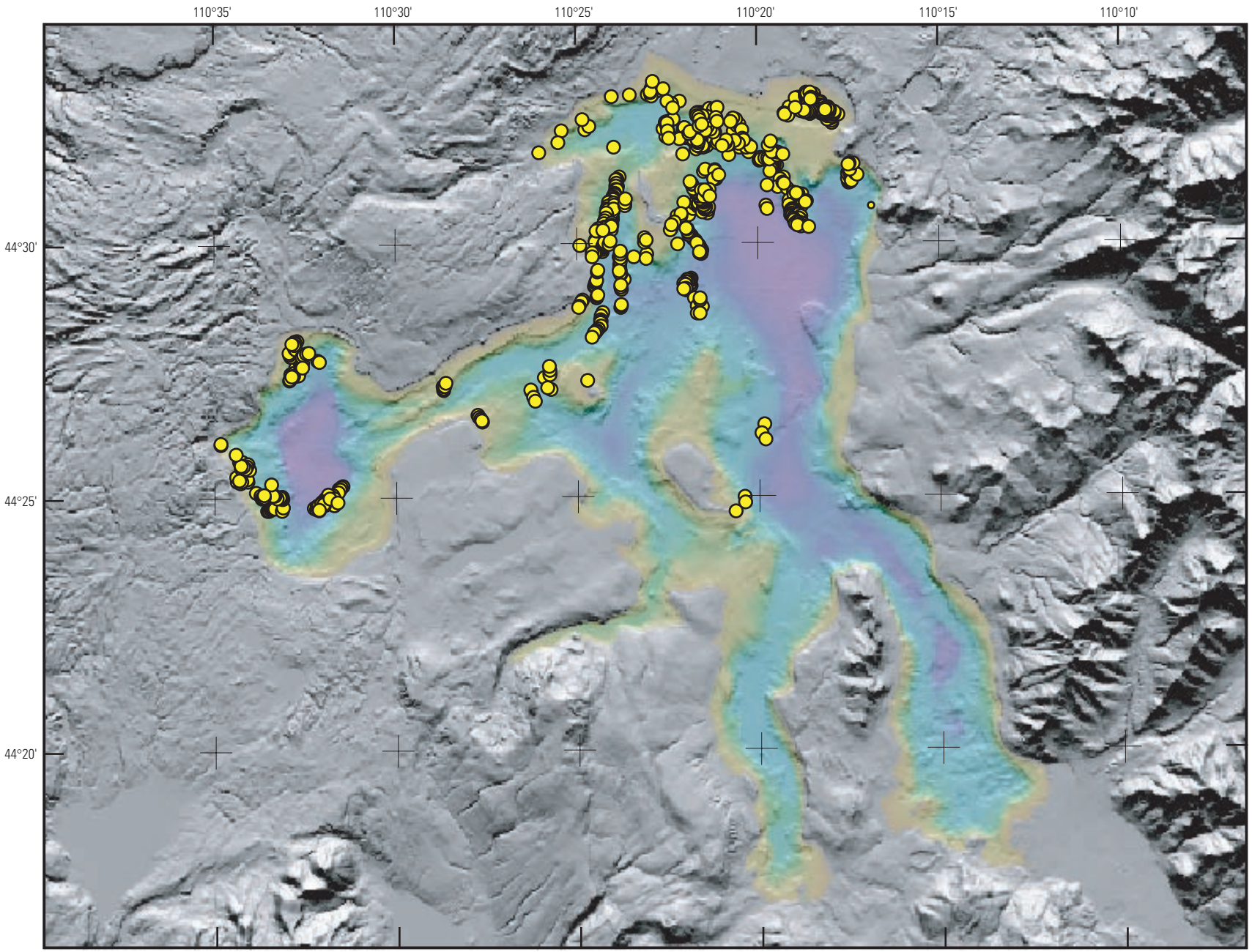

Figure 5. Blue-shaded bathymetric map of Yellowstone Lake surrounded by a gray-shaded topographic map of the surrounding area shows the distribution of hydrothermal vents, shown as yellow dots, in the lake. More than 660 active and inactive hydrothermal-vent structures have been identified in this recent mapping effort.

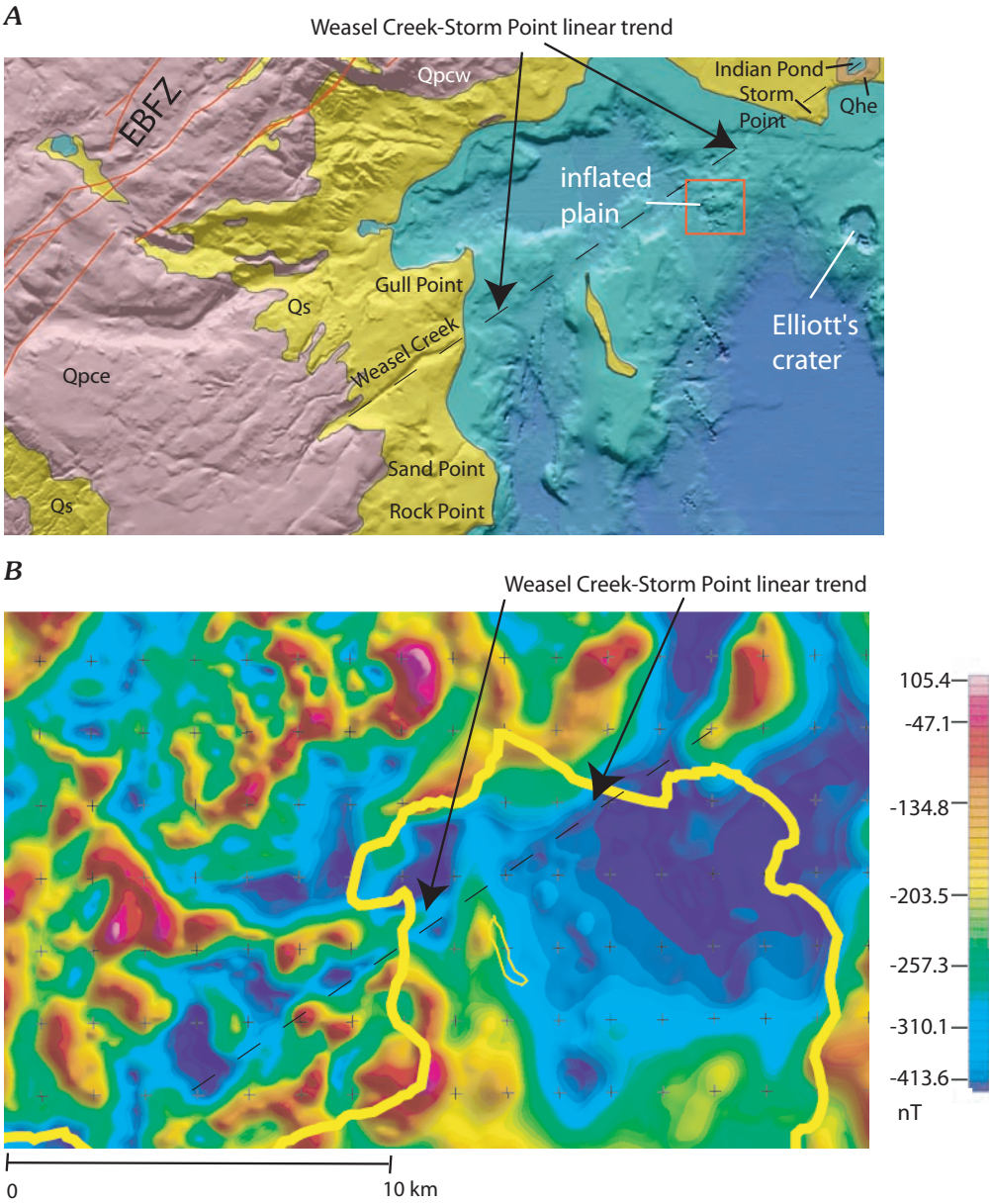

Figure 6. High-resolution images and simplified map of the "inflated plain" in northern basin of Yellowstone Lake.

A, High-resolution blue-shaded-relief bathymetric map of the northern basin of Yellowstone Lake highlighting the location of the "inflated plain," Storm Point, Elliott's hydrothermal-explosion crater, Elephant Back fissure zone (EBFZ), and the northeast-trending Weasel Creek–Storm Point linear trend. A geologic shaded-relief map of the area surrounds the lake (U.S. Geological Survey, 1972). Geologic units shown are in pink (Qpce, Quaternary Elephant Back flow; Qpcw, Quaternary West thumb flow), yellow (Qs, Quaternary sediments), and tan (Qhe, Quaternary hydrothermal-explosion deposit).

B, High-resolution aeromagnetic map (Finn and Morgan, 2002) of the area shown in figure 6A. The shoreline of Yellowstone Lake is represented by a thick, solid-yellow line; Stevenson Island is shown as a thin, solid-yellow line. Note the location of the "Weasel Creek–Storm Point linear trend."

C, Simplified map of Yellowstone National Park highlighting location of the topographic margin of the Yellowstone caldera, its two resurgent domes (Mallard Lake dome and Sour Creek dome), the Elephant Back fissures, and Yellowstone Lake. Superimposed on this, in black, are contour lines (in mm) showing the amount of total caldera uplift that occurred between 1923–1975 (modified from Dzurisin and others, 1994). The Weasel Creek–Storm Point linear trend is shown in purple and coincides approximately with the 450-mm-uplift contour interval.

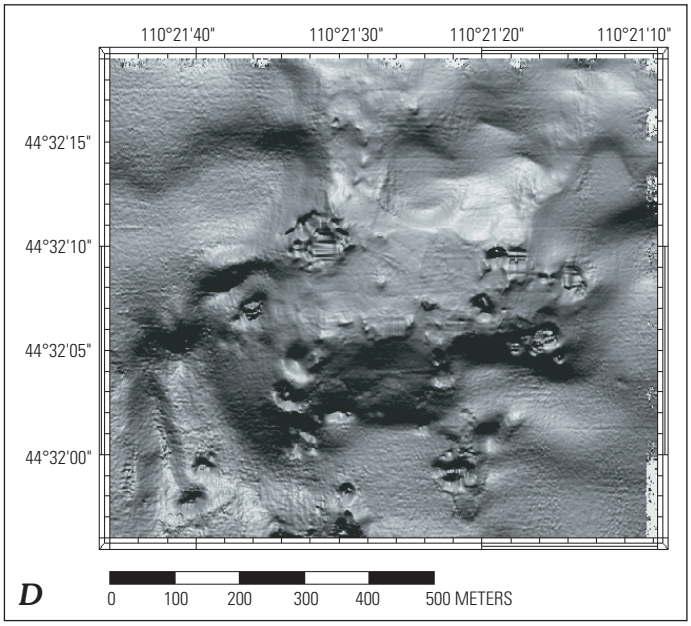

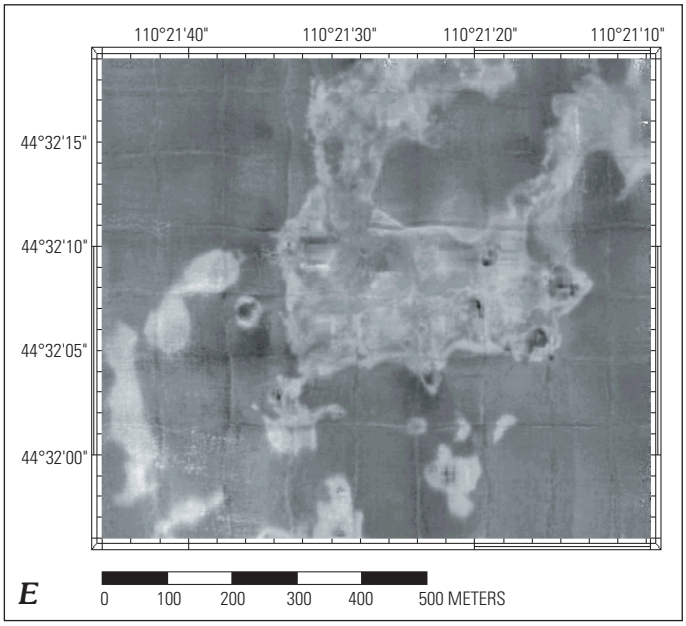

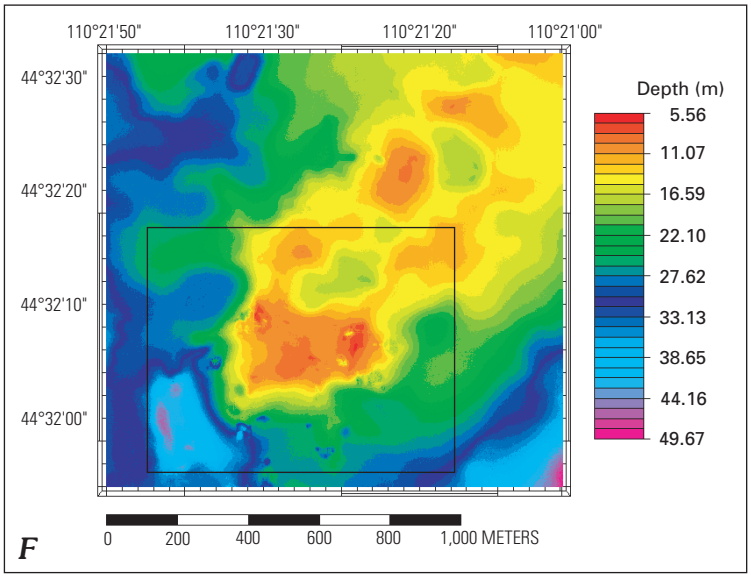

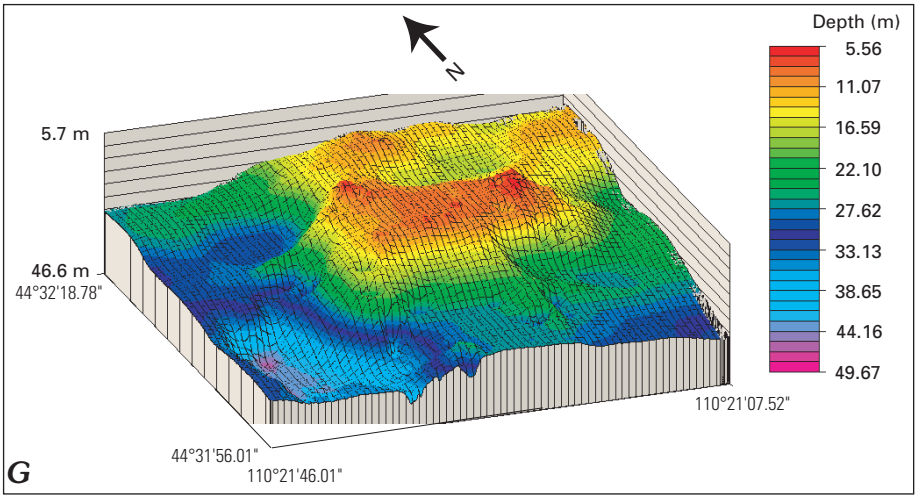

D, Gray-shaded-bathymetric close-up image of the "inflated plain." Illumination is from due north with a sun-angle of 45°.
E, Gray-scale backscatter-amplitude map of the same area shown in figure 6D. Bright areas are reflective due to their relative hardness and degree of silicification. Dark areas are sites of active hydrothermal vents. The range of reflectivity is from 26 to –20 dB.
F, Two-dimensional color-bathymetric map of the "inflated plain." Area shown in black box is the area shown in figures 6D and 6E. Total depth ranges from 5.56 to 49.76 m.
G, Three-dimensional color-shaded-relief image of the "inflated plain." Area shown is same as area in figure 6F; the image is rotated so that north is at 340° and is tilted 20°. Total depth ranges from 5.56 to 49.76 m. Data shown in figures 6A, D, E, F, and G are from 2002 mapping when the "inflated plain" was resurveyed.

of hydrothermal fluids is seen beneath and adjacent to hydrothermal vents identified in the seismic-reflection profiles. The areas of opacity in the seismic data and of low values of magnetic intensity in the aeromagnetic data represent larger zones of hydrothermal alteration than those seen in the surficial hydrothermal vents (fig. 5) (Finn and Morgan, 2002) and provide further evidence of lateral migration of hydrothermal fluids.

Many vent areas are associated with smaller domal structures in which the original horizontally laminated, diatomaceous, lacustrine sediments have been arched upward as much as several meters by underlying pockets of gas or gas-charged fluids, presumably rich in steam and possibly CO_2. Hydrothermal fluids, rich in silica, beneath the domes flow into the overlying sediments resulting in their silicification. The cap sediments become sealed, impermeable, and weakly lithified so that their resultant compaction is minimal. In contrast, the unaltered muds surrounding these domes become more compacted over time and contribute to the overall domal morphology. These domal structures may be preserved as domes, may develop into large craters associated with hydrothermal explosions, or may develop smaller craters within the dome that collapse due to dissolution of the underlying sediment. All these scenarios would pose different levels of hazards, from very little associated with a dome to significant, as would be the case for a hydrothermal explosion.

A large domal structure, informally referred to as the "inflated plain" (fig. 6), was originally recognized in the 1999 bathymetric survey of the northern basin (Morgan and others, 1999) and was resurveyed in 2002. The "inflated plain" covers an approximately circular area with a diameter of ~0.7 km, has a relatively flat or plain-like top covered with smaller craters, and stands ~30 m above the surrounding lake floor. The dome hosts numerous active and vigorous hydrothermal vents and smaller domal structures and is the largest dome identified in the lake. Differential analysis of the 1999 data with that collected in 2002 shows no measurable changes in the surface of the structure.

As shown in figure 6*A*, the "inflated plain" lies along a northeast linear trend in line with other structures. Northeast of the dome on land is Storm Point, a 4- to 6-ka hydrothermal dome, and Indian Pond, a 3-ka hydrothermal-explosion crater. Southwest of the "inflated plain" is an unnamed trough in the lake that continues on land into the Weasel Creek drainage, west of Yellowstone Lake (fig. 6*A*). We informally refer to the northeast linear trend as the "Weasel Creek lineament." This 14-km-long structure is subparallel to fissures in the Elephant Back fissure zone to the northwest (fig. 6*A*). Weasel Creek has an unusually straight drainage, as do two smaller subparallel drainages due north and at least one drainage due south of Weasel Creek. These fissures may represent linear zones of weakness, similar in origin to the fissures on Elephant Back Mountain and related to the inflation/deflation cycles of deformation of the Yellowstone caldera (fig. 6*C*) (Dzurisin and others, 1994). The Weasel Creek lineament, the most developed of these zones of weakness south of Elephant Back Mountain, is reflected as a discontinuous linear zone of low magnetic intensity in the high-resolution reduced-to-the-pole magnetic map of the area (fig. 6*B*) and may reflect a zone of upwelling hydrothermal fluids, which have contributed significantly to the demagnetization of the rocks present. This structure appears to left-laterally offset the "outlet graben" to the north from an incipient graben to the south associated with the "fissures" area in the lake, due west of Stevenson Island.

In late summer of 2002, while traversing the "inflated plain" area in the RV *Cutthroat,* we noted several unusual phenomena not observed in our previous surveys, which were conducted in late June and July. Phenomena included a strong scent of H_2S, a 30- to 50-m-diameter plume of fine sediments, and large concentrations of bubbles, many of them quite vigorous, at the lake surface. The fine-sediment plume was first detected by the Fathometer as a strong reflector concentrated ~3 m below the lake surface and later observed. We have reoccupied this site in subsequent years during the early summer and fall, and note that the phenomena observed in late summer 2002 are not apparent in the early summer. This timing coincides with changes in lake levels, which are high in June and July and quickly drop off by late August (fig. 7). Lake level data were calculated from discharge data available at http://nwis.waterdata.usgs.gov/wy/nwis/discharge/?site_no=06186500. We now attribute the observed phenomena in late summer and fall as being associated with a drop in lake level, significant enough to lower the hydrostatic head on active hydrothermal-vent systems. Balistrieri and others (this volume) have considered the cause of lake level drop and have calculated an annual average evaporation rate of 0.17 km^3/y, which is insignificant compared to discharge that averages 1.19 km^3/y. As shown in figure 7, the level of water in Yellowstone Lake increases as much as 1 m over a 2-month period in late spring associated with runoff from melt of snow pack in surrounding mountains. Lake level peaks in late July and drops sharply by late August coinciding when the observed phenomena associated with the "inflated plain" begin. This drop allows finely disseminated clays in the vents to rise to the surface along with an increase in bubble activity which pop at the surface releasing H_2S. Based on lake level changes (fig. 7), it may be that the phenomena described is normal and is obscured from observation due to a rapid increase in lake level for a 2-month period.

A close-up bathymetric image of the "inflated plain" (fig. 6*D*) domal structure pockmarked with numerous hydrothermal vents and craters. Clear evidence of hydrothermal alteration is seen in the amplitude map (fig. 6*E*) where bright areas are reflective due to their relative hardness. We infer that these brighter areas reflect higher degrees of silicification and may represent silicified caprock material, whereas the darker and less hard areas are places where little silicification has occurred. Figures 6*F* and 6*G* show the "inflated plain" in 2-dimensional and 3-dimensional perspectives, respectively, and plainly show how this feature rises as much as 30 m from the lake floor. Note smaller domal structures lie immediately northeast of the "inflated plain" in line with the Weasel Creek linear trend.

Our seismic-reflection studies clearly identify sublacustrine hydrothermal vents with associated hydrothermal feeders (Johnson and others, 2003). Much of the deformation and alteration can be attributed to hydrothermal-vent channelways, subsurface migration, and ascent of hydrothermal fluids. In contrast, areas devoid of inferred hydrothermal vents show well-laminated seismic-reflection profiles characteristic of lake sediments. More than 660 individual hydrothermal vents have been mapped in Yellowstone Lake (fig. 5)—most occur in the northern and West Thumb basins, and several thermal areas also are identified in the central basin. These fields contain dozens of small hydrothermal vents in various stages of development and activity.

Siliceous Spires

Siliceous spires in Bridge Bay (fig. 2*B,* pl. 2) in the northern basin of Yellowstone Lake were discovered by one of us (Lovalvo) in 1997 and are described here because they represent an end-member of hydrothermal-deposit development in the lake clearly imaged by multibeam-sonar studies. Approximately 12–18 spires are identified in water depths of 15 m. These approximately conical structures (fig. 8*A*) are as much as 8 m in height and up to 10 m wide at the base. A small 1.4-m-tall spire collected from Bridge Bay in cooperation with the National Park Service in 1999 shows the spire base to be shallow (~0.5 m below the sediment-water interface), irregular, and rounded; spire material above the sediment-water interface constitutes about 75 percent of the entire structure. The sediment-water interface on the lake floor is recorded on the spire as a zone of banded ferromanganese-oxide-stained clay-rich and diatomaceous sediments. Below the sediment-water interface, the spire is not oxidized, whereas above it, the spire has a dark reddish-brown oxide coating (fig. 8*B*). The interior of the collected spire is white, finely porous, and has thin (from 0.3- to <3-cm diameter), anastomosing vertical channels through which hydrothermal fluids flowed. Little oxide occurs in the interior of the spire structure, but oxidation surfaces are present on former growth fronts (fig. 8*B*). Chemical and oxygen-isotope analyses and scanning electron microscope (SEM) studies of spire samples show them to be composed of silicified filamentous bacteria, diatom tests, and amorphous silica produced by sublacustrine hydrothermal-vent processes (fig. 8*C*). Geochemical studies of lake waters, hydrothermal-vent fluids, and waters in tributary streams show that Yellowstone Lake waters and vent fluids are enriched in As, Mo, Tl, Sb, and W (Balistrieri and others, this volume). Similarly, the Bridge Bay spires are strongly enriched in As, Ba, Mn, Mo, Tl, Sb, and W (fig. 8*D*). Oxygen-isotopic values suggest formation of the spires at about 70–90°C. Uranium-series disequilibrium dating of two samples from one spire yields dates of about 11 ka (ages were determined by Neil C. Sturchio, University of Illinois at Chicago, written commun., 1998); thus, the spire analyzed is immediately postglacial. Spires may be analogous in formation to black-smoker chimneys, well-documented hydrothermal features associated with deep-seated hydrothermal processes at oceanic plate boundaries that precipitate on the seafloor due to mixing between hydrothermal fluids and cold bottom waters (Tivey, 1995).

Analogous subaerial features to the spires in Bridge Bay may be found at Monument Geyser Basin located along the western edge of the Yellowstone caldera (fig. 1*A*) on a ridge top along a northwest-trending fissure in altered Lava Creek Tuff (fig. 9*A*). As shown in figure 9*B*, the number and distribution of the siliceous spire-like structures at Monument Basin is similar to what is seen in Bridge Bay. In Bridge Bay, the spires are cold and inactive. The structures at Monument Basin, like the spires in Bridge Bay, have irregular forms and similar dimensions (figs. 9*C*, 9*D*, 9*E*, and 9*F*). Currently Monument Geyser Basin sits about 250 m above the water table and emits highly acidic steam (Gemery and others, this volume) consistent with the intense alteration of the Lava Creek Tuff host rock. It is unlikely the monuments formed from an acid-steam system because steam has a very limited carrying capacity for SiO_2. We hypothesize that these deposits formed from a hot-water system in an aqueous environment, probably related to a glacially dammed lake during the waning stages of the Pinedale glaciation about 15–12 ka.

Fissures and Faults

Features identified in the western area of the northern and central basins (figs. 2*B,* 2*C,* and 3; pl. 1*F*) include: (1) a set of subparallel, elongate, north–northeast-trending fissures west of Stevenson Island extending southward on the east and west sides of Dot Island (fig. 2*B* and 2*C*) and continuing southward to Eagle Bay; (2) a series of en echelon, linear, northwest-trending, fissure-controlled, small depressions east and southeast of Stevenson Island; and (3) a graben north of Stevenson Island, nearly on strike with Lake Village (figs. 1*B* and 3).

Subparallel sets of fissures west of Stevenson Island (figs. 2*B* and 2*C*) cut as much as 10–20 m into the soft-sediment lake floor. Due west of Stevenson Island, a parallel set of north- to south-trending fissures occurs 1.3 km northeast of Sand Point (fig. 2*B*). Farther south along this trend, the fissures appear to have well-developed hydrothermal-vent craters, although investigations with the submersible show only weak or inactive vent fields in the central basin. These fissures represent extension fractures whose orientation is controlled by regional north-south structural trends, recognized as faults both north and south of Yellowstone Lake (Christiansen, 2001). Active hydrothermal activity is localized along fissures 0.5 km southeast of Sand Point as shown by dark oxide precipitates and warm shimmering fluids upwelling from them. The fissures, inspected with the submersible ROV for about 160 m along their NNE. trend, are narrow (2 to <10 m wide) and cut vertically into soft laminated sediments. No vertical or strike-slip displacement is observed at this location. Continuing southward along this trend, however, seismic-reflection profiles record a series of small, en

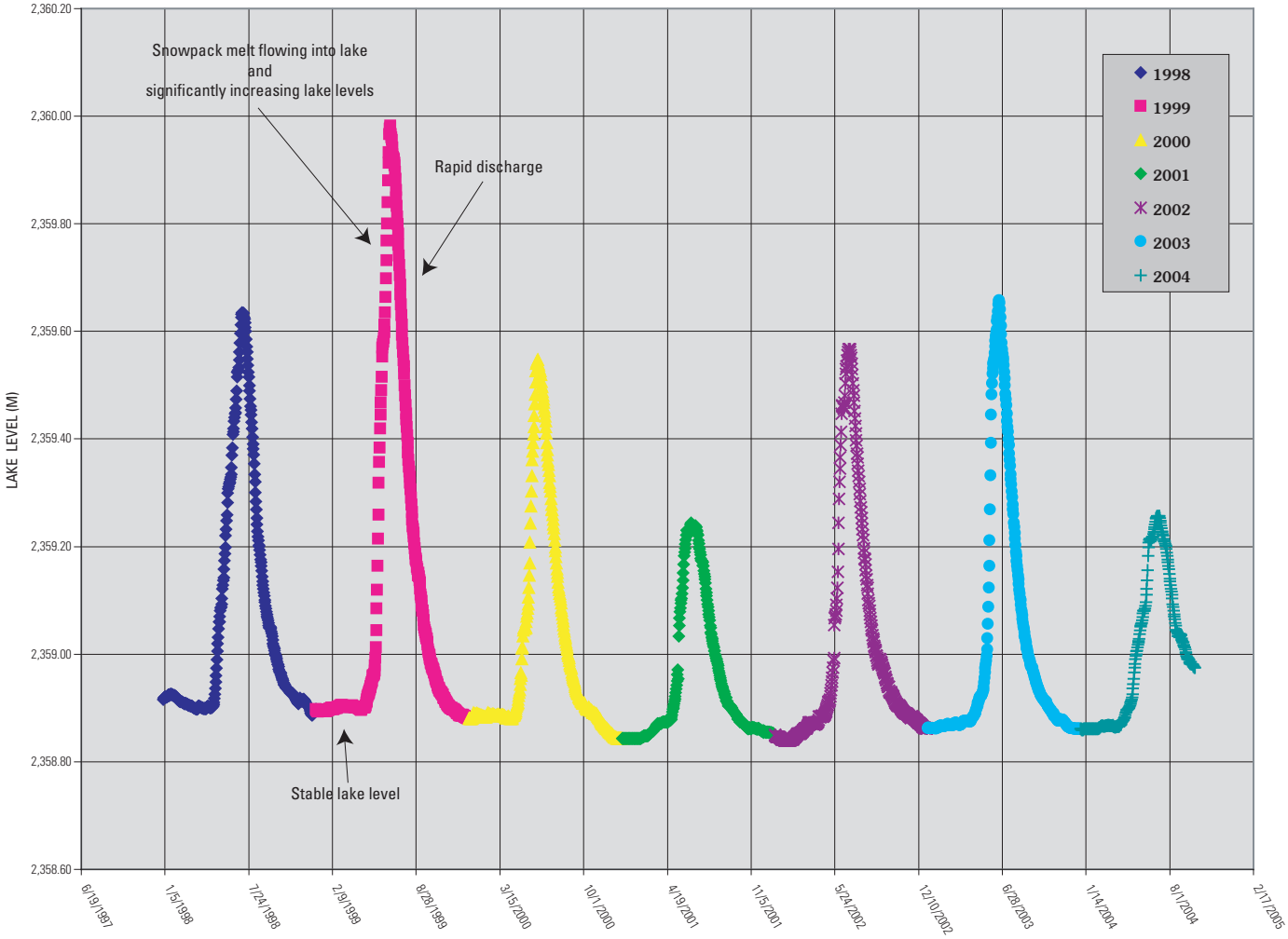

Figure 7. Lake-level variations in Yellowstone Lake from 1998 through early 2005 (http://nwis.waterdata.usgs.gov/wy/nwis/discharge/?site_no=06186500). The average annual change in lake level is ~<1-m total. As shown in the diagram, the highest lake levels occur within approximately a 3-month interval starting in late May–early June and continuing until late July when the runoff from snowpack melt in the mountains surrounding the lake basin is at a maximum. Lake levels are at a maximum in late July and rapidly decrease during the month of August. Lake levels are stable and lower during the nine-month interval between peak runoff and discharge.

echelon, normal faults with displacements of several tens of centimeters to 1–2 meters that occur due southwest of Rock Point (fig. 2*C*). Examination of the high-resolution magnetic-intensity map of this area shows a linear zone of relatively lower magnetic intensities that spatially coincides with the fissures and graben to the north, referred to as the Lake Hotel graben (figs. 1*C*, 2*C,* 2*D,* and 3).

Observation of the features east of Stevenson Island (fig. 2*B*) using the submersible ROV indicates that small, well-developed hydrothermal vents coalesce along northwest-trending fissures. These may be similar to, but more developed, than those vents and fissures west of Stevenson Island. A large hydrothermal vent at the south end of the northernmost set of aligned vents, in the deepest part of Yellowstone Lake, at 133 m (pl. 3*B*), emits hydrothermal fluids as hot as 120°C.

Finally, east–west seismic-reflection profiles across the down-dropped block north of Stevenson Island reveal a north–northwest-trending graben structure bounded by normal faults. This graben, the Lake Hotel graben, was identified by previous investigations (Kaplinski, 1991; Otis and others, 1977; Shuey and others, 1977) but our studies, using differential GPS navigation and high-resolution seismic and bathymetric data, provide the first accurate information on location and displacement on this important structure. Measured displacements along the two bounding faults are variable, but displacement along the western boundary is generally ~6 m, whereas displacement along the eastern normal fault is ~2 m. The eastern bounding fault cuts Holocene lake sediments, indicating recent movement. Analyses of the seismic profiles across the graben indicate the graben developed during three main events: the initial phase between 15–12 ka, a second event at 12–7.5 ka, and the most recent event between 2.5 and 0.1 ka (Johnson and others, 2003). The graben projects (or strikes) toward Lake Village (figs. 1*B* and 2*B*), posing a potential seismic hazard in that area.

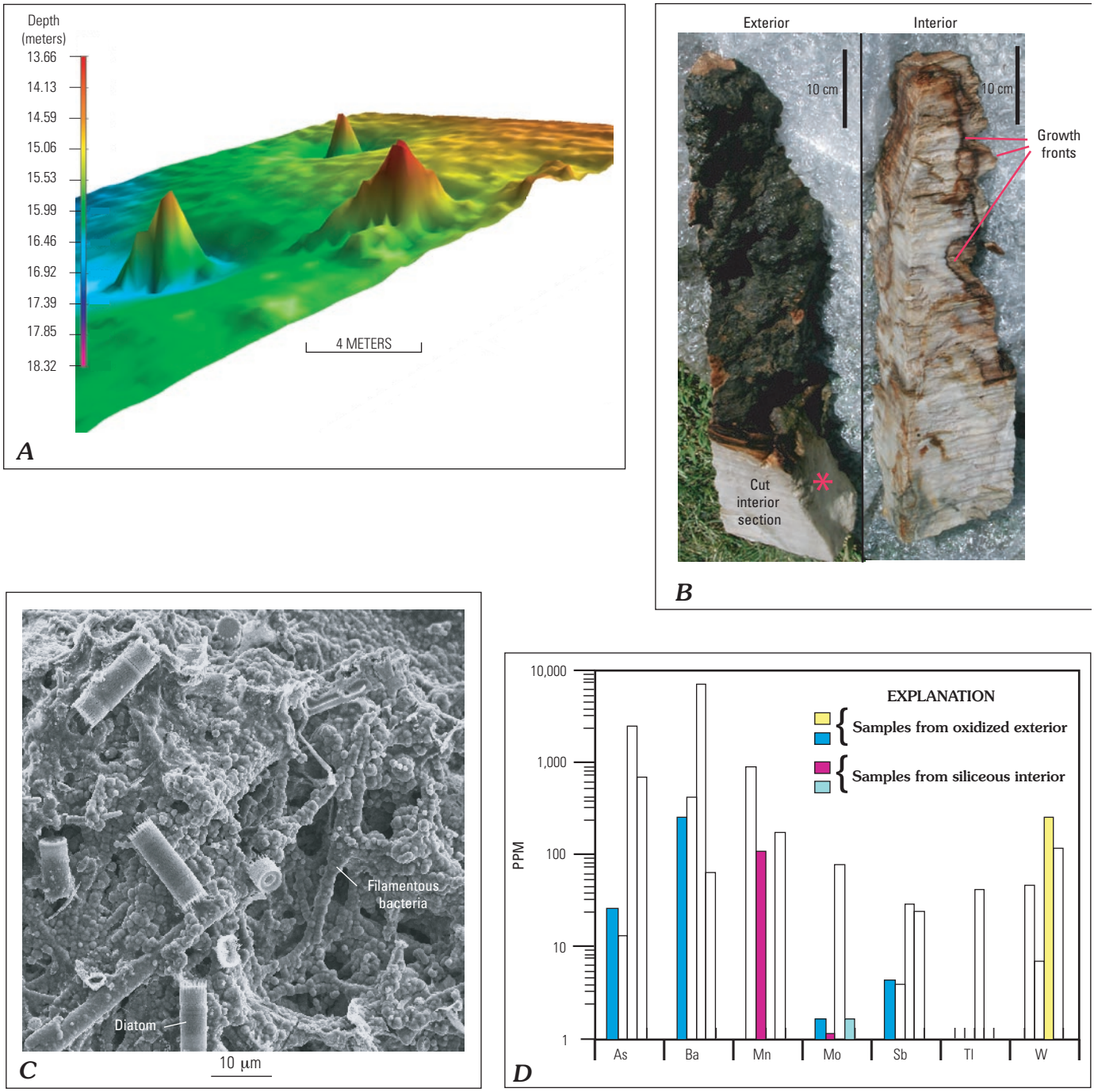

Figure 8. Siliceous spires in Bridge Bay in northern basin of Yellowstone Lake. *A*, Bathymetric image of spires in Bridge Bay showing their approximately conical shapes. Approximately a dozen such siliceous sinter spires—some are as tall as 8 m—occur near Bridge Bay. Many of the spires occupy lake-bottom depressions (possible former explosion or collapse craters). *B*, Photographs of the exterior and interior of a 1.4-m-tall spire sample recovered from Bridge Bay by National Park Service divers. The sediment–water interface of this spire is apparent near the base of the exterior section as seen in the dramatic color change from the outer rind of red-brown ferromanganese oxide to the light-gray interior. (The red asterisk on the photograph of the exterior is on a natural external surface of the spire below the sediment–water interface.) Former growth fronts on the spire can be seen as shown in the photograph of the interior section. *C*, SEM image of diatoms, silicified filamentous bacteria, and amorphous silica from a spire sample. *D*, Summary bar graph of chemical analyses of spire samples showing substantial concentrations of the potentially toxic elements arsenic, barium, manganese, molybdenum, antimony, thallium, and tungsten.

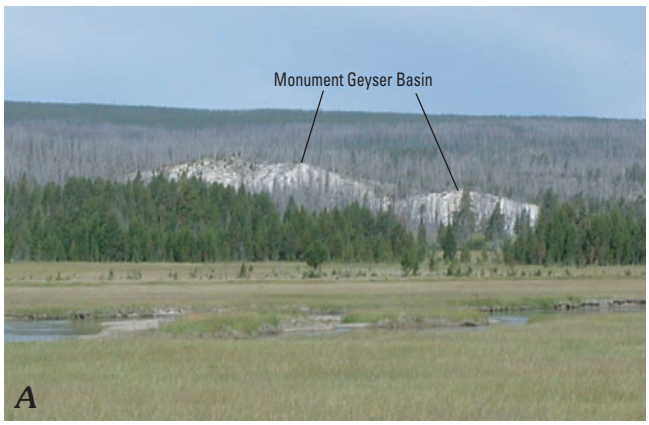
Monument Geyser Basin
A

C

D

E

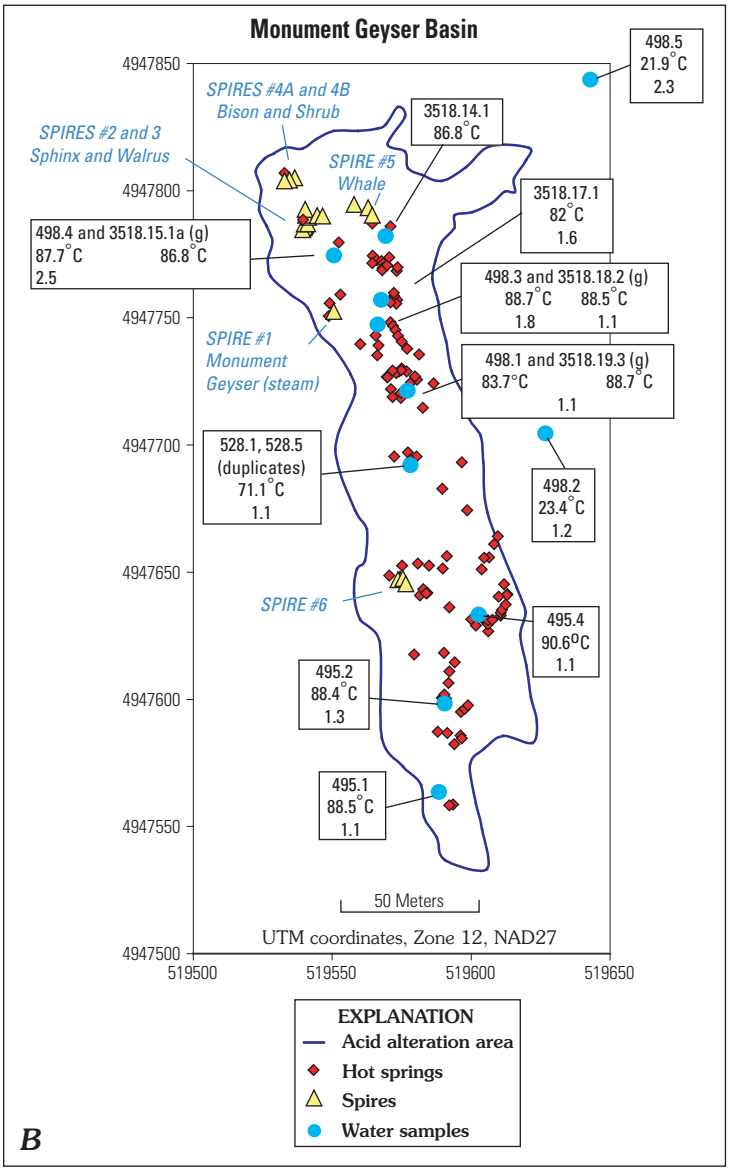
Monument Geyser Basin
SPIRES #4A and 4B
Bison and Shrub
SPIRES #2 and 3
Sphinx and Walrus
SPIRE #5
Whale
SPIRE #1
Monument
Geyser (steam)
SPIRE #6
498.5
21.9°C
2.3
3518.14.1
86.8°C
3518.17.1
82°C
1.6
498.4 and 3518.15.1a (g)
87.7°C 86.8°C
2.5
498.3 and 3518.18.2 (g)
88.7°C 88.5°C
1.8 1.1
498.1 and 3518.19.3 (g)
83.7°C 88.7°C
1.1
528.1, 528.5
(duplicates)
71.1°C
1.1
498.2
23.4°C
1.2
495.4
90.6°C
1.1
495.2
88.4°C
1.3
495.1
88.5°C
1.1
4947850
4947800
4947750
4947700
4947650
4947600
4947550
4947500
519500
519550
519600
519650
50 Meters
UTM coordinates, Zone 12, NAD27
EXPLANATION
Acid alteration area
Hot springs
Spires
Water samples
B

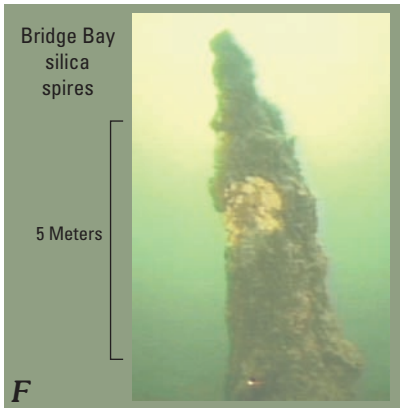
Bridge Bay
silica
spires
5 Meters
F

The set of fissures west and southwest of Stevenson Island may be an incipient graben that is offset from and forming to the south–southwest of the Lake Hotel graben. This structure is on trend with the Eagle Bay fault system (fig. 3).

The sublacustrine fissures and faults revealed by the high-resolution bathymetry are related to the regional tectonic framework of the northern Rocky Mountains, variable depths to the brittle-ductile transition zone (Fournier, 2000), and the subcaldera magma chamber (Eaton and others, 1975; Fournier, 1989; Fournier and others, 1976; Lehman and others, 1982; Stanley and others, 1991; Wicks and others, 1998) and play important roles in shaping the morphology of the floor of Yellowstone Lake. Many recently identified features along the western margin of the northern and central basins, such as the active fissures west of Stevenson Island, the faults southwest of Rock Point, and the Lake Hotel graben in the northern basin, are oriented approximately north–south and probably are related to a regional structural feature in western Yellowstone Lake on strike with the Neogene Eagle Bay fault zone (fig. 1*B*) (Locke and Meyer, 1994; Pierce and others, 1997). Seismicity maps of the Yellowstone region (see U.S. Geological Survey Yellowstone Volcano Observatory Web site: http://volcanoes.usgs.gov/yvo) show concentrations of epicenters at various locations in Yellowstone Lake, including the western and eastern portions of West Thumb basin, west of Stevenson Island, southwest of Rock Point, east of Breeze Point (fig. 2*C*), east and west of Dot Island, the northern basin, and a northwest-trending set west of Park Point.

Figure 9. Monument Geyser Basin. *A*, Photograph of Monument Geyser Basin as seen looking west. Monument Geyser Basin caps a larger hydrothermal system along a north–northwest-trending fissure. Area in white is composed of hydrothermally altered Lava Creek Tuff and sinter. *B,* Index map of Monument Geyser Basin, surveyed using a total field station, showing extent of hydrothermal alteration and distribution of spire-like structures, hot springs, and water-sample localities. Values in the boxes represent individual sample numbers (data found in Gemery and others, this volume), temperatures of hot springs, and pH. *C,* View looking south into Monument Geyser Basin. Note that the basin has a central trough and contains as many as seven spire-like siliceous structures. Person in the mid-foreground provides scale. *D,* Photograph of one of the spire-like structures, informally referred to as the Walrus, in the northern edge of the basin. Person in background provides scale. *E,* Photograph of another spire-like structure, known as Monument Geyser or Thermos Bottle, actively venting steam and H_2S. This structure is ~2 m tall. *F,* Underwater photograph of a large (~8 m) spire structure in Bridge Bay in the northern basin of Yellowstone Lake. The subaerial structures at Monument Geyser Basin are very similar to the spires in Bridge Bay (in terms of size, scale, and distribution) and are irregular in form.

Landslide Deposits

Multibeam-bathymetric data reveal hummocky lobate terrain at the base of slopes along the margins—especially along the northeast, eastern, and western margins—of the lake basin (figs. 2*A* and 3, pl. 1*F*). Seismic-reflection data indicate that the deposits range in thickness from ≥10 m at the eastern edge of the lake and are recognizable as thin (<1 m) units extending as far as 500 m into the interior of the lake basin (Johnson and others, 2003). We interpret these as landslide deposits. The thickness of the lacustrine-sediment cap deposited above the landslide deposits is variable and suggests that the landslides were generated by multiple events. We suggest that the landslides were triggered by ground shaking associated with earthquakes and (or) hydrothermal explosions. Alternatively, some landslide deposits may represent water-saturated debris flows coming off the steep slopes of the adjacent Absaroka Range directly east of Yellowstone Lake. The eastern shore of Yellowstone Lake, near where many of these landslide deposits occur, marks the margin of the Yellowstone caldera (Christiansen, 1984, 2001; Hildreth and others, 1984; U.S. Geological Survey, 1972) and abuts steep terrain of the Absaroka Range to the east, both possible factors contributing to landslide events. Certainly the area along this eastern boundary with high, hydrothermally altered terrane is susceptible to major slide-block development as interpreted to occur in the eastern part of Yellowstone Lake near Elk and Signal Points. The volume of material identified in these deposits as well as the smaller landslide deposits would result in a significant displacement of lake water and may pose a potential hazard on shore.

Submerged Shorelines

Several submerged former lake shorelines form underwater benches in the West Thumb, northern, and central basins of Yellowstone Lake (figs. 2*A*, 2*B*, and 2*C*). The submerged, shallow margins (depth <15–20 m) of the northern basin are generally underlain by one to three relatively flat, discontinuous, postglacial terraces that record the history of former lake levels. Correlation of these submerged shoreline terraces around the lake is based primarily on continuity inferred from multibeam bathymetric data and shore-parallel seismic-reflection profiles. These data indicate that lake levels were significantly lower in the past. An extensive bench occurs south of Steamboat Point and along the western shore of the northern basin south of Gull Point (fig. 2*B*). In Bridge Bay, pebbly, submerged beach sand, 5.5 m below the present lake level, yielded a carbon-14 date of 3,835 yr (Pierce and others, 2002). Well-developed submerged shoreline terraces are present in West Thumb basin, especially along its southern and northern edges.

Relief on these terraces is as much as 2–3 m, a measure of postdepositional vertical deformation. Documentation of the submerged terraces adds to a database of as many as nine separate emergent terraces around the lake (Locke and Meyer, 1994; Locke and others, 1992; Meyer and Locke, 1986; Pierce

and others, 2002). Significant, non-seasonal changes in lake level during the last 9,500 radiocarbon years have occurred primarily in response to episodic uplift and subsidence (inflation and deflation) of the central part of the Yellowstone caldera (Dzurisin and others, 1994; Pelton and Smith, 1982; Pierce and others, 1997, 2002; Pierce, Cannon, and others, this volume; Wicks and others, 1998). Holocene changes in lake level recorded by these terraces have been variably attributed to intra-caldera magmatic processes, hydrothermal processes, climate change, regional extension, and (or) glacioisostatic rebound (Dzurisin and others, 1994; Locke and Meyer, 1994; Meyer and Locke, 1986; Pierce and others, 1997, 2002; Wicks and others, 1998).

Glacial Deposits and Features

Yellowstone Lake straddles the southeast corner of the Yellowstone caldera, with approximately 40 percent of the lake southeast and outside of the caldera margin. This area is dominated by deposits and features of glacial, alluvial, and colluvial origin. Flat Mountain, South, and Southeast Arms are fault-bounded valleys enhanced by glacial scour.

The area around the Southeast Arm and the floor of much of the Southeast Arm is characterized with a hummocky bathymetry with many depressions reflective of kettle and glacial-meltwater terrain seen elsewhere in Yellowstone and Grand Teton National Parks (see fig. 2*D*; pl. 1*F*). Blocks of ice from the last glacial recession appear to have ponded in the southern and central parts of the Southeast Arm. These kettle-like features do not seem as abundant in the South Arm; however, Alder Lake is most likely a former kettle (fig. 2*D*). These features are very similar to "The Potholes" in Jackson Hole, Wyo. (see inset in fig. 2*D*), where glacial-meltwater streams deposited sand and gravel around blocks of stagnant ice (Good and Pierce, 1996). Upon melting, voids left by the ice were later partially filled with slumped sediment leaving large (tens of meters), irregularly shaped depressions.

Discussion

Newly Discovered Features in Yellowstone Lake Pose Potential Geologic Hazards

The bathymetric, seismic, and submersible surveys of Yellowstone Lake have identified various geologic deposits and features that indicate significant potential hazards may exist on the lake floor and adjacent near-shore areas. Potential hazards include hydrothermal explosions, seismic activity, landslides, and possible sudden collapse of hydrothermally altered areas of the lake floor through fragmentation of hydrothermally altered caprock material. Any of these events could result in a sudden shift in lake level generating large waves or seiches that could cause rapid local flooding. Evidence for previous seiche activity can be found in deposits now exposed along the wave-cut cliffs of the northern shore of the lake. Here, dark, well-sorted, crossbedded to planar-bedded, generally fine grained, nonindurated sands are present at the base of and within the 13.0-ka (Pierce, Cannon and others, this volume) Mary Bay explosion-breccia deposit. The sand unit is variable in thickness and in appearance and is similar in character to what has been described for other paleoseismites (Bartholomew and others, 2002). We suggest that this sand deposit represents deposition from a possible earthquake-generated wave that led to displacement of water above a large and sealed hydrothermal system in Mary Bay. The sudden displacement of water may have significantly reduced the total hydrostatic head over Mary Bay, resulting in a rapid decrease in the confining pressure around the hydrothermal system and triggering a large hydrothermal explosion.

Ejecta from past hydrothermal explosions that formed craters in and around Yellowstone Lake extend several kilometers from their crater rims and include rock fragments in excess of several meters in diameter (Hamilton, 1987; Love and others, this volume; Pierce, Cannon, and others, this volume; Morgan and others, 1998; Richmond, 1973, 1974, 1976, 1977). About 12–15 large hydrothermal-explosion craters have been mapped in or near Yellowstone Lake and within the Yellowstone caldera. All of these formed since the last glacial recession about 16 ka and have ^{14}C radiometric ages from 13.0 ka to 3.0 ka (Pierce, Cannon, and others, this volume; Richmond, 1973, 1976; Morgan and others, 1998). On land, deposits from the 3.0-ka Indian Pond hydrothermal-explosion event extend northeast as much as 3 km from its crater and are as thick as 3–4 m (Pierce and others, 2002). The potential of another large hydrothermal-explosion event may exist, as indicated by the abundance of hydrothermal venting and domal structures observed especially in the northern basin where heat-flow values and measured fluid temperatures are extremely high. The area covered by the large hydrothermal dome, informally referred to as the "inflated plain," is comparable in scale to its neighboring features: Storm Point, on land and Elliott's crater, in the lake. Northeast of the "inflated plain," Storm Point, a 850-m-diameter, 6- to 4-ka (Pierce, Cannon, and others, this volume) hydrothermal dome, stands at about 40 feet above the surrounding landscape and is capped with multiple smaller collapse craters. East of the "inflated plain" is the 800-m-diameter, ~8.0-ka Elliott's hydrothermal-explosion crater (figs. 2*B* and 6*A*), containing many smaller craters and active hydrothermal vents. In addition to hazards affecting humans, hydrothermal explosions are likely to be associated with the rapid release of steam and hot water into the lake (Fournier and others, 1991), possibly affecting water chemistry by the release of potentially toxic trace metals. Such changes could have significant impact on the fragile ecosystem of Yellowstone Lake and vicinity (Shanks and others, 2001; Chaffee, Shanks, and others, this volume).

Do Rhyolitic Lava Flows Control Hydrothermal Activity?

One of the basic observations from our surveys is that a close spatial relationship exists between the distribution of hydrothermal vents, explosion craters, and sublacustrine rhyolitic lava flows. Does the presence of fully cooled lava flows in a subaqueous environment affect the distribution of hydrothermal vents? Could the identification of rhyolitic lava flows be used as a tool to help predict where some hydrothermal activity may occur in the future?

The floor of Yellowstone Lake, two-thirds of which is within the Yellowstone caldera, lies above a large magma chamber that may be periodically replenished (Eaton and others, 1975; Fournier, 1989; Fournier and others, 1976; Lehman and others, 1982; Stanley and others, 1991; Wicks and others, 1998). The relationship between sublacustrine hydrothermal features and the areas of high relief, interpreted here as rhyolitic lava flows, can be seen in figures 1*B*, 2*A*, 2*B*, 3, 5, and 10*D*. Based on our observations of the abundant present-day distribution of hydrothermal vents, we infer that fully cooled, post-Yellowstone caldera rhyolitic lava flows exert a fundamental influence on subsurface hydrology and hydrothermal-vent locations. We speculate that upwelling hydrothermal fluids are focused preferentially through rhyolitic lava flows, whereas hydrothermal fluids conducted through lake and glacial sediments tend to be more diffuse (fig. 10). In addition, convective flow moves laterally away from thicker, more impermeable segments of the rhyolite flow toward the fractured-flow margin, where the majority of hydrothermal activity is observed (fig. 10*E*).

In order to evaluate the effect of rhyolitic lava flows on convective-fluid flow in the sublacustrine environment, three simple 2-dimensional flow models were constructed (fig. 10). Flow modeling was carried out using the program Basin2, v. 4.0.1, 1982–1999, developed by Craig Bethke, University of Illinois. This program uses finite-difference methods to solve Darcy's law for fluids of varying density. The program allows the user to model topographic, compaction-driven, and (or) convective flow by setting parameters related to fluid density and viscosity, heat capacity, heat flow, porosity, and permeability.

The first model involves fluid flow in a sediment volume 1 km thick by 10 km wide (fig. 10*B*) covered by lake water 200 m deep. Both left and right edges of the sediment volume are open to flow. Closing left and right boundaries results in an almost stagnant-flow situation, so that option was not pursued further. Vertical-direction permeability (z) is 10^{-15} m^2 and horizontal-direction (x) permeability is 10^{-14} m^2, properties expected for lacustrine or glacial sediments. In order to simulate a magma chamber at depth, heat flow through the base of the section is set at 4 HFU or 167.6 mW/m^2 (1 heat flow unit = 10^{-6} cal/cm^2/sec = 41.9 mW/m^2), close to the bottom of the range of a typical continental value of 40–70 mW/m^2. The basal heat-flow value used in these calculations produces the highest possible thermal gradient without violating the assumptions of the modeling approach (boiling not allowed, fluid density and viscosity extremes not allowed, and fluid temperature <300°C). Results of this fluid-flow model (fig. 10*B*) indicate uniform increase of temperature with depth to a maximum of 114°C, recharge at the surface, flow out of both ends, and low fluid-flow rates of <1 mm/yr.

Addition of a sublacustrine 190-m-thick caprock, in this case a fully cooled lava flow, on top of the model sedimentary section (fig. 10*C*) produces dramatic changes in fluid flow. The fractured lava flow is assigned permeabilities of 2.5×10^{-14} m^2 in the z-direction and 5×10^{-14} m^2 in the x-direction, within the range measured for fractured-volcanic rocks. Results indicate that a sublacustrine lava flow atop the sediment causes focusing of intense thermal upflow through the lava flow and strong discharge at the surface of the flow into the overlying lake waters. In contrast to the simple sedimentary model, fluid-flow rates beneath the lava-flow caprock are as much as 150 mm/yr and temperatures are ≥140°C.

Our bathymetric mapping shows that hydrothermal vents in the lake are concentrated along lava-flow margins and structures, such as the caldera margin and fissures in the northern and central basins. To simulate the affects of a lava flow with a thick impermeable cap that thins toward its margins and has a basal breccia zone, a 3-layer model was applied. In this case, the lower sedimentary prism is unchanged but is overlain by a thin (20 m) basal unit with the properties of a fractured lava flow that is capped by a 170-m-thick unfractured lava flow with low permeability. In this case, the unfractured portion of the lava flow is assigned permeabilities of 6.3×10^{-16} m^2 in the z-direction and 6.3×10^{-15} m^2 in the x-direction, within the range measured for unfractured-volcanic rocks.

Results of this model (fig. 10*E*) indicate strong convective upflow under the lava flow, with maximum subsurface temperatures of 150°C and flow rates as much as 160 mm/yr. As expected, upflow is strongly influenced by the overlying low-permeability unfractured lava flow and is deflected laterally to the edges of the flow. Lateral flow proceeds within the 20-m-thick "basal" fractured zone away from the central upwelling zone toward the flow edges on either side, resulting in hydrothermal venting on the lake floor near the margins of lava flows. This physical model explains the preferential distribution of hydrothermal vents near or at the edges of rhyolitic lava flows in Yellowstone Lake (fig. 10*D*). In fact, this relationship can also be seen on land where hydrothermal fields and vents are located along the margins of rhyolitic lava flows or where several lava flows have flowed into a common area creating a depression, such as at Pocket Basin, which is surrounded by the Summit Mountain, Nez Perce, and Elephant Back flows or along the edge of the Pitchstone Plateau flow, just to list two examples.

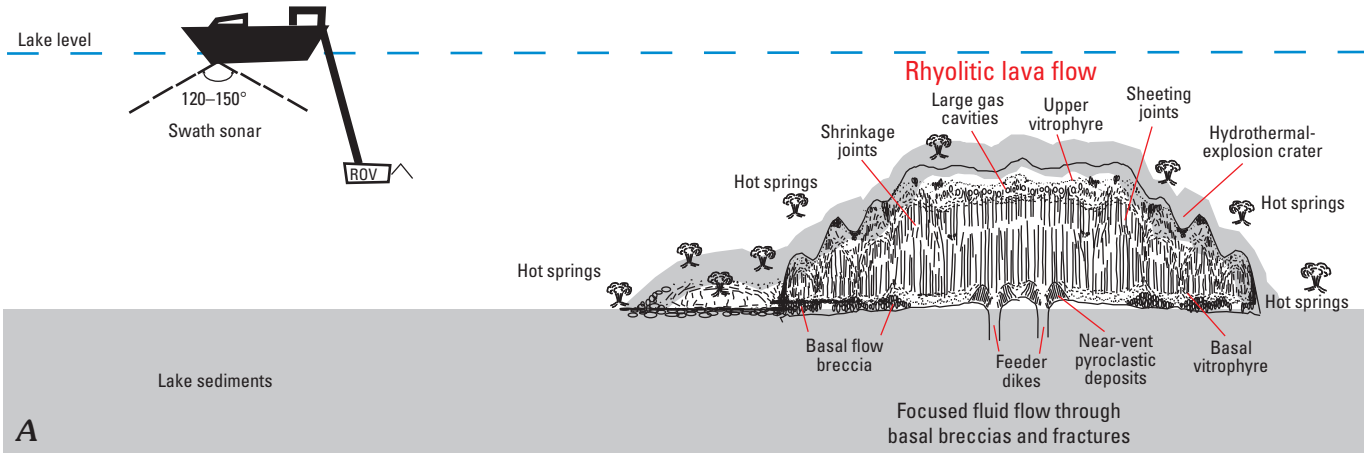

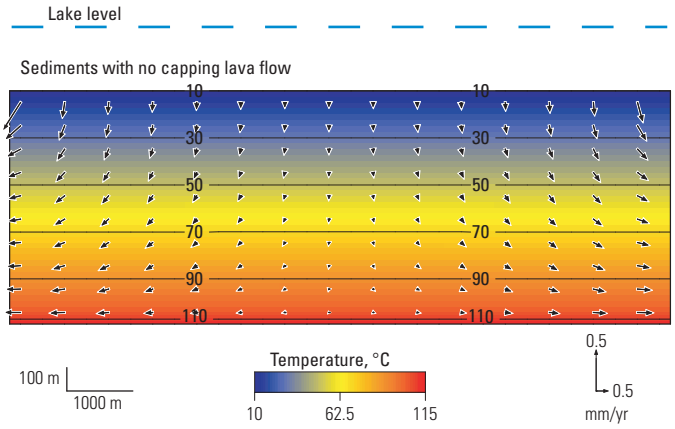

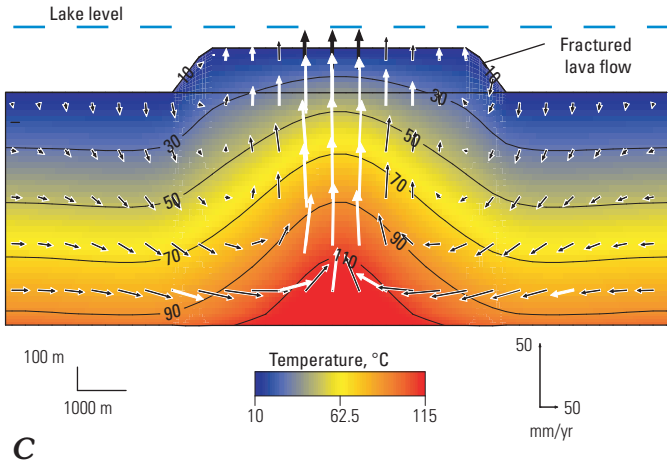

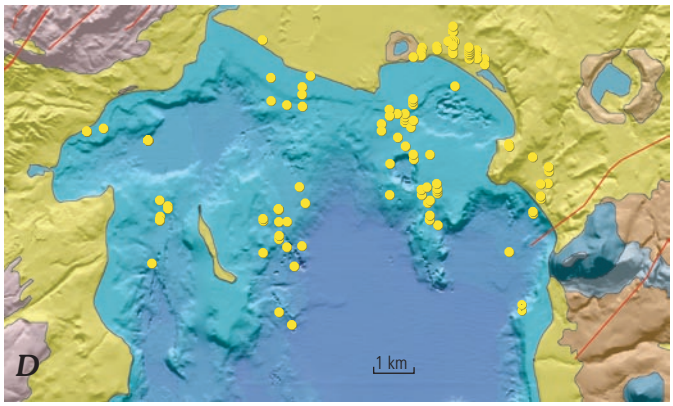

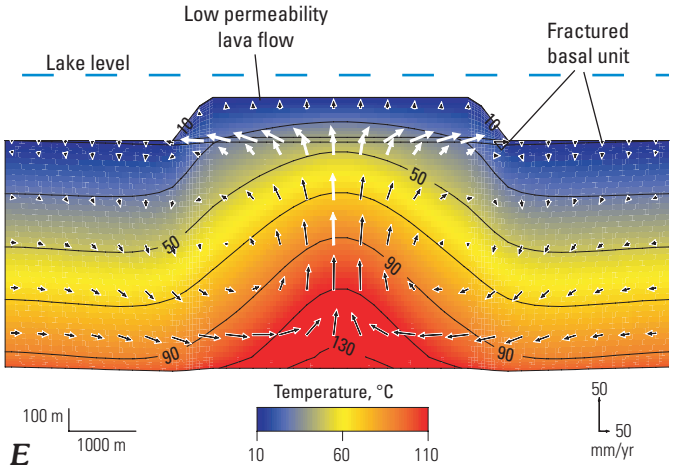

Figure 10. Flow model for hydrothermal vents and rhyolitic lava flows in Yellowstone Lake. *A,* Schematic diagram showing physical features of a rhyolitic lava flow (modified from Bonnichsen and Kauffman, 1987). *B,* Two-dimensional fluid-flow model with simple glaciolacustrine-sedimentary aquifer (no caprock) that results in low flow velocities, recharge at the surface, and lateral flow out of both ends of the model aquifer. Subsurface temperatures never exceed 114°C, as indicated by contours and color map. Fluid-flow rates are low (<0.7 mm/yr) as indicated by velocity vectors. *C,* Fluid-flow model with a fully cooled rhyolitic lava flow acting as caprock. The

Summary and Conclusions

Mapping in Yellowstone Lake extends subaerial geologic mapping, allowing the lake basin to be understood in the geologic context of the rest of the Yellowstone region (Blank, 1974; Christiansen, 1974, 2001; Richmond, 1973; U.S. Geological Survey, 1972). Rhyolitic lava flows contribute greatly to the geology and morphology of Yellowstone Lake, as they do to the subaerial morphology of the Yellowstone Plateau. We infer from our high-resolution bathymetry and aeromagnetic data that Stevenson, Dot, and Frank Islands are underlain by large-volume rhyolitic lava flows (figs. 2*B,* 2*C,* and 3). Mapped late Pleistocene glaciolacustrine-sediment deposits on these islands (Otis and others, 1977; Richmond, 1974; Richmond and Waldrop, 1975; Shuey and others, 1977) merely mantle or blanket the flows. Similarly, the hydrothermally cemented beach deposits exposed on Pelican Roost, located ~1 km southwest of Steamboat Point (fig. 2*B*), blanket another submerged large-volume rhyolite flow. The margin of the Yellowstone caldera (Richmond, 1974; Richmond and Waldrop, 1975) passes through the central part of the lake through Frank Island and northward along the lake's eastern edge (fig. 1). We suggest that postcollapse rhyolitic lava flows are present along much of the caldera margin beneath Yellowstone Lake and control much of the distribution of the sublacustrine hydrothermal vents—this is similar to most of the rest of the topographic margin of the Yellowstone caldera (fig. 1*A*). Many potential hazards have been identified in our mapping effort. Next steps will include hazard assessments and the determination of methodologies to be employed in monitoring these potentially dangerous features; this will be done under the aegis of the Yellowstone Volcano Observatory.

underlying sedimentary aquifer and heat flow are exactly the same as in the previous model. The addition of a 200-m-thick fractured crystalline-rock cap strongly focuses the upward limb of an intense convection cell under the caprock. In this model, fluid temperatures reach 140°C and flow velocities are as high as 150 mm/yr. *D,* Locations of hydrothermal vents on the northern lake floor mapped using seismic reflection. Lava flow boundaries are based on high-resolution bathymetry and aeromagnetic data. *E,* Fluid-flow model that includes a basal breccia zone beneath an impermeable lava flow. In this case, the lower sedimentary unit is overlain by a thin, fractured, lava-flow unit (20 m thick) that extends the entire width of the sedimentary prism. Above the more permeable basal unit is a 170-m-thick low-permeability unfractured lava flow. Flow vectors indicate strong upflow under the lava flow with maximum subsurface temperatures of ~150°C and flow rates up to 160 mm/yr. Upflow is deflected laterally within the 20-m-thick "basal" fractured zone toward the flow edges resulting in hydrothermal venting on the lake floor near the margins of lava flows.

References Cited

Bartholomew, M.J., Stickney, M.C., Wilde, E.M., and Dundas, R.G., 2002, Late Quaternary paleoseismites—Syndepositional features and section restoration used to indicate paleoseismicity and stress-field orientations during faulting along the main Lima Reservoir fault, southwestern Montana, *in* Ettensohn, F.R., Rast, N., and Brett, C.E., eds., Ancient seismites: Geological Society of America Special Paper 359, p. 29–48.

Blank, H.R., 1974, Geologic map of the Frank Island quadrangle, Yellowstone National Park, Wyoming: U.S. Geological Survey Geologic Quadrangle Map GQ-1209a, scale 1:62,500.

Bonnichsen, B., and Kauffman, D.F., 1987, Physical features of rhyolite lava flows in the Snake River Plain volcanic province, southwestern Idaho, *in* Fink, J.H., ed., The emplacement of silicic domes and lava flows: Geological Society of America Special Paper 212, p. 119–145.

Browne, P.R.L., and Lawless, J.V., 2001, Characteristics of hydrothermal eruptions, with examples from New Zealand and elsewhere: Earth-Science Reviews, v. 52, p. 299–331.

Christiansen, R.L., 1974, Geologic map of the West Thumb quadrangle, Yellowstone National Park, Wyoming: U.S. Geological Survey Geologic Quadrangle Map GQ-1191, scale 1:62,500.

Christiansen, R.L., 1984, Yellowstone magmatic evolution—Its bearing on understanding large-volume explosive volcanism, *in* Explosive volcanism—inception, evolution, and hazards: Washington, D.C., National Academy Press, p. 84–95.

Christiansen, R.L., 2001, The Quaternary and Pliocene Yellowstone Plateau volcanic field of Wyoming, Idaho, and Montana: U.S. Geological Survey Professional Paper 729-G, 145 p.

Christiansen, R.L., and Blank, H.R., Jr., 1975, Geologic map of the Canyon Village quadrangle, Yellowstone National Park, Wyoming: U.S. Geological Survey Geologic Quadrangle Map GQ-1192, scale 1:62,500.

Dzurisin, D., Yamashita, K.M., and Kleinman, J.W., 1994, Mechanisms of crustal uplift and subsidence at the Yellowstone caldera, Wyoming: Bulletin of Volcanology, v. 56, p. 261–270.

Eaton, G.P., Christiansen, R.L., Iyer, H.M., Pitt, A.M., Mabey, D.R., Blank, H.R., Jr., Zietz, I., and Gettings, M.E., 1975, Magma beneath Yellowstone National Park: Science, v. 188, no. 4190, p. 787–796.

Finn, C.A., and Morgan, L.A., 2002, High-resolution aeromagnetic mapping of volcanic terrain, Yellowstone National Park: Journal of Volcanology and Geothermal Research, v. 115, p. 207–231.

Fournier, R.O., 1989, Geochemistry and dynamics of the Yellowstone National Park hydrothermal system: Annual Review of Earth and Planetary Sciences, v. 17, p. 13–53.

Fournier, R.O., 2000, Hydrothermal processes related to movement of fluid from plastic into brittle rock in the magmatic-epithermal environment: Economic Geology, v. 94, p. 1,193–1,212.

Fournier, R.O., Thompson, J.M., Cunningham, C.G., and Hutchinson, R.A., 1991, Conditions leading to a recent small hydrothermal explosion at Yellowstone National Park: Geological Society of America Bulletin, v. 103, p. 1,114–1,120.

Fournier, R.O., White, D.E., and Truesdell, A.H., 1976, Convective heat flow in Yellowstone National Park, *in* Second U.N. symposium on the development and use of geothermal resources, proceedings: Washington D.C., San Francisco, U.S. Government Printing Office, v. 1, p. 731–739.

Good, J.M., and Pierce, K.L, 1996, Interpreting the landscapes of Grand Teton and Yellowstone National Parks—Recent and ongoing geology: Grand Teton National Park, Moose, Wyoming, Grand Teton Natural History Association, 58 p.

Hague, A., Weed, W.H., and Iddings, J.P., 1896, Yellowstone National Park: U.S. Geological Survey Geologic Atlas of U.S., Folio 30, 20 p.

Hamilton, W.L., 1987, Water level records used to evaluate deformation within the Yellowstone caldera, Yellowstone National Park: Journal of Volcanology and Geothermal Research, v. 31, nos. 3–4, p. 205–215.

Hildreth, W., Christiansen, R.L., and O'Neil, J.R., 1984, Catastrophic isotopic modification of rhyolitic magma at times of caldera subsidence, Yellowstone Plateau volcanic field: Journal of Geophysical Research, v. 89, no. 10, p. 8,339–8,369.

Johnson, S.Y., Stephenson, W.J., Morgan, L.A., Shanks, W.C., III, and Pierce, K.L., 2003, Hydrothermal and tectonic activity in northern Yellowstone Lake, Wyoming: Geological Society of America Bulletin, v. 115, no. 8, p. 954–971.

Kaplinski, M.A., 1991, Geomorphology and geology of Yellowstone Lake, Yellowstone National Park, Wyoming: Flagstaff, Northern Arizona University, M.S. thesis, 82 p.

Klump, J.V., Remsen, C.C., and Kaster, J.L., 1988, The presence and potential impact of geothermal activity on the chemistry and biology of Yellowstone Lake, Wyoming, *in* DeLuca, M., and Babb, I., eds., Global venting, midwater and benthic ecological processes: NOAA Symposium on Undersea Research, v. 4, p. 81–98.

Lehman, J.A., Smith, R.B., and Schilly, M.M., 1982, Upper crustal structure of the Yellowstone caldera from seismic delay time analyses and gravity correlations: Journal of Geophysical Research, v. 87, p. 2,713–2,730.

Locke, W.W., and Meyer, G.A., 1994, A 12,000 year record of vertical deformation across the Yellowstone caldera margin—The shorelines of Yellowstone Lake: Journal of Geophysical Research, v. 99, p. 20,079–20,094.

Locke, W.W., Meyer, G.A., and Pings, J.C., 1992, Morphology of a postglacial fault scarp across the Yellowstone (Wyoming) caldera margin, United States, and its implications: Bulletin of the Seismological Society of America, v. 82, no. 1, p. 511–516.

Mason, B.G., Pyle, D.M., and Oppenheimer, Clive, 2004, The size and frequency of the largest explosive eruptions on Earth: Bull. Volcanology, v. 66, p. 735–748.

Merrill, M.D., 1999, Yellowstone and the Great West—Journals, letters, and images from the 1871 Hayden Expedition: Lincoln and London, University of Nebraska Press, 315 p.

Meyer, G.A., and Locke, W.W., 1986, Origin and deformation of Holocene shoreline terraces, Yellowstone Lake, Wyoming: Geology, v. 14, p. 699–702.

Morgan, L.A., and Shanks, W.C., III, 2005, Influences of rhyolitic lava flows on hydrothermal processes in Yellowstone Lake and on the Yellowstone Plateau, *in* Inskeep, W.P., and McDermott, T.R., eds., Geothermal biology and geochemistry in Yellowstone National Park: Proceeding of the Thermal Biology Institute workshop, Yellowstone National Park, Wyoming, p. 31–52.

Morgan, L.A., Shanks, W.C., Lovalvo, D., Johnson, S.Y., Stephenson, W.J., Harlan, S.S., White, E.A., Waples, J., and Klump, J.V., 1999, New discoveries from the floor of Yellowstone Lake—Results from sonar imaging, seismic reflection, and magnetic surveys [abs.]: Geological Society of America, Abstracts with Programs, v. 31, no. 7, p. A-207.

Morgan, L.A., Shanks, W.C., III, Lovalvo, D., Johnson, S.Y., Stephenson, W., Pierce, K.L., Harlan, S., Finn, C., Lee, G., Webring, M., Schulze, B., Duhn, J., Sweeney, R., and Balistrieri, L., 2003, Exploration and discovery *in* Yellowstone Lake—Results from high-resolution sonar imaging, seismic reflection profiling, and submersible studies: Journal of Volcanology and Geothermal Research, v. 2003, no. 122, p. 221–242.

Morgan, L.A., Shanks, W.C., III, and Pierce, K.L., 2002, Possible earthquake-generated wave deposits near Yellowstone Lake—Clues into triggering mechanisms of a large hydrothermal explosion crater [abs.]: Eos, Transactions of the American Geophysical Union, v. 83, no. 47, p. F1,423.

Morgan, L.A., Shanks, W.C., III, Pierce, K.L., and Rye, R.O., 1998, Hydrothermal explosion deposits in Yellowstone National Park—Links to hydrothermal processes [abs.]: Eos, Transactions of the American Geophysical Union, fall annual meeting, v. 79, p. F964.

Morgan, P., Blackwell, D.D., Spafford, R.E., and Smith, R.B., 1977, Heat flow measurements in Yellowstone Lake and the thermal structure of the Yellowstone caldera: Journal of Geophysical Research, v. 82, p. 3,719–3,732.

Muffler, L.J.P., White, D.E., and Truesdell, A.H., 1971, Hydrothermal explosion craters in Yellowstone National Park: Geological Society of America Bulletin, v. 82, p. 723–740.

Otis, R.M., Smith, R.B., and Wold, R.J., 1977, Geophysical surveys of Yellowstone Lake, Wyoming: Journal of Geophysical Research, v. 82, p. 3,705–3,717.

Pelton, J.R., and Smith, R.B., 1982, Contemporary vertical surface displacements inYellowstone National Park: Journal of Geophysical Research, v. 87, p. 2,745–2,751.

Pierce, K.L., 1974, Surficial geologic map of the Tower Junction quadrangle and part of the Mount Wallace quadrangle, Yellowstone National Park, Wyoming and Montana: U.S. Geological Survey Miscellaneous Investigations Series Map I-647, scale 1:62,500.

Pierce, K.L., 1979, History and dynamics of glaciation in the northern Yellowstone National Park area: U.S. Geological Survey Professional Paper 729-F, 89 p.

Pierce, K.L., Cannon, K.P., and Meyer, G., 1997, Yellowstone caldera “heavy breathing” based on Yellowstone Lake and River changes in post-glacial time [abs.]: Eos, Transactions of the American Geophysical Union, v. 78, p. 802.

Pierce, K.L., Cannon, K.P., Meyer, G.A., Trebesch, M.J., and Watts, R., 2002, Post-glacial inflation-deflation cycles, tilting, and faulting in the Yellowstone caldera based on Yellowstone Lake shorelines: U.S. Geological Survey Open-File Report 02-142, 65 p.

Remsen, C.C., Klump, J.V., Kaster, J.L., Paddock, R., Anderson, P., and Maki, J.S., 1990, Hydrothermal springs and gas fumaroles in Yellowstone Lake, Yellowstone National Park, Wyoming: National Geographic Research, v. 6, p. 509–515.

Richmond, G.M., 1973, Surficial geologic map of the West Thumb quadrangle, Yellowstone National Park, Wyoming: U.S. Geological Survey Miscellaneous Investigations Series Map I-643, scale 1:62,500.

Richmond, G.M., 1974, Surficial geologic map of the Frank Island quadrangle, Yellowstone National Park, Wyoming: U.S. Geological Survey Miscellaneous Investigations Series Map I-642, scale 1:62,500.

Richmond, G.M., 1976, Surficial geologic history of the Canyon Village quadrangle, Yellowstone National Park, Wyoming: U.S. Geological Survey Bulletin 1427, 35 p., for use with map I-652.

Richmond, G.M., 1977, Surficial geologic map of the Canyon Village quadrangle, Yellowstone National Park, Wyoming: U.S. Geological Survey Miscellaneous Investigations Series Map I-652, scale 1:62,500.

Richmond, G.M., and Waldrop, H.A., 1975, Surficial geologic map of the Norris Junction quadrangle, Yellowstone National Park, Wyoming: U.S. Geological Survey Miscellaneous Investigations Series Map I-650, scale 1:62,500.

Ruzycki, J.R., and Beauchamp, D.A., 1997, A bioenergetics modeling assessment of the lake trout impact on Yellowstone Lake, *in* Hamre, R., ed., Wild trout VI: Fort Collins, Colo., Trout Unlimited and Federation of Fly Fishers, p. 127–133.

Shanks, W.C., III, Balistrieri, L., Alt, J., Morgan, L.A., Meeker, G., Rye, R.O., Sturchio, N., Lovalvo, D., Cuhel, R., and Klump, J.V., 2001, Geochemical studies of hydrothermal vents and sublacustrine siliceous deposits in Yellowstone Lake, *in* Agenda and abstracts, Yellowstone Lake—Hotbed of chaos or reservoir of resilience? [abs.]: 6th Biennial Scientific Conference on the Greater Yellowstone Ecosystem, Yellowstone National Park, October 8–10, 2001, National Park Service, p. 35–36.

Shuey, R.T., Ugland, R.O., and Smith, R.B., 1977, Magnetic properties and secular variation in cores from Yellowstone and Jackson Lakes, Wyoming: Journal of Geophysical Research, v. 82, p. 3,739–3,746.

Smedes, H.W., and Prostka, H.J., 1972, Stratigraphic framework of the Absaroka Volcanic Supergroup in the Yellowstone National Park region: U.S. Geological Survey Professional Paper 729-C, 33 p.

Smith, R.B., 1991, Earthquake and geodetic surveillance of Yellowstone: Seismological Research Letters, v. 62, p. 27.

Stanley, W.D., Hoover, D.B., Sorey, M.L., Rodriguez, B.D., and Heran, W.D., 1991, Electrical geophysical investigations in the Norris-Mammoth corridor, Yellowstone National Park, and the adjacent Corwin Springs Known Geothermal Resources Area: U.S. Geological Survey Water Resources Investigations, v. 91-4052, p. D1–D18.

Tivey, M.K., 1995, Modeling chimney growth and associated fluid flow at seafloor hydrothermal vent sites, *in* Humphris, S.E., Zierenberg, R.A., Mullineaux, L.S., and Thomson, R.E., eds., Seafloor hydrothermal systems; physical, chemical, biological, and geological interactions: Washington, D.C., American Geophysical Union Monograph 91, p. 158–177.

U.S. Geological Survey, 1972, Geologic map of Yellowstone National Park: U.S. Geological Survey Miscellaneous Investigations Series Map I-711, scale 1:125,000.

Wicks, C.W., Jr., Thatcher, W.R., and Dzurisin, D., 1998, Migration of fluids beneath Yellowstone caldera inferred from satellite radar interferometry: Science, v. 282, no. 5388, p. 458–462.

Wold, R.J., Mayhew, M.A., and Smith, R.B., 1977, Bathymetric and geophysical evidence for a hydrothermal explosion crater in Mary Bay, Yellowstone Lake, Wyoming: Journal of Geophysical Research, v. 82, no. 26, p. 3,733–3,738.

Appendix

Appendix D-1. Digital Models and Visualizations of Bathymetry and Topography in the Yellowstone Lake Area

By Gregory K. Lee[1] and Michael W. Webring[2]

Data Processing

High-resolution multi-beam swath sonar data were collected using a SeaBeam 1180 instrument that uses 126 beams covering a 150-degree ensonification angle to map a swath width of 7.4 times water depth. The studies produced approximately 244 million soundings across the lake, which occupies 34,157.9 hectares (341.579 km^2, or 131.9 mi^2) and has a shoreline length of 227 km (141 mi). According to data collected for this study, maximum lake depth is 120.7 m (396 ft).

Data collected in 1999 covered the northern basin of the lake; 2000 data included West Thumb basin; 2001 data covered the central part of the lake; and the 2002 survey covered the southern extent of the lake, including the "arms" (Morgan and others, 2003, this volume). Figure 1 shows the approximate areas of Yellowstone Lake that were covered by the four separate surveys. Recorded measurements included beam identifier, signal return time, transmission signal strength, return signal amplitude, and real-time recordings of shipboard parameters such as position, azimuth, roll, pitch, heave, and yaw. These data, together with sound velocity profiles, were used to calculate depth (meters), backscatter amplitude (decibels), latitude (decimal degrees), and longitude (decimal degrees) for each beam sounding. Gridded bathymetric models of the four sections of the lake were calculated from these data and were merged to produce a composite grid of the entire lake bottom. The bathymetric grid was then combined with 10-m digital elevation data that cover the entire park, obtained from the National Elevation Dataset (NED), available online at URL http://ned.usgs.gov/, to produce a digital elevation model of Yellowstone National Park (the Park) that includes the bottom of Yellowstone Lake.

The spatial coordinates of data from each survey were projected from decimal degrees, WGS 84 spheroid and datum, to Universal Transverse Mercator meters, zone 12, using the GRS 1980 spheroid and North American Datum of 1983. Point data from each of the four surveys, totaling approximately 244 million observations, were transformed to regularly spaced grid arrays, using a minimum curvature gridding algorithm (Webring, 1982) to create bathymetric grid

[1]U.S. Geological Survey, Mail Stop 973, Box 25046, Denver, CO, 80225.

[2]U.S. Geological Survey, Mail Stop 964, Box 25046, Denver, CO, 80225.

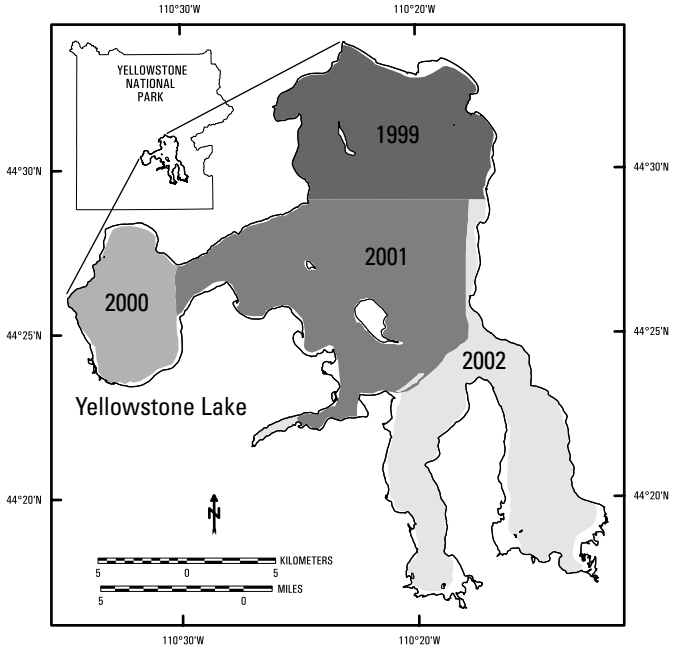

Figure 1. Approximate areas of multi-beam swath sonar surveys conducted in Yellowstone Lake, 1999–2002.

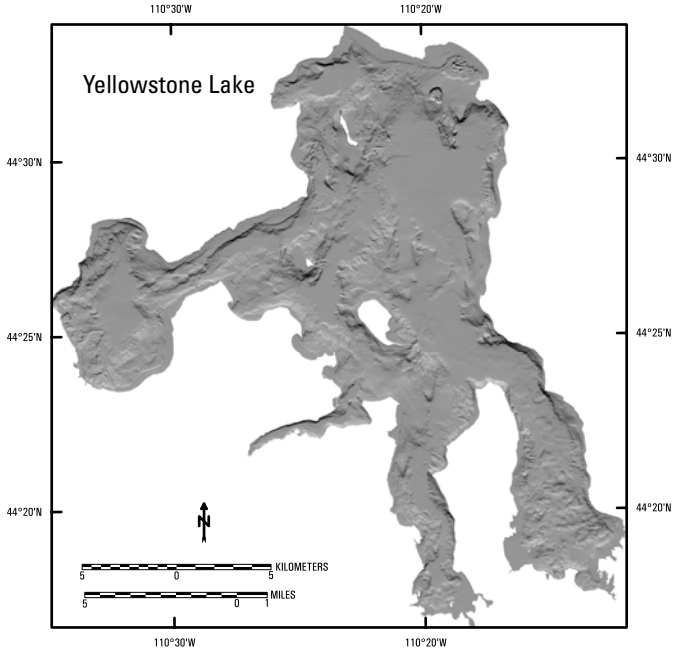

Figure 2. Shaded relief of bathymetric model of Yellowstone Lake.

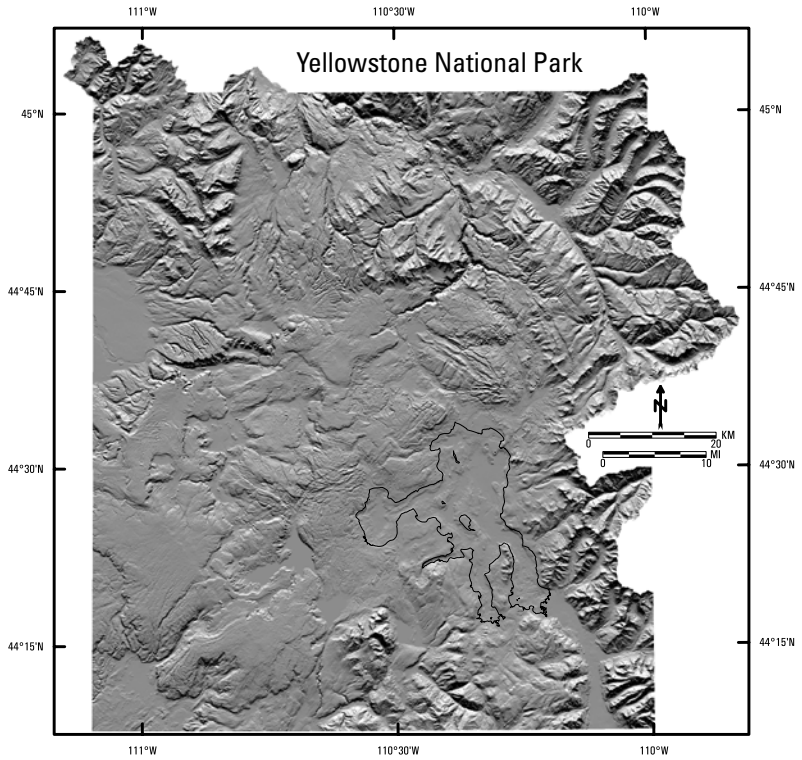

Figure 3. Shaded-relief image of Yellowstone National Park, including the floor of Yellowstone Lake (shoreline shown in black).

models of lake depth. The algorithm was modified to select the median (instead of mean) depth value for the typical case in which a grid cell contained multiple soundings. Successive iterations of low- and high-pass filtering were implemented at various grid cell dimensions to identify and remove false artifacts in the data, while retaining features more likely to be real.

The shoreline of Yellowstone Lake, including its islands, was digitized from 1:24,000-scale Digital Raster Graphics (DRG) images of nine 1:24,000-scale 7.5-minute USGS topographic map quadrangles (Lake, WY; Lake Butte, WY; Sylvan Lake, WY; Frank Island, WY; Dot Island, WY; West Thumb, WY; Heart Lake, WY; Alder Lake, WY; and Trail Lake, WY) that contain square grid cell edge dimensions of approximately 2.4 m. The digitized shoreline was then "densified," using ERDAS IMAGINE software, to produce nearly 121,000 closely spaced zero-depth points to provide control for the gridding algorithm at the lake edge, beyond the spatial extents of the survey swaths.

Using IMAGINE software applications, the bathymetric depth grids were converted to elevation models in terms of feet above mean sea level, using the North American Vertical Datum of 1988 (NAVD88). These grids were merged to create an elevation model of the entire bottom of Yellowstone Lake (fig. 2). Grid spacing of each of the models is 10 m.

The collars of twelve 7.5-minute (1:24,000-scale) lake-area DRGs (Beach Lake, Lake, Lake Butte, Mount Chittenden, Sylvan Lake, Frank Island, Dot Island, West Thumb, Mount Sheridan, Heart Lake, Alder Lake, and Trail Lake) were removed, and the resulting clipped images were mosaicked to provide a single DRG covering the vicinity of Yellowstone Lake.

We created a 10-m digital elevation model (DEM) of Yellowstone National Park by merging a USGS DEM of 10-m-elevation data (available at http://seamless.usgs.gov/) covering the Park using the NAVD88 elevation datum. Eight retrievals were required to accommodate download-file-size limitations. These were received in ArcGrid format and converted to IMAGINE files. The 8 digital elevation files were mosaicked and the combined result was clipped to exclude areas outside the Park. These data were merged with the Yellowstone Lake bathymetric-elevation model to produce a digital elevation model of the entire Park that includes the floor of Yellowstone Lake. Figure 3 shows a shaded-relief image of Yellowstone National Park that includes the bathymetry of Yellowstone Lake.

References Cited

Morgan, L.A., Shanks, W.C., III, Lovalvo, D.A., Johnson, S.Y., Stephenson, W.J., Pierce, K.L., Harlan, S.S., Finn, C.A., Lee, G., Webring, M., Schulze, B., Dühn, J., Sweeney, R., and Balistrieri, L., 2003, Exploration and discovery in Yellowstone Lake: results from high-resolution sonar imaging, seismic reflection profiling, and submersible studies: Journal of Volcanology and Geothermal Research, v. 122, p. 221–242.

Webring, Michael, 1982, MINC, a gridding program based on minimum curvature: U.S. Geological Survey Open-File Report 81-1224, 43 p.

Postglacial Inflation-Deflation Cycles, Tilting, and Faulting in the Yellowstone Caldera Based on Yellowstone Lake Shorelines

E

By Kenneth L. Pierce, Kenneth P. Cannon, Grant A. Meyer, Matthew J. Trebesch, and Raymond D. Watts

Chapter E *of*

Integrated Geoscience Studies in the Greater Yellowstone Area—Volcanic, Tectonic, and Hydrothermal Processes in the Yellowstone Geoecosystem

Edited by Lisa A. Morgan

U.S. Geological Survey Professional Paper 1717

U.S. Department of the Interior
U.S. Geological Survey

Contents

Abstract 131
Introduction 132
Previous Studies of Postglacial Shorelines 132
Holocene Lake- and River-Level Changes and Their Chronology 135
Lake-Level Rise After Lake Low 4–3 ka 143
Yellowstone Lake 143
Outlet Reach of the Yellowstone River 143
S-Meander and Rise of Lake ~9.7–8.6 ka 145
Subaerial Shoreline Sequence ~8.0 ka S2 to ~14.4 ka S6 146
S2 Shoreline 146
S3 Shoreline 149
S4 Shoreline 149
S5 Shoreline 149
S5.5 Shoreline 150
S6 Shoreline 151
Possible Lake-Level Culminations Near 4.5 and 2.5 ka 151
Summary of Postglacial Lake-Level Chronology 152
Uplift of Le Hardys Rapids Indicated by Submerged Localities 153
Faulting 155
Local Deformation of Shorelines 157
Discussion 157
Decreases in Lake Level 158
Holocene Outlet Erosion and Pleistocene Glacial Damming 158
Tectonic Stretching 159
Yellowstone Lake Ceasing to Overflow 159
Increases in Lake Level 159
Inflation by Magma Intrusion 159
Tectonic Compression 160
Possible Increases or Decreases in Lake Level 160
Faulting and Local Warping 160
Glacial-Isostatic Rebound 160
Oscillations in Lake Level 160
Two Favored Explanations for Record of Oscillations 162
Hydrothermal Inflation and Deflation 162
Inflation by Magma Intrusion and Subsidence by Other Mechanisms 162
Local Doming and Faulting of Shorelines 163
Conclusions 163
Acknowledgments 164
References Cited 164

Figures

1. Map showing Yellowstone National Park, the Yellowstone caldera, Yellowstone Lake and River, and contours on the historic dome of uplift from1923–1975 133
2. Map of the Yellowstone Lake area, including some important localities and ages outside the LIDAR area 134
3. Vertical surface displacements measured by repeated first-order leveling surveys along a traverse from Lake Butte north-northwestward across the floor of Yellowstone caldera to Canyon Junction....135
4. Reconstruction of changes in Yellowstone Lake level during the last 15 k.y. 136
5. LIDAR image showing the "outlet reach" of the Yellowstone River from the outlet to Le Hardys Rapids 144
6. Diagram of uplift of Le Hardys Rapids after 3 ka 145
7. Profile section of the S-meander based on LIDAR data 146
8. Cross section across the S-meander showing location of channel gravels, ~9.2-ka charcoal, and S3 and S2 shorelines 147
9. Comparison of outlet reach during S-meander time (~9.7 ka) with that during formation of S3/S2 shorelines (8.6–8.0 ka) 147
10. LIDAR image of the northern lakeshore area showing shorelines S2–S6 as well as unlabeled intermediate shorelines 148
11. Drawings of projectile points from shorelines on the north shore of Yellowstone Lake....150

12–15. LIDAR profiles:

- 12. Of northern Yellowstone Lake shorelines S2–S6 151
- 13. Along S5.5 barrier beach mantled by Mary Bay hydrothermal-explosion deposit....152
- 14. Showing faulting and tilting of shorelines across the Fishing Bridge peninsula....154
- 15. Of S4, S2 and two younger shorelines (S1.8 and S1.6) from the Storm Point geothermal center west to Pelican Creek....156

16. Diagrams showing mechanisms for inflation and deflation of Yellowstone caldera....158

Tables

1. ^{14}C and other ages associated with levels of Yellowstone Lake....137
2. Submerged Yellowstone Lake and River levels, and their normalization to the outlet 153
3. Offsets on the Fishing Bridge fault and associated tilting across Fishing Bridge....154
4. Processes for decreases, increases, and oscillations in Yellowstone Lake and River levels in postglacial time....157
5. Change in altitude of shorelines S2, S4, and S5 161

Postglacial Inflation-Deflation Cycles, Tilting, and Faulting in the Yellowstone Caldera Based on Yellowstone Lake Shorelines

By Kenneth L. Pierce,[1] Kenneth P. Cannon,[2] Grant A. Meyer,[3] Matthew J. Trebesch,[1] and Raymond D. Watts[4]

Abstract

The Yellowstone caldera, like many other late Quaternary calderas of the world, exhibits dramatic unrest. Between 1923 and 1985, the center of the Yellowstone caldera rose nearly 1 m along an axis between its two resurgent domes (Pelton and Smith, 1979; Dzurisin and Yamashita, 1987). From 1985 until 1995–1996, the caldera subsided at about 2 cm/yr (Dzurisin and others, 1990). More recent radar-interferometry studies show renewed inflation of the northeastern resurgent dome between 1995 and 1996; this inflation migrated to the southwestern resurgent dome from 1996 to 1997 (Wicks and others, 1998).

We extend this record back in time using dated geomorphic evidence of postglacial Yellowstone Lake shorelines around the northern shore and Yellowstone River levels in the outlet area. We date these shorelines using carbon-isotopic and archeological methods. Following Meyer and Locke (1986) and Locke and Meyer (1994), we identify the modern shoreline as S1 (1.9±0.3 m above the lake-gage datum), map paleoshoreline terraces S2 to S6, and infer that the prominent shorelines were cut during intracaldera-uplift episodes that produced rising water levels. Doming along the caldera axis reduces the gradient of the Yellowstone River from Le Hardys Rapids to the Yellowstone Lake outlet and ultimately causes an increase in lake level. The 1923–1985 doming is part of a longer uplift episode that has reduced the Yellowstone River gradient to a "pool" with a drop of only 0.25 m over most of this 5-km reach. We also present new evidence that doming has caused submergence of some Holocene lake and river levels.

Shoreline S5 is about 14 m above datum and estimated to be ~12.6 ka because it postdates a large hydrothermal-explosion deposit from the Mary Bay area that occurred ~13 ka. S4 formed about 8 m above datum ~10.7 ka as dated by archeology and ^{14}C and was accompanied by offset on the Fishing Bridge fault. About 9.7 ka, the Yellowstone River eroded the "S-meander," followed by a ~5-m rise in lake level to S2. The lowest generally recognizable shoreline is S2; it is ~5 m above datum (3 m above S1) and is ~8 ka, as dated on both sides of the outlet. Yellowstone Lake and the Yellowstone River near Fishing Bridge were 5–6 m below their present level about 4–3 ka, as indicated by ^{14}C ages from submerged beach deposits, drowned valleys, and submerged Yellowstone River gravels. Thus, the lake in the outlet region has been below or near its present level for about half the time since a 1-km-thick ice cap melted from the Yellowstone Lake basin about 16 ka.

The amplitude of two rises in lake and river level can be estimated based on the altitude of Le Hardys Rapids, indicators of former lake and river levels, and reconstruction of the river gradient from the outlet to Le Hardys Rapids. Both between ~9.5 ka and ~8.5 ka, and after ~3 ka, Le Hardys Rapids was uplifted about 8 m above the outlet at Fishing Bridge, suggesting a cyclic deformation process. Older rises in lake level are suggested by locations where the ~10.7-ka S4 truncates older shorelines and where valleys were truncated by the ~12.6-ka S5 shoreline. Using these controls, a plot of lake level through time shows five to seven millennial-scale oscillations since 14.4 ka.

Major cycles of inflation and deflation are thousands of years long. Le Hardys Rapids has twice been uplifted ~8 m relative to the lake outlet. These two locations span only the central 25 percent of the historic caldera doming; so if we use historic doming as a model, total projected uplift would be ~32 m. This "heavy breathing" of the central part of the Yellowstone caldera may reflect a combination of several possible processes: magmatic inflation; tectonic stretching and deflation; and hydrothermal-fluid sealing and inflation, followed by cracking of the seal, pressure release, and deflation. Over the entire postglacial period, subsidence has balanced or slightly exceeded uplift as shown by older shorelines that *descend* toward the caldera axis. We favor a hydrothermal mechanism for inflation and deflation because it provides for both inflation and deflation with little overall change. Other mechanisms, such as inflation by magma intrusion and deflation by extensional stretching, require two separate geologic processes to alternate and yet result in no net elevation change.

[1]U.S. Geological Survey, Northern Rocky Mountain Science Center, Box 173492, Montana State University, Bozeman, MT 59717.

[2]National Park Service, Midwest Archeological Center, Federal Building, Lincoln, NE 68508-3873.

[3]Department of Earth and Planetary Sciences, University of New Mexico, Albuquerque, NM 87131-1116.

[4]U.S. Geological Survey, 4512 McMurry Ave., Fort Collins, CO 80525-3400.

In addition to inflation and deflation, new LIDAR (Light Detection and Ranging) data demonstrate previously unrecognized local deformation along the north shore of Yellowstone Lake. The newly recognized Fishing Bridge fault shows a progressive increase in offset from 0.5 m for the ~8-ka S2 to perhaps 5 m for the ~12.6-ka S5. Uplift of the Storm Point hydrothermal center tilts shorelines westward as much as 6 m/km. A local anticline has as much as 3 m of relief in 0.5 km. LIDAR data also show the Mary Bay hydrothermal-explosion debris has a surface relief of about 1 m over 100 m, and that it overlies S5.5 and S6 shorelines, but not S5. Although the postglacial deformation record does not indicate voluminous magma accumulation or other large-scale eruption precursors, strong local deformation associated with hydrothermal centers does suggest the possibility of future hydrothermal explosions and associated hazards.

Introduction

The Yellowstone caldera (fig. 1) is the youngest of three large rhyolitic calderas formed in greater Yellowstone in the last 2.1 m.y. (Christiansen, 1984, 2001). It collapsed with eruption of ~1,000 km^3 of ash flows from two overlapping ring-fracture systems at ~640 ka. Shortly thereafter, the central part of the caldera was uplifted to form the Sour Creek (northeast) and Mallard Lake (southwest) resurgent domes. Voluminous extrusion of rhyolitic lavas from 150 ka to 70 ka covered much of the caldera except the Sour Creek dome and small areas in the eastern part of Yellowstone Lake (Morgan and Shanks, 2005) (fig. 2). At present, this caldera shows remarkable signs of unrest, consistent with many other young calderas around the world (Newhall and Dzurisin, 1988; Dvorak and Mastrolorenzo, 1991). A resurvey of 1923 level lines in 1975–1977 along the road system of Yellowstone showed doming within the caldera (fig. 1), with maximum uplift at Le Hardys Rapids (LHR) of about 0.8 m (Pelton and Smith, 1979). Between 1976 and 1985, resurveys revealed an additional 0.15-m uplift of LHR, with a pattern similar to that between 1923 and 1976 (Dzurisin and Yamashita, 1987). Thus, from 1923 to 1985, maximum uplift was about 0.95 m over 62 years at an average rate of about 15 mm/yr. Uplift unexpectedly ceased in 1985, and between 1986 and 1996, the caldera subsided at a maximum rate of about 20 mm/yr in a pattern essentially inverse to the uplift (fig. 3). Recent radar-interferometry studies define a more complex temporal pattern, with renewed inflation of the Sour Creek resurgent dome area from 1995 to 1996 and migration of inflation to the Mallard Lake dome area from 1996 to 1997 (Wicks and others, 1998). Global positioning system (GPS) measurements from 1987 to 1995 (Smith and others, 1997; Meertens and others, 2000) show caldera-wide subsidence of as much as 15 mm/yr accompanied by radial-caldera contraction of up to 10 mm/yr.

Spurred by these records of uplift and subsidence in the Yellowstone caldera over the last century, we employed geomorphic criteria to assess the character and magnitude of deformation during the last 15,000 years. Paleoshorelines of Yellowstone Lake and drowned subaerial features, such as stream valleys and beach sediment, allow us to construct a record of vertical deformation in the central part of the Yellowstone caldera. New ^{14}C and projectile-point ages obtained in archeological surveys and excavations, as well as geological studies, provide improved age control (Pierce and others, 1994; Cannon and others, 1994, 1995, 1997). Cyclic inflation and deflation of the caldera in the last 100 years has been called "breathing" (see, for example, Pelton and Smith, 1979); we use the term "heavy breathing" for longer, higher amplitude cycles of inflation and deflation.

We build this study on the detailed surveying of Yellowstone Lake shorelines by Meyer and Locke (1986), Locke (1986), Meyer (1986), and Locke and Meyer (1994). Our findings are in general agreement with their mapping and correlation of shorelines; however, new dating and archeological studies indicate that the lower shorelines are much older than previously thought. LIDAR imagery of the northern lakeshore permits more continuous tracing and elevation measurement of shorelines and revision of some shoreline correlations east of Pelican Creek. LIDAR imagery also allowed us to locate previously unrecognized features, including the Fishing Bridge fault and low-relief beach-ridge shorelines that are strongly tilted away from the Storm Point geothermal center. Because of delays in publication, Pierce and others (2002) made available an earlier version of this study.

Previous Studies of Postglacial Shorelines

Richmond first mapped shorelines from 3 m to more than 50 m above present Yellowstone Lake (Richmond, 1973, 1974, 1976, 1977; Richmond and Pierce, 1972). He considered shorelines at and below 18–20 m to represent an open, postglacial lake, whereas higher shorelines were associated with deglaciation of the lake basin. Richmond's work predated recognition of active deformation in the Yellowstone caldera, and he assumed that (1) shorelines could be correlated by height alone, and (2) lake level underwent a relatively simple and continuous decline over postglacial time.

Drawing on this earlier work, Meyer and Locke (1986) mapped and correlated about nine shorelines around northern Yellowstone Lake. They designated the present shoreline as S1 and shorelines up to about 30 m above S1 as S2 to S9. Shoreline profiles were surveyed to centimeter accuracy (with closure) using the Bridge Bay lake-level gage zero mark as a datum, and shoreline elevations were interpreted to the decimeter. Meyer and Locke (1986) inferred that prominent shorelines were cut by rising lake levels due to episodic uplift within the Yellowstone caldera. This work was later continued around the entire lake (Locke and Meyer, 1994). In contrast to earlier work that relied on rapid hand leveling, these studies showed that many shorelines were deformed, both inside and

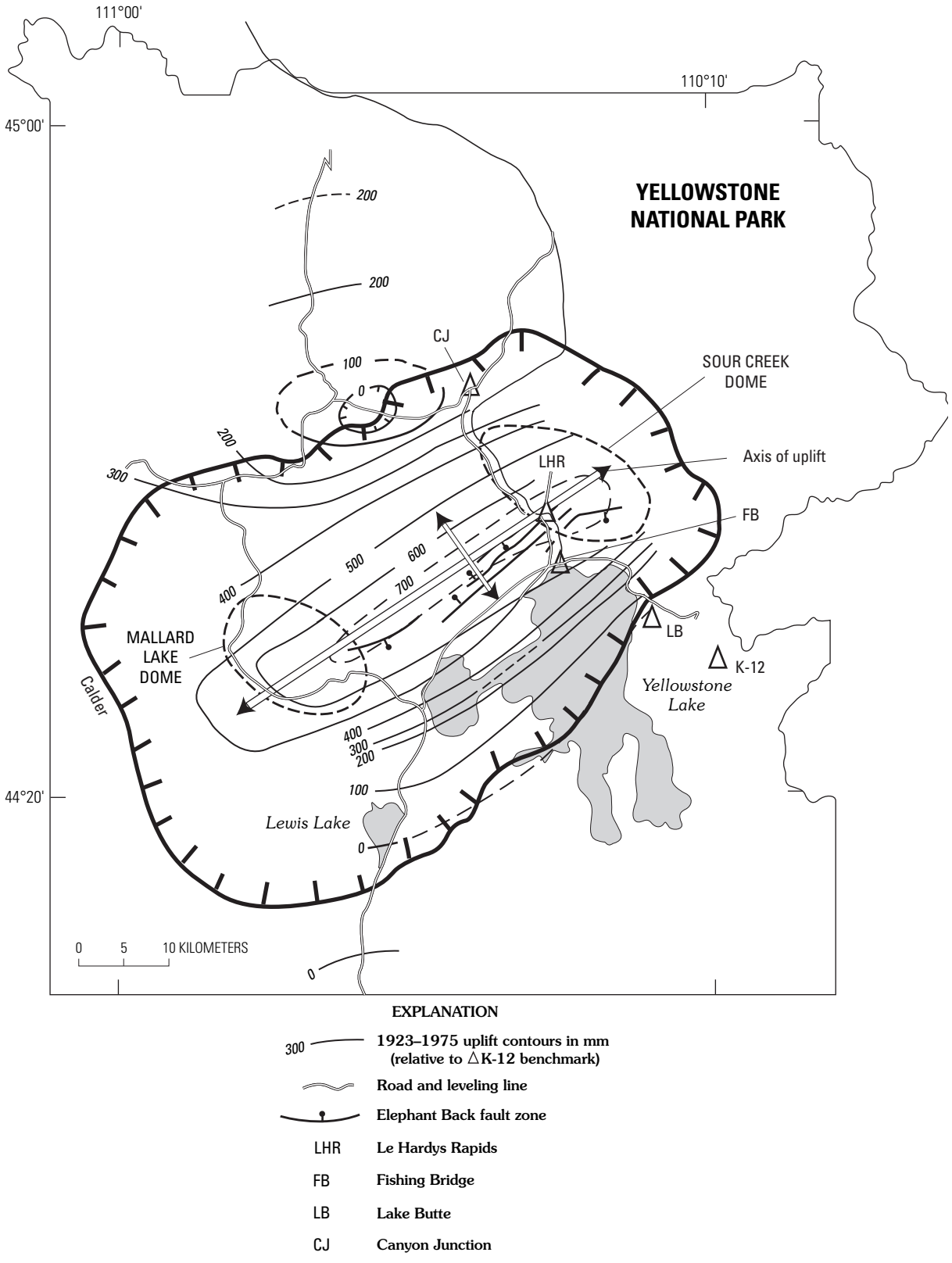

Figure 1. Map showing Yellowstone National Park, the Yellowstone caldera, Yellowstone Lake and Yellowstone River, and contours on the historic dome of uplift from 1923–1975 (after Pelton and Smith, 1982). Uplift is primarily within the Yellowstone caldera, and the axis of uplift extends between the Sour Creek and Mallard Lake domes. Note that upstream from Le Hardys Rapids (LHR) uplift also raises the level of the Yellowstone River and Yellowstone Lake and thus ties the level of Yellowstone Lake to uplift and subsidence at LHR.

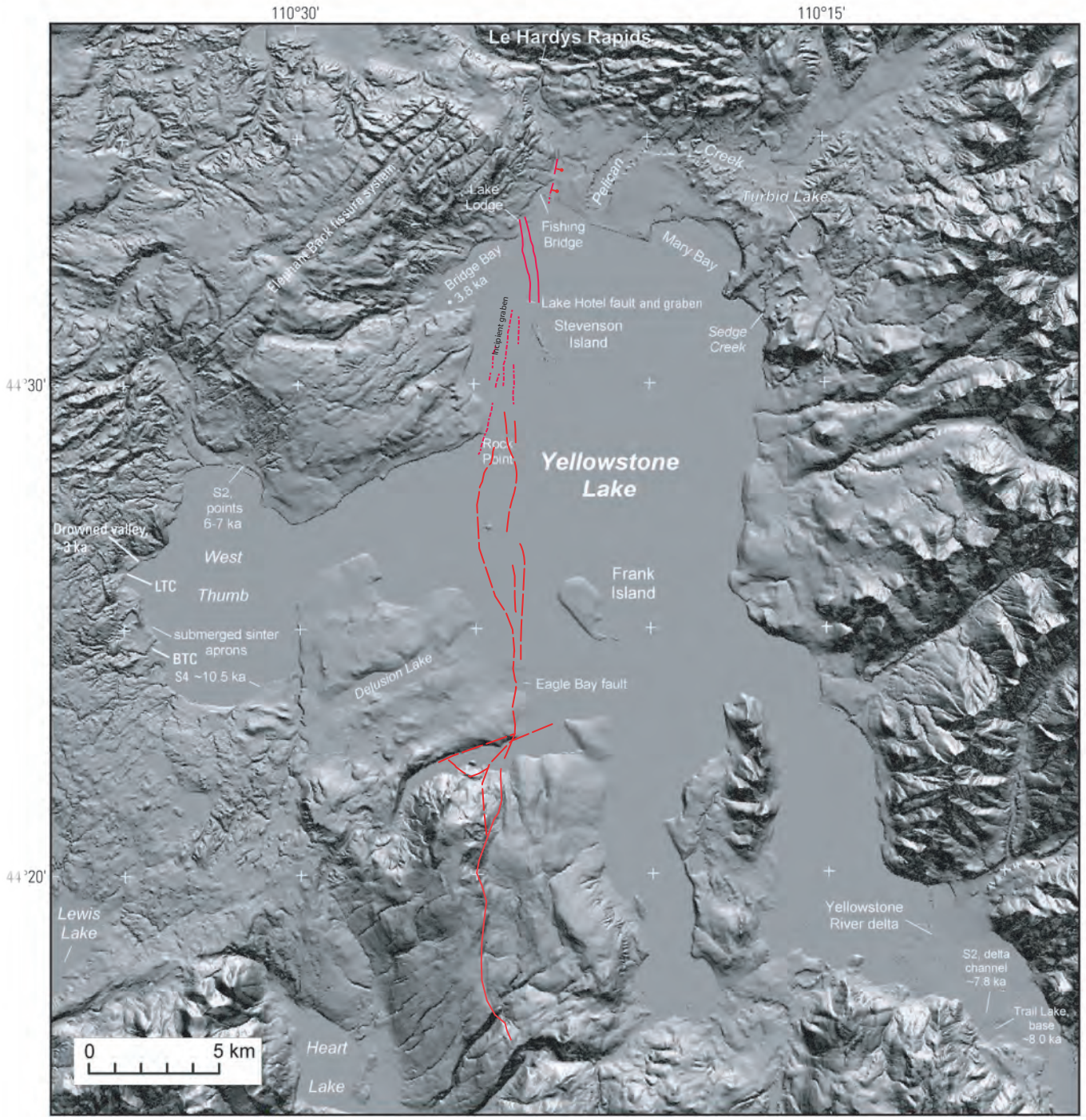

Figure 2. Digital elevation model of the Yellowstone Lake area, including some important localities and ages outside the LIDAR area. LIDAR data (figs. 5 and 10) cover the north shore from near the Lake Lodge to Mary Bay. Lake-floor surveys (Morgan and others, this volume) suggest a zone of faulting and fissuring connecting the Holocene Eagle Bay fault (Locke and others, 1992) in the southern lake area with the Lake Hotel graben. BTC, Big Thumb Creek; LTC, Little Thumb Creek.

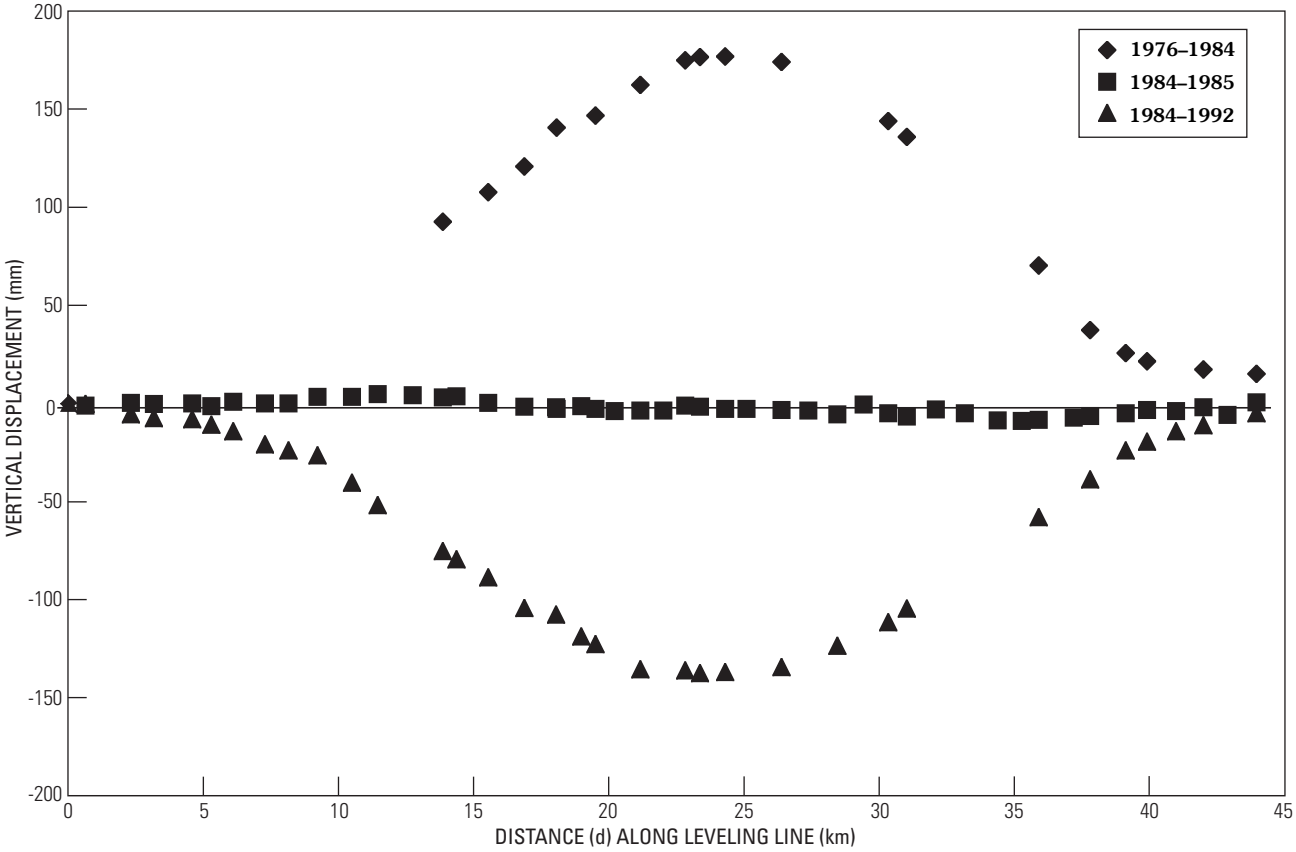

Figure 3. Vertical surface displacements measured by repeated first-order leveling surveys along a traverse from Lake Butte (d=0) north-northwest across the floor of Yellowstone caldera to Canyon Junction (d=44 km). The traverse was measured in 1923, 1975–1977 (labeled 1976 in the plot), each year from 1983 to 1993, 1995, and 1998. Shown here are the net displacements of benchmarks along the traverse for three contiguous time periods: 1976–1984, 1984–1985, and 1984–1992 (after Dzurisin and others, 1994). The uplift profile for 1976–1984 is essentially the mirror image of the subsidence profile for 1984–1992, which suggests a common source region and a remarkable unity of the uplift and subsidence processes. The transition from uplift to subsidence occurred during 1984–1985 when the observed surface displacements were negligibly small.

outside the caldera. Except for local areas of greater tilting and faulting, most shorelines were found to be gently warped. Given that historic intracaldera uplift and subsidence rates of 10–20 mm/yr could produce 50–100 m of vertical deformation in 5,000 yr, Locke and Meyer (1994) noted that net intracaldera deformation during the Holocene must be small because most shorelines are subhorizontal and the highest, oldest postglacial shorelines are at similar elevations inside and outside of the caldera (±~8 m). In these studies, a small number of radiocarbon dates were obtained on organic matter in lagoonal sediments associated with shorelines, but these provided only minimum ages.

During archeological studies near the outlet of Yellowstone Lake, Reeve (1989) initially recognized a discrepancy between Richmond's declining lake model and the occurrence of late Pleistocene–early Holocene (paleo-indian) projectile points within a few meters of present lake level, but he did not note that his archeological studies required considerably older ages than the minimum-limiting dates of Meyer and Locke (1986). Hamilton and Bailey (1990) recognized submerged shorelines of Yellowstone Lake at depths of 3–30 m below the present lake surface and constructed a complex history of postglacial lake-level changes but with little age control or means of correlation. Submerged shorelines are also described by Johnson and others (2003).

Holocene Lake- and River-Level Changes and Their Chronology

In this section we present the data used to construct the detailed lake-level chronology of figure 4. Table 1 describes the radiocarbon sample locations and gives the calibrated (corrected) ages. We use "ka" to indicate thousand years ago in calibrated (corrected) ages. Elevation is relative to the Bridge Bay gage. We first present evidence for low lake and river levels that were followed by a *rise* in lake and river levels because this is the key observation indicating caldera inflation. We then describe

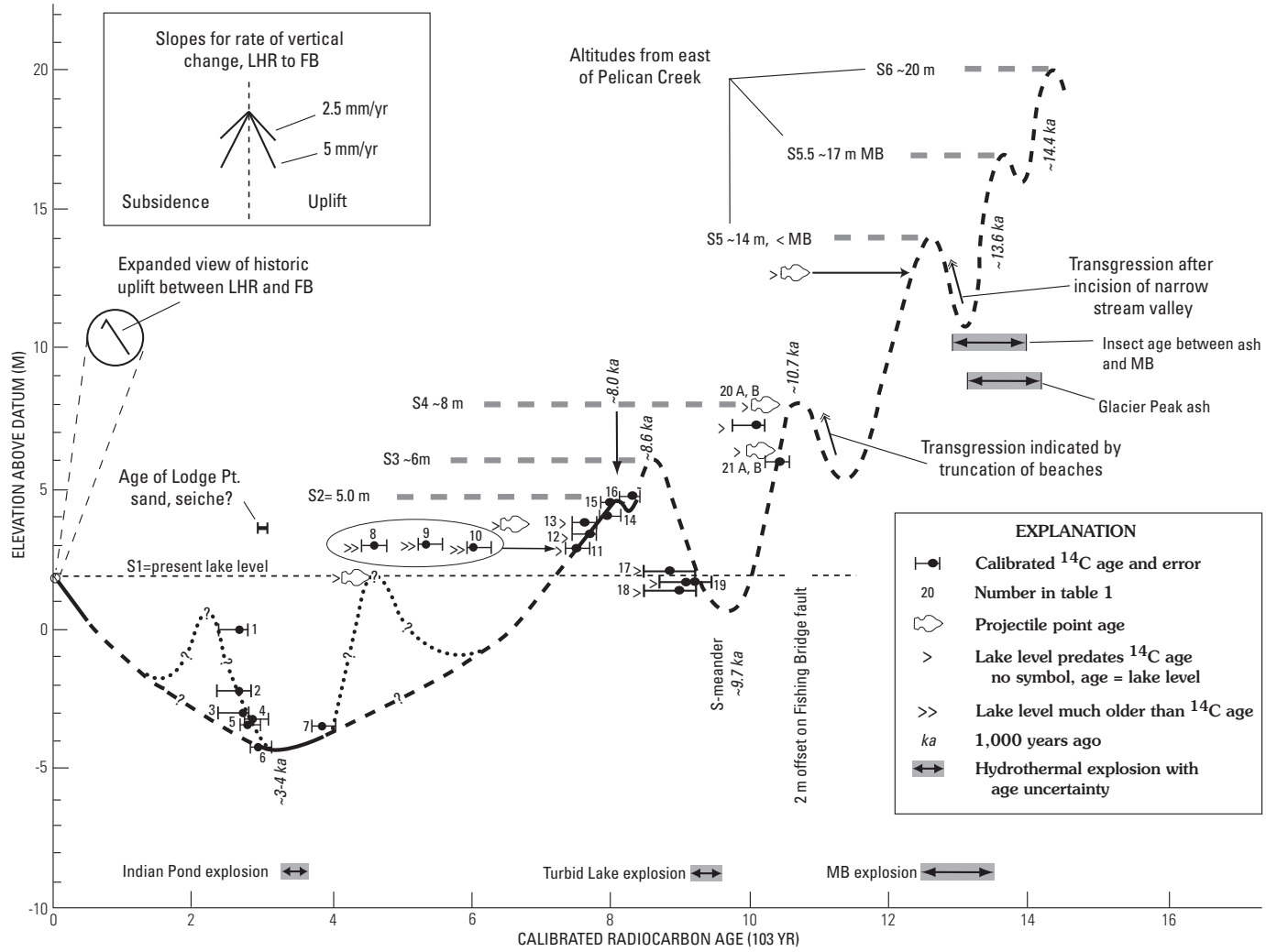

Figure 4. Reconstruction of changes in Yellowstone Lake level during the last 15 k.y. Shoreline altitude is relative to gage at Bridge Bay Marina and for the northern lake area. Radiocarbon ages and their conversion to calendar ages are given in table 1. LHR, Le Hardys Rapids; FB, Fishing Bridge; MB, Mary Bay explosion.

subaerial shorelines in order of *increasing* age because this is how we resolved the chronology shown in figure 4.

Airborne LIDAR elevation data were incorporated into this study. The survey contractor, Eaglescan, Inc., flew its instrumented airplane approximately 1,500 m above ground level. Aircraft position was recorded using base-station-corrected global positioning system (GPS) measurements, and aircraft attitude was measured with an inertial navigation system (INS). The laser was in the near-infrared wavelength (1.069 micron) and recorded returns from the land and water surface, reflecting these from a cross-track scanning mirror. The same laser that generated the transmissions amplified ground-return pulses for detection and measurement of the round-trip time of light. Recording equipment was configured to log the last return pulse, thus discarding a large fraction of vegetation signals. Each LIDAR pulse was approximately 15 cm thick along its flight path (this is the instrumental resolution limit for elevation determinations) and approximately 1 m in diameter at its intersection with the ground.

The contractor's postflight data-processing combined GPS positions, INS attitude measurements, mirror positions, and laser-pulse time-of-flight measurements to determine the georeferenced location of each reflection point in UTM coordinates (Zone 12, WGS84 reference system). The scanning mirror operated within 15° of nadir, measuring a swath width of 800 m along each flight line. Geometric factors degrade the accuracy of position determinations at points farther from nadir; errors at 15° are approximately 1 m. The laser-pulse-repetition frequency and mirror-scan rate were sufficient to sample elevations at a nominal 2-m spacing across-track and 5-m spacing along-track.

Postflight processing included winnowing of returns that came from vegetation and other features above the mean neighborhood surface. The remaining returns, presumed to come from the ground or from low ground-cover vegetation,

Table 1. Carbon-14 and other ages associated with levels of Yellowstone Lake, generally in order of increasing age.

[Localities and ages in bold type are critical to interpretation of lake-level history. YR, Yellowstone River; FB, Fishing Bridge]

Location, sample identifier, depth Samples numbered 1 to 23 are plotted in fig. 4	Age (yr B.P.) Lab number(s)	Corrected age (yr) (2-sigma range) Method A	Meters above datum	Remarks
		A. Subaerial samples lower and younger than S-2 shoreline		
1. Pelican Cr. Paleo-barrier beach	**2,550±60**	2,735	0-1	From depth of 1.65 m in eolian sand and 0.25 m above top of openwork beach gravel near present Yellowstone Lake level.
94P33b, 165 cm	Beta-78912	(2,362–2,775)		
	CAMS-17814			
Pelican Cr. East reentrant	2,800±50	2,874–2,917	4.5	Charcoal from mixed zone on 4.5 m beach, provides minimum age for post-S2
97P29, 81 cm	WW-1635	(2,778–3,057)		beach.
97P30, 65 cm	2,670±50	2,770	4.2	Charcoal from mixed zone on 4.2 m beach, provides minimum age for post-S2
	WW-1636	(2,739–2,865)		beach.
97P31, 65 cm	Modern		?	Pine needles, brown.
Storm Point	**2,160±60**	2,133–2,148	3.43	Charcoal from open platy platform gravels of shoreline 4.3 m above datum on
95P61, 90 cm	WW-724	(1, 954–2,335)		east side of Storm Point. Anomalously young age probably explained by uplift of
	CAMS-28372			Storm Point geothermal center.
	1,160±40	1,060	3.62	Charcoal from eolian deposits overlying the above sample. May be local young
95P61, 67 cm	WW-723	(968–1,174)		uplift of Storm Point.
	CAMS-28371			
		B. Samples from below present lake level		
2. Drowned YR channel	**2,518±100**	2,712–2,622	-2.37	Wood from 280 cm below slough surface near base of parting sand.
91P46, 280 cm	_____	(2,345–2,837)		
3. Drowned YR channel	**2,560±70**	2,738	-3.08	Pine needles from 353 cm below water surface. Depth based on 1991 water
92P28, 384 cm	Beta-63807	(2,361–2,781)		levels. Occurs 20 cm above channel gravel.
	CAMS-7692			
4. Drowned YR channel	**2,750±86**	2,848	-3.39	Charcoal (hard chunk) in gravel at depth of 415–418 cm, 3.85 m below water
91P46, 415–418 cm	_____	(2,743–3,136)		level of slough.
5. Drowned YR channel	**2,710±60**	2,781	-3.40	Wood from upper part of gravel at depth of 415–423 cm in drowned
91P46, 415–423 cm	Beta-63806	(2,745–2,948)		paleochannel of Yellowstone River about 1 km downstream from Fishing Bridge.
	CAMS-7691			
6. West Thumb area	**2,880±60**	2,980	-4.3	Wood from about 17 ft below lake level of culvert across “north” Little Thumb
93P3	Beta-63809	(2,851–3,210)		Creek, West Thumb. Insects indicate wetland environment. Depth 23.5–24 ft
	CAMS-7693			below road, est. altitude 7,717 ft. Wood probably conifer but not pine.
7. Bridge Bay	**3,560±60**	3,835	-3.43	Wood from 497 cm. Upper part of beach sands 40 cm thick in 2.6 m water on 1.8
94P31b, 497 cm	Beta-78911	(3,690–4,036)	(approx.)	m soft lake sediments and above firm lake sediments.
	CAMS-17813			
Pelican Creek drowned valley	11,720±60	13,805	-4.3?	Carbonized plant fragments or roots. From highway boring at Pelican Creek at
PC5, 26–27.5 ft	_____	(13,446–15,123)		depth of 26–27.5 ft and about 16 ft below present lake level. Sample in lower part
				of fill near edge of drowned valley of Pelican Creek.
		C. Samples lower and younger than S2 and mostly older than submerged shoreline samples		
Lodge Point sand	**130±50**	2,261	3.7	Charcoal, probably intrusive from above.
97P46A, +85 cm	WW-1640	(0–291),		

Table 1. Carbon-14 and other ages associated with levels of Yellowstone Lake, generally in order of increasing age—*Continued*.

Location, sample identifier, depth Samples numbered 1 to 23 are plotted in fig. 4	Age (yr B.P.) Lab number(s)	Corrected age (yr) (2-sigma range) Method A	Meters above datum	Remarks
C. Samples lower and younger than S2 and mostly older than submerged shoreline samples—*Continued*				
Lodge Point sand	**2,980±50**	3,083–3,205	3.4	Charcoal near top of fine-bedded sand. Pulse of well-bedded sand into paleo-
97P46F, +65 cm	WW-1638	(2,968–3,335)		lagoon with Lodge Point soil on S2 shoreline. One possibility is seiche of Yellowstone Lake into basin.
97P46, 45 cm	2,870±40	2,962	3.2	Charcoal in middle of fine-bedded sand section. Fine-bedded sand deposited
	WW-1845	(2,868–3,158)		rapidly, perhaps during a seiche of Yellowstone Lake.
8. Lodge Point soil that	**4,160±60**	4,650–4,810	2.91	Charcoal 20 cm below top of buried soil that formed after lake dropped from S2
postdates S2	WW-564	(4,451–4,845)		level. Soil developed and then was buried by Lodge Point sand (see above) and
95P7, 185 cm	CAMS-23265			by eolian deposits. Age of S2 (here at 5.16 m above datum) is significantly greater than these three soil ages.
9. Lodge Point soil that	**4,710±60**	5,333–5,466	2.96	Charcoal sample from 33 cm below top of soil postdating S2 shoreline. Soil
postdates S2	WW-521	(5,310–5,591)		developed and then was buried while lake was at or below present level. Age of
95P7, 198 cm	CAMS-22090			S2 significantly greater than these soil ages.
10. 97P46, 10 cm	5,300±40	5,998–6,167	2.85	Charcoal near base of fine-bedded sand. Overlies soil dated 4,110±60 yr B.P.
	WW-1846	(5,937–6,196)		nearby. Age may be near 3,000 yr based on continuous well-bedded sand section that includes above two samples at 45 and 65 cm.
95P9, 190–200 cm	4,110±60	4,572–4,778	~2.8	Charcoal from 20–30 cm below top of buried soil that postdates S2 shoreline.
	WW-565	(4,423–4,831)		Age of S2 significantly greater than these soil ages.
	CAMS-23266			
D. Samples associated with S-2 shoreline				
11. Pelican Cr. terrace	**6,740±90**	7,587–7,606	~2.5	From 105–110 cm depth in paleochannel on Pelican Creek terrace that truncates
truncating S2	Beta-65468	(7,432–7,745)		S2 west of Pelican Creek. Top of terrace 1.2 m below S2 at UTM 550420 East,
95P15, 105–110 cm	CAMS-8671			493900 North.
12. Shoreline below S2	**6,820±50**	7,666	3.1	Charcoal from base of mixed zone; may be limiting age for local 3-m beach at
(S 1.6)	WW-1639	(7,574–7,746)		west end of uplift associated with Storm Point (see fig. 15). Also provides
97P32B, 70 cm				minimum age for S2 beach.
13. Archeological excavation	**6,800±90**	7,621–7,660	3.9	At depth of 2.6 m beneath S2 surface at 4.3 m above datum at east part of Fishing
on S2	Beta-65467	(7,493–7,791)	S2=4.3	Bridge peninsula near Pelican Creek terrace (Cannon and others, 1994).
S568/E432	CAMS-8670			
14. S2 on Lodge "bay"	**7,210±50**	7,979–8,008	4.07	Charcoal sample dates time of occupation of S-2 shoreline at 5.16 m above datum
95P4, 94 cm	WW-563	7,878–8,158		on Lodge Point. Occurs beneath thick molic soil at depth of 94 cm.
	CAMS-23264			
15. S2 on Lodge "bay"	**7,210±60**	7,979–8,008	4.48	Charcoal in diatomaceous cap of progradational bar deposits of S2 shoreline and
96P50, 53 cm	WW-1174	(7,875–8,168)		provides age for abandonment of S2 shoreline.
E. Possibly associated with S3 shoreline				
16. S3(?) behind FB	**7,565±70**	8,378	4.75	In old ball field behind General Store. Site in Fishing Bridge S4 paleolagoon.
General Store	Beta 63092	(8,190–8,451)		Sample from level 10 at base of mixed zone (Cannon and others, 1994). S3 water
N248-9/W126, level 10	ETH-10616			may have filled into this area from Yellowstone River.
F. Abandoned S-meander				
17. Bottom of S-meander	**7,968±118**	8,781–8,978	~2	Charcoal at auger depth of 109 cm in S-meander.
91P34		(8,457–9,245)		

Table 1. Carbon-14 and other ages associated with levels of Yellowstone Lake, generally in order of increasing age—*Continued*.

Location, sample identifier, depth Samples numbered 1 to 23 are plotted in fig. 4	Age (yr B.P.) Lab number(s)	Corrected age (yr) (2-sigma range) Method A	Meters above datum	Remarks
		F. Abandoned S-meander—*Continued*.		
18. Bottom of S-meander	**8,030±240**	9,000	2	Charcoal 2.12–2.20 m below pit datum and 4.2 m from pit end. On top of channel
Yell 92-15	56712	(8,371–9,527)		gravel. See below.
19. Bottom of S-meander	**8,250±130**	9,152–9,263	2.2	Charcoal 2 m below surface and 10–20 cm above river gravel. Dates drowning by
Yell 92-14, 92P30	Beta-56711	(8,812–9,528)		rising waters in ponded reach of Yellowstone River. Minimum age for top of Yellowstone River channel gravels that extend down to <1 m and probably <0 m above datum. Shorelines S3(?) and S2 are younger than sample.
		G. Samples related to the S4 shoreline		
20. Fishing Bridge Peninsula	**8940±60**	10,154	7.8	Charcoal at depth of 1.6 m above beach gravels and in lower part of mixed zone
S375/E512	Beta-65466	(9,795–10,219)	S4=8.2	of eolian sand and beach sand. One-meter-square archeological excavation near
	CAMS-8669			easternmost extent of S4 surface at 9 m above datum. From northern end on old campground loop. Unit S375/E512 (Cannon and others, 1994, their fig. 44).
21. S4 in Fishing Bridge area	**~8,800 to ~9,400**	9,790–9,890	9–7.5	Cody Complex points (late paleo-indian) on S4 between Yellowstone River and
		10,580–10670		Pelican Creek (Cannon and others, 1995).
		H. Samples associated with hydrothermal-explosion deposits		
Indian Pond	**3,090±50**	3,272; 3,337		Charcoal in soil beneath Indian Pond explosion deposit exposed in culvert
96P45, 102 cm	WW-1173	(3,082–3,445))		excavation for highway halfway from Indian Pond east to lake margin. Maximum age for Indian Pond deposit. On S5 shoreline of Meyer and Locke (1986).
Beneath Indian Pond expl.	4,220±40	4,828		Charcoal in soil beneath 2.5 m of Indian Pond explosion deposit, 0.3 km east of
deposit	WW-2161	(4,624–4,852)		Indian Pond and above S5 shoreline. Age of explosion deposit ~3 ka, so this was
98P25				an older charcoal fragment in the buried soil.
"Little" Storm Point	**3,080±50**	3,270; 3,330	9.4	Humic wetland deposit buried by greenish Indian Pond hydrothermal-explosion
beneath Indian Pond expl.	WW-725	(3,082–3,386)		deposit. Sample 40 cm above shoreline platform at 8.95 m above datum.
deposit	CAMS-28373			
95P64B, 32 cm				
Beneath Indian Pond expl.	3,500±250	3,727; 3,825		Richmond (1976, section 74) reported this age for a sample beneath diamicton
deposit	W-2734	(3,170–4,501)		now recognized as Indian Pond hydrothermal-explosion deposit. Occurs above Mary Bay explosion deposit.
"Little Storm Point" section	430±50	505		Charcoal in weak soil in eolian sand 40 cm below surface. *Numbers for distance*
96P47, +140 cm	WW-1169	(323–539)		*above(+) and below (-) arbitrary datum.*
96P47, +47 cm	420±50	502		Charcoal in soil in eolian sand 160 cm below surface.
	WW-1166	(319–536)		
96P47, 0 cm	1,780±40	1,707		Charcoal. Overlies Indian Pond deposit and provides minimum age for deposit
	WW-1164	(1,570–1,820)		and for base of eolian sand.
96P47, –40 cm	**2,940±60**	3,078–3,154	8.95	Charcoal. Immediately underlies Indian Pond explosion deposit and provides best
	WW-1165	(2,890–3,323)		maximum age for deposit.
96P47, –70 to 75 cm	5,160±60	5,916		Charcoal in soil pendant on platform of S4.5(?) shoreline cut across Mary Bay
	WW-1167	(5,748–6,167)		explosion deposit.
96P47, –75 cm	3,970±50	4,419		Blackened material including charcoal. Similar to charcoal sample directly above.
	WW-1168	(4,259–4,566)		

Table 1. Carbon-14 and other ages associated with levels of Yellowstone Lake, generally in order of increasing age—*Continued.*

Location, sample identifier, depth Samples numbered 1 to 23 are plotted in fig. 4	Age (yr B.P.) Lab number(s)	Corrected age (yr) (2-sigma range) Method A	Meters above datum	Remarks
		Lake bluffs southeast of Indian Pond and east of "Little Storm Point"		
	4,040±60	4,451– 4,521	8.06	Sample below two buried soils in tree-throw wedge pulled from platform gravels of
95P53, 103 cm	WW-722	(4,412–4,806)		7-m S4(?) shoreline.
	CAMS-28370			
	4,050±60	4,453–4,524		Charcoal below buried soil in disturbed zone 20 cm above platform gravels at ~7 m
95P10B, 85 cm	WW-522	4,411–4,813		above datum in bluffs south of Indian Pond and 85 cm below buried soil.
	CAMS-22091			
	5,290±60	5,922–6,166	9.2	Charcoal fragments in molic buried soil above stone line of platform of 10.6-m
95P64B, 48–50 cm	WW-726	(5,922–6,271)		S5(?) shoreline that is eroded on Mary Bay explosion deposit.
	CAMS-28374			
	5,890±40	6,678–6,722	8.36	Charcoal at base of platform gravels very close to the S4(?) shoreline. Overlain by
98P11	WW-2157	(6,574–6,844)		buried soil and by Indian Pond explosion deposit. From east of 8-ka samples.
Indian Pond Creek West	**2,200±50**	2,156–2,298	13	Charcoal in eolian sand deposit above level of sample 95P51. May be intrusive from
section	WW-720	(2,060–2,340)		above.
95P6c, 80 cm	CAMS-28368			
Indian Pond Creek West	**8,160±50**	9,032–9,124	10	Charcoal in sheet-bedded sands about 10 cm above platform gravel of pre-S4 lake
95P51, 105 cm	WW-721	(9,007–9,394)		level, ~11 m above datum when Mary Bay explosion deposit predates S4(?)
	CAMS-28369			shoreline and postdates Glacier Peak ash (11,400 yr B.P.) and age of 11,400 yr B.P.
				Scott Elias (Univ. Colorado) obtained on insect in fibrous lacustrine peat deposit.
Indian Pond Creek West	**11,400±90**	13,411	~4.8?	Scott Elias (Univ. Colorado) obtained this age on caterpillar mandibles from
	CAMS-17388	(13,042–13,800)		lacustrine stringy peat about 1 m above Glacier Peak ash and several meters below
				Mary Bay explosion deposit.
		Lake bluff south of Indian Pond and just east of cemented column		
95P66	**8,110**±60	9,025	7.64	Charcoal from grass and brush fire above platform gravels at 7.64 m above datum
	WW-727	(8,791–9,262)		S4(?) shoreline at ~9 m above datum. Occurs below two phases of Indian Pond
	CAMS-28375			deposit.
98P14	**8,340±40**	9,328–9,419	7.0	Charcoal in platform gravel (base 6.9 m, top 7.15 m) of nearby S4(?) shoreline that
	WW-2159	(9,150–9,484)		truncates Mary Bay hydrothermal-explosion deposit and overlies lake sediments
				on Mary Bay explosion deposit.
98P13	**8,210±40**	9,132–9,243	7.0	Charcoal from platform gravel of S4(?). Site at same position and very near 98P14.
	WW-2158	(9,027–9,397)		Overlies lake sediments on Mary Bay hydrothermal-explosion deposit.
Richmond (1977, section 74)	10,720±350	12,857	~5–6?	Charcoal 2.6 m above Glacier Peak ash and beneath Mary Bay explosion deposit.
	W-2738	(11,344–13,437)		

Table 1. Carbon-14 and other ages associated with levels of Yellowstone Lake, generally in order of increasing age—*Continued*.

Location, sample identifier, depth Samples numbered 1 to 23 are plotted in fig. 4	Age (yr B.P.) Lab number(s)	Corrected age (yr) (2-sigma range) Method A	Meters above datum	Remarks
		Lake bluff south of Indian Pond and just east of cemented column—*Continued*		
Glacier Peak ash	11,450±50	13,436 (13,160–13,800)	~2.8	Below MB explosion deposit and beneath S4(?) and by inference S5 shoreline. Collected by Ken Pierce and determined by Andre Sarna to have mixture of shards of both Glacier Peak and Yellowstone affinities. Probably same ash 2.92 m above datum at Richmond's section (1976, section 74). First two ages from Whitlock (1993), third from Mehringer and others (1984), and last from Doerner and Carrara (2001).
	12,100±50	14,100 (13,690–15,360)		
	11,200±50?	13,155 (12,910–13,750)		
	>11,510±70	13,460 (13,170–13,820)		
		Turbid Lake explosion deposit		
Turbid Lake explosion deposit 98P21B	8,410±40 WW-2160	9,437–9,469 (9,300–9,525)	~76 m	Charcoal from high in bluff of Bear Creek beneath 2 m of Turbid Lake explosion deposit. Altitude near 7,800 ft.
Turbid Lake explosion deposit 98P21B	8,000±500 W-2486	8,819–8,986 (7,792–10,190)	do.	Sample of charcoal from beneath Turbid Lake explosion deposit along Bear Creek. Section 58 of Richmond (1977). Air conditioning problem in lab at time of analysis.
Turbid Lake explosion deposit 98P21B	8,310±300 W-1944	9,300–9,398 (8,435–10,150)	do.	Sample collected by Dave Love from beneath diamicton now considered to be Turbid Lake explosion deposit.
		I. Old lake sediment ages		
Bridge Bay Marina 94P23, 897 cm	11,890±60 Beta 78910 CAMS-17812	13,840 (13,624–15,250)	-7.97	Twigs from 8.97 m below platform (0.27 m above water surface on 8/5/94) with beach(?) sand at about 4 m below datum.
Lodge Point Yell 92-13	13,040±90 Beta-56710	15,678 (14,605–16,173)	~3?	Sedge peat 30–40 cm below diatomite identified by Ed Theriott (Academy of Natural Sciences, Philadelphia). Old carbon dioxide effect?
Lodge bay	13,360±320 Beta-40764	16,053 (14,622–16,928)	~3?	Sedge peat, Lodge Point, collected by Wayne Hamilton (NPS, retired). Old carbon dioxide effect?
		J. Samples from southern part of Yellowstone Lake		
22. 00P52 and archeological site 48YE409	**9,360±60** Beta-148567	10,570 (10,294–10,737)	5.8	Charcoal from base of mixed zone on shoreline gravels that are the 7.0-m S4 of Bill Locke (Montana State Univ., written commun., 2000). Site 1 km east of Grant Village sewage disposal plant.
23. Osprey Beach site 48YE409	**~8,800 to 9,400**	~9,800 to 10,300	~5.8	Same as 00P52. Point types of late paleo-indian age in the 8,800–9,400 yr B.P. time range. Cody Complex points in base of mixed zone above beach gravels to 5.7 m above datum on 7.4-m S4 of Bill Locke (Montana State Univ., written commun., 2000).
Plainview projectile point from Osprey Beach site.	~500 years older than Cody Complex	~10 to 11.6 ka (see above)	~5.8?	A Plainview point was found either (1) recently slumped to the present beach (Ann Johnson, NPS, oral commun., 2002) or (2) inland 30 m and on a surficial linear concentration of archeological material (Don Blakeslee, Univ. Wichita, written commun., 2002).
Samples associated with S2 97P54, 215 cm	**6990±40** WW-1848	7,790–7,815 (7,689–7,933)	5.5	Wood near base of paleochannel in Yellowstone delta aggraded to ~9 m above datum or ~7,760–7,765 ft alt. This landform dams off Trail Lake (7,751 ft, see below). Age is similar to S2 shoreline in NW. part of lake.

Table 1. Carbon-14 and other ages associated with levels of Yellowstone Lake, generally in order of increasing age—*Continued*.

Location, sample identifier, depth Samples numbered 1 to 23 are plotted in fig. 4	Age (yr B.P.) Lab number(s)	Corrected age (yr) (2-sigma range) Method A	Meters above datum	Remarks
		J. Samples from southern part of Yellowstone Lake—*Continued*		
Yellowstone River Delta at S2 level	**7,215±70** _____	7,980–8,010 (7,871–8,17)	6.1 (lake level)	Cathy Whitlock (Montana State Univ.) obtained this age for the base of a core from Trail Lake. Trail Lake is probably dammed by a delta of the Yellowstone River at the S2 level. Trail Lake altitude is 7,751 ft.
Eagle Bay	4,540±40 ETH-3987	5,294 (5,046–5,317)		Colluvium on fault scarp eroded by S4 shoreline (Locke and others, 1992).
		Sites in or near modern Yellowstone River delta		
97P51, 51 cm	1,570±40 WW-1847	1420–1508 (1,350–1,541)	~2	Dead duck delta 5 ft above present lake. In kettle lake connected to Yellowstone Lake northwest of Trail Creek cabin. Local delta top is about 7,738 ft.
97P56, 56 cm	850±40 WW-1850	738 (674–908)	~1	Stabilized beach with grass and trees at (7,739 ft), east side of delta. Dates beach deposition near or slightly above present lake level.
97P55, 240 cm below dune top	340±40 WW-1849	328–431 (301–504)	~1	Northern point on modern delta. Dates beach deposition near or slightly above present lake level.

defined a triangulated irregular network (TIN). The data were interpolated to a 2-m-square grid by sampling the triangular facets of the TIN at the grid points. We used the lake-level gage at Bridge Bay Marina, (0.44 m) when the LIDAR was flown, to calibrate to the datum used in previous studies (see, for example, Meyer and Locke, 1986). The altitude of the zero mark on the gage was measured at 2,356.48 m in 1985 by level surveys.

Lake-Level Rise After Lake Low 4–3 ka

Yellowstone Lake

Many of the lower ends of stream valleys entering Yellowstone Lake appear to be drowned. Several streams, both north and south of the West Thumb Geyser Basin, have drowned valleys upstream from their entrances into Yellowstone Lake, commonly with standing water grading upstream into alluvial wetlands. Two such streams are Big Thumb Creek and Little Thumb Creek (fig. 2). The next stream north of Little Thumb Creek (here called "Little Thumb Creek North") has water standing in a drowned valley on the upstream (west) side of the highway. Highway borings in the center of this drowned valley encountered wood at a depth of 4.3 m below datum with an age ~3.0 ka (2,880±60 yr B.P.; table 1, no. 6). Insect faunae studied by Scott Elias (University of Colorado, written commun., 1993) indicate a shallow wetland environment was associated with the wood. Since this time, the level of Yellowstone Lake has risen about 5–6 m, but this small stream has not yet transported enough sediment to fill in the drowned valley.

Immediately offshore from the West Thumb Geyser Basin, aprons of siliceous sinter around active and inactive hydrothermal vents extend well below lake level. Divers from the National Park Service sampled these vents at depths of 4.9 and 5.5 m below datum. Analysis of the oxygen-isotope composition show the sinter formed subaerially and not under Yellowstone Lake (Pat Shanks, oral commun., 2000). Shoreline data (Locke, 1986; Locke and Meyer, 1994) also suggest substantial local downwarping in the West Thumb area, although the lower shorelines are poorly defined and poorly correlated there.

We cored Yellowstone Lake about 6 km southwest of the outlet in the relatively quiet water of Bridge Bay (fig. 2), which is sheltered from wave action generated by the prevailing southwesterly winds. A wood sample from a coarse-sand deposit 5 m below the surface (3.45 m below datum) yielded an age of ~3.8 ka (3,560±60 yr B.P.; table 1, no. 7). The sand is well sorted and 0.5 m thick, similar to the modern beach. It is underlain by firm deep-water lake sediments and overlain by poorly consolidated, fine, lake sediments. We infer that the sand represents a beach deposit drowned by a lake-level rise after ~3.8 ka. This site is 3.2 km west of the north-trending, down-to-the-east Lake Hotel fault, and thus its submergence is not related to downdropping on that fault.

Two other drowned valleys adjacent to Yellowstone Lake and cored by the Federal Highways Administration indicate low lake levels. (1) Pelican Creek is a drowned valley as suggested by the high, steep, stream-cut scarps that now flank the exceptionally wide, low-gradient flood plain. An aggrading stream will have a wide valley, and the necessity of the aggrading stream at times occupying the valley edge where it can undercut the banks is part of this process. Borings for a proposed causeway across Pelican Creek encountered gravelly sands above finer lake sediments. These gravelly sands extend to a depth of 4 to 5 m below datum. We interpret the gravelly sand to represent a drowned channel of Pelican Creek eroded into lake sediments. Although no carbon samples were obtained from the gravelly sand, an age of ~13.8 ka (11,720±60 yr B.P.; table 1) was obtained from the lake sediments just below the gravelly sands. (2) Sedge Creek is nearly at the caldera margin and has a lower valley similar to Pelican Creek. At Sedge Creek, gravelly sediment extends to 18 m below datum and is underlain by about 6 m of fine-grained lake sediment that overlies a lower gravelly material, possibly glacial till or outwash. This may suggest the possibility of a drowned valley extending to 18 m below datum near the caldera margin at Lake Butte and as distant as possible within the caldera from the central part of the caldera where historic inflation and deflation has been greatest.

Outlet Reach of the Yellowstone River

The outlet reach of the Yellowstone River (fig. 5) is anomalous and extends from the outlet at Fishing Bridge to Le Hardys Rapids (LHR). The river has recently deposited sandbars in the *outsides* of meanders, effectively straightening its channel and indicating a substantial reduction in stream power (Meyer, 1986, his fig. 17; Locke and Meyer, 1994). The present river has very low gradient (0.05 m/km). For low discharge in September, both surveying (Dan Dzurisin, oral commun., 1993) and LIDAR data indicate a total drop of only 0.25 m in the 5-km distance from the outlet to just upstream from LHR. During higher discharges in June, the water surface would have a somewhat steeper gradient. The only bedrock forming the channel bed in this reach is at LHR, where an erosionally resistant unit in the Lava Creek Tuff acts as a weir that controls water level in the outlet reach (Hamilton, 1987). Uplift or subsidence of this bedrock threshold therefore has the potential to control both the river gradient and the level of Yellowstone Lake. Downstream from LHR, the river has a gradient of 1.8 m/km, more than 30 times steeper than above LHR.

Although the river is now essentially a continuous, low-velocity "pool" in the outlet reach, steep, high cutbanks on the outsides of the meanders indicate that the older, more sinuous channel contained an energetic river (fig. 5). These scarps were so actively being undercut that they were unvegetated and served as a source for thick eolian sand now preserved at the top of the bank (fig. 5, see also fig. 8). About 1 km downstream from the outlet, an outer meander of the old channel forms a slough that is isolated from the present active channel by a sand bar.

A core in this slough encountered 3.5 m of fine sediment over river gravel at a depth of 4 m (3.4 m below datum). The

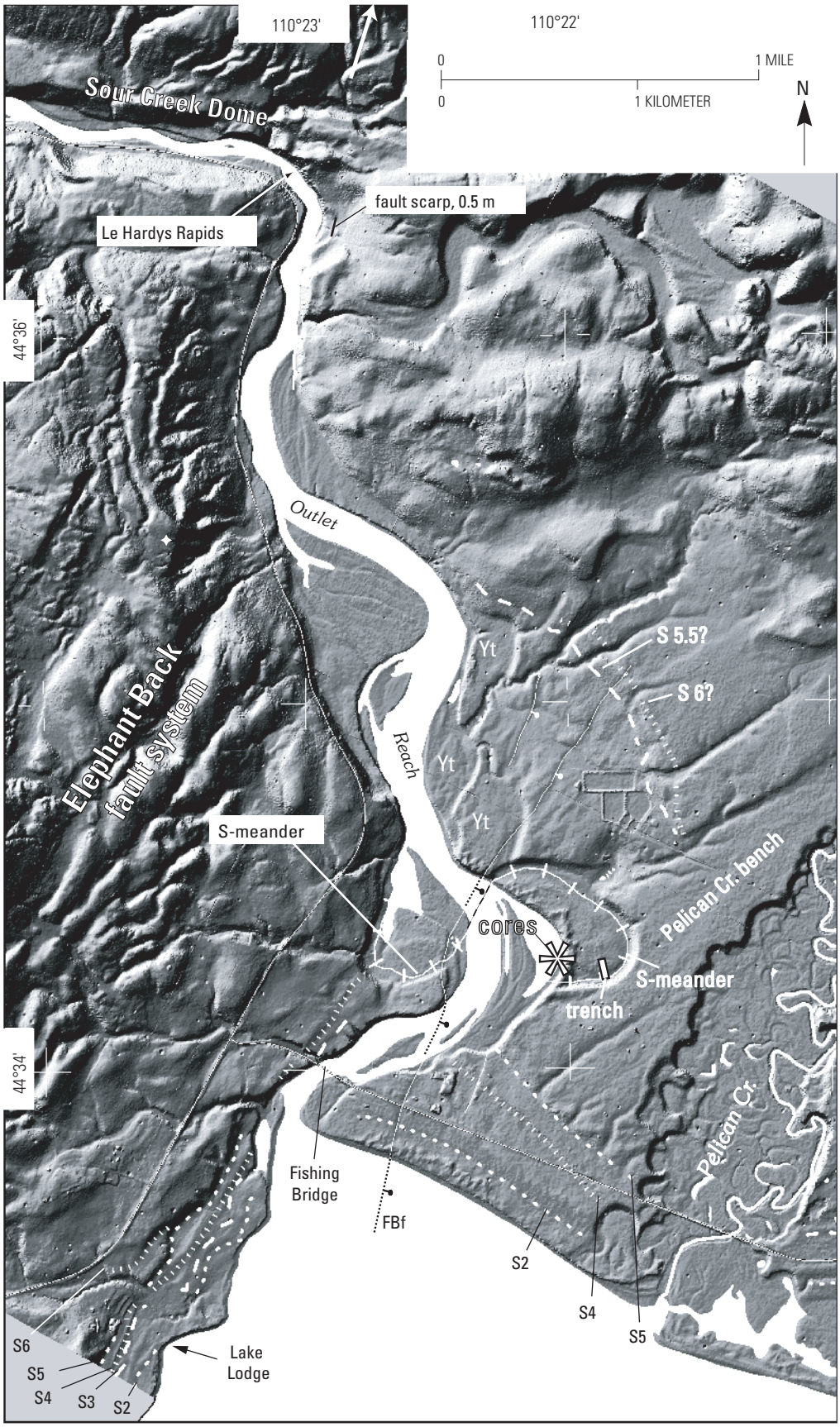

Figure 5. LIDAR image showing the "outlet reach" of the Yellowstone River from the outlet at Fishing Bridge to Le Hardys Rapids. The outlet reach has a drop of only 0.25 m over a distance of more than 4 km. Sand deposition along the outlet reach indicates the gradient has been diminishing and the channel has been straightening. FBf, Fishing Bridge fault; Yt, Yellowstone River terraces; S2–S6, shorelines. S-meander denoted by thin white line crossed by heavy white bars. LIDAR shown with artificial illumination from the west.

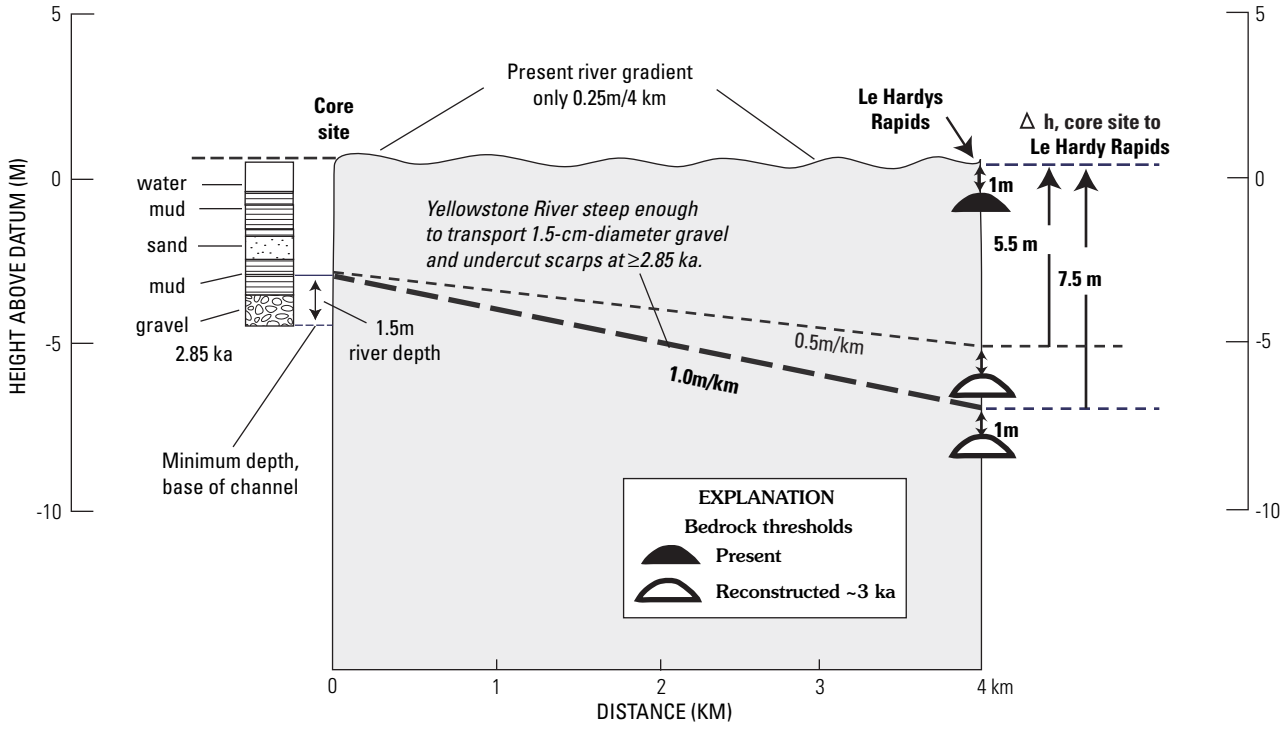

Figure 6. Diagram approximating uplift of Le Hardys Rapids after 3 ka. Note that gravel at the core site is below the bedrock threshold at Le Hardys Rapids (LHR). The present drowned profile (upper horizontal wavy line) is compared to a reconstructed profile at ~3 ka when the gradient is estimated to have been 1m/km to the bedrock threshold at LHR (heavy dashed line, see text). At ~3 ka, the outlet reach of the Yellowstone River was a vigorous, gravel-transporting, bank-eroding stream.

gravel is at least 1 m thick; wood and charcoal samples from the upper gravel yielded ages of ~2.8 ka (2,710±60 and 2,750±86 yr B.P.; table 1, nos. 4 and 5). We infer that the sedimentary sequence (fig. 6) represents a reduction of gradient and velocity because of relative uplift of the bedrock threshold at LHR downstream, and the fine sediment has accumulated since abandonment and drowning of the channel bend. The top of the river gravel is now about 3 m *below* the threshold at LHR, whereas at the time of deposition it would have been significantly above the threshold.

Therefore, at the time of active transport of the river gravels, the Yellowstone River had a considerably steeper gradient and sufficient energy to undercut banks 15 m high. Based on median sediment diameter of 1.5 cm and 1.5-m water depth, Waite Osterkamp (written commun., 1996) used the Shields equation to estimate the paleo-river gradient of 1m/km for significant transport of 1.5-cm gravel and 0.5 m/km for incipient transport. Figure 6 shows a graphical solution for the uplift of LHR relative to the core site. With a gradient of 1 m/km, uplift is 7.5 m, and if this gradient is extended from the core site to the outlet, uplift of LHR relative to the outlet is 8.5 m. We acknowledge this paleo-river gradient is poorly constrained and only estimated at one site. Consideration of potential errors indicates that the gradient could have been as low as 0.5 m/km—a drop of 2.5 m over the 5-km outlet reach. This yields a minimum estimated uplift of LHR of 5.5 m relative to the outlet (fig. 6).

S-Meander and Rise of Lake ~9.7–8.6 ka

The "S-meander" is an abandoned (relict) set of meander bends of the Yellowstone River about 1–2 km north of the outlet (fig. 5). The downstream meander bend was partly filled with a sand bar or spit during a rise of Yellowstone Lake (Meyer and Locke, 1986; Locke and Meyer, 1994). LIDAR data and field measurements show this sand spit is offset 1.2–1.8 m by the Fishing Bridge fault (fig. 7). Data from the S-meander indicate that the former vigorous river at ~9.7 ka was converted to an arm of Yellowstone Lake by ~8.6 ka (fig. 4).

A trench in the S-meander on the east side of the river revealed buried charcoal resting on channel gravels, showing that drowning of the river was underway by 9 ka (fig. 8; table 1, nos. 17, 18, and 19). The full suite of landforms and dated river and shoreline deposits on both sides of the modern Yellowstone River imply the following sequence: (1) formation of the S-meander with river transport of 3-cm gravel and vigorous bank undercutting to produce steep scarps 15 m high, (2) loss of current and cessation of gravel transport and deposition of charcoal by 9 ka, (3) continued drowning until Yellowstone Lake rose into this area and cut the S3 shoreline into the meander scarp at 5.5 m above datum, perhaps at ~8.6 ka, (4) lowering of the lake about 2 m and cutting of the S2 shoreline at ~4.1 m above datum, dated nearby at ~8.1 ka, and (5) lowering of lake and river to levels below present-day level by 4–3 ka (fig. 4).

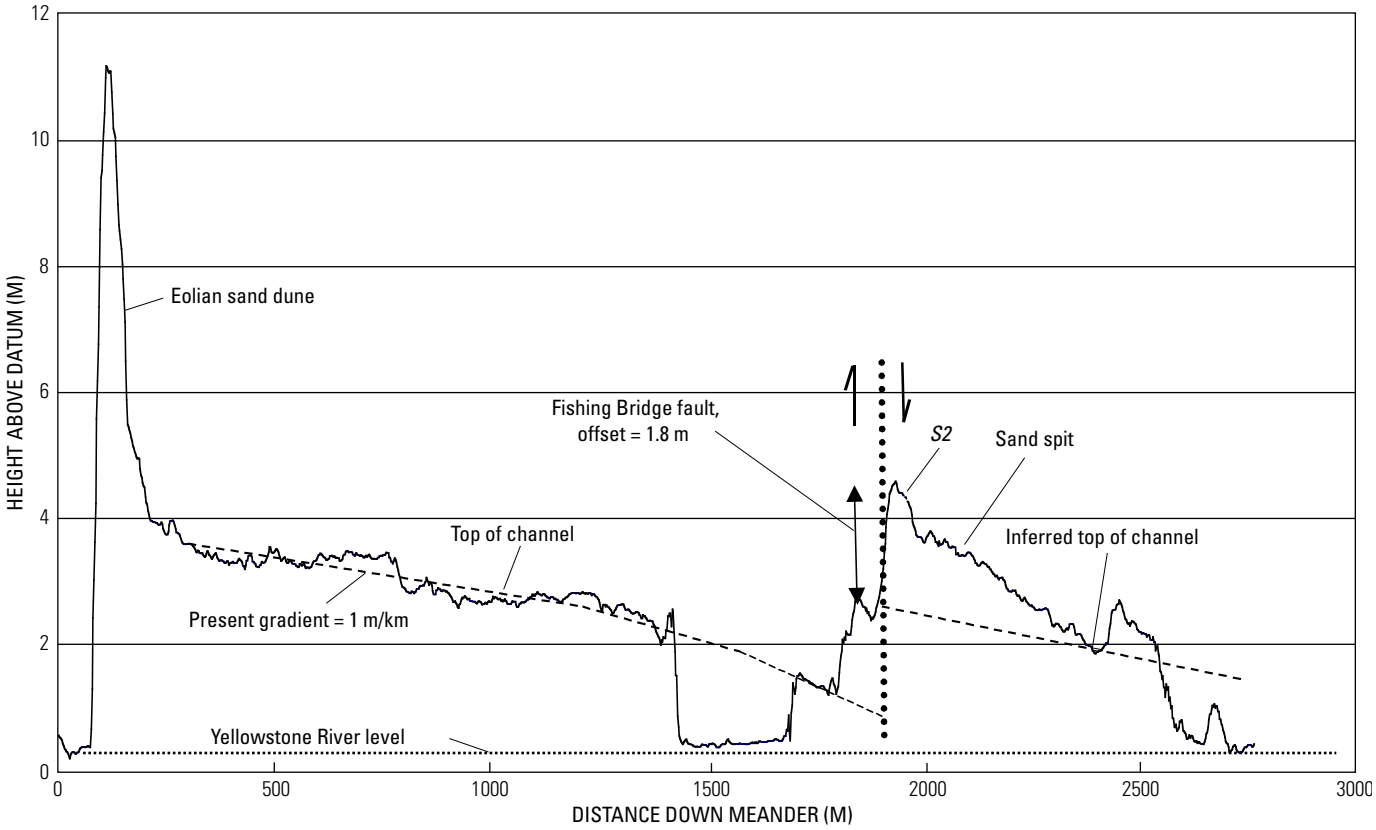

Figure 7. Profile section of the S-meander based on LIDAR data. Position of S-meander shown by line with single crosshatch in figure 5. The meander was drowned, starting by ~9.2 ka, and invaded by Yellowstone Lake, including the S2 sand spit, at ~ 8 ka. The Fishing Bridge fault has offset this sand spit ~1.8 m. The eolian sand dune filled the upper end of the S-meander when the present drowned channel was more active at about 3 ka (see fig. 5). The thalweg of the S-meander has a consistent gradient of about 1 m/km across its entire length except where it is offset by the Fishing Bridge fault. The S-meander thalweg now descends below the surface of the outlet reach at the downstream end of the S-meander.

The drowning of the S-meander is a remarkably similar sequence to the more recent drowning of the Yellowstone River reach, particularly the increase in water level to 4–5 m above channel gravels (compare figs. 6, 7, 8, and 9). We postulate that uplift centered on LHR is also responsible for drowning of the S-meander. A field estimate of the median gravel diameter in the S-meander is ~3 cm, twice that noted in the presently drowned channel that was active about 3 ka. A median diameter of 3 cm with a 1.5-m water depth yields a gradient of 1 m/km for incipient movement of pebbles and 2 m/km for significant transport of pebbles. We use the conservative 1m/km gradient in figure 9 because some coarser gravel may have been introduced into the stream channel from the high, adjacent cutbank in sandy gravel ("plsg," Pinedale lacustrine sandy gravel of Richmond, 1977). This 1m/km gradient yields uplift of LHR relative to the trench site of 7.3 m and 8.3 m relative to the outlet (fig. 9). If we use the 2 m/km gradient, then uplift of LHR relative to this S-meander site would be 11.3 m, and 13.3 m relative to the lake outlet. The S-meander is drowned at its downstream end by the present river, which may reflect a combination of uplift downstream by either warping or faulting, and drowning associated with post-3-ka uplift discussed earlier.

Subaerial Shoreline Sequence, ~8.0 ka S2 to ~14.4 ka S6

S2 Shoreline

Numerous ages on both sides of the outlet date the S2 shoreline (fig. 10) at about 8.0 ka (fig. 4). Directly in front of the Lake Lodge, lagoonal sediments between the wave-cut S2 shoreline and its barrier beach (now partly eroded) are exposed in the present wave-cut bluff. Two charcoal samples from the upper part of these diatomaceous sediments above crossbedded sands yielded ages of 8.0 ka (7,210±60 and 7,210±50 yr B.P.; table 1, nos. 14 and 15; fig. 4). Other samples from or above a humic soil that is below S2 and clearly postdates it, yield ages of 6.0, 5.5–5.3, 4.8–4.7, and 4.8–4.6 ka (~5,300, 4,710, 4,160, and 4,110 yr B.P.; table 1, nos. 10, 9, 8, and not numbered) and thus provide additional support for the surprisingly old age of ~8.0 ka for S2.

On the Fishing Bridge peninsula east of the outlet, a sample from beneath a 2-m-thick eolian sand mantling S2 yielded an age of 7.7–7.6 ka (6,800±90 yr B.P.; Cannon and

others, 1994, their fig. 40). Just east of this site, a terrace of Pelican Creek truncates S2. A sample from a paleochannel on this terrace yielded an age of 7.6 ka (6,740±90 yr B.P.; table 1). We infer an age here for S2 of ~8 ka or 0.4 k.y. older than this minimum age because following deposition of S2, (1) lake level lowered, and a wide terrace of Pelican Creek formed and eroded out S2, and (2) an active channel on this terrace was abandoned and then accumulated charcoal-bearing sediment about 7.6 ka. A mid-Holocene projectile point was collected from the surface of the S2 in the old campground loops D and E (Cannon and others, 1997, their fig. 41h). The eared and basally notched point is similar to those recovered from Layer 30 at Mummy Cave dated ~5 ka (4,420±150 yr B.P.; Husted and Edgar, 2002).

Southeast of Yellowstone Lake and 4 km upstream from the margin of the Yellowstone River delta is a terrace of an older delta with a prominent paleodistributary channel graded to ~7–8 m above datum (fig. 2). Local damming of this channel has facilitated accumulation of more than 2 m of organic-rich sediment. Wood from a depth of 2.15 m just above channel sands in this paleochannel is 7.8 ka (6,990±40 yr B.P.; table 1, part I). Trail Lake (fig. 2) is

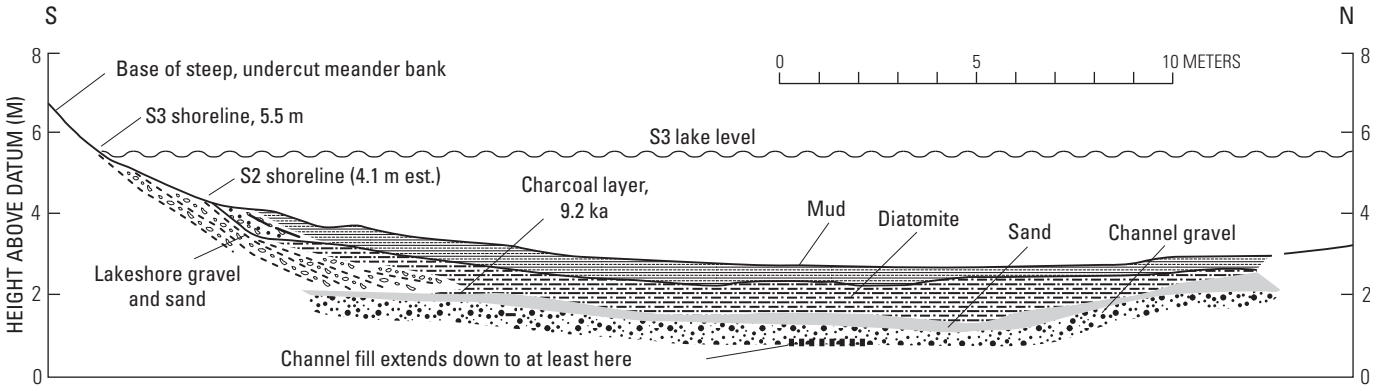

Figure 8. Cross section across the S-meander showing location of channel gravels, ~9.2-ka charcoal, and S3 (5.5 m) and S2 (4.1 m) shorelines. This section is based on four nearly connected trenches across the paleochannel labeled "trench" in figure 5.

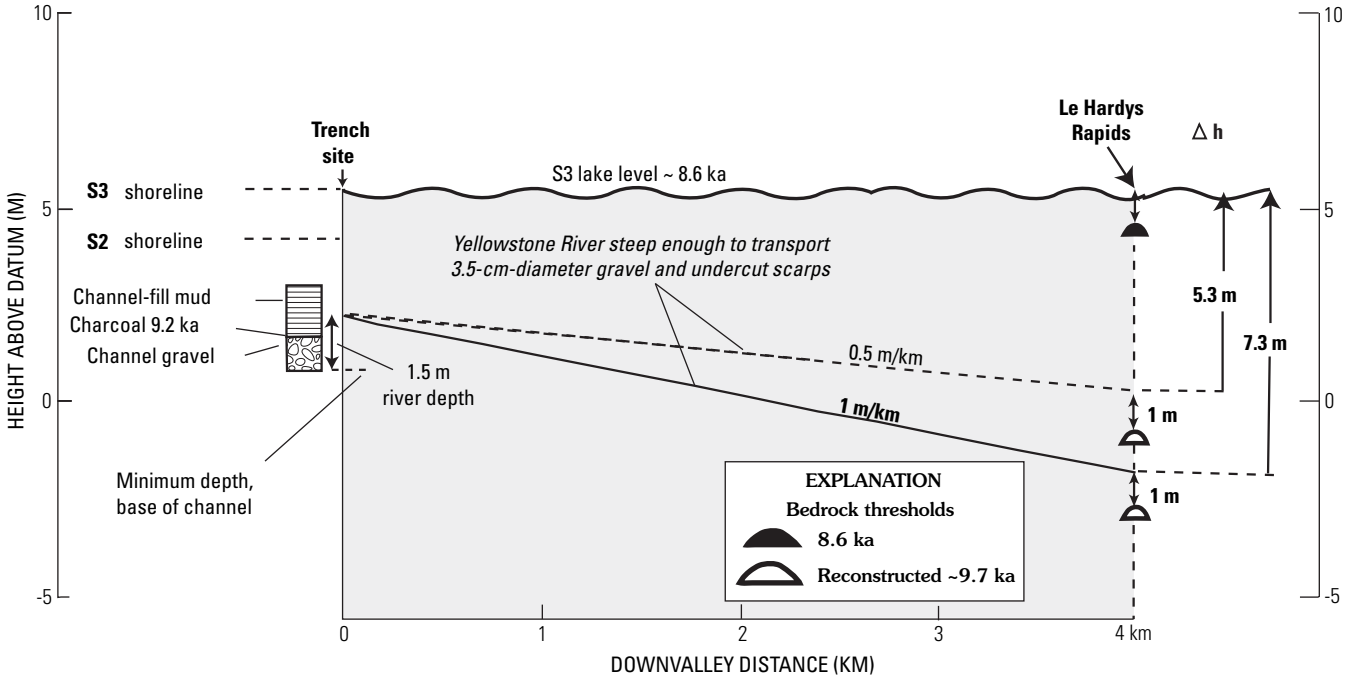

Figure 9. Comparison of outlet reach during S-meander time (~9.7 ka and gradient of 1m/km) with outlet reach during formation of S3 and S2 shorelines (8.6–8.0 ka). This diagram shows uplift of Le Hardys Rapids between ~9.7 and ~8.6 ka was about 7 m, similar to that between 3 ka and present (fig. 6). The S-meander was converted from a relatively vigorous stream carrying gravel and undercutting its steep banks (fig. 5) to an arm of Yellowstone Lake.

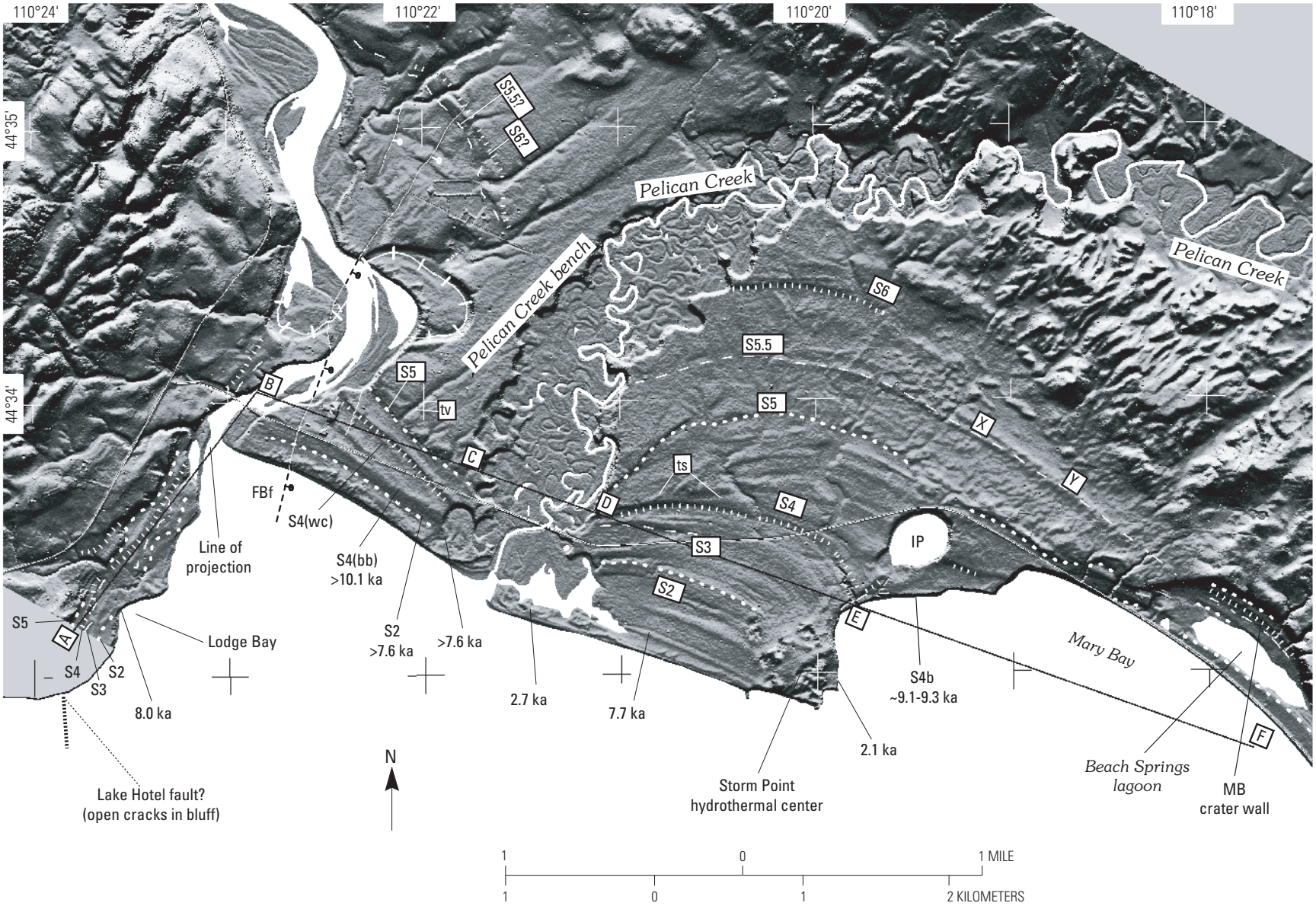

Figure 10. LIDAR image of the northern lakeshore area showing shorelines S2–S6 as well as unlabeled intermediate shorelines. Artificial illumination of LIDAR data from the north. Note surface texture of MB (Mary Bay explosion deposit) northeast of Mary Bay, which is profiled in figure 13 along S5.5 between X and Y. FBf, Fishing Bridge fault; IP, Indian Pond; MB, Mary Bay explosion; tv, truncated valley; ts, truncated shorelines. For S4 both barrier beach (bb) and wave cut (wc) shorelines locally identified, as well as a lower phase near Indian Pond (S4b). ABCDEF, line of projection for figure 12.

also dammed by this paleodelta. Basal ages from Trail Lake are 8.0 ka (7,215±70 yr B.P.; Cathy Whitlock, Montana State University, oral commun., 1999). These ages of 8.0 to 7.8 ka are essentially the same as those for the S2 shoreline in the outlet area. Thus, a delta at ~7–8 m above datum well outside the Yellowstone caldera has similar ages to the S2 shoreline 4–5 m above datum in the outlet area. This difference of 2–4 m over a distance of 34 km yields an overall tilt of only 0.06–0.1 m/km toward the caldera center.

S3 Shoreline

The S3 shoreline is mapped in the area from the Lake Lodge to the outlet and east of Pelican Creek (fig. 10), but is not well represented on the Fishing Bridge peninsula (Meyer and Locke, 1986). S2 and S3 are best represented in the S-meander by the tops of two small deltas at 5.5 m (S3) and 4.75 m (S2) above datum that were built into the S-meander by the drainage that comes from the area of the present sewage disposal plant (rectangular dikes shown on fig. 5). S3 is not readily recognizable and seems closely linked with S2, and is here locally referenced as S2/S3. Gravelly deposits at the approximate altitude of S3 do occur in the paleolagoon of the S4 shoreline on the Fishing Bridge peninsula. There, at an elevation of 4.75 m above datum, at a depth of 1 m, and just above well-sorted sands is charcoal with an age of 8.5– 8.2 ka (7,565±70 yr B.P.; Cannon and others, 1994, their fig. 14). Excavations by SUNY-Albany also produced two large side-notched projectile points from the inferred position of the S3 shoreline in the S4 Fishing Bridge paleolagoon (Reeve, 1989, his figs. 13h and 13i). One point is similar to the Blackwater side-notched projectile-point style recovered from Layer 16 in Mummy Cave and radiocarbon dated 9.0–8.0 ka (7,630±170 yr B.P.; Husted and Edgar, 2002). The depth of the S4 paleolagoon is such that in S3 time, and perhaps S2 time, Yellowstone Lake may have extended into the northern part of this lagoon.

S4 Shoreline

On the Fishing Bridge peninsula, a wave-cut shoreline and a barrier beach to the south, with an intervening paleolagoon, represent the S4 shoreline (fig. 10). The General Store at Fishing Bridge lies on the crest of the S4 barrier beach. In the old Fishing Bridge campground area, archeological excavations commonly exposed a meter or more of eolian sand overlying S4 barrier-beach pebbly sand. Charcoal ~10.2 ka (8,940±60 yr B.P.) was collected from 1.6-m depth in disturbed sediment filling the root void of a tree throw in beach gravel. Tree throw occurs when a tree topples to the ground and the tree roots pull up the material held by the roots and thus disturb any stratification present. The beach gravel is covered with 1.3 m of mixed material—mostly eolian sand (Cannon and others, 1994, their fig. 44).

Two Scottsbluff projectile points and one Cody knife all from the late paleo-indian Cody Cultural Complex have been found on the S4 barrier beach (fig. 11). Ages for the Cody Cultural Complex range from 10.6–9.7 ka (8,800–9,400 yr B.P.; Frison, 1991, his table 2.2) and support an age of ~10.7 ka for S4. Six additional late paleo-indian projectile points were recovered from excavations on the S4 surface on the Fishing Bridge peninsula. These stylistically variable projectile points conform to lanceolate-projectile-point styles of the Foothills-Mountains tradition that date between 10(?) and 8.8(?) ka (9,000 and 8,000 yr B.P.; Frison, 1992).

On the south shore of West Thumb, similar constraints for the age of S4 are found at the Osprey Beach archeological site (48YE409) 3 km east of Grant Village (fig. 2). A gravel bench at 6.4 m above datum extends back to a nearby wave-cut shoreline ~6.8 m above datum. At a nearby transect, Bill Locke (Montana State University, written commun., 2001, his profile Z54) places S4 at 7.0 m and S5 at 8.8 m above datum. Just above beach gravels and beneath 60 cm of non-bedded mixed material (pebbly sand of mostly eolian origin), charcoal is 10.7–10.3 ka (table 1). Cody Complex material was found in the basal part of the mixed zone just above the beach gravels, as well as in recently slumped material from the wave-cut cliff onto the modern beach below (Shortt, 2001). Cody Complex ages are from 10.6–9.7 ka (see discussion above for age). A Goshen (or Plainview?) point was also found 30 m back from the bluff (Don Blakeslee, Wichita University, written commun., map, 2002). Goshen (or Plainview?) points are perhaps 500 years older than the Cody Complex, or ~11.6 to 10 ka (Ann Johnson, National Park Service, oral commun., 2002). This may indicate a slightly older age for this shoreline than S4 in the Fishing Bridge area, although, because occupation of the shoreline occurs after its deposition, the ages also may be the same.

S5 Shoreline

We trace S5 along the north shore of Yellowstone Lake and along the present outlet reach of the Yellowstone River. LIDAR imagery (figs. 10 and 12) shows that S5 on the east side of Pelican Creek probably extends east to the shoreline that Meyer and Locke (1986) mapped as S6 near Mary Bay. The LIDAR imagery also shows a deposit with hummocky surface texture higher than and north of S5 with a relief of about 1 m over 50–100 m (fig. 13). We identify this as the large hydrothermal-explosion deposit from Mary Bay exposed on land and designate it as Mary Bay explosion deposit (MB). In the bluffs south of Indian Pond, MB overlies sandy lake sediment that contains charcoal at 2.6 m below MB that dates 13.4–11.3 ka (10,720±350 yr B.P.; Richmond, 1977). The sandy lake sediment grades downward into coarsely varved lake sediment that contains ash 4.6 m below MB. The ash contains a mixture of shards probably from the ash of Glacier Peak (layers B or G) apparently contaminated by reworked shards from a Yellowstone source (Andre Sarna-Wojcicki, written commun., 1999). Several dated localities place the age of

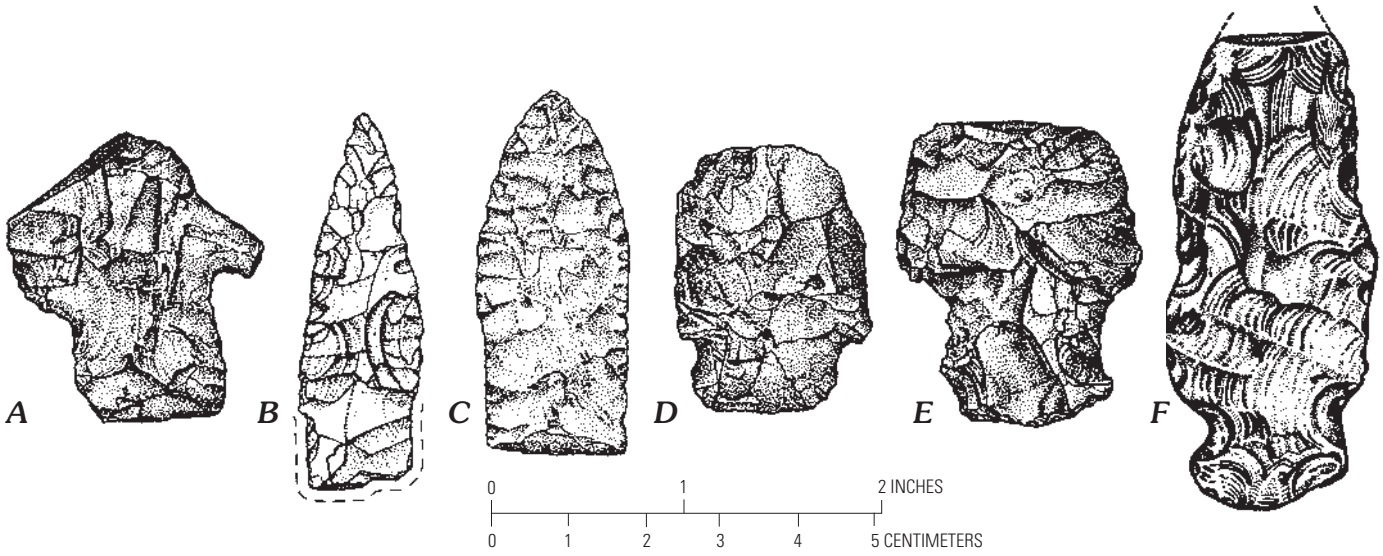

Figure 11. Drawings of projectile points from shorelines on the north shore of Yellowstone Lake. A Cody knife (A) and Scottsbluff projectile points of the Cody Complex (B, C) (~10.7–9.8 ka) were on S4 deposits on the Fishing Bridge peninsula. Projectile points D and E are late Pleistocene and early Holocene (~10,000–9,000 yr B.P.; ~11.3–10 ka) stemmed points similar in age to Cody Complex points from the S4 paleolagoon. F is a mid-Holocene side-notched point (~6,000–5,500 yr B.P.; ~7–6.4 ka) from the S2(?) barrier beach that encloses the Beach Springs lagoon (fig. 10). It had been weakly abraded by either wind blown sand or wave action.

the ash of Glacier Peak at between 14 and ~13.4 ka (table 1). In the Yellowstone–Grand Teton region, Whitlock (1993) obtained ages of 14.1–13.4 ka (12,100–11,450 yr B.P.) for a Glacier Peak ash (table 1). Although a Glacier Peak ash in west-central Montana has been dated as 13.2 ka (11,200 yr B.P.; table 1) (Mehringer and others, 1984), studies in west-central Idaho indicate an age older than 13.4 ka (11,510±70 yr B.P.; table 1) (Doerner and Carrara, 2001). Based on the charcoal and ash ages and assuming that the lake sediment accumulated rapidly, we estimate an age of ~13 ka for the MB hydrothermal-explosion deposits and ~12.6 ka for the S5 shoreline (fig. 4). The S5 shoreline is the highest shoreline eroded into the steep crater walls north of Mary Bay (fig. 12, Beach Spring area), which also shows that S5 formed soon after the MB explosion, as S5.5 is not found higher on the crater wall. The S5 shoreline is now tilted down toward the caldera axis (fig. 12). From 16–17 m above datum on the Mary Bay crater wall, the S5 shoreline descends to about 13 m above datum on the east side of the Fishing Bridge peninsula and descends to 9 m across the peninsula.

On the Fishing Bridge peninsula, the S5 shoreline truncates an extensive fill terrace of Pelican Creek (fig. 10, Pelican Creek bench). This terrace postdates S5.5 because this shoreline is not developed on the terrace but is present on both sides (figs. 5 and 10). A narrow valley of a small stream was eroded into this Pelican Creek terrace, but it abruptly terminates at the S5 shoreline (fig. 10). This incised valley and the Pelican Creek bench into which it is incised must have extended farther south to a lower lake level than the S5 shoreline. Lake level then rose (fig. 4), and bluff erosion by the S5 shoreline truncated the stream valley and Pelican Creek bench.

S5.5 Shoreline

The S5.5 shoreline is a double-crested barrier beach that extends from Mary Bay to Pelican Creek. Hydrothermal-explosion deposits from the MB event mantle the shoreline terrain of Mary Bay to within at least 1 km of Pelican Creek (fig. 10; see also fig. 13). This mantle extends from just above S5 across S5.5 to above S6. The S5.5 barrier beach shows up clearly through this mantle about 1 km east of Pelican Creek, where field measurements indicate that the explosion deposits are more than 1 m thick. Eastward toward the Mary Bay source, the MB explosion deposit thickens until it completely obscures the S5.5 barrier beach about 0.5 km west of the crater rim (fig. 10).

Shoreline S5.5 becomes totally obscured within 1 km of the valley of Pelican Creek (fig. 10), apparently by a diamicton locally exposed at the top of Pelican Creek banks. This diamicton may be distal MB or it may be explosion debris that came down Pelican Creek valley. The correlation of S5.5 is less certain west of Pelican Creek because S5.5 is eroded away or buried by the extensive gravel bench along Pelican Creek above the S5 shoreline on the Fishing Bridge peninsula. Northwest of this terrace, S5.5 may correlate to a possible wave-cut scarp east of the Yellowstone River that has a tilt subparallel to that of S5 (figs. 5, 10, and 12). An age for S5.5 of ~13.6 ka is estimated based on its position in the shoreline sequence and the mantle of S5.5 by MB deposits estimated to be ~13 ka based on relations to Glacier Peak ash and radiocarbon ages on insect parts (fig. 4).

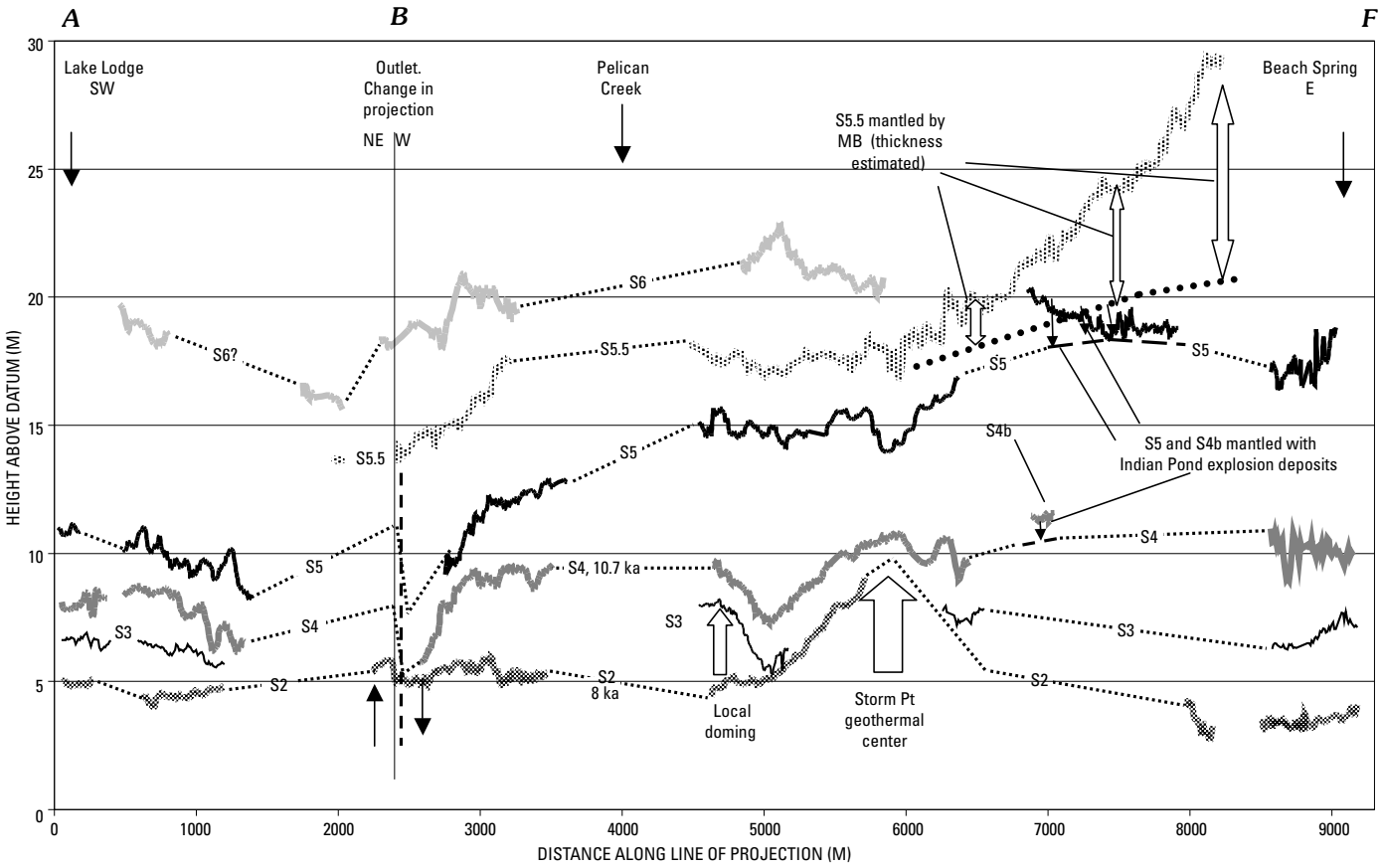

Figure 12. LIDAR profiles of northern Yellowstone Lake shorelines S2–S6. The LIDAR altitude of the mapped shorelines was projected at 10-m spacing onto line ABCDEF of figure 10. S2 is ~8.0 ka, S4 is ~10.7 ka, and S5 is ~12.6 ka. In the outlet area, there is a general sag at the Fishing Bridge fault. Westward from the Mary Bay crater wall at Beach Springs, the S5.5 shoreline is mantled with a decreasing thickness of MB (Mary Bay explosion deposits) (open arrow symbol). The S5 shoreline is mantled with Indian Pond explosion deposits whose thickness was measured at the position of the black arrows westward to where its thickness became too great. Note local doming associated with the Storm Point geothermal center and the smaller dome just east of Pelican Creek (open arrows).

S6 Shoreline

The S6 shoreline is best expressed just east of Pelican Creek with a well-defined 3-m-high wave-cut scarp (fig. 10). Farther east, a mantle of hydrothermal-explosion deposits obscures it. Assuming an age of about 13 ka for the MB explosion deposit that mantles both S6 and the next lower S5.5, we estimate that the age of S6 is ~14.5–14 ka.

Possible Lake-Level Culminations Near 4.5 and 2.5 ka

From the present (S1) time back to the recession from S2 about 8 ka, the northwest part of Yellowstone Lake has been near or below its present level. From 4–3 ka, lake and river levels were ~5–6 m below present, but several lines of evidence suggest the lake was near its present level (S1 shoreline) ~4.5 and ~2.5 ka (fig. 4). Thus, we find rationales for either a simple or more complex lake-level history between 6 ka and 1 ka (fig. 4). The possible culminations near 4.5 and 2.5 ka have some supporting data, but require rather rapid changes in lake level.

Behind the modern barrier beach just east of the mouth of Pelican Creek, charcoal, dated at 2.7 ka (2,550±60 yr B.P.; table 1, loc. 1, sample 94P33b), was collected at the base of 1.65 m of eolian sand, 25 cm above beach gravels. During or following deposition of these beach gravels ~1 m above datum, Pelican Creek entered the lake to the east of this site. It has subsequently established its inlet west of this site. Rising lake levels to the present shoreline would facilitate this change near 2.5 ka. In addition to the Pelican Creek site, the sandy part of the fine-grained section in the core from the drowned Yellowstone River (fig. 6) contains wood 2.37 m below datum with an age of 2.7 ka (2,518±100 yr B.P.; table 1, loc. 2), indicating a river level somewhat below present. In an adjacent core, an age of 2.7 ka (2,560±70 yr B.P.; table 1, loc. 3) indicates a maximum age for the sand and a time when the Yellowstone River was near its present level.

In the recently uplifted Storm Point geothermal center, slabby, openwork-platform gravels 3.43 m above datum contain charcoal dated at 2.1 ka (2,160±60 yr B.P.; table 1, section A, sample not numbered). This uplifted beach here is

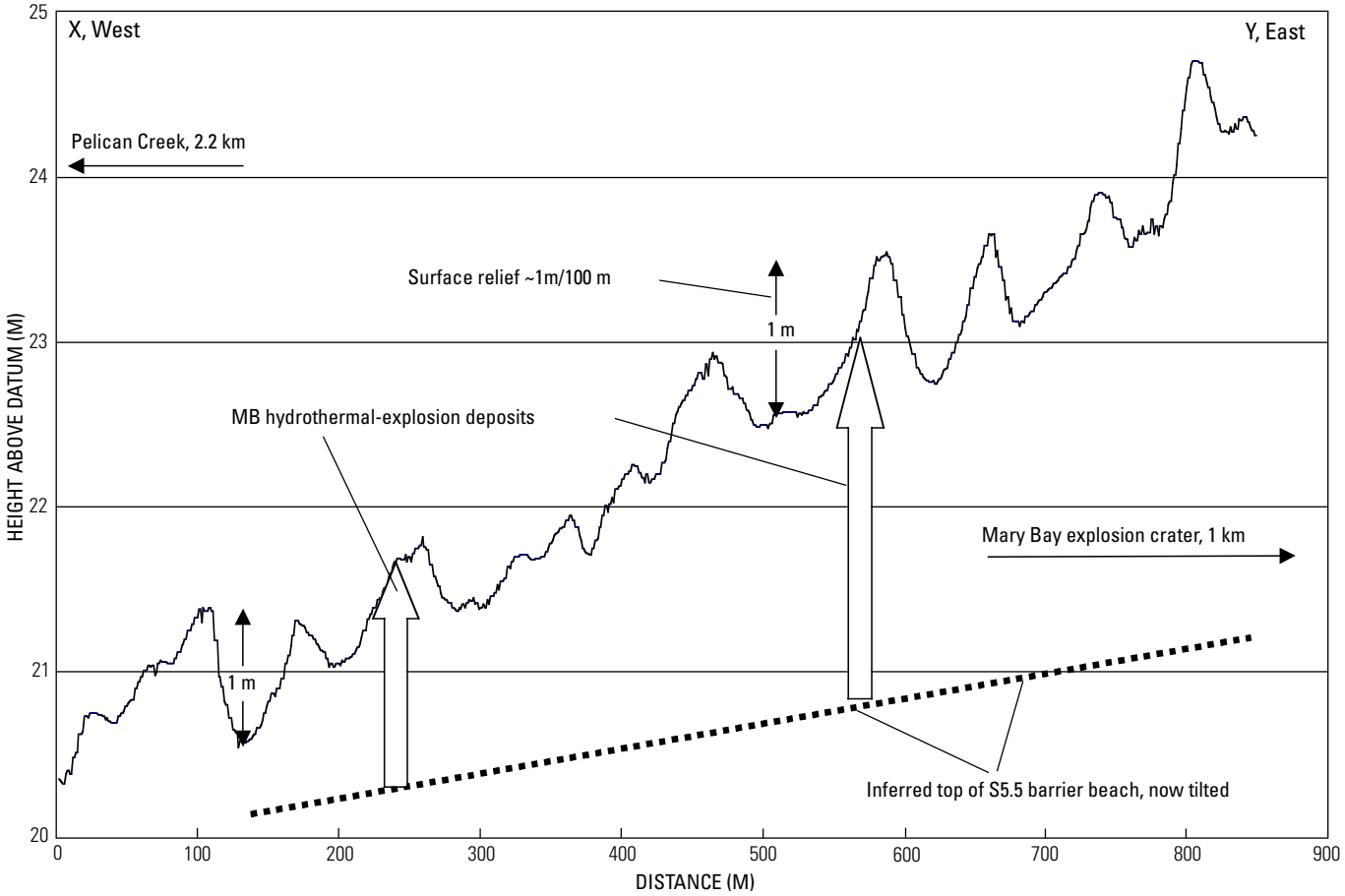

Figure 13. LIDAR profile along S5.5 barrier beach mantled by MB (Mary Bay hydrothermal-explosion deposits). Profile is on barrier beach between X and Y on figure 10. The barrier beach would be smooth (see figs. 14 and 15), but the explosion deposit has a surface texture with an amplitude of 1 m over a distance of 100 m. The increase in altitude to the east results from an increase in thickness of MB deposits, perhaps supplemented by tilting away from the source in the Mary Bay explosion crater.

distinct from the modern beach, S1, and also appears to indicate a culmination a little older than 2 ka.

About halfway from Lodge Point to the outlet, a relict barrier beach (fig. 5) with a clearly developed soil occurs at the same level as modern storm deposits, including that from high water of 1996 and 1997. The soil has a 12-cm-thick color B-horizon (10YR4/3, moist) and four, 1-cm-thick clay lamellae at depths between 12 and 35 cm, consistent with an age of several millennia. The soil is buried by 35 cm of modern beach deposits, particularly that of 1996 and 1997. A projectile point recovered from this beach in the collections of the Yellowstone Museum (no. FS-1911) is of the Hanna type. This Northern Plains projectile-point style was originally defined by Wheeler (1954) and represents a Middle Archaic index artifact dating between 4,500 and 2,800 yr B.P. (Greiser, 1986), suggesting a calibrated age in the 4±1 ka range (fig. 4, projectile point symbol at ~4.1 ka).

In eastern Mary Bay north of Holmes Point, a shoreline 1 m above modern high water has a tree cover, significant soil development, and artifacts of obsidian flakes, all indicating a lake level just above that of the present. This shoreline is several thousand years old but is younger than 8 ka.

Summary of Postglacial Lake-Level Chronology

Figure 4 plots the history of Yellowstone Lake and Yellowstone River level changes in the northern Yellowstone Lake area over the last ~15,000 yr. Both S5.5 and S6 are older than the ~13-ka MB explosion deposit and are estimated to be 13.6 and 14.4 ka, respectively. Shorelines S6 and S5.5 are younger than deglaciation of the ice cap on the Yellowstone Lake and Yellowstone Plateau area. Above the Yellowstone delta area (fig. 2), Richmond and Pierce (1972) note that a very prominent ~18- to 20-m shoreline at Beaverdam Creek correlates by outwash relations with late Pinedale mountain-valley glaciation, somewhat younger than an age of 16.3–14.7 ka (13,140±700 yr B.P.; Richmond and Pierce, 1972, their section 14; Porter and others, 1983, their table 4–7, locality E). Locke and Meyer (1994, their fig. 4), however, surveyed the shoreline elevation at this locality to 27.6 m above datum and correlated it with their S9 shoreline. We note that S7 of Locke and Meyer (1994) in the Southeast Arm may correlate with S5 in the northern Yellowstone area because the LIDAR imagery shows that S5 adjacent to Pelican Creek traces to S7 of Locke and Meyer (1994) near Mary Bay.

Table 2. Submerged lake and river levels and their normalization to the outlet.

[Δh is change in height; #2, #7, and so forth is the numerical value listed in the row with that number in this table]

	Location	Le Hardy Rapids (LHR)	Drowned channel to outlet	Bridge Bay	Little Thumb Cr.-North
			1923–1975 parameters		
1.	1923–1975 uplift	800 mm	600 mm	470 mm	460 mm
2.	Δh to LHR (1923–1976)	0	200 mm	330 mm	340 mm
3.	Δh site/Δh at outlet	---	1×	1.65×	1.70×
4.	#2/Δh-LHR (% total)	0%	25%	41%	43%
			Old submerged sites		
5.	A. Age (yr B.P.)		2,750	3,560±60	2,880±60
	B. Corrected age (yr)		2,848	3,835	2,970
6.	Depth below datum			3.43 m	4.3 m
7.	Depth below S1 (present lake) (1.8 m+#6)			5.2 m	6.1 m
8.	#7/#3 (normalized to outlet)			3.2 m	3.6 m
9.	*Total Δh to LHR = #7+5m*[1]		*(8.5 m)*[2]	*10.2*	*11.1m*
10.	**Normalized to outlet, Δh to LHR, #8+5m**[1]		**(8.5 m)**[2]	**8.2 m**	**8.6 m**
11.	Net rate to present between site and LHR, (#10/#5B)		3.0 mm/yr	2.7 mm/yr	3.9 mm/yr
12.	Rate (1923–1975), site to LHR (#2/52 yr)		3.9 mm/yr	6.3 mm/yr	6.5 mm/yr

[1] Paleoriver drop of 5 m from the outlet to Le Hardy Rapids (LHR) based gradient of 1m/km.
[2] Estimated uplift as shown in figure 6.

Radiocarbon ages from the Yellowstone Lake area suggest that deglaciation had occurred by 16.2 ka (>14,000 yr B.P.; Porter and others, 1983; Whitlock, 1993; Pierce, 2003). At the time of the Deckard Flats readjustment, the ice cap on the Yellowstone Plateau had greatly receded but was probably still present (Pierce, 1979; Sturchio and others, 1994). The radiocarbon chronology of deglaciation is several thousand years older than that produced by cosmogenic surface-exposure dating that places the Deckard Flats readjustment at ~13.8±0.4 ka (Licciardi and others, 2001). We cannot resolve why cosmogenic ages are younger than radiocarbon ages, but we suggest either one or both dating systems may be in error.

S5 is estimated to be ~12.6 ka because it is bracketed as younger than the ~13-ka MB explosion deposit and older than the ~10.7-ka S4 (fig. 4). S4 was constructed about 10.7 ka, as dated by Cody Complex projectile points and a ^{14}C age. Subsequent formation of the S-meander indicates a relatively low lake level about 2 m above the present level at ~9.5 ka. S3 is incompletely preserved and is not well dated but was formed after initial drowning of the S-meander and before formation of S2. S2 is the best dated shoreline at ~8.0 ka based on multiple ages on both sides of the outlet.

After formation of the ~8-ka S2 shoreline, lake levels have been below or near the present level (fig. 4). Lake level was ~4 m below datum from 4–3 ka. Two options are shown for lake levels immediately before and after 4–3 ka (fig. 4): (1) a gradual lowering to 4–3-ka levels followed by a gradual increase to present lake level and (2) possible culminations near the present level ~4.5 ka and ~2.5 ka that bracket low levels between 4 and 3 ka and also define lake-level lows before ~4.6 ka and after 2.2 ka. Both options are shown (fig. 3) with question marks because present information may be interpreted to favor either option. Either option after ~2 ka is consistent with the historic rise of LHR relative to the outlet at a rate of about 4 mm/yr (fig. 4).

Uplift of Le Hardys Rapids Indicated by Submerged Localities

Table 2 shows calculations of the uplift of Le Hardys Rapids relative to sites in the lake as well as at the outlet by normalizing localities to the outlet based on the 1923–1976 uplift dimensions. These calculations indicate between 8 and 9 m of uplift of the Le Hardys Rapids relative to the outlet following the lowstand 4–3 ka (table 2, line 10). Uplift of LHR relative to the Bridge Bay and Little Thumb Creek North sites is calculated to be 10.2 and 11.1 m, respectively (table 2, line 9). Normalization of these sites to the outlet based on the 1923–1976 uplift pattern yields values of 8.2 and 8.6 m, similar to the 8.5 m calculated for the outlet (fig. 6). From the lowstand at 4–3 ka to the present, the net rate of uplift is less than the historic rate from 1923–1975 (table 2, compare lines 11 and 12), although this does not consider a possible highstand near 2 ka and possible submergence after that, as shown by the second option in figure 4. Historic uplift or subsidence of LHR relative to the outlet is only about one-quarter of the total uplift and subsidence relative to the areas beyond the caldera margin (figs. 1 and 3). These rates of ~3–4 mm/yr, if extended to the caldera margin and multiplied by 4, would be 12–16 mm/yr. This is within the range of 16 mm/yr for the 1923–1985 uplift as well as for other calderas such as Campi Flegrei, Italy, where rates of 10–20 mm/yr have been observed

Table 3. Offsets on the Fishing Bridge fault and associated elevation change across the Fishing Bridge peninsula (fig. 5) based on offset shorelines, elevation change due to tilt of shorelines into the fault, and shoreline projections shown in figure 14.

Shoreline/age	Height above datum (m)	Elevation change[1] (m)	Total offset (m)	Offset/elevation change (%)	Interval offset (m)
S2/8.0 ka	6	0.8	0.5	63	0.5
*S4*bb/10.7 ka (bb, barrier beach)	9	1.8	1.0	55	0.5(?)
*S4*wc/10.7 ka (wc, wave-cut)	9	~4.8	~2.9[2]–3.2[3]	60[2]	1.9–2.2
S5/12.6 ka	12	~6.7	~4.0[2]–5.5[3]	60[2]	1.1–2.3

[1]Elevation change across Fishing Bridge peninsula to Fishing Bridge fault.
[2]Based on fault offset being 60 percent of elevation change as averaged from S2 and S4bb.
[3]Offset based on projection of S4wc and S5 across fault as shown in figure 14.

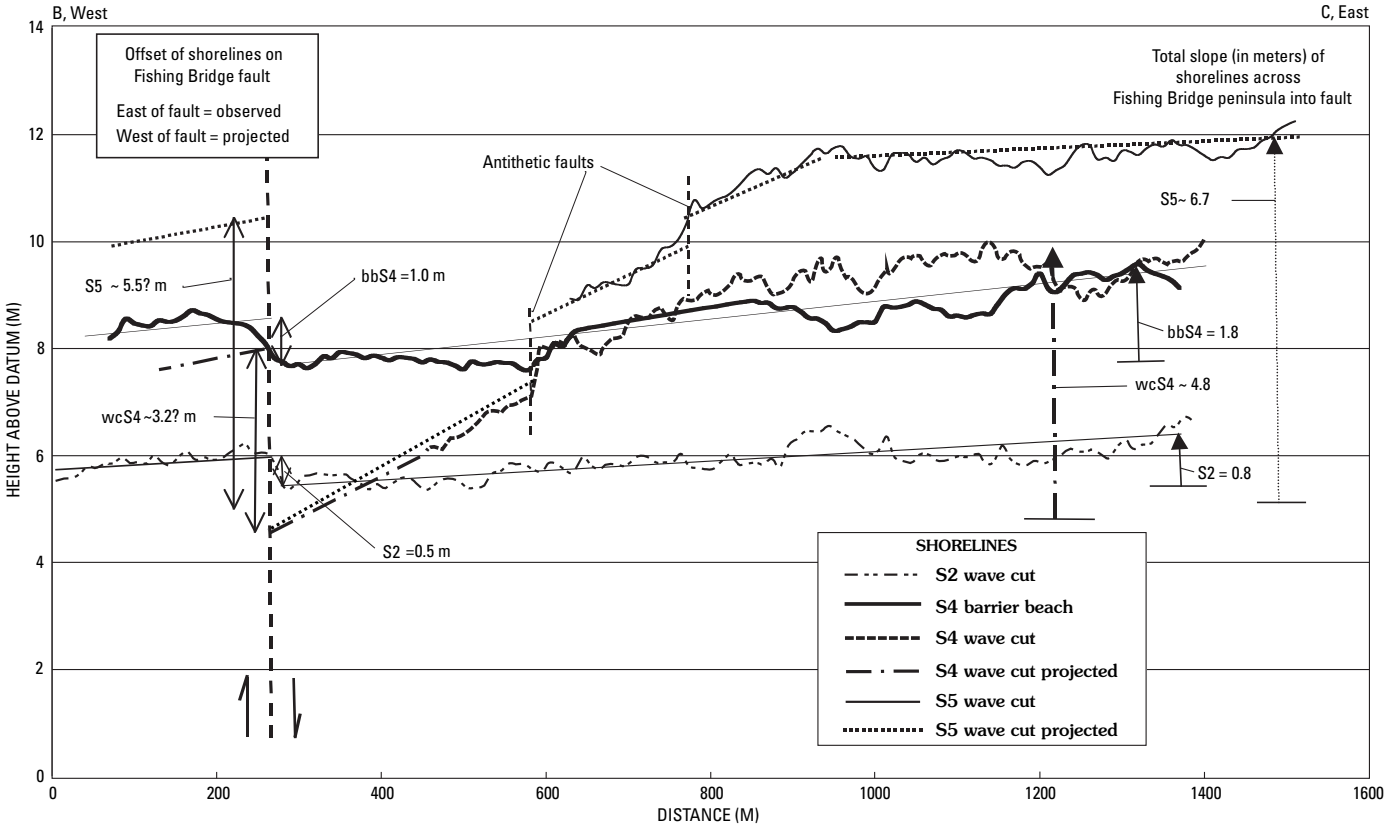

Figure 14. LIDAR profiles showing faulting and tilting of shorelines across the Fishing Bridge peninsula. Location is along line of projection between B and C on figure 10. Four shoreline profiles indicate increased deformation from S2 to S5 time (see table 3). The fault does not cross the S4 or S5 shorelines, but the shorelines show increasing tilt toward the fault with age. S2 is offset 0.5 m. The S4 barrier beach (bbS4) is faulted 1 m, but slightly older wave-cut S4 (wcS4) is projected to be offset ~3.2 m suggesting about 2 m of offset during S4 time (see text).

over millennial time scales (Dvorak and Mastrolorenzo, 1991). In a compilation of data for more than 100 calderas worldwide showing signs of unrest, Newhall and Dzurisin (1988) found rates of uplift and subsidence of tens of millimeters to greater than 100 mm/yr.

Faulting

Late Quaternary faulting has broken many parts of the Yellowstone Plateau, especially outside of the caldera, but locally within it as well (Christiansen, 2001; Machette and others, 2001). Because of high thermal gradients and shallow young intrusions within the caldera, the brittle-ductile transition may lie at a depth of only 3–5 km, limiting faulting to shallow crustal levels. Compared to sites where the brittle-ductile transition is about 15 km deep, maximum earthquakes are of lesser magnitude (Smith and Braille, 1993). In contrast to the large subsided half-graben basins and uplifted blocks of adjacent Basin-and-Range terrain (for example, Jackson Hole and the Teton Range), normal-fault systems in the caldera have little net offset and commonly form grabens and fissure-like structures.

The Elephant Back fissure system, the most prominent set of young faults within the caldera, strikes northeasterly from the Sour Creek resurgent dome to east of the Mallard Lake dome (fig. 1). This fissure zone is nearly parallel to the caldera long axis and also forms the axis of historical uplift and subsidence. The fissures of the Elephant Back system may result from general extension or from fracturing associated with localized uplift and subsidence along the caldera axis. These young faults cut the 150-ka Elephant Back flow, but leveling resurveys of benchmarks across the northeast end of the Elephant Back zone show no apparent steps or offsets suggesting structural changes since the first survey in 1923 (Dzurisin and others, 1994; Dan Dzurisin, oral commun., 1995).

LIDAR imagery reveals a fault that offsets postglacial surfaces across the west tip of the Fishing Bridge peninsula and extends 3 km to the NNE (fig. 5). Figure 14 shows local shoreline profiles, shoreline tilts, and fault offset, which are tabulated in table 3. Only shorelines S2 and the barrier beach of S4 are preserved actually crossing the fault. S2 and the S4 barrier beach at the east end of the Fishing Bridge peninsula are higher than their upfaulted remnant at the west end of the peninsula (fig. 14), although farther eastward S2 and S4 are horizontal (figs. 12 and 14). The ratio of fault offset to total shoreline-elevation change across the Fishing Bridge peninsula produced by tilting into the fault is about 60 percent (table 3, S2 and S4bb). Two methods were used to estimate offset of wave-cut S4 and S5 that do not cross the fault. One is based on the fault offset equaling 60 percent of the tilt into the fault (table 3). The other method was a visual projection of the shoreline across the fault (fig. 14) consistent with the shoreline west of the fault (fig. 12). Table 3 outlines the sequence of tilting and surface-offset faulting events.

We infer that a faulting event occurred between erosion of the S4 wave-cut shoreline and construction of the S4 barrier beach on the Fishing Bridge peninsula. Faulting and subsidence of the hanging wall apparently submerged the west end of the wave-cut S4 shoreline. Longshore drift of sediment from Pelican Creek then prograded a barrier beach across the south side of the drowned area to form a lagoon. Because the strongly tilted S4 wave-cut shoreline and much less tilted S4 barrier beach are at the same elevation on the east side the Fishing Bridge peninsula (east side of fig. 14), lake level did not change significantly before construction of the barrier beach, and faulting did not affect the lake outlet level. The S4 interval is the only time during the period of shoreline-terrace formation that a barrier beach and lagoon existed on the Fishing Bridge peninsula. This relationship also links the time of tilting and offset with barrier beach and lagoon formation.

Features in the area of the S-meander are also offset by the Fishing Bridge fault (figs. 5 and 7). A S2 sand spit built across the S-meander is offset 1.8 m (fig. 7). The higher bench just south of and older than the S-meander is offset 1.2 m (fig. 5), indicating no increase in offset going back to at least the ~9.7-ka age of the S-meander. Figure 7 shows that the gradient of the channel of the S-meander is ~1 m/km along most of the meander. No other fault strands offset the wide belt occupied by the S-meander. Farther north, a Yellowstone River terrace that predates the S-meander is offset 1.5–1.8 m by the Fishing Bridge fault (fig. 5). The fault continues northward with surface offsets of 1 m or less and dies out above the S6 shoreline. Surfaces older than the ~9.7-ka S-meander on both sides of the Yellowstone River are offset less than 2 m.

An ~1-km-wide graben is located on the floor of Yellowstone Lake 0.5 km southeast of the Lake Hotel (fig. 2). Seismic reflection profiles by Otis and others (1977) first revealed this graben, and Kaplinski (1991) mapped it in greater detail. Because of its potential involvement in shoreline deformation, Locke and Meyer (1994) termed this structure the Outlet graben. However, recent detailed mapping with GPS control (Morgan and others, 2003 and this volume; Johnson and others, 2003) shows that it is about 1 km west of where originally mapped and has a more northwesterly strike. The primary fault on the west side of the graben strikes about N. 10° W. from the north end of Stevenson Island (figs. 2 and 10). Because it does not appear to intercept the outlet, we call this fault the Lake Hotel fault. No faulting of shorelines has been observed in the Lodge Bay area, but, along the lakeshore in Lodge Bay directly below the General Store parking lot (fig. 10), vertical fractures with 10- to 20-cm openings in compact “lacustrine till” suggest extensional deformation, possibly due to lateral spread. Directly above these fractures, S5 platform gravels at 10–11 m above datum are not offset. Farther north along this trend, the Lake Hotel fault may extend onshore to a prominent escarpment behind the Lake Lodge and continues northward to the outlet area. No evidence of offset of surface sediments has been observed in the field or with LIDAR data, however, and the S5 barrier beach adjoins this escarpment but is not offset (fig. 5). Therefore, any fault offset on this escarpment is older than S5, and in S5 time this was a wave-cut cliff.

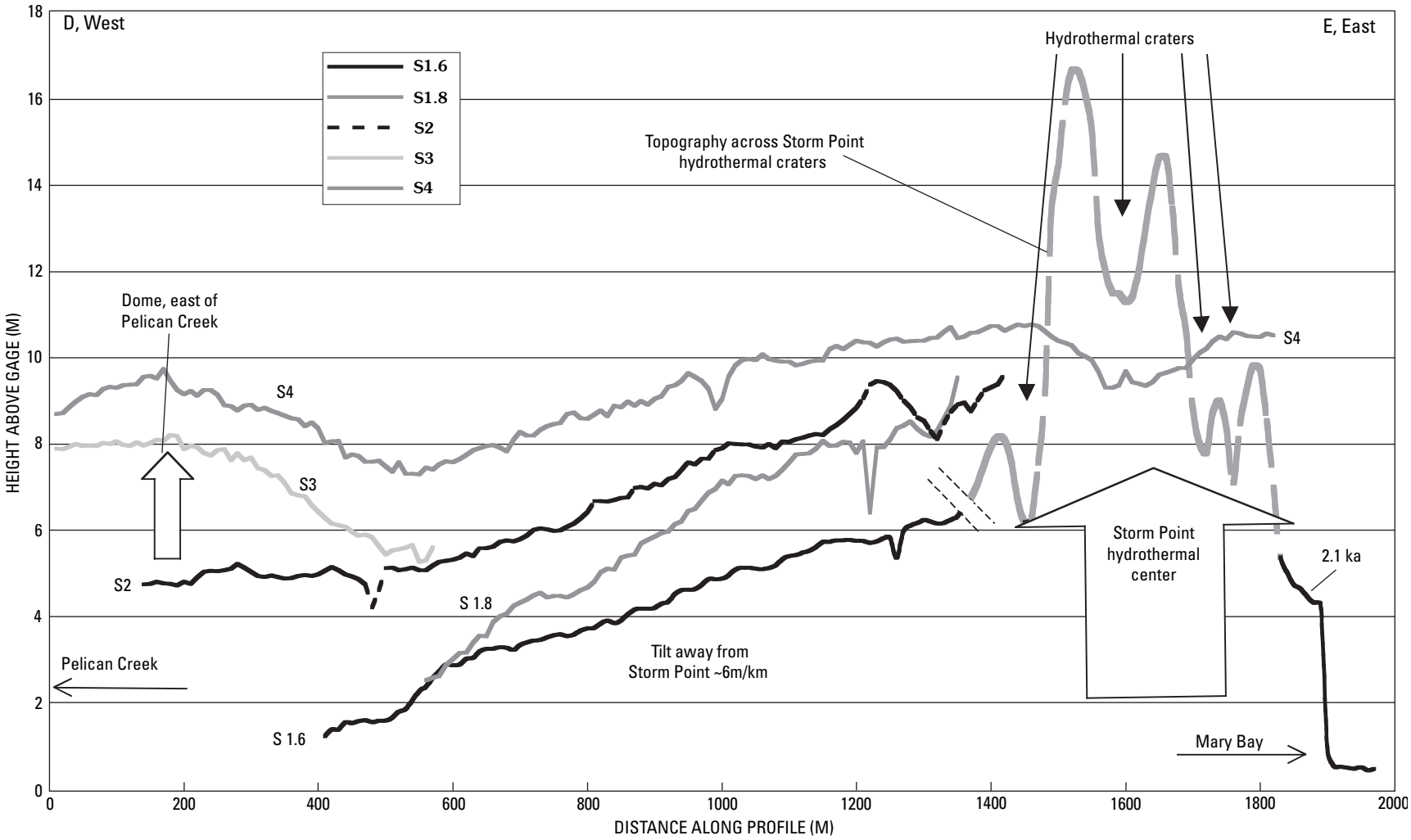

Figure 15. LIDAR profiles of S4, S2, and two younger shorelines (S1.8 and S1.6) from the Storm Point geothermal center west nearly to Pelican Creek. Location is along line of projection between D and E on figure 10. The shorelines rise as steeply as 6m/km to the Storm Point geothermal center. A local anticline interrupts this westward tilt and is well shown by S4 and S3 just west of Pelican Creek. East of 1,400 m, the dashed broad gray line is a topographic profile that shows the craters of the Storm Point hydrothermal center.

Local Deformation of Shorelines

LIDAR data define strong local tilting away from the Storm Point geothermal center (fig. 15). The shorelines that intersect the center (S2, S1.8, and S1.6) show steep subparallel tilts of as much as 6 m/km. The shorelines that skirt north of the center show lesser tilting; S4 shows a gentle 4-m-high dome, and S5 is apparently not affected. This tilting resembles Holocene bulges on the floor of Yellowstone Lake inferred to be related to hydrothermal pressures (Morgan and others, 2003 and this volume; Johnson and others, 2003).

A local dome just east of Pelican Creek has about 3 m of relief in S3 and S4 (fig. 15). Shorelines on the east limb of the dome form a sharp syncline with the shorelines tilted away from the Storm Point hydrothermal center (figs. 10, 12, and 15). We have observed no hydrothermal features or faulting in the immediate vicinity, but this dome may imply subsurface pressure buildup and merits additional investigation to understand the cause of deformation and any associated hazard. South of the dome, the beach sands on the shore of Yellowstone Lake are hot at a shallow depth and are the site of a rare thermophilic(?) sand verbena, *Abronia ammophila* (Whipple, 2001). In February of 2004, water vapor indicated heat just offshore of this beach. This may reflect hydrothermal processes associated with the anticline.

Discussion

The pattern of both rises and falls of lake level (fig. 4) combined with the historically observed inflation and deflation suggests intriguing volcanic, hydrothermal, and (or) other processes may be involved. Table 4 outlines the many processes for changing Yellowstone Lake and Yellowstone River levels. In the following, we discuss most of these processes emphasizing those most relevant to our study. We attribute the overall decrease in lake level observed during the first half of the record to lowering of the outlet by a combination of erosion and subsidence. We suggest that a millennial-scale oscillation occurred combined with an overall lowering of lake and river levels during the first

Table 4. Processes for decreases, increases, and oscillations in Yellowstone Lake and Yellowstone River levels in postglacial time.

[The pattern of historic changes and the present drowned "outlet reach" of the Yellowstone River suggest that changes in the altitude of Le Hardy Rapids are important. Processes in italics are discussed only in this table]

Change and process	Comments
I. Decrease in lake level	
A. Glacial damming	A. During glacial recession, glaciers from Beartooth uplift dammed lakes in Yellowstone Lake-Hayden Valley area, particularly above S6 level.
B. Outlet erosion	B. At Le Hardy Rapids, very resistant threshold formed by 1–3 m ledge with interlocking micro-spherulites near base of Lava Creek Tuff. Much more erodible units above and below.
C. *Magmatic cooling*	C. *Contraction due to cooling of batholith beneath Yellowstone caldera. Subsidence estimated to be 0.6–0.7 mm/yr by Fournier and Pitt (1985).*
D. Tectonic stretching	D. Crustal thinning and downwarping above magma chamber and other ductile material.
E. Yellowstone Lake ceasing to overflow	E. A greater-than-likely drying of climate because loss from lake now about 15 percent by evaporation and 85 percent by overflow.
II. Increase in lake level	
A. Magma intrusion and inflation	A. Magma and associated heat are probably being added from hotspot source. Magma likely to be permanent volumetric addition to caldera unless intruded radially to outside caldera.
B. Tectonic compression	B. Local compression, particularly squeezing of a ductile magma chamber, could produce doming.
III. Possible increases or decreases in lake level	
A. Faulting	A. Faulting of appropriate magnitude and timing not apparent. Overall sag of shorelines and offset on Fishing Bridge fault noted in outlet area.
B. Glacial-isostatic rebound	B. Glacial load nearly uniform over Yellowstone Lake basin producing even uplift. Rebound fast and mostly during deglaciation because brittle-ductile transition is shallow in caldera.
IV. Oscillations in lake level	
A. Geothermal inflation and deflation	A. Geothermal sealing, pressure buildup, and inflation followed by rupture of seal, release of geothermal fluids, and deflation. A cycle produces no net change in lake level consistent with paleoshorelines not rising toward caldera center.
B. Combinations from any of the above (I, II, and III)	B. For increase, magna intrusion (II-A) is plausible. For decrease, tectonic stretching (II-D) is plausible.

half of this record, and this oscillation is the primary cause of lake level changes during the second half of this record (fig. 4). We suggest that this millennial-scale oscillation in lake levels, in part, reflects caldera-wide inflation and deflation similar to that recognized from releveling surveys and radar-interferometry studies. Our radiocarbon and archeologically dated history (fig. 4) provides a temporal scale two orders of magnitude longer than the historic studies. New observations of faulting and local shoreline deformation are based on LIDAR data. In addition to investigating the processes responsible for lake-level change, the history itself provides a framework for archeology, including possible human habitation of both subaerial and now-submerged shorelines.

A rising water level greatly enhances landward erosion and the development of wave-cut shorelines, a process described by the Bruun rule (Bruun, 1988; Schwartz, 1987). The better developed shorelines (S1 to S6 and higher) recognized by Meyer and Locke (1986) and Locke and Meyer (1994) appear to have been developed under rising lake conditions, as suggested by the Bruun rule and as discussed for the history of each shoreline in this report.

Decreases in Lake Level

Holocene Outlet Erosion and Pleistocene Glacial Damming (I-A and 1-B in Table 4)

Above ~20 m at LHR, the Yellowstone River appears to have been downcutting mostly through unconsolidated glacial and alluvial material. Farther north in Hayden Valley, Richmond (1977) maps ice-dammed lake sediments of Pinedale age (pkl) to 2,375 m and locally to 2,390 m (~20 m locally to 33 m above datum; LHR is ~1 m below datum). Thus Yellowstone Lake levels from ~20 m above datum and higher, or above S6, may have been dammed by recessional glaciers from the

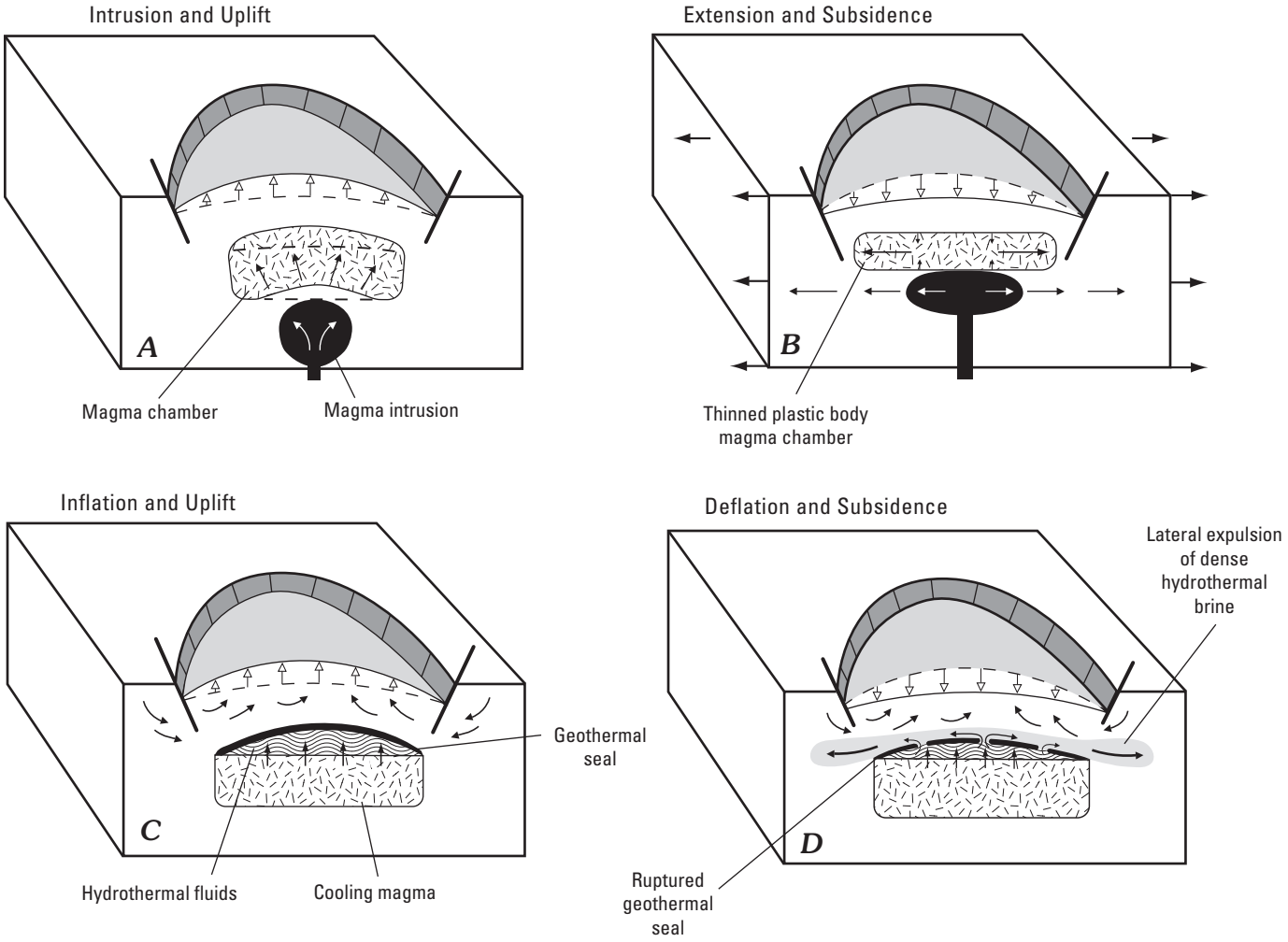

Figure 16. Diagrams showing mechanisms for inflation and deflation of Yellowstone caldera. Only some mechanisms are diagrammed. (A) Intrusion of magma and uplift. (B) Extension of crust and contained magma body resulting in subsidence above magma body. (C) Geothermal pressure buildup below seal and uplift. (D) Geothermal pressure release with rupture of seal and deflation accompanied by deep outward movement of dense fluids. Diagrams C and D are after Fournier (written commun., 1997).

Beartooth uplift during Deckard Flats and younger times (Pierce, 1979).

Figure 4 shows a pattern of oscillating lake levels with a net lowering from ~20 m above datum for S6 at ~14.4 ka to about the present lake level at S-meander time (~10 ka). Assuming LHR has returned to the same vertical position for each shoreline, erosion of LHR at ~5 m/k.y. is indicated from 14.4 to 10 ka. Conversely, the change in shoreline levels may have been accompanied either by (1) tectonic sagging of LHR, in which case the rate of erosion would be less, or (2) net uplift of LHR, in which case the rate of erosion would be greater. Our correlations of shorelines from Fishing Bridge to the Mary Bay area are based on new LIDAR data and indicate a pronounced sagging; notably, S5 sags from ~18 m to ~10 m above datum from Mary Bay to the outlet.

Figure 4 also shows that, after 10 ka, lake levels have oscillated but with no clear trend. Hamilton and Bailey (1990, their fig. 3) draw a bedrock threshold at LHR 5 m above datum. Bedrock is locally mapped to 20 m above datum on the west side of LHR (Christiansen and Blank, 1975). An erosionally resistant zone near the base of the Lava Creek Tuff forms the bedrock ledge of Le Hardys Rapids (R.L. Christiansen, oral commun., 2002). This little-fractured, ~1- to 3-m-thick devitrified zone is composed largely of interlocking microspherulites 1–3 mm across, making it quite resistant to erosion. Above this spherulite zone is a devitrified zone with joints on a decimeter scale that is more readily eroded. Below the spherulite zone, the Yellowstone River will next encounter the basal vitrophyre that is also much more fractured and also will be more readily eroded. The resistant bedrock zone appears to have been base level for the Yellowstone River for a considerable time, perhaps all of Holocene time. The ~3-ka gravel channel of the outlet reach is now below the level of this bedrock threshold. The 9.7-ka S-meander channel is drowned at its downstream end and thus projects at or below this bedrock threshold, suggesting little erosion of LHR over this time interval. The shorelines also show general sagging toward the outlet area (fig. 12) and thus toward the central part of the caldera (fig. 1), however, so some of the low altitude of the ~9.7-ka S-meander channel is probably from this sagging. The erosion rate of the bedrock threshold at LHR over the last 10 k.y. must be low in any case, as would be expected given the low bed-load transport rate at LHR. Bed-load supply in the outlet reach is limited to sand and fine gravel supplied by bank erosion and material carried to the outlet by longshore wave transport.

Tectonic Stretching (I-D in Table 4)

A crystallizing batholith probably exists beneath Yellowstone (see Christiansen, 2001, and references therein). Yellowstone is along the east margin of the Basin-and-Range structural province where tectonic extension is occurring. In addition, the Elephant Back fault zone offsets the 150-ka Elephant Back flow (fig. 5) indicating either significant SE–NW extension perpendicular to the caldera axis or keystone faulting associated with resurgent doming. Given that ductile material is as shallow as 4–5 km beneath the caldera (Smith and Bruhn, 1984; Fournier and Pitt, 1985; Smith and Braille, 1993), tectonic extension would stretch and thin the ductile body and cause subsidence perhaps accompanied by fissuring and faulting in the brittle material above (see fig. 16*B*). LHR lies along the axis of the caldera where the greatest subsidence due to extension might be expected. (See comment under "tectonic compression" regarding subsidence associated with convergence.)

Yellowstone Lake Ceasing to Overflow (I-E in Table 4)

Hamilton and Bailey (1988) observed submerged shorelines and suggested that they might indicate that Yellowstone Lake ceased to overflow. Locke and Meyer (1994) considered that Holocene climatic change was unlikely to have caused closed-basin conditions because an average of 45 percent of annual precipitation in the Yellowstone Lake basin currently discharges at the lake outlet. Studies of oxygen isotopes of water entering and exiting Yellowstone Lake suggest that about 15 percent of the inflow evaporates from the lake surface at present (Pat Shanks, oral commun., 2000). For Yellowstone Lake to cease overflowing, the ratio of evaporation to inflow would have to increase by more than six times, necessitating a very major climatic change. Pollen records from the Yellowstone Lake basin do not show evidence for dramatic late Holocene vegetation and climatic changes (Whitlock, 1993; Baker, 1976; Waddington and Wright, 1974). The simplest argument against closed-basin conditions is the drowned outlet channel of the Yellowstone River, which now lies well below the level of the bedrock threshold farther downstream at LHR. This channel was cut 4–3 ka when Yellowstone Lake was more than 5 m below its present level, yet, the lake was clearly overflowing and transporting gravel and undercutting its banks (fig. 6).

Increases in Lake Level

Inflation by Magma Intrusion (II-A in Table 4)

Decompression melting in the mantle from the Yellowstone hotspot source is thought to generate basaltic magma that rises upward to the base of the rhyolitic magma chamber (fig. 16*A*). Uplift or inflation because of magma intrusion is quite plausible (Pelton and Smith, 1982; Dzurisin and others, 1994). Modeling indicates that the historic inflation is consistent with a volume expansion involving either magmatic or hydrothermal fluids, primarily in the 3- to 6-km depth range (Vasco and others, 1990), or 8-km depth (Wicks and others, 1998). Uplift may relate either directly to this basaltic magma influx or to a rhyolitic magma generated by its heat and intruded at shallow levels within the caldera.

Tectonic Compression (II-D in Table 4)

Local compression of a ductile magma chamber would produce uplift (Meertens and Levine, 1985). GPS studies show that radial contraction was accompanied by subsidence, suggesting the opposite effect (Smith and others, 1997; Meertens and others, 2000). This pattern (contraction and subsidence) suggests that subsidence is caused primarily by depressurization of a subcaldera source rather than by tectonic stretching.

Possible Increases or Decreases in Lake Level

Faulting and Local Warping (III-A in Table 4)

A north-trending fault system includes the Lake Hotel fault on the lake floor and the Fishing Bridge fault (see section on faulting discussed earlier). Although the Fishing Bridge fault offsets shoreline S5 and the wave-cut shoreline of S4 by several meters, it offsets the ~9.7-ka S-meander and surfaces that predate the S-meander by less than 2 m. The shorelines show an overall sag across the outlet area (fig. 12). The S2 shoreline is dated at ~8 ka on both sides of the Fishing Bridge fault and is only offset 0.5 m by the fault (fig. 14; table 3).

For the Lake Hotel graben, Johnson and others (2003) recognize 7.5 m of total offset on the western fault and 3.4 m of offset on the eastern antithetic fault; this results in a net offset of 4.1 m. The lake floor is offset 2.7 m across the Lake Hotel graben (only 1.4 m less than the net offset of 4.1 m). Based on sedimentation rates (Johnson and others, 2003), the last and by far the largest offset was 5.7 m on the western strand with a net offset of 2.9 m within the last 2 k.y. We infer that such faulting dies out northward because the 8-ka S2 shoreline is essentially horizontal (fig. 12) and is offset only 0.5 m by the Fishing Bridge fault.

Tiller (1995) suggests that faulting might be responsible for increases in lake and river levels. Except for the Fishing Bridge fault, no faults with offset of shorelines have been recognized in the outlet area, including shorelines shown on bedrock and surficial geologic maps (Christiansen and Blank, 1975; Richmond, 1977) and those shorelines studied by Meyer and Locke (1986), Locke and Meyer (1994), Hamilton and Bailey (1990), and Pierce and others (1997). Just east of Le Hardy Rapids, John Good and Ken Pierce found a fault scarp with ~1 m of down-to-the-northwest offset (fig. 5), which is opposite to that needed to raise the level of the outlet reach. The present drowned channel from the outlet to LHR does not change its nearly flat gradient or wide width as it might if a young fault crossed and uplifted the river channel (fig. 5). The submerged shoreline deposits at Bridge Bay and at Little Thumb Creek North, as well as the many drowned valleys around the lake, are not within any recognized graben, and thus local faulting did not cause their submergence.

Based on isostatic considerations and observed altitude changes after normal faulting, extensional faulting and associated crustal thinning is expected to produce 80 percent of the subsidence of the downthrown block and only 20 percent of the uplift of the upthrown block (Barrientos and others, 1987). Because the brittle-ductile transition zone in the caldera is only 20–35 percent as deep as normal in the Basin-and-Range, extensional structures arising from horizontal extension may have less vertical structural relief and may express extension through fissures and grabens.

Glacial-Isostatic Rebound (III-B in Table 4)

At the last glacial maximum, the ice cap on the Yellowstone Plateau reached an altitude greater than 3,350 m above Yellowstone Lake (altitude 2,358m) (Good and Pierce, 1998). The ice cap above the present Yellowstone Lake was about 1 km thick as demonstrated by flow from the lake area northward to over the top of Mount Washburn (altitude 3,125 m; Pierce, 1979) as well as flow eastward through Sylvan Pass at such high levels that it backfilled high into the valley of Middle Creek (Richmond and Pierce, 1972). With total compensation and an upper crust density of 2.7 gm/cm^3, isostatic depression from 1-km-thick ice (density ~0.9 gm/cm^3) would be 330 m. Because the lithosphere is likely to be warm and more ductile beneath Yellowstone, a relatively high fraction of total potential compensation might have occurred close to the center of the load. In addition, because of this ductile material, the rate of rebound may be much greater than in continental craton areas. The thickness and load of ice above the Yellowstone Lake basin was relatively uniform (Good and Pierce, 1996), and thus near-uniform rebound is expected in the lake area, although cooler and stiffer crust is expected outside the caldera. Because both inflation and deflation have taken place during historic time as well as postglacial time (fig. 4), differential isostatic rebound is an unlikely mechanism to explain the historic shoreline record. This view is shared by Pelton and Smith (1982) and Locke and Meyer (1994).

This unweighting during deglaciation of about 1 km of ice (pressure ~90 bars) provides a natural experiment for evaluating the hazard of volcanic eruptions. During deglaciation, pressures in magmas beneath the Yellowstone Plateau were not high enough that the 90-bar reduction in confining pressure resulted in an eruption. In other areas—such as Hawaii (Porter, 1979), Iceland, and the "tuyas" of British Columbia—volcanic eruptions occurred through glacial ice that was melting and unloading during deglaciation. Thus, the pressure in the magmatic system beneath Yellowstone was not great enough to produce a volcanic eruption when rapid deglaciation about 14 ka reduced confining pressure on the system by 90 bars.

Oscillations in Lake Level

Figure 4 shows oscillations in lake level that can be divided into two parts: (1) an oscillating lowering to the S4 level >14 ka to ~10.7 ka and (2) oscillations near the present level from 10.7 ka to the present. The oscillating part of this pattern may be an

Table 5. Change in altitude of *S2, S4,* and *S5* from near the caldera axis in the outlet to sites farther away, but in the caldera, to sites outside the caldera.

[Under the "Site" headings, first number is the shoreline altitude (in meters) above datum, and the second number is the distance from the caldera axis of historic uplift (in kilometers) (see fig. 1). For the outlet area, altitudes are for the eastern part of the Fishing Bridge peninsula]

Shoreline and age	Site in outlet area	Site in caldera but farther from axis	Site outside caldera	Vertical decrease in height toward caldera axis over distance
S2 8.0 ka	5 m/4 km	No site dated	7–8 m/35 km delta in SE. arm	2–3 m/30 km
S4 10.7 ka	8–9 m/4 km	7 m/17 km S. shore, West Thumb	No site dated	–1 to –2 m/13 km, increases toward caldera axis
*S5** 12.6 ka	10–13 m/4 km	14 m/13 km caldera margin at Lake Butte	19 m/35 km* Yellowstone River delta area	6–9 m/31 km total. 5 m/22 km outside caldera, 1–4 m/9 km inside caldera

* *S5* uses height above datum as shown in figure 10 to Mary Bay crater wall, where *S5* is the same as *S7* of Locke and Meyer (1994, their fig. 4) and continues the same as *S7* of Locke and Meyer (1994) along the east shore of Yellowstone Lake.

extension of the observed 1923–1999 pattern of inflation and deflation based on releveling and radar-interferometry studies. The time intervals and amplitudes of inferred Holocene cycles are much greater, although rates are compatible.

The increase in lake level that defines the oscillations to the S5 and S4 shorelines is based on truncation of shorelines and valleys shown in figures 5 and 10. The amplitude is not known, but is estimated to be at least several meters. The increase in lake level both after the S-meander and after the 4- to 3-ka low is estimated to be 8.3 m between LHR and the outlet. Extending farther from the caldera axis, our studies of lake-level changes suggest differential uplift of ~10–11 m at localities that span ~41–43 percent of the 1923–1976 doming (table 2); the average long-term rate of uplift from 4–3 ka to the present is in the 0.7 to 1.2 cm/yr range if extrapolated to the caldera margin at the outer limit of the 1923–1975 doming.

The oscillations suggesting rises near 5 ka and 2 ka (fig. 4) are not well established and are included as options because of evidence for a lake level near that of the present-day at about 4 and 2 ka. These oscillations suggest more rapid rates of uplift and subsidence between the outlet and LHR, and we are reticent to suggest that such rates are established (note slopes of uplift and subsidence on fig. 4). From 1923–1985, uplift of LHR relative to the outlet was 0.25 m at a rate of 4 mm/yr; to produce 8 m of uplift at this rate would take 2 k.y.

Many of the prominent erosional shorelines, especially the ones designated S1–S5, were formed during rising lake levels and were most likely produced by an inflation episode. Locke and Meyer (1994) inferred that rising water levels resulting from the current episode of inflation (including inflation before the historic measurement period) were probably effective in producing the prominent modern wave-cut shorelines noted around Yellowstone Lake. This process probably accounts for the major past shorelines as well.

Unrest of calderas is common (Newhall and Dzurisin, 1988). The Phlegraean Fields caldera, Italy, a smaller trachytic caldera about 15 km across, has a 5,500-year record useful for comparison of rates, amplitudes, and patterns of inflation and deflation relative to Yellowstone (Dvorak and Mastrolorenzo, 1991). For the Phlegraean Fields caldera, Grindley (1976) charts 55 m of uplift from about 3,500 to 500 B.C. at about 18 mm/yr, followed by 15 m of subsidence from about 500 B.C. to about A.D.1000 at a rate of 11 mm/yr. Subsequently, about 12 m of uplift led to an eruption in A.D.1528 followed by about 8 m of subsidence (A. Parascandola, cited in Yokoyama, 1971). These values are comparable to the historical values of uplift (15 mm/yr) and subsidence (20–30 mm/yr) for the center of the Yellowstone caldera.

If the 1923–1985 caldera inflation at 15 mm/yr were to continue for 1,000 to 4,000 years, uplift would total 15 to 60 m. The subaerial shorelines do not have deformation of this magnitude, and the tilts are generally toward the caldera axis rather than away from it (fig. 12) (Locke and Meyer, 1994). Table 5 shows a compilation of overall apparent tilts with distance from the caldera axis for three shorelines. We selected S2 and S4 because they are independently dated over long distances. We selected S5 because this shoreline feature has been nearly continuously mapped (fig. 12) (Locke and Meyer, 1994). S5 of this paper along the northern lakeshore is the same as S7 of Locke and Meyer (1994) on the hydrothermal-explosion-crater rim above Beach Springs. S5 shows a significant tilt toward the caldera axis, and most of this occurs outside the caldera (table 5). S2 shows a 2- to 3-m tilt within the caldera toward the axis, whereas S4 shows a 1- to 2-m tilt away from the axis. In summary, net postglacial tilting of two of three shorelines shows gentle subsidence toward the axis of the caldera, and one shoreline shows a slight increase within the limits of measurement and dating. One explanation for the gentle tilts is that the prominent subaerial shorelines were formed at the culmination of an inflation cycle, and they are near-horizontal at present because the present shoreline may also be forming at the culmination of an inflation cycle. This has returned the older shorelines to approximately their original horizontal positions. The cumulative gentle overall subsidence toward the caldera

axis might be due to magmatic cooling. Fournier and Pitt (1985) estimate subsidence of 0.6–0.7 mm/yr due to cooling; over the age of S5 (14.6 ka), this would total 7.5 m, which is within the range of estimates of subsidence (table 5).

Two Favored Explanations for Record of Oscillations

A nearly steady state process with little net volume change in postglacial time within the caldera seems to be required to produce the observed deformation history (table 5). Inflation and deflation of the caldera in the last 100 years has been called "breathing;" we use the term "heavy breathing" for millennial-scale, larger episodes of inflation and deflation. This "heavy breathing" of the central part of the Yellowstone caldera may reflect magmatic inflation and tectonic stretching and deflation, or (our preferred interpretation) hydrothermal-fluid sealing and inflation followed by cracking and deflation (fig. 16). The other factors noted in table 4 may also be involved. Listed below are two explanations, one involving only hydrothermal processes and the other a hybrid of volcanic and tectonic processes.

Hydrothermal Inflation and Deflation (IV-A in Table 4)

A large, magmatically driven hydrothermal system exists principally within the 640-ka Yellowstone caldera (Fournier and Pitt, 1985; Fournier, 1989; Christiansen, 2001). At a depth of about 5 km, a seal may be created by mineral deposition and ductile flow, separating a deep zone associated with crystallizing magma and its expelled fluids and in which pore pressures can approach lithostatic, from a shallower zone, where pore pressures are hydrostatic (Fournier and Pitt, 1985; Fournier, 1989). Hydrothermal-pressure buildup of the confined hydrothermal fluids beneath this seal would produce uplift. Eventual rupture of the seal, perhaps during an earthquake or hydrofracturing, would permit these confined hydrothermal fluids to escape and result in subsidence, perhaps back to the original level. This mechanism could explain why even latest Pleistocene shorelines show little net deformation, with net inflation being equal to net deflation.

Fournier (1989) calculated that the volume of magmatic fluids released by magma crystallization is adequate to explain historic uplift rates. Fournier (oral commun., 2002) also estimates that no more than a 10-percent increase in surface manifestation of geothermal fluids has occurred, but that dense brines from beneath the ruptured seal might not be vented directly to the surface. Instead, the brines may be expelled laterally at depth. Friedman (this volume) finds that there has been a decrease in chloride representing hydrothermal heat output of about 10 percent since the early 1980s, about when subsidence started in 1985. Friedman also notes that years and seasons of increased precipitation also correlate with increased chloride release. We suggest that the 10-percent decrease noted by Friedman might reflect the general drought that has occurred since about 1980 (Despain, oral commun., 2002) and thus does not necessarily contradict the postulate of geothermal release producing the subsidence after 1985. Dzurisin and others (1994, p. 268) note a cluster of hydrothermal and earthquake events (Nagy and Smith, 1988; Waite and Smith, 2002) within and outside the caldera that may relate to the 1985 change from inflation to deflation and may be associated with rupture of a deep hydrothermal seal and release of hydrothermal fluids. In this regard, it is interesting to note that the banding of vein deposits, commonly noted in mineralized areas around intrusions, may also indicate pulsations in the outflow of hydrothermal fluids (Fournier, 1999).

A correlation between hydrothermal explosions and associated reduction of deep, confined hydrothermal pressures might also result in lowering of LHR and lake levels. Figure 4 shows that the ages of three hydrothermal explosions do not clearly correlate with times of lake-level lowering, although the dating of the explosions and lake level both have considerable uncertainty. Other explosions—such as Duck Pond, Fern Lake, the subaqueous Elliott's crater (age ~13–8 ka; Johnson and others, 2003), and other craters—need to be dated to fully evaluate this possible relation.

Inflation by Magma Intrusion and Subsidence by Other Mechanisms (IV-B in Table 4)

Because Yellowstone is an active volcanic field, a magmatic explanation is obviously plausible (Pelton and Smith, 1982; Dzurisin and others, 1994). The inflation has been modeled with the largest volume expansions in the 3.0- to 6.0-km-depth range (Vasco and others, 1990). The overall horizontality of shorelines (table 5) indicates that there has been no net doming by buildup of postglacial intrusions. The subsidence part of the oscillation is more difficult to explain by evacuation of the emplaced magma, although the radially outward earthquake patterns may represent outward magma movements. Subsidence due to tectonic stretching of ductile material, primarily of the batholithic magma chamber, is predictable given Yellowstone's location on the margin of the extending Basin-and-Range. The Elephant Back fault system indicates SE–NW extension that may reflect either fracturing associated with localized doming along the caldera axis or regional extension; such doming does not provide an explanation for subsidence, but regional extension does. Outside of the Yellowstone caldera, extensional Basin-and-Range faults are clearly active, including the Teton fault, the east Sheridan fault, and the Hebgen earthquake faults. Such extension might be episodic and produce subsidence of the caldera. The Eagle Bay fault has been active in Holocene time and extends into the caldera from the south (fig. 2).

Subsidence due to cooling is almost certainly occurring and estimated to be 0.6–0.7 mm/yr (Fournier and Pitt, 1985), but it can account for only a small fraction of the historically observed rates of about 15- to 30-mm/yr uplift and subsidence (Dzurisin and others, 1994, their fig. 4). This suggests that

cooling is a minor factor in subsidence. If inflation is explained by magma intrusion and deflation is explained by extension or other processes, the following questions are of concern: (1) why would the volume of magma intrusion and associated uplift equal the volume of extension and subsidence?, and (2) why would these alternate systematically in time?

Local Doming and Faulting of Shorelines

In addition to the changes in lake level, remarkable local deformation is recorded by shoreline faulting and tilting. The cause of the tilting and doming is locally associated with hydrothermal centers. For example, west from the Storm Point hydrothermal center with its dramatic craters (fig. 10), uplift is 6 m over a kilometer (fig. 15). A localized anticline just east of Pelican Creek has no surface hydrothermal features, although hot beach sand and steamy unfrozen lake margin is noted along trend to the south and merits further investigation. On the lake floor, domal areas attributed to hydrothermal processes have even greater relief than these onshore sites (Johnson and others, 2003). Outside of the northern Yellowstone Lake study area, Locke and Meyer (1994) show broad uplift of the Rock Point area and subsidence of the West Thumb area.

The Fishing Bridge fault shows increasing offset of older shorelines. Tilting of shorelines into the fault is equal to or greater than fault offset. Over a distance of about 1.1 km across the Fishing Bridge peninsula, tilt of shorelines into the Fishing Bridge fault increase from 0.8 m for S2 to 6.7 m (projected) for S5 (fig. 14; table 3).

Conclusions

S2 (8 ka) and related shorelines are tilted as much as 6 m/km away from the Storm Point hydrothermal center. Just west of this tilted area is a local dome more than 2 m high and about 0.5 km wide. Both of these uplifts suggest shallow emplacement of a volume, presumably of magma or hydrothermal fluids. This, and similar features on the lake floor and perhaps elsewhere, may represent a significant hazard.

LIDAR data permit recognition of the Fishing Bridge fault and its history of Holocene offset. Near Fishing Bridge, the fault offsets the S2 shoreline 0.5 m and the S4 barrier beach 1 m. About 2 m of faulting occurred after eroding the wave-cut S4 but before building the S4 barrier beach. The Fishing Bridge fault, 0.5–1.5 km farther north, offsets by 1–2 m the S2 sand spit filling the S-meander, but it offsets less than 2 m adjacent surfaces that predate the S-meander—indicating offset after ~11 ka (S4) is the same as that after 8 ka (S2). Curiously, late Holocene activity on the Fishing Bridge fault has been minimal (table 2), whereas activity on the *offshore* Lake Hotel fault (Johnson and others, 2003) has been mostly late Holocene.

Shorelines S2 and S4 are correlated by independent dating from the north to south shores of the lake and are essentially horizontal, and, significantly, they do not rise toward the caldera axis. Our correlation of S5, a well-represented shoreline along the north and east side of the lake, gently slopes toward the caldera axis. This overall near-horizontality contrasts with local doming and faulting of shorelines where structural relief exceeds 5 m.

We reconstruct the following postglacial history of changes for Yellowstone Lake and adjacent areas (fig. 4).

1. MB hydrothermal explosion occurred about 13 ka and mantles S5.5 and S6, but not S5. The steep crater wall on the north side of Mary Bay was formed during the MB explosion, and S5 was cut into the crater wall.

2. Using LIDAR images, S5 can be traced from Pelican Creek to Mary Bay, where it is S6 of Meyer and Locke (1986) and S7 of Locke and Meyer (1994). S5 postdates the MB hydrothermal explosion and is ~12.6 ka.

3. The S4 shoreline is ~10.7 ka and is 7–9 m above datum in the Fishing Bridge area and 7–8 m above datum east of the Grant Village area. Locke and Meyer (1994) note local uplift of S4 of about 4 m in the Mary Bay and Rock Point area to about 12 m above datum.

4. The S-meander represents a low level of Yellowstone Lake and LHR that occurred after the S4 shoreline and before S2 and S3 shorelines. Uplift of LHR by more than 8 m relative to the outlet converted this once vigorously flowing reach of the river to an arm of the lake.

5. The S2 shoreline is about 4–6 m above datum on both sides of the outlet and dates ~8 ka on both sides of the outlet, confirming little or no deformation.

6. Yellowstone Lake has been near or below its present level from after S2 time (~8 ka) to present.

7. About 4–3 ka in Bridge Bay and in the drowned valley of Little Thumb Creek North, lake level was 5.4 and 6.3 m lower, respectively, than the present S1 shoreline. The outlet reach of the Yellowstone River is presently a drowned channel that had a much higher gradient before 4–3 ka. Estimation of original river gradients indicates uplift of LHR relative to the outlet was about 8 m and thus converted this reach from a once vigorously flowing river to the present "pool."

8. Other evidence of now-submerged lake-level features that is widespread but not yet dated includes (1) drowned valleys such as Pelican Creek, Sedge Creek, and Little Thumb Creek, (2) submerged shorelines noted by Johnson and others (2003) 2–4 m below datum (their S^{-1}) and 10–13 m below datum (their S^{-3}), and (3) shorelines submerged 15–30 m below datum noted by Hamilton and Bailey (1990) at many tens of locations. Better dating and correlation are needed to understand these submerged shorelines.

The overall pattern of lake level changes (fig. 4) suggests an oscillating lowering of lake level from at least the S6 level at ~14.4 ka to about S4 time at 10.7 ka. This is easiest to explain by

erosion of the outlet accompanied by inflation-deflation cycles; however, the tilt of S5 toward the caldera axis (table 5) may indicate 6–9 m of post-S5 subsidence of the threshold at LHR. After S4 time, lake oscillations predominate over outlet erosion. After S2 time (~8 ka), the lake has been below or near its present level also indicating little outlet erosion. The increase in lake level from 4–3 ka to present (fig. 4) can be explained by uplift of LHR.

The cyclic model suggested by historic deflation and inflation explains many aspects of the record throughout the last 15 k.y. In particular, it explains lake-wide net deformation of shorelines of generally less than 10 m in contrast to historical rates of uplift and subsidence of up to 1–2 cm/yr (10–20 m/1,000 yr). If shorelines were cut during intervals of rising (transgressing) lake level as suggested by Locke and Meyer (1994), the present lake level (S1) and shorelines S3, S4, and S5 probably represent lake-level culminations. This sequence of shorelines is subhorizontal or declines toward the caldera axis, apparently because they represent culminations of uplift in an oscillating pattern that has produced no net uplift. Because the present time appears to be a culmination, the other culminations may also appear essentially horizontal. This history and geometry support cycles of inflation and deflation with an amplitude of about 8 m between LHR and the outlet and a frequency of perhaps 1–3 k.y.

For caldera inflation or deflation, several mechanisms are likely to be operating: magma intrusion, crustal stretching, batholithic cooling, and hydrothermal pressure changes. The mechanism of uplift by hydrothermal-pressure buildup beneath a hydrothermal seal, followed by subsidence due to rupture of the seal and release of fluids, is appealing because, by itself, it explains the present large-scale near-horizontality of shorelines. Local sagging of shorelines may be explained by extension and faulting, whereas local doming may result from hydrothermal or magmatic buildup. Subaerial shorelines that represent inflation culminations and relative lake-level highstands are subhorizontal. Submerged shorelines that formed during deflation episodes and overall lower lake levels might be expected to be more tilted than shown by Johnson and others (2003), but, as suggested by the Bruun rule, even the submerged shorelines might represent minor culminations of lake level during longer period oscillations. Because subaerial postglacial shorelines do not strongly slope away from the caldera axis, either voluminous magma intrusions have not accumulated or the uplift volume of such intrusions has been fortuitously balanced by subsidence processes such as tectonic stretching or batholithic cooling. Inflation appears responsible for the lake-level rises (fig. 4), but such inflation has not resulted in volcanic eruptions or cumulative doming of shorelines tilting away from the caldera axis. The inflation-deflation cycles seem to represent an essentially zero-sum process with little net subsurface volume change, which seems most readily explained by buildup and release of hydrothermal fluids.

Hydrothermal explosions are likely associated with lowering of pressure of the confined hydrothermal system and subsidence. Wicks and others (1998) conclude that transfer of fluids over tens of kilometers between the two resurgent domes has occurred in a few years, which would indicate that caldera-scale interconnections may occur on a similar time scale. The ages of three hydrothermal explosions do not clearly correlate with times of lake-level deflation (fig. 4), although the dating of the explosions and lake level both have considerable uncertainty. Other hydrothermal-explosion craters—such as Duck Lake, Fern Lake, the subaqueous Cutthroat Crater, and other craters—need to be dated to better evaluate this hypothesis.

The Yellowstone caldera was covered with about 1 km of glacial ice about 20–16 ka. Deglaciation and the reduction in pressure by about 90 bars was not accompanied by volcanic eruptions, suggesting the magmatic system was not then, and perhaps not now, at pressures high enough for eruption.

Acknowledgments

We appreciate the work of the crew of the Midwest Archeological Center in finding archeological and charcoal material for dating, and we particularly appreciate the surveying work of George Crothers. The Park Service staff at Lake Village was particularly helpful, including John Lounsbury, Dan Reinhart, Bruce Sefton, Loyd Kortge, Harlan Credit, Dan Mahony, and the NPS dive team. Kerry Cook and Dan Lofgren of the Federal Highways Administration provided records and samples from borings. We appreciate field conferences with Bob Christiansen, Pat Muffler, Rick Hutchinson, and Wayne Hamilton. Bob Fournier greatly aided our understanding of hydrothermal processes and their relation to uplift and subsidence processes. Bob Smith provided GPS data on the ongoing deformation. Dan Dzurisin provided surveying data and advice concerning deformation processes. Pierce particularly appreciates field work together and discussions with Lisa Morgan and Pat Shanks regarding the lake floor and hydrothermal explosions. Bill Locke did the definitive surveying of the shorelines and discussed his interpretations freely with us. Bill Locke and Dan Dzurisin provided very helpful reviews, and Tom Judkins provided thorough editing.

References Cited

Baker, R.G., 1976, Late Quaternary vegetation history of the Yellowstone Lake basin, Wyoming: U.S. Geological Survey Professional Paper 729-E, p. E1–E48.

Barrientos, S.E., Stein, R.S., and Ward, S.N., 1987, Comparison of the 1959 Hebgen Lake, Montana, and the 1983 Borah Peak, Idaho, earthquakes from geodetic observations: Bulletin of the Seismological Society of America, v. 77, p. 784–808.

Bruun, P., 1988, The Bruun rule of erosion by sea-level rise—A discussion on large-scale two- and three-dimensional usages: Journal of Coastal Resources, v. 4, p. 627–648.

Cannon, K.P., Crothers, G.M., and Pierce, K.L. 1994, Archeological investigations along the Fishing Bridge Peninsula, Yellowstone National Park, Wyoming—The archeology, geology and paleoenvironment: Lincoln, Nebr., National Park Service, Midwest Archeological Center Technical Report on file, 367 p.

Cannon, K.P., Pierce, K.L., and Crothers , G.M., 1995, Caldera unrest, lake levels, and archeology—The view from Yellowstone Lake: Park Science, v. 15, no. 3, p. 28–31.

Cannon, K.P., Pierce, L.L., Stormberg, P., and MacMillian, M.V., 1997, Results of archeological and paleoenvironmental investigations along the north shore of Yellowstone Lake, Yellowstone National Park, Wyoming—1990–1994: Lincoln, Nebr., National Park Service, Midwest Archeological Center Technical Report on file, 458 p.

Christiansen, R.L., 1984, Yellowstone magmatic evolution—Its bearing on understanding large-volume explosive volcanism, *in* Explosive volcanism—Inception, evolution, and hazards: Washington, D.C., National Academy Press, p. 84–95.

Christiansen, R.L., 2001, The Quaternary and Pliocene Yellowstone Plateau volcanic field of Wyoming, Idaho, and Montana: U.S. Geological Survey Professional Paper 729-G, 145 p.

Christiansen, R.L., and Blank, H.R., Jr., 1975, Geologic map of the Canyon Village quadrangle, Yellowstone National Park, Wyoming: U.S. Geological Survey Geologic Quadrangle Map GQ-1192, scale 1:62,500.

Doerner, J.P., and Carrara, P.E., 2001, Late Quaternary vegetation and climatic history of the Long Valley area, west-central Idaho, U.S.A.: Quaternary Research, v. 56, p. 103–111.

Dvorak, J.J., and Mastrolorenzo, Giuseppe, 1991, The mechanisms of recent crustal movements in Campi Flegrei caldera, southern Italy: Geological Society of America Special Paper 263, 47 p.

Dzurisin, Daniel, Christiansen, R.L., and Pierce, K.L., 1995, Yellowstone—Restless volcanic giant: U.S. Geological Survey Open-File Report 95-59 (Fact Sheet), 2 p.

Dzurisin, Daniel, Savage, J.C., and Fournier, R.O., 1990, Recent crustal subsidence at Yellowstone caldera, Wyoming: Bulletin of Volcanology, v. 52, p. 247–270.

Dzurisin, Daniel, and Yamashita, K.M., 1987, Vertical surface displacements at Yellowstone caldera, Wyoming, 1976–1986: Journal of Geophysical Research, v. 92, no. B13, p. 13,753–13,766.

Dzurisin, Daniel, Yamashita, K.M., and Kleiman, J.W., 1994, Mechanisms of crustal uplift and subsidence at the Yellowstone caldera, Wyoming: Bulletin of Volcanology, v. 56, p. 261–270.

Fournier, R.O., 1989, Geochemistry and dynamics of the Yellowstone National Park hydrothermal system: Annual Review Earth Planetary Science, v. 17, p. 13–53.

Fournier, R.O., 1999, Hydrothermal processes related to movement of fluid from plastic into brittle rock in the magmatic-epithermal environment: Economic Geology, v. 94, p. 1,193–1,212.

Fournier, R.O., and Pitt, A.M., 1985, The Yellowstone magmatic-hydrothermal system, *in* Stone, Claudia, ed., International symposium on geothermal energy, international volume: Geothermal Resources Council Transactions, p. 319–327.

Frison, G.C., 1991, Prehistoric hunters of the High Plains (2d ed.): New York, Academic Press, 532 p.

Frison, G.C., 1992, The foothills-mountains and the open plains—The dichotomy in paleoindian subsistence strategies between two ecosystems, *in* Stanford, D.J., and Day, J.S., eds., Ice Age hunters of the Rockies: Niwot, Colo., University Press of Colorado, p. 323–362.

Good, J.D., and Pierce, K.L., 1996, Interpreting the landscapes of Grand Teton and Yellowstone National Parks, recent and ongoing geology: Grand Teton National History Association, 58 p., 57 illus., 2d printing, 1998.

Greiser, S.T., 1986, Artifact collections from ten sites at Canyon Ferry Reservoir: Archeology in Montana, v. 27, no. 1-2, p. 1–190.

Grindley, G.W., 1976, Relation of volcanism to Earth movements, Bay of Naples, Italy, *in* Gonzales-Ferran, O., ed., Proceedings symposium on Andean and Antarctic volcanology problems: Rome, IAVEC, p. 598–612.

Hamilton, W.L., 1987, Water level records used to evaluate deformation within the Yellowstone caldera, Yellowstone National Park: Journal of Volcanology and Geothermal Research, v. 31, p. 205–215.

Hamilton, W.L., and Bailey, A.L., 1988, Holocene deformation deduced from shorelines at Yellowstone Lake, Yellowstone caldera, I: Historical summary and implications:Eos, Transactions of the American Geophysical Union, v. 69, no. 44, p. 1,472.

Hamilton, W.L., and Bailey, A.L., 1990, Holocene deformation history of the Yellowstone caldera at Yellowstone Lake inferred from abandoned shorelines and sediments: Yellowstone Physical Sciences Laboratory, Yellowstone National Park, Report 90-3, 24p., 13 figs. [draft of 8 June, 1990].

Husted, W.M., and Edgar, R., 2002, The archeology of Mummy Cave, Wyoming—An introduction to Shoshonean prehistory: Lincoln, Nebr., National Park Service, Midwest Archeological Center Special Report 4 and Southeast Archeological Center Technical Report Series 9, 231 p.

Johnson, S.Y., Stephenson, W.J., Morgan, L.A., Shanks, W.C., III, and Pierce, K.L., 2003, Postglacial geologic processes in northern Yellowstone Lake, Wyoming: Geological Society of America Bulletin, v. 115, no. 8 p. 954–971.

Kaplinski, M.A., 1991, Geomorphology and geology of Yellowstone Lake, Yellowstone National Park, Wyoming: Flagstaff, Northern Arizona University, M.S. thesis, 82 p.

Licciardi, J.M., Clark, P.U., Brook, E.J., Pierce, K.L., Kurz, M.D., Elmore, D., and Sharma, P., 2001, Cosmogenic ^{3}He and ^{10}Be chronologies of the northern outlet glacier of the Yellowstone ice cap, Montana, USA: Geology, v. 29, p. 1,095–1,098.

Locke, W.W., 1986, Shoreline elevation data for the roaded portion of Yellowstone Lake shore, *in* Locke, W.W., unnamed editor, Quaternary evolution of the Yellowstone region: Friends of the Pleistocene, Rocky Mountain Cell, Guidebook, p. 52–53.

Locke, W.W., and Meyer, G.A., 1994, A 12,000-year record of vertical deformation across the Yellowstone caldera margin—The shorelines of Yellowstone Lake: Journal of Geophysical Research, v. 99, no. B10, p. 20,079–20,094.

Locke, W.W., Meyer, G.A., and Pings, J.C., 1992, Morphology of a post-glacial fault scarp across the Yellowstone (Wyoming) caldera margin and its implications: Bulletin of the Seismological Society of America, v. 82, p. 511–516.

Machette, M.N., Pierce, K.L., McCalpin, J.P., Haller, K.M., and Dart, R.L., 2001, Map and data for Quaternary faults and folds in Wyoming: U.S. Geological Survey Open-File Report 01-461, 155 p., map.

Mehringer, P.J., Jr., Sheppard, J.C., and Foit, F.F., Jr., 1984, The age of the Glacier Peak tephra in west-central Montana: Quaternary Research, v. 21, p. 36–41.

Meertens, C.M., and Levine, J., 1985, Compressive tectonic strain as a possible mechanism for long-term vertical deformation of the Yellowstone caldera: Eos, Transactions of the American Geophysical Union, v. 66, no. 46, p. 853.

Meertens, C.M., and Smith, R.B., 1991, Crustal deformation of the Yellowstone caldera from first GPS measurements—1987–1989: Geophysical Research Letters, v. 18, p. 1,763–1,766.

Meertens, C.M., Smith, R.B., and Puskas, C.M., 2000, Crustal deformation of the Yellowstone caldera from campaign and continuous GPS surveys, 1987–2000 [abs.]: Eos, Transactions of the American Geophysical Union, v. 78, no. 46, p. V22F-19.

Meyer, G.A., 1986, Morphology of the Yellowstone River below the nominal lake outlet at Fishing Bridge and topographic map of the Lake Lodge area, *in* Locke, W.W., unnamed editor, Quaternary evolution of the Yellowstone region: Friends of the Pleistocene, Rocky Mountain Cell, Guidebook, p. 47–49.

Meyer, G.A., and Locke, W.W., 1986, Origin and deformation of Holocene shoreline terraces, Yellowstone Lake, Wyoming: Geology, v. 14, p. 699–702.

Morgan, L.A., and Shanks, W.C., 2005, Influences of rhyolitic lava flows on hydrothermal processes in Yellowstone Lake and on the Yellowstone Plateau, *in* Inskeep, W.P., and McDermott, T.R., eds., Geothermal biology and geochemistry in Yellowstone National Park: Proceeding of the Thermal Biology Institute workshop, Yellowstone National Park, Wyoming, p. 53–72.

Morgan, L.A., Shanks, W.C., III, Lovalvo, D.A., Johnson, W.J., Pierce, K.L., Harlan, S., Finn, C.A., Lee, G., Webring, M., Schulze, B., Duhn, J., Sweeney, R., and Balistrieri, L., 2003, Exploration and discovery in Yellowstone Lake—Results form high-resolution sonar imaging, seismic reflection profiling, and submersible studies: Journal of Volcanology and Geothermal Research, v. 122, p. 221–242.

Nagy, W.C., and Smith, R.B., 1988, Seismotectonic implications of the 1985–86 Yellowstone earthquake swarm from velocity and stress inversion: Seismological Research Letters, v. 59, p. 20.

Newhall, C.G., and Dzurisin, Daniel, 1988, Historic unrest at large calderas of the world: U.S. Geological Survey Bulletin 1855, 1,108 p., 2 vols.

Otis, R.R., Smith, R.B., and Wold, R.J., 1977, Geophysical surveys of Yellowstone Lake, Wyoming: Journal of Geophysical Research, v. 82, p. 3,705–3,717.

Pelton, J.R., and Smith, R.B., 1979, Recent crustal uplift in Yellowstone National Park: Science, v. 206, p. 1,179–1,182.

Pelton, J.R., and Smith, R.B., 1982, Contemporary vertical surface displacements in Yellowstone National Park: Journal of Geophysical Research, v. 87, no. B4, p. 2,745–2,761.

Pierce, K.L., 1979, History and dynamics of glaciation in the northern Yellowstone National Park area: U.S. Geological Survey Professional Paper 729-F, 91 p.

Pierce, K.L., 2003, Pleistocene glaciations of the Rocky Mountains, *in* Gillespie, A.R., Porter, S.C., and Atwater, B.F., eds., The Quaternary Period in the United States—Developments in Quaternary Science, v. 1: Amsterdam, Elsevier, p. 63–76.

Pierce, K.L., Cannon, K.P., and Crothers, G.M., 1994, Archeological implications of changing lake levels of Yellowstone Lake, Yellowstone National Park, Wyoming: Current Research in the Pleistocene, v. 11, p. 106–108.

Pierce, K.L., Cannon, K.P., and Meyer, G.A., 1997, Yellowstone caldera "heavy breathing" based on Yellowstone Lake and River changes in post-glacial time: Eos, Transactions of the American Geophysical Union, v. 78, no. 46, p. F802.

Pierce, K.L., Cannon, K.P., Meyer, G.A., Trebesch, M.J., and Watts, Raymond, 2002, Post-glacial inflation-deflation cycles, tilting, and faulting in the Yellowstone caldera based on Yellowstone Lake shorelines: U.S. Geological Survey Open-File Report 02-0142, 30 p., 16 figs., 5 tables.

Porter, S.C., 1979, Hawaiian glacial ages: Quaternary Research, v. 12, p. 161–187.

Porter, S.C., Pierce, K.L., and Hamilton, T.D., 1983, Late Pleistocene glaciation in the Western United States, *in* Porter, S.C., ed., The late Pleistocene, v. 1, *of* Wright, H.E., Jr., ed., Late Quaternary environments of the United States: Minneapolis, Minn., University of Minnesota Press, p. 71–111.

Reeve, S.A., 1989, Prehistoric settlements at the Yellowstone Lake outlet, Yellowstone National Park, Wyoming: Lincoln, Nebr., National Park Service, Midwest Archeological Center Technical Report on file , 161 p.

Richmond, G.M., 1973, Surficial geologic map of the West Thumb quadrangle, Yellowstone National Park, Wyoming: U.S. Geological Survey Miscellaneous Investigations Series Map I-643, scale 1:62,500.

Richmond, G.M., 1974, Surficial geologic map of the Frank Island quadrangle, Yellowstone National Park, Wyoming: U.S. Geological Survey Miscellaneous Investigations Series Map I-642, scale 1:62,500.

Richmond, G.M., 1976, Surficial geologic history of the Canyon Village quadrangle, Yellowstone National Park, Wyoming, for use with Map I-652: U.S. Geological Survey Bulletin 1427, 35 p.

Richmond, G.M., 1977, Surficial geologic map of the Canyon Village quadrangle, Yellowstone National Park, Wyoming: U.S. Geological Survey Miscellaneous Investigations Series Map I-652, scale 1:62,500.

Richmond, G.M., and Pierce, K.L., 1972, Surficial geologic map of the Eagle Peak quadrangle, Yellowstone National Park and adjoining area, Wyoming: U.S. Geological Survey Miscellaneous Investigations Series Map I-637, scale 1:62,500.

Schwartz, M.L., 1987, The Bruun rule—twenty years later: Journal of Coastal Resources, v. 3, p. ii–iv.

Shortt, M. W., 2001, The Osprey Beach site—A Cody Complex occupation on the south shore of West Thumb [abs.]: 6th Biennial Scientific Conference on the Greater Yellowstone Ecosystem, abstracts, p. 37.

Smith, R.B., and Braile, L.W., 1993, Topographic signature, space-time evolution, and physical properties of the Yellowstone–Snake River Plain volcanic system—The Yellowstone hotspot, *in* Snoke, A.W., Steidtmann, J.R., and Roberts, S.M., eds., Geology of Wyoming: Geological Survey of Wyoming Memoir 5, p. 694–754.

Smith, R.B., and Bruhn, R.L., 1984, Intraplate extensional tectonics of the western U.S. Cordillera—Inferences on the structural style from seismic reflection data, regional tectonics and thermal-mechanical models of brittle-ductile deformation: Journal of Geophysical Research, v. 89, p. 5,733–5,762.

Smith, R.B., Meertens, C.M., Lowry, A.R., Palmer, Randy, and Ribe, N.M., 1997, Evolution and active processes of the Yellowstone hotspot: Eos, Transactions of the American Geophysical Union, v. 78, no. 46, p. F801.

Sturchio, N.C., Pierce, K.L., Murrell, M.T., and Sorey, M.L., 1994, Uranium-series ages of travertines and timing of the last glaciation in northern Yellowstone area, Wyoming-Montana: Quaternary Research, v. 41, p. 265–277.

Tiller, C.C., 1995, Postglacial sediment stratigraphy of large lakes in Greater Yellowstone—Scenarios of tectonic and climatic forcing: Minneapolis, University of Minnesota, M.S. thesis, 193 p.

Vasco, D.W., Smith, R.B., and Taylor, C.L., 1990, Inversion for sources of crustal deformation and gravity change at the Yellowstone caldera: Journal of Geophysical Research, v. 95, no. B12, p. 19,839–19,856.

Waddington, J.C.B., and Wright, H.E., Jr., 1974, Late Quaternary vegetation changes on the east side of Yellowstone Park, Wyoming: Quaternary Research, v. 4, p. 175–184.

Waite, G.P., and Smith, R.L., 2002, Seismic evidence for fluid migration accompanying subsidence of the Yellowstone caldera: Journal of Geophysical Research, v. 107, no. B9, 2177, doi:10.1029/2001JB000586.

Wheeler, R.P., 1954, Two new projectile point types—Duncan and Hanna Points: Plains Anthropologist, no. 1, p. 7–14.

Whipple, J.J., 2001, Yellowstone sand verbena—A Yellowstone Lake endemic [abs.], *in* Yellowstone Lake, hotbed or chaos or reservoir of resilience?: 6th Biennial Scientific Conference on the Greater Yellowstone Ecosystem, Yellowstone National Park, Wyoming, Oct. 8–10, 2001, p. 17.

Whitlock, Cathy, 1993, Postglacial vegetation and climate of Grand Teton and southern Yellowstone National Parks: Ecological Monographs, v. 63, no. 2, p. 173–198.

Wicks, Charles, Jr., Thatcher, Wayne, and Dzurisin, Daniel, 1998, Migration of fluids beneath Yellowstone caldera inferred from satellite radar interferometry: Science, v. 282, p. 458–462.

Yokoyama, I., 1971, Pozzuoli event in 1970: Nature, v. 229, p. 532–534.

The Influence of Sublacustrine Hydrothermal Vent Fluids on the Geochemistry of Yellowstone Lake

F

By Laurie S. Balistrieri, Wayne C. Shanks, III, Russell L. Cuhel, Carmen Aguilar, and J. Val Klump

Chapter F *of*
Integrated Geoscience Studies in the Greater Yellowstone Area—Volcanic, Tectonic, and Hydrothermal Processes in the Yellowstone Geoecosystem
Edited by Lisa A. Morgan

U.S. Geological Survey Professional Paper 1717

U.S. Department of the Interior
U.S. Geological Survey

Contents

Abstract 173
Introduction 173
Acknowledgments 174
Study Area 174
Methods 175
Field Methods 175
Laboratory Methods 177
Results and Discussion 177
Systematics of Stable Isotopes ($\delta^{18}O$ and δD) 177
Mass-Balance Calculations 178
Chloride Concentrations in Hydrothermal Vent Fluids and Lake Water: Mixing of End-Member Solutions 181
Relationships Between Major Anions and pH in Hydrothermal Vent Fluids and Lake Water 181
Normalized Concentrations of Elements in Hydrothermal Vent Fluids and Lake Water 184
SiO_2 184
B and Alkali Metals 185
Alkaline Earth Elements 186
Trace Anions and Mercury 186
Species Related to Gas Dissolution 187
Redox-Sensitive Species 187
Element Enrichment Due to Hydrothermal Activity 188
δD and Cl: An Estimate of the Concentration of Cl in the Hydrothermal Source Fluid to the Lake 188
Concentrations of Selected Elements and Species in Boiled Hydrothermal Source Fluid to the Lake 193
Summary 195
References 197

Figures

1. Maps of Yellowstone National Park and Yellowstone Lake bathymetry 176
2. Hydrogen- and oxygen-isotope compositions of Yellowstone Lake water, inflowing streams, and sublacustrine hydrothermal vent fluids 178
3. Box model used for mass-balance calculations 179
4. Results of mass-balance calculations 180

5–7. Dissolved concentrations of:

5. Cl in flow-weighted inflow to Yellowstone Lake, in lake water as a function of depth and location, and in hydrothermal vent water as a function of location 183
6. B and Li as a function of dissolved Cl concentrations in inflow and lake water, in hydrothermal vent fluids, and in the mixing experiments between Yellowstone River water and subaerial geyser fluids 184

7. As and W as a function of dissolved Cl concentrations in inflow and lake water, in hydrothermal vent fluids, and in the mixing experiments between Yellowstone River water and subaerial geyser fluids 185
8. Ternary diagram showing relationships among dissolved Cl, SO_4, and HCO_3 in inflow, hydrothermal, and lake water 186
9–15. Cl-normalized concentrations of dissolved:
9. Inorganic carbon (ΣCO_2*) relative to pH for hydrothermal vent fluids and Yellowstone Lake water 187
10. SiO_2 in Yellowstone Lake waters 188
11. B, Li, Na, K, Rb, and Cs in Yellowstone Lake waters 189
12. Mg, Ca, Sr, and Ba in Yellowstone Lake waters 190
13. As, Ge, Hg, Mo, Sb, and W in Yellowstone Lake waters 191
14. SO_4, ΣCO_2, and HCO_3 in Yellowstone Lake waters 192
15. Fe and Mn in Yellowstone Lake waters 192
16. Plot of δD versus dissolved Cl concentrations 194
17. Concentrations of elements in the predicted hydrothermal source fluid to Yellowstone Lake and in subaerial geysers relative to predicted concentrations in the deep thermal fluid in Yellowstone National Park 197

Tables

1. Volume and flux relations for water budget of Yellowstone Lake 179
2. Temperature and average chemical composition of Yellowstone Lake water, inflow water, and hydrothermal vent fluids 182
3. Regulatory limits and potential health-related effects of selected elements 193
4. Comparisons of predicted chemical compositions of boiled geothermal source fluid to Yellowstone Lake water and deep thermal reservoir fluid with measured compositions of subaerial geothermal water 196

The Influence of Sublacustrine Hydrothermal Vent Fluids on the Geochemistry of Yellowstone Lake

By Laurie S. Balistrieri,[1] Wayne C. Shanks, III,[2] Russell L. Cuhel,[3] Carmen Aguilar,[3] and J. Val Klump[3]

Abstract

The geochemical composition of Yellowstone Lake water is strongly influenced by sublacustrine hydrothermal vent activity. The evidence for this conclusion is twofold. First, mass-balance calculations indicate that the outflow from Yellowstone Lake is enriched in dissolved As, B, Cl, Cs, Ge, Li, Mo, Sb, and W relative to inflowing waters. Calculations involving stable isotopes of hydrogen and oxygen (δD and $\delta^{18}O$, respectively) and mass-balances indicate about 13 percent evapoconcentration in the lake, which is inadequate to account for the enrichment of these elements in the water column. Second, linear relationships between the concentration of Cl and many other elements in the lake and in hydrothermal vent fluids suggest that Yellowstone Lake water is a mixture of inflowing surface water and hydrothermal source fluid. The conservative behavior of many elements is further demonstrated in mixing experiments that utilize subaerial geyser fluids and Yellowstone River water sampled at the lake outlet.

The hydrothermal source fluid feeding the lake is identified by comparing theoretical predictions of the Cl and δD content of boiled, deep, thermal-reservoir fluid with observed compositions of water-column, pore-water, and vent samples from Yellowstone Lake. This comparison indicates that the hydrothermal source fluid has a temperature of 220°C and a Cl content of 570 mg/kg (~16 mM or millimoles per liter) and it evolved by boiling of a deep reservoir fluid with δD equal to –149 per mil and Cl content of 310 mg/kg. The concentrations of other elements in the hydrothermal source fluid are estimated using the observed linear relationships between Cl and other elements in lake and hydrothermal vent fluids. These concentrations indicate strong enrichment of Cl, Si, B, Li, Na, K, Rb, As, Ge, Mo, Sb, and W in sublacustrine hydrothermal vent fluids. In general, the composition of the hydrothermal source fluid is similar to the composition of subaerial geyser water in Yellowstone National Park (the Park).

The Cl concentration in the hydrothermal source fluid indicates that Yellowstone Lake water is about 1 percent hydrothermal source fluid and 99 percent inflowing stream water. The flux of hydrothermal source fluid into the lake is about 8×10^9 kg of water per year, based on mass-balance calculations for Cl. If the concentration of Cl in deep reservoir fluid, rather than in hydrothermal source fluid, is used, then the flow is calculated to be 1.5×10^{10} kg of water per year. Using the latter estimate, sublacustrine vents in Yellowstone Lake account for ~10 percent of the total flux of deep, thermal reservoir water in the Park, as estimated from Cl in streams (Friedman and Norton, 2000, this volume). Although the volumetric input of water into the lake from hydrothermal vents is small, the impact of the vent fluids on the geochemistry of Yellowstone Lake is large because of the great enrichment of many elements in these fluids. Because about 41 million kg per day of element-enriched deep thermal water flows into the lake, and recent swath sonar studies show the presence of numerous newly recognized hydrothermal features, Yellowstone Lake should be considered one of the most significant hydrothermal basins in the Park.

Introduction

Isotopic and geochemical studies suggest that the spectacular subaerial thermal basins in Yellowstone National Park (the Park) are a result of interaction between deeply recharged meteoric water and a magma chamber in the upper crust beneath the Yellowstone caldera (Fournier and others, 1979; Fournier, 1989, 2000). A deep, hot (360°C), and Cl-enriched (~9 mM Cl) reservoir (Rye and Truesdell, 1993, this volume) is thought to feed a series of intermediate reservoirs that vary in temperature and composition because of conductive cooling to surrounding rocks, boiling and steam separation, and mixing and dilution of ascending hydrothermal fluids with colder meteoric water (Truesdell and others, 1977; Fournier and others, 1979). These processes, in addition to water-rock interactions and mineral precipitation, result in the diverse geochemical compositions of subaerial geysers in Yellowstone National Park.

[1]U.S. Geological Survey, University of Washington, School of Oceanography, Box 355351, Seattle, WA 98195.

[2]U.S. Geological Survey, Box 25046, MS 973, Denver, CO 80225.

[3]Great Lakes Water Institute, University of Wisconsin-Milwaukee, Milwaukee, WI 53201.

The work of White and others (1988) and Fournier (1989) indicates the presence of three main types of hydrothermal waters and their hybrids within the Park. The first main type typically is boiling springs that are characterized by nearly neutral pH and high concentrations of Cl, B, alkali metals (for example, Li, Na, K), As, and Si. The boiling springs deposit siliceous sinter and consist primarily of the concentrated liquid that remains after boiling and steam separation of ascending thermal fluids. The second type of hydrothermal water is acidic, and it has high concentrations of SO_4 and NH_4. This water contains volatile gases (CO_2, H_2S, and NH_3) that separate from boiling, chloride-rich ascending fluids and then condense into colder meteoric waters. Such solutions are acidic due to addition of hydrogen ions during the dissolution of CO_2 and the dissolution and oxidation of H_2S (Xu and others, 1998). Fe, Al, Ca, and Mg are generally in greater concentrations than Na and K. These steam-heated, acid-sulfate waters tend to be above shallow, boiling, and chloride-rich fluids. Both types of hydrothermal waters are thought to originate from intermediate reservoirs in rhyolitic lava flows and ignimbrites and to have temperatures of 180° to 270°C. The third main type of hydrothermal fluid is mainly in the Mammoth Hot Springs area. In contrast to the other two water types, it ascends to the surface through sedimentary rocks composed of carbonates and gypsum-bearing shale. This water has nearly neutral pH; it has high concentrations of HCO_3, SO_4, Mg, and Ca and low concentrations of Si; and it originates from reservoirs with temperatures <100° to 120°C.

During the past 15 years, researchers from the University of Wisconsin-Milwaukee and Marquette University and, more recently, the U.S. Geological Survey have studied hydrothermal vents in Yellowstone Lake (Klump and others, 1988). The sublacustrine vents are thought to be submerged counterparts to the subaerial geysers that are present throughout the Park. Our integrated studies relate the geology and chemistry of the hydrothermal vents to the composition of water and solids in the lake, and also to the productivity and physiological characteristics of the biological communities in and near the hydrothermal fluids that enter the lake. This report focuses on the geochemistry of Yellowstone Lake water, the processes that control its composition, and the steady supply of potentially toxic elements to the Yellowstone Lake ecosystem by sublacustrine hydrothermal vents. Such information is critical for understanding and, ultimately, for managing the complex relationships between geology and biological communities in Yellowstone National Park.

Acknowledgments

This work could not have been done without the support of the National Park Service, especially Dan Reinhart, Dan Mahoney, and Jim Ruzycki. The help of Dave Lovalvo of Eastern Oceanics, Inc., who designed and operated the remotely operated vehicle (ROV) and the research vessel (R.V. *Cutthroat*), was invaluable. Jim Maki, of Marquette University, and associated graduate students and Tony Remsen and Rob Paddock of the University of Wisconsin-Milwaukee-Great Lakes Water Institute hauled anchors, deployed and retrieved the ROV, collected samples, and maintained the logbook in addition to doing their own research. Al Meier, Paul Briggs, Jim Crock, and Pete Theodorakos of the U.S. Geological Survey and Pat Anderson of the University of Wisconsin-Milwaukee-Great Lakes Water Institute analyzed samples. Rick Sanzolone, Kirk Miller, and Pam Gemery of the U.S. Geological Survey collected river samples, analyzed samples, and assisted with the mixing experiments. Special thanks go to Bob Seal of the U.S. Geological Survey for assistance in evaluating the stable-isotopic evaporation equations and to Lisa Morgan of the U.S. Geological Survey for her insights on the geology of Yellowstone National Park.

The U.S. Geological Survey (Mineral Resources Surveys Program) and the National Science Foundation (Environmental Geochemistry and Biogeochemistry) provided financial support for this research.

Study Area

Yellowstone National Park is a region of young and active tectonism and volcanism that is related to its current position over the Yellowstone hotspot (Christiansen, 1984). Migration of the North American plate over the Yellowstone hotspot, beginning 16 Ma, produced a string of silicic volcanic fields containing caldera complexes along the Snake River Plain. This track of silicic magmatism is reflected in the topographically low Snake River Plain; the hotspot is now centered in the topographically high Yellowstone Plateau (Morgan and others, 1984; Morgan, 1992; Pierce and Morgan, 1992). Large-volume, high-silica, rhyolitic ignimbrites and lava flows have erupted from overlapping and nested calderas in the Yellowstone Plateau volcanic field, producing an estimated volume of rock of 6,700 km^3 (Christiansen, 1984). Major caldera-forming eruptions occurred at 2.1 Ma, 1.3 Ma, and 0.64 Ma (K-Ar ages cited in Christiansen and Blank, 1972; Obradovich, 1992; Christiansen, 2001). The 0.64-Ma Yellowstone caldera is the locus of most of the active hydrothermal activity in the Park. Seismic studies suggest that a zone of magma is present below the caldera at a depth of about 4–6 km (Christiansen, 1984; Smith and Rubin, 1994). Magmatic heat drives the abundant and spectacular hydrothermal activity of Yellowstone National Park. One area in the Park outside the Yellowstone caldera that has extensive hydrothermal activity is in the Norris-Mammoth corridor. This is a system of north-trending faults and thermal areas that extends from Norris Geyser Basin to Mammoth Hot Springs.

Located in the southeastern part of the Park (fig.1), Yellowstone Lake, at an altitude of 2,357 m and covering an area of more than 341 km^2, is the largest high-altitude lake in North America (Kaplinski, 1991). Multiple geologic forces, including volcanic, hydrothermal, and glacial activity, have

shaped the Yellowstone Lake basin. The northern portion of the lake is mostly within the 0.64-Ma Yellowstone caldera (fig. 1). The eastern and northeastern boundary of the lake is the eastern edge of the Yellowstone caldera. Mary Bay, a large scalloped embayment on the north edge of the lake, formed approximately 10.8 ka as a series of sublacustrine hydrothermal-explosion events (Wold, and others, 1977; Morgan and others, 1998). West Thumb, in the western part of Yellowstone Lake, formed when the 128-ka tuff of Bluff Point erupted, forming the West Thumb caldera (Christiansen, 1984; L.A. Morgan and W.C. McIntosh, oral communs., 1998). Areas in Yellowstone Lake that are within the Yellowstone caldera have exceptionally high heat flow (Morgan and others, 1977) and are characterized by abundant sublacustrine hydrothermal activity (Kaplinski, 1991) (fig. 1). The South and Southeast Arms of the lake are far outside the caldera boundary, are of glacial origin, and exhibit no evidence of hydrothermal activity.

Methods

Field Methods

Because there are very few water-quality data or discharge measurements for surface-water flow into Yellowstone Lake, samples were collected during August and September 1998, and July 1999, from 21 of the major streams that enter the lake. GPS measurements were obtained, and the temperature and pH of the water were determined at each site. The pH meter was calibrated each day using known buffer solutions. Either point-source or integrated water samples were collected in 500-mL polyethylene bottles and brought to a field-based laboratory for processing. The bottles had been acid-cleaned and well rinsed with distilled, deionized water before use. Estimates of discharge were made either by timing a float and determining the cross-sectional area of the stream (1998) or by measuring the flow rate at 1 to 20 locations in a cross section of the stream using a velocity meter (1999). The accuracy of the flow estimates varied between years and sampling sites because different individuals used different methods at different times, and because some streams could not be waded.

A large-volume (20 L) sample from the Yellowstone River at its outlet from Yellowstone Lake (near Fishing Bridge) was placed into a plastic cubitainer in July of 1999. The sample was collected using teflon tubing, an in-line 0.45-µm filter capsule, and a peristaltic pump. The sample was returned to the field-based laboratory for processing and for use in the mixing experiments described below. Because the U.S. Geological Survey (USGS) gages the Yellowstone River at its outlet from the lake (station 06186500), continuous discharge measurements from this site are available (http://mt.water.usgs.gov; accessed 8/2000). Outflows from the lake during our sampling periods were 52 ± 3 and 156 ± 9 m^3/s in 1998 and 1999, respectively.

Hydrothermal vent samples for this study were collected in West Thumb, in Mary Bay, and near Stevenson Island in the summers of 1996 through 1999 (fig. 1). The West Thumb vent samples were from several vent fields at depths of 29–53 m. Vent fluids were collected nearshore off Steamboat Point and near Pelican Creek. These were shallow vents with depths of 7–10 m. Hydrothermal fluids were also collected from a deep hole in Mary Bay at depths of 48–54 m. Samples collected near Stevenson Island were from the deepest vents (95–110 m). All vent samples were collected with a tethered and submersible remotely operated vehicle (ROV) designed and piloted by Dave Lovalvo of Eastern Oceanics, Inc. Klump and others (1992) described an early version of that vehicle. Although the exact set-up of the vehicle varied from year to year, it always collected vent-fluid samples using piston-operated plastic syringes that were connected by polypropylene tubing to an articulated and extensible probe. The temperature of the vent was continuously monitored during sample collection, and the probe was maintained in position using electrical and video connections to the surface. After retrieval of the ROV, samples were transferred through three-way valves from the syringes on the vehicle into other syringes for biological and chemical measurements. The vent samples were returned to the field-based laboratory for processing.

Samples from different depths in the water column of Yellowstone Lake were collected in Southeast Arm, West Thumb, and Mary Bay in July 1997 and 1998, and near Stevenson Island in July 1998, using a trace-metal-clean hydrobottle (no internal cords) attached either to a Kevlar line, a HYDROLAB™ cable, or the hydrowire on the research boat. All wire types produced consistent results, with no evidence of contamination for the elements of interest. The water-column samples in Mary Bay were collected directly above the vents in the deep hole in Mary Bay. The water-column samples near Stevenson Island were collected close to, but not directly above, the vents that were sampled. In contrast, water-column samples from West Thumb were collected 3–4 km from the sampled hydrothermal vent fields. Water-column samples from Southeast Arm were collected at least 10 km from any known hydrothermal vents. Water-column samples were placed in 500-mL acid-cleaned and well-rinsed polyethylene bottles on board the boat and returned to the field-based laboratory. In-place measurements of temperature, pH, conductivity, redox potential, and dissolved oxygen concentrations in the water column were taken as a function of depth, using a HYDROLAB™, prior to collection of water samples. Those profiles were used to determine the depths for collection of the water samples and to confirm that the entire water column was oxic at every site.

Lake-bottom sediment was collected in Mary Bay and West Thumb using a gravity corer. Pore water was obtained from cores at the field-based laboratory, using the whole-core squeezing method of Jahnke (1988). The pore water was filtered through acid-washed, 0.2-µm disposable filters.

Water samples from two subaerial geysers were collected from West Thumb Geyser Basin (Black Pool and Vandalized Pool) in September of 1998, using a plastic bottle. They were immediately filtered on-site using a 0.45-µm filter. During July of 1999, water samples were collected from three subaerial

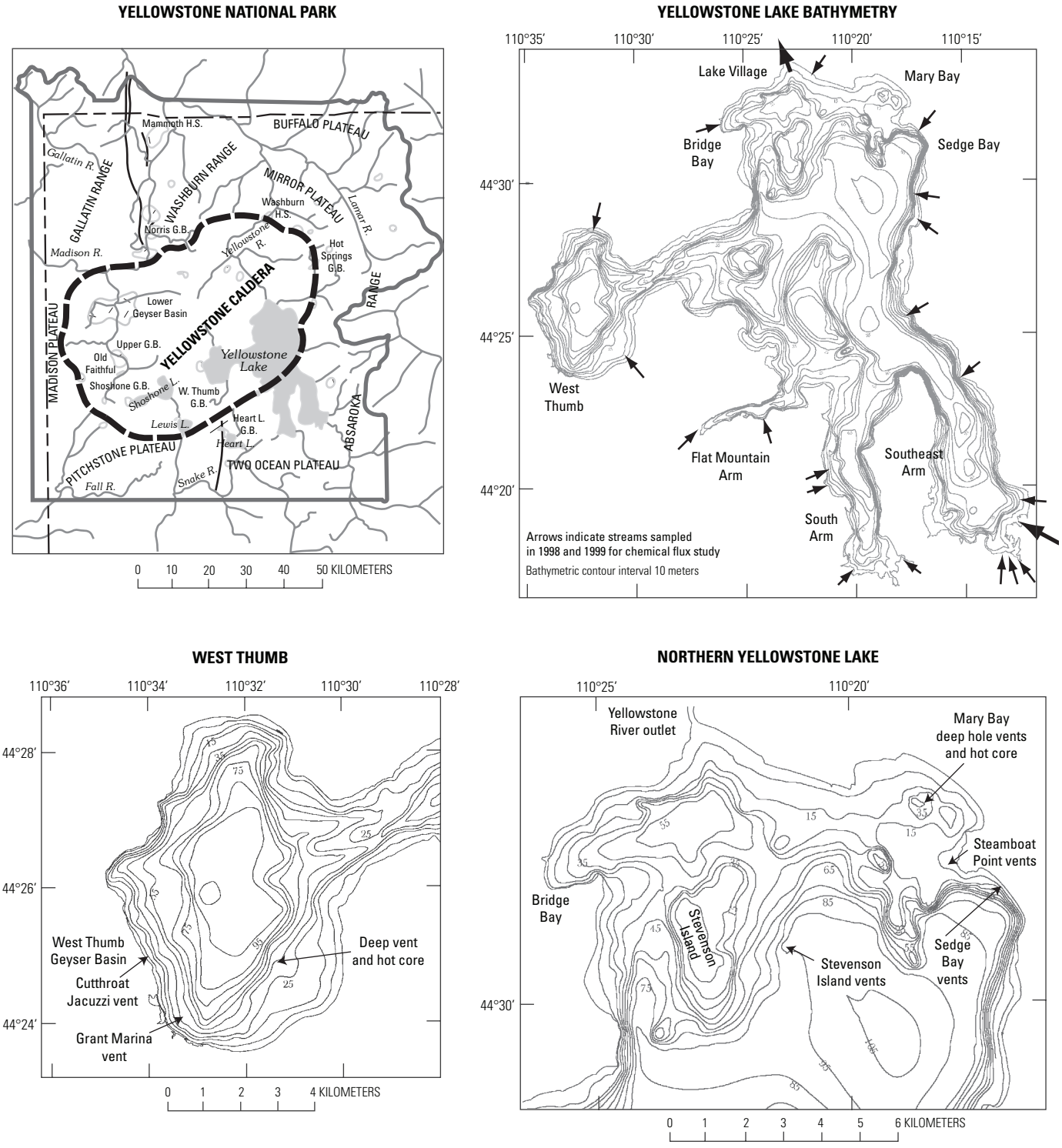

Figure 1. Maps of Yellowstone National Park and Yellowstone Lake with detailed maps of West Thumb and northern Yellowstone Lake showing locations of the sampling sites. G.B., geyser basin; H.S., hot spring; R., River; L., Lake. Base bathymetry from Kalinski (1991).

geysers in Norris Geyser Basin (Green Dragon, Echinus, and Porkchop Geysers) and from Black Pool at West Thumb Geyser Basin using a peristaltic pump loaded with teflon tubing and an in-line 0.45-µm filter capsule. These particular geysers were chosen because they are indicative of the spectrum of hydrothermal fluids observed in the Park. Water samples from Porkchop, Black Pool, and Vandalized Pool are neutral to alkaline and Cl-rich. The hydrothermal fluids from Green Dragon and Echinus are acidic and enriched in SO_4 and Cl. Geyser waters collected in 1999 were immediately mixed with filtered water collected from the Yellowstone River in 500-mL polyethylene bottles in proportions ranging from 0 to 100 percent geyser water. The temperatures of the mixtures were maintained by insulating the bottles. The samples were processed at the field-based laboratory less than 2 hours after mixing.

Laboratory Methods

Values of pH of vent fluids, water-column samples, and mixed solutions were determined at the field-based laboratory after standardizing a pH meter and electrode using six buffer solutions ranging from pH 1.68 to 10. Subsamples of all water samples except pore water were taken for analysis of dissolved elements, Hg, anions, isotopes ($\delta^{18}O$ and δD), and either alkalinity or dissolved inorganic carbon. Because of the limited volumes of pore water, only selected samples were analyzed for anions and isotopes. Samples for anion and dissolved-element determinations were obtained by filtering the water through 0.45-µm disposable nylon filters into new polyethylene bottles for anions; into acid-cleaned, well-rinsed polyethylene bottles for dissolved elements; and into acid-cleaned glass bottles with teflon caps for Hg. Anion samples were kept cool, whereas samples to be analyzed for dissolved elements were preserved by adding one drop of re-distilled concentrated nitric acid per 10 mL of solution. Samples for dissolved Hg analyses were preserved with 1.5 mL-Ultrex concentrated HNO_3, saturated with sodium dichromate, per 60 mL of sample. Anion analyses of vent, water-column, and pore-water samples were done by ion chromatography at the field-based laboratory; anion analyses of the river water and mixing experiments were done by ion chromatography in the USGS laboratories in Denver, Colo. Dissolved elements were determined at the USGS laboratories in Denver, using inductively coupled plasma–atomic emission spectrometry (ICP–AES) (major ions and B), inductively coupled plasma–mass spectrometry (ICP–MS) (minor elements), and cold vapor generation with atomic-fluorescence detection (Hg). Samples for water isotopes ($\delta^{18}O$ and δD) were placed in 20-mL glass scintillation vials, tightly capped, and analyzed at the USGS laboratories in Denver by isotope-ratio mass spectrometry. Water samples were prepared for hydrogen-isotopic analyses using the Zn reduction technique, and for oxygen-isotope analyses using an automated CO_2 equilibration technique. Values of $\delta^{18}O$ and δD are relative to Vienna Standard Mean Ocean Water (VSMOW); they have reproducibility of approximately 0.1 and 1.0 per mil, respectively. Alkalinity was determined using either a Chemetrics test kit (stream samples) or by Gran titration (mixing experiment samples) (Stumm and Morgan, 1996) at the field-based laboratory. The dissolved inorganic carbon or sum CO_2 content of the vent fluids and water-column samples was determined by flow-injection analyses at the field-based laboratory.

Blank samples using distilled, deionized water were included with each batch of 20 samples. The blank samples had element concentrations below detection limits. Standard reference solutions, either from the USGS or from the National Institute of Standards and Technology, were included in each batch of samples to determine accuracy and precision of the ICP-AES and ICP-MS analyses.

Results and Discussion

Systematics of Stable Isotopes ($\delta^{18}O$ and δD)

Hydrogen and oxygen isotopes are powerful tools for understanding the origin and evolution of waters in and around Yellowstone Lake. A plot of δD versus $\delta^{18}O$ clearly indicates that Yellowstone Lake deep waters plot off the global meteoric water line of Craig (1961), along an evaporation trend with a slope of about 5 (fig. 2). In contrast, samples from the majority of streams that drain into Yellowstone Lake have isotope values of typical atmospheric waters that plot on or near the global meteoric water line. Examination of the data for lake water reveals three important observations: (1) lake water is progressively more evaporated with increased distance from the Yellowstone River inlet, which is at the south end of Southeast Arm (fig. 1), (2) sublacustrine hydrothermal vent water is mainly lake water, probably due to mixing in the shallow subsurface or entrainment of lake water during sampling of the hydrothermal vent fluids, and (3) vent-water samples and water-column samples above vent sites tend to form nearly vertical arrays that indicate mixing with water whose composition is similar to the thermal pore water collected from Mary Bay and West Thumb sediments. Pore-water samples were collected from near-surface sediments as close as possible to known sublacustrine vent sites.

Studies by Craig and others (1963), Craig and Gordon (1965), and Gilath and Gonfiantini (1983) showed that the effects of evaporation, which are dependent on both kinetic and equilibrium liquid-vapor isotope-fractionation effects, can be calculated if temperature, relative humidity, and the isotopic values (oxygen or hydrogen isotopes) of surface inflow waters and atmospheric vapor are known. In practice, the isotope values of atmospheric vapor are calculated assuming equilibrium with precipitation. Krabbenhoft and others (1990) showed that the equilibrium assumption is valid, at least for $\delta^{18}O$ calculations. Parameters used in stable-isotopic-evaporation calculations are listed in table 1. Using the equations in Gilath and Gonfiantini (1983) and the appropriate $\delta^{18}O$ data, we calculate that Yellowstone Lake water has evaporated approximately 13 percent

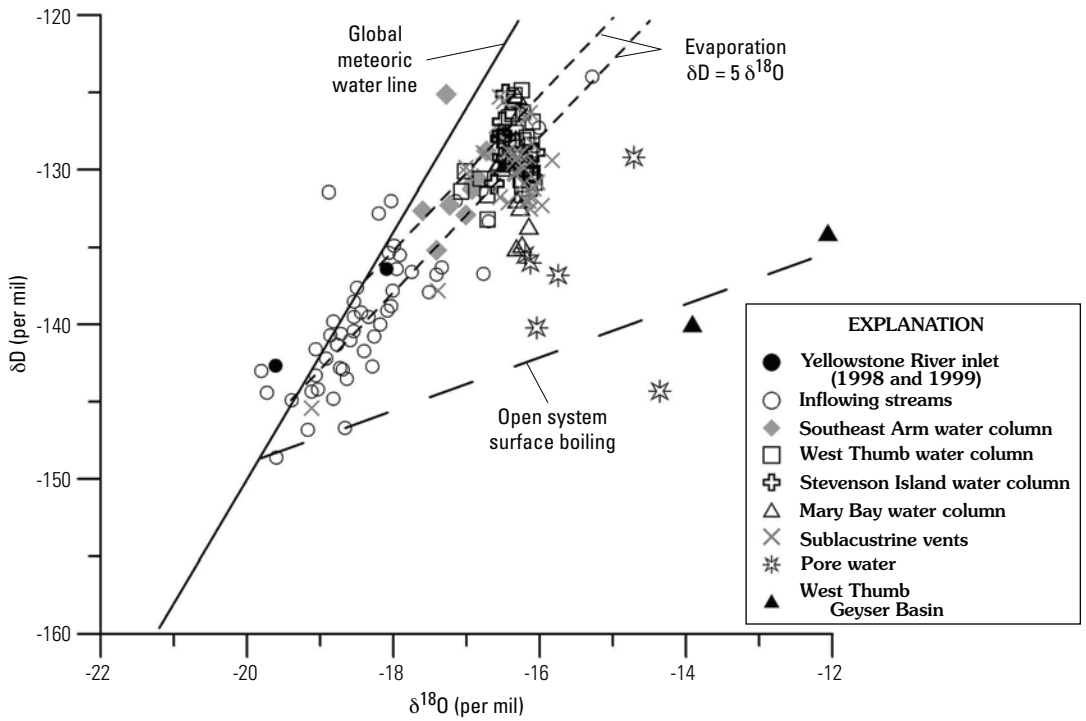

Figure 2. Hydrogen- and oxygen-isotope compositions of Yellowstone Lake (water columns in Southeast Arm, West Thumb, near Stevenson Island, and Mary Bay), inflowing streams, and sublacustrine hydrothermal vent fluids. Cl-rich pore waters collected near sublacustrine hydrothermal vents and two subaerial geyser waters from West Thumb Geyser Basin are shown for comparison.

during the 14±3-year residence time of the water in the lake. Hostetler and Giorgi (1995) compiled and calculated meteorological data for Yellowstone Lake, and their estimates of evaporation from meteorological data allow a direct comparison with estimates from stable-isotope fractionation. Using Kaplinski's (1991) estimate of total lake volume and the mean annual evaporation rate for Yellowstone Lake based on the global-climate model of Hostetler and Giorgi (1995), we calculate net evaporation during the 14-year residence time of about 16 percent, very similar to that estimated from the isotopic calculations (table 1). Furthermore, the simulations and meteorological data of Hostetler and Giorgi (1995) indicate that the volume of water lost due to evaporation and gained from precipitation is 3–4 times less than the volume of water flowing into and out of the lake. Thus, evaporation is very important in controlling the stable-isotopic composition of Yellowstone Lake water, but it is not the major flux of water from the lake.

Mass-Balance Calculations

Mass-balance calculations are used to identify elements for which hydrothermal vents may be an important source to Yellowstone Lake. These calculations consider the change in concentration of an element or species in a system as a function of time (Schnoor, 1996). The change in concentration as a function of time is the difference between the inputs (or sources) and outputs (or sinks) of elements or species to the system. For Yellowstone Lake, we consider only changes in dissolved concentrations of elements or species. Figure 3 illustrates potential sources and sinks of dissolved elements or species to Yellowstone Lake. Potential sources include precipitation (rain and snow), inflowing streams, and hydrothermal vents. Potential sinks for this system are evaporation, outflow via the Yellowstone River at the north end of the lake, and removal processes occurring within the lake that transform dissolved elements into particulate elements (for example, mineral precipitation, adsorption, or biological uptake). Ground water may be an important potential source or sink of elements. However, its impact is not known because a thorough hydrologic balance and detailed analyses of ground-water compositions have not yet been done for this system.

The mathematical expression to describe changes in the concentration (C) of a dissolved element or species as a function of time (t) (that is, $\frac{\delta C}{\partial t}$ with units of moles/L/s) in terms of these potential inputs and outputs is:

$$\frac{\delta C}{\delta t} = \frac{(Qprec*Cprec)}{V} + \frac{\sum(Qin*Cin)}{V} + \frac{(Qvent*Cvent)}{V} - \frac{(Qevap*Cevap)}{V} - \frac{(Qout*Cout)}{V} - J \pm \frac{(Qgw*Cgw)}{V} \quad (1)$$

where Q is discharge in m^3/s of precipitation (prec), inflow (in), hydrothermal vent water (vent), evaporation (evap), outflow (out), and ground water (gw), C is the dissolved concentration of an element or species of interest in moles/L in precipitation, inflow, hydrothermal vent water, evaporation, outflow, or ground water, J is a generic removal term in moles/L/s to account for transformations from dissolved to particulate phases, and V is the volume of the lake in m^3.

Contributions from precipitation and evaporation are insignificant because their element concentrations (Drever, 1988) and discharges are very low (table 1) compared to other hydrologic components considered in equation 1. Therefore, neither evaporation nor precipitation is considered further in the

Table 1. Volume and flux relations for water budget of Yellowstone Lake.

Average ice-free relative humidity	77%	Hostetler and Giorgi (1995)
Average ice-free annual temperature	11.6°C	Hostetler and Giorgi (1995)
$\delta^{18}O$ flow-weighted surface inflow	–19.0‰	this study
$\delta^{18}O$ atmospheric moisture*	–28.8‰	
Mean annual evaporation rate	0.19 km^3/yr	Hostetler and Giorgi (1995)
Mean annual precipitation rate	0.17 km^3/yr	Hostetler and Giorgi (1995)
Aug.–Sept. 1998 stream inflow	0.67 km^3/yr	this study
July 1999 stream inflow	3.6 km^3/yr	this study
Lake surface area	341 km^2	Kaplinski (1991)
Lake volume	16.54 km^3	Kaplinski (1991)
Discharge at USGS gaging station 06186500 Yellowstone River at Yellowstone Lake outlet	1.19±0.29 km^3/yr	USGS; from 67-year record [http://mt.water.usgs.gov]
Average residence time	14±3 yr	Calc. as volume/discharge
Net evaporation rate	1.12%/yr	
Net evaporation calculated from hydrologic data and residence time	16±3%	For one residence time of lake water
Net evaporation calculated from $\delta^{18}O$	13%	For one residence time of lake water

*Calculated by equilibrium with precipitation.

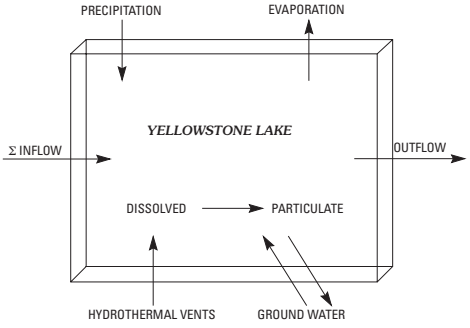

Figure 3. A box model, the basis for the mass-balance calculations, illustrates the potential sources and sinks of elements in Yellowstone Lake.

mass-balance calculations. In addition, if we assume that the system is at steady state (that is, $\frac{\delta C}{\partial t} = 0$ or there is no change in the dissolved concentration of an element or species in lake water as a function of time), then equation 1 can be rearranged to indicate that inputs due to inflow and hydrothermal vents equal outputs by outflow and other biochemical removal processes. Ground water can act either as a source or a sink of elements.

$$\Sigma(Qin*Cin) + (Qvent*Cvent) = (Qout*Cout) \pm (Qgw*Cgw) + (J*V) \quad (2)$$

By dividing both sides of the equation by *Qout* and rearranging, the dissolved concentration of an element or species at the lake outlet can be compared with that in the flow-weighted inflow.

$$Cout - [\frac{\sum(Qin*Cin)}{Qout}] = \frac{(Qvent*Cvent)}{Qout} \pm \frac{(Qgw*Cgw)}{Qout} - \frac{(J*V)}{Qout} \quad (3)$$

If the dissolved concentration of a chemical species in the outflow is greater than the flow-weighted dissolved concentration of the same species in the inflow, there is a net source of that species in the lake. If the difference between the dissolved concentrations of the outflow and flow-weighted inflow is negative, then the lake is acting as a net sink for the element or species. If the dissolved concentration of a chemical species in the outflow is equal to the flow-weighted dissolved concentration of the same species in the inflow, there is no net source or sink in the lake.

The mass-balance calculations were made using two synoptic estimates of the flow and dissolved concentrations of elements or species in streams, determined during low-flow (August and September of 1998) and high-flow (July of 1999) conditions. Sampling times were chosen to represent extremes in discharge and element or species concentrations associated with those flows, and they were intended to span the range of variations. The mass-balance calculations are instantaneous pictures. A more detailed evaluation that looks at changes in daily, monthly, or seasonal fluxes can be done only when a hydrologic balance for the lake is determined and samples for element analyses of the inflows and outflows are collected and analyzed at higher frequencies throughout a long time interval.

The Yellowstone River at its inlet to Yellowstone Lake in Southeast Arm is the major contributor (that is, 70 percent in 1998 and 86 percent in 1999) of water to the lake. Because the Yellowstone River at its inlet to Yellowstone Lake is a braided stream, it is difficult to measure its discharge without an established and calibrated gaging station. Hence, of all the terms on the left side of equation 3, the value for *Qin* likely has the largest error. We estimate this error by examining the water balance for the time intervals of our samplings. This calculation considers that the change in the volume (V) of the lake as a function of time (t) (that is, $\frac{\partial V}{\partial t}$ in units of m^3/s) is equal to the discharge or flux of water into the lake minus the flux of water out of the lake, that is,

$$\frac{\partial V}{\partial t} = Qprec + Qin + Qvent - Qevap - Qout \pm Qgw \quad (4)$$

To calculate the value of *Qin* for comparison with our measured value, we used published values of *Qprec* and *Qevap* for this area (table 1) and assumed that *Qvent* and *Qgw* are negligible relative to the other discharges. In addition, the value for $\frac{\partial V}{\partial t}$ for each of the river sampling intervals (8/24–9/1/98 and 7/12–7/21/99) was estimated by first determining the relationship between gage height and discharge at Yellowstone River at its out-

let from the lake, from the long-term gaging records (http://mt.water.usgs.gov; accessed 8/2000). The change in discharge at the Yellowstone River outlet during the sampling periods was converted to a change in gage height using the relationship. Then, the change in gage height was multiplied by the surface area of the lake (table 1) to determine the change in volume during the sampling intervals. Solving equation 4 with the above assumptions yields calculated values for *Qin*, which is the sum of all inflows, of 27 m^3/s in 1998 and 93 m^3/s in 1999. The measured values for ΣQin during our sampling periods were 21 m^3/s in 1998 and 115 m^3/s in 1999. Our measured values for ΣQin are within 22 percent of the calculated values.

Because our discharge estimates are relatively well constrained ($\pm$22 percent), we can evaluate the role of internal sources of elements to the lake by plotting the ratio of the concentration of an element in the outflow to the concentration in the flow-weighted inflow (fig. 4). On this log plot, positive values of the ratio indicate that there is a net source of the element into the lake, whereas negative values indicate that the lake is a net sink for the element. Values of zero indicate that there is little or no net source or sink for the element, or that a small source or sink term is not resolved by this approach. Given the assumptions and error estimates above, we conservatively assume that values of the ratio within 1 log unit of zero indicate no net source or sink.

The mass-balance calculations for 1998 and 1999 indicate that many elements have larger dissolved concentrations (by at least a factor of 10) in the outflow from Yellowstone Lake relative to the flow-weighted inflow, suggesting that there is a supply of these elements within the lake (fig. 4). The magnitude of the loading of elements or species into the lake appears to be seasonal (that is, generally loading is greater during high flow), but more detailed information about temporal changes in discharges and associated element concentrations is needed. Elements that definitely show a source within the lake (that is, log [$\text{concentration}_{\text{outflow}}/\text{concentration}_{\text{flow-weighted inflow}}$] ≥ 1) for one or both years include As, (possibly) B, Cl, Cs, Cu, Ge, Li, Mo, Sb, and W. Probable mechanisms for increased concentrations of many elements in the lake include evapoconcentration and supply from hydrothermal vents and ground water. The stable isotopes ($\delta^{18}O$ and δD) indicate that evapoconcentration accounts for a change of about 13 percent in the concentrations of elements during the residence time of water in the lake. This change is within our analytical error, and it is much too small to account for the results of our mass-balance calculations. Because most of these elements (As, B, Cl, Cs, Li, Mo, Sb, and W) are known signature elements for the suberial hydrothermal waters (Beeson and Bargar, 1984; Stauffer and Thompson, 1984; Sturchio and others, 1986; White and others, 1991), we conclude that enrichment of these elements in the lake outflow is due to hydrothermal input. Other elements (that is, Ce, La, Mn, Sc and U) show removal within the lake during one or both years. Processes such as oxidation and (or) mineral precipitation (Mn) or sorption by particles (Ce and U) may be responsible for dissolved-metal loss from the water column (Stumm and Morgan, 1996).

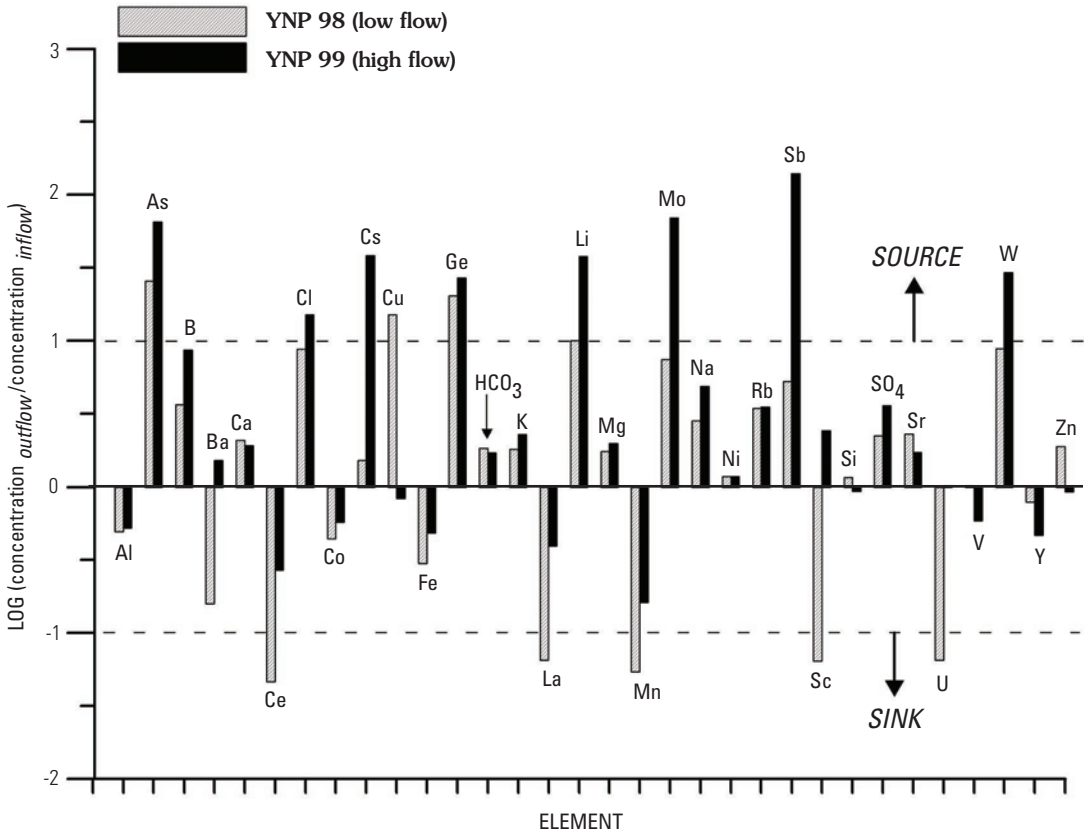

Figure 4. Results of mass-balance calculations that compare element concentrations in the flow-weighted inflow to and outflow from Yellowstone Lake. Values of the log of the ratios ($\text{concentration}_{\text{outflow}}/\text{concentration}_{\text{inflow}}$) ≥ 1 indicate a net source of elements to the lake; log ratios ≤ 1 indicate a net loss or sink of elements within the lake. If the log ratio = 0 ± 1, then there is no net source or sink of elements.

Chloride Concentrations in Hydrothermal Vent Fluids and Lake Water: Mixing of End-Member Solutions

Chloride is a major indicator of hydrothermal fluids. Geochemical interpretations of geyser basin fluids indicate that the subsurface deep-reservoir fluids that feed the thermal basins in the Park contain about 10 mM (360 mg/kg) Cl (Truesdell and others, 1977; Fournier, 1989). As these fluids ascend to the surface, boiling and steam separation occur; the concentration of Cl in the boiled water can be as high as 20 to 21 mM (710 to 750 mg/kg) (Truesdell and others, 1977). Chloride concentrations in the boiled water depend on the steam-separation mechanism (that is, single stage, continuous, or a combination) and dilution by local meteoric waters.

Chloride is an excellent tracer of hydrothermal water in Yellowstone Lake because the major source of water to the lake, that is the Yellowstone River, contains almost no Cl (<6 μM or micromoles per liter). The flow-weighted inflow for August and September of 1998 and July of 1999 had Cl concentrations of 15 and 9 μM, respectively. Those values are at least three orders of magnitude smaller than Cl concentrations in the deep source water or boiled thermal water.

Dissolved chloride concentrations for the flow-weighted inflow waters, hydrothermal vent fluids, and lake water as a function of depth are compared in figure 5 and table 2. The vent fluids and lake water are significantly enriched in Cl relative to the inflowing water. However, the vent fluids, with a few exceptions, have about the same concentration of Cl as the lake water, and that concentration (100 to 200 μM) is substantially lower than dissolved Cl concentrations in deep thermal water (10 to 20 mM). Thus, the vent fluids that we collected appear to be highly diluted hydrothermal source water. Furthermore, Cl concentrations in the water column vary with location in the lake. This observation is not expected for a conservative element in a lake that has a water residence time of 14±3 years. These differences in Cl concentrations, as well as other elements (table 2), suggest that there is variable dilution by lake water or there are variable inputs of hydrothermal fluids into the lake.

The dilution hypothesis is supported by relationships between the concentrations of Cl and other elements in lake and vent waters. The results of the mixing experiments between Yellowstone River water and subaerial geyser fluids are also instructive. Linear relationships between Cl and other element concentrations are expected for mixing of end-member solutions when no removal reactions (for example, precipitation of minerals) occur. The slopes of such lines are indicative of the concentrations in the end-member solutions. The concentrations of selected elements that show enrichments in the outflow relative to the inflow (B, Li, As, and W) are plotted with respect to Cl in figures 6 and 7 for the flow-weighted inflow, water column, hydrothermal vent fluids, and mixing experiments. The correlation coefficients for the linear relationships between Cl and B, Li, As, and W for these solutions are significant at the 99 percent confidence interval (Rohlf and Sokal, 1995). Other dissolved components that show linear relationships between their concentrations and Cl concentrations in lake water and vent fluids at the 99 percent confidence interval are SiO_2, Na, K, Rb, Cs, Ge, Mo, Sb, HCO_3, and SO_4. There are no correlations between dissolved Cl and the alkaline earth elements (Mg, Ca, Sr, Ba) in lake water and vent fluids. Alkaline earth elements are independent of Cl concentration, indicating that end members have very similar concentrations or that the hydrothermal source fluid has negligible concentrations of these elements. The linear relationships between Cl and many elements or species in vent fluids and lake water strongly indicate that end-member mixing is occurring and that the most likely end members that define the chemical composition of Yellowstone Lake water are inflow water and hydrothermal source fluids. This is further demonstrated by linear correlations between Cl and other elements or species, including the alkaline earth elements, for the experiments in which river water and subaerial geyser fluids were mixed.

To compare differences in the compositions of hydrothermal vent fluids and their influence on the geochemistry of the water column in the lake, we normalized element concentrations in these waters to an average concentration of Cl in the deep water of the lake. This normalization eliminates the variable dilution of these waters as end-member mixing occurs.

$$[Me^*] = \frac{[Me]}{[Cl]} * [ClDW] \quad (5)$$

where $[Me^*]$ is the normalized-element or species concentration, $[Me]$ is the measured concentration of the element or species, $[Cl]$ is the measured Cl concentration, and $[ClDW]$ is the average concentration of Cl in the deep water of Yellowstone Lake and is 140 μM.

Relationships Between Major Anions and pH in Hydrothermal Vent Fluids and Lake Water

The principal anions in the subaerial hydrothermal systems in the Park are Cl, SO_4, and HCO_3 (Henley and others, 1984). The relative proportions of those anions in hydrothermal waters and their pH reflect the processes (for example, boiling, dissolution of gases and rocks, and mixing) that occur as deep thermal fluids ascend and interact with ground water, surrounding rocks, and surface water. For example, deep thermal fluids may flow directly to the surface, producing boiling springs that have nearly neutral to alkaline pH and Cl-rich water. Acid-SO_4 waters of low pH (<3) and low Cl contents are produced when H_2S volatilizes from deep thermal fluids during boiling and then condenses into colder ground water. The H_2S can then oxidize and release hydrogen ions and SO_4 to solution. Volatilization of CO_2 from boiling thermal fluids and dissolution into ground water produces HCO_3-rich waters. Mixtures of these waters form hybrid solutions, such as acid-SO_4-Cl waters.

Table 2. Temperature and average chemical composition of Yellowstone Lake water, including streams that enter the lake (flow-weighted inflow), deep lake water (DW; >25 m deep) in Southeast Arm (SE. Arm), in West Thumb (WT), near Stevenson Island (SI), and in Mary Bay (MB), and lake-bottom hydrothermal vent fluids in West Thumb, near Stevenson Island, and in Mary Bay.

Parameter, element, or species	Units	1999 Flow-weighted inflow	SE. Arm DW	WT DW	SI DW	MB DW	WT vents	SI vents	MB nearshore vents	MB deep-hole vents
temp.	°C	14.6	4.8	7.3	9.3	12	8.7–68	15–106	28.3–93	30–103
pH		5.7	7.5	7.3	7.4	6.9	5.4–8.6	5.1–7.1	5.4–7.3	4.8–6.9
Cl	μM	8.7	120	160	140	170	50–1,150	130–140	120–140	140–170
SiO_2	μM	170	170	210	190	200	180–1,600	160–330	150–350	150–400
B	μM	1.1	7.4	8.1	7.5	9.7	3.2–68	5.7–8.3	6.5–9.2	7.4–13
Li	μM	0.8	5.7	7.9	6.5	8.1	8.8–88	6.2–7.8	4.9–7.2	4.9–8.5
Na	μM	72	350	470	400	440	440–3,900	360–420	300–390	270–430
K	μM	16	31	38	36	36	17–200	36–41	33–61	31–51
Rb	nM	13	56	69	60	68	61–550	56–69	47–96	55–85
Cs	nM	0.4	24	31	22	31	22–630	17–24	17–280	8.3–660
Mg	μM	42	98	110	110	110	8.2–120	90–130	74–140	66–120
Ca	μM	59	130	130	130	130	87–140	120–160	100–210	90–140
Sr	nM	230	500	490	490	520	75–550	470–730	410–1,140	380–730
Ba	nM	41	61	59	60	65	36–120	71–590	29–1,240	57–490
As	nM	2.9	160	270	190	240	120–2,800	130–290	88–230	49–720
Ge	nM	0.1	2.7	5.5	3.3	3.9	5.5–140	2.7–5.5	2.7–4.1	2.7–5.5
Hg	pM	<25	<25	55	<25	<25	<25–800	<25–850	<25–160	<25–140
Mo	nM	0.4	11	16	11	11	18–380	0.4–21	9.5–33	1–28
Sb	nM	<0.2	4.1	6.3	4.9	6.5	0.8–140	<0.2–7.8	<0.2–90	<0.2–107
W	nM	0.9	7.3	11	6.9	9.5	87–440	5.4–10	6.5–260	7.1–540
ΣCO_2	mM	0.25	0.62	0.69	0.69	0.79	0.76–5.5	0.64–9.8	0.92–2.4	0.83–27
HCO_3	μM	240	560	680	620	610	510–3,040	460–700	400–720	230–620
SO_4	μM	21	76	78	82	89	21–130	78–120	71–150	78–150

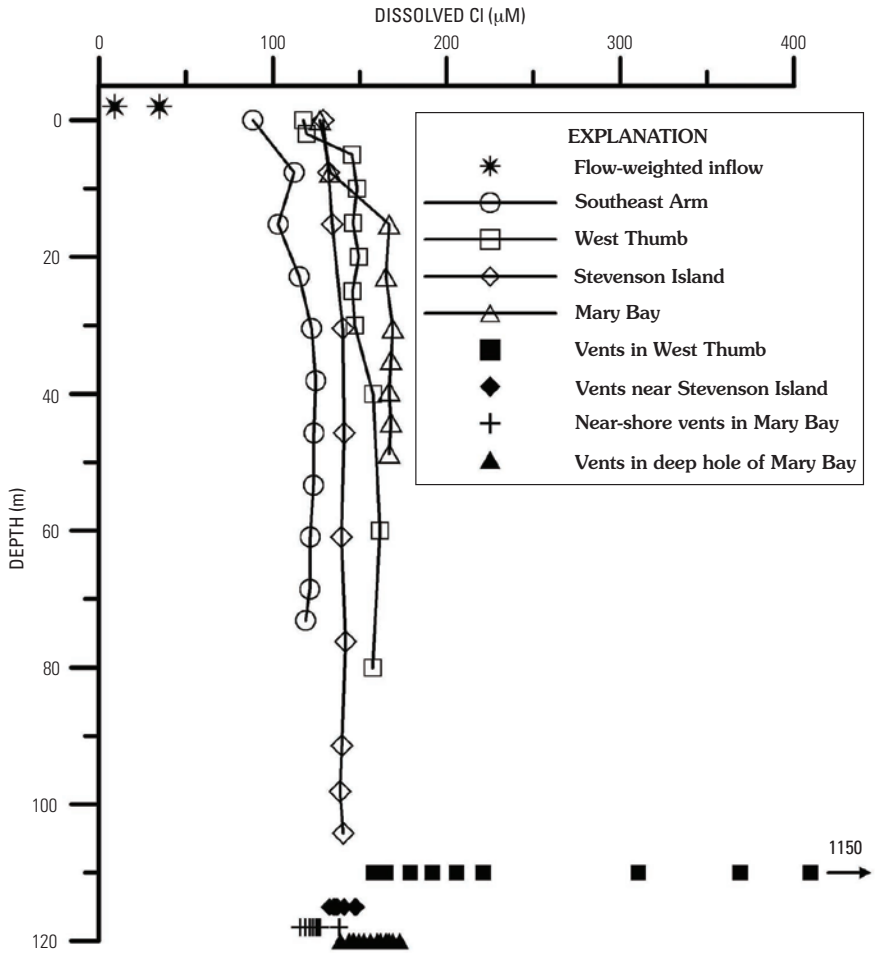

Figure 5. Dissolved Cl concentrations in flow-weighted inflow to Yellowstone Lake, lake water as a function of depth and location, and hydrothermal vents as a function of location. Inflow data were collected in the summers of 1998 and 1999, water-column data in the summer of 1998, and vent data in the summers of 1996–1999.

A ternary diagram illustrates the relative importance of Cl, SO_4, and HCO_3 in vent fluids and lake water (fig. 8). Data from the acid and nearly neutral geyser water collected from Norris Geyser Basin and West Thumb Geyser Basin are also plotted for comparison. The first observation is that the dominant anion in almost all vent fluids and lake water is HCO_3, whereas the water in subaerial geysers tends to be dominated by Cl (Porkchop), Cl and SO_4 (Green Dragon and Echinus), or Cl and HCO_3 (Black Pool). Second, the water from some vents near Stevenson Island and in the deep hole of Mary Bay have a larger proportion of SO_4 relative to Cl or HCO_3, whereas the water from vents in West Thumb has a larger proportion of Cl relative to SO_4 and HCO_3. This observation suggests that water in certain vents near Stevenson Island and in the deep hole of Mary Bay is influenced more by the volatile gas H_2S. The relative proportions of anions in lake water are between the proportions in the two vent types, but closer to the relative proportions observed in water from the Mary Bay and Stevenson Island vents.

The mixing lines between Yellowstone River water at the inlet to the lake and subaerial geyser water suggest that the source fluid for vents near Stevenson Island and in the deep hole of Mary Bay has a larger component of acid-SO_4-Cl water, whereas the source fluid for some vents in West Thumb has a larger component of nearly neutral, Cl-rich water. The lake water is a composite of these source fluids and inflowing surface water.

The pH of hydrothermal vent fluids is regulated by the amount of volatile gases (CO_2 and H_2S) dissolved into solution. In figure 9, normalized concentrations of total dissolved carbonate (ΣCO_2*) are plotted with respect to pH (measured at 25°C) for the hydrothermal vents and water in Yellowstone Lake. Also shown in that figure is a prediction, using the chemical-equilibrium-modeling computer program MINEQL+ (Schecher and McAvoy, 1998), of pH based on injection of variable concentrations of CO_2 into a closed system. There is excellent agreement between the measured and predicted pH. Values of pH are lower when there are higher amounts of total-dissolved-carbonate species in solution. The contribution of H_2S, depicted by concentrations of its oxidized form (SO_4), is <13 percent of the sum of ΣCO_2* and SO_4*. Thus, the dominant dissolved gas controlling the pH of these waters likely is CO_2. The observed data indicate that water in all vents, except a few in West Thumb and near the shore in Mary Bay, are acidic (pH < 7). The most acidic and CO_2-enriched vents are near Stevenson Island and in the deep hole of Mary Bay. In contrast, lake water has low concentrations of total dissolved carbonate, and it is nearly neutral to alkaline.

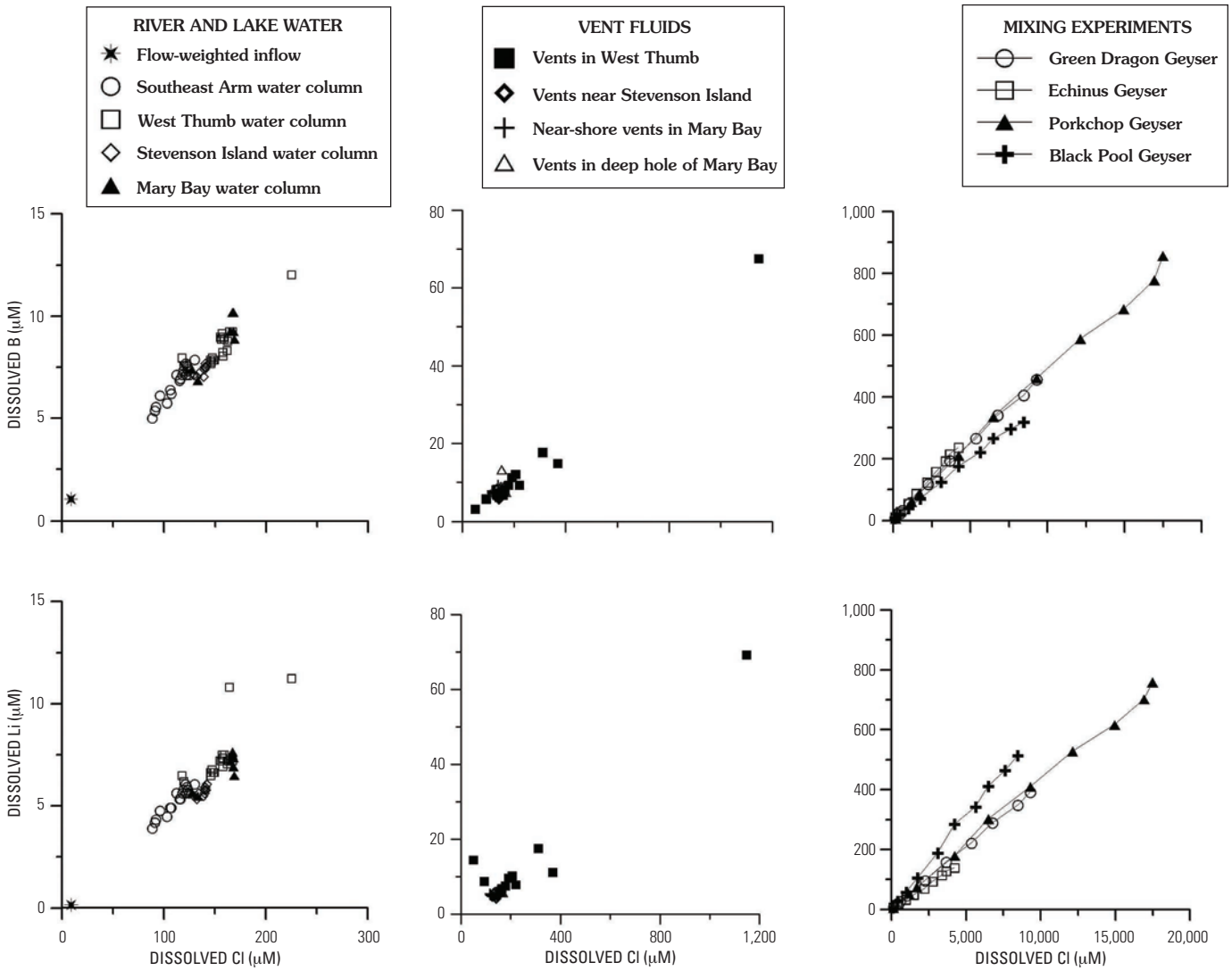

Figure 6. Dissolved concentrations of B and Li as a function of dissolved Cl concentrations in inflow and lake water, hydrothermal vent fluids, and in the mixing experiments between Yellowstone River water and subaerial geyser fluids. Note changes in scale for both x- and y-axes.

Normalized Concentrations of Elements in Hydrothermal Vent Fluids and Lake Water

The anion and pH data for hydrothermal vents in Yellowstone Lake suggest that there are some differences in the compositions of source fluids to the lake and that the compositions of the source fluids may vary as a function of location within the lake. To further explore these differences, we examined the concentrations of SiO_2, B, alkali metals (Li, Na, K, Rb, Cs), alkaline earth elements (Mg, Ca, Sr, Ba), trace anions and mercury (As, Ge, Hg, Mo, Sb, W), species related to gas dissolution (HCO_3, SO_4), and redox-sensitive species (Fe, Mn) in inflow water, lake water, and hydrothermal vent fluids. Because lake water is a variable mixture of inflow water and hydrothermal source fluids and vent fluids are variable mixtures of lake water and hydrothermal source fluids, we evaluated their Cl-normalized concentrations as a function of depth and location for lake water and as a function of location for vent water. The concentrations of elements in flow-weighted inflow water were not normalized because this water is an end-member fluid. The comparisons of different water are intended to emphasize the influence of hydrothermal vent fluids on the composition of Yellowstone Lake water and to characterize the geochemical signature of hydrothermal source fluids to the lake water.

SiO_2

The flow-weighted inflow concentration of SiO_2 (fig. 10) is slightly lower than the average, but within the range, of the Cl-normalized concentration in the water column of the lake (170 compared to 200±20 µM). The concentration of SiO_2* as a function of depth in Yellowstone Lake water is fairly uniform, with a variation of only 12 percent about the mean.

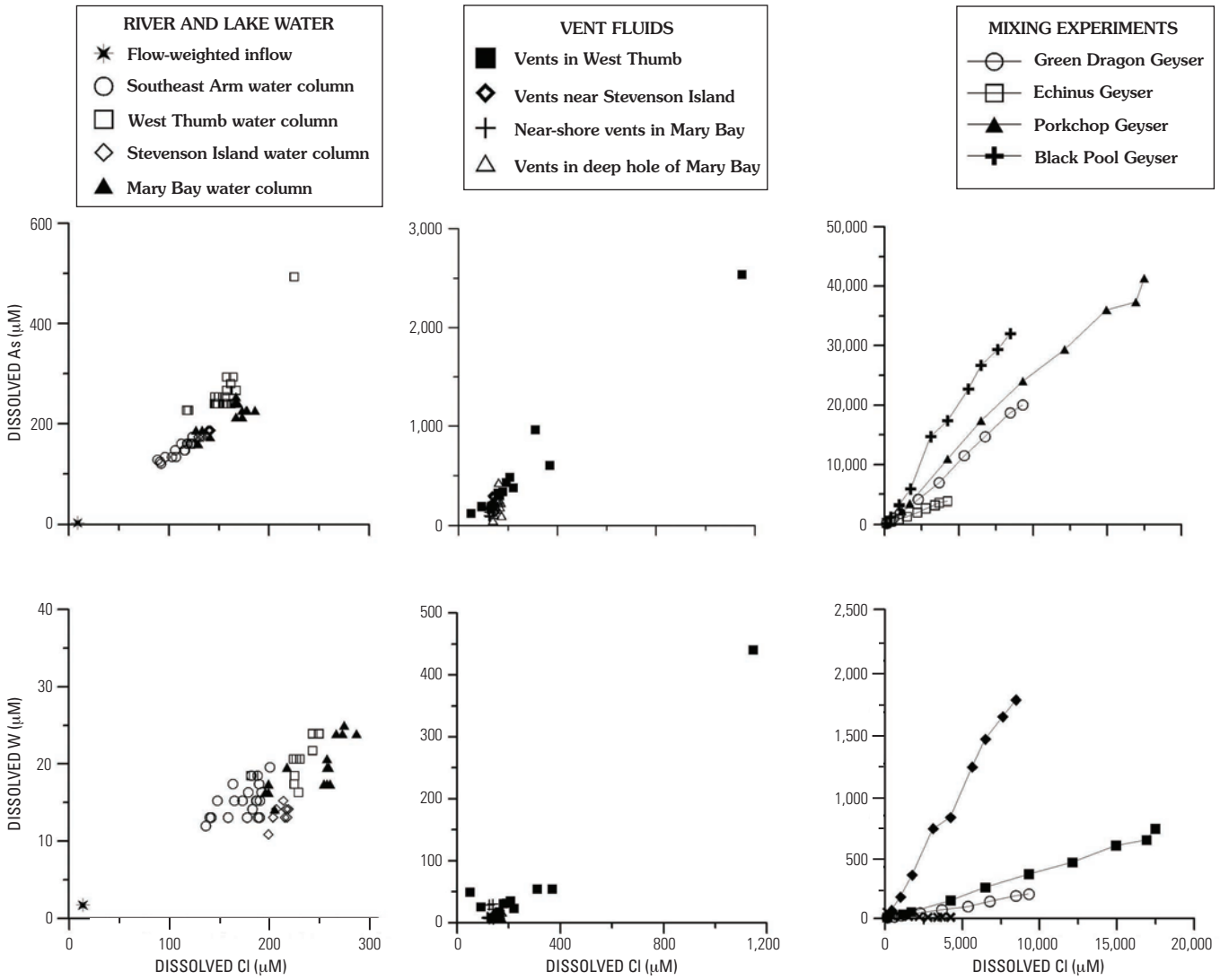

Figure 7. Dissolved concentrations of As and W as a function of dissolved Cl concentrations in inflow and lake water, hydrothermal vent fluids, and in the mixing experiments between Yellowstone River water and subaerial geyser fluids. Note changes in scale for both x- and y-axes.

Several of the hydrothermal vent fluids, particularly those in Mary Bay and near Stevenson Island, show some enrichment in SiO_2* relative to lake water.

B and Alkali Metals

Lake water is enriched in all of these elements, relative to the flow-weighted inflow water (fig. 11). The average Cl-normalized concentrations of B, Li, and Rb in the water column of Yellowstone Lake are 7.9 µM B*, 6.3 µM Li*, and 63 µM Rb*. There is little variation (<8 percent) in Cl-normalized concentrations with depth or location for these elements throughout the lake. This observation is consistent with the small variations in the average concentrations of these elements (6.6–8.6 µM B*, 4.8–6.2 µM Li*, 61–68 µM Rb*) in hydrothermal vent fluids collected from different sites in the lake.

The average concentration of Na* in lake water is 390±40 µM, with water below the thermocline (>15 m) in Mary Bay at the low end of the range and water in Southeast Arm at the high end of the range. Concentrations of Na* in vent fluids from different sites are generally similar.

Concentrations of K* in the water column are 41±6 µM (15 percent variation), with the deep water of Mary Bay and West Thumb at the lower end of the range, compared to lake water near Stevenson Island. Water in Southeast Arm appears to be more enriched in K, compared to water in the other areas. Water from some vents in West Thumb and the deep hole in Mary Bay has lower concentrations of K* than water from other vents.

Vent fluids from sites that are generally more acidic and enriched in CO_2 (Mary Bay and Stevenson Island; see fig. 9) tend to have lower concentrations of Cs* than do fluids from more neutral West Thumb vents (average concentrations of 21–25 µM compared to 39 µM). However, the influence of

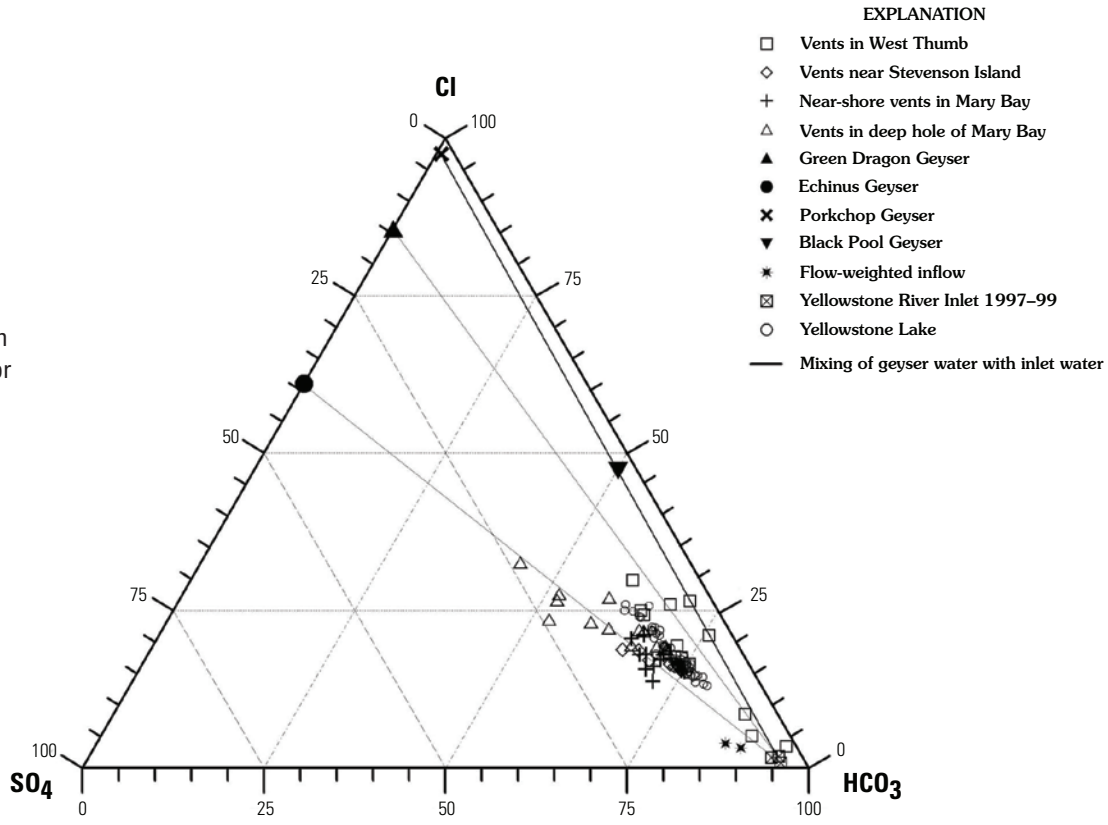

Figure 8. Ternary diagram showing relationships between dissolved Cl, SO_4, and HCO_3 in inflow, hydrothermal, and lake water. Data for subaerial geysers in Norris Geyser Basin (Green Dragon, Echinus, Porkchop) and West Thumb Geyser Basin (Black Pool) are plotted for comparison.

vent fluids on the concentration of Cs* in the water column is small (26±3 µM). Concentrations in the water column near Stevenson Island are slightly lower than those at other sites in the lake.

The above data suggest that the composition of the hydrothermal source fluid is similar in its B, Li, Na, K, and Rb contents throughout the lake. Only the vent-water data for Cs* suggest that slightly more enriched vent fluids are present in West Thumb, compared to the other vent sites.

Alkaline Earth Elements

Concentrations of alkaline earth elements (fig. 12), especially Mg, Ca, and Sr, in flow-weighted inflow water tend to be lower than those in the water column. Water-column profiles of Mg*, Ca*, Sr*, and Ba* indicate that the average concentrations are 110 µM, 130 µM, 510 nM (nanomoles per liter), and 64 nM, respectively, and the profiles show variations of only 11–13 percent in concentration with depth and location. Although these variations are small, the deep water in Mary Bay and West Thumb has lower concentrations of these elements, relative to those of deep water near Stevenson Island and in Southeast Arm.

The hydrothermal vent fluids may have some influence on water-column geochemistry at some sites. Although the Cl-normalized concentrations of the alkaline earth elements vary widely, vent fluids in West Thumb and the deep hole in Mary Bay generally have lower average concentrations of Mg*, Ca*, and Sr*, compared to concentrations in vent fluids near Stevenson Island and near the shore in Mary Bay (65–83 µM versus 110 µM Mg*, 82–100 µM versus 140 µM Ca*, and 330–470 nM versus 580–590 nM Sr*). Large concentrations of Ba* are present in some hydrothermal vent fluids near Stevenson Island and in the deep hole of Mary Bay.

Trace Anions and Mercury

Concentrations of As*, Ge*, Mo*, Sb*, and W* in the water column of Yellowstone Lake (fig. 13) are higher than those in flow-weighted inflow water. Concentrations of Hg in flow-weighted inflow water and water-column samples are below or very close to the detection limit (< 25 pM or picomoles per liter). However, Hg* concentrations in vent water are as high as 320 pM.

The average Cl-normalized concentrations of As, Ge, Mo, Sb, and W in lake water are 210 nM, 3.7 nM, 12 nM, 5.2 nM, and 8.4 nM, respectively. Variations with depth and location range from a low of 10 percent for Sb* to a high of 20 percent for Ge*. The water column in West Thumb generally has the highest concentrations of these elements.

All of the trace elements and mercury show large variations in their Cl-normalized concentrations in the hydrothermal vent fluids. In general, concentrations of all these elements tend to be higher in vent fluids from West Thumb, compared to the other sites (average concentrations: 290 nM versus 170–220 nM As*, 7.6 nM versus 3.3–3.9 nM Ge*, 53 pM versus 16–34 pM Hg*, 22 nM versus 6–17 nM Mo*, 9.9 nM versus 4.1–6.5 nM Sb*, and 22 nM versus 8.5–13 nM W*). The vent fluids, enriched in As, Ge, Mo, and W in West Thumb, appear to enrich the water column at that site, relative to other sites in the lake.

Species Related to Gas Dissolution

The water column of Yellowstone Lake is enriched in SO_4, ΣCO_2, and HCO_3 (fig. 14) relative to flow-weighted inflow water (table 2), and the profiles show a variation of 8 percent in SO_4*, 7 percent in ΣCO_2*, and 12 percent in HCO_3* concentrations as a function of depth and location. Average Cl-normalized concentrations of lake water are 81 µM SO_4*, 0.69 mM ΣCO_2*, and 640 µM HCO_3*. However, HCO_3* concentrations indicate that there is less HCO_3 at depth at the station over the deep hole of Mary Bay compared to concentrations at other locations in the lake.

The hydrothermal vent fluids show clear differences in SO_4* concentrations as a function of location in the lake. Hydrothermal vent fluids in West Thumb have lower concentrations (51±20 µM) than do fluids from vents near Stevenson Island and in Mary Bay (93–100±20 µM). Some vent fluids in Mary Bay and near Stevenson Island are greatly enriched in ΣCO_2* and, as indicated previously, dissolution of CO_2 probably is responsible for the low pH values of these fluids. Vent water in West Thumb and in the deep hole in Mary Bay tends to have lower average concentrations of HCO_3* (390–460 µM) than does water from vents near Stevenson Island and near the shore in Mary Bay (590–620 µM).

Redox-Sensitive Species

In contrast to most of the other examined elements, the concentrations of Fe and Mn (fig. 15) in the flow-weighted inflow are generally greater than or equal to Cl-normalized concentrations in the water column. The water-column data indicate that there are differences between sites. There are enrichments in the very bottom water for Fe or below the thermocline for Mn at the site over the deep hole in Mary Bay, whereas enrichments in Mn are present in the bottom water near Stevenson Island.

Hydrothermal vent fluids near Stevenson Island and in the deep hole of Mary Bay are significantly enriched in Fe (13–20 times the average concentration in lake water) and Mn (15–28 times the average concentration in lake water). This suggests that both Fe and Mn are in their reduced forms in the vent fluids, and they oxidize and precipitate when they mix with oxic lake water. The different behaviors of Fe and Mn with depth in the water column in both Mary Bay and near Stevenson Island likely reflect the fact that the oxidation rate of Fe is faster than that of Mn (Stumm and Morgan, 1996). The difference in oxidation rates allows dissolved Mn to diffuse higher in the water column before it is removed by oxidation and precipitation.

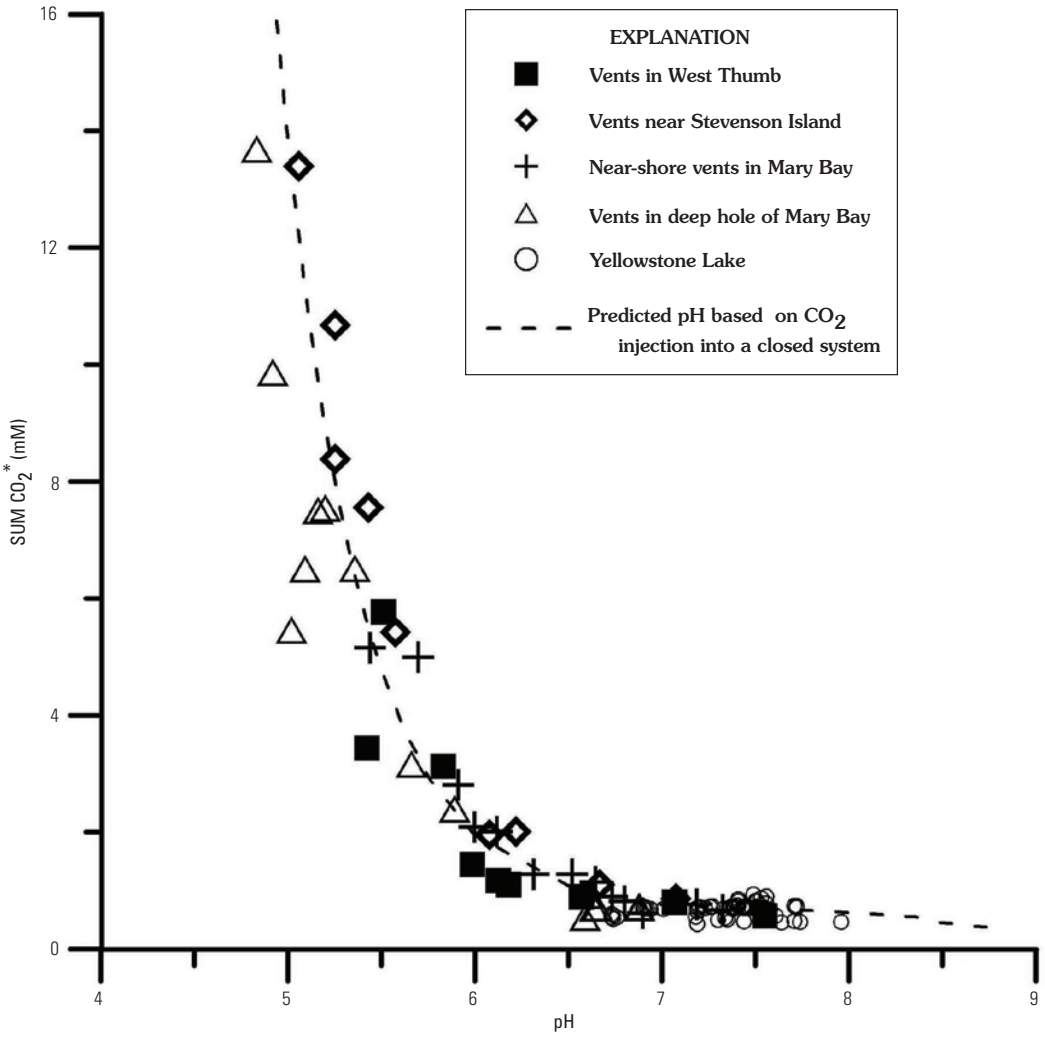

Figure 9. Cl-normalized concentrations of total dissolved inorganic carbon (ΣCO_2*) versus pH for hydrothermal vent fluids and lake water in Yellowstone Lake. The dashed line is a prediction of pH for variable injections of CO_2 into a closed system.

Element Enrichment Due to Hydrothermal Activity

The above observations indicate that Yellowstone Lake water is enriched in some elements and species (Cl, B, alkali metals, alkaline earth elements, As, Ge, Mo, Sb, W, SO_4, and HCO_3) relative to concentrations in inflowing waters. This enrichment includes water in Southeast Arm that is outside of the caldera and away from known hydrothermal activity. Although there may be some local influences of hydrothermal inputs on some water-column profiles, in general, these elements and species tend to vary little in concentration (less than 13 percent for major ions and up to 20 percent for minor ions) with location or depth in the lake, if dilution effects are taken into account. Enrichment of these elements and species in the lake is consistent with the mass-balance calculations that use only inflow and outflow concentrations and water fluxes. Only two elements (Fe and Mn) show variations with depth and location in the lake when dilution effects are considered. These variations are due to processes that affect the speciation of the elements after they enter the lake.

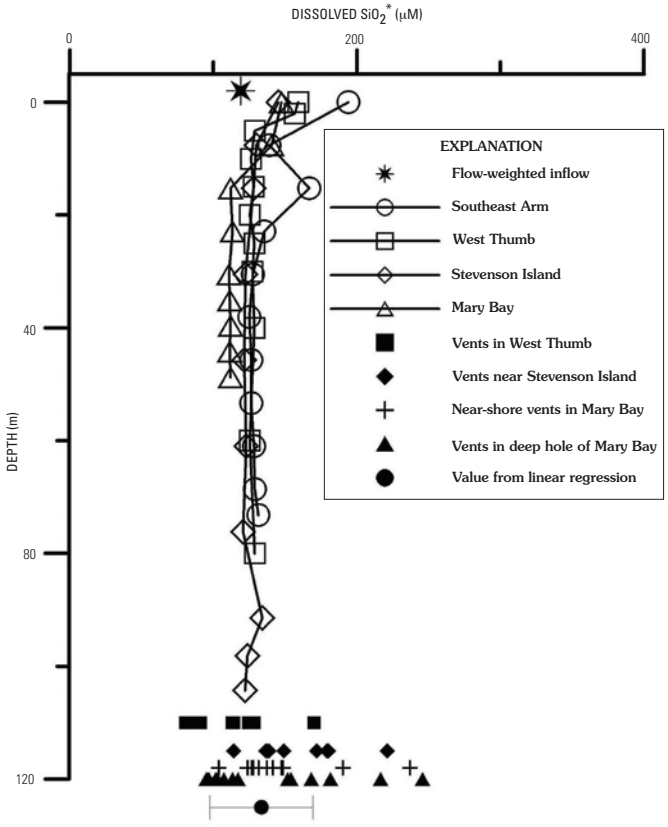

Figure 10. Cl-normalized concentrations of dissolved SiO_2 in inflowing waters to Yellowstone Lake, lake water as a function of depth and location, and hydrothermal vents as a function of location. The average value and standard deviation determined from the Cl-element regression at 140 µM (micromoles per liter) Cl are also shown.

Our studies of lake water, stream water, and hydrothermal vent fluids indicate that there is enrichment of As, B, Cl, Cs, Ge, Hg, Li, Mo, Sb, and W in lake water and in sublacustrine hot springs. What is the significance of this list of elements? All of these elements are relatively mobile in the aqueous environment: Cs, Hg, and Li exist as cations; Cl is a simple anion; and As, B, Ge, Mo, Sb, and W exist as oxyanions. Consequently, all of these elements are likely to remain in solution in the Yellowstone River for considerable distances downstream from Yellowstone Lake. Table 3 summarizes established regulatory limits on these elements in drinking water and seafood, and it summarizes known human health effects of these elements. Some elements (As, Hg, Li, Mo, and Sb) are toxic or potentially toxic above specified concentrations, but only dissolved concentrations of Sb in Yellowstone Lake and in hydrothermal vent fluids exceed presently established limits for Sb in drinking water. Dissolved As and Sb in subaerial geyser fluids sampled in Norris and West Thumb Geyser Basins and Cl concentrations in fluids sampled in West Thumb Geyser Basin exceed current drinking-water standards, and those element concentrations may have important local consequences for biota in the Greater Yellowstone ecosystem.

δD and Cl: An Estimate of the Concentration of Cl in the Hydrothermal Source Fluid to the Lake

Truesdell and others (1977) presented an elegant quantitative description of the effect of subsurface boiling on the isotopic and Cl composition of subaerial hydrothermal water in Yellowstone National Park. Their calculations showed that the δD values of hydrothermal fluids are a function of the boiling mechanism. They considered two end-member boiling mechanisms—single-stage steam separation, wherein steam remains mixed with the water until it separates at a given temperature, and continuous steam separation, wherein steam separates from solution as it is formed. Although concentrations of dissolved Cl are about the same for the two mechanisms, values of δD are considerably lower for continuous separation compared to values for the single-stage steam-separation mechanism. One assumption of these calculations is that there is a single, deep, thermal reservoir containing fluid with the following characteristics: 360°C, 310 mg/kg Cl (8.7 mM Cl), and –149 per mil δD. Analyses of δD and $\delta^{18}O$ of recharge waters in the Park indicate that this deep reservoir fluid is isotopically lighter than recharge waters in the caldera, and either it has a remote recharge area in the northwest corner of the Park or it has a residual component of water from the last glacial event (Rye and Truesdell, 1993; this volume). In the Truesdell and others (1977) model calculations, deep reservoir fluid ascends to the surface while boiling. Mixing between deep thermal water and cold, dilute local meteoric water (5°C, 2 mg/kg Cl [56 µM Cl] and a range of δD values [–142 to –133 per mil]) is also considered. Such mixtures then can ascend to the surface with additional boiling.

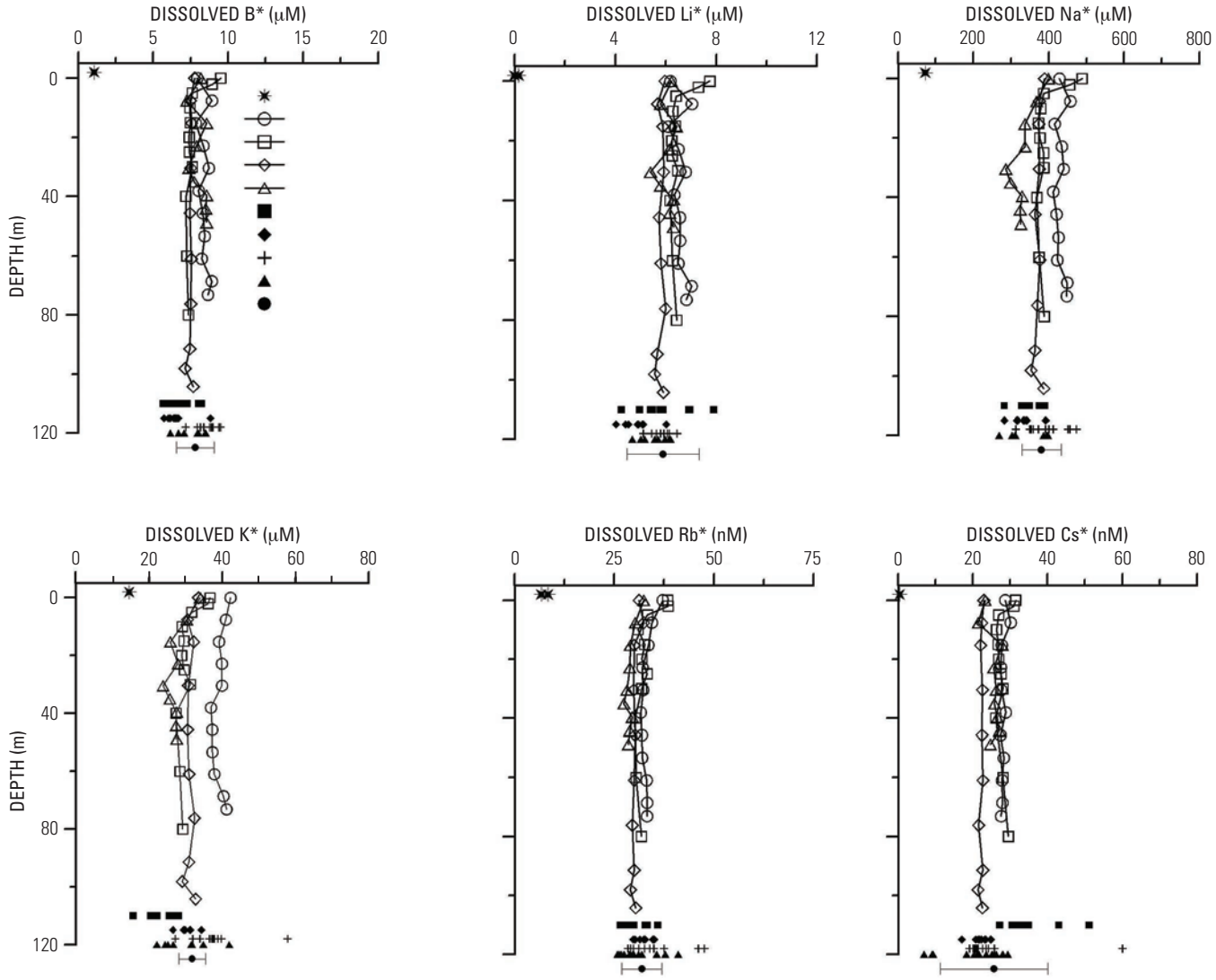

Figure 11. Cl-normalized concentrations of dissolved B, Li, Na, K, Rb, and Cs in inflowing waters to Yellowstone Lake, lake water as a function of depth and location, and hydrothermal vent fluids as a function of location. The average values and standard deviations determined from the Cl-element regression at 140 μM (micromoles per liter) Cl are also shown.

We use the approach of Truesdell and others (1977), with modifications, and our isotopic and Cl data for inflow water, water-column samples, pore water from shallow sediments, and hydrothermal vent fluids in Yellowstone Lake to estimate a value for the concentration of Cl in the end-member hydrothermal-source fluid to the lake. First, we calculate the composition of water produced by mixing between deep thermal water and meteoric water that has the composition of our flow-weighed inflow water (5°C, 1.4 mg/kg Cl [39 μM Cl], -141 per mil δD). The solid line with open diamonds in figure 16, along with associated temperatures of the mixtures, shows this process.

Next, we reproduce the Truesdell and others (1977) boiling curves for continuous and single-stage steam separation for deep thermal fluid. Calculations are done at 5°C intervals for continuous steam separation. The solid lines with open circles and open squares, along with associated temperatures, represent boiling of the deep thermal fluid by continuous steam separation and single-stage steam separation, respectively (fig. 16).

The next step is to calculate the Cl-δD compositions for situations in which first there is mixing between meteoric water and deep thermal fluid, and then there is boiling to a temperature of 220°C by the two different steam-separation mechanisms. These cases are depicted in figure 16 by solid lines with closed triangles (continuous separation) and open triangles (single-stage separation). Temperatures of the mixtures before boiling are given in parentheses above the open triangles. We chose a boiling temperature of 220°C, for reasons that will be apparent later. The calculations were done for a range of boiling temperatures, but those results would further complicate the figure and are not included in the figure.

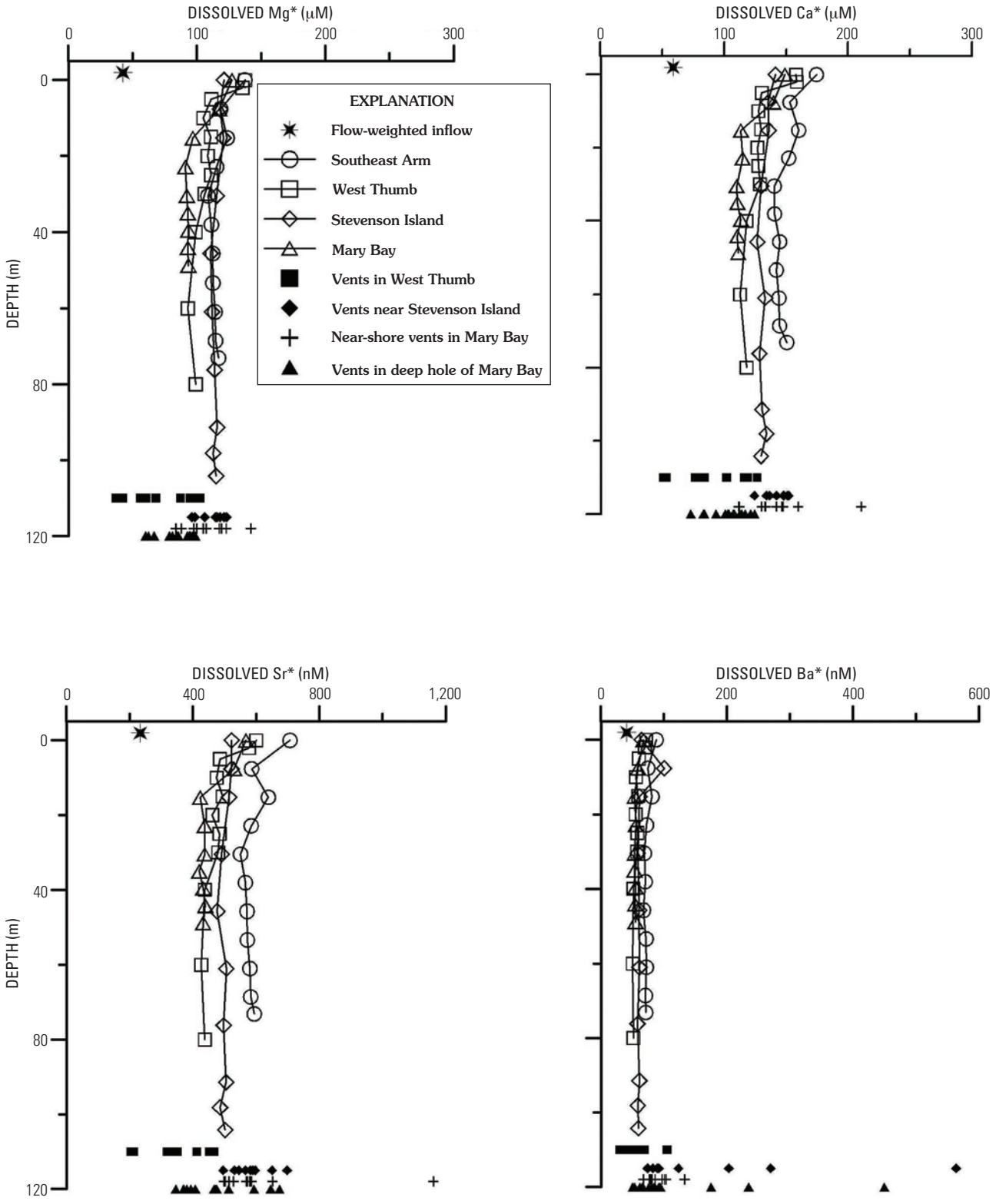

Figure 12. Cl-normalized concentrations of dissolved Mg, Ca, Sr, and Ba in inflowing waters to Yellowstone Lake, lake water as a function of depth and location, and hydrothermal vent fluids as a function of location.

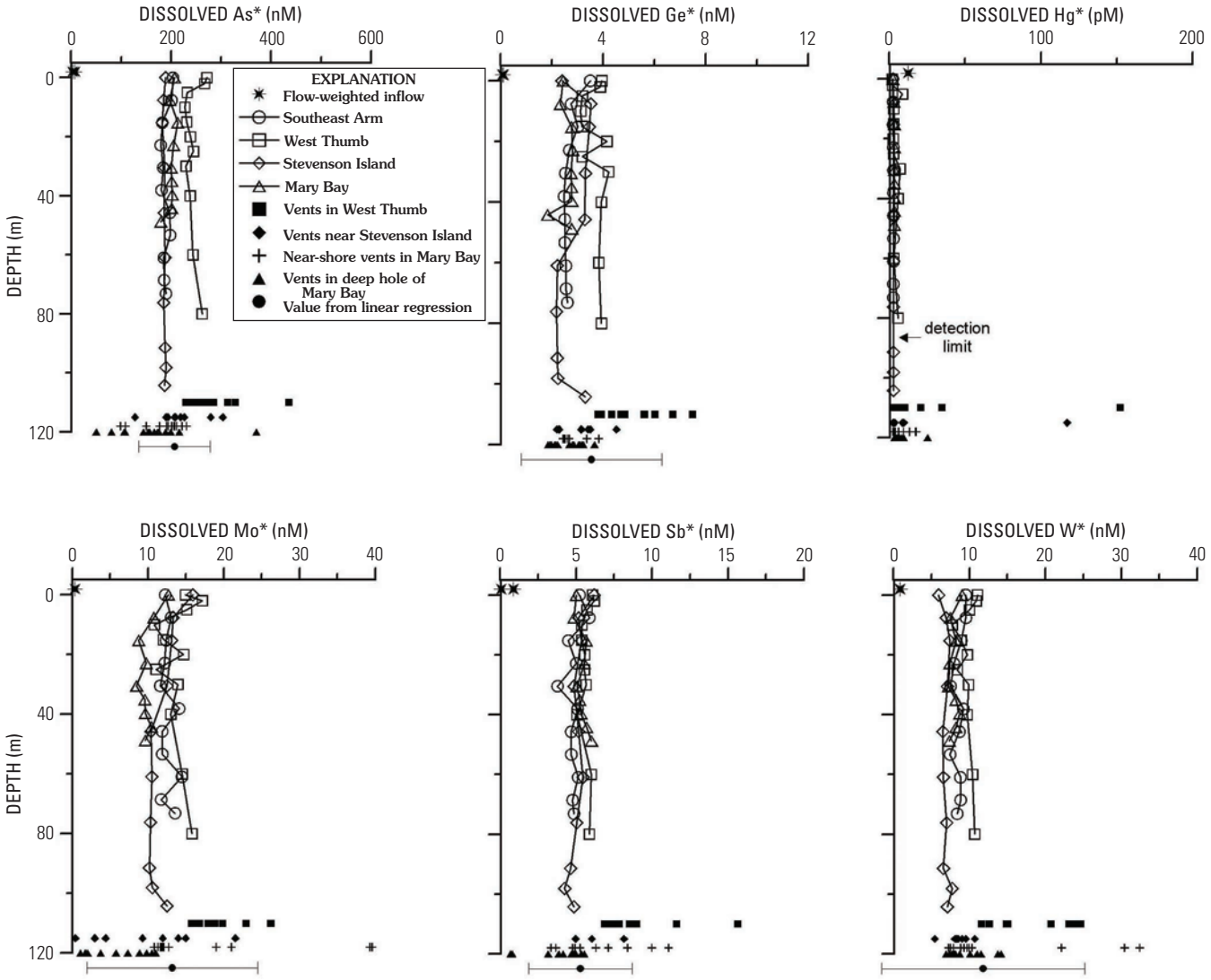

Figure 13. Cl-normalized concentrations of dissolved As, Ge, Hg, Mo, Sb, and W in inflowing waters to Yellowstone Lake, lake water as a function of depth and location, and hydrothermal vent fluids as a function of location. The average values and standard deviations determined from the Cl-element regression at 140 µM (micromoles per liter) Cl are also shown.

Our final theoretical consideration is mixing between boiled thermal water and bottom water of Yellowstone Lake. The bottom water of Yellowstone Lake contains 4.4–5.9 mg/kg Cl (~120–170 µM Cl), and it has δD values that range from –128 to –131 per mil. The temperature of the bottom water ranges from 4.8°C to 12°C, depending on location. We use the temperature of bottom water in Mary Bay (12°C) in our calculations of mixing because some of our pore-water data are from that site. Mixing between Yellowstone Lake bottom water and hydrothermal waters that boil at a variety of temperatures and by different mechanisms can be portrayed by a series of straight lines between end members. For simplicity, only mixing between the bottom water of Yellowstone Lake and boiled deep thermal water with continuous steam separation to 220°C is shown in figure 16 (dashed lines). The temperatures of the mixtures are indicated by stars along the dashed line and are given as numbers in brackets.

Boiling and mixing calculations provide the theoretical framework needed to calculate a value for the Cl concentration in the hydrothermal source water to the lake. As indicated earlier, almost all of the collected hydrothermal vent fluids are very dilute, with Cl-δD values not much different from those of lake water (fig. 16). On the other hand, one vent sample and several pore-water samples have higher Cl concentrations and lower values of δD than other samples. These values, along with values for the most concentrated vent fluids in West Thumb and the lower range of values from Yellowstone Lake bottom water, form a straight line. This line best represents mixing between the bottom water of Yellowstone Lake and boiled deep thermal water. This boiled deep thermal water is the hydrothermal source fluid to the lake. The line intersects the boiling curves at 220°C, for both steam-separation mechanisms. The Cl concentrations for boiled thermal water at 220°C are 553 mg/kg (~15.6 mM) for single-stage steam

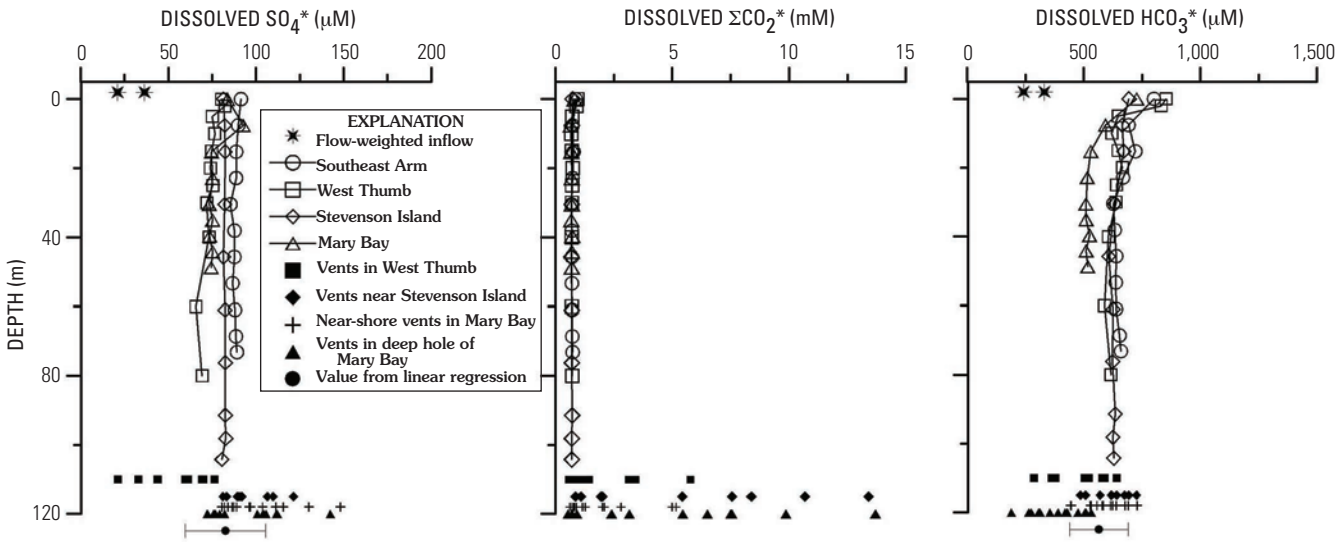

Figure 14. Cl-normalized concentrations of dissolved SO_4, ΣCO_2, and HCO_3 in inflowing waters to Yellowstone Lake, lake water as a function of depth and location, and hydrothermal vent fluids as a function of location. The average values and standard deviations determined from the Cl-element regression at 140 μM (micromoles per liter) Cl are also shown.

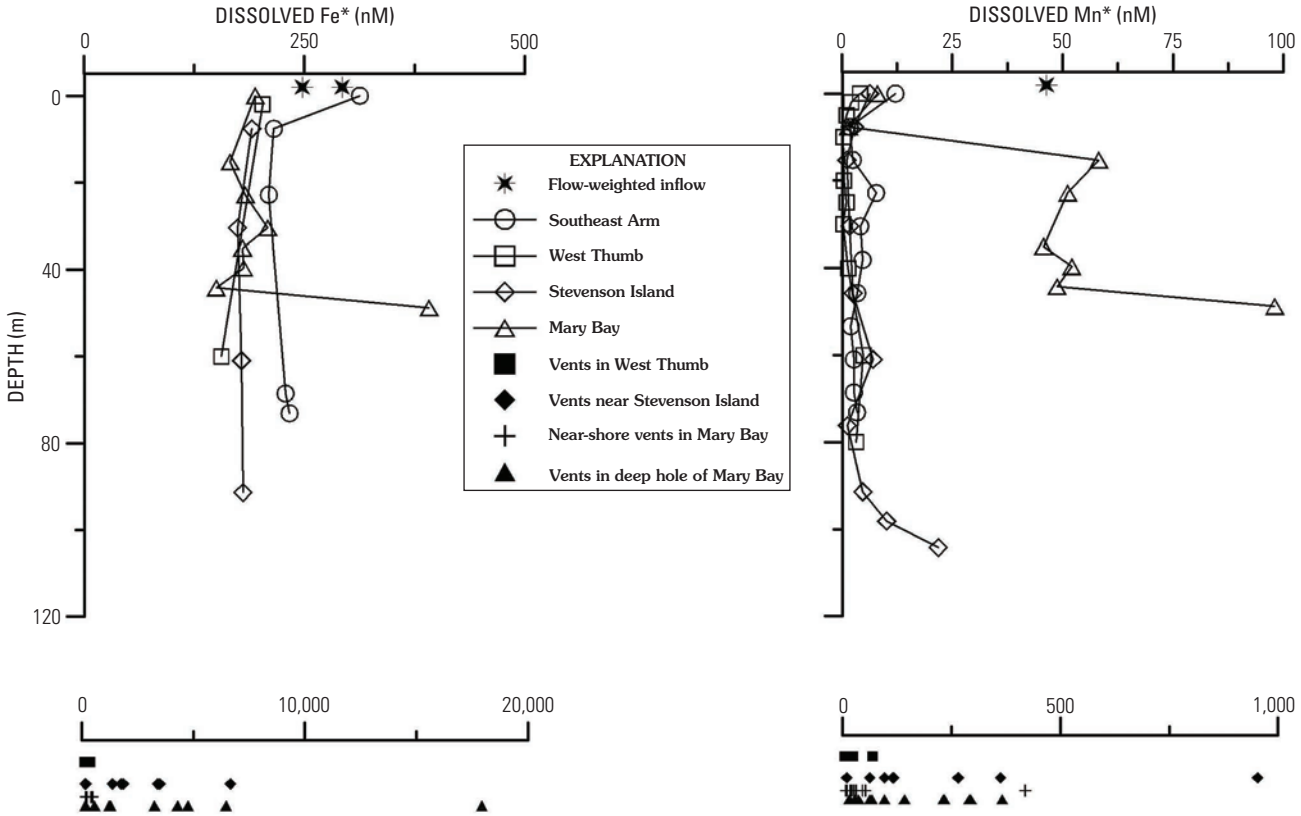

Figure 15. Cl-normalized concentrations of dissolved Fe and Mn in inflowing waters to Yellowstone Lake, lake water as a function of depth and location, and hydrothermal vent fluids as a function of location. Note the change in concentration scales.

separation and 586 mg/kg (~16.5 mM) for continuous steam separation. We interpret this to mean that deep thermal reservoir fluid boils with steam loss from about 360°C to 220°C during ascent, and then it mixes with cold ambient lake water.

Is 220°C a reasonable boiling temperature for the hydrothermal fluids entering the bottom of Yellowstone Lake? Using the relationship between boiling-point and depth (or pressure) in Henley and others (1984), we calculate that the boiling-point temperatures at the depths of the lake-bottom vents are 105°C for the shallow (7–10 m) vents in Mary Bay, 158°–160°C for vents in the deep hole of Mary Bay, 140–160°C for vents at depths of 29–53 m in West Thumb, and 180°–185°C for the deep (95–110 m) vents near Stevenson Island. These boiling temperatures compare with 93°C temperatures for the subaerial geysers in Yellowstone National Park. The estimated boiling temperature of the hydrothermal source fluid to the lake (220°C) therefore is higher than expected from the calculated boiling-point temperatures at lake-bottom pressures for all sampled vents. This difference suggests that either mixing with lake water occurs in the shallow subsurface beneath the lake bottom or that submersible sampling of vent fluids has not allowed measurement of the maximum temperatures of venting.

A check on the estimated 220°C temperature can be made by calculating the temperature along the mixing line between bottom water in Mary Bay (12°C) and the hydrothermal end member (220°C) and then comparing those temperatures to the temperature of the pore water and sediment at the bottom of the core from Mary Bay (270 mg/kg Cl [~7.7 mM Cl], –140.2 per mil δD). The Cl and δD values place the pore water exactly on the mixing line (fig. 16). Unfortunately, it was not possible to measure the temperature of the pore water and sediment at the bottom of the core. However, some constraints on the temperature can be made by observations at the time of core collection. The core was too hot to touch and the core liner was severely deformed by the heat. The melting point for cellulose acetate butyrate, the material of core liners, is >135°C (http://hazard.com/msds). Calculations for temperatures of mixtures of bottom water from Mary Bay and the boiled thermal water place the temperature of the deepest pore-water sample between 95°C and 137°C (fig. 15), close to the temperature at which core liner melts. This temperature exceeds the maximum measured vent-fluid temperatures in the deep hole in Mary Bay (103°C), suggesting there is mixing of lake water and hydrothermal fluids below the sediment-water interface.

Concentrations of Selected Elements and Species in Boiled Hydrothermal Source Fluid to the Lake

If our assessment of the Cl-δD relationships and pore-water data is correct, then we can estimate the concentrations of some elements in the hydrothermal source fluid to the lake from linear relationships between Cl and elements in lake water and vent fluids. The extrapolations take us far beyond the measured Cl concentrations in lake water and vent fluids. However, the laboratory experiments indicate that mixing of dilute Yellowstone River water and element-enriched geyser water with Cl concentrations between 4.2 mM and 19 mM (150 mg/kg and 660 mg/kg) results in no observed losses for the elements of interest. In other words, only dilution is occurring, and all of the examined elements or species behave conservatively. Hence, there is experimental justification for extrapolating beyond the range of Cl and element concentrations in the lake and vent waters.

Table 3. Regulatory limits and potential health-related effects of certain elements.

[Data from Smith and Huyck (1999) and references cited therein, with additional information from EPA and FDA Web sites. MCL, maximum contaminant level; $^{+}$, primary EPA standard; $^{\#}$, secondary EPA standard; *, shellfish; **, methyl mercury in fish (usually approximates total mercury); P, possible or suspected; Y, proven or established; T, toxic metals with multiple effects; S, special conditions required; t, metals with potential for toxicity; E, embryocidal. Leaders (--) indicate no known health effect. Little or no data are available for health effects of Cs, Ge, or W]

Element	EPA drinking water MCL (mg/L)	FDA action levels in seafood (mg/kg wet weight)	Essential for human health	Toxicity	Carcinogenic	Teratogenic (interferes with growth of embryo or fetus)
As	0.050^{+}	76–86*	P	T	Y	Y/E
B	--	--	P	--	--	--
Cl	250$^{\#}$	--	Y	--	--	--
Cs	--	--	--	--	--	--
Ge	--	--	--	--	--	--
Hg	0.002^{+}	1.0**	--	T	--	Y/E
Li	--	--	P	S	--	--
Mo	--	--	Y	t	--	Y
Sb	0.006^{+}	--	--	t	--	--
W	--	--	--	--	--	--

The predicted concentrations of selected elements and species in the boiled hydrothermal source fluid to the lake are compared to the observed compositions of selected subaerial geyser fluids in Yellowstone National Park (table 4). The concentrations of elements in the hydrothermal source fluid were calculated by assuming that the Cl concentration in the fluid is 16 mM (570 mg/kg), which is the average of the values predicted for deep thermal water boiled from 360°C to 220°C by single-stage and continuous steam separation. If the elements and species of interest, except those affected by gas loss (HCO_3 and SO_4), are conservative during the boiling process, then we can also estimate the compositions of selected elements in the deep thermal fluid by assuming that the Cl concentration is 8.7 mM (310 mg/kg) (table 4). This solution is the parent fluid for the boiled hydrothermal water entering the lake, and it is more dilute because it has not yet lost water through steam separation.

The ratios of the predicted compositions of hydrothermal source fluids or measured compositions of subaerial geyser fluids to the predicted composition of deep thermal fluid are presented in figure 17. On this log plot, a value of zero indicates that the concentration of an element in a given fluid (that is, hydrothermal source fluid or subaerial geyser water) is the same as that in the deep thermal fluid. Values greater than zero indicate that an element is enriched relative to the parent fluid. Enrichment occurs if the element remains in solution and is concentrated during steam loss. Values less than zero indicate that the element is depleted in a given fluid relative to the parent fluid. Elements may be lost from solution during steam separation by adsorption, precipitation, or volatilization. The comparisons indicate that the compositions of all the hydrothermal fluids are within a factor of 2 to 5 for many elements (Cl, Si, B, Li, Na, K, Rb, and As) (fig. 17). Concentrations of Ge, Mo, Sb, and W in the hydrothermal source fluid to the lake and in the neutral to alkaline subaerial geyser fluids are generally within a factor of 2 to 5 of the concentrations in the deep thermal fluid. The predicted hydrothermal source fluid and the deep thermal reservoir fluid are greatly enriched (>10 to >100 times) in Mo, Sb, and W relative to the acid-Cl-SO_4 subaerial geyser waters.

Another test of the predicted composition of the hydrothermal source fluid to Yellowstone Lake is to calculate the in-place temperature for a hydrothermal fluid of such composition using chemical geothermometers. Using the equations in Fournier (1981) and Kharaka and Mariner (1988), equilibrium temperatures are predicted to be 158°C (Na-K), 202°C (amorphous SiO_2), 277°C (quartz with maximum steam loss), and 331°C (chalcedony) for the geothermometers. Calculations using the Na-K-Ca or Mg geothermometers could not be done because we do not have estimates for the concentrations of alkaline earth elements in

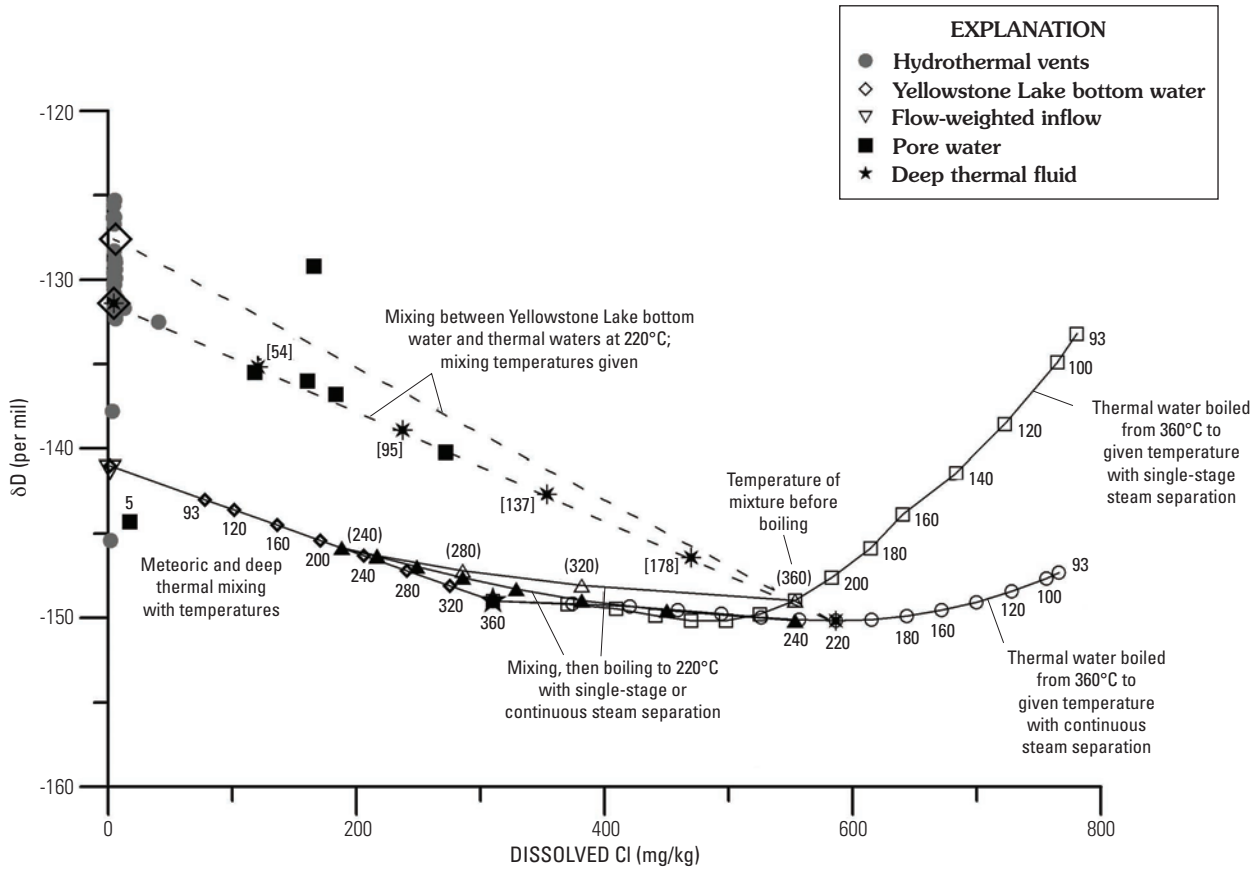

Figure 16. Plot of δD versus dissolved Cl concentrations derived from theoretical calculations and for data from inflow water, lake water, hydrothermal vent fluids, or pore waters in Yellowstone Lake. See text for further discussion. Diagram adapted from Truesdell and others (1977).

the hydrothermal source fluid. The estimated temperature of the boiled hydrothermal source water using pore-water data and Cl-δD relationships is 220°C (fig. 16), within about 60°C of the Na-K geothermometer and within 20°C of the Si geothermometer using amorphous SiO_2. These temperatures are consistent with the observation that vent deposits and the underlying lake sediments are mostly amorphous silica.

Our final calculations assess the fraction of hydrothermal source fluid that is in the water column of Yellowstone Lake and estimate the flow of water from hydrothermal vents into the lake. The calculations are done using Cl concentrations. Cl and other element concentrations in the water column of Southeast Arm, West Thumb, near Stevenson Island, and Mary Bay differ because of variable inputs of hydrothermal source fluid (table 2). Using a predicted concentration of 16 mM Cl in the hydrothermal end member, the percentage of hydrothermal source fluid in the bottom water (>15m depth) of Yellowstone Lake is lowest in Southeast Arm (0.74±0.04 percent) and it increases from near Stevenson Island (0.87±0.01 percent) and West Thumb (0.95±0.04 percent) to the highest values in the deep hole of Mary Bay (1.04±0.01 percent). The flow of water from hydrothermal vents is estimated by rearranging equation 2, assuming that J = 0 for a conservative element such as Cl, ΣQin = 0.67 to 3.6 km^3/yr (table 1), ΣQin = 9 to 15 µM Cl, *Qout* = 1.19 km^3/yr (table 1), *Cout* = 130 µM Cl, *Cvent* = 16 mM Cl, ground-water contributions are negligible, and solving for *Qvent*. This calculation indicates that the flow of hydrothermal source fluid to the lake is 0.006 to 0.009 km^3 of water per year or about 8 x 10^9 kg of water per year. Although the flow rate of hydrothermal source water to the lake is small compared to the flow rate of water from streams, the flux or loading of elements to the lake from sublacustrine vents is very significant because of the high concentrations of Cl and other elements in the hydrothermal source water.

Using the same procedure, we also estimate the flux of hydrothermal water in terms of the deep thermal reservoir fluid. This fluid has a predicted Cl concentration of 8.7 mM. Substituting that concentration into equation 2 and using the same parameters for inflow and outflow water yields a discharge from the deep thermal reservoir of 0.01 to 0.02 km^3 of water per year or about 1.5 x 10^{10} kg of water per year. Studies of Cl in streams indicate that in 1999 there was a total flux of deep thermal water of about 16 x 10^{10} kg/yr from all thermal areas in the Park (Friedman and Norton, 2000, this volume). This means that, according to this estimate, sublacustrine vents in Yellowstone Lake account for ~10 percent of the total flux of deep thermal reservoir water in the Park. This estimate is very similar to that of Fournier and others (1976) based on Cl content at the lake outflow at Fishing Bridge in 1972. Because we estimate that 41 million kg/d of deep hydrothermal fluid flows into the lake and recent studies have revealed the presence of numerous hydrothermal features on the lake bottom (Morgan and others, 1999; Shanks and others, 1999), Yellowstone Lake should now be considered one of the most important thermal basins in the Park.

Summary

Mass-balance calculations and comparisons of concentrations of elements in inflowing surface water and in the water column indicate that Yellowstone Lake is enriched in a suite of elements, most of which are also enriched in subaerial geyser waters. Relationships between the concentrations of Cl and many elements in both lake water and hydrothermal vent fluids indicate that mixing of end-member solutions is occurring. Yellowstone Lake appears to be a slightly evaporated mixture of inflowing stream water and hydrothermal fluids.

The chemical composition of lake and hydrothermal water is dominated by Na and HCO_3. Although lake water is nearly neutral, most of the vent fluids are acidic. This acidity is due mainly to dissolution of CO_2, a volatile gas associated with ascending hydrothermal fluids. Vent fluids in Mary Bay and near Stevenson Island have a larger component of SO_4 than do some vent fluids from West Thumb. This observation indicates that dissolution and oxidation of H_2S are important processes in the Mary Bay and Stevenson Island vent water. Although sulfide-oxidation processes contribute to acidity, dissolution of CO_2 dominates the pH of vent fluids in Mary Bay and near Stevenson Island.

Variable mixing or dilution of end members occurs throughout the lake. Once dilution is taken into account, almost all of the elements show little variation in their Cl-normalized concentrations as a function of depth within the water column or as a function of location in the lake. The notable exceptions are Fe and Mn, for which large enrichments are observed in some vent fluids relative to lake water, especially those in Mary Bay and near Stevenson Island. These enrichments in hydrothermal vent fluids translate into enrichments in the bottom water near Stevenson Island and in Mary Bay. The Cl content of the hydrothermal source fluid to the lake is about 16 mM (570 mg/kg). This value was determined by using the Cl and δD contents of pore water, lake water, and hydrothermal vent water in the lake, following Truesdell and others (1977), with modifications to account for conditions at the bottom of the lake and mixing between lake water and hydrothermal source water. We estimate that the final boiling temperature of the hydrothermal source fluid is 220°C, within the temperature range estimated for intermediate reservoirs of hydrothermal source fluids for geyser basins in the Park. We interpret this to indicate that deep thermal reservoir fluid boils with steam loss from about 360°C to 220°C during ascent, and then it mixes with cold ambient lake water. The concentrations of selected elements in the hydrothermal source fluid were calculated from the linear relationships between Cl and elements in lake water and hydrothermal vent fluids, assuming that the Cl concentration of the hydrothermal source fluid is 16 mM. The predicted concentrations of many elements are consistent with concentrations in subaerial geyser fluids. The geochemistry of Yellowstone Lake indicates that it is a mixture of about one percent hydrothermal source fluid

Table 4. Comparisons of predicted chemical compositions of boiled geothermal source fluid to Yellowstone Lake water (YL) and deep thermal reservoir fluid with measured compositions of subaerial geothermal waters in Norris Geyser Basin (Porkchop, Echinus, and Green Dragon) and West Thumb Geyser Basin (Black Pool and Vandalized Pool).

[Note change in units compared to table 2. n.d., not determined]

Parameter, element, or species	Units	Predicted composition of geothermal source fluid to YL[a]	Predicted composition of deep thermal reservoir fluid[a]	Porkchop July 1999	Black Pool Sept. 1998	Black Pool July 1999	Vandalized Pool Sept. 1998	Echinus July 1999	Green Dragon July 1999
temp.	°C	220	360	57	n.d.	72.3	n.d.	68.8	79.9
pH		n.d.	n.d.	6.6	8.2	7.9	8.2	3.2	2.6
Cl	mM	16	8.7	17	8.5	8.5	8.7	4.2	9.3
SiO_2	mM	16	8.7	6.8	6.0	4.8	5.3	4.5	7.8
B	µM	920	500	860	n.d.	320	n.d.	240	500
Li	µM	950	510	1,400	620	560	520	160	890
Na	mM	37	20	17	16	18	16	7.5	9.7
K	µM	1,000	570	1,460	490	500	310	1,330	1,170
Rb	µM	7.4	4.0	5.7	1.8	2.3	1.2	4.1	4.6
Cs	µM	9.0	4.8	4.4	1.8	2.3	0.60	0.61	2.3
Mg	µM	n.d.	n.d.	0	0	0	0.4	21	13
Ca	µM	n.d.	n.d.	130	19	22	17	120	100
Sr	nM	n.d.	n.d.	150	21	23	18	84	130
Ba	nM	n.d.	n.d.	76	0	0	0	420	240
As	µM	32	20	41	21	32	21	3.9	23
Ge	µM	1.6	1.0	0.55	0.44	0.74	0.44	0.14	0.34
Mo	µM	4.6	2.8	2.9	0.93	1.1	1.0	0.06	0.33
Sb	µM	1.7	1.1	1.2	0.82	0.82	0.82	0.007	0.046
W	µM	5.5	3.4	0.87	1.3	2.1	1.4	0.01	0.27
HCO_3[b]	mM	13	n.d.	0.12	7.0	9.0	7.0	0	0
SO_4	mM	5.1	n.d.	0.33	0.41	0.47	0.49	2.7	1.6

[a] Predictive calculations discussed in text.
[b] Calculated by charge balance.

and 99 percent inflowing surface water. Mass-balance calculations suggest that the flow of hydrothermal source fluid into the lake is about 0.008 km^3/yr, which accounts for about 10 percent of the total flux of deep thermal fluid in the Park. Thus, Yellowstone Lake is one of the most important thermal basins in the Park.

References

Beeson, M.H., and Bargar, K.E., 1984, Major and trace element analyses of drill cores from thermal areas in Yellowstone National Park, Wyoming: U. S. Geological Survey Open-File Report 84-373, 40 p.

Christiansen, R.L., 1984, Yellowstone magmatic evolution—Its bearing on understanding large-volume explosive volcanism, *in* National Research Council Geophysics Study Committee, ed., Explosive volcanism—Inception, evolution, and hazards—Studies in geophysics: Washington, D.C., National Academy Press, p. 84–95.

Christiansen, R.L., 2001, The Quaternary and Pliocene Yellowstone plateau volcanic field of Wyoming, Idaho, and Montana: U.S. Geological Survey Professional Paper 729-G, 156 p.

Christiansen, R.L., and Blank, H.R., 1972, Volcanic stratigraphy of the Quaternary rhyolite plateau in Yellowstone National Park: U. S. Geological Survey Professional Paper 729-B, 18 p.

Craig, H., 1961, Isotopic variations in meteroic waters: Science, v. 133, p. 1,702–1,703.

Craig, H., and Gordon, L.I., 1965, Deuterium and oxygen-18 variations in the ocean and the marine atmosphere, *in* Tongiorgi, E., ed., Stable isotopes in oceanographic studies and paleotemperature: Pisa, Spoleto, Consiglio Nazionale delle Ricerche, Laboratorio di Geologia Nucleare, p. 1–22.

Craig, H., Gordon, L.I., and Horibe, Y., 1963, Isotopic exchange effects in the evaporation of water: Journal of Geophysical Research, v. 68, p. 5,079–5,087.

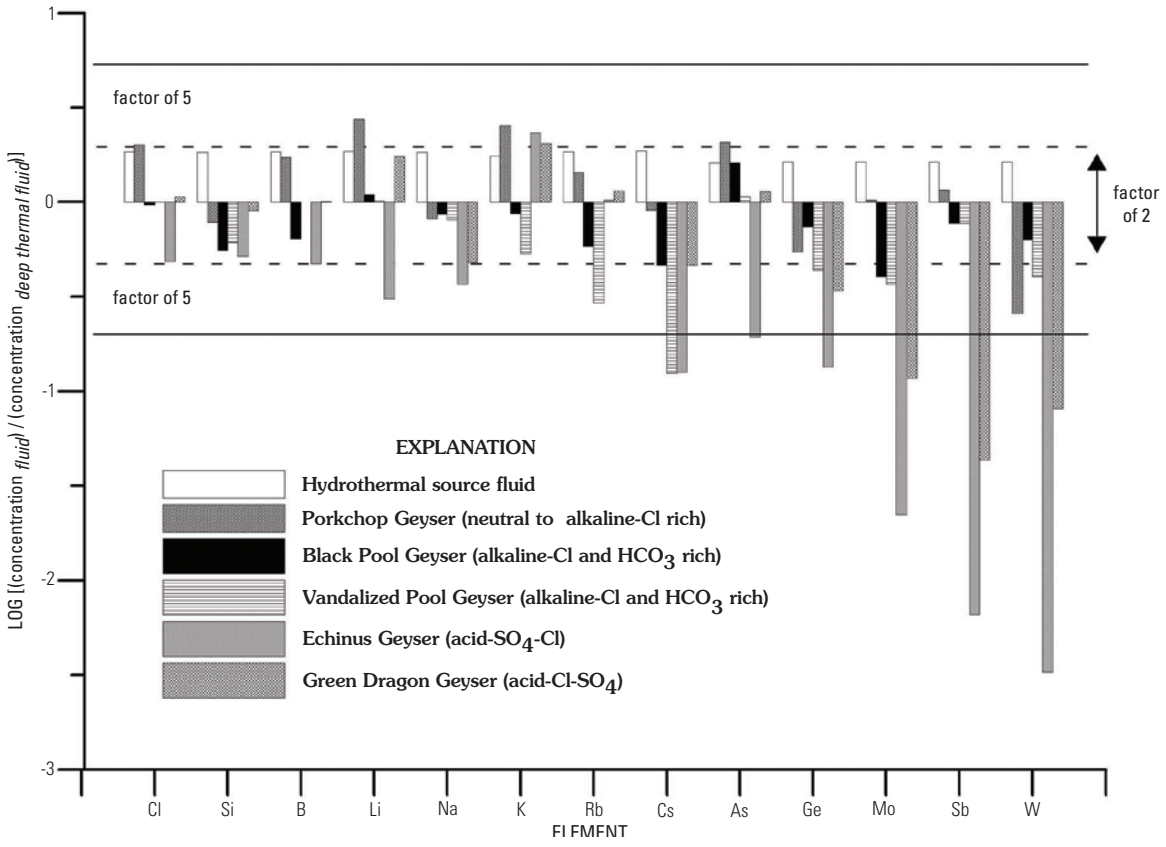

Figure 17. Concentrations of elements in the predicted hydrothermal source fluid to Yellowstone Lake and in subaerial geysers (Porkchop, Black Pool, Vandalized Pool, Echinus, and Green Dragon) relative to predicted concentrations in the deep thermal fluid in Yellowstone National Park. When the ratio equals 0 on this log plot, the concentrations are the same. Ratios greater than 0 indicate enrichment relative to deep thermal water; ratios less than 0 indicate depletions relative to deep thermal water. Lines are drawn to represent concentrations within factors of 2 or 5 of each other.

Drever, J.I., 1988, The geochemistry of natural waters (2nd ed.): Englewood Cliffs, N.J., Prentice Hall, 437 p.

Fournier, R.O., 1981, Application of water geochemistry to hydrothermal exploration and reservoir engineering, *in* Rybach, L., and Muffler, L.J.P., eds., Hydrothermal systems—Principles and case histories: New York, Wiley, p. 109–143.

Fournier, R.O., 1989, Geochemistry and dynamics of the Yellowstone National Park hydrothermal system: Annual Review of Earth and Planetary Sciences, v. 17, p. 13–53.

Fournier, R.O., 2000, Hydrothermal processes related to movement of fluid from plastic into brittle rock in the magmatic-epithermal environment: Economic Geology, v. 94, p. 1,193–1,212.

Fournier, R.O., Estep, M.L.F., and Macko, S.A., 1979, Geochemical and hydrologic considerations and the use of enthalpy-chloride diagrams in the prediction of underground conditions in hot-spring systems: Journal of Volcanology and Geothermal Research, v. 5, no. 1–2, p. 1–16.

Fournier, R.O., White, D.E., and Truesdell, A.H., 1976, Convective heat flow in Yellowstone National Park, *in* Proceedings second U.N. symposium on the development and use of geothermal resources, San Francisco, 1975: Washington, D.C., U.S. Government Printing Office, p. 731–739.

Friedman, I., and Norton, D.R., 2000, Data used for calculating chloride flux out of Yellowstone National Park for the water years 1983–1999: U. S. Geological Survey Open-File Report 00-0194, 48 p.

Gilath, C., and Gonfiantini, R., 1983, Lake dynamics—Guidebook on nuclear techniques in hydrology: International Atomic Energy Agency Technical Report Series, p. 129–161.

Henley, R.W., Truesdell, A.H., Barton, P.B., Jr., and Witney, J.A., 1984, Fluid-mineral equilibria in hydrothermal systems: Reviews in Economic Geology, Society of Economic Geologists, v. 1, 268 p.

Hostetler, S.W., and Giorgi, F., 1995, Effects of a 2 X CO_2 climate on two large lake systems: Pyramid Lake, Nevada and Yellowstone Lake, Wyoming: Global and Planetary Change, v. 10, p. 43–54.

Jahnke, R.A., 1988, A simple, reliable, and inexpensive porewater sampler: Limnology and Oceanography, v. 33, no. 3, p. 483–487.

Kaplinski, M.A., 1991, Geomorphology and geology of Yellowstone Lake, Yellowstone National Park, Wyoming: Flagstaff, Northern Arizona University, M.S. thesis, 82 p.

Kharaka, Y.K., and Mariner, R.H., 1988, Chemical geothermometers and their application to formation waters from sedimentary basins, *in* Naeser, N.D., and McCulloh, T.H., eds., Thermal history of sedimentary basins—Methods and case histories: New York, Springer-Verlag, p. 99–117.

Klump, J.V., Paddock, R., and Lovalvo, D., 1992, A multiple-loop, ROV controlled, in-situ water sampler: Journal of Great Lakes Research, v. 18, no. 2, p. 309–315.

Klump, J.V., Remsen, C.C., and Kaster, J.L., 1988, The presence and potential impact of geothermal activity on the chemistry and biology of Yellowstone Lake, Wyoming, *in* DeLuca, M.P., and Babb, I., eds., Global venting, midwater, and benthic ecological processes: National Undersea Research Program, Research Report 88-4, p. 81–98.

Krabbenhoft, D.P., Bowser, C.J., Anderson, M.P., and Valley, J.W., 1990, Estimating groundwater exchange with lakes; 1. The stable isotope mass balance method: Water Resources Research, v. 26, no. 10, p. 2,445–2,453.

Morgan, L.A., 1992, Stratigraphic relations and paleomagnetic and geochemical correlations of ignimbrites of the Heise volcanic field, eastern Snake River Plain, eastern Idaho and western Wyoming, *in* Link, P.K., Kuntz, M.A., and Platt, L.B., eds., Regional geology of eastern Idaho and western Wyoming: Geological Society of America Memoir 179, p. 215–226.

Morgan, L.A., Doherty, D.J., and Leeman, W.P., 1984, Ignimbrites of the eastern Snake River Plain; evidence for major caldera-forming eruptions: Journal of Geophysical Research, v. 89, no. 10, p. 8,665–8,678.

Morgan, L.A., Shanks, W.C., Lovalvo, D., Johnson, S.Y., Stephenson, W.J., Harlan, S.S., White, E.A., Waples, J., and Klump, J.V., 1999, New discoveries from the floor of Yellowstone Lake—Results from sonar imaging, seismic reflection, and magnetic surveys [abs.]: Geological Society of America Abstracts with Programs, v. 31, p. A-207.

Morgan, L.A., Shanks, W.C., Pierce, K.L., and Rye, R.O., 1998, Hydrothermal explosion deposits in Yellowstone National Park—Links to hydrothermal processes [abs.]: Eos, Transactions of the American Geophysical Union, Abstracts, v. 79, p. F964.

Morgan, P., Blackwell, D.D., Spafford, R.E., and Smith, R.B., 1977, Heat flow measurements in Yellowstone Lake and the thermal structure of the Yellowstone caldera: Journal of Geophysical Research, v. 82, p. 3,719–3,732.

Obradovich, J.D., 1992, Geochronology of the late Cenozoic volcanism of Yellowstone National Park and adjoining areas, Wyoming and Idaho: U.S. Geological Survey Open-File Report 92-408, 45 p.

Pierce, K.L., and Morgan, L.A., 1992, The track of the Yellowstone hot spot; volcanism, faulting, and uplift, *in* Link, P.K., Kuntz, M.A., and Platt, L.B., eds., Regional geology of eastern Idaho and western Wyoming: Geological Society of America Memoir 179, p. 1–53.

Rohlf, F.J., and Sokal, R.R., 1995, Statistical tables (3d ed.): New York, W.H. Freeman, 219 p.

Rye, R.O., and Truesdell, A.H., 1993, The question of recharge to the geysers and hot springs of Yellowstone National Park: U.S. Geological Survey Open-File Report 93-384, 40 p.

Schecher, W.D., and McAvoy, D.C., 1998, MINEQL+, A chemical equilibrium modeling system, version 4.0 for Windows, User's manual: Hallowell, Maine, Environmental Research Software, 318 p.

Schnoor, J.L., 1996, Environmental modeling—Fate and transport of pollutants in water, air, and soil: New York, Wiley, 682 p.

Shanks, W.C., III, Morgan, L.A., Johnson, K.M., Lovalvo, D., Johnson, S.Y., Stephenson, W.J., Harlan, S.S., White, E.A., Waples, J., and Klump, J.V., 1999, The floor of Yellowstone Lake is anything but quiet—New discoveries from sonar imaging, seismic reflection, and magnetic surveys [abs.]: Eos, Transactions of the American Geophysical Union, Abstracts, v. 80, p. F1162.

Smith, K.S., and Huyck, H.L.O., 1999, An overview of the abundance, relative mobility, bioavailability, and human toxicity of metals, *in* Plumlee, G.S., and Logsdon, M.J., eds., The environmental geochemistry of mineral deposits Part A—Processes, techniques, and health issues: Reviews in Economic Geology, Society of Economic Geologists, Inc., p. 29–70.

Smith, R.B., and Rubin, A.M., 1994, Rapid reversal of uplift to subsidence at the Yellowstone caldera by magmatic processes imaged by earthquakes: Seismological Research Letters, v. 65, no. 1, p. 56.

Stauffer, R., and Thompson, J.M., 1984, As and Sb in geothermal waters of Yellowstone National Park: Geochimica et Cosmochimica Acta, v. 48, p. 2,547–2,561.

Stumm, W., and Morgan, J.J., 1996, Aquatic chemistry (3d ed.): New York, Wiley, 1,022 p.

Sturchio, N.C., Muehlenbachs, K., and Seitz, M.G., 1986, Element redistribution during hydrothermal alteration of rhyolite in an active geothermal system—Yellowstone drill cores Y-7 and Y-8: Geochimica et Cosmochimica Acta, v. 50, no. 8, p. 1,619–1,631.

Truesdell, A.H., Nathenson, M., and Rye, R.O., 1977, The effects of subsurface boiling and dilution on the isotopic compositions of Yellowstone thermal waters: Journal of Geophysical Research, v. 82, no. 26, p. 3,694–3,704.

White, D.E., Heropoulos, C., and Fournier, R.O., 1991, Gold and other minor elements associated with the hot springs and geysers of Yellowstone National Park, Wyoming, supplemented with data from Steamboat Springs, Nevada: U.S. Geological Survey Bulletin 2001, 19 p.

White, D.E., Hutchinson, R.A., and Keith, T.E.C., 1988, The geology and remarkable thermal activity of Norris Geyser Basin, Yellowstone National Park, Wyoming: U.S. Geological Survey Professional Paper 1456, 84 p.

Wold, R.J., Mayhew, M.A., and Smith, R.B., 1977, Bathymetric and geophysical evidence for a hydrothermal explosion crater in Mary Bay, Yellowstone Lake, Wyoming: Journal of Geophysical Research, v. 82, no. 26, p. 3,733–3,738.

Xu, Y., Schoonen, M.A.A., Nordstrom, D.K., Cunningham, K.M., and Ball, J.W., 1998, Sulfur geochemistry of hydrothermal waters in Yellowstone National Park; I. Origin of thiosulfate in hot spring waters: Geochimica et Cosmochimica Acta, v. 62, no. 23/24, p. 3,729–3,743.

G

Geochemistry of Sublacustrine Hydrothermal Deposits in Yellowstone Lake—Hydrothermal Reactions, Stable-Isotope Systematics, Sinter Deposition, and Spire Formation

By Wayne C. Shanks, III, Jeffrey C. Alt, and Lisa A. Morgan

Chapter G *of*
Integrated Geoscience Studies in the Greater Yellowstone Area—Volcanic, Tectonic, and Hydrothermal Processes in the Yellowstone Geoecosystem
Edited by Lisa A. Morgan

U.S. Geological Survey Professional Paper 1717

U.S. Department of the Interior
U.S. Geological Survey

Contents

Abstract 205
Introduction 205
Geologic Setting 206
Acknowledgments 206
Methods 210
Occurrence and Mineralogy of Hydrothermal Deposits in Yellowstone Lake 210
    Siliceous Vent Deposits 216
    Siliceous Spires 217
    Yellowstone Lake Sediments and Altered Vent Sediments 223
Geochemistry 225
    Major-Element Systematics 225
    Trace Elements in Vent Fluids and Sinter Deposits 226
Stable-Isotope Systematics 226
    Oxygen Isotopes in Siliceous Deposits and Altered Sediments 226
    Sulfur Isotopes in Lake Water, Vent Fluids, and Vent Deposits 228
Geochemical Model for Silica Transport and Deposition 228
Summary and Conclusions 232
References Cited 232

Figures

1. Bathymetric maps of:
    A. Yellowstone Lake 207
    B. West Thumb showing locations of hydrothermal sites 207
    C. Northern Yellowstone Lake showing locations of hydrothermal sites 207
2. Lake-bottom photographs of hydrothermal deposits off Grant Marina, West Thumb:
    A. Silicified hydrothermal conduits protruding above lake floor 216
    B. Flat and branching plates of siliceous material atop sediment 216
    C. Irregular, "blobby"-shaped conduit 216
3. Seismic-reflection profile of shallow subsurface sediments at Stevenson Island vent site 217
4. Photographs of vent conduit samples:
    A. Portion of silicified conduit with partly silicified lake sediment adhering to outer walls 222
    B. Close-up of mass of interconnected small siliceous tubes 222
    C. Siliceous conduit showing main orifice and smaller orifices branching off the sides 222
    D. Mass of interconnected small siliceous tubes 222
    E. Portion of 4-cm-diameter conduit with silica-rich walls and ~2-cm-diameter main conduit 222
    F. Mushroom-shaped conduit 222

5. Scanning electron micrographs of siliceous conduit:
   A. Inner conduit lining consisting of amorphous silica precipitate 223
   B. Outer surface of conduit with detrital material and diatoms 223
6. Underwater photomosaic of a Bridge Bay spire with scanning electron micrograph of siliceous spire texture 224
7. Ternary diagram of SiO_2-Al_2O_3-CaO for sinter deposits and Yellowstone Lake sediments 225
8. Plots of results of sediment leaching calculations 225
9. Enrichment-depletion diagram for trace elements in vent deposits and vent muds relative to average unaltered West Thumb sediment 227
10. Plots of oxygen-isotope values of hydrothermal silica deposits versus calculated temperatures 228
11. Oxygen-isotope composition of hydrothermal end-member fluids 229
12. Incremental reaction models for:
   A. Equilibration of hydrothermal fluid with amorphous silica 230
   B. Silica precipitation by advective mixing 230
   C. Silica precipitation by conductive cooling 230
13. Schematic diagram of spire growth 231

Tables

1. Mineralogy of vent deposits and vent muds from X-ray diffraction and scanning electron microscopy 208
2. Major element and stable-isotope data for vent deposits and vent muds 211
3. Minor and trace-element data for vent deposits and vent muds 218

Geochemistry of Sublacustrine Hydrothermal Deposits in Yellowstone Lake—Hydrothermal Reactions, Stable-Isotope Systematics, Sinter Deposition, and Spire Formation

By Wayne C. Shanks, III,[1] Jeffrey C. Alt,[2] and Lisa A. Morgan[1]

Abstract

Geochemical and mineralogical studies of hydrothermal deposits and altered vent muds from the floor of Yellowstone Lake indicate that these features form due to hydrothermal fluid quenching in shallow flow conduits or upon egress into bottom waters. Siliceous precipitates occur as conduits within the uppermost sediments, as tabular deposits that form along sedimentary layers, and as spires as much as 8 m tall that grow upward from crater-like depressions on the lake bottom. These deposits are enriched in As, Cs, Hg, Mo, Sb, Tl, and W.

Variations in major-element geochemistry indicate that subaerial sinters from West Thumb and spire interiors are nearly pure SiO_2, whereas sublacustrine conduits are less SiO_2 rich and are similar in some cases to normal Yellowstone Lake sediments due to incorporation of sediments into conduit walls. Vent muds, which are hydrothermally altered lake sediments, and some outer conduit walls show pervasive leaching of silica (~63 weight percent silica removal). This hydrothermal leaching process may explain the occurrence of most sublacustrine vents in holes or vent craters, but sediment winnowing by vent fluids may also be an important process in some cases.

Stable-isotope studies indicate that most deposits formed at temperatures between 78°C and 160°C and that vent fluids had oxygen-isotope values of –3.2 to –11.6 per mil, significantly higher than lake waters (–*16.5 per mil). Sulfur-isotope studies indicate that vent waters and lake waters are dominated by sulfur derived from volcanic rocks with $\delta^{34}S$ ~ 2.5 per mil.

Geochemical reaction modeling indicates that spires form from upwelling hydrothermal fluids that are saturated with amorphous silica at temperatures 80°–96°C. Reaction calculations suggest that silica precipitation on the lake bottom is initially caused by mixing with cold bottom waters. Once a siliceous carapace is established, more rapid silica precipitation occurs by conductive cooling. Silicification of thermophilic bacteria is a very important process in building spire structures.

Introduction

Yellowstone Lake at 2,356 m altitude is the largest high-altitude lake in North America and is an important scenic attraction and pristine environment in America's first National Park. Famous for abundant and spectacular hydrothermal activity, Yellowstone National Park (the Park) is home to hundreds of geysers, boiling pools, terraces, and acid-steam environments—and thus results from recent high-resolution bathymetric and seismic mapping that indicate hundreds of hydrothermal vents on the lake floor generally are consistent with distributions of thermal features in major subaerial geyser basins (Morgan and others, 2003).

Studies of hydrothermal vent fluids in Yellowstone Lake have shown that a number of elements, including B, Li, Cs, Cl, As, Sb, Hg, Mo, and W, are strongly enriched in vent fluids and in the lake water column due to hydrothermal venting (Balistrieri and others, this volume; Gemery-Hill and others, this volume). Moreover, these studies, combined with Park-wide studies of Cl fluxes in streams (Friedman and Norton, this volume), indicate that 10 percent of the flux of deep hydrothermal water in Yellowstone National Park occurs on the Yellowstone Lake bottom as sublacustrine hydrothermal vents (Balistrieri and others, this volume). The sublacustrine vents and associated deposits represent several of the most important thermal fields in Yellowstone National Park, comparable in size and hydrothermal flux to Norris Geyser Basin or the Old Faithful area.

Yellowstone Lake also holds a unique position in the geoecosytem of the Park; the native and threatened cutthroat trout in the lake are particularly important because they spawn in the rivers and are important food sources for otter, bear, and eagles. Indeed, geochemical studies of trace metals and stable isotopes show that mercury in sublacustrine hydrothermal vents is incorporated into cutthroat trout and occurs as significantly elevated mercury content in the hair of bears that feed near Yellowstone Lake (Chaffee, Shanks, and others, this volume, Felliceti and others, 2004).

[1]U.S. Geological Survey, Box 25046, Mail Stop 973, Denver Federal Center, Denver, CO 80225.

[2]Department of Geological Sciences, C.C. Little Building, The University of Michigan, Ann Arbor, MI 48109.

In this report, we document the occurrence of sublacustrine hydrothermal deposits and their mineralogy, chemistry, and stable-isotope composition in order to understand their origins and implications for processes involving hydrothermal fluids venting on the lake bottom.

Geologic Setting

Yellowstone National Park occupies a region of young and active tectonism and volcanism related to its current position over a deep long-lived thermal disturbance (Humphreys and others, 2000; Christiansen and others, 2002) refered to as the Yellowstone hotspot (Pierce and Morgan, 1992; Smith and Braile, 1994). Migration of the North American plate over the Yellowstone hotspot beginning at ~16 Ma has produced a progression of silicic volcanic fields containing nested caldera complexes along the Snake River Plain (Pierce and Morgan, 1992). This track of silicic magmatism is exposed along the margins of and reflected in the topographically low Snake River Plain (Armstrong and others, 1975; Morgan and others, 1984; Perkins and Nash, 2002; Kellogg and others, 1994; Morgan, 1992; Leeman, 1982; Hughes and McCurry, 2002; Bonnichsen, 1982); the hotspot is now centered on the topographically high Yellowstone Plateau (Pierce and Morgan, 1992; Pierce and others, this volume).

Large-volume, high-silica rhyolitic ignimbrites and lava flows have erupted from overlapping and nested calderas in the Yellowstone Plateau volcanic field producing an estimated total eruptive volume of 3,700 km^3 (Christiansen, 2001). Major caldera-forming eruptions occurred at 2.05 Ma, 1.3 Ma, and 0.64 Ma (Christiansen, 2001). The 0.64-Ma Yellowstone caldera is the locus of most active hydrothermal activity in the Park. Seismic studies (Christiansen, 2001; Miller and Smith, 1999) suggest that a zone of magma below the caldera, at about 5–6 km deep, fuels the hydrothermal activity of Yellowstone National Park. Further, Fournier (1999) argues that the hydrothermal fluids circulate above the depth of brittle-ductile transition depth (3–5 km) and that there may be periodic exchange of magma or brine across this interface.

Yellowstone Lake straddles the southeastern topographic margin of the 0.64-Ma Yellowstone caldera (fig. 1), resulting in the northern two-thirds of the lake lying within the caldera and containing most of the sublacustrine hydrothermal activity. The eastern boundary of the northern part of the lake corresponds with the eastern edge of the Yellowstone caldera (Morgan and others, 2003). Mary Bay, a large scalloped embayment on the northern edge of the lake, formed around 13,600 years ago as a series of sublacustrine hydrothermal-explosion events (Wold and others, 1977; Morgan and others, 1998; Pierce and others, 2002). West Thumb basin, in the western reaches of Yellowstone Lake, formed during eruption of the ~140-ka tuff of Bluff Point (Obradovich, 1992) and subsequent collapse of the West Thumb caldera (Christiansen, 2001).

Hydrothermal vent areas in Yellowstone Lake have been known since the first surveys of the area in the late 1800s (Hayden, 1878). Bathymetric and additional geophysical surveys conducted by Wold and others (1977), Otis (1975), Otis and others (1977), and Kaplinski (1991) and vent sampling by the University of Wisconsin-Milwaukee (Klump and others, 1988; Remsen and others, 1990) better established the existence and location of several hydrothermal vent fields within the lake. These studies clearly show that abundant sublacustrine hydrothermal activity occurs within the Yellowstone caldera (fig. 1). West Thumb basin and the northern basin (fig. 1) related to exceptionally high heat flow (Morgan and others, 1977). The South and Southeast Arms of the lake, well outside the caldera boundary, are of glacial origin and exhibit little evidence of hydrothermal activity.

More recently, USGS high-resolution bathymetric mapping of Yellowstone Lake from 1999–2002 has identified more than 300 hydrothermal vents on the lake floor, mainly in the West Thumb and northern basins but also in the central basin (Morgan and others, 2003; Morgan and others, this volume). Exploration, photographic documentation, and sampling with a submersible remotely operated vehicle (ROV) has revealed different types of hydrothermal deposits on the lake bottom, including siliceous conduits formed due to hydrothermal fluid flow through surficial sediments in areas of active or previously active venting and a spectacular group of 12–15 spires of siliceous sinter as much as 8 m tall. Siliceous sinter deposits in Yellowstone Lake are of broad interest because they may be analogous to some important ancient mineral deposits that are hosted by siliceous sinter in lake beds (Cunneen and Sillitoe, 1989; Ebert and Rye, 1997). Similar small sublacustrine sinter deposits have been reported from Lake Taupo, New Zealand (de Ronde and others, 2002). Inactive siliceous spires have been observed in one area in Crater Lake, Oregon (Robert Collier, Oregon State University, written commun.; Bacon and others, 2002), but they have not been studied in detail.

Acknowledgments

This work could not have been done without the support of the National Park Service, especially Mike Finley, John Varley, Tom Olliff, Paul Doss, Dan Reinhart, Rick Fey, John Lounsbury, Dan Mahoney, Jim Ruzycki, Todd Koel, and the Aquatic Resources Group at Lake Station. We are particularly indebted to Dave Lovalvo of Eastern Oceanics, Inc., who designed, built, and piloted the ROV and the research vessel (R.V. *Cutthroat*) and generously shared his incredible knowledge of Yellowstone Lake. We thank Kate Johnson, Ed du Bray, Geoff Plumlee, Pat Leahy, Steve Bohlen, Tom Casadevall, Linda Gundersen, Denny Fenn, Elliott Spiker, and Dick Jachowski for supporting this work. We thank Dan Reinhart, Paul Doss, Ann Deutch, Christie Hendrix, Pam Gemery-Hill, Rick Sanzolone, Al Meier, Pete Theodorakos, Jim Bruckner, Bree Burdick, Steve Harlan, Greg Meeker, Jim Waples, Bob Evanoff, Wes Miles, Rick Mossman, Gary Nelson, Eric White, and many others for assistance with field and laboratory studies. We especially

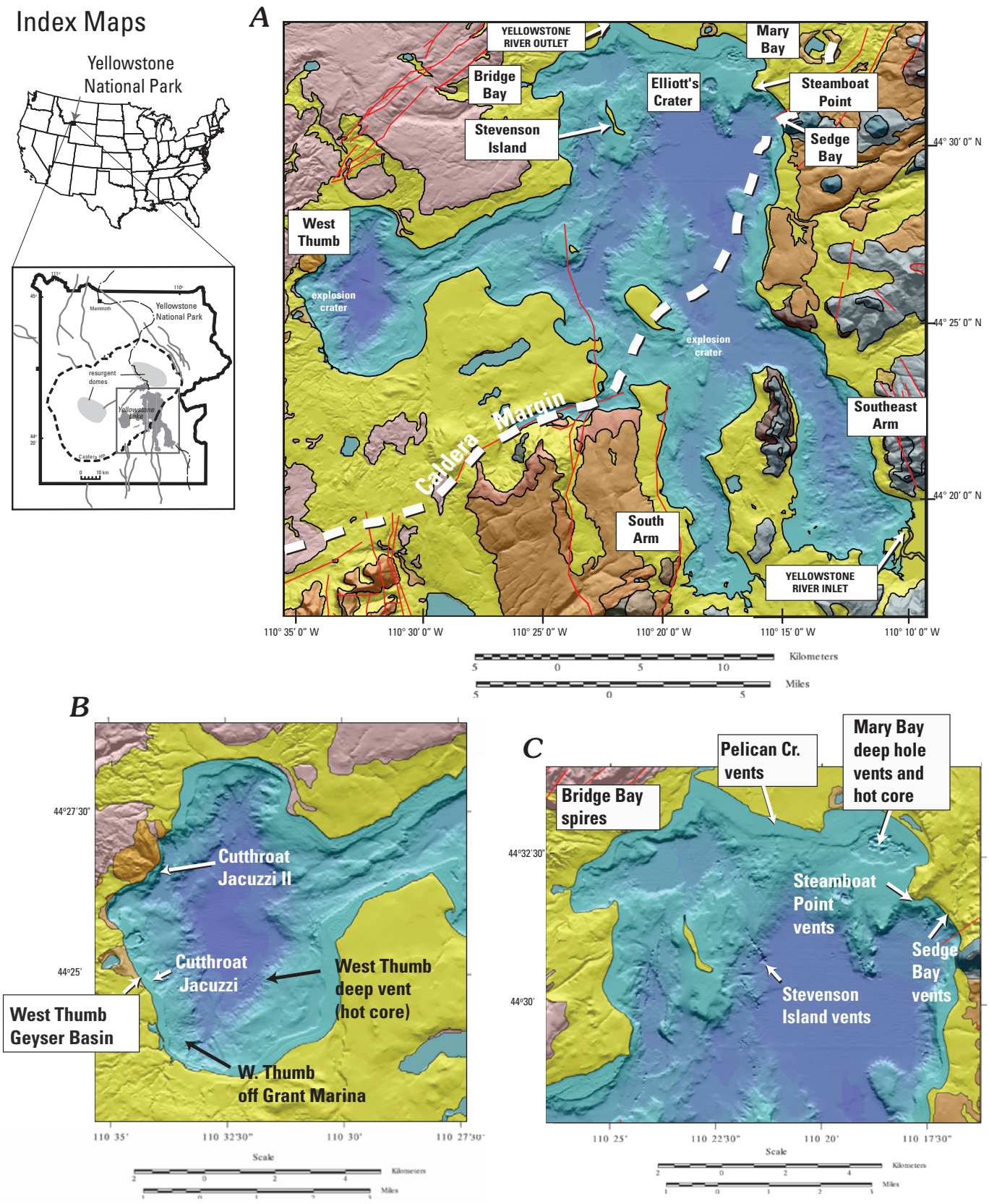

Figure 1. *A,* Bathymetric map of Yellowstone Lake. *B,* Detailed bathymetric map of West Thumb showing locations of hydrothermal sites. *C,* Detailed bathymetric map of northern Yellowstone Lake showing locations of hydrothermal sites.

Table 1. Mineralogy of vent deposits and vent muds from X-ray diffraction (XRD) and scanning electron microscopy.

[Co, conduit; Cr, crust; Sed, sediment; Ab, albite; Sm, smectite; Vill, villyaellenite—a Mn-As oxyhydroxide: $(MnCaZn)_5(AsO_3OH)_2(AsO_4)_2.4(H_2O)$—Am, amorphous; Gt, goethite; Interst, interstitial; Am Si, amorphous silica]

Sample	Type	Description	XRD			Location
			Major	Minor	Trace	
		Vent deposits				
BS 8	co	~3-cm-diameter conduit; porous gray, hard gray, soft buff	Qz, Ab, Opal		Ill, Sm	Mary Bay
			Opal	Qz, Ab	Sm, Ill	Mary Bay
			Opal		Qz, Ab	Mary Bay
94-7-1(D-7)	cr	Irregular gray "crust" and conduits; composed of lithified sediment				Mary Bay
94-11-2	co	1- to 2-cm-diameter conduits; gray inner, buff outer; porous white and red-brown precipitates	Qz, Ab, Opal;	Sm, Illite		Mary Bay
			Opal	Qz, Ab	Sm, Ill	Mary Bay
			Opal			Mary Bay
94-12-2	co	3- to 4-cm-diameter conduit; harder inner and softer outer layers; composed of lithified sediment?	Qz, Ab	Opal	Sm, Ill, Gyp	Mary Bay
94-12-4	cr	Soft, buff-colored "crust" composed of semilithified sediment?				Mary Bay
94-13-2	co	1-cm-diameter white-buff conduit; hard gray-brown lining; sedimentary layering?				Mary Bay
94-23-1	cr	1- to 2.5-cm-thick "crust;" harder gray core (lithified sediment?); red-brown stains				Mary Bay
94-24-2 tube	co	2.5-cm-diameter conduit; white, hard gray, soft buff				Mary Bay
94-24-2 crust	cr	1–2 cm thick; irregular, semilithified sediment; buff; 0.5-mm-diameter holes	Qz, Ab	Opal	Sm, Ill	Mary Bay
94-?	co+cr	2-cm-diameter conduit and crust with sediment (conduit?); all are buff; lithified sediment?				Mary Bay
98-3	cond	~15-cm-long double conduit; stained by iron oxide				Mary Bay
98-11	co	3- to 4-cm-diameter conduit; 1.5 cm internal diameter; 0.5–2 cm wall (7×10-inch relict conduit)				Mary Bay
	cr	1- by 3- to 5-cm-crust fragments (7×10-inch relict conduit, inverted mushroom)				Mary Bay
YNP 89 SBS-11	tubes	Aggregrate of 1 mm gray tubes; lt gray sed interst; pyrite	Pyrite		Vill>Qz, Ab, Sm, Ill	Sedge Bay
94-14-1 Stv Is	co/cr	Irregular conduit?; hard gray, softer gray, yellow coat; tiny crystal rosettes	Na-Jarosite, Gyp		Qz, Ab, Opal	Stevenson Island
94-14-4	co	1.5 cm buff-orange conduits; hard brown silica lining				Stevenson Island
97 WTGB	sinter	Chunk of subaerial sinter	Opal only			West Thumb Geyser Basin
98-16 cond	co	19-inch-long conduit; 2–10 mm walls; brown iron oxide coating, mud fill	Qz	Opal	Sm, Ill	W Thumb, off marina
98-17 cond	co	12-inch-long relict conduit; sediment ridges; 2-inch-diameter and 3-mm-thick wall				W Thumb, off marina
98-18 crust	cr	10×13-inch crust (vein in sed?); 3 mm–3 cm thick; variably silicified; brown FeMn oxide stain				W Thumb, off marina
98-18 sntr	sinter	1×2-inch fragment of white sinter/crust (similar to above sample?)				W Thumb, off marina
98-21	co	6×8-inch mushroom conduit; section through neck; Am Si, native S; mud	Opal		Qz, Ab, Sm	W Thumb, deep
			Opal		Qz, Ab, Sm	
			Opal		Qz, Ab, Ill	
98-22	co	Double conduit; section through throat, tip of neck, and soft outer mud				W Thumb, deep

Table 1. Mineralogy of vent deposits and vent muds from X-ray diffraction (XRD) and scanning electron microscopy—*Continued*.

Sample	Type	Description	XRD			Location
			Major	Minor	Trace	
98-23D-A	co	4×6.5-inch conduit; 2-cm-diameter neck; iron oxide stained; hard 2–3 cm fragments at base; sediment and silica veins				W Thumb, deep
98-24	co	9×10-inch relict conduit with lacy network of tubes; 1-inch-diameter irregular center conduit stained and cemented by red-brown iron oxide				W Thumb, deep
		Bridge Bay spires				
97 BB-1	spire	Chunk of spire	Opal		Ab, Sm, Ill	Bridge Bay spire
	spire	Outer surface	Opal, Am. FeOx		Gt (broad pks)	Bridge Bay spire
97 BB-2	spire	Chunk of spire	Opal only			Bridge Bay spire
		Vent muds				
98-3	mud	Associated with conduit; olive green mud				Mary Bay
98 core 3	mud	1: 0–10 cm long; dark green-black mud; hot (~50 cm core)	Qz, Ab	Sm	Gyp, Ill	Mary Bay
98 core 3	mud	2: 20–30 cm long; dark green-black mud; hot	Qz, Ab	Gyp	Sm, Ill	Mary Bay
98 core 3	mud	3: 40–45 cm long; dark green-black mud; hot	Qz, Ab	Gyp	Ill	Mary Bay
98-26	mud	Dark olive brown mud around active 60°C vent	Qz, Ab	Ill, Sm		Mary Bay
98-27	sed	Dark olive brown mud and consolidated sediments at active 103°C vent	Qz, Ab, Sm	Gyp	Illite	Mary Bay
98-SB 0-1cm	sand	Brown sand; diver core over active vent/bubbler				Sedge Bay
98-SB 5-6 cm	sand	Gray sand				Sedge Bay
98-29	mud	Dark olive brown mud at active vent				E of Stevenson Is
98-29	sed	Gray-black consolidated mud; 1–3 cm clasts				E of Stevenson Is
98-29	sulfide	Pyrite and native S veins and blobs				E of Stevenson Is
98-30	mud	Gray mud from edge of large inactive hole (1–2 ft diameter)	Chl	Sm	Qz, Ab, Ill	E of Stevenson Is
98-32	mud	Mud from around active vents	Chl, Qz	Sm, Ab	Ill	E of Stevenson Is
98-16 in mud	mud	Mud inside conduit; brown-buff				W Thumb, off marina
98-16 out mud	mud	Mud outside conduit; when wet is dark green-brown				W Thumb, off marina
98-17 sedmnt	sed	Consolidated green mud with black FeMn oxide veins and coatings				W Thumb, off marina
98-19	sed	Consolidated gray sediment; stained red-brown by iron oxide	Qz	Chl	Ab, Ill	W Thumb, deep
98-20	sed	Green-gray lithified sediment; angular coarse sandstone and obsidian fragments				W Thumb, deep
		Unaltered West Thumb sediment				
WT89 sediment core	sed	25–26 cm long; tan sediment	Opal		Ab, Qz, Illite, Sm	West Thumb
WT89 sediment core	sed	26–27 cm long; tan sediment	Opal		Ab, Qz, Illite, Sm	West Thumb

thank Greg Lee and Mike Webring of the USGS for turning raw data into beautiful maps. We thank Val Klump, Russell Cuhel, Tony Remsen, and Carmen Aguilar of the University of Wisconsin-Milwaukee for introducing us to Yellowstone Lake vent studies and for sharing samples. Marty Goldhaber and Rich Wanty provided constructive reviews that substantially improved the manuscript. This research was supported by the U.S. Geological Survey, the National Park Service, the National Science Foundation (Environmental Geochemistry and Biogeochemistry), and the Yellowstone Foundation.

Methods

Representative samples of siliceous hydrothermal deposits and sediments were collected from the lake bottom in conjunction with hydrothermal-water-sampling operations (Balistrieri and others, this volume). Most samples were collected with a submersible remotely operated vehicle (ROV) designed and piloted by Dave Lovalvo of Eastern Oceanics, Inc. Although the exact configuration of the vehicle varied from year to year, it was equipped with a motorized scoop for collecting solid samples by remotely maneuvering the submersible while making video observations in the control room of the support boat. Some sediment samples were collected by gravity coring.

Minerals were characterized by X-ray diffraction (XRD) analysis, performed on sample powders using an automated Scintag diffractometer with Cu kα radiation. Samples also were examined by scanning electron microscopy (SEM), using a HITACHI S-3200N SEM, equipped with a Noran X-ray energy-dispersive system (EDS). Mineralogy of samples is summarized in table 1.

Samples were crushed and ground to <200 mesh for chemical analyses. All chemical and isotopic analyses were done in the USGS laboratories in Denver, Colo. Major-element analyses were carried out on fused pellets by wavelength-dispersive X-ray fluorescence (table 2). Forty trace and minor elements were analyzed by inductively coupled plasma–mass spectrometry (ICP–MS) following sample dissolution in HNO_3-HF solution. Mercury was analyzed on separate acid dissolutions using flameless atomic absorption (AA) analysis. Trace- and minor-element data are summarized in table 3.

Silicate samples for oxygen-isotope analysis were reacted with BrF_5 in nickel reaction vessels (Clayton and Mayeda, 1963) to liberate O_2, which was converted to CO_2. Oxygen-isotope values ($\delta^{18}O$) were analyzed on a Finnigan 252 isotope ratio mass spectrometer and calibrated relative to the VSMOW (Vienna Standard Mean Ocean Water; Coplen, 1995) standard with reproducibility of approximately 0.2 per mil. Sulfur-bearing phases were analyzed for $\delta^{34}S$ using an automated elemental analyzer interfaced to a Micromass Optima isotope ratio mass spectrometer (Giesemann and others, 1994). $\delta^{34}S$ error is estimated to be 0.2 per mil. Stable-isotope data are included in table 2.

Occurrence and Mineralogy of Hydrothermal Deposits in Yellowstone Lake

Active hydrothermal vents and associated vent deposits have been observed at many locations in Yellowstone Lake (fig. 1) including shallow-water vents in nearshore locations in West Thumb, Mary Bay, off Steamboat Point, and in Sedge Bay; moderate-depth (25–50 m) vents in West Thumb basin and in the Mary Bay hydrothermal-explosion-crater complex; and in the deepest part of the lake (95–110 m) off Stevenson Island

Large hydrothermal-explosion craters (>500-m diameter) are known in subaerial hydrothermal areas in Yellowstone National Park and elsewhere (Browne and Lawless, 2001; Morgan, Shanks, and others, 1998; Muffler and others, 1971). High-resolution bathymetric surveys in recent years have identified a number of large hydrothermal-explosion craters on the lake floor (Morgan and others, this volume; Morgan and others, 2003). These include the Mary Bay crater complex, a large crater southeast of Storm Point informally named Elliott's Crater (Morgan and others, 2003; Morgan and others, this volume; Johnson and others, 2003), a nearshore crater in West Thumb north of West Thumb Geyser Basin, and a crater south of the caldera margin in the central lake (fig. 1). Hydrothermal activity has been observed in many of these explosion craters, and additional data on related vent fluids is presented in Gemery-Hill and others (this volume).

High-resolution bathymetric mapping has located more than 650 vent craters in Yellowstone Lake (Morgan and others, this volume; Morgan and others, 2003). At sublacustrine vent sites, shimmering hydrothermal fluids, with or without bubbles, typically exit from small (~1–5 cm in diameter) vents within unconsolidated or semi-indurated sediment, at temperatures of ~10°–120°C. Most sublacustrine hydrothermal vents in Yellowstone Lake occur within localized bathymetric deeps or small craters, here called vent craters, which are most commonly ~1–10 m wide and ~10–20 m deeper than the surrounding lake floor. The largest of the vent craters is off the eastern shore of Stevenson Island (fig. 1*C*) and is about 220 m wide and 50 m deeper than the surrounding lake bottom (fig. 2). This structure is in the northernmost set of three northwest-trending fissures; its location is at the southeastern end of the line of vents (fig. 1). It contains numerous individual vents, as indicated by seismic reflection profiles across this structure (Johnson and others, 2003) and by photographic documentation with the ROV exploration and sampling of thermal fluids and solids.

Sediment is exposed in the walls of many of these vent craters, especially in West Thumb basin and off the eastern shore of Stevenson Island. Solid samples and submersible observations show that the sediments are laminated, semi-indurated, fractured, and jointed, breaking into angular centimeter- to decimeter-size blocks. Recent unconsolidated sedi-

Table 2. Major element and stable-isotope data for vent deposits and vent muds.

[Chemical analyses by wavelength-dispersive X-ray fluorescence (WD-XRF) and by inductively coupled plasma–mass spectrometry (ICP-MS). LOI, loss on ignition]

Sample number/description	Location	$\delta^{34}S$	$\delta^{18}O$	SiO_2* (wt %)	Al_2O_3 (wt %)	CaO (wt %)	$FeTO_3$ (wt %)	K_2O (wt %)	MgO (wt %)	MnO (wt %)	Na_2O (wt %)	P_2O_5 (wt %)	TiO_2 (wt %)	S (wt %)	LOI (925°C)	Total	Analytical method
98-11, MB relict conduit	Mary Bay			76.4	7.54	1.8	2.26	1.14	0.7	0.02	1.27	0.18	0.3	0.12	7.2	98.9	WD-XRF
98-11, MB crust	Mary Bay			77.1	7.56	1.83	1.84	1.13	0.83	0.02	1.29	0.13	0.3	0.25	7.7	100.0	WD-XRF
94-11-2, MB bulk conduit	Mary Bay			84.1	5.10	0.84	1.30	0.73	0.40	0.023	0.71	0.27	0.17	0.20			ICP-MS
94-11-2, MB inner conduit	Mary Bay		8.6	87.4	2.83	0.56	1.22	0.42	0.25	0.008	0.49	0.14	0.13	0.40			ICP-MS
94-11-2, MB outer conduit	Mary Bay			80.1	7.18	1.20	1.86	1.11	0.50	0.046	1.15	0.37	0.33	< 0.1			ICP-MS
94-12-2, MB bulk conduit	Mary Bay			81.9	5.29	1.23	2.43	0.80	0.46	0.026	0.96	0.41	0.17	0.20			ICP-MS
94-12-4, MB crust	Mary Bay			74.5	9.83	2.38	2.14	1.45	0.93	0.039	1.75	0.37	0.50	< 0.1			ICP-MS
94-13-2, MB bulk conduit	Mary Bay			84.4	4.53	0.92	1.57	0.65	0.41	0.046	0.67	0.37	0.17	0.10			ICP-MS
94-13-2, MB inner conduit	Mary Bay		8.5	89.5	2.27	0.42	0.56	0.33	0.20	0.009	0.32	0.09	0.10	0.10			ICP-MS
94-13-2, MB outer conduit	Mary Bay			83.6	4.91	0.95	1.72	0.73	0.43	0.194	0.75	0.41	0.17	< 0.1			ICP-MS
94-14-4, MB outer conduit	Mary Bay			72.0	10.0	1.82	4.72	1.57	0.53	0.101	1.75	0.50	0.50	0.40			ICP-MS
94-23-1, MB bulk crust	Mary Bay			82.2	5.86	1.13	1.72	0.75	0.50	0.023	0.88	0.32	0.33	0.20			ICP-MS
94-23-1, MB inner crust	Mary Bay			84.5	4.35	1.09	1.43	0.60	0.51	0.022	0.75	0.27	0.17	0.20			ICP-MS
94-23-1, MB outer crust	Mary Bay			76.2	8.50	2.38	2.14	1.18	0.65	0.074	1.35	0.46	0.33	0.60			ICP-MS
94-24-2-A, MB crust	Mary Bay			77.2	7.75	1.96	2.57	1.14	0.90	0.058	1.48	0.50	0.33	< 0.1			ICP-MS
94-24-2-B, MB bulk conduit	Mary Bay		16.3	77.9	7.75	1.96	2.00	1.11	0.99	0.037	1.35	0.32	0.33	0.10			ICP-MS
94-3, MB bulk conduit	Mary Bay			81.2	6.05	1.54	1.57	0.92	0.63	0.101	1.13	0.23	0.33	0.20			ICP-MS
94-7-1, MB crust	Mary Bay			77.3	7.94	2.10	2.00	1.16	1.03	0.039	1.48	0.32	0.33	0.20			ICP-MS
BS8, MB bulk conduit	Mary Bay		9.8	83.0	6.05	0.85	1.20	0.86	0.32	0.018	0.86	0.23	0.33	0.20			ICP-MS
BS8, MB inner conduit	Mary Bay			88.0	2.83	0.56	0.79	0.42	0.25	0.007	0.47	0.09	0.13	0.30			ICP-MS
BS8, MB outer conduit	Mary Bay			82.3	6.05	0.95	1.43	0.94	0.38	0.022	0.98	0.27	0.33	0.20			ICP-MS
YNP-89-SBS-11, pyritic tubes w/ sediment	Sedge Bay			13.1	5.10		44.32	0.08	0.03	0.001		0.09	0.17	31.00			ICP-MS
98-29, SI sediment & pyrite veins	Stevenson Island													23			WD-XRF
94-14-1, SI bulk conduit	Stevenson Island			73.9	9.45	1.82	3.29	1.33	0.63	0.021	1.62	0.32	0.33	1.20			ICP-MS
94-14-1, SI inner conduit/crust	Stevenson Island		13.5	81.8	5.67	1.15	1.72	0.84	0.50	0.013	1.09	0.18	0.33	0.60			ICP-MS
94-14-1, SI outer conduit	Stevenson Island			75.4	8.50	1.82	2.86	1.20	0.66	0.019	1.62	0.32	0.33	1.10			ICP-MS
94-14-4, SI bulk conduit	Stevenson Island			68.6	12.3	2.10	4.86	1.81	0.65	0.046	2.02	0.50	0.50	0.50			ICP-MS
94-14-4, SI inner conduit	Stevenson Island			84.1	4.91	0.92	1.40	0.76	0.28	0.023	0.89	0.18	0.17	0.20			ICP-MS
98-22, WT double conduit	West Thumb deep vent			88.1	2.02	0.31	0.46	0.42	< 0.10	0.01	0.19	0.1	0.07		6.6	98.2	WD-XRF

Table 2. Major element and stable-isotope data for vent deposits and vent muds—*Continued*.

Sample number/description	Location	$\delta^{34}S$	$\delta^{18}O$	SiO_2* (wt %)	Al_2O_3 (wt %)	CaO (wt %)	$FeTO_3$ (wt %)	K_2O (wt %)	MgO (wt %)	MnO (wt %)	Na_2O (wt %)	P_2O_5 (wt %)	TiO_2 (wt %)	S (wt %)	LOI (925°C)	Total	Analytical method
98-23D, WT slab	West Thumb deep vent		17.1	91.1	0.60	0.08	0.33	0.15	< 0.10	< 0.01	< 0.15	0.08	0.04	0.08	5.9	98.3	WD-XRF
98-23d, WT conduit	West Thumb deep vent			93.6	0.72	0.09	0.32	0.17	< 0.10	0.03	< 0.15	0.09	0.04	b.d.	3.8	98.9	WD-XRF
98-24, WT relict, lacy conduit	West Thumb deep vent			81.0	2.87	0.45	3.26	0.34	0.17	1.91	0.19	0.29	0.09	b.d.	7.5	98.1	WD-XRF
98-16, WT conduit	West Thumb off Grant			78.8	6.64	0.7	2.37	1.85	0.23	0.95	1.22	0.28	0.23	b.d.	5.6	98.8	WD-XRF
98-18, WT sinter crust	West Thumb off Grant		20.3	91.1	1.09	0.16	0.73	0.22	< 0.10	0.48	< 0.15	0.08	0.05	b.d.	4.8	98.7	WD-XRF
BRIDGE BAY SPIRES																	
97-BB1, dark outer sinter	NE Bridge Bay		16.1	89.1	2.27	0.28	0.81	0.19	0.25	0.106	0.22	0.37	0.05	0.20			ICP-MS
97-BB1, white/tan inner sinter	NE Bridge Bay		13.7	83.3	6.42	0.81	1.19	0.60	0.53	0.010	0.70	0.18	0.15	<0.1			ICP-MS
97-BB2, dark outer sinter	NE Bridge Bay		8.0	73.3	8.31	1.33	7.43	0.72	0.68		0.77	0.96	0.17	0.20			ICP-MS
97-BB2, white/tan inner sinter	NE Bridge Bay		14.7	88.8	1.57	0.14	2.57	0.10	0.17	0.015	0.07	0.41		<0.2			ICP-MS
WEST THUMB SINTERS																	
97-WTGB-1, WT sinter	Sinter terrace WTGB		20.7	93.6	0.38	<0.07	0.04	0.09	<0.02	< 0.01	0.32	<0.05	<0.02	<0.1			ICP-MS
98P94-A, WT sinter	Fishing Cone, 4 ft deep		21.4	91.7	0.52	0.15	0.1	0.12	< 0.10	< 0.01	< 0.15	0.06	< 0.02		5.3	98.0	WD-XRF
98P94-B, WT sinter	Fishing Cone, 7 ft deep			92.0	0.50	0.1	0.1	0.11	< 0.10	< 0.01	< 0.15	0.06	0.030		5.9	98.8	WD-XRF
98P94-C, WT sinter	50m N of Fishing Cone, 4.5 ft deep			90.6	0.40	0.09	0.1	0.05	< 0.10	< 0.01	< 0.15	< 0.05	< 0.02		7.5	98.7	WD-XRF

Table 2. Major element and stable-isotope data for vent deposits and vent muds—*Continued* .

Sample number/description	Location	$\delta^{34}S$	$\delta^{18}O$	SiO_2* (wt %)	Al_2O_3 (wt %)	CaO (wt %)	$FeTO_3$ (wt %)	K_2O (wt %)	MgO (wt %)	MnO (wt %)	Na_2O (wt %)	P_2O_5 (wt %)	TiO_2 (wt %)	S (wt %)	LOI (925°C)	Total	Analytical method
WEST THUMB SINTERS—*Continued*																	
98P95-B, WT sinter	70 m off Fishing Cone, 14.5 ft deep		20.6	93.7	0.35	0.07	0.1	0.07	< 0.10	< 0.01	< 0.15	< 0.05	< 0.02		4.6	98.9	WD-XRF
98P96-B, WT sinter	70m/20 deg S of Fishing Cone, 18 ft deep			92.7	1.10	0.11	0.2	0.10	< 0.10	0.01	< 0.15	0.08	0.030		4.8	99.2	WD-XRF
VENT MUDS																	
98-03, vent mud	Mary Bay	4.6	8.8	67.2	14.7	2.80	3.57	2.05	1.34	0.027	2.16			0.0010			ICP-MS
98-26, vent mud	Mary Bay	0.7	8.4	65.6	14.7	2.94	4.43	1.93	2.16	0.043	2.02			0.03			ICP-MS
98-27, vent mud	Mary Bay	0.8	8.1	70.1	14.9	1.54	3.29	1.20	1.82	0.027	0.89			0.03			ICP-MS
Core 3-1 (0–10 cm), vent mud	Mary Bay	3.4	7.0	70.1	12.7	2.52	3.15	2.05	1.29	0.031	2.02			0.01			ICP-MS
Core 3-2 (20–30 cm), vent mud	Mary Bay	5.7	7.2	70.6	11.9	2.66	3.43	1.81	1.33	0.032	2.16			0.0020			ICP-MS
Core 3-3 (40–45 cm), vent mud	Mary Bay	3.7	8.3	68.8	12.8	2.80	3.72	1.93	1.66	0.039	2.02			0.01			ICP-MS
98-29, vent mud	Stevenson Island	3.4	-3.5	64.4	17.0	0.14	10.58	0.20	1.24	0.015	0.13			0.15			ICP-MS
98-30a, vent mud	Stevenson Island	3.4	-1.5	69.1	14.4	0.28	9.44	0.22	0.27	0.023	0.08			0.14			ICP-MS
98-30b, vent mud	Stevenson Island	3.6	-1.3	70.4	14.0	0.42	8.01	0.30	0.36	0.063	0.15			0.15			ICP-MS
98-32, vent mud	Stevenson Island	3.7	8.1	74.4	12.7	0.78	4.00	0.72	0.73	0.028	0.47			0.05			ICP-MS
98-19, vent mud	West Thumb deep vent	-3.8		71.9	16.1	0.56	2.86	1.02	1.38	0.015	0.04			0.01			ICP-MS
98-16a, vent mud	West Thumb off Grant		11.2	72.8	10.2	1.11	4.29	1.57	1.66	1.291	0.97			0.0004			ICP-MS
98-16b, vent mud	West Thumb off Grant		12.1	73.9	12.7	0.76	2.29	2.29	0.70	0.023	1.28			0.0002			ICP-MS
98-17, vent mud	West Thumb off Grant		10.8	66.7	15.7	1.96	2.86	3.01	1.36	0.045	2.29			0.0001			ICP-MS

Table 2. Major element and stable-isotope data for vent deposits and vent muds—*Continued*.

Sample number/description	Location	$\delta^{34}S$	$\delta^{18}O$	SiO_2* (wt %)	Al_2O_3 (wt %)	CaO (wt %)	$FeTO_3$ (wt %)	K_2O (wt %)	MgO (wt %)	MnO (wt %)	Na_2O (wt %)	P_2O_5 (wt %)	TiO_2 (wt %)	S (wt %)	LOI (925°C)	Total	Analytical method
WEST THUMB SEDIMENTS																	
WT core, 25–26 cm, mud	Central West Thumb			85.5	3.21	0.56	2.00	0.43	0.56	0.112	0.34	0.69	0.12	0.30			ICP-MS
WT core, 25–26 cm, mud	Central West Thumb			85.0	3.40	0.56	2.14	0.47	0.60	0.127	0.35	0.78	0.13	0.30			ICP-MS
WT core, 26–27 cm, mud	Central West Thumb			81.3	5.48	1.04	2.57	0.77	1.18	0.112	0.59	0.37	0.17	0.30			ICP-MS
WT core, 27–28 cm, mud	Central West Thumb			85.5	3.97	0.70	1.57	0.52	0.68	0.070	0.40	0.23	0.13	0.10			ICP-MS
WT core, 28–29 cm, mud	Central West Thumb			84.8	4.35	0.70	1.72	0.57	0.75	0.074	0.44	0.27	0.15	0.10			ICP-MS
WT core, 28–29 cm, mud	Central West Thumb		16.4	85.4	3.97	0.70	1.57	0.58	0.68	0.072	0.43	0.27	0.13	0.10			ICP-MS
WT core, 29–30 cm, mud	Central West Thumb			84.5	3.21	0.56	2.29	0.45	0.53	0.155	0.35	1.51	0.12	0.20			ICP-MS
WT core, 30–31 cm, mud	Central West Thumb			84.3	3.78	0.56	2.14	0.51	0.71	0.142	0.40	0.96	0.13	0.20			ICP-MS
WT core, 31-–32 cm, mud	Central West Thumb			85.6	3.59	0.56	1.72	0.52	0.58	0.098	0.39	0.55	0.13	0.10			ICP-MS
WT core, 32–33 cm, mud	Central West Thumb		17.3	85.7	3.40	0.56	1.72	0.48	0.61	0.111	0.38	0.73	0.12	0.10			ICP-MS
WT core, 33–34 cm, mud	Central West Thumb			86.0	3.40	0.56	1.72	0.48	0.65	0.071	0.38	0.27	0.12	0.20			ICP-MS
WT core, 34–35 cm, mud	Central West Thumb			84.9	3.97	0.70	1.86	0.54	0.65	0.093	0.46	0.41	0.13	0.20			ICP-MS
WT core, 35–36 cm, mud	Central West Thumb			84.6	4.35	0.70	1.86	0.59	0.71	0.074	0.47	0.27	0.17	0.10			ICP-MS

Table 2. Major element and stable-isotope data for vent deposits and vent muds—*Continued*.

Sample number/description	Location	$\delta^{34}S$	$\delta^{18}O$	SiO_2* (wt %)	Al_2O_3 (wt %)	CaO (wt %)	$FeTO_3$ (wt %)	K_2O (wt %)	MgO (wt %)	MnO (wt %)	Na_2O (wt %)	P_2O_5 (wt %)	TiO_2 (wt %)	S (wt %)	LOI (925°C)	Total	Analytical method
WEST THUMB SEDIMENTS—*Continued*																	
WT core, 35–36 cm, mud	Central West Thumb			85.0	4.16	0.70	1.72	0.59	0.66	0.074	0.46	0.27	0.15	0.10			ICP-MS
WT core, 36–37 cm, mud	Central West Thumb			85.5	3.78	0.70	1.72	0.54	0.66	0.070	0.43	0.23	0.13	0.10			ICP-MS
WT core, 37–38 cm, mud	Central West Thumb			85.7	3.78	0.56	1.72	0.51	0.70	0.067	0.40	0.23	0.13	0.10			ICP-MS
WT core, 38–39 cm, mud	Central West Thumb			86.4	3.40	0.56	1.57	0.49	0.60	0.067	0.38	0.23	0.12	0.10			ICP-MS
WT core, 39–40 cm, mud	Central West Thumb			86.2	3.40	0.56	1.57	0.47	0.53	0.080	0.38	0.37	0.12	0.20			ICP-MS
WT core, 40–41 cm, mud	Central West Thumb			85.5	3.40	0.56	1.86	0.45	0.56	0.102	0.36	0.73	0.12	0.20			ICP-MS
WT core, 41–42 cm, mud	Central West Thumb			85.1	3.21	0.56	2.14	0.46	0.53	0.129	0.36	1.05	0.12	0.20			ICP-MS
WT core, 44–45 cm, mud	Central West Thumb		15.0	86.2	2.83	0.42	2.00	0.41	0.46	0.123	0.31	0.82	0.10	0.20			ICP-MS

*SiO_2 for samples analyzed by ICP-MS is calculated by difference, assuming LOI = 6.1 wt %, the average value for measured vent deposits. Sulfur in vent muds as sulfide, done gravimetrically by CrC_{12} extraction.

ment drapes the walls and floors of the craters in Mary Bay and West Thumb basin and can be clearly seen in seismic-reflection images (Johnson and others, 2003). An excellent example is a profile across the deep hole vent field east of Stevenson Island; this vent field and other nearby vents are related to a set of northwest-trending fissures (figs. 1 and 2).

Siliceous Vent Deposits

Hydrothermal precipitates occur on the lake bottom near active hydrothermal vents and at former vent sites that are now inactive. Hydrothermal deposits, such as in Mary Bay, in West Thumb basin, and southeast and east of Stevenson Island are characterized by centimeter- to decimeter-size tubular to irregularly shaped and branching siliceous conduits once filled with thermal fluids (fig. 3). Most common are 1- to 8-cm-diameter irregular tubes that contain 0.5- to 5-cm-diameter open conduits, in some cases filled with sediment (fig. 4). Individual conduit samples are as long as 40 cm. The outer surface of many conduits consists of soft to friable clay-rich sediment mainly comprised of diatoms, plus minor quartz, albite, smectite, and illite. The diatoms are progressively recrystallized and cemented by amorphous silica toward the center of the tube, forming the dense inner wall of the conduits. The inner conduit walls are lined or clogged with amorphous silica, the colloform texture of which indicates precipitation from hydrothermal fluids (fig. 5*A*). In many samples, there are long filamentous structures suggestive of replaced or mineralized bacteria.

Hydrothermal deposits are observed in the following settings: (1) at the bottom of or perched on the walls of hydrothermal vent areas or craters, (2) sticking out of softer sediment, or (3) lying flat on the sediment surface. In one upright conduit protruding from soft(?) sediment in West Thumb basin, native sulfur occurs as thin layers within the walls and lining the open conduit (fig. 4*E*). The native sulfur most likely results from microbial oxidation of H_2S in hydrothermal fluids. Active communities of bacteria form large mats around many active hydrothermal vent areas in Yellowstone Lake, as photographically documented and sampled with the ROV (Remsen and others, 1990). The outer surface of a conduit sample from the Stevenson Island deep vent site is coated with gypsum and yellowish natrojarosite that forms when hydrothermal sulfide oxidizes within the conduit walls. Also present in small amounts are as much as 20-cm aggregates of tiny (~1 mm) open siliceous tubes, with or without interstitial sediment present. These are essentially a smaller-scaled version of the deposits described above. Similar tubes also have been found in gravelly material at shallow depths of less than a few meters in Sedge Bay, associated with ~1-mm grains of pyrite.

In Mary Bay, irregular, "blobby"-looking conduits are typically perched on the walls of explosion craters and form an irregular surface composed of small, irregular structures, which appear to protrude directly into the water from the lake floor (fig. 3*C*). Field observations suggest that these conduits are connected at depth with fractures in the underlying sediment and have formed within the soft sediment, the structure shape controlled by fluid flow and relative porosities in the sediment. The random-appearing structures were most likely formed

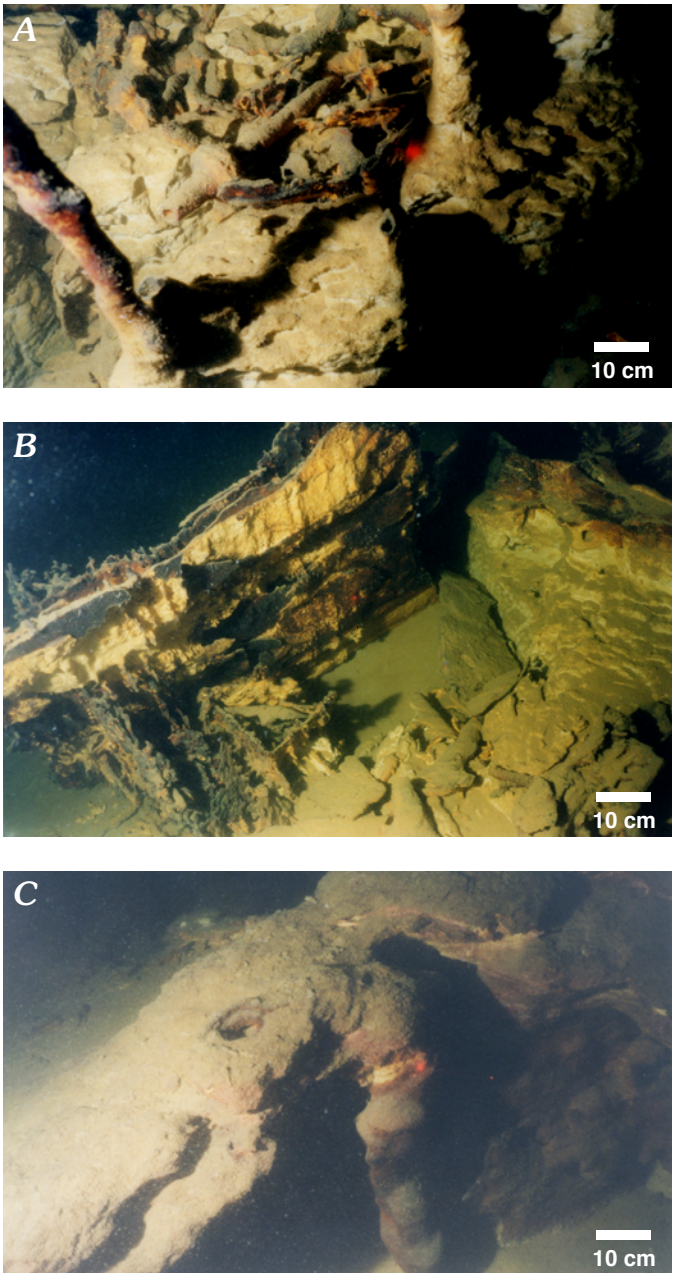

Figure 2. Lake-bottom photographs (by David Lovalvo, Eastern Oceanics, Inc.) of hydrothermal deposits from the vent area off of Grant Marina, West Thumb. All three of these areas are now exposed on the lake bottom due to sediment removal by slumping, winnowing, or dissolution. *A,* Silicified hydrothermal conduits protruding above the lake floor within vent deep. Water depth is 108 ft. *B,* Flat and branching plates of siliceous material lie on top of the sediment within deeps of West Thumb and probably formed as veins within the sediment. Water depth is 108 ft. *C,* Irregular, "blobby"-shaped conduit that terminates in surficial, flange-silicified sediments. Water depth is 73 ft.

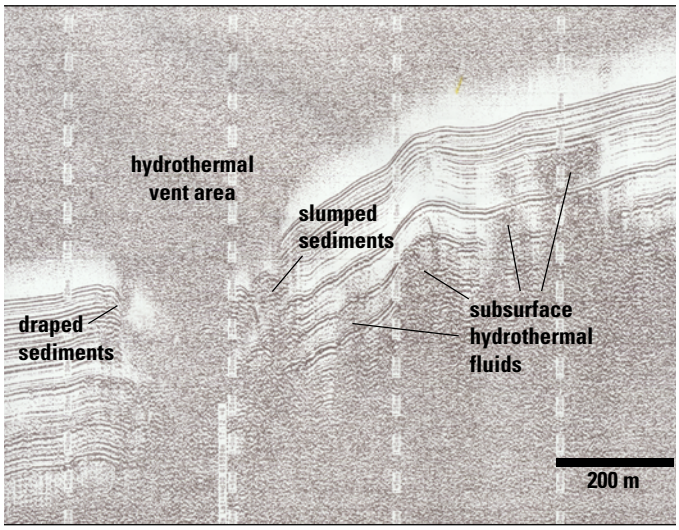

Figure 3. Seismic-reflection profile of shallow subsurface sediments at the Stevenson Island vent site.

below the sediment-water interface within sediments along conduits or vents. The structures may have been exposed later when the surrounding, unconsolidated, unaltered host sediment slumped off the harder, mineralized hydrothermal vent structure or was winnowed away by currents associated with individual vents or current dispersion on the lake floor, possibly combined and enhanced with active dissolution processes. Most of the conduit deposits are approximately 20 cm high or less. An alternative explanation for the formation of these structures is as chimneys above the sediment-water interface; however, this process is inconsistent with the horizontally layered diatomaceous sediments incorporated within the walls and onto the outside of the conduits (figs. 2 and 4). The layering and composition of these layers is very comparable to the laminated sediments found on the undisturbed lake floor.

The occurrence, morphology, and mineralogy of the siliceous conduits and tubes suggest that they formed as fluid conduits within the sediment and that the sediment between the conduits was subsequently removed, exposing the deposits at the sediment surface, where many have toppled over. Many of these conduits occur at the bottom of the vent craters, requiring a process that enables sediment to be winnowed out of 20- to 50-m-deep craters. Recent observations have noted a large (50-m diameter) sediment plume in the water column above active sets of vigorous vents in the northern basin, indicating fine-grained sediments are entrained in the hydrothermal vents during some venting processes and, if vigorous enough and sustained for a long enough time, this process might produce significant deep crater areas. In addition, geochemical studies suggest that sediment dissolution by hydrothermal fluids may be a very important process in explaining much of the detailed landscape in hydrothermal areas on the lake floor (see below).

In the West Thumb basin, irregular flat and branching horizontal plates of siliceous material, <1 cm thick by as much as tens of centimeters across, occur locally atop the sediment associated with the other hydrothermal material (figs. 2*C*, 4*D*, and 4*F*). This platy material is essentially identical to the walls of the tubes described above and may have formed as crusts on top of or veins within more permeable zones within the layered sediment (fig. 3). Lacy, fragile, network-like branching conduits (figs. 2*B* and 4*B*; table 1, sample 98-24) occur in West Thumb basin hydrothermal fields and most likely formed within sediment beneath the sediment-water interface. Joints are common in the semi-indurated sediment exposed within some craters and act as conduits for several active vents in West Thumb basin (fig. 3*B*). This process suggests that siliceous veins could be actively forming in the subsurface at these locations.

Many of the inactive siliceous conduits are stained red to dark brown as the result of coating with iron oxyhydroxides during exposure on the lake bottom, perhaps due to oxidation of hydrothermal fluids during mixing with ambient, oxygenated lake water. The iron oxides are mostly X-ray amorphous, but broad, weak peaks of goethite occur in some diffraction patterns.

Siliceous Spires

Another significant hydrothermal structure found in Yellowstone Lake consists of hard, porous siliceous material protruding vertically from crater-like depressions as irregular, conically shaped “spires” discovered in Bridge Bay in 1997. A group of 12–15 spires, as tall as 8 m with average diameters of 1–2 m, project above the diatomaceous sediment surface at a water depth of 15 m (fig. 6). Spire samples and a small (1.4 m tall), complete spire were recovered by National Park Service scuba divers in 1997 and 1999. Macroscopically, spire samples consist of white or tan, porous, punky siliceous interior with a distinctly red-brown to black outer zone. Scanning electron microscope and X-ray diffraction studies indicate that the spire deposits consist of globules of amorphous silica. The globules are about 5–10 μm in diameter (fig. 6) and form irregular aggregates, interconnecting masses, and cylinders or tubes of aggregated globules. These textures are similar to those observed for silica in active submarine hydrothermal deposits from mid-ocean ridges (Alt and others, 1987; Juniper and Fouquet, 1988). Common, tiny (~1 μm) holes in the silica are probably dissolution effects and could be microbial in origin. The overall texture suggests silica precipitation on bacterial filaments as documented in New Zealand hydrothermal systems (Jones and Renaut, 1996; Jones and others, 1997). Diatoms are sparse in the spire interiors while diatoms are abundant within spire walls, especially near the outer surface of the wall and where the spire roots extend below the sediment-water interface.

Trace amounts of smectite and quartz in the spires are probably detrital material trapped within the hydrothermal pre-

Table 3 (continued on facing page). Minor and trace-element data for vent deposits and vent muds (Ag–Hf).

[Chemical analyses by inductively coupled plasma–mass spectrometry (ICP-MS). Elements measured in parts per million]

Sample number/description	Location	Ag	As	Au	Ba	Be	Bi	Cd	Co	Cr	Cs	Cu	Ga	Ge	Hf
VENT DEPOSITS															
98-11, MB relict conduit	Mary Bay	0.31	69		840	1.4		0.08	6.0	82	37	13	10	1.5	
98-11, MB crust	Mary Bay	0.31	140		860	1.6		0.08	6.7	82	42	14	11	1.9	
94-11-2, MB bulk conduit	Mary Bay		2200		380	0.9	0.08	<0.1	3.4		36	6	<0.1	2.1	1
94-11-2, MB inner conduit	Mary Bay		3200		280	0.8	0.08	<0.1	3.2		18	10	<0.1	0.9	0.6
94-11-2, MB outer conduit	Mary Bay		440		630	1.4	0.1	<0.1	4		64	10	<0.1	2.1	2
94-12-2, MB bulk conduit	Mary Bay		310		520	1.4	0.06	0.5	6.5		28	10	<0.1	1.8	1
94-12-4, MB crust	Mary Bay		74		840	1.6	0.1	<0.1	6		38	10	<0.1	2.4	2
94-13-2, MB bulk conduit	Mary Bay		190		490	0.5	0.06	<0.1	4.1		37	6	<0.1	1.9	1
94-13-2, MB inner conduit	Mary Bay		44		220	0.5	<0.05	<0.1	1.6		28	6	<0.1	0.8	0.5
94-13-2, MB outer conduit	Mary Bay		200		440	0.5	0.05	0.6	12		50	10	<0.1	1.8	1
94-14-4, MB outer conduit	Mary Bay		380		980	2	0.1	0.2	16		46	20	<0.1	2.5	3
94-23-1, MB bulk crust	Mary Bay		330		420	0.9	0.07	0.1	5		30	8	<0.1	1.7	2
94-23-1, MB inner crust	Mary Bay		460		370	0.9	0.2	<0.1	4.6		18	20	<0.1	1	0.8
94-23-1, MB outer crust	Mary Bay	0.2	190		740	1.9	0.1	<0.1	9.4		60	10	<0.1	2.1	2
94-24-2-A, MB crust	Mary Bay	<0.1	240		640	1	0.08	<0.1	5.6		16	6	<0.1	2.5	2
94-24-2-B, MB bulk conduit	Mary Bay	<0.1	91		620	1.2	0.08	<0.1	5.4		20	8	<0.1	2	2
94-3, MB bulk conduit	Mary Bay	<0.1	83		490	0.8	<0.05	0.5	5.8		20	8	<0.1	1.8	1
94-7-1, MB crust	Mary Bay	<0.1	89		630	1.2	0.08	<0.1	5.5		21	8	<0.1	2	2
BS8, MB bulk conduit	Mary Bay	0.2	230		510	1.5	0.1	0.2	3.8		60	20	<0.1	2	2
BS8, MB inner conduit	Mary Bay	0.9	420		280	0.7	<0.05	<0.1	2.8		18	8	<0.1	0.9	0.7
BS8, MB outer conduit	Mary Bay	0.1	230		500	1.2	0.09	0.4	4.4		65	30	<0.1	1.6	2
YNP-89-SBS-11, pyritic tubes w/ sediment	Sedge Bay	0.2	5000		19	0.4	0.09	0.2	26		1.6	120	<0.1	0.4	0.9
98-29, SI sediment & pyrite veins	Stevenson Island	0.27	1000		15	0.18		0.13	42	44	0.92	50	6.6	0.33	
94-14-1, SI bulk conduit	Stevenson Island		160		750	1.4	0.1	<0.1	7.4		24	10	<0.1	1.6	2
94-14-1, SI inner conduit/crust	Stevenson Island		120		520	0.7	0.1	<0.1	4.3		14	10	<0.1	0.9	1
94-14-1, SI outer conduit	Stevenson Island		140		770	1.3	0.09	0.2	6.2		24	10	<0.1	1.3	2
94-14-4, SI bulk conduit	Stevenson Island		220		1000	1.6	0.1	<0.1	13		42	20	<0.1	3.5	3
94-14-4, SI inner conduit	Stevenson Island		95		550	1	0.06	<0.1	5		26	10	<0.1	1.1	1
98-22, WT double conduit	West Thumb deep vent	0.17	76		150	0.94		0.11	0.96	21	68	10	8.5	7.6	
98-22, WT deep vent conduit	West Thumb deep vent	0.04	1200		250	1.2		0.2	3.2	22		10	23	15	
98-23D, WT slab	West Thumb deep vent	0.08	790		47	0.45		0.04	0.38	<10	31	8.6	4.9	3.1	
98-23D, WT conduit	West Thumb deep vent	0.09	290		72	0.82		0.12	0.80	12	48	9.2	6.8	4.0	
98-24, WT relict, lacy conduit	West Thumb deep vent	0.08	930		880	4.2		0.72	23	20	25	20	16	4.4	
98-16, WT conduit	West Thumb off Grant	0.51	550		750	2.6		0.17	10	24	46	7.4	16	3.6	
98-18, WT sinter crust	West Thumb off Grant	0.18	390		270	2.4		0.27	5.2	<10	11	7.8	5.8	2.4	
98-18, WT brown slab	West Thumb off Grant	0.02	500		410	3.5		0.3	7.7	10		7	10	3.4	
BRIDGE BAY SPIRES															
97-BB1, dark outer sinter	NE Bridge Bay	0.12	28	<0.05	130	20	<0.05	0.3	2.1		2.7	5	4.8	0.6	<0.5
97-BB1, white/tan inner sinter	NE Bridge Bay	0.13	13	<0.05	330	16	0.06	<0.1	4.1		6.3	4	8.5	2.4	0.7
97-BB2, dark outer sinter	NE Bridge Bay	0.05	1700	<0.05	6600	12	<0.05	0.8	45		8.2	33	16	6.8	0.5
97-BB2, white/tan inner sinter	NE Bridge Bay	0.37	510	<0.1	59	23	<0.1	<0.2	2		2.1	<6	5.6	1	<1
WEST THUMB SINTERS															
97-WTGB-1, WT sinter	Sinter terrace WTGB	0.1	4	<0.05	5	28	0.06	<0.1	<0.1		86	<3	130	0.4	<0.5
98P94-A, WT sinter	Fishing Cone, 4 ft deep	0.08	4.9		28	71		0.02	0.24	29	200	6.9	170	0.70	0.35
98P94-B, WT sinter	Fishing Cone, 7 ft deep	0.05	5.9		30	28		0.02	0.14	<10	49	1.8	100	3.8	1.6
98P94-C, WT sinter	50m N of Fishing Cone, 4.5 ft deep	0.03	2		32	8.3		0.01	<0.1	<10	40	10	46	2.1	0.11
98P95-B, WT sinter	70 m off Fishing Cone, 14.5 ft deep	0.03	9.0		34	19		0.01	0.32	<10	69	14	170	1.1	0.43

Table 3 (continued from facing page). Minor and trace-element data for vent deposits and vent muds (Hg–Zr).

[Chemical analyses by inductively coupled plasma–mass spectrometry (ICP-MS). Elements measured in parts per million]

Hg	Li	Mo	Nb	Ni	Pb	Rb	Sb	Sc	Se	Sn	Sr	Ta	Th	Tl	U	V	W	Y	Zn	Zr
VENT DEPOSITS																				
	12	2.1		20	13	47	2.8		0.3		440	0.77	6.1	0.3	1.7	52	13		31	
	12	2.8		21	14	48	3.4		0.3		450	1.0	6.5	0.3	1.8	51	25		31	
6.1	8.9	1.7	6.8	12	6.8	31	3.3	4	<1	0.9	180	0.4	3.4	0.2	0.99	36	36	8.6	20	75
	5.6	2.2	5	11	<0.1	16	5.1	2	<1	<0.5	120	0.5	2.2	0.1	0.66	23	17	5.8	10	46
	12	2.9	9.6	12	51	52	3.2	5.4	<1	0.6	260	0.8	5	0.3	1.5	48	61	12	20	100
0.26	6.8	3.8	6.4	16	7.3	26	3.4	4	<1	0.8	260	0.4	3.4	0.2	0.91	40	30	9.3	30	70
0.55	14	1.7	6.6	22	13	44	1.9	7.2	<1	1	460	0.4	6.5	0.3	1.6	52	15	14	36	140
2.7	8.9	2	7	13	6.8	26	2.4	4	<1	0.6	180	0.4	3.4	0.2	0.97	35	58	8.4	20	68
1.6	5	1.3	4	7	1	17	1.5	2	<1	<0.5	84	0.3	1.7	0.1	0.5	18	9.9	4.5	8	34
	11	4.1	7.3	15	88	33	4.1	4	<1	<0.5	180	0.5	4.1	0.2	1.3	41	150	11	20	66
1.8	12	9.7	14	23	16	60	9.3	8.4	<1	5	430	1	7.2	0.3	1.9	83	71	17	39	140
0.68	11	2.2	9	18	7.8	26	3.1	4	<1	2	220	0.4	3.8	0.2	1.1	41	29	10	20	80
	8.7	2.1	8.3	17	7.5	20	3.4	3	<1	<0.5	200	0.5	3.2	<0.1	1.2	31	18	9.8	20	70
	17	2.8	13	23	13	45	4.8	6.7	<1	<0.5	360	0.7	6.4	0.3	1.7	60	77	16	30	120
0.48	12	1.8	6.2	19	10	32	2	6.1	<1	0.9	370	0.3	5	0.3	1.5	44	39	12	30	100
0.18	14	1.4	8.6	20	9.8	32	1.3	5.6	<1	0.8	370	0.5	4.9	0.2	1.4	39	19	11	20	100
0.95	9.7	1.5	5.4	24	5.6	26	1.4	5	<1	<0.5	280	0.2	3.4	0.4	1	27	30	7.8	20	74
0.38	14	1.4	9.1	21	10	33	1.3	5.8	<1	0.8	380	0.5	4.9	0.2	1.3	41	19	11	30	100
14	11	3.6	7.8	11	10	42	4.9	5	<1	1	210	0.5	4.3	0.2	1.2	42	23	11	20	88
55	5.9	2	4.8	11	4.4	17	2.4	2	<1	<0.5	120	0.3	2.1	0.2	0.54	21	7.9	6.2	10	43
3.1	11	2.6	8.3	13	12	45	2.3	5	<1	2	210	0.6	4.2	0.2	1.3	39	41	12	36	90
9.1	0.2	100	22	5.2	110	22	<0.05	240	4	7	5.3	6.2	<0.5	2.5	4.4	0.89	35	12	6.6	53
	0.4	35		240	27	0.32	18		2.6		3.6	0.89	3.5	1.3	1.0	40	120		45	
0.51	14	2.5	12	26	12	37	3.9	6.4	<1	1	400	0.8	5.6	0.3	1.4	57	15	14	34	120
	9.1	1.6	7.7	16	8.1	24	2.8	4	<1	0.8	250	0.6	3.7	0.1	0.96	33	8.8	8.6	20	78
	14	2.2	12	22	11	39	3.6	5.7	<1	0.7	390	1.2	5.7	0.2	1.4	53	16	13	30	120
2.2	14	8.6	15	27	16	62	7.9	9.2	<1	2	500	1.1	7.7	0.4	1.9	89	36	19	46	170
1	5.4	2.4	6.9	13	6.6	31	3.3	4	<1	0.5	220	0.5	3.3	0.1	0.9	35	14	10	20	63
	5.4	0.78		6.7	4.3	26	5.6		0.2		42	0.37	1.7	0.2	0.74	8.8	26		11	
	8.7	2.1		6.7	8.1	49	11		<1		89		3.1	0.6	1.6	32	78		10	
	1.2	3.9		3.0	2.0	12	26		<0.2		12	0.2	0.73	0.1	0.36	6.8	18		<5	
	2.3	3.0		5.9	2.9	18	5.5		0.1		17	0.2	1.1	0.2	0.79	10	51		5.5	
	8.3	17		150	4.3	18	15		0.5		67	<0.2	3.0	12	2.2	60	450		29	
	18	13		29	14	75	22		0.5		100	1.3	12	2.4	3.4	25	200		35	
	5.7	25		46	2.8	13	40		0.2		23	<0.2	1.8	5.1	0.93	15	260		11	
	13	16		70	4.3	16	18		<1		38		3.2	8	1	24	250		20	
BRIDGE BAY SPIRES																				
	6.7	1.9	8.3	16	3.6	6.3	6	1	<1	<0.5	53	<0.1	1	0.1	1.6	13	40	8.6	10	9.2
	16	1.3	7.2	16	7.2	19	5.4	2	<1	0.7	150	0.1	2.9	0.2	1.6	28	6.8	6.8	10	51
	60	57	0.5	520	5.8	22	20	3	<1	<0.5	250	<0.1	3.2	27	2.8	180	390	15	52	8.7
	4	2	19	21	5.9	4.1	14	<1	<2	<1	21	<0.2	1	<0.2	2.5	44	110	5.8	<6	18
WEST THUMB SINTERS																				
	9.4	0.2	0.2	0.4	1	13	55	<0.5	<1	<0.5	3	<0.1	<0.05	0.2	0.2	<1	4.3	0.8	<3	0.4
	5.7	0.96	<2	16	1.7	23	12	<0.3	<0.2		6.9	<0.2	0.44	0.2	0.15	<0.4	1.0	1.5	<5	
	6.0	0.23	2.1	<1	1.5	14	37	<0.3	<0.2		5.8	<0.2	0.49	0.1	0.44	1.4	3.9	1.5	<5	
	3.1	0.2	<2	<1	1.3	9.2	44	<0.3	<0.2		2.9	<0.2	0.30	0.06	0.14	1.1	3.7	0.51	<5	
	5.4	0.74	<2	1.3	1.2	12	66	<0.3	<0.2		6.4	<0.2	0.29	0.07	0.16	0.8	1.4	0.68	<5	

Table 3 (continued on facing page). Minor and trace-element data for vent deposits and vent muds (Ag–Hf)—*Continued.*

Sample number/description	Location	Ag	As	Au	Ba	Be	Bi	Cd	Co	Cr	Cs	Cu	Ga	Ge	Hf
WEST THUMB SINTERS—*Continued*															
98P96-B, WT sinter	70m/20 deg S of Fishing Cone, 18 ft deep	0.05	17		130	25		0.02	0.26	<10	49	6.8	88	3.2	3.0
VENT MUDS															
98-03, vent mud	Mary Bay	<0.02	77		1100	1.7	0.06	0.1	12	120		20	17	2.5	
98-26, vent mud	Mary Bay	0.06	140		1200	1.6	0.08	0.2	13	140		20	18	2.1	
98-27, vent mud	Mary Bay	0.06	150		600	1.6	0.1	0.1	8.6	170		20	24	1.2	
Core 3-1 (0–10cm), vent mud	Mary Bay	0.08	130		1100	1.6	0.1	0.2	11	110		20	17	2.2	
Core 3-2 (20–30cm), vent mud	Mary Bay	0.03	130		960	1.7	0.1	0.2	11	110		20	16	2.2	
Core 3-3 (40–45cm), vent mud	Mary Bay	0.06	130		1100	1.9	0.1	0.2	12	110		20	18	2.1	
98-29, vent mud	Stevenson Island	<0.02	330		99	1.7	0.2	0.2	41	120		75	36	0.7	
98-30a, vent mud	Stevenson Island	0.08	240		110	1.4	0.1	0.2	38	150		64	28	1.2	
98-30b, vent mud	Stevenson Island	0.1	340		190	1.9	0.2	0.2	39	120		56	27	2.3	
98-32, vent mud	Stevenson Island	0.1	220		370	1.8	0.1	0.2	23	110		55	24	5.6	
98-19, vent mud	West Thumb deep vent	1.1	93		230	2.8		0.07	3.6	150		20	32	1.9	
98-16a, vent mud	West Thumb off Grant	0.03	860		870	5.2	0.1	0.3	17	62		30	67	9.4	
98-16b, vent mud	West Thumb off Grant	0.04	160		710	2.6	0.2	0.1	5.8	72		20	23	10	
98-17, vent mud	West Thumb off Grant	0.08	75		1100	2.8	0.3	<0.1	15	110		20	20	2.3	
WEST THUMB SEDIMENTS															
WT core (25–26 cm), mud	Central West Thumb	0.4	430	0.001	230	3.8	0.1	0.2	7.4		13	20	<0.1	21	1
WT core (25–26 cm), mud	Central West Thumb	<0.1	480	0.002	230	3.5	0.1	0.2	7.7		13	20	<0.1	21	1
WT core (26–27 cm), mud	Central West Thumb	0.2	620	<0.0007	400	5.4	0.3	0.7	12		21	33	<0.1	21	2
WT core (27–28 cm), mud	Central West Thumb	<0.1	240	<0.0007	280	3.5	0.2	0.2	5.4		15	10	<0.1	11	1
WT core (28–29 cm), mud	Central West Thumb	<0.1	260	0.002	320	3.9	0.2	0.2	5.8		16	20	<0.1	14	2
WT core (28–29 cm), mud	Central West Thumb	<0.1	250	0.0008	290	2.9	0.2	0.2	5.5		15	20	<0.1	13	1
WT core (29–30 cm), mud	Central West Thumb	<0.1	540	0.001	260	3.2	0.2	0.2	6.6		13	20	<0.1	17	1
WT core (30–31 cm), mud	Central West Thumb	<0.1	410	0.0008	280	3.3	0.2	0.2	7.1		14	20	<0.1	16	1
WT core (31–32 cm), mud	Central West Thumb	<0.1	360	0.003	280	3.3	0.2	0.2	6.4		14	20	<0.1	15	1
WT core (32–33 cm), mud	Central West Thumb	<0.1	330	0.0009	260	3.2	0.1	0.3	6.5		13	10	<0.1	15	1
WT core (33–34 cm), mud	Central West Thumb	<0.1	320	<0.0007	260	3.4	0.2	0.2	5.9		12	20	<0.1	14	1
WT core (34–35 cm), mud	Central West Thumb	<0.1	260	<0.0007	290	3.4	0.2	0.7	6.9		13	20	<0.1	14	1
WT core (35–36 cm), mud	Central West Thumb	<0.1	300	0.003	340	4.1	0.2	0.3	6.8		14	20	<0.1	13	2
WT core (35–36 cm), mud	Central West Thumb	<0.1	300	<0.0007	310	3.1	0.2	0.2	6.6		13	20	<0.1	12	1
WT core (36–37 cm), mud	Central West Thumb	<0.1	270	<0.0007	300	3.7	0.2	0.4	6.4		13	10	<0.1	13	1
WT core (37–38 cm), mud	Central West Thumb	<0.1	240	0.002	290	4	0.2	0.2	6.6		13	10	<0.1	14	1
WT core (38–39 cm), mud	Central West Thumb	<0.1	270	0.001	270	3.5	0.1	0.2	5.7		12	20	<0.1	14	1
WT core (39–40 cm), mud	Central West Thumb	<0.1	330	0.001	260	3.8	0.2	0.2	5.7		12	10	<0.1	16	1
WT core (40–41 cm), mud	Central West Thumb	<0.1	340	0.001	260	4.4	0.2	0.4	6.1		12	10	<0.1	15	1
WT core (41–42 cm), mud	Central West Thumb	<0.1	580	0.001	260	4.5	0.2	0.4	7.8		12	20	<0.1	18	1
WT core (44–45 cm), mud	Central West Thumb	<0.1	430	0.002	230	4	0.1	0.2	6.5		10	10	<0.1	18	1

Table 3 (continued from facing page). Minor and trace-element data for vent deposits and vent muds (Hg–Zr)—*Continued.*

Hg	Li	Mo	Nb	Ni	Pb	Rb	Sb	Sc	Se	Sn	Sr	Ta	Th	Tl	U	V	W	Y	Zn	Zr
WEST THUMB SINTERS—*Continued*																				
	8.3	0.1	2.0	1.5	1.7	11	23	<0.3	<0.2		8.8	0.2	0.76	0.1	0.24	2.3	7.2	2.1	14	
VENT MUDS																				
	21	2.3		39	26	54	3.7		<1	2	490		9.1	0.4	2.3	83	16		61	
	29	3.1		45	19	58	5.2		<1	2	580		9.2	0.5	2.2	96	26		62	
	41	7		28	17	40	9.1		<1	3	240		10	0.3	2.9	120	52		41	
	29	2		35	19	57	4.7		<1	2	500		9.3	0.4	2.4	80	16		50	
	32	2		39	20	53	4.3		<1	2	500		8.2	0.4	2.2	78	16		56	
	29	2.2		37	21	67	4		<1	3	550		9.7	0.4	2.4	81	12		54	
	43	24		120	60	2.4	13		<1	3	34		5.5	0.6	3.5	170	93		77	
	73	7.8		140	39	5.6	5		<1	3	25		7.8	0.8	3.4	130	43		100	
	64	7.7		140	42	8.7	5		<1	3	45		9.1	0.6	3.5	150	70		100	
	38	14		73	29	24	9.7		<1	3	140		9	0.4	3.6	130	58		79	
16	26	5.8		11	35	50	7.6		0.6		46		24	0.5	6.5	110	140		59	
	55	15		78	17	62	63		<1	3	180		11	5.8	4	81	410		74	
	27	70		19	23	84	42		<1	5.3	190		14	0.9	5	100	95		55	
	40	1.6		26	26	110	1.9		<1	5	350		15	0.7	4.2	96	39		83	
WEST THUMB SEDIMENTS																				
1.1	12	16	4.7	35	5.5	18	44	3	<1	0.6	76	0.3	3.1	0.3	1.6	48	36	12	32	62
	12	16	4.6	36	5.2	18	44	3	<1	0.6	76	0.3	2.9	0.3	1.6	51	36	12	33	62
	20	24	7.8	69	12	30	61	5.2	1	7	130	0.5	5.1	0.5	2.6	74	56	19	66	110
2.3	15	12	5.4	28	7	21	35	4	<1	0.7	93	0.3	3.5	0.3	1.6	46	35	13	36	74
1.8	16	13	6.1	29	7.2	23	38	4	<1	0.9	100	0.4	4	0.3	1.9	50	41	14	41	83
	15	12	5.3	27	6.8	22	35	4	<1	0.7	94	0.3	3.7	0.3	1.7	47	38	13	38	74
2.1	12	19	4.8	35	5.8	18	44	3	<1	0.6	79	0.3	3.3	0.3	1.7	45	40	12	32	64
2.1	14	12	4.8	34	6.6	20	34	4	<1	0.6	92	0.2	3.6	0.3	1.8	49	38	13	33	65
2	14	13	5.2	29	6.6	20	37	3	<1	0.7	81	0.3	3.6	0.3	1.8	48	42	13	34	68
1.8	13	12	4.7	29	6.1	19	34	3	<1	0.6	79	0.2	3.2	0.3	1.8	46	39	12	32	65
1.8	13	14	5	33	6.3	19	34	3	<1	0.6	80	0.3	3.2	0.3	1.7	46	39	12	33	65
1.7	14	13	5.7	32	7.2	21	32	4	<1	0.7	96	0.3	3.6	0.3	1.7	47	38	13	36	72
1.5	15	13	6.4	33	12	23	36	4	<1	0.9	110	0.4	4.3	0.3	2	51	43	15	40	86
	14	12	5.8	31	9.8	22	33	4	<1	0.8	100	0.3	3.6	0.3	1.7	49	37	13	39	78
1.9	14	12	5.2	31	6.4	20	33	3	<1	0.7	95	0.3	3.6	0.3	1.7	46	39	13	35	72
2.1	14	12	5.3	32	6.9	19	32	3	<1	0.7	91	0.3	3.4	0.3	1.6	45	38	12	33	72
2	12	12	5	29	6.4	19	32	3	<1	0.6	81	0.3	3.3	0.3	1.7	43	39	12	34	66
2.3	12	13	4.6	28	5.7	18	35	3	<1	0.6	79	0.3	3.2	0.3	1.8	44	42	12	31	63
2.1	11	14	4.4	31	5.6	17	36	3	<1	0.5	78	0.2	3.1	0.3	1.8	47	42	12	30	63
2.4	12	14	4.5	32	5.7	17	38	3	<1	0.5	77	0.3	3.2	0.4	1.8	49	46	12	30	63
1.7	11	13	4.1	30	5	16	34	3	<1	0.6	66	0.3	2.8	0.3	1.7	43	44	11	30	55

A

D

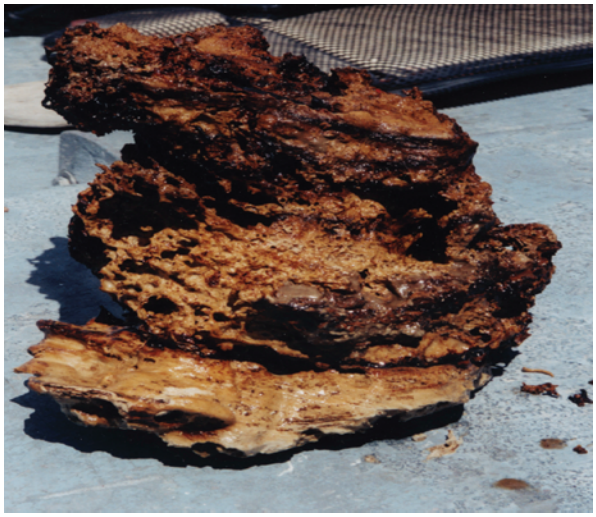

B

E

C

F

cipitates. The reddish coating from the outer portion of the spire is goethite plus amorphous iron oxyhydroxide. Goethite peaks are broad, suggesting poorly crystalline material or very small grain size. Similar materials have been observed in seafloor iron-oxyhydroxide deposits from seamounts (Alt and others, 1987) and form in low-energy venting situations where Fe-bearing hydrothermal fluids mix with oxygenated bottom waters.

The Bridge Bay spires must have formed in place above the sediment-water interface by growth of chimney-like features from lake-bottom hydrothermal vents, similar to seafloor hydrothermal-sulfide chimneys. No currently active hydrothermal venting is associated with spires in Yellowstone Lake, and spires are only known from the Bridge Bay field. Preliminary studies using uranium-isotope disequilibria suggest the spires formed about 11 ka (Neil Sturchio, University of Illinois at Chicago, written commun., 1998), after the last glacial event when ice receded from the central Yellowstone Lake basin (~16 ka; Pierce and others, this volume). Studies of past Yellowstone Lake shorelines (Meyer and Locke, 1986; Pierce, 1997; Pierce and others, 2002) have indicated that the lake was above present level during most of the period since the last glacial event, and there is no evidence that lake level was lower than about 5 m below present lake level. Moreover, the fragile, upright spire structures could not have formed subaerially above a lowered lake level and survived submergence with the attendant wave activity and winter ice flows.

Figure 4. Photographs of vent conduit samples. *A*, Portion of silicified conduit with partly silicified buff-gray lake sediment adhering to outer walls and partly stained by Fe-oxides. Not visible is central conduit partly filled with gray amorphous silica. Top is at right. *B,* Close-up of portion of material from sample 98-24, shown in figure 4D, showing network of interconnected millimeter-size siliceous tubes stained by Fe-oxides. Sample 72198-23D from West Thumb in water depth of 165 ft. *C,* Siliceous conduit (10 × 17 cm; top at right) with main orifice at right and smaller orifices branching off the sides (top and bottom). Exposed portion of conduit (at right) is stained red-brown (dark) by Fe-oxides. Sample 98-23D from West Thumb in water depth of 165 ft. *D*, Mass of interconnected, small (~1-mm diameter) siliceous tubes with lake sediment filling interstices. Irregular 2.5-cm central conduit runs through sample, which is 22 cm high by 25 cm wide. Base of sample (bottom) is buff-colored, similar to lake sediment, whereas exposed upper portion is stained red-brown by Fe-oxides. Sample 98-24 from West Thumb in water depth of 203 ft. *E,* Portion of 4-cm-diameter conduit with 0.5- to 1.0-cm-thick silica-rich walls and ~2-cm-diameter main conduit filled with buff sediment. Sample 98-11 from Mary Bay in water depth of 137 ft. *F,* Mushroom shaped conduit, 15 cm across × 18 cm high, in metal scoop on ROV. Upper portion of sample is semi-indurated and stained red-brown by Fe-oxides, and base of sample consists of softer gray-buff sediment. Central 2.5- to 4.0-cm-diameter conduit is lined with amorphous silica and native sulfur (not visible in photo). Sample 98-21 from West Thumb in water depth of 167 ft.

Yellowstone Lake Sediments and Altered Vent Sediments

Hydrothermally altered and unaltered sediments were sampled at several sites in the lake. A 50-cm-long core from West Thumb (sample no. YNP89) provides a sample of typical unaltered sediment accumulating on the lake bottom (table 1). Unaltered lake sediment consists mainly of opal (diatoms), as well as traces of quartz, albite, smectite, and illite, and is similar to material on the outside of siliceous hydrothermal conduits described above.

Consolidated, laminated, gray sediment exposed within the walls of hydrothermal vent craters in West Thumb consists of fine-grained quartz, smectite, and chlorite, as well as traces of illite and albite (table 1). Sediment associated with outer walls of inactive silicified conduits within the craters consists of typical modern background material (mainly opal, plus minor quartz, albite, smectite, and illite).

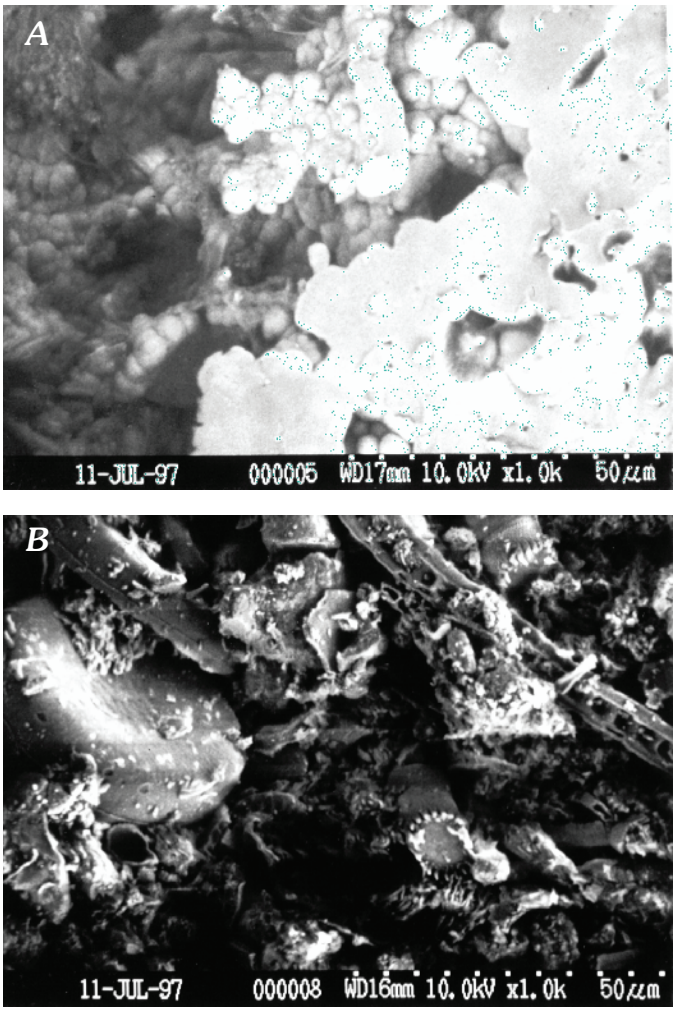

Figure 5. Scanning electron micrographs of siliceous conduit. Sample 94-11-2. *A*, Inner conduit lining consisting of amorphous silica precipitate. *B,* Outer surface of conduit with detrital material and diatoms clearly visible.

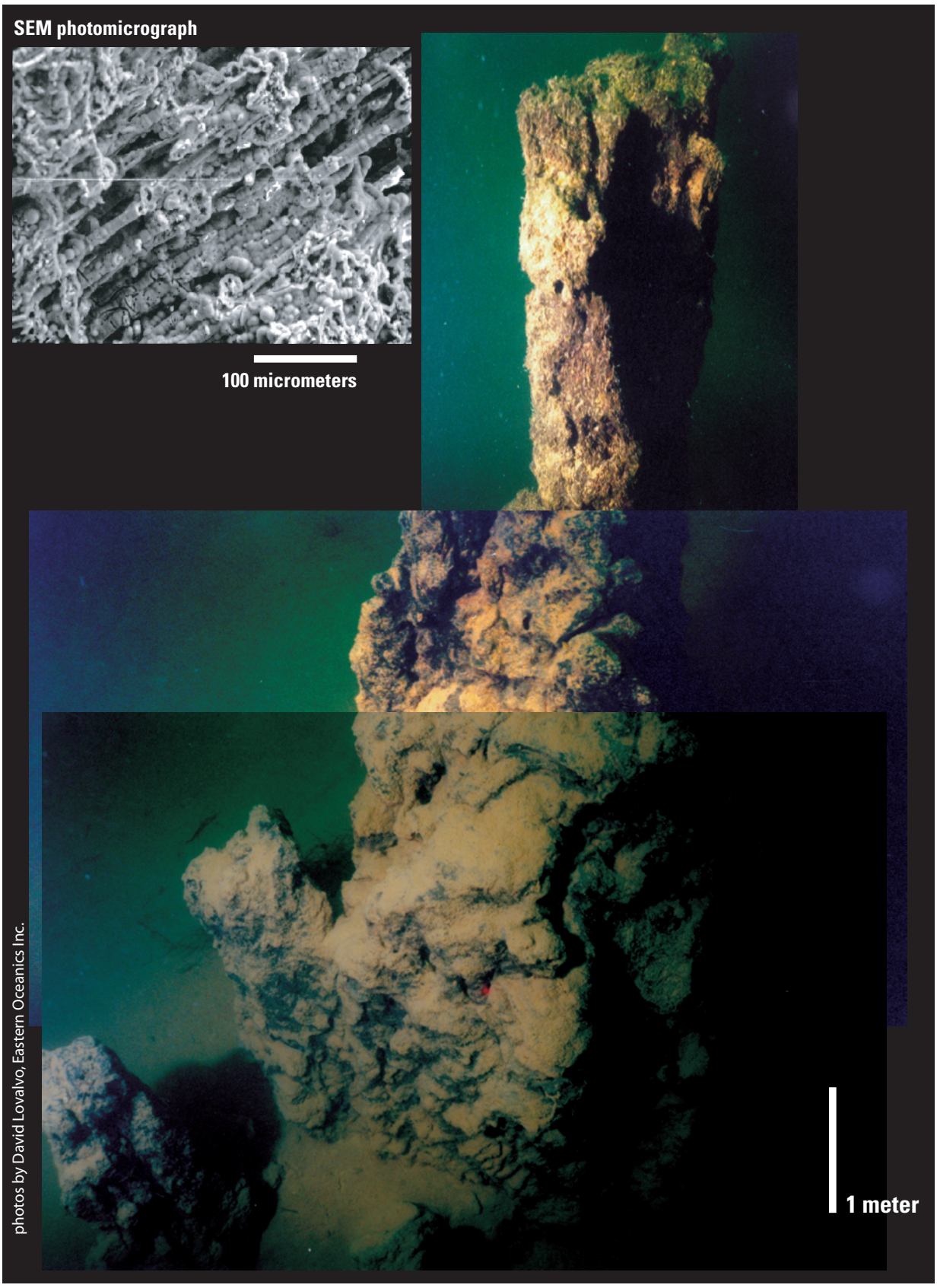

Figure 6. Underwater photomosaic of a Bridge Bay spire. Underwater photographs by David Lovalvo, Eastern Oceanics, Inc. Inset is scanning electron micrograph of siliceous spire texture.

Gray and olive-brown muds at active and inactive vents in vent craters east of Stevenson Island consist of chlorite and quartz, in addition to lesser albite, smectite, and illite. Opal in recent sediment has been recrystallized to quartz, and chlorite may be derived from hydrothermal-alteration processes. One sample of unconsolidated mud through which fluid was actively venting at a temperature of 114°C contains <1- to 2-mm blobs of native sulfur plus plates of pyrite, as much as 5 mm thick and 30 mm across.

Olive-green to black muds sampled at active 60°–120°C vents in Mary Bay by ROV and by gravity coring nearby contain quartz, albite, smectite, illite, and minor gypsum. Gypsum may have formed from oxidation of H_2S in pore waters or from oxidation of fine-grained pyrite. Opal in these sediments is completely recrystallized to quartz. There is no significant change in mineralogy along the 50-cm depth interval of the core, or between core samples and surface-sediment samples collected by ROV in this area. Altered muds in the core smelled of sulfide when sampled, and two additional cores taken nearby smelled of petroleum-like hydrocarbons. Plastic core liners used in these cores, which melt at temperatures >135°C, were partially melted and strongly deformed, reflecting high temperatures in the shallow subsurface. Boiling temperatures in Mary Bay are 140°–160°C at the depths of the Mary Bay vents, but actual measured temperatures of venting fluids are ≤120°C, suggesting hotter fluids in the very shallow subsurface. The Mary Bay hot core and a similar core from West Thumb yielded pore water with high concentrations of Cl reflecting a deep, high-temperature origin (Balistrieri and others, this volume).

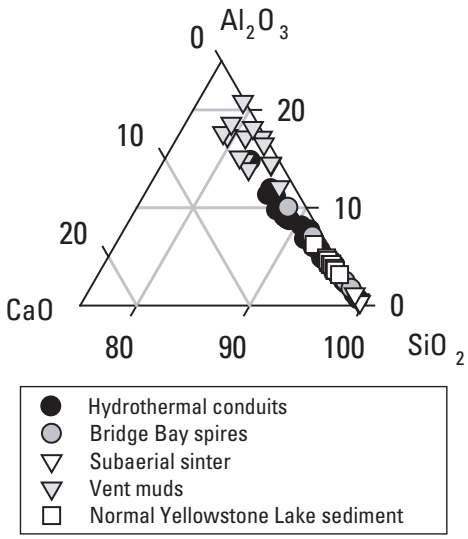

Figure 7. Ternary diagram of SiO_2-Al_2O_3-CaO for sublacustrine sinter deposits and altered and unaltered Yellowstone Lake sediments.

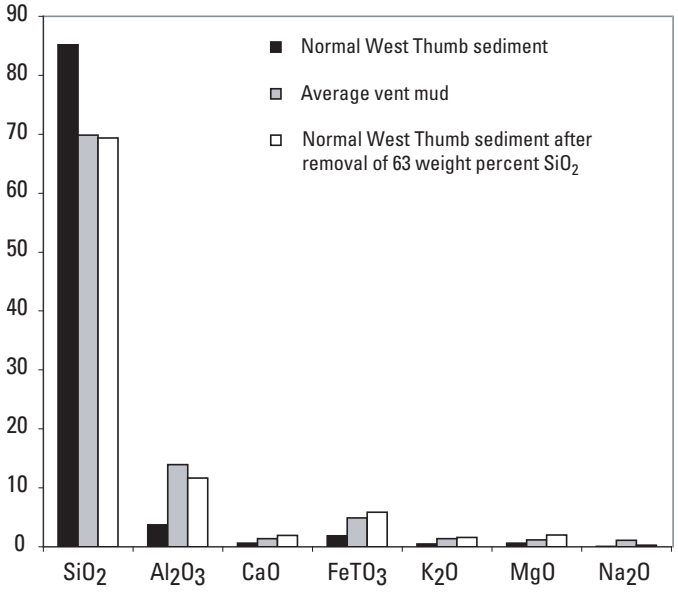

Figure 8. Plots of sediment leaching calculations showing that removal of 63 weight percent SiO_2 from average unaltered West Thumb sediment produces a sediment very close in composition to the hydrothermally altered vent muds.

Geochemistry

Major-Element Systematics

Unaltered West Thumb lake sediments (table 2) have high SiO_2 contents (81.3–86.4 weight percent), Al_2O_3 (2.8–5.5 weight percent), minor amounts of CaO, Na_2O, and K_2O (<1 percent each), low $FeTO_3$ (1.6–2.6 weight percent; $FeTO_3$ indicates total iron calculated as Fe_2O_3), and MgO (0.5–1.2 weight percent). In contrast, altered muds from hydrothermal vents have lower contents of SiO_2 and greater Al_2O_3, CaO, Na_2O, K_2O, $FeTO_3$, and MgO than the modern opal-rich background sediment. This reflects dissolution of opal and passive enrichment of other components. Dilution by hydrothermal addition of chlorite could not explain the Ca-Na-K enrichments.

Chemical variations between altered and unaltered sediments, compared with hydrothermal deposits, are illustrated on a ternary diagram of SiO_2-Al_2O_3-CaO (fig. 7). This projection shows that the altered mud samples (vent muds) are depleted in SiO_2, strongly enriched in Al_2O_3, and somewhat enriched in CaO relative to unaltered Yellowstone Lake sediment. In order to test whether these trends fit a silica dissolution model, silica removal and its affect on sediment chemistry was calculated by removing successive amounts of silica and recalculating to 100 percent. Results show that the average chemistry of the vent muds is consistent with removal of 63 weight percent SiO_2 from average unaltered West Thumb sediment (fig. 8). This calculation slightly underestimates the amount of Al_2O_3 and Na_2O in altered muds and overestimates CaO, K_2O, and MgO, especially for Stevenson Island vent muds. Also, $FeTO_3$ is quite enriched in Stevenson Island vent muds compared to the calculated values.

These results suggest that, in West Thumb and Mary Bay vent muds, silica leaching is accompanied by the addition of Na_2O and Al_2O_3. In the Stevenson Island vent field, silica leaching is accompanied by the addition of $FeTO_3$ and the

removal of CaO, K_2O, and MgO, and Na_2O. These trends are consistent with the more intense alteration observed in Stevenson Island vent muds, with abundant chlorite that must be iron-rich to account for the increased $FeTO_3$ in the altered sediment.

Could these trends be produced by physical winnowing of fine-grained sediments or is a chemical process required? Obviously, the simple calculation done here cannot differentiate between physical and chemical removal of SiO_2. However, the indicated removal of alkalis and alkaline earth elements from the Stevenson Island muds, coupled with the addition of iron to form chlorite, favors a chemical process. In addition, chemical variation in hydrothermal conduits (fig. 7), which are basically vent sediments cemented in place and silicified in the inner annulus, suggests a similar silica-leaching process. SiO_2 in conduits varies from values close to pure silica, such as subaerial sinter, to SiO_2-Al_2O_3-CaO abundances similar to vent muds. Because physical winnowing is precluded in the conduit wall, where original sedimentary layering is often preserved, we conclude that chemical-leaching processes can produce the observed chemical changes in conduit-wall sediments. Vent muds show more extreme chemical changes than conduits, which may be attributed to more intense chemical leaching or perhaps to a combination of leaching and entrainment of diatom-rich fractions of the sediment due to vent-fluid advection.

Dissolution of sediments probably is caused by heating of the sediments due to hydrothermal fluid circulation, causing dissolution of amorphous silica as solubility increases. In detail, this process is complicated and influenced by fluid composition and by the kinetics of recrystallization to quartz. Balistrieri and others (this volume) have concluded from δD-Cl systematics that sublacustrine hydrothermal fluids boil on ascent due to pressure release. Steam that separates from ascending fluids is expected to be initially silica-poor but, upon condensation associated with cooling, would equilibrate by dissolving amorphous silica. Reaction with condensed steam may be the driving mechanism causing dissolution in vent craters. Possibly, simple mixing of hydrothermal fluid with ambient pore waters may lead to silica undersaturation during sublacustrine venting.

Trace Elements in Vent Fluids and Sinter Deposits

Hydrothermal fluids in Yellowstone National Park have compositions that are strongly affected by boiling and by mixing in the shallow subsurface (Fournier, 1989). In most of the Park, hot springs deposit siliceous sinter; the exceptions are areas like Mammoth Geyser Basin where hydrothermal fluids that have reacted with Paleozoic or Mesozoic carbonates in the subsurface and deposit travertine at the surface. Hydrothermal vent fluids in Yellowstone Lake have much in common with other thermal waters in the Park, including a common source from deep thermal water that has δD values of –149 per mil and Cl of ~315 mg/L (Truesdell and others, 1977; Balistrieri and others, this volume).

Chemical analyses of sublacustrine hydrothermal vent fluids indicate that active vents in Mary Bay, Stevenson Island, and West Thumb have different compositional signatures (Gemery-Hill and others, this volume). West Thumb vent fluids are more enriched in hydrothermal-indicator elements B, As, Cs, Ge, Li, Mo, Sb, and W (Balistrieri and others, this volume) relative to vents in Mary Bay.

Chemical analyses of siliceous hydrothermal deposits (table 3; fig. 9) indicate that West Thumb deposits are enriched in As, Cs, Hg, Tl, and W. Mary Bay and Stevenson Island hydrothermal deposits are commonly enriched in Ba and Cs and depleted in Cu, Mn, Mo, and Sb with respect to normal lake sediments. Bridge Bay spire samples are enriched in As, Ba, Co, Mo, Tl, and W relative to normal Yellowstone Lake sediments. Vent muds are enriched in Ba, Co, Cs, Cu, Fe, Ni, Tl, and V and are depleted in As, Mn, Mo, and Sb suggesting a possible source for the hydrothermal-indicator elements in vent fluids and vent deposits. However, the hydrothermal-indicator elements are the same throughout the Yellowstone Plateau, suggesting that subsurface reaction with underlying rhyolitic lava flows and ignimbrites must be the major source of these elements. None of the sublacustrine sinter deposits are enriched in Au or Ag.

Stable-Isotope Systematics

Oxygen Isotopes in Siliceous Deposits and Altered Sediments

Oxygen-isotope values in sublacustrine sinter and vent-mud samples range from –3.5 to 20.3 per mil (table 2), with the lower values indicating formation at higher temperatures. Unaltered West Thumb sediments have $\delta^{18}O$ values from 15.0 to 17.3 per mil, and subaerial West Thumb sinter samples have values from 20.6 to 21.4 (table 2).

Stable isotopes of hydrogen and oxygen have been analyzed on river, creek, lake, and vent-fluid waters (Balistrieri and others, this volume; Gemery-Hill and others, this volume). The water isotopes show that vent-fluid samples have values very similar to lake waters, -16.5 ± 0.5 per mil, because they are diluted by lake water during sampling or mixing in the shallow subsurface. Recharge waters for the deep hydrothermal systems in the Park initially had $\delta^{18}O$ values of about –20 per mil, corresponding to meteoric waters with δD values of –149 per mil, which is interpreted as a mixture of glacial-age waters and present-day recharge (Rye and Truesdell, this volume). However, as the recharge waters are heated in subsurface hydrothermal systems, oxygen isotopes exchange with silicate rocks and evolve by water-rock interaction to higher $\delta^{18}O$ values. Boiling of hydrothermal fluids during ascent must also influence the

$\delta^{18}O$ values, and this process will also cause ^{18}O enrichment as isotopically light steam is lost from the system. Thus, the $\delta^{18}O$ values of end-member hydrothermal fluids cannot be directly measured in our vent-fluid samples because they are >95 percent ambient lake water. Values of Cl and δD for pore fluids from the hot cores (Balistrieri and others, this volume) suggest that hydrothermal fluids that are as much as 50 percent end-member fluid occur in the very shallow (<1.5 m) subsurface. The $\delta^{18}O$ values have not been measured on these end-member fluids, but $\delta^{18}O$ values of ascending vent fluids, prior to mixing, can be estimated using the measured $\delta^{18}O$ values of hydrothermal deposits and oxygen-isotope fractionation calculations.

Calculated oxygen-isotope fractionation temperatures, assuming reaction of amorphous silica sinter deposits with normal lake water ($\delta^{18}O = -16.5$), indicates a range from 78°C to 164°C (fig. 10). The progression of temperatures calculated (fig. 10) is generally consistent with those expected for the different environments. For example, subaerial West Thumb sinter, which forms from thin sheets of hot-spring waters flowing across the surface of the sinter terraces, must form at temperatures between boiling (94°C at the altitude of West Thumb Geyser Basin) and ambient air temperature. Our calculated temperatures are 51°–55°C based on silica-water oxygen-isotope fractionation.

Similarly, the spires must form at moderately low temperature because they occur in shallow water where the boiling point limits fluid temperature to about 115°C and because they contain abundant bacteria that cannot live at temperatures above 114°C (Jorgensen and others, 1990). Moreover, the spires stick up into the water column and would radiate heat effectively. Calculated oxygen isotope temperatures are 80°–96C°.

At the other end of the spectrum, sinter samples from Mary Bay and Stevenson Island, which occur in deep waters where the boiling temperature is 140°C or higher, give $\delta^{18}O$ temperatures from 127°C to 164°C. Thus, the oxygen-isotope fractionation temperatures for amorphous silica deposits are

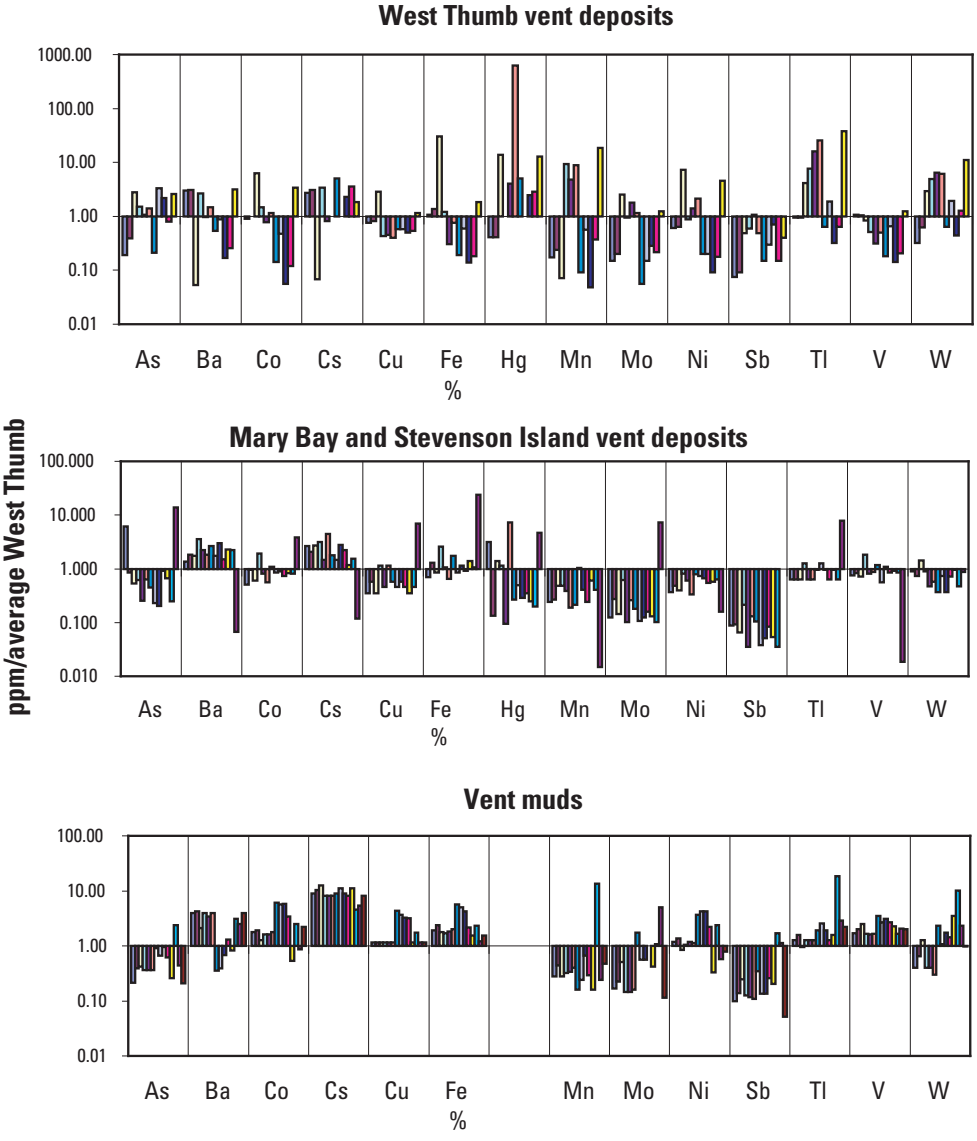

Figure 9. Enrichment-depletion diagram for trace elements in vent deposits and vent muds relative to average unaltered West Thumb sediment.

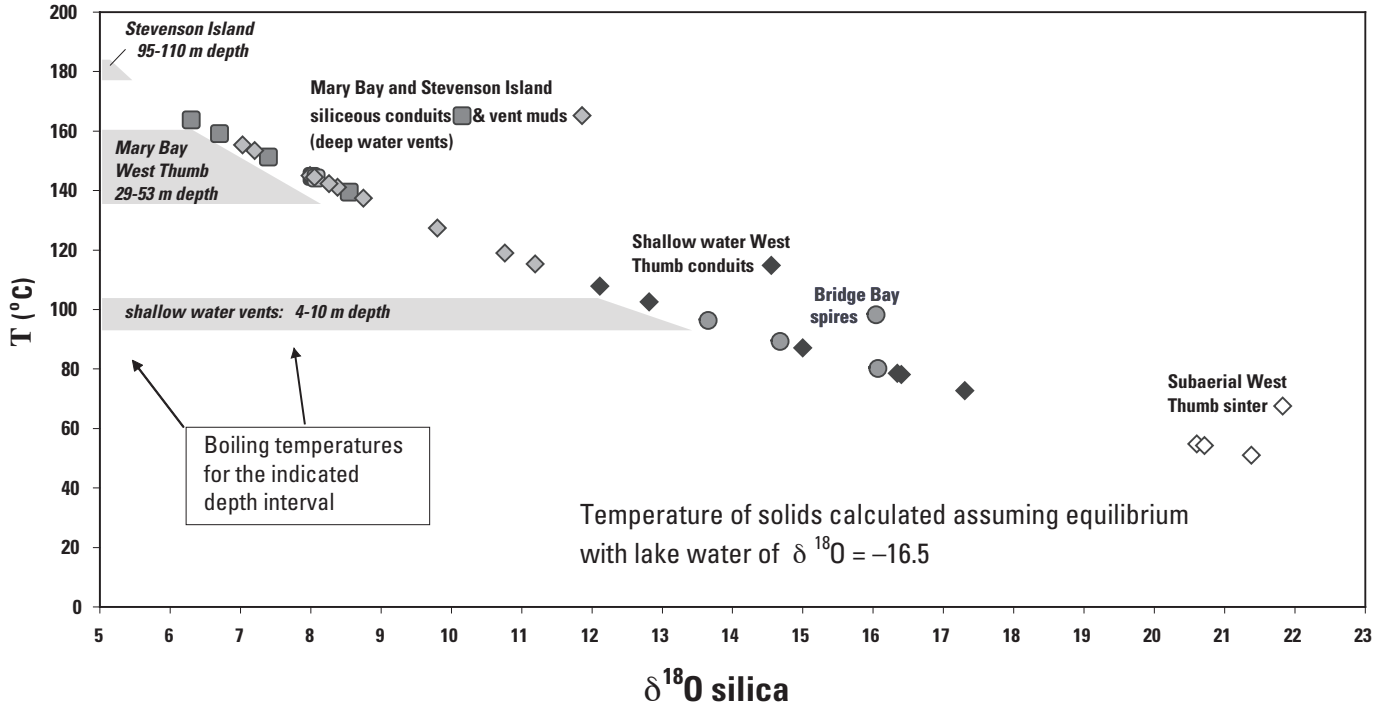

Figure 10. Plots of oxygen-isotope values of hydrothermal silica deposits versus calculated temperatures assuming formation from normal, present-day Yellowstone Lake water with $\delta^{18}O$ value of –16.5 per mil. Lake-floor boiling temperatures, which are upper limits, are noted for deposits from different depth environments.

generally consistent with geologic settings but are probably underestimated because actual vent fluids may have $\delta^{18}O$ values that are higher than –16.5 per mil (ambient lake water) due to sediment-fluid interaction on ascent.

Another approach is to estimate the $\delta^{18}O$ values of vent fluids that reacted in the shallow subsurface with silica deposits and vent muds by assuming the ascending fluids are at the boiling temperature when they reach the lake floor. This is a reasonable assumption because Cl-δD systematics (Balistrieri and others, this volume) indicate that the deep subsurface fluid beneath Yellowstone Lake is Cl rich due to boiling and has a temperature of 220°C. Calculated water $\delta^{18}O$ values, assuming vent fluids were at their boiling temperatures, range from –3.2 to –11.6 per mil (fig. 11), which are reasonable $\delta^{18}O$ values for undiluted hydrothermal fluids that have evolved to higher $\delta^{18}O$ values due to water-rock or water-sediment interaction.

Sulfur Isotopes in Lake Water, Vent Fluids, and Vent Deposits

Sulfur-isotope values of Yellowstone Lake sulfate (table 2) are quite uniform at 2.5 per mil (±0.7 per mil), suggesting that lake-water sulfate is dominated by hydrothermal sulfide. Two major sources of sulfur are possible: (1) vent sulfide that oxidizes to SO_4 in the lake (vent H_2S has measured $\delta^{34}S_{H2S}$ values of –0.5 to 3.6 per mil with an average value of 2.2 per mil) or (2) SO_4 in streams that drain into the lake. Yellowstone River and 44 tributaries that flow into Yellowstone Lake were sampled in August–September 1998; the most important streams (that is, those streams with highest flow rates and chemical fluxes) were resampled in July 1999. Sulfur-isotope analyses indicate $\delta^{34}S_{SO4}$ values range from –3.6 to 10.7 per mil with an average (not weighted for flow) of 2.6 per mil. Sufficient contrast does not exist in these data to determine whether sulfur in the lake is dominated by surface discharge into the lake or by sublacustrine hydrothermal vents. Basically, sulfur in Yellowstone Lake is dominated by volcanically derived sulfur. $\delta^{34}S$ values of sulfides in vent muds range from –3.8 to 5.7 per mil, similar to the range in stream waters.

Geochemical Model for Silica Transport and Deposition

Abundant silica deposition is unusual in hydrothermal vents on modern mid-ocean ridges, and several studies have suggested that this is because conductive cooling rather than mixing is necessary to form siliceous deposits in the subaqueous environment of the seafloor (Janecky and Seyfried, 1984; Janecky and Shanks, 1988). Moreover, high-temperature seafloor vents begin their ascent to the seafloor at quartz saturation at 350°–400°C, whereas lower

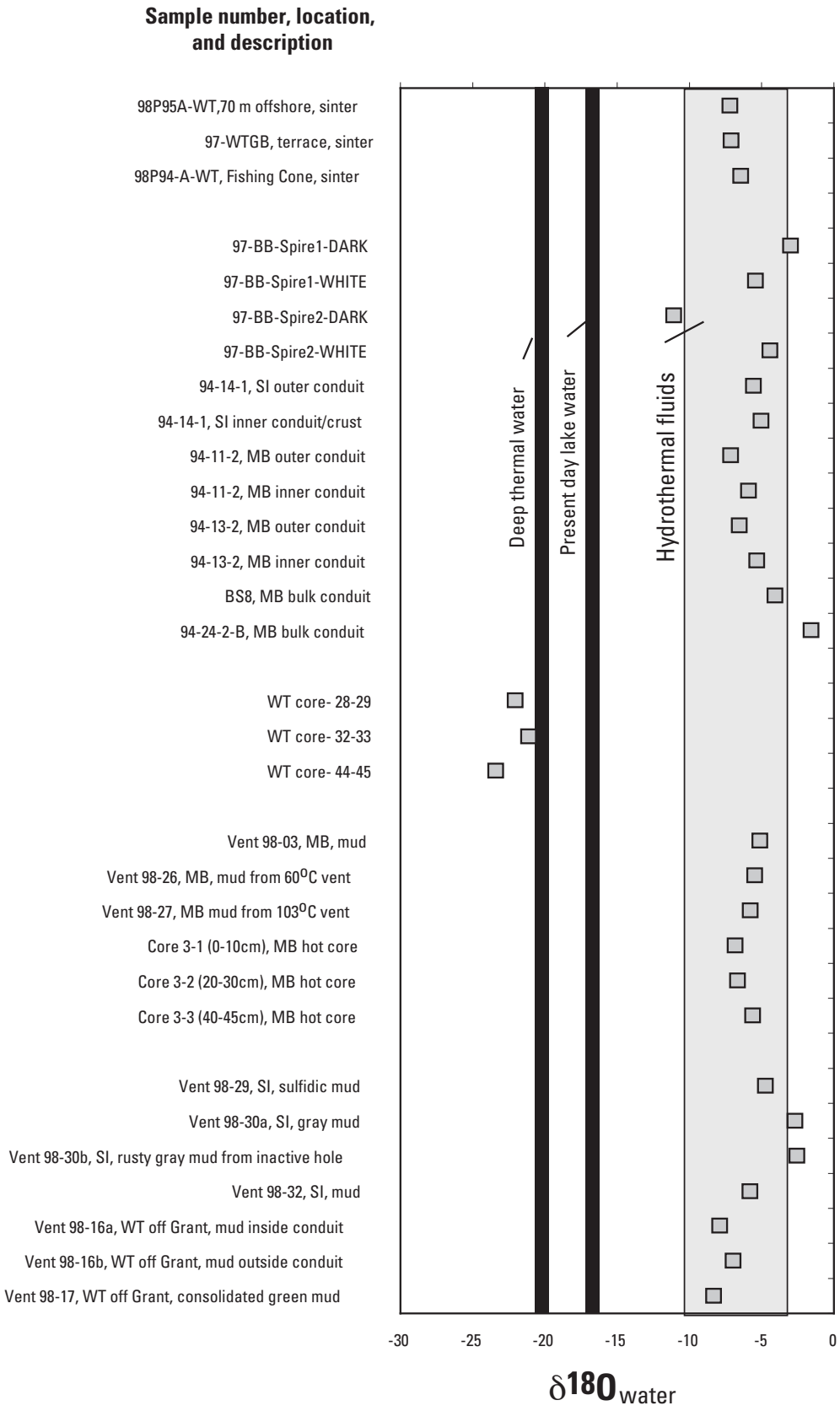

Figure 11. Oxygen-isotope composition of hydrothermal end-member fluids calculated by assuming vent fluids are in equilibrium with amorphous silica at boiling temperatures on the lake bottom when the vent deposits or vent muds formed. This approach gives a range of $\delta^{18}O$ values from –2.3 to –11.6 per mil.

temperature fluids ascending through rhyolitic glass and diatomaceous sediments beneath Yellowstone Lake may be at the much higher silica concentrations required for amorphous silica saturation.

The Yellowstone Lake silica spires are mainly amorphous silica and they apparently grew as "chimneys" above lake-bottom hydrothermal vents, based on geological arguments. In order to determine reaction and transport processes, geochemical modeling was carried out using the Geochemist's WorkBench™ incremental reaction modeling code developed by Craig Bethke and associates at the University of Illinois (Bethke, 1994).

The silica-reaction model was set up to simulate saturation of ascending solutions with amorphous silica. This was accomplished by suppressing precipitation of less soluble silica phases such as quartz, chalcedony, cristobalite, and coesite (fig. 12*A*). Precipitation of amorphous silica due to advective mixing/cooling by dilution or due to conductive cooling within the spire was tested in additional reaction models using the amorphous silica-saturated solution.

Results of these calculations (fig. 12*B*) indicate that precipitation during advective mixing of cold lake water occurs if fluids vent at temperatures >145°C. Returning to the analogy with seafloor "black smoker" sulfide chimneys, precipitation of anhydrite due to advective mixing is the initial reaction that establishes a $CaSO_4$ carapace and allows intitial chimney growth (Haymon, 1983; Styrt and others, 1981; Tivey and others, 1995). The anhydrite shell forms the leading edge of chimney growth that protects the venting hydrothermal fluid from extreme dilution due to mixing with cold bottom waters. This allows sulfide minerals to precipitate due to conductive cooling inside the chimney wall.

Similar advective mixing and amorphous silica precipitation could serve the same function in the growth of silica spires in Yellowstone Lake. Once a carapace is established, conductive cooling (without dilution) precipitates approximately 40 times as much silica sinter as advective mixing (fig. 12*C*). However, the spires occur in approximately 15-m water depth, which is too shallow due to boiling constraints for the 145°C temperature required for silica precipitation during mixing. A boiling temperature of 145°C requires about 32-m water depth, and there is no evidence that water at this site was 17 m deeper 11 ky ago (Pierce and others, this volume). Alternatively, thermophilic bacteria living at sublacustrine vent sites may have provided a protected site for silica precipitation at lower temperatures at the lake bottom. Whatever the mechanism for initially generating the spire walls, silicified bacterial filaments appear to be important in the process, and conductive cooling of vent fluids probably accounted for most of the silica precipitation.

Results of the chemical reaction modeling and other observations, as applied to spire growth, are conceptually summarized in figure 13. Oxygen-isotope analyses of silica deposits in spires indicate formation at temperatures between 80°C and 96°C. Hydrothermal circulation beneath the lake floor brings ascending hot fluids in contact with volcanic glass and with diatom-rich lake sediments. Subsurface fluid

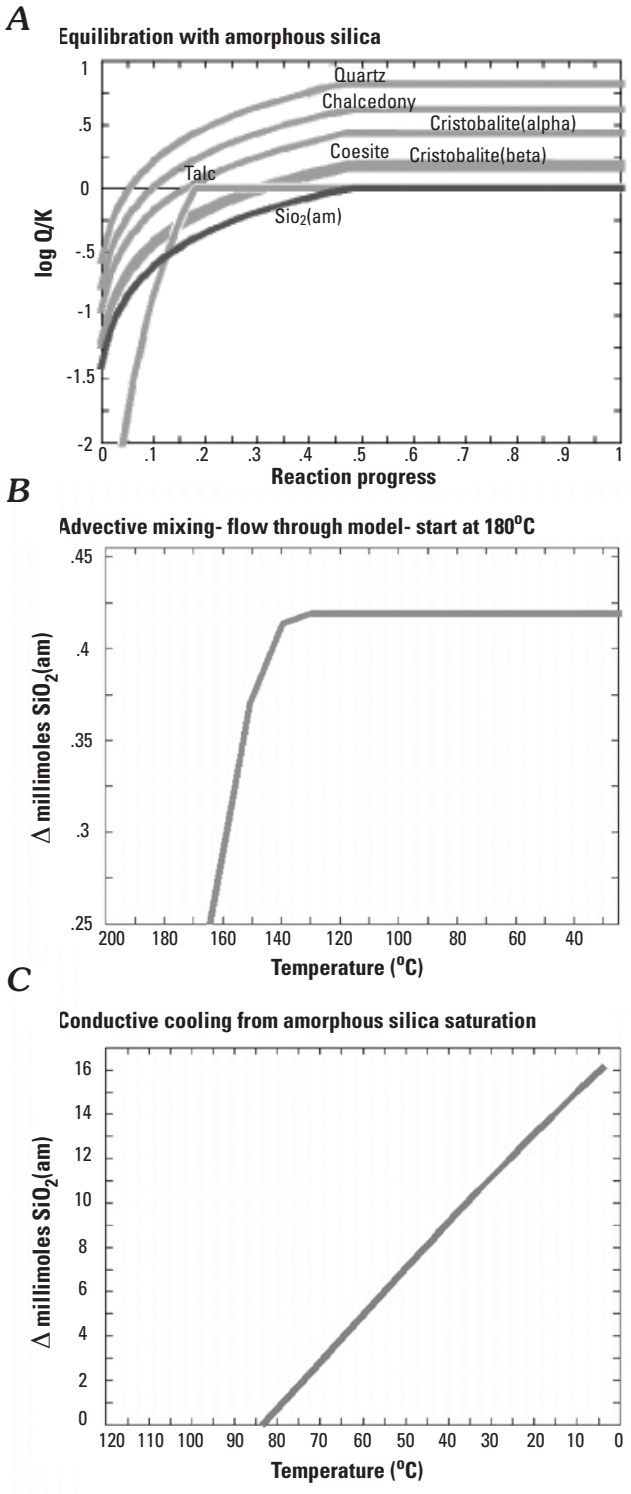

Figure 12. Incremental reaction models for: *A,* Equilibration of hydrothermal fluid with amorphous silica. *B,* Silica precipitation by advective mixing. *C,* Silica precipitation by conductive cooling.

reactions with these solids at temperatures to as much as 220°C, as indicated by vent fluid δD-Cl studies (Balistrieri and others, this volume), brings the hot fluids to saturation with amorphous silica. When these silica-rich fluids vent on the lake floor, mixing with silica-depleted, cold lake water results in precipitation of amorphous silica (fig. 13). This initial stage of spire formation produces an outer siliceous, solid shell around the vent orifice. Thus, amorphous silica precipitation is necessary to form the outer carapace of the spire and initiate spire growth. Once the shell is established, additional vent fluids traveling up the central portion of the structure can be cooled by conductive heat loss, without significant dilution due to mixing, resulting in even more rapid silica precipitation and upward growth of spires from the lake bottom.

Diatoms entrained from surficial sediments and (or) diatoms settling out of the water column, perhaps stimulated by advection of silica-rich vent fluids, are incorporated into the growing spire walls. Similarly, thermophilic bacteria that thrive in the sublacustrine vent environment are replaced and encrusted by silica as the spires grow upward from the lake floor. Bacteria are probably very important in establishing the structure that allows silicification and spire growth, but the process is not yet fully understood. It is unlikely that bacteria at the vent site have a chemical effect on the vent fluids, but sublacustrine bacterial masses and their eventual silicification may be a critical element of spire development. Perhaps bacterial mats or encrustations on the outer walls of growing spires protect vent fluids from mixing with cold dilute waters, leading to efficient silica precipitation by conductive cooling.

Why do large spires occur in shallow (15 m) water near Bridge Bay and not elsewhere in the lake? Relevant observations are (1) high resolution bathymetric mapping (Morgan and others, 2003) shows conclusively that large spires occur only in the Bridge Bay spire field, (2) spires contain abundant silicified filamentous masses (fig. 6), (3) chemical and isotopic studies indicate that spires are hydrothermal, (4) geological reasoning indicates that spires formed in-place on the lake bottom in shallow water, and (5) there are many presently active hydrothermal vents on the floor of Yellowstone Lake and some of these are in shallow-water settings similar to the Bridge Bay spire field. Observations of the silica-encased filamentous textures suggest the original thermophilic bacteria may have been cyanobacteria, which have an upper temperature limit of 73°C and are photosynthetic. We speculate that the spires require a site shallow enough to be in the photic zone so cyanobacteria can flourish around the periphery of the vents. In order to carry and deposit abundant silica, the spires must form from hot water (not steam or gas) vents. This may be a rare combination because most shallow-water vents are very gas-rich and therefore are poor transporters of silica.

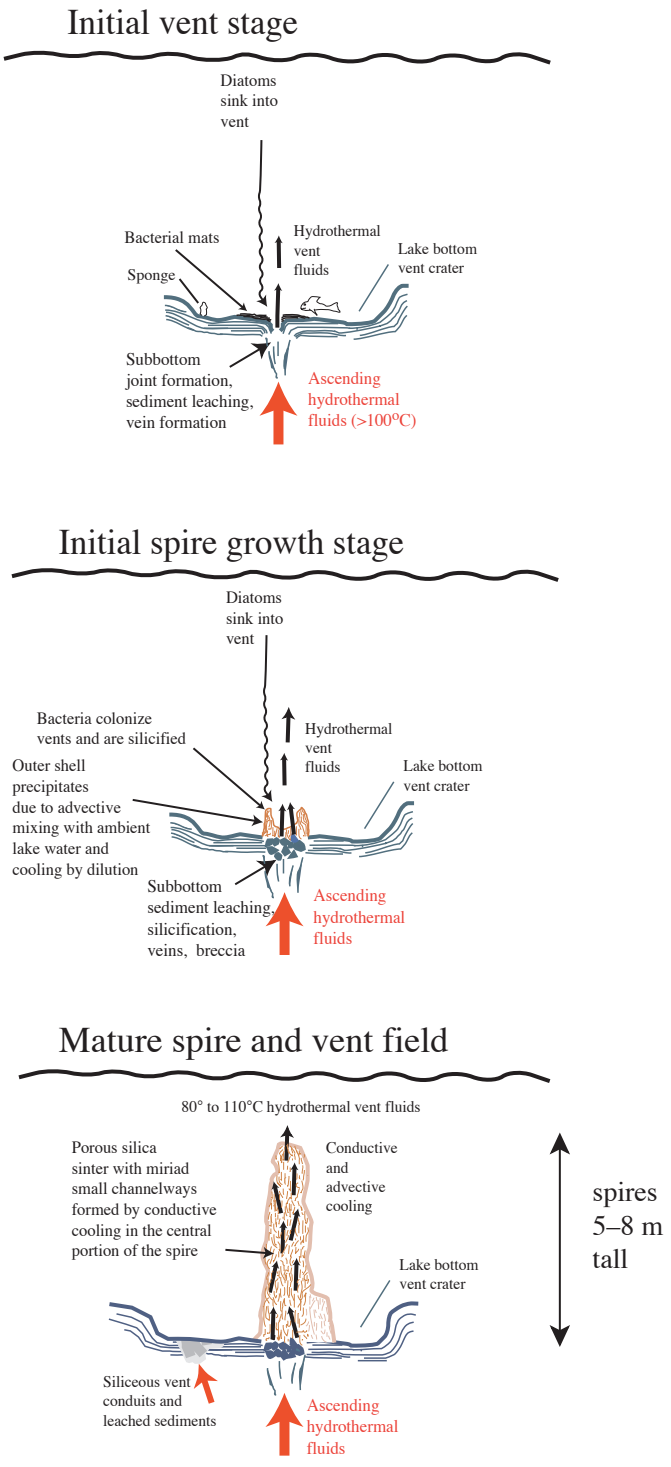

Figure 13. Schematic diagram of spire growth based on geological and geochemical observations and results of incremental reaction modeling.

Summary and Conclusions

Sublacustrine hydrothermal deposits in Yellowstone Lake are an interesting analog to ancient high-level epithermal systems. Hydrothermal elements As, Cs, Hg, Mo, Sb, Tl, and W are concentrated in the deposits but Au and Ag are not. Studies of δD and Cl in vent fluids and pore waters (Balistrieri and others, this volume) conclude that the hydrothermal fluids in Yellowstone Lake are derived from deep thermal water with about 315 mg/L Cl and are boiled on ascent to a temperature of 220°C and a Cl concentration of ~570 mg/L. This ascending fluid is mixed with lake water as it approaches and then vents on the lake floor. Boiling and mixing likely removed much of the H_2S from the ascending fluids leading to precipitation of Au at depth as sulfide-complexing breaks down.

Hydrothermal vent processes lead to development of siliceous conduits in the shallow subsurface. These pipelike features are typically filled with amorphous silica and have an outer zone that is poorly to densely silicified lake sediments. Later removal of surficial sediments by slumping or currents exposes conduit deposits in active or inactive vent fields. Vent conduits form at temperatures between 78°C and 164°C, based on oxygen-isotope geothermometry, and are limited by sublacustrine boiling temperatures at individual vent depths.

In Bridge Bay, remarkable large siliceous spires grow upward from the lake floor to heights of 8 m in water depths of 15 m. Twelve to fifteen spires are estimated to occur in Bridge Bay, and spires are unknown in other localities in the lake. Spires form at ~80°–96°C based on oxygen-isotope geothermometry, and silica deposition is caused by cooling of vent fluids initially by mixing with bottom waters and later by conductive cooling within the growing spire. Much of the spire interior appears to be silicified bacteria, suggesting that thermophilic bacteria are important in spire growth.

Hydrothermal vents in Yellowstone Lake almost invariably occur in craters on the lake bottom. These vent craters are most likely formed by sediment dissolution by vent fluids and (or) sediment entrainment and physical winnowing by vent fluids. Chemical mass-balance calculations that compare vent muds with unaltered lake sediments indicate removal of 63 weight percent SiO_2 accompanied by variable, but minor, addition or removal of the other major elements.

References Cited

Alt, J.C., Lonsdale, P., Haymon, R., and Muehlenbachs, K., 1987, Hydrothermal sulfide and oxide deposits on seamounts near 21°N., East Pacific Rise: Geological Society of America Bulletin, v. 98, p. 157–168.

Armstrong, R.L., Leeman, W.P., and Malde, H.E., 1975, K-Ar dating, Quaternary and Neogene volcanic rocks of the Snake River Plain, Idaho: American Journal of Science, v. 275, no. 3, p. 225–251.

Bacon, C.R., Gardner, J.V., Mayer, L.A., Buktenica, M.W., Dartnell, P., Ramsey, D.W., and Robinson, J.E., 2002, Morphology, volcanism, and mass wasting in Crater Lake, Oregon: Geological Society of America Bulletin, v. 114, no. 6, p. 675–692.

Bethke, C.M., 1994, The geochemist's workbench™, version 2.0—A user's guide to Rxn, Act2, React, and Gtplot: Champagne-Urbana, University of Illinois, Hydrogeology Program.

Bonnichsen, B., 1982, The Bruneau-Jarbidge eruptive center, southwestern Idaho: Idaho Bureau of Mines and Geology Bulletin , v. 26, p. 237–254.

Browne, P.R.L., and Lawless, J.V., 2001, Characteristics of hydrothermal eruptions, with examples from New Zealand and elsewhere: Earth-Science Reviews, v. 52, p. 299–331.

Christiansen, R.L., 1984, Yellowstone magmatic evolution—It's bearing on understanding large-volume explosive volcanism, *in* Explosive volcanism—Inception, evolution, and hazards: National Academy Press, p. 84–95.

Christiansen, R.L., 2001, The Quaternary and Pliocene Yellowstone Plateau volcanic field of Wyoming, Idaho, and Montana: U.S. Geological Survey Professional Paper 729-G, 145 p.

Christiansen, R.L., Foulger, G.R., and Evans, J.R., 2002, Upper-mantle origin of the Yellowstone hotspot: Geological Society of America Bulletin, v. 114, p. 1,245–1,256.

Clayton, R.N., and Mayeda, T.K., 1963, The use of bromine pentafluoride in the extraction of oxygen in oxides and silicates for isotopic analysis: Geochimica Cosmochimica Acta, v. 27, p. 43–52.

Coplen, T.B., 1995, Discontinuance of SMOW and PDB: Nature (London), v. 375, p. 285.

Cunneen, R., and Sillitoe, R.H., 1989, Paleozoic hot spring sinter in the Drummond Basin, Queensland, Australia: Economic Geology, v. 84, p 135–142.

de Ronde, C.E.J., Stoffers, P., Garbe-Schonberg, D., Christenson, B.W., Jones, B., Manconi, R., Browne, P.R.L., Hissmann, K., Botz, R., Davy, B.W., Schmitt, M., and Battershill, C.N., 2002, Discovery of active hydrothermal venting in Lake Taupo, New Zealand: Journal of Volcanology and Geothermal Research, v. 115, p. 257–275.

Ebert, S.W., and Rye, R.O., 1997, Secondary precious metal enrichment by steam-heated fluids in the Crowfoot-Lewis hot spring gold-silver deposit and relation to paleoclimate: Economic Geology, v. 92, p. 578–600.

Felicetti, L.A., Schwartz, C.C., Rye, R.O., Gunther, K.A., Crock, J.G., Haroldson, M.A., Waits, L., and Robbins, C.T., 2004, Use of naturally occurring mercury to determine the importance of cutthroat trout to Yellowstone grizzly bears: Canadian Journal of Zoology, v. 82, p. 493–501.

Fournier, R.O., 1989, Geochemistry and dynamics of the Yellowstone National Park hydrothermal system: Annual Review of Earth and Planetary Sciences, v. 17, p. 13–53.

Fournier, R.O., 1999, Hydrothermal processes related to movement of fluid from plastic into brittle rock in the magmatic-epithermal environment: Economic Geology, v. 94, p. 1,193–1,212.

Giesemann, A., Jager, H.-J., Norman, A.L., Krouse, H.R., and Brand, W.A., 1994, On-line sulfur-isotope determination using an elemental analyzer coupled to a mass spectrometer: Analytical Chemistry, v. 66, p. 2,816–2,819.

Hayden, F.V., 1878, Survey of the territories—A report of progress of the exploration in Wyoming and Idaho for the year 1878. Part II. Yellowstone National Park; geology-thermal springs-topography: U.S. Geological and Geographical Survey, Twelfth Annual Report, 503 p.

Haymon, R.M., 1983, Growth history of hydrothermal black smoker chimneys: Nature, v. 301, p. 695–698.

Hughes, S.S., and McCurry, M., 2002, Bulk major and trace element evidence for a time-space evolution of Snake River Plain rhyolites, Idaho, *in* Bonnichsen, B., White, C.M., and McCurry, M., eds., Tectonic and magmatic evolution of the Snake River Plain volcanic province: Idaho Geological Survey Bulletin 30, p. 161–176.

Humphreys, E.D., Dueker, K.G., Schutt, D.L., and Smith, R.B., 2000, Beneath Yellowstone; evaluating plume and nonplume models using teleseismic images of the upper mantle: GSA Today, v. 10, no. 12, p. 1–7.

Janecky, D.R., and Seyfried, W.E., Jr., 1984, Formation of massive sulfide deposits on oceanic ridge crests—Incremental reaction models for mixing between hydrothermal solutions and seawater: Geochimica Cosmochimica Acta, v. 48, p. 2,723–2,738.

Janecky, D.R., and Shanks, W.C., III, 1988, Computational modeling of chemical and sulfur isotopic reaction processes in seafloor hydrothermal systems—Chimneys, mounds, and subjacent alteration zones: Canadian Mineralogist, v. 26, p. 805–825.

Johnson, S.Y., Stephenson, W.J., Morgan, L.A., Shanks, W.C., III, and Pierce, K.L., 2003, Hydrothermal and tectonic activity in northern Yellowstone Lake, Wyoming: Geological Society of America Bulletin, v. 115, p. 954–971.

Jones, B., and Renaut, R.W., 1996, Influence of thermophilic bacteria on calcite and silica precipitation in hot springs with water temperatures above 90° C; evidence from Kenya and New Zealand: Canadian Journal of Earth Science, v. 33, no. 1, p. 72–83.

Jones, B., Renaut, R.W., and Rosen, M.R., 1997, Biogenicity of silica precipitation around geysers and hot-spring vents, North Island, New Zealand: Journal of Sedimentary Research, v. 67, no. 1, p. 88–104.

Jorgensen, B.B., Zawacki, L.X., and Jannasch, H.W., 1990, Thermophilic bacterial sulfate reduction in deep-sea sediments at the Guaymas Basin hydrothermal vent site (Gulf of California): Deep-Sea Research, Part A—Oceanographic Research Papers, v. 37, no. 4(A), p. 695–710.

Juniper, S.K., and Fouquet, Y., 1988, Filamentous iron-silica deposits from modern and ancient hydrothermal sites: Canadian Mineralogist, v. 26, p. 859–869.

Kaplinski, M.A., 1991, Geomorphology and geology of Yellowstone Lake, Yellowstone National Park, Wyoming: Flagstaff, Northern Arizona University, M.S. thesis, 82 p.

Kellogg, K.S., Harlan, S.S., Mehnert, H.H., Snee, L.W., Pierce, K.L., Hackett, W.R., and Rogers, D.W., 1994, Major 10.2-Ma rhyolitic volcanism in the eastern Snake River Plain, Idaho—Isotopic age and stratigraphic setting of the Arbon Valley Tuff Member of the Starlight Formation: U.S. Geological Survey Bulletin 2091, 18 p.

Klump, J.V., Remsen, C.C., and Kaster, J.L., 1988, The presence and potential impact of geothermal activity on the chemistry and biology of Yellowstone Lake, Wyoming, *in* DeLuca, M., and Babb, I., eds., Global venting, midwater and benthic ecological processes: NOAA Symposium on Undersea Research, p. 81–98.

Leeman, W.P., 1982, Rhyolites of the Snake River Plain-Yellowstone Plateau Province, Idaho and Wyoming; a summary of petrogenetic models: Idaho Bureau of Mines and Geology Bulletin, v. 26, p. 203–212.

Meyer, G.A., and Locke, W.W., 1986, Origin and deformation of Holocene shoreline terraces, Yellowstone Lake, Wyoming: Geology, v. 14, no. 8, p. 699–702.

Miller, D.S., and Smith, R.B., 1999, P and S velocity structure of the Yellowstone volcanic field from local earthquake and controlled-source tomography: Journal of Geophysical Research, v. 104, no. 7, p. 15,105–15,121.

Morgan, L.A., 1992, Stratigraphic relations and paleomagnetic and geochemical correlations of ignimbrites of the Heise volcanic field, eastern Snake River Plain, eastern Idaho and western Wyoming, *in* Link, P.K., Kuntz, M.A., and Platt, L.B., eds., Regional geology of eastern Idaho and western Wyoming: Geological Society of America Memoir 179, p. 215–226.

Morgan, L.A., Doherty, D.J., and Leeman, W.P., 1984, Ignimbrites of the eastern Snake River Plain; evidence for major caldera-forming eruptions: Journal of Geophysical Research, v. 89, no. 10, p. 8,665–8,678.

Morgan, L.A., Shanks, W.C., III, Lovalvo, D., Johnson, S.Y., Stephenson, W., Pierce, K.L., Harlan, S., Finn, C., Lee, G., Webring, M., Schulze, B., Duhn, J., Sweeney, R., and Balistrieri, L., 2003, Exploration and discovery in Yellowstone Lake—Results from high-resolution sonar imaging, seismic reflection profiling, and submersible studies: Journal of Volcanology and Geothermal Research, v. 122, p. 221–242.

Morgan, L.A., Shanks, W.C., III, Pierce, K.L., and Rye, R.O., 1998, Hydrothermal explosion deposits in Yellowstone National Park—Links to hydrothermal processes [abs.]: Eos, Transactions of the American Geophysical Union, Fall Annual Meeting, v. 79, p. F964.

Morgan, P., Blackwell, D.D., Spafford, R.E., and Smith, R.B., 1977, Heat flow measurements in Yellowstone Lake and the thermal structure of the Yellowstone caldera: Journal of Geophysical Research, v. 82, p. 3,719–3,732.

Muffler, L.J.P., White, D.E., and Truesdell, A.H., 1971, Hydrothermal explosion craters in Yellowstone National Park: Geological Society of America Bulletin, v. 82, p. 723–740.

Obradovich, J.D., 1992, Geochronology of the late Cenozoic volcanism of Yellowstone National Park and adjoining areas, Wyoming and Idaho: Open-File Report 92-408, 45 p.

Otis, R.M., 1975, Interpretation and digital processing of seismic reflection and refraction data from Yellowstone Lake, Wyoming: Salt Lake City, University of Utah, Ph.D. dissertation, 223 p.

Otis, R.M., Smith, R.B., and Wold, R.J., 1977, Geophysical surveys of Yellowstone Lake, Wyoming: Journal of Geophysical Research, v. 82, p. 3,705–3,717.

Perkins, M.E., and Nash, B.P., 2002, Explosive silicic volcanism of the Yellowstone hotspot; the ash fall tuff record: Geological Society of America Bulletin, v. 114, no. 3, p. 367–381.

Pierce, K.L., 1997, Yellowstone caldera "heavy breathing" based on Yellowstone Lake and River changes in post-glacial time: Eos, Transactions of the American Geophysical Union, v. 78, p. F802.

Pierce, K.L., Cannon, K.P., Meyer, G.A., Trebesch, M.J., and Watts, R., 2002, Post-glacial inflation-deflation cycles, tilting, and faulting in the Yellowstone caldera based on Yellowstone Lake shorelines: U.S. Geological Survey Open-File Report 02-142, 62 p.

Pierce, K.L., and Morgan, L.A., 1992, The track of the Yellowstone hot spot; volcanism, faulting, and uplift, *in* Link, P.K., Kuntz, M.A., and Platt, L.B., eds., Regional geology of eastern Idaho and western Wyoming: Geological Society of America Memoir 179, p. 1–53.

Remsen, C.C., Klump, J.V., Kaster, J.L., Paddock, R., Anderson, P., and Maki, J.S., 1990, Hydrothermal springs and gas fumaroles in Yellowstone Lake, Yellowstone National Park, Wyoming: National Geographic Research, v. 6, p. 509–515.

Smith, R.B., and Braile, L.W., 1994, The Yellowstone hotspot: Journal of Volcanology and Geothermal Research, v. 61, p. 121–187.

Styrt, M.M., Brackmann, A.J., Holland, H.D., Clark, B.C., Pisutha-Arnond, V., Eldridge, C.S., and Ohmoto, H., 1981, The mineralogy and the isotopic composition of sulfur in hydrothermal sulfide/sulfate deposits on the East Pacific Rise, 21°N. latitude: Earth and Planetary Science Letters, v. 53, no. 3, p. 382–390.

Tivey, M.K., 1995, Modeling chimney growth and associated fluid flow at seafloor hydrothermal vent sites, *in* Humphris, S.E., Zierenberg, R.A., Mullineaux, L.S., and Thomson, R.E., eds., Seafloor hydrothermal systems; physical, chemical, biological, and geological interactions: Third RIDGE Theoretical Institute, American Geophysical Union Monograph, v. 91, p. 158–177.

Truesdell, A.H., Nathenson, M., and Rye, R.O., 1977, The effects of subsurface boiling and dilution on the isotopic compositions of Yellowstone thermal waters: Journal of Geophysical Research, v. 82, no. 26, p. 3,694–3,704.

Wold, R.J., Mayhew, M.A., and Smith, R.B., 1977, Bathymetric and geophysical evidence for a hydrothermal explosion crater in Mary Bay, Yellowstone Lake, Wyoming: Journal of Geophysical Research, v. 82, no. 26, p. 3,733–3,738.

The Question of Recharge to the Deep Thermal Reservoir Underlying the Geysers and Hot Springs of Yellowstone National Park

H

By Robert O. Rye and Alfred H. Truesdell

Chapter H *of*
Integrated Geoscience Studies in the Greater Yellowstone Area—Volcanic, Tectonic, and Hydrothermal Processes in the Yellowstone Geoecosystem
Edited by Lisa A. Morgan

U.S. Geological Survey Professional Paper 1717

U.S. Department of the Interior
U.S. Geological Survey

Contents

Abstract 239
Introduction 240
Thermal Features of Yellowstone National Park 240
Recognition of a Deep-Water Component in the Thermal System:
Comparison of δD of Water from Drill Holes and Thermal Springs 242
Methodology for Tracing Recharge Sources 242
Use of δD in Hydrology Studies of Geothermal Areas 242
Climatic Controls on the Regional Distribution of the δD of Cold Waters
in the Yellowstone Area 243
$\delta^{18}O$ and δD Values of Precipitation and Cold Waters in Yellowstone National Park 245
δD of Precipitation in Yellowstone National Park and Its Relationship to δD
of Infiltrating Water 247
Relationship of δD of Ground Waters to δD of Streams and Rivers 250
Sampling of Streams for δD Analyses 250
Results: δD of Surface Water in the Greater Yellowstone Area 259
Areas North of the Park 259
Gallatin Range 261
Washburn Range 261
Buffalo Plateau 261
Absaroka Range 261
Madison Plateau 261
Central Plateau 261
Yellowstone Lake and Yellowstone River 262
Mirror Plateau 262
Pitchstone Plateau and Areas South and West of the Park 262
Snake River Drainage 262
Discussion 262
Yearly Variations in δD Values at Individual Sites 263
Source of Recharge of Deep Thermal Water If It Occurred During the Holocene 263
Volume of Deep Thermal Water in the Western Side of the Caldera 264
Age of the Deep Water 267
Source of Recharge of Deep Thermal Water If a Substantial Component Remains
from the Pleistocene 267
Conclusions 268
Acknowledgments 268
References Cited 268

Figures

1. Sketch map of Yellowstone National Park 241
2. Generalized mixing and boiling model for Norris Geyser Basin waters 243

3. Enthalpy-chloride diagram for Lower, Upper, Norris, Heart Lake, and Shoshone Geyser Basins....244
4. $\delta^{18}O$-chloride relations for neutral-chloride hot-spring waters from Heart Lake, Upper, Lower, Norris, Shoshone, and West Thumb Geyser Basins....245
5. δD- $\delta^{18}O$ of precipitation, creeks, streams, rivers, lakes, cold springs, wells, rain, and snow showing relationship to the global meteoric water line....247
6. δD of monthly precipitation collections from rain gages at Old Faithful from August 1978 through January 1981....250
7. Sketch map of Yellowstone National Park and adjacent area showing select topographic features and the δD of cold waters at each sample site....260
8. δD of fall discharge of eight Yellowstone streams....263
9. Geologic sketch map of Yellowstone National Park showing possible recharge area for deep thermal waters of the geyser basins....265
10. Schematic north-south cross section through the west side of Yellowstone National Park showing possible recharge for deep thermal water and shallow mixing waters at Lower and Shoshone Geyser Basins....266

Tables

1. δD of drill-hole, hot-spring, and cold-water samples from Yellowstone National Park geyser basins....242
2. δD of precipitation in Yellowstone National Park....246
3. δD and $\delta^{18}O$ of streams, rivers, springs, lakes, and precipitation in Yellowstone National Park....248
4. δD of cold waters in Yellowstone National Park and adjacent areas....251

The Question of Recharge to the Deep Thermal Reservoir Underlying the Geysers and Hot Springs of Yellowstone National Park

By Robert O. Rye[1] and Alfred H. Truesdell[2]

Abstract

The extraordinary number, size, and unspoiled beauty of the geysers and hot springs of Yellowstone National Park (the Park) make them a national treasure. The hydrology of these special features and their relation to cold waters of the Yellowstone area are poorly known. In the absence of deep drill holes, such information is available only indirectly from isotope studies. The δD-$\delta^{18}O$ values of precipitation and cold surface-water and ground-water samples are close to the global meteoric water line (Craig, 1961). δD values of monthly samples of rain and snow collected from 1978 to 1981 at two stations in the Park show strong seasonal variations, with average values for winter months close to those for cold waters near the collection sites. δD values of more than 300 samples from cold springs, cold streams, and rivers collected during the fall from 1967 to 1992 show consistent north-south and east-west patterns throughout and outside of the Park, although values at a given site vary by as much as 8 ‰ from year to year. These data, along with hot-spring data (Truesdell and others, 1977; Pearson and Truesdell, 1978), show that ascending Yellowstone thermal waters are modified isotopically and chemically by a variety of boiling and mixing processes in shallow reservoirs. Near geyser basins, shallow recharge waters from nearby rhyolite plateaus dilute the ascending deep thermal waters, particularly at basin margins, and mix and boil in reservoirs that commonly are interconnected. Deep recharge appears to derive from a major deep thermal-reservoir fluid that supplies steam and hot water to all geyser basins on the west side of the Park and perhaps in the entire Yellowstone caldera. This water ($T \geq 350°C$; $\delta D = -149 \pm 1$ ‰) is isotopically lighter than all but the farthest north, highest altitude cold springs and streams and a sinter-producing warm spring ($\delta D = -153$ ‰) north of the Park.

Derivation of this deep fluid solely from present-day recharge is problematical. The designation of source areas depends on assumptions about the age of the deep water, which in turn depend on assumptions about the nature of the deep thermal system. Modeling, based on published chloride-flux studies of thermal waters, suggests that for a 0.5- to 4-km-deep reservoir the residence time of most of the thermal water could be less than 1,900 years, for a piston-flow model, to more than 10,000 years, for a well-mixed model. For the piston-flow model, the deep system quickly reaches the isotopic composition of the recharge in response to climate change. For this model, stable-isotope data and geologic considerations suggest that the most likely area of recharge for the deep thermal water is in the northwestern part of the Park, in the Gallatin Range, where major north-south faults connect with the caldera. This possible recharge area for the deep thermal water is at least 20 km, and possibly as much as 70 km, from outflow in the thermal areas, indicating the presence of a hydrothermal system as large as those postulated to have operated around large, ancient igneous intrusions. For this model, the volume of isotopically light water infiltrating in the Gallatin Range during our sampling period is too small to balance the present outflow of deep water. This shortfall suggests that some recharge possibly occurred during a cooler time characterized by greater winter precipitation, such as during the Little Ice Age in the 15th century. However, this scenario requires exceptionally fast flow rates of recharge into the deep system.

For the well-mixed model, the composition of the deep reservoir changes slowly in response to climate change, and a significant component of the deep thermal water could have recharged during Pleistocene glaciation. The latter interpretation is consistent with the recent discovery of warm waters in wells and springs in southern Idaho that have δD values 10–20 ‰ lower than the winter snow for their present-day high-level recharge. These waters have been interpreted to be Pleistocene in age (Smith and others, 2002). The well-mixed model permits a significant component of recharge water for the deep system to have δD values less negative than –150 ‰ and consequently for the deep system recharge to be closer to the caldera at a number of possible localities in the Park.

[1]U.S. Geological Survey, Box 25046, Mail Stop 963, Denver Federal Center, Denver, CO 80225.

[2]700 Hermosa Way, Menlo Park, CA 94025.

Introduction

Extraordinary geysers, hot springs, and fumaroles are distributed widely in Yellowstone National Park (the Park), and they constitute one of its major attractions. Public law (The Geothermal Steam Act of 1970 (30 U.S.C. 1001–1025) as amended by Section 28 in 1988) requires that significant thermal features in the Park be protected from the effects of exploration and exploitation for geothermal energy outside of the Park—determination of possible effects are to be based on scientific evidence from monitoring studies by the U.S. Geological Survey. For the purposes of this act, Yellowstone National Park is considered to be a single significant geothermal system, and it is protected in its entirety.

Extensive scientific study of the thermal areas of Yellowstone National Park began with the Hayden Expedition of 1871 (Hayden, 1872) and continued with the geochemical studies of Gooch and Whitfield (1888) and Allen and Day (1935). Since 1960, the U.S. Geological Survey has been active in the study of Yellowstone, with topographic and geologic mapping and geophysical, geothermal, and volcano hazard studies. For a bibliography of these studies from 1965 to 1986, see Bargar and Dzurisin (1986); also see the review by Fournier (1989) and investigations reported in Sorey (1991), Rye and Truesdell (1993), and other papers in this volume. Initial studies of the hydrothermal system(s) in Yellowstone concentrated on the surface thermal features—their character, chemistry, and output. In 1967, as part of a study to understand the geochemistry and hydrology of the thermal areas, we began isotopic studies of cold waters around the geyser basins in an attempt to locate the recharge area(s) for the thermal waters. Chemical and isotopic modeling (Truesdell and others, 1977) indicated that probably all of the hot-spring and geyser basins on the west side of the Yellowstone caldera are underlain by deep meteoric water of constant isotopic and chemical composition. This deep water is modified isotopically and chemically as it cools by boiling and mixing with local cold waters. The recharge area(s) for the deepest parts of the Yellowstone system have not been located. The purpose of this paper is to compare the isotopic compositions of deep thermal-reservoir waters indicated by analyses of hot-spring, geyser and research-well waters (Truesdell and others, 1977) with the compositions of meteoric waters, for the purpose of constraining the source(s) of recharge for the deep waters. A unique solution is not possible because the age of the deep water is not known. If the deep thermal water in the Yellowstone geothermal system is Holocene in age, the most likely area for its meteoric water recharge is in the Gallatin Range in and northwest of the Park. However, if a component of the deep water was recharged during Pleistocene glaciation and if the deep reservoir is well mixed, the recharge area could be multiple localities within the Park, close to the caldera.

Thermal Features of Yellowstone National Park

The areal distribution of active thermal areas in the Park and their relationships to surface drainage and major geologic and topographic features are shown in figure 1. Most of the active thermal areas are (1) in the 0.6-Ma Yellowstone caldera, close to the outer margin (for example, Hot Spring Basin and Washburn Hot Springs) and in the topographically low area near the two resurgent domes (for example, Upper and Lower Geyser Basins) or (2) along north-south-trending faults that extend outside the caldera (for example, Norris and Heart Lake Geyser Basins). Geophysical evidence indicates that an active magma system underlies much of the Yellowstone caldera at depths of about 5–6 km, and it currently produces inflation and deflation of the area (Eaton and others, 1975; Dzurisin and Yamashita, 1987; Dzurisin and others, 1990; Smith and Rubin, 1994; Pierce and others, 1997; Wicks and others, 1999; Pierce and others, this volume).

A variety of thermal features is present in individual basins. In general, alkaline-chloride hot springs are in basins on the west side of the caldera, where one would expect to find cold-water springs. These alkaline-chloride springs deposit thick mounds and terraces of silica on glacial till, welded tuff, and rhyolite. In areas where boiling water does not emerge at the surface, H_2S in the steam that separates from the water commonly oxidizes and forms H_2SO_4 at the surface, and it produces acid-sulfate pools and mud pots. Small travertine-producing springs are present at the margins of geyser basins in which CO_2-charged waters cool by mixing with cold ground water before they have a chance to boil. The thermal features in the east side of the Park have little water discharge and typically consist of fumaroles surrounded by sulfur and steam-heated pools of acid-sulfate water containing little chloride. Because this area is higher than the adjacent valleys, the water table seldom intersects the surface. However, recent studies indicate that there is discharge of chloride-rich waters into Yellowstone Lake from sublacustrine vents (Balistrieri and others, this volume). Large travertine deposits outside of the caldera, such as those at Mammoth Hot Springs and adjacent to the Snake River, occur at the low-temperature margins of the Yellowstone system where thermal fluids flow through thick limestone sequences.

Figure 1. Sketch map of Yellowstone National Park (dashed dot-dot line) showing general locations of geyser basins (dark gray) and their relation to the Yellowstone caldera (heavy black line), important north-south faults (dot dashed line), resurgent domes (diagonal pattern), surface drainage (fine lines), and selected topographic and physiographic features (text and wavy pattern for lakes). Also shown are location of Mammoth and Old Faithful (large white dots), the Continental Divide (open dotted line), roads (short dashed line), and State boundaries (thin dashed lines). Caldera outline, resurgent domes, and faults generalized from Christiansen (1984).

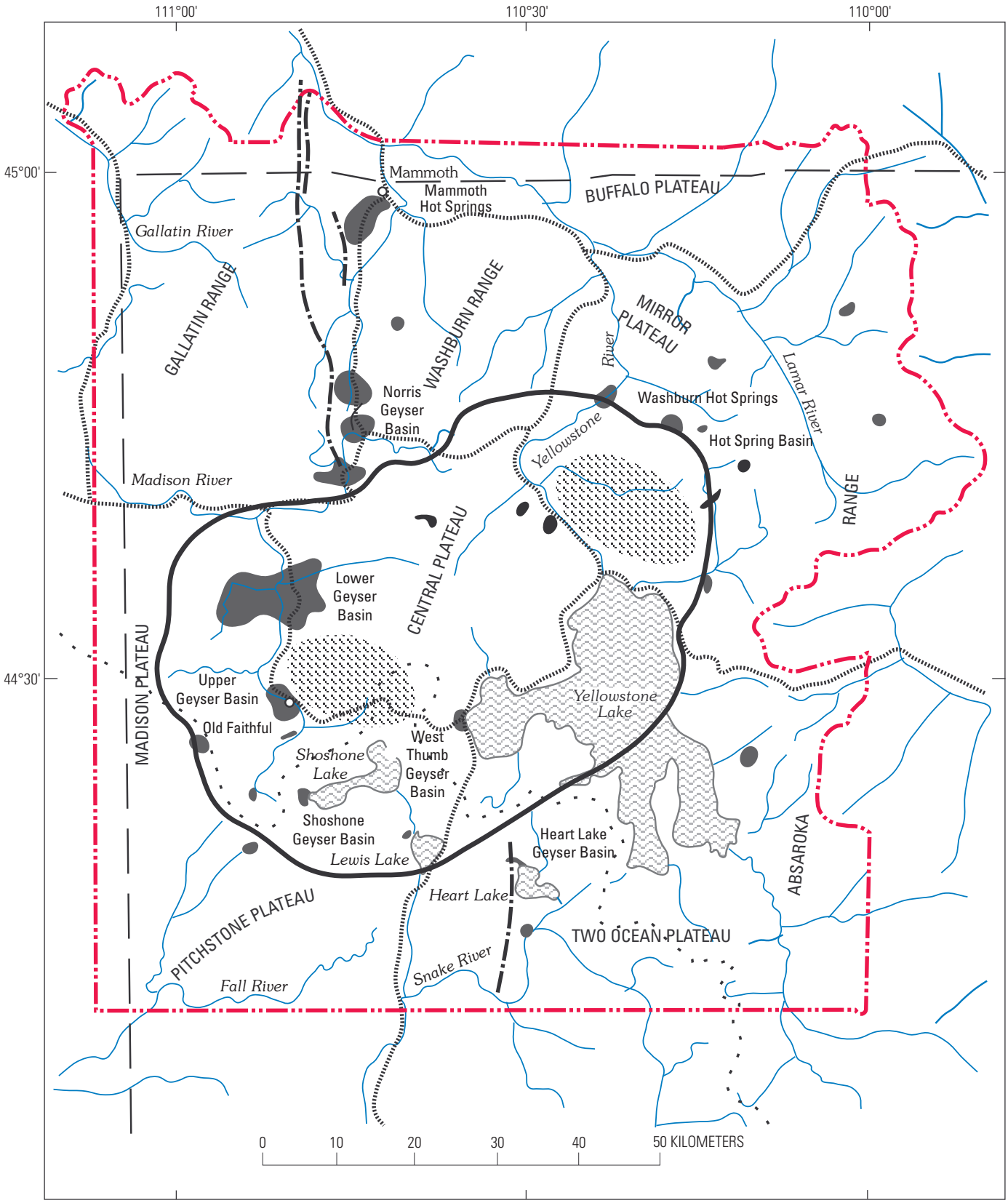
111°00'
110°30'
110°00'
45°00'
44°30'
Mammoth
Mammoth Hot Springs
BUFFALO PLATEAU
Gallatin River
GALLATIN RANGE
WASHBURN RANGE
MIRROR PLATEAU
Yellowstone River
Lamar River
Norris Geyser Basin
Washburn Hot Springs
Hot Spring Basin
Madison River
CENTRAL PLATEAU
RANGE
Lower Geyser Basin
MADISON PLATEAU
Upper Geyser Basin
Old Faithful
Yellowstone Lake
West Thumb Geyser Basin
Shoshone Lake
Shoshone Geyser Basin
Lewis Lake
Heart Lake Geyser Basin
ABSAROKA
Heart Lake
PITCHSTONE PLATEAU
TWO OCEAN PLATEAU
Snake River
Fall River
0 10 20 30 40 50 KILOMETERS

Recognition of a Deep-Water Component in the Thermal System: Comparison of δD of Water from Drill Holes and Thermal Springs

Early isotope studies showed that essentially all of the thermal waters in Yellowstone Park and elsewhere in the world were derived from meteoric water (Craig and others, 1956). Hundreds of additional samples from Yellowstone and other thermal areas throughout the world have been analyzed, and that conclusion still holds, with few exceptions. In order to better understand the geochemistry and hydrodynamics of the thermal areas, in 1967 we began a search for the recharge areas for the thermal water in the Yellowstone geyser basins. At that time, we assumed that the hot springs in each basin were recharged locally by water from the surrounding rhyolite plateaus. Analyses of water collected from shallow (65–332 m depth) research holes drilled in 1967 and 1968 required us to abandon that assumption. The δD values of waters from drill holes and nearby hot-water springs and local meteoric water from Lower, Norris, and Shoshone Geyser Basins are summarized in table 1. The striking feature of the data in table 1 is that δD values of waters from hot springs and drill holes were more negative than those of local meteoric waters. For example, the δD values of water from drill holes at Norris and Lower Geyser Basins were –146 to –151 ‰, whereas those of local meteoric water were –140 to –145 ‰. Recognition of this difference led to modeling of the δD of thermal waters in terms of isotope effects due to boiling and mixing (Truesdell and others, 1977). The results of that modeling for Norris Geyser Basin are illustrated in figure 2. The boiling and mixing model enabled interpretation of the measured δD of spring waters in terms of δD of deep water prior to boiling and (or) mixing. The deep thermal waters mix with cool water from local sources in shallow reservoirs, and these mixtures boil to produce the chemical and isotopic compositions of the surface thermal waters. Because most boiling and mixing occurs in shallow aquifers, the δD values of waters recovered from drill holes approximate the primary compositions of thermal waters prior to boiling and mixing. This modeling indicated that hot springs in the Norris Geyser Basin have a deep-water component that was derived from meteoric water having a δD significantly lower than that of present local meteoric waters. Truesdell and others (1977) showed that the compositions of thermal waters at Lower and Shoshone Geyser Basins also are consistent with derivation from the same deep water of δD = –148 to –150 ‰. Balistrieri and others (this volume) extended the Truesdell and others (1977) modeling to sublacustrine vents and associated pore waters in Yellowstone Lake, at Mary Bay. Their studies indicated that the deep reservoir probably underlies the entire caldera and that the prevalence of steam in the eastern caldera is due more to altitude effects than to a fundamental difference in the geothermal systems.

Table 1. δD of drill-hole, hot-spring, and cold-water samples from Yellowstone National Park geyser basins.

Basin	Drill holes	Hot springs	Cold waters
Norris	–149 to –151	–139 to –149	–140 to –144
Lower	–146 to –149	–140 to –146	–140 to –145
Shoshone		–135 to –139	–130 to –135

A single, deep-source water for Yellowstone surface-thermal-water discharges also is indicated by chemical arguments. When chloride compositions and geothermometer temperatures of the thermal waters are plotted on enthalpy-chloride diagrams (fig. 3), the temperatures and chloride concentrations of all major thermal waters in the Park are consistent with derivation from a single deep fluid of 320 ppm chloride and 360°C temperature (Truesdell and Fournier, 1976). Research wells do not exist for West Thumb and Heart Lake Geyser Basins, and mixing of partially evaporated water from Yellowstone and Heart Lakes complicates the δD values of their thermal waters. However, as shown in figure 4, the $\delta^{18}O$ versus chloride systematics of some Heart Lake and West Thumb hot springs are similar to those of waters from Norris, Upper, Lower, and Shoshone Geyser Basins. The fact that the compositions of some thermal waters at Heart Lake and West Thumb fall on the same mixing line as other spring waters suggests that they possibly evolved from the same deep water. All of our data from Yellowstone are consistent with the hypothesis that an isotopically and chemically homogeneous fluid underlies all of the thermal areas on the west side of the caldera.

Methodology for Tracing Recharge Sources

Use of δD in Hydrology Studies of Geothermal Areas

Hydrogen- and oxygen-isotopic compositions of water show variations related to the source and history of the water. For most cold-water systems, these isotopes may be used interchangeably because processes of evaporation and condensation affect both isotopes similarly. For geothermal systems, both isotopes are affected by subsurface processes of mixing, boiling, and steam separation, as discussed and modeled in our earlier paper emphasizing thermal waters (Truesdell and others, 1977). In geothermal systems such as Yellowstone, however, oxygen isotopes in water exchange with those in rock so that $\delta^{18}O$ values of water depend on the temperature and duration of rock-water interaction, on the ratio of water to rock, and on the character of the rock, as well as on mixing and evaporation-condensation processes. This exchange, called the “oxygen isotope shift,” complicates interpretation of the $\delta^{18}O$ values as indicators of recharge. In contrast, hydrogen-isotope exchange between water and rock minerals is not significant (except at very low water/rock ratios), and interpretation

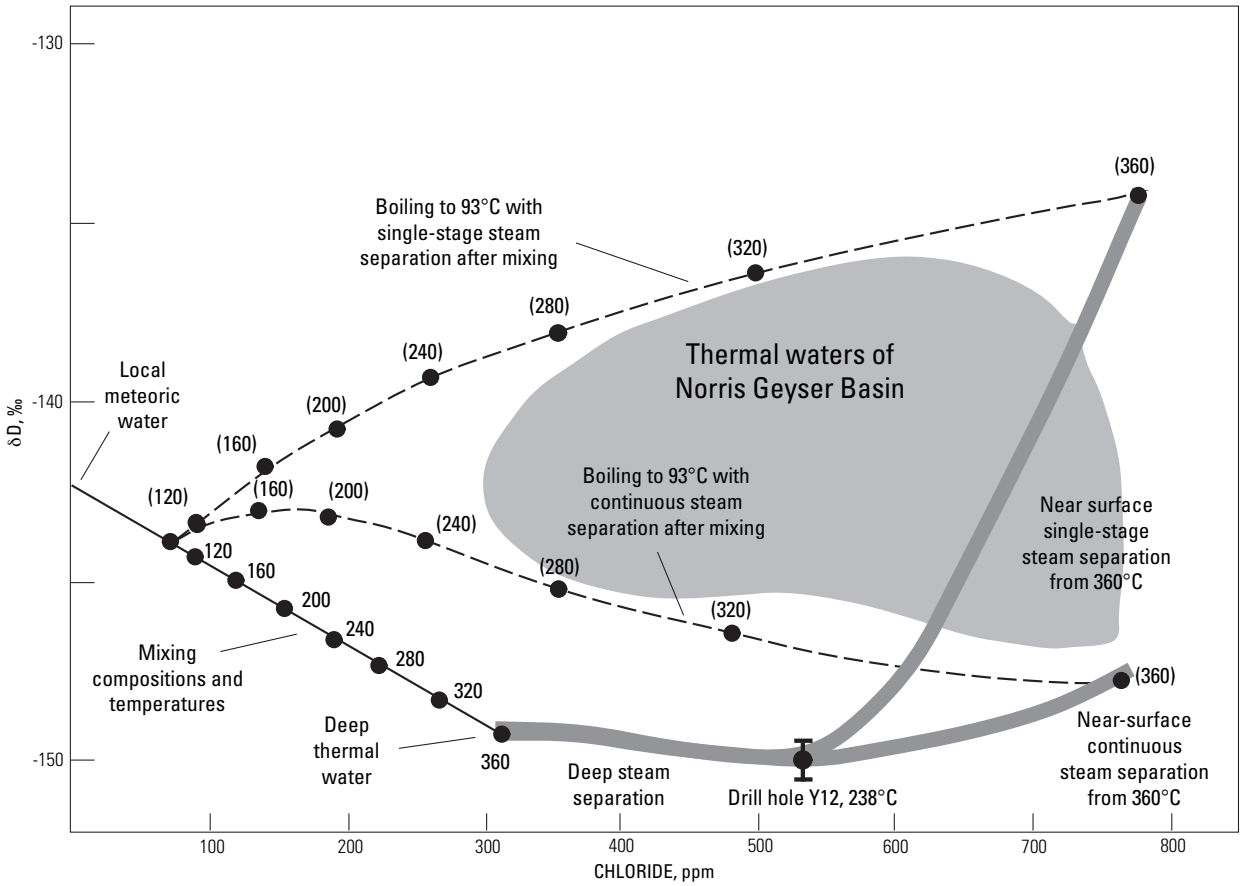

Figure 2. Generalized mixing and boiling model for Norris Geyser Basin waters (from Truesdell and others, 1977). Solid straight line shows compositions and temperatures for mixtures of deep thermal water and surface water. Wide dark-gray lines shows evolved composition of deep waters that undergo single-stage or continuous steam separation from 360° to 93 °C without mixing. Dashed lines show compositions at 93°C for mixed waters after undergoing single-stage or continuous steam separation from mixtures having the indicated starting temperatures (shown in parentheses). Gray field shows compositions of Norris Geyser Basin neutral-chloride hot-spring waters. Similar diagrams using the same deep-water compositions can explain the compositions of hot springs at Upper, Lower, and Shoshone Geyser Basins (Truesdell and others, 1977).

of δD values of water is more straightforward. For this reason, we concentrated our study of Yellowstone recharge on the δD values of possible infiltrating waters in relation to the δD values of the thermal-source water described earlier.

Determination of the recharge area for the deep thermal water requires samples that are representative of infiltrating waters. As is discussed later, possible infiltrating waters are best sampled during dry periods in the fall when most streams and rivers in Yellowstone National Park are fed largely by springs and seeps (the springs and seeps received most of their recharge from snowmelt during the previous spring). More than 300 δD analyses were made of possible infiltrating waters from cold springs, wells, streams, and rivers in a 15,000 km^2 region in and adjacent to the Park. Most of the samples were collected in the fall from 1967 to 1990. The remainder of this section focuses on validating the use of δD analyses of these samples as an indicator of the composition of infiltrating waters. To aid in this validation, $\delta^{18}O$ analyses also were made on some of these samples.

Climatic Controls on the Regional Distribution of the δD of Cold Waters in the Yellowstone Area

A recent study of more than 4,800 δD values of surface waters in the conterminous United States shows the mountainous Yellowstone Plateau to be within a large area with δD values lower than –130 ‰, in which δD contours closely match topographic contours (Kendall and Coplen, 1991, 2001). Yellowstone Park is in a part of North America that is affected by Arctic, Gulf of Mexico, and Pacific air masses (Bryson and Hare, 1974). The general distribution of δD values of cold waters in the Park area reflects the influence of both complex weather patterns and altitude.

Precipitation records in Yellowstone Park were summarized by Dirks and Martner (1982). River runoff records were summarized by Norton and Friedman (1991), and weather patterns were interpreted by Despain (1987). According to precipitation

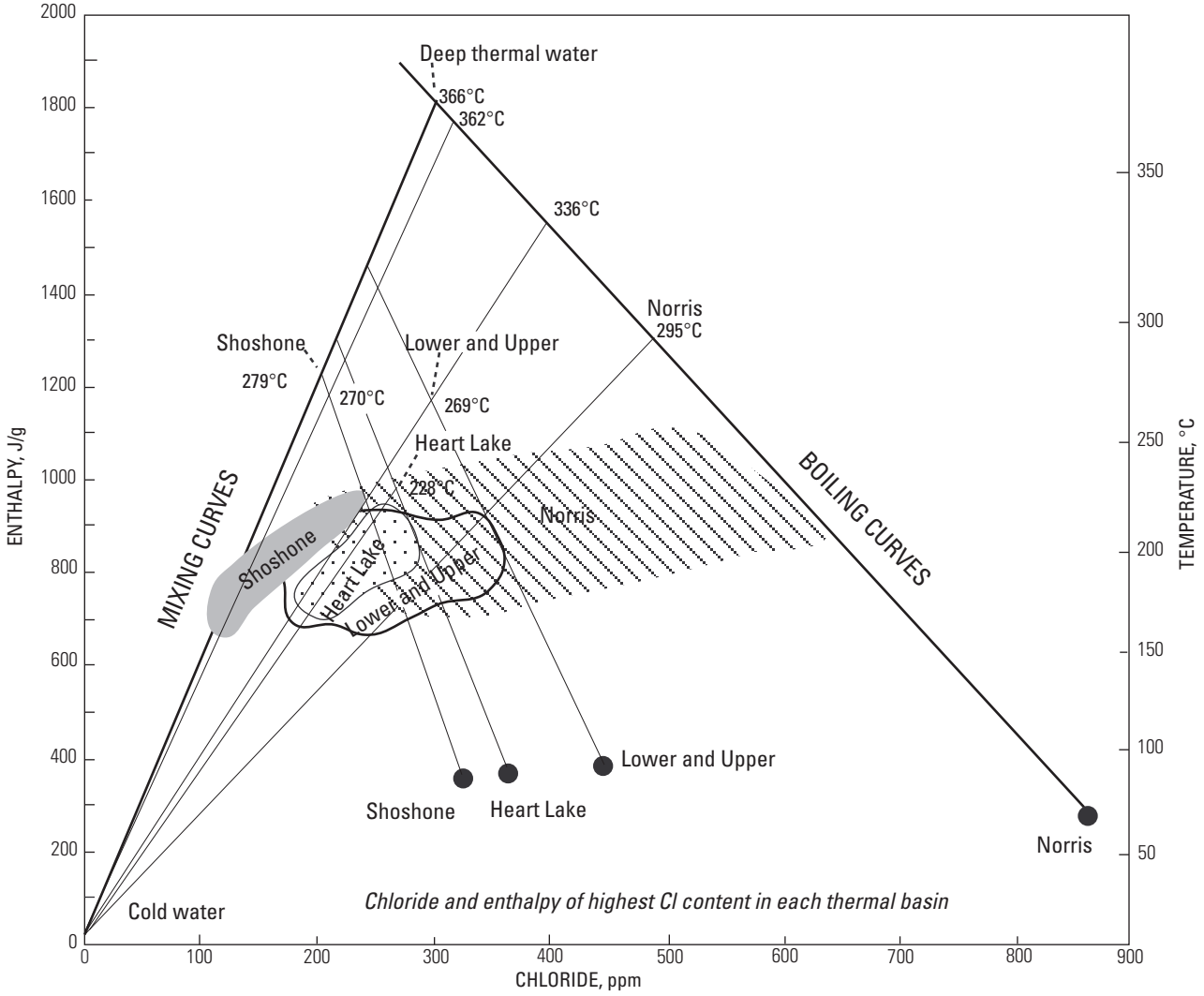

Figure 3. Enthalpy-chloride diagram for Lower, Upper, Norris, Heart Lake, and Shoshone Geyser Basins (from Truesdell and Fournier, 1976). Pattern areas outline compositions for hot neutral-chloride waters in respective geyser basins. Because little heat is lost by conduction and chloride is conservative, all enthalpy and chloride compositions must be a result of mixing and boiling. Diagram shows that all compositions for all basins can be explained as a result of mixing and boiling combinations of a single deep-thermal water having about 320 ppm chloride at 360°C and dilute cold waters.

summaries by Dirks and Martner (1982), precipitation in the region is fairly well distributed throughout the year, with the exception that large storms occur in mid-winter and dry periods frequently occur in the fall. As much as 75 percent of the total precipitation in Yellowstone Park falls during winter snowstorms from October through May. The remainder falls primarily during local warm-season thunderstorms. Because the valleys in the Park tend to be dry, seasonal river-flow measurements for the major drainage basins, such as the Madison River, indicate that most of the precipitation is concentrated at higher altitudes and that it accumulates there as snow, causing high river volumes during spring snowmelt. The largest amount of precipitation falls on the high plateaus in the southwestern part of the Park; the Central Plateau is in the rain shadow of the higher areas to the southwest (Dirks and Martner, 1982; Norton and Friedman, 1991; Farnes, 1997).

The largest storms, from the Pacific, enter the Park region from the Snake River Plain to the southwest. Winter weather in Yellowstone reflects the relative strengths and positions of Arctic and Pacific air masses. The increase in δD values in all directions away from the mountainous Yellowstone Plateau reflects the influence of high altitudes and the complex weather patterns in the region involving Pacific, Arctic, and Gulf air masses. The northward decrease in δD values, shown in our data in a succeeding section, reflects both increases in altitude and the general south-to-north path of storm trajectories, as well as the rain shadow produced by the southwestern mountains. The trend to less negative δD values for cold water in the northeastern part of mountainous regions possibly reflects the importance of Gulf air masses in the eastern part of the region.

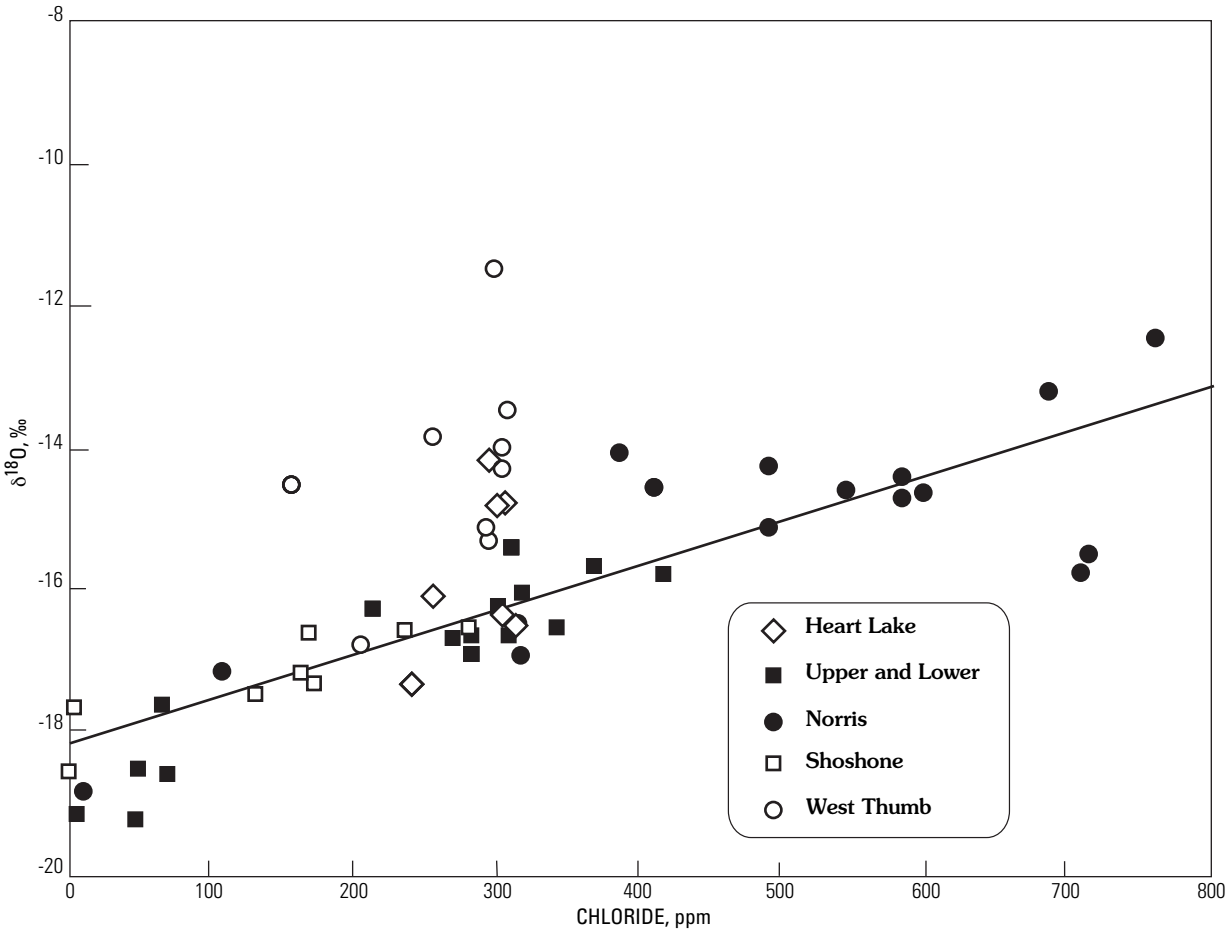

Figure 4. $\delta^{18}O$-chloride relations for neutral-chloride hot-spring waters from the Heart Lake, Upper, Lower, Norris, Shoshone, and West Thumb Geyser Basins. The less negative $\delta^{18}O$ values for hot waters and Heart Lake and West Thumb reflect the mixing of evaporated waters from Heart and Yellowstone Lakes, respectively. The compositions of all hot waters fall on a trend, suggesting the possibility that they evolved from the same deep thermal water. Different isotopic compositions of hot waters in different basins reflect, in large part, mixing of the deep thermal water with local shallow water of different compositions.

$\delta^{18}O$ and δD Values of Precipitation and Cold Waters in Yellowstone National Park

The δD and $\delta^{18}O$ values for precipitation samples collected in the Yellowstone National Park region during May and June and during November and December, 1970 through 1977, are given in table 2. These data and values of cold-water samples from streams, rivers, cold springs, and lakes collected in May and June and in September and October, 1967 through 1982 (table 2), are plotted in figure 5. The data for the precipitation samples plot very close to the global meteoric water line (GMWL) (Craig, 1961) with δD values from –64 to –168 ‰. These data establish that the local meteoric water line (LMWL) in the Yellowstone region is identical within error to the GMWL. Similar results were obtained by Thordsen and others (1992) from snow core samples.

The δD and $\delta^{18}O$ values of the stream, river, and spring samples straddle the GMWL, with δD values from –126 to –153 ‰. These samples are typical of those analyzed only for δD. The conformity of their compositions to the GMWL indicates that our surface-water samples did not undergo significant evaporation during precipitation, infiltration, or inflow into streams. The δD-$\delta^{18}O$ values of lake samples, however, in a fashion typical of evaporated waters, plot off the GMWL. Our data from streams, rivers, and springs contrast with those of Thordsen and others (1992). Their data for springs show increased isotope spreads for higher $\delta^{18}O$ values typical of evaporation trends. Many of their samples show values similar to values we observed for lakes (figure 5) or for streams flowing from lakes. Their study differed from ours in that it included many samples from low-altitude springs and seeps collected during summer months. Water from seeps and small springs is likely to undergo evaporation in the summer. Summer rainfall in the low-altitude valleys of Yellowstone Park, which recharges the seeps and small springs, also is likely to undergo evaporation during precipitation. Such waters will not have compositions typical of infiltrating waters that are derived from melting snow in the spring.

Table 2. δD of precipitation in Yellowstone National Park.

Date sampled	Collection	Amount (cm)	δD (‰)
	Mammoth		
5/30/77	May 1977		–118
1/26/78	Jan. 1978	1.9	–152
10/23/78	June 1978 to Oct. 1978		–90
1/12/79	Jan. 12, 1979	0.8	–206
3/7/79	Mar. 1–7, 1979	6.1	–184
7/30/79	July 1979	3.3	–94
8/31/79	Aug. 1979	5.2	–73
10/15/79	Oct. 15, 1979	1.3	–83
11/12/78	Oct.1 to Nov. 12, 1979		–163
	Old Faithful		
8/31/78	Aug. 1978		–61
10/31/78	Oct. 1978	1.0	–115
3/4/79	Feb. 1979	6.5	–189
3/31/79	Mar. 1979	6.3	–167
5/1/79	Apr. 1979	4.1	–160
5/1/79	Apr. 1979	4.1	–161
5/31/79	May 1979	3.1	–154
6/31/79	June 1979	3.3	–120
7/31/79	July 1979	1.3	–103
8/30/79	Aug. 1979	5.8	–79
9/30/79	Sep. 1979	1.5	–68
11/2/79	Oct. 1979	5.6	–142
12/2/79	Nov. 1979	1.7	–171
1/2/80	Dec. 1979	2.4	–153
1/31/80	Jan. 1980	7.8	–151
3/2/80	Feb. 1980	5.2	–135
4/3/80	Mar. 1980	1.7	–151
5/1/80	Apr. 1980	2.5	–122
6/1/80	May 1980	11.2	–120
7/1/80	June 1980	3.2	–112
8/1/80	July 1980	8.5	–102
9/4/80	Aug. 1980	4.7	–85
11/4/80	Oct. 1980	5.6	–93
12/4/80	Nov. 1980	1.7	–114
1/1/81	Dec. 1980	8.0	–156
7/30/82	July 1982	5.6	–124
9/1/82	Aug. 1982		–113
10/1/82	Sep. 1982	3.3	–186
11/30/92	Nov. 1982	6.9	–143
12/31/82	Dec. 1982	7.7	–188
1/31/83	Jan. 1983	3.1	–138

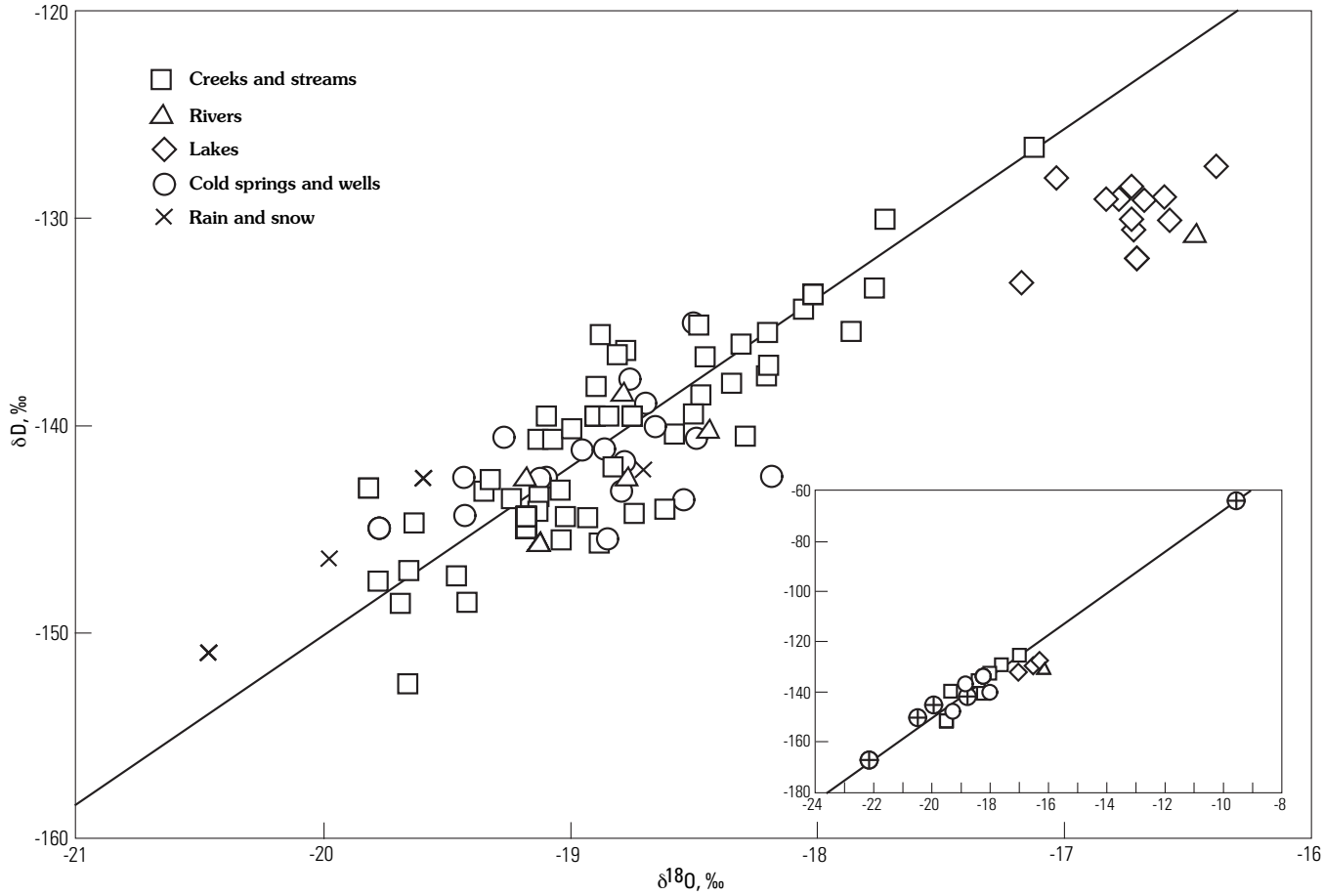

Figure 5. δD-δ^{18}O of precipitation, creeks, streams, rivers, lakes, cold springs, wells, rain, and snow from Yellowstone National Park region showing relationship to Craig's (1961) global meteoric water line. Insert shows same data set with two additional precipitation samples with extreme compositions.

δD of Precipitation in Yellowstone National Park and Its Relationship to δD of Infiltrating Water

Precipitation in a given drainage area can have a wide range of δD values, depending on the temperature, source, and history of air masses responsible for individual storms. Samples collected monthly by Park rangers from rain and snow gages at Mammoth and Old Faithful, from May 1977 through January 1983, allowed us to study the variation of δD of precipitation at those locations during a period of several years. The δD values of the precipitation, along with amounts of precipitation for the collection periods, are summarized in table 3. The δD values ranged from –206 ‰ for a single storm of 0.8 cm of precipitation at Mammoth on January 12, 1979, to –68 ‰ for 1.5 cm of precipitation during September 1979. The δD values of precipitation at Mammoth are similar to those at Old Faithful for the few months that collections were made at both sites. The data for Old Faithful, where precipitation samples were available for nearly every month during a 2-year period, are plotted in figure 6. The δD values of the monthly precipitation collections at Old Faithful show cyclic seasonal variations, in which the most negative values are derived from samples collected during the winter and the least negative values are derived from samples collected during the summer.

The weighted average δD for precipitation during winter months (September–May) of –134 ‰ (table 3) is close to the average value observed for the water supply at Old Faithful (table 4 and next section). Thus, it is likely that ground waters receive most of their recharge from melting snow during spring runoff. Because precipitation in a given drainage area can have a wide range of δD values, determination of the δD of the recharge for the thermal water involves locating cold waters that have the δD value of average infiltrating waters.

In 1967, we assumed that water from wells and cold springs that have steady discharge from ground-water reservoirs, in which water has a relatively long residence time, should give the best average values for water available for recharge. Unfortunately, there are very few such cold springs in the geyser basins where most of the subsurface water at low altitudes is thermal. Collection from cold springs outside the geyser basins is difficult because the springs seldom are located on maps, and they are likely to be small and ephemeral so that the δD of discharging water possibly reflects the most recent

Table 3. δD and $\delta^{18}O$ of streams, rivers, springs, lakes, and precipitation in Yellowstone National Park.

Sample	Description	Date sampled (mo/day/yr)	Temperature (°C)	$\delta^{18}O$ (‰)	δD (‰)
		Streams			
R-25	Tributary of Solfatara Creek	09/10/67	38	–18.6	–144
W-3	Glen Creek	09/21/71		–19.7	–149
W-4	Nez Perce Creek	09/24/71		–19.2	–144
W-13	Glen Creek	10/11/71	7	–19.8	–148
W-18	DeLacy Creek	10/11/71	7	–18.5	–138
W-25	Unnamed creek 2 mi north of Lake	10/12/71	7	–19.7	–145
W-33	Nez Perce Creek	10/04/72	13	–18.8	–144
W-2	Little Creek	10/10/75		–18.8	–136
W-3	Arnica Creek	10/10/75		–19.3	–144
W-4	Cub Creek	10/10/75		–18.9	–135
W-5	Antelope Creek	10/10/75		–19.7	–148
W-6	Tower Creek	10/10/75		–19.4	–143
W-7	Crystal Creek	10/10/75		–18.8	–142
T73-87	Fall Creek	09/10/73		–17.7	–130
T76-14	Creek near Gibbon River	09/10/76	5	–19.4	–142
T76-15	Creek near Dunraven picnic area	09/10/76	5	–19.1	–140
T76-16	Antelope Creek	09/10/76	6	–19.7	–147
T76-17	Tributary of Soda Butte Creek	09/10/76	6	–17.1	–126
T76-18	Soda Butte Creek	09/10/76	6	–18.7	–140
T76-19	Amphitheater Creek	09/10/76	5	–18.6	–141
T76-20	Pebble Creek	09/10/76	5	–19.2	–141
T76-??	DeLacy Creek	09/10/76		–18.4	–138
T76-28	Tributary of Clear Creek	09/10/76		–18.9	–138
T76-29	Cub Creek	09/10/76		–18.8	–136
T76-40	Glen Creek	09/30/76	8	–19.7	–153
T76-43	Tributary to Grayling Creek	09/30/76		–18.6	–140
T76-44	Tributary to Grayling Creek	09/30/76		–19.8	–143
T76-45	Tributary to Grayling Creek	09/30/76		–19.5	–148
T76-46	Tributary to Grayling Creek	09/30/76		–19.5	–147
T76-47	Grayling Creek	09/30/76		–18.6	–140
W-1002	Delacy Creek	06/14/77		–18.1	–134
W-1003	Grayling Creek	06/14/77		–17.8	–133
W-1004	Cub Creek	06/14/77		–19.1	–146
W-1008	Tributary of Grayling Creek	06/14/77		–18.2	–136
W-1009	Pebble Creek	06/14/77		–19.0	–144
W-1010	Glen Creek	06/14/77		–18.2	–138
W-1012	Creek near Virginia Meadows	06/14/77		–18.3	–141
W-1013	Antelope Creek	06/14/77		–19.0	–140
W-1014	Tributary of Barronette Creek	06/14/77		–17.9	–135
W-1015	Dunraven Peak Creek	06/14/77		–18.9	–146
W-1017	Tributary of Clear Creek	06/14/77		–19.1	–143
W-1018	Black Butte Creek	06/14/77		–19.1	–145
W-1019	Tributary of Grayling Creek	06/14/77		–18.2	–137
W-1020	Soda Butte Creek	06/14/77		–19.2	–144
H78-1	Grayling Creek	05/09/78	3	–18.5	–136
H78-2	Grayling Creek	05/09/78	4	–18.5	–135
H78-5	Black Butte Creek	05/09/78	6	–19.2	–145
H78-7	Cub Creek	05/10/78	2	–19.1	–141
H78-10	Glen Creek	05/10/78	4	–19.2	–144
H78-11	Apollinaris Creek	05/10/78	8	–18.5	–141
H78-13	Creek north of Soda Butte	05/11/78	1	–18.5	–140
H78-14	Soda Butte Creek	05/11/78	3	–18.9	–140
H78-15	Pebble Creek	05/11/78	3	–18.9	–140

Table 3. δD and $\delta^{18}O$ of streams, rivers, springs, lakes, and precipitation in Yellowstone National Park—*Continued*.

Sample	Description	Date sampled (mo/day/yr)	Temperature (°C)	$\delta^{18}O$ (‰)	δD (‰)
		Streams—*Continued*			
SH86-11	Shoshone Creek	09/10/86		–18.3	–136
SH86-12	Shoshone Creek	09/10/86		–18.0	–134
		Rivers			
R-41	Gibbon above Virgina Cascades	09/10/67		–18.5	–140
W-2	Gibbon above Virgina Cascades	09/21/71		–18.8	–142
W-12	Gardiner River	10/11/71	8	–19.2	–146
W-17	Little Firehole River	10/11/71	14	–18.8	–138
W-43	Yellowstone River	10/04/72	10	–16.5	–131
W-8	Lamar River	10/10/75		–19.2	–143
T76-13a	Gibbon River	09/10/76		–18.6	–141
		Lakes			
T75-23	Yellowstone Lake, Fishing Bridge	10/06/75		–16.7	–132
T75-24	Yellowstone Lake, Pumice Point	10/06/75		–16.7	–132
T76-30	Yellowstone Lake, Steamboat Point	10/08/75		–16.6	–130
T76-31	Yellowstone Lake, Fishing Bridge	10/08/75		–16.7	–131
T76-32	Yellowstone Lake, Pumice Point	10/08/75		–16.7	–130
W-1005	Yellowstone Lake, Pumice Point	06/14/77		–16.7	–129
W-1006	Yellowstone Lake, Steamboat Point	06/14/77		–17.0	–128
W-1011	Yellowstone Lake, Fishing Bridge	06/14/77		–16.8	–129
W-1016	Yellowstone Lake, Fishing Bridge	06/14/77		–16.8	–129
H78-6	Yellowstone Lake, Pumice Point	05/10/78		–16.7	–129
H78-8	Yellowstone Lake, Steamboat Point	05/10/78		–16.6	–129
H78-9	Yellowstone Lake, Fishing Bridge	05/10/78		–17.2	–133
T81-20	Shoshone Lake	09/19/81		–16.4	–128
		Springs			
F-381	Midway picnic area spring	10/19/67		–18.9	–145
W-1	Midway picnic area water supply	09/29/71		–19.2	–142
W-6	Midway picnic area spring	09/29/71		–19.0	–141
W-9	Above Black Sand Basin	10/10/71		–19.1	–142
W-10	New Old Faithful	10/10/71		–18.8	–138
W-11	Apollinaris	10/10/71		–18.9	–141
F-571	West of Sylvan Springs	09/10/72		–19.3	–140
T73-20	Grants Pass	09/07/73		–18.5	–135
T74-49	Apollinaris	08/10/74		–18.8	–143
T74-59	Apollinaris	10/10/74		–18.8	–143
T75-73	Apollinaris	10/10/74		–18.2	–142
T76-37	Grants Pass	09/10/76		–18.7	–139
W-1007	Apollinaris	06/14/77		–18.6	–140
W-1022	Cold spring	06/14/77		–19.4	–142
H78-3	Near tributary of Grayling Creek	05/09/78		–19.8	–145
H78-4	Cold spring east of culvert	05/09/78		–19.4	–144
H78-11	Apollinaris	05/10/78		–18.5	–141
T82-5	West of Emerald pool	10/01/82		–18.8	–142
T82-19	Apollinaris	10/04/82		–18.6	–144
		Precipitation			
F-486	Near Gibbon	05/27/70		–18.7	–142
T75-87	Mammoth	12/10/75		–22.4	–168
T75-85	Mammoth	11/10/75		–20.0	–146

Table 3. δD and $\delta^{18}O$ of streams, rivers, springs, lakes, and precipitation in Yellowstone National Park—*Continued*.

Sample	Description	Date sampled (mo/day/yr)	Temperature (°C)	$\delta^{18}O$ (‰)	δD (‰)
		Precipitation—*Continued*			
T75-86	Old Faithful	12/10/75		–20.5	–151
T75-84	Old Faithful	11/10/75		–19.6	–142
W-1021	Old Faithful	06/14/77		–9.4	–64

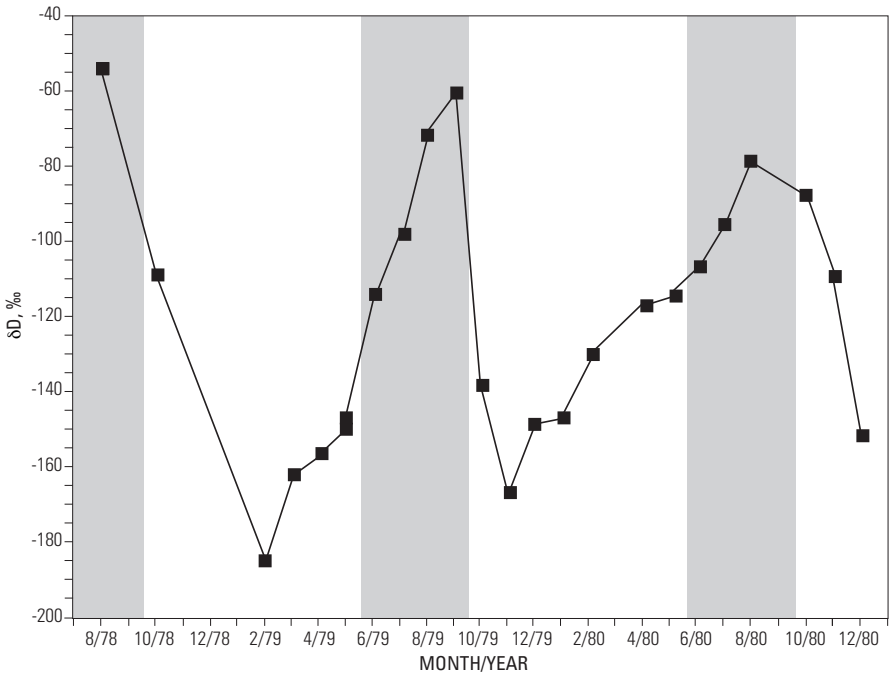

Figure 6. δD of monthly precipitation collections from rain gages at Old Faithful from August 1978 through January 1981.

precipitation rather than a long-term average value. Much of the drinking water in the Park is not from wells but from surface water in reservoirs where evaporation is likely. Because relatively few cold springs and wells were accessible, most of our samples collected after 1967 were from fast-moving cold streams and rivers.

Relationship of δD of Ground Waters to δD of Streams and Rivers

Because sampling of Yellowstone streams was largely limited to the fall season, the isotope systematics of individual streams throughout the year and the relationship of δD values of stream samples to average values for ground water must be predicted by analogy from studies of small cold streams that have been sampled frequently over a period of several years (principles reviewed by Fritz, 1981). In alpine basins with small ground-water-storage capacity, the inflow of ground water causes small sinusoidal annual changes of about ±5 ‰ in δD, with summer values isotopically heavy and winter values light (Hermann and others, 1978). Only the δD of streams during the dry period at the end of summer showed the composition of ground water with a value near that of the average for winter precipitation. Such studies suggest that stream samples collected in the early fall, after the end of summer thunderstorms and before the start of winter storms, probably are representative of ground waters that were recharged largely during the previous spring. Supporting this assumption is an observation that in the Yellowstone region δD values of streams in the fall are mostly within ±4 ‰ of the value recorded for the previous spring (table 4). We do not expect perfect agreement between the values for the spring runoff and fall stream discharge because the ground-water-storage capacity of the reservoirs for springs that feed individual streams probably varies considerably, and some spring reservoirs possibly retain water from several previous years.

Sampling of Streams for δD Analyses

Ideally, the water in streams and rivers should undergo little isotopic change during flow; it should closely reflect the average δD for local ground water feeding the streams through springs and seeps. Ideal streams are those that are fed exclusively from large subsurface reservoirs in which water has a relatively long residence time and has flowed

Table 4. δD of cold waters in Yellowstone National Park and adjacent areas.

Sample	Name	Elevation (meters)	Latitude (N.)	Longitude (W.)	Date (mo/day/yr)	Location	Temperature (°C)	δD (‰)
				GALLATIN RANGE—northwest of Yellowstone National Park				
MH78-21	Spanish Creek	1,620	45°29'	111°16'	10/1/78	before Gallatin River along US 191		-136
MH78-22	Squaw Creek	1,650	45°26'	111°14'	10/1/78	before Gallatin River along US 191		-145
MH78-23	Portal Creek	1,670	45°19'	111°11'	10/1/78	before Gallatin River along US 191		-142
MH78-2	Dudley Creek	1,830	45°15'	111°14'	9/7/78	before Gallatin River along US 191	9	-147
MH78-3	Dudley Creek Spring	1,830	45°15'	111°14'	9/7/78	north of Dudley Creek	14	-149
MH78-4	Porcupine Creek	1,860	45°13'	111°15'	9/7/78	before Gallatin River along US 191	13	-147
MH78-5	Beaver Creek	1,860	45°13'	111°11'	9/7/78	before Gallatin River along US 191		-145
MH78-6	Buck Creek	1,920	45°10'	111°15'	9/7/78	before Gallatin River along US 191		-147
MH78-7	Elkhorn Creek	1,920	45°09'	111°15'	9/7/78	before Gallatin River along US 191	7.5	-148
MH78-1	Buffalo Horn Creek	1,950	45°06'	111°13'	9/6/78	before Gallatin River along US 191	15	-144
MH78-8	Taylor Fork	2,040	45°04'	111°16'	9/7/78	before Wapati Creek	15	-138
MH78-9	Wapiti Creek	2,040	45°04'	111°16'	9/7/78	north of Taylor Creek	15	-139
MH78-10	Taylor Fork Spring	2,010	45°04'	111°10'	9/8/78	at rockpile near Taylor Fork	17	-135
MH78-11	Sage Creek	2,010	45°04'	111°11'	9/7/78	before Big Spring Creek	15	-137
MH78-12	Snowflake Spring	2,010	45°04'	111°11'	9/9/78	1/4 mile south of US 191	12	-152
				ABSAROKA-BEARTOOTH RANGE—*WEST*				
R78-28	Pine Creek		45°30'	110°21'	10/2/78	at quarry 3 mile east of US 89		-141
R78-29	Mill Creek	1,980	45°16'	110°29'	10/2/78	1/2 mile east of Anderson Creek		-143
R78-30	Montanapolis Spring	1,800	45°17'	110°31'	10/2/78	north of Mill Creek Ranch		-152
R78-31	West Fork Mill Creek tributary	1,980	46°14'	110°34'	10/2/78	1/2 mile south Coffee Pot Creek		-147
R78-32	West Mill Creek	1,860	45°16'	110°35'	10/2/78	before Arrastra Creek		-144
R78-33	Arrastra Creek	2,100	45°16'	110°36'	10/2/78	at road to Barbara Ann mine		-148
R78-34	East Fork Mill Creek	1,740	45°19'	110°31'	10/2/78	at Snowy Range Ranch		-148
R78-35	Emigrant Creek	1,830	45°18'	110°41'	10/2/78	end of road in Emigrant Gulch		-142
R78-36	Six Mile Creek	1,620	45°17'	110°46'	10/2/78	at fork in road to Dailey Lake		-144
R78-37	Cedar Creek	1,740	45°09'	110°47'	10/2/78	at road crossing west of ranch		-145
R78-38	Pine Creek	2,100	45°05'	110°37'	10/2/78	at road crossing north of Jardine		-145
R78-39	North Fork Bear Creek	2,120	45°05'	110°38'	10/2/78	at Bear Creek Trail west of Jardine		-149
R78-40	Bear Creek	1,980	45°05'	110°38'	10/2/78	at Jardine		-146
				ABSAROKA-BEARTOOTH RANGE—*CENTRAL*				
R78-19	Stillwater River	1,560	45°21'	109°54'	9/30/78	at campground .5 mile west Beartooth Ranch		-138
R78-20	Woodbine Creek	1,560	45°21'	109°53'	9/30/78	below falls trail before Stillwater River		-137
R78-21	Stillwater River	1,100	45°39'	109°18'	9/30/78	before Yellowstone River near Columbus		-138
R78-22	Boulder River	2,040	45°16'	110°15'	10/1/78	at Box Canyon Guard Station		-148
R78-23	Four Mile Creek	1,860	45°20'	110°14'	10/1/78	before Boulder River		-147
R78-24	Speculator Creek	1,710	45°23'	110°12'	10/1/78	before Boulder River		-147

Table 4. δD of cold waters in Yellowstone National Park and adjacent areas—*Continued*.

Sample	Name	Elevation (meters)	Latitude (N.)	Longitude (W.)	Date (mo/day/yr)	Location	Temperature (°C)	δD (‰)
				ABSAROKA-BEARTOOTH RANGE—*CENTRAL—Continued*				
R78-25	East Chippy Creek	1,680	45°26'	110°11'	10/1/78	before Boulder River (near Weasel Creek)		-146
R78-26	Boulder River	1,460	45°40'	110°06'	10/1/78	before east Boulder River on State 298		-144
R78-27	West Boulder River	1,490	45°37'	110°15'	10/1/78	before Boulder River on road to Livingston		-145
				ABSAROKA-BEARTOOTH RANGE—*EAST*				
R78-12	Cook City Creek	2,350	45°01'	109°55'	9/29/78	on east side of Cooke City on US 212		-139
R78-13	Clarks Fork River	2,130	44°57'	109°48'	9/29/78	below Pilot Creek at US 212 bridge		-136
R78-14	Rock Creek	2,130	45°04'	109°24'	9/29/78	before Lake Fork on US 212		-140
R78-15	W. Fork Rock Creek	2,350	45°10'	109°29'	9/29/78	at Camp Senia		-141
R78-16	East Rosebud Creek	1,890	45°12'	109°39'	9/30/78	at outlet from east Rosebud Lake		-138
R78-17	East Rosebud Creek spring	1,770	45°13'	109°38'	9/30/78	north side east Rosebud 1 mile east of lake		-145
R78-18	West Rosebud Creek	1,370	45°27'	109°30'	9/30/78	before Fishtail Creek at Highway near Fishtail		-139
				GALLATIN RANGE YNP				
W-12	Gardiner River	2,260	44°54'	110°45'	10/11/71	at US 89 near Indian Creek campground		-146
R82-31	Gardiner River	2,260	44°54'	110°45'	9/22/82	at US 89 near Indian Creek campground	5.5	-145
R82-32	Gardiner River	2,260	44°54'	110°45'	9/28/82	at service road before Panther-Indian Creeks	5	-147
R78-6	Gardiner River	2,260	44°54'	110°45'	9/29/78	at bridge on Grand Loop Road		-140
R90-35	Gardiner River	2,260	44°54'	110°45'	9/12/90	at Fawn Pass trail crossing	15	-142
F-478	Glen Creek	2,230	44°56'	110°44'	5/25/70	north of Rustic Falls on US 89		-147
W-3	Glen Creek	2,230	44°56'	110°44'	9/29/71	north of Rustic Falls on US 89		-149
W-13	Glen Creek	2,230	44°56'	110°44'	10/11/71	north of Rustic Falls on US 89		-148
T76-40	Glen Creek	2,230	44°56'	110°44'	9/30/76	north of Rustic Falls on US 89		-153
W-1010	Glen Creek	2,230	44°56'	110°44'	6/14/77	north of Rustic Falls on US 89		-138
T78-66	Glen Creek	2,230	44°56'	110°44'	9/29/78	north of Rustic Falls on US 89		-153
R79-23	Glen Creek	2,230	44°56'	110°44'	9/24/79	north of Rustic Falls on US 89		-148
R82-33	Glen Creek	2,230	44°56'	110°44'	9/28/82	north of Rustic Falls on US 89 (after storms)	5	-152
R82-14	Glen Creek	2,230	44°56'	110°44'	9/28/82	north of Rustic Falls on US 89	9	-151
R90-25	Glen Creek	2,230	44°56'	110°44'	9/12/90	north of Rustic Falls on US 89 (10:50 AM)	7	-147
R90-37	Glen Creek	2,230	44°56'	110°44'	9/12/90	north of Rustic Falls on US 89 (6:00 PM)	13	-148
R90-26	East Fawn Creek	2,410	44°57'	110°49'	9/12/90	on Fawn Pass trail	12	-141
R90-27	East Fawn Creek spring	2,530	44°57'	110°49'	9/12/90	spring north of Fawn at west end of marshes	7	-147
R90-32	East Fawn Creek spring	2,410	44°57'	110°48'	9/12/90	middle spring south of above	4.5	-147
R90-33	East Fawn Creek spring	2,410	44°57'	110°48'	9/12/90	easternmost spring south of above	5	-146
MH78-14	Indian Creek	2,260	44°53'	110°45'	9/29/78	at Indian Creek campground below Panther Creek		-140
R90-39	Indian Creek	2,260	44°53'	110°45'	9/14/90	trail crossing near Panther Creek (11:00 AM)	9	-138
R90-42	Indian Creek	2,260	44°53'	110°45'	9/14/90	same location (3:00 PM)	13	-138
R90-41	Indian Creek	2,270	44°52'	110°48'	9/14/90	before gravel flats	8	-135

Table 4. δD of cold waters in Yellowstone National Park and adjacent areas—*Continued*.

Sample	Name	Elevation (meters)	Latitude (N.)	Longitude (W.)	Date (mo/day/yr)	Location	Temperature (°C)	δD (‰)
				GALLATIN RANGE YNP—*Continued*				
R90-40	Panther Creek	2,380	44°53'	110°49'	9/14/90	on Bighorn Pass trail	6. 5	-139
R67-2	Apollinaris Spring	2,230	44°51'	110°44'	9/1/67	east of US 89		-144
R82-4	Daly Creek	2,070	45°04'	111°08'	9/22/82	before Gallatin River at US 191	14	-151
R90-10	Daly Creek	2,070	45°04'	111°08'	9/12/90	before Gallatin River at US 191	5	-146
W-807	Black Butte Creek	2,200	45°03'	111°07'	9/30/76	before Gallatin River at US 191		-149
W-1018	Black Butte Creek	2,200	45°03'	111°07'	6/14/77	before Gallatin River at US 191		-145
MH78-15	Black Butte Creek	2,200	45°03'	111°07'	9/30/78	before Gallatin River at US 191		-148
R79-8	Black Butte Creek	2,200	45°03'	111°07'	9/23/79	before Gallatin River at US 191	6	-143
R82- 5	Black Butte Creek	2,200	45°03'	111°07'	9/22/82	before Gallatin River at US 191	9	-151
R90-11	Black Butte Creek	2,200	45°03'	111°07'	9/12/90	before Gallatin River at US 191	4	-146
MH78-16	Specimen Creek	2,200	45°01'	111°05'	9/30/78	before Gallatin River at US 191		-147
R79-7	Specimen Creek	2,200	45°01'	111°05'	9/23/79	before Gallatin River at US 191	6	-144
R82-6	Specimen Creek	2,200	45°01'	111°05'	9/22/82	before Gallatin River at US 191	9	-146
R90-12	Specimen Creek	2,200	45°01'	111°05'	9/12/90	before Gallatin River at US 191	4	-139
R79-6	Fan Creek	2,230	44°57'	111°04'	9/23/79	before Gallatin River at US 191	6	-139
R90-17	Fan Creek	2,230	44°57'	111°04'	9/12/90	before Fawn Creek on Fawn Pass trail	15	-144
R90-13	Fawn Creek trail spring	2,230	44°57'	111°04'	9/12/90	westernmost spring south of Fawn Creek	5.5	-145
R90-15	Fawn Creek trail spring	2,230	44°57'	111°04'	9/12/90	easternmost spring south of Fawn Creek	5.5	-142
R90-16	Fawn Creek trail spring	2,230	44°57'	111°04'	9/12/90	just above Fan Creek on Fawn Pass trail	12	-142
MH78-17	Gallatin River	2,200	44°56'	111°04'	9/30/78	at Bighorn Pass trail head at US 191		-143
R79-9	Gallatin River	2,200	44°56'	111°04'	9/23/79	at Bighorn Pass trail head at US 191	6	-139
T76-47	Grayling Creek	2,160	44°53'	111°03'	9/30/76	before main creek turns S at US 191		-140
W-1003	Grayling Creek	2,160	44°53'	111°03'	6/14/77	before main creek turns S at US 191		-133
MH78-18	Grayling Creek	2,160	44°53'	111°03'	9/30/78	before main creek turns S at US 191		-139
R90-18	Grayling Creek	2,160	44°53'	111°03'	9/12/90	before main creek turns S at US 191	11	-138
R79-5	Grayling Creek	2,160	44°53'	111°03'	9/23/79	before main creek turns S at US 191	6	-135
T76-46	Grayling Creek spring	2,160	44°52'	111°03'	9/30/76	Spring near US 191 between above and below		-147
MH78-24	Grayling Creek spring	2,160	44°52'	111°03'	10/1/78	Spring near US 191 between above and below		-143
R79-4	Grayling Creek spring	2,160	44°52'	111°03'	9/23/79	Spring near US 191 (very little flow)	6	-136
T76-44	Grayling Creek tributary	2,100	44°51'	111°03'	9/30/76	east tributary at State boundary and US 191		-143
W-1019	Grayling Creek tributary	2,100	44°51'	111°04'	6/22/77	east tributary at State boundary and US 191		-137
T76-43	Grayling Creek tributary	2,100	44°51'	111°04'	9/30/76	1 mi southwest of State boundary on US 191		-140
W-1008	Grayling Creek tributary	2,100	44°51'	111°04'	6/14/77	1 mi southwest of State boundary on US 191		-136
R79-3	Grayling Creek tributary	2,100	44°51'	111°04'	9/23/79	1 mi southwest of State boundary on US 191	6.5	-139
R82-7	Grayling Creek tributary	2,100	44°51'	111°04'	9/22/82	1 mi southwest of State boundary on US 191		-145
MH78-19	Duck Creek	2,040	44°47'	111°07'	9/30/78	at US 191		-141
R79-1	Duck Creek	2,040	44°47'	111°07'	9/23/79	at US 191	9.5	-137
R90-19	Duck Creek	2,040	44°47'	111°07'	9/12/90	at US 191	18	-136
MH78-20	Cougar Creek	2,000	44°45'	111°07'	9/30/78	at US 191		-142

Table 4. δD of cold waters in Yellowstone National Park and adjacent areas—*Continued*.

Sample	Name	Elevation (meters)	Latitude (N.)	Longitude (W.)	Date (mo/day/yr)	Location	Temperature (°C)	δD (‰)
				GALLATIN RANGE YNP—*Continued*				
R79-2	Cougar Creek	2,000	44°45'	111°07'	9/23/79	at US 191	9	-138
R90-21	Pipe Creek	2,180	45°02'	110°52'	9/11/90	tributary to Mol Heron Creek, .5 mi N. of Park	6	-141
R90-24	Reese Creek	1,700	45°03'	110°47'	9/11/90	1.5 mi southwest of US 89	7	-143
				WASHBURN RANGE				
R78-1	Lava Creek	2,070	44°56'	110°38'	9/29/78	before Lupine at Lava Creek Campground		-146
R82-15	Lava Creek	2,070	44°56'	110°38'	9/22/82	before Lupine at Lava Creek Campground	9.5	-148
R82-34	Lava Creek	2,070	44°56'	110°38'	9/28/82	before Lupine at Lava Creek (after storm)	6	-150
R90-3	Lava Creek	2,070	44°56'	110°38'	9/10/90	before Lupine at Lava Creek Campground	15	-146
R90-4	Lupine Creek	2,070	44°56'	110°38'	9/10/90	before Lava Creek	15	-147
R78-2	Blacktail Creek	2,070	44°56'	110°36'	9/29/78	after Deer Creek		-145
R82-16	Blacktail Creek	2,070	44°56'	110°36'	9/22/82	after Deer Creek	11	-144
R82-35	Blacktail Creek	2,070	44°56'	110°36'	9/28/82	after Deer Creek (after storms)	5	-149
R90-5	Blacktail Creek	2,070	44°56'	110°36'	9/10/90	after Deer Creek	16	-145
R90-6	Deer Creek	2,070	44°57'	110°36'	9/10/90	east of Blacktail Creek	14	-141
R78-3	Elk Creek	2,040	44°56'	110°27'	9/29/78	at Grand Loop highway (after storms)		-147
R82-17	Elk Creek	2,040	44°56'	110°27'	9/22/82	at Grand Loop highway	6.5	-147
R90-7	Elk Creek	2,040	44°56'	110°27'	9/10/90	at Grand Loop highway	12	-143
W75-6	Tower Creek	2,040	44°55'	110°25'	11/5/75	above Tower falls		-144
R78-4	Tower Creek	2,040	44°55'	110°25'	9/29/78	above Tower falls		-144
R82-18	Tower Creek	2,040	44°55'	110°25'	9/22/82	above Tower falls	11	-146
R82-41	Tower Creek	2,040	44°55'	110°25'	9/28/82	above Tower falls (after storms)	6	-150
R90-8	Tower Creek	2,040	44°55'	110°25'	9/10/90	above Tower falls	13	-144
W75-5	Antelope Creek	2,130	44°54'	110°23'	11/5/75	at Grand Loop highway		-148
W-785	Antelope Creek	2,130	44°54'	110°23'	9/27/76	at Grand Loop highway		-153
W-1014	Antelope Creek	2,130	44°54'	110°23'	6/14/77	at Grand Loop highway		-147
R78-5	Antelope Creek	2,130	44°54'	110°23'	9/29/78	at Grand Loop highway		-152
R79-10	Antelope Creek	2,130	44°54'	110°23'	9/24/79	at Grand Loop highway		-149
R82-19	Antelope Creek	2,130	44°54'	110°23'	9/22/82	at Grand Loop highway		-150
R90-9	Antelope Creek	2,130	44°54'	110°23'	9/10/90	at Grand Loop highway	13	-147
W-784	Dunraven Peak Creek	2,590	44°46'	110°27'	9/27/76	at Grand Loop highway		-144
W-1015	Dunraven Peak Creek	2,590	44°46'	110°27'	6/14/77	at Grand Loop highway		-146
MH78-13	Dunraven Peak Creek	2,590	44°46'	110°27'	9/29/78	at Grand Loop highway		-143
				BUFFALO PLATEAU				
R77-7	Buffalo Plateau creek	1,950	44°59'	110°26'	10/10/77	at Hellroaring Creek, .5 mi S. State boundary		-150
R77-10	Little Cottonwood Creek	1,770	45°00'	110°29'	10/10/77	at Black Canyon Yellowstone trail		-146
R77-11	Black Canyon trail spring	1,760	45°00'	110°30'	10/10/77	small spg. on Black Canyon Yellowstone trail		-159

Table 4. δD of cold waters in Yellowstone National Park and adjacent areas—*Continued*.

Sample	Name	Elevation (meters)	Latitude (N.)	Longitude (W.)	Date (mo/day/yr)	Location	Temperature (°C)	δD (‰)
				BUFFALO PLATEAU—*Continued*				
R78-11	Slough Creek	1,920	44°57'	110°31'	9/29/78	above Buffalo Creek		-142
R82-24	Slough Creek	1,920	44°57'	110°31'	9/22/82	below Buffalo Creek at campground	12	-142
R82-36	Slough Creek	1,920	44°57'	110°31'	9/28/82	same (after storm)		-146
R90-48	Slough Creek	1,920	44°57'	110°31'	9/12/90	below Buffalo Creek at campground	16	-140
R82-38	Slough Creek campground well	1,920	44°57'	110°31'	9/28/82	well at Buffalo Creek campground		-143
R90-49	Slough Creek campground well	1,920	44°57'	110°31'	9/12/90	well at Buffalo Creek campground	18	-141
R82-37	Buffalo Creek	1,920	44°57'	110°31'	9/28/82	above Slough Creek (after storm)	6	-143
				MADISON PLATEAU				
R78-41	Little Firehole River	2,380	45°29'	110°52'	10/5/78	just above Mystic Falls		-139
R67-1	Little Firehole River	2,380	45°29'	110°52'	9/1/67	just above Mystic Falls		-142
R82-26	Little Firehole River	2,380	45°29'	110°52'	9/23/82	just above Mystic Falls	11	-141
R90-56	Little Firehole River	2,380	45°29'	110°52'	9/15/90	just above Mystic Falls	14	-141
W-9	Black Sand Basin spring	2,320	45°27'	110°52'	10/10/71	base of Rhyolite cliffs above Black Sand basin		-143
R78-42	Black Sand Basin spring	2,320	45°27'	110°52'	10/5/78	base of Rhyolite cliffs above Black Sand basin	4	-139
R82-25	Black Sand Basin spring	2,320	45°27'	110°52'	9/23/82	base of Rhyolite cliffs above Black Sand basin	10	-143
R90-38	Black Sand Basin spring	2,320	45°27'	110°52'	9/13/90	base of Rhyolite cliffs above Black Sand basin	11	-141
W-5	Lonestar road spring	2,320	45°26'	110°48'	9/29/71	by road to Lonestar geyser		-142
R82-27	Madison River	2,040	45°39'	111°01'	9/29/82	at Madison Range overlook	17	-145
R82-42	Madison River	2,040	45°39'	111°01'	9/28/82	at Madison Range overlook	11	-146
R82-72	Boundary Creek	2,040	44°11'	111°00'	9/30/82	1/2 mi before Bechler River on Bechler trail	11	-136
R82-73	Snow Creek	2,040	44°15'	111°06'	10/1/82	at Park boundary road 509	7	-135
R82-74	South Fork Partridge Creek	2,040	44°20'	111°08'	10/1/82	1 mi north of Snow Creek at Park boundary	3	-135
				CENTRAL PLATEAU				
R67-41	Gibbon River	2,380	44°43'	110°39'	9/1/67	just above Virginia Cascades	7	-140
F-486	Gibbon River	2,380	44°43'	110°39'	5/25/70	just above Virginia Cascades		-142
W-2	Gibbon River	2,380	44°43'	110°39'	9/29/71	just above Virginia Cascades		-142
W-782	Gibbon River	2,380	44°43'	110°39'	9/27/76	just above Virginia Cascades		-142
R82-9	Gibbon River	2,380	44°43'	110°39'	9/21/82	just above Virginia Cascades	10	-143
R90-20	Gibbon River	2,380	44°43'	110°39'	9/11/90	just above Virginia Cascades	15	-140
W-783	Gibbon River	2,380	44°43'	110°38'	9/27/76	Virginia Meadows area		-144
W-1012	Gibbon River	2,380	44°43'	110°38'	6/14/77	Virginia Meadows area		-142
MH78-25	Gibbon River	2,380	44°43'	110°38'	10/5/78	Virginia Meadows area		-143
W-27	Gibbon Hill stream	2,320	44°43'	110°41'	10/2/72	small unnamed stream on Gibbon Hill		-141
T78-63	Norris Geyser Basin	2,290	44°44'	110°42'	10/5/78	cold water supply		-140
W-33	Nez Perce Creek	2,200	44°35'	110°47'	10/4/72	at gate to service road		-144
W-4	Nez Perce Creek	2,200	44°35'	110°47'	9/29/71	at gate to service road		-144

Table 4. δD of cold waters in Yellowstone National Park and adjacent areas—*Continued*.

Sample	Name	Elevation (meters)	Latitude (N.)	Longitude (W.)	Date (mo/day/yr)	Location	Temperature (°C)	δD (‰)
				CENTRAL PLATEAU—*Continued*				
R82-29	Nez Perce Creek	2,200	44°35'	110°47'	9/25/82	1 mile east of gate to service road	19	-149
R90-43	Nez Perce Creek	2,200	44°35'	110°47'	9/14/90	100 yds. east of US 89	16.5	-145
W-6	Midway Geyser Basin spring	2,260	44°32'	110°50'	9/29/71	at Lower Basin picnic ground		-141
W75-1	Midway Geyser Basin spring	2,260	44°32'	110°50'	10/10/75	at Lower Basin picnic ground		-142
W-18	Delacy Creek	2,440	44°26'	110°41'	10/11/71	about 100 yards north of US 89		-138
W-792	Delacy Creek	2,440	44°26'	110°41'	9/28/76	about 100 yards north of US 89		-141
W-1002	Delacy Creek	2,440	44°26'	110°41'	6/21/77	about 100 yards north of US 89		-134
MH78-26	Delacy Creek	2,440	44°26'	110°41'	10/5/78	about 100 yards north of US 89		-136
R79-16	Delacy Creek	2,440	44°26'	110°41'	9/24/79	about 100 yards north of US 89		-138
R90-55	Delacy Creek	2,440	44°26'	110°41'	9/15/90	about 100 yards north of US 89	8	-137
R90-54	Dry Creek	2,440	44°26'	110°41'	9/15/90	north of bridge on highway	6	-138
W-10	Old Faithful drinking water	2,240	44°26'	110°48'	10/10/71	cold water supply		-138
MH78-27	Old Faithful drinking water	2,240	44°26'	110°48'	10/5/78	cold water supply		-134
W-25	Lake Junction area creek	2,380	44°35'	110°23'	10/12/71	small creek 2 mi north Lake Junction		-145
R90-44	Lake Junction area creek	2,380	44°35'	110°23'	9/14/90	small creek 2 mi north Lake Junction	9	-140
R82-11	Yellowstone Lake area creek	2,380	44°33'	110°25'	9/21/82	small creek 2 miles north of Yellowstone Lake	10	-148
W-43	Yellowstone River	2,380	44°36'	110°22'	10/4/72	near Cascade campground		-125
R82-10	Yellowstone River	2,380	44°36'	110°22'	9/21/82	near Cascade campground		-130
	Yellowstone River	2,380	44°36'	110°22'	10/5/78	at Fishing bridge		-130
R79-21	Yellowstone River	2,380	44°34'	110°22'	9/24/79	at Fishing bridge		-127
R90-45	Yellowstone Lake	2,380	44°34'	110°22'	9/14/90	at Fishing bridge	20	-128
W75-3	Arnica Creek	2,380	44°28'	110°32'	10/10/75	north of Grand Loop Road		-144
	Arnica Creek	2,380	44°28'	110°32'	10/5/78	north of Grand Loop Road		-148
R79-17	Arnica Creek	2,380	44°28'	110°32'	9/24/79	north of Grand Loop Road		-143
R82-12	Arnica Creek	2,380	44°28'	110°32'	9/21/82	north of Grand Loop Road	14	-146
R90-2	Arnica Creek	2,380	44°28'	110°32'	9/10/90	north of Grand Loop Road	16	-146
W75-2	Little Thumb Creek	2,350	44°25'	110°35'	10/10/75	west of US 89		-137
R79-22	Little Thumb Creek	2,350	44°25'	110°35'	9/24/79	west of US 89		-133
				MIRROR PLATEAU				
R76-13	Specimen Ridge trail spring	2,680	44°49'	110°14'	9/30/76	on Specimen trail		-144
R76-14	Amethyst Creek	2,010	44°53'	110°14'	9/30/76	on Specimen trail		-145
W75-7	Crystal Creek	1,890	44°55'	110°18'	10/5/75	above Lamar River on US 212		-143
R90-52	Crystal Creek	1,890	44°55'	110°18'	9/14/90	above Lamar River on US 212	10	-145
				ABSAROKA RANGE				
R76-5	Lamar River	2,130	44°52'	110°11'	9/30/76	at trail before Lamar River		-142
R76-6	Miller Creek	2,130	44°46'	110°06'	9/30/76	at trail before Lamar River		-143

Table 4. δD of cold waters in Yellowstone National Park and adjacent areas—*Continued*.

Sample	Name	Elevation (meters)	Latitude (N.)	Longitude (W.)	Date (mo/day/yr)	Location	Temperature (°C)	δD (‰)
				ABSAROKA RANGE—*Continued*				
R76-7	Calfee Creek	2,100	44°47'	110°07'	9/30/76	at trail before Lamar River		-142
R76-10	Cache Creek	2,040	44°50'	110°10'	9/30/76	at trail before Miller Creek		-140
W75-8	Larmar River	2,010	44°52'	110°12'	10/5/75	after Soda Butte		-142
R78-7	Larmar River	2,010	44°52'	110°11'	9/29/78	after Soda Butte		-141
R82-23	Larmar River	2,010	44°52'	110°11'	9/22/82	after Soda Butte		-143
R82-40	Larmar River	2,010	44°52'	110°11'	9/28/82	after Soda Butte (very muddy after storm)		-157
R82-21	Larmar River	2,010	44°52'	110°11'	9/22/82	after Soda Butte	7	-142
R90-51	Larmar River	2,010	44°52'	110°11'	9/14/90	after Soda Butte	10	-139
W-789	Pebble Creek	2,070	44°55'	110°07'	9/27/76	at Pebble Creek campground		-146
W-1009	Pebble Creek	2,070	44°55'	110°07'	6/14/77	at Pebble Creek campground		-144
R78-9	Pebble Creek	2,070	44°55'	110°07'	9/29/78	at Pebble Creek campground		-142
R79-13	Pebble Creek	2,070	44°55'	110°07'	9/24/79	at Pebble Creek campground		-143
R82-22	Pebble Creek	2,070	44°55'	110°07'	9/22/82	at Pebble Creek campground	10	-144
R90-50	Pebble Creek	2,070	44°55'	110°07'	9/14/90	at Pebble Creek campground	13	-139
R78-11	Soda Butte Creek	2,200	45°00'	110°00'	9/29/78	at park entrance		-140
W-1020	Soda Butte Creek	2,010	44°55'	110°06'	6/14/77	above Amphitheater		-144
W-787	Soda Butte Creek	2,010	44°52'	110°11'	9/27/76	above Lamar		-142
R82-20	Soda Butte Creek	2,010	44°52'	110°11'	9/22/82	above Lamar		-142
R82-39	Soda Butte Creek	2,010	44°52'	110°11'	9/28/82	above Lamar (after storm)	8	-147
W-788	Amphitheater Creek	2,100	44°55'	110°06'	9/27/76	above Soda Butte		-136
R79-14	Amphitheater Creek	2,100	44°55'	110°06'	9/24/79	above Soda Butte		-142
R82-21	Amphitheater Creek	2,100	44°55'	110°06'	9/22/82	above Soda Butte		-142
W75-4	Cub Creek	2,560	44°30'	110°12'	11/5/75	at US 20		-137
W-1004	Cub Creek	2,560	44°30'	110°12'	6/14/77	at US 20		-146
W-795	Cub Creek	2,560	44°30'	110°12'	9/28/76	at US 20		-142
W-796	Cub Creek	2,560	44°30'	110°12'	10/1/76	at US 20		-142
MH78-30	Cub Creek	2,560	44°30'	110°12'	10/5/78	at US 20		-141
R79-18	Cub Creek	2,560	44°30'	110°12'	9/26/79	at US 20		-137
R90-46	Cub Creek	2,560	44°30'	110°12'	9/14/90	at US 20	16	-139
W-795	Clear Creek	2,560	44°29'	110°10'	10/1/76	at US 20		-142
W-1017	Clear Creek	2,560	44°29'	110°10'	6/14/77	at US 20		-143
R79-20	Clear Creek	2,560	44°29'	110°10'	9/26/79	at US 20		-133
R82-75	Clear Creek	2,560	44°29'	110°10'	10/3/82	at US 20		-142
				PITCHSTONE PLATEAU AND SNAKE R. DRAINAGE—*PITCHSTONE PLATEAU*				
R82-45	North Boone Creek	1,950	44°06'	110°56'	9/29/82	at Reclamation road (snowing)	4	-137
R82-46	Calf Creek	2,200	44°08'	110°53'	9/29/82	at Reclamation road (1 ft snow on ground)	3	-136
R82-49	Glade Creek	2,200	44°07'	110°47'	9/29/82	at Reclamation road (Lakes in Drainage)	3	-132
R82-58	Rock Creek	1,930	44°07'	111°06'	9/29/82	at Cave Falls road	6	-131

Table 4. δD of cold waters in Yellowstone National Park and adjacent areas—*Continued*.

Sample	Name	Elevation (meters)	Latitude (N.)	Longitude (W.)	Date (mo/day/yr)	Location	Temperature (°C)	δD (‰)
PITCHSTONE PLATEAU AND SNAKE R. DRAINAGE—*PITCHSTONE PLATEAU—Continued*								
R82-59	Beaver Creek	1,800	44°07'	111°08'	9/29/82	at Cave Falls road	6.5	-133
R82-60	Robinson Creek	1,740	44°08'	111°10'	9/29/82	at end of Sawmill Creek road	10	-133
R82-61	Porcupine Creek	1,710	44°05'	111°13'	9/29/82	at Cave Falls road		-132
R82-73	Snow Creek	2,070	44°15'	111°06'	10/1/82	at Park boundary road 509	7	-135
R82-74	North Fork Partridge Creek	2,290	44°20'	111°09'	10/1/82	1 mile north of Snow Creek at Park boundary	3	-135
PITCHSTONE PLATEAU AND SNAKE R. DRAINAGE—*BECHLER RIVER*								
R82-62	Bechler River	2,130	44°15'	110°56'	9/30/82	at stock crossing of river	7	-134
R82-63	Bechler River area creek	2,130	44°15'	110°56'	9/30/82	small creek 100 yards from stock ford	5	-131
R82-64	Bechler River area spring	2,100	44°15'	110°56'	9/30/82	30-40 gallon/minute spring on Bechler trail	6	-134
R82-65	Bechler River area spring	2,040	44°15'	110°56'	9/30/82	14 gallon/minute spring Bechler trail	4	-132
R82-66	Bechler River area spring	2,010	44°15'	110°56'	9/30/82	3 gallon/minute spring Bechler trail	3.5	-134
R82-69	Bechler River area spring	1,980	44°14'	110°57'	9/30/82	spring near fall tree fishing hole	4	-135
R82-72	Boundary Creek	1,890	44°11'	111°00'	9/30/82	at south edge of Bechler Meadow		-136
PITCHSTONE PLATEAU AND SNAKE R. DRAINAGE—*SHOSHONE LAKE AREA*								
T73-20	Grants Pass Spring	2,410	44°23'	110°49'	9/00/73	at Grant Pass on Howard Eaton trail		-135
W-804	Grants Pass Spring	2,410	44°23'	110°49'	10/4/76	at Grant Pass on Howard Eaton trail		-143
T73-87	Shoshone Fall Creek	2,410	44°23'	110°47'	9/00/73	above thermal area		-130
PITCHSTONE PLATEAU AND SNAKE R. DRAINAGE—*HEART LAKE AREA*								
T78-38	North Fork of Witch Creek	2,320	44°18'	110°30'	10/4/78	at Fissure group		-137
T78-39	South Fork of Witch Creek	2,320	44°18'	110°30'	10/4/78	at Fissure group		-142
T78-44	Witch Creek	2,320	44°17'	110°32'	10/4/78	above all thermal springs		-140
PITCHSTONE PLATEAU AND SNAKE R. DRAINAGE—*SNAKE RIVER AREA*								
R78-43	Snake River	2,070	44°06'	110°40'	10/6/78	at bridge on US 89		-136
R82-1	Snake River	2,070	44°06'	110°40'	9/21/82	at bridge on US 89	11	-133
R82-50	Snake River	2,070	44°06'	110°40'	9/29/82	at bridge on US 89	8	-132
R90-1	Snake River	2,070	44°06'	110°40'	9/9/90	at bridge on US 89	17	-131
R82-51	Crawfish Creek	1,950	44°09'	110°41'	9/29/82	above Moose Falls on US 89	14	-139
R82-52	Polecat Creek	2,070	44°07'	110°42'	9/29/82	1 mile west of Flagg Ranch	14	-126

short distances with minimum evaporation. Those streams are likely to have temperatures only slightly higher than that of the ground water. Even on warm days in the Yellowstone region, temperatures of streams were seldom observed to be more than 10°C higher than temperatures recorded in local cold springs, and the δD of the streams did not change during the day as their temperatures rose. Such streams are the most likely streams to have fairly uniform δD values from year to year when sampled in the fall at times that specifically avoid major storms.

Isolating the effect of possible evaporation on the δD of stream water is difficult in mountainous regions because the inflow is from many inconspicuous sources along the courses of the streams. Where gradients are steep, the water comes from a range of altitudes, possibly with different isotopic compositions. However, evaporation is expected to be limited at the low temperatures of the springs and within the short average distances of flow from the springs to our sampling points. This assumption is supported by the clustering of data around the GMWL in figure 5 and by isotope studies of rivers (Friedman and others, 1964; Fritz, 1981) that have shown that flowing water in temperate climates normally undergoes very little change in δD due to evaporation. Even the Nile River undergoes a δD increase of only 3 ‰ during its 2,900-km journey from source to ocean (Friedman and others, 1964). Thus, it is not surprising that we observed no change in δD of the Stillwater River in sample sites 65 km apart (table 4).

Lake water, however, with a long residence time, generally shows significant increases in δD and $\delta^{18}O$ due to evaporation (Friedman and others, 1964; Gat, 1981). The compositions of lake waters in figure 5 plot on a typical evaporation trend. The difference in δD values between Yellowstone Lake (–128 to –133 ‰) and the average of accessible inflowing streams (–135 ‰) is due largely to evaporation. The isotopic change occurs over the 10-year average residence time (Pearson and Truesdell, 1978) of water in Yellowstone Lake. In order to minimize possible effects of evaporation, we avoided streams that traversed standing bodies of water, such as lakes, or that received significant inflow from swampy meadows.

Results: δD of Surface Water in the Greater Yellowstone Area

The δD values of nearly 300 water samples from cold springs, wells, cold creeks, and rivers, collected from 1967 to 1990, and their locations are listed in table 4. More detailed locations, on U.S. Geological Survey Yellowstone National Park or quadrangle topographic maps, can be obtained from the information in table 4. General sample locations, δD values, and pertinent physiographic features are shown in figure 7.

Areas North of the Park

In 1979, streams draining Precambrian to Mesozoic volcanic, igneous, and sedimentary rocks of the Gallatin and Madison Ranges north and west of the Park were sampled from Highway 191 along the Gallatin River drainage for nearly 40 km north of the Park. The highest peaks are higher than 3,350 m (11,000 ft) altitude, and steams flowing into the Gallatin River have steep gradients to the sampling points at 1,525–1,825 m (5,000–6,000 ft) altitude. The δD values of most streams ranged from –144 to –147 ‰. A spring a short distance outside of the Park had a δD value of –152 ‰, and a spring 40 km north of the Park boundary had a value of –149 ‰, differing considerably from values of nearby streams. These springs have not been sampled over a time interval to determine whether the lower δD values reflect recharge at higher altitudes than the inflow for the streams or ephemeral recharge from the last storm in the area.

The Absaroka Mountains to the north of the Park between the Yellowstone and Boulder-Stillwater Rivers are characterized by volcanic and Precambrian terrain. That area was sampled in a road traverse in 1978. Much of the area is higher than 3,050 m (10,000 ft) altitude; samples were collected from altitudes of 1,525–2,450 m (5,000–8,000 ft) from streams with steep gradients. The δD values of most of the sampled streams near the Park ranged from –144 to –149 ‰. The δD values of water in the Stillwater River and its tributaries did not vary significantly over a distance of nearly 65 km and over an altitude change of 1,225 m (4,000 ft) before the Stillwater flowed into the Yellowstone River suggesting that, for this stream, typical of those we studied, evaporation and mixing of water from different altitudes had minimal effect on δD values. In 1978, the Montanapolis warm spring had a δD value of –153 ‰, 6–10 ‰ lower than the value of local recharge in the area. This spring possibly was recharged during a colder climate than the nearby cold streams and was warmed by deep circulation. The low δD value of this warm spring, relative to local recharge water, is consistent with a similar relationship of δD values for water from deep warm wells and springs, relative to local recharge water in an area from southeastern California to the Snake River Plain in southern Idaho (Smith and others, 2002). As pointed out by these authors, the water in these wells was probably recharged during Pleistocene glaciation.

The area north of the Park between the Stillwater River and U.S. Highway 212 contains the Beartooth Wilderness Area with peaks higher than 3,650 m (12,000 ft) chiefly composed of Precambrian rocks. Suitable sampling sites were limited along the road traverse because many drainages in the high country contain glacial lakes. However, the sampled streams and rivers adjacent to the Beartooth Range have a remarkably narrow range of δD values (–137 to –141 ‰). The single spring sampled had a lower δD value of –144 ‰. The δD values of streams in the Beartooth region are higher (less negative) than those farther west in the Absaroka and Gallatin Ranges.

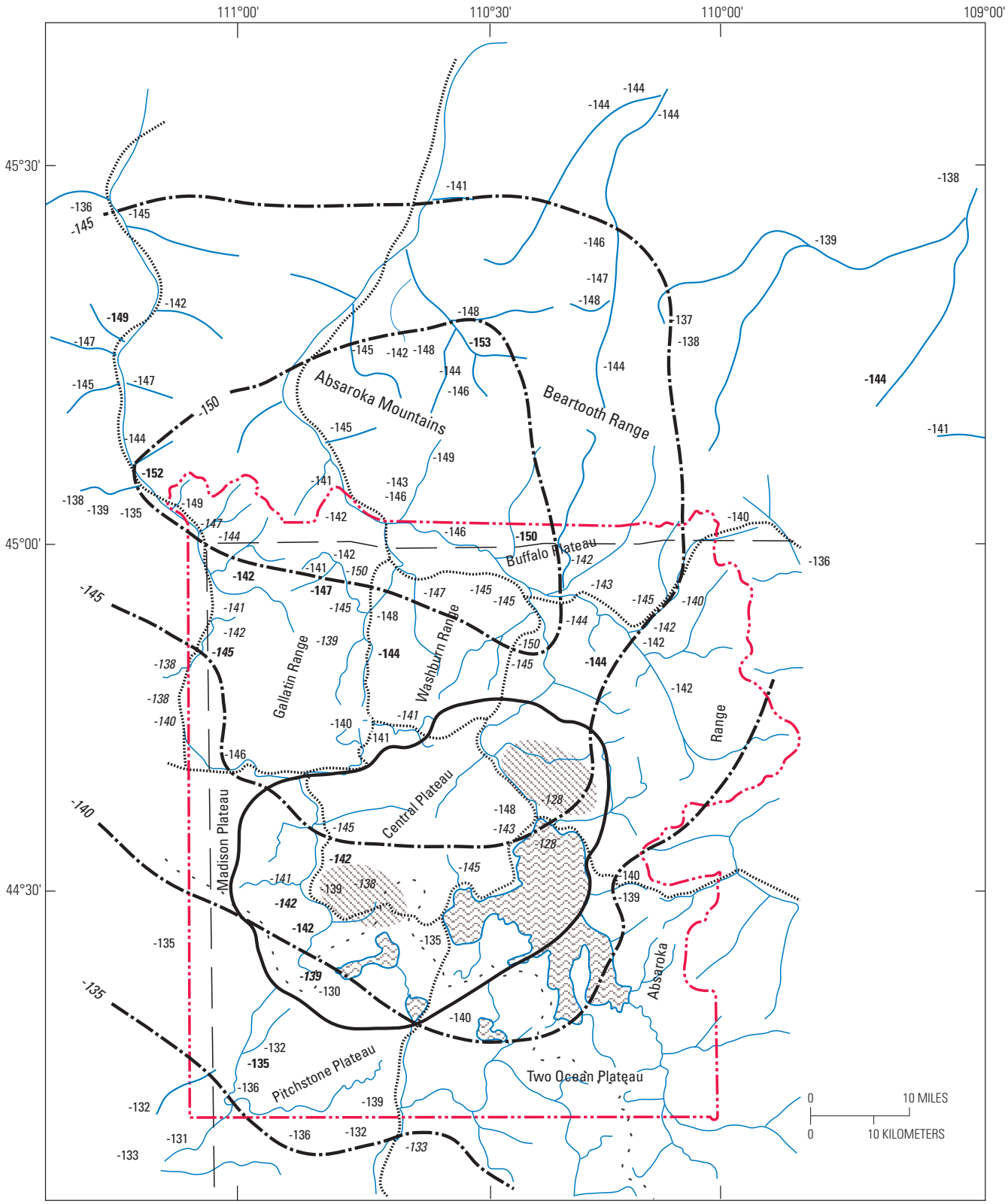

Figure 7. Sketch map of Yellowstone National Park and adjacent area showing select topographic features and the δD of cold waters at each sample site. The δD values are plotted in the general vicinity of sample sites. For detailed locations see table 4. Bold numbers indicate samples of springs and wells. Italics indicate average values for several years. Plain numbers indicate only one sample analyzed. Contours (dot dashed lines) are drawn around the most negative δD values, guided by values for samples believed to be most representative of infiltrating waters. See figure 1 for meaning of other lines and patterns.

Gallatin Range

The Gallatin Range in the northwestern part of the Park is bounded by the Gallatin River on the west, the Gardiner River on the northeast, and the Madison River on the south. The range contains some of the highest altitudes and the largest area of high mountains in the Park. On the north side, δD values from the Gardiner River ranged from –140 to –147 ‰, whereas δD values from Glen Creek (sampled almost yearly from 1970 to 1990) ranged from –147 to –153 ‰. In 1990, the δD value of (east) Fawn Creek was –141 ‰, whereas values from springs along the north and south sides of the creek were –146 to –147 ‰. On the west side, δD values of Daly, Black Butte, Specimen, Fan, and (west) Fawn Creeks ranged from –139 to –151 ‰. In 1990, the δD values of springs along the south side of (east) Fawn Creek were –142 to –145 ‰. The δD value of cold streams in the southern part of the range were less negative (–135 to –142 ‰), based on data from Duck, Cougar, Panther, and Indian Creeks. A small spring with variable flow near Grayling Creek has δD values of –136 to –147 ‰. It appears that, for a given year, the δD values of the fall stream discharges from the northern Gallatin Range are an average of about 5 ‰ lower than those from the southern part of the range.

Washburn Range

The Washburn Range, north of the caldera and including the area surrounded by the northern loop of the Yellowstone Highway, contains watersheds that drain into the Gardiner, Gibbon, and Yellowstone Rivers. This area includes Mount Washburn, with an altitude higher than 3,100 m (10,200 ft). On the north side of the range, Lava, Blacktail Deer, Elk, and Tower Creeks had δD values from –143 to –148 ‰, whereas Antelope Creek, on the east side of the range, which is probably recharged at higher altitudes on Mount Washburn, had lower δD values (from –147 to –153 ‰). This is one of the few cases in which we observed clear variation of δD with altitude for inflow in a given basin. The δD values of the Gibbon River above Virginia Meadows ranged from –140 to –143 ‰, consistent with an increase in the δD values of surface waters to the south.

Buffalo Plateau

The Buffalo Plateau is north of the Yellowstone and Lamar Rivers and Slough Creek, and it extends outside the Park. The highest altitudes are higher than 3,050 m (10,000 ft) largely on Precambrian rocks. A small, but fast moving, cold stream draining the high plateau had a δD value of –150 ‰ in 1977. Slough Creek, Little Cottonwood Creek, and Buffalo Creek had δD values of –140 to –146 ‰ from 1977 to 1990.

Absaroka Range

The Absaroka Range is a large north-south-trending chain of mountains in the entire eastern part of the Park and north of the Park where it joins the Beartooth Wilderness Area on the east and the Gallatin National Forest region on the west. Along the eastern margin of the Park, the Absaroka Range consists of intermediate-silica volcanics—remnants of Eocene stratovolcanoes. Topography is steep, and peaks along the ridge of the range are commonly higher than 3,050 m (10,000 ft). The δD values from streams in the Lamar River–Soda Butte drainage ranged from –139 to –144 ‰, with an average value of –142 ‰. In the area near Sylvan Pass, δD values from Cub Creek ranged from –133 to –142 ‰, with an average value of –139 ‰. The streams near Sylvan Pass were sampled at altitudes from higher than 2,600 m (8,500 ft) to lower than 2,200 m (7,200 ft). It is clear that δD values of small streams decrease from south to north, as was the case on the Central Plateau to the west.

Madison Plateau

The Madison Plateau along the rim of the Yellowstone caldera is composed of Plateau Rhyolite. The highest surfaces are slightly higher than 2,550 m (8,400 ft) altitude. Discharge from this plateau was sampled at three sites from 1971 to 1990: a cold spring at the base of rhyolite cliffs about 3 km west of Old Faithful Geyser, the Little Firehole River above Mystic Falls, and a cold spring adjacent to the old road to Lonestar Geyser. The total range of δD values during the 11-year collection interval for these waters was only –139 to –143 ‰. The cold spring at Grants Pass on the Howard Eaton trail to Shoshone Lake, which could be recharged on the Madison Plateau or to the east in the hills north of Shoshone Lake, had δD values of –135 ‰ in 1973 and –143 ‰ in 1976. Values from cold springs in the vicinity of Shoshone Geyser Basin ranged from –135 to –138 ‰. The δD of the subsurface discharge appears to decrease slightly from south to north in the plateau area.

Central Plateau

The Central Plateau borders the major geyser basins and covers the western resurgent dome of the Yellowstone caldera. The highest altitudes on the Central Plateau are about 2,625 m (8,600 ft), and much of the plateau is higher than 2,550 m (8,400 ft). Nez Perce Creek, which drains the largest watershed in the Central Plateau, was sampled at an altitude of about 2,200 m (7,200 ft). δD values of –143 to –147 ‰ were measured from 1971 to 1990. The values are within the –143 to –148 ‰ range observed from 1975 to 1982 for Arnica Creek, which has a much steeper gradient, near the southeastern margin of the Central Plateau. δD values of –140 to –148 ‰ were obtained between 1971 and

1990 for unnamed creeks with steep gradients draining the 2,625-m (8,600-ft) altitude Elephant Back Mountain on the east side of the plateau. The δD values of the Gibbon River, which has some tributaries on the north margin of the Central Plateau, ranged from –140 to –144 ‰ from 1967 to 1990. The δD values of cold streams and wells on the west margin of the Central Plateau were slightly less negative. On the west margin of the plateau, the δD values of water from cold wells for water supplies at the Midway picnic ground in Lower Geyser Basin and at the Old Faithful and Norris Geyser Basins ranged from –138 to –143 ‰. Substantially higher δD values were obtained from streams on the south margin of the plateau. DeLacy Creek has a small drainage starting at about 2,550 m (8,400 ft) altitude. δD values of DeLacy Creek ranged from –136 to –142 ‰ during a 20-year period. Even less negative values of –133 to –137 ‰ were obtained for Little Thumb Creek that drains similar altitudes about 8 km east of DeLacy Creek. The δD values of all discharge from the central, northern, and eastern margins of the Central Plateau ranged from –138 to –148 ‰, and they averaged about –143 to –145 ‰. The δD values of discharge from the south margin were about 5–7 ‰ greater.

Yellowstone Lake and Yellowstone River

The δD values of Yellowstone Lake water at the outlet to the Yellowstone River near Fishing Bridge and at Pumice and Steamboat Points were measured between 1975 and 1990 at –128 to –133 ‰. The δD value of the Yellowstone River at Buffalo Ford was –125 to –130 ‰. The enrichment of this water in deuterium relative to water in inflow streams reflects evaporation in the lake. This enrichment is not surprising because the residence time of water in the lake is about 10 years (Pearson and Truesdell, 1978).

Mirror Plateau

The Mirror Plateau borders the fumarolic thermal areas east of the Yellowstone caldera. The highest altitudes are higher than 2,900 m (9,600 ft), and much of the plateau is higher than 2,675 m (8,800 ft). Most of the streams sampled are in steep drainages, and δD values should be representative of discharging springs in the area. Streams from the Mirror Plateau and Specimen Ridge had δD values of –143 to –145 ‰ between 1975 and 1990. These values are similar to those from the streams and rivers draining the Absaroka Range to the east and north and the Central Plateau to the west during a longer period of time. Most of the Mirror Plateau drainage flows north into the Yellowstone River along its Grand Canyon.

Pitchstone Plateau and Areas South and West of the Park

The Pitchstone Plateau is southwest of the caldera at altitudes as high as 2,675 m (8,800 ft). Springs that probably recharged on the plateau were sampled in 1982 at altitudes below 2,050 m (6,800 ft) during a single traverse along the trail on the east side of the Bechler River. δD values of the water from the springs ranged from –132 to –135 ‰, similar to values observed for the Bechler River (–134 ‰). The δD values of streams and rivers areas south (Boone, Calf, and Glade Creeks) and west (Strong, Rock, Beaver, and Robinson Creeks) of the Pitchstone Plateau outside of the Park, also sampled in 1982, have essentially the same range of δD (–131 to –137 ‰). These values are clearly less negative than those obtained from streams in the Central and Madison Plateaus to the north.

Snake River Drainage

We have not sampled the Two Ocean Plateau between the Snake and Yellowstone Rivers. However, δD values increased southward in the Park, and no cold streams or springs with δD values lower than –144 ‰ were obtained from waters south of lat 44°30'N. Cold springs in the Shoshone Geyser Basin ranged from –135 to –138 ‰ in 1973. Witches Creek, above the thermal springs at Heart Lake, had a δD value of –140 ‰ in 1978. The cold spring at Grants Pass on the Howard Eaton trail to Shoshone Lake, which could be recharged on the Madison Plateau or to the east in the hills north of Shoshone Lake, had δD values of –135 ‰ in 1973 and –143 ‰ in 1976. The Snake River at Flagg Ranch had δD values of –131 to –136 ‰ from 1978 to 1990.

Discussion

δD values of the cold-water samples for Yellowstone National Park and surrounding areas given in table 4 are summarized in figure 7. Five relationships are evident from the data in figure 7: (1) δD values of surface water north of the Park and in the northern part of the Park become more negative from south to north and from east to west, (2) δD values of surface water more negative than –144 ‰ are not present in the southern half of the Park, (3) except for two small cold streams (both of which probably are influenced by local storms), surface waters with δD values of –148 to –150 ‰ are not found near the geyser basins, (4) localities where the δD values of streams or springs are ≤ –150 ‰ are exclusively north of the caldera and are relatively scarce, and (5) the lowest δD value for a warm sinter-depositing spring (Montanapolis) north of the Park is lower than local recharge and lower than the value modeled for the deep thermal water in the Park.

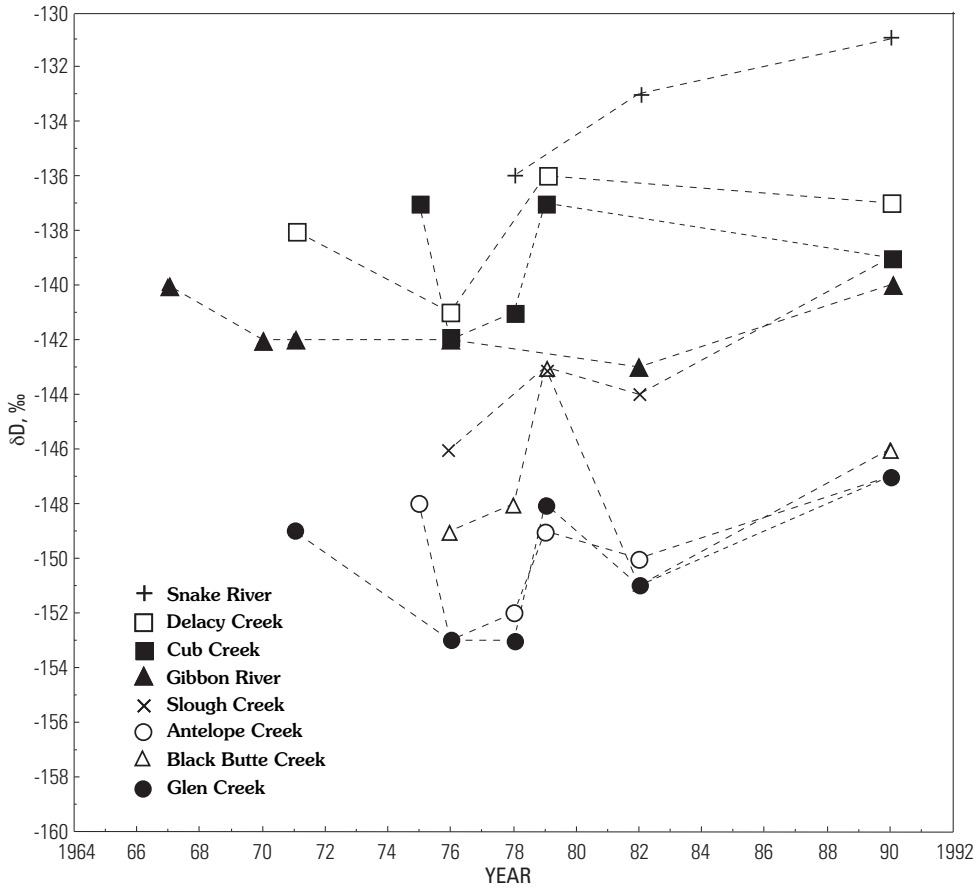

Figure 8. Yearly variations in δD of fall-season discharge of eight Yellowstone National Park streams sampled repeatedly from 1967 to 1990.

Yearly Variations in δD Values at Individual Sites

The pattern of δD distribution for cold waters in the Park, developed in the course of our study, is dependent in part on analyses of water from sites collected only once or twice. In order to determine if δD values from a specific site were consistent from year to year and if the same relative differences between waters from different locations persisted in different years, we collected samples from selected accessible sites during a span of years.

The maximum variation in δD for an individual stream over the collection period from 1967 to 1990 was 8 ‰. Although there were exceptions, the δD values of most streams varied by about the same amount from year to year. This pattern is illustrated in figure 8, which shows similar patterns for δD variations of eight representative streams at different locations in the Park from 1967 to 1990. The important point is that the average δD value for each locality provides a valid picture of the spatial variations in δD of possible infiltrating waters.

Our database is not sufficient to permit us to understand all of the factors controlling the detailed δD of precipitation in the area. A detailed understanding must await data for individual storms, collected over an extended period of time, and information on the residence times of infiltrating precipitation that recharges the streams. As indicated in figure 8, the least negative δD values are for stream samples collected in 1990, whereas the most negative values are for stream samples collected in 1976. The late 1980s were characterized by below normal winter precipitation, whereas the early 1970s were characterized by above normal winter precipitation, as indicated by the yearly average discharge of major rivers in the Yellowstone region (Norton and Friedman, 1991). Although most of the fall stream flow was recharged during the previous spring runoff, possibly a substantial component remained from previous years. Much more detailed studies are needed; however, the average δD values of the streams for a given year apparently correlate with the winter precipitation in the preceding year.

Source of Recharge of Deep Thermal Water If It Occurred During the Holocene

For a system in which the deep thermal water has a short residence time and whose composition responds rapidly to changes in climate, possible recharge areas are constrained by low δD values (–148 to –150 ‰) comparable to those of the deep thermal waters. If the deep thermal water was recharged under the present climatic conditions, the location of recharge must have been in the mountainous areas north and northwest of the caldera. These include (1) the Gallatin Range in the northwest part of the Park and north of the Park between the Gallatin

and Yellowstone Rivers, (2) the Washburn Range, (3) the Buffalo Plateau, and (4) the Absaroka Mountains north of the Park.

From geologic considerations (figs. 9 and 10), the most likely recharge area for deep thermal water underlying the geyser basins on the west side of the caldera is the Gallatin Range between Highways 191 and 89 in the northwestern part of the Park and probably extensions of that range north of the Park. This high-altitude area is bounded by several major north-south-trending faults (fig. 9) that parallel regional faults known from earthquake data to be active (Christiansen, 1984; Pitt, 1987; Pierce and others, 1991; Smith and Rubin, 1994). Large segments of the faults are covered by glacial till and river gravel that are excellent aquifers for recharge of water along the faults to deep levels. Runoff from snowmelt in the spring supplies water to the gravel and that water can infiltrate along the faults to deep levels of the Yellowstone thermal areas. This area also is characterized by large areas of fractured Precambrian basement, Paleozoic and Mesozoic sedimentary rocks with karst topography in limestones, and Eocene volcanics that possibly have permeable contacts. Recharge water may also flow along some northwest-southeast-trending faults in the northwest part of the Park. Those faults parallel major active faults west of the Park (Holdahl and Dzurisin, 1991). Additional recharge could come from the Washburn Range, but, because faults in the Yellowstone Tuff also are oriented north-south, water from this area is more likely to recharge the gas-rich thermal areas on the east side of the caldera. Tectonic and sedimentary structures on the east side of the caldera do not favor recharge from the Absaroka Mountains to the east. The recharge area for deep thermal waters in the Gallatin Range is at least 20 km from outflow at Norris Geyser Basin, 30 km from the outflow at Lower Geyser Basin, and as far as 60–70 km from outflow at the Shoshone and Heart Lake Geyser Basins, respectively. Such distances for deep recharge indicate the presence of an extremely large hydrothermal system. However, these distances are consistent with the size of fossil systems inferred from isotope studies to have been driven by large plutons (Taylor, 1986; Criss and Taylor, 1986).

We need to consider whether precipitation in the Gallatin Range is sufficient to recharge the deep reservoir that supplies the geyser basins on the west side of the caldera. Measured discharge rates of the rivers and chloride concentrations in river waters have been used to calculate the rate of total discharge of the deep component of the hot-spring waters (Fournier, 1989; Norton and Friedman, 1991; Friedman and Norton, this volume). The amount of deep water (that is, water heated to ≥350°C and having 360 ppm Cl) from the west side of the caldera, measured by the chloride flux (Norton and Friedman, 1991; Friedman and Norton, this volume) in the Madison and Snake Rivers, averages about 7.5×10^{10} kg/yr of water with nearly 90 percent derived from the Madison River. The map area of the Gallatin Range in the Park between Highways 191 and 89 is about 1,000 km^2, of which about 400 km^2 is above 2,550 m (8,400 ft) altitude. The annual mean precipitation at West Yellowstone and Old Faithful is about 75 cm/yr on the basis of precipitation summaries by Dirks and Martner (1982). Much more precipitation is expected at altitudes higher than 2,550 m (8,400 ft) in the Gallatin Range. Indeed, precipitation summaries by Dirks and Martner (1982) indicate that the annual mean precipitation in the Gallatin Range is close to 150 cm; most of it is winter snow. Thus, probably 6×10^{11} kg/yr of precipitation falls on the high altitudes of the Gallatin Range within the Park. The amount of runoff from the topographically high areas of the Gallatin Range within the Park is approximately eight times the 7.5×10^{10} kg/yr of deep water estimated to be discharged from the thermal basins on the west side of the caldera each year (Norton and Friedman, 1991; Friedman and Norton, this volume). Additional recharge could be received from the extension of this possible recharge area to the north and northwest of the Park.

The watershed where δD of cold waters is –150 ‰ is limited to the northernmost Gallatin Range, and it does not appear to be large enough to recharge the deep levels of the thermal areas on the west side of the caldera. Furthermore, the δD of much of the possible infiltrating cold water in the southern part of the Gallatin Range is less negative than –148 ‰. Consequently, there is not enough infiltrating cold water of the right composition in the Gallatin Range to account for all of the deep thermal water on the west side of the caldera. This possibly indicates that some recharge is received from ranges east of the Gallatin Range or, more likely, that the deep thermal water was recharged during a colder time interval during which there was greater winter snow accumulations and lower δD values of precipitation. Judging from variations observed in figure 8, we expect δD values of precipitation to be quite sensitive to increases in snowfall. High snowfall accumulations are recorded for the Yellowstone region near the end of the 19th century (Dirks and Martner, 1982), and they also are expected to have occurred during prolonged cold periods such as those observed in Europe in the 15th, 17th, and 18th centuries (Ferronsky and others, 1983). Of course the δD of precipitation was low during the Pleistocene when a large ice cap covered the Yellowstone Plateau as late as 15,000 years ago, and alpine glaciers were active until 11,000 years ago (Pierce, 1979).

Volume of Deep Thermal Water in the Western Side of the Caldera

A schematic north-south cross section through the west side of the caldera (fig. 10) shows hot-spring activity and inferred recharge of local shallow and deep thermal waters. According to R.L. Christiansen (written commun., 1990), the caldera consists of cylindrical cores that originally collapsed and later formed the resurgent domes with shallow tensional faults. The resurgent domes are surrounded by a thick zone of steeply dipping concentric faults that form the main ring-fracture zone of the caldera. The outer part of the caldera consists of large slump blocks that extend along shallow faults to the structural wall of the caldera. The locations of hot-spring activity in Yellowstone probably are controlled primarily by

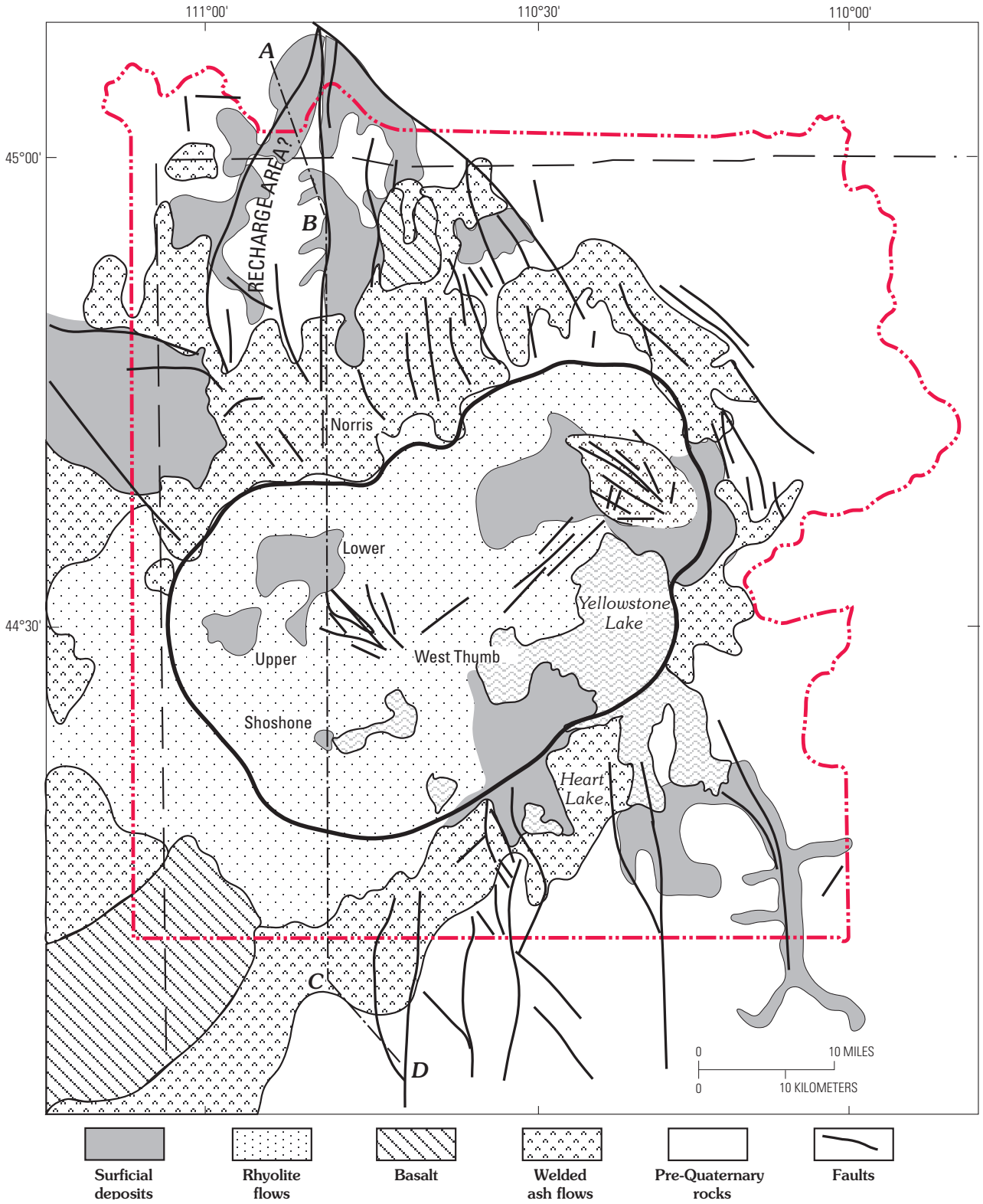

Figure 9. Geologic sketch map of Yellowstone National Park showing possible recharge area for deep thermal waters of the geyser basins on the basis of δD values of cold waters in figure 7. Also shown (dashed dot line ABCD) is location of cross section in figure 10. The area marked RECHARGE AREA? is the center of the most likely source of recharge for thermal waters at Norris, Lower, and Upper Geyser Basins and possibly more distal geyser basins at West Thumb, Shoshone, and Heart Lake. If the deep water contains a component of Pleistocene water and is well mixed, the recharge could be much closer to the caldera inside the Park. See figure 1 for meaning of other lines and patterns.

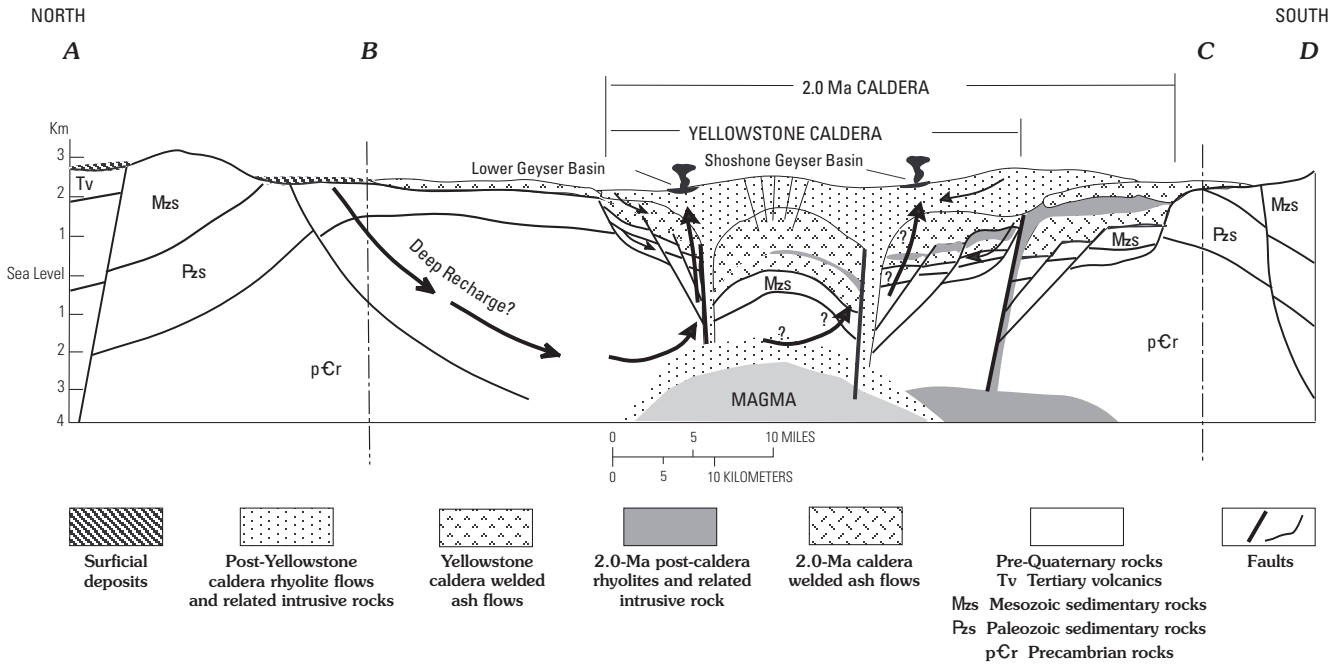

Figure 10. Schematic north-south cross section through the west side of Yellowstone National Park (along ABCD line in fig. 9) showing possible recharge for deep thermal water and shallow mixing waters at Lower and Shoshone Geyser Basins. Caldera structure based on a sketch from R.L. Christiansen (written commun., 1990). The deep recharge is shown for a system in which the deep water has a short residence time and whose δD values respond rapidly to climate changes. If the deep water contains a component of Pleistocene water and is well mixed, the recharge could be much closer to the caldera.

the main ring-fracture faults that are related to the formation of the caldera and also to younger north-south faults inside and outside of the caldera. Individual springs, such as those at Upper and Lower Geyser Basins, however, may be along shallow faults that parallel those in the resurgent dome to the east. The shallow structures at the margins of the caldera probably permit a wedge of cold water to mix with deep thermal water within the caldera.

The maximum volume of the deep thermal-fluid reservoir in the west side of the caldera can be assumed to be the volume of a cylinder approximately 30 km in diameter, the diameter of the outer ring fracture of the caldera. The bottom of the reservoir is the lower limit of circulation of meteoric water, at which seismic activity maintains permeability in the rocks. This depth probably is about 4 km as indicated by the deepest focal depth of earthquakes beneath the caldera (Fournier and Pitt, 1985; Smith and Rubin, 1994; Fournier, 2000). Deeper circulation of water possibly took place in the past, and water possibly circulated into the magma during the recurrent explosive activity that occurred during and immediately after formation of the caldera (Hildreth and others, 1984). Today the circulation depth of meteoric water is probably limited by the depth at which rock deformation changes from primarily brittle-fracture to quasi-plastic flow (Fournier, 1989, 1991, 2000). This transition probably coincides with a thin zone of thermal cracking that migrates inward toward the magma with time as the rocks are cooled (Lister, 1974, 1983). Recharge of cold water along active faults possibly results in thermal cracking of intrusive rocks at depth creating a continuous supply of permeable rocks deep in the thermal areas (Christiansen, 1984). The top of the deep reservoir (defined as thermal water not influenced by shallow recharge) possibly extends in some areas to depths as shallow as 0.5 km, as indicated by the depth to the unmixed deep thermal water indicated from modeling (Truesdell and others, 1977) of the isotopic and chemical compositions of hot-spring waters. Thus, the maximum thickness of the reservoir for deep thermal water probably is about 4 km.

The maximum volume of water in this reservoir can be calculated if assumptions are made about the average porosity of the reservoir. The rocks in the caldera are a heterogeneous mixture of porous rhyolite flows, dense welded tuff, and some sediments from volcanic episodes. Studies of intracaldera volcanics associated with a smaller caldera at Long Valley, Calif., indicated porosities between 1 and 10 percent (Sorey and others, 1978). The higher figure probably is not realistic for the Yellowstone caldera because the Lava Creek and Huckleberry Ridge Tuffs are dense, and the deep thermal water is concentrated in highly fractured and permeable rhyolite and is not uniformly distributed throughout the caldera. The maximum average porosity for the intracaldera volcanics at Yellowstone is assumed to be about 5 percent (R.L. Christiansen, oral commun., 1991). Assuming an average porosity between 1 and 5 percent, the amount of thermal water in the deep reservoir on the west side of the caldera is between 28 and 141×10^{12} kg.

Age of the Deep Water

There are few constraints on the age of the deep water. The absence of such constraints leads to two possible models for the deep recharge. Pearson and Truesdell (1978) determined from tritium measurements that most of the thermal waters are mixtures of two waters—one containing tritium from an open, well-mixed reservoir of relatively short residence time, the other containing no detectable tritium, presumably derived from a deep source. The deep water contains no detectable tritium. Therefore, the deep water is at least 60 years old, based on the 12.3-year half life of tritium. Carbon-14 was not detected in CO_2 from fumarolic steam, as would be expected for a system swamped by CO_2 of igneous or sedimentary origin (F. J. Pearson, Jr., unpubl. data, 1978).

A maximum age of the deep water can be estimated from the discharge rate for deep water of about 7.5×10^{10} kg/yr, as measured from Cl inventory considerations (Norton and Friedman, 1991; Friedman and Norton, this volume) and from the estimates calculated above for the minimum and maximum volume of the deep water reservoir. The reservoir would be emptied in 370–1,900 years assuming a piston flow model in which water does not mix within the reservoir and assuming there is only one point of recharge. These times are generally consistent with the maximum time (1,150 years) for water-rock reaction estimated from a solution and recoil model for radium isotope supply to the hydrothermal system published by Clark and Turekian (1990). However, the times are not consistent with an age of at least 10,000 years based on He-4 flux measurements by Kennedy and others (1987, 1988). Such an old age is consistent with well-mixed models.

Are such recharge ages suggested by short residence times for the deep water hydrologically realistic? Fractured crystalline rocks generally have hydraulic conductivities in the range of 1 to 1×10^{-4} km/yr (deMarsily, 1986, p. 79). Clearly, the high end of this range is more than adequate to account for the proposed recharge of the deep thermal reservoir. The actual hydraulic conductivities are unknown. However, Caine and Forster (1999) calculated a similar range of conductivities for four representative types of fault-zone architectures. Fracture flow through uniformly fractured ignimbrites and flows or along major and continuous fault zones could provide the pathway for fluid recharge from the mountain ranges north of the caldera. However, not all major faults show field evidence of Quaternary activity (Pierce and others, 1991). Furthermore, based on preliminary flow modeling, special conditions are required to provide a flow path as long as that shown in figure 10 that does not break into a series of convection cells recharged from local waters (W.C. Shanks, oral commun., 1999).

Well-mixed models permit the possibility of older ages for the deep water. Also possible Pleistocene water has recently been discovered in warm-water wells and springs from southeastern California to southern Idaho. This water has consistently lower δD values than those of surrounding local recharge (Smith and others, 2002). A possible example of one of these springs is the sinter-producing warm spring (Montanapolis) in the Absaroka Range north of the Park. This spring has a δD of –153 ‰, about 5 per mil lower than that of local ground water. If the water from these springs and wells is proven to be Pleistocene in age, the time required to flush the entire deep reservoir of the Yellowstone hydrothermal system may be longer than 11,000 years.

Source of Recharge of Deep Thermal Water If a Substantial Component Remains from the Pleistocene

The present climate cycle is characterized by variable warm and cold periods (Vance and others, 1992; Feng and Epstein, 1993; Whitlock, 1993) and produces small but significant variations in the δD of precipitation. During the Pleistocene, the variations of δD of recharge water were probably much less than today as most of Yellowstone National Park, particularly the topographically high northern areas, was buried by thick ice (Pierce, 1979). The presence of thermal kanes indicates that some of the hot springs were flowing during the last glacial period. Given the fact that ice caps and glaciers commonly have a layer of water at their base (Patterson, 1981), the meteoric-water hydrologic head on the thermal system was probably much larger than today. The δD of recharge from glacier meltwaters underneath the ice cap during the Pleistocene likely was isotopically uniform, and it possibly had a value of about –160 ‰, similar to the value of the deep, warm, well water observed in southern Idaho (Smith and others, 2002). The contribution of chloride to the deep reservoir during the Pleistocene was probably the same as it is today. The uniformity of temperature, chloride, and δD in the deep thermal water indicates that the deep water probably has a uniform source of heat and chloride. The uniform chloride source could be produced by thermal-stress cracking and leaching by meteoric water of chloride from the freshly exposed rock (Lister, 1974; Christiansen, 1984; White and others, 1992) or by contribution from a magma across a brine-meteoric water interface (Fournier, 1989).

If the deep reservoir contains a component of Pleistocene water and if it is well mixed, the current deep recharge could have δD values as large as –140 to –145 ‰ depending on the size of the deep reservoir and the residence time of water in the reservoir. Waters of such composition could enter the deep system at geologically favorable sites around the caldera (fig. 9). Large uncertainties currently exist about the size of the deep reservoir on the west side of the caldera because it may be connected to the deep reservoir on the east side. Until more is known about the age, residence time, and mixing rates of the deep thermal water, the simplest interpretation is that most recharge for the deep thermal water in the west part of the Park is likely in the Gallatin Range within and northwest of the Park.

Conclusions

An extensive Park-wide program of collection and analysis of cold-water samples was undertaken to determine the sources of recharge to the deep thermal water underlying the geyser and hot-spring basins of Yellowstone National Park. Earlier chemical and isotopic modeling of boiling and mixing processes, as well as the compositions of waters from 200- to 300-m-deep drill holes, showed that δD of deep thermal water (–148 to –150 ‰) is significantly lower than that of local cold waters that enter thermal reservoirs only near the surface. Cold waters in the central, southern, and eastern parts of the Park are isotopically too heavy (generally δD = –130 to –144 ‰) to provide deep recharge. The deep water is at least 60 years old on the basis of tritium measurements, but it could be younger than 1,900 years or older than 10,000 years depending on the model used for volume and flow calculations. For a deep reservoir whose water has a short residence time, only in the Gallatin Range in and northwest of the Park are cold-water δD values sufficiently low and geologic structures appropriate to carry recharging water into the deep caldera reservoir. In this model, the possible source of recharge for the deep thermal water is at least 20 km, and possibly as much as 70 km, from outflow areas. These distances require remarkable flow rates for recharge and a young age for the deep water. The volume of high-altitude infiltration with δD ≤ –148 ‰ in this area is not sufficient at present to match the measured thermal outflow as determined from chloride-flux studies. In this model, this shortfall requires that infiltrating waters were recharged during a period characterized by somewhat cooler climate with more winter snowfall that at present. Such conditions occurred during the Little Ice Age (in the 15th century). There is reason to believe, however, on the basis of data from warm springs and wells from southern Idaho to southern California, that the residence time for the deep water could be more than 10,000 years. If the deep water is well mixed, a portion of deep thermal water (δD = –160 ‰) may have been contributed during Pleistocene glaciation. Under such conditions, the δD for the present recharge for the deep thermal water could be as large as –140 to –145 ‰, and it could enter the deep system at a number of geologically favorable areas around the caldera.

Acknowledgments

Many people contributed to the logistics, sample collection, analyses, and discussions of this work in the nearly 25 years during which the project was conducted. We particularly thank Bob Christiansen, Tyler Coplen, Bob Fournier, Irving Friedman, Mark Huebner, Pat Muffler, Joe Pearson, Joe Whelan, and Don White of the U.S. Geological Survey; Wayne Hamilton and Rick Hutchinsen of the National Park Service; and many other visiting scientists, students, and spouses who joined us on the many memorable field trips in the Yellowstone area. We are particularly indebted to Pat Shanks for discussions regarding modeling of residence times of water in the deep reservoir. This study was recommended by Don White, who was a wonderful mentor to the authors when they were young scientists beginning to fathom the wonders of Yellowstone.

References Cited

Allen, E.T., and Day, A.L., 1935, Hot springs of the Yellowstone National Park: Carnegie Institution of Washington Publication 466, 525 p.

Bargar, K.E., and Dzurisin, Daniel, 1986, Bibliography and brief history of the studies by the U.S. Geological Survey in Yellowstone National Park, Wyoming, Idaho, and Montana: U.S. Geological Survey Open-File Report 86-573, 27 p.

Bryson, R.A., and Hare, F.K., 1974, Climates of North America, *in* Landsberg, H.E., ed., World survey of climatology: Amsterdam, Elsevier, p. 1–47.

Caine, J.S., and Forster, C.B., 1999, Fault zone architecture and fluid flow—Insights from field data and numerical modeling, *in* Haneberg, W.C., Mozley, P.S., Moore, J.C., and Goddwin, L.B., eds., Faults and subsurface fluid flow in the shallow crust: American Geophysical Union Geophysical Monograph 113, p. 101–127.

Christiansen, R.L., 1984, Yellowstone magmatic evolution—Its bearing on understanding large-volume explosive volcanism, *in* Explosive volcanism—Inception, evolution, and hazards: Washington, D.C., National Academy of Sciences (U.S. National Research Council Geophysics Study Committee), p. 84–95.

Clark, J.F., and Turekian, K.K., 1990, Time scale of hydrothermal water-rock reactions in Yellowstone National Park based on radium isotopes and radon: Journal of Volcanology and Geothermal Research, v. 40, p. 169–180.

Craig, Harmon, 1961, Standard for reporting concentrations of deuterium and oxygen-18 in natural waters: Science, v. 133, p. 1,833–1,834.

Craig, Harmon, Boato, Giovanni, and White, D.E., 1956, Isotope geochemistry of thermal waters: National Academy of Sciences, National Research Council Publication, v. 19, p. 29–39.

Criss, R.E., and Taylor, H.P., Jr., 1986, Meteoric-hydrothermal systems, *in* Valley, J.W., Taylor, H.P., and O'Neil, J.R., eds., Stable isotopes in high temperature geologic processes: Reviews in Mineralogy, v. 16, p. 373–424.

deMarsily, Ghislain, 1986, Quantitative hydrogeology: San Diego, Calif., Academic Press, 440 p.

Despain, D.G., 1987, The two climates of Yellowstone National Park: Montana Academy of Science Proceedings, v. 47, p. 11–19.

Dirks, R.A., and Martner, B.E., 1982, The climate of Yellowstone and Grand Teton National Parks: U. S. Department of Agriculture, National Park Service, Occasional paper no. 6, 26 p.

Dzurisin, Daniel, Savage, J.C., and Fournier, R.O., 1990, Recent crustal subsidence at Yellowstone caldera, Wyoming: Bulletin of Volcanology, v. 52, p. 247–270.

Dzurisin, Daniel, and Yamashita, K.M., 1987, Vertical surface displacements at Yellowstone caldera, Wyoming, 1976–1985: Journal of Geophysical Research, v. 92, p. 13,753–13,766.

Eaton, G.P., Christiansen, R.L., Iyer, H.M., Pitt, A.M., Mabey, D.R., Blank, H.R., Jr., Zietz, Isidore, and Gettings, M.E., 1975, Magma beneath Yellowstone National Park: Science v. 188, p. 787–796.

Farnes, P.E., 1997, The snows of Yellowstone: Yellowstone Center for Resources, Yellowstone Science, v. 5, p. 8–11.

Feng, Xiahong, and Epstein, Samuel, 1993, An [A] D/H ratio time series (1000–8000 BP) from bristlecone pine, White Mountains, California—climatic implications [abs.]: Geological Society of America Programs with Abstracts, v. 25, no. 6, p. A-256.

Ferronsky, V.I., Vlasova, L.S., Esikov, A.D., Polyakov, V.A., Seletsky, Y.B., Punning, Y.M.K., and Vajkmyaeh, R.A., 1983, Relationships between climatic changes and variations in isotopic composition of groundwater, precipitation, and organic soil matter in the Quaternary Period, *in* Paleoclimates and paleowater, a collection of environmental isotope studies: Vienna, International Atomic Energy Agency, p. 13–25.

Fournier, R.O., 1989, Geochemistry and dynamics of the Yellowstone National Park hydrothermal system: Annual Reviews Earth Planetary Sciences, v. 17, p. 13–53.

Fournier, R.O., 1991, The influences of depth of burial and the brittle-plastic transition on the evolution of magmatic fluid [abs.], *in* Hedenquist, J.W., ed., Magmatic contributions to hydrothermal systems, Extended Abstracts: Japan-U.S. seminar on magmatic contributions to hydrothermal systems, p. 43–44.

Fournier, R.O., 2000, Hydrothermal processes related to movement of fluid from plastic into brittle rock in the magmatic-epithermal environment: Economic Geology, v. 94, p. 1,193–1,212.

Fournier, R.O., and Pitt, A.M., 1985, The Yellowstone magmatic-hydrothermal system, *in* Stone, Claudia, ed., International symposium on geothermal energy: United States, Geothermal Research Council, International Volume, p. 319–327.

Friedman, Irving, Redfield, A.C., Schoen, Beatrice, and Harris, J.L., 1964, The variation of the deuterium content of natural waters in the hydrologic cycle: Reviews of Geophysics, v. 2, p. 177–224.

Fritz, Peter, 1981, River waters, *in* Gat, J.R., and Gonfiantini, R., eds., Stable isotope hydrology deuterium and oxygen-18 in the water cycle: Vienna, International Atomic Energy Agency, Technical Report Series no. 210, p. 177–202.

Gat, J.R., 1981, Groundwater, *in* Gat, J.R., and Gonfiantini, R., eds., Stable isotope hydrology, deuterium and oxygen-18 in the water cycle: Vienna, International Atomic Energy Agency, Technical Report Series no. 210, p. 223–240.

Gooch, F.A., and Whitfield, J.E., 1888, Analyses of water of the Yellowstone National Park, with an account of the methods of analysis employed: U.S. Geological Survey Bulletin 47, 84 p.

Hayden, F.V., 1872, Preliminary report of the United States Geological Survey of Montana and portions of adjacent territories, being a fifth annual report of progress, Part I: Washington, D.C., U.S. Government Printing Office, p. 13–204.

Hermann, A., Martinec, J., and Stichler, W., 1978, Study of snowmelt-runoff components using isotope measurements, *in* Colbeck, S.C., and Ray, M., eds., Modeling of snow cover runoff: Hanover, N.H., U.S. Army Cold Regions Research and Engineering Laboratory, p. 228–265.

Hildreth, Wes, Christiansen, R.L., and O'Neil, J.R., 1984, Catastrophic isotopic modification of rhyolitic magma at times of caldera subsidence, Yellowstone Plateau volcanic field: Journal of Geophysical Research, v. 89, p. 8,339–8,369.

Holdahl, S.R., and Dzurisin, Daniel, 1991, Time-dependent models of vertical deformation for the Yellowstone-Hebgen Lake region, 1923–1987: Journal of Geophysical Research, Part B, v. 96, p. 2,465–2,483.

Kendall, Carol, and Coplen, T.B., 1991, Identification of vapor-source effects versus local environmental effects on the delta D and delta O^{18} compositions of stream samples in the USA [abs.]: Geological Society of America Abstracts with Programs, v. 23, no. 5, p. A269–270.

Kendall, Carol, and Coplen, T.B., 2001, Distribution of oxygen-18 and deuterium in river waters across the United States: Hydrological Processes, v. 15, p. 1,363–1,393.

Kennedy, B.M., Reynolds, J.H., Smith, S.P., and Truesdell, A.H., 1987, Helium isotopes, Lower Geyser Basin, Yellowstone National Park: Journal of Geophysical Research, Part B, v. 92, p. 12,477–12,489.

Kennedy, B.M., Reynolds, J.H., and Smith, S.P., 1988, Noble gas geochemistry in the thermal springs: Geochimica et Cosmochimica Acta, v. 52, p. 1,919–1,928.

Lister, C.R.B., 1974, On the penetration of water into hot rock: Royal Astronomical Society Geophysical Journal, v. 39, p. 465–509.

Lister, C.R.B., 1983, The basic physics of water penetration into hot rock, *in* Rona, P.A., Bostrom, K., Laubier, L., and Smith, K.L., Jr., eds., Hydrothermal processes at seafloor spreading centers: New York, Plenum Press, p. 141–168.

Norton, D.R., and Friedman, Irving, 1991, Chloride flux and surface water discharge out of Yellowstone National Park, 1982–1989: U.S. Geological Survey Bulletin 1959, 42 p.

Patterson, W.S.B., 1981, The physics of glaciers (2d ed.): New York, Pergamon International Library of Science, Technology, Engineering and Social Studies, 380 p.

Pearson, F.J., Jr., and Truesdell, A.H., 1978, Tritium in the waters of the Yellowstone National Park, *in* Zartman, R.E., ed., Short papers of the Fourth International Conference—Geochronology, cosmochronology, isotope geology: U.S. Geological Survey Open-File Report 78-701, p. 327–329.

Pierce, K.L., 1979, History and dynamics of glaciation in the northern Yellowstone National Park area: U.S. Geological Survey Professional Paper 729-F, 90 p.

Pierce, K.L., Adams, K.D., and Sturchio, N.C., 1991, Geologic setting of the Corwin Springs Known Geothermal Resources Area–Mammoth Hot Spring Area in and adjacent to Yellowstone National Park, *in* Sorey, M.L., ed., Effects of potential geothermal development in the Corwin Springs Known Geothermal Resource Area, Montana, on the thermal features of Yellowstone National Park: U.S. Geological Survey Water Resources Investigations Report 91-4052, p. C1–C37.

Pierce, K.L., Cannon, K.P., and Meyer, G.A., 1997, Yellowstone caldera "heavy breathing" based on Yellowstone Lake and River changes in the postglacial time: Eos, Transactions, American Geophysical Union, v. 78, no. 46, p. F802.

Pitt, A.M., 1987, Tectonics of the Hebgen Lake–northwest Yellowstone Park region from earthquake hypocenters and focal mechanisms: Seismological Research Letters, v. 58, 29 p.

Rye, R.O., and Truesdell, A.H., 1993, The question of recharge to the geysers and hot springs of Yellowstone: U.S. Geological Survey Open-File Report 93-384, 40 p.

Smith, G.I., Friedman, Irving, Guida, Veronda, and Johnson, C.A., 2002, Stable isotope compositions of water in the Great Basin, United States, Part 3—Comparison of ground waters with modern precipitation: Journal of Geophysical Research, v.107, no. D19, p. ACL 1–16.

Smith, R.B., and Rubin, A.M., 1994, Rapid reversals of uplift to subsidence at the Yellowstone caldera by magmatic processes imaged by earthquakes: Seismological Research Letters, v. 65, p. 56.

Sorey, M.L., ed., 1991, Effects of potential geothermal development in the Corwin Springs Known Geothermal Resource Area, Montana, on the thermal features of Yellowstone National Park: U.S. Geological Survey Water-Resources Investigations Report 91-4052, 193 p.

Sorey, M.L., Lewis, R.W., and Olmsted, F.H., 1978, The hydrothermal system of Long Valley caldera, California: U.S. Geological Survey Professional Paper 1044-A, 60 p.

Taylor, H.P., Jr., 1986, Igneous rocks II—Isotopic case studies of circumpacific magmatism, *in* Valley, J.W., Taylor, H.P., Jr., O'Neil, J.R., eds., Stable isotopes in high temperature geological processes: Reviews in Mineralogy, v. 16, p. 273–318.

Thordsen, J.J., Kharaka, Y.K., Mariner, R.H., and White, L.D., 1992, Controls on the distribution of stable isotopes of meteoric water and snow in the greater Yellowstone National Park region, USA, *in* Kharaka, Y.K., and Maest, A.S., eds., Water-rock interaction: Rotterdam, Balkema, p. 591–595.

Truesdell, A.H., and Fournier, R.O., 1976, Conditions in the deeper parts of hot spring systems of Yellowstone National Park: U.S. Geological Survey Open-File Report 76-428, 29 p.

Truesdell, A.H., Nathenson, Manuel, and Rye, R.O., 1977, The effects of subsurface boiling and dilution on the isotopic compositions of the Yellowstone thermal waters: Journal of Geophysical Research, v. 82, p. 3,694–3,704.

Vance, R.E., Mathews, R.W., and Clague, J.J., 1992, 7,000 year record of lake-level change on the northern Great Plains—A high-resolution proxy of past climate: Geology, v. 20, p. 879–882.

Whitlock, Cathy, 1993, Postglacial vegetation and climate of the Grand Teton and southern Yellowstone National Parks: Ecological Monographs, v. 63, p. 173–198.

Wicks, Charles, Jr., Thatcher, Wayne, and Dzurisin, Daniel, 1999, Migration of fluids beneath the Yellowstone caldera inferred from satellite radar interferometry: Science, v. 282, p. 485–461.

White, A.F., Chuma, N.J., and Goff, Frazer, 1992, Mass transfer constraints on the chemical evolution of an active hydrothermal system, Valles caldera, New Mexico: Journal of Volcanology Geothermal Research, v. 49, p. 233–253.

Is Yellowstone Losing Its Steam?—Chloride Flux Out of Yellowstone National Park

By Irving Friedman and Daniel R. Norton

Chapter I *of*
Integrated Geoscience Studies in the Greater Yellowstone Area—Volcanic, Tectonic, and Hydrothermal Processes in the Yellowstone Geoecosystem
Edited by Lisa A. Morgan

Professional Paper 1717

U.S. Department of the Interior
U.S. Geological Survey

Contents

Abstract 275
Acknowledgments 275
Introduction 275
Definition of Water Year 276
Site Descriptions 276
Experimental Results 276
    Chloride Analysis 276
    Stream Discharge Measurements and Sampling 276
    Problems in Acquiring Discharge Measurements for the Fall and Madison Rivers 277
    Annual Discharge Values 279
    Annual Discharge Measurements by Two Different Protocols 279
    Relation Between River Discharge and Chloride Concentration 279
Chloride Flux 282
    Calculation of Chloride Flux 282
    Calculation of Thermal-Chloride Flux 284
    Thermal-Chloride Flux from the Major Rivers 284
    Thermal-Chloride Flux from the West Boundary of the Park 284
    Seasonal Variation of Chloride Flux 284
Modeling of Thermal and Non-Thermal Inputs to the Major Rivers 285
    Gardner River 285
    Fall River 286
    Madison River 286
    Snake River 286
    Yellowstone River 286
Origin of the Seasonal Increase of Chloride in the Major Rivers of Yellowstone National Park 286
Long-Term Variations in Chloride Flux 288
    Effect of Climate on Chloride Flux 288
    Long-Term Changes in Thermal-Water Outflow from Mammoth Hot Springs 290
Is Yellowstone Losing Its Steam? 291
Heat Flow from the Yellowstone Hydrothermal System 292
Summary and Conclusions 292
References 296

Figures

1. Map showing stream-gaging stations 277
2. Diagram of the Fall River showing diversions for irrigation 279
3. Relationship of annual discharges of six rivers 282

4–17. Graphs showing:

    4. Chloride concentrations of water samples from six rivers, plotted against discharges measured at the times of collection 283

5. Instantaneous values for discharge and chloride flux for the Fall, Firehole, Gibbon, Madison, Snake, and Yellowstone Rivers for water years 1983 through 1994 and 1997 through 2001 287
6. Chloride concentration vs. discharge for the Gardner River 288
7. Chloride concentration vs. discharge for the Fall River....289
8. Chloride concentration vs. discharge for the Madison River 290
9. Chloride concentration vs. discharge for the Snake River....291
10. Chloride concentration vs. discharge for the Yellowstone River 292
11. Annual thermal-chloride flux for the Fall, Madison, Snake, and Yellowstone Rivers for the water years 1983–1994 and 1997–2001....293
12. Sums of annual precipitation collected at five sites in the Park, discharges of the four rivers that drain the Park, and annual chloride fluxes of those four rivers....293
13. Unadjusted and adjusted annual thermal-chloride flux out of Yellowstone Park for each water year....294
14. Annual precipitation and the annual discharge from the Park....295
15. Sum of annual precipitation measurements from five measuring stations in Yellowstone Park vs. the annual river discharge from the Park for the water years 1986–2001....295
16. Annual thermal-chloride water discharge from Mammoth Hot Springs into the Gardner River and for water years 1985–2003....296
17. Annual average of the interval between eruptions of Old Faithful Geyser....296

Tables

1. Gaging site descriptions....278
2. Annual discharge from the Fall, Firehole, Gibbon, Madison, Snake, and Yellowstone Rivers 280
3. Comparison of annual discharges of rivers that drain the Park....281
4. Annual chloride flux, total and thermal, from the Fall, Madison, Snake, and Yellowstone Rivers 285
5. Percent thermal chloride as compared to total chloride for each river, and percent of thermal chloride compared to total thermal chloride exiting in the Park 285
6. Total thermal-chloride flux from Yellowstone Park, water years 1983–2003 286
7. Model data for the Gardner River 289
8. Model data for the Fall River....290
9. Model data for the Madison River 291
10. Model data for the Snake River....292
11. Model data for the Yellowstone River 293

Is Yellowstone Losing Its Steam?— Chloride Flux Out of Yellowstone National Park

By Irving Friedman[1] and Daniel R. Norton[2]

Abstract

Chloride flux, a surrogate for heat flow, was determined for the four rivers draining Yellowstone National Park (the Park) for the water years (October 1 through September 30) 1983 through 2003, with the exception of 1995 and 1996. The chloride emitted by the geothermal system underlying Yellowstone Park is designated "thermal chloride," and it constitutes 94 percent of the total chloride exiting the Park. The remainder of the chloride is contributed by rainfall, rock weathering, and a minor amount due to human impact.

Of this 94 percent, the Fall, Madison, Snake, and Yellowstone Rivers have been determined to discharge 93 percent of the chloride leaving the Park; the remaining 7 percent exits along the west boundary into the Henrys Fork River. The chloride flux for each river varied seasonally and annually, and we postulate that it depended primarily on the flow of hot springs. This flow, in turn, depended on the height of the local water table, which increased during spring runoff and varied annually in synchronism with changes in precipitation.

The sum of the annual chloride fluxes for the four rivers varies as much as 20 percent year-to-year. This sum, when corrected for the climatic factors, shows a decline of 10 percent during the past 20 years. A lengthening in the period between eruptions of Old Faithful Geyser has also been observed. We believe that these changes may be related to deflation of the Yellowstone caldera documented by changes in ground levels surrounding Yellowstone Lake.

Acknowledgments

We thank John Varley, Director, Center for Resources, Yellowstone National Park, for financial aid and encouragement. We are especially indebted to Jake Jacobson, Chief, Idaho Falls field office, USGS, who was responsible for establishment of stream gages on the Fall River when diversion of the river for power generation impacted the accuracy of measurements at the historic river-gaging site and provided assistance in collecting data from remote sites. Dale Swanson, Fremont-Madison Water District (Ashton, Idaho), provided discharge data for the irrigation canals that diverted water from the Fall River. The Ida-West Energy Company (Boise, Idaho) provided data on the power generated by diversion of the Fall River water through the Marysville Canal. Ron Shields, Montana District, U.S. Geological Survey (USGS), was very helpful in our study of the Yellowstone and Madison River drainages. Gary Cottrell, USGS National Water Quality Laboratory, was of great assistance in the chloride analysis. The late Rick Hutchinson, Yellowstone National Park geologist, provided great service in the field and acted as coordinator for the sample collectors. Unpublished data on the frequency of eruptions of Old Faithful was furnished by Rick Hutchison and Tom Hougham, Yellowstone National Park. Funding for this research was provided by both the National Park Service and the U.S. Geological Survey.

Introduction

The heart of the Yellowstone National Park (the Park) ecosystem resides in the thermal flux generated by a magma body under the Park. This heat flux manifests itself in the many geysers and hot springs that are the features that originally caused the region to be set aside as the world's first national park. This report discusses an attempt to monitor the state of the thermal flux in the Park and to relate changes in the flux to changes in other aspects of the ecosystem.

Direct measurements of thermal flux or heat flow are difficult to determine. Chloride flux, which is more easily determined, has been used as a surrogate for heat flow (Ellis and Wilson, 1955; Fournier and others, 1976; Norton and Friedman, 1985; Friedman and Norton, 1990; Norton and Friedman, 1991; Friedman and others, 1993).

Norton and Friedman (1985) determined that 94 percent of the chloride exiting Yellowstone is from the geothermal system. The remainder of the chloride is derived from the atmosphere, low-temperature rock weathering, subsurface leaching of rocks, and human waste.

[1]U.S. Geological Survey.

[2]U.S. Geological Survey, Box 25046, Mail Stop 973, Denver Federal Center, Denver, CO, 80225.

The rationale for previous investigations varied from purely scientific objectives to the practical need to establish baseline data to assess adverse impacts on thermal features of the Park from proposed commercial development of water, geothermal, oil, and gas resources adjacent to Yellowstone. Those investigations have been used to relate temporal changes in the plumbing system that connects the magmatic reservoir to changes in the shallow hydrothermal systems underlying Yellowstone. This report extends the investigation of Norton and Friedman (1985) of the chloride flux leaving the Park via four major rivers: Fall, Madison, Snake, and Yellowstone. The chloride flux exiting the Park was estimated to be 94 percent of the total flux—the remainder exiting along the west boundary of the Park in the Henrys Fork drainage (Norton and Friedman, 1985; Friedman and others, 1993).

This study, a cooperative effort between the U.S. Geological Survey (USGS) and the National Park Service (NPS), includes data for water years (WY) 1982–1989, published by Norton and Friedman (1991). The data for WY 1982–1989 have been recalculated using improved protocols, and they are included with data acquired for WY 1990–2003. No samples were collected during WY 1995 and 1996. Collection resumed in WY 1997.

Definition of Water Year

All reported values of annual data, with the exception of figure 12, are calculated for the water year (WY) defined as 12 months beginning on October l and ending on September 30. In figure 12 the data are given for the calendar year.

Site Descriptions

The locations of stream-gaging sites are shown in figure 1, and the site descriptions are listed in table 1. All of the sites are USGS gaging stations. Sites for discharge measurements were selected on the Fall, Madison, Snake, and Yellowstone Rivers where the rivers exit the Park. The Madison River was gaged from September 1982 to October l986, and from 1990 through 2003. For the 3 years that the Madison River site was inoperative, we used data from stations on the Firehole and Gibbon Rivers, which converge to become the Madison, to calculate discharge and chloride flux for the Madison River.

Water samples for chloride analysis were collected at the gaging sites (fig.1) with the exception of the Yellowstone River samples. To exclude chloride input from La Duke Hot Spring, which is outside the Park and discharges into the river 3.2 km upstream from the gaging site, also outside the Park, the Yellowstone River water samples were collected l km upstream from where the hot-spring water enters the river.

Experimental Results

Chloride Analysis

For WY 1983 through 1989, chloride determinations were made by a modification of the thiocyanate-spectrophotometric method of Skoustad and others (1979), in which an automated segmented-sample analyzer replaced the discrete-sample analyzer. To increase the accuracy of the method, we introduced our chloride standard solutions between every 10 to 15 samples. The laboratory results were normalized against these standards, which were prepared gravimetrically from pure NaCl. This resulted in an accuracy of ±2 percent.

For WY 1990 through 2003, chloride concentrations were determined utilizing an ion chromatography method described by Fishman and Friedman (1989). A series of gravimetrically prepared KCl standard solutions were inserted at the beginning, middle, and end of each group of 20 samples, and the laboratory results were normalized to those standards. The digital readout of the automated chloride-analysis apparatus limited the precision of the method. The precision varied from 1 percent relative standard deviation for chloride concentrations higher than 50 ppm, to 3 percent for concentrations lower than 10 ppm. Prior to 2000, the National Water Quality Laboratory of the USGS made all of the chloride analyses. After 2000 the analyses were made by the USGS Volcano Hazards Laboratory in Menlo Park, Calif.

Stream Discharge Measurements and Sampling

The river discharge and chloride concentration data were published by Friedman and Norton (2000). That publication shows plots of river discharge and chloride concentration.

Discharge measurements were obtained from the Water Resources Division (WRD) of the USGS, which used standard hydrologic methods and automated recorders. Their methods are described in standard textbooks, in Carter and Davidian (1968), in Rantz (1982), and are reported to have an accuracy of ±5 percent.

The water samples for chloride analyses were collected with 50-mL plastic syringes. They were filtered on-site through 5-µm membrane filters into plastic bottles before submittal to the WRD National Water Quality Laboratory in Denver, Colo., for analysis. The 5-µm filter was chosen because it is the smallest porosity filter that could be used without becoming plugged by solids that were present in the water. Beginning in 2001, a 0.4-µm filter was used.

Our schedule for water sampling of the rivers was monthly for January, February, November, and December; bi-monthly for March, April, September, and October; and weekly for May, June, July, and August. The 28-sample

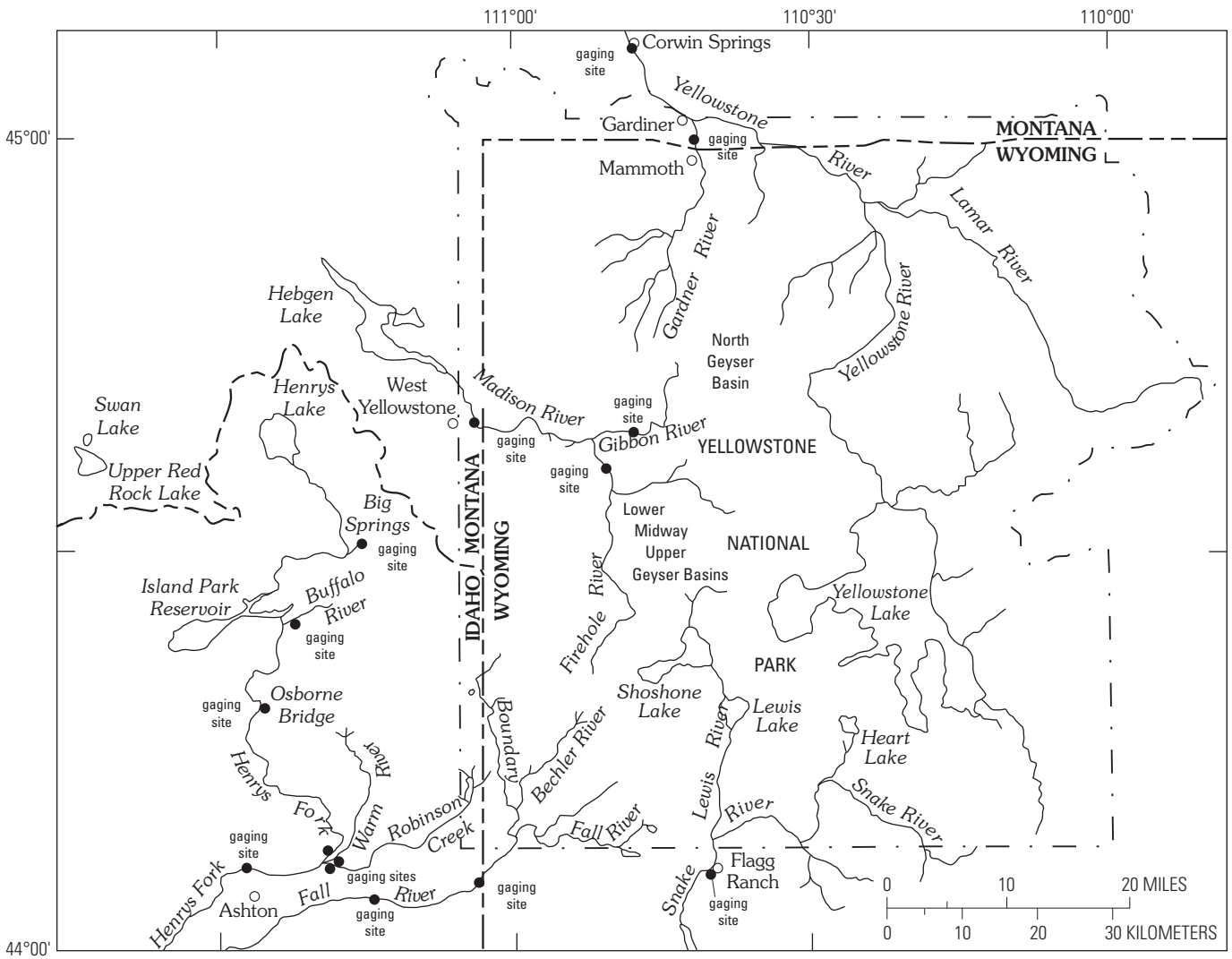

Figure 1. Map showing stream-gaging stations.

protocol resulted in greater accuracy than the normal WRD sampling protocol, particularly during the period of high runoff in the spring and summer. The usual water-sampling protocol used by WRD is to collect a sample at each site every 6 weeks. Using data from both sampling protocols, we calculated the annual chloride flux for 1985 and 1986 for the four major rivers that drain the Park. The flux calculated for individual rivers by the two protocols differs by as much as 12 percent. The discrepancy depends on the specific dates of sampling as related to the timing of snowmelt runoff. In view of those results, we designed our sampling schedule to include additional sampling during the period of high discharge. To the 28 samples per year for each site that we collected, we added some of the 9 samples collected by the WRD.

In WY 1999, collections began on the Henrys Fork at Ashton, Idaho, to quantify the estimates of chloride leaving the Park on its west boundary, as reported by Norton and Friedman (1985).

Problems in Acquiring Discharge Measurements for the Fall and Madison Rivers

Measurements of the discharges of the Fall and Madison Rivers had to be reconstructed for certain intervals. The following is a description of the methods used to calculate the data.

The flow of the Fall River was measured at the USGS gaging site at Squirrel, Idaho (USGS site 13047500), for the period October 1, 1983, through August 31, 1993. Two irrigation canals (Marysville and Yellowstone) diverted water above the gaging site. The sum of the measured diversions through these two canals was added to the river discharge measured at the Squirrel gage to derive a value of the total flow of the river as it exits the Park.

A major diversion of the Fall River through the Marysville Canal for power generation began operation on September 1, 1993. An alternate gaging station (USGS site 13046995) upstream from the diversions did not begin operation until mid-November 1993 (fig. 2 shows the positions of the Fall

Table 1. Gaging site descriptions.

USGS station no.	Site name and location	Topographic map[b]	Drainage[c] area (km^2)
13047500	Fall River[d] near Squirrel, Idaho, 14.0 km from southwest corner of Yellowstone National Park	Porcupine Lake, Idaho	909
13046995	Fall River above Yellowstone Canal, 9 km from southwest corner of Yellowstone National Park and upstream from all irrigation diversions	Porcupine Lake, Idaho	909
06036905	Firehole River, 4.2 km upstream from Madison Junction	Madison Junction, Wyo.	730
06191000	Gardner River near Mammoth, Yellowstone National Park	Mammoth, Wyo.-Mont.	202
06037000	Gibbon River, 6.4 km upstream from Madison Junction	Madison Junction, Wyo.	306
13046000	Henry's Fork River near Ashton, 0.4 km downstream from power dam	Ashton, Idaho	1,040
06037500	Madison River near West Yellowstone, Mont. (gaging site not shown on 7.5′ quad.; shown on older 15′ quad.	W. Yellowstone, Mont.-Wyo.	1,088
13010200	Snake River at Flagg Ranch, Wyo., 3.7 km south of Snake River Station, at bridge on U.S. Hwy. 287	Flagg Ranch, Wyo.	405
06191500	Yellowstone River at Corwin Springs, Mont.,	Electric Peak, Mont.-Wyo.	6,793

[a] Detailed descriptions of gaging sites are given in the USGS water-data reports for Idaho, Montana, and Wyoming. See Brennan and others (1996), Shields and others (1996), and Smalley and others (1995).

[b] Topographic maps are USGS 7.5-minute quadrangle maps.

[c] Drainage area from USGS water-data reports for Idaho, Montana, and Wyoming. See water-data reports in references.

[d] The Falls River, named by the fur trappers in the early 1800s, was renamed Fall River in 1997.

River gaging sites and diversions). An estimate of the Fall River discharge during the period for which no data were available (September, October, and early November of 1993) was made as follows:

1. The average daily water flow through the power station for September, October, and November of the following year (1994) was calculated by subtracting the sum of the daily discharges measured at Squirrel (USGS site 13047500) and the daily irrigation diversions from the Fall River, from the daily total flow of the river measured at a newly established gaging station upstream from the diversions from the Fall River (USGS site 13046995).

2. The resulting power-station discharge was plotted against the daily average electrical power generated, as recorded at the power station.

3. Power-station discharge for the months for which there was no data was calculated using the relation between power generated and turbine discharge, as calculated in step 2.

4. Power-station discharge was added to the sum of the measured Fall River discharge gaged at the Squirrel site and at the measured diversions for irrigation upstream from that gage.

Although this estimate, calculated on the basis of the sum of four measurements (flow in each of the two irrigation canals, the flow of the river at the Squirrel gage, and the calculated power-plant discharge), is less accurate than a direct measurement of the flow, the added error to the annual discharge is small. This is true because the stage of the river during the period from September through early November was low and constituted only approximately 6 percent of the annual discharge of the Fall River.

The discharge and chloride flux for the Madison River were not measured for WY 1987, 1988, and 1989. However, the Firehole and Gibbon Rivers were gaged for these years above their confluence where they form the Madison River. Because no known streams or hot springs discharge into the Madison River in the Park, we used the sum of the discharges of the Firehole and Gibbon Rivers as a proxy for the discharge of the Madison River.

To determine the amount of subsurface inflow and chloride flux into the Madison River between the confluence of the Firehole and Gibbon Rivers and the Madison River gaging site 24 km downstream, we used data for times when all three rivers were gaged and compared the discharge of the Madison at West Yellowstone with the sum of the discharges of the Firehole and Gibbon Rivers near their confluence. The chloride fluxes were compared in a similar manner.

The first set of calculations, using data for 1984, 1985, and 1986 (Norton and Friedman, 1991), indicated that the discharge of the Madison River measured at West Yellowstone, Wyo., was 11.7 percent greater than the sum of the discharges of the Firehole and Gibbon Rivers. The chloride flux was

3.6 percent greater in the Madison River than the sum of the fluxes of the Firehole and Gibbon Rivers.

Calculations from data reported in this paper, using data for 1990–1994 in addition to data for 1984, 1985, and 1986, resulted in new values for these factors; 6.7 percent added discharge and 5.7 percent added chloride flux in the Madison River compared to the sum of the values of the Firehole and Gibbon Rivers. We used our calculated factors to derive the discharge and chloride flux for the Madison River in 1987, 1988, and 1989, when the discharge of the Madison River was not measured.

Annual Discharge Values

The annual integrated discharge values for the Fall, Firehole, Gibbon, Madison, Snake, and Yellowstone Rivers are given in table 2. In calculating the annual discharge, it is necessary to integrate the instantaneous discharge measurements from the beginning to the end of the water year. For sites where samples had not been collected on October 1 and September 30, we used the published average daily discharges for those days.

In a few cases, the annual discharges as published by the WRD and derived from integration of river-stage measurements made every 15 minutes to calculate annual discharge, showed large disagreement with our data (table 3). For example, the results of our data for the Madison River for WY 1993 are 8 percent greater than those published by the WRD (table 3). Another example is the Gibbon River for WY 1989—we calculated 12.7 percent less discharge than the WRD published value.

By examining our data sets in table 3 (data for 1 water year for one river constitutes a data set), we noted that, in 14 cases out of 91, samples were not collected on the dates prescribed by our collection protocol. To correct the data sets, we added to our data the published average daily discharge values for the dates on which samples were missed. The data added to our original data sets were identified in Friedman and Norton (2000) (no times were listed under the column heading "time" in their report). Both the corrected data sets and the uncorrected data sets (in parentheses) are given in table 3.

Annual Discharge Measurements by Two Different Protocols

In this research we assumed that the river sampling by our protocol where 28 samples (collected at strategic times throughout the water year—weekly at periods of rapid change in discharge and less frequently at times of stable flow rates) would yield accurate measurements of annual river discharge and chloride flux for the river. To test this assumption, we compared the total annual discharge of each river, as calculated by our protocol, and the total annual discharge published by the WRD.

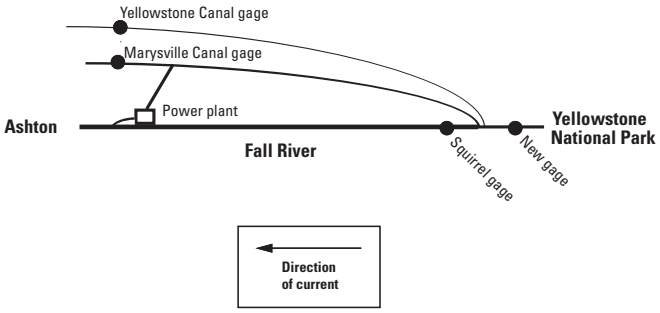

Figure 2. Diagram (not to scale) of the Fall River showing locations of gaging stations and water diversions from the river.

Comparisons of our data with WRD data are given in table 3. The percent differences are given for each river and year. Plots of the discharges calculated by our protocol versus those published by the WRD are shown in figure 3.

For 19 years of record, the average difference in stream flow between the two collection protocols is 0.3 percent with a standard deviation of 4 percent. Because the WRD stage values were collected at 15-minute intervals (35,040 measurements per year), those values are taken to be the true measures of the discharge. The agreement between these two sets of data (fig. 3) indicates that our collection protocol involving only 28 discrete samples is adequate to accurately determine annual discharge of the individual rivers.

Relation Between River Discharge and Chloride Concentration

Plots for each river of the relationship between the chloride concentration and river discharge recorded at the time each sample was taken (fig. 4) show that the relationships are power functions. This indicates that the relation between chloride concentration and river discharge cannot be explained by simple dilution by snow meltwater to the base flow of the river. The base flow is assumed to have a constant input of thermally derived chloride.

We believe that the chloride in the rivers is derived partly from chloride stored in the shallow ground-water system and released by increased ground-water head generated by snowmelt, and partly by a steady flux from deep thermal aquifers that are not affected by changes in the height of the water table. In addition, a small "non-thermal" chloride flux (~7 percent) is attributed to rock weathering, precipitation, and human waste. The contributions from these non-thermal sources can be estimated by examining the chloride concentration of non-thermal streams in the Park, which typically have chloride concentrations of 0.7 to 1 mg/L, in contrast to chloride concentrations of water samples from the streams and rivers that drain thermal features and have chloride concentrations from 2 to 500 mg/L (Norton and Friedman, 1985).

Table 2. Annual discharge from the Fall, Firehole, Gibbon, Madison, Snake, and Yellowstone Rivers.

Water year	Fall River		Firehole River		Gibbon River		Madison River		Snake River		Yellowstone River		Sum of four rivers[a]	
	cfs×10^{10}	m^3×10^8	cfs×10^{10}	m^3×10^8	cfs×10^{10}	m^3×10^8	cfs×10^{10}	m^3×10^8	cfs×10^{10}	m^3×10^8	cfs×10^{10}	m^3×10^8	cfs×10^{10}	m^3×10^8
1983	2.95	8.36					1.73	4.89	3.22	9.11	9.14	25.9	17.1	48.3
1984	3.72	10.52	4.04	1.14	1.17	3.32	1.72	4.86	3.29	9.33	11.4	32.4	20.3	57.5
1985	2.75	7.78	3.43	0.97	1.81	5.01	1.6	4.52	2.47	7.00	8.45	23.9	15.3	43.2
1986	3.17	8.98	4.15	1.17	1.27	3.61	1.95	5.52	3.59	10.2	11.7	33.1	11.8	33.3
1987	1.98	5.60	2.82	0.799	9.46	2.68	1.31[b]	3.71[b]	1.72	4.87	6.77	19.1		
1988	1.84	5.20	2.63	0.744	8.64	2.45	1.16[b]	3.29[b]	1.68	4.76	6.18	17.5	10.9	30.9
1989	2.44	6.92	4.01	1.13	8.82	2.5	1.41[b]	3.99[b]	2.64	7.47	8.80	24.9	15.3	43.4
1990	2.31	6.53	3.61	1.02	9.04	2.56	1.39	3.95	2.62	7.42	9.57	27.1	15.9	45.0
1991	2.43	6..87	4.06	1.15	9.33	2.64	1.47	4.17	2.77	7.83	10.29	29.1	16.9	48.0
1992	1.88	5.32	3.37	0.955	8.23	2.33	1.38	3.92	1.91	5.42	9.04	25.6	14.2	40.3
1993	3.12	8.83	5.16	1.46	9.37	2.65	1.65	4.67	2.86	8.09	11.23	31.8	18.8	53.4
1994	1.96	5.56	3.43	0.972	9.05	2.56	1.52	4.31	1.84	5.21	7.42	21.0	12.7	36.1
1995													18.1[c]	51.2[c]
1996													21.8[c]	61.7[c]
1997	4.31	12.2					2.44	6.92	4.57	12.9	15.91	45.1	27.2	77.1
1998	3.24	9.19					1.94	5.50	3.44	9.73	10.89	30.8	19.6	55.5
1999	3.20	9.05					2.05	5.81	3.61	10.4	12.12	34.3	21.0	59.4
2000	2.71	7.42					1.71	4.84	2.59	7.33	9.14	25.9	16.1	45.7
2001	1.94	5.50					1.42	4.02	1.63	4.50	6.55	18.6	11.5	32.6
2002	2.22	5.14					1.34	3.81	2.50	7.08	8.36	23.7	14.4	39.7
2003	2.41	6.82					1.65	3.83	2.32	6.57	8.70	24.6	15.1	41.8

[a] Sum of the Fall, Madison, Snake, and Yellowstone Rivers.

[b] Calculated value, sum of the discharges of the Firehole and Gibbon Rivers × 1.067. The factor 1.067 is a correction for inflow to the Madison River between the confluence of the Firehole and Gibbon Rivers and the Madison River gaging site at West Yellowstone—see text.

[c] From published USGS WRD data.

Table 3. Comparison, by two different data-collection protocols, of annual discharges of rivers that drain Yellowstone National Park.

[Discharges measured in acre-feet×10^4. Discharges on Fall River from 1983 to 1994 do not include diversions above the gaging station for irrigation. A, data from this report; WRD, data from published values by U.S. Geological Survey Water Resources Division; D, percent difference: ((WRD–A)/WRD)×100. Numbers in parentheses are uncorrected values, as discussed in the text]

Water year	Fall River			Firehole River			Gibbon River			Madison River			Snake River			Yellowstone River		
	A	WRD	D	A	WRD	D	A	WRD	D	A	WRD	D	A	WRD	D	A	WRD	D
1983	68.34	69.53	–2.2	--	--	--	--	--	--	39.67	--	--	73.87	--	--	210.0	219.2	–4.2
1984	85.73	83.05	3.2	26.82	25.79	4.3	9.265	9.494	–2.4	39.43	38.59	2.2	75.62	--	--	262.7	255.2	2.9
1985	60.21	62.06	–3.0	25.17	24.76	1.7	8.147	8.283	–1.6	36.65	37.02	–1.0	56.72	59.64	–4.9	194.0	195.0	–0.5
				(26.11)		(5.5)	(7.867)		(–5.0)				(54.88)		(–8.0)	(187.3)	(–4.2)	
1986	71.10	73.04	–2.6	29.30	28.90	1.4	9.515	9.691	–1.8	44.76	44.57	0.4	82.33	83.32	–1.2	268.1	264.7	–1.3
				(30.43)		(5.3)										(273.1)	(3.3)	
1987	42.69	43.55	–2.0	21.72	21.85	–0.6	6.481	6.477	0.1	31.59	--	--	39.47	40.38	–2.3	155.1	151.5	2.4
																(135.9)	(–10.3)	
1988	39.24	40.68	–3.6	19.84	19.19	3.4	6.035	5.988	0.8	27.86	--	--	38.55	38.18	1.0	142.0	143.3	–0.9
1989	53.10	54.02	–1.7	20.25	21.10	–4.0	9.195	8.771	4.8	30.92	--	--	60.57	62.96	–3.8	202.0	202.8	–0.4
							(7.656)		(–12.7)						(216.3)	(6.7)		
1990	49.83	51.59	–3.2	20.77	20.95	–0.9	8.286	8.152	1.6	31.98	31.99	0.0	60.12	58.54	2.7	219.8	216.6	1.5
																(226.2)	(2.1)	
1991	53.31	51.95	2.6	21.42	21.74	–1.5	9.319	9.365	–0.5	33.78	34.96	–3.4	63.47	63.04	0.7	236.2	231.4	2.1
							(9.000)		(–3.9)									
1992	41.22	42.14	–2.2	18.90	19.33	–2.2	7.744	7.853	–1.4	31.75	31.92	–0.5	43.91	45.09	–2.5	207.6	200.2	3.7
							(6.802)		(–13.4)									
1993	67.68	69.64	–2.8	21.51	21.86	–1.6	11.84	11.49	–3.0	37.82	37.29	–1.4	65.55	65.39	0.2	257.7	251.6	2.4
										(40.29)		(8.0)	(60.40)		(–7.6)			
1994	48.19	--	--	20.76	20.63	0.6	7.88	7.81	0.9	34.96	33.73	3.3	42.23	44.35	–4.8	170.4	174.0	–2.1
1995	--	63.36	--	--	--	--	--	--	--	--	39.95	--	--	71.13	--	--	240.3	--
1996	--	75.45	--	--	--	--	--	--	--	--	48.50	--	--	48.24	--	--	327.7	--
1997	99.0	99.2	–0.2	--	--	--	--	--	--	56.18	57.11	–1.6	104.8	111.4	–5.9	365.2	373.4	–2.2
1998	76.73	74.82	2.6	--	--	--	--	--	--	44.58	44.39	0.04	78.92	77.12	2.3	249.9	255.8	–2.3
1999	73.40	74.45	–1.4							47.20	46.45	1.6	82.97	85.36	–2.8	278.3	281.1	–1.0
2000	62.13	59.94	3.7							39.25	39.86	–1.5	59.42	60.99	–2.5	209.9	511.2	–0.6
2001	44.5	43.33	2.9							32.55	32.18	1.0	37.31	38.33	–2.7	150.4	145.5	3.4
2002	50.91	51.55	–1.2							30.85	30.89	–0.1	57.38	58.68	–2.2	192.0	194.0	–1.0
2003	55.30	56.59	–2.2							31.05	31.51	–1.5	53.22	54.74	–2.8	199.8	202.4	–1.3

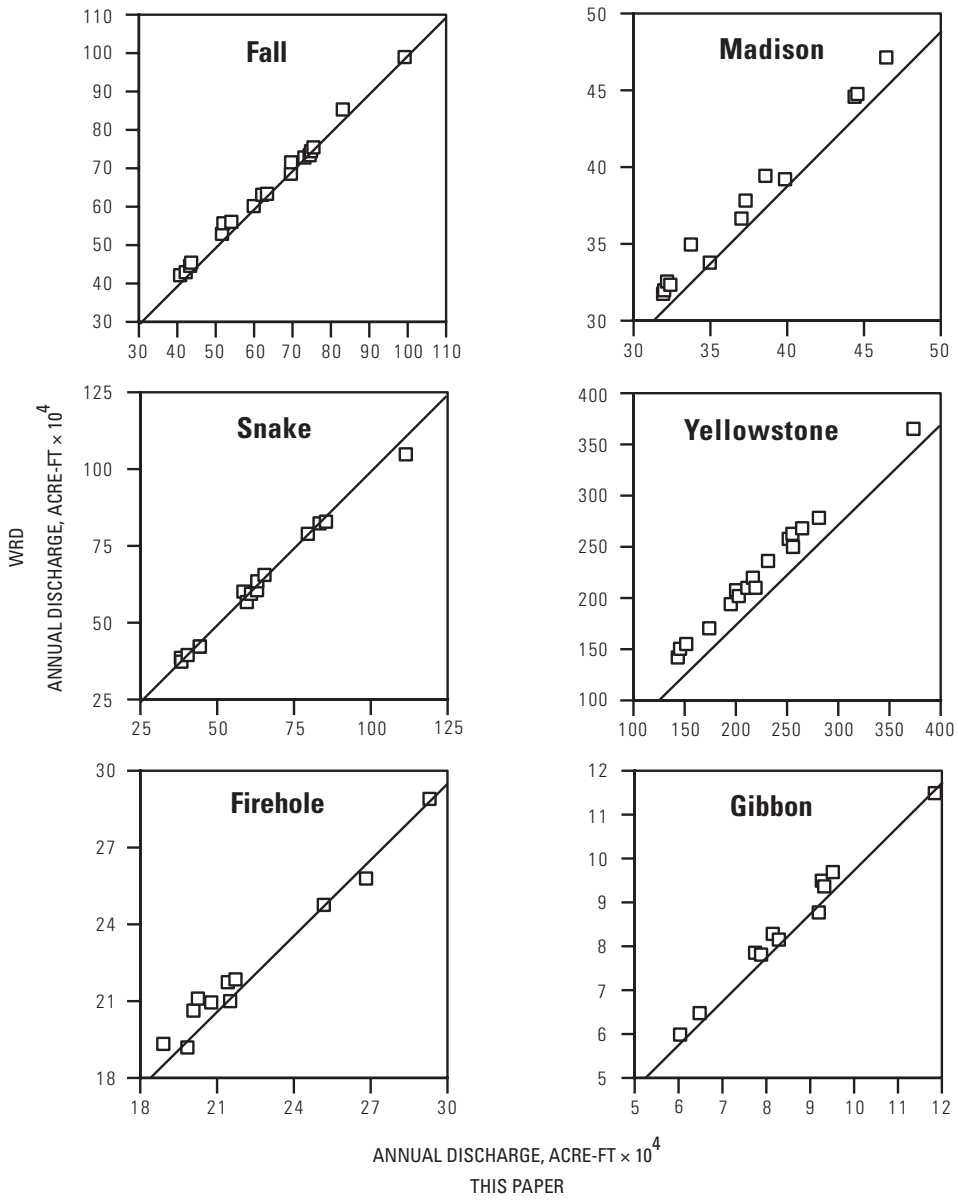

Figure 3. Relationship of annual discharges of six rivers, as calculated in this paper, plotted against discharges published by Water Resources Division of the USGS.

Chloride Flux

Calculation of Chloride Flux

Instantaneous chloride fluxes, tabulated in Friedman and Norton (2000), were calculated by multiplying the chloride concentrations of the samples by the river discharges recorded at the time of sample collection. Annual summations were made by integrating between calculated values for each sample from the beginning of the water year (October 1) to the end of the water year (September 30). If samples had not been collected on October 1 and September 30, the published average daily values of discharge were used, and the chloride concentrations for these discharges were calculated by linear interpolation. Errors introduced by these interpolations are small because at that time of the year the discharges of the rivers were close to minimum flow, and they were changing slowly with time. For other scheduled dates on which no samples were collected, we calculated the chloride concentrations of the water by using the plotted relationships between chloride concentrations and discharges for each river. Those relationships were determined for each river for the measured chloride concentrations of water samples versus the discharge recorded at the time each sample was taken (fig. 4). Integrations were carried out for each water year, and the results are shown in table 4.

The error assigned to the the instantaneous chloride flux calculations is ±5.4 percent. This value is derived from the error of the individual chloride concentration (E=2 percent) and the discharge measurements (E=5 percent) as follows, where E=error.

$$\text{Chloride flux error} = \sqrt{\bar{E}^2_{\text{chloride}} + \bar{E}^2_{\text{discharge}}}$$

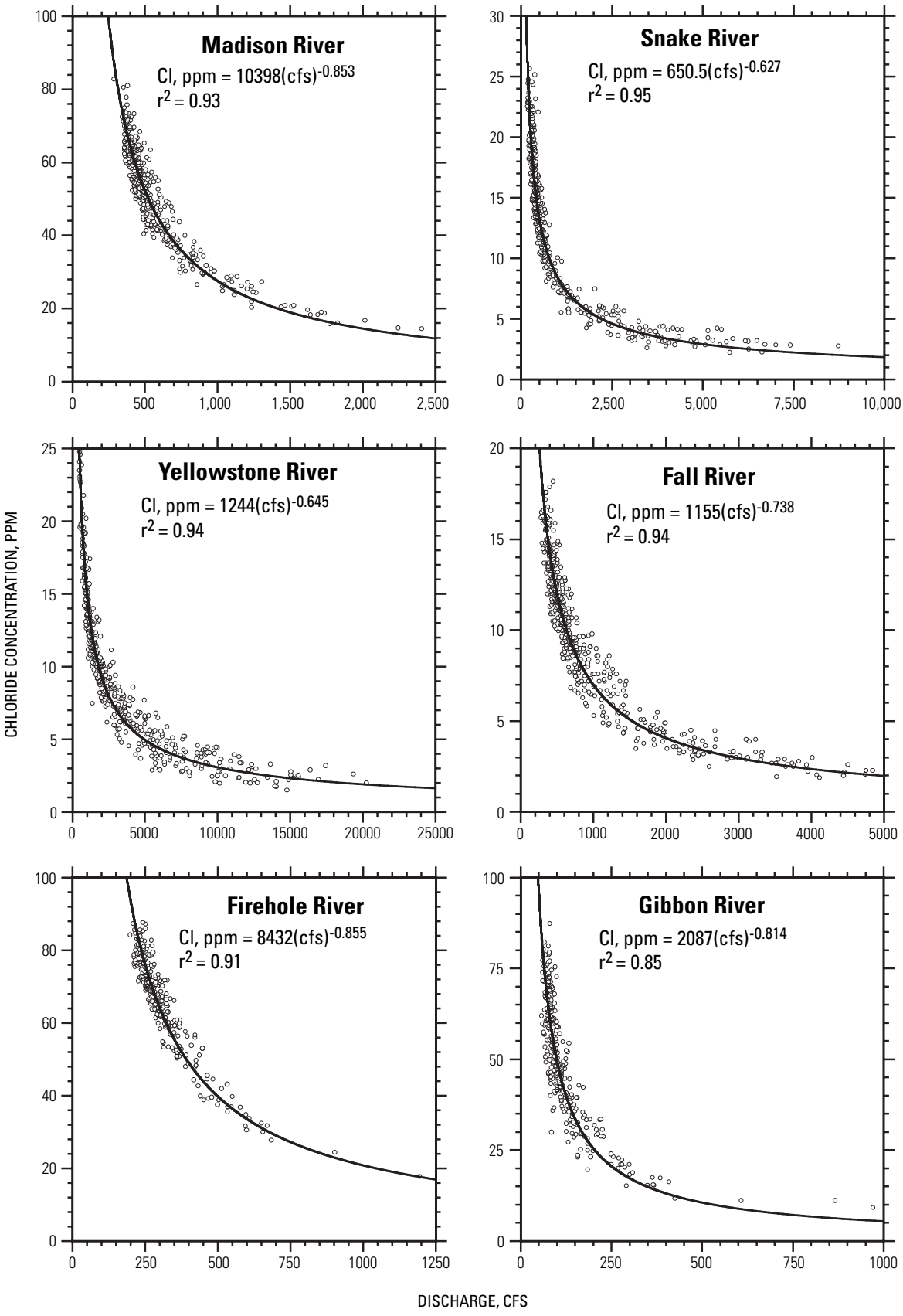

Figure 4. Graphs of chloride concentrations of water samples from six rivers, plotted against discharges measured at the times of collection.

Calculation of Thermal-Chloride Flux

Norton and Friedman (1985) estimated that the background average concentration of non-thermal chloride in the rivers exiting the Park was 0.7 mg/L. This was the sum of chloride contributed by surface-rock weathering, precipitation, and human waste. If this value of non-thermal chloride is subtracted from all of the experimentally determined chloride values, the remaining chloride concentrations represent the thermal chloride derived directly from the hydrothermal system. In this report, the chloride-flux values quoted are thermal chloride unless otherwise stated.

Calculations of the percent of non-thermal chloride for the 19 years of recorded data (table 4) show that it is 7 percent of the total chloride, in comparison to 6 percent reported by Norton and Friedman (1985) on the basis of a much smaller database.

The percentage of thermal chloride compared to total chloride flux differs for each river (table 5). These differences are mainly related to the different proportions of non-thermal chloride versus chloride derived from thermal inflow.

Thermal-Chloride Flux from the Major Rivers

The percent of the total thermal-chloride flux from the Park via each of the major rivers (not including the flux from the west boundary of the Park) for the 19 years of measurement is given in table 5. These values do not differ significantly from those reported earlier by Norton and Friedman (1985).

Thermal-Chloride Flux from the West Boundary of the Park

In their paper on chloride flux from Yellowstone National Park, Norton and Friedman (1985) calculated the chloride flux from the west boundary of the Park as 5 percent of the total leaving the Park. That value was derived from published data (Whitehead, 1978) on stream flow and chloride concentration from several streams that flow from the west boundary into the Henrys Fork River. The data derived from several samples of each stream, collected at infrequent intervals over a period of several years. In 1998, we established a collection site on the Henrys Fork River near Ashton, Idaho (fig. 1), to quantify this important source of chloride. This site is southwest of the Park, and it should record all of the thermal chloride that leaves the Park along the west boundary. For water year 1999, the total chloride flux was 5.5×10^9 g, of which 4.1×10^9 g was thermal chloride. This thermal chloride was 7.6 percent of the total thermal chloride (53.3×10^9 g) that exited the Park during that water year. The total annual chloride flux exiting the Park via the four major rivers, as well as the total that includes that exiting via the Henrys Fork River, are shown in table 6.

Seasonal Variation of Chloride Flux

Because 93 percent of the chloride exiting the Park is hydrothermally derived chloride, we would not expect this flux to show short time (seasonal) variations. However, Fournier and others (1976), Norton and Friedman (1985), and the present authors noted seasonal changes in flux, with a maximum that coincided with the peak of snowmelt runoff (fig. 5). Fournier and others (1976) and Ingebritsen and others (2001) ascribed these seasonal variations in chloride flux to entrapment of thermal chloride in the soil during winter months, associated with freezing, and subsequent release of the trapped chloride during snowmelt. However, the deep snow cover over most of Yellowstone National Park during the winter insulates the ground and prevents the soil from freezing, making this explanation improbable. In addition, the ground in the major thermal areas remains unfrozen and free of snow in the winter. Don White (oral commun., 1984) postulated that the seasonal variations of chloride were caused by entrapment of chloride in the soil during summer and fall, associated with increased temperatures and reduced water-table levels. Although some storage of chloride in the soil probably occurs, it is difficult to associate the synchronism between river discharge and chloride flux to this process. The present authors offer another explanation.

Friedman and Norton (1990) and Friedman and others (1993) reported that samples from individual thermal springs, collected close to their orifices, showed seasonal changes in discharge similar to those of the major rivers. Although the hot-spring discharges increased during snowmelt and decreased in the fall and winter, the chloride concentrations changed very little. They suggested that the major cause of this seasonality in hot-spring discharge was changes in the height of the local water table. Increased water-table height during snowmelt increased hydrostatic pressure above the aquifers that fed the springs and enhanced their flow. Because the hot-spring aquifers and the local water-table water did not mix—at least not in the short time represented by our collections—the chloride concentrations in the hot-spring effluent did not change, and they were independent of discharge rates. As a result, the increased hot-spring discharges during times of high water table associated with snowmelt runoff caused increases in chloride flux during those periods. Because chloride in the rivers is derived mainly from thermal springs, this increase in chloride derived from hot springs explains the observed seasonal increase in chloride flux in the rivers.

It is important to note that the seasonal increases in discharge and chloride flux for the Madison, Firehole, and Gibbon Rivers are not as large as those for the Fall, Snake, and Yellowstone Rivers (fig. 5). This may be explained by the fact that the former rivers drain the major geyser-containing areas of the Park—Upper, Midway, and Lower Geyser Basins, as well as Norris Geyser Basin. We believe that the geyser basins receive a greater proportion of thermal water of deep origin that is isolated from the effects of the local water table than do the thermal features that drain into the Fall, Snake, and Yellowstone Rivers. Another contributing factor that tends to lower the seasonal variation in discharge and chloride flux in the Madison, Firehole, and Gibbon Rivers is the presence of large areas of thermally heated ground in the drainage areas of these rivers. During the winter, snow melting on these heated areas reduces the amount of snow remaining to contribute to early summer runoff.

Table 4. Annual chloride flux, both total and thermal, from the Fall, Madison, Snake, and Yellowstone Rivers.

[All values reported in grams × 10^9]

Water year	Fall River		Madison River		Snake River		Yellowstone River		Sum of four rivers	
	Total	Thermal	Total	Thermal	Total	Thermal	Total	Thermal	Total	Thermal
1983	6.18	5.59	24.85	24.51	7.23	6.60	19.57	17.10	57.83	53.79
1984	6.34	5.60	23.64	23.30	7.17	6.51	20.19	17.92	57.34	53.34
1985	6.24	5.70	23.59	23.28	7.25	6.05	17.49	15.64	54.57	50.67
1986	6.35	5.71	24.95	24.57	8.13	7.42	21.66	19.20	61.09	56.89
1987	5.67	5.28	21.77	21.71	5.80	5.21	16.58	15.18	49.82	47.37
1988	5.11	4.75	21.62	21.60	5.26	4.93	14.38	13.13	46.37	44.40
1989	5.55	5.06	23.18	23.12	6.42	5.90	17.24	15.49	52.39	49.58
1990	6.23	5.77	24.68	24.40	7.33	6.81	18.81	16.90	57.05	53.89
1991	6.16	5.68	23.91	23.62	7.21	6.66	18.93	16.66	56.22	52.62
1992	5.57	5.20	23.51	23.24	6.03	5.65	15.88	14.09	50.99	48.17
1993	6.12	5.42	23.91	22.90	7.41	6.54	17.48	15.11	54.32	49.97
1994	5.59	5.16	23.49	23.19	5.58	5.21	15.33	13.86	49.99	47.42
1995										
1996										
1997	6.86	6.00	24.35	23.86	8.05	7.15	20.73	17.58	59.99	54.59
1998	5.17	4.55	22.16	21.31	6.98	6.18	18.08	15.92	52.39	47.96
1999	5.19	4.53	23.46	23.05	6.58	5.86	18.19	15.79	53.42	49.23
2000	5.74	5.22	22.77	22.15	6.46	5.95	16.02	14.20	50.99	47.51
2001	5.66	5.18	22.31	22.03	5.75	5.43	16.09	14.84	49.81	47.48
2002	5.37	4.80	22.62	22.35	7.59	7.05	15.09	13.46	50.67	48.02
2003	5.31	4.83	21.71	21.45	5.86	5.40	15.55	13.82	48.43	45.50

Modeling of Thermal and Non-Thermal Inputs to the Major Rivers

The following is an attempt to model the various inputs to the major rivers to explain the chloride versus discharge data (fig. 4) and the seasonal changes in chloride concentrations that are observed (fig. 5).

Gardner River

In modeling inputs to the Gardner River, we have used the base flow of the river as measured at the gaging station located at the confluence of the Gardner with the Yellowstone River as one input, with an inflow of 70 cfs and a chloride concentration of 0.7 ppm. This is the non-thermal chloride concentration reported by Norton and Friedman (1985) for streams within the Park that do not contain thermal water and includes chloride input from rock weathering. Another input to the river is snow meltwater, which varies in quantity from zero to a maximum of 800 cfs and has a chloride concentration of 0.2 ppm, as reported by Norton and Friedman (1985). The final input is thermal chloride from Mammoth Hot Springs, with a measured chloride of 170 ppm and a seasonally varying flow of 22 cfs at base-flow conditions to 27 cfs at maximum river flow. The amount of this hot-spring water that enters the river at base flow was calculated from the amount necessary to satisfy the chloride concentration of the river at base flow (41 ppm). The amount that discharges into the river at snowmelt maximum is also calculated to satisfy the measured chloride concentration of the Gardner River at maximum discharge (~6 ppm). Table 7 shows the details of these calculations of discharge and chloride concentrations at various river flows. The calculated chloride concentration versus discharges from table 7 are plotted as large filled circles on a plot of measured chloride concentration versus discharge in figure 6. The calculated data from table 7 fits precisely with the least-mean-squares average for the measured data.

To observe the result of assuming that the thermal water input does not vary seasonally as assumed in table 7, we have plotted data presuming that the thermal water from Mammoth Hot Springs is constant at 22 cfs, the postulated input

Table 5. Percent thermal chloride as compared to total chloride for each river, and percent thermal chloride compared to total thermal chloride exiting in the Park.

River	Percent thermal chloride compared to total chloride for each river	Percent thermal chloride for each river compared to total chloride exiting the Park
Fall	91.5	10
Madison	98.6	46
Snake	91.4	12
Yellowstone	88.7	32

Table 6. Total thermal-chloride flux from Yellowstone National Park, Wyoming, water years 1983–2003.

Water year	Four rivers[a] thermal-chloride flux g×10^{10}	Four rivers plus Henrys Fork River thermal-chloride flux[b] g×10^{10}
1983	5.38	5.76
1984	5.33	5.70
1985	5.07	5.42
1986	5.69	6.08
1987	4.74	5.07
1988	4.44	4.75
1989	4.96	5.31
1990	5.39	5.77
1991	5.26	5.63
1992	4.82	5.16
1993	5.00	5.35
1994	4.72	5.05
1995		
1996		
1997	5.46	5.84
1998	4.80	5.14
1999	4.92	5.26
2000	4.74	5.07
2001	4.75	5.08
2002	4.80	5.14
2003	4.55	4.87

[a] The totals are the sums of the values for the Fall, Madison, Snake, and Yellowstone Rivers.

[b] Total flux is calculated by summing the flux from the four rivers and multiplying by 1.07. The factor 1.07 corrects the total thermal flux for thermal-chloride flux discharged via the Henrys Fork River.

to the Gardner River at base flow. The results of this calculation are shown as squares enclosing a cross in figure 6, and these points deviate from the least-mean-squares average for the measured data points. This comparison lends credence to the assumption that the inflow of thermal water varies seasonally, increasing by 23 percent at high river discharge.

Fall River

A calculation for inflow to the Fall River similar to that made for the Gardner is given in table 8. In this calculation, the thermal-water chloride concentration (85 ppm) is that reported by Friedman and others (1993) for springs in the southwestern part of the Park that enter the Fall River. The input of thermal water varies seasonally from 70 to 115 cfs, a 62 percent increase during the time of maximum snowmelt input. The data derived from the model plots (large filled circles in fig. 7) almost exactly on the least-mean-squares average to the measured data as plotted on figure 4. As before, we have plotted the data assuming that the amount of thermal water input is constant, and again these data deviate from the least-mean-squares line.

Madison River

For the Madison River, we used a value of 400 ppm for the thermal water input. This is based on published values for the analysis of many of the geysers and hot springs in the Upper, Midway, Lower, and Norris Geyser Basins reported by Thompson and others (1975). A 31-percent seasonal increase in thermal chloride is assumed. Again, the data calculated from the model (table 9 and fig. 8) fits the least-mean-squares average for the measured chloride concentration versus discharge (fig. 4), whereas the data calculated assuming a constant thermal-chloride water input does not fit the measured data.

Snake River

Thermal input to the Snake River was assumed to have a chloride concentration of 300 ppm and to increase from 14 cfs at base flow to 55 ppm at maximum flow of the river, a seasonal change of 293 percent (table 10 and fig. 9). Again, the model data fits the measured least-mean-squares average (fig. 4), whereas the data using a seasonally unvarying input does not fit the average.

Yellowstone River

For the Yellowstone River we used two sources of thermal water—thermal water input from Mammoth Hot Springs, for which we used the data in table 7, and other thermal water introduced upstream from the confluence of the Gardner River. This second source was assumed to have a chloride concentration of 30 ppm and to vary seasonally from 500 to 950 cfs. The results of these calculations are given in table 11 and plotted in figure 10. Again, results from the seasonally varying input of thermal water fit the measured data, but the data calculated assuming a fixed amount of thermal water input does not agree with the measured data.

Origin of the Seasonal Increase of Chloride in the Major Rivers of Yellowstone National Park

From the measured values of chloride flux in the rivers of the Park, it is obvious that the flux increases during snowmelt. In the above modeling of water inflow to the individual rivers, we have shown that this increase in chloride flux is mainly due to seasonal changes in thermal chloride input. However, it is not proven that all of this thermal chloride input is caused by an increased flow of hot springs. It is possible that these seasonal changes in chloride flux result from changes in the concentration of chloride in snowmelt runoff due to solution of chloride stored in the soil during summer. This latter process

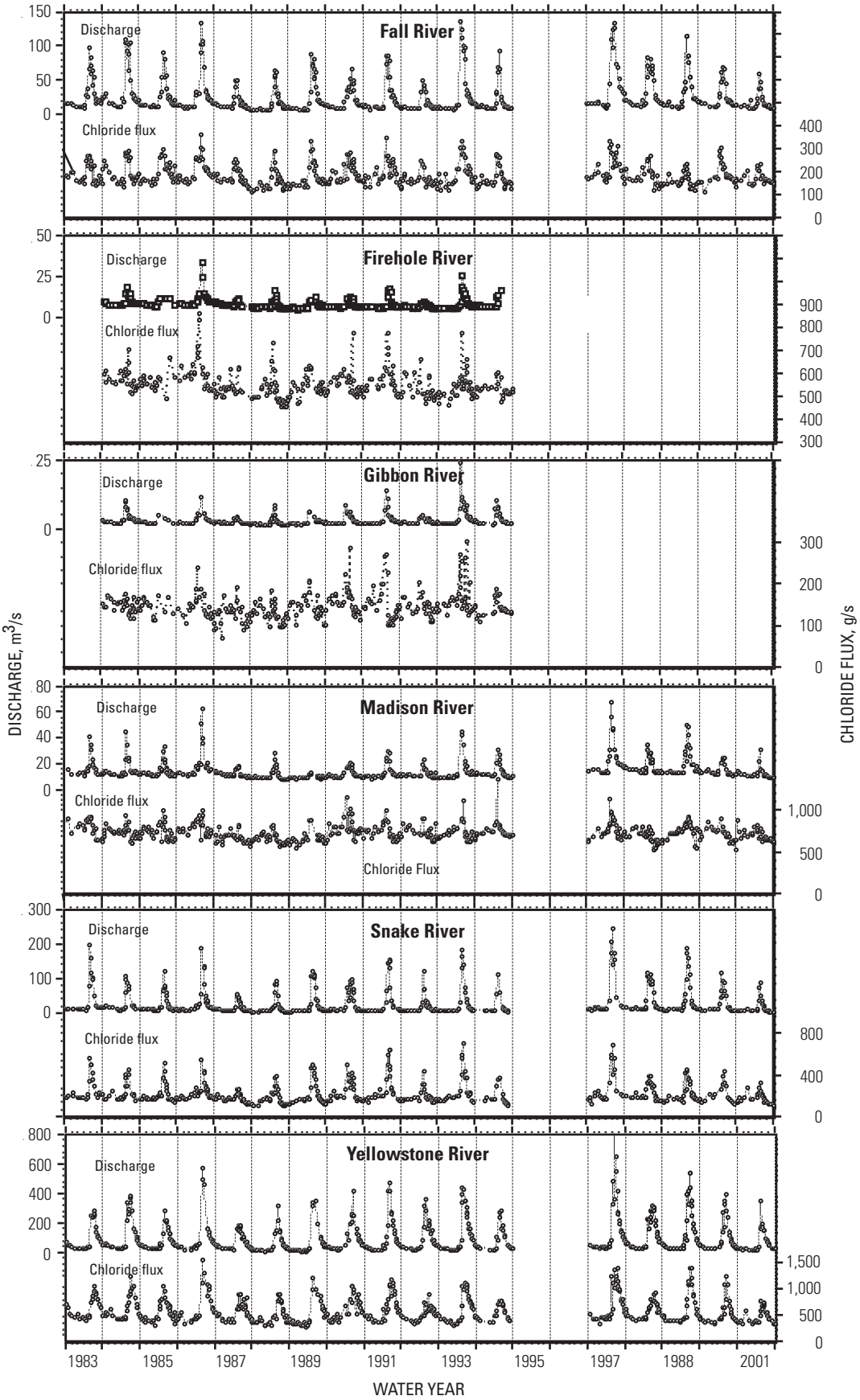

Figure 5. Graph showing instantaneous values for discharge and chloride flux for the Fall, Firehole, Gibbon, Madison, Snake, and Yellowstone Rivers for water years 1983 through 1994 and 1997 through 2001.

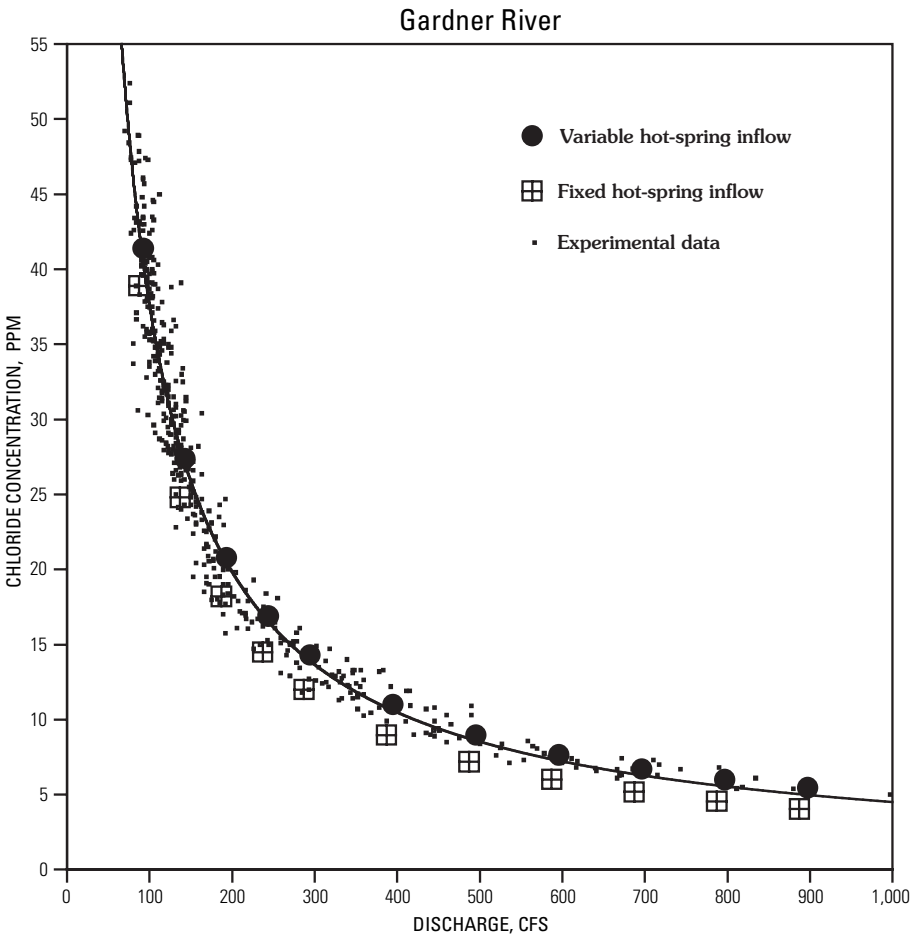

Figure 6. Graph of chloride concentration versus discharge for the Gardner River showing experimental data and models of inflow to the river from various sources.

may be a factor in explaining the seasonality of chloride flux in the rivers. However, we have observed that some springs have a constant chloride concentration that does not change when the discharge of the spring increases during snowmelt. For example, the discharge of Norris Geyser Basin measured at Tantalus Creek can vary by a factor of three, but the chloride concentration of the discharge remains constant at 450±50 ppm. In addition, thermal streams in the Boundary Creek area of the Park display a similar pattern of behavior, where the discharges of these streams increases many fold during snowmelt, but their chloride concentration remains constant throughout the year. Based on these observations, we favor the explanation for the anomalous chloride flux during snowmelt to increased flow of hot springs that discharge into the rivers.

Long-Term Variations in Chloride Flux

In addition to seasonal changes in flux that we attribute to the height of the shallow ground-water table, there are longer term changes, as illustrated in figure 11, showing a plot of the annual thermal-chloride flux from the Madison, Yellowstone, Snake, and Fall Rivers for the 19 years of measurement (21 years of record). These longer term changes also are reflected in the sum of the annual chloride fluxes from the four rivers. The 21-year record of total thermal chloride exiting the Park via the four major rivers shows a decline of about 0.4 percent/year (fig. 12). This change does not appear to be significant due to the scatter in the data that is indicated by the low coefficient of determination (r^2=0.26). In the next section we show that correcting these annual thermal-chloride values for climatic factors that affect the flux results in significant changes in the corrected chloride flux during the 21-year interval.

Effect of Climate on Chloride Flux

The annual chloride fluxes in the rivers are related to the discharges of the rivers, which in turn are related to variations of annual precipitation on their drainage areas (fig. 12). Thus, annual variations in climate affect the chloride flux exiting the Park.

Because of the relationship between thermal-chloride flux and river discharge, which we document, we corrected the thermal-chloride flux for variations in river discharge. To adjust the thermal-chloride flux for river discharge, we normalized the annual chloride-flux data to a common river discharge, which was the average discharge for the 19 years of measurement. This was done by adding to each value

of the annual thermal-chloride flux a factor 2.5 times the difference between the river-discharge value for that year and the average discharge. This correction increased the r^2 value of the linear least-mean-squares regression fit to the data from 0.26 to 0.57.

The factor 2.5 that was used to make these adjustments was determined by trial and error to obtain the largest regression coefficient for the linear least-mean-squares regression. It is important to note that the slope of the regression line shows a significant decrease of 0.5 percent per year in chloride flux, in contrast to the unadjusted flux decrease of 0.4 percent per year, which we previously did not consider significant due to the scatter in the uncorrected data. During the time in which the chloride flux showed a decrease (1983–2001), both precipitation and river discharge decreased (from 1983 to 1990), and then increased from 1991 to 2003 (fig. 13). The adjusted results, together with the unadjusted annual chloride flux, are plotted in figure 13.

Inasmuch as variations in precipitation and river discharge are correlated (figs. 14 and 15), it should be possible to use precipitation to correct the thermal-chloride flux for the effect of climate. There are only five precipitation collection sites in Yellowstone National Park. However, the correlation (r^2=0.83) between the sum of the precipitation measurements at the five sites and the total discharge of the four rivers draining the park (fig. 15) indicates that the sum of the data from the five precipitation-collection sites, which are distributed throughout the Park, is a good approximation of the precipitation over the Park, and therefore it can be used to correct the annual thermal-chloride flux for the influence of climate on chloride flux.

To determine whether correction of the annual thermal-chloride flux for annual changes in precipitation will result in a data set with less scatter than the data set that was corrected for annual changes in river discharge, we normalized the unadjusted annual thermal-chloride values to a common precipitation value, which is the average precipitation for the years in which we measured chloride flux. This was done by adding 5 times the difference between the annual-precipitation values and the average precipitation from the annual thermal-chloride flux values. The factor 5 was determined by trial and error to obtain the largest regression coefficient for the linear least-mean-squares regression. This resulted in a data set with an r^2=0.37 and an annual decline of 0.7 percent. We conclude that correcting the annual thermal-flux values for changes in annual river discharge yields a data set with slightly less scatter than a data set corrected for changes in annual precipitation.

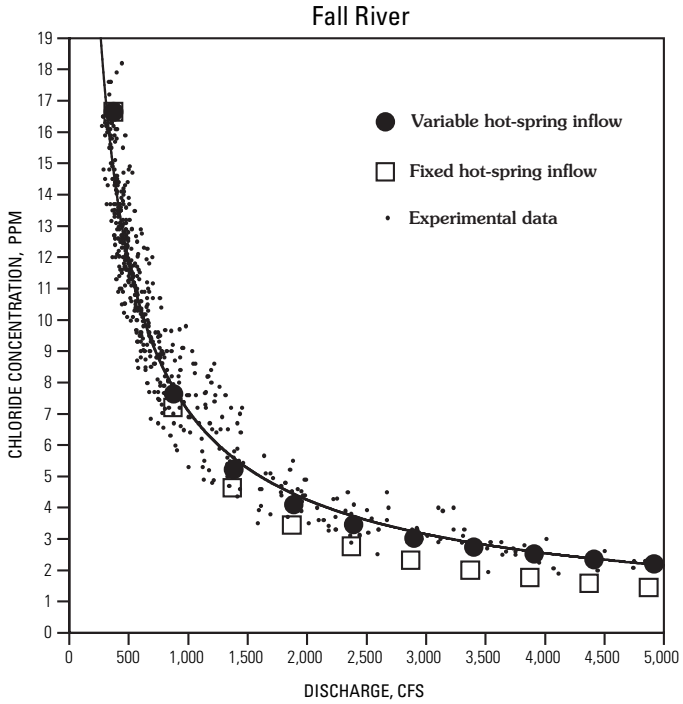

Figure 7. Graph of chloride concentration versus discharge for the Fall River showing experimental data and models of inflow to the river from various sources.

Table 7. Model data for the Gardner River.

River input		Runoff		Hot spring		Total	
cfs	Cl (ppm)	cfs	Cl (ppm)	cfs	Cl (ppm)	cfs[a]	Cl (ppm)[b]
70	0.7	0		22	170	92	41.2
70	0.7	50	0.2	22.5	170	142.5	27.3
70	0.7	100	0.2	23	170	193	20.6
70	0.7	150	0.2	23.5	170	243.5	16.7
70	0.7	200	0.2	24	170	294	14.2
70	0.7	300	0.2	24.5	170	394.5	10.8
70	0.7	400	0.2	25	170	495	8.8
70	0.7	500	0.2	25.5	170	595.5	7.5
70	0.7	600	0.2	26	170	696	6.6
70	0.7	700	0.2	26.5	170	796.5	5.9
70	0.7	800	0.2	27	170	897	5.4

[a] Total cfs equals the sum of the flows of River input, Runoff, and Hot spring.
[b] Chloride concentration in "Total cfs" calculated as follows:
[(column 1)(column 2)+(column 3)(column 4)+(column 5)(column 6)]/column 7.

The long-term changes in chloride flux that we observed contradict the statement made by Ingebritsen and others (2001) who considered the limited data available to them and stated "***the Cl-flux data set shows little evidence of decadal-scale trends in hydrothermal discharge." This contradiction underscores the necessity of securing long-term data sets.

Long-Term Changes in Thermal-Water Outflow from Mammoth Hot Springs

A recent decline in the thermal-water output of a major thermal feature in Yellowstone was noted by Sorey and Colvard (1997). They documented a decline of 15 percent in the output of thermal water from Mammoth Hot Springs from 1987 to 1994 (1.8 percent per year). Their approach involved direct measurement of the flow of Hot River (also known as Boiling River), the major surface discharge from the area, with adjustments to the data to correct for Gardner River inflow into Hot River above its gaging site via a sinkhole in the Gardner River. Beginning in 1985, we used a different method to monitor the thermal-chloride flux discharge of Mammoth Hot Springs. We measured the chloride flux in the Gardner River downstream from the point where both surface and subsurface discharges of the Mammoth Hot Springs enter the river. Measurements of chloride flux in the Gardner River above and below Mammoth Hot Springs show that 90 percent of the chloride in the Gardner River below Mammoth Hot Springs is contributed by the hot springs. We used the chloride flux as measured in the Gardner River at its gaging station below Mammoth Hot Springs to monitor the discharge of chloride from the Mammoth Hot Springs system. To correct these measurements for chloride in the river water before it reaches Mammoth Hot Springs, we multiplied the chloride concentration by 0.9. This coefficient was determined by comparing the chloride concentration of samples collected at high and low river stages at a site below the "High Bridge" (several miles above Mammoth Hot Springs) to the chloride values determined from samples collected below the hot springs. These values then were used to calculate thermal-chloride flux. Our data for 1987–1994, the same period as that used by Sorey and Colvard, shows a decline of 20 percent, as compared to the 15 percent found by them. However, the data from 1995 to 2003, if fitted by a linear least-mean-squares solution—the solid line in figure 16—shows a decline of 1 percent during the past 19 years. Note that the relatively constant thermal chloride flux for the Mammoth Hot Springs system is in contrast with the decline in thermal chloride flux for the entire Yellowstone hydrothermal system.

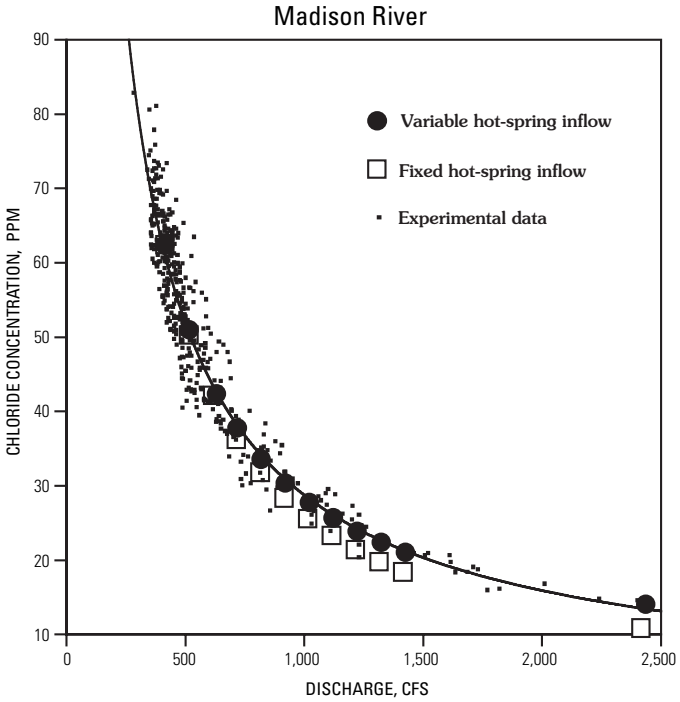

Figure 8. Graph of chloride concentration versus discharge for the Madison River showing experimental data and models of inflow to the river from various sources.

Table 8. Model data for the Fall River.

River input		Runoff		Hot spring		Total	
cfs	Cl (ppm)	cfs	Cl (ppm)	cfs	Cl (ppm)	cfs[a]	Cl (ppm)[b]
300	0.7	0		70	85	370	16.7
300	0.7	500	0.2	75	85	875	7.64
300	0.7	1,000	0.2	80	85	1,380	5.22
300	0.7	1,500	0.2	85	85	1,885	4.10
300	0.7	2,000	0.2	90	85	2,390	3.46
300	0.7	2,500	0.2	95	85	28,955	3.03
300	0.7	3,000	0.2	100	85	3,400	2.74
300	0.7	3,500	0.2	105	85	3,905	2.52
300	0.7	4,000	0.2	110	85	4,410	2.35
300	0.7	4,500	0.2	115	85	4,915	2.21

[a] Total cfs equals the sum of the flows of River input, Runoff, and Hot spring.
[b] Chloride concentration in "Total cfs" calculated as follows:
[(column 1)(column 2)+(column 3)(column 4)+(column 5)(column 6)]/column 7.

Is Yellowstone Losing Its Steam?

The rapid decline in output of thermal-chloride flux from the Yellowstone National Park hydrothermal system documented by this study, added to the decrease in the frequency of eruptions of Old Faithful Geyser (fig.17), give cause for concern. However, if the decrease in activity of the Yellowstone hydrothermal system is a response to deflation of the caldera, as measured by depression of the area under Yellowstone Lake that occurred from 1985 through 1995, then the decrease possibly will be reversed in response to future tectonic changes in Yellowstone National Park. The area occupied by Yellowstone Lake increased in elevation about 2 cm/yr from about 1923 to 1984 (Dzurisin and others, 1994). It was stable from 1984 through 1985; it decreased in elevation by 2 cm/yr from 1985 through 1995 and has begun to inflate again (Wicks and others, 1998). The inflation of the caldera was explained by Dzurisin and others (1994) as follows. The deep hydrothermal system was pressurized by fluids released from a crystallizing body of rhyolitic magma beneath the caldera. It then was trapped beneath a self-sealing layer near the base of the hydrothermal system. Subsequently, there was aseismic intrusion of magma into the lower part of the sub-caldera magma body. They attributed the subsidence that followed inflation of the caldera to depressurization and fluid loss from the deep hydrothermal system and sagging of the caldera floor in response to regional crustal extension. Our evidence suggests that, during inflation, increased fluid pressure at depth results in increased loss of vapor to the shallow hydrothermal system and that, during deflation, lower fluid pressure results in less vapor released from the magma to interact with the shallow geothermal system.

It is possible that the caldera will continue to inflate and deflate over 10- to 20-year intervals and that the hydrothermal system will fluctuate in synchronism with the inflation-deflation. The lack of previous monitoring data related to the Yellowstone hydrothermal system makes it difficult to predict future changes, and it underscores the necessity for future monitoring.

In addition to climatic factors, flux changes might be due to cooling and crystallization of the magma or to changes in the magma-effusion rate beneath the Park (Fournier, 1989). The first process is slow, and it should not result in any observed changes in chloride flux over periods of 50–100 years. The second process is episodic and can result in rapid changes in heat and chloride fluxes.

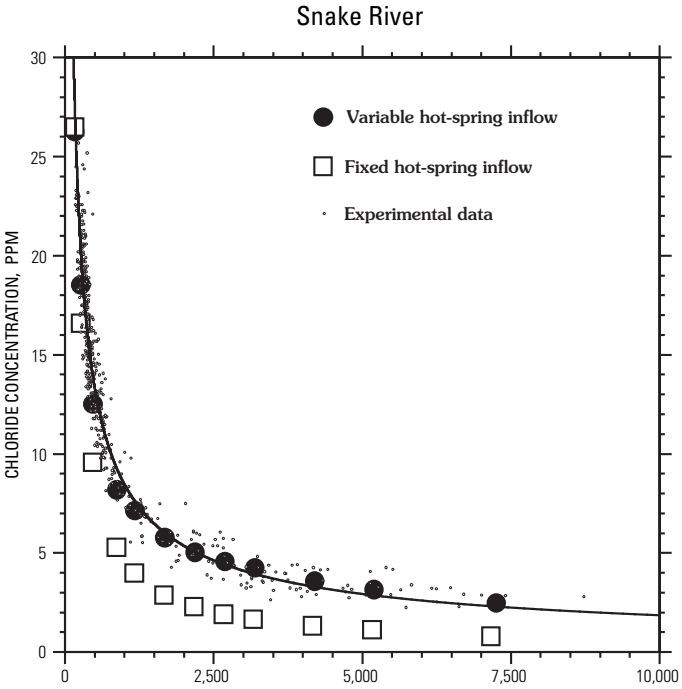

Figure 9. Graph of chloride concentration versus discharge for the Snake River showing experimental data and models of inflow to the river from various sources.

Table 9. Model data for the Madison River.

River input		Runoff		Hot spring		Total	
cfs	Cl (ppm)	cfs	Cl (ppm)	cfs	Cl (ppm)	cfs[a]	Cl (ppm)[b]
350	0.7	0		64	400	414	62.4
350	0.7	100	0.2	65	400	515	51.0
350	0.7	200	0.2	66	400	630	42.4
350	0.7	300	0.2	67	400	717	37.8
350	0.7	400	0.2	68	400	818	33.6
350	0.7	500	0.2	69	400	919	30.4
350	0.7	600	0.2	70	400	1,020	27.8
350	0.7	700	0.2	71	400	1,121	25.7
350	0.7	800	0.2	72	400	1,222	23.9
350	0.7	900	0.2	73	400	1,323	22.4
350	0.7	1,000	0.2	74	400	1,424	21.1
350	0.7	2,000	0.2	84	400	2,434	14.1

[a] Total cfs equals the sum of the flows of River input, Runoff, and Hot spring.
[b] Chloride concentration in "Total cfs" calculated as follows:
[(column 1)(column 2)+(column 3)(column 4)+(column 5)(column 6)]/column 7.

Heat Flow from the Yellowstone Hydrothermal System

Fournier and others (1976) estimated that about 41,500 metric tons of chloride and more than 100 million metric tons of water are discharged annually by Yellowstone hot springs. Using the chloride inventory method of Ellis and Wilson (1955), Fournier and others estimated the convective heat flow from the Park to be 4.02×10^{16} cal/yr. Our data, covering a 21-year interval, yields an average thermal-chloride flux of 50,200 metric tons of chloride. Use of the Ellis and Wilson method and the assumptions of Fournier and others (1976) result in a calculated convective heat flow of 4.86×10^{16} cal/yr, a value about 20 percent greater than the estimate of Fournier and others (1976).

Summary and Conclusions

1. Using our collection protocol of 28 samples per year and collecting samples frequently during the spring runoff peak and less frequently during periods of reduced flow, we calculated annual discharges of the rivers draining Yellowstone National Park that agree within 0.3 percent with the values of discharges calculated by the WRD using instrumented stage measurements recorded every 15 minutes (35,040 measurements/yr).

2. Normalization of the laboratory determinations of chloride concentrations to gravimetrically prepared chloride standards yields chloride determinations that are accurate to 1–3 percent (average 2 percent) of the amount present.

3. The accuracy of the calculated annual chloride flux (±5.4 percent) resulted from the combination of our sampling and analytical protocols.

4. One year of measurement of the chloride flux exiting the west boundary of the Park via the Henrys Fork River indicates that 7.6 percent of the total thermal chloride exiting the Park left along the west boundary.

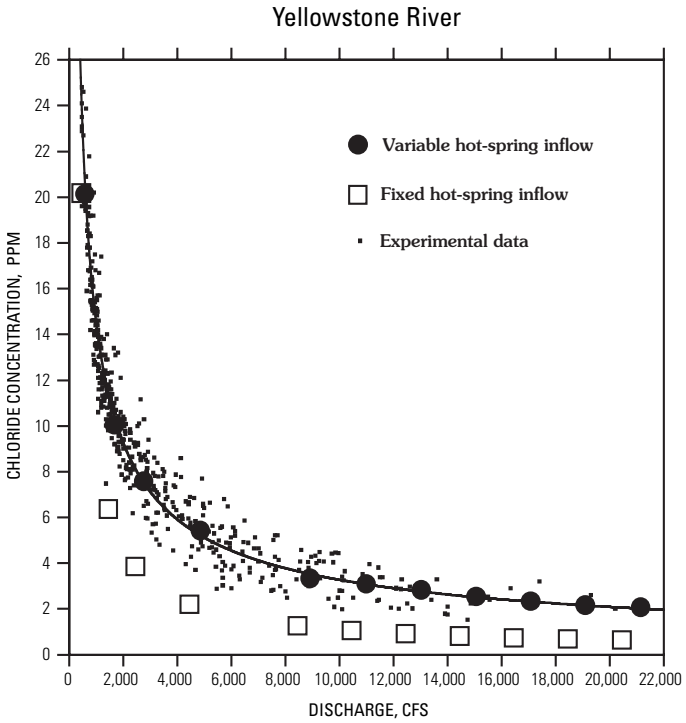

Figure 10. Graph of chloride concentration versus discharge for the Yellowstone River showing experimental data and models of inflow to the river from various sources.

Table 10. Model data for the Snake River.

River input		Runoff		Hot spring		Total	
cfs	Cl (ppm)	cfs	Cl (ppm)	cfs	Cl (ppm)	cfs[a]	Cl (ppm)[b]
150	0.7	0		14	300	164	26.3
150	0.7	100	0.2	16	300	266	18.5
150	0.7	300	0.2	19	300	469	12.5
150	0.7	700	0.2	23	300	872	8.19
150	0.7	1,000	0.2	27	300	1,175	7.15
150	0.7	1,500	0.2	31	300	1,678	5.78
150	0.7	2,000	0.2	35	300	2,182	5.04
150	0.7	2,500	0.2	39	300	2,686	4.58
150	0.7	3,000	0.2	43	300	3,190	4.26
150	0.7	4,000	0.2	47	300	4,194	3.58
150	0.7	5,000	0.2	51	300	5,196	3.16
150	0.7	7,000	0.2	55	300	7,250	2.48

[a] Total cfs equals the sum of the flows of River input, Runoff, and Hot spring.
[b] Chloride concentration in "Total cfs" calculated as follows:
[(column 1)(column 2)+(column 3)(column 4)+(column 5)(column 6)]/column 7.

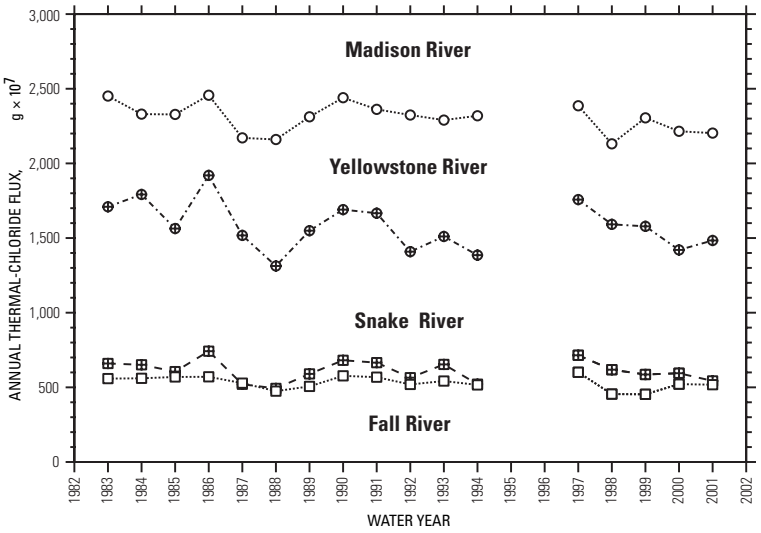

Figure 11. Graph of the annual thermal-chloride flux for the Fall, Madison, Snake, and Yellowstone Rivers for the water years 1983–1994 and 1997–2001.

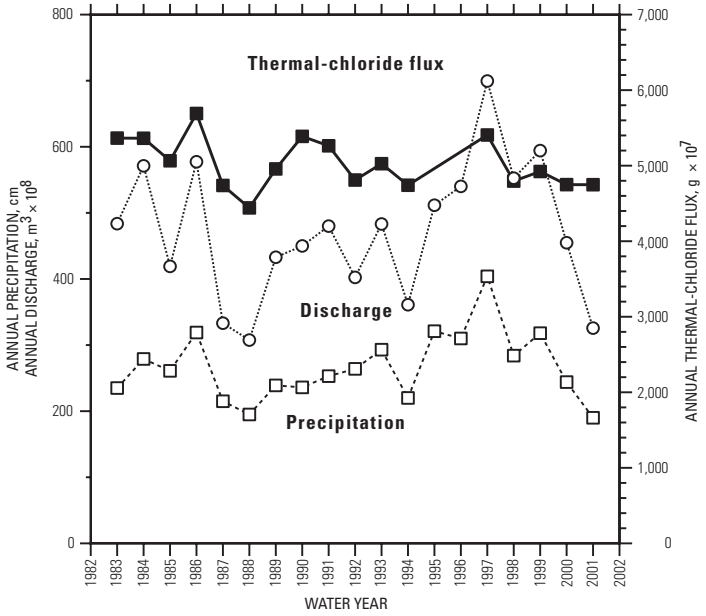

Figure 12. Graph of sums showing annual precipitation collected at five sites in the Park, annual discharges of the four rivers that drain the Park, and annual chloride fluxes of those four rivers.

Table 11. Model data for the Yellowstone River.

[Column "Other hot springs" includes all thermal-water inflow other than Mammoth Hot Springs]

River input		Runoff		Mammoth Hot Springs		Other hot springs		Total	
cfs	Cl (ppm)	cfs	Cl (ppm)	cfs	Cl (ppm)	cfs	Cl (ppm)	cfs[a]	Cl (ppm)[b]
400	0.7	0	0.2	22	170	150	50	572	20.1
400	0.7	1,000	0.2	22.5	170	250	50	16,723	10.1
400	0.7	2,000	0.2	23	170	325	50	2,748	7.58
400	0.7	4,000	0.2	23.5	170	425	50	4,849	5.43
400	0.7	8,000	0.2	24	170	475	50	8,899	3.34
400	0.7	10,000	0.2	24.5	170	550	50	10,974	3.09
400	0.7	12,000	0.2	25	170	600	50	13,025	2.84
400	0.7	14,000	0.2	25.5	170	620	50	15,045	2.55
400	0.7	16,000	0.2	26	170	640	50	17,066	2.34
400	0.7	18,000	0.2	26.5	170	660	50	19,086	2.17
400	0.7	20,000	0.2	27	170	700	50	21,127	2.08

[a] Total cfs equals the sum of flows of River input, Runoff, Mammoth Hot Springs, and Other hot springs.

[b] Chloride concentration in the "Total cfs" calculated as follows:

[(column 1)(column 2)+(column3)(column 4)+(column 5)(column 6)+(column 7)(column 8)]/column 9.

5. The calculated seasonal variations in chloride flux in the rivers exiting the Park are believed to be related to changes in the discharge of thermal springs caused by changes in the height of the water table.

6. The effect of the height of the water table on hot-spring discharge has been observed for several thermal springs in the southwest area of Yellowstone Park. In effluent from these springs, the chloride concentration in the streams remained constant even though the discharge increased greatly during spring runoff.

7. Models have been constructed for the thermal- and non-thermal-water inflow to the Fall, Gardner, Madison, Snake, and Yellowstone Rivers above their stream gages. These models fit the observed chloride concentration–river discharge measurements and require that the amount of thermal-water inflow to each river vary seasonally, increasing during periods of snowmelt and decreasing during base flow of the rivers.

8. Although the year-by-year amount of total thermal chloride exiting the Park varies by as much as 20 percent, the average thermal-chloride flux for the 19 years of measurement, conducted over an interval of 21 years, shows a decline of 0.5 percent per year. The annual variation in thermal-chloride flux correlates with river discharge and with precipitation on the Park.

9. Correction of the total annual thermal-chloride flux for changes in river discharge from the Park results in corrected thermal-flux values that indicate a decline of 11 percent (0.5 percent/yr) from 1983 to 2003. This decline is mirrored by a decline in the frequency of eruptions of Old Faithful Geyser. Decreased output

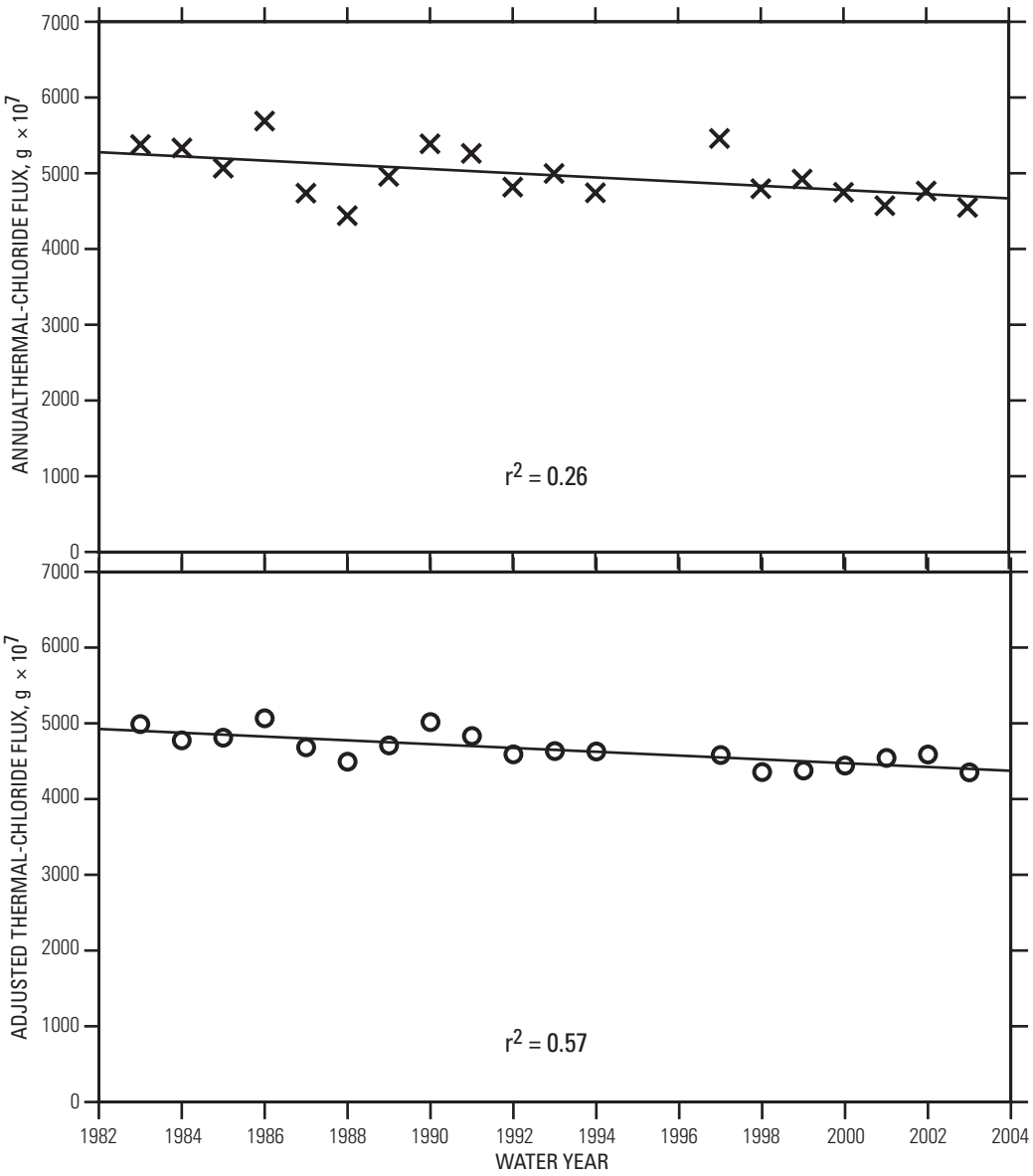

Figure 13. Graphs of the unadjusted and adjusted annual thermal-chloride flux out of Yellowstone Park for each water year.

of thermal water from the Yellowstone system may be a result of volcano-tectonic changes related to subsidence of the Yellowstone caldera.

10. The average annual total thermal-water discharge from Yellowstone is 130 million tons per year. This is equal to 96,000 acre-feet or a flow of 59,000 gallons per minute or 132 cubic feet per second.

11. The development of water, geothermal, gas, or oil resources adjacent to the Park would affect the water flux and pressure in the aquifer system beneath the Park. The aquifers are complex. In many places, thermal waters of very different chemical compositions exit in close proximity; consequently, it is difficult to predict the exact effect on individual thermal features by disturbances to either the hydrothermal system or to the cold-water recharge to hydrothermal aquifers. For this reason, we believe that, in addition to monitoring the rivers, it is necessary to monitor as many separate parts of the Yellowstone geothermal system as possible.

12. Because of the relation between chloride exiting the Park and climatic factors, it is necessary to accumulate continuous records, spanning at least 30 years, to properly assess natural changes in the hydrothermal system. Our measurement of chloride flux during the 21 years of record provides a minimal base from which to observe future disturbances to the Yellowstone hydrothermal system.

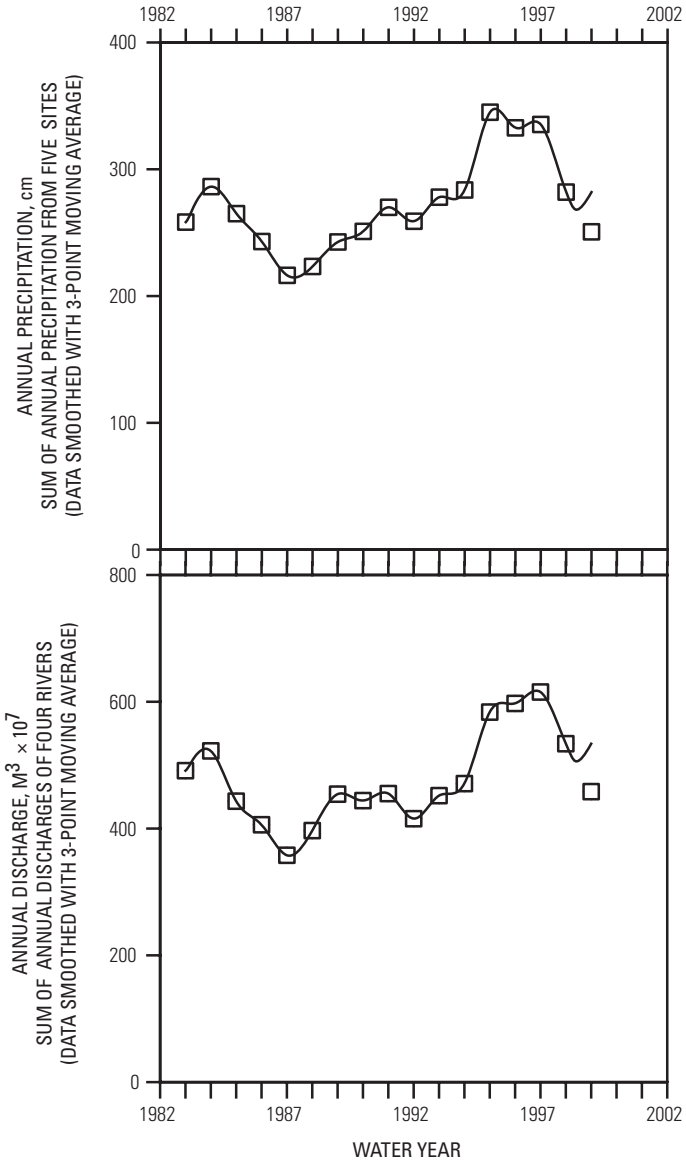

Figure 14. Graphs showing the annual precipitation and the annual discharge from the Park.

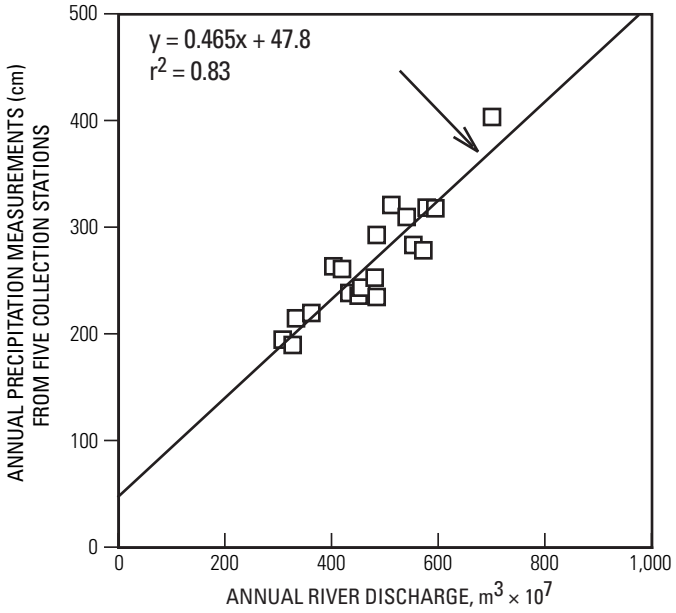

Figure 15. Graph of the sum of annual precipitation measurements from five measuring stations in Yellowstone Park versus the annual river discharge from the Park for the water years 1986–2001.

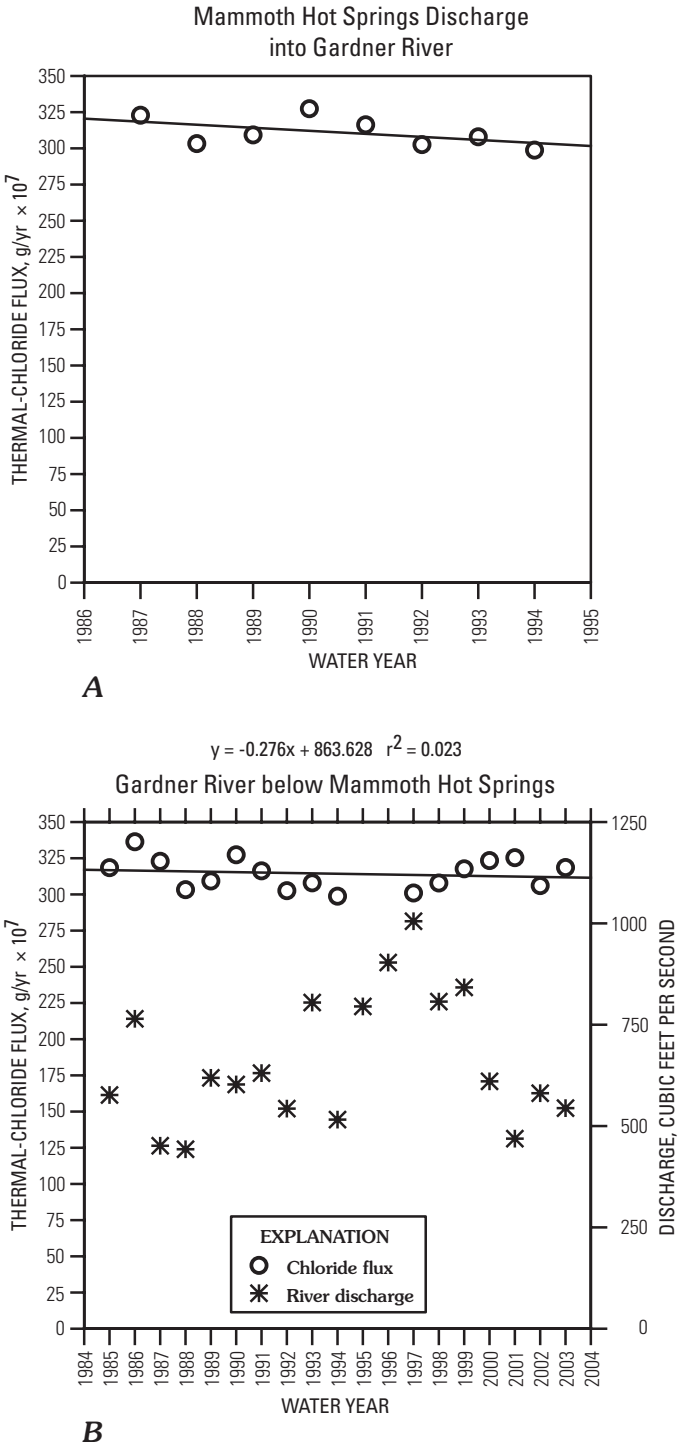

Figure 16. *A*, Graph of the annual thermal-chloride water discharge from Mammoth Hot Springs into the Gardner River. *B*, Annual thermal chloride discharge form Mammoth Hot Springs into the Gardner River for the water years 1985–2003. The annual discharge of the Gardner River is also shown.

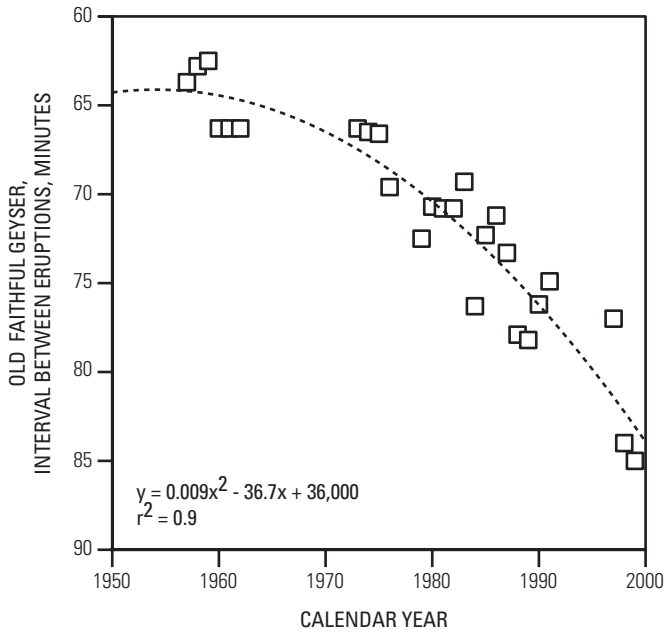

Figure 17. Graph of the annual average of the interval between eruptions of Old Faithful Geyser.

References

Brennan, T.S., O'Dell, I., Lehmann, A.K., and Tungate, A.M., 1996, Water resources data, Idaho, water year 1995, v. 1, Great Basin and Snake River Basin above King Hill: U.S. Geological Survey Water-Data Report ID-95-1, 452 p.

Carter, R.W., and Davidian, Jacob, 1968, General procedure for gaging streams: U.S. Geological Survey Techniques of Water-Resources Investigations, book 3, chap. A6, 13 p.

Dzurisin, D., Yamashita, K.M., and Kleinman, J.W.,1994, Mechanisms of crustal uplift and subsidence at the Yellowstone caldera, Wyoming: Bulletin of Volcanology, v. 56, p. 261–270.

Ellis, A.J., and Wilson, S.H., 1955, The heat from the Wairakei-Taupo thermal region calculated from the chloride output: New Zealand Journal of Science and Technology, sec. B, v. 36, p. 622–631.

Fishman, M.J., and Friedman, L.C., eds., 1989, Methods for determination of inorganic substances in water and fluvial sediments, *in* Techniques of water-resources investigations of the United States Geological Survey, 3rd ed., book 5: U.S. Geological Survey, chap. A1, p. 523–530.

Fournier, R.O., 1989, Geochemistry and dynamics of the Yellowstone National Park hydrothermal system: Annual Review of Earth and Planetary Sciences, v. 17, p. 13–53.

Fournier, R.O., White, D.D., and Truesdell, A.H., 1976, Convective heat flow in Yellowstone National Park: San Francisco, Calif., Proceedings of the United Nations Symposium on the Development and Uses of Geothermal Resources, v. 1, p. 731–739.

Friedman, Irving, Hutchinson, R.A., and Norton, D.N., 1993, Monitoring of thermal activity in southwestern Yellowstone National Park and vicinity, 1980–1993: U.S. Geological Survey Bulletin 2067, 19 p.

Friedman, Irving, and Norton, D. R., 1990, Anomalous chloride flux discharges from Yellowstone National Park: Journal of Volcanology and Geothermal Research, v. 42, p. 225–234.

Friedman, Irving, and Norton, D.R., 2000, Data used for calculating chloride flux out of Yellowstone National Park: U.S. Geological Survey Open-File Report 00-194, 48 p.

Friedman, Irving, and Sorey, M.L.,1991, Effects of potential geothermal development on the thermal features of Yellowstone National Park: GSA Today, v. 4, p. 291–299.

Friedman, Irving, and Sorey, M.L., 1992, Effects of potential geothermal development on the thermal features of Yellowstone National Park: GSA Today, v. 5, p. 3–21.

Ingebritsen, S.E., Galloway, D.L., Colvard, E.M., Sorey, M.L., Mariner, R.H., 2001, Time-variation of hydrothermal discharge at selected sites in the Western United States—Implications for monitoring: Journal of Volcanology and Geothermal Research, v. 111, p. 1–23.

Norton, D.R., and Friedman, Irving, 1985, Chloride flux out of Yellowstone National Park: Journal of Volcanology and Geothermal Research, v. 26, p. 231–250.

Norton, D.R., and Friedman, Irving, 1991, Chloride flux and surface water discharge out of Yellowstone National Park, 1982–1989: U.S. Geological Survey Bulletin 1959, 42 p.

Rantz, S.E., and others, 1982, Measurement and computation of streamflow—Volume 1. Measurement of stage and discharge: U.S. Geological Survey Water-Supply Paper 2175, 631p.

Shields, R.R., White, M.K., Ladd, P.B., and Chambers, C.L., 1996, Water resources data, Montana, water year 1995: U.S. Geological Survey Water-Data Report MT-95-1, 521 p.

Skoustad, M.W., Fishman, M.J., Friedman, L.C., Erdmann, D.E., and Duncan, S.S., eds., 1979, Methods for determination of inorganic substances in water and fluvial sediments, *in* Techniques of Water-Resources Investigations of the U.S. Geological Survey, book 5, chap. A1, 626 p.

Smalley, M.L., Woodruff, R.E., Clark, M.L., and McCallam, P.B., 1995, Water resources data, Wyoming, water year 1995: U.S. Geological Survey Water-Data Report WY-95-1, 393 p.

Sorey, M.L., ed., 1991, Effects of potential geothermal development in the Corwin Springs Known Geothermal Resources Area, Montana, on the thermal features of Yellowstone National Park: U.S. Geological Survey Water-Resources Investigations Report 91-4052, 203 p.

Sorey, M.L., and Colvard, E.M., 1997, Hydrologic investigations in the Mammoth Corridor, Yellowstone National Park and vicinity, U.S.A.: Geothermics, v. 26, p. 221–249.

Thompson, J.M., Presser, T.S., Barnes, R.B., and Bird, D.B., 1975, Chemical analysis of the waters of Yellowstone National Park, Wyoming from 1965 to 1973: U.S. Geological Survey Open-File Report 75-25, 58 p.

Wicks, C., Jr., Thatcher, W., and Dzurisin, D., 1998, Migration of fluids beneath Yellowstone caldera inferred from satellite radar interferometry: Science, v. 282, p. 458–462.

Whitehead, R.L., 1978, Water resources of the upper Henry's Fork basin in eastern Idaho: Idaho Department of Water Resources Water Information Bulletin No. 46, 89 p.

J

Applications of Trace-Element and Stable-Isotope Geochemistry to Wildlife Issues, Yellowstone National Park and Vicinity

By Maurice A. Chaffee, Wayne C. Shanks, III, Robert O. Rye, Charles C. Schwartz, Monique G. Adams, Robert R. Carlson, James G. Crock, Pamela A. Gemery-Hill, Kerry A. Gunther, Cynthia L. Kester, Harley D. King, and Shannon R. Podruzny

Chapter J *of*
Integrated Geoscience Studies in the Greater Yellowstone Area—Volcanic, Tectonic, and Hydrothermal Processes in the Yellowstone Geoecosystem

Edited by Lisa A. Morgan

U.S. Geological Survey Professional Paper 1717

U.S. Department of the Interior
U.S. Geological Survey

Contents

Abstract 303
Introduction 304
Associations Between the Chemistry of Rock, Stream Sediment, and the Scat of Bison (*Bison bison*), Elk (*Cervus elaphus*), and Moose (*Alces alces*) 305
Collection, Preparation, and Analysis of Samples 306
Results of Analyses 307
Results of Factor Analysis 307
Distributions of Anomalies for Selected Variables 310
Discussion 317
Impact of Sublacustrine Hydrothermal Elements on Cutthroat Trout and Grizzly Bears in the Yellowstone Lake Ecosystem 319
Collection, Preparation, and Analysis of Samples 321
Metal Concentrations in Trout 322
Sources of Metals 323
Carbon-, Nitrogen-, and Sulfur-Isotope Studies of Grizzly Bears (*Ursus arctos*) and Their Foods in the Yellowstone Ecosystem 325
Grizzly Bear Food Sources 325
Collection, Preparation, and Analysis of Samples 326
Results 327
Discussion 327
Carbon-Isotope Variations in the Food Chain 327
Nitrogen-Isotope Trophic Enrichment in the Grizzly Bear Food Chain 327
Sulfur-Isotope Variations in Grizzly Bears and Their Food Sources 329
Stable-Isotope Data as Tracers of Geologic and Environmental Sources and Processes in Ecosystems 329
Conclusions 330
Acknowledgments 332
References 332

Figures

1. Map of Yellowstone National Park showing sampling sites for scat samples 306
2–8. Maps showing distribution of:
2. Lanthanum in scat samples 313
3. Cesium in scat samples 317
4. Arsenic in scat samples 318
5. Molybdenum in scat samples 319
6. Zinc in scat samples 320
7. Scat samples high in percent ash 321
8. Scat samples low in percent ash 322
9–12. Mercury concentrations in:
9. Cutthroat and lake trout 323

10. Common species of domestic and imported fish 324
11. Muscle tissue of cutthroat and lake trout 325
12. Plants and animals, greater Yellowstone ecosystem 326
13. $\delta^{15}N$ and $\delta^{13}C$ values for bear tissue, bear food sources, and lake trout 329
14. $\delta^{15}N$ and $\delta^{34}S$ values for bear tissue, bear food sources, and lake trout 329
15. $\delta^{13}C$ and $\delta^{34}S$ values for bear tissue, bear food sources, and lake trout 330

Tables

1–3. Summary statistics for analyses of 36 variables in:
1. 48 samples of bison scat 308
2. 67 samples of elk scat 309
3. 2 samples of moose scat 310
4–5. Factor-loading values for 30 variables in:
4. 48 samples of bison scat 311
5. 67 samples of elk scat 312
6. Percentage of scat sample sites with anomalies for selected elements 313
7. Composition of biological samples from Yellowstone Lake and the greater Yellowstone ecosystem 314
8. Summary of stable-isotope data on grizzly bear tissue and their food sources 328

Applications of Trace-Element and Stable-Isotope Geochemistry to Wildlife Issues, Yellowstone National Park and Vicinity

By Maurice A. Chaffee,[1] Wayne C. Shanks, III,[1] Robert O. Rye,[2] Charles C. Schwartz,[3] Monique G. Adams,[1] Robert R. Carlson,[1] James G. Crock,[1] Pamela A. Gemery-Hill,[1] Kerry A. Gunther,[4] Cynthia L. Kester,[2] Harley D. King,[1] and Shannon R. Podruzny[3]

Abstract

Reconnaissance investigations have been conducted to identify how geochemical techniques can be applied to biological studies to assist wildlife management in and near Yellowstone National Park (the Park). Many elements (for example, As, B, Be, Ce, Cl, Cs, F, Hg, K, Li, Mo, Rb, S, Sb, Si, and W) are commonly enriched in (1) thermal waters in the Yellowstone area, (2) rocks altered by these waters, (3) sinter and travertine deposits, and (4) soils and stream sediments derived from these rocks. Some of these elements, such as As, F, Hg, and Mo, may be toxic to wildlife and could be passed up the food chain to many species of animals.

Three investigations are described here. The first discusses the abundance and distribution of selected elements in the scat (feces) of bison *(Bison bison*), elk (*Cervus elaphus*), and moose (*Alces alces*) collected in and near the Park from areas underlain by both unaltered and hydrothermally altered rock. As compared to mean values for stream-sediment analyses, those of scat analyses collected in the Yellowstone area show relatively high concentrations for 12 elements. This suite of elements comprises (1) hydrothermally related elements (As, Br, Cs, Mo, Sb, and W), (2) essential major elements for plants (Ca and K) and some trace elements (Ba, Rb, and Sr) that commonly proxy (substitute) for Ca or K, and (3) zinc. The behavior of zinc is not understood. It is an essential element for plants and animals but does not normally proxy for either Ca or K. Zinc is also not related to hydrothermal activity. This unique behavior of zinc is discussed in other parts of this investigation.

Six elements (Cr, Hg, Ni, Pb, Se, and U) that can be toxic to wildlife are present in low concentrations in scat, reflecting their generally low concentrations in rock and stream-sediment samples collected throughout the Park.

The chemistry of large-animal scat provides information on the feeding habits of large animals in the Park. Scat chemistry shows a high spatial correlation with fossil or active thermal areas or with areas immediately downstream from thermal areas. The longer that animals forage in these localities, the more likely it is that they may ingest significant amounts of potentially toxic elements such as arsenic.

A second investigation describes the concentration levels of hydrothermal mercury and other elements in cutthroat trout (*Oncorhynchus clarki bouvieri*) and lake trout (*Salvelinus namaycush*). These elements are derived from sublacustrine hot springs and their habitats in Yellowstone Lake, and this study demonstrates that mercury can be used as a tracer in animal ecology studies. Mercury concentrations are significant in the muscle (average 0.9 ppm, dry weight for both) and liver (average cutthroat = 1.6 ppm, dry weight; average lake trout = 2.1 ppm) of cutthroat and lake trout populations. The mercury levels in fish are believed to be related to mercury introduced to the lake by sublacustrine hot springs, which have dissolved mercury concentrations of as much as 0.170 ppb. Methylation of mercury in thermal waters is probably carried out by methanogenic or sulfate-reducing bacteria that live around sublacustrine hot springs and are consumed by crustaceans such as amphipods, which are a major food source for the cutthroat trout. The mercury levels in the cutthroat trout are transferred to lake trout and to land animals that eat trout. For example, hair of grizzly bears that have been collected near Yellowstone Lake have high mercury levels (0.6–1.7 ppm, dry weight), whereas hair of bears sampled at more remote areas in the greater Yellowstone ecosystem have low mercury contents (0.006–0.09 ppm, dry weight). This observation provides strong evidence that mercury in grizzly bears is derived from feeding on spawning cutthroat trout in the spring and early summer. Studies of mercury and metal contents in other grizzly bear food sources (plants and animals) show that only cutthroat trout are strongly enriched in mercury. These data can potentially be used to quantify the percentage of the bear population that eats cutthroat trout and to determine how far individual bears travel to Yellowstone Lake to eat them.

[1]U.S. Geological Survey, Box 25046, MS 973, Federal Center, Denver, CO 80225-0046.

[2]U.S. Geological Survey, Box 25046, MS 963, Federal Center, Denver, CO 80225-0046.

[3]U.S. Geological Survey, Box 172780, Bozeman, MT, 59717-0278.

[4]National Park Service, Box 424, Yellowstone National Park, WY 82190.

A third investigation describes carbon-, nitrogen-, and sulfur-isotope compositions in grizzly bears and in some of their foods and describes how these data can be applied to studies of grizzly bear demographics. $\delta^{13}C$ values in the Yellowstone ecosystem range from –21.7 ‰ to –30.4 ‰, a range that reflects the influence of C_3 plants on the carbon reservoir and probably the effect of elevation on physiological processes. $\delta^{15}N$ values range from –2.3 ‰ to 11.0 ‰ and show classical trophic enrichments with respect to most grizzly bear food sources. Cutthroat trout $\delta^{15}N$ values (8.3±1.0 ‰) may reflect the importance of sublacustrine hydrothermal springs to the food chain in Yellowstone Lake. Lake trout have even larger $\delta^{15}N$ values (11.0±0.4 ‰) that are consistent with their feeding on cutthroat trout. Grizzly bear $\delta^{15}N$ values range from 7.0 ‰ to 8.8 ‰. Although grizzly bears are known to eat cutthroat trout, trophic enrichment in $\delta^{15}N$ above values found in trout is not apparent in analyses of bear hair. This discrepancy occurs because $\delta^{15}N$ values are averaged over one year and include the significantly lower $\delta^{15}N$ values of vegetable food sources consumed by bears while their hair is growing. $\delta^{34}S$ values in the ecosystem range from –3.1 ‰ to 11.1 ‰. $\delta^{34}S$ values of fish (1.2±0.5 ‰) are nearly the same as those in sulfate from thermal springs. Vegetation (clover, cow parsnip, and spring beauty), ungulates (deer, elk, and bison), and moths show a greater range of $\delta^{34}S$ values (–3.3 ‰ to 3.2 ‰). However, bears show higher $\delta^{34}S$ values (3.2 ‰ to 5.4 ‰ in muscle and 6.1 ‰ to 8.7 ‰ in hair) that are consistent with the consumption of whitebark pine nuts ($\delta^{34}S$ = 8.3 ‰ to 11.4 ‰). $\delta^{34}S$ values in bears and their food sources seem to be constrained by the major sources of sulfate and sulfide sulfur in the igneous and sedimentary rocks that underlie much of the Park. The large $\delta^{34}S$ values found in bear tissues are consistent with the documented fact that most grizzly bears eat substantial amounts of whitebark pine nuts when available. This consumption occurs during hair growth in the fall, thus providing an isotopic marker that may be useful in quantifying nut consumption in individual bears.

These three studies show some different ways that geochemical techniques can be applied to biologic issues. The results suggest that integration of geochemistry into specific biologic studies may help address issues of interest to wildlife managers in Yellowstone National Park and the greater Yellowstone ecosystem.

Introduction

Yellowstone National Park (the Park) is known worldwide for spectacular scenic beauty, awesome hydrothermal features, and varied wildlife. These are intertwined and closely associated with the geology and geochemistry of the Park. We describe below how trace-element and stable-isotope geochemical techniques can be applied to wildlife issues in Yellowstone National Park. The greater Yellowstone ecosystem is an excellent natural laboratory in which to examine the relationship between geochemistry and wildlife because of (1) the large knowledge base acquired by geoscientists from many years of investigating the chemistry of rocks and thermal waters and (2) the unique chemical and isotopic signatures that result from hydrothermal activity. The trace-element and isotopic compositions of the unaltered Tertiary and Quaternary volcanic rocks that compose the bedrock in the Park are well known or easily inferred. Hydrothermal fluids, which are characterized by enrichments in elements such as As, B, Be, Ce, Cl, Cs, F, Hg, K, Li, Mo, Rb, S, Sb, Si, and W, leave a well-understood trace-element and stable-isotope imprint on hot-spring deposits and altered rocks. These differences between the trace-element content and stable-isotope compositions of altered rocks and hot-spring deposits and those in unaltered rocks can be used as indicators of animal diet, ecology, and demographics. Many of the trace elements that are enriched in thermal waters are potentially toxic to wildlife. However, few studies of such toxicity have been conducted.

In cooperation with the National Park Service, the U.S. Geological Survey investigated three aspects of the relationship between environmental and isotopic geochemistry and the wildlife of Yellowstone National Park. In the first study, samples of bison (*Bison bison*), elk (*Cervus elaphus*), and moose (*Alces alces*) scat were collected from areas in and near the Park, including areas of hydrothermally altered rocks in active geyser basins, areas of rocks altered by fossil hydrothermal activity, and areas of unaltered rocks. When large animals forage in areas of hydrothermally altered rock, they eat plant material, which commonly includes some attached inorganic substrate. Both the plant material and the inorganic matter may contain high concentrations of potentially toxic elements. Those animals that forage mostly in hydrothermally affected areas thus have a greater risk for trace-element poisoning.

Previous investigations (Garrott and others, 2002) showed that the health of elk living in some areas in the Park was significantly impacted by high hydrothermal fluorine concentrations in their diet. Except for fluorine, we know very little about the effects of hydrothermal elements on large Park animals. Although we can demonstrate that animals are ingesting potentially toxic elements, we do not know how much of a given element is accumulated in the animals and what levels may impact their health.

A second study evaluated the concentrations of selected elements in trout collected from Yellowstone Lake. The native cutthroat trout (*Oncorhynchus clarki bouvieri*), a threatened species, is particularly important to the lake ecosystem because they spawn in the tributaries to the lake and are important food sources for otters, bears, and eagles. The presence of exotic, predatory lake trout (*Salvelinus namaycush*) in Yellowstone Lake severely threatens the viability of the native cutthroat. Cutthroat trout have been observed to congregate and feed around shallow-water hydrothermal vents in Yellowstone Lake and, therefore, accumulation of trace metals in the fish was investigated. Further, transference of potentially toxic trace elements, especially mercury, from cutthroat trout into the food chain was evaluated in conjunction with stable-isotope studies of grizzly bear food sources.

In the third study, stable isotopes were measured in the hair and flesh of grizzly bears (*Ursus arctos*) and in several

common bear foods. The grizzly bear is listed as a threatened species in the conterminous United States. In the greater Yellowstone ecosystem, grizzly bears rely on an array of plant and animal foods, but the majority of the diet comprises four major items: ungulates, cutthroat trout, army cutworm moths, and vegetation, especially whitebark pine nuts. Historically, biologists have used scat analysis to determine bear diets, but differential rates of digestion make quantitative assessments of intake difficult. We explored the possibility of using stable-isotope signatures in the hair and tissue of the grizzly to help quantify food consumption and eating habits. Stable-isotope studies of grizzly bear tissue (hair from living bears and muscle tissue from carcasses) and the most important foods in bear diets show a large range in $\delta^{13}C$, $\delta^{15}N$, and $\delta^{34}S$ values. These variations reflect geologic and environmental sources in the greater Yellowstone ecosystem and well as trophic enrichments in the food chain.

These three investigations demonstrate how geochemical techniques widely used in the earth sciences can be applied to biological studies to assist wildlife management in Yellowstone National Park as well as in the greater Yellowstone ecosystem.

Associations Between the Chemistry of Rock, Stream Sediment, and the Scat of Bison (*Bison bison*), Elk (*Cervus elaphus*), and Moose (*Alces alces*)

In Yellowstone National Park, the chemistry of thermal waters and their associated deposits is largely controlled by that of the underlying bedrock. Most of the fossil and active thermal areas are in or near exposures of Quaternary rhyolitic volcanic rocks. In these areas, as discussed in Rye and Truesdell (1993; this volume), meteoric waters percolate to various depths; become heated as they approach hotter rocks at depth; accumulate magmatic gases such as He, CO_2, and H_2S; and rise to the surface through an elaborate plumbing system in geyser and hot-spring basins. As they migrate to the surface, these waters leach elements from the rock units through which they pass. They also mix with local ground waters, which results in a diversity of hydrothermal-water compositions that may vary significantly, even on a local scale.

Recent Park-wide studies (Miller and others, 1997) have shown that a generally common suite of elements, including As, B, Be, Ce, Cl, Cs, F, K, Li, Mo, Rb, S, Sb, Si, and W, is brought to the surface by thermal waters. Many of these elements are deposited in hydrothermally altered rocks. Our study of the chemistry of fresh and hydrothermally altered rocks and related travertine and sinter deposits, as well as stream sediments eroded from these source areas and carried downstream through, and out of, the Park (Chaffee and others, this volume), indicates that altered volcanic rocks are commonly enriched in as many as 11 elements (As, Au, Br, Cs, F, Hg, Mo, S, Sb, Se, and W). Similarly, Sturchio and others (1986), in a study of hydrothermal alteration in drill core from Yellowstone thermal areas, found strong enrichment of Cs, Li, and Sb. Arsenic, F, Hg, Mo, and possibly Sb are of particular interest because they are potentially toxic to wildlife.

Siliceous-sinter deposits in major geyser and hot-spring basins, such as the Upper, Midway, Lower, Shoshone, and Norris Basins, as well as sediments derived from these deposits, are enriched in many of these same 11 elements listed above (Thompson and DeMonge, 1996; Fournier and others, 1994). Less abundant travertine deposits in hot-spring areas such as Mammoth are underlain by carbonate bedrock (mainly the Mississippian Madison Group). Thermal waters from these areas tend to be enriched in calcium (Thompson and DeMonge, 1996; Fournier and others, 1994) but also contain many of the 11 elements listed above.

Plant species growing in hydrothermally altered areas take up varying amounts of the hydrothermally derived elements, some of which are essential for growth. As an example, analyses of some plant species growing in, or downstream from, altered areas in the Park yield tens of parts per million arsenic (dry weight basis) (James Otton, oral commun., 2000). Some hydrothermally derived elements may also be present as wind-borne surface coatings or rain-splatter deposits on plant parts. By inference, other hydrothermal elements could be present in elevated concentrations in plants growing in hydrothermally affected areas.

Some of the elements discussed here (for example, As, F, Hg, and Mo) can adversely affect the health of wildlife (Gough and others, 1979; Shupe and others, 1984). Although these elements have long been known to be present in surface waters in and near the hydrothermally altered areas of the Park (see, for example, Ball and others, 1998; Miller and others, 1997; Stauffer and others, 1980), it was not known whether large animals such as bison (*Bison bison*), elk (*Cervus elaphus*), and moose (*Alces alces*) actually ingest significant quantities of these elements in their food. To better understand the chemistry of material ingested and excreted by bison and elk, and to a lesser extent by moose, we analyzed samples of their scat (feces) collected from areas of unaltered (mainly volcanic) rocks located throughout the Park and vicinity and from areas of hydrothermally altered rocks, which crop out mainly in geyser basins. These data were then compared to similar data for rock and stream sediment collected from throughout the Park and vicinity.

Only two articles in the literature (Day and others, 1985; Robinson, 1986) were found to contain analytical data for scat. These data, however, were presented in the context of exploration for mineral deposits in Alaska and Arizona, respectively. Thus, no chemical baseline existed for animal scat in Yellowstone National Park prior to this study. The scat chemical data determined for this investigation were evaluated to determine (1) the abundances and distributions of elements and (2) the common associations of elements. The spatial variations of selected elements were examined to investigate whether there are spatial relationships between (1) anomalous elements in scat samples and (2) geyser basins and other thermal features. The results of these studies identify some hydrothermally associated, potentially toxic elements that have been consumed by large animals and suggest how far these animals may have traveled from the time they consumed the plants in an altered area until they deposited their scat.

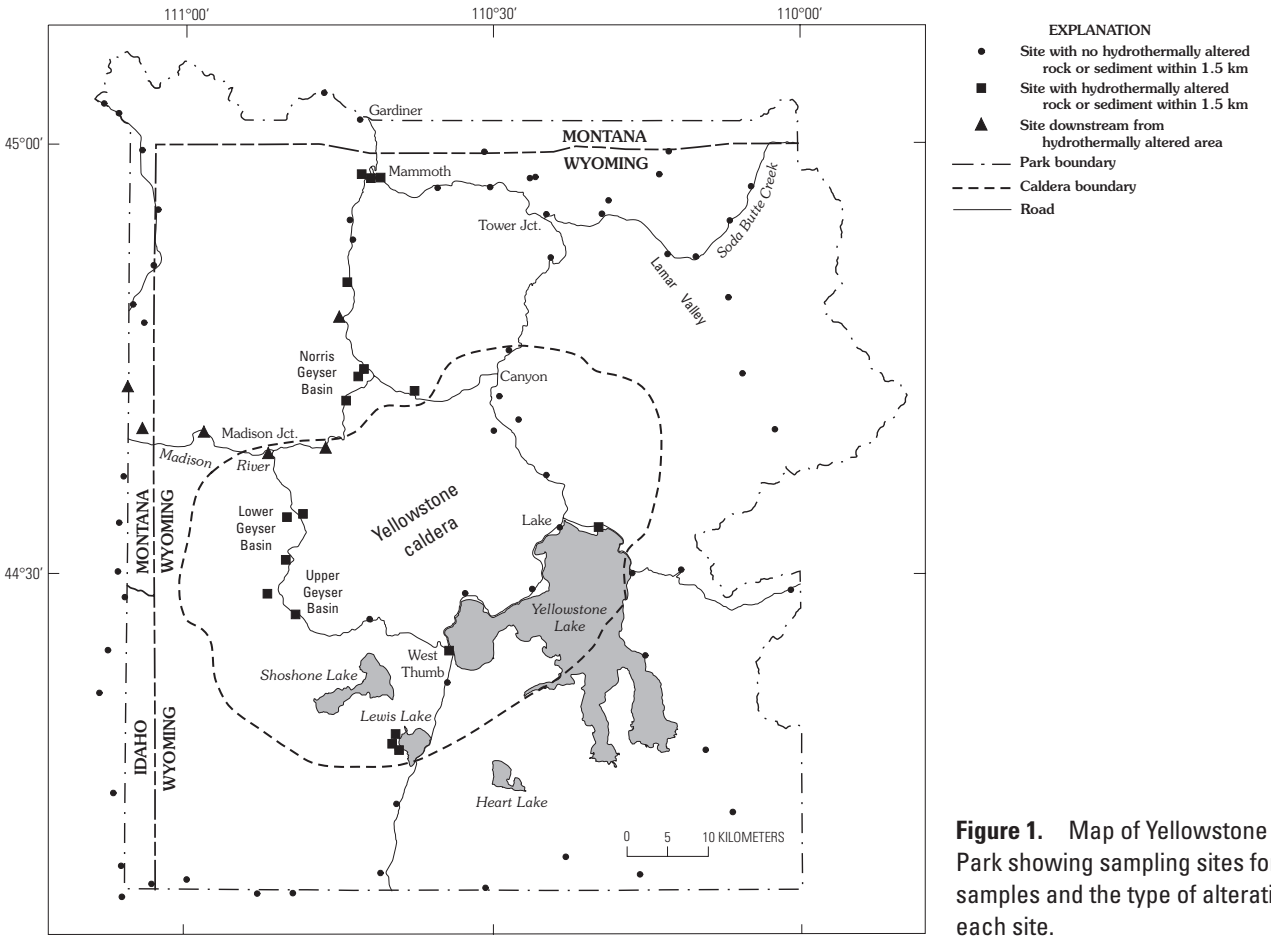

Figure 1. Map of Yellowstone National Park showing sampling sites for scat samples and the type of alteration for each site.

Collection, Preparation, and Analysis of Samples

The geology of Yellowstone National Park is complex and is discussed in detail in Christiansen (2001). Only a brief summary is included here. Further summaries are given in some of the papers in this volume. The oldest rocks in the Park consist mostly of Precambrian metasedimentary rocks that locally include quartz monzonite and diorite intrusions. These units crop out in several localities in the north-central part of the Park, generally north of the Lamar Valley (fig. 1). Paleozoic sedimentary rocks, composed mostly of quartzite, sandstone, and limestone, are found in scattered localities, mainly around the perimeter of the Park. Tertiary andesites are found mostly along the eastern perimeter of the Park. Quaternary felsic volcanic rocks crop out throughout much of the Park and are the most common rock type found. Deposits of Quaternary alluvium and glacial till locally cover all older units.

Figure 1 shows sites in the Park where scat samples were collected. These sites have been placed into the following groups: (1) sites containing generally fresh rock or sediment with no hydrothermally altered rock any closer than about 1.5 km of the plotted site (solid circles), (2) sites containing hydrothermally altered rock or sediment within about 1.5 km of the plotted site (solid squares), and (3) sites near streams but more than about 1.5 km downstream from any altered outcrops (solid triangles).

We collected 48 samples of bison scat, 67 samples of elk scat, and 2 samples of moose scat from 87 sites in and near Yellowstone National Park (fig. 1). At 29 of these sites, we collected both bison and elk scat. Each sample was composited (pooled) with material collected within a roughly 30-m (about 100-ft) radius of the plotted sample site. Care was taken to avoid including substrate material present underneath the scat. Most elk scat consisted of desiccated, winter pellets that were deemed to be as much as a year old but still appeared to be fresh with no obvious signs of decomposition. Bison scat was also relatively fresh. Most samples were desiccated; however, many were still moist. After drying, all scat material was pulverized to a coarse powder. Samples were analyzed in a random order. Internal standards and duplicate samples were also analyzed to monitor accuracy and precision.

In the laboratory, a sample aliquot was pelletized and analyzed for 35 elements (Ag, As, Au, Ba, Br, Ca, Ce, Co, Cr, Cs, Eu, Fe, Hf, Hg, Ir, K, La, Lu, Mo, Na, Nd, Ni, Rb, Sb, Sc, Se, Sm, Sr, Ta, Tb, Th, U, W, Yb, and Zn) by neutron activation analysis by Activation Laboratories, Ltd., Ancaster, Ontario, Canada. In addition, aliquots of the macerated material were combusted to ash in a muffle furnace to determine the amount of noncombustible (inorganic) material. This amount is defined as "percent ash." In the case of bison, elk, and moose scat, the organic material is composed largely of vegetable matter, and the inorganic material is composed mainly of grains of mineral matter in the soil attached to plant roots and of residue compounds, such as silica, that remain after ashing of certain plant species.

Results of Analyses

The results of the analyses are summarized in tables 1–3 for bison, elk, and moose scat, respectively. For some elements, some of the analyses were determined to be below the lower limit of determination (qualified analyses). Analyses in these tables shown as "unqualified" are those that the analysts reported as being above the lower limit of determination for the analytical method used.

Four elements (Ag, Hg, Ir, and Se) in the bison data set (table 1), five elements (Ag, Hg, Ir, Ni, and Se) in the elk data set (table 2), and 13 elements (Ag, Au, Cs, Eu, Hg, Ir, Nd, Ni, Se, Ta, Tb, U, and W) in the moose data set (table 3) did not have sufficient unqualified analyses in order to calculate a meaningful geometric mean value. The geometric mean values for elements in stream-sediment samples (table 1 in Chaffee, Carlson, and King, this volume) give a good estimate of the overall chemistry of surface mineral matter present in and near Yellowstone National Park and thus provide a context for the mean concentrations found in the scat samples. To determine which of 30 selected elements had unusual concentrations in the scat, we normalized geometric mean concentrations in the scat against those of the stream sediment. The resulting ratios, based on arbitrarily selected ratio threshold values, show relatively high values for an identical suite of 12 elements in both bison and elk scat. We did not have sufficient data to adequately evaluate element enrichment in moose scat. Elements with a ratio of ≥0.20 for bison scat include, in order of ratio value: Br (1.76), Zn (1.13), Mo (0.97), Ca (0.85), Sr (0.63), Cs (0.56), W (0.35), Sb (0.34), As (0.33), K (0.24), Ba (0.22), and Rb (0.20). Those with a ratio of ≥0.10 for elk scat include Zn (1.41), Br (1.31), Ca (0.99), Mo (0.50), Sr (0.49), Cs (0.20), Ba (0.18), K (0.17), Sb (0.16), Rb (0.16), As (0.14), and W (0.10). These 12 elements seem to fall into three groups: (1) hydrothermally related elements (As, Br, Cs, Mo, Sb, and W); (2) major elements (Ca and K), which are essential elements for plants, and trace elements (Ba, Rb, and Sr) that commonly proxy for Ca or K; and (3) zinc. The behavior of zinc is not known. It is an essential element for plants and animals but does not proxy for either Ca or K. Zinc is also not related to hydrothermal activity.

Published analyses (see, for example, King and others, 1984; Shacklette, 1972, 1980) indicate that the typical ash content for the above-ground parts of plants is in a range of about 3–7 percent. In contrast, the values for percent ash for the scat samples for bison and elk range from about 10 percent to more than 44 percent (tables 1 and 2). The values, although limited, for moose are about 4 percent (table 3). The amount of ash, which represents the amount of inorganic material in a sample, is thus much higher in the bison and elk scat samples than what would be expected if the animals consumed only above-ground plant material. However, some sedges and other types of plants growing in the vicinity of sinter-rich areas are known to contain a high natural ash content as a result of the high content of silica accumulated in these species (James Otton, written commun., 2001). Comparisons of the mean and maximum values for percent ash for bison and elk scat (tables 1 and 2) and the values for percent ash for the sample pairs from individual sites (not shown here) clearly indicate that bison ingest more mineral matter containing hydrothermal elements than do elk. Comparison of the geometric mean values for all samples for bison (25.5 percent) and elk (14.2 percent) (tables 1 and 2) indicates that the ash content for bison is roughly 1.8 times that of elk. The range of values for percent ash for each species suggests, however, that this ratio will vary in detail for sample pairs collected at a given site. Nevertheless, this value of 1.8 is a good first approximation of the general percent-ash contents between the two species. We think that the differences in ash content for each species reflect their foraging habits. Bison and elk, which mainly consume grasses, ingest significant quantities of mineral matter, most of which is probably soil material attached to plant-root masses. The percent-ash values for elk are generally lower than those for bison because elk probably consume a higher percentage of the above-ground parts of plants and therefore a lower percentage of soil mineral matter.

In contrast to the data for bison and elk, the two samples of moose scat show a very low percent ash, probably emphasizing their different diet. Moose mostly feed in wetlands and tend to be browsers rather than grazers. Their browse evidently contains much less soil substrate, surface contaminants, or plants with a high silica content.

Results of Factor Analysis

Variables selected from tables 1 and 2 were examined for covariance using R-mode factor analysis. Details concerning this mathematical treatment of analytical data are given in Chaffee, Carlson, and King (this volume). Of the original 36 variables determined for the bison and elk scat, 30 (As, Ba, Br, Ca, Ce, Co, Cr, Cs, Eu, Fe, Hf, K, La, Lu, Mo, Na, Nd, Rb, Sb, Sc, Sm, Sr, Ta, Tb, Th, U, W, Yb, Zn, and percent ash) were selected for factor analysis. Five elements were deleted from the data set prior to the factor analysis because each had very few or no unqualified values. Additionally, gold was deleted because the sample aliquots used for analysis were deemed to be too small to provide meaningful analyses.

Tables 4 and 5 show the factor loading values for bison and elk scat, respectively. Factor scores, also generated in the analysis but not tabulated for this report, give an indication of how well an individual sample correlates with a given factor. The distributions of samples with high factor scores can thus be used to identify any spatial relationship between the chemistry of a given sample and the various types of altered or unaltered rocks present near the sample site or upstream from the site.

For the bison samples (table 4) a four-factor model explains 84 percent of the total variance in the data set. Factor 1 contains variables (19 elements plus percent ash) associated with the overall chemistry of major rock units

Table 1. Summary statistics for analyses of 36 variables in 48 samples of bison scat, Yellowstone National Park and vicinity.

[Concentrations are shown in dry weight and in ppm, unless "(ppb)" or "(%)" shown after element symbol. N, not detected at the lower limit of determination shown in parentheses. Mean values based on unqualified values only. "---" in geometric mean column indicates no meaningful value]

Element	Range of values		Number unqualified	Percent unqualified	Geometric mean
	Minimum	Maximum			
Ag	N(0.3)	N(0.3)	0	0	---
As	0.33	18	48	100	2.0
Au (ppb)	N(0.10)	3.9	42	88	0.66
Ba	84	490	48	100	170
Br	2.6	10	48	100	5.1
Ca (%)	0.68	3.60	48	100	1.37
Ce	1.4	28	48	100	9.3
Co	0.3	6.1	48	100	1.3
Cr	1.4	63	48	100	9.4
Cs	0.28	20	48	100	2.0
Eu	N(0.05)	0.44	46	96	0.12
Fe (%)	0.055	1.27	48	100	0.33
Hf	0.11	2.6	48	100	0.90
Hg	N(0.05)	0.73	2	4	---
Ir (ppb)	N(0.10)[1]	N(0.10)[1]	0	0	---
K (%)	N(0.05)	1.20	46	96	0.51
La	0.91	19	48	100	5.8
Lu	0.006	0.19	48	100	0.05
Mo	N(0.05)	15	47	98	3.3
Na	220	6,500	48	100	1,800
Nd	0.60	11	48	100	3.3
Ni	N(2)	18	9	19	8.4
Rb	5.0	37	48	100	17
Sb	0.048	3.1	48	100	0.23
Sc	0.16	4.1	48	100	0.95
Se	N(0.10)	0.50	5	10	---
Sm	0.12	1.8	48	100	0.59
Sr	N(10.)	280	40	83	120
Ta	N(0.05)	0.42	33	69	0.16
Tb	N(0.10)	0.30	25	52	0.15
Th	0.10	3.8	48	100	1.2
U	N(0.01)	1.1	46	96	0.34
W	N(0.05)	44	30	63	2.6
Yb	0.059	1.27	48	100	0.38
Zn	33	160	48	100	79
Ash (%)	18.2	44.0	48	100	25.5

[1]Lower limit of determination reported as 0.20 for 17 samples.

(mainly unaltered rhyolites and andesites) exposed in the Park. Samples strongly correlated with this factor are from sites located throughout the study area and are not closely related to any one geologic unit. Percent ash is most strongly loaded on this factor, reflecting a close association between ash content and the chemistry of rock material included in bison scat.

Factor 2 contains elements associated with chemical enrichment related to hydrothermal activity (Cs, W, Sb, As, Br, and Mo). Samples strongly correlated with this factor are mainly from hydrothermally altered areas in geyser basins or hot-spring areas, or from localities immediately downstream from these features.

Factor 3 contains only zinc. A zinc factor is also present for the elk samples (table 5). The reason for zinc not being associated with variables in other factors is not clear. Factor scores do not indicate that there is any close association of samples containing anomalous zinc with any particular geologic unit. As noted previously, zinc seems to be enriched in scat as compared to stream sediment, and its chemical affinity is not clearly understood. We speculate that bison and elk may metabolize zinc differently than they do other elements.

Table 2. Summary statistics for analyses of 36 variables in 67 samples of elk scat, Yellowstone National Park and vicinity.

[Concentrations are shown in dry weight and in ppm, unless "(ppb)" or "(%)" shown after element symbol. N, not detected at the lower limit of determination shown in parentheses. Mean values based on unqualified values only. "---" in geometric mean column indicates no meaningful value]

Element	Range of values		Number unqualified	Percent unqualified	Geometric mean
	Minimum	Maximum			
Ag	N(0.3)	N(0.3)	0	0	---
As	0.10	18	67	100	0.83
Au (ppb)	N(0.10)	7.7	57	85	0.59
Ba	60	280	67	100	140
Br	1.5	20	67	100	3.8
Ca (%)	0.67	3.40	67	100	1.60
Ce	0.8	22	67	100	4.8
Co	0.40	2.3	67	100	0.83
Cr	0.90	14	67	100	3.9
Cs	0.12	19	67	100	0.72
Eu	N(0.05)	0.19	40	60	0.08
Fe (%)	0.05	0.53	67	100	0.15
Hf	N(0.05)	2.3	66	99	0.44
Hg	N(0.05)	0.24	2	3	---
Ir (ppb)	N(0.10)[1]	N(0.10)[1]	0	0	---
K (%)	N(0.05)	1.70	66	99	0.37
La	0.66	14	67	100	3.6
Lu	0.003	0.185	67	100	0.027
Mo	0.23	12	67	100	1.7
Na	180	3,800	67	100	730
Nd	N(0.5)	8.7	66	99	2.0
Ni	N(2)	6.0	3	4	---
Rb	2.0	67	67	100	13
Sb	0.029	8.2	67	100	0.11
Sc	0.12	1.8	67	100	0.43
Se	N(0.10)	0.60	8	12	---
Sm	0.05	1.4	67	100	0.33
Sr	N(10.)	320	61	91	94
Ta	N(0.05)	0.38	31	46	0.10
Tb	N(0.10)	0.30	13	19	0.12
Th	N(0.10)	2.6	66	99	0.55
U	N(0.01)	0.85	61	91	0.16
W	N(0.05)	24	38	57	0.74
Yb	0.23	1.2	67	100	0.19
Zn	49	270	67	100	99
Ash (%)	5.1	28.6	66	99	14.2

[1]Lower limit of determination reported as 0.20 for 12 samples.

Zinc may also be concentrated in their forage. However, other undefined factors may also be involved.

Factor 4 is strongly loaded with calcium and potassium. This factor may be related to alkali and alkaline-earth elements commonly enriched in plants. Factor scores do not reveal a close spatial association with any particular geologic substrate.

Table 5 shows the factor loading values for a five-factor model for the elk samples. This model explains 81 percent of the variance in the data set. Variables strongly loaded on factors 1 and 4 include those related to lithology. Loading values and factor scores indicate that factor 1 (Sc, Fe, Cr, Na, percent ash, Eu, Co, Hf, Th, and U) is most closely associated with samples from areas containing andesitic volcanic rocks, which crop out mostly in the northern and eastern parts of the Park. Factor 4 (La, Sm, Nd, Ce, Lu, Yb, Th, Hf, Tb, Ta, Eu, and Ba) is more closely associated with samples from areas of rhyolitic volcanic rocks, which are most commonly found in the central, southern, and western parts of the Park.

Factor 2 (W, Cs, As, Sb, Mo, and Br) is associated with elements enriched in altered rocks from areas of past or present hydrothermal activity. Samples with high scores for this

Table 3. Summary statistics for analyses of 36 variables in 2 samples of moose scat, Yellowstone National Park and vicinity.

[Concentrations are shown in dry weight and in ppm, unless "(ppb)" or "(%)" shown after element symbol. N, not detected at the lower limit of determination shown in parentheses. Mean values based on unqualified values only. "---" in geometric mean column indicates no meaningful value]

Element	Range of values		Number unqualified	Percent unqualified	Geometric mean
	Minimum	Maximum			
Ag	N(0.3)	N(0.3)	0	0	---
As	0.20	0.21	2	100	0.20
Au (ppm)	N(0.10)	0.80	1	50	---
Ba	150	190	2	100	170
Br	1.5	2.4	2	100	1.9
Ca (%)	0.89	1.40	2	100	1.12
Ce	0.9	0.9	2	100	0.9
Co	0.30	0.50	2	100	0.39
Cr	1.7	1.8	2	100	1.7
Cs	0.06	0.14	2	100	0.09
Eu	N(0.05)	N(0.05)	0	0	---
Fe (%)	0.04	0.05	2	100	0.04
Hf	0.09	0.14	2	100	0.11
Hg	N(0.05)	N(0.05)	0	0	---
Ir (ppb)	N(0.10)	N(0.10)	0	0	---
K (%)	0.11	0.12	2	100	0.11
La	0.51	0.53	2	100	0.52
Lu	0.006	0.006	2	100	0.006
Mo	0.26	0.29	2	100	0.27
Na	120	160	2	100	140
Nd	N(0.5)	N(0.5)	0	0	---
Ni	N(2)	N(2)	0	0	---
Rb	2.0	3.0	2	100	2.4
Sb	0.035	0.038	2	100	0.036
Sc	0.12	0.13	2	100	0.12
Se	N(0.10)	0.2	1	50	---
Sm	0.05	0.06	2	100	0.05
Sr	40	70	2	100	53
Ta	N(0.05)	N(0.05)	0	0	---
Tb	N(0.1)	N(0.1)	0	0	---
Th	0.10	0.10	2	100	0.10
U	N(0.01)	0.03	1	50	---
W	N(0.05)	0.52	1	50	---
Yb	0.032	0.041	2	100	0.036
Zn	160	180	2	100	170
Ash (%)	3.8	4.3	2	100	4.0

factor show a close spatial correlation with sites near hydrothermally altered areas. Factor 3 is loaded with alkali and alkaline-earth elements (K, Ca, Rb, and Sr), which are most commonly associated with major rock-forming minerals but also may be enriched in plant ash. However, samples with high factor scores for this factor do not show a close spatial association with any one geologic unit.

Factor 5 is loaded primarily with zinc and secondarily with cobalt. This segregation of zinc was previously identified in the bison factor analysis. Samples with high scores for this factor also do not show a close spatial correlation with any one rock unit.

Distributions of Anomalies for Selected Variables

Figures 2–9 show the distributions of anomalies for selected variables in scat samples. The threshold values for each animal species and variable were selected after examining histograms showing concentration distributions and plots of values for each variable. For most variables, the histograms show a single population, suggesting a single source for that variable. For those variables, approximately the top 30 percent of the values were deemed anomalous. Arsenic, however, seems to be distributed bimodally, but the two populations are

not easily separated. Consequently, the top 30 percent of the values is anomalous for arsenic as well. Zinc shows a much clearer bimodal distribution, suggesting two separate sources for this element. The threshold selected for zinc includes most of the samples in the population with the higher concentrations. Thus, 40 percent of the bison scat samples and 52 percent of the elk samples are anomalous for zinc.

Figure 2 shows the distribution of anomalous lanthanum (>7.0 ppm in bison scat; >4.6 ppm in elk scat). Lanthanum is a trace element commonly found in rocks in rock-forming accessory minerals. This element is strongly loaded on factor 1 for bison scat (table 4) and factor 4 for elk scat (table 5). Both of these factors are chemically related to rock lithology.

The highest lanthanum concentrations are found in scat from areas of both fresh and hydrothermally altered rock, mainly in the widespread rhyolites that crop out in the central, southern, and western parts of the Park. It is also enriched locally in a few samples from areas of unaltered rocks in the northern and eastern part of the Park that are underlain by Tertiary andesites, Precambrian metamorphic rocks, or Paleozoic sedimentary rocks (Chaffee, Carlson, and King, this volume; Christiansen, 2001). Lanthanum in scat is anomalous in hydrothermally altered areas, such as the Upper, Lower, and Norris Geyser Basins, and also in localities where no geothermal activity has occurred, such as in the northern part of the Park, between Mammoth and Soda Butte Creek.

Table 6 shows the percentage of sample sites with anomalies for selected elements. Elements with a high percentage of anomalous samples from altered sites are clearly related to hydrothermal activity. The data in table 6 indicate that only a minority of samples from either altered or unaltered sites are anomalous for lanthanum or zinc, emphasizing the fact that these elements are not closely associated with hydrothermal activity. Anomalies of lanthanum in hydrothermal areas are therefore largely the result of primary rock chemistry and not the overprinting of elements enriched in hydrothermal fluids. This conclusion has also been demonstrated mathematically by applying factor analysis to chemical data sets composed of rock and (or) stream-sediment samples collected Park-wide (Chaffee, Carlson, and King, this volume). Lanthanum is not an essential element for animal nutrition (Gough and others, 1979). Its concentration in scat samples is probably related to inorganic material ingested along with plant matter. Individual samples of bison and elk tissue from Park animals were analyzed for this study. Both contained 1.5 ppm La (table 7)

Figure 3 shows the distribution of cesium in scat samples. Cesium is a trace element whose distribution in rocks of the Yellowstone area is closely associated with hydrothermal activity (Chaffee, Carlson, and King, this volume). Cesium commonly proxies for potassium in minerals such as feldspars and micas. Sites whose samples contain anomalous cesium (>3.8 ppm, bison; >1.0 ppm, elk) (fig. 3) are commonly located near or downstream from hydrothermally affected areas (fig. 1). From 79–94 percent of the samples from altered sites contain anomalous cesium (table 6), whereas only 4 percent of the samples from nonaltered sites are anomalous.

Table 4. Factor-loading values for 30 variables in 48 samples of bison scat, Yellowstone National Park and vicinity.

[Four-factor model, varimax loading, based on log-normalized values]

Factor 1 (lithology)		Factor 2 (hydrothermal)		Factor 3 (zinc)		Factor 4 (alkali metals and alkaline earths)	
La	0.97	Cs	0.86	Zn	0.78	K	0.70
Ce	0.97	W	0.86			Ca	0.55
Sm	0.97	Sb	0.84				
Hf	0.96	As	0.81				
Nd	0.95	Br	0.81				
Na	0.93	Mo	0.66				
Yb	0.93	Sr	–0.87				
Th	0.93						
Eu	0.89						
Lu	0.85						
U	0.82						
Fe	0.78						
Tb	0.77						
Rb	0.71						
Sc	0.69						
Ta	0.65						
%Ash	0.65						
Co	0.63						
Cr	0.60						
Ba	0.58						
Percent variability explained							
49%		27%		4%		4%	

The highest cesium concentrations are in scat samples collected near hydrothermal areas in the Upper and Lower Geyser Basins, south of Madison Junction, and near Norris Geyser Basin. Studies of cesium radionuclides (see, for example, Hakonson, 1967) indicate that cesium is most commonly concentrated in muscle tissue. However, it is probably not an essential element for animals. Samples of bison and elk tissue from Park animals contained 0.25 ppm Cs and 1.3 ppm Cs, respectively (table 7). Kabata-Pendias (2001) showed that cesium is not an essential component of plant tissue.

Figure 4 shows the distribution of anomalous arsenic (>2.7 ppm, bison; >1.0 ppm, elk) in scat. Arsenic is abundant in the thermal waters in Yellowstone (Ball and others, 1998; Miller and others, 1997; Thompson and DeMonge, 1996) and is present in anomalous concentrations in water, sinter deposits, and stream sediment in most areas affected by thermal activity. The mineral residence of arsenic in the Park is uncertain, but it is probably present in sulfur-rich minerals, such as pyrite or native sulfur. The spatial correlation of arsenic anomalies in scat with sites near or downstream from hydrothermally altered areas is similar to that of cesium. High percentages of the samples from altered sites contain anomalous arsenic (table 6), and only 4–8 percent

Table 5. Factor-loading values for 30 variables in 67 samples of elk scat, Yellowstone National Park and vicinity.

[Five-factor model, varimax loading, based on log-normalized values. Elements in italics are secondary loading values]

Factor 1 (mafic rocks)		Factor 2 (hydrothermal)		Factor 3 (alkali metals and alkaline earths)		Factor 4 (felsic rocks)		Factor 5 (zinc)	
Sc	0.94	W	0.88	K	0.87	La	0.94	*Co*	*0.56*
Fe	0.91	Cs	0.86	Ca	0.76	Sm	0.93	Zn	0.52
Cr	0.91	As	0.84	Rb	0.72	Nd	0.93		
Na	0.75	Sb	0.84	Sr	0.56	Ce	0.87		
%Ash	0.75	Mo	0.67			Lu	0.85		
Eu	0.72	Br	0.67			Yb	0.84		
Co	0.68					Th	0.67		
Hf	0.56					Hf	0.66		
Th	0.56					Tb	0.59		
U	0.46					Ta	0.56		
						Eu	*0.49*		
						Ba	0.41		
Percent variability explained									
42%		17%		10%		8%		4%	

of the samples from nonaltered sites are anomalous, emphasizing the strong hydrothermal association of this element. Like cesium, the highest arsenic concentrations are found in samples collected in the Upper and Lower Geyser Basins, south of Madison Junction, near Norris Geyser Basin, and in the Mammoth Hot Springs area. Other anomalies are present at scattered localities, mainly near active thermal areas (fig. 4). Few arsenic analyses of tissue from large animals found in the Park are available. However, a sample of bison tissue analyzed for this study contained 0.3 ppm As and a sample of elk tissue, 0.4 ppm As (table 7). No analyses were determined for moose in the Park. Studies conducted elsewhere indicate that arsenic is concentrated in animal organs such as livers and kidneys (Puls, 1988). In very small concentrations, arsenic is considered a necessary element for animals. High concentrations of arsenic tend to enhance the toxic effects of selenium in animals (Speidel and Agnew, 1982). In human beings, arsenic can be carcinogenic (Gough and others, 1979). Toxic levels for the large Park animals, and the eventual long-term effects of ingestion of arsenic by these animals, are not known.

Figure 5 shows the distribution of anomalous molybdenum (>3.9 ppm, bison; >2.4 ppm, elk) in the scat samples. Anomalous molybdenum is found in most of the samples collected from sites associated with geothermal activity (fig. 1). Like cesium and arsenic, molybdenum is anomalous in a high percentage of samples from altered sites (table 6) and is anomalous in only a small percentage of samples from nonaltered sites, indicating a strong association with geothermal activity. The highest molybdenum concentrations are found in samples from the Upper and Lower Geyser Basins and Norris Geyser Basin. Factor analysis studies of molybdenum in sediment samples (Chaffee, Carlson, and King, this volume) also indicate that this element is associated with geothermal activity. However, unlike arsenic, molybdenum also exhibits a strong lithologic association, mainly with the felsic volcanic rocks but also locally with other lithologies. The mineral residence of molybdenum in the Yellowstone area is not known.

Molybdenum is known to be present in high concentrations in some plant species (Gough and others, 1979). At low concentration levels, it is an essential element for animals. Individual samples of bison and elk tissue from Park animals both contained <0.1 ppm Mo (table 7). Studies of domestic livestock have shown that molybdenum ingested in relatively large amounts over a long period of time can, under certain conditions, be toxic, particularly where available copper concentrations in the food are very low or sulfur concentrations are very high (Gough and others, 1979; Puls, 1988). Whether these conditions exist in terms of forage for animals in Yellowstone is not known.

The distributions of anomalous zinc (>85 ppm, bison; >100 ppm, elk) are shown in figure 6. Zinc is an essential nutrient for both plants and animals (Gough and others, 1979; Puls, 1988). Although rare, high (>5,000 ppm) concentrations of zinc in the diet of cattle may be toxic (Puls, 1988). Samples of bison and elk tissue analyzed for this study contained 210 ppm and 112 ppm, respectively (table 7). Zinc is a common trace constituent in iron- and magnesium-rich rock-forming accessory minerals and is highly mobile in many weathering environments. Both factor

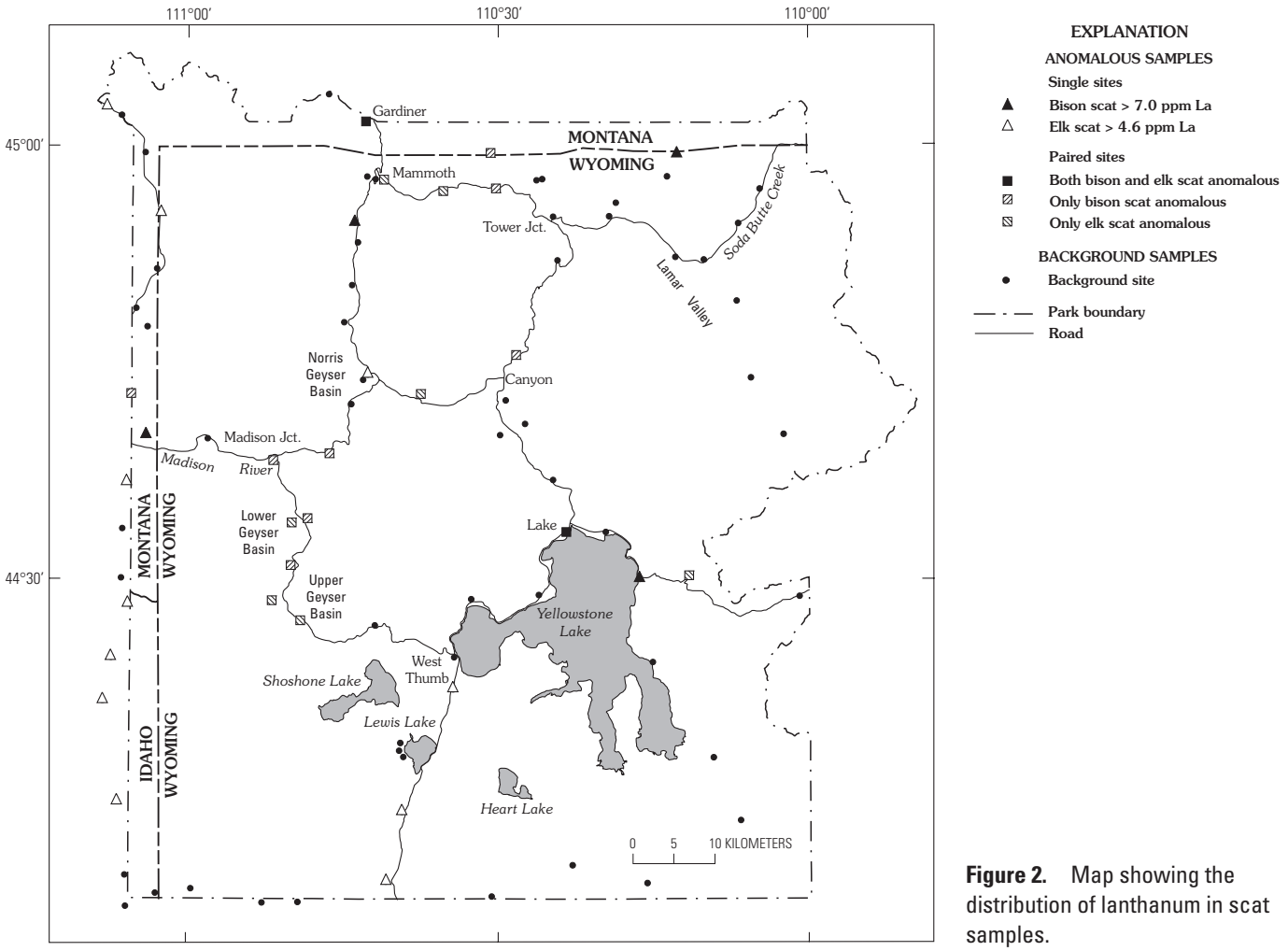

Figure 2. Map showing the distribution of lanthanum in scat samples.

Table 6. Percentage of scat sample sites with anomalies for selected elements.

Element	Altered sites		Nonaltered sites	
	Bison sites (%)	Elk sites (%)	Bison sites (%)	Elk sites (%)
La	42	39	25	27
Cs	79	94	4	4
As	68	89	4	8
Mo	74	83	4	10
Zn	58	78	32	47

analyses (tables 4 and 5) classify zinc separately from most of the other variables.

Although a majority of the samples collected from altered sites contain anomalous zinc (table 6), a relatively high percentage of samples from nonaltered sites are also anomalous, emphasizing that zinc behaves differently from the other elements discussed here. Zinc is not closely associated chemically with hydrothermal activity in the Park.

Anomalous zinc is present in bison scat collected from scattered localities between the Upper and Norris Geyser Basins and the Park boundary near the town of West Yellowstone, near Yellowstone Lake, along the Yellowstone River near Canyon, and in the Mammoth-Gardiner (Mont.) area. In contrast, samples of elk scat with anomalous zinc are generally confined to the southern and western parts of the study area. The two moose samples are strongly anomalous (160 ppm and 180 ppm Zn, respectively), suggesting that moose are consuming plants that have relatively high concentrations of zinc. Analyses of moose pellets from Alaska (Day and others, 1985) show consistently high zinc concentrations, confirming our observations in Yellowstone.

Concentrations of zinc for both bison and elk scat exhibit a bimodal distribution, suggesting two sources for this element. We speculate that one source is ingested plant material and the other is inorganic rock material attached to

Table 7. Composition of biological samples from Yellowstone Lake and the greater Yellowstone ecosystem.

[All units are ppm. Leaders (---) indicate no data]

Sample type	Ag	Al	As	Ba	Be	Bi	Ca	Cd	Ce	Co	Cr	Cs	Cu	Fe
Gill-net macrophytes	< 0.01	90	2.8	8.4	0.32	< 0.005	560	0.03	0.74	0.07	---	1.1	0.4	120
Algal pod	< 0.01	40	1.8	3.2	< 0.01	0.01	1,100	0.04	0.69	0.12	---	0.12	< 3	110
Mat from above vent	0.01	500	6.3	16	0.98	0.01	300	< 0.01	5.3	0.18	---	6.8	< 3	340
60-µm near shore	< 0.01	380	7.9	6.3	0.28	0.02	400	0.03	9.6	0.26	---	2.7	0.8	350
Plankton- 243 µm	< 0.01	50	7.2	6.5	< 0.01	< 0.005	2,700	0.04	0.16	0.09	---	2.5	0.6	70
Plankton- 11µm at 1m	0.02	220	5.2	5.6	0.06	0.02	1,600	0.32	0.87	1.5	---	1.3	11	710
Trout														
Average cutthroat trout stomach contents	< 0.02	681	15	161	0.088	0.013	38,605	0.21	---	0.53	2.1	28.2	39.1	1,008
Average lake trout stomach contents	< 0.02	1,861	46	278	0.247	0.035	26,013	1.55	---	1.31	3.2	18.5	33.1	3,433
Average spawning cutthroat trout muscle	< 0.02	45.0	0.57	9.7	0.003	0.005	8,373	0.03	< 0.5	0.13	2.7	26.2	4.7	107
Average cutthroat trout muscle	<0.02	< 8	0.23	< 0.5	< 0.001	< 0.005	2,201	< 0.003	< 0.5	< 0.1	8.6	83.0	4.6	< 50
Average lake trout muscle	< 0.02	< 8	1.4	< 0.5	< 0.001	< 0.005	2,492	0.006	< 0.5	< 0.1	10.5	69.3	3.7	< 50
Average cutthroat trout liver	< 0.02	24.6	2.0	0.59	0.013	0.030	441	0.49	---	0.30	0.2	21.0	496.3	1,142
Average lake trout liver	< 0.02	15.4	9.6	0.94	0.001	0.015	361	1.36	---	0.57	0.1	13.8	56.3	973
Plants														
Pine nut	< 0.02	46.2	< 0.1	< 0.5	< 0.001	0.006	75.0	0.09	< 0.5	0.11	2.7	0.02	10.9	< 50
Pine nut	< 0.02	< 8	< 0.1	< 0.5	< 0.001	< 0.005	34.5	0.1	< 0.5	< 0.1	0.86	0.02	4.9	< 50
Pine nut	< 0.02	40.8	< 0.1	< 0.5	< 0.001	< 0.005	47.1	0.08	< 0.5	0.13	1.5	0.02	6.4	< 50
Pine nut	< 0.02	20.1	< 0.1	< 0.5	< 0.001	< 0.005	41.7	0.05	< 0.5	< 0.1	1.2	0.01	4.3	< 50
Pine nut	< 0.02	58.8	< 0.1	< 0.5	< 0.001	< 0.005	69.3	0.12	< 0.5	< 0.1	1.6	0.02	8.7	< 50
Pine nut	< 0.02	35.6	< 0.1	< 0.5	< 0.001	< 0.005	49.7	0.08	< 0.5	< 0.1	1.4	0.02	9.5	< 50
Equisetum	0.02	32.9	< 0.1	24.3	0.008	0.02	5,020	1.9	< 0.5	0.23	1.5	0.24	10.8	110
Clover	< 0.02	63.6	< 0.1	39.5	0.002	0.007	3,140	0.007	< 0.5	0.27	0.77	0.004	3.7	130
Perodecidia gairdnew	< 0.02	332	0.2	24.0	0.02	0.01	884	0.30	0.98	0.14	1.6	0.05	7.8	310
Heracleum	< 0.02	125	< 0.1	52.1	0.001	0.006	5,490	0.08	< 0.5	0.22	1.2	0.02	7.3	210
Cirsuim scariagm	< 0.02	55.5	< 0.1	197	0.005	< 0.005	3,080	0.10	< 0.5	< 0.1	1.2	0.02	2.1	60
Animals														
Bison flesh	< 0.02	10.7	0.3	0.58	0.003	0.006	107	0.006	< 0.5	< 0.1	2.3	0.25	5.7	190
Mule deer flesh	< 0.02	16.2	< 0.1	< 0.5	< 0.001	0.005	177	0.08	< 0.5	< 0.1	2.1	0.03	16.1	160
Elk flesh	< 0.02	< 8	0.4	< 0.5	0.004	0.005	86.3	0.006	< 0.5	< 0.1	1.8	1.3	6.2	110
Hayden Valley grizzly bear flesh	< 0.02	< 8	< 0.1	< 0.5	0.005	< 0.005	159	0.04	< 0.5	< 0.1	2.0	0.35	7.5	230
Gallatin NF grizzly bear flesh	< 0.02	7.9	< 0.1	< 0.5	0.002	< 0.005	133	0.05	< 0.5	< 0.1	2.0	0.09	7.3	300
Gallatin NF grizzly bear hair	< 0.02	202	< 0.1	10.0	< 0.001	0.02	639	0.11	< 0.5	< 0.1	2.2	0.04	11.4	140
Shoshone NF grizzly bear hair	0.18	452	0.1	7.3	0.02	0.18	356	0.02	0.75	0.55	2.9	0.05	13.6	740
Yellowstone Lake grizzly bear hair	0.05	297	0.5	7.3	< 0.001	0.09	627	0.06	0.66	0.33	8.3	0.30	12.4	600
Yellowstone Lake grizzly bear hair	< 0.02	140	0.1	2.2	0.003	0.02	219	0.02	< 0.5	< 0.1	3.2	0.04	9.3	120

Table 7. Composition of biological samples from Yellowstone Lake and the greater Yellowstone ecosystem—*Continued*.

Sample type	Ga	Hg	K	La	Li	Mg	Mn	Mo	Na	Nb	Ni	P	Pb
Gill-net macrophytes	< 0.01	---	610	0.5	0.8	190	22	0.28	100	0.05	0.96	230	0.22
Algal pod	< 0.01	---	180	0.41	0.61	320	9.4	0.13	170	0.01	2.2	110	0.13
Mat from above vent	< 0.01	---	190	2.8	3.5	910	29.0	0.09	120	0.04	1	140	0.84
60-µm near shore	< 0.01	---	60	4.7	1.2	280	17.0	0.13	40	0.08	0.42	30	3.7
Plankton- 243 µm	< 0.01	< 0.2	2,000	0.09	28	1,400	3.2	0.98	6,500	0.01	0.67	1,200	0.46
Plankton- 11µm at 1m	< 0.01	< 0.2	710	0.44	9.9	710	18.0	0.49	3,600	0.01	590	360	15
						Trout							
Average cutthroat trout stomach contents	0.43	0.82	10,343	---	1.2	1,552	273	0.6	5,225	< 2	3.0	11,925	0.7
Average lake trout stomach contents	1.23	1.19	9,400	---	1.8	1,352	423	0.8	4,587	< 2	4.0	11,867	2.0
Average spawning cutthroat trout muscle	0.21	0.99	16,417	0.15	0.4	1,237	5.6	< 0.1	3,522	< 2	1.3	20,500	0.1
Average cutthroat trout muscle	0.026	0.9	44,698	< 0.3	< 0.2	2,852	1.6	< 0.1	7,161	< 2	< 1	26,199	< 0.2
Average lake trout muscle	0.023	0.9	42,880	< 0.3	< 0.2	2,774	0.9	< 0.1	7,982	< 2	< 1	24,949	< 0.2
Average cutthroat trout liver	0.09	1.56	13,965	---	0.4	486	6.3	1.1	6,057	< 2	< 1	11,283	0.7
Average lake trout liver	0.09	2.10	10,603	---	0.2	688	14.7	0.3	4,743	< 2	< 1	11,000	0.1
						Plants							
Pine nut	0.06	0.006	8,720	< 0.3	< 0.2	1,780	150	< 0.1	12	< 2	9.1	5,500	< 0.2
Pine nut	0.02	0.006	3,750	< 0.3	< 0.2	818	55.1	< 0.1	7	< 2	< 1	2,300	< 0.2
Pine nut	0.03	0.005	6,860	< 0.3	< 0.2	1,230	88.0	< 0.1	11	< 2	1.8	3,600	< 0.2
Pine nut	0.02	0.005	3,560	< 0.3	< 0.2	857	72.1	0.2	7	< 2	< 1	2,400	0.2
Pine nut	0.03	0.006	7,960	< 0.3	< 0.2	1,280	90.7	< 0.1	10	< 2	2.2	3,500	< 0.2
Pine nut	0.04	0.006	6,920	< 0.3	< 0.2	1,470	96.0	< 0.1	9	< 2	2.0	4,200	< 0.2
Equisetum	0.07	0.028	---	< 0.3	< 0.2	4,240	44.2	0.32	236	< 2	1.1	6,600	5.4
Clover	0.03	0.004	23,200	< 0.3	< 0.2	2,000	33.3	0.48	30	< 2	< 1	1,700	0.2
Perodecidia gairdnew	0.2	<0.004	19,900	0.51	0.2	1,000	42.0	0.42	78	< 2	< 1	4,500	0.5
Heracleum	0.1	0.007	---	< 0.3	< 0.2	2,630	36.6	2.00	86	< 2	2.2	7,600	0.2
Cirsuim scariagm	0.03	<0.004	---	0.49	< 0.2	710	11.9	0.44	39	< 2	< 1	2,100	< 0.2
						Animals							
Bison flesh	0.1	<0.004	18,800	< 0.3	1.5	656	0.98	< 0.1	3,850	< 2	< 1	9,400	< 0.2
Mule deer flesh	0.09	0.005	14,800	< 0.3	< 0.2	956	1.10	< 0.1	3,100	< 2	< 1	9,500	0.2
Elk flesh	0.08	0.008	13,700	< 0.3	1.5	978	0.63	< 0.1	1,670	< 2	< 1	8,900	< 0.2
Grizzly bear flesh	0.07	0.006	11,000	< 0.3	< 0.2	748	0.87	< 0.1	5,330	< 2	< 1	7,600	< 0.2
Grizzly bear flesh	0.09	0.014	19,400	< 0.3	< 0.2	1,080	0.89	0.1	2,510	< 2	< 1	11,000	< 0.2
Grizzly bear hair	0.06	0.09	518	< 0.3	< 0.2	466	21.4	0.1	220	< 2	< 1	330	0.50
Grizzly bear hair	0.2	0.08	258	0.33	< 0.2	538	18.0	0.2	315	5.6	1.1	270	0.58
Grizzly bear hair	0.1	0.61	2,680	0.35	< 0.2	344	7.9	0.23	952	< 2	1.6	880	1.4
Grizzly bear hair	0.05	1.7	122	< 0.3	< 0.2	103	4.1	< 0.1	124	< 2	< 1	240	0.59

Table 7. Composition of biological samples from Yellowstone Lake and the greater Yellowstone ecosystem—*Continued*.

Sample type	Rb	Sb	Sc	Se	Sr	Ta	Th	Ti	Tl	U	V	Y	Zn
Gill-net macrophytes	1.5	0.55	< 0.05	< 0.1	5	< 0.01	0.02	<10	0.02	0.04	0.4	0.39	15
Algal pod	0.3	0.02	< 0.05	< 0.1	6.9	< 0.01	0.03	<10	< 0.01	0.01	0.2	0.23	1
Mat from above vent	2.3	0.53	< 0.05	< 0.1	6.3	< 0.01	0.25	<10	0.02	0.11	0.4	1.4	3
60-µm near shore	1.1	0.05	0.1	< 0.1	4.1	< 0.01	1.4	<10	0.02	0.14	0.3	2.5	3
Plankton- 243 µm	8	0.23	< 0.05	0.1	23	< 0.01	< 0.005	<10	< 0.01	0.009	0.6	0.08	13
Plankton- 11 µm at 1m	2.3	0.04	0.07	< 0.1	13	< 0.01	0.04	<10	< 0.01	0.05	0.5	0.29	690
Trout													
Average cutthroat trout stomach contents	64.4	< 0.02	---	3.5	293	---	---	26.8	0.158	0.09	1.7	---	159
Average lake trout stomach contents	43.7	< 0.02	---	4.7	199	---	---	63.3	0.300	0.18	5.1	---	276
Average spawning cutthroat trout muscle	64.8	< 0.02	< 0.3	1.4	56	< 0.2	0.043	< 40	0.087	0.01	0.9	< 0.3	44.9
Average cutthroat trout muscle	201.5	< 0.02	< 0.3	2.9	10.1	< 0.2	< 0.03	< 40	0.15	< 0.02	< 0.4	< 0.3	85.5
Average lake trout muscle	167.2	< 0.02	< 0.3	4.1	8.9	< 0.2	< 0.03	< 40	0.21	< 0.02	< 0.4	< 0.3	26.1
Average cutthroat trout liver	79.0	< 0.02	---	7.5	1.3	---	---	< 40	0.733	0.02	1.2	---	117
Average lake trout liver	56.5	< 0.02	---	9.6	1.6	---	---	< 40	1.900	0.01	1.3	---	98.4
Plants													
Pine nut	22.7	< 0.02	< 0.3	< 0.2	0.09	< 0.2	0.18	< 40	< 0.003	< 0.02	0.5	< 0.3	47.1
Pine nut	4.9	< 0.02	< 0.3	< 0.2	< 0.05	< 0.2	0.04	< 40	< 0.003	< 0.02	< 0.4	< 0.3	30.1
Pine nut	16.9	< 0.02	< 0.3	< 0.2	0.05	< 0.2	0.06	< 40	< 0.003	< 0.02	< 0.4	< 0.3	34.4
Pine nut	12.6	< 0.02	< 0.3	< 0.2	0.08	< 0.2	0.04	< 40	< 0.003	< 0.02	< 0.4	< 0.3	23.0
Pine nut	6.6	< 0.02	< 0.3	< 0.2	0.20	< 0.2	0.03	< 40	< 0.003	< 0.02	< 0.4	< 0.3	47.8
Pine nut	8.7	< 0.02	< 0.3	< 0.2	0.06	< 0.2	< 0.03	< 40	< 0.003	< 0.02	< 0.4	< 0.3	41.4
Equisetum	65.8	< 0.02	0.3	< 0.2	126	0.43	1.2	< 40	0.007	< 0.02	0.4	< 0.3	55.9
Clover	3.1	< 0.02	< 0.3	< 0.2	105	< 0.2	0.25	< 40	0.003	< 0.02	< 0.4	< 0.3	9.6
Perodecidia gairdnew	7.6	< 0.02	< 0.3	< 0.2	17.0	0.22	0.59	< 40	0.008	< 0.02	0.8	< 0.3	24.5
Heracleum	23.3	< 0.02	< 0.3	< 0.2	134	< 0.2	0.15	< 40	0.004	< 0.02	0.6	< 0.3	28.6
Cirsuim scariagm	40.5	< 0.02	< 0.3	< 0.2	137	< 0.2	< 0.03	< 40	0.006	< 0.02	< 0.4	< 0.3	< 5
Animals													
Bison flesh	10.9	< 0.02	< 0.3	< 0.2	0.64	< 0.2	0.27	< 40	< 0.003	< 0.02	0.5	< 0.3	210
Mule deer flesh	8.6	< 0.02	< 0.3	0.9	0.65	< 0.2	0.16	< 40	< 0.003	< 0.02	0.5	< 0.3	178
Elk flesh	13.4	< 0.02	< 0.3	0.2	0.17	< 0.2	0.09	< 40	0.003	< 0.02	0.5	< 0.3	112
Grizzly bear flesh	19.3	< 0.02	< 0.3	0.5	0.56	< 0.2	0.06	< 40	0.003	< 0.02	0.5	< 0.3	100
Grizzly bear flesh	17.7	< 0.02	< 0.3	0.6	0.44	< 0.2	0.09	< 40	0.004	< 0.02	0.5	< 0.3	144
Grizzly bear hair	0.67	< 0.02	0.3	0.6	3.3	0.23	0.14	< 40	0.01	< 0.02	1.5	< 0.3	141
Grizzly bear hair	0.73	< 0.02	1.3	0.4	6.2	3.1	22.3	< 40	0.03	0.04	3.5	< 0.3	132
Grizzly bear hair	4.7	< 0.02	1.7	< 0.2	4.3	0.22	0.10	< 40	0.02	0.16	3.5	< 0.3	600
Grizzly bear hair	0.70	< 0.02	0.4	0.5	1.2	0.23	0.10	< 40	0.006	< 0.02	1.2	< 0.3	135

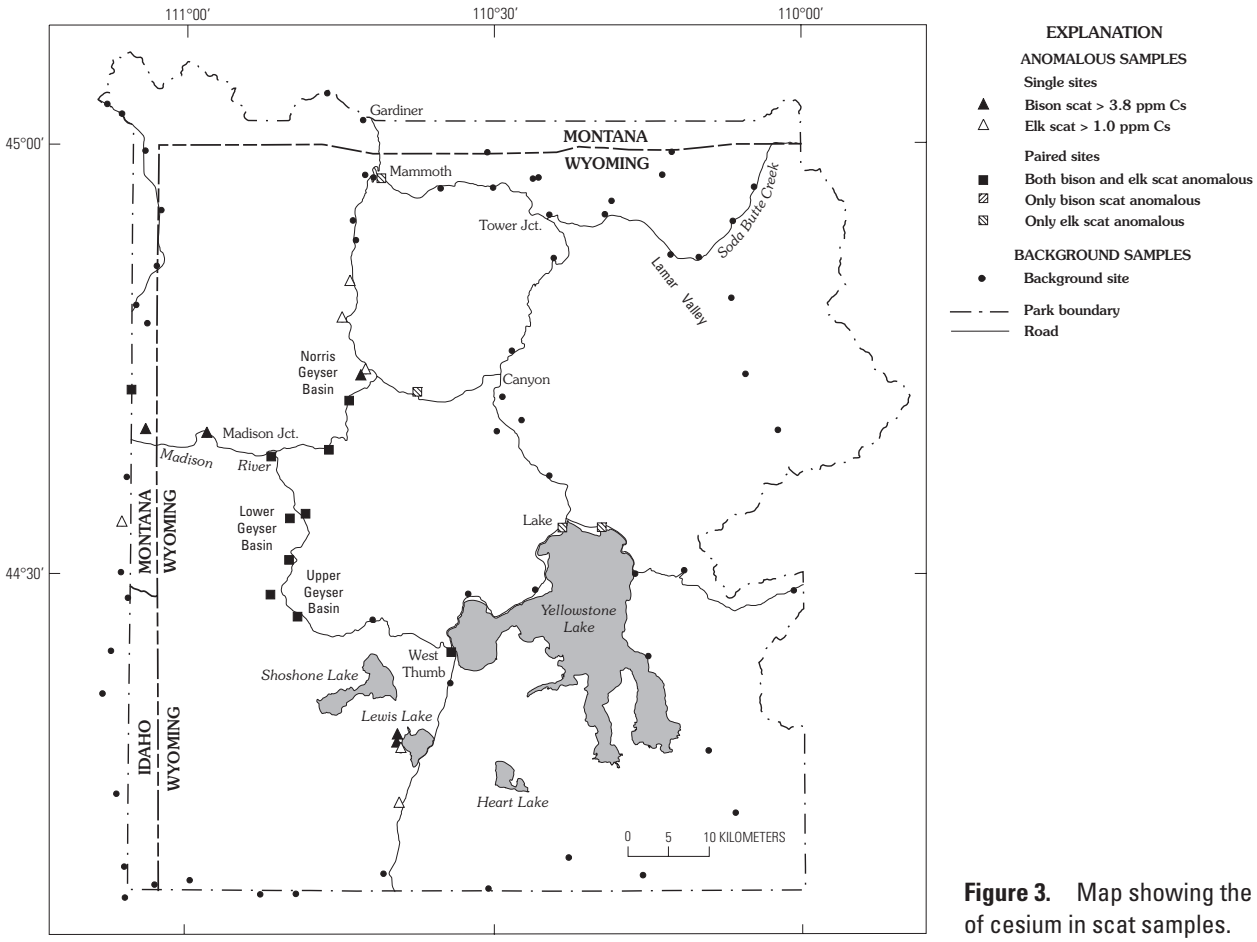

Figure 3. Map showing the distribution of cesium in scat samples.

plant-root masses. The relative distributions of this element in the two environments shown in table 6, as well as its classification into a separate factor by factor analysis, together indicate a relatively poor association of zinc with any particular lithology or with hydrothermal activity.

Figures 7 and 8 show the distributions of high and low concentrations (upper and lower quartiles) of percent ash in bison and elk scat, respectively. High values for both species (fig. 7) are generally concentrated in the Lamar River basin, the Mammoth-Gardiner area, and in the Upper and Lower Geyser Basins. In contrast, low ash values (fig. 8) are most common in samples collected around Yellowstone Lake (mostly bison) and in the southwestern part of the Park and vicinity (mostly elk). Although not plotted on any maps, both moose samples also showed a low percentage of ash (3.8 and 4.3 percent). The distributions of anomalously high or low percent ash for either bison or elk do not show any obvious strong spatial correlations to specific lithologies, or areas of past or present hydrothermal activity. The distribution of percent ash is probably related in part to the types of plants consumed at a given locality but mostly to the amount of soil mineral matter included in each sample.

Discussion

The scat of elk, bison, and moose that forage in thermal areas show enrichments in hydrothermal elements that are characteristically concentrated in thermal waters. These elements are enriched in the rocks altered by these waters and are also found in sinter and travertine deposits.

Fluorine is anomalous in rocks and sediments from many parts of the Park (Chaffee, Carlson, and King, this volume) and is strongly anomalous in geothermal waters (Miller and others, 1997). Anomalous fluorine has also been measured in forage plants growing in some hydrothermally altered areas in parts of the Park (J. Otton, oral commun., 2001; Garrott and others, 2002). Fluorine is the only element examined for this study that has been clearly documented to have a serious negative effect on Yellowstone wildlife (Garrott and others, 2002). This element, which is a necessary nutrient for animals at low concentration levels, has been recognized by biologists for some years as having a serious negative impact on the health and longevity of elk when ingested in large amounts (Shupe and others, 1984). We did not measure the fluorine content in elk-scat samples for this study. However, because it is one of the elements that is strongly associated with hydrothermal activity (Chaffee, Carlson, and King, this volume), one can infer that scat with

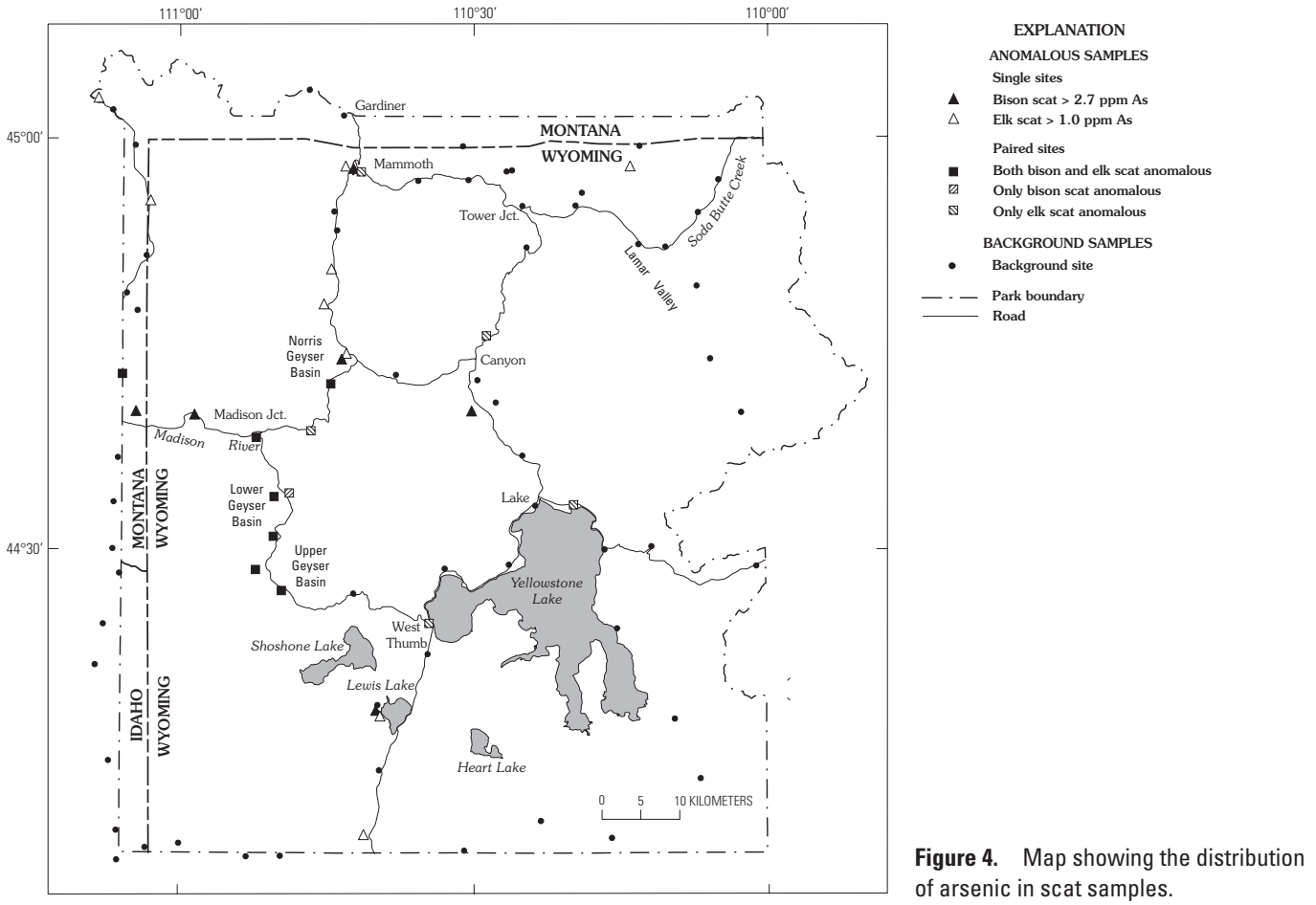

Figure 4. Map showing the distribution of arsenic in scat samples.

high concentrations of elements such as As, Cs, and Mo will probably also contain anomalous concentrations of fluorine.

Elements such as arsenic are also known to be concentrated in plant tissue and may be passed up the food chain to large animals. Some data on the arsenic content of plants are given in table 7. When compared to concentration levels in stream sediment collected in or near Yellowstone National Park, scat samples locally contain unusually high concentrations of the hydrothermally associated elements As, Br, Cs, Mo, Sb, and W, as well as of the vegetation-associated elements Ba, Ca, K, Rb, and Sr. Zinc, an element not related to any one rock type or to hydrothermal activity, is relatively enriched in scat as compared to sediment and is classified in a separate factor by factor analysis. The zinc data set also shows a distinct bimodal distribution. This overall unique behavior of zinc is not understood.

Several other elements that are known to be potentially toxic to wildlife (Cr, Hg, Ni, Pb, Se, and U) were also measured but were found to be present in only very low concentrations in scat. These low values reflect their generally low concentrations in rocks and stream sediments in the region (Chaffee, Carlson, and King, this volume) and in plants (table 7).

The spatial distributions of most of the element anomalies observed in scat for this report in general show no particular correlation with the underlying rock type. However, a spatial correlation between anomalous, hydrothermally related elements in scat and hydrothermally altered rocks does exist. Scat does not seem to be anomalous much more than about a kilometer or two beyond any of the altered areas. However, it may be anomalous downstream from some altered areas. Although most bison and elk in the Park move from place to place seasonally, some elk are nonmigratory in the geyser basins of the Madison River drainage basin. These observations, coupled with our chemical data, suggest that animals spending a considerable amount of time foraging in and near hydrothermal areas may eventually ingest significant amounts of one or more potentially toxic elements.

Additional hydrothermally related elements measured but not discussed in detail in this report include bromine and tungsten. These elements are distributed similarly to samples with anomalous concentrations of other hydrothermally related elements. The effects of ingestion by animals of bromine or tungsten, or any of the other hydrothermal elements discussed except fluorine, are uncertain. According to Puls (1988), a high fluorine uptake by cattle aggravates bromine toxicity. Tungsten in high concentrations is known to be toxic to plants and animals (Gough and others, 1979; Puls, 1988).

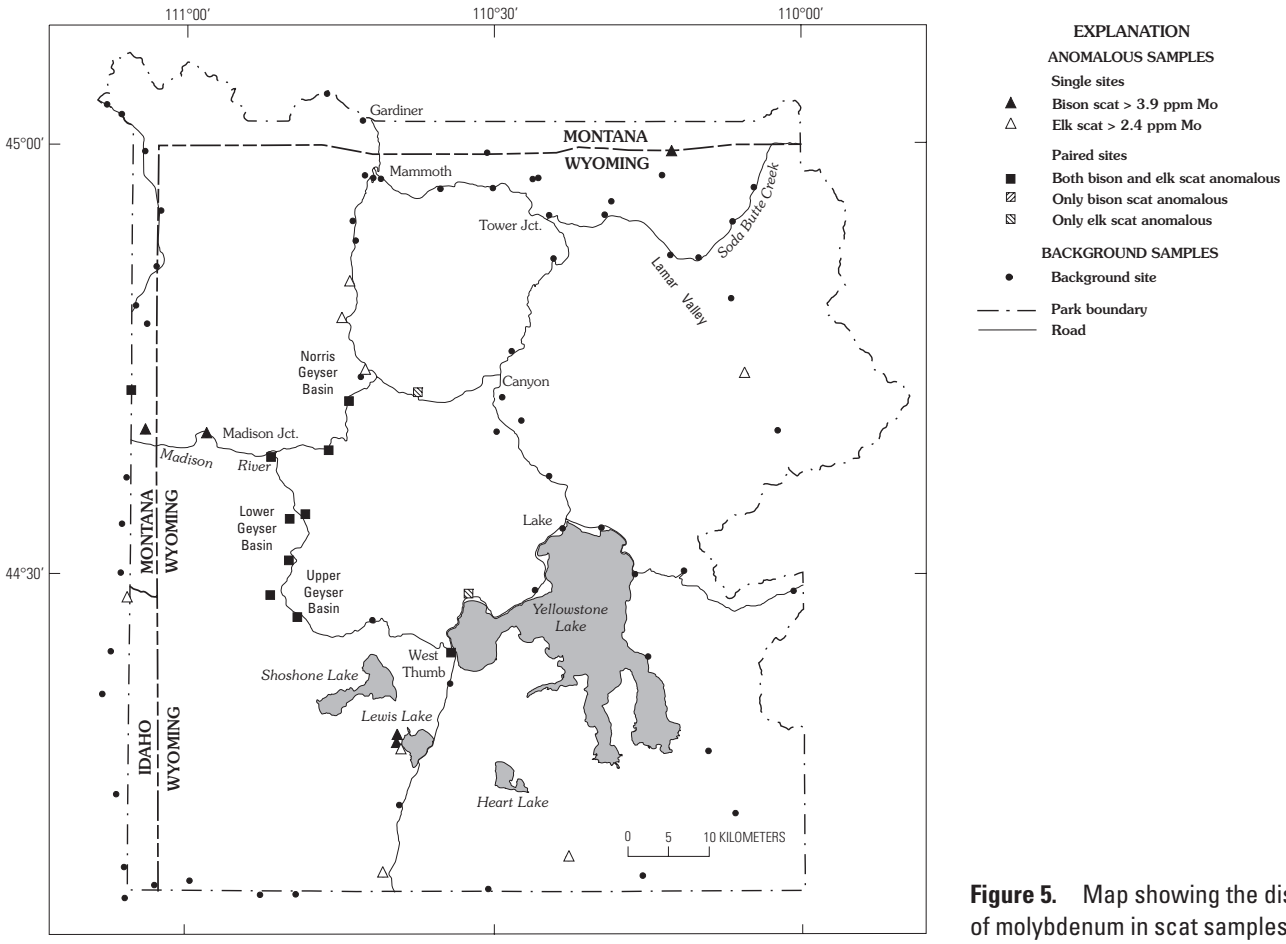

Figure 5. Map showing the distribution of molybdenum in scat samples.

Many plant species can be poisoned by the uptake of relatively large amounts of elements such as Ag, Al, As, B, Br, Cd, Cl, Co, Cr, Cu, F, I, Li, Mn, Mo, Ni, Pb, Tl, U, V, and Zn (Gough and others, 1979; Kabata-Pendias, 2001). This poisoning does not always kill the plants but may weaken them to the point that diseases become a threat. By analogy, this process may occur in animals in the Park but, with the exception of fluorine, may not be visually obvious. However, no obvious effects of bison ingesting toxic doses of any metals have been observed to date (Steve Sweeney, Univ. of Montana, written commun., 2002).

Ingestion of even relatively large amounts of a given element, whether from plants, soils, or water, probably does not demonstrate that the animals retain and accumulate the elements at any particular concentration level in their blood or tissues. Retention and toxicity of many elements depend on the chemical form of the element. Analyses of organs such as livers and kidneys, as well as hair, blood, and urine analysis, will be necessary to demonstrate retention and whether the levels found might be high enough to represent a health problem. Should high levels be found, they should be evaluated for any correlations (1) between high chemical levels in Park animals and incidence of diseases in these animals, and (2) to known areas within the Park having anomalous concentrations of the elements in question in rocks, soils, and (or) plants.

Impact of Sublacustrine Hydrothermal Elements on Cutthroat Trout and Grizzly Bears in the Yellowstone Lake Ecosystem

Yellowstone Lake is the last pristine habitat for the native Yellowstone cutthroat trout (*Oncorhynchus clarki bouvieri*), but the survival of this species is threatened as a result of the illegal or accidental introduction of the piscivorous lake trout (*Salvelinus namaycush*) into the lake. The presence of lake trout was discovered by an angler in 1994 (Kaeding and others, 1996). Since then, lake trout have had a serious, detrimental impact on the Yellowstone cutthroat trout population and have the potential to reduce the native cutthroat trout population by 80–90 percent (McIntyre, 1996).

This predation has led to an aggressive gill-netting program in Yellowstone Lake by the National Park Service to reduce the population of lake trout. Fishing regulations in Yellowstone Lake now allow unlimited catches of lake trout and require that any lake trout caught be killed, the stomach contents be examined, and the findings reported to Park rangers. Ruzycki and Beauchamp (1997) used data on angler-caught and gill-netted lake trout to produce a bioenergetics

model to estimate size-specific consumption of cutthroat trout by lake trout. They estimated that intermediate-size lake trout (301–499 mm long) consume 28 cutthroat trout per year and large lake trout (500–850 mm long) consume an average of 90 cutthroat per year.

The Yellowstone cutthroat trout are of critical importance to the Yellowstone ecosystem because they are an important prey food for grizzly bears, otters, eagles, and osprey. The potamodromous (migrate to and spawn in fresh-water streams) cutthroat trout are an especially important food source for grizzly bears (Mattson and Reinhart, 1995; Mealey, 1980; Reinhart, 1990), which have been designated as a threatened species. Bears feed on massive quantities of trout present in the tributaries to Yellowstone Lake during the spring cutthroat-spawning season. In contrast, the nonmigratory lake trout stay in deep water in the lake and spawn in the lake. Thus, lake trout are not accessible to grizzly bears and do not fill the same environmental niche as the Yellowstone cutthroat trout. Lake trout are also less accessible to otter, osprey, and eagles because of their tendency to stay in deeper water.

Balistrieri and others (this volume) have shown that Yellowstone Lake sublacustrine hydrothermal-vent waters contribute substantial amounts of As, B, Cl, Cs, Ge, Li, Mo, Sb, and W to the lake. Measurements of chloride concentrations in the lake indicate that about 10 percent of the total thermal-water flux in Yellowstone National Park occurs on the floor of Yellowstone Lake, mainly within the Yellowstone caldera, in the north part of the lake, and in the West Thumb area (fig. 1). In addition, Hg and Tl show substantial enrichment in vent fluids and in siliceous deposits near sublacustrine vents (Balistrieri and others, this volume; Shanks and others, this volume). Of these elements, As and Hg have a documented toxicity to wildlife, and Li, Mo, Sb, and Tl are potentially toxic elements (Smith and Huyck, 1999). The possibility that hydrothermal-metal fluxes affect the aquatic ecosystem, and possibly the greater Yellowstone ecosystem, follows from the discovery of three "cutthroat Jacuzzis" in Yellowstone Lake. These are shallow-water, low-temperature vents where schools of as many as 30 cutthroat trout congregate at a given time, presumably because of opportunities to feed on the bacteria and zooplankton that flourish in the nutrient-rich thermal waters.

For this study, metal concentrations in Yellowstone Lake fishes were determined, as were the sources and fates of these metals. Because spawning cutthroat trout are an important food source for the endangered grizzly bear, a special effort was made to measure potentially toxic elements in grizzly bear food sources and in bear tissues. The only previously published data on mercury in fish from Yellowstone National Park are from cutthroat trout sampled from the Yellowstone River, at the lake outlet, as part of the USGS Yellowstone River Basin NAWQA (National Water-Quality Assessment) Program

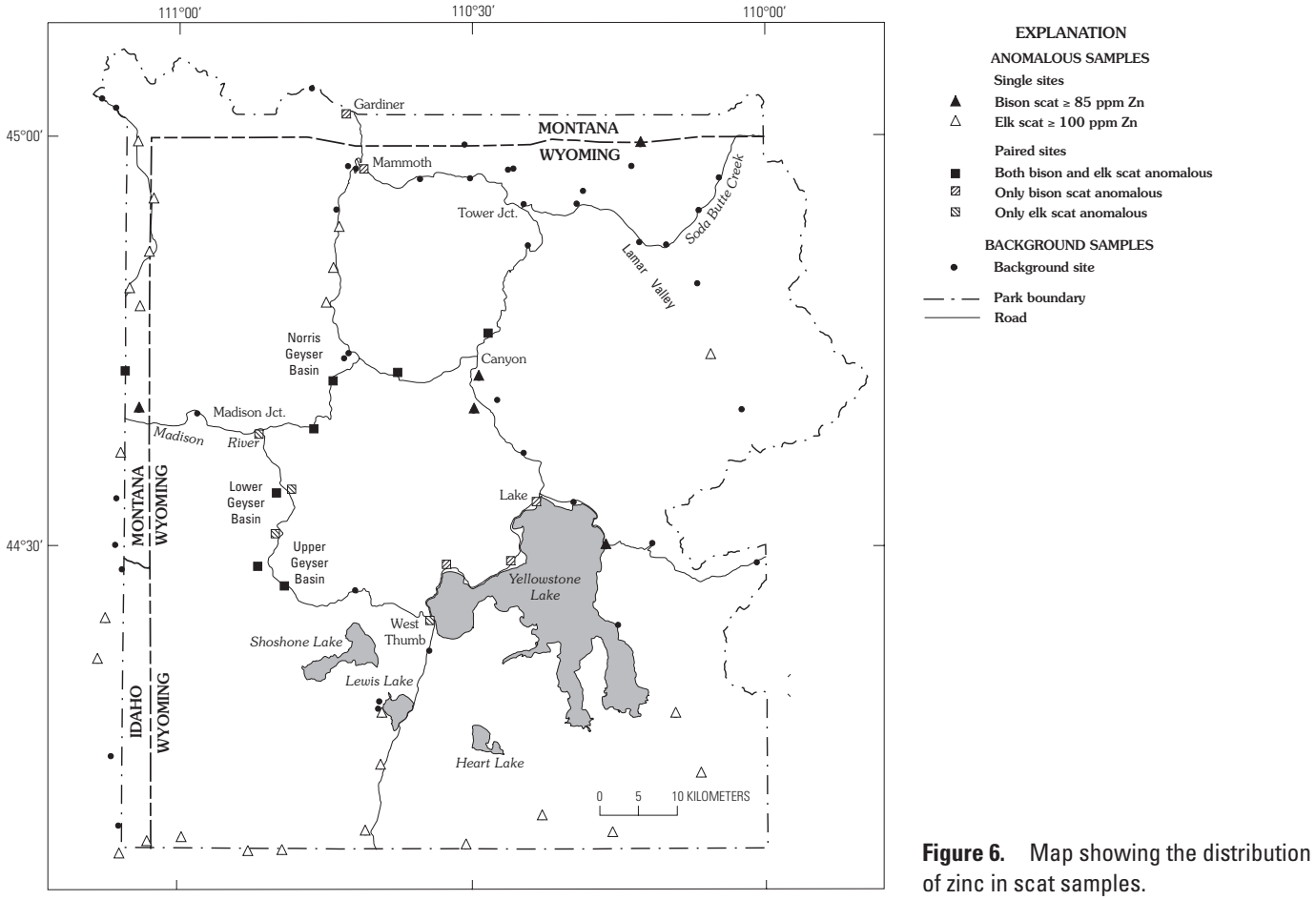

Figure 6. Map showing the distribution of zinc in scat samples.

(Peterson and Boughton, 2000). In that study, five cutthroat trout from this site were collected and their livers were analyzed for organic contaminants, potentially toxic metals, and other elements. Mercury concentrations in fish livers from this site averaged 0.54-ppm Hg (dry weight) and were enriched in comparison to most other fish-liver samples collected in the NAWQA study of the Yellowstone River drainage basin.

Collection, Preparation, and Analysis of Samples

For this study, lake and cutthroat trout were collected from Yellowstone Lake in 1998 and 2000, mostly by gill netting. Additional fish were caught in 1998 by line-fishing at near-shore sites, particularly in areas of known sublacustrine hydrothermal activity. Spawning cutthroat trout were also collected by the Interagency Grizzly Bear Study Team (IGBST). In all, 39 cutthroat trout and 25 lake trout were collected. Sample localities were chosen to give a broad geographical distribution in the lake, and included areas around West Thumb, Dot Island, Frank Island, Southeast Arm, South Arm, Sedge Bay, and Steamboat Point. Fish samples spanned a large range in size, from about 240–640 mm in length.

The 1998 samples were separated into stomach contents, muscle tissue, and liver tissue, which were analyzed separately. Analyses of fish collected in 2000 focused on muscle tissue. Following collection, all samples were frozen and stored in clean, sealed plastic bags until analysis. The 1998 samples were freeze-dried prior to analysis. Weight loss due to freeze-drying allowed calculation of water content, which averaged 76±7 weight percent. Fish collected in 2000 were analyzed directly without drying.

Samples of plants and animals consumed by bears, and of grizzly bear flesh and hair, were collected by the Interagency Grizzly Bear Study Team under direction of Chuck Schwarz, USGS-BRD. Samples selected were broadly representative of the foods grizzly bears are known to consume and were collected from widely separated localities in the Park, as described in the third section of this paper. Samples of bacterial and algal mats, and of plankton in the water column, were also collected from Yellowstone Lake, and subsamples for chemical studies were provided by J.V. Klump and R. Cuhel of the University of Wisconsin-Milwaukee.

All samples were chemically analyzed at the U.S. Geological Survey laboratories in Denver, Colo. The vegetation and tissue samples were first ground; the macerated material was then weighed (usually about 0.5 g) into a flint-glass test tube, 5 mL of concentrated Ultrex nitric acid was added, and the mixture was allowed to stand overnight. For the hair samples, the material was weighed and transferred to the test

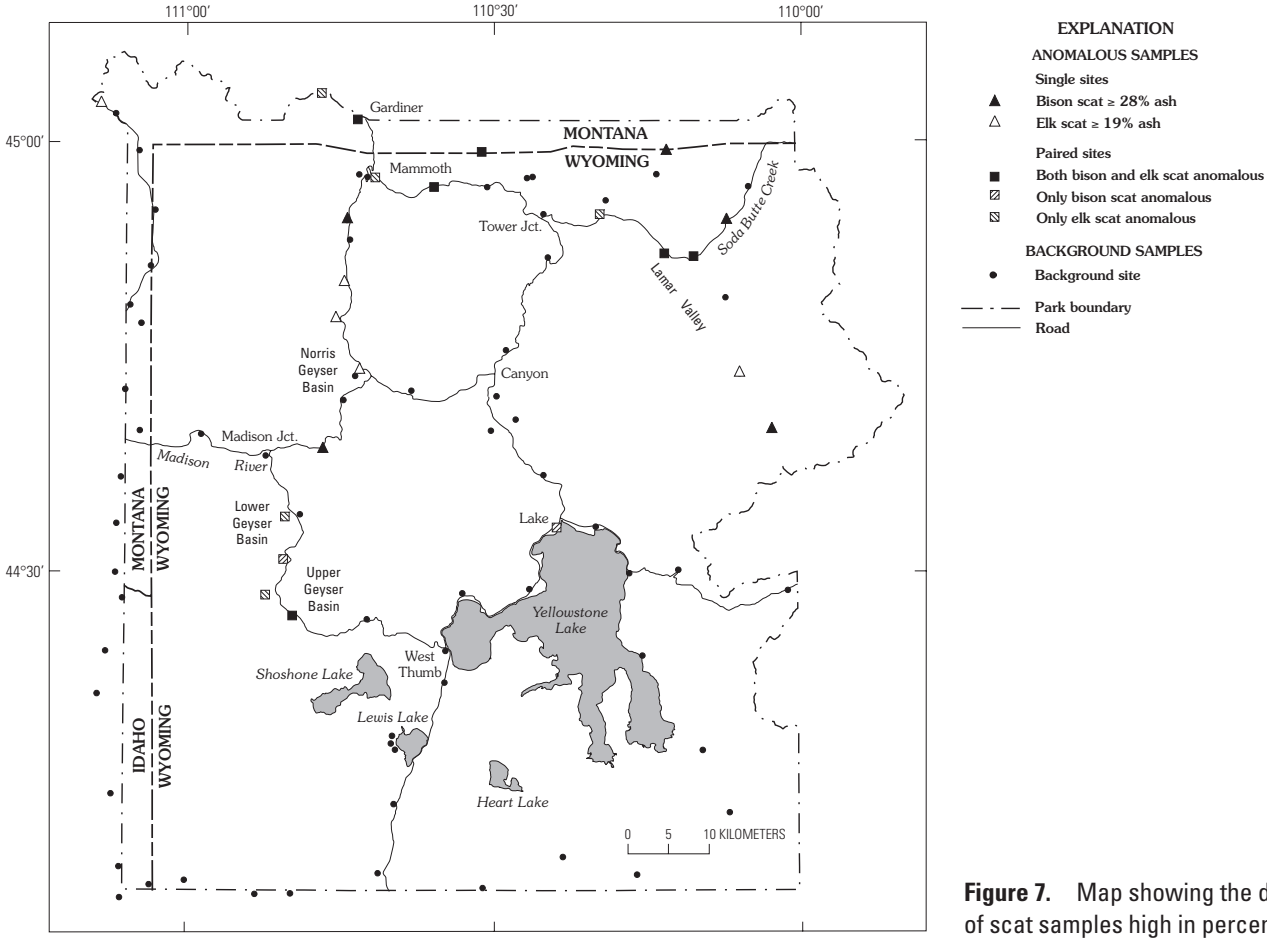

Figure 7. Map showing the distribution of scat samples high in percent ash.

tube. No attempt was made to macerate the material. The test tubes were heated in an aluminum block on a standard laboratory hot plate to about 95°C for about 2 hours. Three 1-mL aliquots of 30-percent hydrogen peroxide were added at 15-minute intervals to the hot digestate while still in the heating block. The resulting solution was heated for an additional hour at 95°C. The test tubes were removed from the hot plate, cooled, and the contents transferred to a new test tube. The volume was brought to a 20-mL volume in a clean test tube with nano-pure water. For the determination of mercury, a 5-mL aliquot of the sample digest was transferred to a clean test tube, 0.5 mL of a nitric acid–sodium dichromate solution was added, and the resulting mixture was brought to a 10-mL volume with nano-pure water. Mercury was determined using the continuous flow, cold-vapor, atomic-absorption spectrometer (CV-AAS) method. Blanks, duplicate samples (where sufficient material permitted), and standard reference materials from the National Institute of Standard Technology were included to insure data quality. The lower limit of determination is solution-based at about 0.1 ppm. Method error has been determined to be less than 5 percent RSD (relative standard deviation). Splits of the same samples were digested by heating in a nitric acid–hydrogen peroxide solution and analyzed for 39 elements by induction coupled plasma–mass spectrometry (ICP–MS) using a Perkin-Elmer model 6000 instrument (Lamothe and others, 1999).

Metal Concentrations in Trout

Concentrations of mercury and 39 other elements were determined in trout tissue and other types of samples (table 7). Mercury in cutthroat and lake trout muscle averaged 0.86 and 0.89 ppm on a dry-weight basis. This translates to an average of about 0.2 ppm on a wet-weight basis, and none of the muscle samples exceeded the 1.0-ppm (wet weight) Food and Drug Administration (FDA) action limit for human consumption (fig. 9). Thus, Yellowstone Lake fishes do not pose an immediate human-health risk, though some samples were close to the FDA's 1.0-ppm wet-weight limit for methyl mercury. Our samples were analyzed for total mercury, but there is good evidence that >95 percent of the Hg in fish tissue occurs as methyl mercury (Bloom, 1992). A comparison of the mercury concentrations in the Yellowstone trout to the mercury contents of marine fishes (from the FDA Web site: http://www.cfsan.fda.gov/~frf/sea-mehg.html) shows that both species of Yellowstone trout have mercury concentrations that are in the normal range, in contrast to species such as shark and swordfish that contain high concentrations of mercury (fig. 10).

Examination of the other metals analyzed (table 7) indicates that cutthroat and lake trout muscle, liver, and

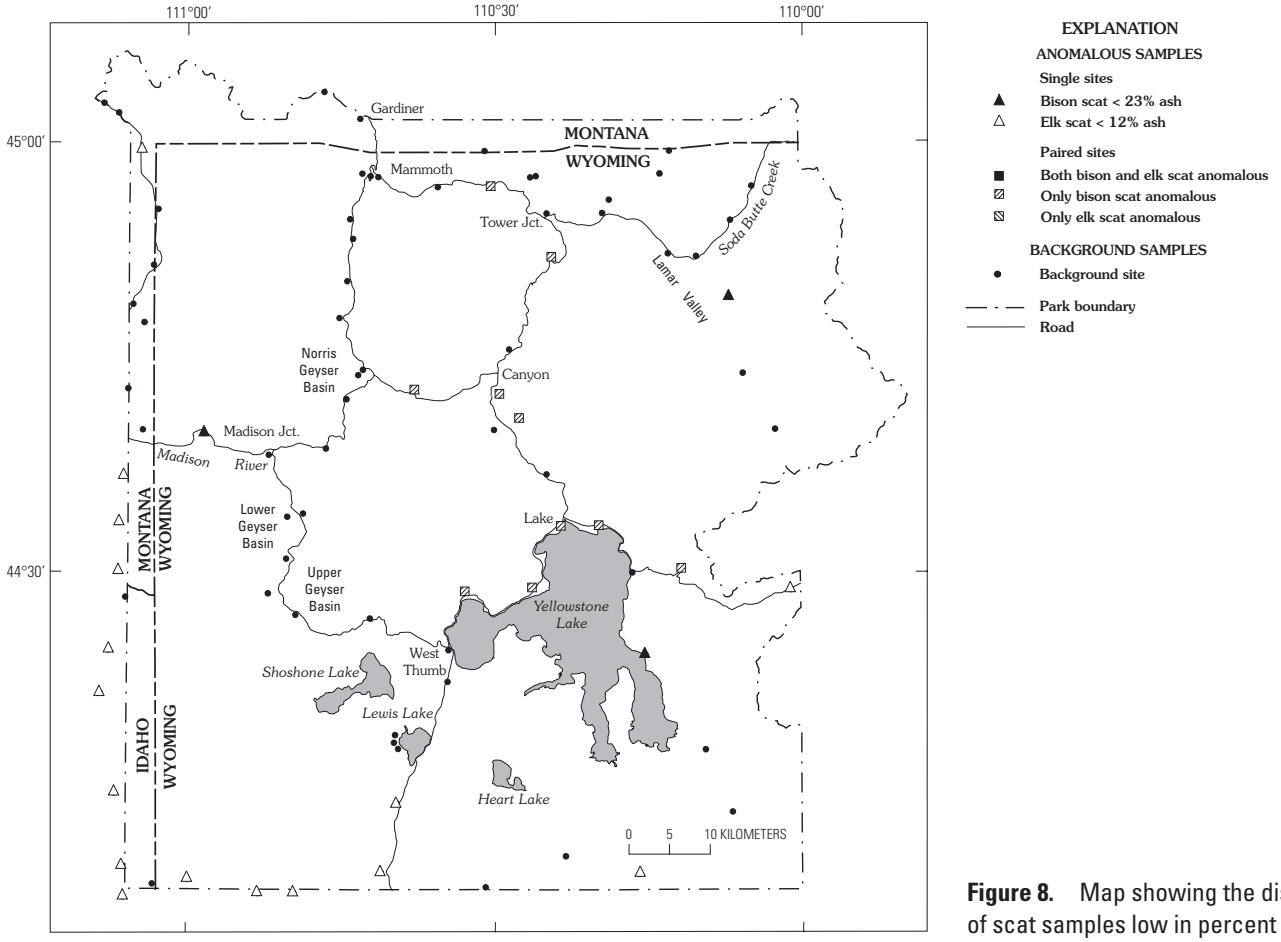

Figure 8. Map showing the distribution of scat samples low in percent ash.

stomach contents have relatively high concentrations of As, Hg, Se, and Tl. The average concentrations of arsenic in Yellowstone Lake fishes (cutthroat trout, 0.23 ppm, and lake trout, 1.4-ppm, dry weight, respectively, in muscle tissue) are well below FDA edible shellfish limits of 76–86-ppm wet weight (U.S. Food and Drug Administration, 2001). FDA limits have not been established for arsenic in fish or for selenium and thallium in seafood.

The average concentration of mercury in lake trout tissue from Yellowstone Lake is the same as that of cutthroat trout; thus, trophic enrichment is not apparent even though cutthroat trout are a major component of lake trout diet. Concentrations of selenium and thallium in muscle tissue show enrichments in lake trout relative to cutthroat trout of about the same factor (1.4). These enrichments may be evidence for trophic enrichment of selenium and thallium. Arsenic concentrations are higher in lake trout muscle than in cutthroat muscle, but many values are near the lower limit of analytical determination, so enrichment factors are probably not reliable for As in muscle. High concentrations of Cd, Cu, Mo, and Zn occur in liver and stomach contents of both cutthroat and lake trout, but these elements are not significantly enriched in the muscle. In addition, the concentration of arsenic in muscle is quite low compared to that in stomach contents, perhaps indicating that arsenic and these other elements are not readily accumulated in muscle tissue.

Sources of Metals

Hydrothermal-vent waters are a probable source of the metals found in the trout of Yellowstone Lake. Mercury ranges from <0.010 to 0.170 ppm in sublacustrine hydrothermal-vent fluids (Balistrieri and others, this volume). Bacterial and algal mats and plankton represent possible food sources for cutthroat trout, but the pathway of metals up the food chain is not known. Mercury must be methylated to be readily accumulated into animal tissue, and it is likely that methylation is caused by methanogenic or sulfate-reducing bacteria, possibly in thermally heated waters. Methylated mercury is also strongly accumulated in phytoplankton such as diatoms (Mason and others, 1995), which are very abundant in Yellowstone Lake. Methyl-mercury studies have not been carried out in the present investigation; only total mercury concentrations have been determined.

Our analyses of the stomach contents of cutthroat trout indicate that zooplankton, such as amphipods, which feed on phytoplankton or bacteria, are consumed by cutthroat trout. In the limited group of samples of bacteria, algae, phytoplankton, and macrophytes analyzed for this study, As, Mo, and Sb were detected in bacteria and plankton. Not enough sample material was available for mercury analysis. Antimony was also detected in the single macrophyte sample (table 7).

Analysis of the stomach contents of lake and cutthroat trout is perhaps the best measure of the metals they consume. All stomach contents were examined by binocular microscope, and several cutthroat trout showed a dominance of

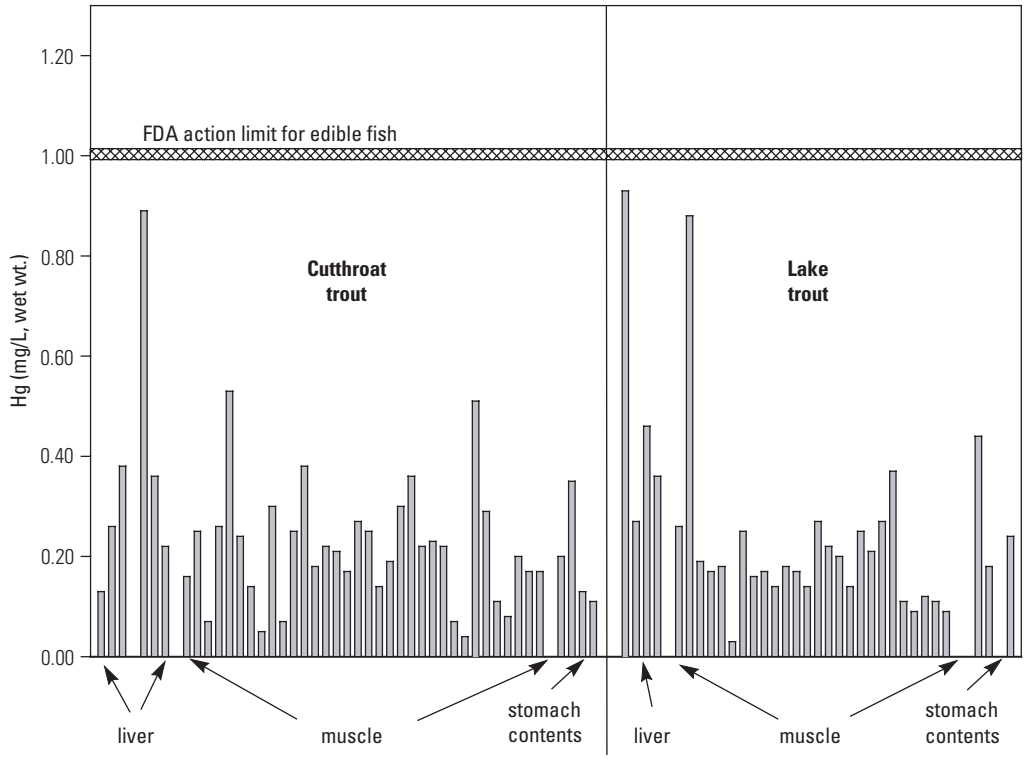

Figure 9. Mercury concentrations in cutthroat and lake trout.

amphipods. Amphipods have frequently been observed by a submersible camera in areas around sublacustrine vents in the lake and may be the principal food for cutthroat trout in vent areas. Arsenic, Cu, Hg, Mo, Se, and Tl are enriched in the stomach contents of both lake and cutthroat trout, whereas cadmium is enriched only in the stomach contents of lake trout (table 7).

The concentrations of As, Se, and Tl are higher in the stomach contents, livers, and muscles of lake trout than in the corresponding parts of cutthroat trout. Mercury is higher in the stomach contents and livers of lake trout than it is in the same parts of cutthroat trout, but it is present in similar concentrations in muscles from both species. For cutthroat trout, a weak correlation was observed between concentrations of mercury and fish size (fig. 11), but no such correlation seems to exist for lake trout. A possible explanation for this apparent lack of correlation in lake trout may be found in the studies of the otoliths (ear bones) of large lake trout from Yellowstone Lake (Ruzycki and Beauchamp, 1997). Some of the otoliths they studied may be from trout that are 20–21 years old. Microchemical studies of these otoliths show that the lake trout originated in Lewis Lake and were illegally introduced to Yellowstone Lake in late 1989 (Munro and others, 2001). Thus, as of this writing, the introduced lake trout have only been consuming mercury-bearing cutthroat trout for a part of their life cycle. Therefore, it is not surprising that trophic enrichment from cutthroat to lake trout is not indicated.

Stable isotope studies of C, N, and S (see study three, below) indicate that whitebark pine nuts and cutthroat trout are important foods for Yellowstone grizzly bears. However, pine nuts are not strongly enriched in any of the trace and minor elements studied (table 7, fig. 12). Other plants and animal flesh show some enrichment in Al, Ba, Mn, Rb, and Sr but not in the potentially toxic elements that are enriched in cutthroat trout. Notably, hair samples from grizzly bears are clearly enriched in mercury and are most strongly enriched in bears that live near Yellowstone Lake. Two hair samples collected near the lake have mercury concentrations of 0.61 ppm and 1.7 ppm (dry weight), respectively (table 7).

The sublacustrine hydrothermal activity in Yellowstone Lake provides a powerful tracer of the importance of fish consumption by grizzly bears. Mercury enrichment in the hair of bears living near Yellowstone Lake almost certainly documents their consumption of spawning cutthroats in early summer. This ability to trace fish consumption through mercury levels in hair is important because it offers a tool to determine how much of the bear population currently consumes fish and how far individual bears may travel to the spawning tributaries of Yellowstone Lake to eat these fish. This information is potentially important to wildlife managers who need to evaluate the ability of the bear population to adjust to possible decrease in cutthroat trout populations due to predation by lake trout.

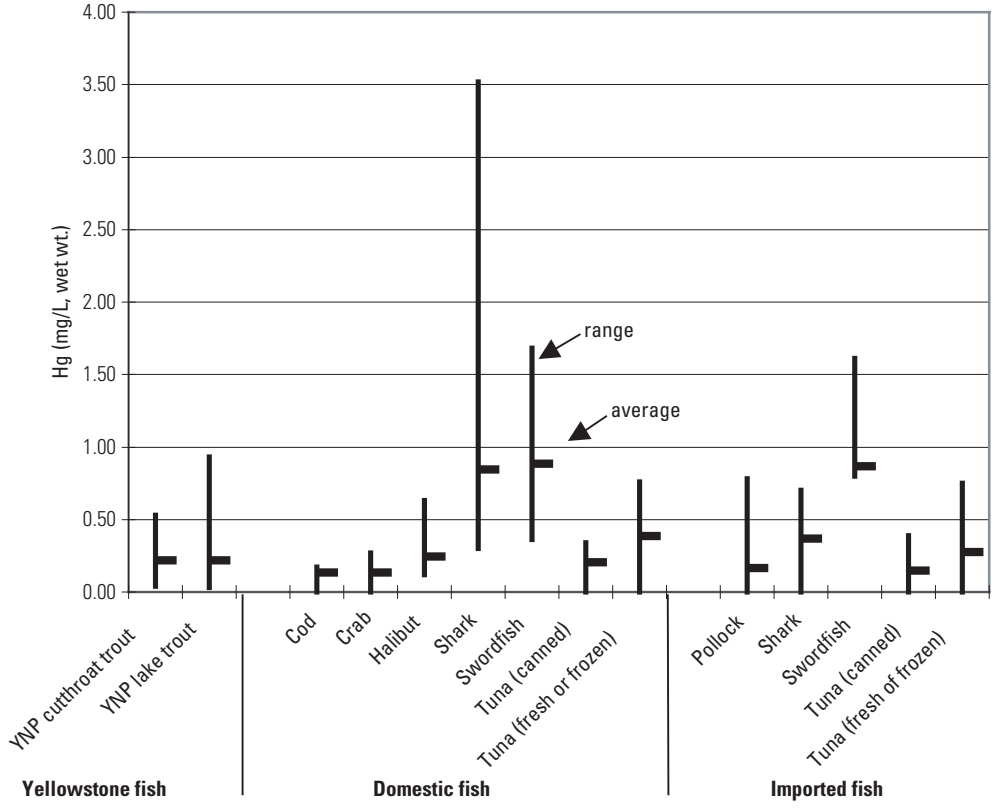

Figure 10. Mercury concentrations in common species of domestic and imported fish.

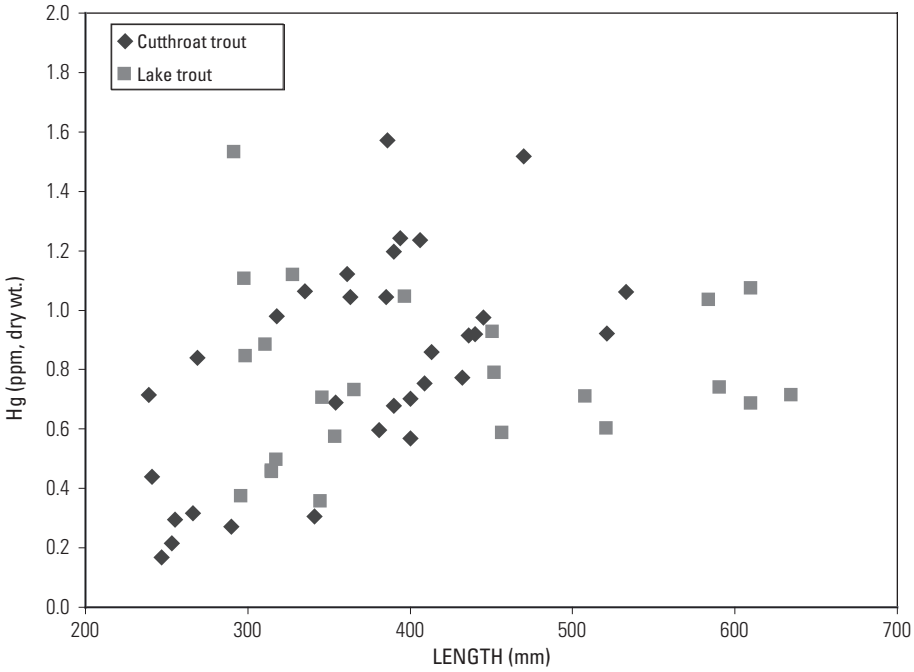

Figure 11. Mercury concentrations in muscle tissue of cutthroat and lake trout.

Carbon-, Nitrogen-, and Sulfur-Isotope Studies of Grizzly Bears (*Ursus arctos*) and Their Foods in the Yellowstone Ecosystem

Beginning in the 1950s with the first isotopic analyses of thermal waters (Craig and others, 1956), stable isotopes have played an important role in understanding the geochemical evolution of the thermal areas and igneous rocks of Yellowstone (see papers in this volume and those referenced in Bargar and Dzurisin, 1986). Recently, stable-isotope studies have been increasingly applied to investigations of ecosystems (Hobson and Wassenaar, 1999; Peterson and Fry, 1987). Stable-isotope applications to diet and food-web studies began with work by DeNiro and Epstein (1981), who showed that carbon- and nitrogen-isotope ($\delta^{13}C$ and $\delta^{15}N$) compositions in animal tissue reflect those of their diet. Fractionation of these isotopes can occur via metabolism and protein synthesis. This fractionation results in higher ratios in consumers relative to their prey; animal tissue is enriched in ^{13}C relative to diet by about 1 ‰ and in ^{15}N by about 3 ‰ (DeNiro and Epstein, 1978, 1981; Fry and Scherr, 1984; Minagawa and Wada, 1984). Sulfur-isotope ($\delta^{34}S$) compositions generally show a small depletion (1–2 ‰) in ^{34}S or no shift in values between consumers and diet (Kester and others, 2001; Krouse, 1989; Neill and Cornwell, 1992; Peterson and Fry, 1987).

This study describes the preliminary results of a stable-isotope study of grizzly bears (*Ursus arctos*) in a part of the greater Yellowstone ecosystem (Schwartz and others, 2002). The purpose of this investigation is to determine the extent to which stable isotopes, particularly those of sulfur in conjunction with carbon and nitrogen, can be used as (1) tracers of nutrient (C, N, and S) sources and processes that occur in the transfer of nutrients, beginning with the elements in rocks and waters and continuing through the rest of the grizzly bear food chain, and (2) aids to understanding the ecology and demographics of grizzly bears. The second aspect of this study is important because some food sources of grizzly bears in the Yellowstone ecosystem may decline, and wildlife managers must understand how the dynamics of this bear population might change in relation to changes in food abundance and distribution.

Grizzly Bear Food Sources

The Interagency Grizzly Bear Study Team (IGBST) was created in 1973 to monitor long-term population status and habitats of Yellowstone grizzly bears. A major goal of the 1993 grizzly bear recovery plan is to provide a scientific basis for the protection of grizzly bear habitat by conducting research on habitat use and food habits. The scientists of the IGBST have identified four major food components in the grizzly bear diet (Mattson and others, 1991). These include whitebark pine (*Pinus albicaulis*) nuts, a significant fall food that is rich in fat (Lanner and Gilbert, 1994); meat from bison (*Bison bison*) and elk (*Cervus elaphus*), which is a significant source of both digestible protein and energy; meat from cutthroat trout (*Oncorchynchus clarki*), also rich in protein; and cutworm moths (*Euxoa auxilaris*), which are high in fat. The abundance of these foods varies both seasonally and annually. For example, the amount of meat from ungulates depends largely on the availability of winter kill, particularly for bison. Bears also consume a wide variety of grasses, sedges, and forbs, as well as other animal matter, such as ants. As discussed below, at least two of the four major food sources in Yellowstone may decline in the

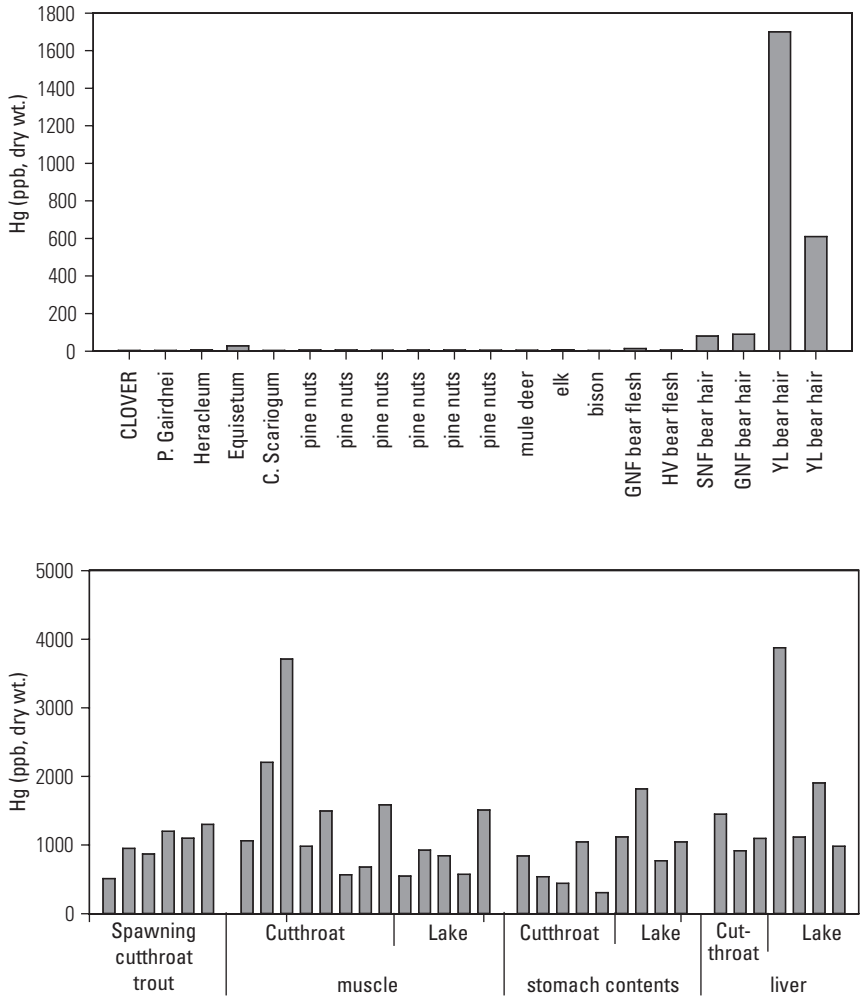

Figure 12. Mercury concentrations in plants and animals in greater Yellowstone ecosystem. GNF, Gallatin National Forest; HV, Hayden Valley; SNF, Shoshone National Forest; YL, Yellowstone Lake.

future. Thus, the need to understand the relationships between the population demographics of grizzly bears and their major food resources is important. Traditionally this type of information has been obtained through long-term telemetry studies, scat analysis, and observations. Stable-isotope studies of hair may offer a cost-effective method to quantify how the grizzly bear population utilizes food resources.

Grizzly bear consumption of spawning cutthroat trout found in tributaries of Yellowstone Lake has been well documented (Mattson and Reinhart, 1995; Mealey, 1980; Reinhart, 1990). The army cutworm moth is also an important, although unquantified, caloric contribution for about one-third of the grizzly bears in the Yellowstone ecosystem (White, 1996; White and others, 1999). The IGBST has identified more than 40 moth sites where grizzly bears feed, primarily in Shoshone National Forest, just to the east of Yellowstone National Park. This moth is an agricultural pest affecting alfalfa and wheat crops on the Great Plains.

Whitebark pine, a masting species, produces significant cone crops at irregular intervals. Cone production varies from as many as 50 per tree to as few as two (Haroldson, 2000). Consumption of pine nuts is considerable in years of abundant crops. Grizzly bear mortality is 1.8–3.3 times greater in years of poor nut crops (Mattson, 1998). Female grizzly bears, especially, tend to feed on pine nuts, a food which may be critical to their reproductive success (Mattson, 2000). Whitebark pine in the Yellowstone ecosystem is infected with an exotic fungus (*Cronartium ribicola*), commonly known as white pine blister rust (Kendall and Keane, 2000). In the Western United States and Canada, 50–100 percent of the extant whitebark pine trees are either dead or dying. Recent surveys (Kendall and Keane, 2000) suggest that this fungus is spreading.

Collection, Preparation, and Analysis of Samples

Samples were collected from a number of widespread localities in the Yellowstone ecosystem (table 8). However, no attempt was made to conduct detailed, systematic sampling. Samples of grizzly bear hair were collected at various sites in the greater Yellowstone ecosystem as part of an ongoing DNA study (Haroldson and Podruzny, 2001). The DNA analyses require only the follicles, so the remainder of each hair sample was

available for stable-isotope and trace-element studies. Theoretically, grizzly bear hair can contain a sequential record of diet. However, growth rates of grizzly bear hair may not be uniform. Samples of hair that are collected from hair corrals for DNA studies are typically samples from hair grown the previous year.

Freeze-dried samples of muscle tissue from two bear carcasses, as well as tissue from elk, bison, and deer road-kill, were also obtained. Vegetation, including clover (*Trifolium* sp.), cow parsnip (*Heracleum* sp.), and spring beauty (*Claytonia* sp.), were collected during the growing season and air dried. Cutthroat and lake trout were collected from Yellowstone Lake using gill nets, and portions of filets were freeze-dried. Spawning cutthroat trout were also collected from a tributary to Yellowstone Lake. Additionally, moths were collected from six sites located throughout the ecosystem, including five lowland agricultural sites east of the Park boundary; these were also freeze-dried. Whitebark pine nuts were collected from several sites in the greater Yellowstone ecosystem and analyzed without further treatment.

Samples were analyzed for carbon- and nitrogen-isotope compositions by continuous-flow methods described by Fry and others (1992) on a Micromass Optima mass spectrometer. Samples were analyzed for sulfur-isotope compositions by continuous-flow methods described by Kester and others (2001) on a Finnigan Delta Plus XL. Hair and meat-tissue samples were analyzed for sulfur directly. Vegetation, moth, and nut samples were first treated with Eschka's mixture to extract sulfur, as described in Kester and others (2001). Results are reported as ratios relative to Peedee limestone ($\delta^{13}C$), atmospheric nitrogen ($\delta^{15}N$), or Canyon Diablo troilite ($\delta^{34}S$) as follows:

$$X = \{[R_{sample}/R_{standard}] - 1\} \times 10^3$$

where X is $\delta^{13}C$, $\delta^{15}N$, or $\delta^{34}S$ and R is $^{13}C/^{12}C$, $^{15}N/^{14}N$, or $^{34}S/^{32}S$. Units are in the per mil (‰) notation, which indicates 0.1 percent deviation from the standard per unit.

Results

The $\delta^{13}C$ values in the Yellowstone ecosystem range from –21.7 ‰ to –30.4 ‰; $\delta^{15}N$ values range from about 1 ‰ in plants to 11 ‰ in lake trout and almost 9 ‰ in bears; $\delta^{34}S$ values for vegetation range from about 3 ‰ for plants to more than 11 ‰ for pine nuts. The $\delta^{34}S$ values for animal tissue range from about –3 ‰ to 9 ‰, with the largest values recorded for bears (table 8). Spawning cutthroat trout show nearly 2 ‰ enrichments in ^{34}S but show no significant corresponding enrichments in ^{13}C or ^{15}N.

Both cutthroat and lake trout from Yellowstone Lake show large but different $\delta^{15}N$ values and similar $\delta^{13}C$ values (fig. 13). Moths show a wide range of $\delta^{15}N$ values and a narrow range of $\delta^{13}C$ values. The values for vegetation (clover and spring beauty), moths, ungulates, and bear tissue (hair and muscle) fall on a trophic-enrichment trend for bear food sources (fig. 13) (Hilderbrand, and others, 1996). The bears and their food sources show distinct $\delta^{15}N/\delta^{34}S$ (fig. 14) and $\delta^{13}C/\delta^{34}S$ (fig. 15) values. In particular, whitebark pine nuts have a distinct $\delta^{15}N/\delta^{34}S$ signature when compared to other bear foods (fig. 14), suggesting that consumption of nuts may be distinguishable by the isotopic signatures of bear tissue. The plot of $\delta^{13}C$ against $\delta^{34}S$ (fig. 15) also suggests that values are relatively invariant across animal food sources but that values for nuts are significantly different from those of other vegetable food sources.

Discussion

Carbon-Isotope Variations in the Food Chain

Carbon isotopes can be used to distinguish between the photosynthetic pathways of C_3 versus C_4 plants (Cerling and Quade, 1993). Stable-carbon-isotope ratios of C_3 plants can range from –20 ‰ to –35 ‰ and C_4 plants can range from –7 ‰ to –15 ‰ (Ehleringer, 1989). The $\delta^{13}C$ values of the grizzly bears, moths, and other animal tissues range from about –26 ‰ to –21 ‰ and are constrained by the –30 ‰ to –22 ‰ values for plants and pine nuts (fig. 13). The $\delta^{13}C$ values for the vegetation are consistent with an organic-carbon reservoir that is dominated by C_3 plants and also show slight trophic enrichments through the food chain. Grizzly bear eating habits also agree with this trend in that the grass component of the diet is in the C_3 category. The difference in $\delta^{13}C$ values in the plants versus the nuts may in part reflect the effect of elevation on the $\delta^{13}C$ values (Körner and others, 1991). Differences in $\delta^{13}C$ values between those of low-elevation plants and those of high-elevation whitebark pine nut samples may be related to the isotope effects associated with the availability of pore water in soils. $\delta^{13}C$ values are higher in dry, upland sites as compared to lower and wetter sites (Angradi, 1994; Ehleringer and Cooper, 1988). Bear hair is slightly more enriched in ^{13}C than is muscle tissue, a fact consistent with physiological differences in carbon-isotope fractionation processes between hair and muscle tissue (Hilderbrand and others, 1996).

Nitrogen-Isotope Trophic Enrichment in the Grizzly Bear Food Chain

Lowland-vegetation and whitebark pine nut $\delta^{15}N$ values (~0 ‰), are similar to atmospheric nitrogen and reflect values for nitrogen from nitrate or ammonia in soil waters, which come mainly from the decomposition of organic material in soils. Comprehensive data for all components of the aquatic ecosystem in Yellowstone Lake do not exist. However, the relatively high $\delta^{15}N$ values for fish from the lake suggest that the aquatic ecosystem acquires nitrogen from a ^{15}N-enriched source, possibly one associated with hydrothermal activity in the lake. Grizzly bears and most of their food sources (fig. 13) show a classical trophic-enrichment pattern as determined from a study of captive and wild bears (Hilderbrand and others, 1996). $\delta^{15}N$ values increase, in order, from plants and nuts to ungulates to bears. Interestingly, the $\delta^{15}N$ values for both cutthroat and lake

Table 8. Summary of stable-isotope data on grizzly bear tissue and their food sources showing average values, standard deviation, and number of analyses.

Sample	Location	Tissue	$\delta^{13}C_{PDB}$		$\delta^{15}N_{AIR}$		$\delta^{34}S_{CDT}$	
			average	1 σ (n)	average	1 σ (n)	average	1 σ (n)
Plants								
Clover *(Trifolium sp.)*	Yellowstone National Park (YNP)	plant	-28.4	0.54 (3)	-1.2	0.6 (2)	3.2	0 (2)
Cow Parsnip (*Heracleum sp.)*	YNP	plant	-28.4	(1)			2.7	(1)
Spring Beauty (*Claytonia sp.)*	Bridger-Teton National Forest	plant	-30.4	0.1 (2)	-1.5	0.0 (2)		
White Bark pine nuts								
(Pinus albicaulis)	Gallatin National Forest	nut	-24.5	0.6 (4)	-2.3	0.1 (3)	11.4	(1)
(Pinus albicaulis)	Gallatin National Forest	nut	-21.7	0.6 (2)	-1.7	0.5 (2)		
(Pinus albicaulis)	Shoshone National Forest	nut	-24.4	0.9 (4)	0.2	0.3 (3)	8.8	0.4 (2)
(Pinus albicaulis)	Custer National Forest	nut	-25.3	0.7 (3)	-1.8	0.0 (2)	9.2	(1)
(Pinus albicaulis)	Beaverhead National Forest	nut	-23.6	0.9 (4)	-0.5	0.6 (2)	8.3	(1)
(Pinus albicaulis)	Targhee National Forest	nut	-24.6	0.8 (7)	-1.0	0.4 (3)	8.5	(1)
Moths								
(Euxoa auxilaris)	Venus	body/wing	-26.2	0.5 (3)	8.0	2.3 (3)		
(Euxoa auxilaris)	Colter Basin	body/wing	-26.3	0.1 (3)	5.5	1.5 (3)		
(Euxoa auxilaris)	Ptarmigan/Clocktower	body/wing	-26.3	0.7 (4)	6.2	1.3 (4)		
(Euxoa auxilaris)	Sunlight	body/wing	-26.0	0.4 (5)	6.8	2.6 (5)		
(Euxoa auxilaris)	Carter Mtn.	body/wing	-26.4	0.7 (22)	6.6	2.1 (21)	-0.1	0.3 (3)
(Euxoa auxilaris)	5 sites in Wyoming	body/wing	-26.2	0.7 (15)	4.1	2.3 (15)	3.9	(1)
Ungulates								
Mule deer (Odocoileus hemionus)	YNP	flesh	-25.1	(1)	4.9	(1)	-3.1	(1)
Elk (Cervus elaphus)	YNP	flesh	-24.7	(1)	3.6	(1)	0.9	(1)
Bison (Bison bison)	YNP	flesh	-23.4	(1)	5.8	(1)	1.7	(1)
Lake trout								
(Alvelinus namaycush)	West Thumb, Yellowstone Lake	filet	-24.6	1.0 (5)	11.0	0.4 (5)	1.0	0.5 (5)
Cutthroat trout								
(Oncorchynchus clark)	West Thumb, Yellowstone Lake	filet	-22.5	1.3 (7)	8.3	1.0 (7)	1.4	0.2 (7)
Spawning cutthroat trout	Clear Creek, YNP	filet	-22.3	2.1 (6)	7.5	0.5 (6)	3.3	0.3 (3)
Grizzly bears								
(Ursus arctos horribilis)	Gallatin National Forest	flesh	-23.0	(1)	8.4	(1)	5.4	(1)
(Ursus arctos horribilis)	Gallatin National Forest	hair	-22.5	(1)	7.1	(1)	8.7	(1)
(Ursus arctos horribilis)	Hayden Valley, YNP	flesh	-23.6	(1)	8.8	(1)	3.2	(1)
(Ursus arctos horribilis)	Yellowstone Lake, YNP	hair	-21.9	0.1 (2)	7.0	1.5 (2)	6.5	0.1 (2)
(Ursus arctos horribilis)	Shoshone National Forest	hair	-21.8	(1)	6.7	(1)	6.1	(1)

trout are equal to, or greater than, the values for grizzly bears. As expected, the $\delta^{15}N$ values for lake trout are larger than the corresponding values for the cutthroat trout on which they routinely feed. The anomalously large $\delta^{15}N$ values for the fish in Yellowstone Lake need to be studied further. However, these values are believed to be related to the fact that the cutthroat trout feed on crustaceans (amphipods) that in turn feed on bacteria that grow around sublacustrine thermal vents. The $\delta^{15}N$ value of the contents (largely amphipods) of a cutthroat stomach was determined to be 5.6 ‰, consistent with this possibility. The fact that the $\delta^{15}N$ values in bears are not larger than those in cutthroat trout reflects the fact that bears are omnivorous, whereas trout are carnivorous. Although some bears eat cutthroat trout during the spawning season, average $\delta^{15}N$ values of hair indicate a significant vegetation-related component to bear diets. Our analyses were of hair that had completed its growth during the previous year. This hair contains an isotopic record of all foods consumed by the bear during the previous year's active (nondenning) season. Because bears only consume cutthroat trout for a short period of time during the spawning season in the spring and early summer, and because a significant portion of their diet the rest of the year is vegetable matter, the $\delta^{15}N$ value of total hair samples cannot be equal to or greater than that of trout. The same argument is valid for bear muscle tissue.

As discussed earlier, cutthroat trout tissues have high mercury concentrations, and high mercury concentrations in bear hair can be used as a tracer of cutthroat consumption. The samples of bear hair do not show large $\delta^{15}N$ values typical of fish consumption because the bears probably grew most of their hair in the fall when they were not eating fish. This interpretation is supported by the fact that the samples of bear hair have large $\delta^{34}S$ values that are consistent with the consumption of ^{34}S-enriched nuts in the fall.

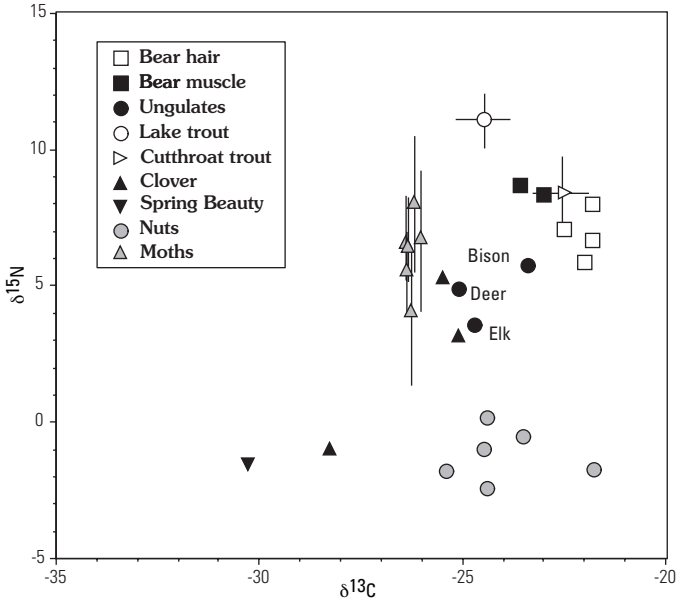

Figure 13. $\delta^{15}N$ and $\delta^{13}C$ values for bear tissue, bear food sources, and lake trout.

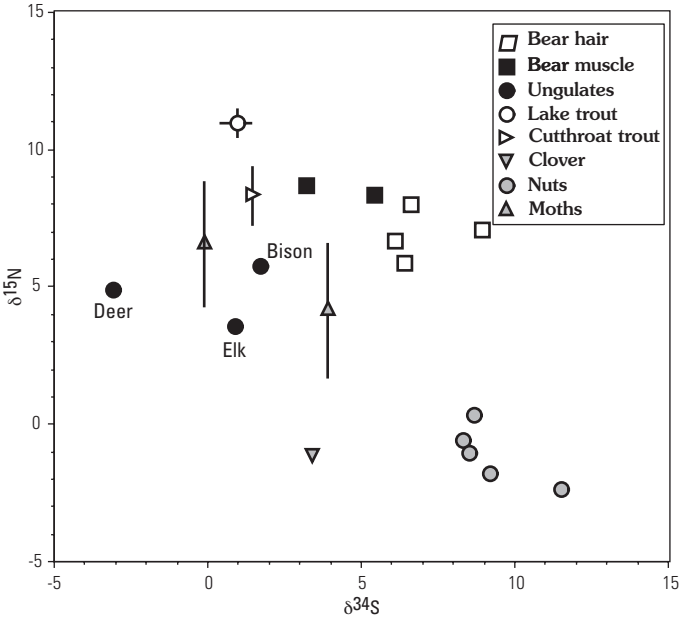

Figure 14. $\delta^{15}N$ and $\delta^{34}S$ values for bear tissue, bear food sources, and lake trout.

Sulfur-Isotope Variations in Grizzly Bears and Their Food Sources

The $\delta^{34}S$ values of grizzly bears (both muscle and hair) are larger than all of their meat food sources. The $\delta^{34}S$ values of whitebark pine nuts are larger than all the other vegetation sources that we measured, which indicates that the pine trees may assimilate sulfur from a different source, an observation consistent with studies of sulfur isotopes in trees from other locations (Krouse, 1980). The range of $\delta^{34}S$ values for grizzly bears and whitebark pine nuts indicates that bears are probably consuming the whitebark pine nuts, an isotopically heavy source of S, during hair growth. Clearly more work is needed on the fractionation of sulfur isotopes in grizzly bears (and food sources) such as described by Hilderbrand and others (1996). If sulfur-isotope fractionations related to physiological processes are not large, as indicated by Kester and others (2001), Krouse (1989), and Peterson and Fry (1987), our sulfur-isotope data are consistent with the possibility that whitebark pine nuts are a substantial component of the diet for some bears during hair growth.

Stable-Isotope Data as Tracers of Geologic and Environmental Sources and Processes in Ecosystems

Detailed sulfur-isotope studies of rocks at Yellowstone have not been made. However, general sulfur-isotope variations can be inferred from sulfur-isotope data from the thermal areas at Yellowstone (Schoen and Rye, 1970). $\delta^{34}S$ values in H_2S from thermal springs, and in sulfate produced from the oxidation of H_2S, range from –5.5 ‰ to 2.3 ‰. The lowest values are found in areas outside of the Yellowstone caldera margin (fig. 1), where thermal waters interact with sedimen-

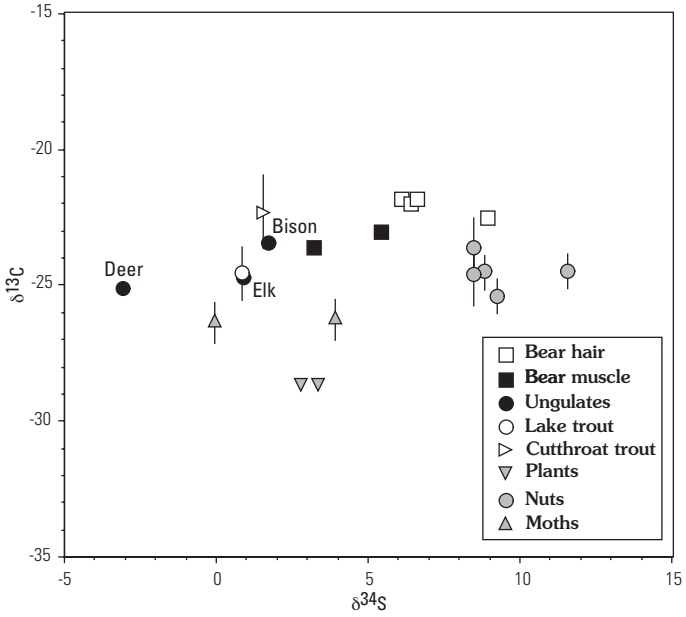

Figure 15. $\delta^{13}C$ and $\delta^{34}S$ values for bear tissue, bear food sources, and lake trout.

tary rocks at depth. The large flux of H_2S to the atmosphere from the thermal areas affects the $\delta^{34}S$ of sulfate in rain and snow in the Yellowstone area (Mast and others, 2001). The weighted-average-$\delta^{34}S$ value for sulfur in the thermal areas, which provide a representative value for the rhyolitic volcanic rocks that underlie much of the Park, is approximately 2±1 ‰. The average $\delta^{34}S$ value for much less abundant sulfate in these igneous rocks can be inferred from the sulfur-isotope fractionations between sulfide and sulfate phases observed in numerous studies of similar igneous rocks (Ueda and Sakai, 1984). This average $\delta^{34}S$ value for sulfate is inferred to be about 8±1 ‰ (Ueda and Sakai, 1984). The $\delta^{34}S$ values of sedimentary sulfide can vary widely but are normally less than 0 ‰ (Ohmoto and Goldhaber, 1997). That this is the case at Yellowstone is indicated by the low $\delta^{34}S$ values for H_2S from thermal areas on the margins of the caldera, where deep fluids interact with sedimentary rocks (Schoen and Rye, 1970). The $\delta^{34}S$ values for sedimentary sulfate depend on the age of the rocks and, in the case of the Mississippian Madison Group in the Yellowstone area, are probably close to 15 ‰ (Holser and Kaplan, 1966). Further work must be done to determine the $\delta^{34}S$ for sulfate and sulfide in volcanic and sedimentary rocks of the Yellowstone area, as well as to calibrate enrichment factors for sulfur isotopes in the Yellowstone food chain. It is encouraging, however, that the $\delta^{34}S$ values determined for the biological samples are bracketed by inferred values for sulfur sources in the igneous and sedimentary rocks, respectively, in the Yellowstone area. Thus, it appears that $\delta^{34}S$ values can be used to trace organic sulfur within the food chain from its origin in specific geologic sources to various flora and fauna.

Nitrogen-isotope values in the Yellowstone ecosystem generally follow trophic-enrichment patterns; however, both species of trout have high $\delta^{15}N$ values relative to those of bears. The large $\delta^{15}N$ values in trout provide a tracer for environmental nitrogen that is related to hot-spring activity in Yellowstone Lake (Estep and Macko, 1984).

Our preliminary study indicates that isotope data (especially when combined with trace-element data) offers an excellent method to trace bear-feeding ecology. In order to realize the full potential of these techniques, it will be necessary to understand the growth rates of bear hair and to determine the fractionations and turnover rates of sulfur in grizzly bears. Once growth rates are understood, the goal will be to sample the hair sequentially so that seasonal changes in food sources can be identified. Our data illustrate the necessity of calibrating bear-hair growth and the time required between consumption of a specific food and change in the isotopic composition of new hair. This type of study is best done with captive bears, such as the work pioneered by Dr. Charlie Robbins and his colleagues and students at Washington State University.

Conclusions

The three studies described here demonstrate how geochemical techniques widely used to investigate rocks and waters at Yellowstone can be applied to biologic problems that are associated with wildlife management.

Elements, including As, B, Be, Ce, Cl, Cs, F, Hg, K, Li, Mo, Rb S, Sb, Si, W, and other elements not described in detail here, are commonly enriched (1) in the thermal waters in the Yellowstone area, (2) in rocks altered by these waters, (3) in sinter and travertine deposits, and (4) in soils and stream sediments derived from these rocks. Although not observed or documented to date, some of these elements, such as As, F, Hg, and Mo, may be at least mildly toxic to wildlife. Many of the hydrothermally associated elements are concentrated in plant tissue and may be passed up the food chain to large animals.

The deleterious effects on wildlife of consuming hydrothermally related elements have only been established for fluorine in elk (Garrott and others, 2002). Some elements consumed by animals are essential in small amounts, some are toxic because they accumulate over time, some become toxic above a threshold level, some may weaken immune systems to the point where disease can be more easily established, and some have no apparent biologic effect and are merely excreted.

The scat of elk, bison, and moose that forage in fossil or active thermal areas show enrichments for many of the above-mentioned elements, as well as for some others. A comparison of the scat analyses with stream-sediment analyses collected in the Yellowstone area shows relatively high concentrations for 12 elements in the scat. This suite of elements includes (1) hydrothermally related elements (As, Br, Cs, Mo, Sb, and W), (2) major elements (Ca and K) that are essential elements for plants, and trace elements (Ba, Rb, and Sr) that commonly proxy for Ca or K, and (3) zinc. The behavior of zinc is not understood. It is an essential element for plants and animals

but does not normally proxy for either Ca or K. Zinc is also not related to hydrothermal activity. The uniqueness of zinc was also identified in other parts of this investigation.

Several other elements that are known to be potentially toxic to wildlife, including Cr, Hg, Ni, Pb, Se, and U, were found to be present in only very low concentrations in bison, elk, and moose scat. However, most of these elements seem to be present in elevated concentrations in one or more of the samples of (1) flesh from trout or mule deer and (or) (2) hair from grizzly bear (table 7). In the case of lead, its presence in flesh or hair and not in scat is the result of initial storage in tissue and gradual excretion in urine rather than feces (Steve Sweeney, written commun., 2002). This process may be true for one or more of the other elements as well.

The chemistry of bison and elk scat may reflect feeding habits. Comparisons of the mean and maximum values for percent ash for bison and elk scat and the values for percent ash for the sample pairs from individual sites both clearly indicate that bison ingest larger amounts of most hydrothermal elements than do elk. These larger amounts probably result from the fact that bison consume more soil substrate than do elk, as reflected in the differences in geometric mean values for percent ash for the two species.

The locations of bison- and elk-scat samples that contain anomalous amounts of hydrothermal elements show a high spatial correlation with fossil or active thermal areas or with areas immediately downstream from thermal areas. The longer that animals forage in these localities, the more likely it is that they may ingest significant amounts of potentially toxic elements such as arsenic.

The scat samples were collected Park-wide at a relatively low density. More detailed sampling in selected basins, which would include soil and forage-plant samples, as well as scat, would help to better identify the distributions, sources, and concentration levels of elements of concern in the food chains of the animal species studied.

Mercury is strongly enriched in trout tissue as compared to other sampled plants and animals of the ecosystem. Significant levels of mercury have been documented in the muscle (average 0.9 ppm, dry weight for both) and liver (average 1.6 ppm for cutthroat and 2.1 ppm for lake trout) of cutthroat and lake trout populations. These mercury levels in fish are thought to be related to sublacustrine hot-spring sources. Methylation of mercury in thermal waters is probably carried out by methanogenic or sulfate-reducing bacteria that are consumed by crustaceans such as amphipods, which are a major food source for the cutthroat trout.

The mercury levels in the cutthroat trout are transferred to the animals that eat them; thus, mercury can be used as a tracer of animal ecology. For example, bear hair collected near Yellowstone Lake has high mercury levels (0.6–1.7 ppm, dry weight), whereas the hair of bears sampled at more remote areas in the greater Yellowstone ecosystem has low mercury contents (0.006–0.09 ppm, dry weight). These data can potentially be used to quantify the percentage of the bear population that eats cutthroat trout and to determine how far individual bears travel to Yellowstone Lake to eat them. Mercury concentrations in bear hair are highest in bears that live near Yellowstone Lake. This observation provides strong evidence that mercury in grizzly bears is derived from feeding on spawning cutthroat trout in the spring and early summer and that mercury levels in bear hair can be used to trace the percentage of grizzly bears that eat spawning cutthroat trout. Additional data are needed to understand the accumulation of mercury in grizzly bears and its possible toxic effects on the bear population.

Reconnaissance stable-isotope studies of grizzly bear tissue (hair from living bears and muscle tissue from carcasses) and major foods show a large range in $\delta^{13}C$, $\delta^{15}N$, and $\delta^{34}S$ values. The $\delta^{13}C$ values of grasses (–30.4 ‰ to –28.4 ‰) and whitebark pine nuts (–24.6 ‰ to –21.7 ‰) reflect the dominance of C_3 plants in the Yellowstone ecosystem. Fine-scale variations within these ranges may reflect the effects of elevation on enrichment factors for carbon isotopes in trees and grasses. The $\delta^{15}N$ values for grizzly bear tissue and some of their food sources show typical trophic enrichments whereby $\delta^{15}N$ values increase at each level of the food chain. The fish tissue from Yellowstone Lake, however, has anomalously high $\delta^{15}N$ values as compared to bear tissue, possibly because of the influence of thermal water on the isotopic composition of nitrogen in the aquatic food chain. The lack of significant ^{15}N enrichment in bear tissue, as compared to cutthroat trout tissue, is probably the result of two factors: (1) bear hair growth may be very slow when they are eating significant amounts of fish, and (2) a considerable percentage of bear diet is vegetable material rather than fish or animal meat.

The $\delta^{34}S$ values for the vegetation and animal tissues that have been analyzed thus far are within the range of sulfide and sulfate sulfur determined or inferred for the igneous and sedimentary rocks that underlie much of the Park. The $\delta^{34}S$ values for both cutthroat and lake trout are nearly identical to those determined for sulfate derived from thermal springs under Yellowstone Lake. Spawning cutthroat trout are enriched in ^{34}S by nearly 2 ‰ over nonspawning trout from the lake. Most of the other food sources have $\delta^{34}S$ values consistent with sulfur derived from reduced sulfur in igneous rocks. Whitebark pine nuts, however, have $\delta^{34}S$ values consistent with derivation of sulfur from sulfate in igneous rocks or possibly from Mississippian-age sedimentary rocks. Although sulfur isotopes may be fractionated during processes that occur in soils and organisms through the food chain, it is probable that the composition of both sulfate and sulfide in the food chain reflects geologic sources. If this interpretation is correct, then the $\delta^{34}S$ data support the conclusion that at least some of the grizzly bears eat whitebark pine nuts during the fall while they are growing a substantial amount of their winter hair.

We conclude that geochemical techniques commonly used to investigate geologic problems provide another tool that can be applied to biologic problems related to wildlife management. The geochemical signatures in rocks and waters in and near Yellowstone National Park that develop as a result of hydrothermal activity may provide unique tracers for studying wildlife ecology and toxicology. Integration of these geochemical techniques into specific biological studies may help address issues of interest to wildlife managers in Yellowstone National Park and the greater Yellowstone ecosystem.

Acknowledgments

In connection with these three studies, we are indebted to the National Park Service, and particularly to Michael Finley, John Varley, Paul Doss, and Dan Reinhart, for providing access, encouragement, and logistical support in Yellowstone. Daniel R. Norton of the USGS assisted us with various parts of the scat investigation.

Peter Theodorakos, Al Meier, and Paul Lamothe of the USGS assisted with field work and chemical analyses for the Yellowstone Lake studies. Jim Ruzycki, Todd Koel, Dan Mahoney, Jim Segelvy, Brian Ertel, of the Aquatic Resources Group of the National Park Service, helped collect fish samples for us during gill-netting operations. Val Klump and Russel Cuhel, of the University of Wisconsin-Milwaukee, provided samples of bacterial and algal mats, macrophytes, and plankton from Yellowstone Lake. We especially thank Dave Lovalvo of Eastern Oceanics, Inc., for designing, operating, and managing submersible operations in the lake and for sharing his substantial knowledge of the floor of Yellowstone Lake. Discussions with Charlie Robbins, Washington State University, and Sean Farley, Alaska Department of Wildlife, materially assisted us in the grizzly bear studies. We thank Doug Stoeser, Craig Johnson, and Steve Sweeney of the USGS for reviewing this paper.

References

Angradi, T.R., 1994, Trophic linkages in the lower Colorado River—Multiple stable isotope evidence: Journal of the North American Benthological Society, v. 13, no. 4, p. 479–495.

Ball, J.W., Nordstrom, D.K., Jenne, E.A., and Vivit, D.V., 1998, Chemical analyses of hot springs, pools, geysers, and surface waters from Yellowstone National Park, Wyoming, and vicinity, 1974–1975: U.S. Geological Survey Open-File Report 98-182, 45 p.

Bargar, K.E., and Dzurisin, Daniel, 1986, Bibliography and brief history of the studies by the U.S. Geological Survey in Yellowstone National Park, Wyoming, Idaho, and Montana: U.S. Geological Survey Open-File Report 86-573, 27 p.

Bloom, N.S., 1992, On the chemical form of mercury in edible fish and marine invertebrate tissue: Canadian Journal of Fisheries and Aquatic Science, v. 49, p. 1,010–1,017.

Cerling, T.E., and Quade, Jay, 1993, Stable carbon and oxygen isotopes in soil carbonates: Geophysical Monograph 78, p. 217–231.

Christiansen, R.L., 2001, The Quaternary and Pliocene Yellowstone Plateau volcanic field of Wyoming, Idaho, and Montana: U.S. Geological Survey Professional Paper 729-G, 145 p.

Craig, Harmon, Boato, Giovanni, and White, D.E., 1956, Isotope geochemistry of thermal waters: National Academy of Sciences, National Research Council Publication, v. 19, p. 29–39.

Day, G.W., Curtin, G.C., Tripp, R.B., and Lewis, J.S., 1985, Analytical results and sample locality map of winter moose pellet samples from the Tanacross quadrangle, Alaska: U.S. Geological Survey Open-File Report 85-268, 23 p., 1 pl., scale 1:250,000.

DeNiro, M.J., and Epstein, Samuel, 1978, Influence of diet on the distribution of carbon isotopes in animals: Geochimica et Cosmochimica Acta, v. 42, p. 495–506.

DeNiro, M.J., and Epstein, Samuel, 1981, Influence of diet on the distribution of nitrogen isotopes in animals: Geochimica et Cosmochimica Acta, v. 45, p. 341–351.

Ehleringer, J.R., 1989, Carbon isotope ratios and physiological processes in arid land plants, *in* Rundel, P.W., Ehleringer, J.R., and Nagy, K.A., eds., Stable isotopes in ecological research: Ecological Studies No. 68, New York, Springer-Verlag, p. 41–54.

Ehleringer, J.R., and Cooper, T.A., 1988, Correlations between carbon isotope ratio and microhabitat in desert plants: Oecologia, v. 76, p. 562–566.

Estep, M.L.F., and Macko, S.A., 1984, Nitrogen isotope biogeochemistry of thermal springs: Organic Geochemistry, v. 6, p. 779–785.

Fournier, R.O., Christiansen, R.L., Hutchinson, R.L., and Pierce, K.L., 1994, A field-trip guide to Yellowstone National Park, Wyoming, Montana, and Idaho—Volcanic, hydrothermal, and glacial activity in the region: U.S. Geological Survey Bulletin 2099, 46 p.

Fry, B., Brand, W., Mersch, F.J., Tholke, K., and Garritt, R., 1992, Automated analysis system for coupled $\delta^{13}C$ and $\delta^{15}N$ measurements: Analytical Chemistry, v. 64, p. 288–291.

Fry, B., and Scherr, E.B, 1984, $\delta^{13}C$ measurements as indicators of carbon flow in marine and freshwater ecosystems: Contributions in Marine Science, v. 27, p. 13–47.

Garrott, R.A., Eberhardt, L.L., Otton, J.K., White, P.J., and Chaffee, M.A., 2002, A geochemical trophic cascade in Yellowstone's geothermal environments: Ecosystems, v. 5, p. 659–666.

Gough, L.P., Shacklette, H.T., and Case, A.A., 1979, Element concentrations toxic to plants, animals, and man: U.S. Geological Survey Bulletin 1466, 80 p.

Hakonson, T.E., 1967, Tissue distribution and excretion of ^{134}Cs in the mule deer: Fort Collins, Colorado State University, M.S. thesis, 121 p.

Haroldson, M.A., 2000, Whitebark pine cone production, *in* Schwartz, C.C., and Haroldson, M.A., eds., Yellowstone grizzly bear investigations: U.S. Geological Survey Report of the Interagency Grizzly Bear Study Team, 1999, Bozeman, Mont., p. 44–47.

Haroldson, M.A., and Podruzny, S.R., 2001, Spawning cutthroat trout numbers on tributary streams to Yellowstone Lake and grizzly bear use of spawning trout, *in* Schwartz, C.C., and Haroldson, M.A., eds., Yellowstone grizzly bear investigations—Annual report of the Interagency Grizzly Bear Study Team, 2000: U.S. Geological Survey, Bozeman, Mont., p. 37–43.

Hilderbrand, G.V., Farley, S.D., Robbins, C.T., Hanley, T.A., Titus, K., and Servheen, C., 1996, Use of stable isotopes to determine diets of living and extinct bears: Canadian Journal of Zoology, v. 74, p. 2,080–2,088.

Hobson, K.A., and Wassenaar, L.I., 1999, Stable isotope ecology—An introduction: Oecologia, v. 120, p. 213–313.

Holser, W.T., and Kaplan, I.R., 1966, Isotope geochemistry of sedimentary sulfates: Chemical Geology, v. 1, p. 93–135.

Kabata-Pendias, Alina, 2001, Trace elements in soils and plants (3d ed.): New York, CRC Press, 413 p.

Kaeding, L.R., Boltz, G.D., and Carty, D.G., 1996, Lake trout discovered in Yellowstone Lake threaten native cutthroat trout: Fisheries, v. 21, p. 16–20.

Kendall, K.C., and Keane, R.E., 2000, Whitebark pine decline—Infection, mortality, and population trends, *in* Tomback, D.F., Arno, S.F., and Keane, R.E., eds., Whitebark pine communities: Ecology and Restoration, Washington, D.C., Island Press, p. 221–242.

Kester, C.L., Rye, R.O., Johnson, C.A., Schwartz, C.C., and Holmes, C.W., 2001, On-line sulfur isotope analysis of organic material by direct combustion—Preliminary results and potential applications: Isotopes Environmental Health Studies, v. 37, p. 53–65.

King, H.D., Curtin, G.C., and Shacklette, H.C., 1984, Metal uptake by young conifer trees: U.S. Geological Survey Bulletin 1617, 23 p.

Körner, C., Farquhar, G.D., and Wong, S.C., 1991, Carbon isotope discrimination by plants follows latitudinal and altitudinal trends: Oecologia, v. 88, p. 30–40.

Krouse, H.R., 1980, Sulfur isotopes in our environment, *in* Fritz, Peter, and Fontes, J. Ch., eds., Handbook of environmental isotope geochemistry: Amsterdam, Elsevier, The Terrestrial Environment, v. 1, p. 435–471.

Krouse, H.R., 1989, Sulfur isotope studies of the pedosphere and biosphere, *in* Rundel, P.W., Ehleringer, J.R., and Nagy, K.A., eds., Stable isotopes in ecological research: New York, Springer-Verlag, Ecological Studies, v. 68, p. 424–444.

Lamothe, P.J., Meier, A.L., and Wilson, S.A., 1999, The determination of forty-four elements in aqueous samples by inductively coupled plasma-mass spectrometry: U.S. Geological Survey Open-File Report 99-151, 14 p.

Lanner, R.M., and Gilbert, B.K., 1994, Nutritive value of whitebark pine seeds, and the questions of their variable dormancy, *in* Schmidt, W.C., and Holtmeier, F.K., eds., Proceedings, International workshop on subalpine stone pines and their environment—The status of our knowledge: U.S. Forest Service General Technical Report INT-GTR-309, p. 206–211.

Mason, R.P., Reinfelder, J.R., and Morel, F.M.M., 1995, Bioaccumulation of mercury and methylmercury: Water, Air, and Soil Pollution, v. 80, p. 915–921.

Mast, M.A., Turk, J.T., Ingersoll, G.P., Clow, D.W., and Kester, C.L., 2001, Use of stable sulfur isotopes to identify sources of sulfate in Rocky Mountain snowpacks: Atmospheric Environment, v. 35, p. 3,303–3,313.

Mattson, D.J., 1998, Changes in mortality of Yellowstone's grizzly bears: Ursus, v. 10, p.129–138.

Mattson, D.J., 2000, Causes and consequences of dietary differences among Yellowstone grizzly bears (*Ursus arctos*): Moscow, University of Idaho, Ph.D. dissertation, 173 p.

Mattson, D.J., Blanchard, B.M., and Knight, R.R., 1991, Food habits of Yellowstone grizzly bears, 1977–1987: Canadian Journal of Zoology, v. 69, p. 1,619–1,629.

Mattson, D.J., and Reinhart, D.P., 1995, Influence of cutthroat trout (*Oncorhynchus clarki*) on behavior and reproduction of Yellowstone grizzly bears (*Ursus arctos*), 1975–1989: Canadian Journal of Zoology., v. 73, p. 2,072–2,079.

McIntyre, J.D., 1996, Review and assessment of possibilities for protecting the cutthroat trout of Yellowstone Lake from introduced lake trout, *in* Varley, J.D., and Schullery, Paul, eds., The Yellowstone Lake crisis—Confronting a late trout invasion: Report to the Director, National Park Service, Wyoming, Center for Resources, Yellowstone National Park, p. 28–33.

Mealey, S.P., 1980, The natural foods habits of grizzly bears in Yellowstone National Park, 1973–1974: Bozeman, Montana State University, M.S. thesis, 158 p.

Miller, W.R., Meier, A.L., and Briggs, P.H., 1997, Geochemical processes and baselines for stream waters for Soda Butte-Lamar Basin and Firehole-Gibbon Basin, Yellowstone National Park: U.S. Geological Survey Open-File Report 97-550, 28 p.

Minagawa, M., and Wada, E., 1984, Stepwise enrichment of ^{15}N along food chains—Further evidence and the relation between ^{15}N and animal age: Geochimica et Cosmochimica Acta, v. 48, p. 1,135–1,140.

Munro, A.R., McMahon, T.E., and Ruzycki, J.R., 2001, Identification of the source population of lake trout in Yellowstone Lake using otolith microchemistry [abs.], *in* Agenda and Abstracts, Yellowstone Lake—Hotbed of chaos or reservoir of resilience?: 6th Biennial Scientific Conference on the Greater Yellowstone Ecosystem, October 8–10, 2001, Yellowstone National Park, National Park Service, p. 26.

Neill, C., and Cornwell, J.C., 1992, Stable carbon, nitrogen, and sulfur isotopes in a prairie marsh food web: Wetlands, v. 12, no. 3, p. 217–224.

Ohomot, Hiroshi, and Goldhaber, M.B., 1997, Sulfur and carbon isotopes, *in* Barnes, H.L., ed., Geochemistry of hydrothermal ore deposits (3d ed.): New York, Wiley, p. 517–612.

Peterson, B.J., and Fry, Brian, 1987, Stable isotopes in ecosystems studies: Annual Review of Ecology and Systematics, v. 18, p. 293–320.

Peterson, D.A., and Boughton, G.K., 2000, Organic compounds and trace elements in fish tissue and bed sediment from streams in the Yellowstone River Basin, Montana and Wyoming, 1998: U.S. Geological Survey Water-Resources Investigations Report 00-4190, 39 p.

Puls, Robert, 1988, Mineral levels in animal health—Diagnostic data: Clearbrook, B.C., Canada, Sherpa International, 240 p.

Reinhart, D.P., 1990, Grizzly bear use of cutthroat trout spawning streams in tributaries of Yellowstone Lake: Bozeman, Montana State University, M.S. thesis, 128 p.

Robinson, Keith, 1986, Cottontail rabbit scat as a biogeochemical prospecting tool in arid desert environments: U.S. Geological Survey Open-File Report 86-506, 19 p.

Ruzycki, J.R., and Beauchamp, D.A., 1997, A bioenergetics modeling assessment of the lake trout impact on Yellowstone Lake, *in* Hamre, R., ed., Wild Trout VI: Fort Collins, Colo., Trout Unlimited and Federation of Fly Fishers, p. 127–133.

Rye, R.O., and Truesdell, A.H., 1993, The question of recharge to the geysers and hot springs of Yellowstone National Park: U.S. Geological Survey Open-File Report 93-384, 40 p.

Schoen, Robert, and Rye, R.O., 1970, Sulfur isotope distributions in solfataras, Yellowstone National Park: Science, v. 170, p. 1,082–1,084.

Schwartz, C.C., Haroldson, M.A., Gunther, K.A., and Moody, D., 2002, Distribution of the grizzly bear in the greater Yellowstone Ecosystem 1900–2000: Ursus, v. 13, p. 203–212.

Shacklette, H.T., 1972, Cadmium in plants: U.S. Geological Survey Bulletin 1314-G, 28 p.

Shacklette, H.T., 1980, Elements in fruits and vegetables from areas of commercial production in the conterminous United States: U.S. Geological Survey Professional Paper 1178, 149 p.

Shupe, J.L., Olson, M.S., Peterson, H.B., and Low, J.B., 1984, Fluoride toxicosis in wild ungulates: Journal American Veterinary Medical Association, v. 185, no. 11, p. 1,295–1,300.

Smith, K.S., and Huyck, H.L.O., 1999, An overview of the abundance, relative mobility, bioavailability, and human toxicity of metals, *in* Plumlee, G.S., and Logsdon, M.J., eds., The environmental geochemistry of mineral deposits, Part A—Processes, techniques, and health issues: Littleton, Colo., Reviews in Economic Geology, Society of Economic Geologists, v. 6A, p. 29–70.

Speidel, D.H., and Agnew, A.F., 1982, The natural geochemistry of our environment: Boulder, Colo., Westview Press, 214 p.

Stauffer, R.E., Jenne, E.A., and Ball, J.W., 1980, Chemical studies of selected trace elements in hot-spring drainages of Yellowstone National Park: U.S. Geological Survey Professional Paper 1044-F, 20 p.

Sturchio, N.C., Muehlenbachs, K., and Seitz, M.G., 1986, Element redistribution during hydrothermal alteration of rhyolite in an active geothermal system; Yellowstone drill cores Y-7 and Y-8: Geochimica et Cosmochimica Acta, v. 50, no. 8, p. 1,619–1,631.

Thompson, J.M., and DeMonge, J.M., 1996, Chemical analyses of hot springs, pools, and geysers from Yellowstone National Park, Wyoming, and vicinity, 1980–1993: U.S. Geological Survey Open-File Report 96–68, 65 p.

Ueda, A., and Sakai, Hitoshi, 1984, Sulfur isotope study of Quaternary volcanic rocks from the Japanese island arc: Geochimica et Cosmochimica Acta, v. 48, p. 1,837–1,848.

U.S.Food and Drug Administration, 2001, Fish and fisheries products—Hazards and controls guidance: U.S. Food and Drug Administration (from Web site: http://www.cfsan.fda.gov/~frf/sea-mehg.html, accessed May 2004).

White, D.D., Jr., 1996, Two grizzly bear studies—Moth feeding ecology and male reproductive biology: Bozeman, Montana State University, Ph.D. dissertation, 79 p.

White, D.D., Jr., Kendall, K.C., and Picton, H.D., 1999, Potential energetic effects of mountain climbers on foraging grizzly bears: Wildlife Society Bulletin, v. 27, p. 146–151.

Environmental Geochemistry in Yellowstone National Park—Natural and Anthropogenic Anomalies and Their Potential Impact on the Environment

K

By Maurice A. Chaffee, Robert R. Carlson, and Harley D. King

Chapter K *of*

Integrated Geoscience Studies in the Greater Yellowstone Area—Volcanic, Tectonic, and Hydrothermal Processes in the Yellowstone Geoecosystem

Edited by Lisa A. Morgan

Professional Paper 1717

U.S. Department of the Interior
U.S. Geological Survey

Contents

Abstract 337
Introduction 337
Previous Investigations 338
Geologic Setting 338
Sampling and Analysis 341
Description and Discussion of Chemical Differences by Media and Location 341
Results of Factor Analysis 342
Descriptions of the Geochemical Maps 345
Environmental Concerns 356
Summary and Conclusions 360
Acknowledgments 361
References Cited 361

Figures

1. Index map of Yellowstone National Park and vicinity 338
2. Generalized geologic maps 339
3. Box plot comparing analytical ranges for 13 elements 342

4–16. Distribution of elements in stream sediment:

4. Lanthanum 344
5. Thallium 346
6. Arsenic 347
7. Gold 349
8. Copper 350
9. Lead 351
10. Sulfur 352
11. Tellurium 353
12. Tungsten 354
13. Molybdenum 355
14. Cesium 357
15. Mercury 358
16. Fluorine 359

Tables

1. Summary statistics for analyses of 49 elements 340
2. Factor loading values for 47 elements 343

Environmental Geochemistry in Yellowstone National Park—Natural and Anthropogenic Anomalies and Their Potential Impact on the Environment

By Maurice A. Chaffee, Robert R. Carlson, and Harley D. King

Abstract

In cooperation with the National Park Service, the U.S. Geological Survey conducted a stream-sediment-based environmental geochemical study in and near Yellowstone National Park (the Park). The main goals of the study were to (1) determine background concentrations for as many as 49 elements in samples of rock and stream sediment, (2) establish a geochemical baseline during the 1990s for future reference, (3) identify the source(s) of anomalies for selected elements, and (4) identify potential chemical impacts on the Park environment, especially on wildlife.

Two areas of the Park containing identified environmental geochemical problems were selected for detailed study: (1) an area in the western part of the Park that includes the Gibbon, Firehole, and Madison River basins, and (2) an area in the northeastern part that includes the Soda Butte Creek and Lamar River basins and part of the Yellowstone River basin. The geology of the first area is characterized mainly by Quaternary felsic volcanic rocks. Localities with major geothermal activity are present in this area. The second area has more complex geology that consists primarily of Tertiary volcanic rocks of intermediate composition and Precambrian schists and gneisses. Also present are scattered exposures of Paleozoic clastic and carbonate rocks and Quaternary felsic volcanic rocks. Geothermal activity is very limited in this area. Both study areas contain extensive deposits of glacial, fluvial, or lacustrine origin.

Analyses for as many as 49 elements in 393 samples of stream sediment collected from throughout the Park were evaluated statistically, including factor analysis. A five-factor model classified the elements on the basis of two lithologic factors, one mineral-deposit-related factor, one geothermal-process-associated factor, and one "miscellaneous" factor.

Data from the factor analysis, when combined with the distributions of anomalies for the elements determined in this study, show that most (34) of the elements are best correlated with rock chemistry. Many of these elements can be used to discriminate between major lithologic units and can therefore be used to assist geologic mapping studies in the Park area.

Anomalies of As, Cs, F, Hg, Mo, S, Sb, Tl, and W were determined to be associated with areas of geothermal activity. Of these nine elements, cesium is the best discriminator between anomalies related to geothermal activity and those related to outcrops of mineralized rock and to past mining activity near the Park. The effects of mineralization and past mining activity in the Cooke City, Mont., area, outside but near the northeastern boundary of the Park, are defined by anomalies of Ag, As, Au, Cu, Fe, Hg, Mo, Pb, S, Sb, Se, Te, Tl, W, and Zn, and possibly F. The effects are delineated best by anomalies of Au, Cu, and Te. Relatively weak anomalies of some of these elements extend as far as 18 km inside the Park.

In the area of Slough Creek, in the northeastern area of the Park, the source for a high concentration of lead was determined to be anthropogenic because of the sample location and a lack of anomalies of other elements that commonly are associated with natural lead anomalies. This anomaly probably is related to past fishing activity.

In high concentrations, a number of the elements associated with geothermal activity in the Park are potentially toxic to animals. Currently, only one of the 49 elements determined (fluorine) is known to affect the health and longevity of wildlife in the Park. Additional studies are needed to determine whether other elements are impacting the Park environment, including wildlife.

Introduction

An important goal in the field of environmental geochemistry is to identify unusually high or low natural concentrations of elements in the surficial environment and to evaluate their potential impact on the environment. An equally important goal is to identify element concentrations that are related to human (anthropogenic) activity. In cooperation with the National Park Service, the U.S. Geological Survey (USGS) conducted a stream-sediment-based environmental geochemical study in and near Yellowstone National Park (the Park). The Park is

U.S. Geological Survey, Box 25046, Mail Stop 973, Denver Federal Center, Denver, CO, 80225.

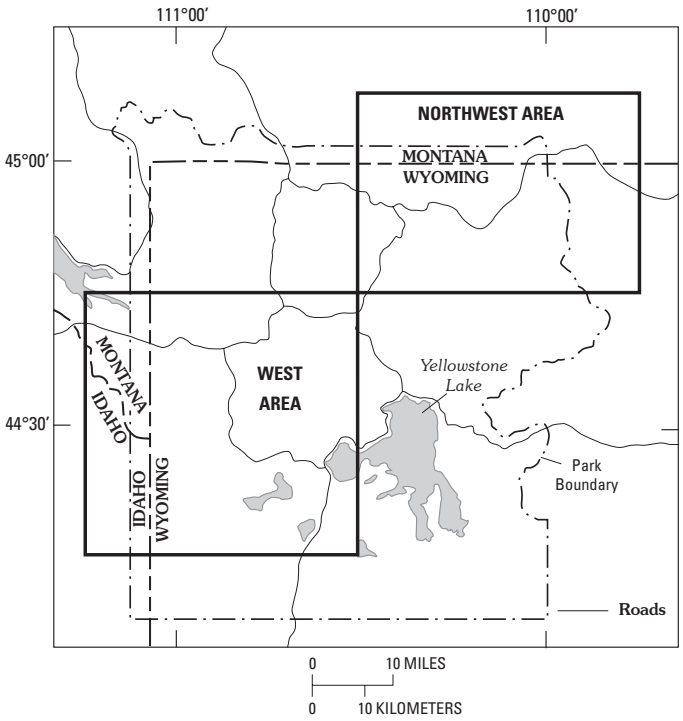

Figure 1. Index map of Yellowstone National Park and vicinity showing locations of the two study areas. Road shown as thin solid line.

mostly located in northwestern Wyoming, with small portions in adjacent areas of Idaho and Montana (fig. 1).

As part of a regional environmental geochemical study of Yellowstone National Park, surficial materials were sampled throughout the Park and in the immediately adjacent area. The main goals of the study were to (1) determine background concentrations for as many as 49 elements in samples of rock and stream sediment, (2) establish a geochemical baseline during the 1990s for future reference, (3) identify the source(s) of anomalies for selected elements, and (4) identify potential chemical impacts on the Park environment, especially on wildlife.

Two areas of the Park containing identified environmental geochemical problem areas have been selected for discussion here (fig. 1). The West Study Area (West Area) includes streams above and below the major geyser basins along the Firehole, Gibbon, and Madison Rivers. The waters of many of these streams contain natural but elevated concentrations of elements such as arsenic, fluorine, and molybdenum (Miller and others, 1997), which may impact the health of animals in the Park.

The Northeast Study Area (Northeast Area) contains the Soda Butte Creek basin, which includes the New World mining district, north of Cooke City, Mont., and the Republic district, south of Cooke City. Soda Butte Creek drains runoff and ground water from predominantly gold- and copper-rich, base- and precious-metal mineral deposits and their associated dumps, tailings piles, and slag heaps in these two districts. That stream flow enters the Lamar and Yellowstone River basins in the Park.

Previous Investigations

Analyses of waters collected in Yellowstone National Park have been described and interpreted by a number of investigators (see, for example, Allen and Day, 1935; Gooch and Whitfield, 1888; Miller and others, 1997; Rowe and others, 1973; Stauffer and others, 1980; Thompson and DeMonge, 1996; Thompson and Hutchinson, 1981; Thompson and Yadav, 1979; Thompson and others, 1975; White and others, 1988). Water and stream-sediment samples were collected in the Park and analyzed (but never adequately evaluated) for the National Uranium Reconnaissance Evaluation Program (Bolivar, Hensley, and others, 1980; Bolivar, Sandoval, and others, 1980; Broxton and others, 1979; Shannon and others, 1980). Geochemical data and interpretations have been published by the U.S. Geological Survey for several of the national forests and wilderness areas surrounding Yellowstone National Park (Antweiler, Love, and others, 1989; Antweiler, Rankin, and others, 1985; Carlson and Lee, 2005; Elliott and others, 1983; Lee and Carlson, 1993; Love and others, 1975; Nelson and others, 1980; Simons and others, 1979; Wedow and others, 1975). A report by Shannon (1982) is the only one that describes the regional geochemistry of stream-sediment samples collected within any part of the Park.

Geologic Setting

The geology of Yellowstone National Park has been described by many workers (see, for example, Bond, 1978; Christiansen and Blank, 1972; Fournier and others, 1994; Keefer, 1972; Love and Keefer, 1975; Taylor and others, 1989; U.S. Geological Survey, 1972; Wilson and Elliott, 1997). Only a brief summary, based on these maps and reports, is included here.

Simplified geologic maps are shown for the two study areas (figs. 2*A* and 2*B*). In the West Area (fig. 2*A*), exposures are almost entirely Quaternary felsic (mostly rhyolitic) volcanic rocks. A few small basalt flows are exposed in the northwestern part of this area. Quaternary alluvial and lacustrine deposits and glacial moraines locally cover the older units.

In contrast, the Northeast Area (fig. 2*B*) is geologically complex. The oldest rocks in the area are in the Beartooth Mountains, in the extreme northeastern part of this area. These rocks are mostly Precambrian granitic gneisses and migmatites, with minor intrusions of mafic rocks (B.S. Van Gosen, written commun., 1998). Areas of Precambrian metasedimentary rocks and quartz monzonite and diorite are present at several localities in the west-central part of the area. Paleozoic sedimentary rocks, mostly quartzite, sandstone, and limestone, are present at scattered localities, mainly in the northeastern part of this area. Tertiary volcanic rocks of the Absaroka Volcanic Supergroup, primarily andesites of intermediate composition, are the most common rock types in the Northeast Area. Exposures of Quaternary felsic volcanic rocks are present in the southwestern part of this study area, mainly in the Yellowstone River basin. Deposits of Quaternary alluvium and glacial moraine locally cover the older rocks.

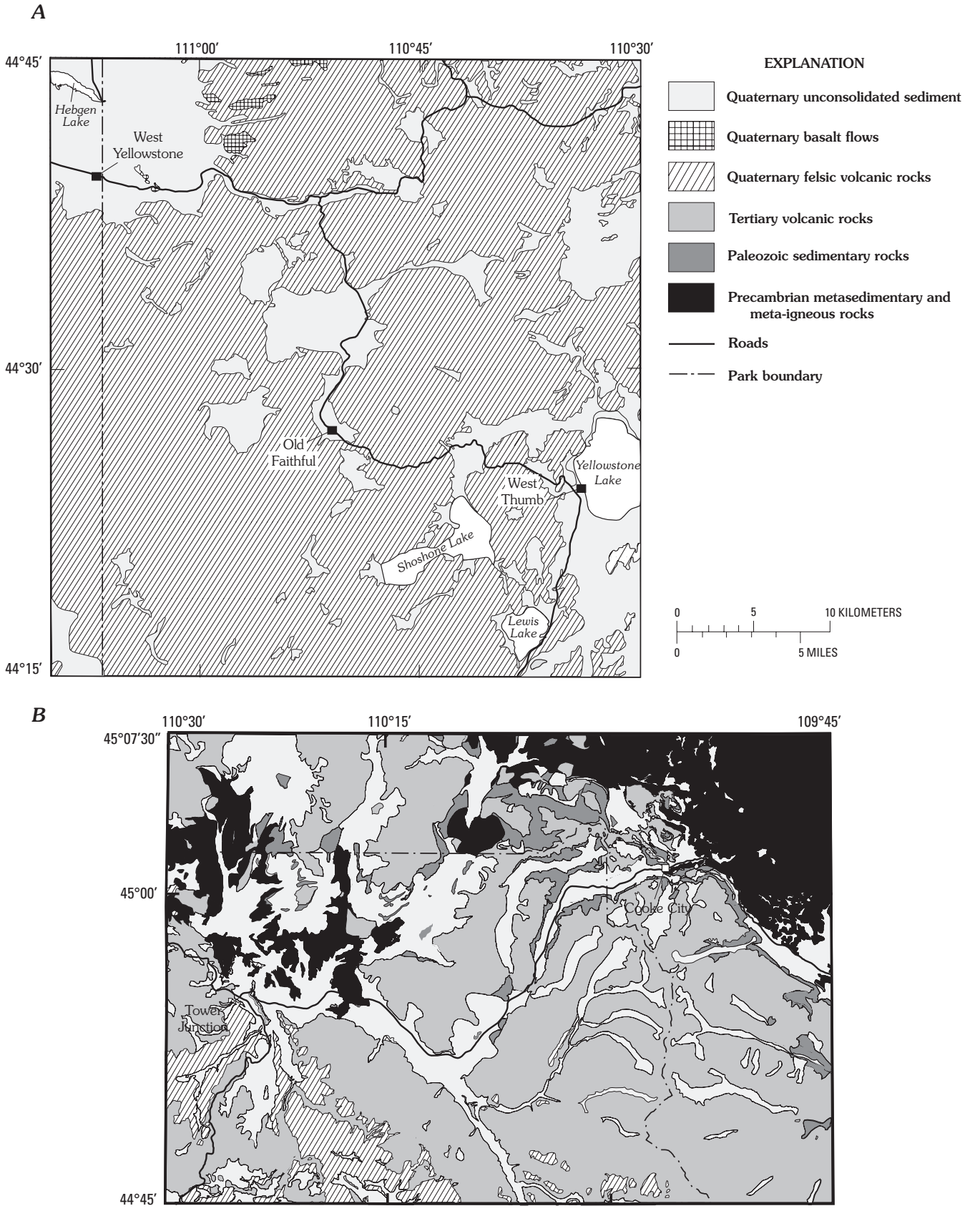

Figure 2. *A,* Generalized geologic map of the West Study Area. Geology modified from Taylor and others (1989), U.S. Geological Survey (1972), and Wilson and Elliott (1997). *B*, Generalized geologic map of the Northeast Study Area. Geology modified from Taylor and others (1989), U.S. Geological Survey (1972), and B.S. Van Gosen (written commun., 1998).

Table 1. Summary statistics for analyses of 49 elements in 393 stream-sediment and 68 rock samples, Yellowstone National Park and vicinity.

[Element symbols in bold identify elements discussed in detail in text. Concentrations for Au shown in ppb; all other values in ppm unless "(%)" shown after element symbol. N, not detected at the lower limit of determination shown in parentheses. Geom., Geometric. Mean values based on unqualified values only. HY, hydride analysis; NA, neutron-activation analysis; AA, atomic-absorption analysis; CVA, cold-vapor atomic-absorption analysis; INST, LECO furnace analysis; ION, specific-ion electrode analysis; no letters, ICP-AES analysis. "<" before a value in mean columns indicates estimated value]

Element	Range of values		Number	Percent	A	B	C	D
	Minimum	Maximum	unqualified	unqualified	Geom. mean 393 sediments	Geom. mean 49 rhyolites	Geom. mean 19 andesites	Crustal[3] abundance
Ag[1]	N(0.4)	7.8	27	7	<0.4	<0.4	<0.4	0.05
Al (%)	0.27	10	393	100	6.04	6.01	7.98	8.04
As-NA[1]	N(0.5)	670	375	95	6.1	4.5	2.1	1.5
Au-NA[1]	N(2.)	14,300	147	37	8.5	4.4	4.2	1.8
Ba-NA	N(50.)	4,000	390	99	760	460	1,000	550
Be	N(2.)	120	144	37	2.9	3.7	2.0	1.5
Br-NA[1]	N(0.5)	20	220	56	2.9	1.7	<0.5	2.5
Ca (%)	0.10	7.8	393	100	1.61	0.37	4.45	3.00
Cd	N(0.5)	7.7	64	16	0.60	0.60	0.77	0.098
Ce-NA	3	780	393	100	93	140	54	64
Co-NA	N(0.5)	52	370	94	9.1	1.8	23	10
Cr-NA	N(5.)	900	337	86	95	9.6	81	35
Cs-NA	N(1.)	870	348	89	3.6	2.9	2.6	3.7
Cu	1.0	630	393	100	8.5	3.4	27	25
Eu-NA	N(0.2)	3.4	388	99	1.2	0.96	1.4	0.88
F-ION	N(20.)	1,600	389	99	440	640	360	625
Fe-NA (%)	0.13	18.3	393	100	2.58	1.28	5.30	3.50
Hf-NA	N(1.)	67	391	99	8.2	9.1	3.6	5.8
Hg-CVA	N(0.02)	50	159	40	0.08	<0.02	<0.02	0.08
K (%)	0.12	5.41	393	100	2.13	4.07	1.51	2.80
La-NA	2.0	550	393	100	57	77	31	30
Lu-NA	N(0.05)	2.36	392	99	0.43	0.83	0.22	0.32
Mg (%)	0.01	5.69	393	100	0.62	0.03	1.81	1.33
Mn	16	11,800	393	100	530	240	720	600
Mo	N(2.)	29	220	56	3.4	4.1	<2.0	1.5
Na-NA (%)	0.10	3.16	393	100	1.92	2.46	2.41	2.89
Nd-NA	N(5.)	360	391	99	36	47	21	26
Ni	2.0	190	393	100	19	2.4	35	20
P (%)	0.003	0.22	393	100	0.04	0.008	0.11	0.07
Pb	N(5.)	190	388	99	20	32	15	12.5
Rb-NA	N(15.)	230	351	89	83	170	63	20
S-INST(%)	N(0.01)	4.25	341	87	0.03	0.02	0.04	0.03
Sb-NA	N(0.1)	150	287	73	0.68	0.38	0.21	0.2
Sc-NA	0.4	49	393	100	7.6	2.1	17	11
Se-HY[1]	N(0.2)	4.6	86	22	0.29	<0.2	<0.2	0.05
Sm-NA	0.20	43	393	100	6.3	9.5	4.3	4.5
Sr	5	1,500[2]	380	97	190	19	710	350
Ta-NA[1]	N(0.5)	8.6	221	56	2.4	3.4	1.2	2.2
Tb-NA	N(0.5)	5	203	52	1.3	1.5	0.60	0.64
Te-AA	N(0.1)	16	46	12	0.19	<0.1	<0.1	0.001
Th-NA	0.50	94	393	100	11	25	3.9	11
Ti (%)	0.01	1.13	393	100	0.24	0.09	0.42	0.30
Tl-AA	N(0.1)	21	343	87	0.45	0.76	0.23	0.75
U-NA[1]	N(0.5)	16	345	88	3.4	5.5	1.3	2.8
V	2	510	393	100	36	2.8	130	60
W-NA[1]	N(1.)	260	99	25	7.4	3.5	<1.0	2.0
Y	2	140	393	100	25	51	13	22
Yb-NA	0.2	15	393	100	2.9	5.7	1.4	2.2
Zn	5	350	393	100	70	63	70	71

[1]Lower limits vary. Lowest reported value shown.

[2]Excludes 13 samples reported as >750 ppm Sr.

[3]Values for Br and F from compilation by Levinson (1974). Value for S from compilation by Rose and others (1979). Value for Hg from Taylor (1964). Value for Te from Coakley (1975). Other elements from compilation by Taylor and McLennan (1995) for upper continental crust.

Sampling and Analysis

This study is based on 393 samples of active sediment from streams throughout the Park and in some of the areas bordering the Park. At each site, sample material was composited from multiple sample points to represent as closely as possible the typical chemical composition of material in the vicinity of the site. These compositions reflect a combination of (1) the chemistry of solid material eroded upstream and transported to the sampling site and (2) chemical elements carried in solution and precipitated on sediment grains at the site. Each sample was sieved to minus 0.18 mm (minus 80 mesh), and the material passing through the sieve was pulverized to less than 0.10 mm (minus 150 mesh).

The samples were submitted for analysis in a random order. Internal standards and duplicates were included to monitor the quality of the analyses. Most samples were analyzed for 49 elements that were included in commercial analytical packages. Concentrations of 25 of the elements were determined by instrumental neutron-activation analysis, and concentrations of 18 elements were determined by inductively coupled plasma atomic-emission spectroscopy. In addition, fluorine was determined by an ion-selective electrode technique, mercury by cold-vapor atomic-absorption analysis, total sulfur by a combustion method, selenium by a hydride technique, and tellurium and thallium by atomic-absorption spectroscopy. The analytical results, including analytical methods used for each element, are summarized in table 1.

Rock samples also were collected from outcrops at scattered localities in Yellowstone National Park and vicinity. For this report, only rock samples collected from relatively fresh, unaltered outcrops were evaluated. These samples first were hand-cobbed to remove surficial weathered material, and then they were crushed and pulverized prior to analysis. For comparison purposes, mean values for the rock analyses for two major rock units are included in table 1.

Description and Discussion of Chemical Differences by Media and Location

Table 1 summarizes concentration ranges, geometric mean values, and other information for 49 elements in 393 stream-sediment samples and 68 rock samples collected in, and in the vicinity of, Yellowstone National Park. Of particular importance in table 1 are columns A, B, C, and D. Column A lists the geometric mean values for all of the elements determined in the stream-sediment samples. These mean values are deemed to approximate the most typical value for each element in stream sediment for Yellowstone National Park. Columns B and C list geometric mean values for 49 rhyolite and 19 andesite samples, respectively, that were collected in or near the Park. All of those samples were fresh rock that was not significantly affected by chemical weathering or by hydrothermal alteration. These means are deemed to represent estimates of regional background values for these two major rock types in the Park area. Column D lists published estimates of crustal abundances for the elements listed in columns A, B, and C (Coakley, 1975; Levinson, 1974; Rose and others, 1979; Taylor, 1964; Taylor and McLennan, 1995).

A comparison of mean values for the two types of unaltered rocks (columns B and C) with crustal abundance values (column D) indicates that at least five elements (As, Au, Be, Cd, and Rb) are relatively enriched in both of these rock types in the Park area, as compared to crustal abundances. Similarly, fresh Yellowstone-area rocks are relatively low in Br, Cs, and Hg. A comparison of the mean values for sediment samples (column A), which includes material derived from both fresh and altered rocks, with the mean values for unaltered rocks (columns B and C) indicates that the sediments are relatively enriched in at least nine elements (shown in bold type in table 2: As, Au, Br, Cs, Hg, Sb, Se, Te, and W) and are relatively depleted only in sodium. Our data indicate that all nine elements, except possibly Br, are enriched in the Yellowstone area as a result of past or current geothermal activity. The mean values for other elements in the sediment samples generally are between the extremes represented by the respective values for the two types of rock samples. In a few cases, no meaningful mean value could be calculated because an insufficient number of analyses has been reported, and an estimated value is given.

Figure 3 is a graphical representation constructed to emphasize concentration differences for selected elements collected in the two study areas. All values determined for this figure were calculated after replacing each qualified value with a value equal to 0.5 times the lower limit of determination. This figure shows that some elements occur within a relatively small range of values in both areas (F, Mo, and Tl, for example), whereas other elements tend to occur over a much wider range (As, Au, Hg, S, and W, for example). The plots also show that the elements As, Cs, F, Hg, La, Mo, Tl, and W are more enriched in the West Area, where geothermal activity is high and rhyolite is the dominant rock type, whereas the elements Au, Cu, and Te are more enriched in the Northeast Area, where contaminated material from mineralized outcrops and past mining activities in the vicinity of the New World and Republic mining districts has entered the Park. Lead and sulfur show similar distribution ranges for both areas, indicating that these two elements probably have multiple sources with similar concentration levels.

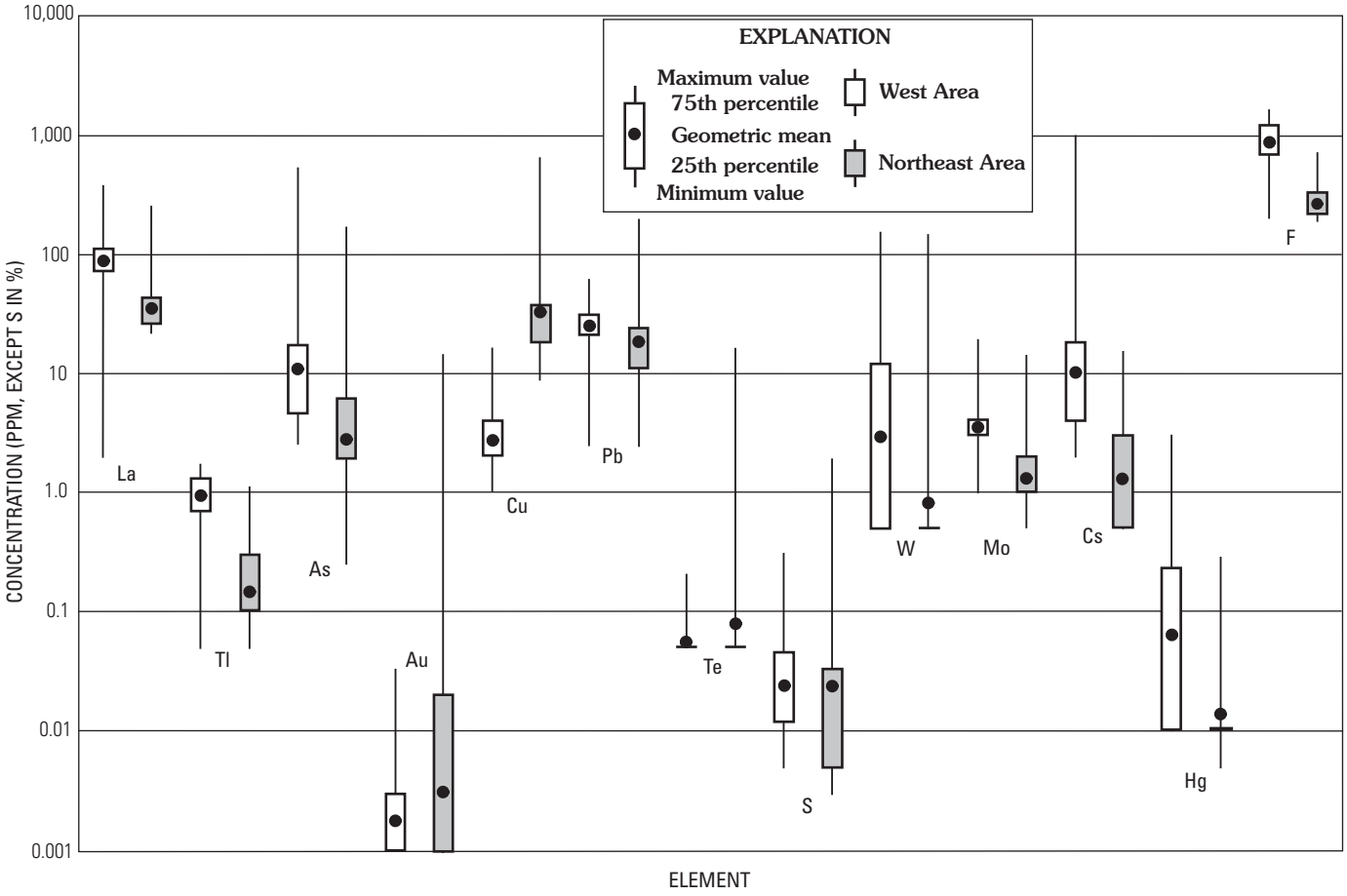

Figure 3. Box plot comparing analytical ranges for 13 elements in the two study areas. The single horizontal line for tellurium in the West Area indicates that all values are below the lower limit of determination.

Results of Factor Analysis

To provide a better understanding of the interrelationships of the group of elements determined for this study, we ran factor analysis. Factor analysis is a mathematical technique that groups variables (in this case, chemical elements) according to how they vary in relation to each other in the samples. As used here, the technique helps to identify suites of elements that have been enriched or depleted in the region (1) as a result of a common process or (2) because the elements are present in a common mineral or suite of minerals. Prior to running the analysis, two elements (cadmium and silver) were deleted from the data set because either there were too few reported values above the lower limit of determination (silver) or there was insufficient analytical variation (cadmium) for proper evaluation by this technique. For the remaining 47 elements, arbitrarily selected values were substituted for all qualified determinations. A value equal to half the lower limit of determination was substituted for each element for all values below the respective lower limit(s) of determination for each element. For values reported as being above an upper limit of determination, a new value equal to the upper limit divided by 0.7 was substituted. Because most of the elements displayed log-normal distributions, logarithms of the analyses were used in the factor analysis. A five-factor model with varimax rotation was selected as best fitting observed geologic conditions. This model accounts for 78 percent of the variance in the data. The loading values for each element, which identify the elements most strongly associated with each factor, are shown for the model in table 2. Factor scores, which rank the samples in each factor and thus show which samples most closely correlate with a given factor, were determined as part of the factor analysis, but they are not included in this report.

Factor 1 is a lithology factor. The factor scores indicate that the elements loaded on this factor are mostly from samples containing minerals commonly associated with felsic igneous rocks, such as rhyolite. These rocks contain sodium- and potassium-rich feldspars and rock-forming accessory minerals that commonly are enriched in uranium and thorium and (or) in lanthanide-series elements, including Ce, Eu, La, Lu, Nd, Sm, and others. Note that molybdenum, an element commonly associated with

Table 2. Factor loading values for 47 elements in 393 samples of stream sediment, Yellowstone National Park and vicinity.

[Five-factor model, varimax loading, based on log-normalized values. Elements in italic indicate secondary loading values]

Factor 1 (Felsic rocks)		Factor 2 (Mafic rocks)		Factor 3 (Geothermal)		Factor 4 (Mineral deposit)		Factor 5 (Miscellaneous)	
La	0.96	Sc	0.91	Sb	0.81	Te	0.85	Zn	0.59
Ce	0.95	Ti	0.90	As	0.77	Se	0.73	Be	0.59
Nd	0.94	Mg	0.89	Hg	0.73	Au	0.71	*Mn*	0.50
Sm	0.94	V	0.88	Cs	0.67	Pb	0.65	F	0.43
Th	0.87	Sr	0.88	S	0.65	*Cu*	0.46	*Br*	0.21
Lu	0.83	Cr	0.87	W	0.61	*S*	0.39		
Yb	0.81	Fe	0.87	*Hf*	0.41	*Zn*	0.33		
Hf	0.80	Ni	0.85	*Tl*	0.33	*W*	0.27		
K	0.78	Co	0.85	*Mo*	0.31	*Fe*	0.21		
Y	0.76	Ca	0.82	*Be*	0.29				
Ta	0.63	Ba	0.78						
Rb	0.63	Cu	0.69						
Tb	0.62	P	0.65						
U	0.61	Mn	0.61						
Mo	0.60	Al	0.60						
Tl	0.51	Eu	0.59						
Pb	0.50								
Na	0.49								
Zn	0.42								
F	0.42								
Br	0.22								
Percent variability explained									
48%		13%		8%		5%		4%	

mineral deposits, has its primary loading on this factor, suggesting that it is mainly associated with felsic-rock lithology in the study areas, rather than with geothermal activity or mineral deposits. Molybdenum is known to occur in many major and accessory rock-forming minerals, as well as in tungsten minerals (Manheim and Landergren, 1978).

Factor 2 also is a lithology factor. The scores indicate that the elements loaded on this factor are mostly from samples containing minerals that commonly are associated with intermediate to mafic igneous rocks, such as andesites, which commonly contain dark minerals such as calcium- and magnesium-rich feldspars, hornblende, biotite, and magnetite. Note that copper, an element sometimes enriched in one or more of these dark minerals, has its highest loading on this factor, emphasizing a moderately strong lithologic affinity for this element.

Factor 3 is a geothermal-process-associated factor. Factor scores indicate that the elements loaded on this factor are associated with samples of altered material from areas of past or present geothermal activity. Note that Mo and Tl have secondary loading values on this factor, indicating more than one source for these elements.

Factor 4 is a mineral-deposit-related factor. The factor scores indicate that the elements loaded on this factor are associated with sample material from the Cooke City, Mont., area, outside the northeast corner of the Park. Much of this material has been eroded from outcrops altered by hydrothermal mineralization or from dumps, tailings piles, or slag heaps related to past mining. Note that Cu, Fe, S, W, and Zn, elements associated with the mineral deposits near Cooke City, have secondary loading values on this factor, indicating their association with more than one source.

Factor 5 is a "miscellaneous" factor containing primary loadings for three elements (Be, F, and Zn) that do not seem to fit well into any of the other factors. By default, they have been mathematically forced into this last factor grouping, and they may or may not have a common natural association. The factor scores indicate that samples associated with this factor are composed mostly of felsic tuffs, Precambrian granites, or strongly altered, geothermally related sinter deposits that commonly are strongly enriched in one or more of the elements in this factor. The manganese-zinc association may be related to manganese scavenging, a natural process that enriches some trace elements when they co-precipitate with manganese as coatings on sediment grains or when they are adsorbed onto manganese-oxide coatings or nodules.

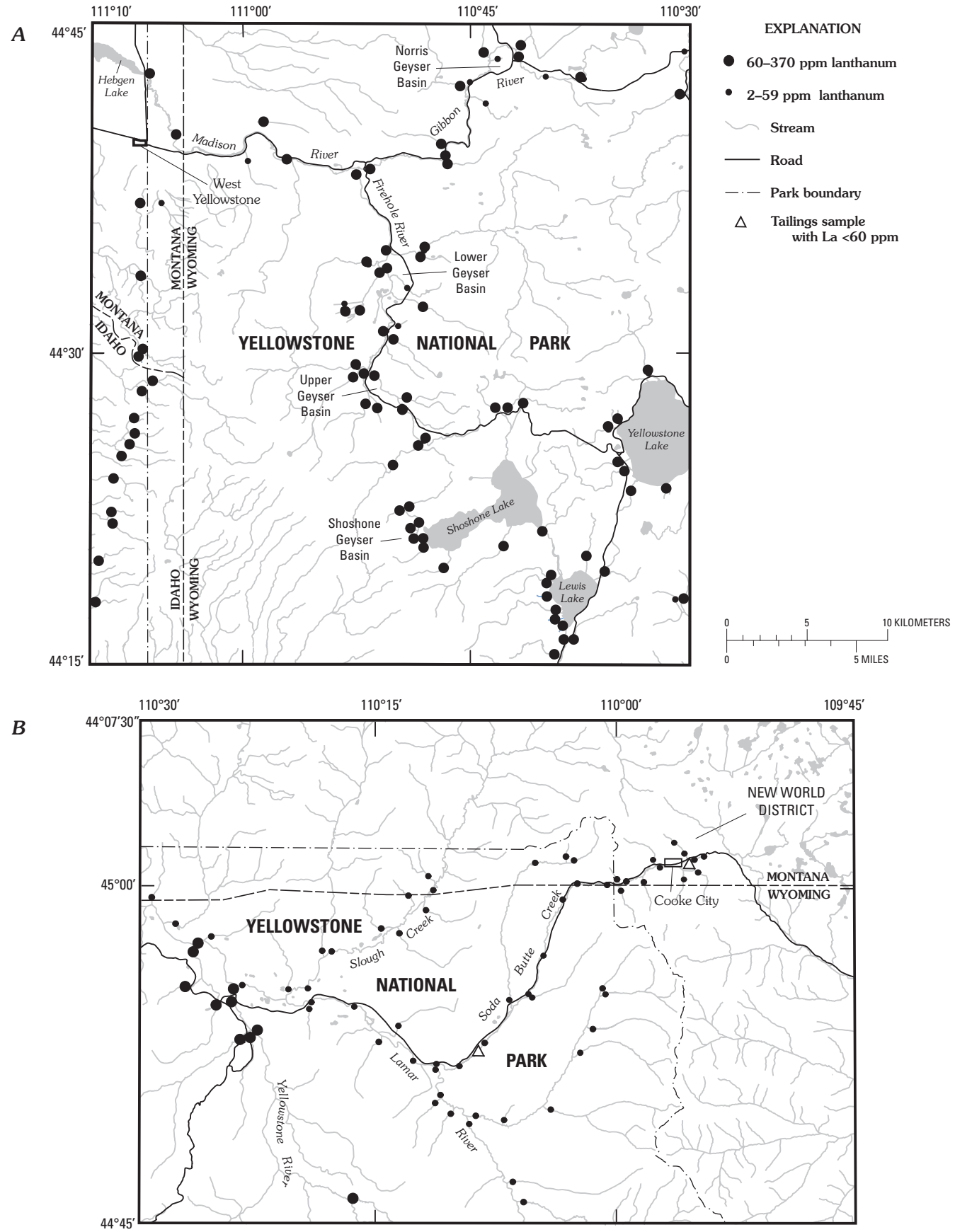

Figure 4. *A,* Distribution of lanthanum in stream sediment, West Area. *B*, Distribution of lanthanum in stream sediment, Northeast Area.

Descriptions of the Geochemical Maps

The distributions of anomalies for 15 elements in 152 of the 393 stream-sediment samples are described in this section. Some elements were selected to illustrate different sources and distribution patterns for the respective anomalies. Others were selected because they could be toxic to plants or animals, or both. The ranges of values shown on each map are for the plotted samples only and not for the complete data set. Sites whose samples fell in the range of values deemed to represent background concentrations for each element are shown as small filled circles on each map. The highest background value (threshold value) for each element was selected after studying (1) the frequency-distribution plots for each element and (2) the spatial distribution for each element plotted on a geologic base map. Anomalous samples are shown as filled squares or large filled circles. In addition to stream-sediment sites, maps for the Northeast Area show the locations of two samples of sediment that consist mostly of mill tailings. The northern one is from near the large tailings pile of the long-abandoned McLaren mine, one of the larger mines in the New World district. The southern one is from a flood-plain deposit adjacent to Soda Butte Creek that is composed of sediment derived from erosion of some of the McLaren mill tailings during a flash flood in 1950 (Meyer, 1993).

Lanthanum.—Lanthanum, the most strongly loaded element on factor 1 (table 2), is an element whose concentration is strongly correlated with lithology. This element is most common in rock-forming accessory minerals. Anomalies for lanthanum (60–370 ppm) are present in most of the West Area (fig. 4*A*) and in the Yellowstone River drainage in the western part of the Northeast Area (fig. 4*B*). The anomalies correlate well with the distribution of Quaternary felsic volcanic rocks in the two areas. Shannon (1982) noted that a number of elements in stream-sediment samples collected by the Department of Energy in the Ashton, Idaho-Montana-Wyoming 1°×2° quadrangle were useful for identifying provenances in parts of the Park. Our study confirms Shannon's observations and suggests that lanthanum, and also many of the other elements listed in factors 1 and 2 of the factor analysis (table 2), should be useful in mapping and correlating selected geologic formations in the region.

Thallium.—Thallium also is loaded on factor 1 (table 2), indicating that its strongest affinity is to lithology, especially to felsic volcanic rocks. However, it has two distinct sources. As a lithology-associated element, thallium is most abundant in potassium-rich minerals such as orthoclase feldspar, micas, and clay minerals. Thallium also occurs in sulfide minerals in some mineral deposit environments (de Albuquerque and Shaw, 1972). In the West Area (fig. 5*A*) and in the Yellowstone River drainage in the Northeast Area (fig. 5*B*), the widespread distribution of anomalous thallium (0.3–1.7 ppm) is similar to that of lanthanum (figs. 4*A* and 4*B*). Anomalous thallium in samples from the Slough Creek area and the stream northeast of Slough Creek probably are related to potassium-rich, Precambrian, felsic intrusive rocks or to glacial deposits containing material derived from these rocks. Thallium also is anomalous (0.3–1.1 ppm) in the New World mining district upstream from Cooke City, Mont., and in the two samples of tailings-rich sediment (0.3 and 0.8 ppm in fig. 5*B*), indicating a weak secondary affinity of this element in mineralized rocks of the district. The specific mineral residence of thallium in the district is not known.

Arsenic and antimony.—Arsenic commonly forms its own minerals, but it also may occur in more complex minerals. Both arsenic and antimony are strongly loaded only on the geothermal factor (table 2). However, arsenic also has two other, less significant, sources. In the West Area (fig. 6*A*), arsenic is strongly anomalous (15–670 ppm) in sediment from many streams. Note that the overall concentrations of arsenic in this area (represented by a relatively high percentage of filled-square and large-circle symbols) are much higher than in the Northeast Area (fig. 6*B*). Many of the weakly anomalous (6–14 ppm) samples in the West Area may be related to fossil geothermal areas, or they may simply represent unusually high background values in some of the felsic volcanic rocks. Arsenic is strongly anomalous (27 ppm) in the Madison River at the western boundary of the Park. The downstream extent of anomalous arsenic in sediment from this stream is not known, but anomalous arsenic in Madison River water is present at least to the junction of this stream with the Jefferson River, about 140 km downstream from the Park boundary at West Yellowstone, Wyo. (Sonderegger and Ohguchi, 1988).

In the Northeast Area (fig. 6*B*), arsenic is weakly to moderately anomalous (6–20 ppm) in most samples of active stream sediment collected from Soda Butte Creek. The highest concentrations (11–20 ppm As) are associated with mineralized outcrops or contaminated material in the New World district. The concentrations decrease rapidly downstream, and they reach background levels (<6 ppm) about 8 km downstream from the Northeast Entrance Park boundary. The moderately to strongly anomalous (15–170 ppm As) samples collected from the Yellowstone River, on the west side of this area, are not mining related. They are mainly enriched as a result of solfataric (geothermal) activity, but some of the enrichment may be related to the local lithology. The sample from the vicinity of the McLaren tailings pile contains 28 ppm As. Note that the downstream flood-plain tailings sample is anomalous (46 ppm As), whereas the adjacent active stream-sediment sample (2.5 ppm) is not. This relationship, which also is true for other elements, clearly indicates the anthropogenic nature and origin of the downstream tailings sample.

Antimony is nearly always closely associated in the natural environment with arsenic, and it commonly proxies for arsenic in arsenic-rich minerals. Because of its close association with arsenic, the distribution of antimony is not shown here. Antimony is the most strongly loaded element on the geothermal factor (table 2). The distributions of anomalies of this element in both study areas (0.5–150 ppm Sb) are generally similar to those of arsenic. In the Northeast Area, antimony is anomalous (1.5 and 1.0 ppm) in the two tailings samples. Unlike arsenic, however, antimony is only anomalous in Soda Butte Creek in the immediate area upstream from Cooke City.

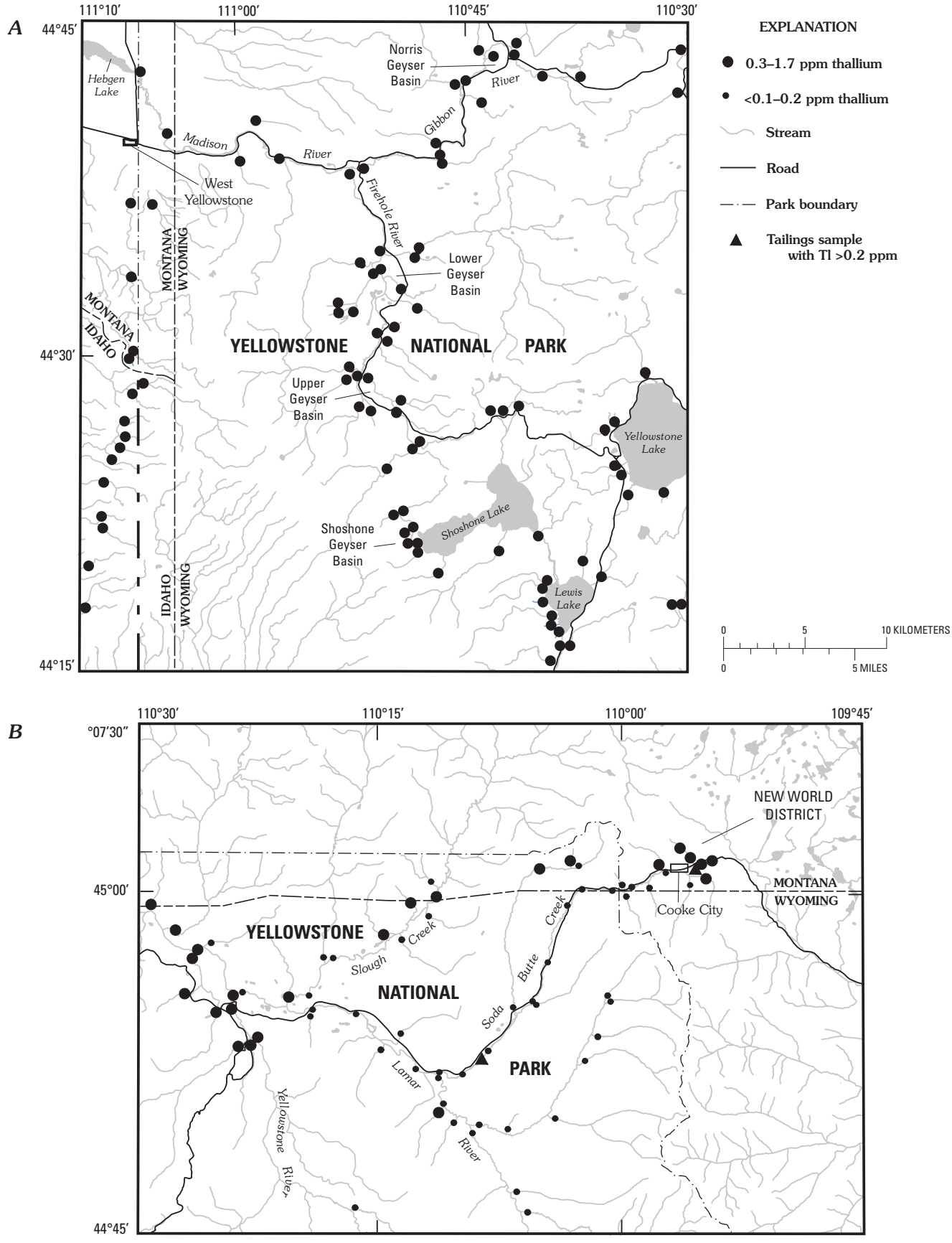

Figure 5. *A*, Distribution of thallium in stream sediment, West Area. *B*, Distribution of thallium in stream sediment, Northeast Area.

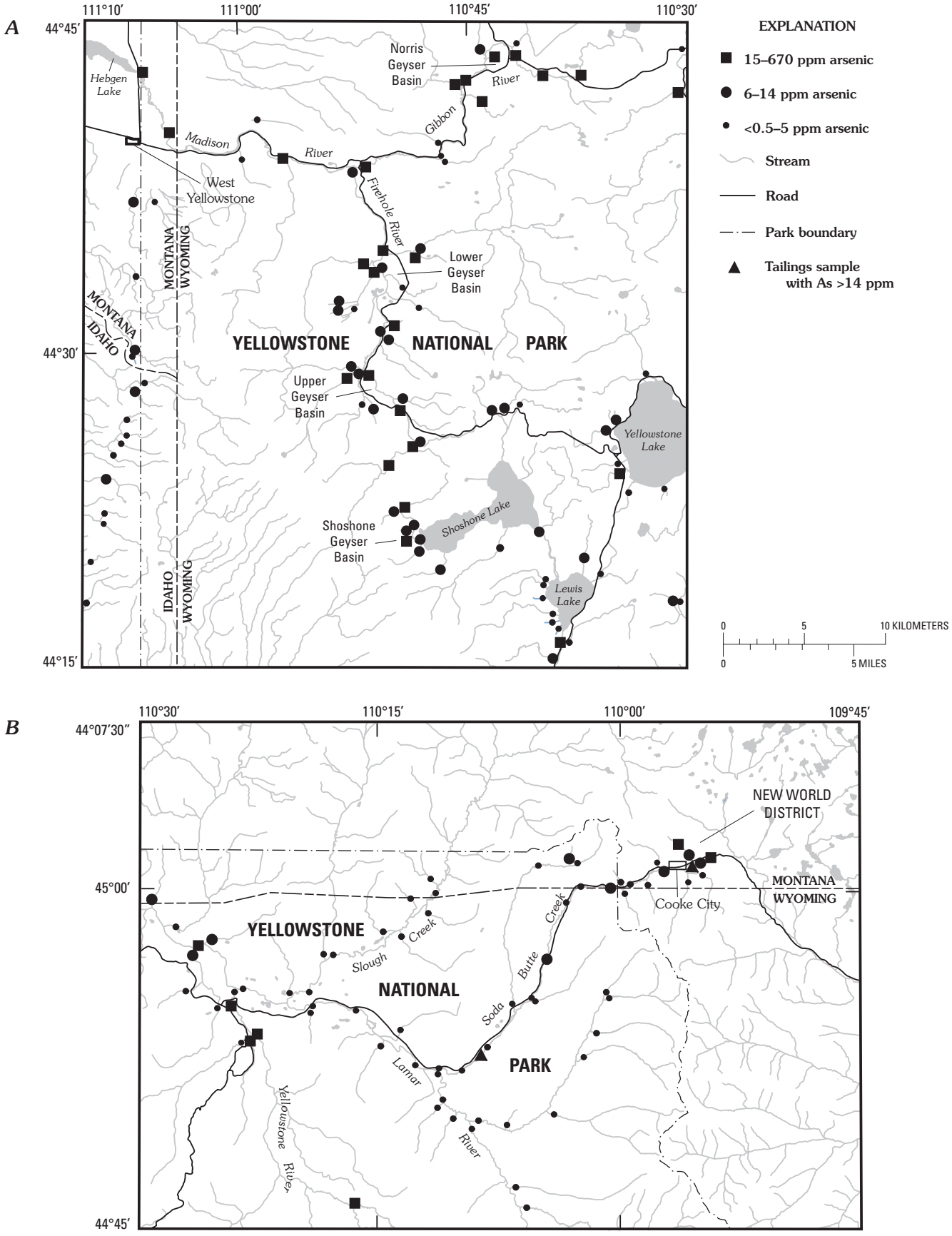

Figure 6. *A*, Distribution of arsenic in stream sediment, West Area. *B*, Distribution of arsenic in stream sediment, Northeast Area.

Gold.—Gold is strongly loaded only on the mineral deposit factor (table 2). However, a second, less significant source for this element exists. In the West Area (fig. 7*A*), anomalous gold (7–33 ppb) related to geothermal processes is present at scattered localities, particularly in the Norris and Shoshone Geyser Basins. The mineral form of this gold is not known.

In the Northeast Area (fig. 7*B*), gold is one of the elements enriched in the mineralized New World district. This element may occur as free gold, or it may be present in the structures of other ore-related minerals, such as pyrite or chalcopyrite. Anomalous gold (7–14,300 ppb) is present in stream-sediment samples collected in the New World district and in samples collected downstream from there in Soda Butte Creek. The anomaly continues to the junction of Soda Butte Creek with the Lamar River, where sediments with low gold concentrations from sources in the upper Lamar River watershed dilute anomalous sediments from Soda Butte Creek to background levels. Four additional samples collected downstream from this junction also are anomalous. The source of the gold in the sample from below the junction of the Lamar and Yellowstone Rivers (27 ppb) is not known. This anomaly, which may represent the "nugget effect" sometimes present in gold-rich sediment samples, may be an additional manifestation of contamination from the Cooke City area. The anomalous (7 ppb Au) sample from the Yellowstone River above its junction with the Lamar River probably is related to geothermally altered rocks. The sources of the gold anomalies in lower Slough Creek and the small stream south of there are not known. Note that both tailings samples are anomalous (5,000 and 730 ppb Au), again emphasizing that most of the anomaly in Soda Butte Creek probably is associated with naturally mineralized rock outcrops or with past mining activity in the New World district.

Copper.—Copper is loaded on two factors (table 2). The primary loading is on factor 2, the mafic rock factor, emphasizing the probable association of copper with dark accessory minerals that are common in the intermediate to mafic volcanic rocks in the Northeast Area (fig. 2*B*). The secondary loading is on factor 4, the mineral deposit factor. Anomalous copper in the Northeast Area is present mainly as chalcopyrite or its weathering products. In this same area, copper (fig. 8) is moderately to strongly anomalous (40–630 ppm) in the highly mineralized areas upstream from Cooke City. A small part of the copper content of samples from the Northeast Area probably is a contribution from the dark-mineral-rich volcanic rocks of the area. However, most of the high copper concentrations are in material eroded from the copper-rich mineral deposits and their associated dumps and tailings and slag piles. The anomaly extends downstream from the Cooke City area and into the Park along Soda Butte Creek to a point past the junction of that stream and the Lamar River. Both tailings samples also are strongly anomalous in copper (530 and 260 ppm).

No copper anomalies are associated with geothermal activity or with the distribution of felsic rocks in either study area. Thus, a copper map for the West Area shows no anomalies and is not shown here. These observations indicate that copper is a good geochemical indicator of both mineralized rock and mining activity in the northeastern part of the Park.

Lead.—Lead is strongly loaded on the mineral deposit factor (table 2). It also has a secondary loading on the felsic-rock factor. We speculate that the lead represented by the loading on the felsic-rock factor probably is related to lead substituting for potassium in potassium-rich feldspars.

In the Northeast Area (fig. 9), lead is anomalous (50–190 ppm) in sediment from streams draining the mineralized New World mining district and adjacent Republic district. However, this anomaly does not extend into the Park in Soda Butte Creek. In the Northeast Area, anomalous lead is mainly associated with galena or oxidation products of this mineral. The anomalous sample collected near the tailings pile contains 86 ppm Pb. Note that the downstream, flood-plain tailings sample is anomalous (100 ppm), whereas the nearby active stream-sediment sample (24 ppm) is not, indicating that anomalous lead in sediment has migrated downstream in the past from the original tailings pile, but it is not currently moving downstream in significant amounts in active sediment.

The anomalous (110 ppm Pb) sample collected in lower Slough Creek is from a site below the Slough Creek Campground. Because of its location and the absence of other anomalous elements in this sample, this anomaly is deemed to be anthropogenic in origin. It might represent contamination from lead fishing weights. In the West Area, a single lead anomaly (61 ppm) is present in a sample collected below Lewis Falls, at the outlet to Lewis Lake, a popular tourist stop. Unlike the sample from Slough Creek, this sample also is anomalous for several elements that compose the geothermal suite (table 2). However, because lead is not an element associated with the geothermal suite, this isolated lead anomaly may be anthropogenic in origin. Because only one sample with anomalous lead was identified in the West Area, no map for that area is included.

Sulfur.—Total sulfur, as determined for this study, consists of the sum of sulfide sulfur, sulfate sulfur, elemental sulfur, and probably minor amounts of other sulfur compounds. Sulfur is primarily loaded on the geothermal factor (table 2). It is secondarily loaded on the mineral deposit factor, indicating more than one source for this element. Sulfide minerals are common in the mineralized New World district. Native sulfur and other sulfur minerals are common in many geothermal areas in the Park.

The strongest sulfur anomalies in the West Area (fig. 10*A*) all are related to geothermal activity. Some of the strong anomalies, such as those for samples collected at sites north of Shoshone Lake, near the Park road and downstream from geothermally altered rhyolite outcrops (0.06–0.07 percent S), are related to fossil geothermal activity. The weak anomalies along the west boundary of the Park, in fresh rhyolitic rocks, probably represent the high end of the background range of values for sulfur. Most of the other anomalies (0.05–0.30 percent S) are related to active geothermal localities. Note that none of the samples collected in the Shoshone Geyser Basin and only one collected in the Upper Geyser Basin are anoma-

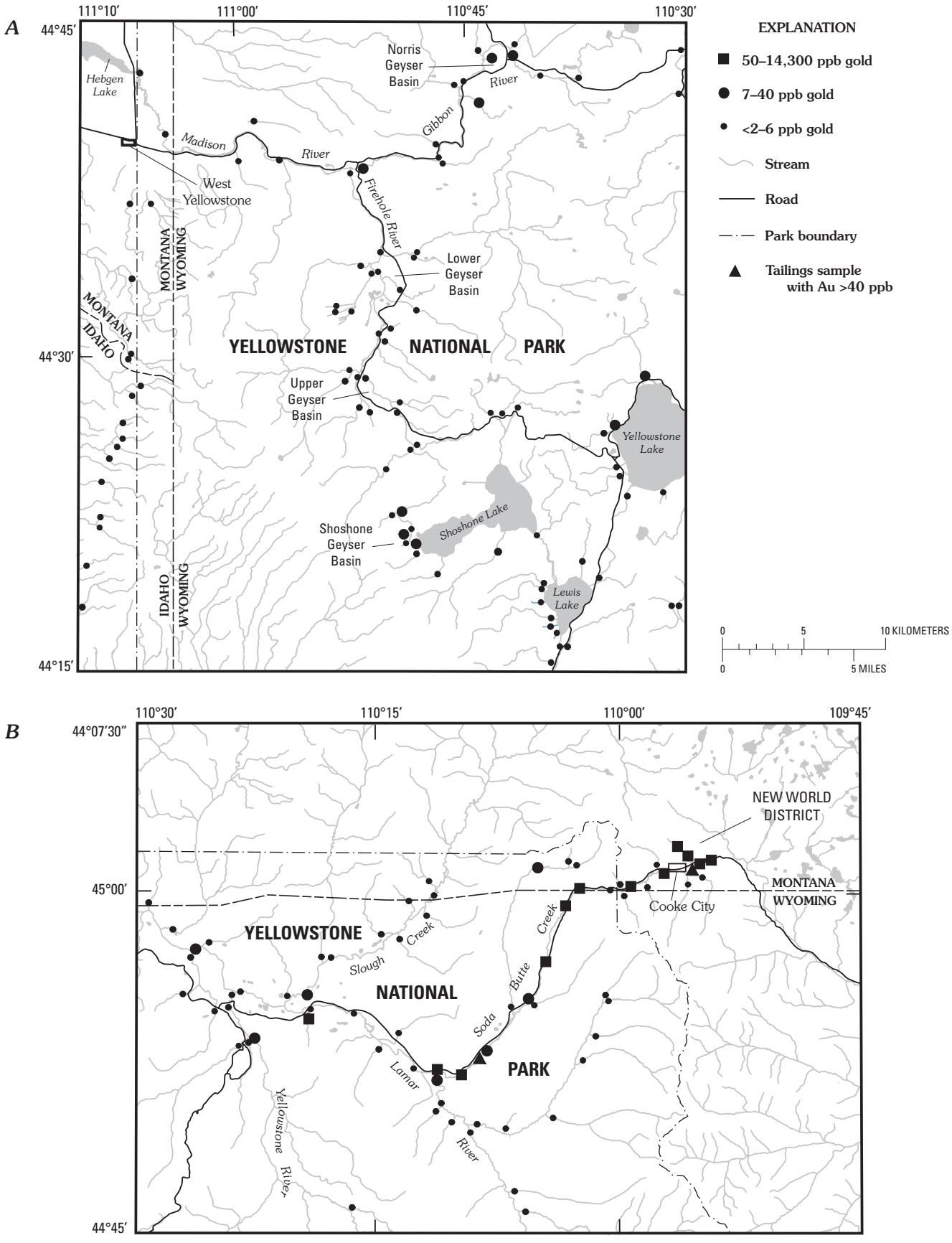

Figure 7. *A*, Distribution of gold in stream sediment, West Area. *B,* Distribution of gold in stream sediment, Northeast Area.

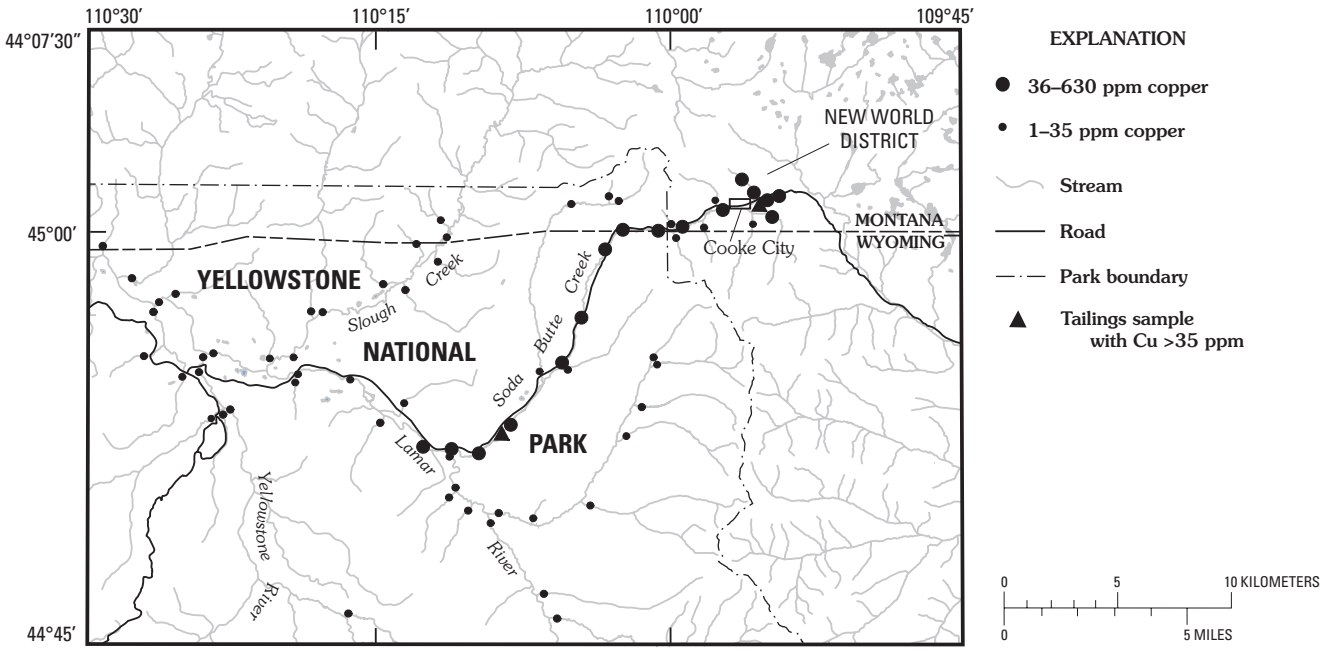

Figure 8. Distribution of copper in stream sediment, Northeast Area.

lous. We speculate that sulfur in these active geothermal areas is still in solution, and it tends to precipitate, mainly in the form of sulfates, only farther downstream where temperatures are lower and (or) evaporation of sulfur-rich water is occurring.

In the Northeast Area (fig. 10*B*), sulfur is weakly to strongly anomalous (0.04–1.86 percent) in the New World mining district and is intermittently anomalous (0.03–0.07 percent) along Soda Butte Creek. Most of this sulfur is derived from the sulfide-rich mineral deposits near Cooke City. Both of the tailings-related samples contain significant concentrations (1.86 percent and 0.27 percent) of sulfur. These observations indicate that sulfides (mainly pyrite) were transported downstream during the 1950 flood and that sulfur is a good geochemical indicator of the effects of the flooding.

The weakly anomalous (0.03 percent) sulfur in the sample from the Lamar River upstream from its junction with Soda Butte Creek and the strongly anomalous (0.05–1.33 percent) sulfur from the samples along the Yellowstone River near its junction with the Lamar River are related to local areas containing sulfur-rich hot springs; they are not related to the sulfides in the Cooke City area. The isolated, anomalous (0.07 percent S) sample collected near the southwest corner of the Northeast Area is from Wrong Creek, downstream from an area of hot springs.

Tellurium and selenium.—Tellurium, which is common in sulfide minerals (especially pyrite), is the most strongly loaded element on the mineral deposit factor (table 2). This association corroborates the distribution of anomalous (0.1–16 ppm) tellurium in the Northeast Area (fig. 11*B*), in the New World district area, and downstream in Soda Butte Creek to its junction with the Lamar River. The two tailings-related samples also are strongly anomalous (16 and 3.6 ppm Te). In the West Area (fig. 11*A*), weakly anomalous (0.01–0.02 ppm) tellurium is present in samples collected in the southeastern corner of the area, near Heart Lake, and in several samples of rhyolite-rich sediment collected along the western boundary of the Park. These anomalies probably represent concentrations that are in the high end of the background range for this element, and thus they have no relationship to any mineral deposits. These observations indicate that tellurium in concentrations >0.2 ppm is a good indicator element for delineating the distribution of mineral-deposit-related material in the Northeast Area.

Selenium is another element that is strongly loaded on the mineral deposit factor (table 2). This element also commonly proxies for sulfur in mineral structures. The distribution of selenium (not shown) is very similar to that of tellurium. It shows only a very restricted anomaly (0.5–4.6 ppm) in the immediate area of the New World district, with no anomaly extending downstream into the Park. Both of the tailings-related samples also are anomalous (3.7 and 1.0 ppm Se). As is the case for tellurium, the selenium anomalies in the West Area are weak (0.04 ppm), and they are confined to three rhyolite-rich sediment samples collected along the western boundary of the Park.

Tungsten.—Tungsten is loaded primarily on the geothermal factor and secondarily on the mineral deposit factor (table 2), emphasizing its association with both the geothermal systems and the mineralized New World district. Although not reflected in the factor analysis, a minor lithologic component also may be present locally. This element commonly occurs as tungstate minerals. However, its mineral residence in the study areas is not known. In the West Area (fig. 12*A*), tungsten is weakly to strongly enriched (1–150 ppm) in stream-sediment samples.

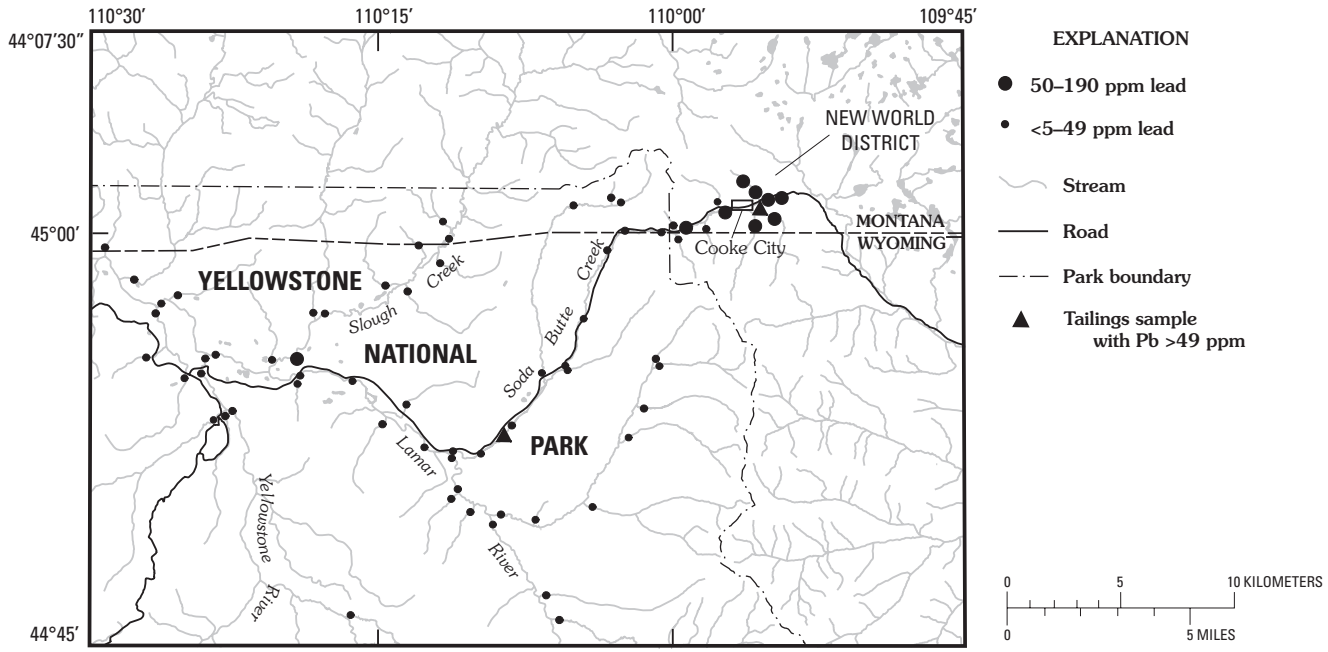

Figure 9. Distribution of lead in stream sediment, Northeast Area.

Most of this enrichment is deemed to be a result of past or present geothermal activity. In a few cases, such as in the two samples southeast of Shoshone Lake and the sample north of Lewis Lake, anomalous tungsten possibly is related locally to elevated background concentrations in felsic volcanic rocks.

With one exception, the distribution of anomalous (3–60 ppm) tungsten in stream-sediment samples in the Northeast Area (fig. 12*B*) is restricted to Soda Butte Creek, mainly upstream from Cooke City. The sample from near the McLaren tailings pile in the New World district is strongly anomalous (140 ppm W). The lower flood-plain tailings sample also is anomalous (21 ppm); however, nearby sediment samples in lower Soda Butte Creek are not anomalous, again emphasizing the tailings-related origin of material in that flood-plain sample. The single anomalous sample on the west side of the area is related to geothermally altered rocks.

Molybdenum.—Molybdenum is loaded on two factors (table 2). Its primary loading is on factor 1, the felsic igneous rock factor. It is secondarily loaded on the geothermal factor, emphasizing at least two sources for this element. Like tungsten, molybdenum forms its own minerals, the most common of which is the sulfide, molybdenite; however, the mineral form of molybdenum in the study areas has not been identified. In the West Area (fig. 13*A*), molybdenum anomalies (3–19 ppm) are widespread. Field observations indicate that some of these anomalies are not related to geothermal activity and that some samples containing geothermally altered material are not anomalous. These observations corroborate the results of the factor analysis and strongly suggest that, in the West Area, molybdenum is enriched both as a result of naturally high background concentrations related to the rhyolite lithology and as a result of geothermal activity.

In the Northeast Area (fig. 13*B*), molybdenum is anomalous (8–14 ppm) in two samples from the New World district, but it shows only background concentrations along Soda Butte Creek. Note that, unlike tungsten, neither tailings-related sample is anomalous. In the Northeast Area, molybdenum also is anomalous in a cluster of samples along the Yellowstone River, near its junction with the Lamar River, and in the isolated sample collected in the southwestern part of the area. These anomalies are deemed to be related to a combination of lithologic and geothermal sources.

Cesium.—Cesium is strongly loaded on the geothermal factor (table 2). Unlike most other elements studied, anomalous cesium is associated solely with geothermal activity. We speculate that this element probably is substituting for potassium in potassium-rich alteration minerals. The highest concentrations of cesium (7–870 ppm) are in sediments collected in the West Area (fig. 14*A*) from smaller streams in the Upper, Lower, and Norris Geyser Basins that drain areas of active geothermal systems. Anomalous concentrations extend downstream from these geyser basins to the Madison River, and thence all the way to the western boundary of the Park. Anomalous cesium also is present in sediments from streams draining hydrothermally altered rocks near Shoshone, Lewis, and Heart Lakes.

In the Northeast Area (fig. 14*B*), anomalous cesium concentrations (10–18 ppm) are only in samples collected along the Yellowstone River, near its junction with the Lamar River. As noted previously, these anomalies are associated with solfataric alteration and hot springs in that area. The absence of anomalous cesium in the Soda Butte Creek drainage emphasizes that this element is not associated with mineralized rock in the Cooke City area. Thus, anomalous cesium is a good

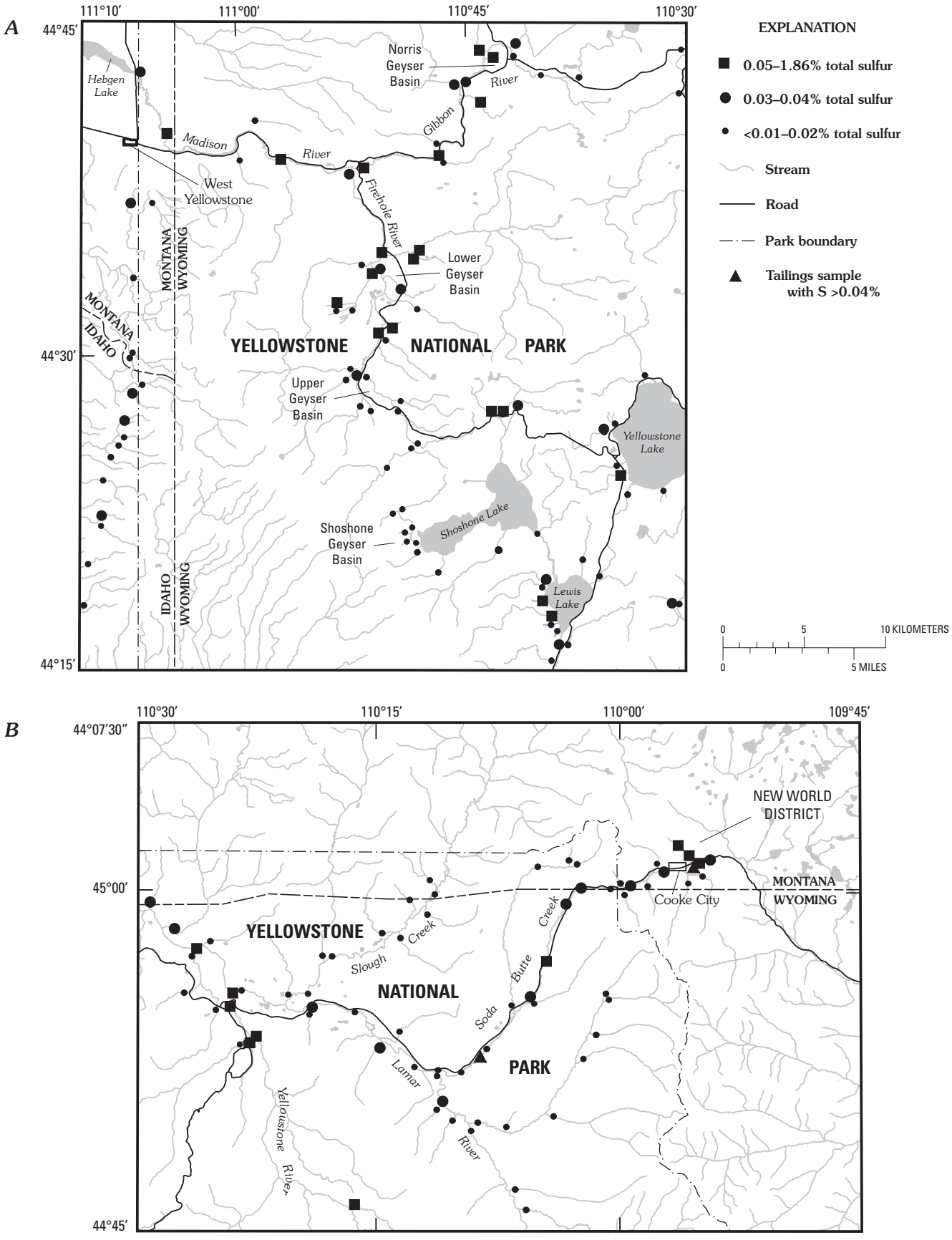

Figure 10. *A*, Distribution of sulfur in stream sediment, West Area. *B,* Distribution of sulfur in stream sediment, Northeast Area.

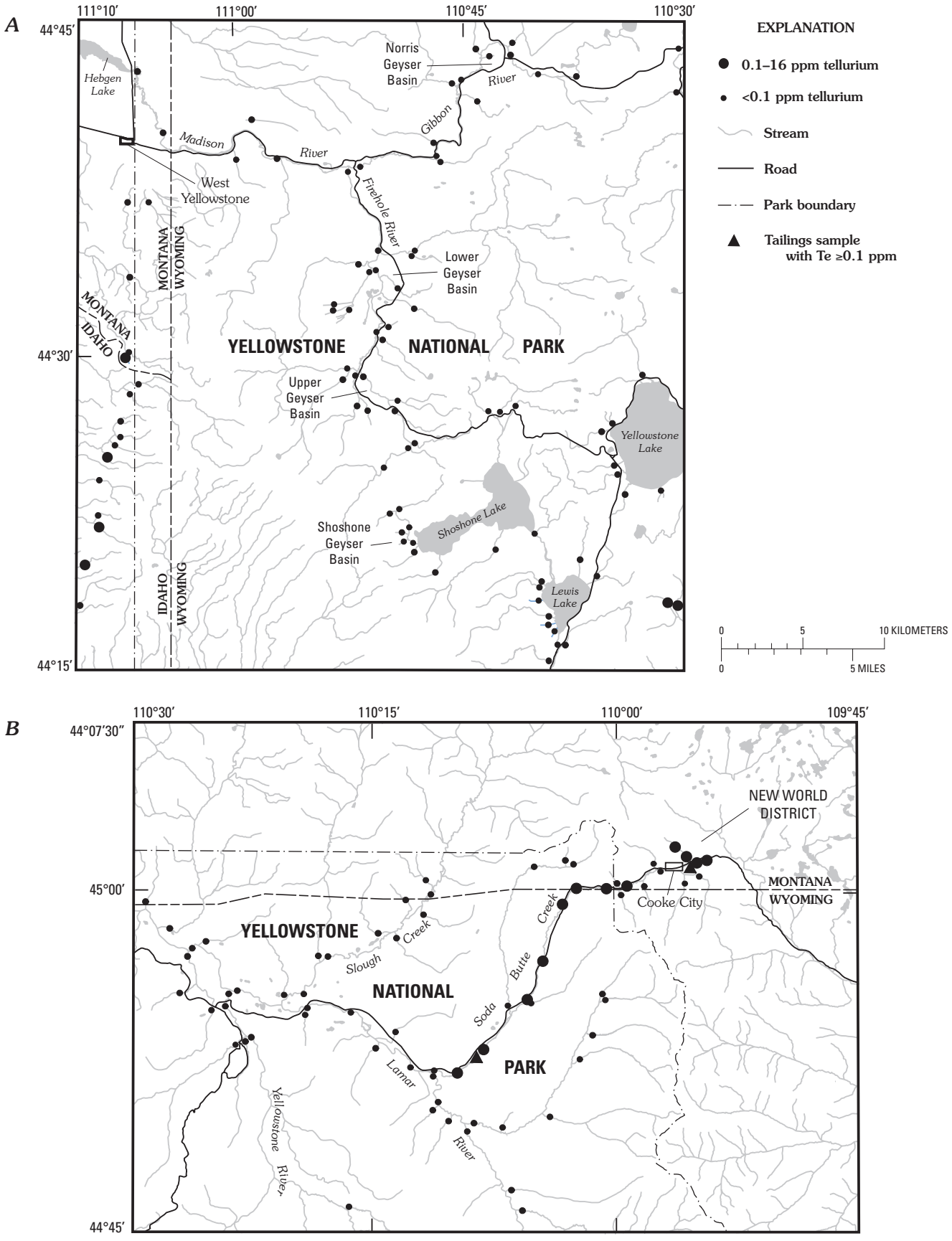

Figure 11. *A,* Distribution of tellurium in stream sediment, West Area. *B,* Distribution of tellurium in stream sediment, Northeast Area.

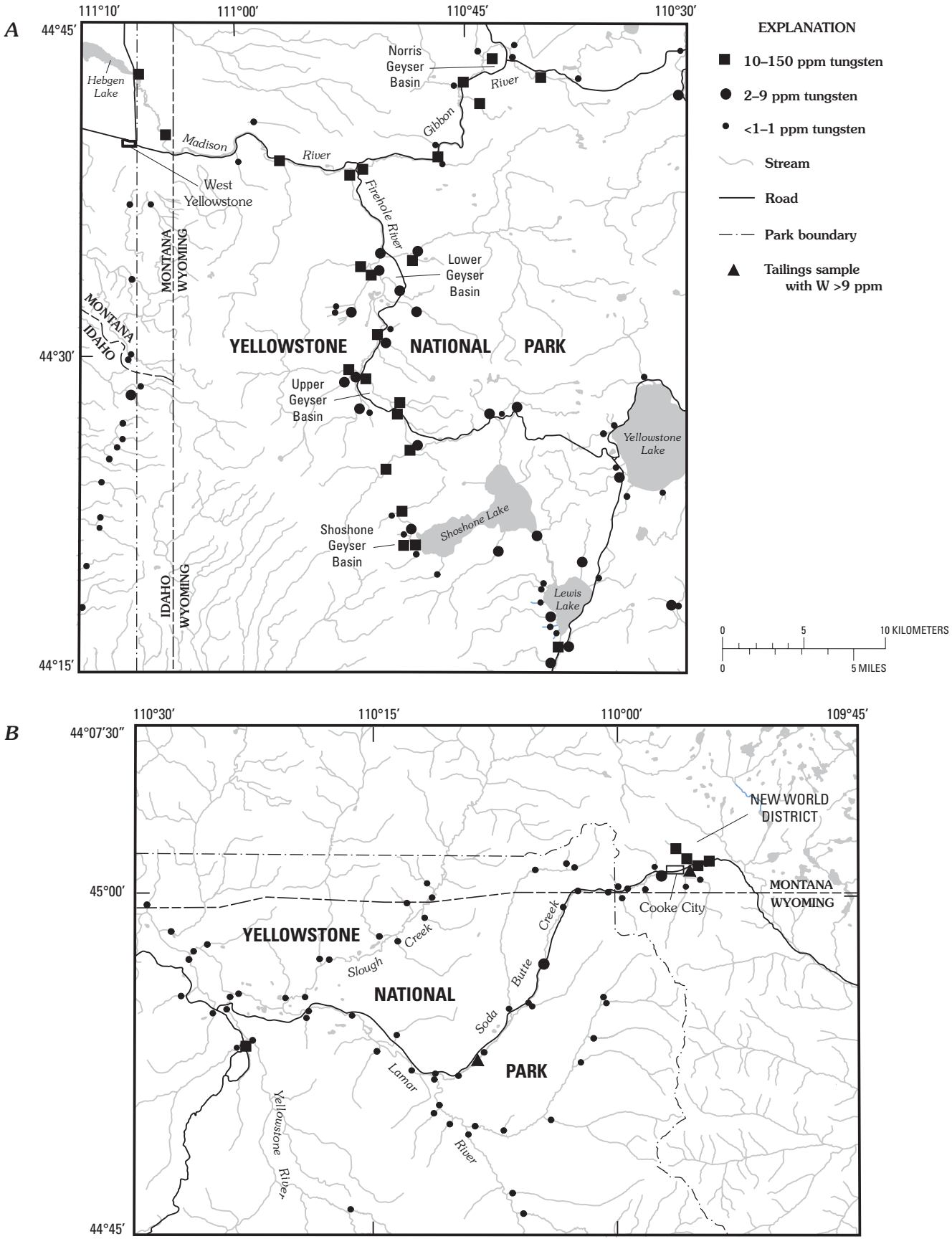

Figure 12. *A*, Distribution of tungsten in stream sediment, West Area. *B,* Distribution of tungsten in stream sediment, Northeast Area.

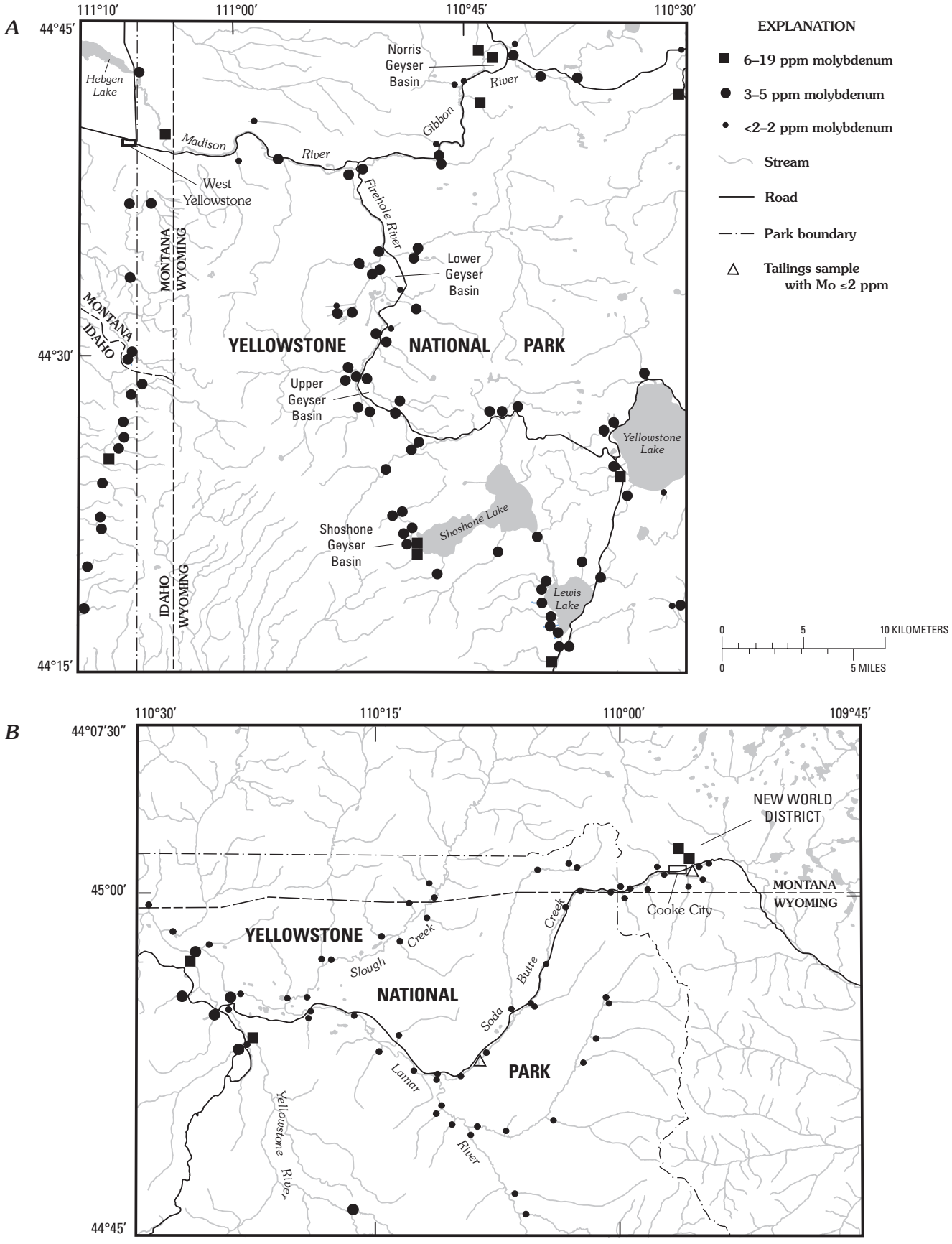

Figure 13. *A,* Distribution of molybdenum in stream sediment, West Area. *B,* Distribution of molybdenum in stream sediment, Northeast Area.

indicator of both past and present geothermal activity in the Yellowstone area.

Mercury.—Mercury is strongly loaded only on the geothermal factor (table 2). However, this element probably has two additional, less significant, sources. The mineral form of mercury in the Yellowstone area has not been determined. It possibly occurs as free mercury or some other mercury mineral, or possibly it is within the structure of one or more sulfide minerals.

Samples with anomalous mercury (0.06–2.85 ppm) are widespread in the West Area (fig. 15*A*) in areas of both active geothermal activity and fossil geothermal systems. Some anomalous samples do not seem to be related to geothermal features. They are thus thought to represent high background concentrations in unaltered rhyolites, as seems to be the case for lead, molybdenum, and tungsten.

In the Northeast Area (fig. 15*B*), mercury is anomalous (0.06–0.28 ppm) in the stream-sediment samples from the immediate area of the New World mining district. The upstream tailings-related sample also is anomalous (0.16 ppm Hg). These observations suggest that this element possibly is a previously unreported minor component of the mineral deposits in the district or, more likely, it was added to the ores during treatment. Low concentrations of mercury also have been detected in areas where mercury-bearing fungicides were applied during reseeding experiments conducted in the New World district. Anomalous (0.07–0.25 ppm) geothermally or lithologically related mercury is also present in the area of active hot springs found along the Yellowstone River near its junction with the Lamar River.

Fluorine.—Fluorine is primarily loaded on the miscellaneous factor (factor 5) (table 2), and it has a secondary loading on the felsic-rock factor. Factor scores indicate that fluorine is closely associated with both fresh and geothermally altered igneous rocks, primarily rhyolites. Kornitnig (1972) noted that fluorine commonly is enriched in rocks with high silica content. This relationship seems to hold in the two study areas. Fluorine can proxy for other elements in silicate structures, and it also may occur in accessory minerals, such as fluorite, topaz, and micas. The mineral residence(s) for fluorine in the Yellowstone area has not been identified.

In the West Area (fig. 16*A*), fluorine is anomalous (450–1,600 ppm) in sediments from streams draining nearly all parts of the area, including localities of fresh rhyolites along the western boundary of the Park and elsewhere and localities of geothermally altered rocks. Fluorine is only anomalous in four of the samples analyzed from the Northeast Area (fig. 16*B*). Three, including two regular sediment samples (480–560 ppm F) and one tailings-related sample (600 ppm F), are from the mineralized area in the New World district upstream from Cooke City. The one other anomalous sample (480 ppm F) is from a tributary of upper Slough Creek. These four samples are from streams that drain areas of either Precambrian metamorphic rocks, Tertiary andesitic rocks, or, in the area upstream from Cooke City, material mined in the New World district.

Environmental Concerns

Concentrations of many of the elements described here may impact the surficial environment of the Park in a variety of ways. Widespread, although generally low-level, concentrations of a number of potentially toxic elements are present in sediments in many parts of the Park. Weakly anomalous, high background levels of As, F, Hg, Mo, Pb, Sb, and (or) W have been identified in stream sediments derived from relatively unaltered felsic volcanic rocks in several parts of the Park. We do not know whether elevated levels of any of these elements are also present in stream waters near these high-background, but anomalous, stream-sediment sample sites. However, our observations suggest that any water stored in the Park for public water supplies should be carefully monitored for quality.

The evaluation of water samples from the Soda Butte Creek drainage by Miller and others (1997) indicates that neither strongly acidic nor strongly basic conditions are currently present in Soda Butte Creek within the Park. Consequently, the leaching into this basin of sulfide minerals from the tailings and dumps of the New World district is not presently significant in terms of impact on water pH.

This study of stream sediment, and that of Miller and others (1997) for water, together suggest that anthropogenic activities in and near the Park, such as mining and recreation, have had only a localized, minimal impact on the surficial environment. When compared to the distributions and concentration levels created by natural processes, such as geothermal features, the distributions and concentration levels of elements enriched by anthropogenic activity are not pronounced.

Little is known about how the health and longevity of wildlife are affected by the naturally occurring surficial chemistry of the Yellowstone-area environment. Anomalous concentrations of many elements in plants and water consumed by animals have been shown to cause health problems (Adriano, 1986; Gough and others, 1979; Lepp, 1981; Speidel and Agnew, 1982; Winston and others, 1973; and references in these publications). Discussion of the many parameters related to the potential toxicity of the elements determined for this study and their impact on wildlife is beyond the scope of this paper. However, an example follows to illustrate one instance in which surficial geochemistry has impacted wildlife.

The health and longevity of elk (*Cervus elaphus*) in the Park recently were studied (Garrott and others, 2002). Elk in the Lamar Valley area live longer than those in the Madison-Firehole area, where geothermal activity has markedly affected surficial chemistry. The longevities of elk in the two areas are closely associated with chemical differences in available food. The food chemistry, in turn, is related to differences in the chemistry of rock, soil, and stream waters of these two areas—differences that are due partly to local geology and partly to the presence or absence of geothermal features. Water, as well as plants and their substrates, is enriched in fluorine and silica in many parts of the Madison-

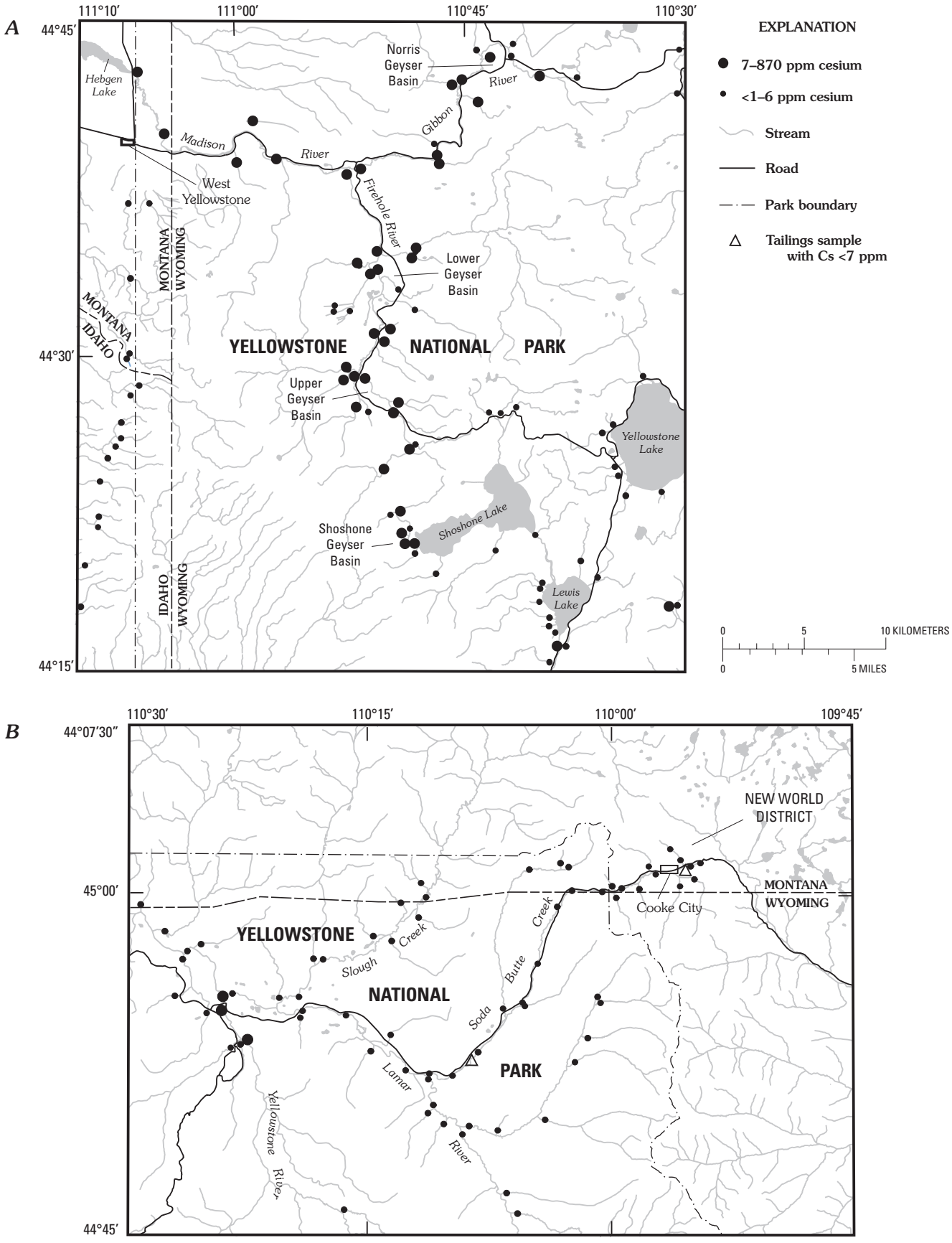

Figure 14. *A*, Distribution of cesium in stream sediment, West Area. *B*, Distribution of cesium in stream sediment, Northeast Area.

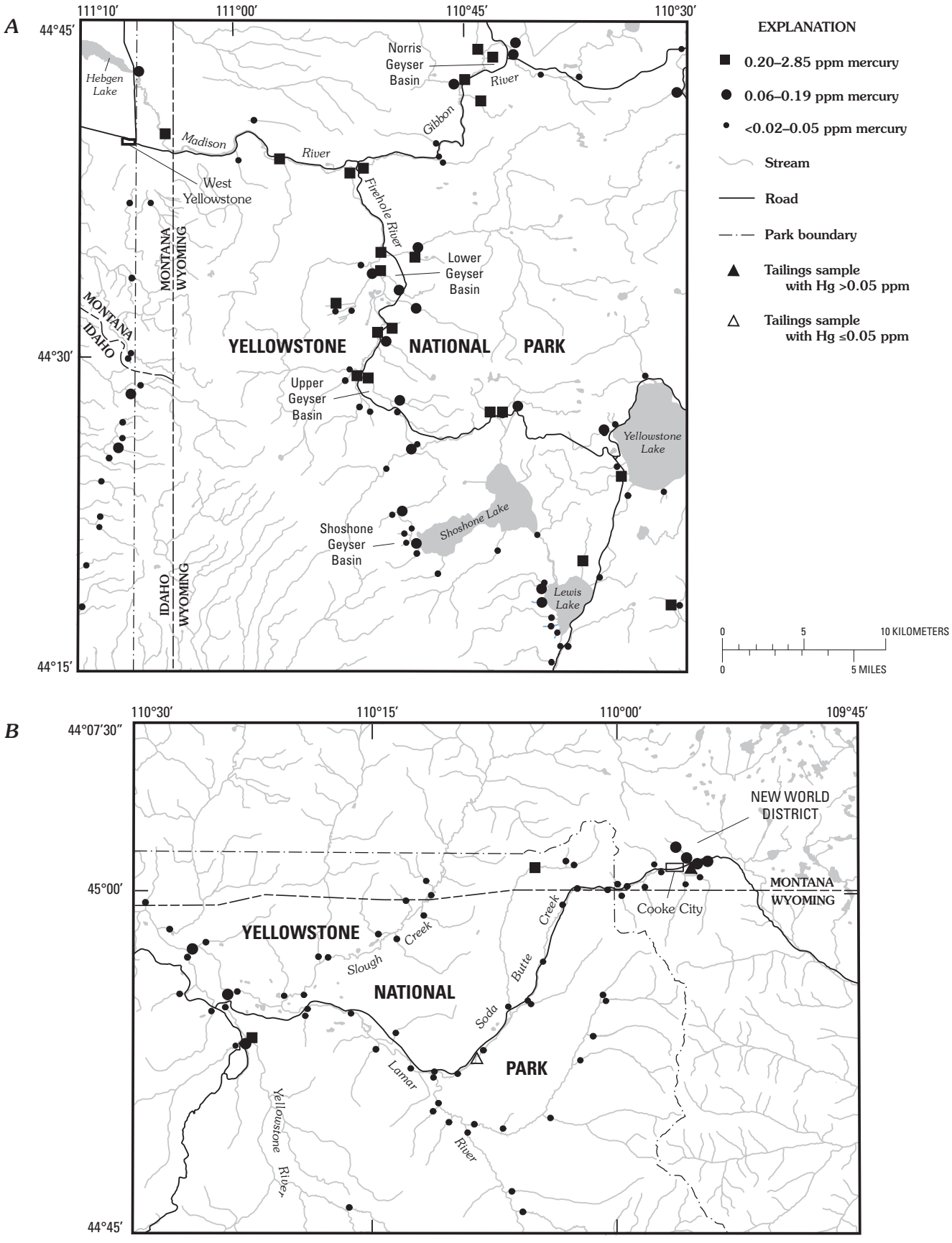

Figure 15. *A,* Distribution of mercury in stream sediment, West Area. *B*, Distribution of mercury in stream sediment, Northeast Area.

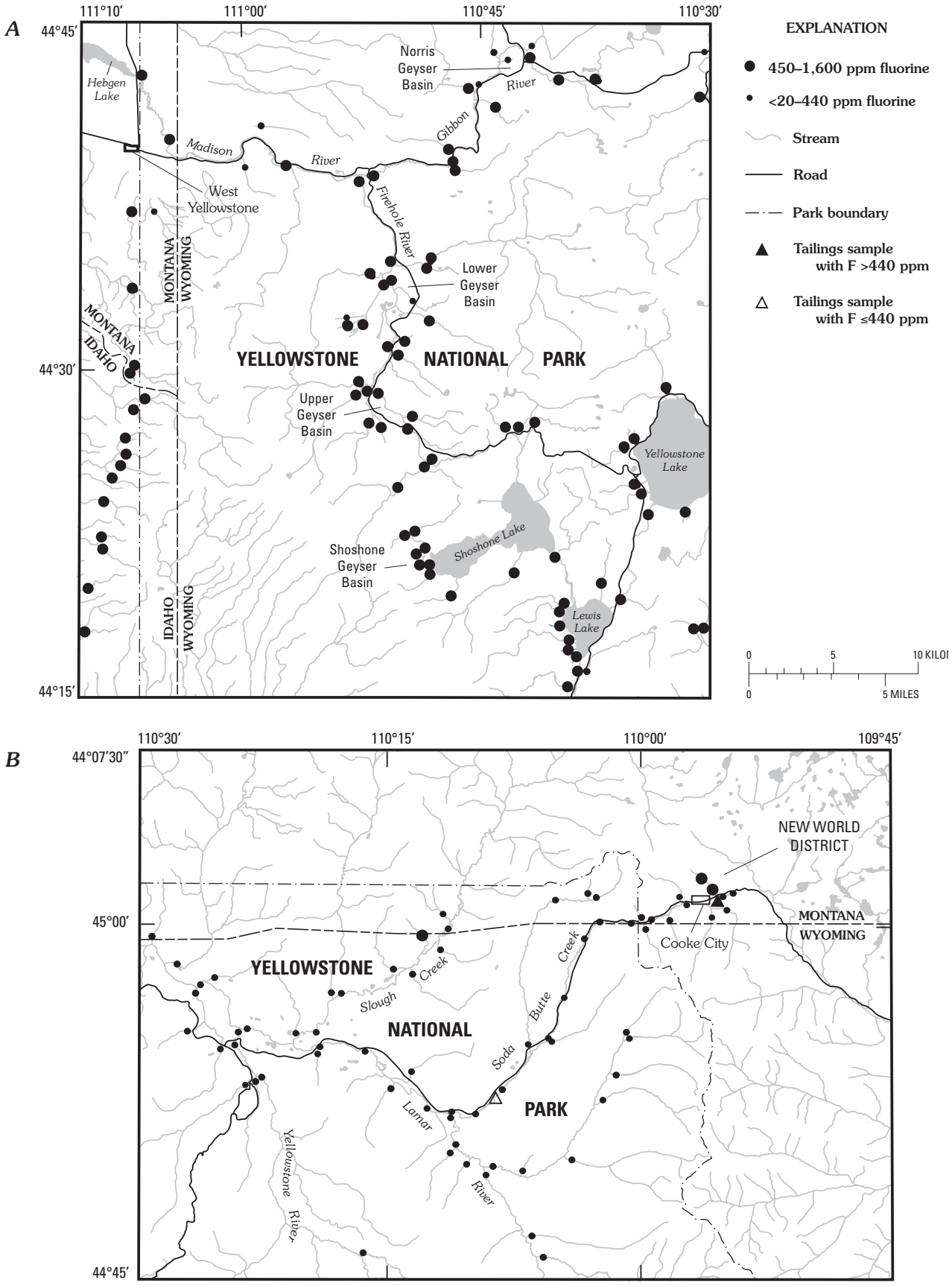

Figure 16. *A,* Distribution of fluorine in stream sediment, West Area. *B*, Distribution of fluorine in stream sediment, Northeast Area.

Firehole area, as compared to the Lamar River valley (Miller and others, 1997; Garrott and others, 2002). Excessive fluorine in the food chain causes severe fluorosis in elk and other ungulates (Shupe and others, 1984), weakening their tooth structure and ultimately destroying their teeth. Additionally, abrasive silica in plants eaten by elk causes abnormal wear of teeth. This fluorine-silica combination causes early loss of teeth and eventual starvation. Our fluorine data clearly show that this element is enriched in samples from many areas of rhyolite outcrops or geothermal features.

Of the elements determined for this study, arsenic, molybdenum, fluorine, and silicon probably have the greatest potential for affecting the health of Park animals. To the best of our knowledge, the effects of arsenic and molybdenum on elk (*C. elaphus*), bison (*Bison bison*), moose (*Alces americana*), or other animals living in or near the Park have not been documented. The impacts of other potentially toxic elements, such as mercury, thallium, selenium, tungsten, and lead, on the health of wildlife in the Park also are not known.

We have also determined the content of selected elements in samples of elk and bison scat collected at localities throughout the Park. The distributions of anomalous elements in these samples closely reflect the chemistry of the underlying rocks. This observation indicates that animals grazing in or near geothermal areas are ingesting plant material (and probably water) that is high in potentially toxic elements such as fluorine, arsenic, and molybdenum. Except for fluorine and silicon, we do not know what elements are being accumulated in Park animals and the effects of any such accumulation. Low levels of potentially toxic elements may not kill animals, but may stress their systems to a point at which they are more susceptible to disease. Further studies of the effects of trace elements on wildlife are clearly needed.

Summary and Conclusions

This study indicates that many elements are relatively enriched in rock, stream-sediment, and water samples collected from localities in and near Yellowstone National Park. Of the elements described here, many have multiple sources, whereas some have only one. The source(s) of many of these elements can be determined by examining their respective distributions on maps and their multivariate statistical associations as determined by factor analysis. Different suites of elements can be used to characterize and differentiate anomalies related to natural causes (such as rock lithology, undisturbed mineral deposits, and geothermal activity) and those related to anthropogenic causes (such as mining and recreation). For many of the elements examined, the strongest anomalies in the Park are related to natural causes rather than to anthropogenic activities. When compared to anomalies caused by geothermal activity, those related to past mining are relatively minor.

Spatial differences in concentrations of 34 of the 49 elements determined for this study are primarily associated with differences in rock type. Many of these elements can be used to discriminate between major lithologic units and thus can be used to assist geologic mapping in the Park area.

Elements discussed in this study that are most closely associated spatially with areas of geothermal activity or source rocks for geothermal waters include As, Cs, Hg, S, Sb, Tl, and W. Of these, cesium, which is enriched only in sediment from geothermal areas, is the best geochemical indicator of geothermal activity. Elements associated with mineral deposits near Cooke City, Mont., include Ag, As, Au, Cu, Fe, Hg, Mo, Pb, S, Sb, Se, Te, Tl, W, Zn, and possibly F. Of these, Au, Cu, and Te are especially useful for identifying the dispersion of mineral-deposit-related contamination, which extends from the New World and Republic districts near Cooke City downstream into the extreme northeastern corner of the Park. Relatively weak anomalies of some of these elements extend as far as 18 km inside the Park, as measured from the Northeast Entrance.

In the area of Slough Creek, in the northeastern part of the Park, a high concentration of lead in one sample was deemed to be anthropogenic because of a lack of anomalies of other elements that commonly are associated with natural lead anomalies. This anomaly probably is related to past fishing activity.

The present-day, active geothermal waters in the Park probably are modern analogs to those that formed certain types of gold deposits in many parts of the world. Studies of Yellowstone's geothermal features can help geologists to better understand the genesis of gold deposits, and possibly other types of mineral deposits.

Many of the elements in stream sediment studied here are also known to be present in anomalous concentrations in the stream waters draining geothermal areas. Some of these elements also are concentrated in plants in these areas; thus, they are in the food chain for wildlife that feed in the geothermal areas of the Park. The impact on Park animals and plants of high chemical concentrations in water, soil, or sediment is not well understood, and it needs to be addressed by scientists. Weakly anomalous concentrations of elements such as As, Mo, Pb, and W occur locally in relatively unaltered felsic rocks and also in stream sediments. In some cases, they occur in stream water, suggesting that water stored in the Park for public water supplies should be carefully monitored for quality.

Significant amounts of As, Cs, Hg, Mo, Sb, W, and probably other elements, are being carried out of the Park in sediment (and, in many cases, in water) in the Madison River and possibly in other streams that exit the Park. Although the downstream environmental effects of a number of elements in the waters of the Madison River have been documented, the chemical contents and effects of sediment downstream from the Park have not been investigated in any detail. Further investigations may be warranted.

Acknowledgments

We are grateful to the National Park Service for its cooperation and assistance in this study. We also acknowledge the assistance of D.R. Norton, A.L. Olson, and R.R. Tidball of the U.S. Geological Survey in various phases of this study. We were aided in the field by Dr. Maciej Podemski, Dr. Jadwiga Slosarz, and Krzysztof Lason, all of the Polish Geological Institute. The analyses for Hg, S, Se, Te, and Tl were determined by XRAL Laboratories, Toronto, Ontario, Canada. All other analyses were determined by Activation Laboratories, Ltd., Ancaster, Ontario, Canada.

References Cited

Adriano, D.C., 1986, Trace elements in the terrestrial environment: New York, Springer-Verlag, 533 p.

Allen, E.T., and Day, A.L., 1935, Hot springs of the Yellowstone National Park: Carnegie Institute Publication 466, 525 p.

Antweiler, J.C., Love, J.D., Prostka, H.J., Kulik, D.M., Anderson, L.A., Williams, F.E., Jinks, J.E., and Light, T.D., 1989, Mineral resources of the Teton Wilderness and adjacent areas, Teton, Fremont, and Park Counties, Wyoming: U.S. Geological Survey Bulletin 1781, 105 p.

Antweiler, J.C., Rankin, D.W., Fisher, F.S., Long, C.L., Love, J.D., Bieniewski, C.L., and Smith, R.C., 1985, Mineral resource potential map of the northern part of the Washakie Wilderness and nearby roadless areas, Park County, Wyoming: U.S. Geological Survey Miscellaneous Field Studies Map MF-1597-A, scale 1:125,000.

Bolivar, S.L., Hensley, W.K., Van Haaften, I.J., Pirtle, June, George, W.E., Gallimore, David, Apel, Charles, and Hansel, James, 1980, Uranium hydrogeochemical and stream sediment reconnaissance of the Bozeman NTMS quadrangle, Montana, including concentrations of forty-two additional elements: Los Alamos, N. Mex., Los Alamos Scientific Laboratory Informal Report LA-7504-MS Supplement, 155 p. [*Reissued as* U.S. Department of Energy Report GJBX-235(80), Grand Junction, Colo.].

Bolivar, S.L., Sandoval, W.F., Gallimore, D.L., Talcott, C.L., Martinez, R.G., Hensley, W.K., and Cheadle, J.M., III, 1980, Uranium hydrogeochemical and stream sediment reconnaissance data release for the Cody NTMS quadrangle, Wyoming, including concentrations of forty-two additional elements: Los Alamos, N.Mex., Los Alamos Scientific Laboratory Informal Report LA-7352-MS, 147 p. [*Reissued as* U.S. Department of Energy Report GJBX-233(80), Grand Junction, Colo.].

Bond, J.G., compiler, 1978, Geologic map of Idaho: Idaho Department of Lands, Bureau of Mines and Geology, 1 plate, scale 1:500,000.

Broxton, D.E., Sandoval, W.F., Trujillo, L.A., Minor, M.M., Steinhaus, D.W., Martell, C.J., Hensley, W.K., and Mills, C.F., 1979, Uranium hydrogeochemical and stream sediment reconnaissance data release for the Billings NTMS quadrangle, Montana, including concentrations for forty-three additional elements: Los Alamos, N.M., Los Alamos Scientific Laboratory Informal Report LA-7669-MS, 200 p. [*Reissued as* U.S. Department of Energy Report GJBX-150(79), Grand Junction, Colo.].

Carlson, R.R., and Lee, G.K., 2005, Chapter D, Geochemistry—Stream sediment, *in* Wilson, A.B., Hammarstrom, J.M., and Van Gosen, B.S., Mineral and energy resource assessment of the Gallatin National Forest (exclusive of the Absaroka-Beartooth Study Area), in Gallatin, Madison, Meagher, Park, and Sweet Grass Counties, south-central Montana: U.S. Geological Survey Professional Paper 1654, p. D1–D16.

Christiansen, R.L., and Blank, H.R., 1972, Volcanic stratigraphy of the Quaternary Rhyolite Plateau in Yellowstone National Park: U.S. Geological Survey Professional Paper 729-B, 18 p.

Coakley, G.J., 1975, Tellurium, *in* U.S. Bureau of Mines staff, Mineral facts and problems, 1975 edition: U.S. Bureau of Mines, p. 1103–1108.

de Albuquerque, C.A.R., and Shaw, D.M., 1972, Thallium, *in* Wedepohl, K.H., ed., Handbook of Geochemistry: New York, Springer-Verlag, v. II-5, chap. 81, secs. B–O.

Elliott, J.E., Gaskill, D.L., Raymond, W.H., Peterson, D.L., Stotelmeyer, R.B., Johnson, F.L., Lindsey, D.S., Ridenour, James, Schmauch, S.W., and Zilka, N.T., 1983, Mineral resources of the North Absaroka Wilderness Study Area, Park and Sweet Grass Counties, Montana: U.S. Geological Survey Bulletin 1505, 251 p., 5 plates.

Fournier, R.O., Christiansen, R.L., Hutchinson, R.A., and Pierce, K.L., 1994, A field-trip guide to Yellowstone National Park, Wyoming, Montana, and Idaho—Volcanic, hydrothermal, and glacial activity in the region: U.S. Geological Survey Bulletin 2099, 46 p.

Garrott, R.A., Eberhardt, L.L., Otton, J.K., White, P.J., and Chaffee, M.A., 2002, A geochemical trophic cascade in Yellowstone's geothermal environments: Ecosystems, v. 5, p. 659–666.

Gooch, F.A., and Whitfield, J.E., 1888, Analyses of waters of the Yellowstone National Park, with an account of the methods of analysis employed: U.S. Geological Survey Bulletin 47, 84 p.

Gough, L.P., Shacklette, H.T., and Case, A.A., 1979, Element concentrations toxic to plants, animals, and man: U.S. Geological Survey Bulletin 1466, 80 p.

Keefer, W.R., 1972, The geologic story of Yellowstone National Park: U.S. Geological Survey Bulletin 1347, 92 p.

Koritnig, S., 1972, Fluorine, *in* Wedepohl, K.H., ed., Handbook of Geochemistry: New York, Springer-Verlag, v. II-1, chap. 9, secs. B–O.

Lee, G.K., and Carlson, R.R., 1993, Geochemistry of the Absaroka-Beartooth area, *in* Hammarstrom, J.M., Zientek, M.L., and Elliott, J.E., eds., Mineral resource assessment of the Absaroka-Beartooth study area, Custer and Gallatin National Forests, Montana: U.S. Geological Survey Open-File Report 93-207, chap. D, p. D1–D11, 19 plates.

Lepp, N.W, 1981, Effect of heavy metal pollution on plants, volume 1: Englewood, New Jersey, Applied Science Publishers, Inc., 352 p.

Levinson, A.A., 1974, Introduction to exploration geochemistry: Calgary, Alberta, Applied Publishing Co., 612 p.

Love, J.D., Antweiler, J.C., and Williams, F.E., 1975, Mineral resources of the Teton corridor, Teton County, Wyoming: U.S. Geological Survey Bulletin 1397-A, 51 p.

Love, J.D., and Keefer, W.R., 1975, Geology of sedimentary rocks in southern Yellowstone National Park, Wyoming: U.S. Geological Survey Professional Paper 729-D, 60 p., 1 plate.

Manheim, F.T., and Landergren, S., 1978, Molybdenum, *in* Wedepohl, K.H., ed., Handbook of Geochemistry: New York, Springer-Verlag, v. II-4, chap. 42, secs. B–O.

Meyer, G.A., 1993, Holocene and modern geomorphic response to forest fires and climate change in Yellowstone National Park: Albuquerque, University of New Mexico, Ph.D. dissertation, 402 p.

Miller, W.R., Meier, A.L., and Briggs, P.H., 1997, Geochemical processes and baselines for stream waters for Soda-Butte-Lamar Basin and Firehole-Gibbon Basin, Yellowstone National Park: U.S. Geological Survey Open-File Report 97-550, 28 p.

Nelson, W.H., Prostka, H.J., Williams, F.E., 1980, Geology and mineral resources of the North Absaroka Wilderness and vicinity, Park County, Wyoming, *with sections on* Mineralization of the Sunlight mining region *and* Geology and mineralization of the Cooke City mining district *by* J.E. Elliott, *and a section on* Aeromagnetic survey *by* D.L. Peterson: U.S. Geological Survey Bulletin 1447, 101 p.

Rose, A.W., Hawkes, H.E., and Webb, J.S., 1979, Geochemistry in mineral exploration: New York, Academic Press, 657 p.

Rowe, J.J., Fournier, R.O., and Morey, G.W., 1973, Chemical analysis of thermal waters in Yellowstone National Park, Wyoming, 1960–65: U.S. Geological Survey Bulletin 1303, 31 p.

Shannon, S.S., Jr., 1982, Geochemical provenance of anomalous metal concentrations in stream sediments in the Ashton 1:250,000 quadrangle, Idaho/Montana/Wyoming, *in* Reid, S.G., and Foote, D.J, eds., Geology of Yellowstone Park Area: Wyoming Geological Association Guidebook, 33rd Annual Field Conference, Mammoth Hot Springs, Wyo., September 1982, p. 323–333.

Shannon, S.S., Jr., Sandoval, W.F., Gallimore, D.L., Hansel, J.M., Hensley, W.K., Pritle, June, and Macdonell, C.J., 1980, Uranium hydrogeochemical and stream sediment reconnaissance data release for the Ashton NTMS quadrangle, Idaho/Montana/Wyoming, including concentrations of forty-two additional elements: Los Alamos, N. Mex., Los Alamos Scientific Laboratory Informal Report LA-8009-MS, 166 p. [*Reissued as* U.S. Department of Energy Report GJBX-189(80), Grand Junction, Colo.].

Shupe, J.L., Olson, A.E., Peterson, H.B., and Low, J.B., 1984, Fluoride toxicosis in wild ungulates: Journal American Veterinary Medical Association, v. 185, no. 11, p. 1295–1300.

Simons, F.S., Armbrustmacher, T.J., Van Noy, R.M., Zilka, N.T., Federspiel, F.E., and Ridenour, James, 1979, Mineral resources of the Beartooth Primitive Area and vicinity, Carbon, Park, Stillwater, and Sweet Grass Counties, Montana, and Park County, Wyoming: U.S. Geological Survey Bulletin 1391-F, 125 p.

Sonderegger, J.L., and Ohguchi, Takeshi, 1988, Irrigation related arsenic contamination of a thin alluvial aquifer, Madison River Valley, Montana, U.S.A.: Environmental Geology and Water Sciences, v. 11, no. 2, p. 153–161.

Speidel, D.H., and Agnew, A.F., 1982, The natural geochemistry of our environment: Boulder, Colo., Westview Press, 214 p.

Stauffer, R.E., Jenne, E.A., and Ball, J.W., 1980, Chemical studies of selected trace elements in hot-spring drainages of Yellowstone National Park: U.S. Geological Survey Professional Paper 1044-F, 20 p.

Taylor, S.R., 1964, Abundance of chemical elements in the continental crust; a new table: Geochimica et Cosmochimica Acta, v. 28, p. 1273–1285.

Taylor, R.L., Ashley, J.M., Locke, W.W., Hamilton, W.L., and Erickson, J.B., 1989, Geologic map of Yellowstone National Park: Bozeman, Montana State University, Department of Earth Sciences, approximate scale 1:240,000.

Taylor, S.R., and McLennan, S.M., 1995, The geochemical evolution of the continental crust: Reviews of Geophysics, v. 33, no. 2, p. 241–265.

Thompson, J.M., and DeMonge, J.M., 1996, Chemical analyses of hot springs, pools, and geysers from Yellowstone National Park, Wyoming, and vicinity, 1980–1993: U.S. Geological Survey Open-File Report 96-68, 65 p.

Thompson, J.M., and Hutchinson, R.A., 1981, Chemical analyses of waters from the Boundary Creek thermal area, Yellowstone National Park, Wyoming: U.S. Geological Survey Open-File Report 81-1310, 14 p.

Thompson, J.M., and Yadov, Sandhya, 1979, Chemical analyses of waters from geysers, hot springs, and pools in Yellowstone National Park, Wyoming, from 1974 to 1978: U.S. Geological Survey Open-File Report 79-704, 48 p.

Thompson, J.M., Presser, T.S., Barnes, R.B., and Bird, D.B., 1975, Chemical analysis of the waters of Yellowstone National Park, Wyoming, from 1965 to 1973: U.S. Geological Survey Open-File Report 75-25, 58 p.

U.S. Geological Survey, 1972, Geologic map of Yellowstone National Park: U.S. Geological Survey Miscellaneous Geologic Investigations Map I-711, scale 1:125,000.

Wedow, Helmuth, Jr., Gaskill, D.L., Bannister, D'A.P., and Pattee, E.C., 1975, Mineral resources of the Absaroka Primitive Area and vicinity, Park and Sweet Grass Counties, Montana, *with a section on* Interpretation of geophysical data *by* D.L. Peterson: U.S. Geological Survey Bulletin 1391-B, 115 p.

White, D.E., Hutchinson, R.A., and Keith, T.E.C., 1988, The geology and remarkable thermal activity of Norris Geyser Basin, Yellowstone National Park, Wyoming: U.S. Geological Survey Professional Paper 1456, 84 p.

Wilson, A.B., and Elliott, J.E., compilers, 1997, Geologic maps of western and northern parts of Gallatin National Forest, south-central Montana: U.S. Geological Survey Miscellaneous Geologic Investigations Map I-2584, scale 1:126,720.

Winston, P.W., Hoffman, L., and Smith, W., 1973, Increased weight loss in molybdenum-treated rats in the cold, *in* Hemphill, D.D., ed., Trace substances in environmental health-VII: Columbia, University of Missouri, Proceedings of the 7th annual conference on trace substances in environmental health, June 1973, p. 241–244.

Geochemical Data for Selected Rivers, Lake Waters, Hydrothermal Vents, and Subaerial Geysers in Yellowstone National Park, Wyoming and Vicinity, 1996–2004

By Pamela A. Gemery-Hill, Wayne C. Shanks, III, Laurie S. Balistrieri, and Gregory K. Lee

Chapter L *of*
Integrated Geoscience Studies in the Greater Yellowstone Area—Volcanic, Tectonic, and Hydrothermal Processes in the Yellowstone Geoecosystem
Edited by Lisa A. Morgan

Professional Paper 1717

U.S. Department of the Interior
U.S. Geological Survey

Contents

Abstract 367
Introduction 367
Study Area 368
Methods 368
    Field Methods 368
    Laboratory Methods 371
Results 373
Summary 377
Acknowledgments 379
References Cited 379

Figures

1. Map showing Yellowstone National Park with sampling areas 369
2. Detailed map of Yellowstone Lake with sample locations 370
3–6. Maps showing sample locations in:
    3. Norris Geyser Basin 375
    4. Heart Lake Geyser Basin 376
    5. Gibbon and Monument Geyser Basins area 377
    6. Turbid Lake area 378

Table

1. Analytical methods 372

Appendixes

1. Creeks and water-column profiles 382
2. Hydrothermal vents in Yellowstone Lake 398
3. 1999 mixing experiments 409
4. Subaerial hydrothermal features 419

Geochemical Data for Selected Rivers, Lake Waters, Hydrothermal Vents, and Subaerial Geysers in Yellowstone National Park, Wyoming and Vicinity, 1996–2004

By Pamela A. Gemery-Hill,[1] Wayne C. Shanks, III,[1] Laurie S. Balistrieri,[2] and Gregory K. Lee[1]

Abstract

Analyses of more than 400 water samples collected from creeks and rivers draining into Yellowstone Lake, hydrothermal vents and water-column profiles within Yellowstone Lake, and subaerial hot springs and geysers throughout Yellowstone National Park (the Park) are reported. The samples were collected from 1996 to 2004. All of the water samples were collected and analyzed as part of the USGS Mineral Resources Program Project, Integrated Geoscience Studies of the Greater Yellowstone Area. Goals of this study are to provide state-of-the-art chemical determinations of more than 45 elements and species to help understand the influences of hydrothermal processes within Yellowstone National Park.

Hydrothermal vents within Yellowstone Lake were sampled during 1996–2004. Sampling of creeks contributing to Yellowstone Lake began in 1997 and continued through 1999. Four water-column profiles were collected within Yellowstone Lake in both 1997 and 1998. Water samples were collected from subaerial geysers and hot springs throughout Yellowstone National Park during 1998–2002.

In 1999, mixing experiments were conducted using water samples collected from four subaerial hot springs: three in Norris Geyser Basin and one at West Thumb Geyser Basin. These thermal-water samples were mixed with Yellowstone Lake water to simulate processes at sublacustrine vents and to evaluate conservative–nonconservative behavior of elements during mixing. The results of these experiments are discussed in Balistrieri and others (this volume), and the full data sets are presented here.

The data reported in this paper clearly show the influence of hydrothermal processes on waters within Yellowstone National Park. Yellowstone Lake hydrothermal-indicator elements (As, B, Cl, Cs, Cu, Ge, Hg, Li, Mo, Sb, and W) as defined by Balistrieri and others (this volume) delineate areas of hydrothermal influx. The differences in the levels of these elements between the creek data and water-column profiles indicate an influx of hydrothermal water within Yellowstone Lake. The water-column samples have higher values of the hydrothermal-indicator elements than the creeks flowing into the lake; therefore significant input of hydrothermal-indicator elements from the hydrothermal vents within the lake is indicated.

There are large variations in the values of the indicator elements among vents in Yellowstone Lake. The values of the hydrothermal-indicator elements are elevated for all of the vent samples, but a group of the West Thumb vents contain the highest values. This could indicate more active vents and (or) less mixing with lake water during sampling or during ascent to the lake floor. The subaerial features in the Park also show considerable variations in the values of the indicator elements. Some thermal features in the Park, such as Porkchop and Green Dragon Geysers in Norris Geyser Basin, have highly elevated hydrothermal-indicator-element values, while other features have values similar to Yellowstone Lake water, which is 99 percent meteoric water. These differences must reflect varying amounts of hydrothermal activity and input in these areas.

Introduction

Yellowstone National Park (the Park) was first designated as a National Park in 1872 for its scenic beauty and spectacular hydrothermal activity. Ten thousand thermal features and 300 geysers in the more than 2-million-acre park represent over half of the Earth's known hydrothermal

[1]U.S. Geological Survey, Box 25046, MS 973, Denver Federal Center, Denver, CO 80225.

[2]U.S. Geological Survey, University of Washington, School of Oceanography, Box 357940, Seattle, WA 98195.

features and provide unique opportunities for research. Gooch and Whitfield (1888) were the first to carry out chemical analyses of thermal and surficial waters, and Allen and Day (1935) did the first extensive work. Beginning in the 1960s, the intensity of aqueous geochemical studies in Yellowstone has steadily increased (Ball, Nordstrom, Cunningham, and others, 1998; Ball, Nordstrom, Jenne, and Vivit, 1998; Ball and others, 2001, 2002; Balistrieri and others, this volume; Fournier, 1989; Kharaka and others, 1991, 2000; Thompson and others, 1975; Thompson and Yadav, 1979; Thompson and DeMonge, 1996; White and others, 1970, 1971, 1988). However, the development and widespread use of inductively coupled plasma (ICP) spectrographic methods in the late 1980s and early 1990s has led to a renaissance in trace-element geochemistry, with many more elements determined than by previous methods. For example, Balistrieri and others (this volume) have clearly shown that Mo and W are important geothermal elements, whereas most previous studies did not analyze for these elements. Balistrieri and others (this volume) conclude that As, B, Cl, Cs, Cu, Ge, Hg, Li, Mo, Sb, and W are important geothermal elements based on enrichments in Yellowstone Lake waters and in sublacustrine vent fluids. Shanks and others (this volume) would also include Tl, which is enriched in siliceous sinter deposits related to sublacustrine vents.

In the present study, water samples were collected from various sources throughout Yellowstone National Park and were analyzed for a suite of chemical components and stable-isotopic compositions to provide a basic understanding of the influences of hydrothermal processes on the water, sediments, and biota of Yellowstone Lake and surrounding areas. This report summarizes data on the geochemistry of water samples collected from creeks and rivers draining into and out of Yellowstone Lake, hydrothermal vents and water-column profiles within Yellowstone Lake, and subaerial geysers and hot springs throughout the Park. These different sources of water all contribute valuable information to the water chemistry in Yellowstone Lake and the Park as a whole. Sample locations, methods for collecting and analyzing the water samples, and analytical results are reported.

Study Area

All of the samples reported here were collected in Yellowstone National Park, which is situated in the northwest corner of Wyoming. The samples were collected throughout the Park concentrating around Yellowstone Lake and major hydrothermal areas, but with some lesser known hydrothermal areas also included (fig. 1).

Methods

Field Methods

Because very few water-quality data or discharge measurements were available for surface water flow into Yellowstone Lake, samples were collected during July 1997, August–September 1998, and July 1999 from the major streams that enter the lake (fig. 2). Locations were obtained by global positioning satellite (GPS), and the temperature and pH of the water were determined at each site. Point-source or integrated water samples were collected in 500-mL polyethylene bottles and brought to a field-based laboratory for processing. The bottles had been acid-washed and well rinsed with distilled, deionized water before use.

Estimates of stream discharge were made by timing floats and determining the cross-sectional area of the stream (in 1998) or by measuring the flow rate at 1 to 20 locations in a cross section of the stream using a velocity meter (in 1999). The accuracy of the flow estimates varied between years and sampling sites because different individuals used different methods at different times and because some streams could not be waded. Balistrieri and others (this volume) utilized these flow measurements to calculate a chemical mass balance for Yellowstone Lake and assess chemical fluxes. Because the U.S. Geological Survey (USGS) gages the Yellowstone River at its outlet from the lake (station 06186500), continuous discharge measurements from this site are available (http://waterdata.usgs.gov, accessed 5/18/04). Outflows from the lake during our sampling periods were 52 ± 3 and 156 ± 9 m^3/s in 1998 and 1999, respectively. Balistrieri and others (this volume), by comparing total fluxes into the lake from as many as 44 streams, changes in lake level, and flux out of the lake at Fishing Bridge, were able to calculate a total error for all the stream-flow measurements of ±22 percent relative to the measured flow at the gaging station.

Hydrothermal vent samples for this study were collected in the West Thumb, Mary Bay, and Stevenson Island areas (fig. 2). The West Thumb vent samples were from two shallow ($\leq$5 m deep) vents and several vent fields at depths of 29–53 m. Shallow vent fluids from Mary Bay were collected near the shore off Steamboat Point and near Pelican Creek at depths of 7–10 m. Hydrothermal fluids were also collected from a deep hole in Mary Bay at depths of 48–54 m. Samples collected near Stevenson Island were from the deepest vents (95–110 m) in Yellowstone Lake.

All vent samples were collected with a submersible remotely operated vehicle (ROV) designed and piloted by Dave Lovalvo of Eastern Oceanics, Inc. Klump and others (1992) described an early version of that vehicle. Although the exact configuration of the vehicle varied from year to year, it always collected vent-fluid samples using piston-operated plastic syringes that were connected by

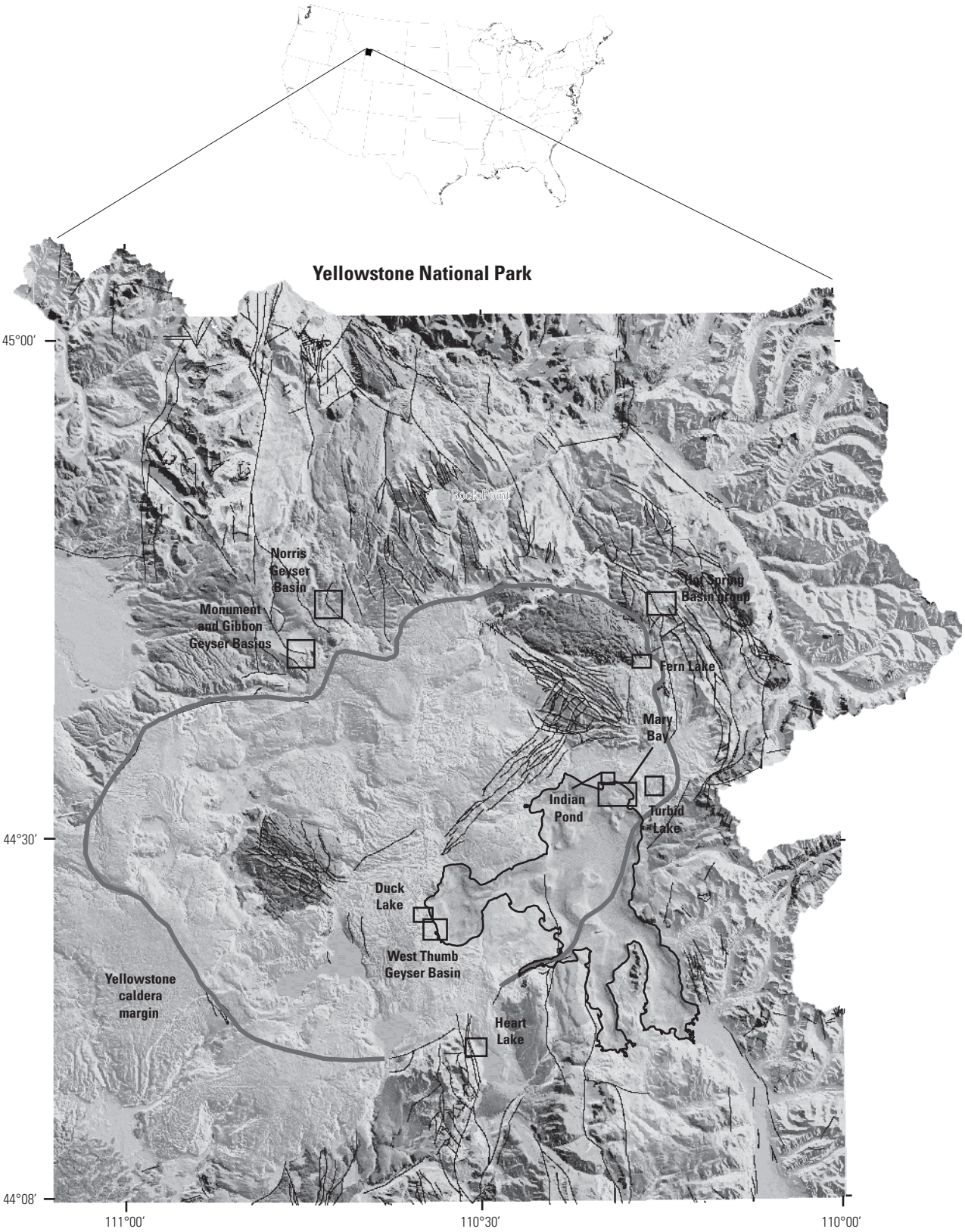

Figure 1. Map of Yellowstone National Park showing topography, faults (narrow black lines), and the caldera margin. Areas where multiple samples were collected are outlined with black rectangles and labeled accordingly.

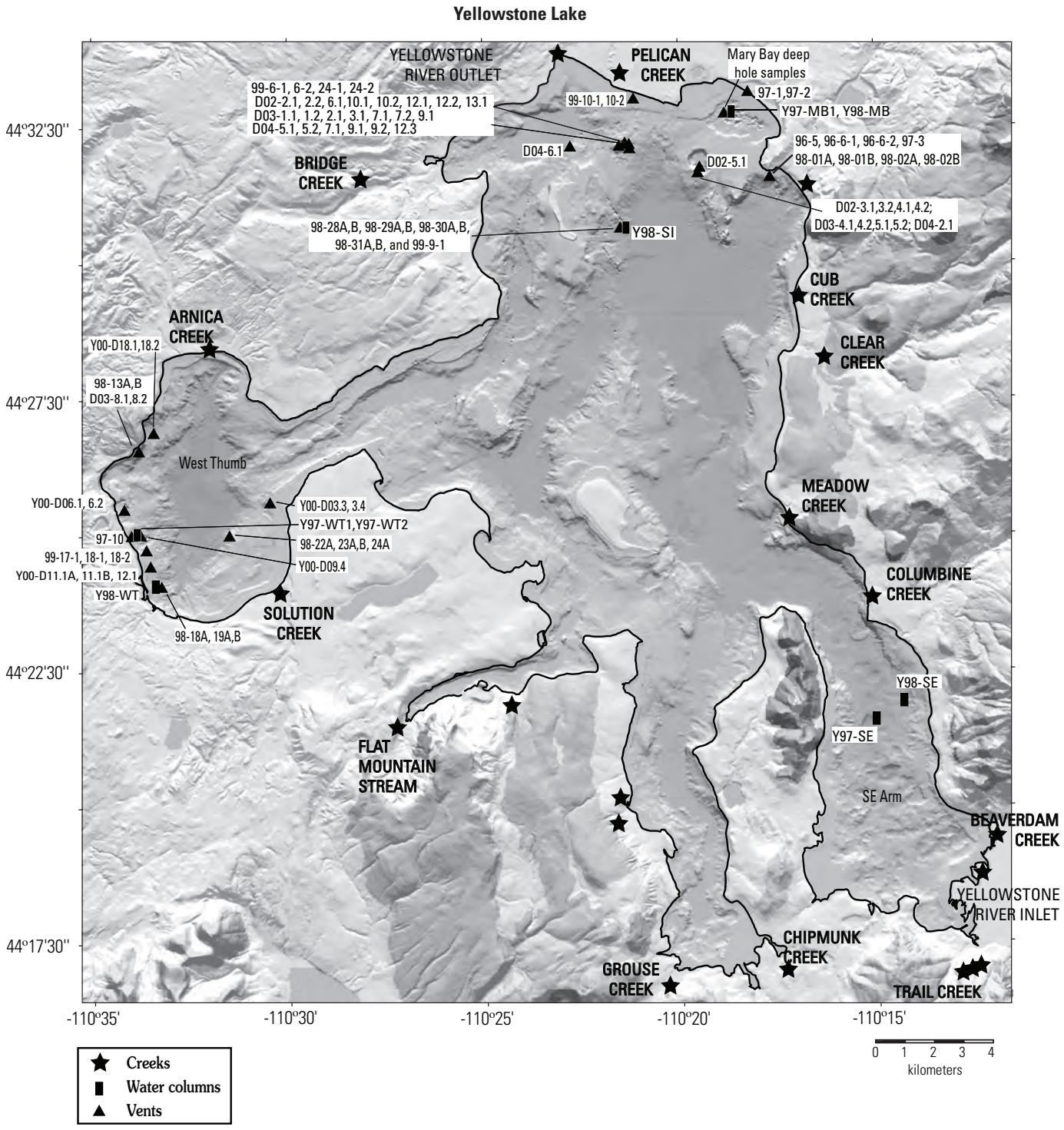

Figure 2. Detailed map of Yellowstone Lake with new bathymetry (see Morgan and others, this volume) showing locations of creeks and samples of water-column profiles and vents. Sampled from 1996–2004.

polypropylene tubing to an articulated and extendible probe. The temperature of each vent was continuously monitored during sample collection, and the probe was maintained in position by remotely maneuvering the submersible while making video observations in the control room of the support boat. After retrieval of the ROV, samples were transferred through 3-way valves from the syringes on the vehicle into other syringes for biological and chemical measurements. The vent samples were returned to the field-based laboratory for processing.

Samples from different depths in the water column of Yellowstone Lake were collected in Southeast Arm, West Thumb, and Mary Bay in July 1997 and 1998 and near Stevenson Island in July 1998 (fig. 2) using a trace-metal-clean hydrobottle (no internal cords) attached either to a Kevlar line, a Hydrolab cable, or the hydrowire on the research boat. All wire types produced consistent results with no evidence of contamination for the elements of interest. The water-column samples in Mary Bay were collected directly above the vents in the deep hole in Mary Bay. The water-column samples near Stevenson Island and from West Thumb were collected close to, but not directly above, known hydrothermal vents. Water-column samples from Southeast Arm were collected at least 10 km from any known hydrothermal vents. Water-column samples were placed in 500-mL acid-cleaned and well-rinsed polyethylene bottles on board the boat and returned to the field-based laboratory. In-place measurements of temperature, pH, conductivity, redox potential, and dissolved oxygen concentrations in the water column were made as a function of depth, using a Hydrolab, prior to collection of water samples. Those profiles were used to determine the depths for collection of water samples and to confirm that the entire water column was oxygenated at every site.

A large-volume (20 L) sample from the Yellowstone River at its outlet from Yellowstone Lake (near Fishing Bridge) (fig. 2) was collected in a low-density polyethylene container in July 1999. The sample was collected using Teflon tubing, an in-line 0.45-µm nylon-filter capsule, and a peristaltic pump. The sample was returned to the field-based laboratory for processing and for use in the mixing experiments described below.

Water samples from two subaerial geysers were collected from West Thumb Geyser Basin (Black Pool and Vandalized Pool) in September 1998. They were immediately filtered on-site using a 0.45-µm nylon filter. During July 1999, water samples were collected from three subaerial geysers in Norris Geyser Basin (Green Dragon, Echinus, and Porkchop Geysers) and from Black Pool at West Thumb Geyser Basin using a peristaltic pump with Teflon tubing and an in-line 0.45-µm nylon-filter capsule. These particular geysers were chosen because they are indicative of the spectrum of hydrothermal fluids observed in the Park. Water samples from Porkchop, Black Pool, and Vandalized Pool are neutral to alkaline and Cl-rich. The hydrothermal fluids from Green Dragon and Echinus are acidic and enriched in SO_4 and Cl. Geyser waters collected in 1999 were immediately mixed with filtered water collected from the Yellowstone Lake outlet at Fishing Bridge in 500-mL polyethylene bottles in proportions ranging from 10- (samples G1–W1) to 100-percent (samples G10–W10) geyser water. The temperatures of the mixtures were maintained by insulating the bottles. The samples were processed at the field-based laboratory less than 2 hours after mixing.

Water samples from many subaerial geysers throughout Yellowstone National Park were collected from 1998 through 2002. The samples generally were collected from the center or most active upwelling area of the geyser pools using an extendable, rigid sampling device. Temperature and pH were measured on site. Samples YNP-00-528.1 and 528.5 are duplicate water samples from an acidic Monument Geyser Basin hot spring. These duplicate samples were used to test for contamination related to an extendible aluminum sampling tool, which we use to place our polyethylene sampling bottles in the hottest portion of the spring. Sample 528.1 was collected using the sampling tool, whereas sample 528.5 was collected from the same spot using a polyethylene bottle on nylon line. Comparison of the data from these 2 samples (see appendix 4) indicates that the sampler is noncontaminating.

Laboratory Methods

Values of pH of vent fluids, water-column samples, and mixed solutions were determined at the field-based laboratory after standardizing a pH meter and electrode using six buffer solutions ranging from pH 1.68 to 10. Subsamples of all water samples were taken for analysis of dissolved elements, Hg, anions, oxygen-isotope values ($\delta^{18}O$), hydrogen isotope values (δD), and either alkalinity or dissolved inorganic carbon. Subsamples of water for sulfur isotopes of sulfide and sulfate ($\delta^{34}S_{H_2S}$, $\delta^{34}S_{SO_4}$) were collected where sufficient water was available. Samples for anion and dissolved-element determinations were obtained by filtering the water through 0.45-µm disposable nylon filters into new polyethylene bottles for anions; into acid-washed, well-rinsed polyethylene bottles for dissolved elements; and into acid-washed glass bottles with Teflon caps for Hg. Samples for dissolved Hg analyses were preserved with Ultrex concentrated HNO_3, saturated with sodium dichromate, to prevent volatilization of Hg. Anion samples were kept cool prior to analysis, whereas samples to be analyzed for dissolved elements were preserved by adding one drop of redistilled concentrated nitric acid per 10 mL of sample solution. Anion analyses of vent and water-column samples from 1996–1999 were by ion chromatography at the field-based laboratory. Anion analyses of all other water samples were by ion chromatography in the USGS laboratories in Denver, Colo. (Theodorakos, 2002). Dissolved elements were determined at the USGS laboratories in Denver, using inductively coupled plasma–atomic

Table 1. Analytical methods.

Descriptor	Method	Species determined (reported)	Equipment used	References or comments
ICP-MS	Inductively coupled plasma–mass spectrometry	Ag, Al, As, Au, Ba, Be, Bi, Ca, Cd, Ce, Co, Cr, Cs, Cu, Dy, Er, Eu, Fe, Ga, Gd, Ge, Hf, Ho, In, K, La, Li, Mg, Mn, Mo, Na, Nb, Nd, Ni, P, Pb, Pr, Rb, Re, Sb, Sc, Se, SiO_2, Sm, Sn, Sr, Ta, Tb, Te, Th, Ti, Tl, Tm, U, V, W, Y, Yb, Zn, Zr	Perkin Elmer Elan 6000 inductively coupled plasma–mass spectrometer	Lamothe and others (2002)
ICP-AES	Inductively coupled plasma–atomic emission spectrometry	B, Ca, K, Mg, Na	Perkin Elmer Optima 3000 simultaneous inductively coupled plasma–atomic emission spectrometer	Briggs (2002)
IC-Aq	Ion chromotography	F^-, Cl^-, NO_3^-, SO_4^{2-}	Dionex Model 2021 or equivalent, guard column AG4A or equivalent, separator column AS4A or equivalent, Dionex anion fiber suppressor (AFS-1) or Dionex micromembrane suppressor (AMMS-1)	Theodorakos (2002)
Hg-CVAFS	Mercury by cold vapor atomic fluorescence spectroscopy	Hg	Lachat QuikChem mercury analyzer with fluorescence detector	Hageman (2002)
ISO1	Oxygen isotopes	$\delta^{18}O$	MultiPrep coupled to a Micromass Optima isotope ratio mass spectrometer	Online method adapted from offline method in Epstein and Mayeda (1953)
ISO2	Hydrogen isotopes	δD	Finnigan MAT 252 isotope ratio mass spectrometer	Kendall and Coplen (1985)
ISO3	Sulfur isotopes on sulfide materials	$\delta^{34}S_{H_2S}$	Carlo Erba NC2500 elemental analyzer coupled to a Micromass Optima isotope ratio mass spectrometer	Giesemann and others (1994)
ISO4	Sulfur isotopes on sulfate materials	$\delta^{34}S_{SO_4}$	Carlo Erba NC2500 elemental analyzer coupled to a Micromass Optima isotope ratio mass spectrometer	Giesemann and others (1994)
ISO5	Carbon isotopes of dissolved total carbonate	$\delta^{13}C_{CO_3}$	A Matt Emmons acid injection multiprep device coupled to a Micromass Optima isotope ratio mass spectrometer	McCrea (1950). There is no reference for the Matt Emmons acid injection device. It consists of a heating block held at 90°C and an autosampler with a double needle that evacuates, injects acid, and then samples the evolved gas.

emission spectrometry (ICP–AES) for major ions and B (Briggs, 2002), inductively coupled plasma–mass spectrometry (ICP–MS) for minor elements (Lamothe and others, 2002), and cold vapor-atomic fluorescence spectroscopy (CVAFS) for Hg (Hageman, 2002).

Water samples for oxygen and hydrogen isotope analyses were placed in 20-mL glass scintillation vials, tightly capped, and analyzed at the USGS laboratories in Denver by isotope ratio mass spectrometry. Water samples were prepared for hydrogen-isotopic analyses using the Zn-reduction technique (Kendall and Coplen, 1985) and for oxygen-isotope analyses using an automated CO_2 equilibration technique (adapted from Epstein and Mayeda, 1953). Values of $\delta^{18}O$ and δD are relative to Vienna Standard Mean Ocean Water (VSMOW); they have reproducibility of approximately 0.2 and 1.0 per mil, respectively. Water samples for sulfur isotope analyses were initially collected in 40-mL glass vials with septa caps, but the 40-mL vials were replaced by 250-mL bottles with septa caps in 2003. The 250-mL bottles also allowed the determination of carbon isotope values of dissolved total carbonate ($\delta^{13}C_{CO_3}$). All water samples for sulfur and carbon isotopes were analyzed at the USGS laboratories in Denver by isotope ratio mass spectrometry following precipitation of Ag_2S from H_2S, $BaSO_4$ from dissolved total SO_4, and $BaCO_3$ from dissolved total CO_3. Sulfur-isotope analyses were performed by combustion using continuous flow techniques described by Giesemann and others (1994). Carbon-isotope analyses were performed by using an on-line acid-digestion method similar to the off-line method described by McCrea (1950). Values of $\delta^{34}S_{H_2S}$ and $\delta^{34}S_{SO_4}$ are relative to the standard Canyon Diablo troilite (CDT) with reproducibility of 0.2 per mil. Values of $\delta^{13}C_{CO_3}$ are relative to Vienna Peedee belemnite (VPDB); they have reproducibility of 0.1 per mil or better.

Alkalinity was determined using either a Chemetrics test kit (hot spring and stream samples) or by Gran titration (Stumm and Morgan, 1996) at the field-based laboratory (water-column and mixing-experiment samples). Dissolved total inorganic carbon content of vent fluids and water-column samples was determined by flow-injection analyses at the field-based laboratory. Table 1 provides a summary of the analytical methods.

Blank samples using distilled, deionized water were included with each batch of 20 samples. The blank samples had element concentrations below detection limits. Standard reference solutions, either from the USGS or from the National Institute of Standards and Technology, were included in each batch of samples. The standards, as well as duplicates of samples, were used to determine accuracy and precision of the analyses.

Results

Appendixes 1–4 tabulate the geochemical data discussed here and in Balistrieri and others (this volume). Each table contains detailed site data and water analyses. The data in this chapter are reported in mass/volume units, which provide a convenient conversion for the data in Balistrieri and others (this volume) that are reported in mol/volume units. Abbreviations for the methods (column 3) correspond to those listed in table 1. Blanks in the data fields exist because not all samples were analyzed by each method, and there were variations in the elements detected by ICP-MS. Samples within each table are sorted by location and then by sample collection date. Longitude and latitude in these tables and in figures 1–6 are referenced to the Clarke 1866 spheroid and North American 1927 datum.

Appendix 1 contains data for the water-column profiles and the creeks flowing into Yellowstone Lake. The pH values range from 2.5 to 8.5, with the majority of samples being in the neutral range (6.5 –7.5). Approximately neutral pH values are expected for samples of fresh water, whereas low values generally reflect hydrothermal influences related to oxidation of H_2S to produce H_2SO_4.

The values for boron and the major cations (Ca, K, Mg, Na) are highly variable. Boron values in the creeks range from <10 to 960 µg/L, with the majority of the values being <10 µg/L. Pelican Creek and Sedge Creek are the sources of the highest values for B (960 µg/L and 650 µg/L, respectively). The range in B values for the water-column data is <10 to 130 µg/L, with the bulk of the values between 50 and 100 µg/L. Boron is a hydrothermal-indicator element (Balistrieri and others, this volume). Therefore, B concentrations in Pelican Creek, Sedge Creek, and the water-column profiles indicate hydrothermal input.

Calcium values in both the creek data and water-column profiles are generally less than 10 mg/L. Potassium is low in both the creek and water-column samples. The highest K value for the creek data is 11 mg/L; in the water-column data, the highest value is 4.3 mg/L (MB-1). Magnesium values range from 1 to 50 mg/L in the creeks; most of the samples have values under 10 mg/L. The majority of the water-column data show a Mg range of 1.9 to 2.5 mg/L. Sodium values in the creek data are generally less than 10 mg/L, and the highest value is 41 mg/L (Pelican Creek). The majority of the water-column data have Na values between 6 and 10 mg/L.

In general, the values of the hydrothermal-indicator elements B, As, Cl, Cs, Cu, Ge, Li, Mo, Sb, and W show an increase from the creek data to the water-column-profile data, indicating that these elements are added within the lake from hydrothermal vents on the lake bottom (Balistrieri and others, this volume). This pattern is evident in appendix1 when comparing these elements between the creek and water-column data. For As, Cl, Cs, Mo, Sb, and W, the majority of the creek data have values very close to the

lower limit of determination, whereas the water-column data have higher values. The values of these hydrothermal-indicator elements in the water-column data are not excessive, only generally higher than the creek data, indicating an addition of these elements from within the lake. A few of the creek samples, such as Pelican Creek and Sedge Creek, have values more consistent with or higher than the water-column data. There are higher values of Li in both the creek and water-column data than the other indicator elements. In the creek data, the Li values range from <0.1 to 190 µg/L, but the majority of the values are less than 20 µg/L. Some of the creek data have values in the 30–60 µg/L range, which is the same range as the water-column data.

The data from hydrothermal vents within Yellowstone Lake are presented in appendix 2. The range in pH values is 4.9 to 8.6. Boron is elevated in some of the vent samples, ranging from 35 to 730 µg/L. The highest value is from a West Thumb vent (sample 98-19a). Values for Ca range from 3.2 to 23 mg/L. The range in values of K and Mg is fairly narrow, <1 to 3.9 mg/L. Sodium values range from 6.0 to 160 mg/L, but the highest value is an anomaly. The majority of Na values are 7–10 mg/L.

West Thumb samples have higher values of most or all of the hydrothermal-indicator elements than other sublacustrine vent areas. Samples 96-2-6a, 97-10, 98-19a, YNP-99-17-1, Y00-D06.1, Y00-D06.2, and Y00-D09.4 have the highest hydrothermal-indicator-element values. Most vent samples have As values between 3.7 and 54 µg/L, but the West Thumb group listed above has values from 72 to 210 µg/L. Chlorine values in the majority of the vent samples range from 3 to 8 mg/L. Chlorine values greater than 23 mg/L are found only in West Thumb samples. The values of Cs for the bulk of the vent samples are less than 10 µg/L. All Cs values above 16 µg/L are West Thumb samples. Li values are quite high in some of the West Thumb samples, ranging from 110 to 1,200 µg/L. The majority of the rest of the vent samples have Li values between 34 and 77 µg/L. Two samples from Elliot's Crater rim (D02-3.2, D02-4.2) have Li values greater than 100 µg/L. Values for Mo are low in most vent samples, with a range of 0.04 to 7.5 µg/L. The highest Mo values (12–36 µg/L) are seen in a few of the West Thumb samples. The range in Sb values for the majority of the vent samples is <0.02–2.6 µg/L. The West Thumb samples listed above have Sb values from 4.2 to 400 µg/L. The values of W in the bulk of the vent samples are low, ranging from 1.0 to 6.4 µg/L. Any values of W greater than 6.4 µg/L correspond to West Thumb samples.

Appendix 3 presents data from the 1999 mixing experiments. The locations of the three geysers sampled from Norris Geyser Basin (Echinus, Green Dragon, and Porkchop) are shown in figure 3. The four geysers used in the mixing experiments were chosen because they represent the spectrum of hydrothermal fluids found in Yellowstone Park. Green Dragon and Echinus Geysers were chosen as the acidic, SO_4- and Cl-rich end member and have pH values of 2.6 and 3.2, respectively. Porkchop Geyser and Black Pool (West Thumb Geyser Basin) represent the neutral to alkaline, Cl-rich end member. Porkchop and Black Pool have pH values of 6.6 and 7.9, respectively.

The geyser waters were mixed with Yellowstone Lake water in varying amounts, so in appendix 3, samples G1, E1, P1, and W1 represent 10-percent geyser water and 90-percent lake water, and G10, E10, P10, and W10 are pure geyser water. Therefore the data in each of the series, progressing from 1 to 10, reflects the increase in geyser water, in 10-percent increments.

Boron is highly enriched in all four of the geyser waters (78–9,360 µg/L); therefore an increase in the value of B is seen in the progression from sample 1 through 10 for each mixing experiment. Calcium, with values from 0 to 5 mg/L, either decreases as geyser water increases or just fluctuates (Porkchop). Magnesium values also decrease through the mixing experiments. The values of K and Na increase with increasing amounts of geyser water. Sodium is quite enriched in the geyser waters, ranging from 159 to 406 mg/L.

Most of the hydrothermal-indicator elements are elevated in the geyser waters as is expected for hydrothermal features. Therefore enrichment in the values of the indicator elements increases as the amount of geyser water increases. The Echinus mixing experiment is the exception for the elements Mo, Sb, and W. The values of these three elements either fluctuate or decrease slightly through the Echinus mixing experiment, indicating similarities in the values of these elements between the lake outflow water and Echinus Geyser.

The As values range from 300 to 2,900 µg/L, Cl from 150 to 660 mg/L, and Cs from 81 to 500 µg/L. Values of Li are the highest of the hydrothermal-indicator-element values, varying from 1,000 to 7,000 µg/L. Molybdenum, Sb, and W are less elevated with ranges of 6.1–240 µg/L, 0.64–130 µg/L, and 5.8–350 µg/L, respectively. Of the four geysers sampled, Echinus Geyser has the lowest values for all hydrothermal-indicator elements. Porkchop Geyser has the highest values for As, Cl, Cs, Li, Mo, and Sb. The highest values for W are from Black Pool.

Data from subaerial features in Yellowstone National Park are summarized in appendix 4. The pH values range from 1.1 to 9.9. Boron values are high for many of the subaerial samples, which is consistent with B being a hydrothermal-indicator element. The range in B values is <10 to 9,360 µg/L. Values for Ca and K range from 1 to 60 mg/L. Magnesium values show the narrowest range, varying from <0.1 to 18 mg/L. Sodium values range from <0.1 to 430 mg/L.

The ranges in the values of the hydrothermal-indicator elements for the subaerial samples are fairly wide and highly variable between samples, even within the same area. The values of As range from 0.4 to 3,100 µg/L. The values of Cl and Cs vary from <0.08 to 660 mg/L and from 0.01 to 580 µg/L, respectively. Lithium values show the larg-

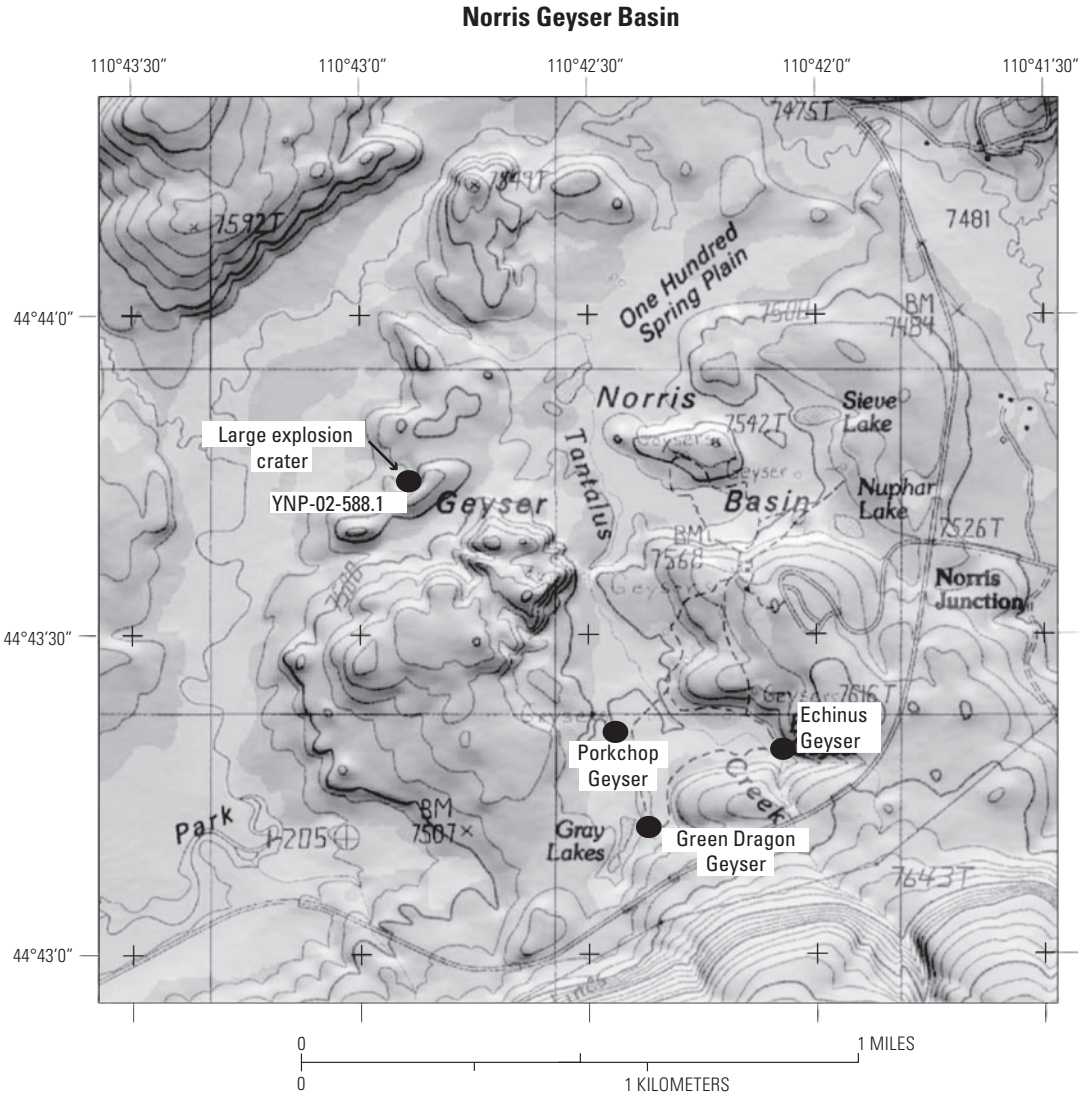

Figure 3. Map of the Norris Geyser Basin area showing sample locations of geysers and explosion crater. Echinus, Green Dragon, and Porkchop Geysers were sampled multiple years including 1999 for the mixing experiments.

est range, with a variation from 0.9 to 10,000 µg/L. The ranges in values for Mo, Sb, and W are smaller than the other indicator elements. Molybdenum values vary from <0.02 to 290 µg/L, whereas the range in Sb values is from <0.02 to 160 µg/L. Values of W vary from 0.2 to 390 µg/L. The variability in the data from the subaerial samples is related to the amount of hydrothermal influence in the samples. The four geysers used in the mixing experiments are also included in appendix 4 because they were sampled at other times unrelated to the mixing experiments. Porkchop Geyser has the highest values for As, B, Cl, Cs, Cu, Ge, Hg, Li, Mo, and Sb, and values of W are highest in Black Pool. The Heart Lake area has some samples with high levels of hydrothermal-indicator elements. Other areas sampled have lower levels of the indicator elements suggesting weaker hydrothermal activity. The differences in the hydrothermal-indicator elements could also be related to water sources and perhaps can help in source-water studies.

The geysers of Norris Geyser Basin reflect the spectrum of hydrothermal fluids found in Yellowstone National Park. Four geysers were sampled in Norris Geyser Basin (fig. 3)—three along the southern boardwalk of Back Basin and one in a large explosion crater to the west of Porcelain Basin. Both acidic and neutral to alkaline fluids are found in the geysers in Norris Geyser Basin. Porkchop Geyser has a neutral pH and very high values of the hydrothermal-indicator elements. Echinus Geyser is acidic and has much lower hydrothermal-indicator-element values than Porkchop.

Heart Lake Geyser Basin is shown in figure 4. Two geysers were sampled in both the Rustic Geyser area and a central geyser area. One geyser from the upper basin was

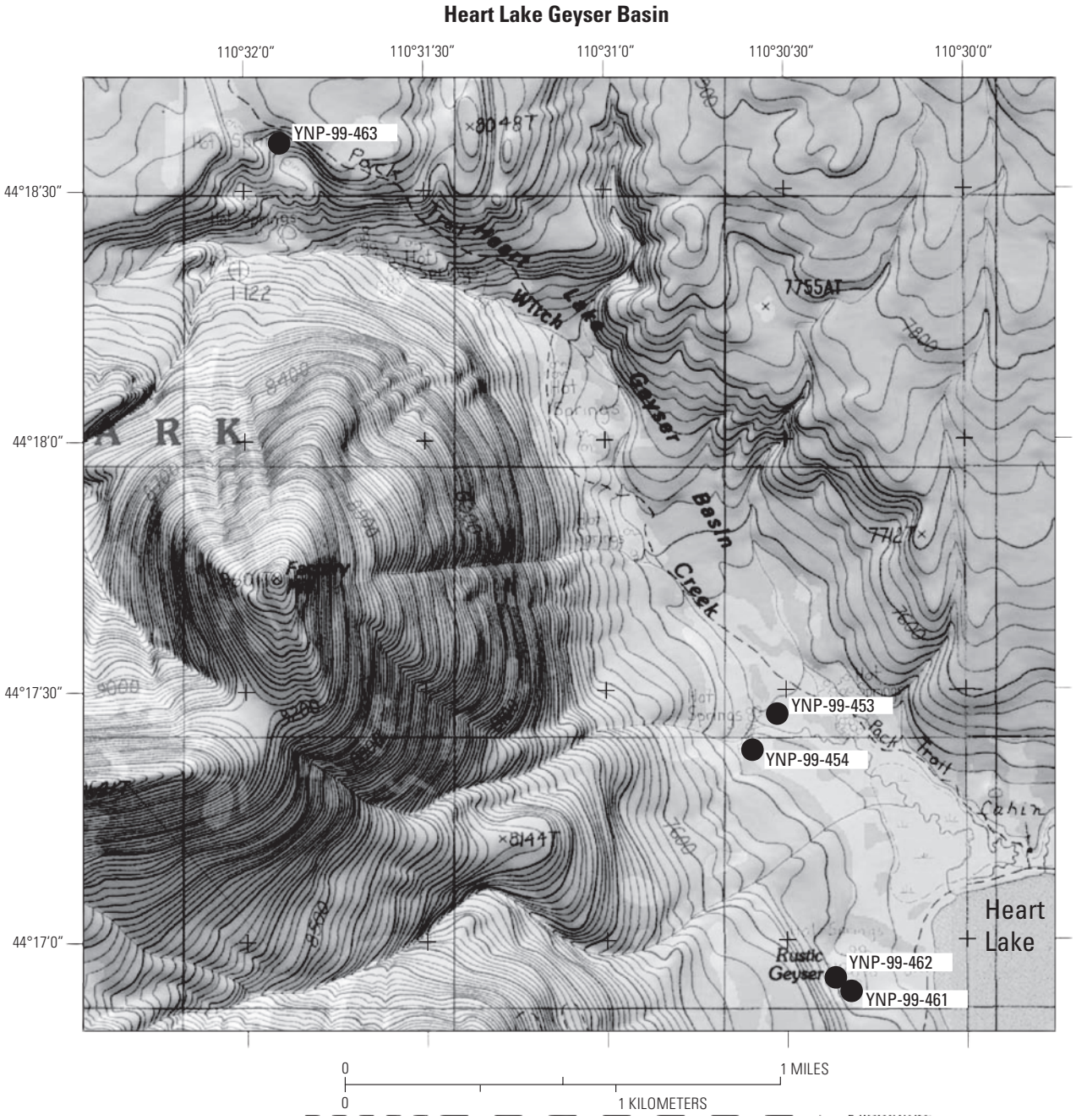

Figure 4. Map of Heart Lake Geyser Basin in northwest corner of Heart Lake. Locations of the five geysers sampled in 1999 are shown.

sampled. Representing the range of hydrothermal fluids found in the Park, two of the geysers are acidic and three are neutral to alkaline. The geyser from the upper basin is the most acidic, with a pH of 2.1, and has the lowest hydrothermal-indicator-element values. Three geysers have very similar high hydrothermal-indicator-element values: the alkaline geyser from the central geyser area (YNP-99-454) and the alkaline and acidic geysers from the Rustic Geyser area (YNP-99-461 and YNP-99-462).

Figure 5 shows both Gibbon and Monument Geyser Basins. Of the geysers sampled, thirteen were in Monument Geyser Basin, six were near the Gibbon River, one was at Artists Paintpots, and two samples were from Gibbon Geyser Basin. The geysers sampled in Monument Geyser Basin are all acidic (pH=1.1 to 2.5). The majority of the geysers near the Gibbon River are neutral to alkaline (pH=6.1 to 7.2), as is the geyser at Artists Paintpots (pH=7.3). In Gibbon Geyser Basin, one sample is near neutral (pH=6.1) and the other is acidic (pH=3.7).

Eight samples were collected around Turbid Lake, and their locations are shown in figure 6. Two samples each were collected at Sedge Creek inlet, Bear Creek inlet, and

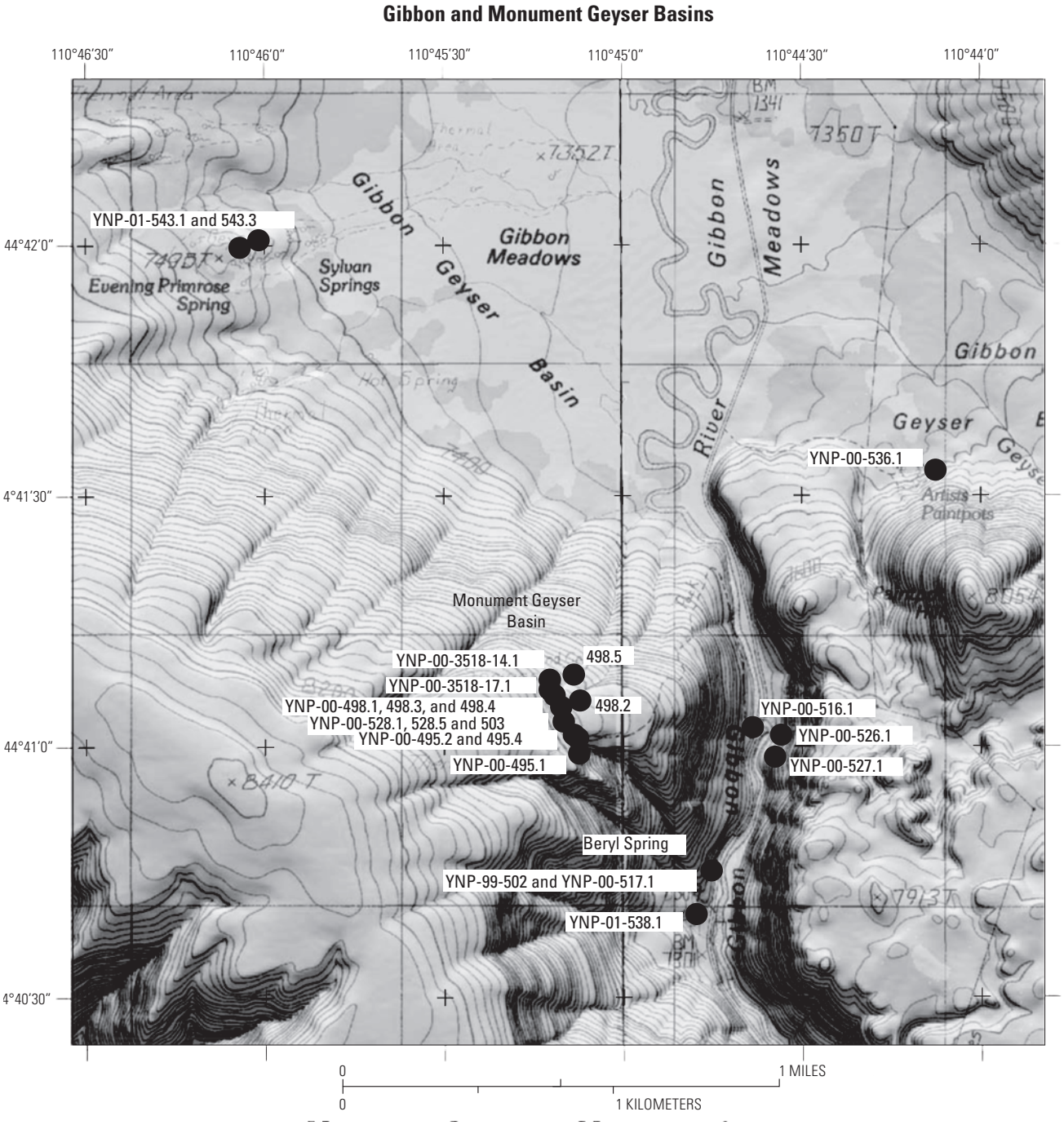

Figure 5. Map of Gibbon and Monument Geyser Basins area. Sample locations are shown in both geyser basins, along the Gibbon River at Beryl Spring, and at Artists Paintpots. Monument Geyser Basin was sampled in multiple years, most extensively in 2000.

the mudpots on the southeast shore. Two samples of lake water were also collected. The samples collected at the inlets to Turbid Lake have the lowest values for the hydrothermal-indicator elements. The mudpots have the highest hydrothermal-indicator-element values, and the lake has intermediate values. Therefore, there must be some input of hydrothermal water within the lake.

Summary

This chapter summarizes data on the geochemistry of more than 400 water samples collected from 1996 to 2004 from creeks and rivers draining into and out of Yellowstone Lake, hydrothermal vents and water-column profiles within Yellowstone Lake, and from subaerial geysers and hot springs

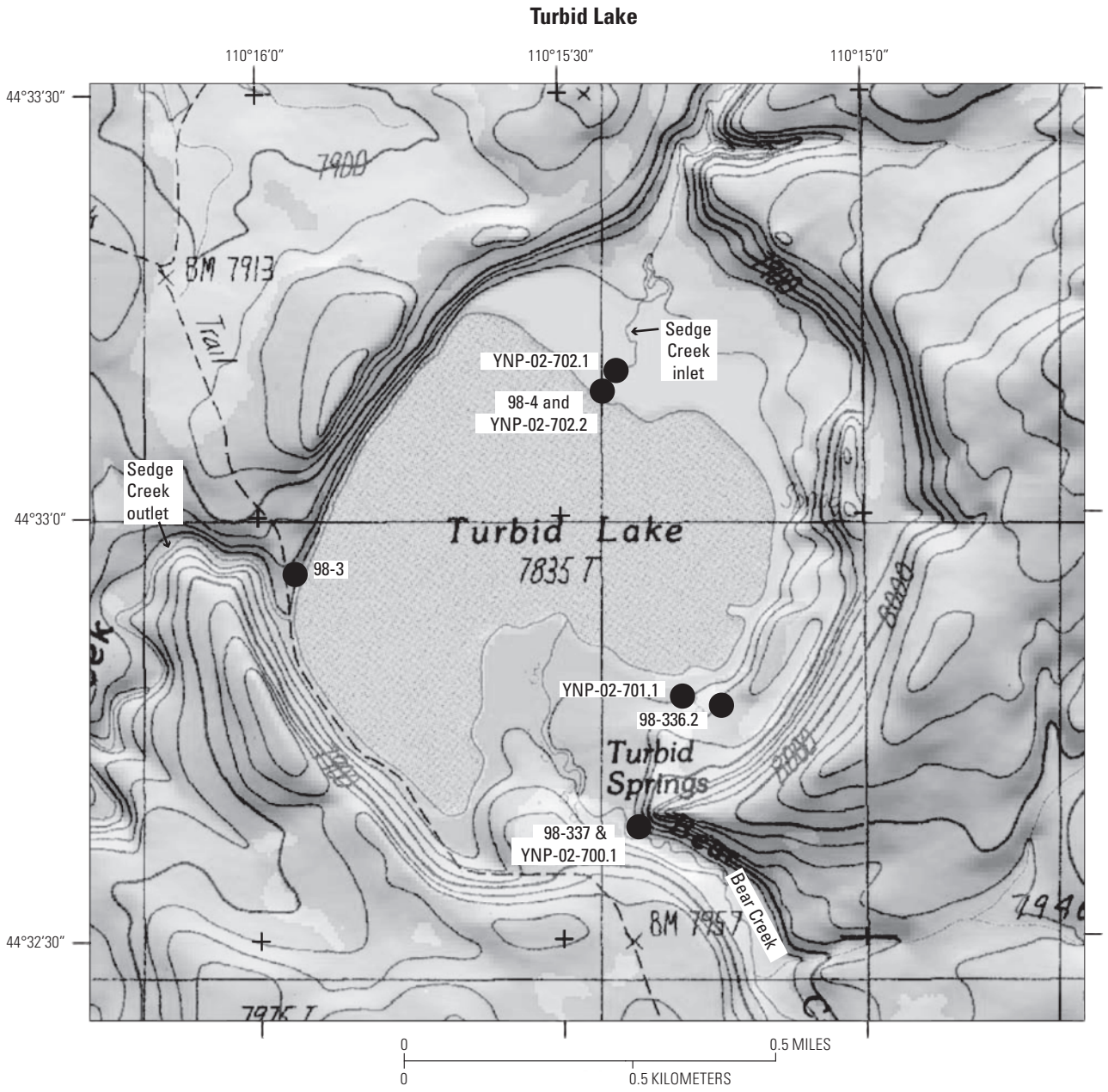

Figure 6. Detailed map of Turbid Lake showing inlets from Sedge and Bear Creeks at the north and south, respectively. The outlet to Sedge Creek is on the west side of the lake. Samples were collected in 1998 and 2002 at approximately the same locations.

throughout the Park. These different sources of water all contribute valuable information to the water chemistry in Yellowstone Lake and the Park as a whole. Goals of the geochemical fluid studies were to provide state-of-the-art chemical determinations of over 45 elements and species to help understand the influences of hydrothermal processes within Yellowstone National Park.

The values of the hydrothermal-indicator elements As, B, Cl, Cs, Cu, Ge, Li, Mo, Sb, and W can highlight hydrothermal activity in the Park (Balistrieri and others, this volume). An increase in the values of these indicator elements from the creek data to the water-column-profile data of Yellowstone Lake indicate that these elements are likely added within the lake from hydrothermal vents on the lake bottom. The increase in concentration of the geothermal-indicator elements in certain areas of the lake (West Thumb) and Park (Heart Lake and Norris Geyser Basins) suggest highly active hydrothermal features.

Acknowledgments

This work could not have been done without the support of the National Park Service, especially Mike Finley, John Varley, Tom Olliff, Paul Doss, Dan Reinhart, Dan Mahoney, Jim Ruzycki, Todd Koel, and Aquatic Resources Group at Lake Station. These studies would not have been possible without Dave Lovalvo of Eastern Oceanics, Inc., who designed and operated the ROV and the research vessel (RV *Cutthroat*) and generously shared his knowledge of Yellowstone Lake. We thank Kate Johnson, Ed du Bray, Geoff Plumlee, Pat Leahy, Steve Bohlen, Tom Casadevall, Linda Gundersen, Denny Fenn, Elliott Spiker, and Dick Jachowski for supporting this work. We thank Dan Reinhart, Paul Doss, Rick Fey, John Lounsbury, Ann Deutch, Christie Hendrix, Rick Sanzolone, Kirk Miller, Jim Bruckner, Bob Evanoff, Wes Miles, Rick Mossman, Gary Nelson, Julie Friedman, Brenda Bietler, Charles Gimbach, Brie Burdick, and many others for assistance with field studies. Al Meier, Paul Briggs, Jim Crock, and Pete Theodorakos of the U.S. Geological Survey and Pat Anderson of the University of Wisconsin-Milwaukee-Great Lakes Water Institute analyzed samples. Jim Crock and Rick Sanzolone provided constructive reviews that substantially improved the manuscript. This research was supported by the U.S. Geological Survey, National Park Service, National Science Foundation (Environmental Geochemistry and Biogeochemistry), and Yellowstone Foundation.

References Cited

Allen, E.T., and Day, A.L., 1935, Hot Springs of the Yellowstone National Park: Washington, Carnegie Institute of Washington, Publication 466, 525 p.

Ball, J.W., McCleskey, R.B., Nordstrom, D.K., Holloway, J.M., and Verplanck, P.L., 2002, Water-chemistry data for selected springs, geysers, and streams in Yellowstone National Park, Wyoming, 1999–2000: U.S. Geological Survey Open-File Report 02-382, 104p.

Ball, J.W., Nordstrom, D.K., Cunningham, K.M., Schoonen, M.A., Xu, Y., and DeMonge, J.M., 1998, Water-chemistry and on-site sulfur-speciation data for selected springs in Yellowstone National Park, Wyoming, 1994–1995: U.S. Geological Survey Open-File Report 98-574, 35p.

Ball, J.W., Nordstrom, D.K., Jenne, E.A., and Vivit, D.V., 1998, Chemical analyses of hot springs, pools, geysers, and surface waters from Yellowstone National Park, Wyoming, and vicinity, 1974–1975: U.S. Geological Survey Open-File Report 98-182, 45p.

Ball, J.W., Nordstrom, D.K., McCleskey, R.B., Schoonen, M.A.A., and Xu, Y., 2001, Water-chemistry and on-site sulfur-speciation data for selected springs in Yellowstone National Park, Wyoming, 1996–1998: U.S. Geological Survey Open-File Report 01-49, 42p.

Briggs, P.H., 2002, The determination of twenty-seven elements in aqueous samples by inductively coupled plasma-atomic emission spectrometry, chap. F *of* Taggart, J.E., Jr., ed., Analytical methods for chemical analysis of geologic and other materials: U.S. Geological Survey Open-File Report 02-223, [10] p.

Epstein, S., and Mayeda, T., 1953, Variations of O^{18} contents of waters from natural sources: Geochimica et Cosmochimica Acta, v. 4, p. 213–224.

Fournier, R.O., 1989, Geochemistry and dynamics of the Yellowstone National Park hydrothermal system: Annual Review of Earth and Planetary Sciences, v. 17, p. 13–53.

Giesemann, A., Jager, H.J., Norman, A.L., Krouse, H.R., and Brand, W.A., 1994, On-line sulfur-isotope determination using an elemental analyzer coupled to a mass spectrometer: Analytical Chemistry, v. 66, p. 2,816–2,819.

Gooch, F.A., and Whitfield, J.E., 1888, Analyses of water of the Yellowstone National Park: U.S. Geological Survey Bulletin 47, 84 p.

Hageman, P.L., 2002, Mercury in water by flow injection-cold vapor-atomic fluorescence spectrometry, chap. N *of* Taggart, J.E., Jr., ed., Analytical methods for chemical analysis of geologic and other materials: U.S. Geological Survey Open-File Report 02-223, [5] p.

Kendall, C., and Coplen, T.B., 1985, Multisample conversion of water to hydrogen by zinc for stable isotope determination: Analytical Chemistry, v. 57, p. 1,437–1,440.

Kharaka, Y.K., Mariner, R.H., Bullen, T.D., Kennedy, B.M., and Sturchio, N.C., 1991, Geochemical investigations of hydraulic connections between the Corwin Springs Known Geothermal Resources Area and adjacent parts of Yellowstone National Park, *in* Sorey, M.L., ed., Effects of potential geothermal development in the Corwin Springs Known Geothermal Resources Area, Montana, on the thermal features of Yellowstone National Park: U.S. Geological Survey Water Resources Investigations Report 91-4052, p. F1–F38.

Kharaka, Y.K., Sorey, M.L., and Thordsen, J.J., 2000, Large-scale hydrothermal fluid discharges in the Norris-Mammoth corridor, Yellowstone National Park, USA: Journal of Geochemical Exploration, v. 69–70, p. 201–205.

Klump, J.V., Paddock, R., and Lovalvo, D., 1992, A multiple-loop, ROV controlled, in-situ water sampler: Journal of Great Lakes Research, v. 18(2), p. 309–315.

Lamothe, P.J., Meier, A.L., and Wilson, S.A., 2002, The determination of forty four elements in aqueous samples by inductively coupled plasma-mass spectrometry, chap. H *of* Taggart, J.E., Jr., ed., Analytical methods for chemical analysis of geologic and other materials: U.S. Geological Survey Open-File Report 02-223, [11] p.

McCrea, J.M., 1950, The isotopic chemistry of carbonates and a paleotemperature scale: The Journal of Chemical Physics, v. 18, p. 849.

Stumm, W., and Morgan, J.J., 1996, Aquatic Chemistry (3rd ed.): New York, Wiley, 1,022 p.

Theodorakos, P.M., 2002, Fluoride, chloride, nitrate, and sulfate in aqueous solution utilizing AutoSuppression chemically suppressed ion chromatography, chap. V *of* Taggart, J.E., Jr., ed., Analytical methods for chemical analysis of geologic and other materials: U.S. Geological Survey Open-File Report 02-223, [7] p.

Thompson, J.M., and DeMonge, J.M., 1996, Chemical analyses of hot springs, pools, and geysers from Yellowstone National Park, Wyoming, and vicinity, 1980–1993: U. S. Geological Survey Open-File Report 96-0068, 66 p.

Thompson, J.M., Presser, T.S., Barnes, R.B., and Bird, D.B., 1975, Chemical analyses of the waters of Yellowstone National Park, Wyoming, from 1965–1973: U.S. Geological Survey Open-File Report 75-25, 59 p.

Thompson, J.M., and Yadav, S., 1979, Chemical analyses of waters from geysers, hot springs, and pools in Yellowstone National Park, Wyoming, from 1974 to 1978: U.S. Geological Survey Open-File Report 79-704, 49 p.

White, D.E., Hinkle, M.E., and Barnes, I., 1970, Mercury contents of natural thermal and mineral fluids—Mercury in the environment: U.S. Geological Survey Professional Paper 713, 67 p.

White, D.E., Hutchinson, R.A., and Keith, T.E.C., 1988, The geology and remarkable thermal activity of Norris Geyser Basin, Yellowstone National Park, Wyoming: U.S. Geological Survey Professional Paper 1456, 84 p.

White, D.E., Muffler, L.J.P., and Truesdell, A.H., 1971, Vapor-dominated hydrothermal systems compared with hot-water system: Economic Geology, v. 66(1), p. 75–97.

Appendixes

Appendix 1. Site and analytical data from creeks and water column profiles.

Field no. Drainage/ description			RS-16-97 Yellowstone River inlet	RS-32-97 Columbine Creek	RS-35-97 Clear Creek	RS-39-97 Sedge Creek	RS-40-97 Pelican Creek	30 Yellowstone River outlet	37 Columbine Creek	39 Clear Creek	41 Sedge Creek	40 Pelican Creek	38 Yellowstone River outlet	RS-1-98 Solution Cr
Latitude			44°18'28"N	44°24'3"N	44°28'35"N	44°31'26"N	44°33'38"N	44°34'3"N	44°24'3"N	44°28'35"N	44°31'26"N	44°33'38"N	44°34'3"N	44°24'22"N
Longitude			110°10'49"W	110°15'7"W	110°16'8"W	110°16'43"W	110°21'9"W	110°22'48"W	110°15'7"W	110°16'8"W	110°16'43"W	110°21'9"W	110°22'48"W	110°30'1"W
NPS no.			40	1099	1095	1089	1085		1099	1095	1089	1085		1163
Date			07/15/97	07/15/97	07/16/97	07/19/97	07/19/97	07/19/97	07/15/97	07/16/97	07/19/97	07/19/97	07/19/97	08/25/98
Depth	m		-	-	-	-	-	-	-	-	-	-	-	-
Treatment/ Sample type			-	Filtered and acidified	Filtered and acidified	Filtered and acidified	Filtered and acidified	Filtered and acidified	Raw and acidified	Raw and acidified	Raw and acidified	Raw and acidified	Raw and acidified	integrated
Collector			Sanzalone	Sanzalone	Sanzalone	Sanzalone	Sanzalone	Sanzalone	Sanzalone	Sanzalone	Sanzalone	Sanzalone	Sanzalone	Sanzolone
pH			7.05	7.07	7.01	3.70	7.03	7.29	-	-	-	-	-	6.25
Conductivity	uS/cm		-	-	-	134	213	89	-	-	-	-	-	-
Temperature	°C		-	-	-	15.5	16.5	14.2	-	-	-	-	-	12.3
Flow	CFS		-	-	-	-	-	-	-	-	-	-	-	6.7
Alkalinity	Mg/L as $CaCO_3$		-	-	-	-	-	-	-	-	-	-	-	35
Sum CO_2	mM		-	0.34	0.58	0.12	1.53	1.04	-	-	-	-	-	-
HCO_3	mM	measured	-	-	-	-	-	-	-	-	-	-	-	-
HCO_3	uM	calculated	-	-	-	-	-	-	-	-	-	-	-	-
Comments			-	-	-	-	-	-	-	-	-	-	-	difficult flow measure-ment
Cl	mg/L	IC-Aq	-	-	-	3.4	11.4	4.4	-	-	-	-	-	0.6
F	mg/L	IC-Aq	-	-	-	-	-	-	-	-	-	-	-	0.3
NO_3	mg/L	IC-Aq	-	-	-	-	-	-	-	-	-	-	-	< 0.1
SO_4	mg/L	IC-Aq	1.2	17.4	1.8	37.2	46.8	6.7	-	-	-	-	-	1.6
Ag	ug/L	ICPMS	0.00	< 0.01	< 0.01	< 0.01	< 0.01	< 0.01	< 0.01	< 0.01	< 0.01	< 0.01	< 0.01	< 0.01
Al	ug/L	ICPMS	16	1200	18	320	320	19	1800	160	470	2500	84	16
As	ug/L	ICPMS	0.3	< 0.2	0.3	9.2	14	12	0.3	0.2	12	29	13	2
Au	ug/L	ICPMS	0.01	< 0.005	< 0.005	< 0.005	< 0.005	< 0.005	< 0.005	< 0.005	< 0.005	< 0.005	< 0.005	0.02
B	ug/L	ICPAES	0	< 10	< 10	280	480	83	< 10	< 10	270	480	82	20
Ba	ug/L	ICPMS	6.8	12	8.4	18	34	8.9	13	10	19	40	9.1	10
Be	ug/L	ICPMS	0.00	< 0.05	< 0.05	< 0.05	0.05	< 0.05	< 0.05	0.05	< 0.05	0.07	0.05	< 0.05
Bi	ug/L	ICPMS	0.00	< 0.01	< 0.01	< 0.01	< 0.01	< 0.01	< 0.01	< 0.01	< 0.01	< 0.01	< 0.01	< 0.01
Ca	mg/L	ICPAES	3.9	5.4	6.7	4.9	12	5.6	5.8	6.9	4.7	13	5.6	8.2
Cd	ug/L	ICPMS	0.00	< 0.02	< 0.02	< 0.02	< 0.02	< 0.02	< 0.02	< 0.02	< 0.02	< 0.02	< 0.02	< 0.02
Ce	ug/L	ICPMS	0.1	2.9	0.2	1.0	0.2	0.05	4.6	0.60	1.4	1.6	0.2	0.3
Co	ug/L	ICPMS	0.0	0.2	0.02	0.4	0.2	< 0.02	0.3	0.08	0.4	0.3	0.06	0.1
Cr	ug/L	ICPMS	0.0	< 0.5	< 0.5	< 0.5	< 0.5	< 0.5	< 0.5	< 0.5	< 0.5	< 0.5	< 0.5	< 1
Cs	ug/L	ICPMS	0.00	0.01	< 0.01	1.9	3.7	2.6	0.02	0.01	2.0	3.8	2.6	0.2
Cu	ug/L	ICPMS	0.0	< 0.5	< 0.5	< 0.5	< 0.5	< 0.5	< 0.5	< 0.5	< 0.5	0.6	< 0.5	0.6
Dy	ug/L	ICPMS	0.01	0.18	0.073	0.12	0.03	< 0.005	0.29	0.12	0.15	0.17	0.008	0.02
Er	ug/L	ICPMS	0.01	0.12	0.058	0.081	0.01	0.005	0.17	0.075	0.073	0.10	0.007	0.02
Eu	ug/L	ICPMS	0.00	0.02	< 0.005	0.01	< 0.005	< 0.005	0.03	0.01	0.02	0.02	0.005	< 0.005
Fe	ug/L	ICPMS	28	170	27	360	110	11	400	110	640	1000	40	130
Ga	ug/L	ICPMS	0.00	0.04	< 0.02	< 0.02	< 0.02	< 0.02	0.08	< 0.02	0.03	0.04	< 0.02	< 0.02
Gd	ug/L	ICPMS	0.02	0.22	0.094	0.13	0.02	< 0.005	0.35	0.14	0.17	0.19	0.02	0.02
Ge	ug/L	ICPMS	0.00	< 0.02	< 0.02	0.2	0.4	0.2	< 0.02	< 0.02	0.2	0.4	0.2	< 0.02
Hf	ug/L	ICPMS	0.00	< 0.05	14	2.1	10	< 0.05	< 0.05	< 0.05	< 0.05	< 0.05	5.7	< 0.05
Ho	ug/L	ICPMS	0.00	0.04	0.02	0.03	0.005	< 0.005	0.055	0.02	0.03	0.03	< 0.005	0.006
In	ug/L	ICPMS	0.00	< 0.01	< 0.01	< 0.01	< 0.01	< 0.01	< 0.01	< 0.01	< 0.01	< 0.01	< 0.01	< 0.01
K	mg/L	ICPAES	1.1	1.1	0.56	1.3	6.6	1.7	1.2	0.61	1.4	6.4	1.6	1.8
La	ug/L	ICPMS	0.09	1.6	0.2	0.50	0.1	0.04	2.3	0.50	0.66	0.72	0.09	0.1
Li	ug/L	ICPMS	0.2	0.9	1.3	25	68	35	0.8	1.1	25	68	35	2.5
Mg	mg/L	ICPAES	1.6	2.7	1.5	2.1	7.2	2.4	2.8	1.5	2.1	7.0	2.3	2.8
Mn	ug/L	ICPMS	2.5	34	4.3	42	46	0.75	36	9.1	43	52	2.3	9.9
Mo	ug/L	ICPMS	0.2	0.2	0.4	0.4	0.50	1.1	0.2	0.5	0.4	0.5	1.1	0.59
Na	mg/L	ICPAES	2.4	3.4	2.6	6.2	22	9.0	3.5	2.6	5.8	21	8.6	2.9
Nb	ug/L	ICPMS	0.00	< 0.02	< 0.02	< 0.02	< 0.02	< 0.02	< 0.02	< 0.02	< 0.02	< 0.02	< 0.02	< 0.02
Nd	ug/L	ICPMS	0.06	1.4	0.26	0.63	0.08	< 0.01	2.0	0.55	0.78	0.82	0.04	0.1
Ni	ug/L	ICPMS	0.6	0.9	0.2	1.1	1.3	0.5	1.0	0.3	1.2	1.6	0.5	1
P	ug/L	ICPMS	180	100	47	110	58	84	170	66	250	220	90	-
Pb	ug/L	ICPMS	0.00	< 0.05	< 0.05	< 0.05	< 0.05	< 0.05	< 0.05	< 0.05	< 0.05	< 0.05	< 0.05	< 0.05
Pr	ug/L	ICPMS	0.02	0.34	0.05	0.1	0.02	< 0.01	0.52	0.1	0.2	0.20	0.02	0.03
Rb	ug/L	ICPMS	1.5	2.5	1.0	3.2	24	5.2	2.5	1.1	3.2	24	5.2	2.6
Re	ug/L	ICPMS	0.00	< 0.02	< 0.02	< 0.02	< 0.02	< 0.02	< 0.02	< 0.02	< 0.02	< 0.02	< 0.02	< 0.02
Sb	ug/L	ICPMS	0.00	< 0.02	0.03	0.2	0.3	0.53	< 0.02	< 0.02	0.2	0.3	0.52	0.1
Sc	ug/L	ICPMS	0.6	0.7	0.6	0.6	2	0.3	0.7	0.4	0.6	2	0.3	1
Se	ug/L	ICPMS	0.0	<0.5	<0.5	<0.5	<0.5	<0.5	<0.5	<0.5	<0.5	<0.5	<0.5	< 0.2
SiO_2	mg/L	ICPMS	18	20	12	20	52	11	20	12	20	53	11	18
Sm	ug/L	ICPMS	0.02	0.22	0.05	0.1	0.03	< 0.01	0.34	0.08	0.2	0.1	0.01	0.02
Sn	ug/L	ICPMS	0.00	< 0.05	< 0.05	< 0.05	< 0.05	< 0.05	< 0.05	< 0.05	< 0.05	< 0.05	< 0.05	< 0.05
Sr	ug/L	ICPMS	27	43	71	40	110	38	44	71	39	110	39	42
Ta	ug/L	ICPMS	0.00	< 0.02	< 0.02	< 0.02	< 0.02	< 0.02	< 0.02	< 0.02	< 0.02	< 0.02	< 0.02	< 0.02
Tb	ug/L	ICPMS	0.00	0.03	0.01	0.02	< 0.005	< 0.005	0.053	0.02	0.02	0.03	< 0.005	0.005
Te	ug/L	ICPMS	0.0	< 0.1	< 0.1	< 0.1	< 0.1	< 0.1	< 0.1	< 0.1	< 0.1	< 0.1	< 0.1	< 0.1
Th	ug/L	ICPMS	0.00	< 0.005	0.02	0.03	0.04	< 0.005	0.02	< 0.005	0.02	0.06	0.007	< 0.005
Ti	ug/L	ICPMS	0.0	1.4	< 0.1	0.2	< 0.1	< 0.1	5.3	1.4	3.4	1.7	0.5	0.2
Tl	ug/L	ICPMS	0.00	< 0.05	< 0.05	< 0.05	< 0.05	< 0.05	< 0.05	< 0.05	< 0.05	< 0.05	< 0.05	< 0.05
Tm	ug/L	ICPMS	0.00	0.02	0.008	0.01	< 0.005	< 0.005	0.02	0.01	0.01	0.02	< 0.005	< 0.005
U	ug/L	ICPMS	0.02	0.02	0.07	0.03	0.05	0.02	0.04	0.09	0.05	0.08	0.02	0.05
V	ug/L	ICPMS	3	1	1	1	2	1	2	1	2	3	1	1
W	ug/L	ICPMS	0.08	0.06	0.03	0.58	0.2	1.8	< 0.02	0.1	1.1	0.2	1.7	0.1
Y	ug/L	ICPMS	0.06	1.1	0.50	0.69	0.1	0.04	1.6	0.78	0.82	0.96	0.07	0.1
Yb	ug/L	ICPMS	0.0	0.1	0.05	0.06	0.02	< 0.01	0.1	0.08	0.08	0.08	< 0.01	0.01
Zn	ug/L	ICPMS	0.0	0.8	< 0.5	1	1	< 0.5	2	< 0.5	0.9	3	1	0.9
Zr	ug/L	ICPMS	0.00	< 0.05	0.2	0.08	0.2	< 0.05	0.08	< 0.05	0.05	< 0.05	0.1	< 0.05
Hg	ng/L	Hg CVAF	-	-	-	-	-	-	-	-	-	-	-	<5
$\delta^{18}O$ vs VSMOW	permil	ISO1	-19.6	-18.89	-18.77	-18.55	-18.06	-16.38	-	-	-	-	-	-15.3
δD vs VSMOW	permil	ISO2	-143	-131.4		-140.4	-135.3	-128.8	-	-	-	-	-	-124.0
$\delta^{34}S$ vs CDT	permil	ISO3	-	-	-	-3.4	4.3	3.3	-	-	-	-	-	-
$\delta^{34}S$ vs CDT	permil	ISO4	-	-	-	-3.6	5.6	3.3	-	-	-	-	-	-

Appendix 1. Site and analytical data from creeks and water column profiles—*Continued*.

Field no. Drainage/ description			RS-2-98	RS-3-98	RS-4-98	RS-5-98 Flat Mt. Stream	RS-6-98	RS-7-98	RS-8-98 West side S. arm	RS-9-98	RS-10-98	RS-11-98	RS-12-98 Alder Lake Outlet	RS-13-98	RS-14-98
Latitude			44°25'35"N	44°24'33"N	44°24'13"N	44°21'36"N	44°22'6"N	44°22'23"N	44°20'34"N	44°19'57"N	44°18'32"N	44°18'7"N	44°20'17"N	44°22'29"N	44°20'1"N
Longitude			110°27'40"W	110°25'5"W	110°24'27"W	110°27'4"W	110°24'16"W	110°23'11"W	110°21'25"W	110°21'23"W	110°20'59"W	110°20'23"W	110°19'2"W	110°17'48"W	110°16'33"W
NPS no.			1161	1158	1157	1155	1147	1143	1138	1137	no #	1131	1119	1118	1115
Date			08/25/98	08/25/98	08/25/98	08/25/98	08/25/98	08/25/98	08/26/98	08/26/98	08/26/98	08/26/98	08/26/98	08/26/98	08/27/98
Depth	m		-	-	-	-	-	-	-	-	-	-	-	-	-
Treatment/ Sample type			point	point	point	integrated	point	point	point	point	point	point	point	point	point
Collector			Sanzolone	Sanzolone	Sanzolone	Sanzolone	Sanzolone	Sanzolone	Sanzolone	Sanzolone	Sanzolone	Sanzolone	Sanzolone	Sanzolone	Sanzolone
pH			5.75	5.71	6.15	6.45	6.83	6.49	6.92	6.90	4.80	7.74	7.41	7.40	7.74
Conductivity	uS/cm		-	-	-	-	-	-	-	-	-	-	-	-	-
Temperature	°C		8.4	15.6	14.5	14.3	11.4	10.2	5.5	5.4	7.5	12.5	14.7	11.6	10.9
Flow	CFS		0.001	0.004	0.009	8.3	3.3	1.3	1.5	5.3	0.3	0.1	0.001	1.3	0.04
Alkalinity	Mg/L as $CaCO_3$		20	20	50	40	25	22	30	32	45	45	100	70	150
Sum CO_2	mM		-	-	-	-	-	-	-	-	-	-	-	-	-
HCO_3	mM	measured	-	-	-	-	-	-	-	-	-	-	-	-	-
HCO_3	uM	calculated	-	-	-	-	-	-	-	-	-	-	-	-	-
Comments			no surface flow to lake	Headwater at Delusion Lake	no surface flow to lake	inlet to Flat Mt. Arm	-	-	-	-	-	-	no surface flow to lake	no surface flow to lake	abundant suspended sed
Cl	mg/L	IC-Aq	0.2	1.0	0.5	0.5	0.4	0.4	0.4	0.4	0.2	0.2	1.2	0.6	1.4
F	mg/L	IC-Aq	0.2	0.2	0.7	0.6	0.4	0.4	0.8	1.4	0.3	0.2	0.2	0.2	0.3
NO_3	mg/L	IC-Aq	< 0.1	< 0.1	< 0.1	< 0.1	< 0.1	< 0.1	< 0.1	< 0.1	< 0.1	< 0.1	0.4	< 0.1	0.2
SO_4	mg/L	IC-Aq	1.4	< 0.5	1.4	2.5	0.9	0.9	1.2	1.6	1.7	1.2	0.9	1.8	< 0.5
Ag	ug/L	ICPMS	< 0.01	< 0.01	< 0.01	< 0.01	< 0.01	< 0.01	< 0.01	< 0.01	< 0.01	< 0.01	< 0.01	< 0.01	< 0.01
Al	ug/L	ICPMS	37	35	31	21	28	18	11	4.6	31	15	5.2	13	84
As	ug/L	ICPMS	0.5	0.6	2	4.9	0.2	< 0.2	0.2	0.3	0.9	0.8	2	0.6	9.2
Au	ug/L	ICPMS	< 0.01	< 0.01	< 0.01	< 0.01	0.01	< 0.01	< 0.01	< 0.01	< 0.01	< 0.01	< 0.01	< 0.01	< 0.01
B	ug/L	ICPAES	12	12	< 10	< 10	< 10	< 10	< 10	< 10	< 10	< 10	10	< 10	11
Ba	ug/L	ICPMS	17	11	16	14	9.7	6.8	5.9	2	14	9.5	32	9.4	28
Be	ug/L	ICPMS	< 0.05	< 0.05	< 0.05	< 0.05	< 0.05	< 0.05	0.05	0.1	< 0.05	< 0.05	< 0.05	< 0.05	< 0.05
Bi	ug/L	ICPMS	< 0.01	< 0.01	< 0.01	< 0.01	< 0.01	< 0.01	< 0.01	< 0.01	< 0.01	< 0.01	< 0.01	< 0.01	< 0.01
Ca	mg/L	ICPAES	5.3	4.2	9.0	9.6	4.8	4.8	6.2	7.5	8.4	8.6	18	21	25
Cd	ug/L	ICPMS	< 0.02	< 0.02	< 0.02	< 0.02	< 0.02	< 0.02	< 0.02	< 0.02	< 0.02	< 0.02	< 0.02	< 0.02	< 0.02
Ce	ug/L	ICPMS	0.76	0.4	0.99	0.2	0.2	0.2	0.1	0.02	0.2	0.1	0.06	0.2	0.83
Co	ug/L	ICPMS	0.1	0.1	1.1	0.03	< 0.02	< 0.02	< 0.02	< 0.02	0.02	0.04	0.1	0.2	1.4
Cr	ug/L	ICPMS	1	< 1	< 1	< 1	14	< 1	< 1	< 1	< 1	< 1	< 1	1	1
Cs	ug/L	ICPMS	0.09	0.06	0.32	0.1	0.01	< 0.01	0.04	0.2	< 0.01	< 0.01	0.02	0.02	0.03
Cu	ug/L	ICPMS	0.6	< 0.5	< 0.5	< 0.5	2	< 0.5	< 0.5	< 0.5	< 0.5	< 0.5	< 0.5	0.5	1
Dy	ug/L	ICPMS	0.089	0.04	0.066	0.02	0.062	0.04	0.02	< 0.005	0.02	0.057	< 0.005	0.01	0.04
Er	ug/L	ICPMS	0.059	0.03	0.058	0.02	0.051	0.04	0.01	< 0.005	0.02	0.05	0.005	0.01	0.02
Eu	ug/L	ICPMS	0.01	< 0.005	0.007	< 0.005	0.005	< 0.005	< 0.005	< 0.005	0.005	< 0.005	< 0.005	< 0.005	0.01
Fe	ug/L	ICPMS	59	140	370	52	29	20	30	17	36	38	170	110	300
Ga	ug/L	ICPMS	< 0.02	< 0.02	< 0.02	< 0.02	< 0.02	< 0.02	< 0.02	< 0.02	< 0.02	< 0.02	< 0.02	< 0.02	0.03
Gd	ug/L	ICPMS	0.090	0.05	0.067	0.01	0.057	0.057	0.02	< 0.005	0.02	0.056	0.006	0.01	0.04
Ge	ug/L	ICPMS	< 0.02	< 0.02	0.04	< 0.02	< 0.02	< 0.02	< 0.02	< 0.02	< 0.02	< 0.02	< 0.02	< 0.02	< 0.02
Hf	ug/L	ICPMS	< 0.05	< 0.05	< 0.05	< 0.05	< 0.05	< 0.05	< 0.05	< 0.05	< 0.05	< 0.05	< 0.05	< 0.05	< 0.05
Ho	ug/L	ICPMS	0.02	0.009	0.02	0.005	0.01	0.01	< 0.005	< 0.005	< 0.005	0.02	< 0.005	< 0.005	0.007
In	ug/L	ICPMS	< 0.01	< 0.01	< 0.01	< 0.01	< 0.01	< 0.01	< 0.01	< 0.01	< 0.01	< 0.01	< 0.01	< 0.01	< 0.01
K	mg/L	ICPAES	2.3	1.4	2.2	2.1	< 1	< 1	< 1	1.1	1.8	2.1	5.0	1.6	3.4
La	ug/L	ICPMS	0.4	0.2	0.3	0.07	0.2	0.2	0.05	0.01	0.09	0.1	0.02	0.1	0.3
Li	ug/L	ICPMS	0.1	1.0	5.9	3.9	1.3	0.6	3.2	3.1	0.3	< 0.1	0.3	0.4	0.6
Mg	mg/L	ICPAES	1.7	1.4	3.4	1.3	1.1	1.1	1.5	1.7	2.8	2.8	6.9	5.1	15
Mn	ug/L	ICPMS	10	30	230	7.3	2.3	0.24	6.4	0.23	2.9	8.4	150	13	500
Mo	ug/L	ICPMS	0.3	0.3	0.5	0.3	0.3	0.2	0.53	0.75	0.2	0.1	0.5	0.09	0.4
Na	mg/L	ICPAES	2.5	2.0	3.2	3.2	2.6	2.6	2.9	3.1	2.5	2.7	7.1	3.9	12
Nb	ug/L	ICPMS	< 0.02	< 0.02	< 0.02	< 0.02	< 0.02	< 0.02	< 0.02	< 0.02	< 0.02	< 0.02	< 0.02	< 0.02	< 0.02
Nd	ug/L	ICPMS	0.43	0.2	0.36	0.06	0.2	0.2	0.06	< 0.01	0.08	0.1	0.03	0.1	0.30
Ni	ug/L	ICPMS	1.0	1.0	3.0	0.6	1.7	1.0	0.3	0.3	0.6	0.7	1.0	1.7	4.6
P	ug/L	ICPMS	-	-	-	-	-	-	-	-	-	-	-	-	-
Pb	ug/L	ICPMS	< 0.05	< 0.05	0.2	< 0.05	0.3	< 0.05	< 0.05	< 0.05	< 0.05	< 0.05	0.1	< 0.05	0.06
Pr	ug/L	ICPMS	0.1	0.05	0.1	0.02	0.04	0.05	0.02	< 0.01	0.03	0.03	< 0.01	0.03	0.09
Rb	ug/L	ICPMS	4.4	2.6	6.0	6.1	1.4	1.3	1.9	1.8	1.4	2.2	3.0	1.8	3.2
Re	ug/L	ICPMS	< 0.02	< 0.02	< 0.02	< 0.02	< 0.02	< 0.02	< 0.02	< 0.02	< 0.02	< 0.02	< 0.02	< 0.02	< 0.02
Sb	ug/L	ICPMS	0.05	0.03	0.04	0.2	< 0.02	< 0.02	< 0.02	< 0.02	< 0.02	< 0.02	< 0.02	< 0.02	0.05
Sc	ug/L	ICPMS	2	0.5	2	2	1	1	1	1	2	2	2	1	1
Se	ug/L	ICPMS	< 0.2	< 0.2	< 0.2	< 0.2	< 0.2	< 0.2	< 0.2	< 0.2	< 0.2	< 0.2	< 0.2	< 0.2	0.2
SiO_2	mg/L	ICPMS	34	7.7	34	40	18	19	26	26	30	38	42	29	28
Sm	ug/L	ICPMS	0.06	0.04	0.06	0.02	0.02	0.03	0.01	< 0.01	0.02	0.04	< 0.01	0.01	0.04
Sn	ug/L	ICPMS	< 0.05	< 0.05	< 0.05	< 0.05	< 0.05	< 0.05	< 0.05	< 0.05	< 0.05	< 0.05	< 0.05	< 0.05	< 0.05
Sr	ug/L	ICPMS	48	35	55	27	32	31	32	28	48	48	89	54	180
Ta	ug/L	ICPMS	< 0.02	< 0.02	< 0.02	< 0.02	< 0.02	< 0.02	< 0.02	< 0.02	< 0.02	< 0.02	< 0.02	< 0.02	< 0.02
Tb	ug/L	ICPMS	0.01	< 0.005	0.01	< 0.005	0.005	0.009	< 0.005	< 0.005	< 0.005	0.008	< 0.005	< 0.005	0.006
Te	ug/L	ICPMS	< 0.1	< 0.1	< 0.1	< 0.1	< 0.1	< 0.1	< 0.1	< 0.1	< 0.1	< 0.1	< 0.1	< 0.1	< 0.1
Th	ug/L	ICPMS	0.02	0.02	0.02	< 0.005	< 0.005	< 0.005	< 0.005	< 0.005	< 0.005	< 0.005	< 0.005	< 0.005	0.01
Ti	ug/L	ICPMS	0.4	0.2	0.4	< 0.1	0.1	< 0.1	< 0.1	< 0.1	0.2	0.1	< 0.1	0.2	0.8
Tl	ug/L	ICPMS	< 0.05	< 0.05	< 0.05	< 0.05	< 0.05	< 0.05	< 0.05	< 0.05	< 0.05	< 0.05	< 0.05	< 0.05	< 0.05
Tm	ug/L	ICPMS	0.01	< 0.005	0.007	< 0.005	0.007	0.006	< 0.005	< 0.005	< 0.005	0.007	< 0.005	< 0.005	< 0.005
U	ug/L	ICPMS	0.02	0.01	0.02	0.06	0.01	0.01	0.03	0.16	0.02	0.04	0.009	0.50	0.66
V	ug/L	ICPMS	2	0.2	0.9	0.5	0.1	< 0.1	0.2	0.2	1	2	0.8	3	4
W	ug/L	ICPMS	0.03	0.04	0.1	0.05	0.02	< 0.02	< 0.02	0.04	0.03	0.05	0.2	< 0.02	0.3
Y	ug/L	ICPMS	0.5	0.2	0.5	0.1	0.3	0.3	0.1	0.03	0.1	0.4	0.02	0.1	0.2
Yb	ug/L	ICPMS	0.07	0.03	0.06	0.02	0.04	0.06	0.02	< 0.01	0.01	0.06	< 0.01	0.02	0.03
Zn	ug/L	ICPMS	2	1	1	0.9	22	1	0.5	0.6	0.5	1	1	0.8	2
Zr	ug/L	ICPMS	0.4	0.3	0.4	< 0.05	0.05	< 0.05	< 0.05	< 0.05	< 0.05	< 0.05	< 0.05	0.1	0.5
Hg	ng/L	Hg CVAF	<5	<5	<5	<5	<5	<5	<5	<5	<5	<5	<5	<5	5
$\delta^{18}O$ vs VSMOW	permil	ISO1	-19.2	-9.7	-17.3	-18.7	-18.0	-17.9	-18.9	-19.1	-18.8	-18.9	-18.8	-18.4	-17.2
δD vs VSMOW	permil	ISO2	-146.8	-92.2	-136.3	-142.8	-134.9	-135.5	-140.7	-143.3	-141.3	-142.2	-144.8	-141.7	-132.0
$\delta^{34}S$ vs CDT	permil	ISO3	-	-	-	-	-	-	-	-	-	-	-	-	-
$\delta^{34}S$ vs CDT	permil	ISO4	-	-	-	6.89	2.94	2.89	-	-	8.63	-	-	-	-

Appendix 1. Site and analytical data from creeks and water column profiles—*Continued*.

Field no.			RS-15-98	RS-16-98	RS-17-98	RS-17R-98	RS-18-98	RS-19-98	RS-20-98	RS-21-98	RS-22-98	RS-23-98	RS-24-98	RS-25-98	RS-26-98
Drainage/ description				Yellowstone River inlet	Beaver Dam Cr	Beaver Dam Cr	Trail Cr					Grouse Cr			Chipmunk Cr
Latitude			44°20'46"N	44°18'28"N	44°19'23"N	44°19'23"N	44°17'27"N	44°17'22"N	44°17'21"N	44°17'36"N	44°17'17"N	44°16'53"N	44°16'38"N	44°16'38"N	44°17'18"N
Longitude			110°13'22"W	110°10'49"W	110°11'6"W	110°11'6"W	110°12'9"W	W	W	W	W	W	W	W	110°17'7"W
NPS no.			1106	40	1107	1107	1108	1109	1110	1111	1126	1125	1123	1122	1121
Date			08/27/98	08/28/98	08/28/98	08/28/98	08/29/98	08/30/98	08/30/98	08/30/98	08/30/98	08/30/98	08/30/98	08/30/98	08/30/98
Depth	m		-	-	-	-	-	-	-	-	-	-	-	-	-
Treatment/ Sample type			point	integrated	integrated	integrated	point	point	point	point	point	point	point	point	point
Collector			Sanzolone	Sanzolone	Sanzolone	Sanzolone	Sanzolone	Sanzolone	Sanzolone	Sanzolone	Sanzolone	Sanzolone	Sanzolone	Sanzolone	Sanzolone
pH			7.90	7.12	7.55		8.50	7.63	7.64	7.95	8.16	7.93	8.04	7.00	8.49
Conductivity	uS/cm		-	-	-	-	-	-	-	-	-	-	-	-	-
Temperature	˚C		9.1	15.1	17.1		13.9	7.9	7.9	17.7	8.8	10.4	11.6	16.0	16.9
Flow	CFS		0.002	500	56		9.0	3.2	7.9	1.0	1.0	10.7	0.5	0.001	21
Alkalinity	Mg/L as $CaCO_3$		70	35	35	35	60	50	55	70	150	110	100	75	50
Sum CO_2	mM		-	-	-	-	-	-	-	-	-	-	-	-	-
HCO_3	mM	measured	-	-	-	-	-	-	-	-	-	-	-	-	-
HCO_3	uM	calculated	-	-	-	-	-	-	-	-	-	-	-	-	-
Comments			-	-	-	duplicate	abundant suspended sed	-	drainage not on 7.5 map	-	-	-	-	-	-
Cl	mg/L	IC-Aq	0.6	0.2	0.2	0.2	0.3	0.3	0.3	0.3	0.5	0.4	0.4	0.3	0.2
F	mg/L	IC-Aq	0.2	0.2	0.2	0.2	0.2	0.2	0.2	0.2	0.3	0.1	0.2	0.2	0.2
NO_3	mg/L	IC-Aq	< 0.1	< 0.1	< 0.1	< 0.1	0.5	< 0.1	< 0.1	< 0.1	< 0.1	< 0.1	< 0.1	< 0.1	< 0.1
SO_4	mg/L	IC-Aq	30	2.3	4.4	4.4	0.8	1.2	1.2	1.2	3.3	4.9	2.5	< 0.5	0.8
Ag	ug/L	ICPMS	< 0.01	< 0.01	< 0.01	< 0.01	< 0.01	< 0.01	< 0.01	< 0.01	< 0.01	< 0.01	< 0.01	< 0.01	< 0.01
Al	ug/L	ICPMS	27	15	14	12	15	16	4.5	24	5.2	3.4	29	40	11
As	ug/L	ICPMS	0.3	0.4	0.5	0.5	0.7	0.3	0.2	0.6	0.3	< 0.2	< 0.2	2	0.4
Au	ug/L	ICPMS	< 0.01	< 0.01	< 0.01	< 0.01	< 0.01	< 0.01	< 0.01	< 0.01	< 0.01	< 0.01	< 0.01	< 0.01	< 0.01
B	ug/L	ICPAES	< 10	< 10	< 10	< 10	< 10	< 10	< 10	< 10	< 10	< 10	< 10	< 10	< 10
Ba	ug/L	ICPMS	23	8.7	13	13	16	33	29	32	280	66	7.9	23	22
Be	ug/L	ICPMS	< 0.05	< 0.05	< 0.05	< 0.05	< 0.05	< 0.05	< 0.05	< 0.05	< 0.05	< 0.05	< 0.05	< 0.05	< 0.05
Bi	ug/L	ICPMS	< 0.01	< 0.01	< 0.01	< 0.01	< 0.01	< 0.01	< 0.01	< 0.01	< 0.01	< 0.01	< 0.01	< 0.01	< 0.01
Ca	mg/L	ICPAES	14	5.8	3.9	3.9	11	10	11	11	40	31	12	14	9.5
Cd	ug/L	ICPMS	< 0.02	< 0.02	< 0.02	< 0.02	< 0.02	< 0.02	< 0.02	< 0.02	< 0.02	< 0.02	< 0.02	< 0.02	< 0.02
Ce	ug/L	ICPMS	0.09	0.07	0.06	0.05	0.2	0.09	0.02	0.1	0.03	0.02	0.4	0.4	0.09
Co	ug/L	ICPMS	0.04	0.04	< 0.02	< 0.02	0.1	< 0.02	< 0.02	0.05	0.07	0.09	< 0.02	0.4	0.04
Cr	ug/L	ICPMS	< 1	< 1	< 1	< 1	< 1	< 1	< 1	< 1	< 1	< 1	< 1	< 1	< 1
Cs	ug/L	ICPMS	< 0.01	< 0.01	< 0.01	< 0.01	0.02	< 0.01	0.01	0.02	< 0.01	< 0.01	0.01	0.02	< 0.01
Cu	ug/L	ICPMS	0.8	< 0.5	< 0.5	< 0.5	0.5	< 0.5	< 0.5	< 0.5	< 0.5	0.5	< 0.5	2	< 0.5
Dy	ug/L	ICPMS	0.04	0.005	0.008	0.01	0.01	0.006	< 0.005	0.01	0.01	< 0.005	0.14	0.03	0.006
Er	ug/L	ICPMS	0.02	< 0.005	< 0.005	0.007	0.008	< 0.005	< 0.005	0.01	< 0.005	< 0.005	0.11	0.02	< 0.005
Eu	ug/L	ICPMS	0.006	< 0.005	< 0.005	< 0.005	< 0.005	0.005	< 0.005	< 0.005	0.02	0.01	0.007	0.01	< 0.005
Fe	ug/L	ICPMS	38	27	14	10	190	32	23	59	96	80	33	140	41
Ga	ug/L	ICPMS	< 0.02	< 0.02	< 0.02	< 0.02	< 0.02	< 0.02	< 0.02	< 0.02	< 0.02	< 0.02	< 0.02	< 0.02	< 0.02
Gd	ug/L	ICPMS	0.052	0.006	0.008	< 0.005	0.02	0.009	< 0.005	0.03	< 0.005	< 0.005	0.18	0.050	< 0.005
Ge	ug/L	ICPMS	< 0.02	< 0.02	< 0.02	< 0.02	< 0.02	< 0.02	< 0.02	< 0.02	0.02	< 0.02	< 0.02	< 0.02	< 0.02
Hf	ug/L	ICPMS	< 0.05	< 0.05	< 0.05	< 0.05	< 0.05	< 0.05	< 0.05	< 0.05	< 0.05	< 0.05	< 0.05	< 0.05	< 0.05
Ho	ug/L	ICPMS	0.01	< 0.005	< 0.005	< 0.005	< 0.005	< 0.005	< 0.005	0.006	< 0.005	< 0.005	0.05	0.008	< 0.005
In	ug/L	ICPMS	< 0.01	< 0.01	< 0.01	< 0.01	< 0.01	< 0.01	< 0.01	< 0.01	< 0.01	< 0.01	< 0.01	< 0.01	< 0.01
K	mg/L	ICPAES	2.2	1.4	1.4	1.4	2.7	2.2	2.3	2.4	1.5	1.1	1.7	1.7	1.8
La	ug/L	ICPMS	0.3	0.05	0.05	0.04	0.1	0.04	< 0.01	0.08	0.02	0.01	0.4	0.2	0.04
Li	ug/L	ICPMS	1.8	< 0.1	< 0.1	< 0.1	< 0.1	0.4	0.6	0.5	1.0	0.6	1.7	0.1	< 0.1
Mg	mg/L	ICPAES	12	2.5	1.5	1.5	4.0	1.7	1.5	3.5	15	10	3.2	5.3	2.1
Mn	ug/L	ICPMS	0.19	5.9	1.1	0.91	43	1.1	0.08	8.8	9.9	12	5.0	67	4.5
Mo	ug/L	ICPMS	0.1	0.2	0.3	0.3	0.2	0.07	0.06	0.09	0.5	0.54	0.52	0.3	0.08
Na	mg/L	ICPAES	4.9	3.7	7.7	7.7	4.3	2.8	2.6	3.1	10	5.1	3.0	4.3	2.5
Nb	ug/L	ICPMS	< 0.02	< 0.02	< 0.02	< 0.02	< 0.02	< 0.02	< 0.02	< 0.02	< 0.02	< 0.02	< 0.02	< 0.02	< 0.02
Nd	ug/L	ICPMS	0.30	0.05	0.04	0.04	0.07	0.04	0.01	0.08	0.02	0.01	0.53	0.26	0.03
Ni	ug/L	ICPMS	1.4	0.7	0.3	0.3	0.8	0.5	0.4	0.9	1.6	1.6	0.5	3.1	0.7
P	ug/L	ICPMS	-	-	-	-	-	-	-	-	-	-	-	-	-
Pb	ug/L	ICPMS	< 0.05	< 0.05	1.3	< 0.05	< 0.05	< 0.05	< 0.05	< 0.05	< 0.05	< 0.05	< 0.05	< 0.05	< 0.05
Pr	ug/L	ICPMS	0.07	0.01	0.01	0.01	0.03	0.01	< 0.01	0.02	< 0.01	< 0.01	0.1	0.06	0.01
Rb	ug/L	ICPMS	2.6	1.6	1.9	1.8	2.8	2.5	2.5	2.2	0.86	0.88	1.7	1.9	2.0
Re	ug/L	ICPMS	< 0.02	< 0.02	< 0.02	< 0.02	< 0.02	< 0.02	< 0.02	< 0.02	< 0.02	< 0.02	< 0.02	< 0.02	< 0.02
Sb	ug/L	ICPMS	< 0.02	< 0.02	< 0.02	< 0.02	< 0.02	< 0.02	< 0.02	< 0.02	0.04	0.03	< 0.02	< 0.02	< 0.02
Sc	ug/L	ICPMS	2	0.9	1	1	1	2	1	1	0.3	0.4	0.6	0.9	1
Se	ug/L	ICPMS	< 0.2	< 0.2	< 0.2	< 0.2	< 0.2	< 0.2	< 0.2	< 0.2	< 0.2	0.2	< 0.2	< 0.2	< 0.2
SiO_2	mg/L	ICPMS	41	23	26	25	27	37	33	29	10	9.2	30	21	24
Sm	ug/L	ICPMS	0.06	0.02	0.01	< 0.01	< 0.01	< 0.01	< 0.01	0.02	< 0.01	< 0.01	0.1	0.06	< 0.01
Sn	ug/L	ICPMS	< 0.05	< 0.05	< 0.05	< 0.05	< 0.05	< 0.05	< 0.05	< 0.05	< 0.05	< 0.05	< 0.05	< 0.05	< 0.05
Sr	ug/L	ICPMS	110	35	27	25	57	46	42	61	350	230	44	100	53
Ta	ug/L	ICPMS	< 0.02	< 0.02	< 0.02	< 0.02	< 0.02	< 0.02	< 0.02	< 0.02	< 0.02	< 0.02	< 0.02	< 0.02	< 0.02
Tb	ug/L	ICPMS	0.005	< 0.005	< 0.005	< 0.005	< 0.005	< 0.005	< 0.005	< 0.005	< 0.005	< 0.005	0.02	0.006	< 0.005
Te	ug/L	ICPMS	< 0.1	< 0.1	< 0.1	< 0.1	< 0.1	< 0.1	< 0.1	< 0.1	< 0.1	< 0.1	< 0.1	< 0.1	< 0.1
Th	ug/L	ICPMS	0.006	< 0.005	< 0.005	< 0.005	< 0.005	< 0.005	< 0.005	< 0.005	< 0.005	< 0.005	0.008	0.005	< 0.005
Ti	ug/L	ICPMS	0.2	0.1	< 0.1	< 0.1	0.2	0.1	< 0.1	0.2	< 0.1	< 0.1	0.1	0.3	< 0.1
Tl	ug/L	ICPMS	< 0.05	< 0.05	< 0.05	< 0.05	< 0.05	< 0.05	< 0.05	< 0.05	< 0.05	< 0.05	< 0.05	< 0.05	< 0.05
Tm	ug/L	ICPMS	< 0.005	< 0.005	< 0.005	< 0.005	< 0.005	< 0.005	< 0.005	< 0.005	< 0.005	< 0.005	0.02	< 0.005	< 0.005
U	ug/L	ICPMS	0.02	0.02	0.02	0.01	0.10	0.06	0.08	0.10	0.48	0.32	0.05	0.03	0.07
V	ug/L	ICPMS	3	3	3	3	3	2	2	3	0.2	0.2	0.6	2	2
W	ug/L	ICPMS	< 0.02	< 0.02	< 0.02	< 0.02	0.05	< 0.02	< 0.02	< 0.02	< 0.02	< 0.02	< 0.02	0.03	< 0.02
Y	ug/L	ICPMS	0.2	0.03	0.04	0.04	0.06	0.04	0.01	0.1	0.06	0.04	0.95	0.2	0.04
Yb	ug/L	ICPMS	0.02	< 0.01	< 0.01	< 0.01	< 0.01	< 0.01	< 0.01	0.02	< 0.01	< 0.01	0.1	0.03	< 0.01
Zn	ug/L	ICPMS	3	0.9	0.7	< 0.5	1	0.5	0.5	0.7	1	0.5	1	1	0.6
Zr	ug/L	ICPMS	0.4	< 0.05	< 0.05	< 0.05	< 0.05	< 0.05	< 0.05	0.1	< 0.05	< 0.05	0.2	0.3	< 0.05
Hg	ng/L	Hg CVAF	<5	<5	<5	<5	<5	<5	<5	5	<5	<5	<5	<5	<5
$\delta^{18}O$ vs VSMOW	permil	ISO1	-18.5	-18.1	-18.5	-18.5	-16.8	-19.4	-19.6	-18.7	-18.6	-18.3	-18.4	-16.0	-18.6
δD vs VSMOW	permil	ISO2	-139.5	-136.4	-137.6	-138.5	-131.3	-144.9	-148.6	-142.9	-141.0	-139.5	-139.2	-127.3	-143.5
$\delta^{34}S$ vs CDT	permil	ISO3	-	-	-	-	-	-	-	-	-	-	-	-	-
$\delta^{34}S$ vs CDT	permil	ISO4	1.205	-	-4.99	-5.01	-	-	-	-	9.28	-	8.14	-	-

Appendix 1. Site and analytical data from creeks and water column profiles—*Continued*.

Field no.			RS-27-98	RS-28-98	RS-29-98	RS-30-98	RS-31-98	RS-32-98	RS-33-98	RS-34-98	RS-35-98	RS-36-98	RS-37-98	RS-38-98	RS-39-98
Drainage/ description					Alluvium Cr			Columbine Cr	Meadow Cr		Clear Cr		Cub Cr	Little Cr	Sedge Cr
Latitude			44°21'47"N	44°22'37"N	44°23'9"N	44°23'41"N	44°23'48"N	44°24'3"N	44°25'37"N	44°27'7"N	44°28'35"N	44°28'47"N	44°29'23"N	44°30'2"N	44°31'26"N
Longitude			W	W	W	W	W	110°15'7"W	110°17'8"W	W	110°16'8"W	W	W	W	110°16'43"W
NPS no.			1103	1101	1100	None	None	1099	1097	1096	1095	1094	1093	1091	1089
Date			08/31/98	08/31/98	08/31/98	08/31/98	08/31/98	09/01/98	09/01/98	09/01/98	09/01/98	09/01/98	09/01/98	09/01/98	09/02/98
Depth	m		-	-	-	-	-	-	-	-	-	-	-	-	-
Treatment/ Sample type			point	point	point	point	point	point	point	point	integrated	point	point	point	point
Collector			Sanzolone	Sanzolone	Sanzolone	Sanzolone	Sanzolone	Sanzolone	Sanzolone	Sanzolone	Sanzolone	Sanzolone	Sanzolone	Sanzolone	Sanzolone
pH			7.77	2.95	2.52	2.74	6.61	6.94	7.31	7.09	7.98	7.31	8.07	7.93	3.43
Conductivity	uS/cm		-	-	-	-	-	-	-	-	-	-	-	-	-
Temperature	˚C		6.8	10.3	12.0	19.5	13.6	9.6	9.6	8.1	14.2	9.5	14	12	13.3
Flow	CFS		1.3	0.2	0.3	-		14	3	0.004	21.4	0.6	7.5	0.8	7.2
Alkalinity	Mg/L as $CaCO_3$		125	-	-	-	75	55	30	25	45	45	90	50	
Sum CO_2	mM		-	-	-	-	-	-	-	-	-	-	-	-	-
HCO_3	mM	measured	-	-	-	-	-	-	-	-	-	-	-	-	-
HCO_3	uM	calculated	-	-	-	-	-	-	-	-	-	-	-	-	-
Comments			-	no surface flow to lake	-	tributary to Columine Cr--2.2 CFS	Columbine Cr above 30, Fe stain, vents, 5 CFS	murky water	no surface flow to lake	no surface flow to lake	-	no surface flow to lake	-	-	-
Cl	mg/L	IC-Aq	0.5	1.1	2.0	1.1	0.4	0.4	0.3	0.5	0.3	0.4	0.5	0.4	5.1
F	mg/L	IC-Aq	0.2	0.2	0.2	0.2	0.2	0.2	0.3	0.3	0.3	0.2	0.3	0.2	0.3
NO_3	mg/L	IC-Aq	< 0.1	< 0.1	0.3	< 0.1	< 0.1	< 0.1	< 0.1	< 0.1	< 0.1	< 0.1	< 0.1	< 0.1	< 0.1
SO_4	mg/L	IC-Aq	83	560	820	360	21	87	1.8	2.7	3.1	1.8	17	15	84
Ag	ug/L	ICPMS	< 0.01	< 0.01	< 0.01	< 0.01	< 0.01	< 0.01	< 0.01	< 0.01	< 0.01	< 0.01	< 0.01	< 0.01	< 0.01
Al	ug/L	ICPMS	73	30000	73000	19000	80	49	29	190	9.7	120	26	94	480
As	ug/L	ICPMS	< 0.2	< 0.2	0.2	0.4	< 0.2	< 0.2	< 0.2	0.2	< 0.2	0.2	0.3	0.6	5.3
Au	ug/L	ICPMS	< 0.01	< 0.01	< 0.01	< 0.01	< 0.01	< 0.01	< 0.01	< 0.01	< 0.01	< 0.01	< 0.01	< 0.01	< 0.01
B	ug/L	ICPAES	< 10	< 10	< 10	< 10	30	25	< 10	< 10	< 10	< 10	24	< 10	650
Ba	ug/L	ICPMS	21	16	12	22	28	30	7.9	9.8	11	11	24	17	37
Be	ug/L	ICPMS	< 0.05	1.1	2.3	1.1	< 0.05	< 0.05	< 0.05	0.1	< 0.05	0.08	< 0.05	< 0.05	0.07
Bi	ug/L	ICPMS	< 0.01	< 0.01	< 0.01	< 0.01	< 0.01	< 0.01	< 0.01	< 0.01	< 0.01	< 0.01	< 0.01	< 0.01	< 0.01
Ca	mg/L	ICPAES	34	53	49	22	15	20	5.6	5.8	9.2	5.5	16	11	8.2
Cd	ug/L	ICPMS	< 0.02	0.03	0.07	< 0.02	< 0.02	< 0.02	< 0.02	< 0.02	< 0.02	< 0.02	< 0.02	< 0.02	< 0.02
Ce	ug/L	ICPMS	0.06	25	63	88	1.8	0.85	0.4	2.3	0.09	1.3	0.08	0.50	2.2
Co	ug/L	ICPMS	0.2	4.5	7.6	0.85	0.4	0.76	< 0.02	< 0.02	< 0.02	0.03	0.03	< 0.02	0.59
Cr	ug/L	ICPMS	< 1	30	74	14	< 1	< 1	< 1	< 1	< 1	< 1	< 1	< 1	< 1
Cs	ug/L	ICPMS	0.02	0.33	0.91	0.42	0.03	0.07	0.01	0.01	< 0.01	0.01	0.06	< 0.01	4.3
Cu	ug/L	ICPMS	0.8	6	10	1	< 0.5	< 0.5	< 0.5	0.7	0.9	0.6	< 0.5	0.6	0.5
Dy	ug/L	ICPMS	< 0.005	0.99	2.6	4.3	0.096	0.02	0.14	0.52	0.03	0.39	0.02	0.098	0.16
Er	ug/L	ICPMS	0.01	0.56	1.4	2.6	0.058	0.02	0.11	0.35	0.02	0.28	0.02	0.068	0.11
Eu	ug/L	ICPMS	< 0.005	0.37	0.93	0.40	< 0.005	0.006	0.007	0.02	< 0.005	0.02	< 0.005	0.008	0.02
Fe	ug/L	ICPMS	73	1700	1800	1800	71	40	33	48	37	100	40	32	870
Ga	ug/L	ICPMS	< 0.02	0.56	1.6	1.2	< 0.02	< 0.02	< 0.02	0.04	< 0.02	0.03	< 0.02	< 0.02	0.02
Gd	ug/L	ICPMS	0.01	1.4	3.7	5.2	0.099	0.04	0.18	0.57	0.03	0.44	0.02	0.088	0.18
Ge	ug/L	ICPMS	< 0.02	0.08	0.1	0.1	< 0.02	< 0.02	< 0.02	< 0.02	< 0.02	< 0.02	< 0.02	< 0.02	0.2
Hf	ug/L	ICPMS	< 0.05	< 0.05	< 0.05	< 0.05	< 0.05	< 0.05	< 0.05	< 0.05	< 0.05	< 0.05	< 0.05	< 0.05	< 0.05
Ho	ug/L	ICPMS	0.006	0.18	0.56	0.95	0.02	0.008	0.05	0.11	0.005	0.099	< 0.005	0.02	0.04
In	ug/L	ICPMS	< 0.01	< 0.01	< 0.01	< 0.01	< 0.01	< 0.01	< 0.01	< 0.01	< 0.01	< 0.01	< 0.01	< 0.01	< 0.01
K	mg/L	ICPAES	2.6	5.9	11	6.7	2.5	3.2	1.1	1.1	< 1	1.1	1.8	1.4	2.1
La	ug/L	ICPMS	0.05	11	23	35	0.80	0.50	0.4	2.0	0.07	1.3	0.07	0.4	0.98
Li	ug/L	ICPMS	9.5	15	19	15	6.0	7.8	1.7	1.1	4.2	0.8	14	2.5	60
Mg	mg/L	ICPAES	35	50	37	15	9.8	14	2.0	1.8	2.3	1.6	10	6.8	4.4
Mn	ug/L	ICPMS	49	510	670	370	79	210	5.0	0.69	3.9	3.6	8.3	0.55	50
Mo	ug/L	ICPMS	0.06	< 0.02	< 0.02	0.04	0.2	0.1	0.52	0.2	0.81	0.2	0.92	0.3	0.3
Na	mg/L	ICPAES	9.3	15	23	10	15	15	2.9	2.8	4.7	2.8	18	6.5	11
Nb	ug/L	ICPMS	< 0.02	< 0.02	< 0.02	< 0.02	< 0.02	< 0.02	< 0.02	< 0.02	< 0.02	< 0.02	< 0.02	< 0.02	< 0.02
Nd	ug/L	ICPMS	0.05	8.7	23	28	0.54	0.27	0.53	2.2	0.1	1.5	0.06	0.38	0.99
Ni	ug/L	ICPMS	3.0	24	22	4.0	2.0	3.2	0.5	0.7	0.6	0.9	0.7	0.8	2.1
P	ug/L	ICPMS	-	-	-	-	-	-	-	-	-	-	-	-	-
Pb	ug/L	ICPMS	< 0.05	0.06	< 0.05	0.2	< 0.05	< 0.05	< 0.05	< 0.05	< 0.05	0.07	< 0.05	< 0.05	0.08
Pr	ug/L	ICPMS	0.01	2.7	7.2	8.7	0.2	0.06	0.1	0.59	0.02	0.41	0.02	0.1	0.29
Rb	ug/L	ICPMS	3.7	13	34	18	5.3	7.5	1.7	1.5	1.3	1.3	4.4	2.5	5.1
Re	ug/L	ICPMS	< 0.02	< 0.02	< 0.02	< 0.02	< 0.02	< 0.02	< 0.02	< 0.02	< 0.02	< 0.02	< 0.02	< 0.02	< 0.02
Sb	ug/L	ICPMS	< 0.02	< 0.02	< 0.02	< 0.02	< 0.02	< 0.02	< 0.02	< 0.02	< 0.02	< 0.02	< 0.02	0.02	0.3
Sc	ug/L	ICPMS	2	4	5.4	2	1	1	0.6	0.7	0.5	0.7	0.7	0.4	0.4
Se	ug/L	ICPMS	< 0.2	< 0.2	0.2	0.5	< 0.2	< 0.2	< 0.2	< 0.2	< 0.2	< 0.2	< 0.2	< 0.2	< 0.2
SiO_2	mg/L	ICPMS	43	88	95	63	31	37	22	24	17	21	27	28	31
Sm	ug/L	ICPMS	< 0.01	1.3	3.6	4.6	0.08	0.03	0.1	0.42	0.02	0.32	0.02	0.08	0.2
Sn	ug/L	ICPMS	< 0.05	< 0.05	< 0.05	< 0.05	< 0.05	< 0.05	< 0.05	< 0.05	< 0.05	< 0.05	< 0.05	< 0.05	< 0.05
Sr	ug/L	ICPMS	240	570	650	240	96	130	44	50	88	50	180	120	73
Ta	ug/L	ICPMS	< 0.02	< 0.02	< 0.02	< 0.02	< 0.02	< 0.02	< 0.02	< 0.02	< 0.02	< 0.02	< 0.02	< 0.02	< 0.02
Tb	ug/L	ICPMS	< 0.005	0.19	0.54	0.79	0.01	0.005	0.02	0.085	< 0.005	0.069	< 0.005	0.02	0.03
Te	ug/L	ICPMS	< 0.1	< 0.1	< 0.1	< 0.1	< 0.1	< 0.1	< 0.1	< 0.1	< 0.1	< 0.1	< 0.1	< 0.1	< 0.1
Th	ug/L	ICPMS	< 0.005	0.14	0.45	0.34	< 0.005	< 0.005	0.008	0.02	< 0.005	0.04	< 0.005	0.009	0.009
Ti	ug/L	ICPMS	0.4	17	20	14	< 0.1	0.3	0.1	0.5	< 0.1	0.4	< 0.1	0.4	0.4
Tl	ug/L	ICPMS	< 0.05	< 0.05	< 0.05	< 0.05	< 0.05	< 0.05	< 0.05	< 0.05	< 0.05	< 0.05	< 0.05	< 0.05	< 0.05
Tm	ug/L	ICPMS	< 0.005	0.063	0.18	0.34	0.006	< 0.005	0.02	0.04	< 0.005	0.04	< 0.005	0.01	0.01
U	ug/L	ICPMS	0.08	0.12	0.36	0.08	0.01	0.009	0.05	0.06	0.12	0.07	0.32	0.10	0.04
V	ug/L	ICPMS	1	4	8.2	10	< 0.1	< 0.1	0.6	0.4	0.6	0.2	0.5	1	1
W	ug/L	ICPMS	< 0.02	< 0.02	< 0.02	< 0.02	< 0.02	< 0.02	< 0.02	< 0.02	0.04	< 0.02	< 0.02	< 0.02	0.4
Y	ug/L	ICPMS	0.07	4.6	12	22	0.53	0.2	0.95	2.8	0.2	2.1	0.1	0.57	0.92
Yb	ug/L	ICPMS	< 0.01	0.48	1.2	2.2	0.04	0.02	0.1	0.31	0.02	0.25	0.02	0.08	0.07
Zn	ug/L	ICPMS	2	20	37	10	6	7	1	2	1	2	1	1	4
Zr	ug/L	ICPMS	< 0.05	0.08	< 0.05	0.2	< 0.05	< 0.05	0.2	0.66	< 0.05	0.50	< 0.05	0.3	< 0.05
Hg	ng/L	Hg CVAF	<5	<5	<5	7	<5	<5	<5	<5	<5	<5	<5	<5	<5
$\delta^{18}O$ vs VSMOW	permil	ISO1	-18.8	-18.2	-19.7	-18.7	-18.0	-18.2	-18.0	-17.8	-18.0	-18.1	-18.3	-17.5	-16.7
δD vs VSMOW	permil	ISO2	-139.8	-132.8	-144.4	-140.6	-138.8	-140.0	-138.9	-136.6	-136.4	-139.1	-140.8	-137.9	-133.3
$\delta^{34}S$ vs CDT	permil	ISO3	-	-	-	-	-	-	-	-	-	-	-	-	-
$\delta^{34}S$ vs CDT	permil	ISO4	1.15	0.225	-0.14	0.35	2.53	0.92	-	-	-	-	3.74	6.05	-3.28

Appendix 1. Site and analytical data from creeks and water column profiles—*Continued*.

Field no. Drainage/ description			RS-40-98 Pelican Cr	RS-41-98 Bridge Cr	RS-42-98 Big Thumb Cr	RS-43-98 Little Thumb Cr	RS-44-98 Arnica Cr	RS-45-98 Weasel Cr	RS-47-98	RS-1-99 Solution Cr	RS-5-99 Flat Mt. Stream	RS-7-99	RS-8-99 West side S arm	RS-9-99	RS-16-99 Yellowstone River Inlet
Latitude			44°33'38"N	44°31'45"N	44°24'18"N	44°26'9"N	44°28'46"N	44°31'17"N	44°32'16"N	44°24'22"N	44°21'36"N	44°22'23"N	44°20'34"N	44°19'57"N	44°18'28.2"N
Longitude			110°21'9"W	W	W	W	W	110°27'4"W	110°27'7"W	110°30'1"W	110°27'4"W	W	W	W	110°10'46.3"W
NPS no.			1085	1196	1168	1176	1182	1192	1199	-	-	-	-	-	-
Date			09/02/98	09/02/98	09/02/98	09/02/98	09/02/98	09/02/98	09/02/98	07/16/99	07/15/99	07/15/99	07/15/99	07/15/99	07/21/99
Depth	m		-	-	-	-	-	-	-	-	-	-	-	-	-
Treatment/ Sample type			integrated	point	point	point	point	point	point	point	point	point	point	point	point
Collector			Sanzolone	Sanzolone	Sanzolone	Sanzolone	Sanzolone	Sanzolone	Sanzolone	Sanzolone	Sanzolone	Sanzolone	Sanzolone	Sanzolone	WRD
pH			7.43	8.09	6.99	6.87	8.39	6.97	6.93	7.17	7.55	7.35	7.55	7.73	?
Conductivity	uS/cm		-	-	-	-	-	-	-	-	-	-	-	-	-
Temperature	°C		14.9	16.5	19.4	16.6	18	11.8	12.5	13.2	12.2	9.2	6.9	5.7	?
Flow	CFS		35	2.1	0.5	0.3	11.7	0.005	0.01	?	4.6	2.2	2.9	3.4	3500
Alkalinity	Mg/L as $CaCO_3$		57	45	75	30	40	45	45	33	35	22	27	28	?
Sum CO_2	mM		-	-	-	-	-	-	-	-	-	-	-	-	-
HCO_3	mM	measured	-	-	-	-	-	-	-	-	-	-	-	-	-
HCO_3	uM	calculated	-	-	-	-	-	-	-	-	-	-	-	-	-
Comments			abundant suspended sed	-	abundant algae	-	-	poor flow, braided channnel	poor flow, braided channnel	600 sq ft x sec--velocity too low to measure	-	-	-	-	CFS estimate-could not wade
Cl	mg/L	IC-Aq	18	1.1	1.0	0.8	1.3	0.6	1.7	3.9	0.5	0.3	0.5	0.5	0.2
F	mg/L	IC-Aq	0.4	4.3	0.9	0.6	5.0	0.4	3.5	0.5	0.6	0.5	0.5	1.3	0.1
NO_3	mg/L	IC-Aq	< 0.1	< 0.1	< 0.1	< 0.1	< 0.1	< 0.1	< 0.1	<.1	0.1	<.1	0.1	0.6	<.1
SO_4	mg/L	IC-Aq	82	2.0	4.5	1.7	1.7	1.7	1.5	5.3	2.3	0.9	1.3	1.6	1.4
Ag	ug/L	ICPMS	< 0.01	< 0.01	< 0.01	< 0.01	< 0.01	< 0.01	< 0.01	<0.01	<0.01	<0.01	<0.01	<0.01	<0.01
Al	ug/L	ICPMS	450	49	14	67	36	31	60	7.8	12	13	5.5	2	5.7
As	ug/L	ICPMS	18	3.7	8.5	2	2.7	0.3	1	11	5.4	0.6	0.5	0.6	<0.4
Au	ug/L	ICPMS	< 0.01	< 0.01	0.02	< 0.01	< 0.01	< 0.01	0.01	< 0.01	< 0.01	< 0.01	< 0.01	< 0.01	< 0.01
B	ug/L	ICPAES	960	19	10	11	16	< 10	< 10	88.4	19.2	14.1	11.9	11.1	5.73
Ba	ug/L	ICPMS	44	16	28	26	6.1	21	14	11	16	7	7.3	3.1	6.6
Be	ug/L	ICPMS	< 0.05	0.07	0.1	< 0.05	0.3	< 0.05	0.5	<0.05	<0.05	<0.05	<0.05	0.05	<0.05
Bi	ug/L	ICPMS	< 0.01	< 0.01	< 0.01	< 0.01	< 0.01	< 0.01	< 0.01	< 0.01	< 0.01	< 0.01	< 0.01	< 0.01	< 0.01
Ca	mg/L	ICPAES	18	8.4	12	5.1	6.9	4.6	7.0	5.21	8.36	4.06	5.08	6.63	3.24
Cd	ug/L	ICPMS	< 0.02	< 0.02	< 0.02	< 0.02	< 0.02	< 0.02	0.03	<0.02	<0.02	<0.02	<0.02	<0.02	<0.02
Ce	ug/L	ICPMS	0.50	0.3	0.1	0.71	0.3	0.78	0.4	0.2	0.2	0.2	0.1	0.04	0.08
Co	ug/L	ICPMS	0.08	< 0.02	< 0.02	0.09	< 0.02	0.07	0.05	0.06	<0.02	<0.02	<0.02	<0.02	0.02
Cr	ug/L	ICPMS	< 1	< 1	< 1	< 1	< 1	< 1	< 1	<1	<1	<1	<1	<1	<1
Cs	ug/L	ICPMS	7.4	3.8	2.2	0.49	2.6	0.02	1.4	1.8	0.1	< 0.01	0.04	0.2	< 0.01
Cu	ug/L	ICPMS	< 0.5	< 0.5	< 0.5	< 0.5	< 0.5	< 0.5	0.7	<0.5	<0.5	<0.5	<0.5	<0.5	<0.5
Dy	ug/L	ICPMS	0.054	0.02	0.02	0.069	0.02	0.075	0.059	0.02	0.03	0.097	0.03	0.009	0.007
Er	ug/L	ICPMS	0.02	0.03	0.02	0.055	0.02	0.057	0.03	0.01	0.02	0.057	0.02	0.007	< 0.005
Eu	ug/L	ICPMS	< 0.005	< 0.005	< 0.005	0.007	< 0.005	0.01	0.006	< 0.005	< 0.005	< 0.005	< 0.005	< 0.005	< 0.005
Fe	ug/L	ICPMS	66	35	64	67	52	17	63	<30	<30	<30	<30	<30	<30
Ga	ug/L	ICPMS	< 0.02	< 0.02	< 0.02	< 0.02	< 0.02	< 0.02	< 0.02	0.02	< 0.02	< 0.02	< 0.02	< 0.02	< 0.02
Gd	ug/L	ICPMS	0.063	0.03	0.02	0.089	0.03	0.076	0.05	0.02	0.03	0.072	0.03	< 0.005	0.01
Ge	ug/L	ICPMS	0.4	0.2	0.2	0.02	0.2	< 0.02	0.04	0.2	< 0.02	< 0.02	< 0.02	< 0.02	< 0.02
Hf	ug/L	ICPMS	< 0.05	< 0.05	< 0.05	< 0.05	< 0.05	< 0.05	< 0.05	-	-	-	-	-	-
Ho	ug/L	ICPMS	0.01	0.008	0.006	0.02	0.005	0.02	0.01	0.006	0.009	0.02	0.009	< 0.005	< 0.005
In	ug/L	ICPMS	< 0.01	< 0.01	< 0.01	< 0.01	< 0.01	< 0.01	< 0.01	-	-	-	-	-	-
K	mg/L	ICPAES	11	4.3	7.8	2.3	2.6	2.5	2.2	1.67	1.79	0.606	0.865	1.02	0.888
La	ug/L	ICPMS	0.2	0.1	0.08	0.3	0.08	0.4	0.2	0.1	0.1	0.3	0.1	0.1	0.07
Li	ug/L	ICPMS	190	43	29	11	55	2.5	18	46	10	6.8	8.9	9.3	5.7
Mg	mg/L	ICPAES	11	1.8	4.5	1.7	1.5	1.6	2.0	2.14	1.15	1.03	1.27	1.56	1.38
Mn	ug/L	ICPMS	26	3.2	11	22	3.3	12	19	11	6.2	0.41	4.8	0.1	2.3
Mo	ug/L	ICPMS	0.5	4.9	16	0.79	5.7	0.4	2.2	1.2	0.4	0.2	0.5	0.78	< 0.2
Na	mg/L	ICPAES	41	11	17	3.5	13	2.6	4.1	7.86	2.72	2.2	2.53	2.85	2.09
Nb	ug/L	ICPMS	< 0.02	< 0.02	< 0.02	< 0.02	< 0.02	< 0.02	< 0.02	0.04	0.04	0.02	0.03	0.04	< 0.02
Nd	ug/L	ICPMS	0.2	0.2	0.1	0.37	0.08	0.36	0.25	0.1	0.1	0.29	0.1	0.02	0.07
Ni	ug/L	ICPMS	1.2	0.4	0.6	0.4	0.2	0.5	1.0	0.4	<0.1	0.4	<0.1	<0.1	0.3
P	ug/L	ICPMS	-	-	-	-	-	-	-	2	4	< 1	< 1	1	17
Pb	ug/L	ICPMS	< 0.05	< 0.05	< 0.05	< 0.05	< 0.05	< 0.05	0.09	<0.05	<0.05	<0.05	<0.05	<0.05	<0.05
Pr	ug/L	ICPMS	0.06	0.04	0.02	0.1	0.02	0.1	0.07	0.03	0.03	0.07	0.02	< 0.01	0.01
Rb	ug/L	ICPMS	35	20	20	6.3	10	5.0	8.6	4.2	5.9	1	1.8	2	1.2
Re	ug/L	ICPMS	< 0.02	< 0.02	< 0.02	< 0.02	< 0.02	< 0.02	< 0.02	-	-	-	-	-	-
Sb	ug/L	ICPMS	0.4	0.09	0.4	< 0.02	0.04	< 0.02	0.03	0.63	0.41	0.05	<0.05	<0.05	<0.05
Sc	ug/L	ICPMS	0.4	0.5	0.5	0.2	0.3	0.2	0.2	< 0.1	< 0.1	< 0.1	< 0.1	< 0.1	< 0.1
Se	ug/L	ICPMS	< 0.2	< 0.2	< 0.2	< 0.2	< 0.2	< 0.2	< 0.2	< 0.3	< 0.3	< 0.3	< 0.3	< 0.3	< 0.3
SiO_2	mg/L	ICPMS	70	88	100	27	56	35	37	9.1	27	14	20	21	14
Sm	ug/L	ICPMS	0.05	0.02	0.01	0.08	0.02	0.08	0.04	0.02	0.03	0.06	0.02	< 0.01	< 0.01
Sn	ug/L	ICPMS	< 0.05	< 0.05	< 0.05	< 0.05	< 0.05	< 0.05	< 0.05	-	-	-	-	-	-
Sr	ug/L	ICPMS	160	33	70	38	19	42	35	38	29	29	32	29	24
Ta	ug/L	ICPMS	< 0.02	< 0.02	< 0.02	0.05	< 0.02	< 0.02	< 0.02	0.03	0.05	< 0.03	< 0.03	0.06	< 0.03
Tb	ug/L	ICPMS	0.006	0.006	< 0.005	0.01	< 0.005	0.009	0.007	< 0.005	< 0.005	0.01	< 0.005	< 0.005	< 0.005
Te	ug/L	ICPMS	< 0.1	< 0.1	< 0.1	< 0.1	< 0.1	< 0.1	< 0.1	-	-	-	-	-	-
Th	ug/L	ICPMS	< 0.005	0.02	< 0.005	0.01	0.01	0.01	0.01	0.07	< 0.02	< 0.02	< 0.02	< 0.02	< 0.02
Ti	ug/L	ICPMS	0.2	0.2	< 0.1	0.2	0.1	0.1	0.2	< 0.2	< 0.2	< 0.2	< 0.2	< 0.2	< 0.2
Tl	ug/L	ICPMS	< 0.05	< 0.05	< 0.05	< 0.05	< 0.05	< 0.05	< 0.05	<0.05	<0.05	<0.05	<0.05	<0.05	<0.05
Tm	ug/L	ICPMS	< 0.005	< 0.005	< 0.005	0.01	< 0.005	0.008	0.006	< 0.005	< 0.005	0.01	< 0.005	< 0.005	< 0.005
U	ug/L	ICPMS	0.10	0.10	0.04	0.02	0.11	0.02	0.06	0.02	0.05	0.02	0.03	0.15	0.009
V	ug/L	ICPMS	1	1	0.3	0.2	0.5	1	0.4	0.56	<0.2	<0.2	<0.2	<0.2	2
W	ug/L	ICPMS	0.2	0.82	0.1	0.08	1.3	0.04	0.05	2.8	1.4	0.98	0.79	0.82	0.18
Y	ug/L	ICPMS	0.2	0.1	0.1	0.5	0.1	0.4	0.3	0.1	0.2	0.5	0.2	0.05	0.04
Yb	ug/L	ICPMS	0.02	0.02	0.02	0.06	0.02	0.06	0.04	0.01	0.02	0.05	0.03	< 0.01	< 0.01
Zn	ug/L	ICPMS	2	2	2	2	0.8	4	82	0.6	0.6	<0.5	<0.5	<0.5	<0.5
Zr	ug/L	ICPMS	< 0.05	0.3	< 0.05	0.1	0.2	0.2	0.2	< 0.2	< 0.2	< 0.2	< 0.2	< 0.2	< 0.2
Hg	ng/L	Hg CVAF	<5	<5	<5	<5	<5	<5	<5	-	-	-	-	-	-
$\delta^{18}O$ vs VSMOW	permil	ISO1	-16.8	-18.7	-17.4	-18.0	-19.1	-18.3	-19.0	-15.6	-18.3	-18.1	-18.5	-18.9	-18.5
δD vs VSMOW	permil	ISO2	-136.7	-146.7	-136.8	-132.0	-141.6	-142.7	-144.2	-124.3	-139.4	-139.3	-141.7	-142.3	-141.7
$\delta^{34}S$ vs CDT	permil	ISO3	-	-	-	-	-	-	-	-	-	-	-	-	-
$\delta^{34}S$ vs CDT	permil	ISO4	5.21	-	10.68	-	-	-	-	-	-	-	-	-	-

Appendix 1. Site and analytical data from creeks and water column profiles—*Continued*.

Field no. Drainage/ description			RS-17-99 Beaver Dam Creek	RS-18-99 Trail Creek	RS-19A-99 no name	RS-19B-99 no name	RS-20-99 no name	RS-23-99 Grouse Creek	RS-26-99 Chipmunk Creek	RS-32-99 Columbine Cr	RS-33-99 Meadow Cr	RS-35-99 Clear Cr	RS-37-99 Cub Cr	RS-39-99 Sedge Cr
Latitude			44°19'24"N	44°17'29.9"N	44°17'21.9"N	44°17'21.3"N	44°17'22.2"N	44°16'54.3"N	44°17'16.6"N	44°24'3"N	44°25'37"N	44°28'35"N	44°29'23"N	44°31'26"N
Longitude			110°11'4.8"W	110°12'4"W	110°12'24.8"W	110°12'20.4"W	110°12'31.4"W	110°20'13.6"W	110°17'0.8"W	110°15'7"W	110°17'8"W	110°16'8"W	W	110°16'43"W
NPS no.			-	-	-	-	-	-	-	-	-	-	-	-
Date			07/20/99	07/20/99	07/20/99	07/20/99	07/20/99	07/21/99	07/21/99	07/16/99	07/16/99	07/13/99	07/13/99	07/12/99
Depth	m		-	-	-	-	-	-	-	-	-	-	-	-
Treatment/ Sample type			integrated	integrated	point	point	point	point	point	integrated	integrated	integrated	integrated	integrated
Collector			Gemery/WRD	Gemery/WRD	Gemery/WRD	Gemery/WRD	Gemery/WRD	Gemery/WRD	Gemery/WRD	Sanzolone	Sanzolone	Sanzolone	Sanzolone	Sanzolone
pH			7.38	7.86	8.03	7.83	8.09	8.24	8.04	6.58	6.75	7.25	7.60	3.66
Conductivity	uS/cm		-	-	-	-	-	-	-	-	-	-	-	-
Temperature	˚C		7.5	21	9	9	7	11	15.5	4.3	5.7	8.4	8.8	16.0
Flow	CFS		85.1	4.67	0.92	0.66	3.52	10.5	34.7	63	6.4	132	57	48
Alkalinity	Mg/L as $CaCO_3$									20	20	22	30	
Sum CO_2	mM		-	-	-	-	-	-	-	-	-	-	-	-
HCO_3	mM	measured	-	-	-	-	-	-	-	-	-	-	-	-
HCO_3	uM	calculated	-	-	-	-	-	-	-	-	-	-	-	-
Comments			-	-	-	-	-	-	-	-	-	-	-	-
Cl	mg/L	IC-Aq	0.2	0.4	0.2	0.3	0.3	0.3	0.3	0.2	0.3	0.2	0.2	1.7
F	mg/L	IC-Aq	0.2	0.2	0.2	0.1	0.2	0.1	0.2	0.2	0.2	0.1	0.2	0.2
NO_3	mg/L	IC-Aq	<.1	<.1	<.1	<.1	0.2	0.1	<.1	<.1	<.1	<.1	<.1	<.1
SO_4	mg/L	IC-Aq	1.9	1.1	1.2	1.2	1.2	4.2	0.7	14	1.4	1.9	3.6	31
Ag	ug/L	ICPMS	<0.01	<0.01	<0.01	<0.01	<0.01	<0.01	<0.01	<0.01	<0.01	<0.01	<0.01	<0.01
Al	ug/L	ICPMS	4.6	12	5.2	20	<0.5	<0.5	5.5	170	38	14	40	140
As	ug/L	ICPMS	<0.4	0.4	<0.4	<0.4	<0.4	<0.4	<0.4	<0.4	<0.4	<0.4	<0.4	5
Au	ug/L	ICPMS	< 0.01	< 0.01	< 0.01	< 0.01	< 0.01	< 0.01	< 0.01	< 0.01	< 0.01	< 0.01	< 0.01	< 0.01
B	ug/L	ICPAES	5.65	9.57	6.08	6.31	5	6.74	<5	12.1	9.8	8.19	10.1	234
Ba	ug/L	ICPMS	11	21	34	25	32	58	24	11	9.2	8.2	9.4	18
Be	ug/L	ICPMS	<0.05	<0.05	<0.05	<0.05	<0.05	<0.05	<0.05	<0.05	0.05	<0.05	<0.05	0.08
Bi	ug/L	ICPMS	< 0.01	< 0.01	< 0.01	< 0.01	< 0.01	< 0.01	< 0.01	< 0.01	< 0.01	< 0.01	< 0.01	< 0.01
Ca	mg/L	ICPAES	2.6	7.38	9.15	5.97	9.5	25.4	7.31	4.83	4.31	5.74	4.7	3.95
Cd	ug/L	ICPMS	<0.02	<0.02	<0.02	<0.02	<0.02	<0.02	<0.02	<0.02	<0.02	<0.02	<0.02	<0.02
Ce	ug/L	ICPMS	0.04	0.2	0.06	0.1	< 0.01	< 0.01	0.07	1.8	0.56	0.2	0.4	0.93
Co	ug/L	ICPMS	<0.02	0.05	<0.02	<0.02	<0.02	<0.02	<0.02	0.1	0.04	<0.02	<0.02	0.2
Cr	ug/L	ICPMS	<1	<1	<1	<1	<1	<1	<1	<1	<1	<1	<1	<1
Cs	ug/L	ICPMS	< 0.01	0.02	< 0.01	< 0.01	0.01	< 0.01	< 0.01	0.01	0.01	< 0.01	0.03	1.4
Cu	ug/L	ICPMS	<0.5	<0.5	<0.5	<0.5	<0.5	<0.5	<0.5	<0.5	0.7	5	<0.5	<0.5
Dy	ug/L	ICPMS	0.01	0.02	0.008	0.02	< 0.005	0.01	0.01	0.11	0.26	0.073	0.14	0.13
Er	ug/L	ICPMS	0.006	0.006	< 0.005	0.02	< 0.005	< 0.005	0.005	0.069	0.17	0.05	0.084	0.078
Eu	ug/L	ICPMS	< 0.005	0.005	< 0.005	< 0.005	< 0.005	< 0.005	< 0.005	0.01	0.02	0.006	0.007	0.02
Fe	ug/L	ICPMS	<30	100	<30	<30	<30	<30	<30	30	<30	<30	<30	290
Ga	ug/L	ICPMS	< 0.02	< 0.02	< 0.02	< 0.02	< 0.02	< 0.02	< 0.02	< 0.02	< 0.02	< 0.02	< 0.02	< 0.02
Gd	ug/L	ICPMS	< 0.005	0.03	< 0.005	0.007	< 0.005	< 0.005	0.01	0.13	0.22	0.065	0.13	0.12
Ge	ug/L	ICPMS	< 0.02	< 0.02	< 0.02	< 0.02	< 0.02	< 0.02	< 0.02	< 0.02	< 0.02	< 0.02	< 0.02	0.1
Hf	ug/L	ICPMS	-	-	-	-	-	-	-	-	-	-	-	-
Ho	ug/L	ICPMS	< 0.005	< 0.005	< 0.005	< 0.005	< 0.005	< 0.005	< 0.005	0.02	0.056	0.02	0.03	0.03
In	ug/L	ICPMS	-	-	-	-	-	-	-	-	-	-	-	-
K	mg/L	ICPAES	1.03	1.85	2.01	2	2.06	0.96	1.6	1	0.898	0.46	0.628	1.12
La	ug/L	ICPMS	0.07	0.2	0.04	0.1	0.02	0.01	0.06	0.94	0.75	0.2	0.57	0.54
Li	ug/L	ICPMS	5.9	6.3	6.9	5.8	6.6	6.2	6.6	6.8	7	7.1	9.9	24
Mg	mg/L	ICPAES	1.02	2.51	1.54	1.61	1.46	8.38	1.6	2.63	1.65	1.26	2.17	1.91
Mn	ug/L	ICPMS	0.42	18	0.33	0.22	0.056	5.9	3	27	9.3	2.9	7.8	27
Mo	ug/L	ICPMS	< 0.2	< 0.2	< 0.2	< 0.2	< 0.2	0.4	< 0.2	0.3	0.3	0.3	0.3	0.2
Na	mg/L	ICPAES	3.1	2.76	2.48	2.29	2.35	3.54	1.75	3.19	2.28	2.12	3.86	4.23
Nb	ug/L	ICPMS	< 0.02	< 0.02	< 0.02	< 0.02	< 0.02	< 0.02	< 0.02	< 0.02	< 0.02	< 0.02	< 0.02	< 0.02
Nd	ug/L	ICPMS	0.08	0.2	0.05	0.1	0.02	0.01	0.09	0.82	0.92	0.29	0.57	0.68
Ni	ug/L	ICPMS	<0.1	0.3	<0.1	<0.1	<0.1	<0.1	0.2	0.5	0.4	2.5	0.4	1
P	ug/L	ICPMS	20	74	62	43	69	< 1	24	< 1	3	< 1	< 1	4
Pb	ug/L	ICPMS	<0.05	<0.05	<0.05	<0.05	<0.05	<0.05	<0.05	<0.05	<0.05	0.4	<0.05	0.07
Pr	ug/L	ICPMS	0.02	0.04	0.01	0.03	< 0.01	< 0.01	0.02	0.25	0.23	0.06	0.1	0.2
Rb	ug/L	ICPMS	1.5	2.6	2.8	3	2.7	0.84	2.3	2	1.7	0.82	1.6	2.3
Re	ug/L	ICPMS	-	-	-	-	-	-	-	-	-	-	-	-
Sb	ug/L	ICPMS	<0.05	<0.05	<0.05	<0.05	<0.05	<0.05	<0.05	<0.05	<0.05	<0.05	<0.05	0.2
Sc	ug/L	ICPMS	< 0.1	< 0.1	< 0.1	< 0.1	< 0.1	< 0.1	< 0.1	< 0.1	< 0.1	< 0.1	< 0.1	< 0.1
Se	ug/L	ICPMS	< 0.3	< 0.3	< 0.3	< 0.3	< 0.3	0.4	< 0.3	< 0.3	< 0.3	< 0.3	< 0.3	< 0.3
SiO_2	mg/L	ICPMS	19	15	29	26	29	6.6	20	18	19	10	14	17
Sm	ug/L	ICPMS	< 0.01	0.03	< 0.01	0.01	< 0.01	< 0.01	0.02	0.2	0.21	0.06	0.1	0.2
Sn	ug/L	ICPMS	-	-	-	-	-	-	-	-	-	-	-	-
Sr	ug/L	ICPMS	21	46	48	39	45	160	47	41	39	67	53	38
Ta	ug/L	ICPMS	< 0.03	< 0.03	< 0.03	< 0.03	< 0.03	< 0.03	< 0.03	< 0.03	< 0.03	< 0.03	< 0.03	< 0.03
Tb	ug/L	ICPMS	< 0.005	< 0.005	< 0.005	< 0.005	< 0.005	< 0.005	< 0.005	0.02	0.04	0.01	0.02	0.02
Te	ug/L	ICPMS	-	-	-	-	-	-	-	-	-	-	-	-
Th	ug/L	ICPMS	< 0.02	< 0.02	< 0.02	< 0.02	< 0.02	< 0.02	< 0.02	< 0.02	< 0.02	< 0.02	< 0.02	< 0.02
Ti	ug/L	ICPMS	< 0.2	< 0.2	< 0.2	< 0.2	< 0.2	< 0.2	< 0.2	< 0.2	0.2	< 0.2	< 0.2	0.5
Tl	ug/L	ICPMS	<0.05	<0.05	<0.05	<0.05	<0.05	<0.05	<0.05	<0.05	<0.05	<0.05	<0.05	<0.05
Tm	ug/L	ICPMS	< 0.005	< 0.005	< 0.005	< 0.005	< 0.005	< 0.005	< 0.005	0.008	0.02	0.007	0.01	0.01
U	ug/L	ICPMS	0.007	0.04	0.06	0.03	0.08	0.27	0.03	0.008	0.06	0.05	0.06	0.04
V	ug/L	ICPMS	1.6	2.6	2.3	2.2	1.9	<0.2	1.8	0.4	0.61	0.52	0.3	0.96
W	ug/L	ICPMS	0.15	0.21	0.14	0.13	0.1	0.08	0.06	0.64	0.52	0.4	0.39	0.71
Y	ug/L	ICPMS	0.06	0.09	0.03	0.1	0.02	0.04	0.06	0.57	1.3	0.4	0.7	0.62
Yb	ug/L	ICPMS	< 0.01	0.01	< 0.01	0.01	< 0.01	< 0.01	< 0.01	0.06	0.2	0.04	0.09	0.1
Zn	ug/L	ICPMS	<0.5	<0.5	<0.5	<0.5	<0.5	<0.5	<0.5	1	<0.5	2	0.7	1
Zr	ug/L	ICPMS	< 0.2	< 0.2	< 0.2	< 0.2	< 0.2	< 0.2	< 0.2	14	< 0.2	< 0.2	< 0.2	< 0.2
Hg	ng/L	Hg CVAF	-	-	-	-	-	-	-	-	-	-	-	-
$\delta^{18}O$ vs VSMOW	permil	ISO1	-18.5	-17.6	-19.3	-18.7	-19.1	-18.0	-18.7	-18.6	-17.4	-18.0	-18.4	-18.1
δD vs VSMOW	permil	ISO2	-138.1	-135.9	-145.8	-141.6	-146.8	-144.0	-141.3	-136.9	-134.5	-131.7	-136.6	-134.4
$\delta^{34}S$ vs CDT	permil	ISO3	-	-	-	-	-	-	-	-	-	-	-	-
$\delta^{34}S$ vs CDT	permil	ISO4	-	-	-	-	-	-	-	-	-	-	-	-

Appendix 1. Site and analytical data from creeks and water column profiles—*Continued*.

Field no. Drainage/ description			RS-39R-99 Sedge Cr	RS-40-99 Pelican Cr	RS-41-99 Bridge Cr	RS-44-99 Arnica Cr	28 Inlet SE Arm	34 Mid SE Arm surface	35 SE Arm further from inlet	36 Inlet SE Arm	42 Mid SE Arm surface	43 SE Arm further from inlet	SE Arm further from inlet	7 SE Arm water column	8 SE Arm water column
Latitude			44°31'26"N	44°33'38"N	44°31'45"N	44°28'46"N	-	-	-	-	-	-	-	44°21'30.5"N	44°21'30.5"N
Longitude			110°16'43"W	110°21'9"W	110°27'48"W	W	-	-	-	-	-	-	-	110°15'0.5"W	W
NPS no.			-	-	-	-	-	-	-	-	-	-	-	-	-
Date			07/12/99	07/12/99	07/12/99	07/12/99	07/15/97	07/15/97	07/15/97	07/15/97	07/15/97	07/15/97	07/15/97	07/24/97	07/24/97
Depth	m		-	-	-	-	-	-	-	-	-	-	surface	2	5
Treatment/ Sample type			integrated	point	point	integrated	Filtered and acidified	Filtered and acidified	Filtered and acidified	Raw and acidified	Raw and acidified	Raw and acidified	Filtered and acidified	Filtered and acidified	Filtered and acidified
Collector			Sanzolone	Sanzolone	Sanzolone	Sanzolone	-	-	-	-	-	-	-	-	-
pH			3.66	7.61	7.93	8.03	7.05	7.05	7.10	-	-	-	7.10	7.41	7.50
Conductivity	uS/cm		-	-	-	-	-	-	-	-	-	-	-	-	-
Temperature	˚C		16.0	17.7	22.1	19.3	-	-	-	-	-	-	-	-	-
Flow	CFS		-	85	1.7	11.5	-	-	-	-	-	-	-	-	-
Alkalinity	Mg/L as $CaCO_3$		-	30	40	38	-	-	-	-	-	-	-	-	-
Sum CO_2	mM		-	-	-	-	0.47	0.48	0.55	-	-	-	0.55	0.55	0.54
HCO_3	mM	measured	-	-	-	-	-	-	-	-	-	-	-	0.5	0.5
HCO_3	uM	calculated	-	-	-	-	-	-	-	-	-	-	-	499	481
Comments			-	estimate-could not wade	-	-	-	-	-	-	-	-	-	-	-
Cl	mg/L	IC-Aq	1.7	9.9	0.9	1	0.2	0.2	3.4				3.4	3.3	3.2
F	mg/L	IC-Aq	0.2	0.3	4.2	5.2	-	-	-	-	-	-	-	-	-
NO_3	mg/L	IC-Aq	<.1	0.4	<.1	<.1	-	-	-	-	-	-	-	-	-
SO_4	mg/L	IC-Aq	31	38	1.6	1.6	1.1	1.4	5.1				5.1	4.5	5.0
Ag	ug/L	ICPMS	<0.01	<0.01	<0.01	<0.01	< 0.01	< 0.01	< 0.01	< 0.01	< 0.01	< 0.01	< 0.01	< 0.01	< 0.01
Al	ug/L	ICPMS	140	150	70	21	16	13	28	530	660	200	28	27	17
As	ug/L	ICPMS	5	11	3.5	2.7	0.3	0.6	9.0	0.4	0.6	9.3	9.0	9.0	9.3
Au	ug/L	ICPMS	< 0.01	< 0.01	< 0.01	< 0.01	0.005	< 0.005	< 0.005	< 0.005	< 0.005	< 0.005	< 0.005	< 0.005	< 0.005
B	ug/L	ICPAES	234	347	15.3	17.9	< 10	< 10	62	< 10	< 10	60	62	60	58
Ba	ug/L	ICPMS	18	30	15	7.7	6.8	6.7	7.9	11	11	8.8	7.9	8.0	8.0
Be	ug/L	ICPMS	0.06	<0.05	0.05	0.2	< 0.05	< 0.05	< 0.05	< 0.05	< 0.05	< 0.05	< 0.05	< 0.05	< 0.05
Bi	ug/L	ICPMS	< 0.01	< 0.01	< 0.01	< 0.01	< 0.01	< 0.01	< 0.01	< 0.01	< 0.01	< 0.01	< 0.01	< 0.01	< 0.01
Ca	mg/L	ICPAES	3.97	9.47	6.68	6.16	3.9	4.1	5.2	4.4	4.7	5.2	5.2	4.9	4.8
Cd	ug/L	ICPMS	<0.02	0.03	<0.02	<0.02	< 0.02	< 0.02	0.04	< 0.02	0.03	0.06	0.04	< 0.02	< 0.02
Ce	ug/L	ICPMS	0.96	0.2	0.4	0.2	0.1	0.1	0.07	1.2	1.3	0.3	0.07	0.06	0.06
Co	ug/L	ICPMS	0.2	0.08	0.03	0.02	0.04	0.03	< 0.02	0.3	0.4	0.06	< 0.02	< 0.02	< 0.02
Cr	ug/L	ICPMS	<1	<1	<1	<1	< 0.5	< 0.5	< 0.5	< 0.5	< 0.5	< 0.5	< 0.5	< 0.5	< 0.5
Cs	ug/L	ICPMS	1.4	2.7	2.6	2.1	< 0.01	0.03	1.8	0.01	0.07	1.9	1.8	1.8	1.8
Cu	ug/L	ICPMS	<0.5	0.6	<0.5	<0.5	< 0.5	< 0.5	0.5	0.7	0.9	0.8	0.5	< 0.5	< 0.5
Dy	ug/L	ICPMS	0.13	0.02	0.072	0.02	0.01	0.006	0.009	0.05	0.04	0.02	0.009	0.005	< 0.005
Er	ug/L	ICPMS	0.071	0.02	0.04	0.02	0.007	0.005	< 0.005	0.02	0.02	0.01	< 0.005	0.006	< 0.005
Eu	ug/L	ICPMS	0.02	< 0.005	0.006	< 0.005	< 0.005	< 0.005	< 0.005	0.01	0.01	0.005	< 0.005	< 0.005	< 0.005
Fe	ug/L	ICPMS	280	33	49	37	28	30	13	300	350	69	13	19	12
Ga	ug/L	ICPMS	< 0.02	< 0.02	< 0.02	< 0.02	< 0.02	< 0.02	< 0.02	0.04	0.05	0.02	< 0.02	< 0.02	< 0.02
Gd	ug/L	ICPMS	0.15	0.02	0.04	0.03	0.02	0.01	0.01	0.04	0.058	0.02	0.01	0.005	0.009
Ge	ug/L	ICPMS	0.1	0.4	0.3	0.2	< 0.02	< 0.02	0.2	< 0.02	< 0.02	0.2	0.2	0.2	0.2
Hf	ug/L	ICPMS	-	-	-	-	< 0.05	< 0.05	8.9	< 0.05	< 0.05	0.53	8.9	0.52	< 0.05
Ho	ug/L	ICPMS	0.03	0.005	0.01	0.005	< 0.005	< 0.005	< 0.005	0.006	0.008	< 0.005	< 0.005	< 0.005	< 0.005
In	ug/L	ICPMS	-	-	-	-	< 0.01	< 0.01	< 0.01	< 0.01	< 0.01	< 0.01	< 0.01	< 0.01	< 0.01
K	mg/L	ICPAES	1.08	5.09	3.19	2.28	1.1	1.0	1.6	1.2	1.3	1.6	1.6	1.5	1.5
La	ug/L	ICPMS	0.55	0.2	0.2	0.1	0.09	0.1	0.06	0.60	0.70	0.2	0.06	0.05	0.05
Li	ug/L	ICPMS	23	75	32	44	0.2	0.5	26	0.1	0.6	26	26	25	26
Mg	mg/L	ICPAES	1.88	5.72	1.74	1.46	1.6	1.6	2.2	1.8	2.0	2.2	2.2	2.2	2.1
Mn	ug/L	ICPMS	27	22	4.2	6.7	2.5	2.8	0.81	9.6	13	2.8	0.81	0.71	0.51
Mo	ug/L	ICPMS	0.2	0.4	3.4	4.4	0.2	0.2	0.86	0.2	0.2	0.87	0.86	0.80	0.85
Na	mg/L	ICPAES	4.3	16.5	7.6	9.9	2.4	2.5	7.1	2.6	2.9	7.0	7.1	6.8	6.9
Nb	ug/L	ICPMS	< 0.02	< 0.02	0.08	0.1	< 0.02	< 0.02	< 0.02	< 0.02	< 0.02	< 0.02	< 0.02	< 0.02	< 0.02
Nd	ug/L	ICPMS	0.67	0.1	0.26	0.09	0.06	0.06	0.02	0.47	0.56	0.1	0.02	< 0.01	0.02
Ni	ug/L	ICPMS	1	1.7	0.6	0.8	0.6	0.5	0.7	1.6	1.9	0.8	0.7	0.5	0.5
P	ug/L	ICPMS	4	< 1	6.5	5.4	180	170	110	260	270	130	110	110	110
Pb	ug/L	ICPMS	0.08	<0.05	<0.05	<0.05	< 0.05	< 0.05	< 0.05	< 0.05	0.2	< 0.05	< 0.05	1.5	< 0.05
Pr	ug/L	ICPMS	0.2	0.03	0.07	0.02	0.02	0.02	< 0.01	0.1	0.2	0.03	< 0.01	< 0.01	< 0.01
Rb	ug/L	ICPMS	2.2	16	16	9.8	1.5	1.6	4.1	1.7	1.8	4.2	4.1	4.2	4.2
Re	ug/L	ICPMS	-	-	-	-	< 0.02	< 0.02	< 0.02	< 0.02	< 0.02	< 0.02	< 0.02	< 0.02	< 0.02
Sb	ug/L	ICPMS	0.61	0.35	0.1	0.08	< 0.02	< 0.02	0.4	< 0.02	< 0.02	0.4	0.4	0.4	0.4
Sc	ug/L	ICPMS	< 0.1	< 0.1	< 0.1	< 0.1	0.6	0.5	0.3	0.6	0.6	0.3	0.3	0.5	0.5
Se	ug/L	ICPMS	< 0.3	< 0.3	< 0.3	< 0.3	<0.5	<0.5	<0.5	<0.5	<0.5	<0.5	<0.5	<0.5	<0.5
SiO_2	mg/L	ICPMS	16	39	56	41	18	17	12	18	17	12	12	13	13
Sm	ug/L	ICPMS	0.1	0.02	0.07	0.02	0.02	0.02	< 0.01	0.07	0.08	0.03	< 0.01	< 0.01	< 0.01
Sn	ug/L	ICPMS	-	-	-	-	< 0.05	< 0.05	< 0.05	< 0.05	< 0.05	< 0.05	< 0.05	< 0.05	< 0.05
Sr	ug/L	ICPMS	38	88	37	23	27	28	35	29	30	36	35	35	35
Ta	ug/L	ICPMS	< 0.03	< 0.03	0.12	0.18	< 0.02	< 0.02	< 0.02	< 0.02	< 0.02	< 0.02	< 0.02	< 0.02	< 0.02
Tb	ug/L	ICPMS	0.02	0.005	0.007	< 0.005	< 0.005	< 0.005	< 0.005	0.007	0.008	< 0.005	< 0.005	< 0.005	< 0.005
Te	ug/L	ICPMS	-	-	-	-	< 0.1	< 0.1	< 0.1	< 0.1	< 0.1	< 0.1	< 0.1	< 0.1	< 0.1
Th	ug/L	ICPMS	< 0.02	< 0.02	< 0.02	< 0.02	< 0.005	< 0.005	0.01	< 0.005	< 0.005	< 0.005	0.01	< 0.005	< 0.005
Ti	ug/L	ICPMS	0.72	< 0.2	1.1	< 0.2	< 0.1	< 0.1	< 0.1	8.9	9.3	1.7	< 0.1	0.1	< 0.1
Tl	ug/L	ICPMS	<0.05	<0.05	<0.05	<0.05	< 0.05	< 0.05	< 0.05	< 0.05	< 0.05	< 0.05	< 0.05	< 0.05	< 0.05
Tm	ug/L	ICPMS	0.01	< 0.005	0.006	< 0.005	< 0.005	< 0.005	< 0.005	< 0.005	< 0.005	< 0.005	< 0.005	< 0.005	< 0.005
U	ug/L	ICPMS	0.04	0.05	0.08	0.07	0.02	0.02	0.02	0.04	0.04	0.03	0.02	0.01	0.02
V	ug/L	ICPMS	0.93	1.5	1.3	0.4	3	3	1	3	3	1	1	1	1
W	ug/L	ICPMS	0.62	0.5	1.2	1.5	0.08	0.07	1.3	0.08	0.09	1.3	1.3	1.2	1.2
Y	ug/L	ICPMS	0.64	0.1	0.3	0.2	0.06	0.06	0.04	0.2	0.2	0.1	0.04	0.04	0.03
Yb	ug/L	ICPMS	0.07	0.01	0.05	0.02	< 0.01	< 0.01	< 0.01	0.02	0.02	< 0.01	< 0.01	< 0.01	< 0.01
Zn	ug/L	ICPMS	1	2	<0.5	<0.5	< 0.5	< 0.5	< 0.5	< 0.5	1	0.9	< 0.5	< 0.5	< 0.5
Zr	ug/L	ICPMS	< 0.2	< 0.2	< 0.2	< 0.2	< 0.05	< 0.05	0.2	< 0.05	< 0.05	0.05	0.2	< 0.05	< 0.05
Hg	ng/L	Hg CVAF	-	-	-	-	-	-	-	-	-	-	-	-	-
$\delta^{18}O$ vs VSMOW	permil	ISO1	-18.0	-17.9	-18.9	-19.0	-19.61	-19.12	-19.81	-	-	-	-19.81	-17.4	-17.6
δD vs VSMOW	permil	ISO2	-138.6	-138.3	-138.7	-145.9	-142.7	-144.3	-143.0	-	-	-	-143.0	-135.2	-132.6
$\delta^{34}S$ vs CDT	permil	ISO3	-	-	-	-	-	-	-	-	-	-	-	3.1	3.4
$\delta^{34}S$ vs CDT	permil	ISO4	-	-	-	-	-	-	-	-	-	-	-	-	-

Appendix 1. Site and analytical data from creeks and water column profiles—*Continued*.

Field no.			9	10	11	12	13	14	15	16	17	18	19	20	21
Drainage/ description			SE Arm water column	SE Arm water column	SE Arm water column	SE Arm water column	SE Arm water column	SE Arm water column	SE Arm water column	SE Arm water column	SE Arm water column	SE Arm water column	SE Arm water column	SE Arm water column	SE Arm water column
Latitude			44°21'30.5"N	44°21'30.5"N	44°21'30.5"N	44°21'30.5"N	44°21'30.5"N	44°21'30.5"N	44°21'30.5"N	44°21'30.5"N	44°21'30.5"N	44°21'30.5"N	44°21'30.5"N	44°21'30.5"N	44°21'30.5"N
Longitude			W	W	W	W	W	W	W	W	W	W	W	W	W
NPS no.			-	-	-	-	-	-	-	-	-	-	-	-	-
Date			07/24/97	07/24/97	07/24/97	07/24/97	07/24/97	07/24/97	07/24/97	07/24/97	07/24/97	07/24/97	07/24/97	07/24/97	07/24/97
Depth	m		9 pump	9 bottle	13	20	30	50	70	90	2	5	9 pump	9 bottle	13
Treatment/ Sample type			Filtered and acidified	Filtered and acidified	Filtered and acidified	Filtered and acidified	Filtered and acidified	Filtered and acidified	Filtered and acidified	Filtered and acidified	Raw and acidified	Raw and acidified	Raw and acidified	Raw and acidified	Raw and acidified
Collector			-	-	-	-	-	-	-	-	-	-	-	-	-
pH			7.51	7.51	7.40	7.38	7.27	7.23	7.20	7.19	-	-	-	-	-
Conductivity	uS/cm		-	-	-	-	-	-	-	-	-	-	-	-	-
Temperature	˚C		-	-	-	-	-	-	-	-	-	-	-	-	-
Flow	CFS		-	-	-	-	-	-	-	-	-	-	-	-	-
Alkalinity	Mg/L as $CaCO_3$		-	-	-	-	-	-	-	-	-	-	-	-	-
Sum CO_2	mM		0.54	0.56	0.57	0.59	0.62	0.62	0.62	0.63	-	-	-	-	-
HCO_3	mM	measured	0.5	0.5	0.5	0.5	0.5	0.5	0.5	0.6	-	-	-	-	-
HCO_3	uM	calculated	507	483	501	539	516	517	519	502	-	-	-	-	-
Comments			-	-	-	-	-	-	-	-	-	-	-	-	-
Cl	mg/L	IC-Aq	3.4	3.8	3.7	4.2	4.1	4.3	4.4	4.6	-	-	-	-	-
F	mg/L	IC-Aq	-	-	-	-	-	-	-	-	-	-	-	-	-
NO_3	mg/L	IC-Aq	-	-	-	-	-	-	-	-	-	-	-	-	-
SO_4	mg/L	IC-Aq	4.9	6.0	5.9	5.4	6.2	6.5	6.8	8.2	-	-	-	-	-
Ag	ug/L	ICPMS	< 0.01	< 0.01	< 0.01	< 0.01	< 0.01	< 0.01	< 0.01	< 0.01	< 0.01	< 0.01	< 0.01	< 0.01	< 0.01
Al	ug/L	ICPMS	21	17	15	18	28	26	33	18	79	83	69	78	62
As	ug/L	ICPMS	10	10	11	12	11	12	12	13	9.1	9.0	10	10	11
Au	ug/L	ICPMS	< 0.005	< 0.005	< 0.005	< 0.005	< 0.005	< 0.005	< 0.005	< 0.005	< 0.005	< 0.005	< 0.005	< 0.005	< 0.005
B	ug/L	ICPAES	66	67	69	77	75	77	81	85	58	58	64	65	67
Ba	ug/L	ICPMS	8.2	8.2	8.4	8.5	8.4	8.5	8.6	8.8	8.2	8.2	8.4	8.4	8.5
Be	ug/L	ICPMS	< 0.05	< 0.05	< 0.05	< 0.05	< 0.05	< 0.05	< 0.05	< 0.05	< 0.05	< 0.05	< 0.05	< 0.05	< 0.05
Bi	ug/L	ICPMS	< 0.01	< 0.01	< 0.01	< 0.01	< 0.01	< 0.01	< 0.01	< 0.01	< 0.01	< 0.01	< 0.01	< 0.01	< 0.01
Ca	mg/L	ICPAES	4.9	5.1	5.1	5.3	5.5	5.5	5.8	5.8	4.9	4.9	5.0	5.1	5.0
Cd	ug/L	ICPMS	< 0.02	< 0.02	< 0.02	< 0.02	< 0.02	< 0.02	< 0.02	< 0.02	< 0.02	< 0.02	< 0.02	< 0.02	< 0.02
Ce	ug/L	ICPMS	0.05	0.05	0.05	0.06	0.07	0.07	0.08	0.04	0.1	0.1	0.1	0.1	0.1
Co	ug/L	ICPMS	< 0.02	< 0.02	< 0.02	< 0.02	< 0.02	< 0.02	< 0.02	< 0.02	0.03	0.02	0.02	0.03	0.02
Cr	ug/L	ICPMS	< 0.5	< 0.5	< 0.5	< 0.5	< 0.5	< 0.5	< 0.5	< 0.5	< 0.5	< 0.5	< 0.5	< 0.5	< 0.5
Cs	ug/L	ICPMS	2.1	2.2	2.3	2.5	2.3	2.4	2.6	2.8	1.9	1.9	2.1	2.1	2.2
Cu	ug/L	ICPMS	< 0.5	< 0.5	< 0.5	< 0.5	< 0.5	< 0.5	< 0.5	< 0.5	< 0.5	< 0.5	< 0.5	< 0.5	0.5
Dy	ug/L	ICPMS	< 0.005	0.006	0.008	0.008	0.006	< 0.005	0.007	0.005	0.007	0.007	0.01	0.008	0.009
Er	ug/L	ICPMS	< 0.005	0.006	< 0.005	< 0.005	0.006	0.006	0.008	< 0.005	0.007	< 0.005	0.007	0.005	0.006
Eu	ug/L	ICPMS	< 0.005	< 0.005	< 0.005	< 0.005	< 0.005	< 0.005	< 0.005	< 0.005	< 0.005	< 0.005	< 0.005	< 0.005	< 0.005
Fe	ug/L	ICPMS	13	12	12	11	14	14	14	10	37	37	29	32	26
Ga	ug/L	ICPMS	< 0.02	< 0.02	< 0.02	< 0.02	< 0.02	< 0.02	< 0.02	< 0.02	< 0.02	< 0.02	< 0.02	< 0.02	< 0.02
Gd	ug/L	ICPMS	< 0.005	0.006	0.01	0.007	0.01	0.01	0.009	0.007	0.01	0.01	0.007	0.01	0.02
Ge	ug/L	ICPMS	0.2	0.2	0.2	0.2	0.2	0.2	0.2	0.2	0.2	0.1	0.2	0.2	0.2
Hf	ug/L	ICPMS	< 0.05	< 0.05	< 0.05	< 0.05	< 0.05	< 0.05	< 0.05	< 0.05	< 0.05	< 0.05	< 0.05	< 0.05	< 0.05
Ho	ug/L	ICPMS	< 0.005	< 0.005	< 0.005	< 0.005	< 0.005	< 0.005	< 0.005	< 0.005	< 0.005	< 0.005	< 0.005	< 0.005	< 0.005
In	ug/L	ICPMS	< 0.01	< 0.01	< 0.01	< 0.01	< 0.01	< 0.01	< 0.01	< 0.01	< 0.01	< 0.01	< 0.01	< 0.01	< 0.01
K	mg/L	ICPAES	1.6	1.6	1.6	1.7	1.6	1.7	1.7	1.7	1.5	1.4	1.5	1.6	1.5
La	ug/L	ICPMS	0.04	0.04	0.05	0.05	0.07	0.07	0.06	0.05	0.09	0.1	0.07	0.08	0.08
Li	ug/L	ICPMS	29	30	30	34	33	34	35	38	26	26	29	30	30
Mg	mg/L	ICPAES	2.2	2.2	2.2	2.3	2.4	2.4	2.5	2.4	2.1	2.1	2.2	2.2	2.2
Mn	ug/L	ICPMS	0.36	0.31	0.33	0.26	0.43	0.34	0.40	0.28	1.9	1.9	1.3	1.6	1.2
Mo	ug/L	ICPMS	0.94	0.96	0.97	1.0	0.97	1.0	1.1	1.1	0.88	0.86	0.93	0.97	0.96
Na	mg/L	ICPAES	7.4	7.6	7.7	8.3	8.4	8.6	9.1	9.4	6.9	7.0	7.4	7.6	7.6
Nb	ug/L	ICPMS	< 0.02	< 0.02	< 0.02	< 0.02	< 0.02	< 0.02	< 0.02	< 0.02	< 0.02	< 0.02	< 0.02	< 0.02	< 0.02
Nd	ug/L	ICPMS	0.02	0.02	0.02	0.02	0.05	0.04	0.04	0.02	0.06	0.04	0.04	0.04	0.04
Ni	ug/L	ICPMS	0.5	0.4	0.5	0.5	0.5	0.5	0.5	0.5	0.5	0.5	0.5	0.6	0.5
P	ug/L	ICPMS	110	98	100	110	120	100	110	110	140	120	110	110	110
Pb	ug/L	ICPMS	< 0.05	< 0.05	< 0.05	< 0.05	< 0.05	< 0.05	< 0.05	< 0.05	< 0.05	< 0.05	< 0.05	< 0.05	< 0.05
Pr	ug/L	ICPMS	< 0.01	< 0.01	< 0.01	< 0.01	0.01	< 0.01	< 0.01	< 0.01	0.02	0.02	0.01	0.01	0.01
Rb	ug/L	ICPMS	4.5	4.6	4.6	4.9	4.8	5.0	5.0	5.4	4.1	4.2	4.4	4.5	4.6
Re	ug/L	ICPMS	< 0.02	< 0.02	< 0.02	< 0.02	< 0.02	< 0.02	< 0.02	< 0.02	< 0.02	< 0.02	< 0.02	< 0.02	< 0.02
Sb	ug/L	ICPMS	0.4	0.4	0.5	0.52	0.5	0.50	0.50	0.55	0.4	0.4	0.4	0.4	0.4
Sc	ug/L	ICPMS	0.4	0.4	0.4	0.4	0.4	0.4	0.4	0.4	0.4	0.4	0.4	0.4	0.3
Se	ug/L	ICPMS	<0.5	<0.5	<0.5	<0.5	<0.5	<0.5	<0.5	<0.5	<0.5	<0.5	<0.5	<0.5	<0.5
SiO_2	mg/L	ICPMS	13	12	12	12	13	12	12	12	12	12	12	12	12
Sm	ug/L	ICPMS	< 0.01	< 0.01	0.01	< 0.01	< 0.01	< 0.01	0.02	< 0.01	0.02	0.01	0.01	< 0.01	< 0.01
Sn	ug/L	ICPMS	< 0.05	< 0.05	< 0.05	< 0.05	< 0.05	< 0.05	< 0.05	< 0.05	< 0.05	< 0.05	< 0.05	< 0.05	< 0.05
Sr	ug/L	ICPMS	36	37	37	38	38	39	39	40	35	35	36	36	36
Ta	ug/L	ICPMS	< 0.02	< 0.02	< 0.02	< 0.02	< 0.02	< 0.02	< 0.02	< 0.02	< 0.02	< 0.02	< 0.02	< 0.02	< 0.02
Tb	ug/L	ICPMS	< 0.005	< 0.005	< 0.005	< 0.005	< 0.005	< 0.005	< 0.005	< 0.005	< 0.005	< 0.005	< 0.005	< 0.005	< 0.005
Te	ug/L	ICPMS	< 0.1	< 0.1	< 0.1	< 0.1	< 0.1	< 0.1	< 0.1	< 0.1	< 0.1	< 0.1	< 0.1	< 0.1	< 0.1
Th	ug/L	ICPMS	< 0.005	< 0.005	< 0.005	< 0.005	< 0.005	< 0.005	< 0.005	< 0.005	< 0.005	< 0.005	< 0.005	< 0.005	< 0.005
Ti	ug/L	ICPMS	0.1	< 0.1	0.1	< 0.1	0.2	0.1	0.1	< 0.1	0.8	0.8	0.7	0.7	0.4
Tl	ug/L	ICPMS	< 0.05	< 0.05	< 0.05	< 0.05	< 0.05	< 0.05	< 0.05	< 0.05	< 0.05	< 0.05	< 0.05	< 0.05	< 0.05
Tm	ug/L	ICPMS	< 0.005	< 0.005	< 0.005	< 0.005	< 0.005	< 0.005	< 0.005	< 0.005	< 0.005	< 0.005	< 0.005	< 0.005	< 0.005
U	ug/L	ICPMS	0.02	0.01	0.01	0.01	0.02	0.02	0.02	0.01	0.02	0.02	0.02	0.02	0.02
V	ug/L	ICPMS	1	1	1	1	1	1	1	0.9	1	1	1	1	1
W	ug/L	ICPMS	1.4	1.4	1.6	1.7	1.5	1.7	1.6	1.8	1.3	1.3	1.4	1.4	1.6
Y	ug/L	ICPMS	0.04	0.04	0.04	0.04	0.05	0.04	0.05	0.04	0.06	0.05	0.05	0.05	0.06
Yb	ug/L	ICPMS	< 0.01	< 0.01	< 0.01	< 0.01	< 0.01	< 0.01	< 0.01	< 0.01	< 0.01	< 0.01	< 0.01	< 0.01	< 0.01
Zn	ug/L	ICPMS	< 0.5	< 0.5	< 0.5	< 0.5	< 0.5	< 0.5	< 0.5	< 0.5	< 0.5	< 0.5	< 0.5	< 0.5	< 0.5
Zr	ug/L	ICPMS	< 0.05	< 0.05	< 0.05	< 0.05	< 0.05	< 0.05	< 0.05	< 0.05	< 0.05	< 0.05	< 0.05	0.2	< 0.05
Hg	ng/L	Hg CVAF	-	-	-	-	-	-	-	-	-	-	-	-	-
$\delta^{18}O$ vs VSMOW	permil	ISO1	-17.0	-17.2	-17.3	-16.9	-16.7	-16.9	-16.9	-16.6	-	-	-	-	-
δD vs VSMOW	permil	ISO2	-132.3	-132.9	-125.1	-131.2	-128.8	-130.9	-130.6	-127.6	-	-	-	-	-
$\delta^{34}S$ vs CDT	permil	ISO3	-	2.1	1.9	4.6	-	1.7	2.4	2.2	-	-	-	-	-
$\delta^{34}S$ vs CDT	permil	ISO4	-	2.0	-	-	-	-	1.8	-	-	-	-	-	-

Appendix 1. Site and analytical data from creeks and water column profiles—*Continued*.

Field no. Drainage/ description			22 SE Arm water column	23 SE Arm water column	24 SE Arm water column	25 SE Arm water column	26 SE Arm water column	South East Arm water column	South East Arm water column	South East Arm water column	South East Arm water column	South East Arm water column	South East Arm water column	South East Arm water column
Latitude			44°21'30.5"N	44°21'30.5"N	44°21'30.5"N	44°21'30.5"N	44°21'30.5"N	44°21'53.8"N	44°21'53.8"N	44°21'53.8"N	44°21'53.8"N	44°21'53.8"N	44°21'53.8"N	44°21'53.8"N
Longitude			W	W	W	W	W	W	W	W	W	W	W	W
NPS no.			-	-	-	-	-	-	-	-	-	-	-	-
Date			07/24/97	07/24/97	07/24/97	07/24/97	07/24/97	07/28/98	07/28/98	07/28/98	07/28/98	07/28/98	07/28/98	07/28/98
Depth	m		20	30	50	70	90	0	7.6	15.2	22.9	30.5	38.1	45.7
Treatment/ Sample type			Raw and acidified	Raw and acidified	Raw and acidified	Raw and acidified	Raw and acidified	Filtered and acidified	Filtered and acidified	Filtered and acidified	Filtered and acidified	Filtered and acidified	Filtered and acidified	Filtered and acidified
Collector			-	-	-	-	-	-	-	-	-	-	-	-
pH			-	-	-	-	-	7.53	7.71	7.56	7.51	7.51	7.46	7.48
Conductivity	uS/cm		-	-	-	-	-	-	-	-	-	-	-	-
Temperature	˚C		-	-	-	-	-	-	-	-	-	-	-	-
Flow	CFS		-	-	-	-	-	-	-	-	-	-	-	-
Alkalinity	Mg/L as $CaCO_3$		-	-	-	-	-	-	-	-	-	-	-	-
Sum CO_2	mM		-	-	-	-	-	-	-	-	-	-	-	-
HCO_3	mM	measured	-	-	-	-	-	0.5	0.5	0.5	0.6	0.6	0.6	0.6
HCO_3	uM	calculated	-	-	-	-	-	504	552	528	548	546	561	562
Comments			-	-	-	-	-	-	-	-	-	-	-	-
Cl	mg/L	IC-Aq	-	-	-	-	-	3.3	4.3	3.8	4.3	4.5	4.7	4.7
F	mg/L	IC-Aq	-	-	-	-	-	0.5	0.5	0.8	0.5	0.5	0.5	0.5
NO_3	mg/L	IC-Aq	-	-	-	-	-	<.1	<.1	<.1	<.1	<.1	<.1	<.1
SO_4	mg/L	IC-Aq	-	-	-	-	-	4.8	5.9	5.4	5.9	6.2	6.4	6.2
Ag	ug/L	ICPMS	< 0.01	< 0.01	< 0.01	< 0.01	< 0.01	0.00	0.00	0.00	0.00	0.00	0.00	0.00
Al	ug/L	ICPMS	64	100	95	92	72	12.00	7.40	9.60	6.00	5.70	5.60	5.40
As	ug/L	ICPMS	12	11	12	12	13	9.60	12.00	10.00	11.00	12.00	12.00	13.00
Au	ug/L	ICPMS	0.005	< 0.005	< 0.005	< 0.005	< 0.005	0.00	0.00	0.00	0.00	0.00	0.00	0.00
B	ug/L	ICPAES	74	73	76	77	84	54.00	76.99	61.99	73.99	81.99	76.99	78.99
Ba	ug/L	ICPMS	8.6	8.7	8.8	8.8	9.1	7.60	8.20	8.20	8.20	8.30	8.60	8.20
Be	ug/L	ICPMS	< 0.05	< 0.05	< 0.05	< 0.05	< 0.05	0.00	0.00	0.00	0.00	0.00	0.00	0.00
Bi	ug/L	ICPMS	< 0.01	< 0.01	< 0.01	< 0.01	< 0.01	0.00	0.00	0.00	0.00	0.00	0.00	0.00
Ca	mg/L	ICPAES	5.4	5.4	5.5	5.5	5.6	4.30	5.20	4.60	5.20	5.50	5.10	5.30
Cd	ug/L	ICPMS	< 0.02	< 0.02	< 0.02	< 0.02	< 0.02	0.00	0.00	0.00	0.00	0.00	0.00	0.00
Ce	ug/L	ICPMS	0.1	0.2	0.2	0.2	0.1	0.04	0.03	0.04	0.02	0.02	0.02	0.03
Co	ug/L	ICPMS	0.02	0.03	0.02	0.03	< 0.02	0.00	0.00	0.00	0.00	0.00	0.00	0.00
Cr	ug/L	ICPMS	< 0.5	< 0.5	< 0.5	< 0.5	< 0.5	0.00	0.00	0.00	0.00	0.00	1.00	0.00
Cs	ug/L	ICPMS	2.5	2.3	2.5	2.5	2.7	2.40	3.20	2.70	3.00	3.20	3.40	3.20
Cu	ug/L	ICPMS	< 0.5	< 0.5	0.5	< 0.5	< 0.5	0.00	0.00	0.00	0.00	0.50	0.00	0.00
Dy	ug/L	ICPMS	0.007	0.02	0.008	0.01	0.005	0.00	0.00	0.01	0.01	0.00	0.00	0.00
Er	ug/L	ICPMS	0.01	0.006	0.005	< 0.005	0.007	0.00	0.00	0.00	0.00	0.00	0.00	0.00
Eu	ug/L	ICPMS	< 0.005	< 0.005	< 0.005	< 0.005	< 0.005	0.00	0.00	0.00	0.00	0.00	0.00	0.00
Fe	ug/L	ICPMS	26	39	38	37	29	11.00	9.60	13.00	9.60	0.00	0.00	0.00
Ga	ug/L	ICPMS	< 0.02	< 0.02	< 0.02	< 0.02	< 0.02	0.00	0.00	0.00	0.00	0.00	0.00	0.00
Gd	ug/L	ICPMS	0.009	0.01	0.008	0.01	0.01	0.00	0.00	0.01	0.00	0.01	0.00	0.00
Ge	ug/L	ICPMS	0.2	0.2	0.2	0.2	0.2	0.20	0.20	0.20	0.20	0.20	0.20	0.20
Hf	ug/L	ICPMS	< 0.05	< 0.05	< 0.05	< 0.05	< 0.05	0.00	0.00	0.00	0.00	0.00	0.00	0.00
Ho	ug/L	ICPMS	< 0.005	< 0.005	< 0.005	< 0.005	< 0.005	0.00	0.00	0.00	0.00	0.00	0.00	0.00
In	ug/L	ICPMS	< 0.01	< 0.01	< 0.01	< 0.01	< 0.01	0.00	0.00	0.00	0.00	0.00	0.00	0.00
K	mg/L	ICPAES	1.6	1.6	1.6	1.6	1.7	1.30	1.60	1.40	1.60	1.70	1.60	1.60
La	ug/L	ICPMS	0.08	0.1	0.09	0.09	0.08	0.03	0.02	0.03	0.03	0.03	0.02	0.02
Li	ug/L	ICPMS	34	32	34	35	38	29.01	38.01	34.01	38.01	40.01	40.01	41.01
Mg	mg/L	ICPAES	2.3	2.4	2.4	2.4	2.5	1.90	2.20	2.00	2.20	2.40	2.20	2.20
Mn	ug/L	ICPMS	0.91	1.4	1.3	1.5	1.6	0.42	0.08	0.10	0.35	0.20	0.23	0.17
Mo	ug/L	ICPMS	1.1	1.0	1.1	1.1	1.1	0.74	1.00	0.87	0.96	0.97	1.20	1.00
Na	mg/L	ICPAES	8.4	8.3	8.5	8.7	9.0	6.20	8.40	7.00	8.20	8.80	8.40	8.50
Nb	ug/L	ICPMS	< 0.02	< 0.02	< 0.02	< 0.02	< 0.02	0.00	0.00	0.00	0.00	0.00	0.00	0.00
Nd	ug/L	ICPMS	0.05	0.06	0.07	0.07	0.04	0.02	0.03	0.04	0.04	0.03	0.02	0.03
Ni	ug/L	ICPMS	0.6	0.6	0.6	0.6	0.5	0.40	0.40	0.40	0.40	0.30	0.40	0.40
P	ug/L	ICPMS	110	110	120	120	120	15.00	15.00	16.00	14.00	16.00	15.00	16.00
Pb	ug/L	ICPMS	< 0.05	< 0.05	< 0.05	< 0.05	< 0.05	0.00	0.00	0.08	0.00	0.00	0.00	0.00
Pr	ug/L	ICPMS	0.01	0.02	0.02	0.02	0.01	0.00	0.00	0.00	0.00	0.01	0.00	0.00
Rb	ug/L	ICPMS	4.9	4.8	5.1	5.1	5.4	4.00	4.70	4.20	4.50	4.80	4.80	4.80
Re	ug/L	ICPMS	< 0.02	< 0.02	< 0.02	< 0.02	< 0.02	0.00	0.00	0.00	0.00	0.00	0.00	0.00
Sb	ug/L	ICPMS	0.50	0.5	0.51	0.52	0.54	0.40	0.57	0.40	0.50	0.40	0.55	0.50
Sc	ug/L	ICPMS	0.4	0.4	0.4	0.3	0.4	0.00	0.00	0.00	0.00	0.00	0.00	0.00
Se	ug/L	ICPMS	<0.5	<0.5	<0.5	<0.5	<0.5	0.00	0.00	0.00	0.00	0.00	0.00	0.00
SiO_2	mg/L	ICPMS	12	12	12	12	12	10.98	9.99	10.98	9.99	9.99	9.99	9.99
Sm	ug/L	ICPMS	0.01	0.01	0.02	0.02	0.01	0.00	0.00	0.00	0.00	0.00	0.00	0.01
Sn	ug/L	ICPMS	< 0.05	< 0.05	< 0.05	< 0.05	< 0.05	0.00	0.08	0.10	0.08	0.09	0.10	0.06
Sr	ug/L	ICPMS	38	38	39	40	40	39.00	41.00	41.00	42.00	42.00	44.00	44.00
Ta	ug/L	ICPMS	< 0.02	< 0.02	< 0.02	< 0.02	< 0.02	0.00	0.00	0.00	0.00	0.00	0.00	0.00
Tb	ug/L	ICPMS	< 0.005	< 0.005	< 0.005	< 0.005	< 0.005	0.00	0.00	0.00	0.00	0.00	0.00	0.00
Te	ug/L	ICPMS	< 0.1	< 0.1	< 0.1	< 0.1	< 0.1	0.00	0.00	0.00	0.00	0.00	0.00	0.00
Th	ug/L	ICPMS	< 0.005	< 0.005	< 0.005	< 0.005	< 0.005	0.00	0.00	0.00	0.00	0.00	0.00	0.00
Ti	ug/L	ICPMS	0.7	1.0	0.8	0.8	0.5	0.20	0.20	0.10	0.00	0.00	0.00	0.00
Tl	ug/L	ICPMS	< 0.05	< 0.05	< 0.05	< 0.05	< 0.05	0.00	0.00	0.00	0.00	0.00	0.00	0.00
Tm	ug/L	ICPMS	< 0.005	< 0.005	< 0.005	< 0.005	< 0.005	0.00	0.00	0.00	0.00	0.00	0.00	0.00
U	ug/L	ICPMS	0.02	0.02	0.02	0.02	0.01	0.02	0.02	0.01	0.02	0.01	0.01	0.01
V	ug/L	ICPMS	1	1	1	1	1	2.00	1.00	2.00	1.00	1.00	1.00	1.00
W	ug/L	ICPMS	1.7	1.7	1.7	1.7	1.8	1.10	1.40	1.20	1.20	1.20	1.50	1.40
Y	ug/L	ICPMS	0.06	0.06	0.06	0.06	0.06	0.03	0.02	0.03	0.02	0.03	0.02	0.03
Yb	ug/L	ICPMS	< 0.01	< 0.01	< 0.01	< 0.01	< 0.01	0.00	0.00	0.00	0.00	0.00	0.00	0.00
Zn	ug/L	ICPMS	< 0.5	< 0.5	< 0.5	< 0.5	0.5	0.00	0.00	0.00	0.00	0.00	0.00	0.00
Zr	ug/L	ICPMS	< 0.05	< 0.05	< 0.05	< 0.05	< 0.05	0.06	0.08	0.08	0.07	0.08	0.07	0.08
Hg	ng/L	Hg CVAF	-	-	-	-	-	<10	<10	<10	<10	<10	<10	<10
$\delta^{18}O$ vs VSMOW	permil	ISO1	-	-	-	-	-	-17.1	-16.7	-17.0	-16.8	-16.3	-16.2	-16.2
δD vs VSMOW	permil	ISO2	-	-	-	-	-	-131	-132	-130	-131	-129	-132	-130
$\delta^{34}S$ vs CDT	permil	ISO3	-	-	-	-	-	-	-	-	-	-	-	-
$\delta^{34}S$ vs CDT	permil	ISO4	-	-	-	-	-	-	-	-	-	-	-	-

Appendix 1. Site and analytical data from creeks and water column profiles—*Continued*.

Field no. Drainage/ description			South East Arm water column	South East Arm water column	South East Arm water column	South East Arm water column	44 West Thumb (WT1) water column	45 West Thumb (WT1) water column	46 West Thumb (WT1) water column	47 West Thumb (WT1) water column	48 West Thumb (WT1) water column	49 West Thumb (WT1) water column	50 West Thumb (WT1) water column
Latitude			44°21'53.8"N	44°21'53.8"N	44°21'53.8"N	44°21'53.8"N	44°24'59.3"N	44°24'59.3"N	44°24'59.3"N	44°24'59.3"N	44°24'59.3"N	44°24'59.3"N	44°24'59.3"N
Longitude			W	W	W	W	110°34'0"W	110°34'0"W	110°34'0"W	110°34'0"W	110°34'0"W	110°34'0"W	110°34'0"W
NPS no.			-	-	-	-	-	-	-	-	-	-	-
Date			07/28/98	07/28/98	07/28/98	07/28/98	07/24/97	07/24/97	07/24/97	07/24/97	07/24/97	07/24/97	07/24/97
Depth	m		53.3	61.0	68.6	73.2	0	2	4	5	5.9	0	2
Treatment/ Sample type			Filtered and acidified	Filtered and acidified	Filtered and acidified	Filtered and acidified	Filtered and acidified	Filtered and acidified	Filtered and acidified	Filtered and acidified	Filtered and acidified	Raw and acidified	Raw and acidified
Collector			-	-	-	-	-	-	-	-	-	-	-
pH			7.45	7.43	7.46	7.41	7.19	7.18	7.30	7.33	7.35	-	-
Conductivity	uS/cm		-	-	-	-	129	115	124	121	120	-	-
Temperature	˚C		-	-	-	-	13.5	11.7	11.4	11.2	10.0	-	-
Flow	CFS		-	-	-	-	-	-	-	-	-	-	-
Alkalinity	Mg/L as $CaCO_3$		-	-	-	-	-	-	-	-	-	-	-
Sum CO_2	mM		-	-	-	-	0.77	0.70	0.67	-	0.68	-	-
HCO_3	mM	measured	0.6	0.6	0.6	0.6	0.7	0.6	0.6	-	0.6	-	-
HCO_3	uM	calculated	559	552	563	557	570	515	490	-	503	-	-
Comments			-	-	-	-	-	-	-	-	-	-	-
Cl	mg/L	IC-Aq	4.6	4.6	4.6	4.4	8.0	5.5	5.6	-	5.6	-	-
F	mg/L	IC-Aq	0.5	0.5	0.5	0.5	-	-	-	-	-	-	-
NO_3	mg/L	IC-Aq	<.1	<.1	<.1	<.1	-	-	-	-	-	-	-
SO_4	mg/L	IC-Aq	6.2	6.2	6.3	6.6	7.6	7.2	7.4	0.0	7.3	-	-
Ag	ug/L	ICPMS	0.00	0.00	0.00	0.00	< 0.01	< 0.01	< 0.01	< 0.01	< 0.01	< 0.01	< 0.01
Al	ug/L	ICPMS	5.20	5.40	6.50	7.30	< 0.01	< 0.01	< 0.01	< 0.01	< 0.01	14	44
As	ug/L	ICPMS	13.00	12.00	12.00	12.00	37	18	18	18	18	37	18
Au	ug/L	ICPMS	0.00	0.00	0.00	0.00	0.006	< 0.005	0.006	< 0.005	< 0.005	0.005	0.006
B	ug/L	ICPAES	79.99	76.99	82.99	78.99	130	99	96	96	97	130	95
Ba	ug/L	ICPMS	8.70	8.60	8.40	8.30	8.7	9.0	8.8	8.7	9.0	8.7	8.9
Be	ug/L	ICPMS	0.00	0.00	0.00	0.00	< 0.05	< 0.05	< 0.05	< 0.05	< 0.05	< 0.05	< 0.05
Bi	ug/L	ICPMS	0.00	0.00	0.00	0.00	< 0.01	< 0.01	< 0.01	< 0.01	< 0.01	< 0.01	< 0.01
Ca	mg/L	ICPAES	5.40	5.20	5.60	5.50	5.6	5.9	5.6	5.7	5.9	5.4	5.6
Cd	ug/L	ICPMS	0.00	0.00	0.00	0.00	< 0.02	< 0.02	< 0.02	< 0.02	< 0.02	< 0.02	< 0.02
Ce	ug/L	ICPMS	0.02	0.02	0.02	0.02	0.02	0.02	0.02	0.02	0.02	0.05	0.04
Co	ug/L	ICPMS	0.00	0.04	0.00	0.00	< 0.02	< 0.02	< 0.02	< 0.02	< 0.02	< 0.02	< 0.02
Cr	ug/L	ICPMS	0.00	0.00	0.00	0.00	< 0.5	< 0.5	< 0.5	< 0.5	< 0.5	< 0.5	< 0.5
Cs	ug/L	ICPMS	3.30	3.20	3.20	3.10	6.9	3.8	3.8	3.8	3.7	6.9	3.7
Cu	ug/L	ICPMS	0.00	0.00	0.00	0.00	< 0.5	< 0.5	< 0.5	< 0.5	< 0.5	< 0.5	< 0.5
Dy	ug/L	ICPMS	0.00	0.00	0.00	0.00	< 0.005	< 0.005	< 0.005	< 0.005	< 0.005	0.005	< 0.005
Er	ug/L	ICPMS	0.00	0.00	0.00	0.00	< 0.005	< 0.005	< 0.005	0.008	0.005	< 0.005	< 0.005
Eu	ug/L	ICPMS	0.00	0.00	0.00	0.00	< 0.005	< 0.005	< 0.005	< 0.005	< 0.005	< 0.005	< 0.005
Fe	ug/L	ICPMS	0.00	0.00	11.00	11.00	< 10	< 10	< 10	< 10	< 10	< 10	< 10
Ga	ug/L	ICPMS	0.00	0.00	0.00	0.00	0.08	< 0.02	0.02	< 0.02	< 0.02	0.08	0.03
Gd	ug/L	ICPMS	0.00	0.01	0.00	0.01	< 0.005	0.006	0.01	< 0.005	< 0.005	0.01	0.008
Ge	ug/L	ICPMS	0.20	0.20	0.20	0.20	0.8	0.3	0.3	0.4	0.4	0.7	0.3
Hf	ug/L	ICPMS	0.00	0.00	0.00	0.00	5.8	1.2	0.1	< 0.05	< 0.05	0.71	5.6
Ho	ug/L	ICPMS	0.00	0.00	0.00	0.00	< 0.005	< 0.005	< 0.005	< 0.005	< 0.005	< 0.005	< 0.005
In	ug/L	ICPMS	0.00	0.00	0.00	0.00	< 0.01	< 0.01	< 0.01	< 0.01	< 0.01	< 0.01	< 0.01
K	mg/L	ICPAES	1.60	1.60	1.70	1.70	2.0	1.8	1.8	1.8	1.8	1.9	1.7
La	ug/L	ICPMS	0.02	0.02	0.03	0.02	0.02	0.02	0.02	0.02	0.02	0.03	0.03
Li	ug/L	ICPMS	40.01	39.01	39.01	39.01	69	46	45	44	45	69	45
Mg	mg/L	ICPAES	2.30	2.30	2.40	2.40	2.4	2.4	2.4	2.3	2.4	2.4	2.3
Mn	ug/L	ICPMS	0.10	0.13	0.13	0.16	0.37	0.31	0.26	0.29	0.25	0.87	0.87
Mo	ug/L	ICPMS	1.00	1.20	0.97	1.10	2.5	1.6	1.6	1.5	1.6	2.5	1.6
Na	mg/L	ICPAES	8.60	8.40	8.90	8.70	14	11	10	10	11	14	10
Nb	ug/L	ICPMS	0.00	0.00	0.00	0.00	< 0.02	< 0.02	< 0.02	< 0.02	< 0.02	< 0.02	< 0.02
Nd	ug/L	ICPMS	0.02	0.03	0.02	0.03	< 0.01	< 0.01	< 0.01	< 0.01	< 0.01	< 0.01	< 0.01
Ni	ug/L	ICPMS	0.50	0.40	0.40	0.40	0.4	0.4	0.4	0.4	0.4	0.4	0.4
P	ug/L	ICPMS	21.00	16.00	15.00	16.00	71	70	69	73	70	73	73
Pb	ug/L	ICPMS	0.10	0.00	0.00	0.00	< 0.05	< 0.05	< 0.05	< 0.05	< 0.05	< 0.05	< 0.05
Pr	ug/L	ICPMS	0.00	0.00	0.00	0.00	< 0.01	< 0.01	< 0.01	< 0.01	< 0.01	< 0.01	< 0.01
Rb	ug/L	ICPMS	4.80	4.90	4.90	4.80	7.9	6.2	6.1	6.1	6.2	7.8	6.2
Re	ug/L	ICPMS	0.00	0.00	0.00	0.00	< 0.02	< 0.02	< 0.02	< 0.02	< 0.02	< 0.02	< 0.02
Sb	ug/L	ICPMS	0.50	0.54	0.50	0.50	1.8	0.79	0.78	0.79	0.79	1.8	0.78
Sc	ug/L	ICPMS	0.00	0.00	0.00	0.00	0.3	0.3	0.3	0.2	0.3	0.3	0.3
Se	ug/L	ICPMS	0.00	0.00	0.00	0.00	<0.5	<0.5	<0.5	<0.5	<0.5	<0.5	<0.5
SiO_2	mg/L	ICPMS	9.99	9.99	9.99	9.99	12	10	10	10	10	12	9.8
Sm	ug/L	ICPMS	0.01	0.00	0.00	0.00	< 0.01	< 0.01	< 0.01	< 0.01	< 0.01	< 0.01	< 0.01
Sn	ug/L	ICPMS	0.10	0.00	0.10	0.10	< 0.05	< 0.05	< 0.05	< 0.05	< 0.05	< 0.05	< 0.05
Sr	ug/L	ICPMS	44.00	44.00	44.00	44.00	40	40	39	39	40	38	40
Ta	ug/L	ICPMS	0.00	0.00	0.00	0.00	< 0.02	< 0.02	< 0.02	< 0.02	< 0.02	< 0.02	< 0.02
Tb	ug/L	ICPMS	0.00	0.00	0.00	0.00	< 0.005	< 0.005	< 0.005	< 0.005	< 0.005	< 0.005	< 0.005
Te	ug/L	ICPMS	0.00	0.00	0.00	0.00	< 0.1	< 0.1	< 0.1	< 0.1	< 0.1	< 0.1	< 0.1
Th	ug/L	ICPMS	0.00	0.00	0.00	0.00	< 0.005	< 0.005	< 0.005	< 0.005	< 0.005	< 0.005	< 0.005
Ti	ug/L	ICPMS	0.00	0.00	0.00	0.00	< 0.1	< 0.1	< 0.1	< 0.1	< 0.1	< 0.1	< 0.1
Tl	ug/L	ICPMS	0.00	0.00	0.00	0.00	< 0.05	< 0.05	< 0.05	< 0.05	< 0.05	< 0.05	< 0.05
Tm	ug/L	ICPMS	0.00	0.00	0.00	0.00	< 0.005	< 0.005	< 0.005	< 0.005	< 0.005	< 0.005	< 0.005
U	ug/L	ICPMS	0.01	0.01	0.02	0.01	0.01	0.01	0.01	0.01	0.01	0.01	0.01
V	ug/L	ICPMS	1.00	1.00	1.00	1.00	0.8	0.9	0.8	0.9	0.9	0.9	0.9
W	ug/L	ICPMS	1.20	1.40	1.40	1.30	6.8	3.2	3.0	2.9	2.9	7.0	3.2
Y	ug/L	ICPMS	0.02	0.03	0.02	0.02	0.03	0.03	0.03	0.02	0.02	0.03	0.04
Yb	ug/L	ICPMS	0.00	0.00	0.00	0.00	< 0.01	< 0.01	< 0.01	< 0.01	< 0.01	< 0.01	< 0.01
Zn	ug/L	ICPMS	0.00	0.00	0.00	0.00	< 0.5	< 0.5	< 0.5	< 0.5	< 0.5	< 0.5	< 0.5
Zr	ug/L	ICPMS	0.06	0.06	0.07	0.30	0.1	< 0.05	< 0.05	< 0.05	< 0.05	< 0.05	2.4
Hg	ng/L	Hg CVAF	<10	<10	<10	<10	-	-	-	-	-	-	-
$\delta^{18}O$ vs VSMOW	permil	ISO1	-16.3	-16.2	-16.2	-16.7	-16.4	-16.2	-16.3	-16.4	-16.2	-	-
δD vs VSMOW	permil	ISO2	-131	-126	-131	-133	-128.2	-127.9	-	-126.6	-128.1	-	-
$\delta^{34}S$ vs CDT	permil	ISO3	-	-	-	-	-	2.5	2.2	2.1	2.4	-	-
$\delta^{34}S$ vs CDT	permil	ISO4	-	-	-	-	-	2.0	-	-	-	-	-

Appendix 1. Site and analytical data from creeks and water column profiles—*Continued*.

Field no.			51	52	53	54	55	56	57	58	59	60	61
Drainage/ description			West Thumb (WT1) water column	West Thumb (WT1) water column	West Thumb (WT1) water column	West Thumb (WT2) water column	West Thumb (WT2) water column	West Thumb (WT2) water column	West Thumb (WT2) water column	West Thumb (WT2) water column	West Thumb (WT2) water column	West Thumb (WT2) water column	West Thumb (WT2) water column
Latitude			44°24'59.3"N	44°24'59.3"N	44°24'59.3"N	44°24'59.3"N	44°24'59.3"N	44°24'59.3"N	44°24'59.3"N	44°24'59.3"N	44°24'59.3"N	44°24'59.3"N	44°24'59.3"N
Longitude			110°34'0"W	110°34'0"W	110°34'0"W	110°34'0"W	110°34'0"W	110°34'0"W	110°34'0"W	110°34'0"W	110°34'0"W	110°34'0"W	110°34'0"W
NPS no.			-	-	-	-	-	-	-	-	-	-	-
Date			07/24/97	07/24/97	07/24/97	07/25/97	07/25/97	07/25/97	07/25/97	07/25/97	07/25/97	07/25/97	07/25/97
Depth	m		4	5	5.9	0	2	4	5	8	0	2	4
Treatment/ Sample type			Raw and acidified	Raw and acidified	Raw and acidified	Filtered and acidified	Filtered and acidified	Filtered and acidified	Filtered and acidified	Filtered and acidified	Raw and acidified	Raw and acidified	Raw and acidified
Collector			-	-	-	-	-	-	-	-	-	-	-
pH			-	-	-	7.96	7.74	7.71	7.64	7.44	-	-	-
Conductivity	uS/cm		-	-	-	117	115	116	118	118	-	-	-
Temperature	˚C		-	-	-	12.3	11.8	11.7	11.5	10.3	-	-	-
Flow	CFS		-	-	-	-	-	-	-	-	-	-	-
Alkalinity	Mg/L as $CaCO_3$		-	-	-	-	-	-	-	-	-	-	-
Sum CO_2	mM		-	-	-	0.72	0.68	0.65	0.68	0.70	-	-	-
HCO_3	mM	measured	-	-	-	0.7	0.6	0.6	0.6	0.6	-	-	-
HCO_3	uM	calculated	-	-	-	514	481	499	486	506	-	-	-
Comments			-	-	-	-	-	-	-	-	-	-	-
Cl	mg/L	IC-Aq	-	-	-	5.8	5.5	5.5	5.7	5.9	-	-	-
F	mg/L	IC-Aq	-	-	-	-	-	-	-	-	-	-	-
NO_3	mg/L	IC-Aq	-	-	-	-	-	-	-	-	-	-	-
SO_4	mg/L	IC-Aq	-	-	-	6.9	7.3	7.2	7.2	7.1	-	-	-
Ag	ug/L	ICPMS	< 0.01	< 0.01	< 0.01	< 0.01	< 0.01	< 0.01	< 0.01	< 0.01	< 0.01	< 0.01	< 0.01
Al	ug/L	ICPMS	10	8.8	10	< 0.01	< 0.01	< 0.01	< 0.01	< 0.01	19	10	16
As	ug/L	ICPMS	18	18	18	22	18	19	18	20	22	18	19
Au	ug/L	ICPMS	< 0.005	< 0.005	< 0.005	< 0.005	< 0.005	< 0.005	< 0.005	0.006	< 0.005	< 0.005	< 0.005
B	ug/L	ICPAES	94	95	94	100	97	96	95	100	99	94	96
Ba	ug/L	ICPMS	8.8	8.9	8.9	8.6	8.8	8.9	8.9	8.9	8.9	8.9	9.1
Be	ug/L	ICPMS	< 0.05	< 0.05	< 0.05	< 0.05	< 0.05	< 0.05	< 0.05	< 0.05	< 0.05	< 0.05	< 0.05
Bi	ug/L	ICPMS	< 0.01	< 0.01	< 0.01	< 0.01	< 0.01	< 0.01	< 0.01	< 0.01	< 0.01	< 0.01	< 0.01
Ca	mg/L	ICPAES	5.6	5.6	5.6	5.6	5.9	5.6	5.8	5.7	5.7	5.7	5.6
Cd	ug/L	ICPMS	< 0.02	< 0.02	< 0.02	< 0.02	< 0.02	< 0.02	< 0.02	< 0.02	< 0.02	< 0.02	< 0.02
Ce	ug/L	ICPMS	0.04	0.04	0.04	0.02	0.01	0.01	0.02	0.01	0.07	0.05	0.06
Co	ug/L	ICPMS	< 0.02	< 0.02	< 0.02	< 0.02	< 0.02	< 0.02	< 0.02	< 0.02	< 0.02	< 0.02	< 0.02
Cr	ug/L	ICPMS	< 0.5	< 0.5	< 0.5	< 0.5	< 0.5	< 0.5	< 0.5	< 0.5	< 0.5	< 0.5	< 0.5
Cs	ug/L	ICPMS	3.7	3.7	3.7	4.4	3.6	3.8	3.8	4.1	4.5	3.7	3.9
Cu	ug/L	ICPMS	< 0.5	< 0.5	< 0.5	< 0.5	< 0.5	< 0.5	< 0.5	< 0.5	< 0.5	< 0.5	< 0.5
Dy	ug/L	ICPMS	0.008	0.007	0.005	0.006	< 0.005	0.005	< 0.005	0.006	0.008	0.006	0.007
Er	ug/L	ICPMS	< 0.005	< 0.005	< 0.005	< 0.005	0.006	< 0.005	< 0.005	< 0.005	< 0.005	0.005	< 0.005
Eu	ug/L	ICPMS	< 0.005	< 0.005	< 0.005	< 0.005	< 0.005	< 0.005	< 0.005	< 0.005	< 0.005	< 0.005	< 0.005
Fe	ug/L	ICPMS	< 10	< 10	< 10	< 10	< 10	< 10	< 10	< 10	11	< 10	11
Ga	ug/L	ICPMS	0.02	0.02	0.02	0.03	0.02	0.02	< 0.02	0.03	0.04	< 0.02	0.02
Gd	ug/L	ICPMS	0.005	0.006	< 0.005	< 0.005	0.01	< 0.005	< 0.005	0.009	0.02	0.01	0.008
Ge	ug/L	ICPMS	0.4	0.3	0.3	0.4	0.3	0.3	0.4	0.4	0.4	0.4	0.4
Hf	ug/L	ICPMS	< 0.05	< 0.05	< 0.05	< 0.05	< 0.05	< 0.05	< 0.05	< 0.05	< 0.05	< 0.05	< 0.05
Ho	ug/L	ICPMS	< 0.005	< 0.005	< 0.005	< 0.005	< 0.005	< 0.005	< 0.005	< 0.005	< 0.005	< 0.005	< 0.005
In	ug/L	ICPMS	< 0.01	< 0.01	< 0.01	< 0.01	< 0.01	< 0.01	< 0.01	< 0.01	< 0.01	< 0.01	< 0.01
K	mg/L	ICPAES	1.8	1.8	1.8	1.8	1.8	1.7	1.7	1.8	1.8	1.7	1.8
La	ug/L	ICPMS	0.03	0.03	0.02	0.02	0.02	0.02	0.02	0.02	0.04	0.04	0.04
Li	ug/L	ICPMS	44	44	43	51	43	45	45	48	50	43	44
Mg	mg/L	ICPAES	2.4	2.3	2.4	2.4	2.4	2.3	2.3	2.4	2.3	2.4	2.4
Mn	ug/L	ICPMS	0.82	0.85	0.87	0.48	0.25	0.38	0.24	0.41	1.5	1.0	1.4
Mo	ug/L	ICPMS	1.5	1.6	1.6	1.7	1.5	1.6	1.5	1.6	1.7	1.5	1.5
Na	mg/L	ICPAES	10	10	10	11	10	10	10	11	11	10	10
Nb	ug/L	ICPMS	< 0.02	< 0.02	< 0.02	< 0.02	< 0.02	< 0.02	< 0.02	< 0.02	< 0.02	< 0.02	< 0.02
Nd	ug/L	ICPMS	< 0.01	< 0.01	< 0.01	< 0.01	< 0.01	< 0.01	< 0.01	< 0.01	< 0.01	< 0.01	< 0.01
Ni	ug/L	ICPMS	0.4	0.4	0.4	0.4	0.3	0.4	0.4	0.4	0.4	0.4	0.4
P	ug/L	ICPMS	74	77	68	71	63	62	66	61	66	76	80
Pb	ug/L	ICPMS	< 0.05	< 0.05	< 0.05	< 0.05	< 0.05	< 0.05	< 0.05	< 0.05	< 0.05	< 0.05	< 0.05
Pr	ug/L	ICPMS	< 0.01	< 0.01	< 0.01	< 0.01	< 0.01	< 0.01	< 0.01	< 0.01	< 0.01	< 0.01	< 0.01
Rb	ug/L	ICPMS	6.3	6.2	6.0	6.5	6.0	6.1	6.2	6.6	6.6	6.2	6.1
Re	ug/L	ICPMS	< 0.02	< 0.02	< 0.02	< 0.02	< 0.02	< 0.02	< 0.02	< 0.02	< 0.02	< 0.02	< 0.02
Sb	ug/L	ICPMS	0.78	0.77	0.78	0.89	0.74	0.80	0.77	0.83	0.91	0.78	0.80
Sc	ug/L	ICPMS	0.2	0.3	0.3	0.2	0.3	0.2	0.3	0.3	0.3	0.2	0.2
Se	ug/L	ICPMS	<0.5	<0.5	<0.5	<0.5	<0.5	<0.5	<0.5	<0.5	<0.5	<0.5	<0.5
SiO_2	mg/L	ICPMS	9.9	9.7	9.7	10	9.5	10	9.6	9.8	10	9.5	9.7
Sm	ug/L	ICPMS	< 0.01	< 0.01	< 0.01	< 0.01	< 0.01	< 0.01	< 0.01	< 0.01	< 0.01	< 0.01	< 0.01
Sn	ug/L	ICPMS	< 0.05	< 0.05	< 0.05	< 0.05	< 0.05	< 0.05	< 0.05	< 0.05	< 0.05	< 0.05	< 0.05
Sr	ug/L	ICPMS	40	40	40	40	40	40	40	40	40	40	40
Ta	ug/L	ICPMS	< 0.02	< 0.02	< 0.02	< 0.02	< 0.02	< 0.02	< 0.02	< 0.02	< 0.02	< 0.02	< 0.02
Tb	ug/L	ICPMS	< 0.005	< 0.005	< 0.005	< 0.005	< 0.005	< 0.005	< 0.005	< 0.005	< 0.005	< 0.005	< 0.005
Te	ug/L	ICPMS	< 0.1	< 0.1	< 0.1	< 0.1	< 0.1	< 0.1	< 0.1	< 0.1	< 0.1	< 0.1	< 0.1
Th	ug/L	ICPMS	< 0.005	< 0.005	< 0.005	< 0.005	< 0.005	< 0.005	< 0.005	< 0.005	< 0.005	< 0.005	< 0.005
Ti	ug/L	ICPMS	< 0.1	< 0.1	< 0.1	< 0.1	< 0.1	< 0.1	< 0.1	< 0.1	< 0.1	< 0.1	< 0.1
Tl	ug/L	ICPMS	< 0.05	< 0.05	< 0.05	< 0.05	< 0.05	< 0.05	< 0.05	< 0.05	< 0.05	< 0.05	< 0.05
Tm	ug/L	ICPMS	< 0.005	< 0.005	< 0.005	< 0.005	< 0.005	< 0.005	< 0.005	< 0.005	< 0.005	< 0.005	< 0.005
U	ug/L	ICPMS	0.01	0.01	0.01	0.01	0.01	0.01	0.01	0.01	0.01	0.01	0.01
V	ug/L	ICPMS	0.9	0.9	0.9	0.9	0.9	0.9	0.9	0.9	0.9	0.9	0.9
W	ug/L	ICPMS	3.0	3.0	2.9	3.5	3.0	3.2	3.1	3.3	3.5	2.9	3.1
Y	ug/L	ICPMS	0.04	0.04	0.03	0.03	0.03	0.03	0.03	0.03	0.04	0.04	0.04
Yb	ug/L	ICPMS	< 0.01	< 0.01	< 0.01	< 0.01	< 0.01	< 0.01	< 0.01	< 0.01	< 0.01	< 0.01	< 0.01
Zn	ug/L	ICPMS	< 0.5	< 0.5	< 0.5	< 0.5	< 0.5	< 0.5	< 0.5	< 0.5	< 0.5	< 0.5	< 0.5
Zr	ug/L	ICPMS	< 0.05	< 0.05	< 0.05	< 0.05	< 0.05	< 0.05	< 0.05	< 0.05	< 0.05	< 0.05	< 0.05
Hg	ng/L	Hg CVAF	-	-	-	-	-	-	-	-	-	-	-
$\delta^{18}O$ vs VSMOW	permil	ISO1	-	-	-	-16.3	-16.3	-16.2	-16.4	-16.4	-	-	-
δD vs VSMOW	permil	ISO2	-	-	-	-127.6	-125.2	-124.9	-125.6	-126.4	-	-	-
$\delta^{34}S$ vs CDT	permil	ISO3	-	-	-	2.6	1.8	2.0	2.2	-	-	-	-
$\delta^{34}S$ vs CDT	permil	ISO4	-	-	-	-	-	-	2.1	-	-	-	-

Appendix 1. Site and analytical data from creeks and water column profiles—*Continued*.

Field no. Drainage/ description			62 West Thumb (WT2) water column	63 West Thumb (WT2) water column	West Thumb water column	West Thumb water column	West Thumb water column	West Thumb water column	West Thumb water column	West Thumb water column	West Thumb water column	West Thumb water column	West Thumb water column
Latitude			44°24'59.3"N	44°24'59.3"N	44°24'3.3"N	44°24'3.3"N	44°24'3.3"N	44°24'3.3"N	44°24'3.3"N	44°24'3.3"N	44°24'3.3"N	44°24'3.3"N	44°24'3.3"N
Longitude			110°34'0"W	110°34'0"W	110°33'19"W	110°33'19"W	110°33'19"W	110°33'19"W	110°33'19"W	110°33'19"W	110°33'19"W	110°33'19"W	110°33'19"W
NPS no.			-	-	-	-	-	-	-	-	-	-	-
Date			07/25/97	07/25/97	07/19/98	07/19/98	07/19/98	07/19/98	07/19/98	07/19/98	07/19/98	07/19/98	07/19/98
Depth	m		5	8	0	2	5	10	15	20	25	30	40
Treatment/ Sample type			Raw and acidified	Raw and acidified	Filtered and acidified	Filtered and acidified	Filtered and acidified	Filtered and acidified	Filtered and acidified	Filtered and acidified	Filtered and acidified	Filtered and acidified	Filtered and acidified
Collector			-	-	-	-	-	-	-	-	-	-	-
pH			-	-	7.49	7.56	7.43	7.57	7.54	7.45	7.44	7.45	7.33
Conductivity	uS/cm		-	-	-	-	-	-	-	-	-	-	-
Temperature	˚C		-	-	-	-	-	-	-	-	-	-	-
Flow	CFS		-	-	-	-	-	-	-	-	-	-	-
Alkalinity	Mg/L as $CaCO_3$		-	-	-	-	-	-	-	-	-	-	-
Sum CO_2	mM		-	-	-	-	-	-	-	-	-	-	-
HCO_3	mM	measured	-	-	0.6	0.6	0.6	0.6	0.6	0.6	0.6	0.6	0.6
HCO_3	uM	calculated	-	-	714	707	670	655	672	707	664	668	679
Comments			-	-	-	-	-	-	-	-	-	-	-
Cl	mg/L	IC-Aq	-	-	5.3	5.2	5.4	5.6	5.5	5.7	5.6	5.6	5.9
F	mg/L	IC-Aq	-	-	0.6	0.6	0.6	0.6	0.6	0.6	0.6	0.6	0.6
NO_3	mg/L	IC-Aq	-	-	<.1	<.1	<.1	<.1	<.1	<.1	<.1	<.1	<.1
SO_4	mg/L	IC-Aq	-	-	7	7	7	7	7.1	7.1	7.1	7.1	7
Ag	ug/L	ICPMS	< 0.01	< 0.01	0.00	0.00	0.00	0.00	0.00	0.00	0.00	0.00	0.00
Al	ug/L	ICPMS	10	17	5.60	3.40	3.50	2.20	3.20	5.50	3.40	2.10	2.10
As	ug/L	ICPMS	18	20	17.00	17.00	18.00	18.00	18.00	19.00	19.00	18.00	20.00
Au	ug/L	ICPMS	< 0.005	< 0.005	0.00	0.00	0.00	0.00	0.00	0.00	0.00	0.00	0.00
B	ug/L	ICPAES	94	99	85.99	81.99	84.99	84.99	83.99	84.99	82.99	85.99	86.99
Ba	ug/L	ICPMS	8.8	8.9	8.30	8.20	8.60	8.10	8.50	8.10	8.30	8.30	8.00
Be	ug/L	ICPMS	< 0.05	< 0.05	0.00	0.00	0.00	0.00	0.00	0.06	0.00	0.00	0.00
Bi	ug/L	ICPMS	< 0.01	< 0.01	0.00	0.00	0.00	0.00	0.00	0.00	0.00	0.00	0.00
Ca	mg/L	ICPAES	5.7	5.8	5.20	4.90	5.00	4.90	4.80	4.80	4.80	4.90	4.90
Cd	ug/L	ICPMS	< 0.02	< 0.02	0.00	0.00	0.00	0.00	0.00	0.00	0.00	0.00	0.00
Ce	ug/L	ICPMS	0.06	0.06	0.02	0.02	0.01	0.01	0.02	0.01	0.02	0.01	0.02
Co	ug/L	ICPMS	< 0.02	< 0.02	0.00	0.00	0.00	0.00	0.02	0.00	0.00	0.02	0.00
Cr	ug/L	ICPMS	< 0.5	< 0.5	0.00	0.00	0.00	0.00	0.00	0.00	0.00	0.00	0.00
Cs	ug/L	ICPMS	3.7	4.1	3.50	3.50	3.70	3.70	3.70	3.80	3.80	3.90	3.90
Cu	ug/L	ICPMS	< 0.5	< 0.5	0.00	0.60	0.00	0.00	0.00	0.00	0.00	0.00	0.00
Dy	ug/L	ICPMS	0.008	< 0.005	0.00	0.00	0.00	0.00	0.00	0.00	0.00	0.00	0.00
Er	ug/L	ICPMS	0.006	< 0.005	0.00	0.00	0.00	0.00	0.01	0.01	0.00	0.00	0.01
Eu	ug/L	ICPMS	< 0.005	< 0.005	0.00	0.00	0.00	0.00	0.00	0.00	0.00	0.00	0.00
Fe	ug/L	ICPMS	< 10	12	0.00	9.60	0.00	0.00	0.00	0.00	0.00	0.00	0.00
Ga	ug/L	ICPMS	0.02	0.03	0.02	0.03	0.04	0.10	0.00	0.06	0.04	0.00	0.07
Gd	ug/L	ICPMS	0.007	0.02	0.00	0.00	0.00	0.00	0.00	0.01	0.00	0.00	0.00
Ge	ug/L	ICPMS	0.4	0.4	0.30	0.30	0.30	0.30	0.30	0.40	0.30	0.40	0.40
Hf	ug/L	ICPMS	< 0.05	< 0.05	0.00	0.00	0.00	0.00	0.00	0.00	0.00	0.00	0.00
Ho	ug/L	ICPMS	< 0.005	< 0.005	0.00	0.00	0.00	0.00	0.00	0.00	0.00	0.00	0.00
In	ug/L	ICPMS	< 0.01	< 0.01	0.00	0.00	0.00	0.00	0.00	0.00	0.00	0.00	0.00
K	mg/L	ICPAES	1.7	1.8	1.50	1.50	1.60	1.50	1.50	1.50	1.50	1.60	1.50
La	ug/L	ICPMS	0.03	0.04	0.01	0.01	0.01	0.02	0.02	0.02	0.01	0.02	0.01
Li	ug/L	ICPMS	43	47	50.01	48.01	52.01	54.02	52.01	54.02	54.02	52.01	55.02
Mg	mg/L	ICPAES	2.3	2.4	2.20	2.10	2.10	2.10	2.10	2.00	2.10	2.10	2.10
Mn	ug/L	ICPMS	1.0	1.6	0.19	0.10	0.06	0.02	0.00	0.03	0.06	0.02	0.09
Mo	ug/L	ICPMS	1.6	1.6	1.20	1.40	1.50	1.10	1.20	1.50	1.10	1.40	1.40
Na	mg/L	ICPAES	10	11	9.40	8.90	9.20	9.20	8.90	9.20	9.20	9.30	9.50
Nb	ug/L	ICPMS	< 0.02	< 0.02	0.00	0.00	0.00	0.00	0.00	0.00	0.00	0.00	0.00
Nd	ug/L	ICPMS	< 0.01	< 0.01	0.02	0.00	0.00	0.01	0.04	0.02	0.00	0.02	0.02
Ni	ug/L	ICPMS	0.4	0.4	0.30	0.30	0.30	0.30	0.30	0.30	0.30	0.30	0.30
P	ug/L	ICPMS	72	77	15.00	12.00	12.00	12.00	15.00	14.00	13.00	16.00	13.00
Pb	ug/L	ICPMS	< 0.05	< 0.05	0.00	0.00	0.00	0.00	0.20	0.00	0.00	0.00	0.00
Pr	ug/L	ICPMS	< 0.01	< 0.01	0.00	0.00	0.00	0.00	0.00	0.00	0.00	0.00	0.00
Rb	ug/L	ICPMS	6.2	6.4	5.50	5.60	5.90	5.60	5.80	5.80	5.90	5.70	5.80
Re	ug/L	ICPMS	< 0.02	< 0.02	0.00	0.00	0.00	0.00	0.00	0.00	0.00	0.00	0.00
Sb	ug/L	ICPMS	0.77	0.84	0.62	0.64	0.72	0.69	0.68	0.72	0.70	0.72	0.69
Sc	ug/L	ICPMS	0.2	0.3	0.10	0.20	0.10	0.00	0.00	0.00	0.00	0.00	0.00
Se	ug/L	ICPMS	<0.5	<0.5	0.00	0.00	0.00	1100.00	0.00	0.00	0.00	220.00	0.00
SiO_2	mg/L	ICPMS	9.5	9.8	11.98	11.98	11.98	11.98	11.98	11.98	11.98	11.98	12.98
Sm	ug/L	ICPMS	< 0.01	< 0.01	0.00	0.02	0.00	0.00	0.00	0.00	0.00	0.00	0.00
Sn	ug/L	ICPMS	< 0.05	< 0.05	0.00	0.00	0.00	0.00	0.00	0.00	0.00	0.00	0.00
Sr	ug/L	ICPMS	40	40	44.00	43.00	44.00	44.00	45.00	43.00	44.00	44.00	43.00
Ta	ug/L	ICPMS	< 0.02	< 0.02	0.00	0.00	0.00	0.00	0.00	0.00	0.00	0.00	0.00
Tb	ug/L	ICPMS	< 0.005	< 0.005	0.00	0.00	0.00	0.00	0.00	0.00	0.00	0.00	0.00
Te	ug/L	ICPMS	< 0.1	< 0.1	0.00	0.00	0.00	0.00	0.00	0.00	0.00	0.00	0.00
Th	ug/L	ICPMS	< 0.005	< 0.005	0.00	0.00	0.00	0.00	0.00	0.00	0.00	0.00	0.00
Ti	ug/L	ICPMS	< 0.1	< 0.1	0.00	0.00	0.00	0.00	0.00	0.00	0.00	0.00	0.00
Tl	ug/L	ICPMS	< 0.05	< 0.05	0.00	0.00	0.00	0.00	0.00	0.00	0.00	0.00	0.00
Tm	ug/L	ICPMS	< 0.005	< 0.005	0.00	0.00	0.00	0.00	0.00	0.00	0.00	0.00	0.00
U	ug/L	ICPMS	0.01	0.01	0.01	0.02	0.02	0.01	0.01	0.01	0.01	0.01	0.01
V	ug/L	ICPMS	0.9	0.9	1.00	1.00	1.00	1.00	1.00	1.00	1.00	1.00	1.00
W	ug/L	ICPMS	3.0	3.4	1.70	1.70	1.90	1.50	1.70	1.90	1.60	1.90	2.00
Y	ug/L	ICPMS	0.03	0.04	0.02	0.02	0.02	0.02	0.02	0.02	0.02	0.02	0.02
Yb	ug/L	ICPMS	< 0.01	< 0.01	0.00	0.00	0.00	0.00	0.00	0.00	0.00	0.00	0.00
Zn	ug/L	ICPMS	< 0.5	< 0.5	0.00	0.70	0.00	0.00	0.00	1.00	0.00	0.00	0.00
Zr	ug/L	ICPMS	< 0.05	< 0.05	0.98	0.10	0.07	0.10	0.05	0.07	0.06	0.06	0.08
Hg	ng/L	Hg CVAF	-	-	<10	-	16	<10	-	<10	-	13	10
$\delta^{18}O$ vs VSMOW	permil	ISO1	-	-	-16.1	-16.1	-16.1	-16.2	-16.1	-16.2	-16.1	-16.1	-16.1
δD vs VSMOW	permil	ISO2	-	-	-130	-130	-128	-130	-130	-130	-129	-127	-131
$\delta^{34}S$ vs CDT	permil	ISO3	-	-	-	-	-	-	-	-	-	-	-
$\delta^{34}S$ vs CDT	permil	ISO4	-	-	-	-	-	-	-	-	-	-	-

Appendix 1. Site and analytical data from creeks and water column profiles—*Continued*.

Field no.												
Drainage/ description			**West Thumb water column**	**West Thumb water column**	**Mary Bay (MB-1) water column**	**Mary Bay (MB-1) water column**	**Mary Bay (MB-1) water column**	**Mary Bay (MB-1) water column**	**Mary Bay (MB-1) water column**	**Mary Bay (MB-1) water column**	**Mary Bay (MB-1) water column**	**Mary Bay (MB-1) water column**
Latitude			44°24'3.3"N	44°24'3.3"N	44°32'42.8"N	44°32'42.8"N	44°32'42.8"N	44°32'42.8"N	44°32'42.8"N	44°32'42.8"N	44°32'42.8"N	44°32'42.8"N
Longitude			110°33'19"W	110°33'19"W	110°18'39.1"W	110°18'39.1"W	110°18'39.1"W	110°18'39.1"W	110°18'39.1"W	110°18'39.1"W	110°18'39.1"W	110°18'39.1"W
NPS no.			-	-	-	-	-	-	-	-	-	-
Date			07/19/98	07/19/98	07/26/97	07/26/97	07/26/97	07/26/97	07/26/97	07/26/97	07/26/97	07/26/97
Depth	m		60	80	0	5	10	12	17	20	30	40
Treatment/ Sample type			Filtered and acidified	Filtered and acidified	Filtered and acidified	Filtered and acidified	Filtered and acidified	Filtered and acidified	Filtered and acidified	Filtered and acidified	Filtered and acidified	Filtered and acidified
Collector			-	-	-	-	-	-	-	-	-	-
pH			7.19	7.26	7.55	7.56	7.61	7.34	6.74	6.73	6.74	6.76
Conductivity	uS/cm		-	-	-	-	-	-	-	-	-	-
Temperature	˚C		-	-	-	-	-	-	-	-	-	-
Flow	CFS		-	-	-	-	-	-	-	-	-	-
Alkalinity	Mg/L as $CaCO_3$		-	-	-	-	-	-	-	-	-	-
Sum CO_2	mM		-	-	0.64	0.65	0.65	0.67	0.79	0.77	0.77	0.76
HCO_3	mM	measured	0.6	0.7	0.6	0.6	0.6	0.6	0.6	0.5	0.5	0.5
HCO_3	uM	calculated	677	691	462	473	483	467	465	441	443	454
Comments			-	-	-	-	-	-	-	-	-	-
Cl	mg/L	IC-Aq	6	5.9	4.6	4.6	4.6	5.0	6.1	6.3	6.6	6.3
F	mg/L	IC-Aq	0.6	0.6	-	-	-	-	-	-	-	-
NO_3	mg/L	IC-Aq	<.1	<.1	-	-	-	-	-	-	-	-
SO_4	mg/L	IC-Aq	6.6	6.5	6.5	6.5	6.1	7.1	7.7	8.7	8.4	8.0
Ag	ug/L	ICPMS	0.00	0.00	0.03	0.02	0.01	0.01	< 0.01	< 0.01	< 0.01	< 0.01
Al	ug/L	ICPMS	2.10	1.90	15	13	12	8.3	9.3	10	10	10
As	ug/L	ICPMS	21.00	22.00	12	12	12	13	17	17	17	17
Au	ug/L	ICPMS	0.00	0.00	0.02	< 0.005	< 0.005	0.01	0.01	< 0.005	0.02	< 0.005
B	ug/L	ICPAES	89.99	88.99	440	430	< 10	< 10	< 10	< 10	11	13
Ba	ug/L	ICPMS	8.00	8.00	8.5	8.5	8.4	8.6	9.4	9.2	9.3	9.3
Be	ug/L	ICPMS	0.00	0.00	< 0.05	< 0.05	< 0.05	< 0.05	< 0.05	< 0.05	< 0.05	< 0.05
Bi	ug/L	ICPMS	0.00	0.00	< 0.01	< 0.01	< 0.01	< 0.01	< 0.01	< 0.01	< 0.01	< 0.01
Ca	mg/L	ICPAES	4.90	5.00	150	150	23	22	11	11	38	38
Cd	ug/L	ICPMS	0.00	0.00	< 0.02	< 0.02	< 0.02	< 0.02	< 0.02	< 0.02	< 0.02	< 0.02
Ce	ug/L	ICPMS	0.01	0.00	0.03	0.04	0.04	0.04	0.06	0.05	0.05	0.05
Co	ug/L	ICPMS	0.03	0.04	< 0.02	< 0.02	< 0.02	< 0.02	< 0.02	< 0.02	< 0.02	< 0.02
Cr	ug/L	ICPMS	0.00	0.00	1	1	2	2	2	2	2	2
Cs	ug/L	ICPMS	4.30	4.40	2.4	2.5	2.5	2.7	3.8	3.8	3.8	3.8
Cu	ug/L	ICPMS	0.00	1.00	< 0.5	< 0.5	< 0.5	< 0.5	< 0.5	< 0.5	< 0.5	< 0.5
Dy	ug/L	ICPMS	0.00	0.01	< 0.005	< 0.005	0.006	0.006	0.006	0.006	0.009	0.006
Er	ug/L	ICPMS	0.00	0.01	0.005	< 0.005	< 0.005	< 0.005	< 0.005	< 0.005	< 0.005	< 0.005
Eu	ug/L	ICPMS	0.00	0.00	< 0.005	< 0.005	< 0.005	< 0.005	< 0.005	< 0.005	< 0.005	< 0.005
Fe	ug/L	ICPMS	10.00	0.00	29	23	16	12	16	14	16	15
Ga	ug/L	ICPMS	0.00	0.06	< 0.02	< 0.02	< 0.02	< 0.02	< 0.02	< 0.02	< 0.02	< 0.02
Gd	ug/L	ICPMS	0.00	0.01	0.007	0.007	0.008	< 0.005	0.006	0.005	0.008	0.005
Ge	ug/L	ICPMS	0.40	0.40	0.2	0.2	0.2	0.2	0.3	0.3	0.3	0.3
Hf	ug/L	ICPMS	0.00	0.00	0.2	0.06	< 0.05	< 0.05	< 0.05	< 0.05	< 0.05	< 0.05
Ho	ug/L	ICPMS	0.00	0.00	< 0.005	< 0.005	< 0.005	< 0.005	< 0.005	< 0.005	< 0.005	< 0.005
In	ug/L	ICPMS	0.00	0.00	< 0.01	< 0.01	< 0.01	< 0.01	< 0.01	< 0.01	< 0.01	< 0.01
K	mg/L	ICPAES	1.60	1.60	4.3	4.3	3.0	3.1	0.93	1.0	1.2	1.2
La	ug/L	ICPMS	0.01	0.01	0.03	0.03	0.03	0.04	0.04	0.04	0.04	0.04
Li	ug/L	ICPMS	56.02	58.02	35	35	36	38	47	48	48	48
Mg	mg/L	ICPAES	2.10	2.10	90	91	6.02	6.07	2.01	2.02	10	10
Mn	ug/L	ICPMS	0.31	0.20	0.35	0.28	0.17	0.94	2.8	2.8	2.8	2.7
Mo	ug/L	ICPMS	1.60	1.70	1.1	1.0	1.0	1.1	1.1	1.1	1.1	1.1
Na	mg/L	ICPAES	9.90	10.00	273	284	36	37	31	32	21	22
Nb	ug/L	ICPMS	0.00	0.00	< 0.02	< 0.02	< 0.02	< 0.02	< 0.02	< 0.02	< 0.02	< 0.02
Nd	ug/L	ICPMS	0.02	0.03	< 0.01	< 0.01	< 0.01	< 0.01	0.02	< 0.01	0.02	0.02
Ni	ug/L	ICPMS	0.30	0.30	0.4	0.4	0.4	0.4	0.5	0.4	0.4	0.5
P	ug/L	ICPMS	19.00	17.00	92	87	85	86	98	92	94	93
Pb	ug/L	ICPMS	0.00	0.00	< 0.05	< 0.05	< 0.05	< 0.05	< 0.05	< 0.05	< 0.05	< 0.05
Pr	ug/L	ICPMS	0.00	0.00	< 0.01	< 0.01	< 0.01	< 0.01	< 0.01	< 0.01	< 0.01	< 0.01
Rb	ug/L	ICPMS	6.00	6.10	4.9	5.0	5.0	5.3	6.0	6.0	6.0	5.9
Re	ug/L	ICPMS	0.00	0.00	< 0.02	< 0.02	< 0.02	< 0.02	< 0.02	< 0.02	< 0.02	< 0.02
Sb	ug/L	ICPMS	0.84	0.80	0.57	0.54	0.54	0.60	0.75	0.75	0.74	0.77
Sc	ug/L	ICPMS	0.00	0.00	0.4	0.3	0.3	0.4	0.4	0.4	0.4	0.4
Se	ug/L	ICPMS	0.00	0.00	<0.5	<0.5	<0.5	<0.5	<0.5	<0.5	<0.5	<0.5
SiO_2	mg/L	ICPMS	12.98	12.98	10	11	11	11	11	12	12	12
Sm	ug/L	ICPMS	0.00	0.00	< 0.01	< 0.01	< 0.01	< 0.01	< 0.01	< 0.01	< 0.01	0.01
Sn	ug/L	ICPMS	0.00	0.00	< 0.05	< 0.05	< 0.05	< 0.05	< 0.05	< 0.05	< 0.05	< 0.05
Sr	ug/L	ICPMS	43.00	43.00	36	37	37	37	38	38	38	38
Ta	ug/L	ICPMS	0.00	0.00	< 0.02	< 0.02	< 0.02	< 0.02	< 0.02	< 0.02	< 0.02	< 0.02
Tb	ug/L	ICPMS	0.00	0.00	< 0.005	< 0.005	< 0.005	< 0.005	< 0.005	< 0.005	< 0.005	< 0.005
Te	ug/L	ICPMS	0.00	0.00	0.4	< 0.1	0.2	< 0.1	< 0.1	< 0.1	< 0.1	< 0.1
Th	ug/L	ICPMS	0.00	0.00	< 0.005	< 0.005	< 0.005	< 0.005	< 0.005	< 0.005	< 0.005	< 0.005
Ti	ug/L	ICPMS	0.00	0.00	0.8	0.3	0.4	0.3	0.2	0.2	0.2	0.1
Tl	ug/L	ICPMS	0.00	0.00	< 0.05	< 0.05	< 0.05	< 0.05	< 0.05	< 0.05	< 0.05	< 0.05
Tm	ug/L	ICPMS	0.00	0.00	< 0.005	< 0.005	< 0.005	< 0.005	< 0.005	< 0.005	< 0.005	< 0.005
U	ug/L	ICPMS	0.01	0.01	0.02	0.02	0.02	0.02	0.01	0.01	0.01	0.01
V	ug/L	ICPMS	1.00	1.00	0.9	0.9	1	0.9	0.9	0.9	0.9	0.9
W	ug/L	ICPMS	2.20	2.20	1.5	1.6	1.6	1.8	2.2	2.2	2.2	2.3
Y	ug/L	ICPMS	0.02	0.02	0.04	0.03	0.04	0.04	0.05	0.04	0.04	0.05
Yb	ug/L	ICPMS	0.00	0.00	< 0.01	< 0.01	< 0.01	< 0.01	< 0.01	< 0.01	< 0.01	< 0.01
Zn	ug/L	ICPMS	0.00	0.60	0.6	< 0.5	< 0.5	< 0.5	< 0.5	< 0.5	< 0.5	< 0.5
Zr	ug/L	ICPMS	0.05	0.07	0.06	< 0.05	< 0.05	< 0.05	< 0.05	< 0.05	< 0.05	< 0.05
Hg	ng/L	Hg CVAF	<10	10	-	-	-	-	-	-	-	-
$\delta^{18}O$ vs VSMOW	permil	ISO1	-16.1	-16.1	-16.5	-16.4	-16.4	-16.3	-16.7	-16.4	-16.5	-16.4
δD vs VSMOW	permil	ISO2	-130	-131	-129.6	-129.1	-129.4	-129.5	-129.3	-129.6	-129.5	-129.5
$\delta^{34}S$ vs CDT	permil	ISO3	-	-	2.4	2.4	1.7	2.1	2.2	3.4	4.2	2.6
$\delta^{34}S$ vs CDT	permil	ISO4	-	-	-	-	-	-	-	-	-	-

Appendix 1. Site and analytical data from creeks and water column profiles—*Continued*.

Field no.												
Drainage/ description			Mary Bay (MB-1) water column	Mary Bay (MB-1) water column	Mary Bay (MB-1) water column	Mary Bay (MB-1) water column	Mary Bay (MB-1) water column	Mary Bay (MB-1) water column	Mary Bay (MB-1) water column	Mary Bay (MB-1) water column	Mary Bay (MB-1) water column	Mary Bay (MB-1) water column
Latitude			44°32'42.8"N	44°32'42.8"N	44°32'42.8"N	44°32'42.8"N	44°32'42.8"N	44°32'42.8"N	44°32'42.8"N	44°32'42.8"N	44°32'42.8"N	44°32'42.8"N
Longitude			110°18'39.1"W	110°18'39.1"W	110°18'39.1"W	110°18'39.1"W	110°18'39.1"W	110°18'39.1"W	110°18'39.1"W	110°18'39.1"W	110°18'39.1"W	110°18'39.1"W
NPS no.			-	-	-	-	-	-	-	-	-	-
Date			07/26/97	07/26/97	07/26/97	07/26/97	07/26/97	07/26/97	07/26/97	07/26/97	07/26/97	07/26/97
Depth	m		48	0	5	10	12	17	20	30	40	48
Treatment/ Sample type			Filtered and acidified	Raw and acidified	Raw and acidified	Raw and acidified	Raw and acidified	Raw and acidified	Raw and acidified	Raw and acidified	Raw and acidified	Raw and acidified
Collector			-	-	-	-	-	-	-	-	-	-
pH			6.73	-	-	-	-	-	-	-	-	-
Conductivity	uS/cm		-	-	-	-	-	-	-	-	-	-
Temperature	˚C		-	-	-	-	-	-	-	-	-	-
Flow	CFS		-	-	-	-	-	-	-	-	-	-
Alkalinity	Mg/L as $CaCO_3$		-	-	-	-	-	-	-	-	-	-
Sum CO_2	mM		0.78	-	-	-	-	-	-	-	-	-
HCO_3	mM	measured	0.5	-	-	-	-	-	-	-	-	-
HCO_3	uM	calculated	470	-	-	-	-	-	-	-	-	-
Comments			-	-	-	-	-	-	-	-	-	-
Cl	mg/L	IC-Aq	6.1	-	-	-	-	-	-	-	-	-
F	mg/L	IC-Aq	-	-	-	-	-	-	-	-	-	-
NO_3	mg/L	IC-Aq	-	-	-	-	-	-	-	-	-	-
SO_4	mg/L	IC-Aq	7.7	-	-	-	-	-	-	-	-	-
Ag	ug/L	ICPMS	< 0.01	< 0.01	< 0.01	< 0.01	< 0.01	< 0.01	< 0.01	< 0.01	< 0.01	< 0.01
Al	ug/L	ICPMS	10	54	64	60	66	65	66	60	66	270
As	ug/L	ICPMS	16	12	13	12	14	18	18	18	18	19
Au	ug/L	ICPMS	0.02	0.007	< 0.005	0.006	< 0.005	0.006	< 0.005	0.02	0.02	< 0.005
B	ug/L	ICPAES	-	-	-	-	-	-	-	-	-	-
Ba	ug/L	ICPMS	9.4	8.7	8.8	8.6	9.0	9.7	9.7	9.5	9.6	11
Be	ug/L	ICPMS	< 0.05	< 0.05	< 0.05	< 0.05	< 0.05	< 0.05	< 0.05	< 0.05	< 0.05	< 0.05
Bi	ug/L	ICPMS	< 0.01	< 0.01	< 0.01	< 0.01	< 0.01	< 0.01	< 0.01	< 0.01	< 0.01	< 0.01
Ca	mg/L	ICPAES	-	-	-	-	-	-	-	-	-	-
Cd	ug/L	ICPMS	< 0.02	< 0.02	< 0.02	< 0.02	< 0.02	< 0.02	< 0.02	< 0.02	< 0.02	< 0.02
Ce	ug/L	ICPMS	0.06	0.1	0.1	0.1	0.1	0.1	0.1	0.1	0.1	0.55
Co	ug/L	ICPMS	0.02	0.02	0.02	< 0.02	0.02	0.03	0.03	0.03	0.03	0.08
Cr	ug/L	ICPMS	2	2	2	3	3	3	3	3	3	4
Cs	ug/L	ICPMS	3.8	2.5	2.5	2.4	2.8	3.8	3.9	3.8	3.8	4.0
Cu	ug/L	ICPMS	< 0.5	< 0.5	< 0.5	< 0.5	< 0.5	< 0.5	< 0.5	< 0.5	< 0.5	0.5
Dy	ug/L	ICPMS	0.006	0.009	0.008	0.008	0.006	0.01	0.009	0.01	0.01	0.03
Er	ug/L	ICPMS	< 0.005	0.007	0.005	< 0.005	0.005	< 0.005	0.006	0.006	< 0.005	0.01
Eu	ug/L	ICPMS	< 0.005	< 0.005	< 0.005	< 0.005	< 0.005	< 0.005	< 0.005	< 0.005	< 0.005	0.005
Fe	ug/L	ICPMS	25	27	29	30	32	41	42	38	40	150
Ga	ug/L	ICPMS	< 0.02	< 0.02	< 0.02	< 0.02	< 0.02	< 0.02	< 0.02	< 0.02	< 0.02	0.03
Gd	ug/L	ICPMS	0.005	0.01	0.01	0.01	0.008	0.009	0.01	0.01	0.01	0.04
Ge	ug/L	ICPMS	0.3	0.2	0.2	0.2	0.2	0.3	0.3	0.2	0.3	0.3
Hf	ug/L	ICPMS	< 0.05	< 0.05	< 0.05	< 0.05	< 0.05	< 0.05	< 0.05	< 0.05	< 0.05	< 0.05
Ho	ug/L	ICPMS	< 0.005	< 0.005	< 0.005	< 0.005	< 0.005	< 0.005	< 0.005	< 0.005	< 0.005	0.005
In	ug/L	ICPMS	< 0.01	< 0.01	< 0.01	< 0.01	< 0.01	< 0.01	< 0.01	< 0.01	< 0.01	< 0.01
K	mg/L	ICPAES	-	-	-	-	-	-	-	-	-	-
La	ug/L	ICPMS	0.04	0.06	0.07	0.07	0.07	0.08	0.08	0.07	0.09	0.3
Li	ug/L	ICPMS	48	35	35	35	38	48	48	48	48	48
Mg	mg/L	ICPAES	-	-	-	-	-	-	-	-	-	-
Mn	ug/L	ICPMS	3.4	1.3	1.4	1.4	1.9	3.4	3.3	3.3	3.4	4.9
Mo	ug/L	ICPMS	1.1	1.0	1.1	1.1	1.0	1.1	1.1	1.1	1.1	1.1
Na	mg/L	ICPAES	-	-	-	-	-	-	-	-	-	-
Nb	ug/L	ICPMS	< 0.02	< 0.02	< 0.02	< 0.02	< 0.02	< 0.02	< 0.02	< 0.02	< 0.02	< 0.02
Nd	ug/L	ICPMS	0.02	0.03	0.02	0.04	0.05	0.05	0.04	0.04	0.06	0.22
Ni	ug/L	ICPMS	0.4	0.5	0.5	0.5	0.5	0.6	0.5	0.5	0.5	0.8
P	ug/L	ICPMS	86	100	91	100	95	120	100	110	110	150
Pb	ug/L	ICPMS	< 0.05	< 0.05	< 0.05	< 0.05	< 0.05	< 0.05	< 0.05	< 0.05	< 0.05	3.6
Pr	ug/L	ICPMS	< 0.01	0.01	0.01	0.01	0.01	0.01	0.02	0.01	0.02	0.06
Rb	ug/L	ICPMS	5.9	5.0	5.0	5.0	5.2	6.0	5.9	5.9	5.9	6.0
Re	ug/L	ICPMS	< 0.02	< 0.02	< 0.02	< 0.02	< 0.02	< 0.02	< 0.02	< 0.02	< 0.02	< 0.02
Sb	ug/L	ICPMS	0.78	0.54	0.53	0.53	0.60	0.75	0.77	0.76	0.75	0.77
Sc	ug/L	ICPMS	0.4	0.4	0.4	0.4	0.4	0.4	0.4	0.4	0.4	0.4
Se	ug/L	ICPMS	<0.5	<0.5	<0.5	<0.5	<0.5	<0.5	<0.5	<0.5	<0.5	<0.5
SiO_2	mg/L	ICPMS	12	11	11	11	11	12	12	12	12	12
Sm	ug/L	ICPMS	0.01	0.02	0.01	< 0.01	0.01	< 0.01	0.01	0.01	0.01	0.04
Sn	ug/L	ICPMS	< 0.05	< 0.05	< 0.05	< 0.05	< 0.05	< 0.05	< 0.05	< 0.05	< 0.05	< 0.05
Sr	ug/L	ICPMS	38	37	37	37	37	38	38	38	38	39
Ta	ug/L	ICPMS	< 0.02	< 0.02	< 0.02	< 0.02	< 0.02	< 0.02	< 0.02	< 0.02	< 0.02	< 0.02
Tb	ug/L	ICPMS	< 0.005	< 0.005	< 0.005	< 0.005	< 0.005	< 0.005	< 0.005	< 0.005	< 0.005	< 0.005
Te	ug/L	ICPMS	< 0.1	0.1	0.3	< 0.1	< 0.1	< 0.1	< 0.1	< 0.1	< 0.1	< 0.1
Th	ug/L	ICPMS	< 0.005	< 0.005	< 0.005	< 0.005	< 0.005	< 0.005	< 0.005	< 0.005	< 0.005	< 0.005
Ti	ug/L	ICPMS	0.2	0.7	0.8	0.9	1.0	0.9	1.1	1.0	1.1	4.0
Tl	ug/L	ICPMS	< 0.05	< 0.05	< 0.05	< 0.05	< 0.05	< 0.05	< 0.05	< 0.05	< 0.05	< 0.05
Tm	ug/L	ICPMS	< 0.005	< 0.005	< 0.005	< 0.005	< 0.005	< 0.005	< 0.005	< 0.005	< 0.005	< 0.005
U	ug/L	ICPMS	0.01	0.01	0.02	0.02	0.02	0.01	0.01	0.02	0.01	0.02
V	ug/L	ICPMS	0.9	1	1	1	1	0.9	1	0.9	0.9	1
W	ug/L	ICPMS	2.2	1.7	1.8	1.6	1.8	2.2	2.2	2.2	2.3	1.9
Y	ug/L	ICPMS	0.05	0.06	0.05	0.05	0.06	0.07	0.06	0.06	0.06	0.2
Yb	ug/L	ICPMS	< 0.01	< 0.01	< 0.01	< 0.01	< 0.01	0.01	< 0.01	< 0.01	< 0.01	0.02
Zn	ug/L	ICPMS	< 0.5	0.7	< 0.5	< 0.5	< 0.5	< 0.5	< 0.5	< 0.5	< 0.5	1
Zr	ug/L	ICPMS	< 0.05	< 0.05	< 0.05	< 0.05	0.2	< 0.05	< 0.05	< 0.05	< 0.05	< 0.05
Hg	ng/L	Hg CVAF	-	-	-	-	-	-	-	-	-	-
$\delta^{18}O$ vs VSMOW	permil	ISO1	-	-16.5	-16.4	-16.5	-16.8	-16.4	-16.4	-16.4	-16.3	-
δD vs VSMOW	permil	ISO2	-	-130.2	-129.1	-129.7	-129.7	-129.7	-129.4	-129.2	-129.2	-
$\delta^{34}S$ vs CDT	permil	ISO3	-	-	-	-	-	-	-	-	-	-
$\delta^{34}S$ vs CDT	permil	ISO4	-	-	-	-	-	-	-	-	-	-

Appendix 1. Site and analytical data from creeks and water column profiles—*Continued*.

Field no. Drainage/ description			Mary Bay water column	Mary Bay water column	Mary Bay water column	Mary Bay water column	Mary Bay water column	Mary Bay water column	Mary Bay water column	Mary Bay water column	Mary Bay water column	off Stevenson Island water column	off Stevenson Island water column
Latitude			44°32'43.5"N	44°32'43.5"N	44°32'43.5"N	44°32'43.5"N	44°32'43.5"N	44°32'43.5"N	44°32'43.5"N	44°32'43.5"N	44°32'43.5"N	44°30'38.7"N	44°30'38.7"N
Longitude			W	110°18'38.5"W	110°18'38.5"W	110°18'38.5"W	W	W	W	W	W	110°21'17.4"W	110°21'17.4"W
NPS no.			-	-	-	-	-	-	-	-	-	-	-
Date			07/24/98	07/24/98	07/24/98	07/24/98	07/24/98	07/24/98	07/24/98	07/24/98	07/24/98	07/25/98	07/25/98
Depth	m		0	7.6	15.2	22.9	30.5	35.1	39.6	44.2	48.8	0	7.6
Treatment/ Sample type			Filtered and acidified	Filtered and acidified	Filtered and acidified	Filtered and acidified	Filtered and acidified	Filtered and acidified	Filtered and acidified	Filtered and acidified	Filtered and acidified	Filtered and acidified	Filtered and acidified
Collector			-	-	-	-	-	-	-	-	-	-	-
pH			7.41	7.52	7.01	6.92	6.91	6.94	6.9	6.9	6.92	7.72	7.72
Conductivity	uS/cm		-	-	-	-	-	-	-	-	-	-	-
Temperature	˚C		-	-	-	-	-	-	-	-	-	-	-
Flow	CFS		-	-	-	-	-	-	-	-	-	-	-
Alkalinity	Mg/L as $CaCO_3$		-	-	-	-	-	-	-	-	-	-	-
Sum CO_2	mM		-	-	-	-	-	-	-	-	-	-	-
HCO_3	mM	measured	0.6	0.6	0.6	0.6	0.6	0.6	0.6	0.6	0.6	0.6	0.7
HCO_3	uM	calculated	658	562	629	604	612	610	623	610	614	636	625
Comments			-	-	-	-	-	-	-	-	-	-	-
Cl	mg/L	IC-Aq	4.6	4.7	6.9	6.3	6.2	6.2	6.2	6.2	6.5	4.6	4.6
F	mg/L	IC-Aq	0.5	0.5	0.5	0.5	0.5	0.5	0.5	0.5	0.5	0.8	0.5
NO_3	mg/L	IC-Aq	<.1	<.1	<.1	<.1	<.1	<.1	<.1	<.1	<.1	<.1	<.1
SO_4	mg/L	IC-Aq	6.6	6.4	7.3	7.3	7.3	7.3	7.3	7.3	7.4	6.7	6.7
Ag	ug/L	ICPMS	0.00	0.00	0.00	0.00	0.00	0.00	0.00	0.00	0.00	0.01	0.00
Al	ug/L	ICPMS	10.00	6.10	5.10	5.40	9.40	5.70	6.10	5.60	5.80	7.70	7.60
As	ug/L	ICPMS	14.00	14.00	19.00	18.00	18.00	18.00	18.00	18.00	16.00	13.00	13.00
Au	ug/L	ICPMS	0.00	0.00	0.00	0.00	0.00	0.00	0.00	0.00	0.00	0.00	0.00
B	ug/L	ICPAES	79.99	73.99	109.99	99.99	95.99	99.99	109.99	109.99	109.99	76.99	75.99
Ba	ug/L	ICPMS	8.40	7.70	8.80	9.00	8.90	8.80	9.00	9.00	9.00	8.20	13.00
Be	ug/L	ICPMS	0.00	0.00	0.00	0.00	0.00	0.00	0.00	0.00	0.00	0.00	0.07
Bi	ug/L	ICPMS	0.00	0.00	0.00	0.00	0.00	0.00	0.00	0.00	0.00	0.00	0.00
Ca	mg/L	ICPAES	5.00	4.80	4.80	5.00	4.50	4.60	5.10	5.10	5.00	5.00	4.90
Cd	ug/L	ICPMS	0.00	0.00	0.00	0.00	0.00	0.00	0.00	0.00	0.10	0.00	0.00
Ce	ug/L	ICPMS	0.03	0.02	0.03	0.03	0.05	0.02	0.03	0.03	0.05	0.02	0.02
Co	ug/L	ICPMS	0.02	0.00	0.02	0.00	0.00	0.09	0.02	0.02	0.05	0.07	0.00
Cr	ug/L	ICPMS	0.00	0.00	0.00	0.00	0.00	0.00	0.00	0.00	0.00	0.00	0.00
Cs	ug/L	ICPMS	2.80	2.70	4.40	4.00	4.20	4.10	4.20	4.30	3.90	2.80	2.80
Cu	ug/L	ICPMS	0.60	0.00	0.50	0.50	0.00	0.00	0.00	0.50	0.50	0.50	0.00
Dy	ug/L	ICPMS	0.00	0.00	0.00	0.01	0.01	0.01	0.01	0.00	0.02	0.00	0.00
Er	ug/L	ICPMS	0.01	0.01	0.01	0.01	0.01	0.00	0.01	0.01	0.01	0.00	0.00
Eu	ug/L	ICPMS	0.00	0.00	0.00	0.00	0.00	0.00	0.00	0.00	0.00	0.00	0.00
Fe	ug/L	ICPMS	9.80	0.00	11.00	12.00	14.00	12.00	12.00	10.00	26.00	0.00	10.00
Ga	ug/L	ICPMS	0.00	0.00	0.07	0.03	0.02	0.00	0.06	0.03	0.05	0.02	0.04
Gd	ug/L	ICPMS	0.00	0.00	0.01	0.01	0.01	0.01	0.01	0.00	0.01	0.00	0.00
Ge	ug/L	ICPMS	0.20	0.20	0.30	0.30	0.30	0.30	0.30	0.20	0.30	0.20	0.30
Hf	ug/L	ICPMS	0.00	0.00	0.00	0.00	0.00	0.00	0.00	0.00	0.00	0.10	0.07
Ho	ug/L	ICPMS	0.00	0.00	0.00	0.00	0.00	0.00	0.00	0.00	0.00	0.00	0.00
In	ug/L	ICPMS	0.00	0.00	0.00	0.00	0.00	0.00	0.00	0.00	0.00	0.00	0.00
K	mg/L	ICPAES	1.50	1.40	1.50	1.60	1.40	1.50	1.60	1.60	1.60	1.50	1.40
La	ug/L	ICPMS	0.02	0.02	0.02	0.02	0.10	0.02	0.02	0.02	0.04	0.02	0.02
Li	ug/L	ICPMS	45.01	44.01	62.02	56.02	54.02	56.02	58.02	57.02	57.02	41.01	41.01
Mg	mg/L	ICPAES	2.10	2.10	2.10	2.20	2.00	2.20	2.30	2.30	2.30	2.10	2.10
Mn	ug/L	ICPMS	0.40	0.08	3.80	3.30	5.80	3.00	3.40	3.20	6.40	0.32	0.15
Mo	ug/L	ICPMS	1.10	0.98	1.00	1.10	0.98	1.10	1.10	1.20	1.10	1.40	1.20
Na	mg/L	ICPAES	8.30	8.00	9.20	9.10	7.90	8.20	9.00	8.90	8.90	8.20	8.10
Nb	ug/L	ICPMS	0.00	0.00	0.00	0.00	0.00	0.00	0.00	0.00	0.00	0.00	0.00
Nd	ug/L	ICPMS	0.02	0.02	0.03	0.02	0.02	0.02	0.04	0.02	0.03	0.03	0.02
Ni	ug/L	ICPMS	0.30	0.40	0.40	0.40	0.40	0.40	0.40	0.30	0.50	0.40	0.30
P	ug/L	ICPMS	13.00	14.00	12.00	14.00	14.00	12.00	14.00	14.00	13.00	10.00	12.00
Pb	ug/L	ICPMS	0.00	0.00	0.00	0.00	0.00	0.00	0.00	0.00	0.00	0.00	0.00
Pr	ug/L	ICPMS	0.00	0.00	0.00	0.00	0.02	0.00	0.00	0.01	0.01	0.00	0.00
Rb	ug/L	ICPMS	5.00	4.90	5.90	5.80	5.80	5.60	6.00	5.90	5.80	4.90	5.20
Re	ug/L	ICPMS	0.00	0.00	0.00	0.00	0.00	0.00	0.00	0.00	0.00	0.00	0.00
Sb	ug/L	ICPMS	0.55	0.56	0.82	0.79	0.74	0.76	0.77	0.83	0.87	0.69	0.59
Sc	ug/L	ICPMS	0.00	0.00	0.00	0.00	0.00	0.00	0.00	0.00	0.00	0.00	0.00
Se	ug/L	ICPMS	1600.00	0.00	0.00	620.00	830.00	1800.00	0.00	0.00	0.00	0.00	0.00
SiO_2	mg/L	ICPMS	11.98	11.98	11.98	11.98	11.98	11.98	11.98	11.98	11.98	11.98	10.98
Sm	ug/L	ICPMS	0.00	0.01	0.01	0.01	0.02	0.00	0.00	0.01	0.00	0.00	0.02
Sn	ug/L	ICPMS	0.00	0.00	0.00	0.00	0.00	0.00	0.00	0.00	0.00	0.00	0.00
Sr	ug/L	ICPMS	45.00	44.00	44.00	45.00	46.00	44.00	45.00	46.00	45.00	42.00	43.00
Ta	ug/L	ICPMS	0.00	0.00	0.00	0.00	0.00	0.00	0.00	0.00	0.00	0.00	0.00
Tb	ug/L	ICPMS	0.00	0.00	0.00	0.00	0.00	0.00	0.00	0.00	0.00	0.00	0.00
Te	ug/L	ICPMS	0.00	0.00	0.00	0.00	0.00	0.00	0.00	0.00	0.00	0.00	0.00
Th	ug/L	ICPMS	0.00	0.00	0.00	0.00	0.00	0.00	0.00	0.00	0.00	0.01	0.00
Ti	ug/L	ICPMS	0.00	0.00	0.00	0.00	0.00	0.00	0.00	0.00	0.00	0.00	0.00
Tl	ug/L	ICPMS	0.00	0.00	0.00	0.00	0.00	0.00	0.00	0.00	0.00	0.00	0.00
Tm	ug/L	ICPMS	0.00	0.00	0.00	0.00	0.00	0.00	0.00	0.00	0.00	0.00	0.00
U	ug/L	ICPMS	0.01	0.01	0.02	0.02	0.02	0.01	0.01	0.02	0.02	0.01	0.01
V	ug/L	ICPMS	1.00	1.00	1.00	1.00	1.00	1.00	1.00	1.00	1.00	1.00	1.00
W	ug/L	ICPMS	1.50	1.30	1.80	1.60	1.60	1.80	1.90	1.80	1.60	1.00	1.20
Y	ug/L	ICPMS	0.02	0.02	0.03	0.02	0.03	0.03	0.03	0.02	0.04	0.02	0.01
Yb	ug/L	ICPMS	0.00	0.00	0.00	0.00	0.00	0.00	0.00	0.00	0.00	0.00	0.00
Zn	ug/L	ICPMS	0.60	1.00	2.00	0.90	1.00	1.00	2.00	0.80	8.00	0.60	0.70
Zr	ug/L	ICPMS	0.06	0.06	0.07	0.07	0.07	0.07	0.05	0.00	0.00	0.20	0.20
Hg	ng/L	Hg CVAF	<10	<10	<10	<10	<10	<10	<10	<10	<10	<10	<10
$\delta^{18}O$ vs VSMOW	permil	ISO1	-16.2	-16.3	-16.2	-16.3	-16.3	-16.3	-16.3	-16.3	-16.3	-16.5	-16.5
δD vs VSMOW	permil	ISO2	-134	-135	-135	-126	-132	-132	-128	-132	-125	-128	-127
$\delta^{34}S$ vs CDT	permil	ISO3	-	-	-	-	-	-	-	-	-	-	-
$\delta^{34}S$ vs CDT	permil	ISO4	-	-	-	-	-	-	-	-	-	-	-

Appendix 1. Site and analytical data from creeks and water column profiles—*Continued*.

Field no. Drainage/ description			off Stevenson Island water column	off Stevenson Island water column	off Stevenson Island water column	off Stevenson Island water column	off Stevenson Island water column	off Stevenson Island water column	off Stevenson Island water column	off Stevenson Island water column	G1 diss Yellowstone River @ outlet	G1 tot Yellowstone River @ outlet	E1 diss Yellowstone River @ outlet
Latitude			44°30'38.7"N	44°30'38.7"N	44°30'38.7"N	44°30'38.7"N	44°30'38.7"N	44°30'38.7"N	44°30'38.7"N	44°30'38.7"N	44°34'3.2"N	44°34'3.2"N	44°34'3.2"N
Longitude			W	W	W	W	W	W	W	W	110°22'45.3"W	110°22'45.3"W	110°22'45.3"W
NPS no.			-	-	-	-	-	-	-	-	-	-	-
Date			07/25/98	07/25/98	07/25/98	07/25/98	07/25/98	07/25/98	07/25/98	07/25/98	07/22/99	07/22/99	07/22/99
Depth	m		15.2	30.5	45.7	61.0	76.2	91.4	98.1	104.2	-	-	-
Treatment/ Sample type			Filtered and acidified	Filtered and acidified	Filtered and acidified	Filtered and acidified	Filtered and acidified	Filtered and acidified	Filtered and acidified	Filtered and acidified	dissolved	total	dissolved
Collector			-	-	-	-	-	-	-	-	Balistrieri	Balistrieri	Balistrieri
pH			7.53	7.44	7.38	7.37	7.39	7.37	7.39	7.39	7.2	7.2	7.3
Conductivity	uS/cm		-	-	-	-	-	-	-	-	87	87	87
Temperature	˚C		-	-	-	-	-	-	-	-	16.1	16.1	19.9
Flow	CFS		-	-	-	-	-	-	-	-	-	-	-
Alkalinity	Mg/L as $CaCO_3$		-	-	-	-	-	-	-	-	-	-	-
Sum CO_2	mM		-	-	-	-	-	-	-	-	-	-	-
HCO_3	mM	measured	0.6	0.6	0.6	0.6	0.6	0.7	0.6	0.6	-	-	-
HCO_3	uM	calculated	640	632	610	621	630	631	616	628	-	-	-
Comments			-	-	-	-	-	-	-	-	temperature @ filter	temperature @ filter	temperature @ filter
Cl	mg/L	IC-Aq	4.8	4.9	5	5.3	5	5	4.9	4.9	4.7	4.7	4.5
F	mg/L	IC-Aq	0.5	0.5	0.5	0.5	0.5	0.5	0.5	0.5	0.5	0.5	0.4
NO_3	mg/L	IC-Aq	<.1	<.1	<.1	<.1	<.1	<.1	<.1	<.1	<.35	<.35	<.35
SO_4	mg/L	IC-Aq	7	7.1	7.1	7.1	7.2	7.1	7.1	7.2	7.2	7.2	7.2
Ag	ug/L	ICPMS	0.00	0.00	0.00	0.00	0.00	0.00	0.00	0.00	<0.01	<0.01	<0.01
Al	ug/L	ICPMS	4.00	3.60	4.40	10.00	3.70	3.60	4.70	4.60	2.4	2	1
As	ug/L	ICPMS	13.00	14.00	14.00	14.00	14.00	14.00	14.00	14.00	11	11	24
Au	ug/L	ICPMS	0.00	0.00	0.00	0.00	0.00	0.00	0.00	0.00	< 0.01	< 0.01	< 0.01
B	ug/L	ICPAES	77.99	80.99	80.99	80.99	81.99	79.99	75.99	82.99	89.4	82.4	124
Ba	ug/L	ICPMS	8.10	8.10	8.40	8.40	8.10	8.40	8.00	8.20	8.5	8.4	8.9
Be	ug/L	ICPMS	0.00	0.00	0.00	0.06	0.00	0.00	0.00	0.00	<0.05	<0.05	<0.05
Bi	ug/L	ICPMS	0.00	0.00	0.00	0.00	0.00	0.00	0.00	0.00	< 0.01	< 0.01	< 0.01
Ca	mg/L	ICPAES	4.90	5.00	4.90	5.00	5.00	4.90	4.70	5.20	5.1	5.1	5
Cd	ug/L	ICPMS	0.00	0.00	0.00	0.00	0.00	0.00	0.00	0.00	<0.02	<0.02	<0.02
Ce	ug/L	ICPMS	0.02	0.01	0.01	0.03	0.01	0.01	0.01	0.02	0.03	0.03	0.02
Co	ug/L	ICPMS	0.00	0.00	0.00	0.03	0.05	0.02	0.03	0.00	<0.02	<0.02	<0.02
Cr	ug/L	ICPMS	0.00	0.00	0.00	0.00	0.00	0.00	0.00	0.00	<1	<1	<1
Cs	ug/L	ICPMS	2.80	3.00	3.00	3.00	2.90	3.00	2.80	3.00	2.2	2.2	2.3
Cu	ug/L	ICPMS	0.00	0.00	0.00	0.00	0.00	0.00	0.00	0.50	<0.5	<0.5	<0.5
Dy	ug/L	ICPMS	0.00	0.00	0.00	0.00	0.01	0.01	0.00	0.01	< 0.005	0.005	0.005
Er	ug/L	ICPMS	0.00	0.00	0.00	0.00	0.00	0.00	0.00	0.00	0.005	< 0.005	< 0.005
Eu	ug/L	ICPMS	0.00	0.00	0.00	0.00	0.00	0.00	0.00	0.00	< 0.005	< 0.005	< 0.005
Fe	ug/L	ICPMS	0.00	9.70	0.00	9.90	0.00	10.00	0.00	0.00	<30	<30	<30
Ga	ug/L	ICPMS	0.03	0.00	0.00	0.00	0.00	0.00	0.04	0.03	< 0.02	< 0.02	< 0.02
Gd	ug/L	ICPMS	0.01	0.00	0.00	0.00	0.01	0.01	0.00	0.00	< 0.005	< 0.005	0.008
Ge	ug/L	ICPMS	0.30	0.30	0.30	0.20	0.20	0.20	0.20	0.30	0.2	0.2	0.2
Hf	ug/L	ICPMS	0.00	0.00	0.00	0.00	0.00	0.00	0.00	0.00	-	-	-
Ho	ug/L	ICPMS	0.00	0.00	0.00	0.00	0.00	0.00	0.00	0.00	< 0.005	< 0.005	< 0.005
In	ug/L	ICPMS	0.00	0.00	0.00	0.00	0.00	0.00	0.00	0.00	-	-	-
K	mg/L	ICPAES	1.50	1.50	1.50	1.50	1.60	1.50	1.40	1.60	1.7	1.6	1.68
La	ug/L	ICPMS	0.03	0.02	0.01	0.03	0.01	0.02	0.02	0.02	0.03	0.02	0.03
Li	ug/L	ICPMS	44.01	45.01	44.01	46.01	45.01	45.01	44.01	45.01	42	42	44
Mg	mg/L	ICPAES	2.10	2.20	2.10	2.20	2.20	2.10	2.10	2.20	2.23	2.18	2.19
Mn	ug/L	ICPMS	0.06	0.10	0.14	0.39	0.07	0.26	0.55	1.20	0.45	0.48	0.38
Mo	ug/L	ICPMS	1.20	1.20	1.00	1.00	1.00	0.97	1.00	1.20	0.95	0.92	5.9
Na	mg/L	ICPAES	8.20	8.60	8.40	8.60	8.60	8.30	8.00	8.90	8.75	8.48	9.19
Nb	ug/L	ICPMS	0.00	0.00	0.00	0.00	0.00	0.00	0.00	0.00	0.07	0.06	< 0.02
Nd	ug/L	ICPMS	0.02	0.02	0.02	0.04	0.01	0.01	0.01	0.02	0.04	0.03	0.03
Ni	ug/L	ICPMS	0.40	0.30	0.40	0.50	0.40	0.40	0.40	0.40	0.4	0.4	0.3
P	ug/L	ICPMS	10.00	12.00	16.00	14.00	16.00	14.00	15.00	14.00	1	4	< 1
Pb	ug/L	ICPMS	0.00	0.00	0.00	0.70	0.00	0.00	0.00	0.00	<0.05	<0.05	<0.05
Pr	ug/L	ICPMS	0.00	0.00	0.00	0.00	0.00	0.00	0.00	0.00	< 0.01	< 0.01	< 0.01
Rb	ug/L	ICPMS	4.90	5.10	5.20	5.10	5.10	5.10	4.90	5.20	4.1	4.1	4.2
Re	ug/L	ICPMS	0.00	0.00	0.00	0.00	0.00	0.00	0.00	0.00	-	-	-
Sb	ug/L	ICPMS	0.62	0.59	0.63	0.66	0.62	0.56	0.51	0.59	0.47	0.45	1.7
Sc	ug/L	ICPMS	0.20	0.10	0.00	0.00	0.00	0.10	0.30	0.00	0.2	0.2	< 0.1
Se	ug/L	ICPMS	0.00	0.00	0.00	1100.00	15.00	0.00	0.00	0.00	< 0.3	< 0.3	< 0.3
SiO_2	mg/L	ICPMS	10.98	10.98	10.98	10.98	10.98	11.98	10.98	10.98	9.7	9.8	8.9
Sm	ug/L	ICPMS	0.00	0.00	0.00	0.00	0.01	0.01	0.00	0.00	< 0.01	< 0.01	< 0.01
Sn	ug/L	ICPMS	0.00	0.00	0.00	0.00	0.00	0.00	0.00	0.00	-	-	-
Sr	ug/L	ICPMS	43.00	43.00	42.00	44.00	44.00	44.00	42.00	44.00	36	36	36
Ta	ug/L	ICPMS	0.00	0.00	0.00	0.00	0.00	0.00	0.00	0.00	0.04	0.05	< 0.03
Tb	ug/L	ICPMS	0.00	0.00	0.00	0.00	0.00	0.00	0.00	0.00	< 0.005	< 0.005	< 0.005
Te	ug/L	ICPMS	0.00	0.00	0.00	0.00	0.00	0.00	0.00	0.00	-	-	-
Th	ug/L	ICPMS	0.00	0.01	0.00	0.00	0.00	0.01	0.00	0.00	< 0.02	< 0.02	< 0.02
Ti	ug/L	ICPMS	0.00	0.00	0.00	0.00	0.00	0.00	0.00	0.00	< 0.2	< 0.2	< 0.2
Tl	ug/L	ICPMS	0.00	0.00	0.00	0.00	0.00	0.00	0.00	0.00	<0.05	<0.05	<0.05
Tm	ug/L	ICPMS	0.00	0.00	0.00	0.00	0.00	0.00	0.00	0.00	< 0.005	< 0.005	< 0.005
U	ug/L	ICPMS	0.01	0.01	0.01	0.02	0.02	0.01	0.01	0.01	0.01	0.02	0.01
V	ug/L	ICPMS	1.00	1.00	1.00	1.00	1.00	1.00	1.00	1.00	0.77	0.76	0.92
W	ug/L	ICPMS	1.30	1.30	1.20	1.20	1.30	1.20	1.40	1.30	0.89	0.97	11
Y	ug/L	ICPMS	0.02	0.02	0.01	0.02	0.02	0.02	0.02	0.02	0.03	0.03	0.02
Yb	ug/L	ICPMS	0.00	0.00	0.00	0.00	0.00	0.00	0.00	0.00	< 0.01	< 0.01	< 0.01
Zn	ug/L	ICPMS	1.00	0.00	0.00	37.01	0.00	0.60	1.00	1.00	<0.5	<0.5	<0.5
Zr	ug/L	ICPMS	0.10	0.08	0.09	0.08	0.10	0.09	0.08	0.07	< 0.2	< 0.2	< 0.2
Hg	ng/L	Hg CVAF	<10	<10	<10	<10	<10	<10	<10	<10	<5	<5	330
$\delta^{18}O$ vs VSMOW	permil	ISO1	-16.5	-16.5	-16.6	-16.1	-16.5	-16.5	-16.5	-16.5	-16.72	-	-16.65
δD vs VSMOW	permil	ISO2	-128	-125	-131	-129	-129	-128	-128	-129	-	-	-
$\delta^{34}S$ vs CDT	permil	ISO3	-	-	-	-	-	-	-	-	-	-	-
$\delta^{34}S$ vs CDT	permil	ISO4	-	-	-	-	-	-	-	-	-	-	-

Appendix 2. Site and analytical data from hydrothermal vents in Yellowstone Lake.

Field No. / Description			96-2-6A West Thumb Trout Jacuzzi	97-10f West Thumb Trout Jacuzzi	97-10r West Thumb Trout Jacuzzi	98-18A West Thumb off Grant	98-19A West Thumb off Grant	98-19B West Thumb off Grant (0.5-1m above 98-19A)	98-22A West Thumb SE central basin vent field	98-23A West Thumb SE central basin vent field	98-23B West Thumb SE central basin vent field (0.5-1m above 98-23A)	98-24A West Thumb SE central basin vent field
Latitude			44°24'59.1"N	44°24'59.1"N	44°24'59.1"N	44°24'3.9"N	44°24'3.9"N	44°24'3.9"N	44°25'0.3"N	44°25'0.3"N	44°25'0.3"N	44°25'0.3"N
Longitude			110°34'10"W	110°34'10"W	110°34'10"W	110°33'14.8"W	110°33'14.8"W	110°33'14.8"W	110°31'28.4"W	110°31'28.4"W	110°31'28.4"W	110°31'28.4"W
Date			-	7/24/97	7/24/97	7/19/98	-	-	-	-	-	-
Temp	˚C		-	31.7	-	30	58-62	-	8.7-10.2	13.6-14.1	-	7.3
pH			-	7.2	-	5.5	8.3	7.6	5.8	6.1	6.6	7.1
Depth	m		5	5	5	37	47	46	52	50	49	63
Treatment			Raw	Filtered	Raw	Filtered	Filtered	Filtered	Filtered	Filtered	Filtered	Filtered
sum CO2	mM		-	1.49	-	5.46	1.71	0.80	2.43	2.20	1.21	0.76
HCO3	mM	measured	-	1.286	-	0.691	1.675	0.752	0.563	0.822	0.756	0.641
HCO3	uM	calc	-	2056	-	679	3036	665	683	966	792	720
Cl	mg/L	IC-Aq	-	4.1	-	5.8	40.7	6.3	5.8	13.1	7.8	5.6
F	mg/L	IC-Aq	-	-	-	-	-	-	-	-	-	-
NO3	mg/L	IC-Aq	-	-	-	-	-	-	-	-	-	-
SO4	mg/L	IC-Aq	-	11.7	-	-	-	-	-	-	-	-
Ag	ug/L	ICPMS	< 0.05	< 0.01	0.03	< 0.01	< 0.01	< 0.01	< 0.01	< 0.01	< 0.01	< 0.01
Al	ug/L	ICPMS	36	59	160	38	160	3.9	4.9	11	4.0	3.9
As	ug/L	ICPMS	210	180	190	22	190	25	24	45	28	24
Au	ug/L	ICPMS	< 0.01	< 0.005	< 0.005	< 0.01	< 0.01	< 0.01	< 0.01	< 0.01	< 0.01	< 0.01
B	ug/L	ICPAES	-	-	-	88	730	100	81	160	100	74
Ba	ug/L	ICPMS	10	8.7	9.2	17	9.2	10	11	11	9.6	10
Be	ug/L	ICPMS	0.2	0.2	0.2	< 0.05	0.2	< 0.05	< 0.05	0.07	< 0.05	< 0.05
Bi	ug/L	ICPMS	< 0.05	< 0.01	< 0.01	< 0.01	< 0.01	< 0.01	< 0.01	< 0.01	< 0.01	< 0.01
Ca	mg/L	ICPAES	-	-	-	4.4	3.6	4.9	4.2	4.2	4.4	4.0
Ca	mg/L	ICPMS	4	3.5	3.6	5.6	4.4	5.2	5.4	5.6	5.2	5.7
Cd	ug/L	ICPMS	< 0.1	< 0.02	0.08	< 0.02	< 0.02	< 0.02	< 0.02	< 0.02	< 0.02	< 0.02
Ce	ug/L	ICPMS	0.05	0.02	0.2	0.2	0.2	0.02	0.03	0.02	0.02	0.02
Co	ug/L	ICPMS	< 0.1	0.02	0.08	0.1	0.08	0.06	0.04	0.05	0.06	0.03
Cr	ug/L	ICPMS	< 5	2	2	< 1	< 1	< 1	< 1	< 1	< 1	< 1
Cs	ug/L	ICPMS	13	37	37	5.4	84	4.6	4.7	15	6.8	4.6
Cu	ug/L	ICPMS	0.8	< 0.5	< 0.5	< 0.5	< 0.5	0.7	< 0.5	< 0.5	< 0.5	< 0.5
Dy	ug/L	ICPMS	< 0.05	0.006	0.01	0.01	0.01	0.005	0.006	0.005	< 0.005	< 0.005
Er	ug/L	ICPMS	< 0.05	< 0.005	0.006	< 0.005	0.006	< 0.005	< 0.005	0.008	< 0.005	< 0.005
Eu	ug/L	ICPMS	< 0.05	< 0.005	< 0.005	< 0.005	< 0.005	< 0.005	< 0.005	< 0.005	< 0.005	< 0.005
Fe	ug/L	ICPMS	< 500	< 10	24	30	19	11	< 10	< 10	< 10	10
Ga	ug/L	ICPMS	1.2	0.81	0.88	0.1	9.8	0.1	0.05	0.94	0.4	0.05
Gd	ug/L	ICPMS	< 0.05	< 0.005	0.01	0.02	0.02	< 0.005	0.006	0.008	< 0.005	< 0.005
Ge	ug/L	ICPMS	5.2	4.6	4.8	0.5	9.8	0.5	0.4	1.6	0.8	0.4
Hf	ug/L	ICPMS	0.2	0.50	0.3	< 0.05	0.2	< 0.05	< 0.05	< 0.05	< 0.05	< 0.05
Ho	ug/L	ICPMS	< 0.05	< 0.005	< 0.005	< 0.005	< 0.005	< 0.005	< 0.005	< 0.005	< 0.005	< 0.005
In	ug/L	ICPMS	< 0.05	< 0.01	< 0.01	< 0.01	< 0.01	< 0.01	< 0.01	< 0.01	< 0.01	< 0.01
K	mg/L	ICPAES	-	-	-	1.5	3.9	1.6	1.5	2.0	1.7	1.4
K	ug/L	ICPMS	2700	2600	2700	1700	7900	1500	1500	3600	1600	1600
La	ug/L	ICPMS	< 0.05	0.02	0.08	0.1	0.1	0.02	0.02	0.02	0.02	0.02
Li	ug/L	ICPMS	240	310	310	63	610	61	61	110	72	61
Lu	ug/L	ICPMS	< 0.05	-	-	-	-	-	-	-	-	-
Mg	mg/L	ICPAES	-	-	-	2.1	1.6	2.3	1.8	1.8	1.9	1.8
Mg	mg/L	ICPMS	1.6	1.6	1.7	2.7	1.9	2.7	2.7	2.7	2.6	2.8
Mn	ug/L	ICPMS	7.8	0.75	1.4	6.7	4.0	0.48	2.4	4.4	2.9	1.1
Mo	ug/L	ICPMS	12	13	13	2.1	36	2.8	2.1	6.6	2.7	1.7
Na	mg/L	ICPAES	-	-	-	8.9	64	9.6	9.3	17	12	8.6
Na	mg/L	ICPMS	39	47	48	11	89	11	11	21	13	11
Nb	ug/L	ICPMS	< 0.1	< 0.02	< 0.02	< 0.02	< 0.02	< 0.02	< 0.02	< 0.02	< 0.02	< 0.02
Nd	ug/L	ICPMS	< 0.05	< 0.01	0.04	0.08	0.06	0.03	0.04	0.01	0.01	0.02
Ni	ug/L	ICPMS	0.4	0.4	3.2	0.4	0.3	0.3	0.3	0.3	0.4	0.3
P	ug/L	ICPMS	-	62	76	150	110	140	150	140	140	150
Pb	ug/L	ICPMS	0.1	< 0.05	0.5	< 0.05	0.05	< 0.05	< 0.05	< 0.05	< 0.05	< 0.05
Pr	ug/L	ICPMS	< 0.05	< 0.01	0.01	0.03	0.03	< 0.01	< 0.01	< 0.01	< 0.01	< 0.01
Rb	ug/L	ICPMS	21	28	28	7.2	47	6.5	6.6	13	7.6	6.3
Re	ug/L	ICPMS	< 0.05	< 0.02	< 0.02	< 0.02	< 0.02	< 0.02	< 0.02	< 0.02	< 0.02	< 0.02
Sb	ug/L	ICPMS	10	11	11	1.1	17	1.8	1.2	2.5	1.4	0.94
Sc	ug/L	ICPMS	0.8	1	1	< 0.1	< 0.1	< 0.1	< 0.1	< 0.1	< 0.1	< 0.1
Se	ug/L	ICPMS	< 5	0.5	0.5	< 0.2	< 0.2	< 0.2	< 0.2	< 0.2	< 0.2	< 0.2
SiO2	mg/L	ICPMS	34	35	37	18	77	13	13	27	16	13
Sm	ug/L	ICPMS	< 0.05	< 0.01	0.01	0.01	0.02	0.01	< 0.01	< 0.01	< 0.01	< 0.01
Sn	ug/L	ICPMS	< 1	< 0.05	< 0.05	< 0.05	0.2	0.09	< 0.05	< 0.05	< 0.05	< 0.05
Sr	ug/L	ICPMS	33	33	33	48	35	46	46	47	44	46
Ta	ug/L	ICPMS	< 0.05	< 0.02	< 0.02	< 0.02	0.02	< 0.02	< 0.02	< 0.02	< 0.02	< 0.02
Tb	ug/L	ICPMS	< 0.05	< 0.005	< 0.005	< 0.005	< 0.005	< 0.005	< 0.005	< 0.005	< 0.005	< 0.005
Te	ug/L	ICPMS	< 0.5	0.3	< 0.1	< 0.1	< 0.1	< 0.1	< 0.1	< 0.1	< 0.1	< 0.1
Th	ug/L	ICPMS	< 0.05	< 0.005	< 0.005	< 0.005	0.02	< 0.005	< 0.005	< 0.005	0.005	< 0.005
Ti	ug/L	ICPMS	< 0.5	0.8	1.4	< 0.1	0.2	< 0.1	< 0.1	< 0.1	< 0.1	< 0.1
Tl	ug/L	ICPMS	0.1	< 0.05	< 0.05	< 0.05	< 0.05	< 0.05	< 0.05	< 0.05	< 0.05	< 0.05
Tm	ug/L	ICPMS	< 0.05	< 0.005	< 0.005	< 0.005	< 0.005	< 0.005	< 0.005	< 0.005	< 0.005	< 0.005
U	ug/L	ICPMS	< 0.02	0.02	0.02	0.02	0.03	0.01	0.009	0.008	0.01	0.01
V	ug/L	ICPMS	0.9	0.7	0.8	1	1	1	1	1	1	1
W	ug/L	ICPMS	48	48	48	2.5	81	5.7	3.2	10	4.3	2.6
Y	ug/L	ICPMS	< 0.1	0.03	0.06	0.06	0.05	0.02	0.02	0.02	0.02	0.03
Yb	ug/L	ICPMS	< 0.05	< 0.01	< 0.01	< 0.01	< 0.01	< 0.01	< 0.01	< 0.01	< 0.01	< 0.01
Zn	ug/L	ICPMS	70	10	10	32	76	10	20	52	20	7
Zr	ug/L	ICPMS	< 0.1	0.1	0.1	0.05	0.4	< 0.05	< 0.05	0.05	< 0.05	< 0.05
Hg	ng/L	Hg CVAF	-	-	-	19	28	15	35	160	50	<10
$\delta^{18}O$ vs VSMOW	per mil	ISO1	-	-15.9	-15.9	-16.21	-16.13	-16.15	-15.97	-16.09	-16.08	-15.83
δD vs VSMOW	per mil	ISO2	-	-126.3	-	-129.9	-132.5	-132	-132.3	-131.7	-131.2	-129.4
$\delta^{34}S_{H2S}$ vs CDT	per mil	ISO3	-	-	-	-	-	-	-	-	-	-
$\delta^{34}S_{SO4}$ vs CDT	per mil	ISO4	-	8.0	-	-	-	-	-	-	-	-
$\delta^{13}C_{CO3}$ vs VPDB	per mil	ISO5	-	-	-	-	-	-	-	-	-	-

Appendix 2. Site and analytical data from hydrothermal vents in Yellowstone Lake—*Continued*.

Field No.			YNP-99-17-1	YNP-99-18-1	YNP-99-18-2	Y00-D03.3	Y00-D03.4	Y00-D06.1	Y00-D06.2	Y00-D09.4	Y00-D11.1A	Y00-D11.1B
Description			West Thumb, SE of Geyser Basin	West Thumb, SE of Geyser Basin	West Thumb, SE of Geyser Basin	West Thumb, E basin bottom water	West Thumb, E basin bottom water	West Thumb, Evil Twin crater	West Thumb, Evil Twin crater	West Thumb, off Geyser Basin	West Thumb, NE of Grant	West Thumb, NE of Grant
Latitude			44°24'43.4"N	44°24'43.4"N	44°24'43.4"N	44°25'37"N	44°25'37"N	44°25'29.1"N	44°25'29.1"N	44°24'59.1"N	44°24'26.9"N	44°24'26.7"N
Longitude			110°33'34.2"W	110°33'34.2"W	110°33'34.2"W	110°30'28"W	110°30'28"W	110°34'12"W	110°34'12"W	110°33'46.7"W	110°33'30.8"W	110°33'33.5"W
Date			7/24/99	7/24/99	7/24/99	7/27/00	7/27/00	7/28/00	7/28/00	7/29/00	7/30/00	7/30/00
Temp	°C		-	-	-	15.6	15.6	17.1	35.2	66.1	27.8	27.8
pH			5.4	6.0	6.2	7.6	7.5	7.0	6.6	6.4	5.9	5.9
Depth	m		21	21	21	10	10	42	31	30	23	23
Treatment			Filtered	Filtered	Filtered	Filtered	Filtered	Filtered	Filtered	Filtered	Filtered	Filtered
sum CO2	mM		-	-	-	-	-	-	-	-	-	-
HCO3	mM	measured	-	-	-	-	-	-	-	-	-	-
HCO3	uM	calc	632	530	514	-	-	-	-	-	-	-
Cl	mg/L	IC-Aq	11	7.3	6.8	4.9	1.2	7.1	24	72	5.1	5.2
F	mg/L	IC-Aq	1.4	0.8	0.7	0.7	0.3	0.8	1.7	2.6	0.7	0.7
NO3	mg/L	IC-Aq	<.35	<.35	<.35	<.08	<.08	0.3	<.08	0.2	0.2	<.08
SO4	mg/L	IC-Aq	9.3	8.4	8.0	6.9	1.8	7.5	8.9	10.0	8.0	8.0
Ag	ug/L	ICPMS	<0.01	<0.01	<0.01	0.03	0.02	0.01	0.01	0.01	<0.01	<0.01
Al	ug/L	ICPMS	22	6.2	2.3	3.4	9.5	4.4	4.9	15	10	8.2
As	ug/L	ICPMS	72	36	32	14	15	81	170	180	20	20
Au	ug/L	ICPMS	< 0.01	< 0.01	< 0.01	< 0.01	< 0.01	< 0.01	< 0.01	< 0.01	< 0.01	< 0.01
B	ug/L	ICPAES	191	130	121	-	-	-	-	-	-	-
Ba	ug/L	ICPMS	11	9.9	9.4	9.5	11	14	22	250	10	9.9
Be	ug/L	ICPMS	<0.05	<0.05	<0.05	<0.05	<0.05	0.06	0.5	0.64	<0.05	<0.05
Bi	ug/L	ICPMS	< 0.01	< 0.01	< 0.01	< 0.01	< 0.01	< 0.01	< 0.01	< 0.01	< 0.01	< 0.01
Ca	mg/L	ICPAES	5.27	5.28	5.55	-	-	-	-	-	-	-
Ca	mg/L	ICPMS	4.5	4.5	4.6	5.2	4.7	4	3.6	23	4.5	4.4
Cd	ug/L	ICPMS	0.02	0.03	0.05	0.04	0.07	<0.02	<0.02	<0.02	0.04	0.02
Ce	ug/L	ICPMS	0.06	0.04	0.01	< 0.01	< 0.01	0.2	0.4	0.1	0.04	0.04
Co	ug/L	ICPMS	0.3	0.04	<0.02	<0.02	0.05	0.04	0.05	0.07	<0.02	0.02
Cr	ug/L	ICPMS	<1	<1	<1	<1	<1	<1	<1	<1	<1	<1
Cs	ug/L	ICPMS	15	6.8	6	2.9	2.8	23	40	110	3.6	3.6
Cu	ug/L	ICPMS	<0.5	<0.5	<0.5	<0.5	<0.5	<0.5	<0.5	0.6	<0.5	<0.5
Dy	ug/L	ICPMS	< 0.005	0.005	< 0.005	< 0.005	< 0.005	0.01	0.04	0.01	< 0.005	< 0.005
Er	ug/L	ICPMS	0.006	0.008	< 0.005	< 0.005	< 0.005	0.01	0.02	0.02	< 0.005	< 0.005
Eu	ug/L	ICPMS	< 0.005	< 0.005	< 0.005	< 0.005	< 0.005	< 0.005	< 0.005	< 0.005	< 0.005	< 0.005
Fe	ug/L	ICPMS	<30	<30	<30	<1	2	19	5	500	9.6	9.2
Ga	ug/L	ICPMS	0.1	0.09	0.07	0.02	0.03	< 0.02	< 0.02	< 0.02	0.02	0.02
Gd	ug/L	ICPMS	0.01	0.005	0.007	< 0.005	< 0.005	0.01	0.02	0.01	< 0.005	0.008
Ge	ug/L	ICPMS	1.5	0.8	0.6	0.4	0.4	1	5.1	15	0.6	0.6
Hf	ug/L	ICPMS	-	-	-	-	-	-	-	-	-	-
Ho	ug/L	ICPMS	< 0.005	< 0.005	< 0.005	< 0.005	< 0.005	< 0.005	0.005	< 0.005	< 0.005	< 0.005
In	ug/L	ICPMS	-	-	-	< 0.01	< 0.01	< 0.01	< 0.01	< 0.01	< 0.01	< 0.01
K	mg/L	ICPAES	2.2	1.86	1.87	-	-	-	-	-	-	-
K	ug/L	ICPMS	2000	1700	1700	1600	1500	2100	3700	14000	1600	1600
La	ug/L	ICPMS	0.03	0.03	0.02	0.03	0.02	0.09	0.2	0.08	0.04	0.04
Li	ug/L	ICPMS	120	71	66	46	45	69	210	1200	50	49
Lu	ug/L	ICPMS	-	-	-	-	-	-	-	-	-	-
Mg	mg/L	ICPAES	2.23	2.29	2.3	-	-	-	-	-	-	-
Mg	mg/L	ICPMS	2	2	2	2.3	2.2	1.7	1.2	12	2.1	2.1
Mn	ug/L	ICPMS	2.3	1.2	0.76	0.31	0.57	14	24	140	2.3	2
Mo	ug/L	ICPMS	4.2	2.3	2.2	1.4	1.4	2	4.5	1	1.6	1.6
Na	mg/L	ICPAES	19	12.6	12.2	-	-	-	-	-	-	-
Na	mg/L	ICPMS	16	11	10	9	9	14	43	160	9.6	9.5
Nb	ug/L	ICPMS	< 0.02	< 0.02	< 0.02	-	-	-	-	-	-	-
Nd	ug/L	ICPMS	0.05	0.04	0.03	0.01	< 0.01	0.09	0.21	0.07	0.02	0.03
Ni	ug/L	ICPMS	0.4	0.3	0.2	0.3	0.5	0.4	0.2	0.2	0.4	0.4
P	ug/L	ICPMS	< 2	< 2	< 2	5	6	7	7	50	6	8
Pb	ug/L	ICPMS	<0.05	0.09	0.07	<0.05	<0.05	0.08	0.2	0.1	0.1	0.2
Pr	ug/L	ICPMS	0.01	0.01	< 0.01	< 0.01	< 0.01	0.02	0.04	0.02	< 0.01	< 0.01
Rb	ug/L	ICPMS	10	7.2	6.8	5.8	6.1	13	24	83	6.2	6.1
Re	ug/L	ICPMS	-	-	-	< 0.02	< 0.02	< 0.02	< 0.02	< 0.02	< 0.02	< 0.02
Sb	ug/L	ICPMS	4.2	1.6	1.3	0.78	0.82	5.5	400	4.9	1.3	2.4
Sc	ug/L	ICPMS	0.4	0.3	0.3	-	-	-	-	-	-	-
Se	ug/L	ICPMS	< 0.3	< 0.3	< 0.3	< 0.2	< 0.2	< 0.2	< 0.2	< 0.2	< 0.2	< 0.2
SiO2	mg/L	ICPMS	16	12	11	9.7	9.8	13	30	95	10	10
Sm	ug/L	ICPMS	0.01	< 0.01	0.01	< 0.01	< 0.01	0.01	0.04	0.01	< 0.01	< 0.01
Sn	ug/L	ICPMS	-	-	-	-	-	-	-	-	-	-
Sr	ug/L	ICPMS	41	42	42	45	44	40	40	510	43	43
Ta	ug/L	ICPMS	0.04	< 0.03	< 0.03	-	-	-	-	-	-	-
Tb	ug/L	ICPMS	< 0.005	< 0.005	< 0.005	< 0.005	< 0.005	< 0.005	< 0.005	< 0.005	< 0.005	< 0.005
Te	ug/L	ICPMS	-	-	-	-	-	-	-	-	-	-
Th	ug/L	ICPMS	< 0.02	< 0.02	< 0.02	< 0.005	< 0.005	< 0.005	< 0.005	< 0.005	< 0.005	< 0.005
Ti	ug/L	ICPMS	< 0.8	< 0.8	< 0.8	-	-	-	-	-	-	-
Tl	ug/L	ICPMS	<0.05	<0.05	<0.05	<0.05	<0.05	<0.05	<0.05	<0.05	<0.05	<0.05
Tm	ug/L	ICPMS	< 0.005	< 0.005	< 0.005	< 0.005	< 0.005	< 0.005	< 0.005	< 0.005	< 0.005	< 0.005
U	ug/L	ICPMS	< 0.005	0.007	0.007	0.02	0.03	0.008	0.02	0.04	0.009	0.01
V	ug/L	ICPMS	0.9	0.8	0.9	0.83	0.98	1.2	1.5	1.6	0.83	0.82
W	ug/L	ICPMS	10	6.4	5.8	2	2.2	9.6	29	40	3.4	3.1
Y	ug/L	ICPMS	0.05	0.03	0.03	0.02	0.01	0.09	0.3	0.2	0.05	0.05
Yb	ug/L	ICPMS	< 0.01	< 0.01	< 0.01	< 0.01	< 0.01	< 0.01	0.02	0.01	< 0.01	< 0.01
Zn	ug/L	ICPMS	22	3	8	6	280	1	3	10	3	6
Zr	ug/L	ICPMS	< 0.2	< 0.2	< 0.2	-	-	-	-	-	-	-
Hg	ng/L	Hg CVAF	6.0	5.0	6.0	0.008	<0.005	0.01	0.07	0.006	0.041	0.048
$\delta^{18}O$ vs VSMOW	per mil	ISO1	-16.0	-16.1	-16.1	-16.1	-16.1	-16.3	-16.2	-16.5	-16.3	-16.3
δD vs VSMOW	per mil	ISO2	-127.8	-127.9	-126.6	-126.8	-126.4	-126.3	-129.8	-134.8	-128.0	-126.8
$\delta^{34}S_{H2S}$ vs CDT	per mil	ISO3	-	-	-	-	-	-	-	-	-	-
$\delta^{34}S_{SO4}$ vs CDT	per mil	ISO4	-	-	-	-	-	-	-	-	-	-
$\delta^{13}C_{CO3}$ vs VPDB	per mil	ISO5	-	-	-	-	-	-	-	-	-	-

Appendix 2. Site and analytical data from hydrothermal vents in Yellowstone Lake—*Continued*.

Field No. Description			Y00-D12.1 West Thumb, NE of Grant	98-13A West Thumb off Bluff Point (Otter Vent)	98-13B West Thumb off Bluff Point (Otter Vent) (0.5m above 98-13A)	D03-8.1 WT, Otter vent	D03-8.2 WT, Otter vent	Y00-D18.1 West Thumb, N of Bluff Point	Y00-D18.2 West Thumb, N of Bluff Point (same vent as Y00-D18.1)	96-5 Steamboat Point vent	96-6-1 Steamboat Point vent
Latitude			44°24'26.7"N	44°26'36.0"N	44°26'36.0"N	44°26'35.998"N	44°26'35.998"N	44°26'56.8"N	44°26'56.8"N	44°31'35.7"N	44°31'35.7"N
Longitude			110°33'33.0"W	110°33'56.1"W	110°33'56.1"W	110°33'56.1"W	110°33'56.1"W	110°33'30.5"W	110°33'30.5"W	110°17'39.5"W	110°17'39.5"W
Date			7/30/00	7/18/98	7/18/98	8/16/03	8/16/03	8/2/00	8/2/00	-	-
Temp	˚C		31.7	68	-	66.9	66.9	42.0	49.3	89	93
pH			-	8.6	8.3	8.1	8	7.1	7.3	-	-
Depth	m		23	5	5	1.7	1.7	59	59	-	-
Treatment			Filtered	Filtered	Filtered	Filtered	Filtered	Filtered	Filtered	Raw	Raw
sum CO2	mM		-	0.91	0.79	-	-	-	-	0.98	1.17
HCO3	mM	measured	-	0.884	0.774	-	-	-	-	-	-
HCO3	uM	calc	-	1384	948	-	-	-	-	-	-
Cl	mg/L	IC-Aq	5.3	1.8	3.3	5	4.7	4.6	4.6	-	-
F	mg/L	IC-Aq	0.7	-	-	0.5	1.6	2.7	3.1	-	-
NO3	mg/L	IC-Aq	<.08	-	-	<.08	<.08	<.08	0.2	-	-
SO4	mg/L	IC-Aq	8.4	-	-	6.9	6.6	6.3	6.1	-	-
Ag	ug/L	ICPMS	<0.01	< 0.01	< 0.01	<0.01	<0.01	<0.01	<0.01	< 0.05	< 0.05
Al	ug/L	ICPMS	30	21	11	4.4	3.3	3.7	4.5	58	40
As	ug/L	ICPMS	18	9.2	14	14	13	15	16	11	15
Au	ug/L	ICPMS	< 0.01	< 0.01	< 0.01	< 0.01	< 0.01	< 0.01	< 0.01	< 0.01	< 0.01
B	ug/L	ICPAES	-	35	62	-	-	-	-	-	-
Ba	ug/L	ICPMS	9.5	5	7.7	7.8	7.9	9.7	9.9	25	11
Be	ug/L	ICPMS	<0.05	< 0.05	0.07	<0.05	<0.05	<0.05	<0.05	< 0.2	< 0.2
Bi	ug/L	ICPMS	< 0.01	< 0.01	< 0.01	< 0.03	< 0.03	< 0.01	< 0.01	< 0.05	< 0.05
Ca	mg/L	ICPAES	-	3.2	3.8	-	-	-	-	-	-
Ca	mg/L	ICPMS	4.3	3.6	4.5	4.2	4.2	3.8	3.7	5.5	4.9
Cd	ug/L	ICPMS	0.04	< 0.02	< 0.02	<0.02	<0.02	<0.02	<0.02	< 0.1	< 0.1
Ce	ug/L	ICPMS	0.04	0.5	0.04	< 0.01	< 0.01	0.04	0.07	0.2	0.1
Co	ug/L	ICPMS	0.02	0.2	0.1	<0.02	<0.02	<0.02	0.03	< 0.1	< 0.1
Cr	ug/L	ICPMS	<1	< 1	< 1	<1	<1	<1	<1	< 5	< 5
Cs	ug/L	ICPMS	3.5	9.3	5.2	3	2.8	3.6	4	1.3	1.2
Cu	ug/L	ICPMS	<0.5	< 0.5	< 0.5	<0.5	<0.5	<0.5	<0.5	0.9	0.6
Dy	ug/L	ICPMS	0.005	0.01	< 0.005	< 0.005	< 0.005	0.005	< 0.005	< 0.05	< 0.05
Er	ug/L	ICPMS	< 0.005	0.006	< 0.005	< 0.005	< 0.005	0.007	0.005	< 0.05	< 0.05
Eu	ug/L	ICPMS	< 0.005	< 0.005	< 0.005	< 0.005	< 0.005	< 0.005	< 0.005	< 0.05	< 0.05
Fe	ug/L	ICPMS	13	< 10	< 10	<2	<2	8.2	10	< 500	< 500
Ga	ug/L	ICPMS	< 0.02	2.4	0.83	0.087	0.054	0.02	0.02	0.2	< 0.1
Gd	ug/L	ICPMS	0.008	< 0.005	0.006	< 0.005	< 0.005	0.006	0.008	< 0.05	< 0.05
Ge	ug/L	ICPMS	0.5	1.4	0.7	0.47	0.38	0.7	0.9	0.2	0.3
Hf	ug/L	ICPMS	-	0.3	< 0.05	<5	<5	-	-	< 0.05	< 0.05
Ho	ug/L	ICPMS	< 0.005	< 0.005	< 0.005	< 0.005	< 0.005	< 0.005	< 0.005	< 0.05	< 0.05
In	ug/L	ICPMS	< 0.01	< 0.01	< 0.01	< 0.01	< 0.01	< 0.01	< 0.01	< 0.05	< 0.05
K	mg/L	ICPAES	-	< 1	1.0	-	-	-	-	-	-
K	ug/L	ICPMS	1700	680	1400	1400	1400	2200	2400	2200	1600
La	ug/L	ICPMS	0.04	0.03	0.02	< 0.01	< 0.01	0.05	0.05	0.1	0.07
Li	ug/L	ICPMS	50	120	77	50	47	64	69	34	40
Lu	ug/L	ICPMS	-	-	-	-	-	-	-	< 0.05	< 0.05
Mg	mg/L	ICPAES	-	< 1	1.3	-	-	-	-	-	-
Mg	mg/L	ICPMS	2	0.20	1.7	1.9	1.9	1.7	1.6	1.8	1.9
Mn	ug/L	ICPMS	4	6.9	2.8	1.2	0.9	13	17	6.4	9.5
Mo	ug/L	ICPMS	1.6	16	7.5	2.4	1.9	4.2	5.1	1.4	1.2
Na	mg/L	ICPAES	-	25	14	-	-	-	-	-	-
Na	mg/L	ICPMS	10	29	17	9.4	8.5	13	14	7.2	7.2
Nb	ug/L	ICPMS	-	< 0.02	< 0.02	-	-	-	-	< 0.1	< 0.1
Nd	ug/L	ICPMS	0.03	0.05	0.03	< 0.01	< 0.01	0.03	0.06	0.1	0.07
Ni	ug/L	ICPMS	0.4	< 0.1	0.2	0.6	0.42	0.4	0.3	0.3	0.5
P	ug/L	ICPMS	8	43	110	< 1	< 1	9	9	-	-
Pb	ug/L	ICPMS	0.08	0.2	< 0.05	<0.05	<0.05	0.06	0.06	0.2	0.09
Pr	ug/L	ICPMS	< 0.01	0.03	< 0.01	< 0.01	< 0.01	< 0.01	0.01	< 0.05	< 0.05
Rb	ug/L	ICPMS	6.8	5.2	5.5	4.7	4.6	11	12	8.2	4.6
Re	ug/L	ICPMS	< 0.02	< 0.02	< 0.02	< 0.02	< 0.02	< 0.02	< 0.02	< 0.05	< 0.05
Sb	ug/L	ICPMS	1.1	0.54	0.82	0.81	0.8	0.89	1.6	0.4	0.6
Sc	ug/L	ICPMS	-	< 0.1	< 0.1	-	-	-	-	< 0.5	< 0.5
Se	ug/L	ICPMS	< 0.2	< 0.2	< 0.2	< 0.2	< 0.2	< 0.2	< 0.2	< 5	< 5
SiO2	mg/L	ICPMS	12	97	45	14	11	41	47	17	12
Sm	ug/L	ICPMS	< 0.01	< 0.01	0.01	< 0.01	< 0.01	0.01	< 0.01	< 0.05	< 0.05
Sn	ug/L	ICPMS	-	< 0.05	< 0.05	-	-	-	-	< 1	< 1
Sr	ug/L	ICPMS	40	6.6	30	36	37	35	35	50	38
Ta	ug/L	ICPMS	-	0.04	< 0.02	-	-	-	-	< 0.05	< 0.05
Tb	ug/L	ICPMS	< 0.005	0.005	< 0.005	< 0.005	< 0.005	< 0.005	< 0.005	< 0.05	< 0.05
Te	ug/L	ICPMS	-	< 0.1	< 0.1	-	-	-	-	< 0.5	< 0.5
Th	ug/L	ICPMS	< 0.005	0.04	0.01	< 0.08	< 0.08	< 0.005	< 0.005	< 0.05	< 0.05
Ti	ug/L	ICPMS	-	0.1	< 0.1	-	-	-	-	1	0.8
Tl	ug/L	ICPMS	<0.05	< 0.05	< 0.05	<0.05	<0.05	<0.05	<0.05	< 0.1	0.1
Tm	ug/L	ICPMS	< 0.005	< 0.005	< 0.005	< 0.005	< 0.005	< 0.005	< 0.005	< 0.05	< 0.05
U	ug/L	ICPMS	0.009	0.03	0.008	0.012	0.013	0.02	0.02	< 0.02	< 0.02
V	ug/L	ICPMS	0.75	0.2	0.7	0.82	0.86	0.63	0.69	0.9	1.3
W	ug/L	ICPMS	2.8	9.1	4.7	3.1	2.7	3.9	4.2	2.2	2.5
Y	ug/L	ICPMS	0.05	0.03	0.01	< 0.01	0.01	0.04	0.06	< 0.1	< 0.1
Yb	ug/L	ICPMS	< 0.01	< 0.01	< 0.01	< 0.01	< 0.01	< 0.01	< 0.01	< 0.05	< 0.05
Zn	ug/L	ICPMS	2	41	10	0.59	<0.5	4	6	12	21
Zr	ug/L	ICPMS	-	6.9	0.4	-	-	-	-	< 0.1	< 0.1
Hg	ng/L	Hg CVAF	0.019	36	12	-	-	<0.005	0.007	-	-
$\delta^{18}O$ vs VSMOW	per mil	ISO1	-16.3	-19.12	-17.39	-16.3	-16.0	-16.8	-17.0	-	-
δD vs VSMOW	per mil	ISO2	-129.1	-145.4	-137.8	-134.8	-131.9	-131.5	-132.2	-	-
$\delta^{34}S_{H2S}$ vs CDT	per mil	ISO3	-	-	-	-	-	-	-	-	-
$\delta^{34}S_{SO4}$ vs CDT	per mil	ISO4	-	-	-	-	2.4	-	-	-	-
$\delta^{13}C_{CO3}$ vs VPDB	per mil	ISO5	-	-	-	-5.8	-5.5	-	-	-	-

Appendix 2. Site and analytical data from hydrothermal vents in Yellowstone Lake—*Continued*.

Field No. Description			96-6-2 Steamboat Point vent	97-3 Steamboat Point vent	98-01A Steamboat Point vent	98-01B Steamboat Pt (1m above 98-01A)	98-02A Steamboat Point vent	98-02B Steamboat Pt (1m above 98-02A)	YNP-99-11-1 Steamboat Point vent	YNP-99-11-2 Steamboat Point vent	96-8(5) Mary Bay deep hole	96-8(6) Mary Bay deep hole	96-8(6) Mary Bay deep hole
Latitude			44°31'35.7"N	44°31'35.7"N	44°31'35.7"N	44°31'35.7"N	44°31'35.7"N	44°31'35.7"N	44°31'35.7"N	44°31'35.7"N	44°32'42.8"N	44°32'42.8"N	44°32'42.8"N
Longitude			110°17'39.5"W	110°17'39.5"W	110°17'39.5"W	110°17'39.5"W	110°17'39.5"W	110°17'39.5"W	110°17'39.5"W	110°17'39.5"W	110°18'39.1"W	110°18'39.1"W	110°18'39.1"W
Date			-	7/19/97	7/15/98	7/15/98	7/15/98	7/15/98	7/21/99	7/21/99	-	-	-
Temp	°C		-	28.3	33	20	55	25	32.0	32.0	-	-	-
pH			-	5.4	5.9	6.6	6.1	6.5	6.3	6.7	-	-	-
Depth	m		-	4	5	4	5	4	5	5	-	-	-
Treatment			Raw	Raw	Filtered	Filtered	Filtered	Filtered	Filtered	Filtered	Raw	Raw	Raw
sum CO2	mM		-	2.08	2.37	0.92	1.74	1.07	-	-	-	-	-
HCO3	mM	measured	-	0.227	0.632	0.610	0.641	0.638	-	-	-	-	-
HCO3	uM	calc	-	397	551	625	545	607	434	476	-	-	-
Cl	mg/L	IC-Aq	-	4.4	4.5	4.5	4.4	4.5	4.1	4.1	-	-	-
F	mg/L	IC-Aq	-	-	-	-	-	-	0.5	0.5	-	-	-
NO3	mg/L	IC-Aq	-	-	-	-	-	-	<.1	<.1	-	-	-
SO4	mg/L	IC-Aq	-	8.2	9.9	7.6	10.9	7.6	8.8	7.6	-	-	-
Ag	ug/L	ICPMS	< 0.05	< 0.01	< 0.01	< 0.01	< 0.01	< 0.01	0.4	0.2	< 0.05	< 0.05	< 0.05
Al	ug/L	ICPMS	100	67	15	9.8	16	10	0.7	2.9	230	780	760
As	ug/L	ICPMS	14	10	6.6	14	7.1	13	13	13	21	54	54
Au	ug/L	ICPMS	< 0.01	< 0.005	< 0.01	< 0.01	< 0.01	< 0.01	< 0.01	< 0.01	< 0.01	< 0.01	< 0.01
B	ug/L	ICPAES	-	-	86	70	83	77	79.8	84.5	-	-	-
Ba	ug/L	ICPMS	14	13	10	9.6	16	9.6	11	15	14	25	26
Be	ug/L	ICPMS	< 0.2	< 0.05	< 0.05	< 0.05	0.07	< 0.05	<0.05	<0.05	< 0.2	< 0.2	< 0.2
Bi	ug/L	ICPMS	< 0.05	< 0.01	< 0.01	< 0.01	< 0.01	< 0.01	0.052	< 0.01	< 0.05	< 0.05	< 0.05
Ca	mg/L	ICPAES	-	-	4.8	4.2	4.8	4.5	5.15	5.06	-	-	-
Ca	mg/L	ICPMS	4.7	4.0	5.3	5.3	5.6	5.3	4.4	4.4	4.9	4.7	4.9
Cd	ug/L	ICPMS	< 0.1	0.04	< 0.02	< 0.02	< 0.02	< 0.02	<0.02	<0.02	< 0.1	< 0.1	< 0.1
Ce	ug/L	ICPMS	0.2	0.1	0.06	0.04	0.06	0.04	0.2	0.04	0.7	2.1	2.1
Co	ug/L	ICPMS	< 0.1	0.04	0.1	0.08	0.03	0.04	0.2	0.07	0.2	0.5	0.5
Cr	ug/L	ICPMS	< 5	3	< 1	< 1	< 1	< 1	<1	<1	< 5	< 5	< 5
Cs	ug/L	ICPMS	1.1	2.5	2.8	2.9	3.0	2.7	2.2	2.3	1.6	1.9	2
Cu	ug/L	ICPMS	0.5	< 0.5	< 0.5	1	< 0.5	< 0.5	<0.5	<0.5	1.2	2.1	2.1
Dy	ug/L	ICPMS	< 0.05	0.009	< 0.005	< 0.005	0.01	< 0.005	0.01	< 0.005	< 0.05	0.1	0.1
Er	ug/L	ICPMS	< 0.05	0.008	< 0.005	0.005	< 0.005	< 0.005	< 0.005	0.007	< 0.05	0.06	0.06
Eu	ug/L	ICPMS	< 0.05	< 0.005	< 0.005	< 0.005	< 0.005	< 0.005	< 0.005	< 0.005	< 0.05	< 0.05	< 0.05
Fe	ug/L	ICPMS	< 500	26	14	13	11	12	<30	<30	< 500	2100	2100
Ga	ug/L	ICPMS	< 0.1	0.02	0.04	< 0.02	0.2	< 0.02	< 0.02	< 0.02	< 0.1	0.2	0.2
Gd	ug/L	ICPMS	< 0.05	0.008	0.01	< 0.005	< 0.005	0.006	0.02	0.01	0.05	0.1	0.1
Ge	ug/L	ICPMS	0.2	0.2	0.2	0.2	0.2	0.2	0.2	0.2	0.3	0.4	0.4
Hf	ug/L	ICPMS	< 0.05	< 0.05	< 0.05	< 0.05	< 0.05	< 0.05	-	-	< 0.05	< 0.05	< 0.05
Ho	ug/L	ICPMS	< 0.05	< 0.005	< 0.005	< 0.005	< 0.005	< 0.005	< 0.005	< 0.005	< 0.05	< 0.05	< 0.05
In	ug/L	ICPMS	< 0.05	< 0.01	< 0.01	< 0.01	< 0.01	< 0.01	-	-	< 0.05	< 0.05	< 0.05
K	mg/L	ICPAES	-	-	1.4	1.2	1.7	1.4	1.52	1.56	-	-	-
K	ug/L	ICPMS	1500	1300	1400	1400	1600	1400	1400	1400	1600	1600	1600
La	ug/L	ICPMS	0.1	0.08	0.04	0.04	0.04	0.03	0.1	0.04	0.4	1	1
Li	ug/L	ICPMS	43	34	42	42	41	43	41	43	51	52	53
Lu	ug/L	ICPMS	< 0.05	-	-	-	-	-	-	-	< 0.05	< 0.05	< 0.05
Mg	mg/L	ICPAES	-	-	2.2	2.0	2.0	2.2	2.2	2.18	-	-	-
Mg	mg/L	ICPMS	2.2	1.9	2.6	2.7	2.5	2.6	2	2.1	2.1	2.6	2.6
Mn	ug/L	ICPMS	4.4	2.3	2.3	1.4	3.8	1.3	1.8	1.2	14	35	34
Mo	ug/L	ICPMS	1.2	1.0	0.93	0.98	0.91	1.0	3.1	1.5	1.1	1.6	1.6
Na	mg/L	ICPAES	-	-	7.4	6.5	7.1	7.2	8.63	8.54	-	-	-
Na	mg/L	ICPMS	8.2	7.0	8.5	8.9	8.5	8.7	7.2	7.4	8.1	9.5	9.7
Nb	ug/L	ICPMS	< 0.1	< 0.02	< 0.02	< 0.02	< 0.02	< 0.02	0.3	0.2	< 0.1	< 0.1	< 0.1
Nd	ug/L	ICPMS	0.1	0.05	0.04	0.04	0.05	0.04	0.09	0.04	0.4	0.9	0.9
Ni	ug/L	ICPMS	0.7	0.5	0.4	0.4	0.2	0.4	0.4	0.4	1.1	2.6	2.6
P	ug/L	ICPMS	-	76	150	150	110	110	2	2	-	-	-
Pb	ug/L	ICPMS	0.2	< 0.05	0.3	< 0.05	< 0.05	< 0.05	<0.05	<0.05	0.3	0.7	0.7
Pr	ug/L	ICPMS	< 0.05	0.01	0.01	0.01	0.01	< 0.01	0.02	< 0.01	0.09	0.2	0.2
Rb	ug/L	ICPMS	4.6	5.7	5.2	5.4	6.9	5.0	4	4.1	5.1	5.6	5.6
Re	ug/L	ICPMS	< 0.05	< 0.02	< 0.02	< 0.02	< 0.02	< 0.02	-	-	< 0.05	< 0.05	< 0.05
Sb	ug/L	ICPMS	0.6	0.1	< 0.02	0.54	< 0.02	0.4	1	0.63	0.7	1.3	1.4
Sc	ug/L	ICPMS	< 0.5	0.4	< 0.1	< 0.1	< 0.1	< 0.1	< 0.1	< 0.1	< 0.5	< 0.5	< 0.5
Se	ug/L	ICPMS	< 5	0.5	< 0.2	< 0.2	< 0.2	< 0.2	0.6	< 0.3	< 5	< 5	< 5
SiO2	mg/L	ICPMS	12	11	12	12	15	12	9.2	9.4	13	18	18
Sm	ug/L	ICPMS	< 0.05	0.02	0.01	< 0.01	< 0.01	< 0.01	0.02	< 0.01	0.06	0.2	0.2
Sn	ug/L	ICPMS	< 1	< 0.05	< 0.05	< 0.05	< 0.05	< 0.05	-	-	< 1	< 1	< 1
Sr	ug/L	ICPMS	38	39	45	46	50	46	36	36	40	42	42
Ta	ug/L	ICPMS	< 0.05	< 0.02	< 0.02	< 0.02	< 0.02	< 0.02	0.28	0.21	< 0.05	< 0.05	< 0.05
Tb	ug/L	ICPMS	< 0.05	< 0.005	< 0.005	< 0.005	< 0.005	< 0.005	< 0.005	< 0.005	< 0.05	< 0.05	< 0.05
Te	ug/L	ICPMS	< 0.5	< 0.1	< 0.1	< 0.1	< 0.1	< 0.1			< 0.5	< 0.5	< 0.5
Th	ug/L	ICPMS	< 0.05	< 0.005	0.005	< 0.005	0.005	< 0.005	< 0.02	< 0.02	< 0.05	< 0.05	0.05
Ti	ug/L	ICPMS	2.3	1.0	< 0.1	< 0.1	< 0.1	< 0.1	< 0.2	< 0.2	6.2	20	20
Tl	ug/L	ICPMS	0.1	< 0.05	< 0.05	< 0.05	< 0.05	< 0.05	0.2	0.05	0.1	0.1	0.1
Tm	ug/L	ICPMS	< 0.05	< 0.005	< 0.005	< 0.005	< 0.005	< 0.005	< 0.005	< 0.005	< 0.05	< 0.05	< 0.05
U	ug/L	ICPMS	< 0.02	0.01	0.01	0.02	0.009	0.007	0.01	0.009	< 0.02	0.04	0.04
V	ug/L	ICPMS	1.4	0.8	1	1	0.9	1	1.4	1	1.7	7	7.1
W	ug/L	ICPMS	2.4	1.9	1.3	1.2	1.2	1.3	1.5	1.4	2.6	3.5	3.5
Y	ug/L	ICPMS	< 0.1	0.06	0.03	0.03	0.04	0.02	0.07	0.02	0.2	0.6	0.6
Yb	ug/L	ICPMS	< 0.05	< 0.01	< 0.01	< 0.01	< 0.01	< 0.01	0.01	< 0.01	< 0.05	0.06	< 0.05
Zn	ug/L	ICPMS	14	20	31	10	3	4	20	4	9.3	< 5	< 5
Zr	ug/L	ICPMS	< 0.1	< 0.05	< 0.05	< 0.05	< 0.05	0.05	< 0.2	< 0.2	0.2	0.3	0.3
Hg	ng/L	Hg CVAF	-	-	31	26	31	18	0.0	10.0	-	-	-
$\delta^{18}O$ vs VSMOW	per mil	ISO1	-	-16.7	-16.33	-16.36	-16.49	-16.35	-16.5	-16.6	-	-	-
δD vs VSMOW	per mil	ISO2	-	-131.8	-130.3	-129.6	-125.6	-130.2	-130.7	-130.0	-	-	-
$\delta^{34}S_{H2S}$ vs CDT	per mil	ISO3	-	3.0	-	-	-	-	-	-	-	-	-
$\delta^{34}S_{SO4}$ vs CDT	per mil	ISO4	-	2.5	-	-	-	-	-	-	-	-	-
$\delta^{13}C_{CO3}$ vs VPDB	per mil	ISO5	-	-	-	-	-	-	-	-	-	-	-

Appendix 2. Site and analytical data from hydrothermal vents in Yellowstone Lake—*Continued*.

Field No.			96-12-1	96-12-2	97-4a	97-4b	97-7a	97-8a	97-8b	97-12f	97-7a	97-8a
Description			Mary Bay deep hole	Mary Bay deep hole	Mary Bay deep hole	Mary Bay deep hole	Mary Bay deep hole	Mary Bay deep hole	Mary Bay deep hole	Mary Bay deep hole	Mary Bay deep hole	Mary Bay deep hole
Latitude			44°32'42.8"N	44°32'42.8"N	44°32'42.8"N	44°32'42.8"N	44°32'42.8"N	44°32'43.5"N	44°32'43.5"N	44°32'42.8"N	44°32'42.8"N	44°32'43.5"N
Longitude			110°18'39.1"W	110°18'39.1"W	110°18'39.1"W	110°18'39.1"W	110°18'39.1"W	110°18'41.4"W	110°18'41.4"W	110°18'39.1"W	110°18'39.1"W	110°18'41.4"W
Date			-	-	7/20/97	7/20/97	7/22/97	7/23/97	7/23/97	7/26/97	7/22/97	7/23/97
Temp	˚C		30	80	65.6	82.2	85.0	79.4	66.1	35.0	85.0	79.4
pH			-	-	5.0	5.2	4.9	6.6	5.7	5.1	4.9	6.6
Depth	m		-	-	-	-	-	53	53	-	-	53
Treatment			Raw	Raw	Raw	Raw	Filtered	Filtered	Filtered	Filtered	Raw	Raw
sum CO2	mM		1.00	1.03	20.79	13.57	26.91	0.84	20.55	22.42	-	-
HCO3	mM	measured	-	-	0.929	0.823	0.964	0.532	3.484	1.168	-	-
HCO3	uM	calc	-	-	233	369	271	364	440	293	-	-
Cl	mg/L	IC-Aq	-	-	6.1	5.2	4.9	5.9	5.1	5.5	3.3	-
F	mg/L	IC-Aq	-	-	-	-	-	-	-	-	-	-
NO3	mg/L	IC-Aq	-	-	-	-	-	-	-	-	-	-
SO4	mg/L	IC-Aq	-	-	11.8	11.0	10.5	8.2	7.5	11.0	5.2	-
Ag	ug/L	ICPMS	< 0.05	< 0.05	< 0.01	< 0.01	0.2	< 0.01	< 0.01	< 0.01	0.09	< 0.01
Al	ug/L	ICPMS	290	1900	600	4000	92	12	530	96	280	60
As	ug/L	ICPMS	23	52	7.4	12	3.7	14	8.3	12	5.2	15
Au	ug/L	ICPMS	< 0.01	< 0.01	< 0.005	0.01	0.2	< 0.005	0.08	0.01	0.02	0.02
B	ug/L	ICPAES	-	-	-	-	-	-	-	-	-	-
Ba	ug/L	ICPMS	14	33	23	70	18	12	58	12	17	11
Be	ug/L	ICPMS	< 0.2	< 0.2	< 0.05	0.2	0.09	< 0.05	0.2	< 0.05	0.08	< 0.05
Bi	ug/L	ICPMS	< 0.05	< 0.05	< 0.01	< 0.01	< 0.01	< 0.01	< 0.01	< 0.01	< 0.01	< 0.01
Ca	mg/L	ICPAES	-	-	-	-	-	-	-	-	-	-
Ca	mg/L	ICPMS	4.7	5.2	3.6	4.5	3.7	4.0	4.8	3.7	3.5	4.0
Cd	ug/L	ICPMS	< 0.1	< 0.1	< 0.02	< 0.02	< 0.02	< 0.02	< 0.02	< 0.02	< 0.02	< 0.02
Ce	ug/L	ICPMS	0.7	7.6	1.1	9.3	0.2	0.06	0.2	0.2	0.96	0.1
Co	ug/L	ICPMS	0.2	1.7	0.07	0.66	0.05	0.05	0.04	0.04	0.05	0.04
Cr	ug/L	ICPMS	< 5	8.4	4	6	3	2	3	3	3	2
Cs	ug/L	ICPMS	1.6	2	3.8	6.0	3.5	3.4	2.3	4.0	3.5	3.4
Cu	ug/L	ICPMS	0.7	6	< 0.5	< 0.5	< 0.5	6	< 0.5	< 0.5	< 0.5	< 0.5
Dy	ug/L	ICPMS	< 0.05	0.4	0.069	0.39	0.01	0.009	0.03	0.01	0.04	0.01
Er	ug/L	ICPMS	< 0.05	0.2	0.04	0.18	0.009	0.005	0.03	0.01	0.03	0.007
Eu	ug/L	ICPMS	< 0.05	0.1	0.01	0.095	< 0.005	< 0.005	< 0.005	< 0.005	0.01	< 0.005
Fe	ug/L	ICPMS	740	2700	280	1300	39	13	340	100	83	34
Ga	ug/L	ICPMS	< 0.1	0.8	0.03	0.4	< 0.02	< 0.02	< 0.02	< 0.02	0.04	< 0.02
Gd	ug/L	ICPMS	0.05	0.5	0.084	0.48	0.02	0.009	0.04	0.02	0.072	0.01
Ge	ug/L	ICPMS	0.4	0.3	0.3	0.2	0.2	0.2	0.2	0.2	0.2	0.2
Hf	ug/L	ICPMS	< 0.05	< 0.05	< 0.05	< 0.05	< 0.05	< 0.05	< 0.05	< 0.05	< 0.05	< 0.05
Ho	ug/L	ICPMS	< 0.05	0.07	0.01	0.072	< 0.005	< 0.005	0.007	< 0.005	0.008	< 0.005
In	ug/L	ICPMS	< 0.05	< 0.05	< 0.01	< 0.01	< 0.01	< 0.01	< 0.01	< 0.01	< 0.01	< 0.01
K	mg/L	ICPAES	-	-	-	-	-	-	-	-	-	-
K	ug/L	ICPMS	1600	1800	1200	1300	1300	1300	1300	1200	1200	1200
La	ug/L	ICPMS	0.4	3.8	0.51	4.6	0.08	0.05	0.07	0.08	0.50	0.08
Li	ug/L	ICPMS	56	55	41	40	38	42	34	44	37	42
Lu	ug/L	ICPMS	< 0.05	< 0.05	-	-	-	-	-	-	-	-
Mg	mg/L	ICPAES	-	-	-	-	-	-	-	-	-	-
Mg	mg/L	ICPMS	2.4	2.8	1.8	2.4	1.6	1.8	2.4	1.8	1.5	1.8
Mn	ug/L	ICPMS	28	22	9.8	20	5.5	2.8	31	5.8	4.4	2.3
Mo	ug/L	ICPMS	1.3	2.7	0.2	0.2	0.1	1.2	0.2	0.4	0.2	1.2
Na	mg/L	ICPAES	-	-	-	-	-	-	-	-	-	-
Na	mg/L	ICPMS	9.9	9.6	6.8	6.7	6.5	7.4	6.2	7.3	6.0	7.2
Nb	ug/L	ICPMS	< 0.1	< 0.1	< 0.02	< 0.02	< 0.02	< 0.02	< 0.02	< 0.02	< 0.02	< 0.02
Nd	ug/L	ICPMS	0.4	3.5	0.54	4.2	0.06	0.03	0.1	0.09	0.38	0.06
Ni	ug/L	ICPMS	1.3	7.6	0.4	3.0	0.2	0.5	0.5	0.4	0.2	0.5
P	ug/L	ICPMS	-	-	200	740	140	140	220	100	140	88
Pb	ug/L	ICPMS	0.2	2.8	< 0.05	0.76	< 0.05	0.3	< 0.05	< 0.05	0.1	< 0.05
Pr	ug/L	ICPMS	0.09	0.9	0.1	1.0	0.02	< 0.01	0.02	0.02	0.1	0.01
Rb	ug/L	ICPMS	5.3	6.2	5.8	7.3	6.4	5.9	5.6	5.9	6.3	5.9
Re	ug/L	ICPMS	< 0.05	< 0.05	< 0.02	< 0.02	< 0.02	< 0.02	< 0.02	< 0.02	< 0.02	< 0.02
Sb	ug/L	ICPMS	0.9	2	0.05	0.02	< 0.02	0.72	0.03	0.2	< 0.02	0.71
Sc	ug/L	ICPMS	< 0.5	0.5	0.5	0.6	0.5	0.4	0.7	0.4	0.5	0.4
Se	ug/L	ICPMS	< 5	< 5	5.0	2	4	0.5	3	3	4	0.6
SiO2	mg/L	ICPMS	14	22	13	17	15	11	20	9.5	14	11
Sm	ug/L	ICPMS	0.06	0.6	0.09	0.65	0.01	< 0.01	0.03	0.01	0.08	0.01
Sn	ug/L	ICPMS	< 1	< 1	< 0.05	< 0.05	< 0.05	< 0.05	< 0.05	< 0.05	< 0.05	< 0.05
Sr	ug/L	ICPMS	40	48	40	54	33	36	58	36	34	37
Ta	ug/L	ICPMS	< 0.05	< 0.05	< 0.02	< 0.02	< 0.02	< 0.02	< 0.02	< 0.02	< 0.02	< 0.02
Tb	ug/L	ICPMS	< 0.05	0.08	0.01	0.070	< 0.005	< 0.005	0.005	< 0.005	0.008	< 0.005
Te	ug/L	ICPMS	< 0.5	< 0.5	< 0.1	< 0.1	0.8	< 0.1	0.2	0.3	< 0.1	< 0.1
Th	ug/L	ICPMS	< 0.05	0.1	< 0.005	< 0.005	< 0.005	< 0.005	< 0.005	< 0.005	< 0.005	< 0.005
Ti	ug/L	ICPMS	7.2	56	12	45	4.5	0.6	3.5	2.8	8.5	1.3
Tl	ug/L	ICPMS	0.1	0.2	< 0.05	< 0.05	< 0.05	< 0.05	< 0.05	< 0.05	< 0.05	< 0.05
Tm	ug/L	ICPMS	< 0.05	< 0.05	0.006	0.03	< 0.005	< 0.005	< 0.005	< 0.005	< 0.005	< 0.005
U	ug/L	ICPMS	< 0.02	0.1	0.02	0.16	0.02	0.02	< 0.005	0.009	0.04	0.02
V	ug/L	ICPMS	2.1	8.4	1	4	0.5	0.8	1	0.8	0.7	0.8
W	ug/L	ICPMS	2.8	1.8	1.8	1.1	1.8	2.2	1.1	3.6	1.8	2.2
Y	ug/L	ICPMS	0.2	2	0.4	1.8	0.09	0.05	0.2	0.1	0.2	0.07
Yb	ug/L	ICPMS	< 0.05	0.2	0.03	0.2	< 0.01	< 0.01	0.03	0.01	0.02	< 0.01
Zn	ug/L	ICPMS	10	12	3	44	0.5	34	< 0.5	1	34	31
Zr	ug/L	ICPMS	0.2	0.4	< 0.05	< 0.05	< 0.05	< 0.05	< 0.05	0.08	0.06	< 0.05
Hg	ng/L	Hg CVAF	-	-	-	-	-	-	-	-	-	-
$\delta^{18}O$ vs VSMOW	per mil	ISO1	-	-	-16.6	-16.6	-16.9	-16.6	-17.1	-17.0	-16.9	-16.8
δD vs VSMOW	per mil	ISO2	-	-	-	-129.9	-130.3	-128.9	-	-128.9	-130.3	-
$\delta^{34}S_{H2S}$ vs CDT	per mil	ISO3	-	-	-0.5	-	3.6	-	3.5	1.5	-	-
$\delta^{34}S_{SO4}$ vs CDT	per mil	ISO4	-	-	3.8	-	4.3	3.6	-	4.2	-	-
$\delta^{13}C_{CO3}$ vs VPDB	per mil	ISO5	-	-	-	-	-	-	-	-	-	-

Appendix 2. Site and analytical data from hydrothermal vents in Yellowstone Lake—*Continued*.

Field No. Description			97-12r Mary Bay deep hole	98-26A Mary Bay deep hole	98-27A Mary Bay deep hole	98-27B Mary Bay deep hole (0.5m above 98-27A)	YNP-99-12-1 Mary Bay deep hole	YNP-99-12-2 Mary Bay deep hole	YNP-99-13-1 Mary Bay deep hole	YNP-99-13-2 Mary Bay deep hole	97-1 Mary Bay nearshore	97-2 Mary Bay nearshore
Latitude			44°32'42.8"N	44°32'42.8"N	44°32'42.8"N	44°32'42.8"N	44°32'43.5"N	44°32'43.5"N	44°32'43.5"N	44°32'43.5"N	44°33'6"N	44°33'6"N
Longitude			110°18'39.1"W	110°18'39.1"W	110°18'39.1"W	110°18'39.1"W	110°18'38.5"W	110°18'38.5"W	110°18'38.5"W	110°18'38.5"W	110°18'9"W	110°18'9"W
Date			7/26/97	7/24/98	7/24/98	7/24/98	7/22/99	7/22/99	7/22/99	7/22/99	7/26/97	7/26/97
Temp	°C		35.0	50	66; max 103	95	30.1	30.1	7.3	7.3	-	-
pH			5.1	5.2	5.9	6.6	5.4	6.7	4.8	6.6	6.3	-
Depth	m		-	50	48	47	41	41	46	46	-	-
Treatment			Raw	Filtered	Filtered	Filtered	Filtered	Filtered	Filtered	Filtered	Filtered	Raw
sum CO2	mM		-	8.35	2.28	0.90	-	-	-	-	-	-
HCO3	mM	measured	-	0.551	0.588	0.578	-	-	-	-	-	-
HCO3	uM	calc	-	468	582	624	514	447	320	447	-	-
Cl	mg/L	IC-Aq	-	6.0	5.7	5.8	5.4	5.2	5.1	5.3	4.7	-
F	mg/L	IC-Aq	-	-	-	-	0.5	0.5	0.5	0.5	-	-
NO3	mg/L	IC-Aq	-	-	-	-	<.1	<.1	<.35	<.35	-	-
SO4	mg/L	IC-Aq	-	-	-	-	11.0	7.7	14.0	8.1	8.3	-
Ag	ug/L	ICPMS	< 0.01	< 0.01	< 0.01	< 0.01	0.61	0.01	0.09	<0.01	< 0.01	< 0.01
Al	ug/L	ICPMS	230	110	23	4.2	14	<0.5	110	2	9.3	210
As	ug/L	ICPMS	13	17	32	19	14	13	8.1	14	12	13
Au	ug/L	ICPMS	0.005	< 0.01	< 0.01	< 0.01	< 0.01	< 0.01	< 0.01	< 0.01	0.007	< 0.005
B	ug/L	ICPAES	-	80	88	85	143	95.9	88.8	97.2	-	-
Ba	ug/L	ICPMS	13	14	15	10	67	9.6	33	9.7	9.9	11
Be	ug/L	ICPMS	< 0.05	< 0.05	< 0.05	< 0.05	0.1	<0.05	0.09	<0.05	< 0.05	< 0.05
Bi	ug/L	ICPMS	< 0.01	< 0.01	< 0.01	< 0.01	0.01	< 0.01	< 0.01	< 0.01	< 0.01	< 0.01
Ca	mg/L	ICPAES	-	3.7	4.0	4.3	6.32	5.31	5.33	5.42	-	-
Ca	mg/L	ICPMS	3.6	5.0	5.2	5.7	5.4	4.3	4.4	4.3	4.1	4.1
Cd	ug/L	ICPMS	< 0.02	< 0.02	< 0.02	< 0.02	<0.02	<0.02	<0.02	0.04	< 0.02	< 0.02
Ce	ug/L	ICPMS	0.5	0.3	0.2	0.04	0.1	0.03	0.3	0.04	0.1	0.4
Co	ug/L	ICPMS	0.06	0.05	0.2	0.05	0.07	0.06	0.04	0.04	0.06	0.1
Cr	ug/L	ICPMS	3	< 1	< 1	< 1	<1	<1	<1	<1	3	3
Cs	ug/L	ICPMS	4.0	4.1	4.3	4.1	3.4	3	3.8	3	2.5	2.5
Cu	ug/L	ICPMS	< 0.5	< 0.5	< 0.5	< 0.5	<0.5	<0.5	<0.5	<0.5	< 0.5	< 0.5
Dy	ug/L	ICPMS	0.03	0.03	0.01	0.007	0.01	< 0.005	0.05	< 0.005	0.009	0.02
Er	ug/L	ICPMS	0.02	0.03	0.01	0.007	0.007	< 0.005	0.03	< 0.005	< 0.005	0.009
Eu	ug/L	ICPMS	0.005	< 0.005	< 0.005	< 0.005	< 0.005	< 0.005	0.007	< 0.005	< 0.005	0.006
Fe	ug/L	ICPMS	150	360	520	13	<30	<30	87	<30	32	150
Ga	ug/L	ICPMS	< 0.02	< 0.02	< 0.02	0.03	< 0.02	< 0.02	< 0.02	< 0.02	< 0.02	0.02
Gd	ug/L	ICPMS	0.02	0.03	0.03	0.008	0.01	< 0.005	0.056	0.006	0.02	0.03
Ge	ug/L	ICPMS	0.2	0.4	0.3	0.3	0.3	0.3	0.3	0.3	0.2	0.2
Hf	ug/L	ICPMS	< 0.05	< 0.05	< 0.05	< 0.05	-	-	-	-	< 0.05	< 0.05
Ho	ug/L	ICPMS	0.006	< 0.005	0.008	< 0.005	< 0.005	< 0.005	0.01	< 0.005	< 0.005	< 0.005
In	ug/L	ICPMS	< 0.01	< 0.01	< 0.01	< 0.01	-	-	-	-	< 0.01	< 0.01
K	mg/L	ICPAES	-	1.3	1.5	1.4	2.22	1.62	1.74	1.64	-	-
K	ug/L	ICPMS	1200	1400	1500	1500	2000	1400	1600	1500	1300	1300
La	ug/L	ICPMS	0.2	0.1	0.1	0.02	0.05	0.03	0.1	0.03	0.06	0.2
Li	ug/L	ICPMS	45	54	55	59	51	50	46	51	36	36
Lu	ug/L	ICPMS	-	-	-	-	-	-	-	-	-	-
Mg	mg/L	ICPAES	-	1.7	1.7	1.8	2.9	2.25	2.39	2.28	-	-
Mg	mg/L	ICPMS	1.8	2.5	2.6	2.7	2.6	2	2.1	2.1	2.0	2.0
Mn	ug/L	ICPMS	6.2	23	28	3.6	26	1.4	12	1.4	14	16
Mo	ug/L	ICPMS	0.53	0.2	0.81	1.0	0.6	1.1	0.2	1	1.1	1.1
Na	mg/L	ICPAES	-	7.4	8.2	8.4	9.9	9.44	9.1	9.7	-	-
Na	mg/L	ICPMS	7.3	9.1	9.7	9.7	8.3	7.8	7.4	7.8	7.2	7.2
Nb	ug/L	ICPMS	< 0.02	< 0.02	< 0.02	< 0.02	0.2	0.2	0.1	0.1	< 0.02	< 0.02
Nd	ug/L	ICPMS	0.20	0.20	0.09	0.03	0.06	0.05	0.21	0.04	0.03	0.2
Ni	ug/L	ICPMS	0.5	0.4	0.5	0.4	0.3	0.4	0.2	0.5	0.4	0.7
P	ug/L	ICPMS	120	300	360	110	25	1	28	3	54	86
Pb	ug/L	ICPMS	< 0.05	< 0.05	< 0.05	< 0.05	<0.05	<0.05	<0.05	0.1	< 0.05	0.09
Pr	ug/L	ICPMS	0.05	0.04	0.02	< 0.01	0.02	< 0.01	0.05	< 0.01	< 0.01	0.05
Rb	ug/L	ICPMS	5.7	5.5	6.3	6.0	6.6	4.7	5.2	4.7	5.5	5.5
Re	ug/L	ICPMS	< 0.02	< 0.02	< 0.02	< 0.02	-	-	-	-	< 0.02	< 0.02
Sb	ug/L	ICPMS	0.2	< 0.02	< 0.02	0.67	0.09	0.63	<0.05	0.63	0.60	0.60
Sc	ug/L	ICPMS	0.3	< 0.1	< 0.1	< 0.1	0.3	< 0.1	< 0.1	< 0.1	0.4	0.4
Se	ug/L	ICPMS	2	< 0.2	< 0.2	< 0.2	0.5	< 0.3	0.5	< 0.3	<0.5	0.5
SiO2	mg/L	ICPMS	9.8	11	16	12	24	9.1	14	9.2	9.9	10
Sm	ug/L	ICPMS	0.03	0.05	0.02	0.01	0.01	< 0.01	0.06	0.02	0.02	0.03
Sn	ug/L	ICPMS	< 0.05	< 0.05	< 0.05	< 0.05	-	-	-	-	< 0.05	< 0.05
Sr	ug/L	ICPMS	36	43	48	48	64	36	46	38	39	38
Ta	ug/L	ICPMS	< 0.02	< 0.02	< 0.02	< 0.02	0.19	0.18	0.14	0.12	< 0.02	< 0.02
Tb	ug/L	ICPMS	< 0.005	< 0.005	< 0.005	< 0.005	< 0.005	< 0.005	0.005	< 0.005	< 0.005	< 0.005
Te	ug/L	ICPMS	0.1	< 0.1	< 0.1	< 0.1	-	-	-		< 0.1	< 0.1
Th	ug/L	ICPMS	< 0.005	< 0.005	< 0.005	0.006	< 0.02	< 0.02	< 0.02	< 0.02	< 0.005	< 0.005
Ti	ug/L	ICPMS	5.1	< 0.1	< 0.1	< 0.1	< 0.2	< 0.2	1.1	< 0.2	0.4	2.5
Tl	ug/L	ICPMS	< 0.05	< 0.05	< 0.05	< 0.05	<0.05	<0.05	<0.05	<0.05	< 0.05	< 0.05
Tm	ug/L	ICPMS	< 0.005	< 0.005	< 0.005	< 0.005	< 0.005	< 0.005	0.006	< 0.005	< 0.005	< 0.005
U	ug/L	ICPMS	0.02	0.007	0.01	0.01	< 0.005	0.009	< 0.005	0.009	0.01	0.02
V	ug/L	ICPMS	1	2	1	1	0.73	0.8	0.53	0.82	0.9	1
W	ug/L	ICPMS	3.6	1.7	1.7	1.6	1.6	1.5	1.3	1.7	2.2	2.1
Y	ug/L	ICPMS	0.2	0.2	0.1	0.03	0.05	0.03	0.3	0.03	0.05	0.1
Yb	ug/L	ICPMS	0.01	0.01	< 0.01	< 0.01	< 0.01	< 0.01	0.04	< 0.01	< 0.01	0.01
Zn	ug/L	ICPMS	10	5	2	5	<0.5	6	<0.5	6	< 0.5	< 0.5
Zr	ug/L	ICPMS	< 0.05	< 0.05	< 0.05	< 0.05	< 0.2	< 0.2	< 0.2	< 0.2	< 0.05	< 0.05
Hg	ng/L	Hg CVAF	-	28	12	<10	5.0	6.0	0.0	8.0	-	-
$\delta^{18}O$ vs VSMOW	per mil	ISO1	-16.7	-16.33	-16.43	-16.19	-16.8	-16.3	-16.6	-16.5	-16.35	-
δD vs VSMOW	per mil	ISO2	-	-129.4	-132.1	-132	-130.4	-130.5	-130.1	-128.2	-129	-
$\delta^{34}S_{H2S}$ vs CDT	per mil	ISO3	-	-	-	-	-	-	-	-	-	-
$\delta^{34}S_{SO4}$ vs CDT	per mil	ISO4	-	-	-	-	-	-	-	-	-	-
$\delta^{13}C_{CO3}$ vs VPDB	per mil	ISO5	-	-	-	-	-	-	-	-	-	-

Appendix 2. Site and analytical data from hydrothermal vents in Yellowstone Lake—*Continued*.

Field No. / Description			98-11A Mary Bay Deep Hole	98-11B 0.5m above 98-11A	98-28A Deep Vent E of Stevenson Island	98-28B Deep Vent E of Stevenson Island	98-29A Deep Vent E of Stevenson Island	98-29B Deep Vent E of Stevenson Island	98-30A Deep Vent E of Stevenson Island	98-30B Deep Vent E of Stevenson Island (0.5m above 98-30A)	98-31A Deep Vent E of Stevenson Island
Latitude			44°32'42.8"N	44°32'42.8"N	44°30'38.7"N	44°30'38.7"N	44°30'38.7"N	44°30'38.7"N	44°30'38.7"N	44°30'38.7"N	44°30'38.7"N
Longitude			110°18'42.5"W	110°18'42.5"W	110°21'17.4"W	110°21'17.4"W	110°21'17.4"W	110°21'17.4"W	110°21'17.4"W	110°21'17.4"W	110°21'17.4"W
Date			7/17/98	7/17/98	7/25/98	7/25/98	7/25/98	7/25/98	7/26/98	7/26/98	7/26/98
Temp	˚C		12	-	95; max 106	55-85	15-25 above vent	8.7-9.7	102	10	39.5
pH			6.9	6.9	5.4	5.3	5.6	6.2	5.1	6.7	6.1
Depth	m		41	41	106	106	107	102	105	105	93
Treatment			Filtered	Filtered	Filtered	Filtered	Filtered	Filtered	Filtered	Filtered	Filtered
sum CO2	mM		0.84	0.83	9.81	9.37	4.16	1.40	4.39	0.65	0.98
HCO3	mM	measured	0.645	0.639	1.055	0.692	0.596	0.595	0.214	0.442	0.340
HCO3	uM	calc	588	581	670	650	599	703	509	647	551
Cl	mg/L	IC-Aq	5.6	5.7	5.2	5.2	4.8	4.8	5.0	4.8	4.8
F	mg/L	IC-Aq	-	-	-	-	-	-	-	-	-
NO3	mg/L	IC-Aq	-	-	-	-	-	-	-	-	-
SO4	mg/L	IC-Aq	-	-	-	-	-	-	-	-	-
Ag	ug/L	ICPMS	< 0.01	< 0.01	< 0.01	< 0.01	< 0.01	< 0.01	< 0.01	< 0.01	< 0.01
Al	ug/L	ICPMS	6.1	6.8	16	20	36	5.2	100	4.4	15
As	ug/L	ICPMS	18	17	10	15	22	15	21	15	14
Au	ug/L	ICPMS	< 0.01	< 0.01	< 0.01	< 0.01	< 0.01	< 0.01	< 0.01	< 0.01	< 0.01
B	ug/L	ICPAES	94	98	68	70	70	69	62	67	68
Ba	ug/L	ICPMS	11	12	81	39	12	11	17	9.8	27
Be	ug/L	ICPMS	< 0.05	< 0.05	0.07	< 0.05	0.07	0.06	< 0.05	< 0.05	< 0.05
Bi	ug/L	ICPMS	< 0.01	< 0.01	< 0.01	< 0.01	< 0.01	< 0.01	< 0.01	< 0.01	< 0.01
Ca	mg/L	ICPAES	4.6	4.6	4.5	4.5	3.7	4.2	3.7	4.1	3.8
Ca	mg/L	ICPMS	5.3	5.2	6.2	6.0	5.2	5.9	5.4	5.7	5.3
Cd	ug/L	ICPMS	< 0.02	< 0.02	< 0.02	< 0.02	< 0.02	< 0.02	< 0.02	< 0.02	< 0.02
Ce	ug/L	ICPMS	0.03	0.03	0.1	0.1	0.4	0.04	0.4	0.04	0.50
Co	ug/L	ICPMS	0.2	0.1	0.07	0.08	0.04	0.1	0.1	0.05	0.5
Cr	ug/L	ICPMS	< 1	< 1	< 1	< 1	< 1	< 1	< 1	< 1	< 1
Cs	ug/L	ICPMS	3.7	3.8	3.1	3.0	2.8	3.2	3.1	3.0	2.2
Cu	ug/L	ICPMS	< 0.5	< 0.5	< 0.5	< 0.5	< 0.5	< 0.5	< 0.5	< 0.5	< 0.5
Dy	ug/L	ICPMS	0.01	< 0.005	0.01	0.01	0.02	0.01	0.03	0.005	0.04
Er	ug/L	ICPMS	< 0.005	< 0.005	< 0.005	0.006	0.02	0.008	0.02	< 0.005	0.02
Eu	ug/L	ICPMS	< 0.005	< 0.005	< 0.005	< 0.005	< 0.005	< 0.005	< 0.005	< 0.005	0.008
Fe	ug/L	ICPMS	13	14	100	130	230	12	130	11	450
Ga	ug/L	ICPMS	0.03	0.02	< 0.02	< 0.02	< 0.02	< 0.02	< 0.02	< 0.02	< 0.02
Gd	ug/L	ICPMS	0.008	0.01	0.02	0.01	0.04	0.008	0.03	< 0.005	0.050
Ge	ug/L	ICPMS	0.3	0.2	0.3	0.3	0.2	0.3	0.2	0.2	0.3
Hf	ug/L	ICPMS	< 0.05	< 0.05	< 0.05	< 0.05	< 0.05	< 0.05	< 0.05	< 0.05	< 0.05
Ho	ug/L	ICPMS	< 0.005	< 0.005	< 0.005	< 0.005	0.006	< 0.005	0.007	< 0.005	0.008
In	ug/L	ICPMS	< 0.01	< 0.01	< 0.01	< 0.01	< 0.01	< 0.01	< 0.01	< 0.01	< 0.01
K	mg/L	ICPAES	1.4	1.4	1.6	1.6	1.4	1.4	1.3	1.4	1.4
K	ug/L	ICPMS	1400	1400	1600	1600	1400	1600	1400	1500	1500
La	ug/L	ICPMS	0.03	0.03	0.07	0.08	0.2	0.04	0.2	0.02	0.2
Li	ug/L	ICPMS	54	53	46	46	48	51	43	48	48
Lu	ug/L	ICPMS	-	-	-	-	-	-	-	-	-
Mg	mg/L	ICPAES	2.1	2.2	2.0	2.1	1.7	1.8	1.5	1.8	1.7
Mg	mg/L	ICPMS	2.6	2.6	3.0	3.1	2.7	2.9	2.4	2.7	2.5
Mn	ug/L	ICPMS	2.7	2.7	23	23	9.4	7.7	30	5.0	76
Mo	ug/L	ICPMS	1.1	1.2	0.3	0.3	0.86	1.3	0.04	1.1	2.0
Na	mg/L	ICPAES	7.8	7.9	7.6	7.7	7.0	7.6	6.5	7.5	7.4
Na	mg/L	ICPMS	9.3	9.1	9.4	9.1	9.1	9.7	8.3	9.4	9.0
Nb	ug/L	ICPMS	< 0.02	< 0.02	< 0.02	< 0.02	< 0.02	< 0.02	< 0.02	< 0.02	< 0.02
Nd	ug/L	ICPMS	0.04	0.05	0.07	0.07	0.21	0.05	0.20	0.01	0.25
Ni	ug/L	ICPMS	0.5	0.3	0.4	0.4	0.4	0.4	0.3	0.4	0.7
P	ug/L	ICPMS	87	140	340	370	190	180	410	130	120
Pb	ug/L	ICPMS	< 0.05	< 0.05	< 0.05	< 0.05	0.07	< 0.05	< 0.05	< 0.05	< 0.05
Pr	ug/L	ICPMS	< 0.01	0.01	0.02	0.02	0.05	< 0.01	0.05	< 0.01	0.06
Rb	ug/L	ICPMS	5.8	5.6	5.8	5.9	5.2	5.8	5.4	5.7	5.0
Re	ug/L	ICPMS	< 0.02	< 0.02	< 0.02	< 0.02	< 0.02	< 0.02	< 0.02	< 0.02	< 0.02
Sb	ug/L	ICPMS	0.83	0.74	< 0.02	< 0.02	< 0.02	0.71	< 0.02	0.58	0.96
Sc	ug/L	ICPMS	< 0.1	< 0.1	< 0.1	< 0.1	< 0.1	< 0.1	< 0.1	< 0.1	< 0.1
Se	ug/L	ICPMS	< 0.2	< 0.2	< 0.2	< 0.2	< 0.2	< 0.2	< 0.2	< 0.2	< 0.2
SiO2	mg/L	ICPMS	12	11	17	17	13	12	20	12	15
Sm	ug/L	ICPMS	0.01	0.02	0.02	0.01	0.03	0.01	0.06	0.01	0.05
Sn	ug/L	ICPMS	< 0.05	< 0.05	< 0.05	< 0.05	< 0.05	< 0.05	< 0.05	< 0.05	< 0.05
Sr	ug/L	ICPMS	46	47	64	60	45	48	48	49	50
Ta	ug/L	ICPMS	< 0.02	< 0.02	< 0.02	< 0.02	< 0.02	< 0.02	< 0.02	< 0.02	< 0.02
Tb	ug/L	ICPMS	< 0.005	< 0.005	< 0.005	< 0.005	< 0.005	< 0.005	< 0.005	< 0.005	< 0.005
Te	ug/L	ICPMS	< 0.1	< 0.1	< 0.1	< 0.1	< 0.1	< 0.1	< 0.1	< 0.1	< 0.1
Th	ug/L	ICPMS	< 0.005	< 0.005	< 0.005	< 0.005	< 0.005	< 0.005	< 0.005	< 0.005	< 0.005
Ti	ug/L	ICPMS	< 0.1	< 0.1	< 0.1	< 0.1	< 0.1	< 0.1	< 0.1	< 0.1	< 0.1
Tl	ug/L	ICPMS	< 0.05	< 0.05	< 0.05	< 0.05	< 0.05	< 0.05	< 0.05	< 0.05	< 0.05
Tm	ug/L	ICPMS	< 0.005	< 0.005	< 0.005	< 0.005	< 0.005	< 0.005	< 0.005	< 0.005	< 0.005
U	ug/L	ICPMS	0.01	0.02	< 0.005	0.007	< 0.005	0.007	0.007	0.01	0.008
V	ug/L	ICPMS	1	1	1	1	2	1	2	1	4
W	ug/L	ICPMS	1.7	1.7	1.6	1.6	1.6	1.6	1.0	1.5	1.9
Y	ug/L	ICPMS	0.03	0.02	0.05	0.05	0.1	0.04	0.1	0.03	0.2
Yb	ug/L	ICPMS	< 0.01	< 0.01	< 0.01	< 0.01	0.02	< 0.01	< 0.01	0.01	0.02
Zn	ug/L	ICPMS	82	32	2	5	2	3	2	5	1
Zr	ug/L	ICPMS	< 0.05	0.05	< 0.05	< 0.05	< 0.05	< 0.05	< 0.05	< 0.05	0.1
Hg	ng/L	Hg CVAF	10	14	16	17	<10	<10	170	<10	<10
$\delta^{18}O$ vs VSMOW	per mil	ISO1	-16.27	-16.43	-16.23	-16.22	-16.14	-16.03	-16.55	-16.11	-16.18
δD vs VSMOW	per mil	ISO2	-129	-128.8	-126.3	-130.9	-131.7	-130.8	-125.3	-128.3	-129.1
$\delta^{34}S_{H2S}$ vs CDT	per mil	ISO3	-	-	-	-	-	-	-	-	-
$\delta^{34}S_{SO4}$ vs CDT	per mil	ISO4	-	-	-	-	-	-	-	-	-
$\delta^{13}C_{CO3}$ vs VPDB	per mil	ISO5	-	-	-	-	-	-	-	-	-

Appendix 2. Site and analytical data from hydrothermal vents in Yellowstone Lake—*Continued*.

Field No. Description			98-31B Deep Vent E of Stevenson Island (0.5m above 98-31A)	YNP-99-9-1 Deep Vent E of Stevenson Island	YNP-99-10-1 nearshore vent between Pelican & Storm	YNP-99-10-2 nearshore vent between Pelican & Storm	YNP-99-6-1 Inflated Plain-hydrothermal vent	YNP-99-6-2 Inflated Plain-hydrothermal vent	YNP-99-24-1 Inflated Plain-hydrothermal vent	YNP-99-24-2 Inflated Plain-hydrothermal vent	D02-2.1 Inflated Plain-hydrothermal vent	D02-2.2 Inflated Plain-hydrothermal vent
Latitude			44°30'38.7"N	44°30'39.9"N	44°33'5.1"N	44°33'5.1"N	44°32'9.9"N	44°32'9.9"N	44°32'9.9"N	44°32'9.9"N	44°32'10.0"N	44°32'10.0"N
Longitude			110°21'17.4"W	110°21'19.4"W	110°21'3.1"W	110°21'3.1"W	110°21'24.5"W	110°21'24.5"W	110°21'24.5"W	110°21'24.5"W	110°21'18.2"W	110°21'18.2"W
Date			7/26/98	7/20/99	7/21/99	7/21/99	7/18/99	7/18/99	7/27/99	7/27/99	8/18/02	8/18/02
Temp	˚C		-	39.6	18.1	18.1	47.2	47.2	8.3	8.3	-	-
pH			7.1	5.3	7.3	7.2	6.0	6.8	5.7	6.9	6.8	5.2
Depth	m		93	105	shallow	shallow	8	8	18	18	-	-
Treatment			Filtered	Filtered	Filtered	Filtered	Filtered	Filtered	Filtered	Filtered	Filtered	Filtered
sum CO2	mM		0.64	-	-	-	-	-	-	-	-	-
HCO3	mM	measured	0.542	-	-	-	-	-	-	-	-	-
HCO3	uM	calc	675	458	504	538	448	469	717	437	-	-
Cl	mg/L	IC-Aq	4.9	4.7	4.3	4.2	4.2	4.2	4.9	4.9	4.7	4.7
F	mg/L	IC-Aq	-	0.5	0.4	0.5	0.5	0.5	0.6	0.5	0.4	0.4
NO3	mg/L	IC-Aq	-	<.1	<.1	<.1	<.1	<.1	<.35	<.35	0.8	0.5
SO4	mg/L	IC-Aq	-	11.0	6.8	6.8	8.4	7.0	14.0	7.6	7.7	14
Ag	ug/L	ICPMS	< 0.01	<0.01	<0.01	<0.01	0.62	0.1	0.02	<0.01	< 3	< 3
Al	ug/L	ICPMS	4.5	51	8.1	7.2	2.4	2	7.4	1.1	10.5	16
As	ug/L	ICPMS	16	16	13	13	14	12	17	13	10.4	10.9
Au	ug/L	ICPMS	< 0.01	< 0.01	< 0.01	< 0.01	< 0.01	< 0.01	< 0.01	< 0.01	-	-
B	ug/L	ICPAES	67	89.9	76	81.8	76.1	76.4	99.8	89.2	-	-
Ba	ug/L	ICPMS	10	12	12	12	10	9.3	170	9.1	8.6	10.2
Be	ug/L	ICPMS	< 0.05	0.05	<0.05	<0.05	<0.05	<0.05	<0.05	<0.05	< 0.05	< 0.05
Bi	ug/L	ICPMS	< 0.01	< 0.01	< 0.01	< 0.01	0.055	< 0.01	< 0.01	< 0.01	< 0.2	< 0.2
Ca	mg/L	ICPAES	4.1	4.97	4.9	4.92	5.05	5.04	9.91	5.15	-	-
Ca	mg/L	ICPMS	5.9	4.7	4.6	4.8	4.4	4.4	8.3	4.4	3.9	3.9
Cd	ug/L	ICPMS	< 0.02	<0.02	<0.02	<0.02	<0.02	<0.02	<0.02	<0.02	< 0.02	< 0.02
Ce	ug/L	ICPMS	0.02	0.4	0.04	0.04	0.04	0.03	0.04	0.02	0.03	0.06
Co	ug/L	ICPMS	0.04	0.4	0.06	0.05	0.04	<0.02	0.07	<0.02	0.03	0.04
Cr	ug/L	ICPMS	< 1	<1	<1	<1	<1	<1	<1	<1	5.2	< 1
Cs	ug/L	ICPMS	3.2	2.6	2.4	2.4	2.4	2.3	2.8	2.5	2.36	2.35
Cu	ug/L	ICPMS	< 0.5	<0.5	<0.5	<0.5	<0.5	<0.5	<0.5	<0.5	0.8	< 0.5
Dy	ug/L	ICPMS	0.005	0.04	0.01	< 0.005	0.006	< 0.005	0.01	< 0.005	0.005	0.005
Er	ug/L	ICPMS	< 0.005	0.02	< 0.005	< 0.005	< 0.005	< 0.005	< 0.005	< 0.005	< 0.005	0.005
Eu	ug/L	ICPMS	< 0.005	< 0.005	< 0.005	< 0.005	< 0.005	< 0.005	< 0.005	< 0.005	< 0.005	< 0.005
Fe	ug/L	ICPMS	10	230	<30	<30	<30	<30	33	<30	< 50	< 50
Ga	ug/L	ICPMS	< 0.02	< 0.02	< 0.02	< 0.02	< 0.02	< 0.02	0.06	0.03	< 0.05	< 0.05
Gd	ug/L	ICPMS	0.006	0.02	< 0.005	0.01	0.007	0.006	< 0.005	0.006	0.005	0.007
Ge	ug/L	ICPMS	0.4	0.3	0.3	0.2	0.2	0.2	0.3	0.3	0.27	0.25
Hf	ug/L	ICPMS	< 0.05	-	-	-	-	-	-	-	-	-
Ho	ug/L	ICPMS	< 0.005	0.006	< 0.005	< 0.005	< 0.005	< 0.005	< 0.005	< 0.005	< 0.005	< 0.005
In	ug/L	ICPMS	< 0.01	-	-	-	-	-	-	-	-	-
K	mg/L	ICPAES	1.4	1.58	1.54	1.54	1.55	1.53	2.78	1.63	-	-
K	ug/L	ICPMS	1600	1500	1500	1500	1400	1400	2400	1400	1340	1300
La	ug/L	ICPMS	0.01	0.2	0.04	0.04	0.03	0.03	0.04	0.02	0.03	0.04
Li	ug/L	ICPMS	49	54	48	50	45	45	43	45	40.4	38.8
Lu	ug/L	ICPMS	-	-	-	-	-	-	-	-	< 0.1	< 0.1
Mg	mg/L	ICPAES	1.8	2.25	2.15	2.17	2.2	2.18	3.89	2.28	-	-
Mg	mg/L	ICPMS	2.8	2.2	2.1	2.2	2	2	3.4	2	2.05	1.98
Mn	ug/L	ICPMS	0.80	9	1.5	0.77	3.2	1.5	34	0.65	1.4	2.3
Mo	ug/L	ICPMS	1.4	0.4	1	0.96	3.2	1.7	1.2	1.2	< 2	< 2
Na	mg/L	ICPAES	7.5	8.5	7.77	7.76	7.98	7.98	10.7	8.42	-	-
Na	mg/L	ICPMS	9.4	8.4	7.5	7.8	7.4	7.2	9	7.2	8.09	7.76
Nb	ug/L	ICPMS	< 0.02	< 0.02	< 0.02	< 0.02	0.4	0.3	< 0.02	< 0.02	< 0.2	< 0.2
Nd	ug/L	ICPMS	0.03	0.21	0.04	0.04	0.04	0.04	0.04	0.02	0.02	0.04
Ni	ug/L	ICPMS	0.4	0.5	0.4	0.4	0.5	0.4	0.1	0.2	0.6	0.7
P	ug/L	ICPMS	140	19	2	3	5.9	5.3	< 2	< 2	< 0.01	< 0.01
Pb	ug/L	ICPMS	< 0.05	<0.05	<0.05	<0.05	<0.05	<0.05	<0.05	<0.05	< 0.05	< 0.05
Pr	ug/L	ICPMS	< 0.01	0.06	< 0.01	0.01	< 0.01	< 0.01	0.01	< 0.01	< 0.01	< 0.01
Rb	ug/L	ICPMS	5.8	4.8	4.6	4.7	4.3	4.2	8	4.9	4.36	4.37
Re	ug/L	ICPMS	< 0.02	-	-	-	-	-	-	-	-	-
Sb	ug/L	ICPMS	0.59	<0.05	0.5	0.54	0.86	0.73	<0.2	0.4	0.53	0.54
Sc	ug/L	ICPMS	< 0.1	< 0.1	< 0.1	< 0.1	0.2	0.1	0.2	0.3	1.2	1.1
Se	ug/L	ICPMS	< 0.2	< 0.3	< 0.3	< 0.3	0.5	< 0.3	< 0.3	< 0.3	< 1	< 1
SiO2	mg/L	ICPMS	12	9.7	11	10	9.7	9.4	21	9.2	3.8	3.8
Sm	ug/L	ICPMS	< 0.01	0.03	0.01	< 0.01	< 0.01	< 0.01	0.01	< 0.01	< 0.01	< 0.01
Sn	ug/L	ICPMS	< 0.05	-	-	-	-	-	-	-	-	-
Sr	ug/L	ICPMS	51	41	40	42	38	37	100	43	35.1	35.3
Ta	ug/L	ICPMS	< 0.02	< 0.03	< 0.03	< 0.03	0.24	0.2	< 0.03	< 0.03	0.06	0.04
Tb	ug/L	ICPMS	< 0.005	< 0.005	< 0.005	< 0.005	< 0.005	< 0.005	< 0.005	< 0.005	< 0.005	< 0.005
Te	ug/L	ICPMS	< 0.1	-	-	-	-	-	-	-	-	-
Th	ug/L	ICPMS	0.006	< 0.02	< 0.02	< 0.02	< 0.02	< 0.02	< 0.02	< 0.02	0.59	< 0.2
Ti	ug/L	ICPMS	< 0.1	< 0.2	< 0.2	< 0.2	< 0.2	< 0.2	< 0.8	< 0.8	< 0.5	< 0.5
Tl	ug/L	ICPMS	< 0.05	<0.05	<0.05	<0.05	0.2	<0.05	<0.05	<0.05	< 0.1	< 0.1
Tm	ug/L	ICPMS	< 0.005	< 0.005	< 0.005	< 0.005	< 0.005	< 0.005	< 0.005	< 0.005	< 0.005	< 0.005
U	ug/L	ICPMS	0.01	< 0.005	0.01	0.01	0.008	0.01	0.005	0.01	< 0.1	< 0.1
V	ug/L	ICPMS	1	1.9	0.9	0.87	1.1	1.1	0.8	1	0.8	0.9
W	ug/L	ICPMS	1.7	1.4	1.4	1.5	1.6	1.6	5.5	4	1.03	1.18
Y	ug/L	ICPMS	0.02	0.1	0.03	0.03	0.04	0.04	0.03	0.02	0.02	0.04
Yb	ug/L	ICPMS	< 0.01	0.02	< 0.01	< 0.01	< 0.01	< 0.01	< 0.01	< 0.01	< 0.005	< 0.005
Zn	ug/L	ICPMS	8	<0.5	10	20	2	4	<0.5	6	13.7	3
Zr	ug/L	ICPMS	0.07	< 0.2	< 0.2	< 0.2	< 0.2	< 0.2	< 0.2	< 0.2	< 0.2	< 0.2
Hg	ng/L	Hg CVAF	<10	5.0	0.0	5.0	26.0	21.0	0.0	0.0	< 5	50
$\delta^{18}O$ vs VSMOW	per mil	ISO1	-16.19	-16.4	-16.6	-16.6	-16.8	-16.7	-16.4	-16.5	-	-16.1
δD vs VSMOW	per mil	ISO2	-126.7	-132.0	-134.3	-131.2	-130.0	-130.3	-131.3	-128.6	-	-127.5
$\delta^{34}S_{H2S}$ vs CDT	per mil	ISO3	-	-	-	-	-	-	-	-	-	-
$\delta^{34}S_{SO4}$ vs CDT	per mil	ISO4	-	-	-	-	-	-	-	-	-	-
$\delta^{13}C_{CO3}$ vs VPDB	per mil	ISO5	-	-	-	-	-	-	-	-	-	-

Appendix 2. Site and analytical data from hydrothermal vents in Yellowstone Lake—*Continued*.

Field No.			D02-10.1	D02-10.2	D02-12.1	D02-12.2	D02-13.1	D02-6.1	D03-1.1	D03-1.2	D03-2.1	D03-3.1
Description			Inflated Plain-hydrothermal vent	Inflated Plain-hydrothermal vent	Inflated Plain-hydrothermal vent	Inflated Plain-hydrothermal vent	Inflated Plain-hydrothermal vent	Inflated Plain-hydrothermal vent	Inflated Plain-hydrothermal vent	Inflated Plain-hydrothermal vent	Inflated Plain-hydrothermal vent	Inflated Plain-hydrothermal vent
Latitude			44°32'10.4"N	44°32'10.4"N	44°32'10.2"N	44°32'10.2"N	44°32'10.2"N	44°32'8.6"N	44°32'5.161"N	44°32'5.161"N	44°32'5.323"N	44°32'8.206"N
Longitude			110°21'15.8"W	110°21'15.8"W	110°21'18.5"W	110°21'18.5"W	110°21'18.5"W	110°21'15.3"W	110°21'15.624"W	110°21'15.624"W	110°21'15.432"W	110°21'15.75"W
Date			9/26/02	9/26/02	9/27/02	9/27/02	9/27/02	8/20/02	8/7/03	8/7/03	8/9/03	8/9/03
Temp	˚C		35	63	85	22	-	77.8	45	61	69	39
pH			5.2	5.8	5.9	6.7	-	-	5.47	6.69	6.7	6.8
Depth	m		29	29	15	16	13	10	23.9	28.4	29.7	7.9
Treatment			Filtered	Filtered	Filtered	Filtered	Filtered	Filtered	Filtered	Filtered	Filtered	Filtered
sum CO2	mM		-	-	-	-	-	-	-	-	-	-
HCO3	mM	measured	-	-	-	-	-	-	-	-	-	-
HCO3	uM	calc	-	-	-	-	-	-	-	-	-	-
Cl	mg/L	IC-Aq	5.2	5.1	5.1	5.2	5.2	-	4.7	4.8	4.9	4.9
F	mg/L	IC-Aq	0.6	0.6	0.7	0.6	0.6	-	0.6	0.5	0.5	0.5
NO3	mg/L	IC-Aq	<.18	<.18	<.18	2	0.3	-	<.08	<.08	<.08	<.08
SO4	mg/L	IC-Aq	12	11	10	8.9	12	-	15	8.6	8.8	7.8
Ag	ug/L	ICPMS	<0.01	<0.01	0.2	<0.01	<0.01	< 3	0.062	0.013	<0.01	<0.01
Al	ug/L	ICPMS	3	3.5	3.2	2.1	2.3	218	28	5.3	4.7	3.7
As	ug/L	ICPMS	15	14	13	13	13	21.8	19	14	13	13
Au	ug/L	ICPMS	< 0.01	< 0.01	< 0.01	< 0.01	< 0.01	-	0.052	0.013	< 0.01	< 0.01
B	ug/L	ICPAES	-	-	-	-	-	-	-	-	-	-
Ba	ug/L	ICPMS	2	2	3	3	3	23.2	13	9.1	8.8	9
Be	ug/L	ICPMS	<0.05	<0.05	<0.05	<0.05	<0.05	< 0.05	<0.05	<0.05	<0.05	<0.05
Bi	ug/L	ICPMS	< 0.03	< 0.03	< 0.03	< 0.03	< 0.03	< 0.2	< 0.03	< 0.03	< 0.03	< 0.03
Ca	mg/L	ICPAES	-	-	-	-	-	-	-	-	-	-
Ca	mg/L	ICPMS	4.8	4.7	4.7	4.7	4.6	4.0	4.3	4.3	4.3	4.2
Cd	ug/L	ICPMS	<0.02	<0.02	<0.02	<0.02	<0.02	0.06	<0.02	<0.02	<0.02	<0.02
Ce	ug/L	ICPMS	0.02	0.01	0.01	0.01	0.01	0.11	0.16	0.052	0.032	0.034
Co	ug/L	ICPMS	<0.02	<0.02	<0.02	<0.02	<0.02	0.12	0.03	0.068	<0.02	<0.02
Cr	ug/L	ICPMS	2	2	1	2	1	< 1	5.4	3.2	<1	<1
Cs	ug/L	ICPMS	2.4	2.4	2.4	2.4	2.3	2.83	2.5	2.4	2.4	2.5
Cu	ug/L	ICPMS	<0.5	<0.5	<0.5	<0.5	<0.5	10.8	<0.5	0.6	<0.5	<0.5
Dy	ug/L	ICPMS	< 0.005	< 0.005	< 0.005	< 0.005	< 0.005	0.008	0.015	0.0054	0.005	< 0.005
Er	ug/L	ICPMS	< 0.005	< 0.005	< 0.005	< 0.005	< 0.005	0.005	0.0074	< 0.005	< 0.005	< 0.005
Eu	ug/L	ICPMS	< 0.005	< 0.005	< 0.005	< 0.005	< 0.005	< 0.005	< 0.005	< 0.005	< 0.005	< 0.005
Fe	ug/L	ICPMS	9	8.3	7	6.2	6.5	87	22	5.7	<2	<2
Ga	ug/L	ICPMS	< 0.02	< 0.02	< 0.02	< 0.02	< 0.02	< 0.05	< 0.02	< 0.02	< 0.02	< 0.02
Gd	ug/L	ICPMS	< 0.005	< 0.005	< 0.005	< 0.005	< 0.005	0.01	0.013	< 0.005	0.005	0.0079
Ge	ug/L	ICPMS	0.3	0.3	0.3	0.3	0.3	0.33	0.31	0.32	0.31	0.33
Hf	ug/L	ICPMS	-	-	-	-	-	-	<5	<5	20	<5
Ho	ug/L	ICPMS	< 0.005	< 0.005	< 0.005	< 0.005	< 0.005	< 0.005	< 0.005	< 0.005	< 0.005	< 0.005
In	ug/L	ICPMS	< 0.01	< 0.01	< 0.01	< 0.01	< 0.01	-	< 0.01	< 0.01	< 0.01	< 0.01
K	mg/L	ICPAES	-	-	-	-	-	-	-	-	-	-
K	ug/L	ICPMS	1700	1700	1600	1600	1600	2000	1600	1500	1500	1500
La	ug/L	ICPMS	0.01	0.02	< 0.01	0.01	< 0.01	0.04	0.079	0.034	0.029	0.024
Li	ug/L	ICPMS	43	43	42	42	42	37.2	43	47	44	44
Lu	ug/L	ICPMS	-	-	-	-	-	< 0.1	-	-	-	-
Mg	mg/L	ICPAES	-	-	-	-	-	-	-	-	-	-
Mg	mg/L	ICPMS	2.4	2.4	2.3	2.3	2.3	1.76	2.1	2.1	2.1	2
Mn	ug/L	ICPMS	0.81	0.076	0.7	0.53	3.8	12.5	2.5	1.6	1.1	1.3
Mo	ug/L	ICPMS	3	2	1.7	1.8	1.6	< 2	4.7	2.8	2	1.8
Na	mg/L	ICPAES	-	-	-	-	-	-	-	-	-	-
Na	mg/L	ICPMS	9.1	9.2	9	9	8.9	10.1	7.9	8	8	7.8
Nb	ug/L	ICPMS	-	-	-	-	-	< 0.2	-	-	-	-
Nd	ug/L	ICPMS	0.01	0.02	0.01	< 0.01	0.01	0.08	0.091	0.032	0.027	0.022
Ni	ug/L	ICPMS	0.4	0.5	0.3	0.4	0.4	1.3	1.4	3	1.1	0.53
P	ug/L	ICPMS	9	6	5	3	< 3	0.02	7.6	5.3	5	1
Pb	ug/L	ICPMS	<0.05	<0.05	<0.05	<0.05	<0.05	1	<0.05	<0.05	<0.05	<0.05
Pr	ug/L	ICPMS	< 0.01	< 0.01	< 0.01	< 0.01	< 0.01	0.02	0.023	0.01	< 0.01	< 0.01
Rb	ug/L	ICPMS	4.8	4.9	4.8	4.8	4.7	7.16	4.7	4.6	4.5	4.6
Re	ug/L	ICPMS	< 0.02	< 0.02	< 0.02	< 0.02	< 0.02	-	< 0.02	< 0.02	< 0.02	< 0.02
Sb	ug/L	ICPMS	0.95	0.85	0.72	0.77	0.89	0.75	0.55	0.92	0.82	0.9
Sc	ug/L	ICPMS	-	-	-	-	-	2.5	-	-	-	-
Se	ug/L	ICPMS	< 0.2	< 0.2	< 0.2	< 0.2	< 0.2	< 1	< 0.2	< 0.2	< 0.2	< 0.2
SiO2	mg/L	ICPMS	10	10	9.9	9.1	9.4	10	9.2	8.5	8.3	8.4
Sm	ug/L	ICPMS	< 0.01	< 0.01	< 0.01	< 0.01	< 0.01	0.01	0.017	< 0.01	< 0.01	< 0.01
Sn	ug/L	ICPMS	-	-	-	-	-	-	-	-	-	-
Sr	ug/L	ICPMS	37	38	37	37	37	45.8	39	39	39	39
Ta	ug/L	ICPMS	-	-	-	-	-	< 0.02	-	-	-	-
Tb	ug/L	ICPMS	< 0.005	< 0.005	< 0.005	< 0.005	< 0.005	< 0.005	< 0.005	< 0.005	< 0.005	< 0.005
Te	ug/L	ICPMS	-	-	-	-	-	-	-	-	-	-
Th	ug/L	ICPMS	< 0.04	< 0.04	< 0.04	< 0.04	< 0.04	< 0.2	< 0.08	< 0.08	< 0.08	< 0.08
Ti	ug/L	ICPMS	-	-	-	-	-	< 0.5	-	-	-	-
Tl	ug/L	ICPMS	<0.05	<0.05	<0.05	<0.05	<0.05	< 0.1	<0.05	<0.05	<0.05	<0.05
Tm	ug/L	ICPMS	< 0.005	< 0.005	< 0.005	< 0.005	< 0.005	< 0.005	< 0.005	< 0.005	< 0.005	< 0.005
U	ug/L	ICPMS	0.005	< 0.005	< 0.005	< 0.005	< 0.005	< 0.1	0.055	0.023	0.015	0.012
V	ug/L	ICPMS	0.9	1	0.9	0.9	0.9	2.5	1.1	0.81	0.84	1.1
W	ug/L	ICPMS	4.2	3.1	3	2.7	2.5	0.82	2.2	2.3	2.2	2.2
Y	ug/L	ICPMS	0.01	0.02	< 0.01	< 0.01	0.01	0.04	0.082	0.032	0.027	0.024
Yb	ug/L	ICPMS	< 0.01	< 0.01	< 0.01	< 0.01	< 0.01	0.007	0.01	< 0.01	< 0.01	< 0.01
Zn	ug/L	ICPMS	0.5	<0.5	<0.5	<0.5	<0.5	31.4	5.1	5.9	5.8	5.4
Zr	ug/L	ICPMS	-	-	-	-	-	< 0.2	-	-	-	-
Hg	ng/L	Hg CVAF	20	10	22	20	16	-	-	-	-	-
$\delta^{18}O$ vs VSMOW	per mil	ISO1	-16.2	-16.3	-16.2	-15.9	-16.0	-	-16.2	-16.3	-16.1	-16.1
δD vs VSMOW	per mil	ISO2	-127.2	-127.4	-127	-125	-126.8	-	-130.3	-129.7	-128.5	-129.7
$\delta^{34}S_{H2S}$ vs CDT	per mil	ISO3	-	-	-	-	-	-	-	-	-	-
$\delta^{34}S_{SO4}$ vs CDT	per mil	ISO4	-	-	-	-	-	-	2.4	2.6	2.1	2.7
$\delta^{13}C_{CO2}$ vs VPDB	per mil	ISO5	-	-	-	-	-	-	-1.5	-6.9	-5.7	-3.4

Appendix 2. Site and analytical data from hydrothermal vents in Yellowstone Lake—*Continued*.

Field No. Description			D03-7.1 Inflated Plain-hydrothermal vent	D03-7.2 Inflated Plain-hydrothermal vent	D03-9.1 Inflated Plain-hydrothermal vent	D04-5.1 Inflated Plain: water sample in sediment plume just above vent	D04-5.2 Inflated Plain: water sample- bubbler from edge of plume hole	D04-7.1 Inflated Plain: water sample from bubbler	D04-9.1 Inflated Plain: same site as D02-12 and D03-7	D04-9.2 Inflated Plain: same site as D02-12 and D03-7	D04-12.3 Inflated Plain: same as D04-5	D02-5.1 Vent in Elliott's Crater
Latitude			44°32'9.281"N	44°32'9.281"N	44°32'5.489"N	44°32'4.98"N	44°32'4.98"N	44°32'10.163"N	44°32'15.521"N	44°32'15.521"N	44°32'8.135"N	44°31'46.4"N
Longitude			110°21'17.964"W	110°21'17.964"W	110°21'16.23"W	110°21'14.7"W	110°21'14.7"W	110°21'30.305"W	110°21'29.921"W	110°21'29.921"W	110°21'15.455"W	110°19'25.6"W
Date			8/14/03	8/14/03	8/17/03	8/10/04	8/10/04	8/11/04	8/13/04	8/13/04	8/13/04	8/20/02
Temp	˚C		70	99.3	87.4				12.1	15.2		57.2
pH			6.5	7.3	6.6	6.5	6.7	6.9	7.0	6.4	4.9	-
Depth	m		13.7	13.7	28.4	15.4	11.2	11.4	12.3	11.9	11.1	61
Treatment			Filtered	Filtered	Filtered	Filtered	Filtered	Filtered	Filtered	Filtered	Filtered	Filtered
sum CO2	mM		-	-	-	-	-	-	-	-	-	-
HCO3	mM	measured	-	-	-	0.50	0.52	0.42	0.52	0.52	-	-
HCO3	uM	calc	-	-	-	-	-	-	-	-	-	-
Cl	mg/L	IC-Aq	5	7.3	4.8	4.8	4.8	4.9	4.9	4.9	5.1	5
F	mg/L	IC-Aq	0.5	0.5	0.9	0.54	0.54	0.57	0.57	0.66	0.62	0.5
NO3	mg/L	IC-Aq	<.08	<.08	<.08	<.08	<.08	<.08	<.08	<.08	0.14	<.08
SO4	mg/L	IC-Aq	7.1	7.4	6.5	8.4	7.9	8.3	7.8	9.8	9.3	8.2
Ag	ug/L	ICPMS	<0.01	<0.01	0.012	<3	<3	<3	<3	<3	<3	< 3
Al	ug/L	ICPMS	7.1	3.6	4.2	4	2.7	2.5	4.3	9	432	3.4
As	ug/L	ICPMS	12	12	12	16.1	15.5	12.8	15.2	14.8	2	13.8
Au	ug/L	ICPMS	0.011	< 0.01	0.018	-	-	-	-	-	-	-
B	ug/L	ICPAES	-	-	-	-	-	-	-	-	-	-
Ba	ug/L	ICPMS	9.2	8.5	9.2	9.47	9.11	8.83	10.1	9.57	16.8	8.44
Be	ug/L	ICPMS	<0.05	<0.05	<0.05	<0.05	<0.05	<0.05	<0.05	<0.05	0.05	< 0.05
Bi	ug/L	ICPMS	< 0.03	< 0.03	< 0.03	< 0.2	< 0.2	< 0.2	< 0.2	< 0.2	< 0.2	< 0.2
Ca	mg/L	ICPAES	-	-	-	-	-	-	-	-	-	-
Ca	mg/L	ICPMS	4.2	4.3	4.4	5.43	5.45	4.86	5.23	5.18	5.13	5.1
Cd	ug/L	ICPMS	<0.02	<0.02	<0.02	<0.02	<0.02	<0.02	<0.02	<0.02	<0.02	< 0.02
Ce	ug/L	ICPMS	0.03	0.015	0.04	0.02	0.03	0.14	0.04	0.04	0.42	0.03
Co	ug/L	ICPMS	<0.02	<0.02	<0.02	0.03	0.06	0.31	0.03	0.04	0.02	0.02
Cr	ug/L	ICPMS	<1	<1	<1	<1	<1	<1	<1	<1	7.6	< 1
Cs	ug/L	ICPMS	2.4	2.4	2.5	2.73	2.78	2.65	2.79	2.76	3.61	2.24
Cu	ug/L	ICPMS	1.8	<0.5	<0.5	0.52	0.87	<0.5	<0.5	<0.5	<0.5	0.87
Dy	ug/L	ICPMS	< 0.005	< 0.005	< 0.005	< 0.005	< 0.005	0.008	< 0.005	0.005	0.02	< 0.005
Er	ug/L	ICPMS	< 0.005	< 0.005	< 0.005	< 0.005	< 0.005	0.005	< 0.005	< 0.005	0.02	< 0.005
Eu	ug/L	ICPMS	< 0.005	< 0.005	< 0.005	< 0.005	< 0.005	< 0.005	< 0.005	< 0.005	0.007	< 0.005
Fe	ug/L	ICPMS	<2	<2	<2	<50	<50	<50	<50	<50	78	< 50
Ga	ug/L	ICPMS	< 0.02	< 0.02	< 0.02	< 0.05	< 0.05	< 0.05	< 0.05	< 0.05	< 0.05	< 0.05
Gd	ug/L	ICPMS	< 0.005	< 0.005	0.007	< 0.005	< 0.005	0.01	0.005	< 0.005	0.03	0.006
Ge	ug/L	ICPMS	0.33	0.33	0.32	0.38	0.36	0.38	0.38	0.36	< 0.05	0.32
Hf	ug/L	ICPMS	7	<5	10							-
Ho	ug/L	ICPMS	< 0.005	< 0.005	< 0.005	< 0.005	< 0.005	< 0.005	< 0.005	< 0.005	0.005	< 0.005
In	ug/L	ICPMS	< 0.01	< 0.01	< 0.01	-	-	-	-	-	-	-
K	mg/L	ICPAES	-	-	-	-	-	-	-	-	-	-
K	ug/L	ICPMS	1500	1500	1500	1.79	1.81	1.71	1.72	1.7	2.4	1720
La	ug/L	ICPMS	0.023	0.011	0.031	0.02	0.02	0.07	0.03	0.02	0.16	0.04
Li	ug/L	ICPMS	42	42	43	46	46.4	45.9	45.6	45.5	47.2	41.2
Lu	ug/L	ICPMS	-	-	-	< 0.1	< 0.1	< 0.1	< 0.1	< 0.1	< 0.1	< 0.1
Mg	mg/L	ICPAES	-	-	-	-	-	-	-	-	-	-
Mg	mg/L	ICPMS	2	2	2	2.4	2.34	2.16	2.29	2.28	2.11	2.31
Mn	ug/L	ICPMS	1.2	1.1	1.2	1.3	1.4	48.9	2.4	2	19.2	1.6
Mo	ug/L	ICPMS	1.2	1.3	1.3	< 2	< 2	< 2	< 2	< 2	< 2	< 2
Na	mg/L	ICPAES	-	-	-	-	-	-	-	-	-	-
Na	mg/L	ICPMS	7.5	7.6	7.8	9.73	9.62	9.38	9.4	9.2	10.4	9.13
Nb	ug/L	ICPMS	-	-	-	< 0.2	< 0.2	< 0.2	< 0.2	< 0.2	< 0.2	< 0.2
Nd	ug/L	ICPMS	0.026	0.012	0.032	0.01	0.02	0.06	0.02	0.02	0.23	0.02
Ni	ug/L	ICPMS	0.61	0.72	0.52	1	1.1	0.8	0.6	0.7	1.1	0.6
P	ug/L	ICPMS	< 1	< 1	5	< 0.01	< 0.01	< 0.01	< 0.01	< 0.01	0.2	< 0.01
Pb	ug/L	ICPMS	<0.05	<0.05	<0.05	<0.05	<0.05	<0.05	<0.05	<0.05	<0.05	< 0.05
Pr	ug/L	ICPMS	< 0.01	< 0.01	< 0.01	< 0.01	< 0.01	0.02	< 0.01	< 0.01	0.06	< 0.01
Rb	ug/L	ICPMS	4.5	4.4	4.6	5.45	5.41	5.13	5.34	5.3	8.42	4.44
Re	ug/L	ICPMS	< 0.02	< 0.02	< 0.02	-	-	-	-	-	-	-
Sb	ug/L	ICPMS	0.71	1	0.69	0.87	0.84	1.18	0.85	0.76	<0.3	0.66
Sc	ug/L	ICPMS	-	-	-	0.8	0.7	0.7	0.7	0.7	2	1
Se	ug/L	ICPMS	< 0.2	< 0.2	< 0.2	< 1	< 1	< 1	< 1	< 1	< 1	< 1
SiO2	mg/L	ICPMS	8.4	8.4	8.1	10.4	9.8	9.6	9.9	9.8	27.1	3.8
Sm	ug/L	ICPMS	< 0.01	< 0.01	< 0.01	< 0.01	< 0.01	0.01	< 0.01	< 0.01	0.04	< 0.01
Sn	ug/L	ICPMS	-	-	-	-	-	-	-	-	-	-
Sr	ug/L	ICPMS	39	39	40	44.8	44	40.4	44.3	43.2	47.3	35.4
Ta	ug/L	ICPMS	-	-	-	0.08	0.07	0.06	0.04	0.03	0.02	0.04
Tb	ug/L	ICPMS	< 0.005	< 0.005	< 0.005	< 0.005	< 0.005	< 0.005	< 0.005	< 0.005	< 0.005	< 0.005
Te	ug/L	ICPMS	-	-	-	-	-	-	-	-	-	-
Th	ug/L	ICPMS	< 0.08	< 0.08	< 0.08	< 0.2	< 0.2	< 0.2	< 0.2	< 0.2	< 0.2	< 0.2
Ti	ug/L	ICPMS	-	-	-	< 0.5	< 0.5	< 0.5	< 0.5	< 0.5	< 0.5	< 0.5
Tl	ug/L	ICPMS	<0.05	<0.05	<0.05	<0.1	<0.1	<0.1	<0.1	<0.1	<0.1	< 0.1
Tm	ug/L	ICPMS	< 0.005	< 0.005	< 0.005	< 0.005	< 0.005	< 0.005	< 0.005	< 0.005	< 0.005	< 0.005
U	ug/L	ICPMS	0.0095	0.01	0.0077	< 0.1	< 0.1	< 0.1	< 0.1	< 0.1	< 0.1	< 0.1
V	ug/L	ICPMS	0.98	0.87	0.94	1.1	1	1.9	1	1.1	2.8	0.9
W	ug/L	ICPMS	2.1	2.1	2.2	1.81	1.6	2.11	1.6	1.55	1.08	1.81
Y	ug/L	ICPMS	0.021	0.014	0.028	0.02	0.02	0.06	0.03	0.02	0.15	0.04
Yb	ug/L	ICPMS	< 0.01	< 0.01	< 0.01	< 0.005	< 0.005	< 0.005	< 0.005	< 0.005	0.02	0.005
Zn	ug/L	ICPMS	0.85	2.7	1.4	3.9	5.5	1.7	1.4	1.9	1.6	3
Zr	ug/L	ICPMS	-	-	-	< 0.2	< 0.2	< 0.2	< 0.2	< 0.2	< 0.2	< 0.2
Hg	ng/L	Hg CVAF	-	-	-	<5	<5	<5	<5	<5		17
$\delta^{18}O$ vs VSMOW	per mil	ISO1	-16.0	-15.7	-16.1	-15.8	-15.8	-15.8	-15.8	-15.7	-16.0	-16.2
δD vs VSMOW	per mil	ISO2	-128.7	-123.5	-129.8	-128.8	-129.8	-128.2	-127.7	-127.0	-127.3	-126.9
$\delta^{34}S_{H2S}$ vs CDT	per mil	ISO3	-	-	-	-	-	-	-	-	-	-
$\delta^{34}S_{SO4}$ vs CDT	per mil	ISO4	2.7	2.4	-	-	-	-	-	-	-	-
$\delta^{13}C_{TDIC}$ vs VPDB	per mil	ISO5	-2.5	-4.0	-4.8							-

Appendix 2. Site and analytical data from hydrothermal vents in Yellowstone Lake—*Continued*.

Field No. Description			D02-3.1 Elliott's Crater rim- Sucker Vent	D02-3.2 Elliott's Crater rim- Sucker Vent	D02-4.1 Elliott's Crater rim- Sucker Vent	D02-4.2 Elliott's Crater rim- Sucker Vent	D03-4.1 Elliott's Crater rim- Sucker Vent	D03-4.2 Elliott's Crater rim- Sucker Vent	D03-5.1 Elliott's Crater rim- Sucker Vent	D03-5.2 Elliott's Crater rim- Sucker Vent	D04-2.1 Chico/Sucker: water sample- vent	D04-6.1 Bubbler N of Stevenson: water sample- new bubbler near edge of lava flow
Latitude			44°31'39.6"N	44°31'39.6"N	44°31'39.6"N	44°31'39.6"N	44°31'39.694"N	44°31'39.695"N	44°31'39.695"N	44°31'39.695"N	44°31'39.179"N	44°32'5.927"N
Longitude			110°19'29.6"W	110°19'29.6"W	110°19'29.6"W	110°19'29.6"W	110°19'30.138"W	110°19'30.138"W	110°19'30.138"W	10°19'30.138"V	110°19'30.24"W	110°22'45.299"W
Date			8/19/02	8/19/02	8/19/02	8/19/02	8/12/03	8/12/03	8/12/03	8/12/03	8/9/04	8/11/04
Temp	˚C		91.1	29.1	59.1	82.2	61	61	96	30		
pH			-	-	-	-	7	7.5	7.1	7.5	6.9	7.2
Depth	m		12	12	14	13	10.2	-	11.1	-	11.9	36.3
Treatment			Filtered	Filtered	Filtered	Filtered	Filtered	Filtered	Filtered	Filtered	Filtered	Filtered
sum CO2	mM		-	-	-	-	-	-	-	-	-	-
HCO3	mM	measured	-	-	-	-	-	-	-	-	0.50	0.48
HCO3	uM	calc	-	-	-	-	-	-	-	-	-	-
Cl	mg/L	IC-Aq	5.7	23	7.3	15	4.7	4.7	4.9	6.9	6.7	4.9
F	mg/L	IC-Aq	0.5	0.8	0.5	0.6	0.5	0.5	0.5	0.5	0.54	0.55
NO3	mg/L	IC-Aq	<.08	<.08	0.4	<.08	<.08	<.08	<.08	<.08	<.08	<.08
SO4	mg/L	IC-Aq	7.6	12	8	9.8	9.4	7.4	9.3	7.4	7.8	7.5
Ag	ug/L	ICPMS	< 3	< 3	< 3	< 3	<0.01	<0.01	<0.01	<0.01	<3	<3
Al	ug/L	ICPMS	6.2	8	60.3	5.6	3.6	2.9	3.2	3.4	4.8	2.1
As	ug/L	ICPMS	13.7	41.5	17.2	33.9	16	13	18	13	17.9	16.5
Au	ug/L	ICPMS	-	-	-	-	< 0.01	< 0.01	< 0.01	< 0.01	-	-
B	ug/L	ICPAES	-	-	-	-	-	-	-	-	-	-
Ba	ug/L	ICPMS	10.2	44.7	14.3	32.2	13	8.9	14	8.9	13	10.5
Be	ug/L	ICPMS	< 0.05	< 0.05	< 0.05	< 0.05	<0.05	<0.05	<0.05	<0.05	<0.05	<0.05
Bi	ug/L	ICPMS	< 0.2	< 0.2	< 0.2	< 0.2	< 0.03	< 0.03	< 0.03	< 0.03	< 0.2	< 0.2
Ca	mg/L	ICPAES	-	-	-	-	-	-	-	-	-	-
Ca	mg/L	ICPMS	4.1	6.2	4.3	5.3	4.5	4.2	4.5	4.2	5.6	5.45
Cd	ug/L	ICPMS	< 0.02	< 0.02	< 0.02	< 0.02	<0.02	<0.02	<0.02	<0.02	<0.02	<0.02
Ce	ug/L	ICPMS	0.02	0.03	0.04	0.03	0.021	0.013	0.028	0.022	0.01	0.04
Co	ug/L	ICPMS	< 0.02	0.02	0.23	0.02	<0.02	<0.02	<0.02	<0.02	0.05	0.03
Cr	ug/L	ICPMS	< 1	< 1	< 1	< 1	<1	<1	<1	<1	<1	<1
Cs	ug/L	ICPMS	3.18	15.6	4.49	9.94	4.2	2.6	4.9	2.6	4.28	2.73
Cu	ug/L	ICPMS	< 0.5	0.5	0.53	< 0.5	<0.5	0.51	0.5	<0.5	<0.5	0.54
Dy	ug/L	ICPMS	< 0.005	< 0.005	< 0.005	< 0.005	< 0.005	< 0.005	0.005	< 0.005	< 0.005	0.005
Er	ug/L	ICPMS	< 0.005	< 0.005	< 0.005	< 0.005	< 0.005	< 0.005	< 0.005	< 0.005	< 0.005	< 0.005
Eu	ug/L	ICPMS	< 0.005	< 0.005	< 0.005	< 0.005	< 0.005	< 0.005	< 0.005	< 0.005	< 0.005	< 0.005
Fe	ug/L	ICPMS	< 50	< 50	56	< 50	<2	<2	<2	<2	<50	<50
Ga	ug/L	ICPMS	< 0.05	0.07	0.05	< 0.05	0.027	< 0.02	0.026	< 0.02	< 0.05	< 0.05
Gd	ug/L	ICPMS	< 0.005	< 0.005	< 0.005	< 0.005	< 0.005	< 0.005	< 0.005	< 0.005	< 0.005	0.007
Ge	ug/L	ICPMS	0.33	1.5	0.46	0.98	0.53	0.34	0.56	0.33	0.54	0.4
Hf	ug/L	ICPMS	-	-	-	-	<5	<5	<5	<5		
Ho	ug/L	ICPMS	< 0.005	< 0.005	< 0.005	< 0.005	< 0.005	< 0.005	< 0.005	< 0.005	< 0.005	< 0.005
In	ug/L	ICPMS	-	-	-	-	< 0.01	< 0.01	< 0.01	< 0.01	-	-
K	mg/L	ICPAES	-	-	-	-	-	-	-	-	-	-
K	ug/L	ICPMS	1430	3160	1610	2470	1700	1500	1800	1500	2	1.8
La	ug/L	ICPMS	0.02	0.02	0.03	0.02	0.019	0.016	0.022	0.015	0.01	0.04
Li	ug/L	ICPMS	47	158	58.5	108	59	46	62	44	60.3	47.2
Lu	ug/L	ICPMS	< 0.1	< 0.1	0.5	< 0.1	-	-	-	-	< 0.1	< 0.1
Mg	mg/L	ICPAES	-	-	-	-	-	-	-	-	-	-
Mg	mg/L	ICPMS	2.04	2.84	2.12	2.55	2.1	2	2.2	2	2.46	2.39
Mn	ug/L	ICPMS	1.6	16.2	4.1	12.9	3	1	4	0.96	3	4
Mo	ug/L	ICPMS	< 2	< 2	< 2	< 2	1.6	1.6	1.4	1.4	< 2	< 2
Na	mg/L	ICPAES	-	-	-	-	-	-	-	-	-	-
Na	mg/L	ICPMS	8.99	26.8	16.9	18.9	10	8	11	7.9	12	9.7
Nb	ug/L	ICPMS	< 0.2	< 0.2	< 0.2	< 0.2	-	-	-	-	< 0.2	< 0.2
Nd	ug/L	ICPMS	0.01	0.01	0.02	0.02	0.018	0.012	0.02	0.02	< 0.01	0.03
Ni	ug/L	ICPMS	0.6	0.6	190	0.5	0.78	0.79	0.4	0.51	1	0.9
P	ug/L	ICPMS	< 0.01	< 0.01	< 0.01	< 0.01	< 1	< 1	4	< 1	< 0.01	< 0.01
Pb	ug/L	ICPMS	< 0.05	< 0.05	< 0.05	< 0.05	<0.05	<0.05	<0.05	<0.05	<0.05	<0.05
Pr	ug/L	ICPMS	< 0.01	< 0.01	< 0.01	< 0.01	< 0.01	< 0.01	< 0.01	< 0.01	< 0.01	< 0.01
Rb	ug/L	ICPMS	5.02	15	6.2	11	6	4.6	6.3	4.7	6.49	5.54
Re	ug/L	ICPMS	-	-	-	-	< 0.02	< 0.02	< 0.02	< 0.02	-	-
Sb	ug/L	ICPMS	1.56	2.64	1.3	2.15	0.92	1.2	1.3	1.1	1.04	0.84
Sc	ug/L	ICPMS	1.3	4.2	1.6	2.9	-	-	-	-	1.1	0.8
Se	ug/L	ICPMS	< 1	< 1	< 1	< 1	< 0.2	< 0.2	< 0.2	< 0.2	< 1	< 1
SiO2	mg/L	ICPMS	4.6	16.6	5.7	11.2	12	8.6	12	8.4	14	10
Sm	ug/L	ICPMS	< 0.01	< 0.01	< 0.01	< 0.01	< 0.01	< 0.01	< 0.01	< 0.01	< 0.01	< 0.01
Sn	ug/L	ICPMS	-	-	-	-	-	-	-	-	-	-
Sr	ug/L	ICPMS	38.6	89.4	45.2	69.2	46	40	47	40	49.9	44.9
Ta	ug/L	ICPMS	0.04	0.04	0.04	0.04	-	-	-	-	0.08	0.07
Tb	ug/L	ICPMS	< 0.005	< 0.005	< 0.005	< 0.005	< 0.005	< 0.005	< 0.005	< 0.005	< 0.005	< 0.005
Te	ug/L	ICPMS	-	-	-	-	-	-	-	-	-	-
Th	ug/L	ICPMS	< 0.2	< 0.2	< 0.2	< 0.2	< 0.08	< 0.08	< 0.08	< 0.08	< 0.2	< 0.2
Ti	ug/L	ICPMS	< 0.5	< 0.5	2.2	< 0.5	-	-	-	-	< 0.5	< 0.5
Tl	ug/L	ICPMS	< 0.1	< 0.1	< 0.1	< 0.1	<0.05	<0.05	<0.05	<0.05	<0.1	<0.1
Tm	ug/L	ICPMS	< 0.005	< 0.005	< 0.005	< 0.005	< 0.005	< 0.005	< 0.005	< 0.005	< 0.005	< 0.005
U	ug/L	ICPMS	< 0.1	< 0.1	< 0.1	< 0.1	0.013	0.012	0.012	0.013	< 0.1	< 0.1
V	ug/L	ICPMS	0.9	0.8	1	1	0.88	0.89	0.9	0.89	1	1
W	ug/L	ICPMS	1.41	3.94	2.14	3.24	2.7	2.3	2.9	2.3	1.59	1.52
Y	ug/L	ICPMS	0.01	0.02	0.02	0.02	0.018	0.015	0.021	0.017	0.01	0.05
Yb	ug/L	ICPMS	< 0.005	< 0.005	< 0.005	< 0.005	< 0.01	< 0.01	< 0.01	< 0.01	< 0.005	< 0.005
Zn	ug/L	ICPMS	< 0.5	0.8	3.3	< 0.5	4.8	5.1	3.1	2.9	0.8	1.8
Zr	ug/L	ICPMS	< 0.2	< 0.2	< 0.2	< 0.2	-	-	-	-	< 0.2	< 0.2
Hg	ng/L	Hg CVAF	< 5	18	10	15	-	-	-	-	<5	<5
$\delta^{18}O$ vs VSMOW	per mil	ISO1	-16.1	-16.3	-16.1	-16.2	-16.2	-16.2	-16.2	-16.1	-15.8	-15.9
δD vs VSMOW	per mil	ISO2	-127	-130.6	-126.8	-131.1	-131.7	-128.5	-130.7	-130	-129.5	-125.4
$\delta^{34}S_{H2S}$ vs CDT	per mil	ISO3	-	-	-	-	-	-	-	-	-	-
$\delta^{34}S_{SO4}$ vs CDT	per mil	ISO4	-	-	-	-	2.4	2.4	2.4	2.2	-	-
$\delta^{13}C_{CO2}$ vs VPDB	per mil	ISO5	-	-	-	-	-4.6	-	-4.7	-7.0		

Appendix 3. Site and analytical data from the 1999 mixing experiments.

Field no. Sample name/ description			G1 diss Norris/Green Dragon	G1 tot Norris/Green Dragon	G2 diss Norris/Green Dragon	G2 tot Norris/Green Dragon	G3 diss Norris/Green Dragon	G3 tot Norris/Green Dragon	G4 diss Norris/Green Dragon
Latitude			44°43'12.2"N	44°43'12.2"N	44°43'12.2"N	44°43'12.2"N	44°43'12.2"N	44°43'12.2"N	44°43'12.2"N
Longitude			110°42'23"W	110°42'23"W	110°42'23"W	110°42'23"W	110°42'23"W	110°42'23"W	110°42'23"W
Collection date			07/22/99	07/22/99	07/23/99	07/23/99	07/23/99	07/23/99	07/23/99
Temp at filter	°C		16.1	16.1	19.1	19.1	17.5	17.5	20.4
pH			7.2	7.2	6.6	6.6	6.2	6.2	5.3
Conductivity	uS/cm		87	87	162	162	223	223	395
Cl	mg/L	IC-Aq	4.7	-	21	-	37	-	80
F	mg/L	IC-Aq	0.5	-	0.8	-	1	-	1.6
NO_3	mg/L	IC-Aq	<.35	-	<.35	-	<.35	-	<.35
SO_4	mg/L	IC-Aq	7.2	-	14	-	20	-	37
Ag	ug/L	ICPMS	<0.01	<0.01	<0.01	<0.01	<0.01	<0.01	<0.01
Al	ug/L	ICPMS	2.4	2	120	140	190	240	570
As	ug/L	ICPMS	11	11	81	82	140	140	310
Au	ug/L	ICPMS	< 0.01	< 0.01	< 0.01	< 0.01	< 0.01	< 0.01	< 0.01
B	ug/L	ICPAES	89.4	82.4	355	354	603	602	1260
Ba	ug/L	ICPMS	8.5	8.4	10	10	11	11	14
Be	ug/L	ICPMS	<0.05	<0.05	0.1	0.09	0.2	0.1	0.5
Bi	ug/L	ICPMS	< 0.01	< 0.01	< 0.01	< 0.01	< 0.01	< 0.01	< 0.01
Ca	mg/L	ICPAES	5.1	5.1	5.04	4.91	5.02	5.06	4.82
Cd	ug/L	ICPMS	<0.02	<0.02	<0.02	<0.02	<0.02	<0.02	<0.02
Ce	ug/L	ICPMS	0.03	0.03	0.4	0.5	0.79	0.86	1.9
Co	ug/L	ICPMS	<0.02	<0.02	<0.02	<0.02	<0.02	<0.02	<0.02
Cr	ug/L	ICPMS	<1	<1	<1	<1	<1	<1	<1
Cs	ug/L	ICPMS	2.2	2.2	17	17	29	29	62
Cu	ug/L	ICPMS	<0.5	<0.5	<0.5	<0.5	<0.5	<0.5	<0.5
Dy	ug/L	ICPMS	< 0.005	0.005	0.052	0.054	0.088	0.11	0.21
Er	ug/L	ICPMS	0.005	< 0.005	0.03	0.04	0.054	0.053	0.12
Eu	ug/L	ICPMS	< 0.005	< 0.005	< 0.005	< 0.005	< 0.005	< 0.005	0.01
Fe	ug/L	ICPMS	<30	<30	<30	<30	<30	<30	100
Ga	ug/L	ICPMS	< 0.02	< 0.02	< 0.02	0.02	0.03	0.04	0.04
Gd	ug/L	ICPMS	< 0.005	< 0.005	0.066	0.054	0.093	0.091	0.21
Ge	ug/L	ICPMS	0.2	0.2	1.3	1.3	2.1	2.1	4.6
Ho	ug/L	ICPMS	< 0.005	< 0.005	0.01	0.02	0.02	0.02	0.04
K	mg/L	ICPAES	1.7	1.6	3.72	3.84	5.8	5.62	10.8
La	ug/L	ICPMS	0.03	0.02	0.2	0.3	0.4	0.4	0.9
Li	ug/L	ICPMS	42	42	210	210	350	340	740
Mg	mg/L	ICPAES	2.23	2.18	2.06	2.09	2.04	2	1.78
Mn	ug/L	ICPMS	0.45	0.48	7.2	7.4	13	13	29
Mo	ug/L	ICPMS	0.95	0.92	1.9	2	2.9	3	5.8
Na	mg/L	ICPAES	8.75	8.48	20.3	19.7	29.8	30	55.2
Nb	ug/L	ICPMS	0.07	0.06	0.07	0.05	0.06	0.05	0.06
Nd	ug/L	ICPMS	0.04	0.03	0.22	0.25	0.36	0.42	0.86
Ni	ug/L	ICPMS	0.4	0.4	0.4	0.4	0.3	0.4	0.3
P	ug/L	ICPMS	1	4	4.2	4	< 1	3	4
Pb	ug/L	ICPMS	<0.05	<0.05	<0.05	<0.05	<0.05	<0.05	<0.05
Pr	ug/L	ICPMS	< 0.01	< 0.01	0.05	0.06	0.1	0.1	0.21
Rb	ug/L	ICPMS	4.1	4.1	21	22	35	36	76
Sb	ug/L	ICPMS	0.47	0.45	2.1	2.1	3.4	3.4	5.8
Sc	ug/L	ICPMS	0.2	0.2	0.2	0.1	< 0.1	< 0.1	< 0.1
Se	ug/L	ICPMS	< 0.3	< 0.3	< 0.3	< 0.3	0.3	0.4	0.9
SiO_2	mg/L	ICPMS	9.7	9.8	25	25	38	37	74
Sm	ug/L	ICPMS	< 0.01	< 0.01	0.06	0.05	0.08	0.09	0.2
Sr	ug/L	ICPMS	36	36	34	35	33	34	31
Ta	ug/L	ICPMS	0.04	0.05	0.06	0.08	0.08	0.04	0.06
Tb	ug/L	ICPMS	< 0.005	< 0.005	0.009	0.009	0.02	0.01	0.04
Th	ug/L	ICPMS	< 0.02	< 0.02	< 0.02	< 0.02	< 0.02	< 0.02	< 0.02
Ti	ug/L	ICPMS	< 0.2	< 0.2	< 0.2	< 0.2	< 0.2	< 0.2	< 0.2
Tl	ug/L	ICPMS	<0.05	<0.05	<0.05	<0.05	<0.05	<0.05	0.1
Tm	ug/L	ICPMS	< 0.005	< 0.005	< 0.005	< 0.005	0.008	0.007	0.02
U	ug/L	ICPMS	0.01	0.02	0.02	0.02	0.02	0.03	0.03
V	ug/L	ICPMS	0.77	0.76	0.85	0.74	0.76	0.7	0.8
W	ug/L	ICPMS	0.89	0.97	2.6	2.8	4.5	4.6	9.4
Y	ug/L	ICPMS	0.03	0.03	0.3	0.3	0.4	0.53	1.2
Yb	ug/L	ICPMS	< 0.01	< 0.01	0.02	0.03	0.05	0.06	0.1
Zn	ug/L	ICPMS	<0.5	<0.5	<0.5	<0.5	<0.5	<0.5	2
Zr	ug/L	ICPMS	< 0.2	< 0.2	< 0.2	< 0.2	< 0.2	< 0.2	< 0.2
Hg	ng/L	Hg CVAF	<5	<5	9	<5	6	6	26
$\delta^{18}O$ vs VSMOW	permil	ISO1	-16.72	-	-16.28	-	-16.08	-	-15.41

Appendix 3. Site and analytical data from the 1999 mixing experiments—*Continued*.

Field no. Sample name/ description			G4 tot Norris/Green Dragon	G5 diss Norris/Green Dragon	G5 tot Norris/Green Dragon	G6 diss Norris/Green Dragon	G6 tot Norris/Green Dragon	G7 diss Norris/Green Dragon	G7 tot Norris/Green Dragon
Latitude			44°43'12.2"N	44°43'12.2"N	44°43'12.2"N	44°43'12.2"N	44°43'12.2"N	44°43'12.2"N	44°43'12.2"N
Longitude			110°42'23"W	110°42'23"W	110°42'23"W	110°42'23"W	110°42'23"W	110°42'23"W	110°42'23"W
Collection date			07/23/99	07/23/99	07/23/99	07/23/99	07/23/99	07/23/99	07/23/99
Temp at filter	°C		20.4	25.6	25.6	24.9	24.9	26.5	26.5
pH			5.3	3.6	3.6	3.1	3.1	2.9	2.9
Conductivity	uS/cm		395	665	665	965	965	1285	1285
Cl	mg/L	IC-Aq	-	130	-	190	-	240	-
F	mg/L	IC-Aq	-	1.6	-	2.1	-	2.7	-
NO_3	mg/L	IC-Aq	-	<.35	-	0.7	-	<.35	-
SO_4	mg/L	IC-Aq	-	57	-	78	-	100	-
Ag	ug/L	ICPMS	<0.01	<0.01	<0.01	0.01	<0.01	<0.01	<0.01
Al	ug/L	ICPMS	560	980	980	1900	1900	2500	2500
As	ug/L	ICPMS	320	520	520	860	870	1100	1100
Au	ug/L	ICPMS	< 0.01	< 0.01	< 0.01	< 0.01	< 0.01	< 0.01	< 0.01
B	ug/L	ICPAES	1260	2080	2090	2860	2900	3670	3680
Ba	ug/L	ICPMS	14	18	18	23	23	26	26
Be	ug/L	ICPMS	0.4	0.7	0.9	1.7	1.7	1.9	2
Bi	ug/L	ICPMS	< 0.01	< 0.01	< 0.01	< 0.01	< 0.01	< 0.01	< 0.01
Ca	mg/L	ICPAES	4.82	4.72	4.63	4.54	4.5	4.4	4.32
Cd	ug/L	ICPMS	<0.02	<0.02	<0.02	<0.02	<0.02	<0.02	<0.02
Ce	ug/L	ICPMS	1.9	3.2	3.2	4.6	4.9	6.1	6.1
Co	ug/L	ICPMS	<0.02	<0.02	<0.02	<0.02	<0.02	<0.02	<0.02
Cr	ug/L	ICPMS	<1	<1	<1	<1	<1	<1	<1
Cs	ug/L	ICPMS	63	100	100	150	150	200	200
Cu	ug/L	ICPMS	<0.5	<0.5	<0.5	<0.5	<0.5	<0.5	<0.5
Dy	ug/L	ICPMS	0.23	0.36	0.4	0.53	0.57	0.71	0.74
Er	ug/L	ICPMS	0.13	0.23	0.21	0.28	0.31	0.39	0.41
Eu	ug/L	ICPMS	0.01	0.02	0.006	0.02	0.02	0.02	0.03
Fe	ug/L	ICPMS	100	190	190	360	370	480	480
Ga	ug/L	ICPMS	0.05	0.07	0.08	0.1	0.1	0.2	0.2
Gd	ug/L	ICPMS	0.18	0.33	0.32	0.47	0.47	0.62	0.55
Ge	ug/L	ICPMS	4.6	7.4	7.5	12	13	16	16
Ho	ug/L	ICPMS	0.04	0.072	0.068	0.1	0.11	0.15	0.14
K	mg/L	ICPAES	10.9	17.2	17.2	24.2	24	31.2	30.6
La	ug/L	ICPMS	0.95	1.6	1.6	2.3	2.3	3	3
Li	ug/L	ICPMS	750	1200	1200	2500	2600	3400	3500
Mg	mg/L	ICPAES	1.78	1.51	1.51	1.24	1.25	0.953	0.949
Mn	ug/L	ICPMS	28	48	48	83	82	110	100
Mo	ug/L	ICPMS	6	9.5	11	15	16	20	21
Na	mg/L	ICPAES	55.6	88.2	86.8	120	122	154	151
Nb	ug/L	ICPMS	0.05	0.06	0.06	0.08	0.08	0.09	0.08
Nd	ug/L	ICPMS	0.87	1.4	1.6	2	2	2.5	2.7
Ni	ug/L	ICPMS	0.3	0.2	0.2	0.2	0.2	0.2	0.2
P	ug/L	ICPMS	4.3	8.1	7.6	21	21	20	20
Pb	ug/L	ICPMS	0.08	0.2	0.2	0.2	0.2	0.3	0.3
Pr	ug/L	ICPMS	0.22	0.37	0.4	0.55	0.55	0.72	0.72
Rb	ug/L	ICPMS	76	120	120	200	200	250	250
Sb	ug/L	ICPMS	5.6	4.8	5.9	7.2	7	7.9	7.2
Sc	ug/L	ICPMS	< 0.1	< 0.1	< 0.1	< 0.1	< 0.1	< 0.1	< 0.1
Se	ug/L	ICPMS	1.2	1.8	1.9	2.9	2.7	3.8	3.8
SiO_2	mg/L	ICPMS	74	120	120	230	230	300	300
Sm	ug/L	ICPMS	0.23	0.33	0.32	0.43	0.52	0.55	0.57
Sr	ug/L	ICPMS	31	27	27	27	27	22	23
Ta	ug/L	ICPMS	0.05	0.06	0.05	0.04	0.04	0.04	0.04
Tb	ug/L	ICPMS	0.03	0.054	0.063	0.084	0.088	0.11	0.11
Th	ug/L	ICPMS	< 0.02	< 0.02	< 0.02	< 0.02	< 0.02	< 0.02	< 0.02
Ti	ug/L	ICPMS	0.3	0.5	0.6	1.2	1.3	1.6	1.6
Tl	ug/L	ICPMS	0.1	0.2	0.2	0.3	0.3	0.4	0.4
Tm	ug/L	ICPMS	0.02	0.03	0.03	0.04	0.05	0.058	0.058
U	ug/L	ICPMS	0.04	0.05	0.07	0.06	0.08	0.08	0.09
V	ug/L	ICPMS	0.82	0.78	0.84	1.3	1.3	1.3	1.3
W	ug/L	ICPMS	9.7	15	18	21	24	30	32
Y	ug/L	ICPMS	1.2	1.9	2	3.2	3.3	4.2	4.3
Yb	ug/L	ICPMS	0.1	0.2	0.2	0.24	0.26	0.3	0.31
Zn	ug/L	ICPMS	2	3	3	5	5	7	6
Zr	ug/L	ICPMS	< 0.2	< 0.2	< 0.2	< 0.2	< 0.2	< 0.2	< 0.2
Hg	ng/L	Hg CVAF	21	51	35	25	55	7	62
$\delta^{18}O$ vs VSMOW	permil	ISO1	-	-14.62	-	-14.05	-	-13.70	-

Appendix 3. Site and analytical data from the 1999 mixing experiments—*Continued*.

Field no. Sample name/ description			G8 diss Norris/Green Dragon	G8 tot Norris/Green Dragon	G9 diss Norris/Green Dragon	G9 tot Norris/Green Dragon	G10 diss Norris/Green Dragon	G10 tot Norris/Green Dragon	E1 diss Norris/Echinus
Latitude			44°43'12.2"N	44°43'12.2"N	44°43'12.2"N	44°43'12.2"N	44°43'12.2"N	44°43'12.2"N	44°43'19.5"N
Longitude			110°42'23"W	110°42'23"W	110°42'23"W	110°42'23"W	110°42'23"W	110°42'23"W	110°42'4.9"W
Collection date			07/23/99	07/23/99	07/23/99	07/23/99	07/23/99	07/23/99	07/22/99
Temp at filter	°C		30.6	30.6	32.1	32.1	30.1	30.1	19.9
pH			2.7	2.7	2.6	2.6	2.6	2.6	7.3
Conductivity	uS/cm		1603	1603	1785	1785	1984	1984	87
Cl	mg/L	IC-Aq	300	-	330	-	330	-	4.5
F	mg/L	IC-Aq	3.1	-	5.6	-	5.6	-	0.4
NO_3	mg/L	IC-Aq	<.35	-	<.35	-	<.35	-	<.35
SO_4	mg/L	IC-Aq	120	-	130	-	150	-	7.2
Ag	ug/L	ICPMS	0.01	0.01	<0.01	<0.01	<0.01	0.01	<0.01
Al	ug/L	ICPMS	3100	3200	3600	3500	4000	4000	1
As	ug/L	ICPMS	1400	1400	1500	1500	1700	1700	24
Au	ug/L	ICPMS	< 0.01	< 0.01	< 0.01	< 0.01	< 0.01	< 0.01	< 0.01
B	ug/L	ICPAES	4370	4440	4920	4930	5430	5460	124
Ba	ug/L	ICPMS	31	30	32	32	35	35	8.9
Be	ug/L	ICPMS	2.8	2.8	2.6	3.4	3.5	3.6	<0.05
Bi	ug/L	ICPMS	< 0.01	< 0.01	< 0.01	< 0.01	< 0.01	< 0.01	< 0.01
Ca	mg/L	ICPAES	4.23	4.21	4.18	4.07	4.02	4.02	5
Cd	ug/L	ICPMS	<0.02	<0.02	<0.02	<0.02	<0.02	<0.02	<0.02
Ce	ug/L	ICPMS	7.5	7.4	8.3	8.3	9.1	9	0.02
Co	ug/L	ICPMS	<0.02	<0.02	<0.02	<0.02	<0.02	<0.02	<0.02
Cr	ug/L	ICPMS	<1	<1	<1	<1	<1	<1	<1
Cs	ug/L	ICPMS	240	240	260	270	300	300	2.3
Cu	ug/L	ICPMS	<0.5	<0.5	<0.5	<0.5	<0.5	<0.5	<0.5
Dy	ug/L	ICPMS	0.87	0.85	0.94	0.95	1	1	0.005
Er	ug/L	ICPMS	0.49	0.45	0.5	0.53	0.55	0.57	< 0.005
Eu	ug/L	ICPMS	0.03	0.03	0.03	0.03	0.04	0.03	< 0.005
Fe	ug/L	ICPMS	600	600	660	660	750	750	<30
Ga	ug/L	ICPMS	0.2	0.2	0.2	0.2	0.3	0.2	< 0.02
Gd	ug/L	ICPMS	0.75	0.75	0.79	0.84	0.84	0.94	0.008
Ge	ug/L	ICPMS	20	20	22	23	25	25	0.2
Ho	ug/L	ICPMS	0.19	0.18	0.19	0.19	0.2	0.21	< 0.005
K	mg/L	ICPAES	37.6	37.4	42	41	45.8	45.7	1.68
La	ug/L	ICPMS	3.7	3.7	4	4	4.4	4.5	0.03
Li	ug/L	ICPMS	4300	4700	5400	5500	6200	6400	44
Mg	mg/L	ICPAES	0.659	0.671	0.502	0.505	0.316	0.316	2.19
Mn	ug/L	ICPMS	130	130	140	140	160	160	0.38
Mo	ug/L	ICPMS	26	26	28	29	32	33	5.9
Na	mg/L	ICPAES	186	188	206	203	224	227	9.19
Nb	ug/L	ICPMS	0.1	0.08	0.09	0.08	0.08	0.08	< 0.02
Nd	ug/L	ICPMS	3.3	3.2	3.6	3.6	3.9	4	0.03
Ni	ug/L	ICPMS	0.1	0.1	<0.1	0.1	<0.1	<0.1	0.3
P	ug/L	ICPMS	21	20	19	17	17	15	< 1
Pb	ug/L	ICPMS	0.4	0.4	0.6	0.5	0.52	0.5	<0.05
Pr	ug/L	ICPMS	0.86	0.87	0.97	0.95	1	1.1	< 0.01
Rb	ug/L	ICPMS	310	310	350	350	390	390	4.2
Sb	ug/L	ICPMS	8	5.6	6.4	4.2	5.6	6	1.7
Sc	ug/L	ICPMS	< 0.1	< 0.1	< 0.1	< 0.1	< 0.1	< 0.1	< 0.1
Se	ug/L	ICPMS	4.4	4.5	4.7	4.4	4.7	4.5	< 0.3
SiO_2	mg/L	ICPMS	370	380	420	420	470	480	8.9
Sm	ug/L	ICPMS	0.75	0.73	0.8	0.82	0.84	0.88	< 0.01
Sr	ug/L	ICPMS	18	18	16	16	13	13	36
Ta	ug/L	ICPMS	0.06	0.04	0.05	0.05	0.05	0.05	< 0.03
Tb	ug/L	ICPMS	0.13	0.13	0.15	0.15	0.16	0.16	< 0.005
Th	ug/L	ICPMS	< 0.02	< 0.02	< 0.02	< 0.02	< 0.02	< 0.02	< 0.02
Ti	ug/L	ICPMS	2.1	1.7	2.1	2	2.1	2.3	< 0.2
Tl	ug/L	ICPMS	0.5	0.5	0.52	0.52	0.58	0.58	<0.05
Tm	ug/L	ICPMS	0.065	0.07	0.078	0.074	0.087	0.083	< 0.005
U	ug/L	ICPMS	0.11	0.12	0.12	0.12	0.13	0.14	0.01
V	ug/L	ICPMS	1.4	1.4	1.4	1.3	1.4	1.4	0.92
W	ug/L	ICPMS	40	40	43	45	50	50	11
Y	ug/L	ICPMS	5.2	5.2	5.8	5.9	6.6	6.6	0.02
Yb	ug/L	ICPMS	0.4	0.37	0.44	0.45	0.51	0.5	< 0.01
Zn	ug/L	ICPMS	8	8	9	9	10	10	<0.5
Zr	ug/L	ICPMS	< 0.2	< 0.2	< 0.2	< 0.2	0.86	< 0.2	< 0.2
Hg	ng/L	Hg CVAF	8	71	10	67	7	80	330
$\delta^{18}O$ vs VSMOW	permil	ISO1	-12.56	-	-12.09	-	-11.59	-	-16.65

Appendix 3. Site and analytical data from the 1999 mixing experiments—*Continued*.

Field no. Sample name/ description			E1 tot Norris/Echinus	E2 diss Norris/Echinus	E2 tot Norris/Echinus	E3 diss Norris/Echinus	E3 tot Norris/Echinus	E4 diss Norris/Echinus
Latitude			44°43'19.5"N	44°43'19.5"N	44°43'19.5"N	44°43'19.5"N	44°43'19.5"N	44°43'19.5"N
Longitude			110°42'4.9"W	110°42'4.9"W	110°42'4.9"W	110°42'4.9"W	110°42'4.9"W	110°42'4.9"W
Collection date			07/22/99	07/23/99	07/23/99	07/23/99	07/23/99	07/23/99
Temp at filter	°C		19.9	20.2	20.2	21.7	21.7	20.2
pH			7.3	6.8	6.8	6.7	6.7	6.2
Conductivity	uS/cm		87	158	158	196	196	313
Cl	mg/L	IC-Aq	-	13	-	17	-	34
F	mg/L	IC-Aq	-	1	-	1.1	-	1.5
NO_3	mg/L	IC-Aq	-	<.35	-	<.35	-	0.4
SO_4	mg/L	IC-Aq	-	22	-	31	-	61
Ag	ug/L	ICPMS	<0.01	<0.01	<0.01	<0.01	<0.01	<0.01
Al	ug/L	ICPMS	2	120	120	170	180	330
As	ug/L	ICPMS	16	31	30	38	39	66
Au	ug/L	ICPMS	< 0.01	< 0.01	< 0.01	< 0.01	< 0.01	< 0.01
B	ug/L	ICPAES	102	246	242	321	328	603
Ba	ug/L	ICPMS	9	12	12	14	15	20
Be	ug/L	ICPMS	<0.05	0.5	0.4	0.6	0.6	1.6
Bi	ug/L	ICPMS	< 0.01	< 0.01	< 0.01	< 0.01	< 0.01	< 0.01
Ca	mg/L	ICPAES	5.09	4.98	5	5.08	5.06	5.04
Cd	ug/L	ICPMS	<0.02	<0.02	<0.02	<0.02	<0.02	<0.02
Ce	ug/L	ICPMS	0.03	2.3	2.4	3.5	3.7	7.1
Co	ug/L	ICPMS	<0.02	<0.02	<0.02	<0.02	<0.02	<0.02
Cr	ug/L	ICPMS	<1	<1	<1	<1	<1	<1
Cs	ug/L	ICPMS	2.3	7.7	7.9	11	11	20
Cu	ug/L	ICPMS	<0.5	<0.5	<0.5	<0.5	<0.5	<0.5
Dy	ug/L	ICPMS	< 0.005	0.41	0.44	0.6	0.66	1.3
Er	ug/L	ICPMS	< 0.005	0.23	0.23	0.35	0.36	0.72
Eu	ug/L	ICPMS	< 0.005	0.01	0.009	0.02	0.02	0.04
Fe	ug/L	ICPMS	<30	63	66	120	130	300
Ga	ug/L	ICPMS	< 0.02	< 0.02	< 0.02	< 0.02	< 0.02	< 0.02
Gd	ug/L	ICPMS	< 0.005	0.32	0.38	0.47	0.55	1
Ge	ug/L	ICPMS	0.2	0.8	0.8	1.1	1.1	2.2
Ho	ug/L	ICPMS	< 0.005	0.088	0.092	0.12	0.14	0.25
K	mg/L	ICPAES	1.64	4.75	4.71	6.44	6.41	11.7
La	ug/L	ICPMS	0.03	0.63	0.73	1.1	1.1	2.1
Li	ug/L	ICPMS	46	110	110	150	150	260
Mg	mg/L	ICPAES	2.2	2.05	2.04	2	1.99	1.8
Mn	ug/L	ICPMS	0.42	14	14	21	22	44
Mo	ug/L	ICPMS	2.8	2.5	2.1	2.1	1.9	2.5
Na	mg/L	ICPAES	8.66	19.1	19.1	24.9	24.9	42.5
Nb	ug/L	ICPMS	< 0.02	< 0.02	< 0.02	< 0.02	< 0.02	< 0.02
Nd	ug/L	ICPMS	0.04	1.2	1.3	1.8	1.9	3.8
Ni	ug/L	ICPMS	0.4	0.3	0.3	0.3	0.3	0.2
P	ug/L	ICPMS	< 1	< 1	< 1	< 1	< 1	< 1
Pb	ug/L	ICPMS	<0.05	<0.05	<0.05	<0.05	<0.05	<0.05
Pr	ug/L	ICPMS	< 0.01	0.29	0.28	0.42	0.46	0.9
Rb	ug/L	ICPMS	4.2	27	28	39	40	77
Sb	ug/L	ICPMS	1	0.86	0.79	0.73	0.68	0.7
Sc	ug/L	ICPMS	< 0.1	< 0.1	< 0.1	< 0.1	< 0.1	< 0.1
Se	ug/L	ICPMS	< 0.3	< 0.3	< 0.3	< 0.3	< 0.3	< 0.3
SiO_2	mg/L	ICPMS	9.2	23	23	30	31	54
Sm	ug/L	ICPMS	< 0.01	0.33	0.35	0.46	0.56	1
Sr	ug/L	ICPMS	37	34	35	34	34	30
Ta	ug/L	ICPMS	< 0.03	< 0.03	< 0.03	< 0.03	< 0.03	< 0.03
Tb	ug/L	ICPMS	< 0.005	0.065	0.069	0.1	0.1	0.21
Th	ug/L	ICPMS	< 0.02	< 0.02	< 0.02	< 0.02	< 0.02	0.05
Ti	ug/L	ICPMS	< 0.2	< 0.2	< 0.2	< 0.2	< 0.2	0.2
Tl	ug/L	ICPMS	<0.05	<0.05	<0.05	<0.05	<0.05	0.08
Tm	ug/L	ICPMS	< 0.005	0.03	0.03	0.04	0.04	0.098
U	ug/L	ICPMS	0.01	0.14	0.14	0.21	0.23	0.4
V	ug/L	ICPMS	0.9	0.79	0.72	0.62	0.62	0.53
W	ug/L	ICPMS	6.3	5.2	4	3.8	3.4	3.5
Y	ug/L	ICPMS	0.03	2	2.2	3.1	3.4	6.6
Yb	ug/L	ICPMS	< 0.01	0.2	0.2	0.29	0.31	0.58
Zn	ug/L	ICPMS	<0.5	<0.5	0.5	1	1	3
Zr	ug/L	ICPMS	< 0.2	< 0.2	< 0.2	< 0.2	< 0.2	< 0.2
Hg	ng/L	Hg CVAF	<5	13	<5	5	<5	5
$\delta^{18}O$ vs VSMOW	permil	ISO1	-	-16.65	-	-16.63	-	-16.55

Appendix 3. Site and analytical data from the 1999 mixing experiments—*Continued*.

Field no. Sample name/ description			E4 tot Norris/Echinus	E5 diss Norris/Echinus	E5 tot Norris/Echinus	E6 diss Norris/Echinus	E6 tot Norris/Echinus	E7 diss Norris/Echinus
Latitude			44°43'19.5"N	44°43'19.5"N	44°43'19.5"N	44°43'19.5"N	44°43'19.5"N	44°43'19.5"N
Longitude			110°42'4.9"W	110°42'4.9"W	110°42'4.9"W	110°42'4.9"W	110°42'4.9"W	110°42'4.9"W
Collection date			07/23/99	07/23/99	07/23/99	07/23/99	07/23/99	07/23/99
Temp at filter	°C		20.2	24.1	24.1	25.9	25.9	28.3
pH			6.2	5.8	5.8	5.1	5.1	3.7
Conductivity	uS/cm		313	463	463	627	627	814
Cl	mg/L	IC-Aq	-	53	-	78	-	98
F	mg/L	IC-Aq	-	2.3	-	4.3	-	2.8
NO_3	mg/L	IC-Aq	-	<.35	-	0.5	-	0.7
SO_4	mg/L	IC-Aq	-	95	-	140	-	180
Ag	ug/L	ICPMS	<0.01	<0.01	<0.01	<0.01	<0.01	0.56
Al	ug/L	ICPMS	370	610	620	910	880	1300
As	ug/L	ICPMS	66	100	100	150	150	200
Au	ug/L	ICPMS	< 0.01	< 0.01	< 0.01	< 0.01	< 0.01	< 0.01
B	ug/L	ICPAES	604	927	945	1320	1330	1690
Ba	ug/L	ICPMS	20	28	28	36	36	42
Be	ug/L	ICPMS	1.3	2.4	2.5	3.5	3.5	4.9
Bi	ug/L	ICPMS	< 0.01	< 0.01	< 0.01	< 0.01	< 0.01	0.048
Ca	mg/L	ICPAES	4.93	5	5.03	4.97	4.98	4.93
Cd	ug/L	ICPMS	<0.02	<0.02	<0.02	<0.02	<0.02	<0.02
Ce	ug/L	ICPMS	7.7	12	13	18	18	23
Co	ug/L	ICPMS	<0.02	<0.02	<0.02	<0.02	<0.02	<0.02
Cr	ug/L	ICPMS	<1	<1	<1	<1	<1	<1
Cs	ug/L	ICPMS	20	32	31	45	44	54
Cu	ug/L	ICPMS	<0.5	<0.5	<0.5	<0.5	<0.5	<0.5
Dy	ug/L	ICPMS	1.4	2.3	2.4	3.3	3.3	4.3
Er	ug/L	ICPMS	0.76	1.2	1.3	1.7	1.9	2.3
Eu	ug/L	ICPMS	0.03	0.061	0.056	0.083	0.088	0.11
Fe	ug/L	ICPMS	310	550	560	810	820	1300
Ga	ug/L	ICPMS	< 0.02	< 0.02	< 0.02	< 0.02	< 0.02	< 0.02
Gd	ug/L	ICPMS	1.1	1.9	2	2.6	2.8	3.7
Ge	ug/L	ICPMS	2.1	3.5	3.5	4.9	4.9	6.8
Ho	ug/L	ICPMS	0.28	0.45	0.46	0.65	0.68	0.84
K	mg/L	ICPAES	11.8	18.1	18.5	25.8	26	34.5
La	ug/L	ICPMS	2.2	3.7	3.7	5.2	5.3	6.6
Li	ug/L	ICPMS	260	410	410	570	570	690
Mg	mg/L	ICPAES	1.81	1.55	1.57	1.31	1.32	1.11
Mn	ug/L	ICPMS	43	74	72	100	110	170
Mo	ug/L	ICPMS	2.3	3.1	3	3.6	3.6	7.6
Na	mg/L	ICPAES	41.6	65.3	65.6	90.1	90.3	117
Nb	ug/L	ICPMS	< 0.02	< 0.02	< 0.02	0.03	< 0.02	0.64
Nd	ug/L	ICPMS	4.1	6.4	6.6	9.1	9.7	12
Ni	ug/L	ICPMS	0.3	0.2	0.2	0.2	0.2	0.2
P	ug/L	ICPMS	< 1	< 1	< 1	1	< 1	6.5
Pb	ug/L	ICPMS	<0.05	<0.05	<0.05	<0.05	<0.05	0.09
Pr	ug/L	ICPMS	0.9	1.5	1.6	2.2	2.2	2.8
Rb	ug/L	ICPMS	77	130	130	180	180	250
Sb	ug/L	ICPMS	0.69	0.75	0.73	0.79	0.74	1.4
Sc	ug/L	ICPMS	< 0.1	< 0.1	< 0.1	< 0.1	< 0.1	3
Se	ug/L	ICPMS	0.3	0.8	0.5	0.9	0.9	2.1
SiO_2	mg/L	ICPMS	54	88	88	120	120	180
Sm	ug/L	ICPMS	1.1	1.7	1.7	2.5	2.6	3.3
Sr	ug/L	ICPMS	30	28	28	22	22	19
Ta	ug/L	ICPMS	< 0.03	0.04	< 0.03	< 0.03	0.03	0.53
Tb	ug/L	ICPMS	0.22	0.35	0.38	0.53	0.52	0.66
Th	ug/L	ICPMS	0.05	0.12	0.16	0.22	0.2	0.35
Ti	ug/L	ICPMS	< 0.2	0.5	0.5	1	1	2.5
Tl	ug/L	ICPMS	0.08	0.1	0.2	0.2	0.2	0.58
Tm	ug/L	ICPMS	0.11	0.17	0.18	0.23	0.25	0.31
U	ug/L	ICPMS	0.47	0.65	0.75	0.94	1.1	1.4
V	ug/L	ICPMS	0.55	0.4	0.5	0.4	0.3	1
W	ug/L	ICPMS	3.3	3.3	3.3	3.2	3	2.1
Y	ug/L	ICPMS	7	12	12	17	18	24
Yb	ug/L	ICPMS	0.63	0.95	1.1	1.5	1.5	1.8
Zn	ug/L	ICPMS	3	5	5	7	8	10
Zr	ug/L	ICPMS	< 0.2	< 0.2	< 0.2	< 0.2	< 0.2	0.2
Hg	ng/L	Hg CVAF	<5	10	<5	7	<5	9
$\delta^{18}O$ vs VSMOW	permil	ISO1	-	-16.77	-	-16.65	-	-16.60

Appendix 3. Site and analytical data from the 1999 mixing experiments—*Continued*.

Field no. Sample name/ description			E7 tot Norris/Echinus	E8 diss Norris/Echinus	E8 tot Norris/Echinus	E9 diss Norris/Echinus	E9 tot Norris/Echinus	E10 diss Norris/Echinus
Latitude			44°43'19.5"N	44°43'19.5"N	44°43'19.5"N	44°43'19.5"N	44°43'19.5"N	44°43'19.5"N
Longitude			110°42'4.9"W	110°42'4.9"W	110°42'4.9"W	110°42'4.9"W	110°42'4.9"W	110°42'4.9"W
Collection date			07/23/99	07/23/99	07/23/99	07/23/99	07/23/99	07/23/99
Temp at filter	°C		28.3	31.8	31.8	34.5	34.5	35.4
pH			3.7	3.4	3.4	3.2	3.2	3.2
Conductivity	uS/cm		814	1008	1008	1144	1144	1272
Cl	mg/L	IC-Aq	-	120	-	130	-	150
F	mg/L	IC-Aq	-	3.9	-	4.3	-	4.8
NO_3	mg/L	IC-Aq	-	<.35	-	<.35	-	<.35
SO_4	mg/L	IC-Aq	-	210	-	240	-	260
Ag	ug/L	ICPMS	0.2	0.1	0.09	0.07	0.05	0.04
Al	ug/L	ICPMS	1300	1600	1600	1800	1800	2000
As	ug/L	ICPMS	200	240	240	270	260	290
Au	ug/L	ICPMS	< 0.01	< 0.01	< 0.01	< 0.01	< 0.01	< 0.01
B	ug/L	ICPAES	1700	2060	2060	2310	2300	2540
Ba	ug/L	ICPMS	42	48	49	55	55	60
Be	ug/L	ICPMS	4.8	5.8	5.9	6.4	6.5	7
Bi	ug/L	ICPMS	< 0.01	< 0.01	< 0.01	< 0.01	< 0.01	< 0.01
Ca	mg/L	ICPAES	4.95	4.88	4.83	4.81	4.82	4.74
Cd	ug/L	ICPMS	<0.02	<0.02	<0.02	<0.02	<0.02	<0.02
Ce	ug/L	ICPMS	23	28	28	32	31	36
Co	ug/L	ICPMS	<0.02	<0.02	<0.02	<0.02	<0.02	<0.02
Cr	ug/L	ICPMS	<1	<1	<1	<1	<1	<1
Cs	ug/L	ICPMS	54	66	65	74	73	81
Cu	ug/L	ICPMS	<0.5	<0.5	<0.5	<0.5	<0.5	<0.5
Dy	ug/L	ICPMS	4.2	5.4	5.4	6.2	5.9	6.7
Er	ug/L	ICPMS	2.4	2.9	2.9	3.4	3.3	3.5
Eu	ug/L	ICPMS	0.12	0.14	0.14	0.15	0.16	0.17
Fe	ug/L	ICPMS	1300	1600	1500	1700	1700	1900
Ga	ug/L	ICPMS	< 0.02	< 0.02	< 0.02	< 0.02	< 0.02	< 0.02
Gd	ug/L	ICPMS	3.6	4.4	4.4	5	5	5.6
Ge	ug/L	ICPMS	6.6	8.1	8.1	8.8	8.9	9.9
Ho	ug/L	ICPMS	0.88	1.1	1.1	1.2	1.2	1.3
K	mg/L	ICPAES	35.1	42.4	42.1	47.3	47.2	51.9
La	ug/L	ICPMS	6.5	8.1	8.2	9.4	8.9	10
Li	ug/L	ICPMS	720	900	890	1000	1000	1100
Mg	mg/L	ICPAES	1.09	0.848	0.842	0.666	0.664	0.499
Mn	ug/L	ICPMS	160	200	190	210	210	230
Mo	ug/L	ICPMS	4.8	5.4	5.1	5.8	5.5	6
Na	mg/L	ICPAES	117	143	140	158	156	172
Nb	ug/L	ICPMS	0.5	0.4	0.3	0.3	0.2	0.2
Nd	ug/L	ICPMS	12	15	14	16	16	18
Ni	ug/L	ICPMS	0.3	0.2	0.1	0.1	<0.1	<0.1
P	ug/L	ICPMS	7.6	7.5	6.4	6.6	4.9	3
Pb	ug/L	ICPMS	<0.05	<0.05	<0.05	0.07	0.05	<0.05
Pr	ug/L	ICPMS	2.8	3.5	3.4	3.9	3.9	4.2
Rb	ug/L	ICPMS	240	290	280	310	310	350
Sb	ug/L	ICPMS	0.85	0.87	0.8	0.82	0.8	0.82
Sc	ug/L	ICPMS	2	1	0.5	0.4	< 0.1	< 0.1
Se	ug/L	ICPMS	1.6	1.6	1.6	1.8	1.8	1.7
SiO_2	mg/L	ICPMS	180	220	220	250	240	270
Sm	ug/L	ICPMS	3.3	4	3.9	4.7	4.5	4.9
Sr	ug/L	ICPMS	19	14	13	10	10	7
Ta	ug/L	ICPMS	0.43	0.36	0.31	0.31	0.26	0.23
Tb	ug/L	ICPMS	0.66	0.86	0.84	0.96	0.99	1
Th	ug/L	ICPMS	0.34	0.45	0.56	0.57	0.6	0.66
Ti	ug/L	ICPMS	2.4	3	2.6	3	3	3.2
Tl	ug/L	ICPMS	0.4	0.5	0.4	0.5	0.5	0.53
Tm	ug/L	ICPMS	0.32	0.41	0.41	0.42	0.45	0.48
U	ug/L	ICPMS	1.4	1.8	1.8	2	2	2.3
V	ug/L	ICPMS	0.67	0.5	0.4	0.3	<0.2	<0.2
W	ug/L	ICPMS	2	2.1	2.2	2.3	2.2	2.1
Y	ug/L	ICPMS	23	29	28	32	31	34
Yb	ug/L	ICPMS	1.8	2.2	2.3	2.6	2.6	2.9
Zn	ug/L	ICPMS	10	10	10	20	10	20
Zr	ug/L	ICPMS	< 0.2	< 0.2	< 0.2	< 0.2	< 0.2	< 0.2
Hg	ng/L	Hg CVAF	7	10	8	12	10	<5
$\delta^{18}O$ vs VSMOW	permil	ISO1	-	-16.62	-	-16.59	-	-16.53

Appendix 3. Site and analytical data from the 1999 mixing experiments—*Continued*.

Field no. Sample name/ description			E10 tot Norris/Echinus	P1 diss Norris/Pork chop	P1 tot Norris/ Pork chop	P2 diss Norris/ Pork chop	P2 tot Norris/ Pork chop	P3 diss Norris/ Pork chop	P3 tot Norris/ Pork chop
Latitude			44°43'19.5"N	44°43'21"N	44°43'21"N	44°43'21"N	44°43'21"N	44°43'21"N	44°43'21"N
Longitude			110°42'4.9"W	110°42'28"W	110°42'28"W	110°42'28"W	110°42'28"W	110°42'28"W	110°42'28"W
Collection date			07/23/99	07/22/99	07/22/99	07/23/99	07/23/99	07/23/99	07/23/99
Temp at filter	°C		35.4	14.6	14.6	15.8	15.8	14.6	14.6
pH			3.2	7.5	7.5	7.4	7.4	7.3	7.3
Conductivity	uS/cm		1272	87	87	223	223	287	287
Cl	mg/L	IC-Aq	-	4.7	-	41	-	60	-
F	mg/L	IC-Aq	-	0.5	-	0.7	-	0.9	-
NO_3	mg/L	IC-Aq	-	<.35	-	0.4	-	<.35	-
SO_4	mg/L	IC-Aq	-	7.2	-	8.6	-	9	-
Ag	ug/L	ICPMS	0.03	<0.01	<0.01	0.01	<0.01	<0.01	0.01
Al	ug/L	ICPMS	1900	2	2	1	1	0.9	1
As	ug/L	ICPMS	280	11	11	170	170	260	260
Au	ug/L	ICPMS	< 0.01	< 0.01	< 0.01	< 0.01	< 0.01	< 0.01	< 0.01
B	ug/L	ICPAES	2590	78	77.2	659	669	940	933
Ba	ug/L	ICPMS	59	8.6	8.7	8.8	8.9	8.8	9
Be	ug/L	ICPMS	7.6	<0.05	<0.05	<0.05	<0.05	<0.05	<0.05
Bi	ug/L	ICPMS	< 0.01	< 0.01	< 0.01	< 0.01	< 0.01	< 0.01	< 0.01
Ca	mg/L	ICPAES	4.74	5.27	5.19	5.3	5.31	5.28	5.17
Cd	ug/L	ICPMS	<0.02	<0.02	<0.02	<0.02	<0.02	<0.02	<0.02
Ce	ug/L	ICPMS	36	0.02	0.03	0.02	0.02	0.02	0.03
Co	ug/L	ICPMS	<0.02	<0.02	<0.02	<0.02	<0.02	<0.02	<0.02
Cr	ug/L	ICPMS	<1	<1	<1	<1	<1	<1	<1
Cs	ug/L	ICPMS	81	2.2	2.2	37	38	54	55
Cu	ug/L	ICPMS	<0.5	<0.5	<0.5	<0.5	<0.5	<0.5	<0.5
Dy	ug/L	ICPMS	6.8	0.006	< 0.005	< 0.005	< 0.005	0.005	0.008
Er	ug/L	ICPMS	3.5	< 0.005	< 0.005	< 0.005	< 0.005	< 0.005	< 0.005
Eu	ug/L	ICPMS	0.17	< 0.005	< 0.005	< 0.005	< 0.005	< 0.005	< 0.005
Fe	ug/L	ICPMS	1800	<30	<30	<30	<30	<30	<30
Ga	ug/L	ICPMS	< 0.02	< 0.02	< 0.02	< 0.02	< 0.02	< 0.02	< 0.02
Gd	ug/L	ICPMS	5.4	0.006	< 0.005	< 0.005	< 0.005	< 0.005	< 0.005
Ge	ug/L	ICPMS	9.6	0.2	0.2	2.3	2.2	3.2	3.2
Ho	ug/L	ICPMS	1.4	< 0.005	< 0.005	< 0.005	< 0.005	< 0.005	< 0.005
K	mg/L	ICPAES	52	1.51	1.56	4.87	4.95	6.49	6.39
La	ug/L	ICPMS	10	0.03	0.03	0.03	0.03	0.03	0.03
Li	ug/L	ICPMS	1100	42	42	400	400	570	580
Mg	mg/L	ICPAES	0.504	2.22	2.23	2.09	2.11	2.03	2
Mn	ug/L	ICPMS	220	0.42	0.42	2.3	2.1	2.9	2.9
Mo	ug/L	ICPMS	5.9	0.87	0.86	12	13	20	20
Na	mg/L	ICPAES	172	8.58	8.62	32.1	32.2	42.9	41.9
Nb	ug/L	ICPMS	0.2	0.1	0.09	0.1	0.1	0.09	0.09
Nd	ug/L	ICPMS	18	0.03	0.03	0.03	0.03	0.03	0.03
Ni	ug/L	ICPMS	<0.1	0.4	0.4	0.3	0.3	0.3	0.3
P	ug/L	ICPMS	2	1	2	2	2	1	2
Pb	ug/L	ICPMS	<0.05	<0.05	<0.05	<0.05	<0.05	<0.05	<0.05
Pr	ug/L	ICPMS	4.2	< 0.01	< 0.01	< 0.01	< 0.01	< 0.01	< 0.01
Rb	ug/L	ICPMS	340	4	4	31	31	44	45
Sb	ug/L	ICPMS	0.79	0.47	0.47	8.8	9.1	14	13
Sc	ug/L	ICPMS	< 0.1	< 0.1	< 0.1	0.3	0.2	0.4	0.3
Se	ug/L	ICPMS	1.6	< 0.3	< 0.3	0.5	0.6	0.8	0.9
SiO_2	mg/L	ICPMS	260	9	9.1	26	26	35	35
Sm	ug/L	ICPMS	5.1	< 0.01	< 0.01	< 0.01	< 0.01	< 0.01	< 0.01
Sr	ug/L	ICPMS	6.8	35	36	35	34	34	35
Ta	ug/L	ICPMS	0.21	0.11	0.09	0.12	0.1	0.11	0.08
Tb	ug/L	ICPMS	1	< 0.005	< 0.005	< 0.005	< 0.005	< 0.005	< 0.005
Th	ug/L	ICPMS	0.6	< 0.02	< 0.02	< 0.02	< 0.02	< 0.02	< 0.02
Ti	ug/L	ICPMS	2.6	< 0.2	< 0.2	< 0.2	< 0.2	< 0.2	< 0.2
Tl	ug/L	ICPMS	0.51	<0.05	<0.05	<0.05	0.05	0.08	0.08
Tm	ug/L	ICPMS	0.51	< 0.005	< 0.005	< 0.005	< 0.005	< 0.005	< 0.005
U	ug/L	ICPMS	2.2	0.01	0.01	0.01	0.01	0.01	0.01
V	ug/L	ICPMS	<0.2	0.82	0.85	1.3	1.2	1.3	1.4
W	ug/L	ICPMS	2.2	1.4	1.3	6.8	7.9	11	11
Y	ug/L	ICPMS	34	0.03	0.02	0.02	0.03	0.02	0.02
Yb	ug/L	ICPMS	2.9	< 0.01	< 0.01	< 0.01	< 0.01	< 0.01	< 0.01
Zn	ug/L	ICPMS	20	<0.5	<0.5	<0.5	<0.5	<0.5	<0.5
Zr	ug/L	ICPMS	< 0.2	< 0.2	< 0.2	< 0.2	< 0.2	< 0.2	< 0.2
Hg	ng/L	Hg CVAF	8	<5	<5	<5	<5	<5	<5
$\delta^{18}O$ vs VSMOW	permil	ISO1	-	-16.60	-	-16.85	-	-16.62	-

Appendix 3. Site and analytical data from the 1999 mixing experiments—*Continued*.

Field no. Sample name/ description			P4 diss Norris/ Pork chop	P4 tot Norris/ Pork chop	P5 diss Norris/ Pork chop	P5 tot Norris/ Pork chop	P6 diss Norris/ Pork chop	P6 tot Norris/ Pork chop	P7 diss Norris/ Pork chop
Latitude			44°43'21"N	44°43'21"N	44°43'21"N	44°43'21"N	44°43'21"N	44°43'21"N	44°43'21"N
Longitude			110°42'28"W	110°42'28"W	110°42'28"W	110°42'28"W	110°42'28"W	110°42'28"W	110°42'28"W
Collection date			07/23/99	07/23/99	07/23/99	07/23/99	07/23/99	07/23/99	07/23/99
Temp at filter	°C		17.1	17.1	19.6	19.6	22.4	22.4	25.6
pH			7.2	7.2	7.1	7.1	7.0	7.0	6.8
Conductivity	uS/cm		591	591	905	905	1220	1220	1565
Cl	mg/L	IC-Aq	150	-	230	-	330	-	430
F	mg/L	IC-Aq	1.4	-	2.4	-	2.8	-	4.4
NO_3	mg/L	IC-Aq	0.5	-	1.3	-	<.35	-	<.35
SO_4	mg/L	IC-Aq	14	-	22	-	25	-	22
Ag	ug/L	ICPMS	0.03	0.03	0.04	0.03	0.04	0.03	0.04
Al	ug/L	ICPMS	4.9	3.8	2.8	3	9.7	1	<0.5
As	ug/L	ICPMS	820	830	1300	1300	1800	1800	2200
Au	ug/L	ICPMS	< 0.01	< 0.01	< 0.01	< 0.01	< 0.01	< 0.01	< 0.01
B	ug/L	ICPAES	2250	2300	3620	3560	4970	4880	6340
Ba	ug/L	ICPMS	11	10	10	10	11	11	11
Be	ug/L	ICPMS	<0.05	<0.05	0.1	<0.05	0.1	<0.05	0.1
Bi	ug/L	ICPMS	< 0.01	< 0.01	< 0.01	< 0.01	< 0.01	< 0.01	< 0.01
Ca	mg/L	ICPAES	5.2	5.38	5.32	5.12	5.22	5.14	5.19
Cd	ug/L	ICPMS	<0.02	<0.02	<0.02	<0.02	<0.02	<0.02	<0.02
Ce	ug/L	ICPMS	0.02	0.02	0.02	0.02	0.02	0.01	< 0.01
Co	ug/L	ICPMS	<0.02	<0.02	<0.02	<0.02	<0.02	<0.02	<0.02
Cr	ug/L	ICPMS	<1	<1	<1	<1	<1	<1	<1
Cs	ug/L	ICPMS	150	150	230	240	320	320	410
Cu	ug/L	ICPMS	<0.5	<0.5	<0.5	<0.5	<0.5	<0.5	<0.5
Dy	ug/L	ICPMS	< 0.005	< 0.005	< 0.005	< 0.005	< 0.005	0.006	< 0.005
Er	ug/L	ICPMS	< 0.005	0.006	< 0.005	< 0.005	< 0.005	< 0.005	< 0.005
Eu	ug/L	ICPMS	< 0.005	< 0.005	< 0.005	< 0.005	< 0.005	< 0.005	< 0.005
Fe	ug/L	ICPMS	<30	<30	<30	<30	<30	<30	<30
Ga	ug/L	ICPMS	< 0.02	< 0.02	0.03	< 0.02	< 0.02	< 0.02	0.02
Gd	ug/L	ICPMS	< 0.005	< 0.005	0.01	0.008	< 0.005	< 0.005	< 0.005
Ge	ug/L	ICPMS	10	10	16	16	22	22	27
Ho	ug/L	ICPMS	< 0.005	< 0.005	< 0.005	< 0.005	< 0.005	< 0.005	< 0.005
K	mg/L	ICPAES	13.9	14.3	21.8	22.2	30.5	30	39.1
La	ug/L	ICPMS	0.02	0.03	0.02	0.03	0.02	0.02	< 0.01
Li	ug/L	ICPMS	2200	2200	3500	3400	5000	5000	6500
Mg	mg/L	ICPAES	1.72	1.76	1.43	1.4	1.1	1.08	0.747
Mn	ug/L	ICPMS	9.3	9.3	14	14	19	19	23
Mo	ug/L	ICPMS	64	65	100	110	150	150	190
Na	mg/L	ICPAES	93.1	96.7	151	150	202	200	262
Nb	ug/L	ICPMS	0.2	0.2	0.2	0.1	0.2	0.2	0.2
Nd	ug/L	ICPMS	0.03	0.03	0.02	0.02	0.02	0.01	0.02
Ni	ug/L	ICPMS	0.4	0.4	0.3	0.3	0.2	0.2	0.1
P	ug/L	ICPMS	16	14	16	17	16	14	13
Pb	ug/L	ICPMS	<0.05	<0.05	<0.05	<0.05	<0.05	<0.05	<0.05
Pr	ug/L	ICPMS	< 0.01	< 0.01	< 0.01	< 0.01	< 0.01	< 0.01	< 0.01
Rb	ug/L	ICPMS	130	130	200	200	280	280	350
Sb	ug/L	ICPMS	39	40	62	62	86	84	110
Sc	ug/L	ICPMS	0.5	0.1	< 0.1	< 0.1	< 0.1	< 0.1	< 0.1
Se	ug/L	ICPMS	2.8	2.9	4.5	4.7	6.3	6.5	8.3
SiO_2	mg/L	ICPMS	110	110	170	170	230	230	290
Sm	ug/L	ICPMS	< 0.01	< 0.01	< 0.01	< 0.01	< 0.01	< 0.01	< 0.01
Sr	ug/L	ICPMS	40	39	33	33	30	30	24
Ta	ug/L	ICPMS	0.15	0.16	0.16	0.12	0.16	0.14	0.17
Tb	ug/L	ICPMS	< 0.005	< 0.005	< 0.005	< 0.005	< 0.005	< 0.005	< 0.005
Th	ug/L	ICPMS	< 0.02	< 0.02	< 0.02	< 0.02	< 0.02	< 0.02	< 0.02
Ti	ug/L	ICPMS	< 0.2	< 0.2	< 0.2	< 0.2	0.4	0.2	0.4
Tl	ug/L	ICPMS	0.2	0.3	0.4	0.4	0.6	0.59	0.77
Tm	ug/L	ICPMS	< 0.005	< 0.005	< 0.005	< 0.005	< 0.005	< 0.005	< 0.005
U	ug/L	ICPMS	0.01	0.01	0.009	0.008	< 0.005	< 0.005	< 0.005
V	ug/L	ICPMS	2.8	2.6	2.7	2.4	2.5	2.4	2.5
W	ug/L	ICPMS	32	34	55	57	79	79	100
Y	ug/L	ICPMS	0.02	0.02	0.02	0.02	0.01	0.02	0.01
Yb	ug/L	ICPMS	< 0.01	< 0.01	< 0.01	< 0.01	< 0.01	< 0.01	< 0.01
Zn	ug/L	ICPMS	<0.5	<0.5	<0.5	<0.5	<0.5	<0.5	<0.5
Zr	ug/L	ICPMS	< 0.2	< 0.2	< 0.2	< 0.2	< 0.2	< 0.2	< 0.2
Hg	ng/L	Hg CVAF	<5	15	<5	<5	10	7	7
$\delta^{18}O$ vs VSMOW	permil	ISO1	-15.98	-	-15.47	-	-15.00	-	-14.34

Appendix 3. Site and analytical data from the 1999 mixing experiments—*Continued*.

Field no. Sample name/ description			P7 tot Norris/ Pork chop	P8 diss Norris/ Pork chop	P8 tot Norris/ Pork chop	P9 diss Norris/ Pork chop	P9 tot Norris/ Pork chop	P10 diss Norris/ Pork chop	P10 tot Norris/ Pork chop
Latitude			44°43'21"N	44°43'21"N	44°43'21"N	44°43'21"N	44°43'21"N	44°43'21"N	44°43'21"N
Longitude			110°42'28"W	110°42'28"W	110°42'28"W	110°42'28"W	110°42'28"W	110°42'28"W	110°42'28"W
Collection date			07/23/99	07/23/99	07/23/99	07/23/99	07/23/99	07/23/99	07/23/99
Temp at filter	°C		25.6	25.3	25.3	28.9	28.9	31.5	31.5
pH			6.8	6.9	6.9	6.7	6.7	6.6	6.6
Conductivity	uS/cm		1565	1865	1865	2080	2080	2300	2300
Cl	mg/L	IC-Aq	-	530	-	600	-	620	-
F	mg/L	IC-Aq	-	5.1	-	5.7	-	6.5	-
NO_3	mg/L	IC-Aq	-	0.5	-	0.5	-	0.5	-
SO_4	mg/L	IC-Aq	-	28	-	30	-	32	-
Ag	ug/L	ICPMS	0.03	0.04	0.04	0.03	0.03	0.03	0.02
Al	ug/L	ICPMS	1	<0.5	<0.5	<0.5	<0.5	<0.5	<0.5
As	ug/L	ICPMS	2200	2700	2600	2800	2800	3100	3100
Au	ug/L	ICPMS	< 0.01	< 0.01	< 0.01	< 0.01	< 0.01	< 0.01	< 0.01
B	ug/L	ICPAES	6200	7390	7470	8400	8330	9250	9360
Ba	ug/L	ICPMS	11	11	11	11	11	11	11
Be	ug/L	ICPMS	0.1	3.6	3	5.5	5.8	5.2	5.2
Bi	ug/L	ICPMS	< 0.01	< 0.01	< 0.01	< 0.01	< 0.01	< 0.01	< 0.01
Ca	mg/L	ICPAES	4.93	5	4.99	5.16	4.93	5.01	5.16
Cd	ug/L	ICPMS	<0.02	<0.02	<0.02	<0.02	<0.02	<0.02	<0.02
Ce	ug/L	ICPMS	< 0.01	< 0.01	< 0.01	< 0.01	< 0.01	< 0.01	< 0.01
Co	ug/L	ICPMS	<0.02	<0.02	<0.02	<0.02	<0.02	<0.02	<0.02
Cr	ug/L	ICPMS	<1	<1	<1	<1	<1	<1	<1
Cs	ug/L	ICPMS	410	490	480	530	530	580	580
Cu	ug/L	ICPMS	<0.5	<0.5	<0.5	<0.5	<0.5	<0.5	<0.5
Dy	ug/L	ICPMS	0.006	< 0.005	< 0.005	< 0.005	< 0.005	< 0.005	< 0.005
Er	ug/L	ICPMS	< 0.005	< 0.005	< 0.005	< 0.005	< 0.005	< 0.005	< 0.005
Eu	ug/L	ICPMS	< 0.005	< 0.005	< 0.005	< 0.005	< 0.005	< 0.005	< 0.005
Fe	ug/L	ICPMS	<30	<30	<30	<30	<30	<30	<30
Ga	ug/L	ICPMS	< 0.02	< 0.02	< 0.02	0.02	0.02	0.03	< 0.02
Gd	ug/L	ICPMS	< 0.005	< 0.005	< 0.005	< 0.005	< 0.005	< 0.005	< 0.005
Ge	ug/L	ICPMS	27	33	32	35	36	40	40
Ho	ug/L	ICPMS	< 0.005	< 0.005	< 0.005	< 0.005	< 0.005	< 0.005	< 0.005
K	mg/L	ICPAES	37.9	46	45.8	52.1	50.8	57.1	57.9
La	ug/L	ICPMS	0.01	0.01	0.01	< 0.01	< 0.01	< 0.01	< 0.01
Li	ug/L	ICPMS	6600	7900	7900	8900	8900	9800	10000
Mg	mg/L	ICPAES	0.73	0.443	0.448	0.232	0.23	<0.1	<0.1
Mn	ug/L	ICPMS	24	28	28	30	30	33	33
Mo	ug/L	ICPMS	190	230	230	250	250	280	280
Na	mg/L	ICPAES	257	306	309	347	342	383	386
Nb	ug/L	ICPMS	0.2	0.2	0.1	0.1	0.1	0.1	0.1
Nd	ug/L	ICPMS	0.02	< 0.01	0.01	< 0.01	< 0.01	< 0.01	< 0.01
Ni	ug/L	ICPMS	<0.1	<0.1	<0.1	<0.1	<0.1	<0.1	<0.1
P	ug/L	ICPMS	12	9.7	9.4	6.8	6.4	5.6	6
Pb	ug/L	ICPMS	<0.05	<0.05	<0.05	<0.05	<0.05	<0.05	<0.05
Pr	ug/L	ICPMS	< 0.01	< 0.01	< 0.01	< 0.01	< 0.01	< 0.01	< 0.01
Rb	ug/L	ICPMS	350	420	410	460	460	490	510
Sb	ug/L	ICPMS	110	130	130	140	140	150	150
Sc	ug/L	ICPMS	< 0.1	< 0.1	< 0.1	< 0.1	< 0.1	< 0.1	< 0.1
Se	ug/L	ICPMS	7.7	9.6	9.2	10	10	9.8	11
SiO_2	mg/L	ICPMS	300	350	350	380	380	410	420
Sm	ug/L	ICPMS	< 0.01	< 0.01	< 0.01	< 0.01	< 0.01	< 0.01	< 0.01
Sr	ug/L	ICPMS	24	20	20	17	17	14	14
Ta	ug/L	ICPMS	0.15	0.14	0.15	0.12	0.12	0.16	0.15
Tb	ug/L	ICPMS	< 0.005	< 0.005	< 0.005	< 0.005	< 0.005	< 0.005	< 0.005
Th	ug/L	ICPMS	< 0.02	< 0.02	< 0.02	< 0.02	< 0.02	< 0.02	< 0.02
Ti	ug/L	ICPMS	< 0.2	0.3	< 0.2	0.3	0.3	0.2	0.5
Tl	ug/L	ICPMS	0.76	0.94	0.92	1	1	1.2	1.2
Tm	ug/L	ICPMS	< 0.005	< 0.005	< 0.005	< 0.005	< 0.005	< 0.005	< 0.005
U	ug/L	ICPMS	< 0.005	< 0.005	< 0.005	< 0.005	< 0.005	< 0.005	< 0.005
V	ug/L	ICPMS	2.4	2.7	2.6	2.7	2.7	2.8	2.8
W	ug/L	ICPMS	110	130	130	140	140	160	160
Y	ug/L	ICPMS	0.01	< 0.01	< 0.01	< 0.01	< 0.01	< 0.01	< 0.01
Yb	ug/L	ICPMS	< 0.01	< 0.01	< 0.01	< 0.01	< 0.01	< 0.01	< 0.01
Zn	ug/L	ICPMS	<0.5	<0.5	<0.5	<0.5	<0.5	<0.5	<0.5
Zr	ug/L	ICPMS	< 0.2	< 0.2	< 0.2	< 0.2	< 0.2	< 0.2	< 0.2
Hg	ng/L	Hg CVAF	<5	14	5	10	<5	7	<5
$\delta^{18}O$ vs VSMOW	permil	ISO1	-	-13.93	-	-13.50	-	-13.03	-

Appendix 3. Site and analytical data from the 1999 mixing experiments—*Continued*

Field no. Sample name/ description			W1 diss West Thumb/ Black pool	W1 tot West Thumb/ Black pool	W2 diss West Thumb/ Black pool	W2 tot West Thumb/ Black pool	W3 diss West Thumb/ Black pool	W3 tot West Thumb/ Black pool	W4 diss West Thumb/ Black pool	W4 tot West Thumb/ Black pool
Latitude			44°25'6"N	44°25'6"N	44°25'6"N	44°25'6"N	44°25'6"N	44°25'6"N	44°25'6"N	44°25'6"N
Longitude			110°34'17"W	110°34'17"W	110°34'17"W	110°34'17"W	110°34'17"W	110°34'17"W	110°34'17"W	110°34'17"W
Collection date			07/22/99	07/22/99	07/24/99	07/24/99	07/24/99	07/24/99	07/24/99	07/24/99
Temp at filter	°C		16.5	16.5	16.6	16.6	19.8	19.8	21.3	21.3
pH			7.5	7.5	7.6	7.6	7.6	7.6	7.7	7.7
Conductivity	uS/cm		87	87	172	172	303	303	490	490
Cl	mg/L	IC-Aq	4.7	-	15	-	35	-	62	-
F	mg/L	IC-Aq	0.5	-	1.7	-	3.8	-	7	-
NO_3	mg/L	IC-Aq	0.5	-	0.4	-	<.35	-	0.5	-
SO_4	mg/L	IC-Aq	7.2	-	8.7	-	11	-	14	-
Ag	ug/L	ICPMS	<0.01	<0.01	<0.01	<0.01	<0.01	<0.01	<0.01	<0.01
Al	ug/L	ICPMS	1	2	14	14	34	33	62	63
As	ug/L	ICPMS	12	12	94	98	240	240	440	460
Au	ug/L	ICPMS	< 0.01	< 0.01	< 0.01	< 0.01	< 0.01	< 0.01	< 0.01	< 0.01
B	ug/L	ICPAES	105	90.4	221	220	432	432	770	782
Ba	ug/L	ICPMS	8.5	8.6	8.3	8.2	7.6	7.8	7	7.3
Be	ug/L	ICPMS	<0.05	<0.05	0.2	0.2	0.7	0.6	1.3	1.3
Bi	ug/L	ICPMS	< 0.01	< 0.01	< 0.01	< 0.01	< 0.01	< 0.01	< 0.01	< 0.01
Ca	mg/L	ICPAES	4.87	4.93	4.84	4.85	4.59	4.52	4.19	4.17
Cd	ug/L	ICPMS	<0.02	<0.02	<0.02	<0.02	<0.02	<0.02	<0.02	<0.02
Ce	ug/L	ICPMS	0.03	0.03	0.02	0.03	0.02	0.02	0.02	0.03
Co	ug/L	ICPMS	<0.02	<0.02	<0.02	<0.02	<0.02	<0.02	<0.02	<0.02
Cr	ug/L	ICPMS	<1	<1	<1	<1	<1	<1	<1	<1
Cs	ug/L	ICPMS	2.3	2.2	16	16	38	37	66	67
Cu	ug/L	ICPMS	<0.5	<0.5	<0.5	<0.5	<0.5	<0.5	<0.5	<0.5
Dy	ug/L	ICPMS	< 0.005	< 0.005	0.007	0.009	< 0.005	0.007	< 0.005	< 0.005
Er	ug/L	ICPMS	< 0.005	< 0.005	< 0.005	< 0.005	< 0.005	< 0.005	< 0.005	< 0.005
Eu	ug/L	ICPMS	< 0.005	< 0.005	< 0.005	< 0.005	< 0.005	< 0.005	< 0.005	< 0.005
Fe	ug/L	ICPMS	<30	<30	<30	<30	<30	<30	<30	<30
Ga	ug/L	ICPMS	< 0.02	< 0.02	0.4	0.4	1.1	1.2	2.2	2.2
Gd	ug/L	ICPMS	< 0.005	< 0.005	< 0.005	< 0.005	0.008	< 0.005	0.005	< 0.005
Ge	ug/L	ICPMS	0.2	0.2	2.1	2.1	5.1	5.1	9.5	9.7
Ho	ug/L	ICPMS	< 0.005	< 0.005	< 0.005	< 0.005	< 0.005	< 0.005	< 0.005	< 0.005
K	mg/L	ICPAES	1.65	1.56	2.25	2.24	3.32	3.42	4.92	4.98
La	ug/L	ICPMS	0.03	0.03	0.03	0.03	0.03	0.03	0.02	0.02
Li	ug/L	ICPMS	40	41	200	200	440	450	810	820
Mg	mg/L	ICPAES	2.16	2.16	2.1	2.08	1.94	1.97	1.74	1.74
Mn	ug/L	ICPMS	0.4	0.44	0.47	0.51	0.62	0.62	0.78	0.78
Mo	ug/L	ICPMS	1.6	1.2	4.6	4.8	11	11	21	22
Na	mg/L	ICPAES	8.76	8.44	26.3	26.3	53.9	53.1	93.5	93.5
Nb	ug/L	ICPMS	< 0.02	< 0.02	< 0.02	< 0.02	0.06	0.04	0.1	0.1
Nd	ug/L	ICPMS	0.03	0.03	0.02	0.03	0.03	0.04	0.02	0.03
Ni	ug/L	ICPMS	0.3	0.3	0.3	0.3	0.3	0.3	0.3	0.2
P	ug/L	ICPMS	< 1	< 1	< 1	< 1	< 1	< 1	< 1	< 1
Pb	ug/L	ICPMS	<0.05	<0.05	<0.05	<0.05	<0.05	<0.05	<0.05	<0.05
Pr	ug/L	ICPMS	< 0.01	< 0.01	< 0.01	< 0.01	< 0.01	< 0.01	< 0.01	< 0.01
Rb	ug/L	ICPMS	3.9	4	11	11	23	23	39	40
Sb	ug/L	ICPMS	1.6	0.94	5.2	5.2	12	12	23	23
Sc	ug/L	ICPMS	< 0.1	< 0.1	< 0.1	< 0.1	< 0.1	< 0.1	< 0.1	< 0.1
Se	ug/L	ICPMS	< 0.3	< 0.3	< 0.3	< 0.3	< 0.3	< 0.3	0.6	0.7
SiO_2	mg/L	ICPMS	8.4	8.7	19	19	36	36	62	63
Sm	ug/L	ICPMS	< 0.01	< 0.01	< 0.01	< 0.01	< 0.01	0.01	< 0.01	< 0.01
Sr	ug/L	ICPMS	35	34	33	35	33	32	28	29
Ta	ug/L	ICPMS	< 0.03	< 0.03	0.04	< 0.03	0.14	0.11	0.25	0.2
Tb	ug/L	ICPMS	< 0.005	< 0.005	< 0.005	< 0.005	< 0.005	< 0.005	< 0.005	< 0.005
Th	ug/L	ICPMS	< 0.02	< 0.02	< 0.02	< 0.02	< 0.02	< 0.02	< 0.02	< 0.02
Ti	ug/L	ICPMS	< 0.2	< 0.2	< 0.2	< 0.2	< 0.2	< 0.2	< 0.2	0.2
Tl	ug/L	ICPMS	<0.05	<0.05	<0.05	<0.05	<0.05	<0.05	<0.05	<0.05
Tm	ug/L	ICPMS	< 0.005	< 0.005	< 0.005	< 0.005	< 0.005	< 0.005	< 0.005	< 0.005
U	ug/L	ICPMS	0.01	0.01	0.01	0.01	0.01	0.01	0.01	0.01
V	ug/L	ICPMS	0.64	0.7	0.69	0.68	0.62	0.63	0.6	0.6
W	ug/L	ICPMS	5.1	3.3	14	15	38	40	77	81
Y	ug/L	ICPMS	0.03	0.02	0.02	0.03	0.03	0.03	0.02	0.02
Yb	ug/L	ICPMS	< 0.01	< 0.01	< 0.01	< 0.01	< 0.01	< 0.01	< 0.01	< 0.01
Zn	ug/L	ICPMS	<0.5	<0.5	<0.5	<0.5	<0.5	<0.5	<0.5	<0.5
Zr	ug/L	ICPMS	< 0.2	< 0.2	< 0.2	< 0.2	< 0.2	< 0.2	< 0.2	< 0.2
Hg	ng/L	Hg CVAF	5	<5	8	<5	5	<5	9	<5
$\delta^{18}O$ vs VSMOW	permil	ISO1	-16.17	-	-16.57	-	-16.56	-	-15.98	-

Appendix 4. Site and analytical data from subaerial hydrothermal features.

Field no. Sample name & description			RS-49-98 Vandalized Pool-West Thumb GB 1998	RS-48-98 Black Pool-West Thumb GB 1998	W10 diss West Thumb/ Black pool	W10 tot West Thumb/ Black pool	W10ADISS West Thumb/ Black pool	W10ATOT West Thumb/ Black pool	98-343 Duck Lake	YNP-99-408 On knob of tuff of Bluff Point,WTGB	YNP-02-705.1 Indian Pond- from shore	98-3 Turbid Lake-West shore	YNP-02-702.2 Turbid Lake water-from shore near Sedge Cr. Inlet
Latitude			44°25'0"N	44°25'6"N	44°25'6"N	44°25'6"N	44°25'6"N	44°25'6"N	44°25'10.7"N	44°26'45.2"N	44°33'22"N	44°32'54.2"N	44°33'8"N
Longitude			110°34'20"	110°34'17"W	110°34'17"	110°34'17"	110°34'17"	110°34'17"	110°34'49.3"	110°33'27.3"	110°19'30"W	110°15'55.3"	110°15'26"W
Collection Date			09/03/98	09/03/98	07/24/99	07/24/99	07/24/99	07/24/99	07/20/98	06/24/99	9/16/2002	07/15/98	9/11/2002
Temperature	°C		-	-	40.2	40.2	1.6	1.6	-	94.0	17.0	24.3	21
pH			8.2	8.2	7.9	7.9	8.3	8.3	5.0	4.2	7.2	3.4	2.5
Conductivity	uS/cm		-	-	2020	2020	-	-	-	-	-	-	-
Sum CO_2	mM		-	-	-	-	-	-	-	-	-	4.37	-
HCO_3	mM	measured	6.8	6.8	-	-	-	-	-	-	-	0.0	-
HCO_3	uM	calculated	6989	6991	-	-	-	-	-	-	-	-	-
Cl	mg/L	IC-Aq	310	300	300	-	290	-	ns	2	310	12	4.5
F	mg/L	IC-Aq	26	25	26	-	25	-	ns	0.1	5.9	0.3	0.2
NO_3	mg/L	IC-Aq	< 0.1	< 0.1	0.5	-	1.2	-	ns	<.35	0.6	1	0.5
SO_4	mg/L	IC-Aq	47	39	45	-	46	-	ns	30	31	40	86
Ag	ug/L	ICPMS	< 0.01	< 0.01	0.04	0.03	<0.01	<0.01	< 0.01	0.3	<0.1	< 0.01	<0.01
Al	ug/L	ICPMS	100	370	300	300	290	290	7.0	630	110	140	370
As	ug/L	ICPMS	1600	1600	2400	2400	2300	2300	0.4	2.1	1200	6.9	16
Au	ug/L	ICPMS	0.01	0.02	< 0.01	< 0.01	< 0.01	< 0.01	< 0.01	-	< 0.1	< 0.01	< 0.01
B	ug/L	ICPAES	3700	3600	3430	3470	3520	3470	< 10	-	-	290	-
Ba	ug/L	ICPMS	< 0.02	< 0.02	0.4	0.4	0.8	2	4	94	20	15	31
Be	ug/L	ICPMS	2.0	7.6	5.4	5.6	7.2	6.8	< 0.05	0.1	<0.5	< 0.05	0.09
Bi	ug/L	ICPMS	< 0.01	< 0.01	< 0.01	< 0.01	< 0.01	< 0.01	< 0.01	-	< 0.3	< 0.01	< 0.03
Ca	mg/L	ICPAES	< 1	< 1	0.86	0.865	0.85	0.851	1.2	-	-	4.0	-
Ca	mg/L	ICPMS	-	-	-	-	-	-	-	-	12	-	6
Cd	ug/L	ICPMS	< 0.02	< 0.02	<0.02	<0.02	<0.02	<0.02	< 0.02	<0.02	<0.2	< 0.02	0.02
Ce	ug/L	ICPMS	0.04	0.06	0.02	0.02	0.02	0.02	0.05	0.41	0.1	0.79	2.2
Co	ug/L	ICPMS	< 0.02	< 0.02	<0.02	<0.02	<0.02	<0.02	0.03	0.06	<0.2	0.3	0.85
Cr	ug/L	ICPMS	< 1	< 1	1	1	<1	<1	< 1	<1	<10	< 1	<1
Cs	ug/L	ICPMS	80	240	300	300	270	270	0.01	-	110	2.0	3.3
Cu	ug/L	ICPMS	0.7	< 0.5	<0.5	<0.5	<0.5	<0.5	0.6	2	<5	0.7	1
Dy	ug/L	ICPMS	< 0.005	< 0.005	< 0.005	< 0.005	< 0.005	< 0.005	< 0.005	0.052	< 0.05	0.10	0.18
Er	ug/L	ICPMS	< 0.005	< 0.005	< 0.005	< 0.005	< 0.005	< 0.005	< 0.005	0.03	< 0.05	0.061	0.097
Eu	ug/L	ICPMS	< 0.005	< 0.005	< 0.005	< 0.005	< 0.005	< 0.005	< 0.005	0.005	< 0.05	0.008	0.02
Fe	ug/L	ICPMS	< 10	< 10	<30	<30	<30	<30	< 10	1800	140	390	1600
Ga	ug/L	ICPMS	6.8	6.5	12	12	12	12	< 0.02	-	0.3	< 0.02	< 0.02
Gd	ug/L	ICPMS	< 0.005	< 0.005	< 0.005	< 0.005	< 0.005	< 0.005	0.01	0.06	< 0.05	0.11	0.2
Ge	ug/L	ICPMS	32	32	54	54	52	53	< 0.02	-	11	0.2	0.4
Hf	ug/L	ICPMS	0.60	0.70	-	-	-	-	< 0.05	-	-	< 0.05	-
Ho	ug/L	ICPMS	< 0.005	< 0.005	< 0.005	< 0.005	< 0.005	< 0.005	< 0.005	0.01	< 0.05	0.02	0.04
In	ug/L	ICPMS	< 0.01	< 0.01	-	-	-	-	< 0.01	< 0.01	< 0.1	< 0.01	< 0.01
K	mg/L	ICPAES	12	20	19.5	19.6	19.1	19.1	1.1	-	-	1.0	-
K	ug/L	ICPMS	-	-	-	-	-	-	-	-	10000	-	1800
La	ug/L	ICPMS	0.01	< 0.01	< 0.01	0.01	< 0.01	< 0.01	0.04	0.2	< 0.1	0.4	1.2
Li	ug/L	ICPMS	3600	4300	3900	3900	4500	4500	0.9	3.2	840	19	38
Mg	mg/L	ICPAES	< 1	< 1	<0.1	<0.1	<0.1	<0.1	< 1	-	-	1.9	-
Mg	mg/L	ICPMS	-	-	-	-	-	-	-	-	3.5	-	3.2
Mn	ug/L	ICPMS	0.65	2.2	2.4	2.6	2.2	2.3	1.3	17	7.2	34	76
Mo	ug/L	ICPMS	100	89	110	110	110	110	0.04	0.9	5.1	0.08	0.4
Na	mg/L	ICPAES	110	430	406	415	404	408	< 1	-	-	4.3	-
Na	mg/L	ICPMS	-	-	-	-	-	-	-	-	230	-	9.1
Nb	ug/L	ICPMS	0.05	0.06	0.72	0.63	0.4	0.3	< 0.02		-	< 0.02	-
Nd	ug/L	ICPMS	< 0.01	0.01	< 0.01	< 0.01	< 0.01	< 0.01	0.06	0.21	< 0.1	0.57	1
Ni	ug/L	ICPMS	0.2	< 0.1	<0.1	<0.1	<0.1	<0.1	< 0.1	0.3	1	0.8	2.4
P	ug/L	ICPMS	-	-	< 2	< 2	< 2	< 2	34	< 6	< 30	180	54
Pb	ug/L	ICPMS	< 0.05	< 0.05	<0.05	<0.05	<0.05	<0.05	< 0.05	<0.05	<0.5	0.2	0.3
Pr	ug/L	ICPMS	< 0.01	< 0.01	< 0.01	< 0.01	< 0.01	< 0.01	0.01	0.05	< 0.1	0.1	0.27
Rb	ug/L	ICPMS	100	150	200	200	200	200	2.7	38	94	2.7	4.6
Re	ug/L	ICPMS	< 0.02	< 0.02	-	-	-	-	< 0.02	-	< 0.2	< 0.02	< 0.02
Sb	ug/L	ICPMS	100	100	100	100	96	96	< 0.02	0.62	34	1.1	0.24
Sc	ug/L	ICPMS	< 0.1	0.3	3	3	< 0.1	< 0.1	< 0.1	-	-	< 0.1	-
Se	ug/L	ICPMS	2	2	4.8	4.7	3.3	3.6	< 0.2	< 0.2	2	< 0.2	< 0.2
SiO_2	mg/L	ICPMS	320	360	290	300	290	300	4	120	76	24	27
Sm	ug/L	ICPMS	< 0.01	< 0.01	< 0.01	< 0.01	< 0.01	< 0.01	0.01	0.06	< 0.1	0.08	0.2
Sn	ug/L	ICPMS	< 0.05	< 0.05	-	-	-	-	< 0.05	-	-	< 0.05	-
Sr	ug/L	ICPMS	1.6	1.8	2	2	2.1	2.1	12	4.5	94	46	61
Ta	ug/L	ICPMS	0.09	0.1	1.1	0.96	0.51	0.52	< 0.02	-	-	< 0.02	-
Tb	ug/L	ICPMS	< 0.005	< 0.005	< 0.005	< 0.005	< 0.005	< 0.005	< 0.005	0.006	< 0.05	0.02	0.03
Te	ug/L	ICPMS	< 0.1	< 0.1	-	-	-	-	< 0.1	-	-	< 0.1	-
Th	ug/L	ICPMS	< 0.005	0.008	< 0.02	< 0.02	< 0.02	< 0.02	< 0.005	-	2.6	0.005	0.11
Ti	ug/L	ICPMS	0.2	0.2	3.5	3.4	3	3	< 0.1	-	-	0.4	-
Tl	ug/L	ICPMS	0.07	0.1	0.2	0.2	0.2	0.2	< 0.05	0.2	<0.5	< 0.05	<0.05
Tm	ug/L	ICPMS	< 0.005	< 0.005	< 0.005	< 0.005	< 0.005	< 0.005	< 0.005	< 0.005	< 0.05	0.01	0.01
U	ug/L	ICPMS	0.02	< 0.005	0.005	0.006	0.007	< 0.005	0.009	0.09	< 0.05	0.02	0.04
V	ug/L	ICPMS	0.9	0.7	0.8	0.8	0.5	0.5	0.2	<0.2	2	2	4
W	ug/L	ICPMS	250	240	390	380	350	350	0.04	0.2	71	0.4	0.74
Y	ug/L	ICPMS	< 0.01	0.01	0.01	0.01	0.01	0.01	0.05	-	< 0.1	0.50	0.99
Yb	ug/L	ICPMS	< 0.01	< 0.01	< 0.01	< 0.01	< 0.01	< 0.01	< 0.01	0.02	< 0.1	0.06	0.1
Zn	ug/L	ICPMS	2	1	<0.5	<0.5	0.6	0.6	2	2	6	2	5
Zr	ug/L	ICPMS	0.2	0.84	0.3	< 0.2	< 0.2	< 0.2	0.1	-	-	0.1	-
Hg	ng/L	Hg CVAF	240	80	28	26	-	-	-	18	10	-	10
$\delta^{18}O$ vs VSMOW	permil	ISO1	-12.06	-13.94	-14.41	-	-14.45	-	-11.2	-14.9	-10.9	-17.51	-17.0
δD vs VSMOW	permil	ISO2	-134.2	-140.1	-	-	-	-	-108.5	-144.8	-107.8	-136.7	-129.9
$\delta^{34}S$ vs CDT	permil	ISO3	14.26	15.18	-	-	-	-	-	-	-	-	-

Appendix 4. Site and analytical data from subaerial hydrothermal features—*Continued*.

Field no. Sample name & description			98-4 Sedge Crk inlet to Turbid Lake-bubbler	YNP-02-702.1 Turbid Lake-Sedge Cr. Inlet	98-336.2 mudpot SE of Turbid Lake	YNP-02-701.1 Turbid Lake-mudpot	98-337 Bear Crk. inlet to Turbid Lake	YNP-02-700.1 Turbid Lake- Bear Creek inlet	98-329.2w Mushpots-U. Pelican Cr.-Black Pond	98-329.3 Mushpots-U. Pelican Cr.-S. end, Clear Pond	98-333.1 new thermal area-N. of mushpots-Frying Pan	98-333.2 new thermal area-N. of mushpots-pool near top
Latitude			44°33'8.2"N	44°32'11.3"N	44°32'47"N	44°32'48"N	44°32'37.8"N	44°32'37.8"N	44°38'3.2"N	44°38'3.2"N	44°38'14.2"N	44°38'14.2"N
Longitude			110°15'26"W	110°15'24"W	110°15'14.5"	110°15'18.5"W	110°15'26.5"	110°15'26.5"W	110°13'35.3"	110°13'35.3"	110°13'33.3"	110°13'33.3"
Collection Date			07/15/98	9/11/2002	07/16/98	9/11/2002	07/16/98	9/11/2002	07/10/98	07/11/98	07/13/98	07/13/98
Temperature	˚C		14.3	14	56.6	49	20.2	13	62.5	76.2	86.0	66.1
pH			7.6	6.2	1.5	1.1	6.2	7.2	2.8	4.3	6.9	2.3
Conductivity	uS/cm		-	-	-	-	-	-	-	-	-	-
Sum CO_2	mM		0.69	-	-	-	0.88	-	2.07	2	1.18	1.4
HCO_3	mM	measured	0.4	-	-	-	0.4	-	0.0	0.0	0.9	0.0
HCO_3	uM	calculated	-	-	-	-	-	-	-	-	-	-
Cl	mg/L	IC-Aq	0.3	2.3	10	6.7	0.8	2.2	1.2	1.5	1	1.1
F	mg/L	IC-Aq	0.2	0.2	0.2	0.5	1.1	0.3	0.2	1.6	0.4	0.2
NO_3	mg/L	IC-Aq	<.1	0.4	<.1	0.9	<.1	<.18	<.1	<.1	<.1	<.1
SO_4	mg/L	IC-Aq	5	4.8	910	2400	10	5.3	460	460	410	540
Ag	ug/L	ICPMS	< 0.01	<0.01	< 0.01	<0.01	0.01	<0.01	< 0.01	0.1	< 0.01	< 0.01
Al	ug/L	ICPMS	14	9.5	7600	19000	29	22	840	25	7.4	7800
As	ug/L	ICPMS	3.1	2.9	12	37	2	5.6	2	3.1	0.4	1
Au	ug/L	ICPMS	< 0.01	< 0.01	< 0.01	< 0.01	< 0.01	< 0.01	< 0.01	0.01	< 0.01	< 0.01
B	ug/L	ICPAES	26	-	1400	-	46	-	56	1100	520	100
Ba	ug/L	ICPMS	6.8	14	36	39	10	9.6	58	78	63	45
Be	ug/L	ICPMS	< 0.05	<0.05	0.05	0.2	< 0.05	<0.05	1.0	0.2	0.2	0.6
Bi	ug/L	ICPMS	< 0.01	< 0.03	< 0.01	< 0.03	< 0.01	< 0.03	< 0.01	< 0.01	< 0.01	< 0.01
Ca	mg/L	ICPAES	3.7	-	2.6	-	4.1	-	51	39	57	38
Ca	mg/L	ICPMS	-	8.6	-	5.2	-	7.7	-	-	-	-
Cd	ug/L	ICPMS	< 0.02	<0.02	0.05	0.07	< 0.02	<0.02	< 0.02	< 0.02	< 0.02	0.08
Ce	ug/L	ICPMS	0.1	0.1	7.1	21	0.3	0.1	4.1	0.3	0.01	4.8
Co	ug/L	ICPMS	0.08	0.1	0.73	5.6	0.1	0.05	7.7	0.04	0.02	6.2
Cr	ug/L	ICPMS	< 1	<1	4	20	< 1	<1	< 1	< 1	< 1	8
Cs	ug/L	ICPMS	0.06	0.1	13	14	0.47	0.02	4.8	9.4	15	8.6
Cu	ug/L	ICPMS	< 0.5	0.8	3	2	< 0.5	0.6	0.9	1	< 0.5	1
Dy	ug/L	ICPMS	0.03	0.02	0.21	0.56	0.058	0.04	0.78	0.02	< 0.005	0.44
Er	ug/L	ICPMS	0.01	0.01	0.087	0.29	0.04	0.02	0.37	0.009	< 0.005	0.18
Eu	ug/L	ICPMS	0.007	< 0.005	0.055	0.2	< 0.005	< 0.005	0.17	< 0.005	< 0.005	0.12
Fe	ug/L	ICPMS	58	200	800	4300	68	100	1100	50	50	2600
Ga	ug/L	ICPMS	< 0.02	< 0.02	2.2	5.1	< 0.02	< 0.02	0.2	0.04	0.07	0.3
Gd	ug/L	ICPMS	0.02	0.02	0.29	0.78	0.061	0.03	0.87	0.02	< 0.005	0.48
Ge	ug/L	ICPMS	< 0.02	0.02	0.6	0.6	< 0.02	< 0.02	0.9	4.5	1.7	0.9
Hf	ug/L	ICPMS	< 0.05	-	< 0.05	-	< 0.05	-	< 0.05	< 0.05	< 0.05	< 0.05
Ho	ug/L	ICPMS	0.005	0.006	0.03	0.11	0.01	0.008	0.14	< 0.005	< 0.005	0.077
In	ug/L	ICPMS	< 0.01	< 0.01	< 0.01	< 0.01	< 0.01	< 0.01	< 0.01	< 0.01	< 0.01	< 0.01
K	mg/L	ICPAES	1.1	-	3.8	-	1.1	-	17	19	24	24
K	ug/L	ICPMS	-	2100	-	8200	-	1700	-	-	-	-
La	ug/L	ICPMS	0.09	0.1	4.3	13	0.2	0.1	1.5	0.2	< 0.01	1.9
Li	ug/L	ICPMS	3.4	10	77	87	6.0	5.2	51	77	49	22
Mg	mg/L	ICPAES	2	-	< 1	-	2.1	-	18	15	9.3	9.3
Mg	mg/L	ICPMS	-	4.8	-	1.4	-	4.2	-	-	-	-
Mn	ug/L	ICPMS	8.1	21	85	120	18	11	740	240	700	540
Mo	ug/L	ICPMS	0.2	0.5	< 0.02	0.82	0.56	0.81	< 0.02	0.2	< 0.02	< 0.02
Na	mg/L	ICPAES	2.5	-	18	-	2.8	-	68	84	70	42
Na	mg/L	ICPMS	-	5.8	-	27	-	4.5	-	-	-	-
Nb	ug/L	ICPMS	< 0.02	-	< 0.02	-	< 0.02	-	< 0.02	< 0.02	< 0.02	< 0.02
Nd	ug/L	ICPMS	0.1	0.09	2.7	7.9	0.21	0.1	3.5	0.1	< 0.01	3.2
Ni	ug/L	ICPMS	0.2	0.8	2.0	14	0.4	0.6	9.8	0.1	0.2	22
P	ug/L	ICPMS	430	31	650	220	160	19	150	480	80	65
Pb	ug/L	ICPMS	0.1	<0.05	1.3	5.8	< 0.05	<0.05	0.1	< 0.05	< 0.05	0.4
Pr	ug/L	ICPMS	0.02	0.02	0.82	2.5	0.05	0.03	0.72	0.04	< 0.01	0.73
Rb	ug/L	ICPMS	2.6	3.3	9.3	12	2.6	2.4	54	71	150	130
Re	ug/L	ICPMS	< 0.02	< 0.02	< 0.02	< 0.02	< 0.02	< 0.02	< 0.02	< 0.02	< 0.02	< 0.02
Sb	ug/L	ICPMS	0.2	0.2	0.2	0.2	0.2	0.2	< 0.02	< 0.02	< 0.02	0.09
Sc	ug/L	ICPMS	< 0.1	-	< 0.1	-	< 0.1	-	4	2	1	2
Se	ug/L	ICPMS	< 0.2	< 0.2	< 0.2	0.3	< 0.2	< 0.2	< 0.2	< 0.2	220	< 0.2
SiO_2	mg/L	ICPMS	33	34	110	100	26	25	190	140	160	160
Sm	ug/L	ICPMS	0.02	0.02	0.37	1.3	0.08	0.03	0.89	0.04	< 0.01	0.66
Sn	ug/L	ICPMS	< 0.05	-	0.6	-	< 0.05	-	< 0.05	< 0.05	< 0.05	< 0.05
Sr	ug/L	ICPMS	36	62	100	190	50	63	460	660	650	580
Ta	ug/L	ICPMS	< 0.02	-	< 0.02	-	< 0.02	-	< 0.02	< 0.02	< 0.02	< 0.02
Tb	ug/L	ICPMS	< 0.005	< 0.005	0.04	0.1	0.008	< 0.005	0.13	0.007	< 0.005	0.093
Te	ug/L	ICPMS	< 0.1	-	< 0.1	-	< 0.1	-	< 0.1	< 0.1	< 0.1	< 0.1
Th	ug/L	ICPMS	0.05	0.08	0.23	2.9	0.006	< 0.04	< 0.005	< 0.005	< 0.005	0.10
Ti	ug/L	ICPMS	0.1	-	4.3	-	0.2	-	1.8	1.7	1.4	3.2
Tl	ug/L	ICPMS	< 0.05	<0.05	< 0.05	<0.05	< 0.05	<0.05	< 0.05	< 0.05	< 0.05	< 0.05
Tm	ug/L	ICPMS	< 0.005	< 0.005	0.01	0.04	0.006	< 0.005	0.056	< 0.005	< 0.005	0.03
U	ug/L	ICPMS	0.03	0.03	0.14	0.37	0.03	0.03	0.32	0.007	< 0.005	0.49
V	ug/L	ICPMS	5	3	4	12	1	0.8	2	0.2	< 0.1	8.7
W	ug/L	ICPMS	0.06	0.3	0.2	1.2	0.05	0.68	0.2	1.2	0.67	0.2
Y	ug/L	ICPMS	0.1	0.1	0.77	2.4	0.3	0.2	3.5	0.2	< 0.01	1.6
Yb	ug/L	ICPMS	0.01	0.01	0.08	0.28	0.03	0.02	0.30	0.01	< 0.01	0.2
Zn	ug/L	ICPMS	0.9	0.9	9	10	0.8	0.8	34	2	0.8	20
Zr	ug/L	ICPMS	0.06	-	0.3	-	0.1	-	< 0.05	0.07	< 0.05	0.08
Hg	ng/L	Hg CVAF	-	11	-	700	-	10	-	-	-	-
$\delta^{18}O$ vs VSMOW	permil	ISO1	-18.66	-18.3	-1.22	-4.8	-18.02	-17.7	-8.89	-9.62	-13.39	-10.6
δD vs VSMOW	permil	ISO2	-140.2	-135.4	-102.5	-102	-137.3	-129.6	-118.7	-126.8	-135.4	-125.4
$\delta^{34}S$ vs CDT	permil	ISO3	-	-	-	-	-	-	-	-	-	-

Appendix 4. Site and analytical data from subaerial hydrothermal features—*Continued*.

Field no. Sample name & description			YNP-01-569.1 Fern Lake	YNP-99-436diss Ponuntpa Springs	YNP-99-438diss crater near Hot Springs Basin Group	98-348 Vermillion Spr.-Sour Crk. Dome	YNP-00-532.1 Black dog beach vent	YNP-99-429.1tot Porkchop Hot Spring, Norris	YNP-99-429.1diss Porkchop Hot Spring, Norris	YNP-99-429.2tot Porkchop Hot Spring, Norris	YNP-99-429.2diss Porkchop Hot Spring, Norris
Latitude			44°40'37.8"N	44°40'10.2"N	44°44'39.2"N	44°35'4.8"N	44°33'17.4"N	44°43'21"N	44°43'21"N	44°43'21"N	44°43'21"N
Longitude			110°16'5.1"W	110°17'26.3"W	110°14'4.3"W	110°18'49.3"	110°19'19.8"W	110°42'28"W	110°42'28"W	110°42'28"W	110°42'28"W
Collection Date			-	07/13/99	07/14/99	07/21/98	09/02/00	07/04/99	07/04/99	07/04/99	07/04/99
Temperature	˚C		44	43.0	86.0	53.1	42.1	55.0	55.0	55.0	55.0
pH			5.5	6.2	1.5	2.3	6.4	7.0	7.0	7.0	7.0
Conductivity	uS/cm		-	-	-	-	-	-	-	-	-
Sum CO_2	mM		-	-	-	-	-	-	-	-	-
HCO_3	mM	measured	-	-	-	-	-	-	-	-	-
HCO_3	uM	calculated	-	-	-	-	-	-	-	-	-
Cl	mg/L	IC-Aq	210	280	4	14	320	-	650	-	660
F	mg/L	IC-Aq	0.7	5.4	0.3	0.8	1.8	-	6.1	-	6.2
NO_3	mg/L	IC-Aq	0.7	1.2	<.1	0.1	0.2	-	<.1	-	<.1
SO_4	mg/L	IC-Aq	290	2.3	1000	350	1.2	-	34	-	34
Ag	ug/L	ICPMS	5.2	0.02	<0.01	< 0.01	<0.01	0.68	0.3	0.2	0.1
Al	ug/L	ICPMS	40	<0.5	19000	36000	45	240	71	86	69
As	ug/L	ICPMS	49	5.5	13	140	240	3100	3000	3000	3100
Au	ug/L	ICPMS	< 0.1	< 0.01	< 0.01	< 0.01	< 0.01	< 0.01	< 0.01	< 0.01	< 0.01
B	ug/L	ICPAES	-	8110	554	1600	-	9120	9140	9040	9070
Ba	ug/L	ICPMS	51	140	68	21	420	12	11	11	11
Be	ug/L	ICPMS	<0.5	5.5	1.3	0.8	<0.05	6.1	5.5	3.5	6.4
Bi	ug/L	ICPMS	< 0.3	< 0.01	< 0.01	< 0.01	< 0.01	< 0.01	< 0.01	< 0.01	< 0.01
Ca	mg/L	ICPAES	-	19.4	10.8	2.5	-	5.15	5.15	5.19	5.04
Ca	mg/L	ICPMS	44	-	-	-	59	-	-	-	-
Cd	ug/L	ICPMS	<0.2	<0.02	0.03	0.03	0.04	<0.02	<0.02	<0.02	<0.02
Ce	ug/L	ICPMS	< 0.1	0.01	24	21	0.03	0.1	0.02	0.02	< 0.01
Co	ug/L	ICPMS	<0.2	<0.02	0.1	0.56	0.77	<0.02	<0.02	<0.02	<0.02
Cr	ug/L	ICPMS	<10	<1	3	4	<1	<1	<1	<1	<1
Cs	ug/L	ICPMS	15	100	1.8	24	0.34	580	570	570	580
Cu	ug/L	ICPMS	<5	<0.5	0.5	0.6	0.6	<0.5	<0.5	<0.5	<0.5
Dy	ug/L	ICPMS	< 0.05	0.006	1.5	1.6	< 0.005	0.009	< 0.005	< 0.005	< 0.005
Er	ug/L	ICPMS	< 0.05	0.008	0.93	0.78	< 0.005	< 0.005	< 0.005	< 0.005	< 0.005
Eu	ug/L	ICPMS	< 0.05	< 0.005	0.24	0.098	< 0.005	< 0.005	< 0.005	< 0.005	< 0.005
Fe	ug/L	ICPMS	75	330	4100	7500	1600	<30	<30	<30	<30
Ga	ug/L	ICPMS	< 0.2	< 0.02	5.8	3.2	< 0.02	3.4	3	3.3	3.3
Gd	ug/L	ICPMS	< 0.05	< 0.005	1.3	1.8	< 0.005	0.01	< 0.005	< 0.005	< 0.005
Ge	ug/L	ICPMS	9	31	0.7	1.4	7.9	39	38	39	39
Hf	ug/L	ICPMS	-	-	-	< 0.05	-	-	-	-	-
Ho	ug/L	ICPMS	< 0.05	< 0.005	0.32	0.30	< 0.005	< 0.005	< 0.005	< 0.005	< 0.005
In	ug/L	ICPMS	< 0.1	-	-	0.02	< 0.01	-	-	-	-
K	mg/L	ICPAES	-	23.3	20.2	12	-	58	58.3	58.8	57.1
K	ug/L	ICPMS	80000	-	-	-	50000	-	-	-	-
La	ug/L	ICPMS	< 0.1	< 0.01	16	8.3	0.03	0.06	0.01	0.02	0.01
Li	ug/L	ICPMS	1600	440	25	250	750	8900	8900	9100	9200
Mg	mg/L	ICPAES	-	6.87	7.88	1	-	<0.1	<0.1	<0.1	<0.1
Mg	mg/L	ICPMS	13	-	-	-	63	-	-	-	-
Mn	ug/L	ICPMS	520	78	44	42	70	34	33	34	34
Mo	ug/L	ICPMS	11	1.2	1.1	0.2	0.5	280	280	290	290
Na	mg/L	ICPAES	-	<0.1	23.5	10	-	379	379	377	380
Na	mg/L	ICPMS	260	-	-	-	>300	-	-	-	-
Nb	ug/L	ICPMS	-	0.2	0.1	< 0.02	-	0.88	0.65	0.5	0.4
Nd	ug/L	ICPMS	< 0.1	< 0.01	8.4	9.8	0.01	0.07	< 0.01	< 0.01	< 0.01
Ni	ug/L	ICPMS	<1	<0.1	0.4	2.2	3.1	<0.1	<0.1	<0.1	<0.1
P	ug/L	ICPMS	740	7.3	62	110	21	16	12	16	10
Pb	ug/L	ICPMS	<0.5	<0.05	5.1	< 0.05	0.1	0.07	<0.05	<0.05	<0.05
Pr	ug/L	ICPMS	< 0.1	< 0.01	2.7	2.6	< 0.01	0.02	< 0.01	< 0.01	< 0.01
Rb	ug/L	ICPMS	240	150	66	65	63	500	480	490	500
Re	ug/L	ICPMS	< 0.2	-	-	< 0.02	< 0.02	-	-	-	-
Sb	ug/L	ICPMS	2.6	1.2	0.32	0.69	0.2	160	160	160	160
Sc	ug/L	ICPMS	-	< 0.1	< 0.1	0.4	-	4	< 0.1	< 0.1	< 0.1
Se	ug/L	ICPMS	< 2	4.6	< 0.3	1300	0.95	12	12	12	12
SiO_2	mg/L	ICPMS	140	130	170	170	170	460	440	460	450
Sm	ug/L	ICPMS	< 0.1	< 0.01	1.6	2.1	< 0.01	< 0.01	< 0.01	< 0.01	< 0.01
Sn	ug/L	ICPMS	-	-	-	0.2	-	-	-	-	-
Sr	ug/L	ICPMS	470	270	130	27	410	14	14	14	14
Ta	ug/L	ICPMS	-	0.31	0.13	< 0.02	-	0.86	0.64	0.56	0.48
Tb	ug/L	ICPMS	< 0.05	< 0.005	0.22	0.31	< 0.005	< 0.005	< 0.005	< 0.005	< 0.005
Te	ug/L	ICPMS	-	-	-	< 0.1	-	-	-	-	-
Th	ug/L	ICPMS	< 0.4	0.04	3.9	2.3	0.38	< 0.02	< 0.02	< 0.02	< 0.02
Ti	ug/L	ICPMS	-	< 0.2	11	1.5	-	1.3	0.6	0.7	0.6
Tl	ug/L	ICPMS	<0.5	0.3	0.2	0.4	<0.05	1.2	1.2	1.2	1.1
Tm	ug/L	ICPMS	< 0.05	< 0.005	0.13	0.11	< 0.005	< 0.005	< 0.005	< 0.005	< 0.005
U	ug/L	ICPMS	< 0.05	< 0.005	0.72	0.60	0.04	< 0.005	< 0.005	< 0.005	< 0.005
V	ug/L	ICPMS	2	0.5	2.1	8.6	0.71	5.7	3.7	3.3	3
W	ug/L	ICPMS	20	36	7.5	0.3	0.2	140	150	150	160
Y	ug/L	ICPMS	< 0.1	0.1	7.7	7.2	0.08	0.04	0.01	< 0.01	< 0.01
Yb	ug/L	ICPMS	< 0.1	0.01	0.88	0.66	< 0.01	< 0.01	< 0.01	< 0.01	< 0.01
Zn	ug/L	ICPMS	<5	<0.5	10	32	4	<0.5	<0.5	<0.5	<0.5
Zr	ug/L	ICPMS	-	< 0.2	0.7	< 0.05	-	0.7	< 0.2	< 0.2	< 0.2
Hg	ng/L	Hg CVAF	10	68	126	-	<0.005	36	-	16	-
$\delta^{18}O$ vs VSMOW	permil	ISO1	-17.6	-17.6	-15.7	-16.9	-17.7	-12.8	-	-12.8	-
δD vs VSMOW	permil	ISO2	-146.8	-149.3	-137.3	-137.4	-144.8	-138.1	-	-137.5	-
$\delta^{34}S$ vs CDT	permil	ISO3	-	-	-	-	-	-	-	-	-

Appendix 4. Site and analytical data from subaerial hydrothermal features—*Continued*.

Field no. Sample name & description			P10 diss Norris/Pork chop	P10 tot Norris/Pork chop	P10Adiss Norris/Pork chop	P10Atot Norris/Pork chop	YNP-99-430.1tot Echinus Hot Spring, Norris	YNP-99-430.1diss Echinus Hot Spring, Norris	YNP-99-430.2tot Echinus Hot Spring, Norris	YNP-99-430.2diss Echinus Hot Spring, Norris	E10 diss Norris/Echinus
Latitude			44°43'21"N	44°43'21"N	44°43'21"N	44°43'21"N	44°43'19.5"N	44°43'19.5"N	44°43'19.5"N	44°43'19.5"N	44°43'19.5"N
Longitude			110°42'28"W	110°42'28"W	110°42'28"W	110°42'28"W	110°42'4.9"W	110°42'4.9"W	110°42'4.9"W	110°42'4.9"W	110°42'4.9"W
Collection Date			07/23/99	07/23/99	07/23/99	07/23/99	07/04/99	07/04/99	07/04/99	07/04/99	07/23/99
Temperature	°C		31.5	31.5	1.6	1.6	80.0	80.0	80.0	80.0	35.4
pH			6.6	6.6	7.0	7.0	3.3	3.3	3.3	3.3	3.2
Conductivity	uS/cm		2300	2300	-	-	-	-	-	-	1272
Sum CO_2	mM		-	-	-	-	-	-	-	-	-
HCO_3	mM	measured	-	-	-	-	-	-	-	-	-
HCO_3	uM	calculated	-	-	-	-	-	-	-	-	-
Cl	mg/L	IC-Aq	620	-	660	-	-	150	-	150	150
F	mg/L	IC-Aq	6.5	-	5.6	-	-	4.7	-	4.8	4.8
NO_3	mg/L	IC-Aq	0.5	-	<.35	-	-	0.7	-	<.1	<.35
SO_4	mg/L	IC-Aq	32	-	36	-	-	250	-	260	260
Ag	ug/L	ICPMS	0.03	0.02	0.01	0.01	<0.01	<0.01	<0.01	<0.01	0.04
Al	ug/L	ICPMS	<0.5	<0.5	<0.3	<0.3	1900	1900	1900	1900	2000
As	ug/L	ICPMS	3100	3100	2800	2900	310	290	280	280	290
Au	ug/L	ICPMS	< 0.01	< 0.01	< 0.01	< 0.01	< 0.01	< 0.01	< 0.01	< 0.01	< 0.01
B	ug/L	ICPAES	9250	9360	9330	9220	2500	2400	2450	2420	2540
Ba	ug/L	ICPMS	11	11	9.4	9.6	61	62	59	61	60
Be	ug/L	ICPMS	5.2	5.2	2.7	2.9	7.5	6.6	7.3	8.1	7
Bi	ug/L	ICPMS	< 0.01	< 0.01	< 0.01	< 0.01	< 0.01	< 0.01	< 0.01	< 0.01	< 0.01
Ca	mg/L	ICPAES	5.01	5.16	5	5.01	4.73	4.66	4.6	4.6	4.74
Ca	mg/L	ICPMS	-	-	-	-	-	-	-	-	-
Cd	ug/L	ICPMS	<0.02	<0.02	<0.02	<0.02	<0.02	<0.02	<0.02	<0.02	<0.02
Ce	ug/L	ICPMS	< 0.01	< 0.01	< 0.01	< 0.01	37	36	36	36	36
Co	ug/L	ICPMS	<0.02	<0.02	<0.02	<0.02	<0.02	<0.02	<0.02	<0.02	<0.02
Cr	ug/L	ICPMS	<1	<1	<1	<1	<1	<1	<1	<1	<1
Cs	ug/L	ICPMS	580	580	500	500	84	86	82	84	81
Cu	ug/L	ICPMS	<0.5	<0.5	<0.5	<0.5	<0.5	<0.5	<0.5	<0.5	<0.5
Dy	ug/L	ICPMS	< 0.005	< 0.005	< 0.005	< 0.005	6.8	6.6	6.6	6.8	6.7
Er	ug/L	ICPMS	< 0.005	< 0.005	< 0.005	< 0.005	3.9	3.7	3.7	3.7	3.5
Eu	ug/L	ICPMS	< 0.005	< 0.005	< 0.005	< 0.005	0.19	0.16	0.18	0.19	0.17
Fe	ug/L	ICPMS	<30	<30	<30	<30	2000	1800	1900	1800	1900
Ga	ug/L	ICPMS	0.03	< 0.02	0.02	0.04	< 0.02	< 0.02	< 0.02	< 0.02	< 0.02
Gd	ug/L	ICPMS	< 0.005	< 0.005	< 0.005	< 0.005	5.6	5.6	5.5	5.6	5.6
Ge	ug/L	ICPMS	40	40	38	37	9.8	10	9.7	9.8	9.9
Hf	ug/L	ICPMS	-	-	-	-	-	-	-	-	-
Ho	ug/L	ICPMS	< 0.005	< 0.005	< 0.005	< 0.005	1.4	1.3	1.4	1.4	1.3
In	ug/L	ICPMS	-	-	-	-	-	-	-	-	-
K	mg/L	ICPAES	57.1	57.9	57.2	57.4	52.2	51.2	50.7	50.7	51.9
K	ug/L	ICPMS	-	-	-	-	-	-	-	-	-
La	ug/L	ICPMS	< 0.01	< 0.01	< 0.01	< 0.01	11	10	10	10	10
Li	ug/L	ICPMS	9800	10000	7000	7000	1100	1100	1100	1100	1100
Mg	mg/L	ICPAES	<0.1	<0.1	<0.1	<0.1	0.503	0.494	0.497	0.49	0.499
Mg	mg/L	ICPMS	-	-	-	-	-	-	-	-	-
Mn	ug/L	ICPMS	33	33	28	29	210	210	200	210	230
Mo	ug/L	ICPMS	280	280	230	240	14	8.5	8	7.1	6
Na	mg/L	ICPAES	383	386	360	359	167	170	168	168	172
Na	mg/L	ICPMS	-	-	-	-	-	-	-	-	-
Nb	ug/L	ICPMS	0.1	0.1	0.03	0.02	0.2	0.2	0.2	0.2	0.2
Nd	ug/L	ICPMS	< 0.01	< 0.01	< 0.01	< 0.01	19	18	19	19	18
Ni	ug/L	ICPMS	<0.1	<0.1	<0.1	<0.1	<0.1	<0.1	<0.1	<0.1	<0.1
P	ug/L	ICPMS	5.6	6	< 2	< 2	2	< 1	1	< 1	3
Pb	ug/L	ICPMS	<0.05	<0.05	<0.05	<0.05	0.2	0.1	0.2	0.1	<0.05
Pr	ug/L	ICPMS	< 0.01	< 0.01	< 0.01	< 0.01	4.5	4.5	4.4	4.4	4.2
Rb	ug/L	ICPMS	490	510	500	480	360	370	360	370	350
Re	ug/L	ICPMS	-	-	-	-	-	-	-	-	-
Sb	ug/L	ICPMS	150	150	130	130	1.5	1.2	1.1	0.98	0.82
Sc	ug/L	ICPMS	< 0.1	< 0.1	< 0.1	< 0.1	< 0.1	< 0.1	< 0.1	< 0.1	< 0.1
Se	ug/L	ICPMS	9.8	11	7.2	7.4	2.4	2.7	2	1.8	1.7
SiO_2	mg/L	ICPMS	410	420	310	320	250	250	240	250	270
Sm	ug/L	ICPMS	< 0.01	< 0.01	< 0.01	< 0.01	5.3	5.1	5.2	5.4	4.9
Sn	ug/L	ICPMS	-	-	-	-	-	-	-	-	-
Sr	ug/L	ICPMS	14	14	13	14	7.2	7.2	7.1	7.3	7
Ta	ug/L	ICPMS	0.16	0.15	0.04	< 0.03	0.2	0.18	0.17	0.17	0.23
Tb	ug/L	ICPMS	< 0.005	< 0.005	< 0.005	< 0.005	1.1	1.1	1	1.1	1
Te	ug/L	ICPMS	-	-	-	-	-	-	-	-	-
Th	ug/L	ICPMS	< 0.02	< 0.02	< 0.02	< 0.02	0.64	0.68	0.78	0.7	0.66
Ti	ug/L	ICPMS	0.2	0.5	< 0.8	< 0.8	2.6	2.2	2.5	2.5	3.2
Tl	ug/L	ICPMS	1.2	1.2	0.98	0.98	0.61	0.59	0.58	0.56	0.53
Tm	ug/L	ICPMS	< 0.005	< 0.005	< 0.005	< 0.005	0.51	0.53	0.53	0.52	0.48
U	ug/L	ICPMS	< 0.005	< 0.005	< 0.005	< 0.005	2.2	2.2	2.2	2.2	2.3
V	ug/L	ICPMS	2.8	2.8	2	2	0.4	0.3	<0.2	<0.2	<0.2
W	ug/L	ICPMS	160	160	110	120	18	8	8.9	4.8	2.1
Y	ug/L	ICPMS	< 0.01	< 0.01	< 0.01	< 0.01	36	36	35	36	34
Yb	ug/L	ICPMS	< 0.01	< 0.01	< 0.01	< 0.01	3	3	2.9	3	2.9
Zn	ug/L	ICPMS	<0.5	<0.5	<0.5	<0.5	20	20	20	20	20
Zr	ug/L	ICPMS	< 0.2	< 0.2	< 0.2	< 0.2	< 0.2	< 0.2	< 0.2	< 0.2	< 0.2
Hg	ng/L	Hg CVAF	7	<5	-	-	7	-	6	-	<5
$\delta^{18}O$ vs VSMOW	permil	ISO1	-13.03	-	-13.09	-	-16.6	-	-16.5	-	-16.53
δD vs VSMOW	permil	ISO2	-	-	-	-	-141.8	-	-142.9	-	-
$\delta^{34}S$ vs CDT	permil	ISO3	-	-	-	-	-	-	-	-	-

Appendix 4. Site and analytical data from subaerial hydrothermal features—*Continued*.

Field no. Sample name & description			E10 tot Norris/Echinus	E10Adiss Norris/Echinus	E10Atot Norris/Echinus	G10 diss Norris/Green Dragon	G10 tot Norris/Green Dragon	G10Adiss Norris/Green Dragon	G10Atot Norris/Green Dragon	YNP-02-588.1 Large explosion crater N of gap, Norris	YNP-99-453 Heart Lake/fissure geyser area
Latitude			44°43'19.5"N	44°43'19.5"N	44°43'19.5"N	44°43'12.2"N	44°43'12.2"N	44°43'12.2"N	44°43'12.2"N	44°43'43.5"N	44°17'27.2"N
Longitude			110°42'4.9"W	110°42'4.9"W	110°42'4.9"W	110°42'23"W	110°42'23"W	110°42'23"W	110°42'23"W	110°42'53"W	110°30'31"W
Collection Date			07/23/99	07/23/99	07/23/99	07/23/99	07/23/99	07/23/99	07/23/99	9/19/2002	07/22/99
Temperature	˚C		35.4	1.6	1.6	30.1	30.1	1.6	1.6	39	92.0
pH			3.2	3.3	3.3	2.6	2.6	2.8	2.8	1.6	7.0
Conductivity	uS/cm		1272	-	-	1984	1984	-	-	-	-
Sum CO_2	mM		-	-	-	-	-	-	-	-	-
HCO_3	mM	measured	-	-	-	-	-	-	-	-	-
HCO_3	uM	calculated	-	-	-	-	-	-	-	-	-
Cl	mg/L	IC-Aq	-	150	-	330	-	360	-	180	140
F	mg/L	IC-Aq	-	4.8	-	5.6	-	4.5	-	4.1	12
NO_3	mg/L	IC-Aq	-	<.35	-	<.35	-	0.5	-	<.18	<.35
SO_4	mg/L	IC-Aq	-	290	-	150	-	160	-	520	110
Ag	ug/L	ICPMS	0.03	<0.01	<0.01	<0.01	0.01	<0.01	<0.01	<0.1	0.3
Al	ug/L	ICPMS	1900	1800	1800	4000	4000	2600	2600	19000	46
As	ug/L	ICPMS	280	300	300	1700	1700	1400	1400	2100	690
Au	ug/L	ICPMS	< 0.01	< 0.01	< 0.01	< 0.01	< 0.01	< 0.01	< 0.01	< 0.1	< 0.01
B	ug/L	ICPAES	2590	2500	2540	5430	5460	5450	5420	-	1700
Ba	ug/L	ICPMS	59	57	59	35	35	28	29	68	5
Be	ug/L	ICPMS	7.6	6.3	6.9	3.5	3.6	2	2.4	3	1.3
Bi	ug/L	ICPMS	< 0.01	< 0.01	< 0.01	< 0.01	< 0.01	< 0.01	< 0.01	< 0.3	< 0.01
Ca	mg/L	ICPAES	4.74	4.78	4.76	4.02	4.02	4.08	4.09	-	3.05
Ca	mg/L	ICPMS	-	-	-	-	-	-	-	6.9	-
Cd	ug/L	ICPMS	<0.02	<0.02	<0.02	<0.02	<0.02	<0.02	<0.02	<0.2	<0.02
Ce	ug/L	ICPMS	36	35	35	9.1	9	7.4	7.3	22	0.01
Co	ug/L	ICPMS	<0.02	<0.02	<0.02	<0.02	<0.02	<0.02	<0.02	0.5	<0.02
Cr	ug/L	ICPMS	<1	<1	<1	<1	<1	<1	<1	<10	<1
Cs	ug/L	ICPMS	81	82	81	300	300	240	230	160	170
Cu	ug/L	ICPMS	<0.5	<0.5	<0.5	<0.5	<0.5	<0.5	<0.5	<5	<0.5
Dy	ug/L	ICPMS	6.8	6.6	6.6	1	1	0.87	0.87	4.6	< 0.005
Er	ug/L	ICPMS	3.5	3.6	3.6	0.55	0.57	0.49	0.52	2.4	< 0.005
Eu	ug/L	ICPMS	0.17	0.18	0.17	0.04	0.03	0.03	0.03	0.4	< 0.005
Fe	ug/L	ICPMS	1800	1900	1900	750	750	590	590	7600	<30
Ga	ug/L	ICPMS	< 0.02	< 0.02	< 0.02	0.3	0.2	0.2	0.2	5	11
Gd	ug/L	ICPMS	5.4	5.6	5.6	0.84	0.94	0.81	0.78	4.1	< 0.005
Ge	ug/L	ICPMS	9.6	11	11	25	25	22	22	18	17
Hf	ug/L	ICPMS	-	-	-	-	-	-	-	-	-
Ho	ug/L	ICPMS	1.4	1.3	1.3	0.2	0.21	0.18	0.18	0.87	< 0.005
In	ug/L	ICPMS	-	-	-	-	-	-	-	< 0.1	-
K	mg/L	ICPAES	52	51.7	51.6	45.8	45.7	45.5	45.8	-	34.8
K	ug/L	ICPMS	-	-	-	-	-	-	-	41000	-
La	ug/L	ICPMS	10	10	10	4.4	4.5	3.6	3.6	9	< 0.01
Li	ug/L	ICPMS	1100	1000	1100	6200	6400	3700	3800	1600	2800
Mg	mg/L	ICPAES	0.504	0.495	0.493	0.316	0.316	0.323	0.316	-	0.104
Mg	mg/L	ICPMS	-	-	-	-	-	-	-	0.9	-
Mn	ug/L	ICPMS	220	230	220	160	160	130	130	110	28
Mo	ug/L	ICPMS	5.9	6.1	6.4	32	33	25	26	18	54
Na	mg/L	ICPAES	172	159	159	224	227	217	212	-	198
Na	mg/L	ICPMS	-	-	-	-	-	-	-	150	-
Nb	ug/L	ICPMS	0.2	< 0.02	< 0.02	0.08	0.08	< 0.02	< 0.02	-	0.3
Nd	ug/L	ICPMS	18	18	18	3.9	4	3.3	3.3	17	< 0.01
Ni	ug/L	ICPMS	<0.1	<0.1	<0.1	<0.1	<0.1	<0.1	<0.1	2	<0.1
P	ug/L	ICPMS	2	< 2	< 2	17	15	3	2	< 30	< 2
Pb	ug/L	ICPMS	<0.05	0.06	<0.05	0.52	0.5	0.4	0.5	3	<0.05
Pr	ug/L	ICPMS	4.2	4.2	4.3	1	1.1	0.88	0.87	3.8	< 0.01
Rb	ug/L	ICPMS	340	400	390	390	390	350	360	230	280
Re	ug/L	ICPMS	-	-	-	-	-	-	-	< 0.2	-
Sb	ug/L	ICPMS	0.79	0.74	0.64	5.6	6	3.1	12	25	23
Sc	ug/L	ICPMS	< 0.1	1	2	< 0.1	< 0.1	0.2	< 0.1	-	2
Se	ug/L	ICPMS	1.6	1.3	1.6	4.7	4.5	4.2	4.1	< 2	2.5
SiO_2	mg/L	ICPMS	260	260	250	470	480	330	330	290	230
Sm	ug/L	ICPMS	5.1	5	5.1	0.84	0.88	0.78	0.76	5	< 0.01
Sn	ug/L	ICPMS	-	-	-	-	-	-	-	-	-
Sr	ug/L	ICPMS	6.8	7.9	7.8	13	13	12	12	17	22
Ta	ug/L	ICPMS	0.21	< 0.03	< 0.03	0.05	0.05	< 0.03	< 0.03	-	0.52
Tb	ug/L	ICPMS	1	1	1	0.16	0.16	0.14	0.14	0.73	< 0.005
Te	ug/L	ICPMS	-	-	-	-	-	-	-	-	-
Th	ug/L	ICPMS	0.6	0.58	0.71	< 0.02	< 0.02	0.05	0.04	1.3	< 0.02
Ti	ug/L	ICPMS	2.6	3	2	2.1	2.3	2	2	-	3.5
Tl	ug/L	ICPMS	0.51	0.5	0.52	0.58	0.58	0.51	0.52	<0.5	0.4
Tm	ug/L	ICPMS	0.51	0.5	0.5	0.087	0.083	0.062	0.073	0.3	< 0.005
U	ug/L	ICPMS	2.2	2.2	2.3	0.13	0.14	0.13	0.12	0.8	0.008
V	ug/L	ICPMS	<0.2	0.2	0.2	1.4	1.4	1	1	4	3
W	ug/L	ICPMS	2.2	6.8	5.8	50	50	36	40	39	97
Y	ug/L	ICPMS	34	38	38	6.6	6.6	5.9	6	21	< 0.01
Yb	ug/L	ICPMS	2.9	2.8	2.8	0.51	0.5	0.4	0.39	2.1	< 0.01
Zn	ug/L	ICPMS	20	20	20	10	10	9	9	40	<0.5
Zr	ug/L	ICPMS	< 0.2	< 0.2	< 0.2	0.86	< 0.2	< 0.2	< 0.2	-	< 0.2
Hg	ng/L	Hg CVAF	8	-	-	7	80	-	-	160	62
$\delta^{18}O$ vs VSMOW	permil	ISO1	-	-16.87	-	-11.59	-	-11.93	-	-9.2	-16.1
δD vs VSMOW	permil	ISO2	-	-	-	-	-	-	-	-117.4	-138.7
$\delta^{34}S$ vs CDT	permil	ISO3	-	-	-	-	-	-	-	-	-

Appendix 4. Site and analytical data from subaerial hydrothermal features—*Continued*.

Field no. Sample name & description			YNP-99-454 Heart Lake/fissure geyser area	YNP-99-461 Heart Lake/Rustic geyser area	YNP-99-462 Heart Lake/Rustic geyser area	YNP-99-463 Heart Lake/upper geyser area	YNP-99-478 Imperial Geyser, at Twin Buttes	YNP-99-501 Boiling River	YNP-99-502 Beryl Springs	YNP-99-502R Beryl Springs	YNP-00-517.1 Beryl Springs	YNP-01-538.1 Lower acid sulfate area near Beryl Springs
Latitude			44°17'22.2"N	44°16'54"N	44°16'55.5"N	44°18'36.9"N	44°31'54.2"N	45°0'0.2"N	44°40'45"N	44°40'45"N	44°40'45"N	44°40'39.5"N
Longitude			110°30'35"W	110°30'20"W	110°30'22"W	110°31'52.1"	110°52'19.4"W	110°40'57.2"	110°44'46"W	110°44'46"W	110°44'46"W	110°44'48.1"W
Collection Date			07/22/99	07/25/99	07/25/99	07/25/99	08/13/99	-	-	-	08/12/00	7/5/2001
Temperature	˚C		88.0	88.0	92.0	94.0	90.0	-	-	-	89.4	84
pH			9.9	4.6	9.2	2.1	8.8	-	-	-	6.8	1.6
Conductivity	uS/cm		-	-	-	-	-	-	-	-	-	-
Sum CO_2	mM		-	-	-	-	-	-	-	-	-	-
HCO_3	mM	measured	-	-	-	-	-	-	-	-	-	-
HCO_3	uM	calculated	-	-	-	-	-	-	-	-	-	-
Cl	mg/L	IC-Aq	360	310	310	4	180	150	540	-	530	400
F	mg/L	IC-Aq	35	23	31	0.2	24	3.4	19	-	17	12
NO_3	mg/L	IC-Aq	<.35	<.35	1.2	0.5	<.35	1.8	<.35	-	<.08	<.18
SO_4	mg/L	IC-Aq	170	140	140	150	16	520	65	-	65	130
Ag	ug/L	ICPMS	0.06	<0.01	<0.01	<0.01	0.58	<0.08	<0.08	<0.08	0.03	0.07
Al	ug/L	ICPMS	260	260	150	2900	160	3	210	200	220	34000
As	ug/L	ICPMS	1600	1400	1400	12	1000	630	2500	2400	2000	12
Au	ug/L	ICPMS	< 0.01	< 0.01	< 0.01	< 0.01	-	< 0.01	< 0.01	< 0.01	< 0.01	< 0.01
B	ug/L	ICPAES	4170	3610	3490	48.3	-	-	-	-	-	-
Ba	ug/L	ICPMS	2	0.6	2	51	<0.06	50	2.6	2.5	2	39
Be	ug/L	ICPMS	4.2	5.1	3.8	0.6	2.3	0.8	3.9	4.6	9.7	3.7
Bi	ug/L	ICPMS	< 0.01	< 0.01	< 0.01	< 0.01	-	< 600	< 600	< 600	< 0.01	< 0.03
Ca	mg/L	ICPAES	0.941	0.898	1.08	0.487	-	-	-	-	-	-
Ca	mg/L	ICPMS	-	-	-	-	-	260	4.1	3.8	3.7	5.2
Cd	ug/L	ICPMS	<0.02	<0.02	<0.02	0.03	<0.02	<0.02	<0.02	<0.02	<0.02	0.2
Ce	ug/L	ICPMS	0.02	0.01	0.02	8.9	< 0.02	0.02	0.06	0.06	0.02	140
Co	ug/L	ICPMS	<0.02	<0.02	<0.02	0.09	<0.02	<0.02	<0.02	<0.02	<0.02	0.4
Cr	ug/L	ICPMS	<1	<1	<1	<1	30	2	<1	<1	<1	2
Cs	ug/L	ICPMS	370	370	180	3.6		160	420	410	440	4.8
Cu	ug/L	ICPMS	<0.5	<0.5	<0.5	<0.5	<0.5	<0.5	<0.5	<0.5	<0.5	9
Dy	ug/L	ICPMS	< 0.005	< 0.005	< 0.005	0.75	< 0.007	< 0.005	0.01	0.006	< 0.005	9.9
Er	ug/L	ICPMS	< 0.005	< 0.005	< 0.005	0.43	< 0.005	< 0.005	< 0.005	< 0.005	< 0.005	5.2
Eu	ug/L	ICPMS	< 0.005	< 0.005	< 0.005	0.079	< 0.005	< 0.005	< 0.005	< 0.005	< 0.005	0.77
Fe	ug/L	ICPMS	<30	<30	<30	420	<30	<9	<9	<9	8.5	3600
Ga	ug/L	ICPMS	23	18	15	0.3	-	< 0.02	14	13	17	1
Gd	ug/L	ICPMS	< 0.005	< 0.005	< 0.005	0.76	< 0.006	< 0.005	0.008	0.008	0.006	10
Ge	ug/L	ICPMS	42	39	37	0.2	-	3.9	26	26	50	0.8
Hf	ug/L	ICPMS	-	-	-	-	-	-	-	-	-	-
Ho	ug/L	ICPMS	< 0.005	< 0.005	< 0.005	0.16	< 0.005	< 0.005	< 0.005	< 0.005	< 0.005	1.9
In	ug/L	ICPMS	-	-	-	-	< 0.01	< 0.01	< 0.01	< 0.01	< 0.01	0.05
K	mg/L	ICPAES	27.7	16.2	9.11	3.15	-	-	-	-	-	-
K	ug/L	ICPMS	-	-	-	-	-	58000	21000	20000	19000	32000
La	ug/L	ICPMS	< 0.01	< 0.01	< 0.01	3.7	< 0.01	0.01	0.03	0.03	0.03	55
Li	ug/L	ICPMS	6400	6400	6200	13	2600	1600	6700	6600	6700	31
Mg	mg/L	ICPAES	<0.1	<0.1	<0.1	0.116	-	-	-	-	-	-
Mg	mg/L	ICPMS	-	-	-	-	-	63	0.06	0.05	<0.01	0.57
Mn	ug/L	ICPMS	0.27	0.91	0.27	11	2.6	27	25	24	18	170
Mo	ug/L	ICPMS	100	96	94	2.1	23	< 0.4	120	110	120	1.4
Na	mg/L	ICPAES	400	372	368	2.13	-	-	-	-	-	-
Na	mg/L	ICPMS	-	-	-	-	-	120	>200	>200	>300	26
Nb	ug/L	ICPMS	0.7	0.5	0.4	< 0.02	-	-	-	-	-	-
Nd	ug/L	ICPMS	< 0.01	< 0.01	< 0.01	4.7	< 0.02	< 0.01	0.02	0.03	0.01	57
Ni	ug/L	ICPMS	<0.1	<0.1	<0.1	0.2	<0.1	<0.1	<0.1	<0.1	<0.1	3.4
P	ug/L	ICPMS	< 2	< 2	< 2	< 2	24	< 10	< 10	< 10	< 5	66
Pb	ug/L	ICPMS	<0.05	<0.05	<0.05	0.4	<0.05	0.2	0.2	<0.1	<0.05	5.5
Pr	ug/L	ICPMS	< 0.01	< 0.01	< 0.01	1.2	< 0.01	< 0.01	< 0.01	< 0.01	< 0.01	16
Rb	ug/L	ICPMS	340	200	110	13	100	300	300	280	310	160
Re	ug/L	ICPMS	-	-	-	-	-	< 0.02	< 0.02	< 0.02	< 0.02	< 0.02
Sb	ug/L	ICPMS	48	59	48	0.73	24	<0.2	72	69	79	0.66
Sc	ug/L	ICPMS	2	0.8	0.8	0.3	-	-	-	-	-	-
Se	ug/L	ICPMS	5.5	4.4	4.1	< 0.3	3	2	6.3	5.7	1.8	< 0.2
SiO_2	mg/L	ICPMS	330	300	340	110	240	50	240	230	250	290
Sm	ug/L	ICPMS	< 0.01	< 0.01	< 0.01	0.9	< 0.01	< 0.01	< 0.01	< 0.01	< 0.01	12
Sn	ug/L	ICPMS	-	-	-	-	-	-	-	-	-	-
Sr	ug/L	ICPMS	13	24	3	3.5	< 0.09	1800	6.8	6.2	6.6	14
Ta	ug/L	ICPMS	1.1	0.75	0.64	< 0.03	-	-	-	-	-	-
Tb	ug/L	ICPMS	< 0.005	< 0.005	< 0.005	0.12	< 0.005	< 0.005	< 0.005	< 0.005	< 0.005	1.6
Te	ug/L	ICPMS	-	-	-	-	-	-	-	-	-	-
Th	ug/L	ICPMS	< 0.02	< 0.02	< 0.02	0.07	-	0.01	0.02	0.044	0.1	32
Ti	ug/L	ICPMS	5.9	4.5	4.3	1	-	-	-	-	-	-
Tl	ug/L	ICPMS	0.52	0.3	0.1	0.06	0.08	0.1	0.2	0.1	0.1	0.5
Tm	ug/L	ICPMS	< 0.005	< 0.005	< 0.005	0.056	< 0.005	< 0.005	< 0.005	< 0.005	< 0.005	0.68
U	ug/L	ICPMS	0.01	0.04	0.05	0.37	0.1	0.07	0.006	< 0.005	< 0.005	2.3
V	ug/L	ICPMS	2	2	2	<0.1	1.3	0.84	3.4	2.3	<0.2	0.2
W	ug/L	ICPMS	280	260	250	12	260	10	140	140	160	1.7
Y	ug/L	ICPMS	< 0.01	< 0.01	< 0.01	3.7	-	0.07	0.05	0.04	0.04	48
Yb	ug/L	ICPMS	< 0.01	< 0.01	< 0.01	0.38	< 0.01	< 0.01	< 0.01	< 0.01	< 0.01	4
Zn	ug/L	ICPMS	<0.5	<0.5	<0.5	8	<0.5	1	1	0.7	<0.5	120
Zr	ug/L	ICPMS	0.4	< 0.2	< 0.2	< 0.2	-	-	-	-	-	-
Hg	ng/L	Hg CVAF	49	51	45	16	27	<5	23	-	0.026	170
$\delta^{18}O$ vs VSMOW	permil	ISO1	-17.0	-16.4	-16.8	-14.0	-17.7	-18.9	-15.2	-	-14.7	-5.5
δD vs VSMOW	permil	ISO2	-141.5	-142.4	-140.9	-123	-143.8	-	-140.3	-	-140.2	-112.6
$\delta^{34}S$ vs CDT	permil	ISO3	-	-	-	-	-	-	-	-	-	-

Appendix 4. Site and analytical data from subaerial hydrothermal features—*Continued*.

Field no. Sample name & description			YNP-99-503 Monument Geyser Basin	YNP-00-495.1 Monument hot pool	YNP-00-495.2 Monument hot pool	YNP-00-495.4 Monument Geyser Basin	YNP-00-498.1 Monument hot pool	YNP-00-498.2 Monument hot pool	YNP-00-498.3 Monument hot pool	YNP-00-498.4 Monument hot pool	YNP-00-498.5 Monument hot pool
Latitude			44°41'4"N	44°40'59.5"N	44°41'0.9"N	44°41'0.9"N	44°41'5"N	44°41'5.5"N	44°41'5"N	44°41'5"N	44°41'8.5"N
Longitude			110°45'10"W	110°45'8"W	110°45'8.5"W	110°45'8.5"W	110°45'10.5"W	110°45'7"W	110°45'10.5"W	110°45'10.5"W	110°45'8"W
Collection Date			-	07/01/00	07/01/00	10/08/00	07/10/00	07/10/00	07/10/00	07/10/00	07/10/00
Temperature	°C		-	88.5	88.4	90.6	83.7	23.4	88.7	87.7	21.9
pH			-	1.1	1.3	-	1.1	1.2	1.8	2.5	2.3
Conductivity	uS/cm		-	-	-	-	-	-	-	-	-
Sum CO_2	mM		-	-	-	-	-	-	-	-	-
HCO_3	mM	measured	-	-	-	-	-	-	-	-	-
HCO_3	uM	calculated	-	-	-	-	-	-	-	-	-
Cl	mg/L	IC-Aq	360	1	0.5	-	<.08	2	2.9	310	110
F	mg/L	IC-Aq	13	0.7	0.2	-	0.4	0.3	0.2	6.1	2.1
NO_3	mg/L	IC-Aq	<.35	<.08	<.08	-	<.08	<.08	0.2	<.08	0.2
SO_4	mg/L	IC-Aq	280	750	300	-	2700	630	1000	310	610
Ag	ug/L	ICPMS	<0.08	<0.01	<0.01	0.2	<0.01	<0.01	<0.01	0.03	0.01
Al	ug/L	ICPMS	5500	19000	3900	39000	86000	20000	11000	5500	12000
As	ug/L	ICPMS	1700	10	5.4	31	18	130	140	1000	800
Au	ug/L	ICPMS	< 0.01	< 0.01	< 0.01	< 0.01	< 0.01	< 0.01	< 0.01	< 0.01	< 0.01
B	ug/L	ICPAES	-	-	-	-	-	-	-	-	-
Ba	ug/L	ICPMS	88	65	89	28	110	69	85	82	59
Be	ug/L	ICPMS	3.8	0.67	0.67	2.8	2.8	2.7	1.8	1.4	2.1
Bi	ug/L	ICPMS	< 600	< 0.01	< 0.01	0.06	0.04	0.1	0.087	< 0.01	< 0.01
Ca	mg/L	ICPAES	-	-	-	-	-	-	-	-	-
Ca	mg/L	ICPMS	1.7	1.1	0.77	3	2.3	1.7	0.61	1.4	1.2
Cd	ug/L	ICPMS	<0.02	0.08	<0.02	0.2	0.06	0.06	<0.02	<0.02	0.03
Ce	ug/L	ICPMS	4.7	24	9	28	67	53	19	7.2	15
Co	ug/L	ICPMS	0.05	0.1	0.1	0.4	0.4	0.3	0.4	0.06	0.08
Cr	ug/L	ICPMS	<1	<1	<1	10	5	<1	<1	<1	<1
Cs	ug/L	ICPMS	260	2.4	2.6	16	4.9	12	18	190	120
Cu	ug/L	ICPMS	<0.5	2	0.6	6	3	1	1	<0.5	1
Dy	ug/L	ICPMS	0.28	1.2	0.54	1.5	3.4	3.8	0.84	0.39	0.78
Er	ug/L	ICPMS	0.15	0.68	0.29	0.69	2	1.8	0.5	0.2	0.4
Eu	ug/L	ICPMS	0.081	0.29	0.094	0.59	1.1	0.56	0.28	0.1	0.27
Fe	ug/L	ICPMS	910	1300	720	1800	5600	4600	1100	1000	1400
Ga	ug/L	ICPMS	1.2	1.8	1.4	14	45	4	12	0.68	3.8
Gd	ug/L	ICPMS	0.23	1.1	0.54	1.6	3.2	3.6	0.72	0.37	0.7
Ge	ug/L	ICPMS	16	0.4	0.3	1.9	1.2	1	1.7	21	11
Hf	ug/L	ICPMS	-	-	-	-	-	-	-	-	-
Ho	ug/L	ICPMS	0.056	0.19	0.084	0.26	0.56	0.56	0.14	0.06	0.12
In	ug/L	ICPMS	< 0.01	0.26	0.01	0.22	0.24	0.07	0.04	< 0.01	0.01
K	mg/L	ICPAES	-	-	-	-	-	-	-	-	-
K	ug/L	ICPMS	43000	13000	6800	20000	36000	17000	7000	29000	19000
La	ug/L	ICPMS	2.7	15	5.8	17	45	31	15	3.8	9.9
Li	ug/L	ICPMS	4500	2.8	7.3	9.4	14	19	27	3500	1300
Mg	mg/L	ICPAES	-	-	-	-	-	-	-	-	-
Mg	mg/L	ICPMS	0.08	0.13	0.14	0.38	0.37	0.3	0.07	0.1	0.11
Mn	ug/L	ICPMS	19	18	15	48	42	39	9.5	14	19
Mo	ug/L	ICPMS	99	0.2	0.5	7.6	0.51	4.4	68	32	14
Na	mg/L	ICPAES	-	-	-	-	-	-	-	-	-
Na	mg/L	ICPMS	>200	6.4	3.8	12	19	12	3.6	190	77
Nb	ug/L	ICPMS	-	-	-	-	-	-	-	-	-
Nd	ug/L	ICPMS	1.8	9.3	3.9	12	25	25	5.7	3	5.5
Ni	ug/L	ICPMS	0.2	0.3	0.2	3.9	1.2	0.8	0.6	0.1	0.4
P	ug/L	ICPMS	< 10	2200	< 5	51	140	5	8	< 5	< 5
Pb	ug/L	ICPMS	1.6	8.5	2.9	26	31	6.4	32	1	4
Pr	ug/L	ICPMS	0.54	2.4	0.97	3.5	7.1	6.2	1.6	0.74	1.6
Rb	ug/L	ICPMS	380	45	36	69	140	100	30	300	180
Re	ug/L	ICPMS	< 0.02	< 0.02	< 0.02	< 0.02	< 0.02	< 0.02	< 0.02	< 0.02	< 0.02
Sb	ug/L	ICPMS	38	0.3	1.9	7.3	1.3	11	42	26	29
Sc	ug/L	ICPMS	-	-	-	-	-	-	-	-	-
Se	ug/L	ICPMS	4	< 0.2	< 0.2	< 0.2	< 0.2	< 0.2	< 0.2	< 0.2	< 0.2
SiO_2	mg/L	ICPMS	210	200	150	290	220	220	190	240	260
Sm	ug/L	ICPMS	0.33	1.5	0.64	2.2	3.7	4.1	0.8	0.49	0.86
Sn	ug/L	ICPMS	-	-	-	-	-	-	-	-	-
Sr	ug/L	ICPMS	8.2	14	5.9	18	41	17	12	9.7	13
Ta	ug/L	ICPMS	-	-	-	-	-	-	-	-	-
Tb	ug/L	ICPMS	0.04	0.18	0.076	0.26	0.44	0.48	0.1	0.052	0.11
Te	ug/L	ICPMS	-	-	-	-	-	-	-	-	-
Th	ug/L	ICPMS	0.46	0.98	0.6	1.4	26	6	5.6	0.59	2.6
Ti	ug/L	ICPMS	-	-	-	-	-	-	-	-	-
Tl	ug/L	ICPMS	0.2	0.3	0.1	0.4	0.62	0.53	0.56	0.2	0.55
Tm	ug/L	ICPMS	0.02	0.099	0.04	0.093	0.27	0.22	0.067	0.03	0.04
U	ug/L	ICPMS	0.52	2	0.27	0.97	2.7	1.1	1.1	0.5	0.8
V	ug/L	ICPMS	1.8	1.9	<0.2	1	7.2	2.8	0.77	<0.2	0.4
W	ug/L	ICPMS	88	0.2	0.2	0.94	0.2	0.3	2.4	23	12
Y	ug/L	ICPMS	1.2	6	3.5	5.2	21	23	5.2	2.4	4.4
Yb	ug/L	ICPMS	0.1	0.75	0.26	0.59	1.7	1.5	0.41	0.2	0.3
Zn	ug/L	ICPMS	7	68	6	38	93	45	37	10	10
Zr	ug/L	ICPMS	-	-	-	-	-	-	-	-	-
Hg	ng/L	Hg CVAF	95	-	0.025	-	0.029	0.074	0.05	0.058	0.031
$\delta^{18}O$ vs VSMOW	permil	ISO1	-12.5	-11.1	-15.5	-9.6	-9.1	-13.1	-11.3	-12.1	-12.0
δD vs VSMOW	permil	ISO2	-56.3	-120.3	-134.4	-115	-114.8	-124.2	-119.8	-126.8	-118.8
$\delta^{34}S$ vs CDT	permil	ISO3	-	-	-	-	-	-	-	-	-

Appendix 4. Site and analytical data from subaerial hydrothermal features—*Continued*.

Field no. Sample name & description			YNP-00-516.1 spring, base of Monument trail	YNP-00-3518-14.1 vent, Monument	YNP-00-3518-17.1 vent, Monument	YNP-00-526.1 Monument, vent across river	YNP-00-527.1 Monument, vent across river	YNP-00-528.1 Monument, sulfur cauldron	YNP-00-528.5 Monument, sulfur cauldron	YNP-00-536.1 Artist's Paint Pots	YNP-01-543.1 Gibbon geyser basin
Latitude			44°41'2.5"N	44°41'8"N	44°41'7.5"N	44°41'1.2"N	44°40'58.2"N	44°41'3"N	44°41'3"N	44°41'33.9"N	44°42'0"N
Longitude			110°44'39"W	110°45'10.9"W	110°45'12.5"W	110°44'33.5"W	110°44'34.2"W	110°45'10.1"W	110°45'10.1"W	110°44'6.6"W	110°46'4.5"W
Collection Date			08/12/00	08/12/00	08/12/00	08/30/00	08/30/00	08/30/00	08/30/00	10/10/00	7/9/2001
Temperature	˚C		81.4	86.6	82.0	90.6	91.6	71.1	71.1	90.7	82.5
pH			7.2	-	1.6	6.1	6.7	1.1	1.1	7.3	6.1
Conductivity	uS/cm		-	-	-	-	-	-	-	-	-
Sum CO_2	mM		-	-	-	-	-	-	-	-	-
HCO_3	mM	measured	-	-	-	-	-	-	-	-	-
HCO_3	uM	calculated	-	-	-	-	-	-	-	-	-
Cl	mg/L	IC-Aq	550	26	2.4	2	2.2	<.08	-	6.2	530
F	mg/L	IC-Aq	18	1.5	0.2	1.2	4	0.7	-	0.3	18
NO_3	mg/L	IC-Aq	<.08	<.08	0.2	<.08	0.3	<.08	-	<.18	<.18
SO_4	mg/L	IC-Aq	53	2300	670	200	190	4000	-	870	170
Ag	ug/L	ICPMS	0.03	<0.01	<0.01	0.02	<0.01	<0.01	<0.01	2	0.6
Al	ug/L	ICPMS	40	26000	10000	98	720	>200000	>200000	160	350
As	ug/L	ICPMS	2100	170	79	5.9	5.3	680	670	2100	3000
Au	ug/L	ICPMS	< 0.01	< 0.01	< 0.01	< 0.01	< 0.01	< 0.01	< 0.01	< 0.1	< 0.1
B	ug/L	ICPAES	-	-	-	-	-	-	-	-	-
Ba	ug/L	ICPMS	8	40	67	83	56	75	70	0.8	6
Be	ug/L	ICPMS	8	2.4	0.49	1.1	2.3	3.5	3.6	1	2
Bi	ug/L	ICPMS	< 0.01	< 0.01	< 0.01	< 0.01	< 0.01	0.1	0.097	< 0.3	< 0.3
Ca	mg/L	ICPAES	-	-	-	-	-	-	-	-	-
Ca	mg/L	ICPMS	3.2	0.69	0.66	18	9.9	5.9	6	6.6	6.6
Cd	ug/L	ICPMS	<0.02	0.07	0.03	<0.02	<0.02	0.3	0.3	<0.2	<0.2
Ce	ug/L	ICPMS	0.05	31	8.9	0.05	0.54	140	140	< 0.1	0.1
Co	ug/L	ICPMS	<0.02	0.08	0.1	<0.02	<0.02	1.6	1.6	<0.2	<0.2
Cr	ug/L	ICPMS	<1	<1	<1	<1	<1	11	12	<10	<10
Cs	ug/L	ICPMS	450	59	9.1	16	20	29	29	420	370
Cu	ug/L	ICPMS	<0.5	1	0.7	2	0.8	2	3	<5	<5
Dy	ug/L	ICPMS	0.03	1.2	0.35	0.02	0.056	5.7	5.6	< 0.05	< 0.05
Er	ug/L	ICPMS	0.01	0.59	0.22	0.01	0.02	3.3	3.2	< 0.05	< 0.05
Eu	ug/L	ICPMS	< 0.005	0.24	0.13	< 0.005	< 0.005	1.5	1.5	< 0.05	< 0.05
Fe	ug/L	ICPMS	71	730	740	26	110	30000	30000	61	90
Ga	ug/L	ICPMS	6.4	32	5.2	0.2	0.3	81	82	12	3
Gd	ug/L	ICPMS	0.02	1.1	0.37	0.006	0.04	5.3	5.2	< 0.05	< 0.05
Ge	ug/L	ICPMS	49	3.5	1.2	1.8	2	2.2	1.9	44	73
Hf	ug/L	ICPMS	-	-	-	-	-	-	-	-	-
Ho	ug/L	ICPMS	< 0.005	0.18	0.064	< 0.005	0.009	0.94	0.96	< 0.05	< 0.05
In	ug/L	ICPMS	< 0.01	0.04	0.01	< 0.01	< 0.01	0.99	1	< 0.1	< 0.1
K	mg/L	ICPAES	-	-	-	-	-	-	-	-	-
K	ug/L	ICPMS	17000	11000	8300	49000	37000	80000	80000	16000	47000
La	ug/L	ICPMS	0.04	27	6.6	0.04	0.3	89	91	< 0.1	0.1
Li	ug/L	ICPMS	5800	270	18	120	130	34	34	4800	5800
Mg	mg/L	ICPAES	-	-	-	-	-	-	-	-	-
Mg	mg/L	ICPMS	0.1	0.06	0.11	0.77	0.24	1.3	1.3	0.2	0.2
Mn	ug/L	ICPMS	25	12	12	710	240	140	150	3.8	23
Mo	ug/L	ICPMS	100	4.7	2.1	0.3	0.87	4.5	4.3	86	170
Na	mg/L	ICPAES	-	-	-	-	-	-	-	-	-
Na	mg/L	ICPMS	>300	19	2.9	64	56	24	24	370	440
Nb	ug/L	ICPMS	-	-	-	-	-	-	-	-	-
Nd	ug/L	ICPMS	0.05	10	2.9	0.03	0.21	43	43	< 0.1	< 0.1
Ni	ug/L	ICPMS	<0.1	0.6	0.7	<0.1	<0.1	3.5	4.2	<1	<1
P	ug/L	ICPMS	< 5	44	< 5	7	< 5	460	470	< 30	< 30
Pb	ug/L	ICPMS	0.05	10	4.8	0.06	0.2	56	54	2	<0.5
Pr	ug/L	ICPMS	0.01	3	0.84	< 0.01	0.06	13	13	< 0.1	< 0.1
Rb	ug/L	ICPMS	270	59	24	350	260	270	270	230	460
Re	ug/L	ICPMS	< 0.02	< 0.02	< 0.02	< 0.02	< 0.02	< 0.02	< 0.02	< 0.2	< 0.2
Sb	ug/L	ICPMS	130	48	7.7	0.4	0.4	1.3	1	120	42
Sc	ug/L	ICPMS	-	-	-	-	-	-	-	-	-
Se	ug/L	ICPMS	1.4	< 0.2	< 0.2	< 0.2	< 0.2	< 0.2	< 0.2	4	5
SiO_2	mg/L	ICPMS	200	260	140	150	190	160	160	180	480
Sm	ug/L	ICPMS	0.01	1.4	0.41	< 0.01	0.03	6.3	6.4	< 0.1	< 0.1
Sn	ug/L	ICPMS	-	-	-	-	-	-	-	-	-
Sr	ug/L	ICPMS	12	13	13	98	40	73	75	4	14
Ta	ug/L	ICPMS	-	-	-	-	-	-	-	-	-
Tb	ug/L	ICPMS	< 0.005	0.15	0.04	< 0.005	0.006	0.75	0.76	< 0.05	< 0.05
Te	ug/L	ICPMS	-	-	-	-	-	-	-	-	-
Th	ug/L	ICPMS	0.17	14	1	0.09	0.1	56	55	5.6	12
Ti	ug/L	ICPMS	-	-	-	-	-	-	-	-	-
Tl	ug/L	ICPMS	<0.05	0.4	0.2	<0.05	0.2	2.4	2.5	0.6	<0.5
Tm	ug/L	ICPMS	< 0.005	0.076	0.03	< 0.005	< 0.005	0.41	0.4	< 0.05	< 0.05
U	ug/L	ICPMS	0.02	1.5	0.28	0.007	0.005	4.1	4.1	0.06	< 0.05
V	ug/L	ICPMS	<0.2	0.98	0.84	<0.2	<0.2	20	20	1	<1
W	ug/L	ICPMS	190	2.8	0.78	0.81	0.69	0.4	0.3	110	160
Y	ug/L	ICPMS	0.2	6.4	2.4	0.2	0.3	36	37	< 0.1	< 0.1
Yb	ug/L	ICPMS	0.01	0.53	0.2	< 0.01	0.02	2.8	2.8	< 0.1	< 0.1
Zn	ug/L	ICPMS	<0.5	24	8	0.8	1	62	67	7	6
Zr	ug/L	ICPMS	-	-	-	-	-	-	-	-	-
Hg	ng/L	Hg CVAF	0.005	0.015	0.01	0.005	0.01	0.014	-	40	150
$\delta^{18}O$ vs VSMOW	permil	ISO1	-15.9	-11.7	-5.9	-16.1	-14.8	-5.0	-	-15.7	-10.2
δD vs VSMOW	permil	ISO2	-144.9	-119.0	-108.1	-138.8	-132.3	-105.9	-	-143.2	-123.7
$\delta^{34}S$ vs CDT	permil	ISO3	-	-	-	-	-	-	-	-	-

The Life Cycle of Gold Deposits Near the Northeast Corner of Yellowstone National Park—Geology, Mining History, and Fate

M

By Bradley S. Van Gosen

Chapter M *of*

Integrated Geoscience Studies in the Greater Yellowstone Area—Volcanic, Tectonic, and Hydrothermal Processes in the Yellowstone Geoecosystem

Edited by Lisa A. Morgan

U.S. Department of the Interior
U.S. Geological Survey

Professional Paper 1717

U.S. Department of the Interior
U.S. Geological Survey

Contents

Abstract 431
Introduction 431
    Study Approach 432
    Significance of the Homestake Deposit 433
Regional Geologic Setting of the New World District 434
    Precambrian Structural Control 434
    Phanerozoic Sedimentation and Laramide Uplift 435
    Eocene Magmatism 436
    Pleistocene and Holocene Erosion 437
Geology and Mineral Deposits of the Northern New World District 437
    Scotch Bonnet Stock 437
    Fisher Mountain Stock and the Como, McLaren, and Fisher Mountain Deposits 437
    Homestake Stock 438
    Homestake Breccia 439
    Homestake and Miller Creek Deposits—Mineralogy and Genesis 441
        Alteration Patterns 441
        Mineral Assemblages and Paragenesis 443
        Geochemistry 445
        Summary of Eocene Ore-Forming Processes 445
    Post-Ore Henderson Mountain Stock 447
    Alice E. Breccia 447
    Postmineralization Dikes and Sills 447
Recent History of the Homestake Deposit—Exploration, Discovery, Mining Attempts, and Controversy 447
    1860s to 1985—Early Prospecting and Mining 447
    1985 to 1996—Rich Discoveries, Controversy, and Federal Government Involvement 449
        Yellowstone National Park 450
        The Summitville Mine Environmental Disaster 450
        Historic Mines in the New World District 450
        Administration Policy 451
    1997 and 1998—Contract Settlement, Congressional Appropriation, and Mineral Withdrawal 452
Acknowledgments 453
References Cited 453

Figures

1. Map showing the New World mining district area, Montana and Wyoming 432
2. Generalized geologic map of the northern part of the New World district 433
3. Generalized geologic map of the Beartooth uplift region, Montana and Wyoming 435
4. Schematic section showing the stratigraphy of the northern New World district 436
5. Photograph of Fisher Mountain 438

6. Photograph of Homestake breccia on Henderson Mountain 439
7. Schematic section illustrating the geologic setting of the stratabound Miller Creek gold-copper-silver deposits relative to the Homestake deposits....440
8–12. Photomicrographs showing:
8. A native gold inclusion along a microfracture in pyrite 443
9. Banded garnets from the core of the Homestake breccia 445
10. Coexisting intergrowth of zoned acicular specularite-magnetite with pyrite grains and interstitial quartz and chlorite....445
11. Zoned acicular crystals of specularite and magnetite enclosed by chalcopyrite 446
12. Gold-rich ore....446

Tables

1. Geologic ore reserves for identified gold-copper-silver deposits in the northern New World district....434
2. Selected assay results for intervals of the Homestake breccia deposits 442
3. List of minerals identified in the Homestake breccia 444

The Life Cycle of Gold Deposits Near the Northeast Corner of Yellowstone National Park—Geology, Mining History, and Fate

By Bradley S. Van Gosen

Abstract

Henderson Mountain, near Cooke City, Mont., about 4.5 mi northeast of the northeast entrance to Yellowstone National Park (the Park), hosts identified resources of at least 2.3 million ounces of gold, 8.9 million ounces of silver, and 130 million pounds of copper. The mineral deposits formed by selective replacement of calcareous blocks and clasts in a complex breccia pipe (the Homestake deposit), and concurrent skarn development replaced limestone adjacent to the breccia pipe (the Miller Creek deposit). The breccia pipe and mineral deposits formed in the middle Eocene during intrusion of the dacitic Homestake stock.

The geologic history of the Homestake and Miller Creek deposits involves Precambrian tectonics, Phanerozoic sedimentation, Eocene magmatism and hydrothermal processes, and Quaternary erosion and sediment deposition. The stocks of the Cooke City area (New World mining district) represent one of several mineralized centers of Eocene intrusive activity associated with the extensive Eocene Absaroka volcanic field in northwestern Wyoming and southwestern Montana. The Cooke City structural zone is a northwest-trending synformal zone developed in the Precambrian basement rocks of the Beartooth uplift. It was a zone of weakness that permitted calc-alkaline magmas to ascend through the crust during the Eocene to form mineralized centers. At the northern end of Henderson Mountain, intrusion of the Homestake stock during the middle Eocene was accompanied by metamorphism. The argillic Cambrian rocks locally were altered, whereas the interlayered Cambrian limestones were only weakly recrystallized and bleached. Intrusion breccias formed during magmatic stoping and injection of dacitic magma, and roof pendants composed of fractured Cambrian sedimentary rocks were lifted above the rising stock. Multiple events of hydrothermal shattering accompanied a flooding of relatively oxidized sulfur-rich fluids upward through intrusion breccias and shatter breccias (collectively and informally called the "Homestake breccia"). Intense argillic alteration formed in deep shatter zones, and limestone clasts and blocks in upper portions of the Homestake breccia were selectively replaced by silver- and copper-bearing sulfide minerals, coeval iron-oxide minerals, and trace native gold with silver. Lateral flow of the fluids into Cambrian limestones along the perimeter of the breccia pipe formed the stratabound and tabular Miller Creek deposit.

Mineral deposits of the Homestake breccia were the target of two significant mining ventures in the 1900s. An eastern part of the Homestake breccia was explored by a haulage adit in the early 1920s, and a power plant, a smelter, and an aerial tramway to haul ore from the mine to the smelter were nearly completed and then abandoned in 1925. The adit stopped a few hundred feet from high-grade gold deposits discovered later by drilling in the 1990s. An extensive drilling program in the northern New World district by Crown Butte Mines, Inc., led to the "blind" discoveries of the Miller Creek and Homestake deposits in 1989 and 1990. In 1990, Crown Butte Mines submitted a plan to State and Federal agencies to mine these deposits by underground methods. The proposed mining venture caused a strong, organized, anti-mine opposition that drew national attention. Because of the close proximity of the proposed mine to Yellowstone National Park, the environmental legacy of historic mines, and concerns about potential threats to the environment, the Federal Government negotiated a settlement with the mining company and the majority claim owner to halt mining in the area. On August 7, 1998, all properties and mineral rights were formally transferred to the U.S. Forest Service. Later, in August 1998, the U.S. Departments of the Interior and Agriculture announced a 20-year withdrawal of Federal locatable minerals in an area of 19,100 acres (7,735 hectares) surrounding Cooke City (the New World district and a buffer zone).

Introduction

Unexposed skarn deposits enriched in gold, copper, and silver are present at Henderson Mountain about 2.5 mi (4 km) north-northwest of Cooke City, Mont., and about 4.5 mi (7.2 km) northeast of the northeast entrance to Yellowstone National Park (the Park) (fig. 1). The deposits under Henderson Mountain are replacement bodies in a complex breccia pipe (informally called the Homestake breccia) and in tabular, stratabound bodies that formed laterally to the breccia pipe. Localization of the ore deposits

U.S. Geological Survey, Box 25046, Mail Stop 973, Denver Federal Center, Denver, CO, 80225.

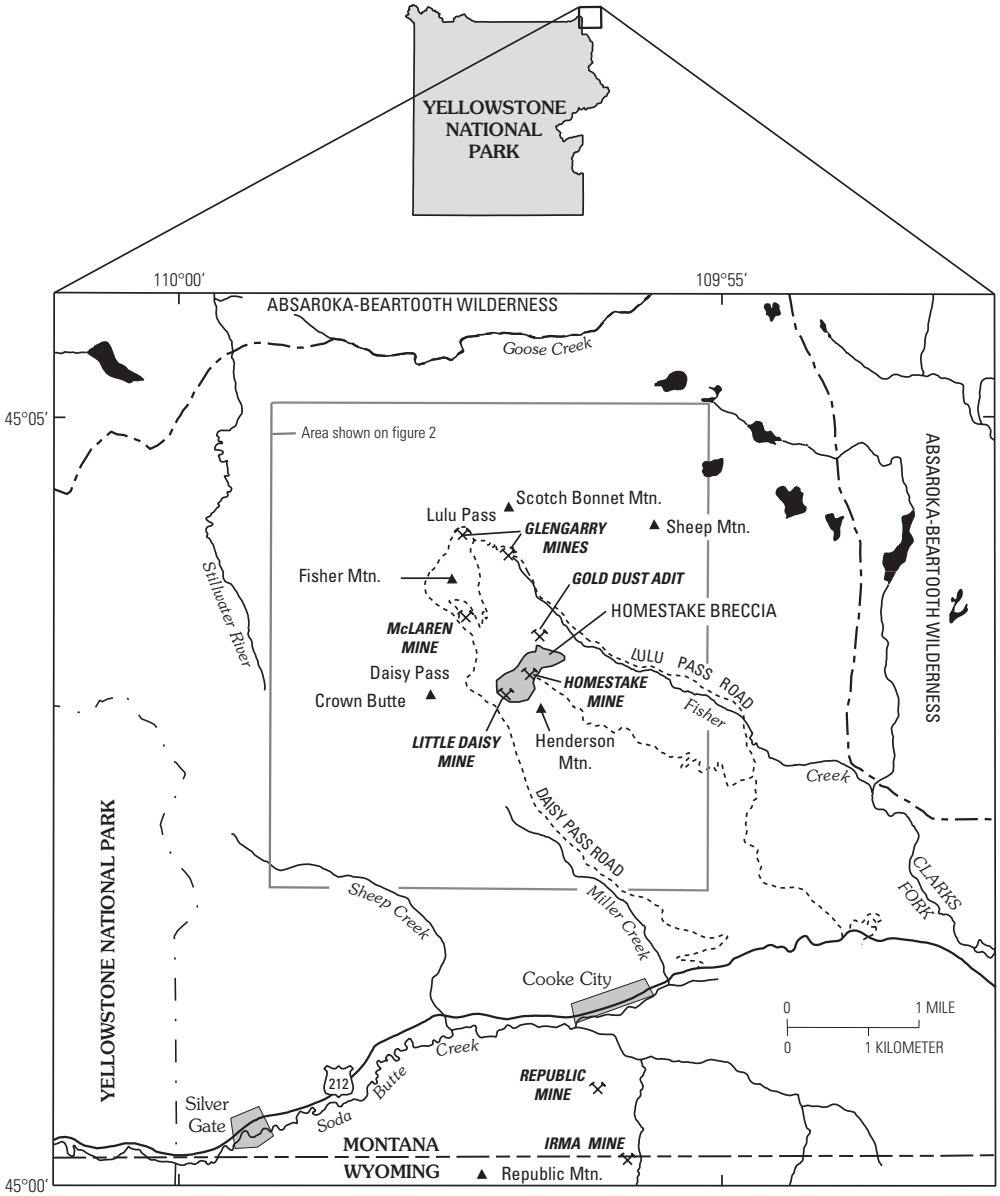

Figure 1. Map of the New World mining district area, Montana and Wyoming showing locations of Homestake breccia, historic mines, and geographic features.

in this particular area and along a northwest-trending zone that cuts across the region was influenced by large-scale structures that originated in the Precambrian. The ores formed in the Eocene during the regional formation of the Absaroka volcanic field (Chadwick, 1970; Smedes and Prostka, 1972; Hausel, 1982; Hiza, 1998, 1999). The gold-rich deposits of Henderson Mountain were targets of mining and (or) prospecting efforts in the 1920s, 1940s, and 1990s.

Study Approach

Crown Butte Mines, Inc., provided to the author subsurface data they collected from their late 1980s to early 1990s exploration- and development-drilling program in the New World district. These data provided a three-dimensional view of a classic ore-forming system. The drill cores were examined as part of a mineralogical and geochemical study of the deposit (Van Gosen, 1994). The extensive drilling array included a number of core holes into the Homestake breccia and stock (fig. 2; drill-hole locations shown in Van Gosen, 1994). Samples were selected to examine the alteration and mineralization patterns within the breccia bodies and their mineral deposits, extending outward into the altered host intrusive and sedimentary rocks.

This report describes the geologic history of these deposits, from the Precambrian structures that set the stage for localization of the intrusions, to the Paleozoic sedimentation that provided the host rock for the ore, to the Eocene magmatic and hydrothermal processes that formed the deposits. The discovery, exploration, and development history of these deposits during the last 125 years also is addressed, with a discussion of the social and political influences that ultimately brought an end, in the 1990s, to possible development of the identified mineral deposits. This study is the first detailed account of the geology, mineralogy, and multiple-element chemistry of this economic breccia-hosted, skarn/replacement deposit.

Significance of the Homestake Deposit

The term "Homestake deposit," as used herein, refers to **all** gold-silver-copper-enriched intervals within, and genetically associated with, the Homestake breccia (fig. 2). This deposit was chosen as the focus of this discussion because of its significant quantities of precious metals, its complex geologic and mining history, and the societal and political controversy that was triggered during the 1990s because of a plan proposed by Crown Butte Mines, Inc., to mine the deposit. That controversy ultimately led to a settlement agreement between the Federal Government, Crown Butte Mines, and the majority claim owner. The agreement officially ended the mine proposal in August 1998, transferring the properties and mineral rights to Gallatin National Forest. That settlement was followed later in the same month by a 20-year withdrawal of Federal locatable minerals in 19,100 acres of the surrounding Federal lands. Thus, the public controversy and Government involvement that centered around the Homestake gold-silver-copper deposit were as complex as the geologic history of the deposit.

On the basis of more than 200 holes through the Homestake breccia, drilled from 1990 to 1992, Crown Butte Mines and Noranda Exploration estimated reserves (as of April 4, 1992) in the Homestake deposit at 6.6 million tons of identified ore with an average grade of 0.224 opt (ounces per ton) gold, 0.71 percent copper, and 0.83 opt silver (table 1). They increased their April 1992 estimate of 1.48 million ounces of gold in the Homestake deposit (table 1) in the following 2 years on the basis of additional drilling and calculations. However, the latter estimates were not published. Additional unidentified mineral resources probably are present in the New World district and vicinity (see Elliott and others, 1992; Hammarstrom, Zientek, and Elliott, 1993; Kirk and others, 1993). The Homestake deposit contains a substantial gold deposit; it is the largest known gold deposit in the New World district (table 1).

The Homestake deposit appears to be geologically unusual in many aspects, although it probably is not unique to the region, as explained in a subsequent section. The gold-silver-copper deposits are part of a complex geologic system that includes polymetallic replacement deposits, skarn deposits, and weak porphyry-style mineralization that is superposed on igneous rocks, reactive rocks in breccia pipes, and adjacent sedimentary layers. The entire breccia-stock-ore complex is genetically related to the middle Eocene intrusion of the dacitic Homestake stock and multiple episodes of associated magmatic and hydrothermal processes.

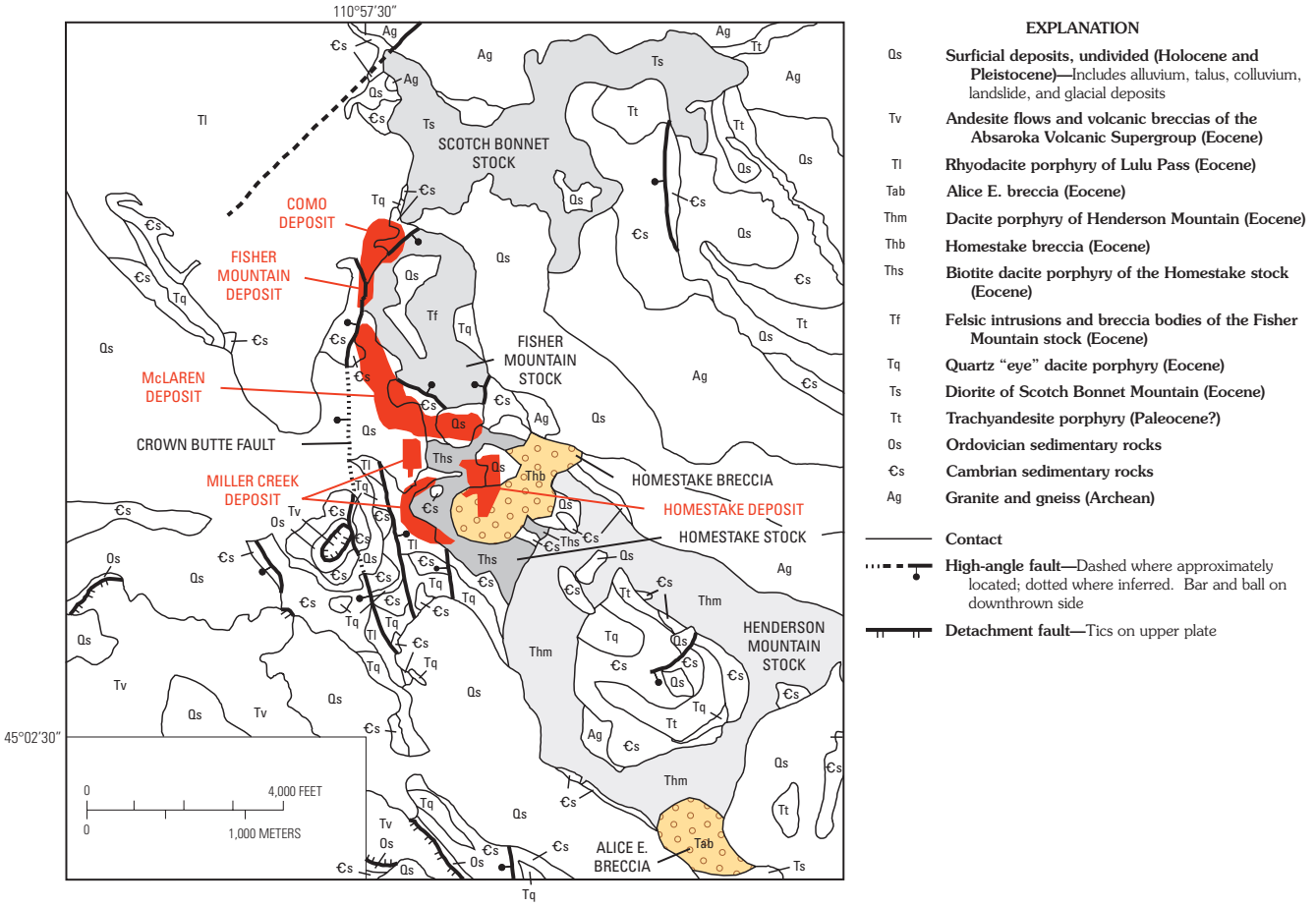

Figure 2. Generalized geologic map of the northern part of the New World mining district showing locations of identified (named) gold-silver-copper deposits, stocks, and Homestake breccia. Note that the ore deposits, shown in red, are projected to the surface in this plan view. Modified from Elliott and others (1992) and Elliott (1979).

Table 1. Geologic ore reserves for identified gold-copper-silver deposits in the northern New World district (fig. 2), as determined by Noranda Exploration and Crown Butte Mines as of April 4, 1992.

[Data from Elliott and others (1992) with their permission. opt, ounces per ton; pct, percent]

Deposit	Tons	Grade			Ounces Au	Pounds Cu	Ounces Ag
		Au (opt)	Cu (pct)	Ag (opt)			
Como	707,318	0.110	1.03	0.546	77,805	14,570,750	386,195
Fisher Mountain	334,200	0.189	0.28	1.130	63,164	1,871,520	377,646
McLaren	2,171,035	0.091	0.70	0.381	197,564	30,394,490	827,164
Miller Creek	2,218,368	0.387	0.87	1.540	858,508	38,599,603	3,416,286
Homestake	6,600,696	0.224	0.71	0.830	1,478,616	93,733,717	5,478,801
Average grade		0.222	0.75	0.870			
Total	12,031,887				2,675,657	179,170,080	10,486,092

Regional Geologic Setting of the New World District

The New World mining district includes areas of past mining and prospecting activity in the vicinity of Cooke City, Mont., including mines in the Republic Mountain area on the south to Lulu Pass on the north, and prospects from Sheep Creek on the west to Sheep Mountain on the east (fig. 1). The New World district is within the "Beartooth uplift," a broad fault-bounded foreland uplift in south-central Montana and northwestern Wyoming (fig. 3). The term Beartooth uplift, as used here, includes the entire continuous mountainous region in south-central Montana between the towns of Gardiner, Livingston, Nye, and Red Lodge (fig. 3). The Beartooth uplift includes the elevated South Snowy, North Snowy, and Beartooth Plateau crustal blocks (fig. 3), named by Foose and others (1961). The blocks were uplifted during the Laramide orogeny. The northwest-trending Cooke City structural zone is the boundary between the Beartooth Plateau block, to the east, and the South Snowy block, to the west (fig. 3).

Precambrian Structural Control

The Cooke City zone is a major structural zone or lineament that crosses the Beartooth uplift, extending from the canyon of the Clarks Fork of the Yellowstone River, on its southeast termination, to the junction of Mill Creek with the Yellowstone River on its northwest termination. Foose and others (1961) first described this zone in a regional context and suggested that it represents a zone of crustal weakness within the uplift, with Precambrian origins. This "sag zone" apparently consists of a down-warped and down-faulted zone that formed in Archean basement rocks of the uplift. Kulik (1992) suggested that the probable origin of the Cooke City zone was "local extension within the uplifted block." The Archean rock surface of the Beartooth Plateau block slopes southwestward toward the Cooke City zone (Foose and others, 1961). Northwest of Cooke City, that surface reverses and slopes northeastward, thereby outlining a structurally downwarped zone within the Archean rocks. Paleozoic (Cambrian through Lower Mississippian) sedimentary rocks are present in the Cooke City "sag zone." These strata were eroded from most of the Beartooth uplift interior. Preservation of these sedimentary rocks within the zone had considerable significance to the formation of the New World district mineral deposits. Limestone units of Cambrian age, preserved in the Cooke City zone within the area of the mining district, subsequently were intruded by Eocene igneous rocks and locally replaced to form the ore bodies. Also, a belt of mineralized Eocene volcanic centers, such as the stocks in the northern part of the New World district (fig. 2), formed along the northwest-southeast trend of the zone, implying that Precambrian structural control was important in the emplacement of the Eocene intrusive centers and their mineral deposits.

In addition to the New World district, the Cooke City zone contains the Independence, Horseshoe Mountain, and Emigrant (slightly offset from the zone) districts and the Sunlight mining region (fig. 3). Each of these areas is associated with Eocene stocks. The Eocene intrusive centers are related spatially, compositionally, and temporally to the Eocene Absaroka Volcanic Province of northwestern Wyoming and south-central Montana (Chadwick, 1970, 1972a, 1972b, 1981; Hiza, 1998, 1999; Smedes and Prostka, 1972). According to Foose and others (1961), the Cooke City zone is a zone of crustal weakness within the Beartooth uplift; it formed along Precambrian structures that were reactivated during the Laramide uplift. Calc-alkaline magmas rose through the crust along this zone of structural weakness during the middle Eocene.

A Precambrian origin of the Cooke City zone is supported by at least two lines of evidence. First, Precambrian mafic dikes, which likely intruded preexisting fracture systems, commonly trend northwestward on the Beartooth Plateau adjacent to the zone (Simons and others, 1979). Second, several faults and shear zones mapped within the zone in the Cooke City area trend northwestward (Lovering, 1929; Parsons, 1958; Elliott, 1979).

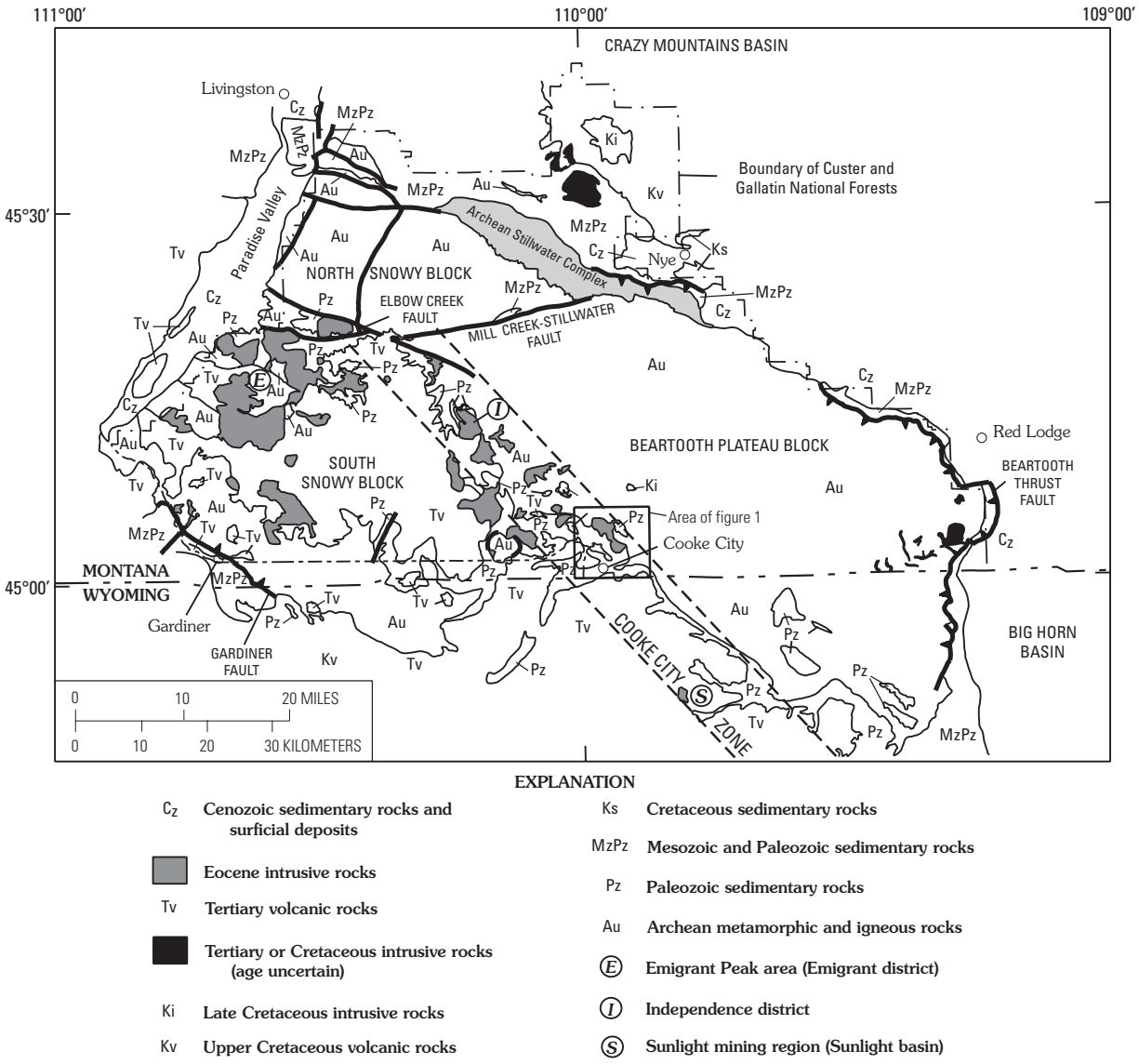

Figure 3. Generalized geologic map of the Beartooth uplift region, Montana and Wyoming, which includes the South Snowy, North Snowy, and Beartooth Plateau blocks as defined by Foose and others (1961).

Phanerozoic Sedimentation and Laramide Uplift

The Beartooth uplift region, including the New World district, had a long period of relative tectonic quiescence during the Paleozoic and most of the Mesozoic. During the Late Proterozoic or Early Cambrian, an erosional plain developed across the surface of the Precambrian rocks of the Beartooth uplift (Hughes, 1933; Thom and others, 1935; Simons and Armbrustmacher, 1976). Throughout the Paleozoic and into the Early Cretaceous, the Beartooth region was a broad, stable platform of shallow-marine inundation on which cyclic offshore carbonates and nearshore and shoreline clastic facies were deposited. During the Early Cretaceous, more rapid subsidence, with concurrent marine transgression and sediment deposition, occurred across the shelf (Foose and others, 1961).

Paleozoic sedimentary rocks totaling 2,800–3,500 ft (853–1,067 m) in thickness record deposition in the region of the Beartooth uplift (on the basis of measurements at the southwestern margin of the uplift by Ruppel (1972), at the southeastern margin by Pierce (1965), and at the northwestern (Livingston, Mont.) corner by Richards (1957)). Carbonate rocks record deposition during the Middle and Late Cambrian in the New World district, specifically the Meagher Limestone and the Pilgrim Limestone (fig. 4). The carbonate rocks later became important host rocks for the Eocene replacement mineral deposits in the district.

Triassic through Upper Cretaceous sedimentary rocks, at least 5,000 ft (1,524 m) in thickness, covered the Paleozoic rocks of the uplift prior to Laramide uplift and erosion (Foose and others, 1961; Pierce, 1965; Richards, 1957; Roberts, 1972; Ruppel, 1972). The final, eastward regression of the shallow

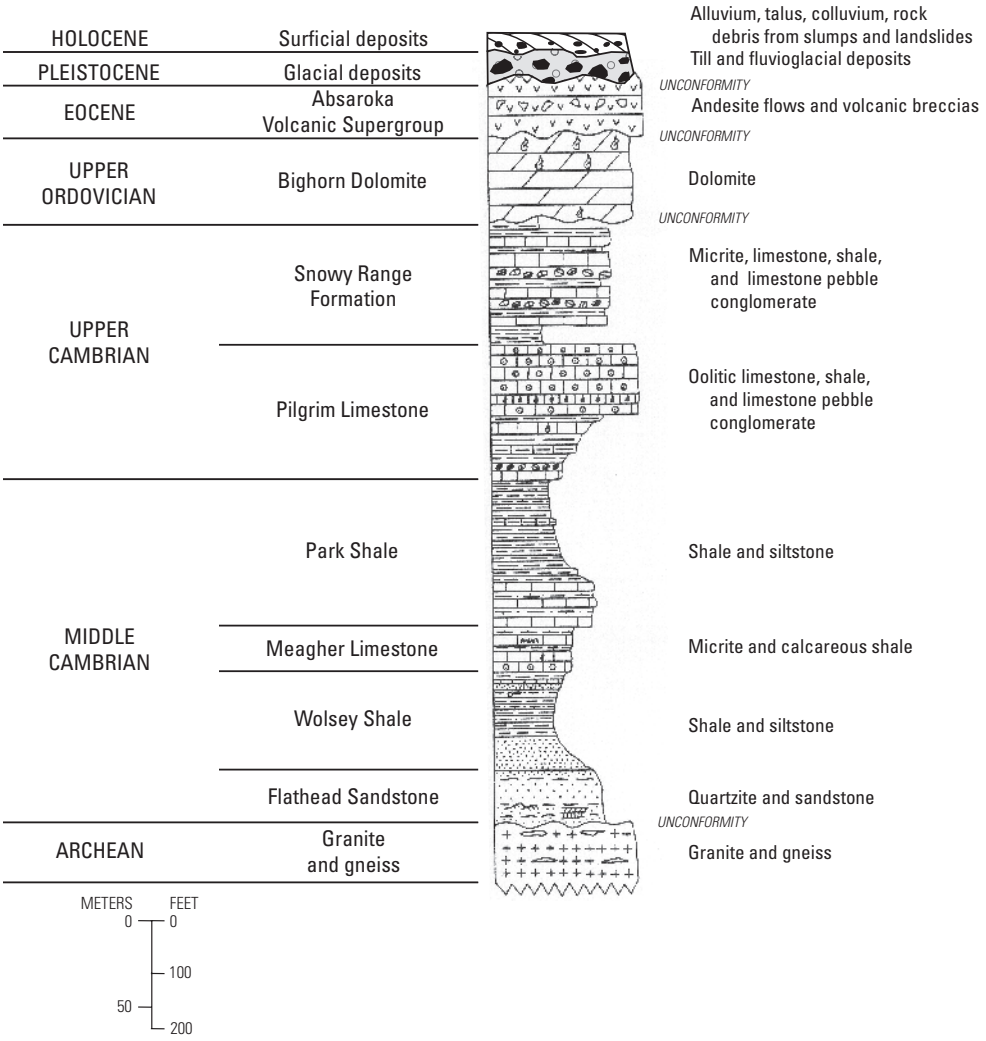

Figure 4. Schematic section showing the stratigraphy of the northern New World mining district. Modified from Elliott and others (1992).

Eagle sea from the region occurred during the Coniacian or early Santonian of the Late Cretaceous (Roberts, 1972). That regression likely coincided with initial stages of regional Laramide uplift. Studies of deposition rates in the Bighorn Basin southeast of the Beartooth uplift (fig. 3) suggest that the climax of the Laramide orogeny here occurred during the middle Paleocene (Hickey, 1980). Laramide uplift and deformation continued in the region until the latest Paleocene or early Eocene (Roberts, 1972). The Laramide orogeny, as elsewhere in the Rocky Mountain province, reactivated and utilized basement structures of Precambrian origin within the Beartooth uplift, such as the Cooke City zone.

Eocene Magmatism

A recent study by Hiza (1998, 1999) suggests that eruptions in the Absaroka volcanic field initiated approximately 53 Ma, during a period of crustal extension. Intrusive centers in the region, such as the stocks in the northern New World district, are temporally and spatially related to thick sequences of volcanic and volcaniclastic rocks of the Eocene Absaroka volcanic field (Smedes and Prostka, 1972). The Eocene intrusive centers are interpreted to represent stratovolcanoes (Hausel, 1982; Parsons, 1958) that now are exposed at various erosional levels. The stratovolcanoes were the sources of the Eocene volcanic and volcaniclastic deposits. Multiple phases of intrusion and eruption are evident at each center, such as the crosscutting stocks, laccoliths, dikes, sills, plugs, and volcanic deposits in the northern New World district (fig. 2) (Elliott, 1979). Hiza (1999) concluded that most of the Absaroka-related volcanic material (more than 60 percent) was erupted between 50 and 48 Ma, with local activity continuing until about 43.5 Ma. At some time during this interval, volcanic deposits blanketed the Cooke City area and buried the newly formed (middle Eocene) mineral deposits, as explained in a subsequent section.

Several studies of the mining districts in the Cooke City zone, including the New World district, have been conducted. Each confirmed the common association of gold-copper-silver mineralization with middle Eocene intrusive activity. Those studies include investigations at (refer to fig. 3) (1) the Independence district (Harlan and others, 1991; Lobanoff-Rostovsky, 1960; Meen, 1985, 1988; Meen and Eggler, 1987; Moyle and Buehler, 1989; Rubel, 1964, 1971; U.S. Geological

Survey and U.S. Bureau of Mines, 1983; Wedow and others, 1975), (2) the Emigrant district (Basler, 1965; Pfau, 1981; U.S. Geological Survey and U.S. Bureau of Mines, 1983; Van Voast, 1964; Wedow and others, 1975), and (3) the Sunlight mining region (Dreier, 1967; Nelson and others, 1980; Osterwald and others, 1966; Parsons, 1937, 1939; Pederson, 1968; Rich, 1974). Hammarstrom, Zientek, Elliott, and others (1993) evaluated the potential for undiscovered mineral deposits associated with intrusive centers in the South Snowy block.

Pleistocene and Holocene Erosion

Much of the present topography of the Beartooth uplift and the Cooke City area formed as a result of Pleistocene glaciation. Glacial landforms, such as sharp peaks and ridges, cirques, deep U-shaped valleys, and a variety of glacial deposits, are widespread throughout the Beartooth Mountains (Elliott and others, 1993; Simons and others, 1979; Wedow and others, 1975). In the northern part of the New World district, glaciation formed hanging valleys on each side of Henderson Mountain in the present valleys of Fisher Creek and Miller Creek. The glaciers uncovered, but spared, most of the Homestake breccia and its mineral deposits. Field mapping suggests that part of the east side of the Homestake breccia possibly was removed by glaciers from the east flank of Henderson Mountain and transported down the Fisher Creek valley. Recent mass wasting also has contributed to exposure of the Homestake breccia.

Geology and Mineral Deposits of the Northern New World District

Eocene stocks, other intrusive bodies, and associated breccia pipes crop out in the northern part of the New World district (fig. 2). These features include the Scotch Bonnet stock, the Fisher Mountain stock, the Homestake stock, the Homestake breccia, the Henderson Mountain stock, and the Alice E. breccia (an informal unit name used locally). Five copper-gold-silver deposits are genetically associated with these features (fig. 2). As summarized by Elliott and others (1992, p. 8), the deposits "are of three principal types: (1) tabular, stratiform, retrograde skarn and replacement deposits hosted mostly by [limestones of] the [Cambrian] Meagher Formation (Como, McLaren, and Miller Creek deposits), (2) replacement and vein deposits along high-angle faults (Fisher Mountain deposit), and (3) sulfide- and iron-oxide-rich replacement deposits of limestone blocks in diatreme and intrusion breccias of the Homestake breccia complex (Homestake deposit)."

Scotch Bonnet Stock

The Scotch Bonnet stock is interpreted to be the oldest major intrusion in the northern part of the New World district (fig. 2). It forms the bulk of Scotch Bonnet Mountain. An age determination of biotite, using the potassium-argon method, indicates the stock solidified 55.3±0.7 Ma (Elliott, 1979). The stock is dark gray to medium-dark gray with a primarily equigranular to fine-grained, subhedral granular texture. The rock ranges in composition from diorite to monzodiorite and is commonly propylitized (Elliott, 1979). Mineral deposits are sparse within the Scotch Bonnet stock. Disseminated pyrite is present in fault zones, and quartz-pyrite veins are present locally along steeply dipping structures (Johnson, 1991). No gold-copper-silver skarn or replacement deposits, such as those associated with the Fisher Mountain and Homestake stocks, have been recognized here.

Fisher Mountain Stock and the Como, McLaren, and Fisher Mountain Deposits

The next major intrusion that formed in the area was the Fisher Mountain stock (fig. 2), a multiphase network of felsic porphyritic intrusions and breccia bodies (Kirk and Johnson, 1993). The intrusion has an elliptical shape in plan view, covering an area of about 4,000 ft (north-south) by 3,500 ft (east-west) (1,219 m by 1,067 m). The Como and McLaren deposits (fig. 2), which are gold-copper-silver skarn and replacement deposits, are present along the perimeter of the stock. The Fisher Mountain gold-silver-copper deposit also is spatially associated with the Fisher Mountain stock. It consists of replaced fault-gouge material in the Crown Butte fault (fig. 2) and local replacement of Pilgrim Limestone and Meagher Limestone adjacent to the fault zone.

Dark-red to reddish-orange, highly fractured, iron-oxide-mineral-bearing rocks are exposed in the Como and McLaren open pits (fig. 5). The geology, alteration, and mineral deposits of the Fisher Mountain stock were described by Johnson (1991, 1992, 1994). He distinguished several phases of intrusion and brecciation in the complex, and he separated them into early and late stages. Crosscutting relationships he noted on Crown Butte (fig. 1) indicate that the Absaroka volcanic rocks in that area were extruded during an interval between the times of intrusion of the early and late stages of the Fisher Mountain stock. Deep drilling by Crown Butte Mines showed that a breccia pipe with open spaces between clasts, enclosed within the stock, reaches at least 2,430 ft (741 m) depth (Johnson, 1991, 1994). It has steep contacts. Collapse of sedimentary strata (as much as 1,700 ft or 518 m) and vertical mixing of clasts are identified in this pipe. According to Johnson (1991, 1994), sericitization and silicification of the rocks are prevalent to depths of 1,150 ft (351 m); propylitization (mainly chlorite and calcite) is dominant from 1,150 to 2,430 ft (351 to 741 m); and weak potassic and sericitic alteration occur below 2,430 ft (741 m) in the pipe.

Figure 5. Photograph of Fisher Mountain, site of the Fisher Mountain stock and mineral deposits, viewed toward the northeast from Daisy Pass (see fig. 1). The disturbed area in the center is the historic McLaren open-pit gold mine—last worked in 1953. Photograph taken in 1992.

Homestake Stock

A stock of biotite dacite porphyry, herein referred to as the Homestake stock, forms the bulk of the intrusive rocks at the north end of Henderson Mountain (fig. 2). The stock is crosscut by magmatic and explosion-collapse, pipe-shaped breccia bodies, referred to here collectively as the Homestake breccia (figs. 1 and 2). The dacite porphyry of the Homestake stock is similar in composition and texture to the biotite dacite porphyry of an early phase of the Fisher Mountain stock. This observation, combined with the crosscutting relations observed by Johnson (1991) for the Fisher Mountain stock, indicate that the Homestake stock predates the extrusive Absaroka Volcanic Supergroup rocks in the immediate area. Zircon was collected from dacite porphyry of the Homestake stock near the historic Homestake mine (fig. 1). Elliott (1979) reported a fission-track age determination of the zircon of 40.6±3.5 Ma. Crosscutting relations between the dacite porphyry and other intrusive rocks suggest that the dacite porphyry was emplaced in several separate events. The 40.6±3.5-Ma age may be a minimum age. If so, emplacement of the stock overlaps the eruptive history of the Absaroka volcanic field in the region (53-43.5 Ma), as determined by Hiza (1998, 1999). In any case, the Homestake stock was emplaced in Henderson Mountain sometime in the middle Eocene.

The Homestake stock, including the breccia-pipe complex (the Homestake breccia) at its center, is approximately circular in plan view, and it has a north-south (longest dimension) diameter of about 4,000 ft (1,219 m) (fig. 2). The deepest core drilling into the stock, to depths of more than 2,300 ft (701 m), did not penetrate the base of the dacite porphyry. The stock is bounded on the east by Cambrian sedimentary rocks and Precambrian granitic rocks, on the south by the younger Henderson Mountain stock, on the west by Cambrian sedimentary rocks, and on the north by Cambrian sedimentary rocks and the Fisher Mountain stock (Elliott, 1979; Van Gosen, 1994, his plate 1). Sill-like bodies of dacite porphyry that radiate outward from the stock intruded Cambrian sedimentary rocks, the Fisher Mountain stock, and Precambrian rocks.

The Homestake stock ranges from dacite to rhyodacite in modal composition. Elliott (1979) mapped the stock as a quartz "eye" rhyodacite. Some parts of the stock tend toward trachytic modal compositions. This likely indicates secondary, hydrothermal, potassium enrichment of the rock as a result of crystallization of potassium feldspar, biotite, or illite. The general visual character of the Homestake stock (Eyrich, 1969; Horral, 1966; Johnson, 1991; Lovering, 1924, 1929; Van Gosen, 1994) is light-gray to very light gray rock with medium- to coarse-grained phenocrysts floating in a holocrystalline, aphanitic to very fine grained groundmass (grain size less than 60 μm). Phenocrysts compose 15–60 percent of the rock, generally forming 30–40 percent of the rock. The phenocrysts are plagioclase, quartz "eyes," biotite, potassium feldspar, hornblende, and accessory apatite, zircon, magnetite, and ilmenite.

Phyllic and propylitic alteration are ubiquitous in the Homestake stock. No rock from this unit examined in outcrop or drill core appeared to be truly fresh and unaltered. Finely disseminated pyrite is common, typically constituting about 1 percent of the rock volume. The pyrite is encased in other alteration products (clay minerals, calcite, and albite(?)).

The Homestake stock was intruded by several dikes and sills of latite porphyry, andesite porphyry, and dacite porphyry. These dikes and sills apparently are spatially, compositionally, and mineralogically related to the main stock.

Homestake Breccia

The Homestake breccia, at the northern end of Henderson Mountain (figs. 1 and 2), is a breccia-pipe complex composed of mineralized and altered bodies of intrusion breccia, shatter breccia composed of sedimentary and intrusive rocks, and diatreme breccia. The term "Homestake breccia" in this discussion refers to all of the brecciated bodies enclosed by the Homestake stock. The Homestake breccia is roughly elliptical in plan view, and, except for a sill-like extension to the northwest, it is elongated in a northeast-southwest direction over a distance of about 2,900 ft (884 m) (fig. 2). It is well exposed on the crest and east-facing slopes of the northern part of Henderson Mountain (fig. 6). The Homestake stock nearly encloses the Homestake breccia on its northern, eastern, and western sides. The Henderson Mountain stock (or laccolith) contacts and intrudes the southern perimeter of the Homestake breccia. In terms of rock volume, the intrusion-breccia bodies are the dominant style of brecciation in the Homestake breccia.

Intrusion of the Homestake and Henderson Mountain stocks displaced Cambrian strata to the south, southeast, and east of the Homestake breccia. Large blocks or "islands" of altered Cambrian strata that were rafted at least 400 ft (122 m) upward by the stocks now are on the crest of Henderson Mountain adjacent to the Homestake breccia (Elliott, 1979).

All of the Cambrian stratigraphic units of the northern New World district, including rocks of the Flathead Sandstone through the Snowy Range Formation (fig. 4), are present as blocks or clasts within the Homestake breccia. The blocks and clasts that originated from clastic intervals (shales and mudstones) of the Cambrian sedimentary section were metamorphosed. They contain a calc-silicate mineral assemblage of epidote, garnet, potassium feldspar, chlorite, and apatite. Calc-silicate alteration in the clastic breccia material is characteristic of all bodies and styles of breccia in the breccia pipe. In the uplifted unbrecciated Cambrian strata adjacent to the breccia pipe, shale- and mudstone-rich horizons also contain calc-silicate alteration of garnet-epidote-chlorite-potassium feldspar with subordinate pyroxene. In contrast, breccia clasts composed of Cambrian limestone, especially those of Meagher Limestone and Pilgrim Limestone (fig. 4), were selectively and nearly completely replaced by sulfide and iron-oxide minerals that constitute the Homestake gold-copper-silver deposit.

Figure 6. Photograph of north-facing view of Homestake breccia on the northern end of Henderson Mountain. Outcrop of strata in the left foreground consists of hornfelsed lower units of Pilgrim Limestone. Lower peak labeled "A" is Fisher Mountain (fig. 5). Homestake breccia, cut by dikes and sills, forms most of the ridge crest and east-facing slopes in the center of the view. Photograph taken in July 1992.

Although many of the mineral deposits in these three breccia facies are widely separated spatially, they are similar in composition. Intense hydrothermal alteration is widespread through all of the breccia types. Overlapping imprints of propylitic and phyllic alteration in the upper zones of the Homestake breccia are indicated by assemblages of chlorite, carbonate minerals (calcite, ankerite, siderite), pyrite, chalcopyrite, hematite (specularite), vein and vuggy quartz, and subordinate epidote and potassium feldspar. The deep holes drilled into the Homestake breccia indicate that argillic alteration is prominent below a depth of about 1,000 ft (305 m). This alteration appears to be comparable to the kaolinite-rich subzone of a copper-porphyry system described by Sillitoe (1973, 1976).

The intrusion breccia bodies are composed of a variety of clasts and blocks of sedimentary and igneous rocks (fig. 7), cemented by an igneous matrix and subsequently altered. The characteristics of this breccia facies are consistent with the term "intrusion breccia" as defined by Sillitoe (1985): "* * * the products of the mechanical fragmentation and incorporation of wall rocks by intrusive magma * * * common * * * near the walls and roofs of subvolcanic stocks, and in porphyry-type deposits." The intrusion breccias likely formed as products of magmatic stoping and injection of magma, processes that followed emplacement of the Homestake stock. Numerous clasts and blocks of dacite porphyry from the Homestake stock are entrained by intrusion breccias, indicating that emplacement of the intrusion-breccia facies followed stock emplacement. Small- and large-scale flow banding in the igneous matrix of the intrusion breccias indicates that this breccia type formed by magmatic processes. Compositionally, the matrix appears to represent a quenched equivalent of the magma that formed the Homestake stock (Van Gosen, 1994, p. 88–89). Considerable rotation and juxtaposition of rock fragments occurred within these breccias. Individual clasts have been displaced by at least 500 ft (152 m) from their expected stratigraphic position. However, the general relic stratigraphy of the Cambrian sedimentary section was crudely retained across the Homestake breccia, including the intrusion breccias.

Parts of the Homestake breccia as wide as 525 ft (160 m) consist of mosaics of rotated large blocks of Cambrian strata, referred to in this discussion as "shatter breccia." These breccia bodies consist mainly of large blocks with little matrix material. Blocks range from a few feet in diameter to several tens of feet across, and they are angular to subangular in shape—suggesting the blocks were transported only short distances in the pipe. The fractures that form the blocks appear to propagate vertically and laterally into the intrusion breccias. The shattering events that formed shatter breccia appear to have concurrently fractured the adjacent bodies of intrusion breccia, indicating that the intrusion breccia was competent or at least partially lithified when fractured. The shatter-breccia zones locally host thick and laterally continuous intervals of high-grade gold concentrations, especially within the horizons dominated by limestone of the Meagher Limestone and Pilgrim Limestone.

Diatreme breccia pipes commonly intruded the bodies of shatter breccia. Fragments of shatter breccia are entrained in the diatreme pipes. Voids between blocks of shatter breccia locally are filled by chloritic-rich rock flour that contains small clasts of wallrocks. This chloritic material is similar to the matrices of the vertical, crosscutting, funnel-shaped diatreme breccia pipes. Microscopic observations indicate that chloritization of the rock flour probably accompanied diatreme emplacement.

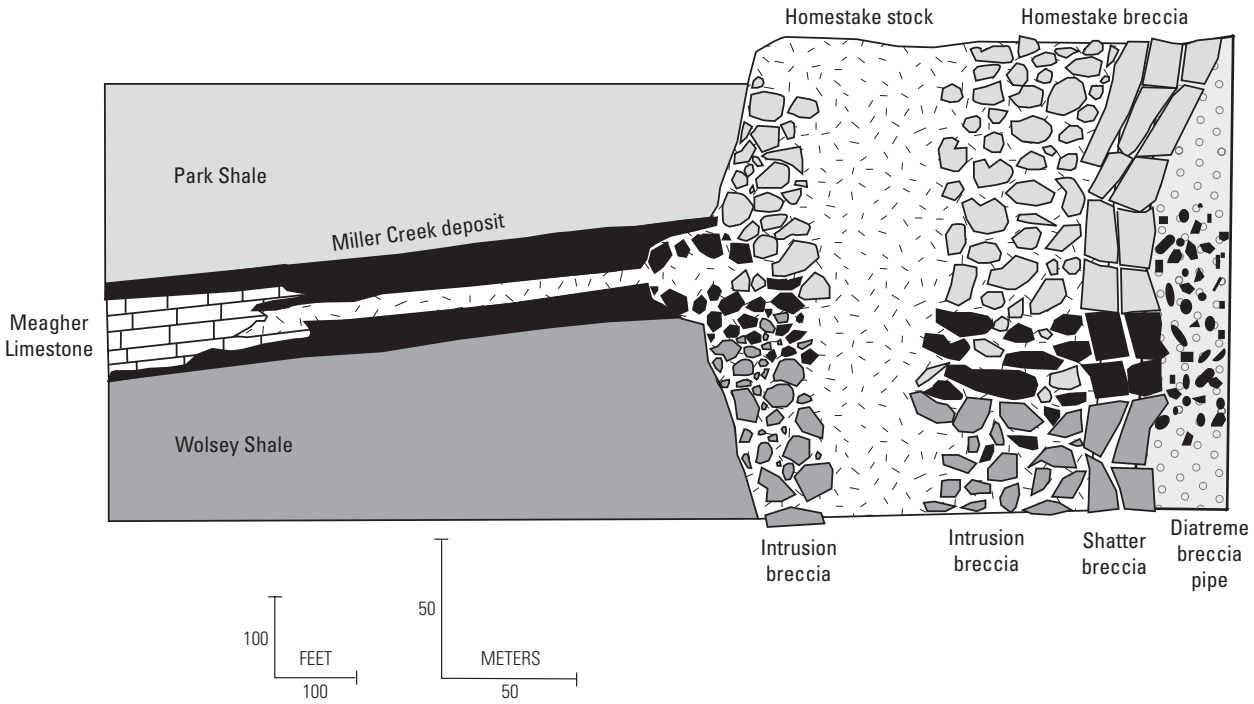

Figure 7. Schematic cross section illustrating the geologic setting of the stratabound Miller Creek gold-copper-silver deposits relative to the Homestake deposits. Replacement deposit material is shown as solid black.

As is the case with the intrusion breccias, relic stratigraphy is crudely maintained in the block-dominated shatter breccias. At a given horizon in the Homestake breccia, most of the clasts were derived from a single sedimentary formation, and those fragments generally are near or below their projected stratigraphic position. Downward movement of fragments probably resulted from the collapse of the entire breccia pipe that accompanied withdrawal of magma from below.

Breccia pipes and pebble dikes with characteristics consistent with phreatic-explosion origin cut across the intrusion and shatter breccias. The largest mass of diatreme breccia, approximately 640 ft (195 m) wide (north-south), is near the center of the Homestake breccia (see plate 1 of Van Gosen, 1994). The diatreme breccia pipes share steep contacts with adjacent intrusive rocks and other breccia bodies. The diatreme breccia pipes are primarily matrix dominated; clasts compose about 20–30 percent of the mass. The matrix typically is dark green; in some places it is dark-gray rock flour that is intensely chloritized. The rock flour is composed of subangular to subrounded, microfractured lithic and mineral fragments that range in size from silt to very fine sand. The silt-size mineral grains are epidote, calcite, or a white clay mineral, likely smectite, with a silky texture. Clasts are subangular to subrounded fragments of Precambrian basement granitic rocks, local Cambrian sedimentary rocks, and dacite porphyry. The diatreme breccia contains rare blocks several tens of feet to more than 100 ft (30 m) in diameter, but clast size typically is 3 to 6 inches (8 to 15 cm) in diameter. The degree of clast rounding likely was controlled by original rock competence and vertical distance of transport. Individual clasts in the diatreme pipes are as high as 500 ft (152 m) above their expected stratigraphic position, but they also commonly are below their normal position. Thus, a late internal collapse of the entire breccia complex is indicated, which occurred subsequent to the upward movement of clasts caused by stock emplacement and breccia-forming processes.

Vertical streaming of clasts and blocks in the diatreme pipes is interpreted on the basis of common rotation of blocks and clasts with their long dimensions oriented subparallel to the dominant vertical-flow foliations defined by fine fragments. The extreme mixture of rock types and the vertical-flow structures within the pipes indicate forceful, high-energy processes such as explosions. The chlorite-rich matrix material that carried small rock fragments was also injected into adjacent wallrocks and older breccias. In addition, the diatreme breccia pipes cut across several zones of gold-silver-copper mineralization. The forceful emplacement of diatreme pipes locally reduced and diluted ore-grade material by fragmenting and vertically spreading zones of gold-copper-silver replacement mineralization. That observation supports the hypothesis that diatreme breccia-pipe emplacement in the Homestake breccia occurred after the intrusion breccias, shatter breccias, and gold-copper-silver deposits had formed. The overall characteristics of the late breccia pipes suggest that they formed from phreatic explosions; therefore they represent diatremes in the upper level of a volcanic system.

Homestake and Miller Creek Deposits—Mineralogy and Genesis

The Homestake deposit consists of several gold-copper-silver-rich intervals of similar composition that are hosted by the Homestake breccia (Kirk and Johnson, 1993). The gold-copper-silver mineralization appears to be discontinuous on a small scale because the deposits consist of selectively replaced, discrete limestone blocks and clasts. At a larger scale, composite intervals maintain high gold grades, both laterally and vertically. Typical high-grade zones are listed in table 2. These and other intervals were the primary targets of the proposed New World mine. These deposits are present mainly as massive sulfide and iron-oxide replacements of limey blocks and clasts from calcareous intervals of the Homestake breccia, particularly breccia horizons that are dominantly clasts of the Meagher Limestone and the lower part of the Pilgrim Limestone (fig. 7). Gold-rich mineralization replaces (1) xenolithic blocks and clasts in intrusion breccias, (2) limey strata within shatter breccias, and (3) transported blocks and clasts in diatreme breccias. Less pervasive and less continuous gold mineralization is in thin pyritic veinlets that cut the bounding Homestake stock.

The primary ore mineral in the Homestake deposit is native gold, which occurs as grains and inclusions ranging from 1 to at least 700 μm in diameter. The gold grains occur in a variety of mineralogical settings; most are associated with pyrite. Gold grains occur (1) as inclusions within pyrite (most common) (fig. 8) and chalcopyrite (less common), (2) in microfractures within pyrite grains, (3) occasionally in interstitial portions (and possibly included within aggregates) of gangue minerals, and, in some cases, (4) intergrown with specularite (Van Gosen, 1994).

Alteration Patterns

The distribution of the gold deposits was controlled by the host protolith. Assays of drill core indicate that the gold-silver-copper-rich intervals are localized along horizons in the Homestake breccia (see plate 2 of Van Gosen, 1994): (1) about 430 ft (131 m) below the crest of Henderson Mountain, where intrusion and shatter breccias contain abundant xenoliths of rafted lower Pilgrim Limestone, and (2) about 500 ft (152 m) deep and lower, where the dominant clast lithology is Meagher Limestone. The Homestake breccia is a heterogenous mixture of fragmented sedimentary, intrusive, and Precambrian granitic rock. In each mineralized-breccia mass, limestone clasts are generally replaced by sulfide minerals. In contrast, in the same breccias, clasts and blocks of siltstone, shale, and mudstone—lithologies that form the bulk of the Park Shale and Wolsey Shale (fig. 4)—consistently contain calc-silicate mineralization and little gold-silver-copper enrichment. Clasts comprised of dacite porphyry typically show low to moderate enrichments of gold, copper, and silver in comparison to the values in calcareous rocks only inches away from the igneous clasts. Fragments of Precambrian granitic rocks, deep in the breccia pipe, are only weakly mineralized.

Table 2. Selected assay results for intervals of the Homestake breccia deposits as reported by Noranda Exploration and Crown Butte Mines.

[Data from Danielson (1991a, 1991c, 1992); Kirk and Johnson (1993); The Northern Miner (1990a, 1990b, 1991a, 1991d). nr, not reported; opt, ounces (troy) per short ton]

Interval thickness (feet)	Interval thickness (meters)	Gold (opt)	Silver (opt)	Copper (percent)
122.5	37.3	0.22	0.48	0.57
49.6	15.1	0.49	1.10	1.01
247.0	75.3	0.32	1.31	1.27
188.4	57.4	0.24	0.59	0.90
120.0	36.6	0.51	1.15	0.43
95.4	29.1	0.24	1.93	1.75
70.0	21.3	0.44	nr	0.66
75.0	22.9	0.27	2.67	0.98
85.0	25.9	0.24	2.01	0.82
379.2	115.6	0.30	nr	nr
126.7	38.6	0.22	0.88	0.77
73.2	22.3	0.23	0.91	0.48
87.1	26.5	0.23	1.47	0.47
117.9	35.9	0.17	0.69	0.64
90.0	27.4	0.26	0.67	0.43
182.0	55.5	0.17	nr	nr
249.0	75.9	0.22	nr	nr
558.0	170.1	0.14	nr	nr
364.0	110.9	0.20	nr	nr

Petrographic and field observations of the Homestake breccia (Van Gosen, 1994) indicate that calc-silicate alteration of the fine-grained detrital rocks was an early phase of metamorphism localized in and around the Homestake stock. Johnson (1991, 1992, 1994) interpreted a similar early hornfels phase for clastic rocks of the Fisher Mountain area. He proposed a local prograde influx of relatively high temperature fluids (hotter than 600°C) that developed during emplacement of the Fisher Mountain stock. A similar hydrothermal process affected the Homestake stock, the Homestake breccia, and the surrounding sedimentary rocks. This early calc-silicate alteration of the fine-grained clastic rocks probably had a strong influence on subsequent gold-copper-silver deposition. The Miller Creek deposits, which consist of tabular stratabound gold-copper-silver skarn mineralization of nearly identical ore mineralogy to that of the Homestake deposit (Kirk and Johnson, 1993), extends laterally outward from the Homestake breccia (fig. 7). These deposits are best developed along the upper and lower contacts of the Meagher Limestone.

The geometries of the Miller Creek deposits (fig. 7) suggest that the early calc-silicate alteration was developed in the overlying Park Shale and underlying Wolsey Shale prior to the introduction of ore-forming hydrothermal fluids. These two clastic units, with their porosities greatly reduced by early epidote-garnet hornfels development, acted as impermeable barriers to upward ore-fluid migration, and the fluids were channeled laterally into the Meagher Limestone. Similarly, hornfelsed blocks of Park Shale apparently sealed the upwelling hydrothermal ore-bearing fluids. The fluids did not reach many of the Pilgrim Limestone blocks (shatter breccia) in the upper Homestake breccia near the present crest of Henderson Mountain. The gold-bearing solutions locally penetrated some upper portions of the breccia pipe through conduits such as faults, fracture systems, and breccia pipes.

Argillic alteration in the dacite porphyry of the Homestake stock, deep within the Homestake breccia, appears to have been coeval with the introduction of sulfide minerals. The overall patterns of argillic alteration deep within the Homestake breccia, overlain by overlapping zones of phyllic and propylitic alteration, suggest that a direct relationship existed between fluids that emanated from the stock below and the replacement ore bodies above. Multiple events of hydrothermal shattering and sulfide deposition within the Homestake stock are evident in core samples from lower intervals of the deepest drill holes.

At depths of about 1,150 ft (351 m) and greater, the Homestake breccia is characterized by angular to subangular clasts with a pyritic matrix and as much as 5 percent chalcopyrite; most of the clasts and matrix material at that depth are shattered dacite porphyry. Sulfide minerals, primarily pyrite, constitute as much as 75 percent of the rock in intervals as thick as 1.5 ft (0.5 m). Breccia in cores from the bottom of drill holes at slightly more than 2,000 ft (610 m) depth are characterized by intense argillic alteration; the original grains are almost completely replaced by kaolinite and quartz. Pyrite, chalcopyrite, and quartz form the matrix of the breccia (probably best described as a magmatic-hydrothermal breccia, as defined by Sillitoe, 1985). These minerals commonly are internally fractured, suggesting multiple episodes of shattering that were likely caused by the explosive pressures of hydrothermal fluids.

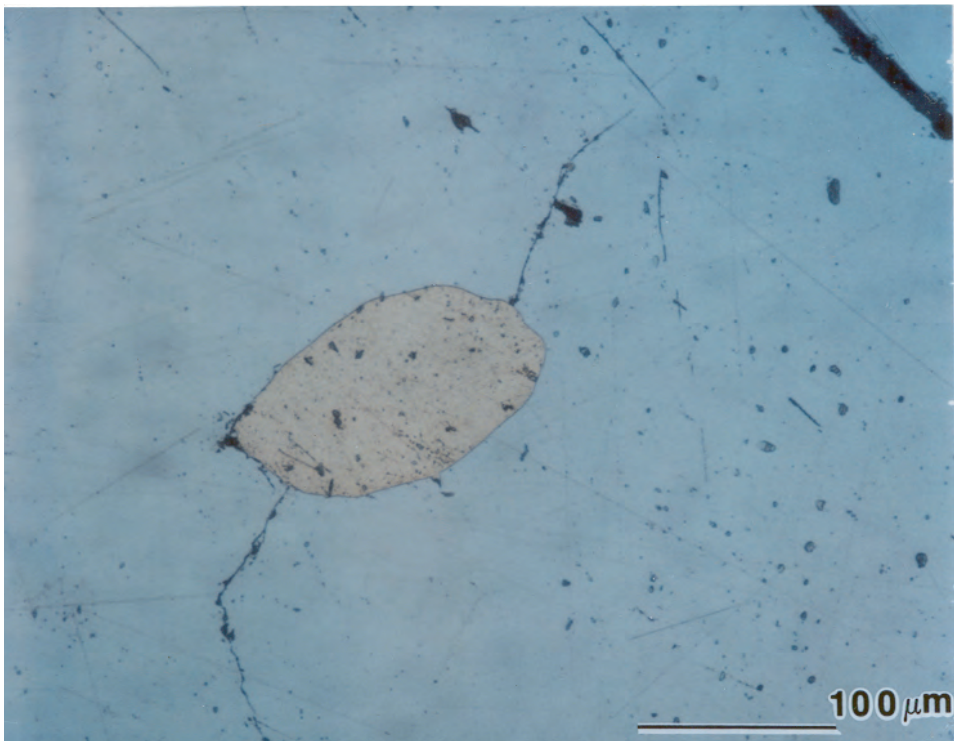

Figure 8. Photomicrograph showing the most common form of native gold in the Homestake deposit—an oblong gold inclusion along a mircofracture in pyrite. Photograph taken in reflected light. Width of view approximately 0.5 mm.

Mineral Assemblages and Paragenesis

The mineral assemblages of the Homestake breccia were studied in outcrop and in drill core samples, by means of microscopic examination of polished thin sections. X-ray diffraction techniques, reflected- and transmitted-light microscopy, and scanning electron microscopy (with semiquantitative analysis capability) were used for mineral identification. The minerals were deposited in four main stages (table 3): (1) *early metamorphism*-assemblage minerals (calc-silicate alteration) formed mostly in clastic-rich Cambrian rocks within and immediately adjacent to the Homestake breccia, (2) *massive ore-deposit-formation*-assemblage minerals that selectively replaced calcareous rocks in the Homestake breccia and limestones adjacent to the breccia pipe (the Miller Creek deposit, figs. 2 and 7), (3) *post-deposit alteration*-assemblage minerals, and (4) *recent-oxidation*-assemblage minerals.

The *early metamorphism* assemblage is characterized by fine-grained garnet (fig. 9), epidote, and potassium feldspar; locally abundant apatite; subordinate amphibole, calcite, and chlorite; and traces of quartz, clay minerals, pyrite, chalcopyrite, specularite, and magnetite (table 3). This calc-silicate hornfels alteration is best developed in the calcareous, fissile laminae of the lower part of the Park Shale. Outcrop, drill core, and microscopic examinations indicate that the early calc-silicate alteration caused the siltstone and shale clasts in the Homestake breccia to be comparatively less enriched in gold, silver, and copper than their less altered limestone and dolomite clast counterparts, which were only bleached and slightly recrystallized by the metamorphism. In breccia clasts that are dominated by closely packed epidote and garnet, the sulfide and iron-oxide ore-bearing minerals are consistently only present in trace quantities, and gold, silver, and copper grades are low.

Following the early calc-silicate alteration, an episode (or, more likely, multiple sequential episodes) of *massive ore-deposit formation* occurred within the Homestake breccia, resulting in deposition of significant sulfide- and iron-oxide-replacement bodies. The highest concentrations of gold, silver, and copper in the Homestake breccia are associated with deposition of these replacement minerals. This mineral assemblage consists mostly of pyrite, chalcopyrite, specularite, and magnetite, with a gangue assemblage of carbonate minerals (calcite, ankerite, and siderite), chlorite, quartz, clay minerals, and potassium feldspars (table 3). Trace amounts of argentiferous galena, native gold, a silver-bismuth-sulfide (unidentified), a copper-bismuth-sulfide (unidentified), mckinstryite, aikinite, and tetrahedrite also formed (table 3).

Pyrite and chalcopyrite are the most plentiful sulfide phases in the assemblage. Pyrite surpasses chalcopyrite in total abundance, although both are common throughout the deposits. All combinations of pyrite grain size and habit are present, but medium grain size and subhedral habit are typical. Locally, pyrite forms as much as 50 percent of the breccia. Chalcopyrite typically is anhedral, but subhedral grains are common. Specularite and magnetite are very abundant in the Homestake deposit. Acicular grains of complexly zoned specularite-magnetite form radiating aggregates of needles without apparent preferred orientations (figs. 10 and 11). Microscopic observations suggest that all of these minerals were deposited simultaneously or nearly so (Van Gosen, 1994). For example, chalcopyrite aggregates in places include very fine grained inclusions of euhedral pyrite and (or) acicular, zoned specularite-magnetite grains. Similarly, the pyrite grains commonly

contain anhedral inclusions of chalcopyrite or acicular specularite-magnetite grains. No consistent relationship of mineral replacement was observed among the pyrite, chalcopyrite, and zoned specularite-magnetite minerals; rather, it appears that they grew intertwined simultaneously. Photomicrographs showing common intergrowth relations of the primary ore minerals are shown in figures 10, 11, and 12. This mineral assemblage, interpreted to have been coeval in deposition, suggests that the precious-metal-bearing fluids that flooded the Homestake breccia were relatively oxidizing, sulfur rich, and acidic. This mineral assemblage, with coeval deposition, is uncommon in the literature.

Several minerals that are common to all portions of the Homestake breccia apparently formed subsequent to the main mineral-deposit-forming stage. These are the *post-deposit alteration* minerals (table 3). Many of these minerals probably grew shortly after the sulfide and iron-oxide phases, and they possibly formed during the cooling of the ore-bearing hydrothermal fluids. Minerals such as red hematite, maghemite, wustite, bornite, and covellite probably precipitated while the sulfide-rich, oxidizing fluids reestablished equilibrium throughout the complex immediately following the fluid-rock interactions associated with deposition of the replacement deposits. For example, the pH and oxidation potential of the hydrothermal fluids in contact with the Homestake breccia likely changed following the replacement processes, contributing to deposition of the post-deposit mineral assemblage.

Coarse-grained, generally euhedral quartz commonly fills and coats vugs throughout the Homestake breccia. Fine- to medium-grained, clear, euhedral dolomite crystals with a yellowish-brown tint commonly encrust the vug-filling late-stage quartz. Subhedral, fine- to medium-grained calcite replaces skeletal grains of acicular specularite-magnetite. The crystalline calcite appears “fresh” compared to earlier generations of calcite. This late-stage calcite and the

Table 3. List of minerals identified in the Homestake breccia, showing their position in the paragenetic sequence.

[Thick lines indicate major phases of deposition for the mineral; thin lines indicate minor phases of deposition. Query (?) indicates uncertainty of mineral's presence in that depositional phase]

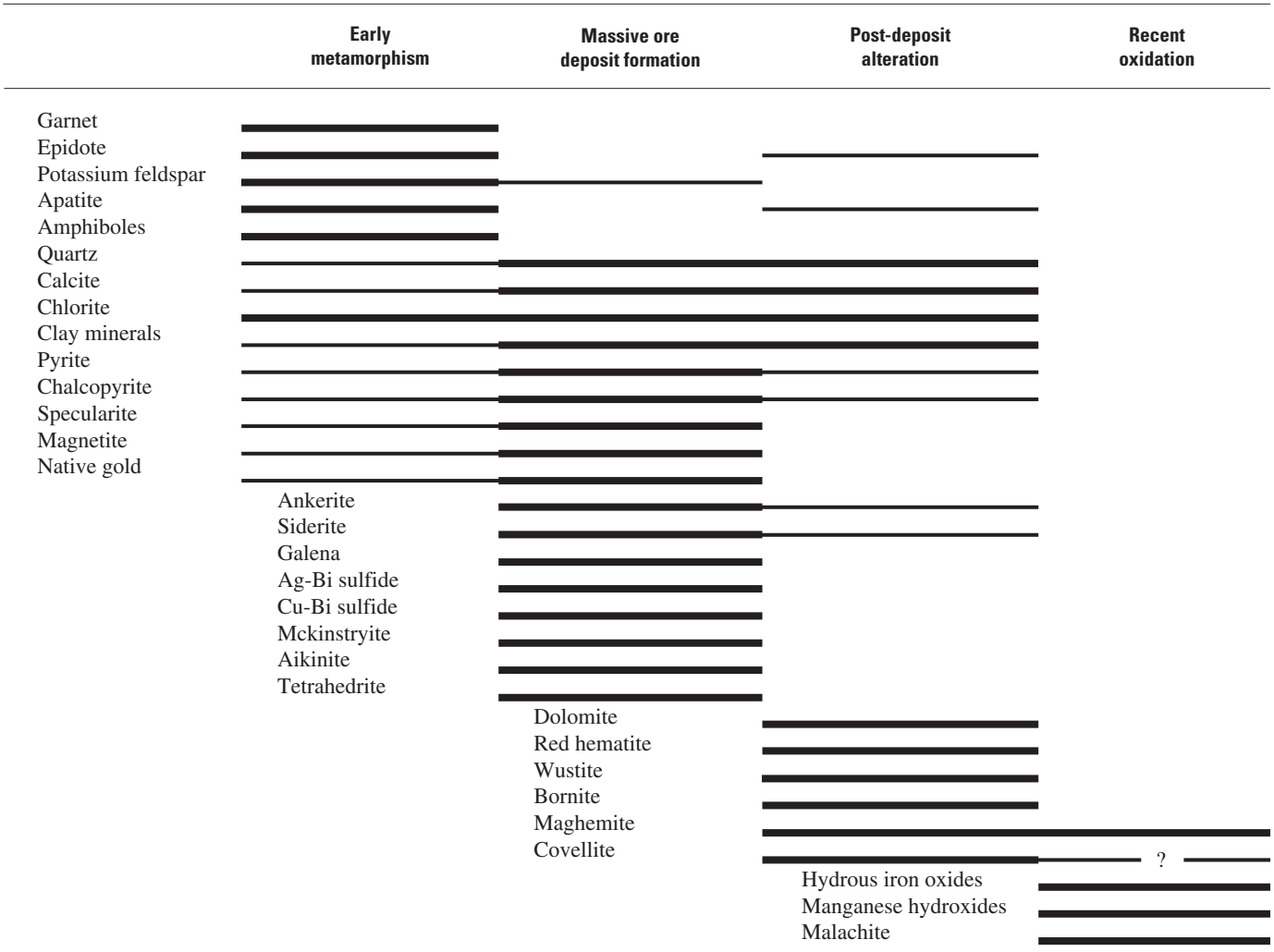

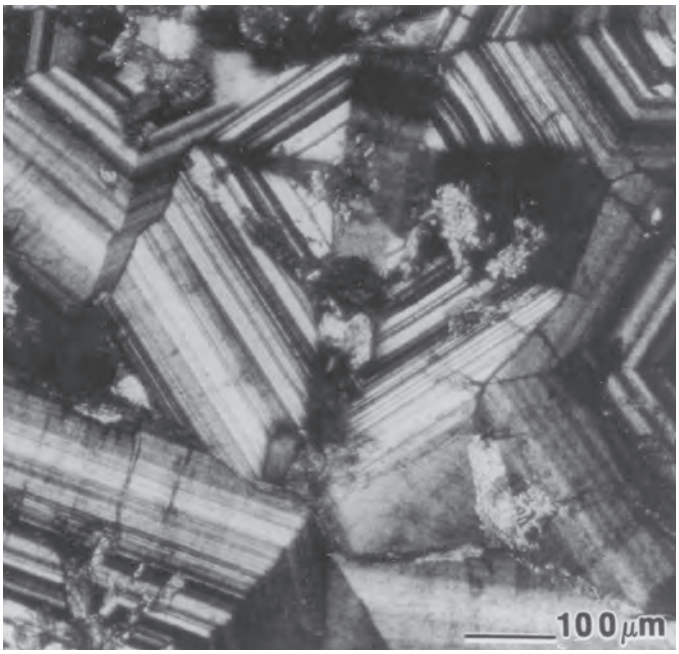

Figure 9. Photomicrograph showing banded garnets from the core of Homestake breccia exhibiting spectacular concentric-growth zonation. Garnets such as these are commonly associated with epidote in mudstone-rich breccia clasts of Homestake breccia; they represent an early calc-silicate hornfels alteration of the detrital rocks. Photograph taken with crossed polarizers. Width of view approximately 1 mm.

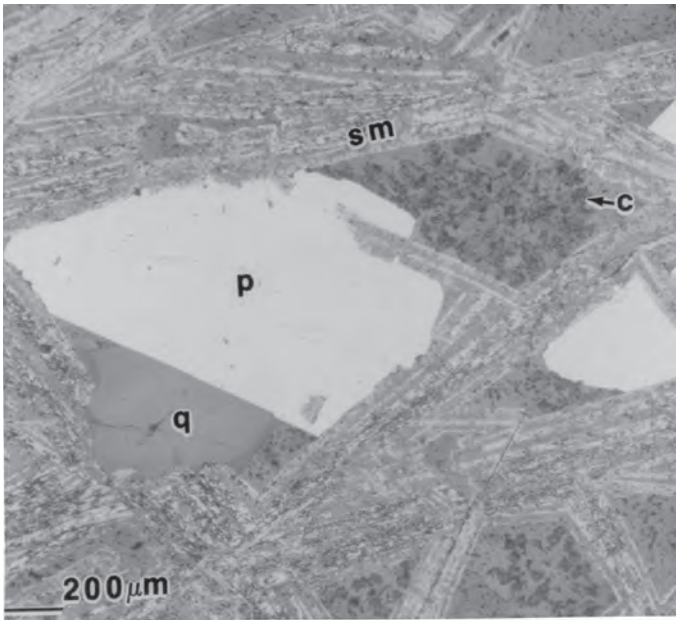

Figure 10. Photomicrograph showing coexisting intergrowth of zoned acicular specularite-magnetite (sm) with euhedral pyrite (p) grains and interstitial quartz (q) and chlorite (c, dark blotches in quartz). Notice that the specularite-magnetite needles are oriented parallel to the edges of the pyrite grains, which is common in the Homestake ores. Photograph taken in reflected light. Width of view approximately 2 mm.

vuggy dolomite probably were derived from magnesium and carbonate liberated during the dissolution and replacement of limestone and dolomite by ore solutions. Some of the clay minerals, ankerite, and siderite that are interstitial to the breccia also may have formed during this stage.

As a result of mass wasting and relatively recent glacial erosion of the Homestake breccia, oxidation of the Homestake deposit has occurred, but only to shallow depths. Core drilling showed that the zone of oxidation extends no more than a few tens of feet (less than 20 m) beneath the surface. Thus, supergene processes negligibly enriched the Homestake ores.

However, outcrops of the Homestake breccia generally are covered by a thin, dark-brown gossan composed of hydrous iron oxides (limonite, goethite) and manganese hydroxides (pyrolusite). The gossan is a product of near-surface *recent oxidation* of specularite, magnetite, and pyrite. The surficial gossan layer typically yields weakly anomalous (<0.05 opt) or trace amounts of gold. Maghemite also replaces magnetite in outcrops and near-surface rocks. Malachite and fine-grained aggregates of covellite locally replace chalcopyrite.

Geochemistry

Coprecipitation of pyrite, chalcopyrite, specularite, and magnetite in the gold-copper-silver-rich mineral assemblage suggests that the precious metal-bearing hydrothermal fluids were oxidizing and were sulfur rich. Inspection of geochemical data (Van Gosen, 1994) and deposit mineralogy indicate that the Homestake mineral deposits contain anomalously high concentrations of Ag, As, Au, Bi, Cu, Fe, Pb, and S, relative to unaltered examples of the host rocks in the region, plus a less substantial enrichment of Nb and, likely, Co. This suite of metals in anomalous amounts, combined with the geology of the Homestake deposit, is consistent with descriptions of gold skarn deposits that are genetically associated with the upper levels of copper-porphyry systems (Cox, 1986; Einaudi, 1982; Meinert, 1989; Sillitoe, 1988, 1991; Theodore and others, 1991; Titley, 1982).

Summary of Eocene Ore-Forming Processes

Based on the relationships described above, the list that follows is a brief summary of the main middle Eocene events and processes (from oldest to most recent) that combined to form the gold-copper-silver-enriched replacement bodies of the Homestake deposit and the closely related Miller Creek deposit.

1. During the middle Eocene, a magma chamber formed deep beneath the present locality of northern Henderson Mountain.

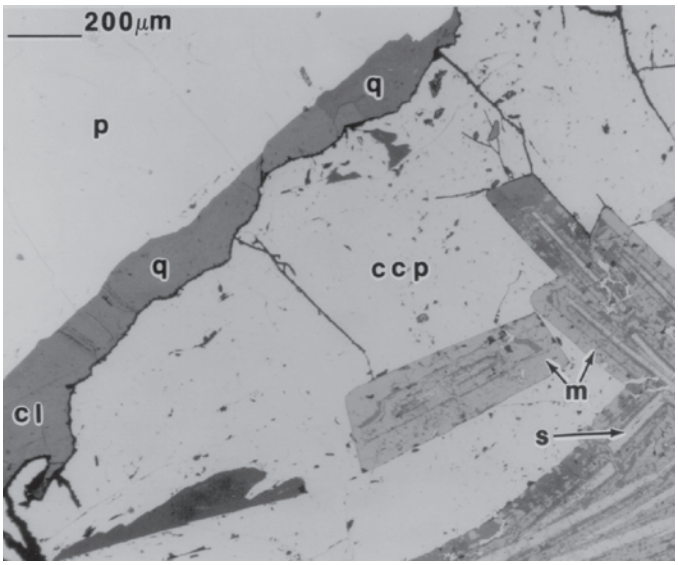

Figure 11. Photomicrograph showing zoned acicular crystals of specularite (s) and magnetite (m) enclosed by chalcopyrite (ccp). Pyrite (p), quartz (q), and calcite (cl) also form parts of this assemblage. Photograph taken in reflected light. Width of view approximately 2 mm.

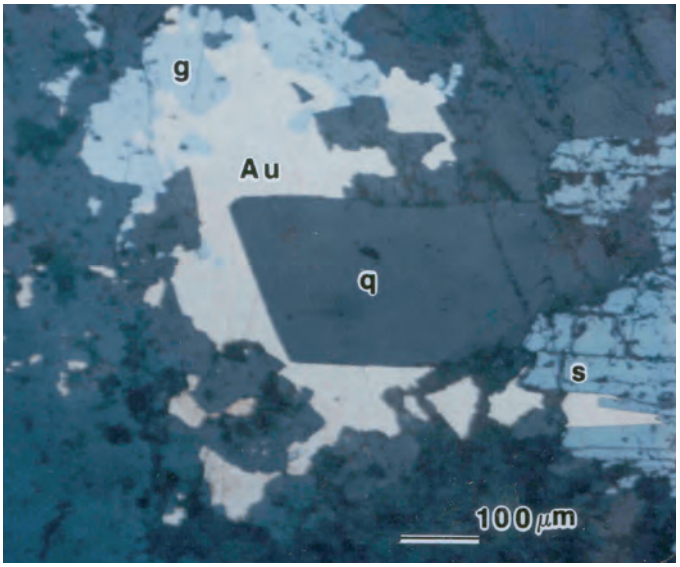

Figure 12. Photomicrograph of a gold-rich ore. Native gold (Au) forms an intergrowth with acicular specularite (s), galena (g), and euhedral late-stage quartz (q). The groundmass of this ore is turbid, fine-grained carbonate minerals, chlorite, and moderate amounts of quartz. Photograph taken in combined reflected and transmitted light for enhancement. Width of view approximately 1 mm.

2. Dacitic magma rose through the crust and the Homestake stock was emplaced concurrently with emplacement of the nearby Fisher Mountain stock (fig. 2). The rising melt utilized a structural zone of crustal weakness with Precambrian ancestry—the Cooke City zone (fig. 3).

3. Intrusion of the Homestake magma was accompanied by calc-silicate metamorphism and low-grade gold mineralization of the clastic Cambrian rocks surrounding the intrusion ("early metamorphism" mineral assemblage, table 3). Interlayered Cambrian limestones were weakly recrystallized and bleached.

4. Intrusion breccias formed during magmatic stoping and injection of dacitic porphyry. This probably followed emplacement of the Homestake stock (on the basis of the presence of numerous dacite porphyry clasts entrained in the intrusion breccias). Cambrian sedimentary wallrocks were assimilated partially, or almost completely, by the ascending dacitic magma. Large sections (roof pendants) of caprocks were rafted upward.

5. Following solidification of the intrusion breccias, multiple events of hydrothermal shattering accompanied a flooding of relatively oxidized, sulfur-rich fluids upward throughout the newly formed Homestake breccia. The hydrothermal shattering formed facies of rotated shatter blocks ("shatter breccia") in the roof pendants. Intense argillic alteration developed in deep shatter zones. Concurrently, limestone clasts and blocks in upper parts of the Homestake breccia were selectively replaced by silver- and copper-bearing sulfide minerals and coeval iron-oxide minerals, accompanied by trace amounts of gold ("massive ore-deposit formation" mineral assemblage, table 3). Blocks and clasts of brecciated Cambrian Meagher Limestone and Pilgrim Limestone were particularly receptive to massive replacement, and they formed the bulk of the Homestake deposit. The lateral flow of the same fluids into Meagher strata along the perimeter of the Homestake breccia formed the adjacent, stratabound and tabular Miller Creek deposit (figs. 2 and 7).

6. Phreatic explosions occurred within the complex breccia pipe, forming vertical pipe-like bodies of diatreme breccia. The explosions probably followed a period of local fracture and fault development. Several diatreme breccia pipes formed in the upper levels of the Homestake breccia. They cut across and violently fragmented several previously formed mineral deposits and spread mineralized fragments upward. The effects were to *locally* dilute and expand previously continuous zones of mineralization.

7. An internal collapse of the entire Homestake breccia complex probably followed formation of the diatreme breccia pipes. Collapse likely accompanied withdrawal of an underlying magma chamber. The result was placement of the Cambrian sedimentary rocks in the Homestake breccia and their replacement deposits at positions below their original stratigraphic position.

Post-Ore Henderson Mountain Stock

The Henderson Mountain stock, possibly a laccolith (Horral, 1966), intruded the southern flank of the Homestake stock and breccia pipe. It is predominantly dacite porphyry. No mineralization is associated with the contacts between the Homestake breccia and the Henderson Mountain stock. Elliott (1979) reported an age of 44.0±4.1 Ma for the porphyry at Henderson Mountain, based on fission-track data from zircon. That age is older than his fission-track age determination for the Homestake stock (40.6±3.5 Ma). The Henderson Mountain stock clearly intrudes, cuts across, and thereby postdates the Homestake stock (Horral, 1966). Although the crosscutting relations indicating the Henderson Mountain stock is younger than the Homestake stock appear to disagree with the age determinations, they do not disagree when the accuracy range of the age-determination method is considered. For example, on the basis of fission-track data, a minimum age of 39.9 Ma is possible for the Henderson Mountain stock, compared to a possible maximum age of 44.1 Ma for the Homestake stock (Elliott, 1979).

Alice E. Breccia

No gold-copper-silver ores are known to occur in the Alice E. breccia (an informal unit of local usage) (fig. 2); however, the breccia shares several alteration and geologic characteristics with the Homestake breccia (Van Gosen, 1994, p. 78–79). The Alice E. is an altered, heterolithologic breccia pipe on the southern boundary of the Henderson Mountain stock (fig. 2). The breccia pipe consists of fragmented and metasomatized Middle Cambrian sedimentary rocks that are mixed with sericitically and propylitically altered porphyritic rocks related to the Henderson Mountain stock (or laccolith) (Cope, 1984). Blocks and clasts of the sedimentary units in the breccia are metamorphosed, and they have alteration assemblages that are similar to those in the subeconomic rocks of the Homestake and Miller Creek deposits. Drilling of the Alice E. breccia by Crown Butte Mines-Noranda Exploration intercepted several sulfide-rich zones with anomalous gold and copper concentrations, mainly in breccia blocks of Meagher Limestone. The grades, however, were below the ore grades for the district. Crown Butte Mines (written commun., 1992) noted that the Meagher is noticeably thinner (50–80 ft or 15–24 m thick) and more silty near the Alice E. breccia than in outcrops near the Homestake breccia and Fisher Mountain stock. The thin and silty character of the Meagher Formation may have contributed to the lack of massive replacement mineralization and the low-grade gold concentrations (<0.05 opt).

Postmineralization Dikes and Sills

A number of dikes and sills cut across the Homestake breccia and its replacement deposits. The dikes and sills are compositionally and spatially related to the Homestake and Henderson Mountain stocks. Porphyritic dikes of dacite (most common) and latite-filled dilation zones in the Homestake breccia intruded along contacts between dissimilar masses (such as different types of breccia bodies). The dikes also filled preexisting open fractures and faults in the country rocks surrounding the stock-breccia-pipe complex, forming concentric and radial patterns centered around the Homestake stock. These dikes and sills commonly are intensely altered, characterized by strong propylitic alteration and weak to moderate phyllic alteration. Replacement minerals include calcite, quartz, iron oxides, and disseminated fine- to very fine grained pyrite. The dikes formed very minor skarn alteration zones (<2 ft or 0.6 m in width) in the rocks they intruded. These late dikes and sills cut breccia masses that are only weakly mineralized, in spite of the favorable presence of dolomite clasts. Thus, the late dikes and sills were not conduits for the ore-bearing fluids. However, possibly they occupy preexisting structural zones that previously had served as plumbing systems for the gold-copper-silver-bearing solutions. Concentric and radial patterns of faults and fractures that formed around an intrusive center are common features in the subvolcanic levels of porphyry copper systems (Heidrick and Titley, 1982). Such patterns are thought to occur early during the emplacement of the pluton; typically they form at high levels in an intrusion system (Knapp and Norton, 1981).

Recent History of the Homestake Deposit—Exploration, Discovery, Mining Attempts, and Controversy

The Cooke City area has been the site of many mineral discoveries and development since the arrival of the first European settlers in the Yellowstone region. The New World district was explored almost continually for more than 125 years. The discovery of the Fisher Mountain, Miller Creek, and Homestake deposits, between 1987 and 1990, was the culmination of the most recent exploration in the area. These resources will be protected for at least the near future by a mineral withdrawal for the area, enacted in 1997.

1860s to 1985—Early Prospecting and Mining

Most of the early mining history of the New World district that follows is summarized from Lovering (1929), who noted that "* * * in the pioneer days of Montana the New World mining district was regarded as one of its most promising camps * * *," and "* * * in the early [eighteen] eighties Cooke [City] had a population of over 2,000."

The earliest exploration for mineral wealth in the New World district area preceded the establishment of Yellowstone National Park by several years. Rich discoveries of lead, silver, and gold within the district apparently were reported (or at least rumored) as early as 1868. However, the first documented discoveries were made in 1869 by four trappers who entered the

area to avoid pursuit by Indians. The trappers were robbed of their horses and supplies by the Indians along Cache Creek in Wyoming. They reportedly "* * * narrowly escaped death and fled north up Cache Creek and crossed the divide that separates its headwaters from Republic Creek [about 5 mi or 8 km south of Cooke City]" (Lovering, 1929). The trappers noted manganese-stained outcrops at the future site of the Republic mine (fig. 1); they panned gold from the streams and reported their findings to the Crow Agency at Columbus, Mont. The district at that time was designated as part of the Crow Indian Reservation. Their news induced prospectors to stake mining and placer claims the next summer (1870) at Miller and Republic Mountains, short distances north and south of the soon-to-be town of Cooke City. A furnace was built in 1875 and lead ore was extracted from the Republic mine (fig. 1) and Miller Mountain (Gardner, 1914). Nez Pierce Indians destroyed the furnace and the mining records in 1878. They absconded with lead bullion, presumably to make bullets.

In 1882, the U.S. Government unilaterally removed the district from the Crow Indian Reservation and several mining claims were quickly established (Gardner, 1914). The "Cooke City or Republic" smelter was built in 1883 and went into production in 1884. Difficulties in smelting the complex ores from the Republic Mountain mine and costly freight rates closed the smelter and mine for the next 20 years. While the Republic mine and smelter remained closed, ore production in the district was intermittent and modest (Gardner, 1914; Brooks, 1921).

"Rich" gold ore was discovered at Henderson Mountain around 1888, at the Little Daisy and Homestake claims. During 1888 and 1889, about 420 tons of ore was produced from those claims (Reed, 1950). From the early 1900s to about 1930, the district and surrounding area was actively developed and several shafts were sunk. However, total district production was modest.

Henderson Mountain, including the Little Daisy and Homestake mines, was a site of development from 1904 until 1925. A 250-kilowatt power plant was built on the Clarks Fork of the Yellowstone River 4 mi (6 km) east of Cooke City in 1915 (Lovering, 1929). A 350-ton copper smelter was nearly completed along Fisher Creek (fig. 1) in 1921, but apparently it never went into production. At that time (1921) an adit was begun at the Gold Dust claim (fig. 1). It entered at the eastern base of Henderson Mountain, in Precambrian granitic rock, and was advanced westward into the Homestake breccia. From the autumn of 1923, until the autumn of 1925, (Lovering, 1929) an aerial tramway was constructed to connect this adit to the unfinished smelter along Fisher Creek. A few of the tramway towers remain standing today.

The high-grade Homestake deposits were not encountered by the Gold Dust adit, and no ore was mined or shipped during this period of development. The financiers of the Gold Dust and tramway developments abandoned the project in 1925, and the claims remained idle until 1947 (Reed, 1950). Stories (no written record) (Allan Kirk, oral commun., 1992) suggest that the primary fundraiser for the Gold Dust mine project embezzled the money collected from investors and fled to Germany with the stolen money. Ironically, the Gold Dust adit came within a couple hundred feet of intercepting high-grade gold deposits that later were delineated by the core drilling of Crown Butte Mines in the 1990s. The Gold Dust adit was driven horizontally into the base of Henderson Mountain as a main haulage adit (see plate 2 of Van Gosen, 1994). However, construction stopped in 1925 when the financial support ended. The workings were less than 200 ft (60 m) from a highly mineralized zone with grades of more than 0.3 opt gold.

In the early 1920s, Lovering completed the first thorough geologic investigation of the New World district. His Ph.D. dissertation (Lovering, 1924) and a report for the U.S. Geological Survey (Lovering, 1929) described the district's general geology and the exposed mineral deposits. Lovering witnessed the development of the Gold Dust adit during the early 1920s, but he completed his field studies before that mining venture was abandoned in 1925.

Modest production (70 tons daily) came from an open pit cut into the Homestake breccia (near the Homestake mine, fig. 1) during the 1940s (Reed, 1950). That modest open-pit operation also only scratched the surface of the Homestake breccia, and it did not encounter the high-grade deposits farther inside the mountain.

Most of the district's production came from the McLaren open-pit mine (fig. 5), which began operation on a small scale in 1933 on the south flank of Fisher Mountain. Production records indicate that from about 1938 to 1953 the McLaren gold mine (operated by Gold Mines, Inc.) yielded 337,000 tons of ore with average grades of 0.184 opt gold, 0.26 opt silver, and 0.59 percent copper (Elliott and others, 1992; Johnson, 1991). A mill along Soda Butte Creek, a short distance east of Cooke City, processed the ores until it burned in 1953, halting all production from the McLaren mine. Tailings at the old mill site and unconsolidated mine material used to fill the old mine pit both assayed at more than 0.1 opt gold (Johnson, 1991).

The Irma and Republic mines (fig. 1) also produced ores from 1938 to 1950. Krohn and Weist (1977) reported that those operations produced about 12,500 tons of ore, averaging 10 percent lead, 5 percent zinc, and 20 opt silver.

From 1962 to 1982, several companies explored the New World district for large-tonnage porphyry copper-molybdenum deposits (Elliott and others, 1992; Lawson, 1981, 1982). Bear Creek Exploration Co. (then part of Kennecott Copper Co.) discovered and drilled the Como copper-silver-gold skarn and replacement deposit (fig. 2) between 1962 and 1973. Additional drilling was completed in the Como area during 1981–1982 by Ranchers Exploration (Hecla Mining Co.) (Engineering and Mining Journal, 1980; The Mining Record, 1980).

Mine Finders and Gulf Resources also actively explored the district for porphyry copper-molybdenum potential during the early 1980s. Apparently, those companies drilled exploratory holes from the top of Henderson Mountain that penetrated the Homestake deposit. However, assays for gold and copper were not conducted because molybdenum was the primary target and the molybdenum values were not considered to be economic.

1985 to 1996—Rich Discoveries, Controversy, and Federal Government Involvement

An exploration program within the district was initiated in 1985 by Plexus, Inc. (Allan Kirk, oral commun., 1992). In 1987, Crown Butte Mines, Inc., was founded by Plexus, Inc., to coordinate drilling for undiscovered reserves at the McLaren deposit area. Noranda Exploration, Inc., became the project manager in late 1987, forming a cooperative effort with Crown Butte Mines. Noranda Exploration–Crown Butte Mines concentrated efforts on exploration for skarn and replacement deposits in Cambrian carbonate rocks adjacent to and within the Eocene stocks in the northern part of the district (Kirk and Johnson, 1993). In the first phase of exploratory drilling, they expanded and delineated the copper-silver-gold reserves at the Como and McLaren deposits (fig. 2). An aggressive drilling program in the northern part of the district led to discovery of three "blind" deposits designated as the Fisher Mountain deposit (found in 1988), the Miller Creek deposit (1989), and the Homestake deposit (1990) (fig. 2). The progress of this exploration program was followed by articles in Rocky Mountain Pay Dirt (1990) and The Northern Miner (1990a,b, 1991a–e, 1992a–c; and Danielson, 1991a–c, 1992) and also discussions by McCulloch and others (1988) and McCulloch (1989).

From 1987 through 1993, Noranda Exploration–Crown Butte Mines drilled a total of 327,031 ft (99,674 m) in 856 exploratory and development holes within the district (Allan Kirk, project manager, written commun., 1994) using reverse circulation and core drilling. Their estimates of the in-place geologic reserves calculated at that time are listed in table 1.

During 1990, Noranda Exploration–Crown Butte Mines submitted a Hard Rock Mine Permit Application to the Montana Department of State Lands and the U.S. Forest Service. The plan included underground mining of the Miller Creek and Homestake deposits by room-and-pillar (or panel) methods, gaining access to the deposits through a 4,000-ft tunnel opening on the east side of Henderson Mountain. As explained by Kirk and others (1993), the extracted ore "will be transported via conveyor through an underground tunnel to the plant site that will be located in the Fisher Creek valley." To avoid controversies associated with cyanide heap-leach ore processing, they proposed fine grinding of the ore, followed by sequential floatation processes to segregate the gold and copper (Kirk and Johnson, 1993; The Northern Miner, 1992a). A tailings impoundment was to be built in the Fisher Creek valley (Satchell, 1995, p. 41). The proposal did not include plans to mine the McLaren and Como open pits and Fisher Mountain underground reserves because of their lower grade; cyanide heap-leach processing was thought necessary to extract the gold from those oxidized materials (Kirk and Johnson, 1993; Kirk and others, 1993). In April of 1993, the permit application was accepted as complete by the authorizing agencies, and an Environmental Impact Study was initiated.

From 1993 until 1997, including the time period in which negotiations occurred between the Federal Government and Crown Butte Mines (in 1996 and 1997, described in a subsequent paragraph), a massive Draft Environmental Impact Statement (DEIS) was prepared. It outlined possible alternatives for mining and "no mine" scenarios, and it analyzed the predicted impacts of each alternative (environmental, social, economic, scenic, and other impacts). This draft was written during a 4-year period by a contractor, using information provided by several Federal and State agencies. The final draft was more than 800 pages in length, not including appendixes and related documents.

The original draft (DEIS) addressed nine alternatives—a "no mine" alternative and eight other possibilities that placed the mill site, tailings disposal, and discharge of mine excess waters at different sites. One of the alternatives required trucking of the "pyritic tailings" (fine-grained mill-processed tailings or waste containing as much as 90 percent pyrite) out of the mine area to a disposal impoundment north of Cody, Wyo. A later draft reduced the alternatives to the "no mine" option and seven scenarios for placements of the mine and mill site, tailings disposal site, and excess mine-water discharge. The last DEIS consisted of 17 chapters and 6 appendixes, addressing issues such as Yellowstone National Park, geology and ground-water hydrology, surface-water hydrology, aquatic resources, cultural resources, area highways, grizzly bear habitat and population, economic conditions, social conditions, and others. A copy of the final DEIS is available through offices of the Gallatin National Forest or the Montana Department of Environmental Quality, the lead agencies responsible for the EIS and the analyses contained in it. The DEIS was not formally published because it never was officially approved for use.

The proposal for a "New World mine" provoked immediate, intense, and organized opposition, including groups such as the Greater Yellowstone Coalition and the Sierra Club. At least four factors were very strong influences on the ultimate success of the anti-mine effort:

1. Proximity of the proposed mine to Yellowstone National Park.
2. Publicity and impact of the 1992 Summitville mine environmental disaster in southwestern Colorado.
3. Environmental legacy of historic mines in the New World district.
4. Opposition to the mine by officials of the Federal Government Executive Branch, including President William Clinton and Secretary of the Interior Bruce Babbitt.

Yellowstone National Park

Yellowstone National Park is regarded as a national and international treasure, at least in part because it was the first national park in the United States and the first designated national park in the world. The unique geothermal, scenic, and ecosystem features of the Park contribute to its stature. The proximity of the proposed New World mine to the Park boundary (less than 5 mi (8 km) from the northeast entrance) contributed to public sentiment in opposition to the mine. In regard to the proposed New World mine, Yellowstone National Park employee Dave Shaver stated that "***the overriding National Park Service concern is the potential for adverse effects of mine operations on park water quality and related resources of the ecosystem" (Shaver, 1996). He added that "***it would be difficult to find an environmentally more sensitive or controversial place to develop a large gold mine." Paul Pritchard, president of the National Parks and Conservation Association, said the mine would cause "***incredible demands on a pristine environment * * * It's about as bad a place to have a human intrusion as you can imagine" (Bama, 1996, p. 10). In December 1995, the World Heritage Committee, affiliated with the United Nations, declared that Yellowstone's status as a United Nation's designated World Heritage Site was in danger due to the mining proposal (Bama, 1996; Wilkinson, 1994). Michael V. Finley became superintendent of Yellowstone National Park in November 1994. He quickly announced his opposition to the proposed mine, stating "How can the logical mind approve this?" (Bama, 1996).

Ironically, during the period of debate over the proposed New World mine, the Mineral Hill gold and silver mine operated about 4 mi northeast of Gardiner and about 2.5 mi north of the Yellowstone National Park boundary; it was visible from Mammoth Hot Springs. The gold at the Mineral Hill mine was extracted from sulfide-bearing, arsenic-rich, iron-formation and quartz veins and boudins adjacent to the iron-formation. The gold is associated with pyrrhotite, pyrite, and arsenopyrite (Hammarstrom, Zientek, Elliott, and others, 1993).

The Summitville Mine Environmental Disaster

From 1985 through 1992, the Summitville mine in southwestern Colorado extracted gold from a large, low-grade, pyritic ore using cyanide heap-leach methods. The mine's operator had ceased mining and had started environmental remediation in 1992. The mining company declared bankruptcy in December of 1992, and abandoned the site. Environmental problems left at the Summitville mine included increased acidic and metal-rich drainage and leakage of cyanide-bearing solutions into nearby rivers. The Environmental Protection Agency immediately took control of the site, and it estimated the cost of cleanup to be $100 million to $120 million. The history and science applied to the Summitville mine were summarized in U.S. Geological Survey Bulletin 2220 (King, 1995). The Summitville mine disaster gained national exposure, thereby focusing public attention on the possible negative effects of metal mining.

The Summitville environmental disaster was used as the showcase example in arguments against the New World mine project. Several national publications described worst-case environmental scenarios for the proposed New World mine (see Parks, 1994, and Wilkinson, 1994), and many of the articles also invoked comparisons to the Summitville mine. For example, an article in U.S. News & World Report (Satchell, 1995) made analogies to the Summitville disaster and said, regarding the New World mine operation, "* * * depending on where the tailings are put, acidic runoff could leach poisonous heavy metals into one of three local creeks that flow into tributaries of the Yellowstone River."

Historic Mines in the New World District

Mining activity in the New World district in the 1950s and earlier left behind abandoned adits and open pits, mine wastes, and acidic drainage near the mines, such as at the McLaren (fig. 5) and Glengarry mines (fig. 1). Photographs of these features are included in articles by Parks (1994), Satchell (1995), and Wilkinson (1994). The poor environmental practices of past mining in the district, although the activities were legal during their times of operation, were used prominently in arguments against the proposed New World mine. For example, Wilkinson (1994, p. 32) wrote the following about the past and proposed mining in the district: "Evidence of what can go wrong ecologically is visible in nearby streams that today run red and sterile with acidic effluent from mining that ceased 40 years ago." Using the historic mines as examples, Satchell (1995, p. 36) wrote, regarding the proposed New World mine, " * * * by far the most feared long-term threat is acid drainage from abandoned mine tunnels and waste-rock tailings."

The compositions of mine-drainage waters collected from several skarn- and polymetallic-replacement-deposit mining districts in the Rocky Mountain region, including the New World district, were studied by Plumlee and others (1999). They noted the following: "Mine-waters draining the skarn deposits at New World are quite acidic and have relatively high levels of dissolved metals * * * We interpret this to reflect the lack of neutralizing reactions between the acid waters and the calc-silicate alteration minerals in the skarns, and the lack of reactions with any carbonate minerals that may remain in the original sedimentary host rocks." Plumlee and others (1999) considered these results to be "intriguing" because in a ranking of acid-drainage potential for seven types of common ore deposits, Kwong (1993) judged skarn deposits to have the least potential to produce acid drainage. Kwong (1993, p. 6) stated that acid drainage "* * * is not known to associate with skarn deposits." It should be noted here that the water samples used in the analyses of Plumlee and others (1999) were obtained from adits and dumps of the Glengarry mine and dumps of the McLaren mine. Those samples thus were waters in contact with the McLaren and Como deposits (fig. 2), and they do not necessarily reflect the chemistry

of waters interacting with the Homestake and Miller Creek deposits, the main target of the proposed New World mine.

Gurrieri (1998) conducted a reconnaissance study of benthic organisms, water quality, and sediments in the upper Stillwater River headwaters downstream from the McLaren mine. Due to natural oxidation of the pyritic materials left exposed in the McLaren open pit (fig. 5), metals and sulfuric acid are released into the waters draining from the mine site in tributaries of the Stillwater River. In this area, Gurrieri (1998, p. 98) found elevated levels of metals in the waters and in the streambed sediments. He stated, "* * * though chronic aquatic life water quality criteria were not exceeded at most main stem sites during the synoptic sampling event, the macroinvertebrate and periphyton communities were impaired." He also modeled the pre-mining sediment conditions and concluded "* * * the magnitude of pre-mining metal enrichment is shown to be small compared to the amplification from mining disturbances" (Gurrieri, 1998, p. 99). Critics of the New World mine argued that similar effects to Fisher Creek and Miller Creek (fig. 1) would result from the new mining operation proposed for adjacent Henderson Mountain.

Other studies in the northern New World district suggested that pre-mining metal concentrations in ground and surface waters might have been underestimated because natural acid drainage has occurred there for thousands of years. A study by Furniss and others (1999) of undisturbed ferricrete deposits at the headwaters area of Fisher Creek, and near Daisy Pass (fig. 1), showed that natural acid drainage carrying heavy metals from the mineral deposits of the northern New World district occurred long before mining began in the area. The ferricrete deposits record ancient acidic runoff in seeps and springs that date to at least 8,800 radiocarbon years before present (Furniss and others, 1999). Geochemical studies of peat bogs, overbank stream deposits, and tree rings in the district by Chamberlain (2000) revealed that (1) these streams have been naturally acidic, with high background levels of metals, for at least 8,000 radiocarbon years; (2) periods during which streams had high metal concentrations correlated with long-term climatic variations; and (3) tree rings show the effects of recent mining and also show that "* * * the streams have a natural buffering capacity that returns streams to background levels within a few 10s of years."

The host rocks and the ore bodies of the Homestake deposit contain large quantities of calcite, and thus they are expected to have an inherent capacity to neutralize acidic solutions produced by oxidation of the pyrite-rich mineral deposits. As noted previously, the Homestake ore minerals selectively replaced carbonate rocks. The calcium, magnesium, and carbon dioxide liberated from the carbonate rocks during replacement and ore deposition were reprecipitated in the mineral deposits and wallrocks as calcite, dolomite, and ankerite. The propylitic alteration that is ubiquitous in the Homestake stock also contains secondary calcite.

In a study of the waters draining from the historic Gold Dust adit (fig. 1), Miller and Gurrieri (1997) determined that "* * * sulfide oxidation is occurring * * * however, a near neutral pH (7.3) and moderate bicarbonate (112 mgL^{-1}) [mg/L], calcium (94 mgL^{-1}) and magnesium (27 mg/L) concentrations indicate that acidity is buffered by the deposit geology." Based on the qualities of the Gold Dust adit waters and the results of humidity cell tests, Miller and Gurrieri (1997) predicted that adit discharges during operation of the New World mine would have "***neutral pH, moderate bicarbonate (>120 mgL^{-1}), sulfate (circa 500 mgL^{-1}), and metal (10 to 100 mgL^{-1} total recoverable Al + Fe + Cu + Ag + Cr + Mn + Pb + Ni + Zn) concentrations."

Because the host-rock environment is so heterogeneous within the Homestake deposits, it is impossible to accurately calculate the gross acid-generating/acid-neutralizing capacity of these rocks. Thus, it would be difficult to estimate the qualities of waters that could emit from an adit that cuts across the Homestake breccia or from seeps that could form on the flanks of Henderson Mountain due to mining. However, processed mill tailings, in which the pyritic material has been concentrated by ore processing, would produce more acidic solutions when finely ground and exposed in oxidized conditions than would the raw, massive ore material.

Administration Policy

On August 25, 1995, President Clinton took a helicopter tour over the New World project. Later he told groups that he was concerned that the proposed mine could endanger the Yellowstone ecosystem, and he expressed his intent to invoke a moratorium on further mining claims on Federal lands in this area for 2 years (the *Federal Register,* Sept. 1, 1995). On August 28, 1995, Secretary of the Interior Bruce Babbitt approved a request to pursue withdrawal of approximately 19,000 acres in the Cooke City area from mineral location and entry for a 20-year period. The request and approval included implementation of a 2-year temporary withdrawal to allow studies to be completed, including preparation of an Environmental Impact Statement. The 2-year moratorium on new mining claims in the area, which did not include the active New World project claims, took effect on September 1, 1995, when it was announced in the *Federal Register.*

During 1996, President Clinton ordered senior Government officials, including Department of Agriculture Secretary Dan Glickman, to negotiate with officials of Crown Butte Resources and its parent company (Noranda Exploration) for a possible buyout or swap of the company's holdings in the New World district for Federal lands elsewhere (Wilkinson, 1996a; The Denver Post, 1996). President Clinton announced on August 12, 1996, at the foot of Baronnette Peak in the northeast part of Yellowstone National Park, that an arrangement had been negotiated with the mining companies during the preceding year (Wilkinson, 1996b). Initially, the plan included a swap of the New World claims for Federal lands worth $65 million.

1997 and 1998—Contract Settlement, Congressional Appropriation, and Mineral Withdrawal

In March of 1997, negotiators on behalf of the Executive Branch of the Federal Government, an attorney for the Sierra Club Legal Defense Fund, and representatives of the Greater Yellowstone Coalition offered a settlement agreement to Crown Butte Mines for the New World mine acquisition (Miniclier, 1997). In the settlement, the land and mineral rights of the New World project claims were to become the property of the U.S. Government; Crown Butte Mines would receive $65 million for their claims and mineral rights, $22.5 million of which would be set aside for reclamation and remediation of historic mine sites in the district. In addition, groups that had sued the company regarding water-quality standards on their properties would refrain from further legal actions (Miniclier, 1997). After a 30-day review of the proposal by Crown Butte Resources, Ltd., of Toronto and Crown Butte Mines, Inc., of Houston, the companies agreed to the deal. Margaret Reeb owned an estimated 65 percent of the mining claims in the project area (Miniclier, 1997) and had leased her claims to Crown Butte-Noranda. In September 1997, Ms. Reeb also agreed to the settlement, and the deal was complete (Billings, 1997). Margaret Reeb reportedly received an undisclosed sum of money from Crown Butte, and she was allowed to keep her claims as long as she agreed not to develop them. She understood that her claims could be mined in the future if allowed by the President and Congress (Billings, 1997).

Some members of Congress were opposed to the settlement plan. However, lawmakers in both parties stated that they wanted the company to leave the district. Also, the buyout concept and the means originally proposed to fund it, such as temporary borrowing from the Conservation Reserve Program, were issues of debate (The Washington Post, 1997). As late as July 1997, some key members of Congress, including House Interior Appropriations Subcommittee Chairman Ralph Regula (R-Ohio), were opposed to inclusion of land purchases in their version of the fiscal year 1998 Department of the Interior appropriations bill (Bettelheim, 1997). Later in 1997, an accord was reached on the terms of funding the settlement.

The New World mine acquisition was authorized by Congress as part of a complex rider attached to the fiscal year 1998 Department of the Interior appropriations bill (Public Lands News, 1998a). The rider included $65 million for acquisition of the New World properties and their mineral rights and $12 million for repairs to the Beartooth Scenic Highway. Crown Butte agreed to transfer $22.5 million to the U.S. Forest Service to remediate historic mine sites in the district.

The proposed contract settlement was filed in Federal court in Montana on June 25, 1998 (Public Lands News, 1998a). A Federal judge approved the contract, and on August 7, 1998, the properties of the New World mine project were formally transferred to the U.S. Forest Service (Public Lands News, 1998b), under the administration of Gallatin National Forest.

The Secretary of Interior earlier (August 1995) had proposed a 20-year withdrawal of Federal locatable minerals in an area of 19,100 acres surrounding Cooke City (basically the historic New World district and a buffer zone). In 1996, public meetings and preparation of an Environmental Impact Statement (EIS) were initiated for the proposed mineral withdrawal. A Draft EIS was released in March 1997. The New World mine issue was not to be considered a "connected action" to withdrawal of the surrounding Federal lands. However, upon completion of the "New World Mine acquisition" on August 7, 1997, the New World project claims, now under the supervision of Gallatin National Forest, were added to the "Cooke City Area Mineral Withdrawal." In August 1997, shortly after transfer of the New World Project claims, the Assistant Secretary of the Interior and the Under Secretary of Agriculture released a joint Record of Decision (MTM84500) that stated their decision to "* * * withdraw from mineral entry, subject to valid existing claims, 22,065 acres of Federal land near Cooke City, Montana." The Cooke City Area Mineral Withdrawal will remain in place for 20 years beginning in August 1997, unless Congressional action makes the withdrawal permanent.

So, after surviving two attempts to develop a mine, one in the 1920s and one in the 1990s, the Homestake gold-silver-copper deposits remain intact inside Henderson Mountain, under the protection of Gallatin National Forest. Geologic inferences suggest that similar deposits possibly are present around Eocene intrusions at Emigrant Peak, in the Independence district, in Sunlight Basin (Sunlight mining region), and potentially elsewhere in the region (Hammarstrom, Zientek, Elliott, and others, 1993).

As noted previously, the settlement agreement between the United States and Crown Butte Mining, Inc., provided $22.5 million for cleanup of specific historic mine sites in the New World district, including properties previously owned and leased by the mining company (such as the McLaren and Glengarry mine properties). Using this funding, the "New World District Response and Restoration Project" was established in 1999, with the U.S. Forest Service acting as the lead agency in charge of administering the project. The main goals of the project were "* * * to assure the achievement of the highest and best water quality practicably attainable" and "* * * to mitigate environmental impacts that are a result of historic mining" (quoted from the project's Web site: http://www.maximtechnologies.com/newworld/index.htm; accessed 3/10/04). The project was to "* * * initially focus on stabilizing the solid mine wastes to prevent or reduce erosion onto adjacent lands or into streams." The project Web site stated that other restoration actions may include temporary water-treatment systems, creating repository sites for waste materials, making capping systems on the waste dumps to minimize further oxidation and acid production, closing adits and shafts, revegetating mining-disturbed areas, and monitoring water quality. This effort (2001) involved several Federal Government agencies with specific responsibilities to the project, including the U.S. Forest Service, the Environmental Protection Agency, the U.S. Department of Agriculture Office of the General Council, and the U.S. Department of the Interior, all in cooperation with the State of Montana through the Montana Department of Environmental Quality.

Acknowledgments

This study was undertaken as a thesis project in partial fulfillment of a Master of Science Degree completed by the author at the Colorado School of Mines, Golden, Colo. (Van Gosen, 1994). The study was supported by the U.S. Geological Survey, Branch of Central Mineral Resources, Lakewood, Colo. The study contributed to a mineral resource assessment of the region (Hammarstrom, Zientek, and Elliott, 1993).

The study was possible because of the cooperation and generosity shown by Crown Butte Mines, Inc., and Noranda Exploration, Inc. These companies provided complete access to their drill core, data, and properties. Allan Kirk (formerly of Crown Butte Mines) and Todd Johnson of Noranda Exploration were especially helpful in sharing and debating their intimate knowledge of the study area.

References Cited

Bama, Lynne, 1996, Yellowstone—A park boss goes to bat for the land: High Country News, v. 28, no. 8, April 29, 1996, p. 1, 8, 9, 10.

Basler, A.L., 1965, Geology of the Emigrant Peak intrusive complex, Park County, Montana: Bozeman, Montana State University, M.S. thesis, 52 p.

Bettelheim, Adriel, 1997, Gold mine near Yellowstone loses luster amid bickering: The Denver Post, July 27, 1997, p. 8A.

Billings, E.P., 1997, Last landowner finally gives in to Crown Butte: Missoula, Mont., The Missoulian [Newspaper], September 26, 1997.

Brooks, L.H., 1921, Cooke City and the New World mining district: Mining and Scientific Press (May 14, 1921), v. 122, p. 682–684.

Chadwick, R.A., 1970, Belts of eruptive centers in the Absaroka-Gallatin volcanic province, Wyoming-Montana: Geological Society of America Bulletin, v. 81, no. 1, p. 267–273.

Chadwick, R.A., 1972a, Igneous activity south and west of the Crazy Mountains Basin, Montana, *in* Lynn, John, Balster, Cliff, and Warne, John, eds., Crazy Mountains Basin, Montana Geological Society, 21st Annual Geological Conference, September 22–24, 1972: Montana Geological Society, p. 141–148.

Chadwick, R.A., 1972b, Volcanism in Montana: Northwest Geology, v. 1, p. 1–20.

Chadwick, R.A., 1981, Chronology and structural setting of volcanism in southwestern and central Montana, *in* Tucker, T.E., ed., Montana Geological Society field conference and symposium guidebook to southwest Montana, 1981: Montana Geological Society, p. 301–310.

Chamberlain, C.P., 2000, Realistic remediation of the New World mining district, MT—Consideration of natural and anthropogenic concentration of metals [abs.]: Geological Society of America Abstracts with Programs, v. 32, no. 5, p. A-6.

Cope, E.L., 1984, Geology of the Alice E. breccia pipe and vicinity, New World mining district, Park County, Montana: Fort Collins, Colorado State University, M.S. thesis, 119 p.

Cox, D.P., 1986, Model 17, descriptive model of porphyry Cu, *in* Cox, D.P., and Singer, D.A., eds., Mineral deposit models: U.S. Geological Survey Bulletin 1693, p. 76–81.

Danielson, Vivian, 1991a, Active drill program at New World project: The Northern Miner, v. 78, no. 24, p. 1, 2, 5.

Danielson, Vivian, 1991b, Noranda increases reserves at New World gold project: The Northern Miner (February 18, 1991), p. 17.

Danielson, Vivian, 1991c, Steady success at New World: The Northern Miner, v. 77, no. 35, p. 1, 17.

Danielson, Vivian, 1992, Crown Butte cuts 247 ft of 0.31 oz at Montana project: The Northern Miner, v. 78, no. 16, p. 1–2.

The Denver Post, 1996, Clinton hopes to stop gold mine: The Denver Post, August 7, 1996, p. 1B, 4B.

Dreier, J.E., Jr., 1967, Economic geology of the Sunlight mineralized region, Park County, Wyoming: Laramie, Wyoming University, M.S. thesis, 81 p.

Einaudi, M.T., 1982, Description of skarns associated with porphyry copper plutons, southwestern North America, *in* Titley, S.R., ed., Advances in geology of the porphyry copper deposits of southwestern North America: Tucson, University of Arizona Press, p. 139–183.

Elliott, J.E., 1979, Geologic map of the southwest part of the Cooke City quadrangle, Montana and Wyoming: U.S. Geological Survey Miscellaneous Investigations Series Map I-1084, scale 1:24,000.

Elliott, J.E., Kirk, A.R., and Johnson, T.W., 1992, Field guide—Gold-copper-silver deposits of the New World district, *in* Elliott, J.E., ed., Guidebook for the Red Lodge-Beartooth Mountains-Stillwater area, Tobacco Root Geological Society, 17th Annual Field Conference, Red Lodge, Mont., August 20–22, 1992: Northwest Geology, v. 20/21, p. 1–19.

Elliott, J.E., Van Gosen, B.S., du Bray, E.A., LaRock, E.J., and Zientek, M.L., 1993, Geology of the Absaroka-Beartooth study area, *in* Hammarstrom, J.M., Zientek, M.L., and Elliott, J.E., eds., Mineral resource assessment of the Absaroka-Beartooth study area, Custer and Gallatin National Forests, Montana: U.S. Geological Survey Open-File Report 93-207, Chapter B, p. B1–B23.

Engineering and Mining Journal, 1980, US—Ranchers Exploration and Development Corp.: Engineering and Mining Journal, November 1980, p. 264.

Eyrich, H.T., 1969, Economic geology of part of the New World mining district, Park County, Montana: Pullman, Washington State University, Ph.D. dissertation, 130 p.

Foose, R.M., Wise, D.U., and Garbarini, G.S., 1961, Structural geology of the Beartooth Mountains, Montana and Wyoming: Geological Society of America Bulletin, v. 72, no. 8, p. 1,143–1,172.

Furniss, G., Hinman, N.W., Doyle, G.A., and Runnells, D.D., 1999, Radiocarbon-dated ferricrete provides a record of natural acid rock drainage and paleoclimatic changes: Environmental Geology, v. 37, nos. 1–2, p. 102–106.

Gardner, E.D., 1914, New World mining district: Mining and Scientific Press, v. 108, no. 21, p. 880–884.

Gurrieri, J.T., 1998, Distribution of metals in water and sediment and effects on aquatic biota in the upper Stillwater River basin, Montana, *in* Gough, L.P., and Marsh, S.P., eds., Fourth International Symposium on Environmental Geochemistry (4th ISEG)—Part I [special issue]: Journal of Geochemical Exploration, v. 64, nos. 1–3, p. 83–100.

Hammarstrom, J.M., Zientek, M.L., and Elliott, J.E., eds., 1993, Mineral resource assessment of the Absaroka-Beartooth study area, Custer and Gallatin National Forests, Montana: U.S. Geological Survey Open-File Report 93-207, 296 p., 19 pls.

Hammarstrom, J.M., Zientek, M.L., Elliott, J.E., Van Gosen, B.S., Carlson, R.R., Lee, G.K., and Kulik, D.M., 1993, Mineral resource assessment for locatable minerals (exclusive of the Stillwater Complex), *in* Hammarstrom, J.M., Zientek, M.L., and Elliott, J.E., eds., Mineral resource assessment of the Absaroka-Beartooth study area, Custer and Gallatin National Forests, Montana: U.S. Geological Survey Open-File Report 93-207, Chapter G, p. G1–G78.

Harlan, S.S., Mehnert, H.H., Snee, L.W., and Meen, J.K., 1991, Preliminary isotopic (K-Ar and $^{40}Ar/^{39}Ar$) age determinations from selected Late Cretaceous and Tertiary igneous rocks in Montana, *in* Baker, D.W., and Berg, R.B., eds., Guidebook of the central Montana alkalic province—Geology, ore deposits and origin: Montana Bureau of Mines and Geology Special Publication 100, p. 136–137.

Hausel, W.D., 1982, General geologic setting and mineralization of the porphyry copper deposits, Absaroka Volcanic Plateau, Wyoming, *in* Reid, S.G., and Foote, D.J., eds., Geology of Yellowstone Park area, Wyoming Geological Association, 33rd annual field conference guidebook, Mammoth Hot Springs, Wyo., September 15–18, 1982: Wyoming Geological Association, p. 297–313.

Heidrick, T.L., and Titley, S.R., 1982, Fracture and dike patterns in Laramide plutons and their structural and tectonic implications—American Southwest, *in* Titley, S.R., ed., Advances in geology of the porphyry copper deposits: Tucson, University of Arizona Press, p. 73–91.

Hickey, L.J., 1980, Paleocene stratigraphy and flora of the Clarks Fork Basin, *in* Gingerich, P.D., ed., Early Cenozoic paleontology and stratigraphy of the Bighorn Basin, Wyoming: Ann Arbor, University of Michigan Papers on Paleontology No. 24, p. 33–49.

Hiza, M.M., 1998, The geologic history of the Absaroka Volcanic Province: Yellowstone Science, v. 6, no. 2, p. 2–7.

Hiza, M.M., 1999, The geochemistry and geochronology of the Eocene Absaroka Volcanic Province, northern Wyoming and southwest Montana, USA: Corvallis, Oregon State University, Ph.D. dissertation, 243 p.

Horral, K.B., 1966, The petrology of the Henderson Mountain laccolith, Park County, Montana: De Kalb, Northern Illinois University, M.S. thesis, 85 p.

Hughes, R.V., 1933, Peneplanation of Beartooth Mountains: Pan-American Geology, v. 59, p. 321–327.

Johnson, T.W., 1991, Geology, hydrothermal alteration, and Cu-Ag-Au skarn and replacement mineralization in the northern part of the New World district, Park County, Montana: Pullman, Washington State University, M.S. thesis, 326 p.

Johnson, T.W., 1992, Geology and paragenesis of the McLaren copper-silver-gold skarn and replacement deposit, New World district, Park County, Montana [abs.], *in* Elliott, J.E., ed., Guidebook for the Red Lodge-Beartooth Mountains-Stillwater area, Tobacco Root Geological Society, 17th annual field conference, Red Lodge, Mont., August 20–22, 1992: Northwest Geology, v. 20/21, p. 61–62.

Johnson, T.W., 1994, Au-Cu-Ag skarn and replacement mineralization in the McLaren deposit, New World district, Park County, Montana: Economic Geology, v. 89, no. 5, p. 969–993.

King, T.V.V., ed., 1995, Environmental considerations of active and abandoned mine lands—Lessons from Summitville, Colorado: U.S. Geological Survey Bulletin 2220, 38 p.

Kirk, A.R., and Johnson, T.W., 1993, Geology and mineral deposits of the New World district, Park County, Montana, *in* Hunter, L.D.V., ed., Energy and mineral resources of central Montana, Montana Geological Society 1993 field conference guidebook, Old Timers' Rendezvous Edition: Montana Geological Society, p. 227–235.

Kirk, A.R., Johnson, T.W., and Elliott, J.E., 1993, Geology and mineral deposits of the New World district, Park County, Montana, *in* SEG Newsletter, January 1993, no. 12: Littleton, Colo., Society of Economic Geologists, p. 1, 12–16.

Knapp, R.B., and Norton, D.L., 1981, Preliminary numerical analysis of processes related to magma crystallization and stress evaluation in cooling pluton environments: American Journal of Science, v. 281, p. 35–68.

Krohn, D.H., and Weist, M.M., 1977, Principal information on Montana mines: Montana Bureau of Mines and Geology Special Publication 75, p. 113–115.

Kulik, D.M., 1992, Gravity and magnetic features in the Beartooth uplift, southwestern Montana and northwestern Wyoming [abs.], *in* Elliott, J.E., ed., Guidebook for the Red Lodge-Beartooth Mountains-Stillwater area, Tobacco Root Geological Society, 17th annual field conference, Red Lodge, Mont., August 20–22, 1992: Northwest Geology, v. 20/21, p. 67–68.

Kwong, Y.T.J., 1993, Prediction and prevention of acid rock drainage from a geological and mineralogical perspective: Saskatoon, Saskatchewan, Canada, National Hydrology Research Institute [NHRI] Contribution CS-92054 [MEND Project 1.32.1], p. 4–6.

Lawson, D.C., 1981, Directory of Montana mining enterprises for 1980: Montana Bureau of Mines and Geology Bulletin 115, 53 p., 1 pl.

Lawson, D.C., 1982, Directory of Montana mining enterprises for 1981, *with a section on* The Stillwater Complex by H.G. McClernan: Montana Bureau of Mines and Geology Bulletin 117, 59 p., 1 pl.

Lobanoff-Rostovsky, Nikita, 1960, Geology of the Independence mining district, Park and Sweet Grass Counties, Montana: New York, Columbia University, M.A. thesis, 67 p.

Lovering, T.S., 1924, A report on the New World mining district, Park County, Montana: Minneapolis, University of Minnesota, Ph.D. dissertation, 102 p.

Lovering, T.S., 1929, The New World or Cooke City mining district, Park County, Montana, *in* Contributions to economic geology (short papers and preliminary reports), 1929, part I—Metals and nonmetals except fuels: U.S. Geological Survey Bulletin 811-A, p. 1–88.

McCulloch, Robin, 1989, Mining and mineral developments in Montana—1989: Montana Bureau of Mines and Geology Open-File Report MBMG 223, 41 p.

McCulloch, Robin, Berg, R.B., and Sholes, M.A., 1988, Mining and mineral developments in Montana—1988: Montana Bureau of Mines and Geology Open-File Report MBMG 206, 20 p.

Meen, J.K., 1985, The origin and evolution of a continental volcano—Independence, Montana: University Park, Pennsylvania State University, Ph.D. dissertation, 917 p.

Meen, J.K., 1988, Petrological and chemical variations in the Independence volcanic complex, Absaroka Mountains, Montana: Northwest Geology, v. 17, p. 21–41.

Meen, J.K., and Eggler, D.H., 1987, Petrology and geochemistry of the Cretaceous Independence volcanic suite, Absaroka Mountains, Montana—Clues to the composition of the Archean sub-Montanan mantle: Geological Society of America Bulletin, v. 98, no. 2, p. 238–247.

Meinert, L.D., 1989, Gold skarn deposits—Geology and exploration criteria, *in* Keays, R.R., Ramsay, W.R.H., and Groves, D.I., eds., The geology of gold deposits—The perspective in 1988: Economic Geology Monograph 6, p. 537–552.

Miller, R.A., and Gurrieri, J.T., 1997, Geochemistry and water quality prediction for skarn deposits in the New World mining district [abs.], *in* Wanty, R.B., Marsh, S.P., and Gough, L.P., eds., 4th International Symposium on Environmental Geochemistry—Program with abstracts: U.S. Geological Survey Open-File Report 97-496, p. 65.

Miniclier, Kit, 1997, Cash offered to block Yellowstone gold mine: The Denver Post, March 13, 1997, p. 1A, 16A.

The Mining Record, 1980, Ranchers Exploration reports plan for open-pit gold mine: Denver, Colo., The Mining Record, October 22, 1980, p. 1.

Moyle, P.R., and Buehler, A.R., 1989, A study of the central part of the Independence mining district, Park and Sweet Grass Counties, Montana, *in* French, D.E., and Grabb, R.F., Geologic resources of Montana, volume I, Montana Geological Society, 1989 field conference guidebook, Montana Centennial edition: Montana Geological Society, p. 383–392.

Nelson, W.H., Prostka, H.J., and Williams, F.E., 1980, Geology and mineral resources of the North Absaroka Wilderness and vicinity, Park County, Wyoming: U.S. Geological Survey Bulletin 1447, 101 p., 2 pls.

The Northern Miner, 1990a, New World reserve estimate increased: The Northern Miner, December 10, 1990, v. 76, no. 40, p. 17.

The Northern Miner, 1990b, New World reserves could rise on basis of 1990 drill program: The Northern Miner, November 12, 1990, v. 76, no. 36, p. 3.

The Northern Miner, 1991a, Crown Butte ups gold content at 100% owned New World: The Northern Miner, December 30, 1991, v. 77, no. 43, p. 2.

The Northern Miner, 1991b, Drilling boosts New World project—Deposit cut off on northwest side only: The Northern Miner, October 7, 1991, p. 17.

The Northern Miner, 1991c, New World preliminary reserves: The Northern Miner, March 4, 1991, v. 77, no. 52.

The Northern Miner, 1991d, Noranda extends zone at New World: The Northern Miner, June 10, 1991, v. 77, no. 14.

The Northern Miner, 1991e, Work has steadily increased Crown Butte's gold reserves: The Northern Miner, November 4, 1991, v. 77, no. 35, p. 17.

The Northern Miner, 1992a, Crown Butte rules out cyanide from New World gold mine plan: The Northern Miner, v. 78, no. 17, p. 11.

The Northern Miner, 1992b, New World reserve estimate boosts contained gold by 69%: The Northern Miner, March 20, 1992, v. 78, no. 4, p. A6.

The Northern Miner, 1992c, U.S. projects closer to production: The Northern Miner, January 6, 1992, v. 77, no. 44, p. 13.

Osterwald, F.W., Osterwald, D.B., Long, J.S., Jr., and Wilson, W.H., 1966, Mineral resources of Wyoming: Geological Survey of Wyoming Bulletin 50, 287 p.

Parks, Richard, 1994, Mining the Clark's Fork drainage: Fly Fisherman, v. 25, no. 6, September 1994, p. 26–30.

Parsons, W.H., 1937, The ore deposits of the Sunlight mining region, Park County, Wyoming: Economic Geology, v. 32, no. 6, p. 832–854.

Parsons, W.H., 1939, Volcanic centers in the Sunlight area, Park County, Wyoming: Journal of Geology, v. 47, p. 1–26.

Parsons, W.H., 1958, Origin, age, and tectonic relationships of the volcanic rocks in the Absaroka-Yellowstone-Beartooth region, Wyoming-Montana, *in* Zieglar, D.L., ed., Beartooth uplift and Sunlight Basin, Billings Geological Society in conjunction with Yellowstone-Bighorn Research Association, 9th annual field conference guidebook, August 14–16, 1958: Billings Geological Society, p. 36–43.

Pederson, Kenneth, 1968, Sulfide mineralization of the northwestern part—Sunlight mining region, Park County, Wyoming: Laramie, University of Wyoming, M.S. thesis, 50 p.

Pfau, Mark, 1981, Geology of the Emigrant Gulch porphyry copper-molybdenum complex, Park County, Montana: Moscow, University of Idaho, M.S. thesis, 89 p.

Pierce, W.G., 1965, Geologic map of the Deep Lake quadrangle, Park County, Wyoming: U.S. Geological Survey Geologic Quadrangle Map GQ-478, scale 1:62,500.

Plumlee, G.S., Smith, K.S., Montour, M.R., Ficklin, W.H., and Mosier, E.L., 1999, Geologic controls on the composition of natural waters and mine waters draining diverse mineral-deposit types, *in* Filipek, L.H., and Plumlee, G.S., eds., The environmental geochemistry of mineral deposits, Part B—Case studies and research topics: Society of Economic Geologists, Reviews in Economic Geology, v. 6B, p. 373–432.

Public Lands News, 1998a, Headwaters, New World acquisitions each move forward a step: Public Lands News, v. 23, no. 15, July 17, 1998.

Public Lands News, 1998b, Baca Ranch one of three big land acquisitions on the move: Public Lands News, v. 23, no. 18, September 11, 1998.

Reed, G.C., 1950, Mines and mineral deposits (except fuels), Park County, Montana: U.S. Bureau of Mines Information Circular 7546, 68 p.

Rich, D.H., 1974, Economic geology of Silvertip Basin, Sunlight mining region, Park County, Wyoming: Oxford, Ohio, Miami University, M.S. thesis, 73 p.

Richards, P.W., 1957, Geology of the area east and southeast of Livingston, Park County, Montana: U.S. Geological Survey Bulletin 1021-L, p. 385–438, pls. 34–36.

Roberts, A.E., 1972, Cretaceous and early Tertiary depositional and tectonic history of the Livingston area, southwestern Montana: U.S. Geological Survey Professional Paper 526-C, 120 p.

Rocky Mountain Pay Dirt, 1990, Crown Butte's New World gold prospect is looking good: Rocky Mountain Pay Dirt, February, 1990, p. 11A.

Rubel, D.N., 1964, Geology of the Independence area, Sweet Grass and Park Counties, Montana: Ann Arbor, University of Michigan, Ph.D. dissertation, 192 p.

Rubel, D.N., 1971, Independence volcano—A major Eocene eruptive center, northern Absaroka Volcanic Province: Geological Society of America Bulletin, v. 82, no. 9, p. 2,473–2,494.

Ruppel, E.T., 1972, Geology of pre-Tertiary rocks in the northern part of Yellowstone National Park, Wyoming: U.S. Geological Survey Professional Paper 729-A, 66 p.

Satchell, Michael, 1995, A new battle over Yellowstone Park: U.S. News & World Report, March 13, 1995, p. 34, 36, 41, 42.

Shaver, Dave, 1996, New World mine—The interface of science and policy outside Yellowstone National Park [abs.]: Geological Society of America Abstracts with Programs, v. 28, no. 7, p. A-20.

Sillitoe, R.H., 1973, The tops and bottoms of porphyry copper deposits: Economic Geology, v. 68, p. 799–815.

Sillitoe, R.H., 1976, A reconnaissance of the Mexican porphyry copper belt: American Institute of Mining and Metallurgical Engineers Transactions, Section B, Applied Earth Science, v. 85, p. B170–B189.

Sillitoe, R.H., 1985, Ore-related breccias in volcanoplutonic arcs: Economic Geology, v. 80, p. 1,467–1,514.

Sillitoe, R.H., 1988, Gold and silver deposits in porphyry systems, *in* Schafer, R.W., Cooper, J.J., and Vikre, P.G., eds., Bulk mineable precious metal deposits of the Western United States: Reno, Geological Society of Nevada, p. 233–257.

Sillitoe, R.H., 1991, Intrusion-related gold deposits, *in* Foster, R.P., ed., Gold metallogeny and exploration: Glasgow, Blackie and Son Ltd., p. 165–209.

Simons, F.S., and Armbrustmacher, T.J., 1976, High-level plateaus of the southeastern Beartooth Mountains, Montana and Wyoming—Remnants of an exhumed sub-Cambrian marine plain: U.S. Geological Survey Journal of Research, v. 4, no. 4, p. 387–396.

Simons, F.S., Armbrustmacher, T.J., Van Roy, R.M., Zilka, N.T., Federspiel, F.E., and Ridenour, James, 1979, Mineral resources of the Beartooth Primitive Area and vicinity, Carbon, Park, Stillwater, and Sweet Grass Counties, Montana, and Park County, Wyoming, *with a section on* Interpretation of aeromagnetic data, by L.A. Anderson: U.S. Geological Survey Bulletin 1391-F, 125 p., 2 pls.

Smedes, H.W., and Prostka, H.J., 1972, Stratigraphic framework of the Absaroka Volcanic Supergroup in the Yellowstone National Park region: U.S. Geological Survey Professional Paper 729-C, 33 p.

Theodore, T.G., Orris, G.J., Hammarstrom, J.M., and Bliss, J.D., 1991, Gold-bearing skarns: U.S. Geological Survey Bulletin 1930, 61 p.

Thom, W.T., Jr., Jones, O.T., and Chamberlin, R.T., 1935, Morphology of the Beartooth Mountain uplift [abs.]: Geological Society of America Proceedings, 1934, p. 117.

Titley, S.R., 1982, The style and progress of mineralization and alteration in porphyry copper systems, *in* Titley, S.R., ed., Advances in geology of the porphyry copper deposits, southwestern North America: Tucson, University of Arizona Press, p. 93–116.

U.S. Geological Survey and U.S. Bureau of Mines, 1983, Mineral resources of the North Absaroka Wilderness Study Area, Park and Sweet Grass Counties, Montana: U.S. Geological Survey Bulletin 1505, 251 p., 5 pls.

Van Gosen, B.S., 1994, Genesis of the Homestake breccia gold-silver-copper deposit near Cooke City, Park County, Montana: Golden, Colorado School of Mines, M.S. thesis, 210 p., 2 pls.

Van Voast, W.A., 1964, General geology and geomorphology of the Emigrant Gulch-Mill Creek area, Park County, Montana: Bozeman, Montana State University, M.S. thesis, 65 p.

The Washington Post, 1997, Proposal to buy out mine near Yellowstone is questioned: The Washington Post, April 7, 1997.

Wedow, Helmuth, Jr., Gaskill, D.L., Banister, D'A.P., and Pattee, E.C., 1975, Mineral resources of the Absaroka Primitive Area and vicinity, Park and Sweet Grass Counties, Montana, *with a section on* Interpretation of geophysical data, by D.L. Peterson: U.S. Geological Survey Bulletin 1391-B, 115 p., 2 pls.

Wilkinson, Todd, 1994, Fool's gold: National Parks, v. 68, nos. 7–8, p. 31–35.

Wilkinson, Todd, 1996a, Talks may halt mine near Yellowstone: The Denver Post, August 1, 1996, p. 4B.

Wilkinson, Todd, 1996b, Clinton hails end to site for mine: The Denver Post, August 13, 1996, p. 4B.

Spectral Analysis of Absorption Features for Mapping Vegetation Cover and Microbial Communities in Yellowstone National Park Using AVIRIS Data

N

By Raymond F. Kokaly, Don G. Despain, Roger N. Clark, and K. Eric Livo

Chapter N *of*
Integrated Geoscience Studies in the Greater Yellowstone Area—Volcanic, Tectonic, and Hydrothermal Processes in the Yellowstone Geoecosystem

Edited by Lisa A. Morgan

Professional Paper 1717

U.S. Department of the Interior
U.S. Geological Survey

Contents

Abstract 463
Introduction 463
Background 464
    Yellowstone Vegetation 464
    Reflectance Spectra of Plants 465
    Remote Sensing of Vegetation in Yellowstone National Park 465
Methods 465
    AVIRIS Data Collection for Yellowstone National Park 465
    AVIRIS Data Calibration 466
    Spectral-Feature Analysis and Mapping Methods 467
        Spectral-Feature Analysis 467
        Spectral Library for Yellowstone Vegetation 467
        The USGS Tetracorder System 468
Results and Discussion 471
    Comparison of Spectra for Vegetation Cover Types 471
        Reflectance Spectra 471
        Continuum-Removed Vegetation-Spectral Features 472
Maps of Vegetation and Microorganisms in Yellowstone National Park Derived from AVIRIS Data 474
    Forest Cover 474
    Nonforest Cover 481
    Hot-Spring Microorganisms 484
Conclusions 486
Acknowledgments 487
References Cited 487

Figures

1. Laboratory reflectance spectra of an oak leaf 465
2. Coverage of AVIRIS data collected on August 7, 1996 466
3. AVIRIS spectra of Doulas fir and lodgepole pine 468
4. Field-reflectance spectrum of a hot-spring bacterial mat 470
5. Representative reflectance spectra for Yellowstone vegetation 472
6. Continuum-removed 0.68-µm chlorophyll-absorption spectra 475
7. Continuum-removed 0.98-µm leaf-water-absorption spectra 479
8–10. Maps of the Mammoth Hot Springs area showing:
    8. Forest cover types 483
    9. Lodgepole pine cover 484
    10. Selected nonforest cover types 485
11. Map showing microbial mats in the Upper and Lower Geyser Basins 486

Tables

1–2. Spectral-library entries for:
   1. Forest cover types 469
   2. Nonforest cover types 470
3. Channels of 1996 AVIRIS data not used in spectral analysis 471
4. Continuum end points used for vegetation-absorption features 477
5–6. Characteristics of:
   5. 0.68-µm chlorophyll-absorption features for vegetation cover types 478
   6. 0.98-µm leaf-water-absorption features for vegetation cover types 482

Spectral Analysis of Absorption Features for Mapping Vegetation Cover and Microbial Communities in Yellowstone National Park Using AVIRIS Data

By Raymond F. Kokaly,[1] Don G. Despain,[2] Roger N. Clark,[1] and K. Eric Livo[1]

Abstract

This report summarizes the application of imaging spectroscopy to the study of biotic components of Yellowstone National Park ecosystems. Maps of vegetation cover and hot-spring microorganisms were generated using spectral-feature analysis of data from the airborne visible and infrared imaging spectrometer (AVIRIS). AVIRIS data were calibrated to surface reflectance using a radiative-transfer model and a ground-calibration target. A spectral library of canopy-reflectance signatures was created by averaging pixels of reflectance data over known occurrences of 27 vegetation cover types in Yellowstone. Distributions of these vegetation types were determined by comparing absorption features of the vegetation in the spectral library with every pixel of the AVIRIS data using continuum removal and spectral analysis in the U.S. Geological Survey's Tetracorder expert system. Analysis of the chlorophyll- and leaf-water-absorption features (centered near 0.68, 0.98, and 1.20 μm, respectively) allowed accurate identification of vegetation cover types. Conifer cover types of lodgepole pine, whitebark pine, Douglas fir, and a mixed Engelmann spruce/subalpine fir class were spectrally identified and their distributions were mapped in AVIRIS images. Field-reflectance measurements revealed a distinct spectral signature of hot-spring microorganisms. These field measurements were added to the vegetation spectral library, and maps showing the distributions of microbial mats in the geyser basins of Yellowstone were produced.

Introduction

Yellowstone National Park (the Park) preserves and protects unique geologic features and biologic systems. This paper reports on efforts of the U.S. Geological Survey (USGS), in cooperation with the National Park Service, to apply imaging spectroscopy to map the distributions of vegetation species and microorganisms in Yellowstone ecosystems. The Park's ecosystems support many large mammals, whose populations and movements are directly and indirectly influenced by vegetation. In Yellowstone, the distributions of forest stands of whitebark pine affect the movements of grizzly bears (*Ursus arctos horribilis*) (Mattson and others, 1992). The large wildfires in 1988 increased interest in fire ecology and demonstrated how dramatically and rapidly the forests and the state of the ecosystem could change. Smaller organisms, the thermophilic bacteria of the hot springs, have received increasing scientific attention. Microorganisms in the unique hydrothermal environments of Yellowstone have been studied by biotechnology researchers because of their potential benefits for human health and their use in environmental remediation (Brock, 1994).

In comparison to multispectral broadband remote sensing, which only uses a few channels, imaging spectrometers measure the radiation upwelling from a surface in hundreds of contiguous, narrow bandwidth channels (Green and others, 1998). *Imaging spectroscopy* refers to analysis techniques that combine the spatial capability of an imaging system and the spectrometer's ability to resolve absorption features caused by the chemical bonds and affected by the physical structure of surface materials (Vane and others, 1993). In addition to imaging spectroscopy, other terms such as imaging spectrometry and hyperspectral, ultraspectral, and superspectral remote sensing have been applied to this type of remote sensing, to contrast it with traditional "multispectral" remote sensing (Clark, 1999). The advantage of spectroscopic over multispectral measurements is the ability to resolve absorption features and determine their specific wavelength positions and characteristic shapes. These absorption features are related to the material or materials causing them; thus, the materials present in a pixel of imaging-spectroscopy data can be identified (Mustard and Sunshine, 1999).

Approaches to mapping the distributions of materials in images have included the use of a reference set of spectra of known materials and "matching" algorithms (Clark and others, 2003; Van der Meer and Bakker, 1997; Adams and others, 1993; Boardman and Goetz, 1991; Clark and others,

[1]U.S. Geological Survey, Box 25046, MS 973, Denver Federal Center, Denver, CO 80225.

[2]U.S. Geological Survey, Biologic Resources Division, Box 173492, Montana State University, Bozeman, MT 59717.

1990; Mustard and Pieters, 1987). Those algorithms exploit the greater number of channels available and also directly take advantage of the spectrometer's power to resolve absorption features. Successful remote-sensing applications of spectral matching to identify Earth-surface materials have been advanced in the geological sciences, particularly with respect to mineral mapping (Swayze and others, 2000; King and others, 2000). These applications were highly successful in part because minerals have specific chemical compositions; thus, reflectance spectra of samples measured in the laboratory and spectra of outcrops on the landscape are comparable.

Vegetation cover has been mapped with imaging-spectroscopy data. In grasslands, the vegetation type and relative amounts of green and dry vegetation have been estimated with respect to soil background (Gamon and others, 1993). Roberts and others (1998) used airborne-spectrometer data, combined with spectral-mixture modeling, to map the distribution of different chaparral vegetation types in the Santa Monica Mountains of California. Airborne-imaging spectroscopy has been applied to forests of the Eastern United States in order to discriminate different forest types in an area of deciduous, mixed deciduous/conifer, and conifer cover (Martin and others, 1998). In those studies and spectral-mixture-analysis studies, a set of end-member spectra representing the vegetation cover, soils, and other surface materials of the area was matched with remotely sensed spectra. In those analyses, the full spectrum (all channels of the instrument) was used in the calculations. Other studies in vegetation analysis with spectroscopy suggested that only channels that correspond to the principal absorption features of vegetation (Kokaly, 2001; King and others, 2000; Kokaly and Clark, 1999; Kokaly and others, 1998) or that seem to offer the greatest separability between materials (Asner and Lobell, 2000) should be used.

In this paper, we report the use of imaging spectroscopy to map biologic materials in Yellowstone National Park using an analysis of spectral features. Vegetation spectra extracted from the AVIRIS data were assembled into a spectral-library database for Yellowstone vegetation. The USGS Tetracorder system (Clark and others, 2003; Clark and Swayze, 1995) was used to compare the spectral features of the AVIRIS pixels to the entries of the spectral library, using the chlorophyll- and leaf-water-absorption features. This approach to mapping vegetation utilized the absorption features caused by the biochemical composition of plants and affected by the architecture of vegetation canopies. This report first presents background information on the vegetation of Yellowstone and on past applications of remote sensing to the mapping of forest cover. Then, spectral-analysis techniques used to detect and map vegetation cover and hot-spring microorganisms are described. The spectral differences between vegetation cover types in Yellowstone National Park are presented and discussed. Finally, the resulting maps of vegetation cover and hot-spring microorganisms are presented, and their contributions to understanding hydrothermal systems and to examining the links between the distributions of plant species and large mammal populations are discussed.

Background

Yellowstone Vegetation

Most of the forests of Yellowstone National Park consist of five conifer species (Despain, 1990): lodgepole pine (*Pinus contorta*), whitebark pine (*Pinus albicaulis*), Douglas fir *(Pseudotsuga menziesii*), Engelmann spruce (*Picea engelmannii*), and subalpine fir (*Abies lasiocarpa*). The temperate forests at high altitudes in the Park receive large amounts of precipitation during the long, cold winter. According to Despain (1990), the mean duration of snow cover at 2,740-m altitude is about 271 days. At lower altitudes, in relatively drier valleys, grasslands and sagebrush steppe communities predominate.

The geology underlying the vegetation in Yellowstone influences the distribution of plants within the Park (Despain, 1990). In areas underlain by andesitic rocks, a higher nutrient content supports climax forests of mixed Engelmann spruce/subalpine fir. Douglas fir is present in moist areas, such as on north-facing slopes. Soils derived from rhyolite volcanic flows have relatively low nutrient content; in these areas, the dominant forest type is lodgepole pine. Thus, a strong geobotanical link is demonstrated between the species composition of conifer-forest stands and the availability of nutrients in soils derived from volcanic rocks.

As a result of fire history and soil conditions, the current dominant forest cover in Yellowstone is lodgepole pine. Despain (1990) delineated five cover-type categories for lodgepole pine based on forest structure and composition, fire characteristics, and age of the stand (LP0, LP1, LP2, LP3, and LP). The youngest age class, LP0, is young forest growth, commonly post-fire regrowth, with an age of 0 to 45 years. Since the large fires in 1988, LP0 has been a major cover type in the Park. LP1 forest stands range in age from approximately 45 to 150 years. These stands are small-diameter lodgepole with very sparse forest-floor vegetation. LP2 cover-type stands are closed canopy stands that still are dominated by lodgepole pine and range in age from 150 to 300 years. The understory is Engelmann spruce and subalpine fir seedlings and saplings. Depending on soil conditions, the final seral stage (older than 300 years) of lodgepole pine is either LP or LP3. Forest stands on rhyolite-derived or other dry soils are dominated by lodgepole pine, with some whitebark pine possibly growing in the overstory and understory (this cover type is designated LP). The LP3 cover type has an uneven canopy composed of a mixture of lodgepole pine, Engelmann spruce, subalpine fir, and whitebark pine. The LP3 understory consists of small and large spruce and fir seedlings and saplings.

Nonforest vegetation in Yellowstone National Park is divided into four major groups: grassland, sagebrush steppe, wet sedge and willow meadow, and alpine meadow. The distributions of these vegetation types are influenced by precipitation and soil characteristics, and, consequently, they

are strongly related to altitude. Big sagebrush grows in dry to moderately moist areas at middle and lower altitudes, such as in the Lamar River valley. Silver sage grows in wetter areas higher than 2,130 m, for example, in the Hayden and Pelican Valleys. Alpine meadows are present at altitudes higher than 3,050 m. Sedge marshes and other wetland vegetation thrive in areas of year-long standing water at various altitudes throughout the Park. Willows and sedges grow along streams and near seeps.

Reflectance Spectra of Plants

Spectroscopy can provide information about a substance by relating the interaction of electromagnetic radiation as a function of wavelength to its chemical composition and physical properties. All vegetation contains the same basic constituents: chlorophyll and other light-absorbing pigments, water, proteins, starches, waxes, and structural biochemical molecules such as lignin and cellulose (Elvidge, 1990). All of these components contribute to the reflectance spectra of vegetation. Figure 1 shows laboratory reflectance spectra of vegetation foliage in both the fresh state and after being dried in an oven for 24 hours. The wavelength regions in which the basic plant components have strong absorption features are indicated on this plot. Because of pigment absorptions, the visible region of green plants shows a maximum reflectance at approximately 0.55 μm and lower reflectance in the blue (0.45 μm) and red (0.68 μm).

Beyond visible wavelengths (longer than 0.70 μm), the spectra of fresh plants show a strong rise in reflectance. The region of high plant reflectance at the short-wavelength end of the near-infrared (0.75–1.30 μm) is called the near-infrared plateau (NIR-plateau). The high reflectance results from an increased amount of light scattering at cell-wall interfaces because of a change in the index of refraction,

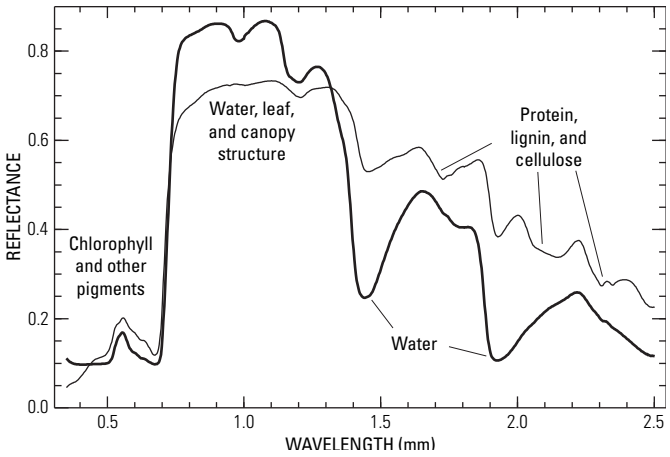

Figure 1. Laboratory reflectance spectra of an oak leaf in fresh (thick line) and dry (thin line) states. The causes of major plant absorption features are indicated. Reflectance is unitless.

the absence of pigment absorptions, and the weakening of overtone absorption of water in leaves at those wavelengths. Two absorption features centered near 0.98 and 1.20 μm are evident on the NIR-plateau. At 1.40 μm, a strong water-absorption feature reduces the reflectance. For fresh leaves, another, even stronger, water absorption is present at 1.90 μm. In dried vegetation, the water absorptions no longer conceal the absorption features at 1.73 μm, 2.10 μm, and 2.30 μm that are caused by organic bonds in plant biochemicals. Proteins, lignin, and cellulose all contribute to these features. C-H, N-H, and C-O bonds in the organic molecules have overtones and combinations that absorb in the near-infrared region of the spectrum (Peterson and Hubbard, 1992; Kokaly, 2001).

Remote Sensing of Vegetation in Yellowstone National Park

Remote sensing of vegetation is rooted in the interpretation of aerial photography. Photographs taken with airborne cameras have very high spatial resolution. By comparison of "textures," which includes the crown shape, density, and color of vegetation, different vegetation species are identified (Howard, 1991). Despain (1990) used aerial photography of Yellowstone National Park to construct a vegetation map. His map showed the distributions of the five major conifer species, the various age classes of lodgepole pine, and nonforest vegetation.

The development of digital sensors flown on satellites allowed vegetation mapping to be conducted on regional scales. These systems now are used routinely to map the distribution and quality of vegetation (Teillet and others, 1997; Huete and others, 1999). In particular, the Landsat MSS (multispectral scanner) and TM (thematic mapper) instruments, with 80- and 30-m resolution, respectively, have been applied widely to regional studies of vegetation. Jakubauskas (1996) used Landsat TM data to map the distribution of forest cover types in Yellowstone National Park. He demonstrated that lodgepole pine forest types had differing reflectance characteristics as a function of age.

Methods

AVIRIS Data Collection for Yellowstone National Park

For this study, the airborne visible and infrared imaging spectrometer (AVIRIS), operated by NASA's Jet Propulsion Laboratory, was used. AVIRIS collects data in 224 continuous channels of approximately 10-nanometer bandpass over the spectral-wavelength range of 0.35 to 2.50 μm (from visible light to near-infrared). In Yellowstone, for the mean altitude of 2,290 m, AVIRIS measured pixels with a nominal size of 17.5 m.

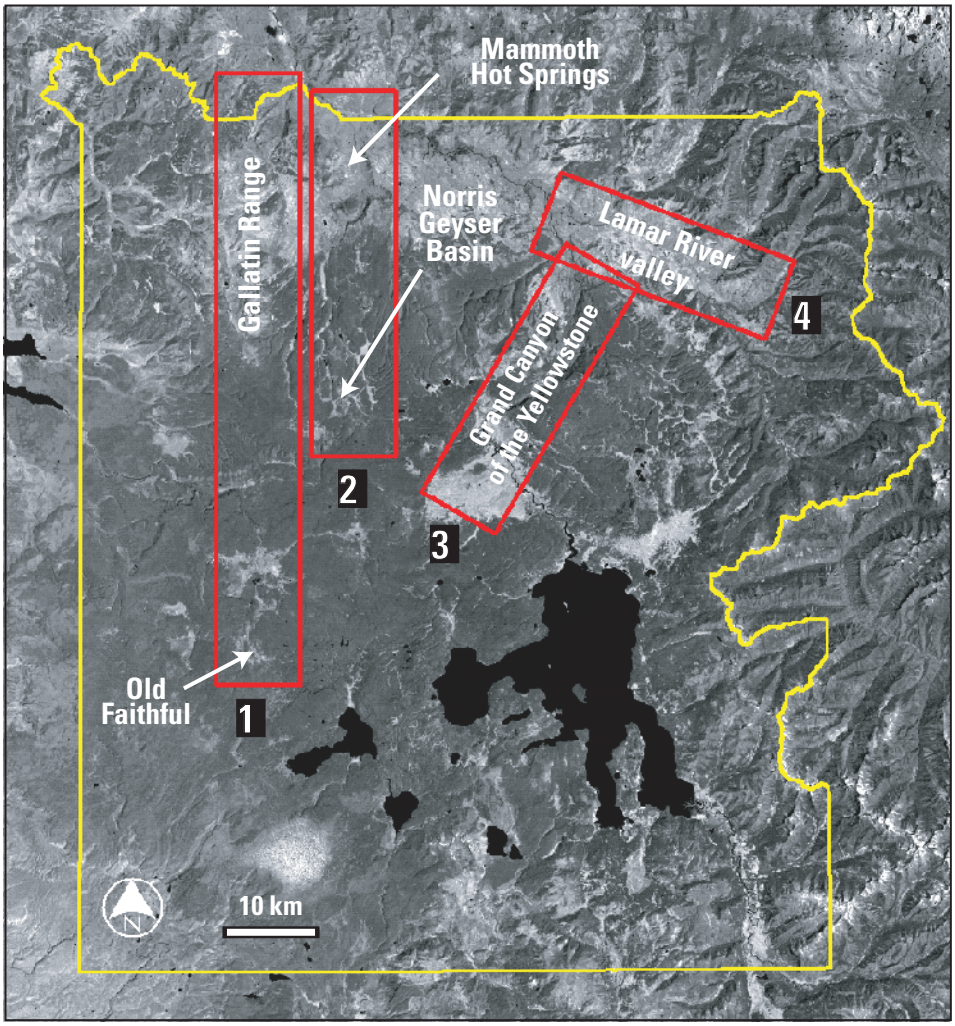

Figure 2. Coverage of AVIRIS data collected on August 7, 1996, over Yellowstone National Park (the Park boundary is indicated). The four flight lines, approximately 10 km wide, include: line 1—north from the Old Faithful area to the Gallatin Range; line 2—north from Norris Geyser Basin to Mammoth Hot Springs and Gardiner, Montana; line 3—Grand Canyon of the Yellowstone River and Mount Washburn; and line 4—Lamar River valley.

The cross-track pixel sampling at nadir was 15.4 m and along-track sampling was 17.5 m, given the aircraft ground speed of approximately 210 m/s. The sensor-swath width was approximately 10 km.

AVIRIS data were collected on August 7, 1996, in four flight lines that included the following areas: Upper and Lower Geyser Basins, Gallatin Mountain Range, Mammoth Hot Springs, Norris Geyser Basin, Grand Canyon of the Yellowstone River, and the Lamar River valley. Those areas were selected to target areas of primary geologic and biologic interest. The outlines of the AVIRIS flight lines are shown in figure 2.

AVIRIS Data Calibration

To convert AVIRIS data from radiance to reflectance, the data were corrected for the influence of several variables, including solar irradiance, atmospheric-gas absorptions, and atmospheric scattering. We employed a two-step procedure for this conversion, as described in Clark and others (2003) and Rockwell and others (2002). First, the atmospheric-removal algorithm (ATREM; Gao and others, 1993, 1997) was applied to the radiance data. This radiative-transfer model removed most of the atmospheric effects. Unfortunately, residual atmosphere absorptions remained in the data, including an overcorrection of the atmospheric-path radiance. An additive correction for path radiance was derived using ATREM reflectance of a vegetation-covered area in shadow (Clark and others, 2003). Next, field-reflectance measurements of a ground-calibration site were used to reduce the atmospheric residuals. A gravel-staging site near Norris Geyser Basin was used for calibration because it was fairly large and homogenous, and it did not contain materials with strong absorption features. On the day of the AVIRIS flight, reflectance measurements of the staging site were made with an analytical spectral device (ASD) full-range field spectrometer. The averaged field measurements were corrected for the small absorption features of the Spectralon (Labsphere, Inc., North Sutton, N.H.) reference-calibration standard. The field measurement was used with the averaged ATREM data over the calibration site to generate the multiplicative correction. The resulting reflectance data are termed radiative-transfer ground-calibrated (RTGC) reflectance data. Kokaly and others (2003) described the calibration procedure in detail.

Spectral-Feature Analysis and Mapping Methods

The approach to vegetation mapping in this study uses comparisons of the spectral features of known vegetation cover types to the spectral features in each pixel of remote-sensing data. The following sections present the critical parts of this approach: (1) techniques of spectral-feature analysis used to isolate and normalize absorption features in reflectance data, (2) the creation of a spectral library of vegetation cover in Yellowstone National Park, and (3) compilation of vegetation maps by applying a spectral-feature-fitting algorithm and expert-system rules in the USGS Tetracorder system to the AVIRIS data and the vegetation spectral library.

Spectral-Feature Analysis

To compare the shapes of the absorption features, this study used a method of normalization called continuum removal. The continuum is simply an estimate of the other absorptions present in the spectrum, not including the one of interest (Clark and Roush, 1984; Clark, 1999). The first step in continuum removal is selection of the continuum endpoints (λ_1 and λ_2), which may be established at the points of minimum absorption surrounding the absorption feature. Following the selection of endpoints, the continuum may be modeled using a linear, polynomial, or other mathematical function. In practice, linear segments can be used to approximate the continuum, offering the advantage of easy computation. However, a Gaussian analysis probably is more accurate for strong overlapping absorptions (for example, see Clark 1981; Sunshine and others, 1990; Sunshine and Pieters, 1993).

After the continuum line (R_L) is established, the continuum-removed spectrum (R_C) is calculated by *dividing* the original reflectance values (R_O) by the corresponding values of the continuum line for all the channels in the wavelength region (λ_1 to λ_2) of the absorption feature:

$$R_C(\lambda) = R_O(\lambda) / R_L(\lambda) \quad (1)$$

To illustrate application of continuum removal, the reflectance spectra of two conifers (shown in fig. 3*A*) are used. By applying linear-continuum removal, it is clear that the reflectance from Douglas fir has a deeper chlorophyll absorption than that of lodgepole pine (fig. 3*B*). The greater depth of the Douglas fir absorption feature is a result of stronger absorption by chlorophyll. At the leaf level, this possibly is caused by greater concentration of the pigment. For reflectance spectra of canopies, the depth of the chlorophyll absorption varies because of many factors including: (1) the concentration of chlorophyll in the understory and overstory, or both; (2) the effects of multiple scattering between canopy elements; and (3) changes in fractional cover of vegetation over the soil background. The depth (D) of the absorption feature at each channel is calculated by

$$D(\lambda) = 1 - R_C(\lambda) \quad (2)$$

The band center (λ_C) of the absorption feature is the wavelength position of the spectrometer channel with the maximum depth. The absorption depth at the band center, D_C, is referred to as the band depth. More complex determinations of the wavelength position of the absorption-band center, which are less instrument specific, are made by fitting of mathematical functions to the channels near the absorption center (see for example, Choquette and others, 1998).

Scaling of absorption features to the same band depth at the band center facilitates visual comparison of the shapes. From the reflectance spectra of the same absorption feature in different samples, the continuum-removed absorption features can be scaled to equal depth at the band center. An example of this is shown in figure 3*C*. The scaling reveals that, in addition to the greater band depth, the reflectance spectrum of Douglas fir has a wider chlorophyll-absorption feature compared to that of lodgepole pine. The spectral differences between these two conifers suggest that spectroscopic remote sensing can be used to distinguish conifer forest cover types based on subtle differences in their reflectance spectra.

Spectral Library for Yellowstone Vegetation

The major cover types in Yellowstone National Park were identified during a field survey. These cover types included all significant forest cover types, including lodgepole pine, whitebark pine, Douglas fir, and a mixed Engelmann spruce/subalpine fir category. Because lodgepole pine covers the greatest area in the Park and is the major colonizing species on recently disturbed ground, five classes of lodgepole pine were used. In addition, areas of nonforest vegetation were identified. These nonforest types included sagebrush, willow, Idaho fescue grasslands, lush sedge habitats, and wetland areas.

To establish spectral signatures of these vegetation types, pixels in the AVIRIS data covering the vegetation types were averaged to generate representative spectra. Thirty-seven areas were identified in the AVIRIS data. More than one area was used for some vegetation cover classes. Table 1 lists the forest cover types (boldface indicates entries for which the spectra are used in figures in this paper). Table 2 lists the nonforest cover types and the names used to label the subsequent plots. These averaged AVIRIS spectra for the vegetation cover types in tables 1 and 2 constitute the reference spectral library used by the Tetracorder system in this study.

In addition to vegetation cover, spectra of hot-spring microorganisms were included in the reference library. During field surveys, we measured the reflectance spectra of hot-spring bacteria and algae. The spectral shapes were

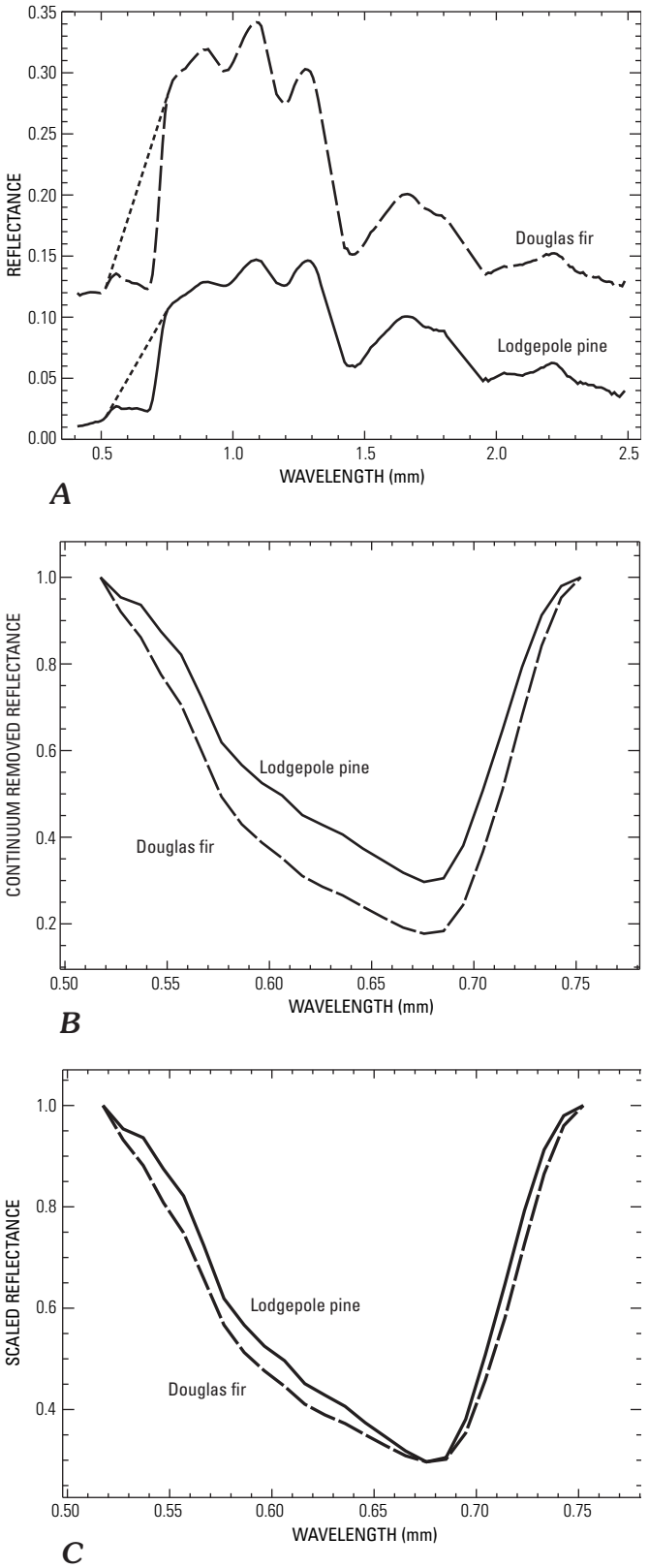

Figure 3. AVIRIS radiative-transfer ground-calibrated reflectance spectra of Douglas fir and lodgepole pine with associated continuum lines. *A*, Reflectance spectra are offset by 0.1 in reflectance. *B,* Continuum-removed chlorophyll absorption-feature spectra. *C,* Scaled chlorophyll absorption features.

unique, compared to those of vegetation. Figure 4 shows a spectrum of a hot-spring-bacteria mat that contains a thick surface layer of the thermophilic bacterium *Synechococcus* sp. Compared to features of vegetation, the chlorophyll absorption is narrow and the water absorptions are very strong. All spectra used in this study are published in Clark and others (2003) and are available online at http://speclab.cr.usgs.gov/spectral-lib.html.

Although the atmospheric correction and ground calibration of AVIRIS data were performed, some channels were deleted from the mapping analysis (and the plotted spectra in this paper) because of residual atmospheric effects. The channels in which detector overlaps are present were also excluded from analyses. These excluded channels are listed in table 3.

The USGS Tetracorder System

Tetracorder is an expert system. It compares the absorption features present in each pixel of AVIRIS data to the characteristic absorption features of materials in a spectral library (Clark and others, 1990, 1991; Clark, Swayze, and others, 1993; Clark and Swayze, 1995; Clark and others, 2003). Tetracorder uses continuum removal to isolate specific absorptions and to remove the effects of changing slopes and overall reflectance levels. It compares the shapes of absorption features in the AVIRIS data with those in each reference sample of the library. A modified least-squares-fitting algorithm numerically determines the best match between the spectral features in a pixel of AVIRIS data and those in the entries of the spectral library. The Tetracorder system can make further refinements to the selection of the closest match with a set of expert-system rules, including definition of threshold values, continuum-slope constraints, and other methods (see detailed explanation in Clark and others, 2003).

Tetracorder uses user-specified continuum endpoints, linear-continuum removal, and a modified, linear, least-squares-fitting algorithm to scale the absorption feature of a library-reference spectrum to match the feature in an AVIRIS pixel (for details see Clark and others, 2003). The least-squares fitting uses all the channels in the feature to adjust the depth of the reference spectrum to the depth of the feature in the spectrum of the unknown material in the AVIRIS pixel. The depth of the feature in the unknown spectrum is calculated as the band depth of the library-reference spectrum that was scaled to it, in order to avoid calculations using the noisier AVIRIS spectrum. In Tetracorder, the correlation coefficient (r) resulting from the least-squares fitting is used to assess the *goodness of fit* between the continuum-removed spectral features of the library and the unknown spectra.

For the comparison of the entries of a spectral library to the spectrum of an AVIRIS pixel using only a single absorption feature, the fit values calculated between the library entries and the pixel are compared and the entry

Table 1. Spectral library entries of forest cover types.

[Bold type indicate entries used in figures of reflectance spectra in this paper]

Forest cover type	Training site location	Number of pixels, averaged
Douglas fir	Mammoth (line 2)	114
Douglas fir	Gallatin Range (line 1)	84
Douglas fir	Lamar Valley (line 4)	207
Whitebark pine	Mt Washburn (line 3)	34
Whitebark pine	Gallatin Range (line 1)	105
Engelmann spruce/subalpine fir	Mt Washburn (line 3)	18
Engelmann spruce/subalpine fir	Mt Washburn (line 3)	20
Engelmann spruce/subalpine fir	Gallatin Range (line 1)	257
Engelmann spruce/subalpine fir	Gallatin Range (line 1)	99
Engelmann spruce/subalpine fir	Gallatin Range (line 1)	126
Aspen	Lamar Valley (line 4)	15
Lodgepole pine age class 0—moderate regrowth	Mammoth (line 2)	371
Lodgepole pine age class 0—vigorous regrowth	Mammoth (line 2)	56
Lodgepole pine age class 1	Mt Washburn (line 3)	72
Lodgepole pine age class 1	Mammoth (line 2)	144
Lodgepole pine age class 1	Norris (line 2)	135
Lodgepole pine age class 1	Mammoth (line 2)	129
Lodgepole pine age class 2	Mammoth (line 2)	30
Lodgepole pine age class 2	Mammoth (line 2)	128
Lodgepole pine age class 3	Mt Washburn (line 3)	132
Lodgepole pine age class 3	Mt Washburn (line 3)	52
Lodgepole climax age class	Norris (line 2)	148
Lodgepole pine meadow mix	Mt Washburn (line 3)	153

with highest fit value (r) is selected as the best match. In Tetracorder, multiple absorption features in a single material (that is, a library entry) are used with a list of user-specified constraints to select the best match (Clark and others, 2003). A standard constraint in the applications of Tetracorder is the definition of a minimum continuum-threshold level. Deeply shadowed pixels have low reflectance (for example, pixels along the north-facing slope of a canyon). Such pixels have a low signal-to-noise ratio, making it difficult to discern absorption features through the high noise level. In Tetracorder, a minimum threshold level of 4-percent reflectance was set arbitrarily for the midpoint of the continuum for all entries in the Yellowstone vegetation spectral library. For pixels with a continuum-reflectance level below this threshold, Tetracorder did not attempt to determine the vegetation cover type.

In this application of Tetracorder to the mapping of vegetation in Yellowstone National Park, we selected three absorption features to use in the comparison of AVIRIS data to the spectral library. The absorptions used were the 0.68-μm chlorophyll-absorption feature, the 0.98-μm leaf-water, and the 1.20-μm leaf-water absorptions. Table 4 shows the continuum endpoints used by the Tetracorder analysis for the three features. A range of wavelengths was selected as the endpoints of the continuum. In the computation of the continuum line, the AVIRIS channels within these ranges were averaged to reduce the effect of noise in the computations (Clark and others, 2003).

In this study, the fit values for each of the three absorption features, the chlorophyll and two water absorptions, were weighted by approximately 0.70, 0.15, and 0.15, respectively, and summed. These weights gave more emphasis to the stronger chlorophyll absorption. Thus, for a pixel in the AVIRIS data, the Tetracorder system calculated a total weighted-fit value for each entry in the spectral library. Subsequently, the "best match" of the AVIRIS pixel to the spectral library was selected as the highest weighted-fit value. For each entry in the spectral library, a raster image was produced by assigning the fit value to the pixels for which the cover type was selected as the best match (all other pixels were set to zero). Thus, for an entry in the spectral library, its raster "fit" image shows the distribution of pixels that have the closest spectral appearance to the entry compared to the other entries in the library. The pixel values are an indication of the closeness of the match between the pixel spectrum and the library spectrum. Thus, the range in values of the pixels is a measure of the degree of confidence in the match, and the image can be processed with simple contrast stretching to represent either the full range of fit values or only the relatively high fit values. By selecting different colors for each cover type, fit images were combined to produce thematic maps of conifer, non-forest, and microbial cover.

Table 2. Spectral library entries of nonforest cover types.

Cover type category	Plot name	Cover type	Major vegetation species occurring in cover type	Training site area	Number of pixels
Sagebrush shrubland	sage1	Sagebrush and grass	*Artemisia tridentata, Festuca idahoensis*	Mammoth (line 2)	216
Sagebrush shrubland	sage2	Sagebrush and grass	*Artemisia tridentata, Festuca idahoensis*	Mammoth (line 2)	81
Sagebrush steppe	sage/fescue1	Mixed sage and grass	*Artemisia tridentata, Festuca idahoensis, Geranium viscosissimum*	Lamar Valley (line 4)	129
Sagebrush steppe	sage/fescue2	Mixed sage and grass on north-facing slope	*Artemisia tridentata, Festuca idahoensis, Geranium viscosissimum*	Lamar Valley (line 4)	51
Grassland	fescue/wheatgrass1	Mixed Idaho fescue and bearded wheatgrass—wet phase	*Festuca idahoensis, Agropyron caninum, Geranium viscosissimum*	Lamar Valley (line 4)	62
Grassland	fescue/wheatgrass2	Mixed Idaho fescue and bearded wheatgrass—dry phase	*Festuca idahoensis, Agropyron caninum*	Lamar Valley (line 4)	56
Grassland	fescue/wheatgrass3	Mixed Idaho fescue and bluebunch wheatgrass	*Festuca idahoensis*, *Agropyron spicatum*	Lamar Valley (line 4)	78
Grassland	fescue/needlegrass	Mixed Idaho fescue and Richardson's needlegrass	*Festuca idahoensis, Stipa richardsonii*	Lamar Valley (line 4)	510
Grassland	bromus	Smooth brome	*Bromus inermis*	Lamar Valley (line 4)	65
Wet nonforest	willow/sedge	Willow and sedge	*Salix* sp., *Carex* sp.	Norris (line 2)	39
Wet nonforest	willow	Willow	*Salix* sp.	Norris (line 2)	30
Wet nonforest	sedge	Sedge	*Carex* sp.	Mammoth (line 2)	183
Wet nonforest	cattail	Cattails	*Typha* sp.	Old Faithful (line 1)	18
Wet nonforest	wetland1	Mixed wetland	Mixed wetland vegetation	Old Faithful (line 1)	11
Wet nonforest	wetland2	Mixed wetland	Mixed wetland vegetation	Norris (line 2)	53

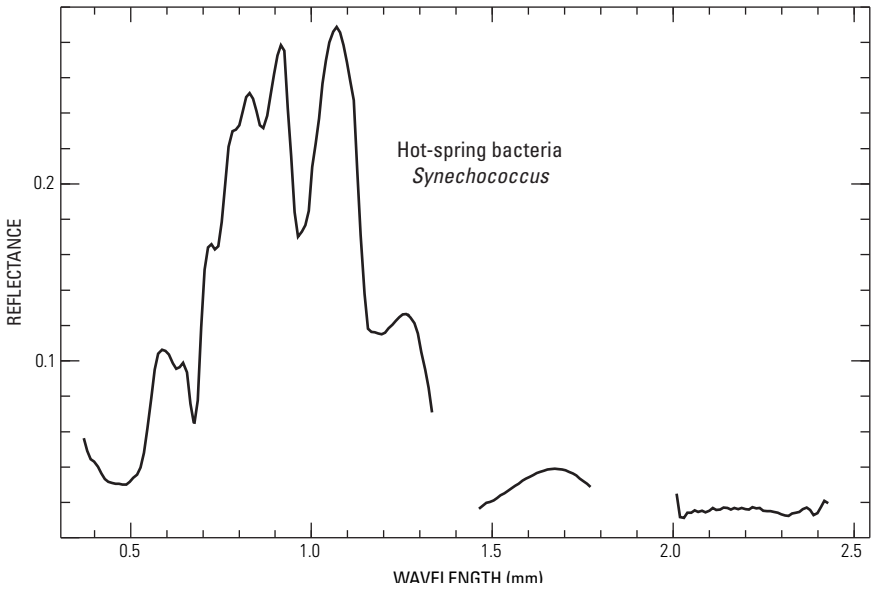

Figure 4. Field-reflectance spectrum of a Yellowstone hot-spring bacterial mat (primary organism is *Synechococcus* sp.).

Table 3. Channels of 1996 AVIRIS data not used in spectral analysis.

[N/A, not applicable]

Deleted channels	Wavelength region	Reason for deletion
1–4	< 0.40 μm	Decreasing signal from ozone absorption and an imprecise correction for atmospheric scattering
32–33	N/A	Overlap in detectors
43	0.71 μm	Oxygen absorption
59–62	centered at 0.98 μm	Atmospheric water vapor
81–84	centered at 1.20 μm	Atmospheric water vapor
95–97	N/A	Overlap in detectors
106–113	centered at 1.40 μm	Atmospheric water vapor
154–167	centered at 1.90 μm	Atmospheric water vapor
173–175	centered at 2.00 μm	Atmospheric carbon dioxide
223–224	> 2.49 μm	AVIRIS instrument performance degrades

Results and Discussion

In this study, vegetation mapping in Yellowstone National Park is focused on a comparison of the spectral features in each pixel of remote-sensing data to the spectral features of known vegetation cover types. The results are reported in the following two sections. First, the reflectance spectra of the vegetation cover types in Yellowstone are presented and the differences in absorption strengths are discussed. This discussion aids in interpretations of the vegetation maps, which are given in the final section.

Comparison of Spectra for Vegetation Cover Types

This section presents the reflectance spectra and continuum-removed absorption features of the vegetation cover types in Yellowstone National Park. For clarity, in the plots of spectra, only one representative spectrum from the spectral library of forest cover types, listed in table 1, is presented.

Reflectance Spectra

Reflectance spectra of the forest cover types are shown in figure 5*A*. In general, the forest cover types are designated by the dominant species: whitebark pine (WB), lodgepole pine (LP), Douglas fir (DF), and mixed Engelmann spruce/subalpine fir forest (SF). In Yellowstone, lodgepole pine covers the largest area in the Park and is the major colonizing species on recently disturbed ground; as a result, Despain (1990) delineated several age classes of lodgepole pine. Representative spectra of the lodgepole age classes, from the entries of forest cover types in the spectral library listed in table 1, are shown in figure 5*B*.

The nonforest vegetation cover types listed in table 2 were divided into three groups. The first group, the "wet" vegetation, is the relatively lush nonforest vegetation that contains a significant amount of chlorophyll and water in leaves. The second group, "grassland," contains vegetation cover types dominated by grass species. The third group, "sagebrush steppe," contains cover types with a significant amount of sagebrush in addition to grasses. The spectra of wet, grassland, and sagebrush steppe nonforest cover types are shown in figures 5*C* to 5*E*, respectively.

In general, the conifer-reflectance spectra in figure 5*A* have a low level of reflectance in the visible spectrum (less than 5 percent from the blue to red portion of the visible spectrum) and a maximum reflectance level of 15–24 percent at 1.1 μm in the near-infrared (NIR) plateau. The reflectance spectra of lodgepole age classes in figure 5*B* show a change in the NIR plateau in young to old stands. The spectrum of the LP0 age class, consisting of young lodgepole pine seedlings, shows the NIR plateau region to have weak leaf-water absorptions that are superposed on a generally positive slope. In contrast, the LP3 stand has strong leaf-water absorption features. The LP3 lodgepole stand has a broken overstory that is beginning to be replaced by a mixed spruce/fir overstory (Despain, 1990). As a result, the ragged canopies of LP3 have gaps in the overstory. The increased water absorption possibly arises from multiscattering of incident light in this variable-height canopy or from higher water content in the understory vegetation, or both.

The wet-nonforest cover types (willows and sedge marshes) have much higher reflectance in the NIR plateau (see fig. 5*C*), compared to the forest cover (fig. 5*A*). These cover types have reflectance from 30–50 percent at 1.1 μm. The leading edge (0.75–0.90 μm) of the NIR plateau shows some variation in slope, from a steep slope for the sedge spectrum to a nearly zero slope for the wetland1 spectrum (fig. 5*C*). The reflectance spectra of the grassland cover types in figure 5*D* show a range in spectral features. The variations are dependent on the moisture regimes in which the different cover types grow. Fescue/wheatgrass1 is in a moisture-rich area. This is reflected in the strong chlorophyll- and water-absorption features in its spectrum. In contrast, fescue/wheatgrass2, a drier phase of the fescue/wheatgrass1, shows the water features to be weaker, and the 2.10- and 2.30-μm absorption features are revealed.

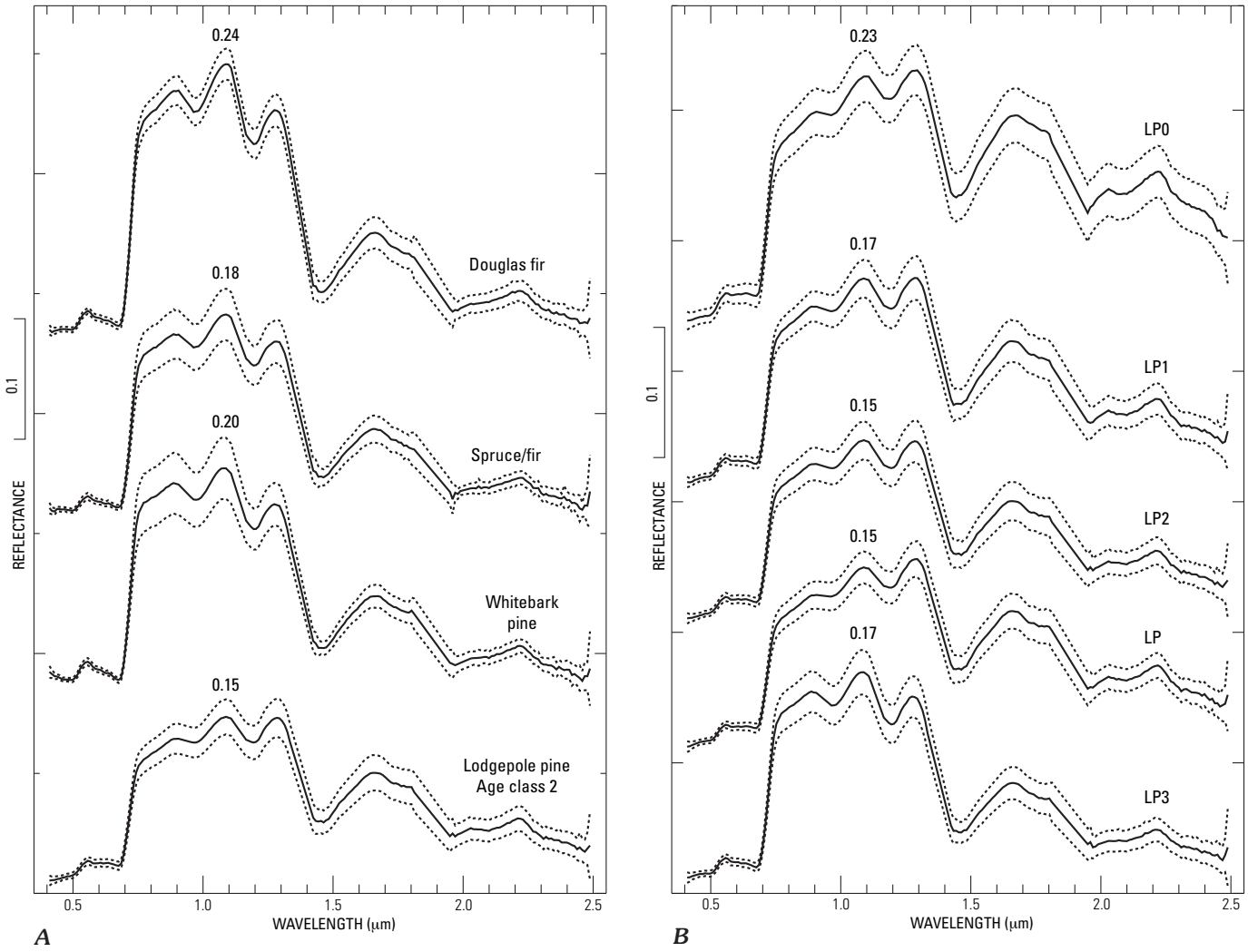

Figure 5. Representative AVIRIS radiative-transfer ground-calibrated reflectance spectra for Yellowstone vegetation (reflectance values at 1.1 μm are given in the figures). *A,* Conifer cover types; spectra are plotted at fixed intervals of 0.1 but offset by 0.15. *B,* Lodgepole pine age classes; spectra are plotted at fixed intervals of 0.1 but offset by 0.10.

The reflectance spectra of sagebrush steppe cover types (fig. 5*E*) differ greatly from those of forest and lush vegetation. These plants grow in sparse groups, and they had low water content at the time of the overflight (August 1996). Thus, the reflectance spectra of sagebrush steppe cover types show weaker absorption because of water. That weaker absorption reveals the longer wavelength absorptions at 2.10 and 2.30 μm that arise from leaf biochemical constituents (primarily lignin and cellulose). In addition to weaker water absorption, sagebrush leaves are covered by fine hairs that are composed mainly of cellulose; the hairs also will increase the longer wavelength absorption features at 2.10 and 2.30 μm. Furthermore, the spectra of the areas dominated by sagebrush (sage1 and sage2) show weak absorption at the 0.68-μm chlorophyll position because sagebrush plants have relatively low chlorophyll content and most grasses in these areas were senescent at the time of the AVIRIS overflight.

Continuum-Removed Vegetation-Spectral Features

The continuum-removed spectra for the chlorophyll-absorption feature are shown in figures 6*A* to 6*E* for the forest and lodgepole and nonforest wet, grassland, and sagebrush steppe cover types, respectively. Calculated band depths and band centers are given in table 5. For the forest-vegetation spectra shown in figure 6*A*, the pines show weaker absorption strengths, with lodgepole pine having the weakest chlorophyll absorption. Douglas fir has the strongest absorption feature. In figure 6*B*, the age classes of lodgepole pine show increasing band depth from the youngest class, LP0, to LP1, to LP2, and finally, to LP3.

The depth of chlorophyll absorption in these remotely sensed canopy spectra is due to both the concentration of chlorophyll in the leaves of the vegetation and the percent

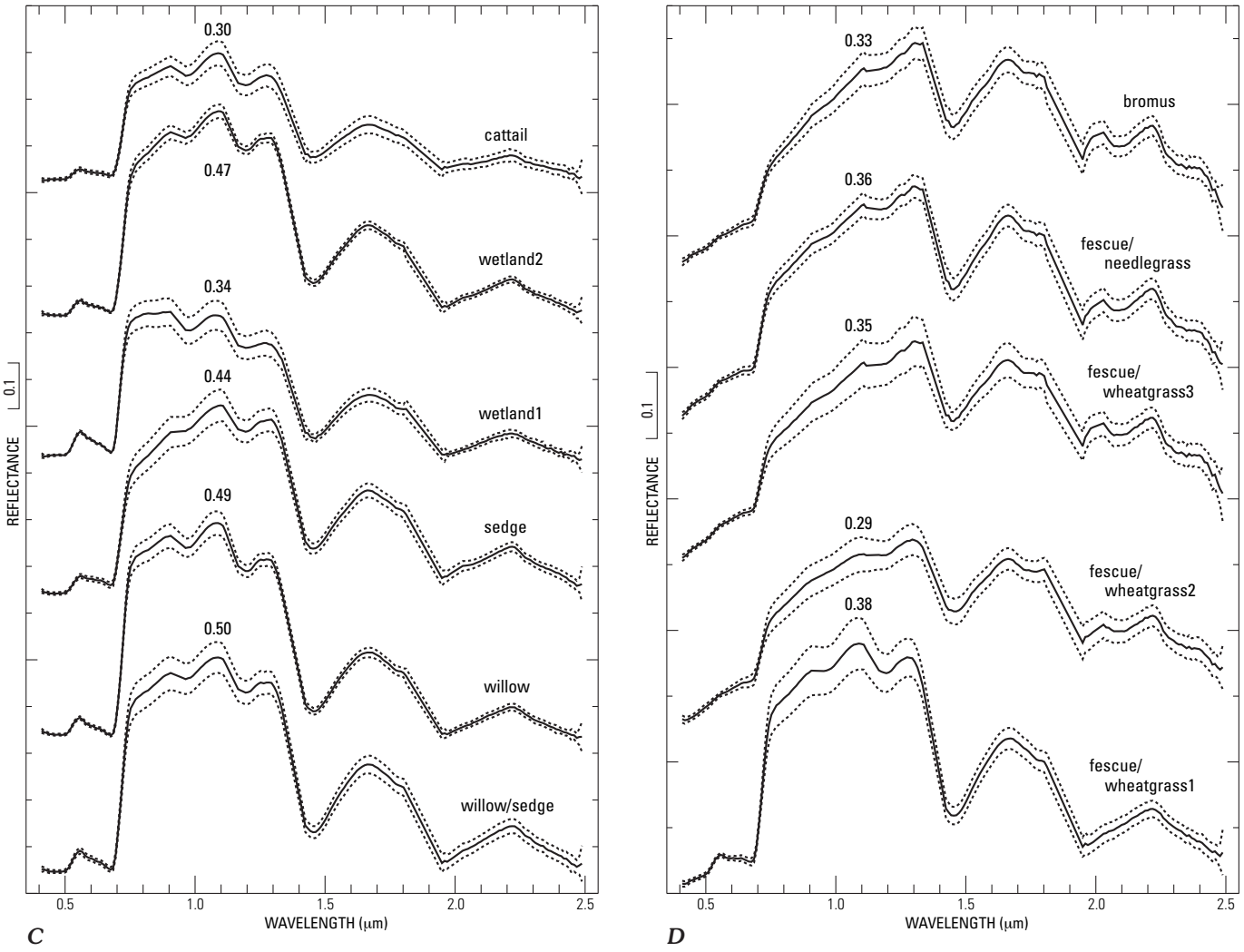

Figure 5 (continued). *C,* Lush nonforest vegetation; spectra are plotted at fixed intervals of 0.1 but offset by 0.25. *D,* Grassland cover types; spectra are plotted at fixed intervals of 0.1 but offset by 0.22.

cover of the vegetation over the background rocks and soils. Multiple scattering effects possibly affect the apparent strength of the chlorophyll absorption. A variable height canopy in LP3 possibly enhances multiple scattering between the overstory mature lodgepole pine and younger subalpine fir and Engelmann spruce in the understory, leading to a stronger absorption feature. The LP1, LP2, and LP age classes all show similar shapes of the chlorophyll absorption. Because of similarities of LP1, LP2, and LP spectra, these age classes of lodgepole pine are difficult to distinguish from one another spectrally, based only on the chlorophyll absorption.

Figure 6*C* shows the continuum-removed chlorophyll-absorption features for the areas of lush nonforest vegetation. In general, all of these features are stronger, in comparison to the other cover types (see the band depths in table 5). Within this group there is considerable variation in the shapes of the feature. This likely is caused by relative differences in concentrations of chlorophyll a and b, carotenes, and other accessory pigments among the cover types. At the time of the flight on August 7, 1996, the leaves of the nonforest plants in Yellowstone National Park were in various stages of senescence.

Figure 6*D* shows that, with the exception of fescue/wheatgrass1, all grassland areas contained low amounts of chlorophyll, as indicated by the shallow absorption feature. The spectra from these sites varied in the shape of the chlorophyll feature, and they are distinct from those of other cover types. The fescue/wheatgrass1 site contains a wet phase of the Idaho fescue/bearded wheatgrass grassland, and the stronger chlorophyll feature is consistent with this site retaining its chlorophyll later in the season because of available water, in comparison to the other grasslands. Figure 6*E* shows the chlorophyll absorption of the sagebrush areas. The mixed sage/grassland sites (sage/fescue1 and sage/fescue2) show more abundant chlorophyll in the vegetation, probably owing to a higher concentration of chlorophyll in the leaves as well as a higher percentage of total plant cover compared to the sage shrub lands (sage1 and sage2).

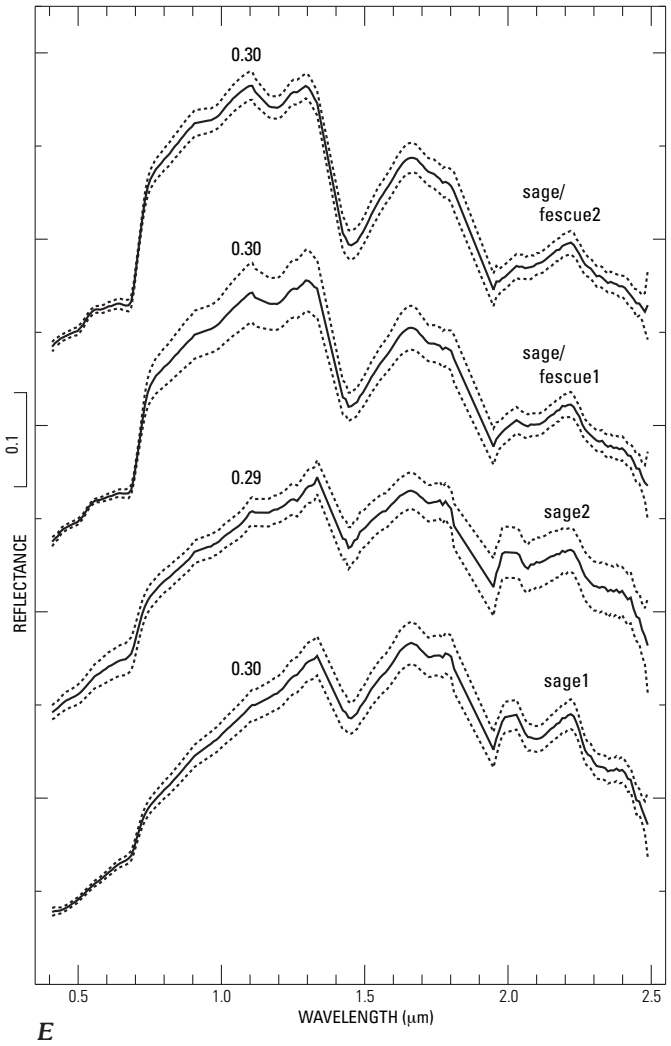

Figure 5 (continued). *E,* Sagebrush steppes; spectra are plotted at fixed intervals of 0.1 but offset by 0.20.

The continuum-removed 0.98-μm water-absorption features for the different forest areas are shown in figure 7*A*. Table 6 shows the band-depth and band-center positions of this absorption feature. In contrast to the chlorophyll-absorption feature, this feature shows that whitebark pine forest has stronger absorption than mixed Engelmann spruce/subalpine fir forest. Figure 7*B* shows that the LP1- and LP2- absorption features are extremely similar. The LP3 age class has the greatest water-absorption strength (band depth = 0.1074), at 0.98 μm, and LP0 has the weakest, at a band depth of 0.0601. The LP class has a weaker absorption than LP1 or LP2, but the overall shapes of the features are similar.

Figure 7*C* shows the 0.98-μm absorption feature owing to leaf water in the lush nonforest-vegetation types. The most distinguishing element of the shapes of these features, compared to other cover types, is the broad, flat bottoms of the features. The features here are flat from approximately 0.962 to 0.982 μm. In contrast, the forest-vegetation spectra show a narrow feature with a distinct band minimum at 0.982 μm (figs. 7*A* and 7*B*). Figure 7*D* shows that the 0.98-μm water-absorption features are weak for the grassland cover types, again with the exception of the fescue/wheatgrass1 site. The same features in the sagebrush sites are also weak, with depths of 3.5 percent or less (see fig. 7*E* and table 6). The absorption features for the sage shrub lands (sage and sage2) are extremely weak (<2 percent band depth). As a result, noise affects the shape of the absorption feature.

For the forest and lodgepole cover types, the shapes and band depths show similar trends in the 1.20-μm water-absorption feature as those for the 0.98-μm water-absorption feature (see Kokaly and others, 2003). Again, the wetland cover types have water absorption at 1.20 μm, with broad flat bottoms like those observed at 0.98 μm. Similar band depths and band-shape trends are present for the 1.20-μm water-absorption feature, when compared to the trends observed in the 0.98-μm water-absorption features for the grassland and sagebrush steppe cover types.

Maps of Vegetation and Microorganisms in Yellowstone National Park Derived from AVIRIS Data

Forest Cover

Using the results of the USGS Tetracorder system applied to the calibrated AVIRIS data and the vegetation spectral library, forest cover maps were produced that revealed distributions of conifer stands for areas of the Park covered by AVIRIS data. In this report, we focus on two specific areas of the Park for discussion: Mammoth Hot Springs and Mount Washburn. The map of forest cover for the Mammoth Hot Springs area of Yellowstone National Park is presented in figure 8. In this figure, the colored pixels representing the different forest cover types are overlaid on a gray-scale background image (the pixels in this figure that do not have mature forest cover are depicted in gray-scale tones).

The image for the area around Mammoth Hot Springs (fig. 8) shows that the forest cover is predominately lodgepole pine of various age classes (LP and LP1 to LP3). The fires of 1988 reduced much of the mature lodgepole forests in the southern half of the image in fig. 8. In the northern part of the scene, near Mammoth Hot Springs, large stands of Douglas fir (DF) are mapped. These stands also were indicated in aerial-photograph interpretations (Despain, 1990). This part of the scene was subject to much field verification, and agreement between both types of remote-sensing analysis and the field survey was good.

In another area of the scene, in the vicinity of Mount Everts, there was disagreement between the AVIRIS and aerial-photograph maps. The Tetracorder analysis of the AVIRIS data identified many pixels as either mixed Engelmann spruce/subalpine fir

Figure 6. Continuum-removed 0.68-μm chlorophyll-absorption spectra. *A,* Conifer cover types. *B,* Lodgepole pine age classes. *C,* Lush nonforest vegetation. *D,* Grassland cover types. *E,* Sagebrush steppes.

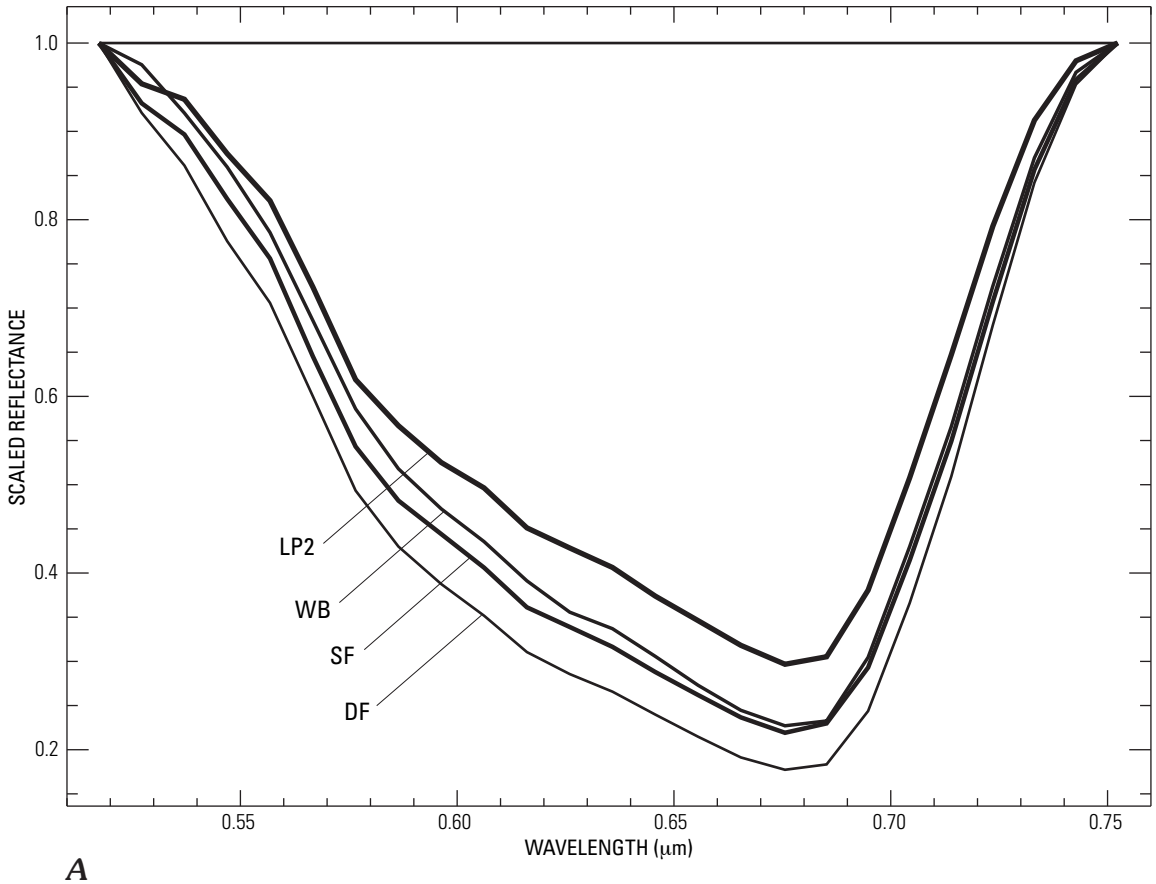
1.0
0.8
0.6
0.4
0.2
SCALED REFLECTANCE
LP2
WB
SF
DF
0.55
0.60
0.65
0.70
0.75
WAVELENGTH (μm)

A

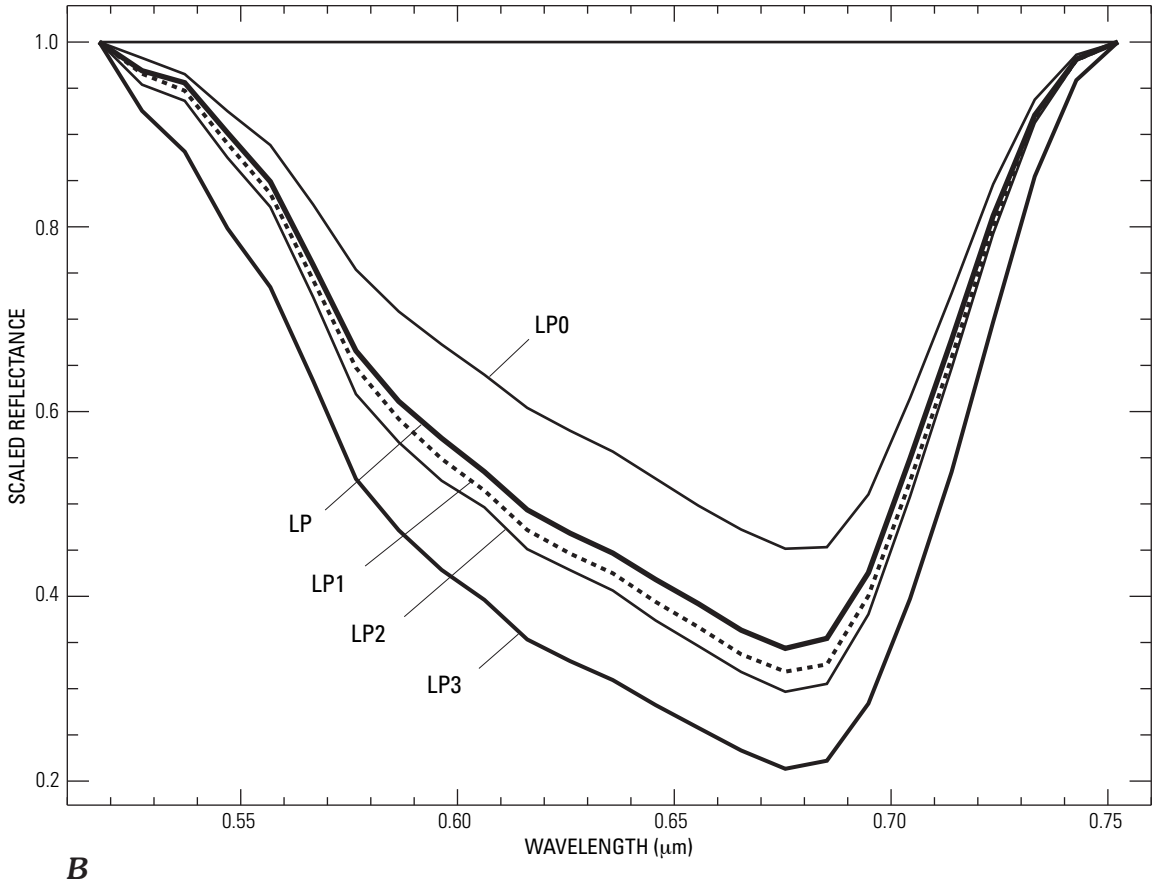
1.0
0.8
0.6
0.4
0.2
SCALED REFLECTANCE
LP0
LP
LP1
LP2
LP3
0.55
0.60
0.65
0.70
0.75
WAVELENGTH (μm)

B

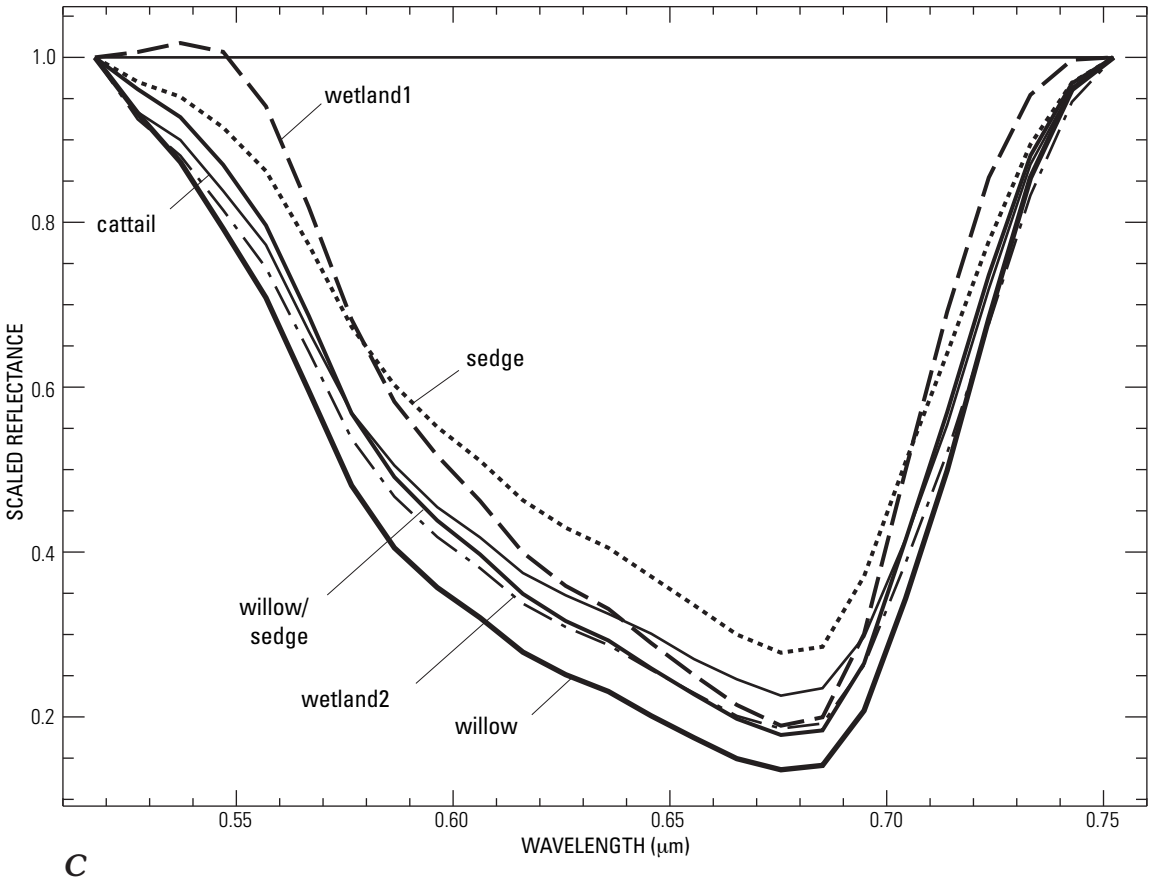
1.0
0.8
0.6
0.4
0.2
SCALED REFLECTANCE
wetland1
cattail
sedge
willow/
sedge
wetland2
willow
0.55
0.60
0.65
0.70
0.75
WAVELENGTH (μm)

C

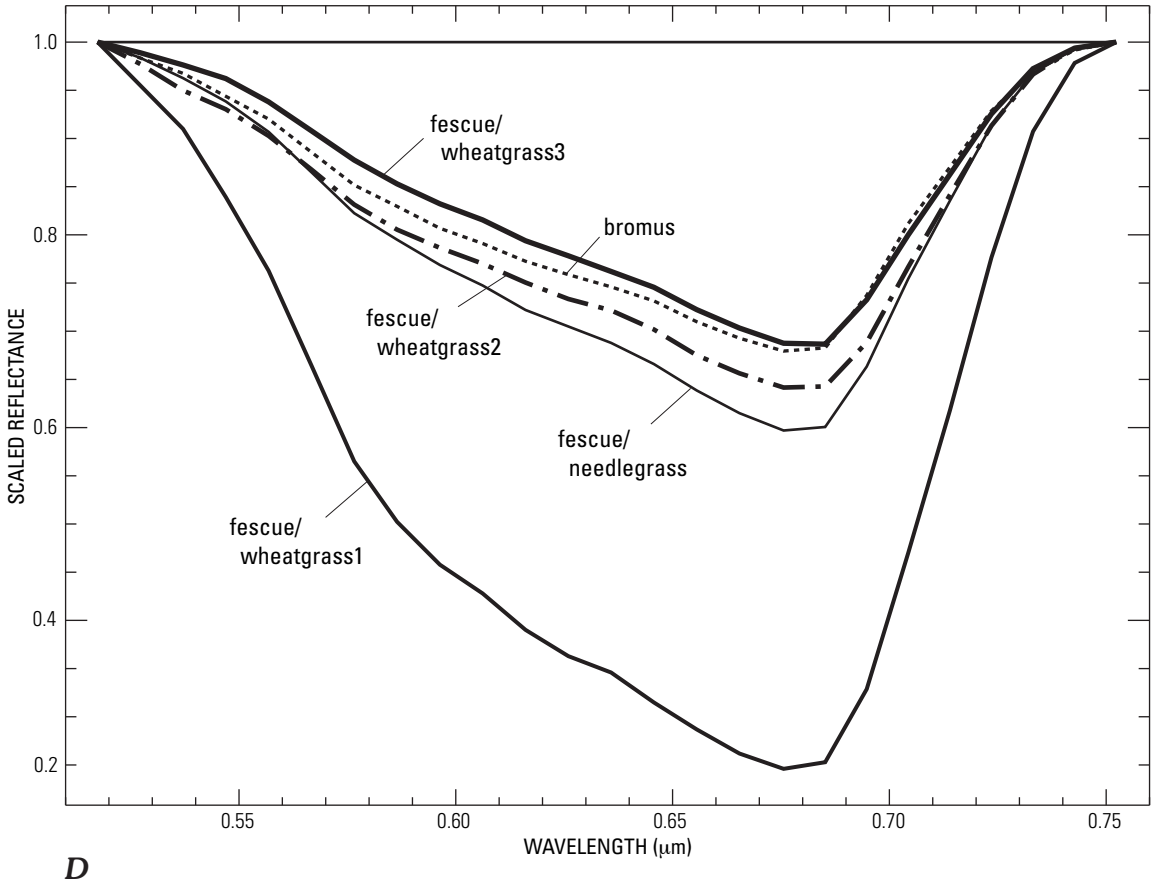
1.0
0.8
0.6
0.4
0.2
SCALED REFLECTANCE
fescue/
wheatgrass3
bromus
fescue/
wheatgrass2
fescue/
needlegrass
fescue/
wheatgrass1
0.55
0.60
0.65
0.70
0.75
WAVELENGTH (μm)

D

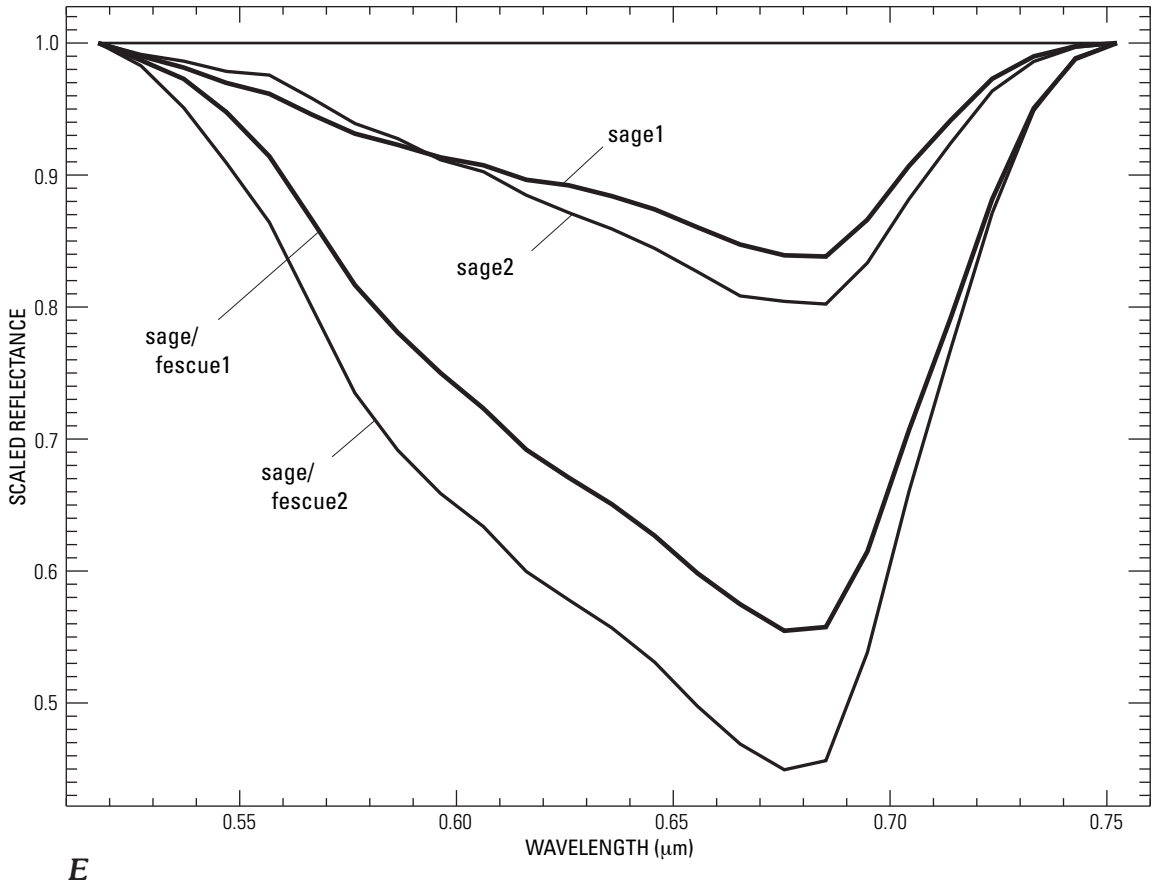

E

(SF) or Douglas fir (DF). However, the aerial-photograph analysis of Despain (1990) showed only Douglas fir in this area. Field checking revealed that, in addition to the indicated Douglas fir, there were many stands of Engelmann spruce (subalpine fir was not present). Thus, the spectral analysis was consistent in identifying the best match to these Engelmann spruce stands as being the Engelmann spruce/subalpine fir category. The map of forest cover derived from AVIRIS (fig. 8) also indicated the presence of a stand of whitebark pine (WB) in the northeast corner of the image that did not agree with the aerial-photograph interpretations. The presence of whitebark pine in these pixels was verified by field survey, and the spectral-analysis results for this area thus were confirmed.

The distributions of lodgepole pine regrowth (LP0) after the fires of 1988 also were mapped (fig. 9). During a preliminary examination of AVIRIS pixels over areas burned by the 1988 fires, we noted that some areas of LP0 cover class showed very strong chlorophyll- and water-absorption features. Consequently, the LP0 class was divided into two categories: moderate regrowth and vigorous regrowth (see the entries in table 1 and the blue and red pixels in fig. 9). When the Tetracorder results for the Mammoth Hot Springs area

Table 4. Continuum end points used for vegetation absorption features.

Cover type	Absorption feature	Left continuum range (μm)	Right continuum range (μm)
Forest			
	Chlorophyll (0.68 μm)	0.512–0.542	0.737–0.767
	Water (0.98 μm)	0.870–0.900	1.055–1.085
	Water (1.20 μm)	1.083–1.113	1.270–1.300
Nonforest			
	Chlorophyll (0.68 μm)	0.512–0.542	0.737–0.767
	Water (0.98 μm)	0.895–0.925	1.055–1.085
	Water (1.20 μm)	1.083–1.113	1.270–1.300
Bacteria			
	Chlorophyll (0.68 μm)	0.512–0.542	0.737–0.767
	Water (0.98 μm)	0.870–0.900	1.055–1.085
	Water (1.20 μm)	1.083–1.113	1.270–1.300

Table 5. Characteristics of the 0.68-µm chlorophyll-absorption feature for vegetation cover types of Yellowstone National Park.

Cover type (plot name)	Band center (µm)	Band depth	Continuum slope (μm^{-1})
	Forest		
Whitebark pine	0.6756	0.7729	0.5728
Spruce/fir	0.6756	0.7808	0.4137
Douglas fir	0.6756	0.8227	0.6714
Lodgepole pine—LP0	0.6756	0.5485	0.5103
Lodgepole pine—LP1	0.6756	0.6815	0.4300
Lodgepole pine—LP2	0.6756	0.7033	0.3744
Lodgepole pine—LP3	0.6756	0.7867	0.4747
Lodgepole pine—LP	0.6756	0.6563	0.3619
	Nonforest		
Sagebrush (sage1)	0.6852	0.1618	0.4095
Sagebrush (sage2)	0.6852	0.1978	0.4269
Sagebrush steppe (sage/fescue1)	0.6756	0.4453	0.5972
Sagebrush steppe (sage/fescue2)	0.6756	0.5506	0.6652
Grassland (fescue/wheatgrass1)	0.6756	0.7541	0.9975
Grassland (fescue/wheatgrass2)	0.6756	0.3584	0.5459
Grassland (fescue/wheatgrass3)	0.6852	0.3134	0.5933
Grassland (fescue/needlegrass)	0.6756	0.4030	0.6684
Grassland (bromus)	0.6756	0.3206	0.5222
Wet nonforest (willow/sedge)	0.6756	0.8219	1.4396
Wet nonforest (willow)	0.6756	0.8641	1.4956
Wet nonforest (sedge)	0.6756	0.7221	1.0331
Wet nonforest (cattail)	0.6756	0.7742	0.7975
Wet nonforest (wetland1)	0.6756	0.8106	1.1717
Wet nonforest (wetland2)	0.6756	0.8141	1.2318

were examined, several large areas were identified with a high concentration of vigorous lodgepole pine regrowth (indicated by red pixels in fig. 9). These areas were checked by field survey; the lodgepole pines in these areas had grown to much greater heights (more than 2 m) and densities than most of the surrounding lodgepole regrowth (≤ 1-m height). Areas of vigorous growth had high soil moisture. The higher growth rates may be related to soil moisture. The spectral differences are explained by seedling densities in the two areas. Areas of slower regrowth were a mix of grass cover and lodgepole seedlings. Areas of vigorous regrowth had an almost 100-percent cover of lodgepole pine. The spectrum of the vigorous regrowth was intermediate between that of the slower growing LP0 class and the older LP1 class.

In figures 8 and 9, a triangle-shaped patch of older lodgepole pine in the southeast corner of the AVIRIS scene was clearly indicated by the spectral analysis. The trees in this stand were interpreted to be in two age categories: 50- to 150-year-old LP1 and 150- to 300-year-old LP2. The identified age classes of lodgepole pine derived from AVIRIS data match the age classes indicated on the maps compiled from aerial-photograph interpretations; however, the spatial patterns differ. In comparing the spectra from the various areas of LP1 and LP2 age classes, overlap was observed between the spectral shapes and depths. Such a high degree of spectral similarity was not observed between other forest cover types. Consequently, it appears that additional work needs to be done to refine the age-class discriminations. Although three age classes of lodgepole pine apparently can be distinguished (LP0, LP1/LP2, and LP3), the finer discrimination of LP1 from LP2 was not always successful. This possibly is due to the fact that the two age classes do not have a clear distinguishing boundary. Indeed, the classes are age-based divisions of a continuous series. Different divisions possibly need to be developed for spectral remote-sensing data. The new age classes should correspond to observable differences in canopy spectra that result from changes in species composition, canopy structure, and percent cover of forest stands. A field study linking forest age and structure with AVIRIS canopy reflectance is needed to explore more detailed application of AVIRIS to discrimination of the ages of lodgepole stands.

The forest cover map for Mount Washburn (not pictured in this paper; see Kokaly and others, 2003) shows that most of this area is covered by lodgepole pine. However, Douglas fir (DF)

Figure 7. Continuum-removed 0.98-µm leaf-water absorption spectra. *A,* Conifer cover types. LP2, intermediate-age lodgepole pine; SF, Engleman spruce/subalpine fir; WB, whitebark; DF, Douglas fir. *B,* Lodgepole pine age classes. *C,* Lush nonforest vegetation. *D,* Grassland cover types. *E,* Sagebrush steppes.

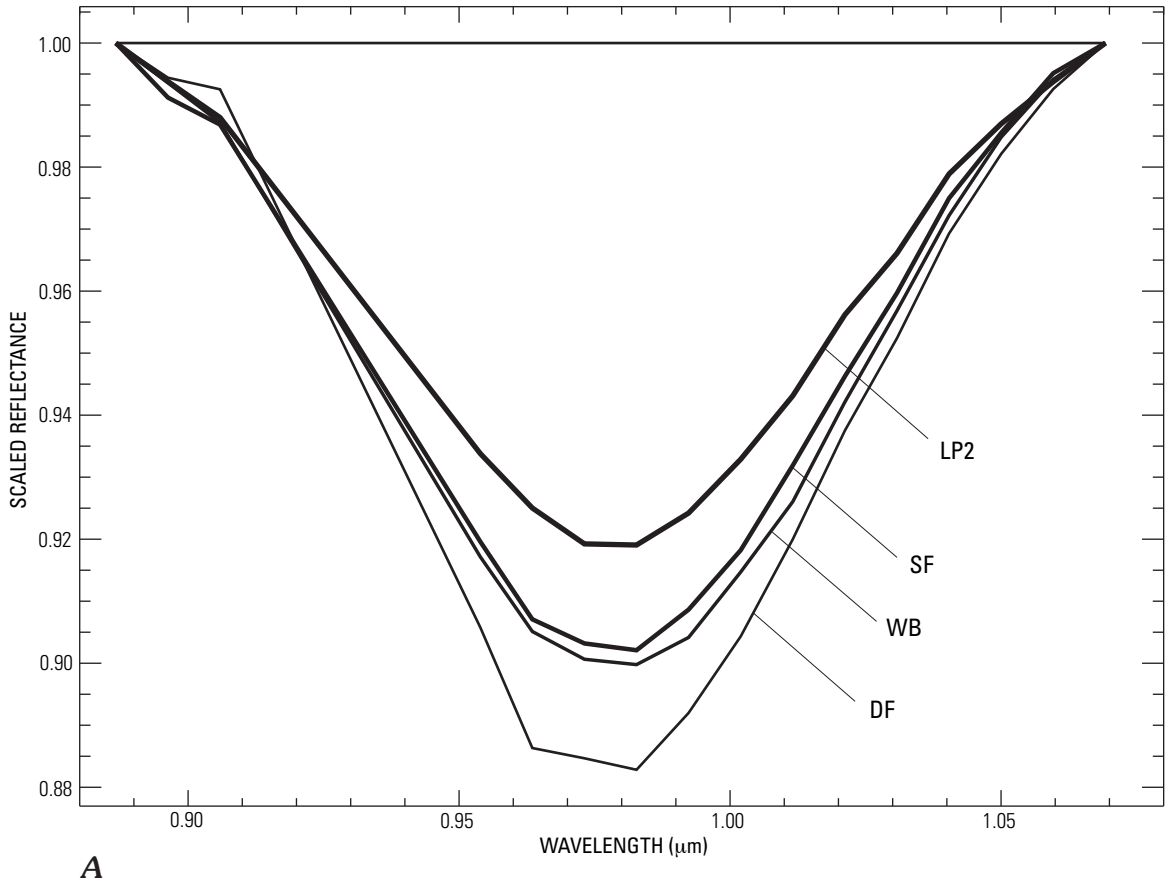
1.00
0.98
0.96
0.94
0.92
0.90
0.88
SCALED REFLECTANCE
0.90
0.95
1.00
1.05
WAVELENGTH (μm)
LP2
SF
WB
DF

A

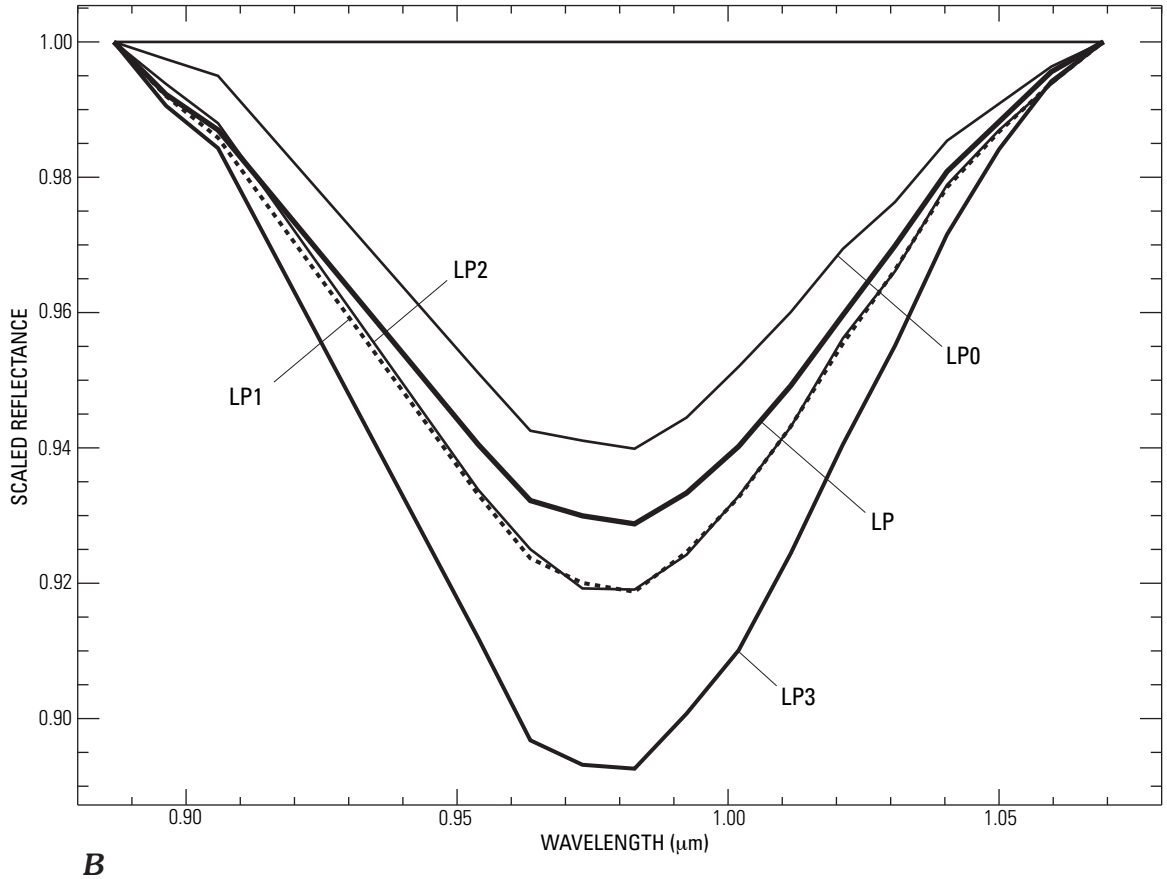
1.00
0.98
0.96
0.94
0.92
0.90
SCALED REFLECTANCE
0.90
0.95
1.00
1.05
WAVELENGTH (μm)
LP2
LP1
LP0
LP
LP3

B

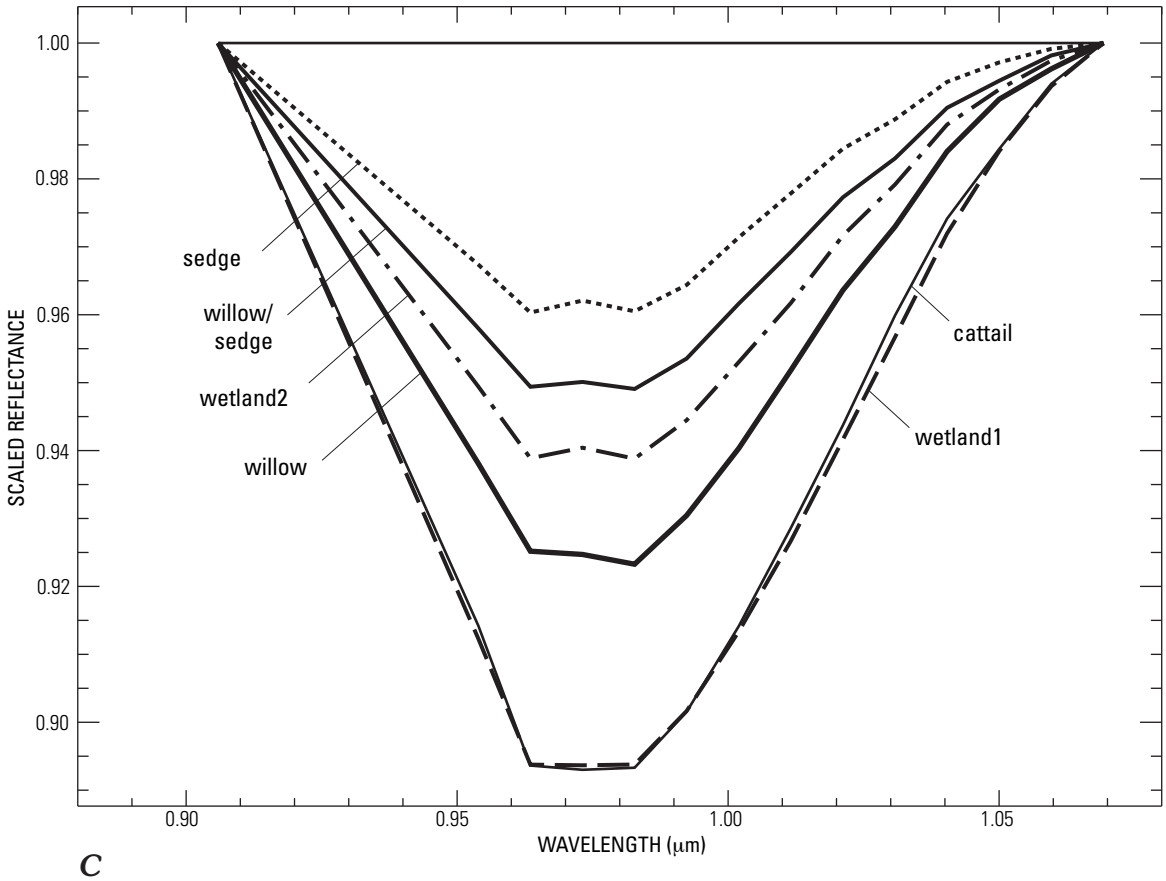
1.00
0.98
0.96
0.94
0.92
0.90
SCALED REFLECTANCE
0.90
0.95
1.00
1.05
WAVELENGTH (μm)
sedge
willow/
sedge
wetland2
willow
cattail
wetland1

C

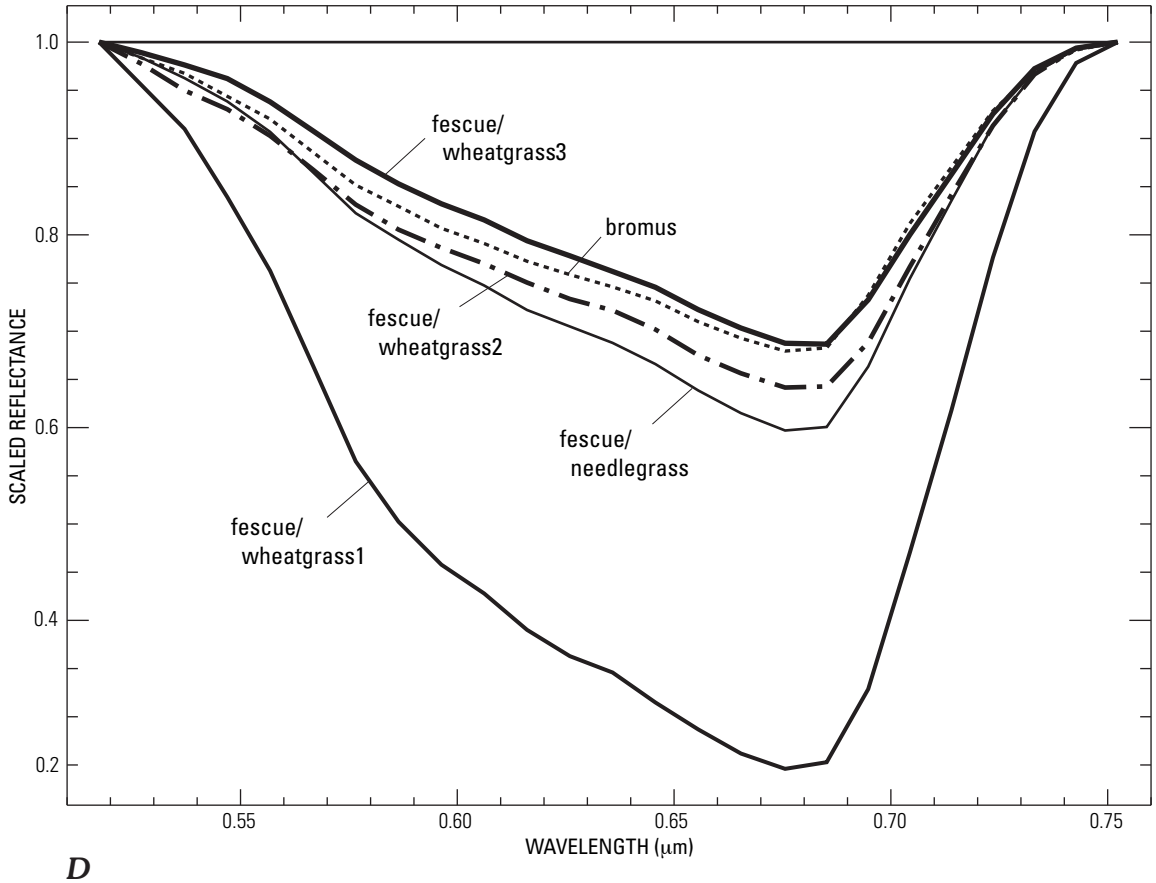
1.0
0.8
0.6
0.4
0.2
SCALED REFLECTANCE
0.55
0.60
0.65
0.70
0.75
WAVELENGTH (μm)
fescue/
wheatgrass3
bromus
fescue/
wheatgrass2
fescue/
needlegrass
fescue/
wheatgrass1

D

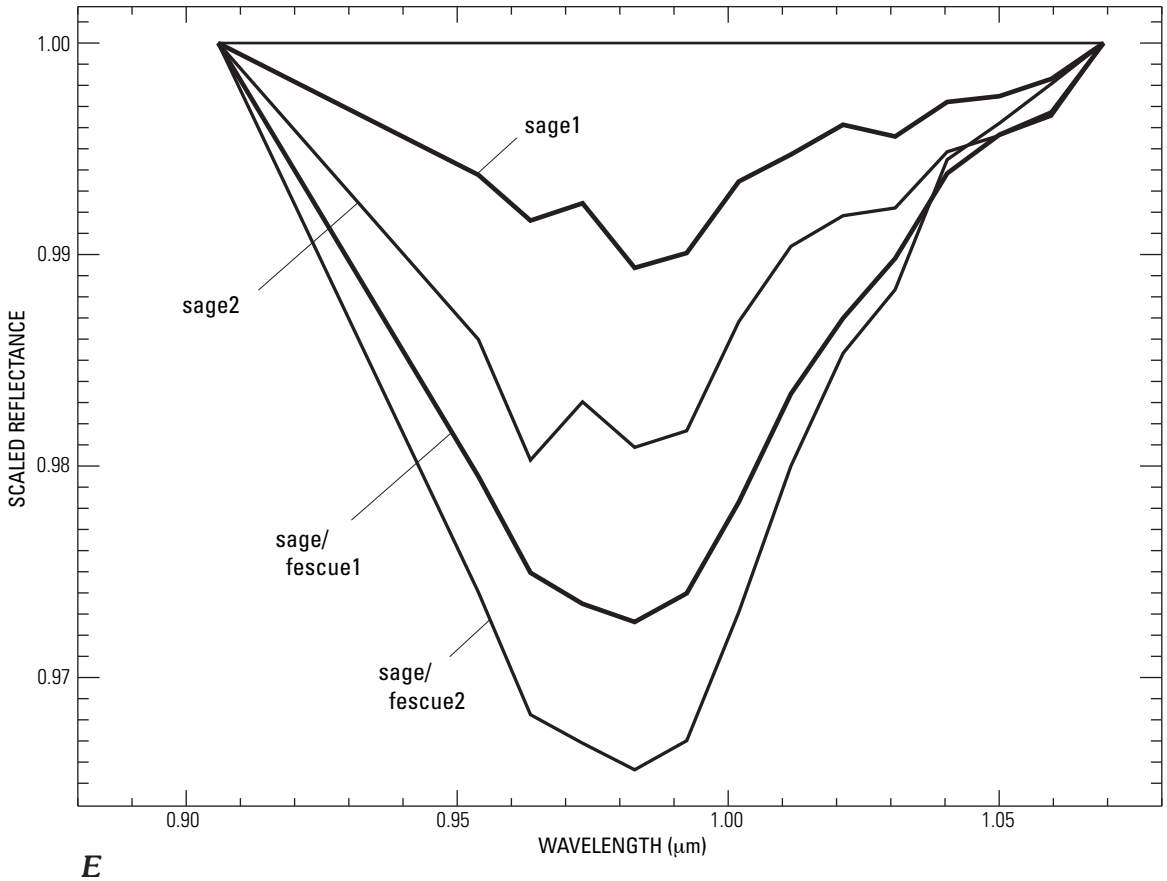

E

dominates the forest cover in the Grand Canyon of the Yellowstone River. Whitebark pine (WB) was mapped in high concentrations on the upper slopes of Mount Washburn. The mixed Engelmann spruce/subalpine fir category (SF) was present on the southern slopes of Mount Washburn at lower altitudes, and it was not present in such solid concentrations as were the other forest cover types. The high abundance of WB on the south and west slopes of Mount Washburn was confirmed by field surveys.

Overall, the distributions of forest cover types that were mapped using the Tetracorder system applied to the AVIRIS data agreed with existing maps that were compiled by Despain (1990) using aerial-photograph interpretation. Kokaly and others (2003) quantified this agreement at 74 percent (kappa statistic of 0.62). This agreement was remarkable, considering that the analytical methods of the two different types of remote-sensing data were different. In contrast to the spectral methods used here, aerial-photograph interpretation involved classification of the texture of the forest cover (including crown shapes, sizes, and shadowing). Comparison of the AVIRIS mapping results to interpreted aerial photographs revealed that the pixel-by-pixel nature of the spectral-analysis methods showed greater short-distance variation in forest cover. However, in general, the polygons drawn for different forest stands from the aerial photographs matched with the distributions derived from the AVIRIS data (compare Despain, 1990, to Kokaly and others, 2003). The distributions of whitebark pine also agreed with the expected altitude ranges of those forests; for example, whitebark pine is present at altitudes above 2,620 m (Despain, 1990). In the entire AVIRIS data set for Yellowstone National Park, whitebark pine rarely was mapped by the Tetracorder system at altitudes lower than this. The distribution of whitebark pine was confirmed in the Mount Washburn area along the trail from Dunraven Pass to the summit of Mount Washburn.

The map generated for the Mount Washburn area is used to assist in studying other parts of the Yellowstone geo-ecosystem. Whitebark pine was mapped along the slopes of Mount Washburn in areas where grizzly bears forage for food. The link between whitebark pine and grizzly bears is red squirrels, which store cones from the trees in middens; the middens are raided by grizzly bears in the fall (Mattson and others, 1992; Mattson and Reinhart, 1997). Future work in linking the AVIRIS-derived forest cover distributions with other data in a GIS analysis possibly will be useful for grizzly bear habitat delineation.

Nonforest Cover

The distributions of selected nonforest vegetation cover types for the Mammoth Hot Springs area, derived from the spectral analysis of AVIRIS data, are shown in figure 10. In this figure, the colored pixels representing the different nonforest cover types are overlaid on a gray-scale background image. Pixels that are covered by different types of vegetation or materials are depicted in gray scale. In general, white and light-gray pixels are bare ground, dark-gray pixels are forests,

Table 6. Characteristics of the 0.98-µm leaf-water-absorption feature for vegetation cover types of Yellowstone National Park.

Cover type (plot name)	Band center (µm)	Band depth	Continuum slope (μm^{-1})
	Forest		
Whitebark Pine	0.9827	0.1002	0.0658
Spruce/Fir	0.9827	0.0979	0.0765
Douglas Fir	0.9827	0.1172	0.1075
Lodgepole Pine - LP0	0.9827	0.0601	0.1430
Lodgepole Pine - LP1	0.9827	0.0813	0.1098
Lodgepole Pine - LP2	0.9827	0.0809	0.0944
Lodgepole Pine - LP3	0.9827	0.1074	0.0767
Lodgepole Pine - LP	0.9827	0.0712	0.1097
	Nonforest		
Sagebrush (sage1)	0.9827	0.0106	0.2627
Sagebrush (sage2)	0.9635	0.0197	0.1851
Sagebrush Steppe (sage/fescue1)	0.9827	0.0274	0.2238
Sagebrush Steppe (sage/fescue2)	0.9827	0.0344	0.2097
Grassland (fescue/wheatgrass1)	0.9827	0.0423	0.2418
Grassland (fescue/wheatgrass2)	0.9923	0.0093	0.2259
Grassland (fescue/wheatgrass3)	0.9923	0.0182	0.2926
Grassland (fescue/needlegrass)	0.9923	0.0221	0.2876
Grassland (bromus)	0.9923	0.0156	0.3524
Wet nonforest (willow/sedge)	0.9827	0.0509	0.1943
Wet nonforest (willow)	0.9827	0.0767	0.1586
Wet nonforest (sedge)	0.9635	0.0397	0.3195
Wet nonforest (cattail)	0.9731	0.1070	0.1518
Wet nonforest (wetland1)	0.9731	0.1063	-0.0459
Wet nonforest (wetland2)	0.9827	0.0595	0.2606

and black pixels are areas of water or deep shadows. Note that we chose not to represent all of the nonforest cover types in figure 10 in order to enhance the ability to see the depicted vegetation types in context. The other nonforest vegetation types that were identified, but not depicted, in this scene include the drier grassland vegetation types listed in table 2.

Figure 10 clearly shows where areas of sedge, willow, and wetland vegetation types are present. The riparian areas along Obsidian Creek and adjacent to Swan Lake show a mosaic pattern of dense willow stands (magenta pixels), mixed sedge and willow areas (red pixels), and areas of sedge and other wetland cover types listed in table 2 (yellow pixels). The Mammoth Hot Springs area also shows small patches of these relatively lush cover types. These patches are influenced by the geology and climate of this area. The extensive deposits of hot-spring travertine are easily penetrated by precipitation. The amount of precipitation is high in Yellowstone National Park, in part owing to the altitude of the volcanic plateaus. The precipitation likely filters through the porous travertine into depressions in the Mammoth area. The valley in which the Mammoth Hot Springs is located was shaped by glaciers that left a mosaic of depressions and mounds that concentrate water in certain areas. Similar glacial terrain on Mount Everts also is dotted with sedge and other wetland vegetation as well as small ponds. In contrast, on the rhyolitic volcanic plateau, shown in the southern two-thirds of the image in figure 10, wetland vegetation is present primarily along riparian corridors of streams.

Sagebrush shrub lands are present in two areas of the image in figure 10. Lower altitudes along the Gardner River west of Mammoth Hot Springs receive a relatively low amount of moisture compared to higher altitudes of the plateau. This climate favors growth of big sagebrush on the west slope of the Gardiner Canyon, as indicated by the results of the spectral analysis of the AVIRIS data (see blue pixels in fig. 10). At higher altitudes, near 2,194 m in the Gardner's Hole area in the vicinity of Swan Lake, the silver sagebrush cover type was mapped by the spectral analysis of the AVIRIS data (the center-left part of the image in fig. 10, also indicated by blue pixels).

Sagebrush shrub lands also were mapped in the image of the Lamar River valley (not pictured here; see Kokaly and others, 2003). At lower altitudes of the Lamar valley, pixels matched the spectra of the sage shrubland area. The higher slopes of the valley matched the areas with a higher percentage of grass relative to sagebrush (corresponding to entries of sage/fescue listed in table 1). In addition to the sagebrush cover types, much of Lamar River valley contains Idaho fescue grasslands that are mixed with

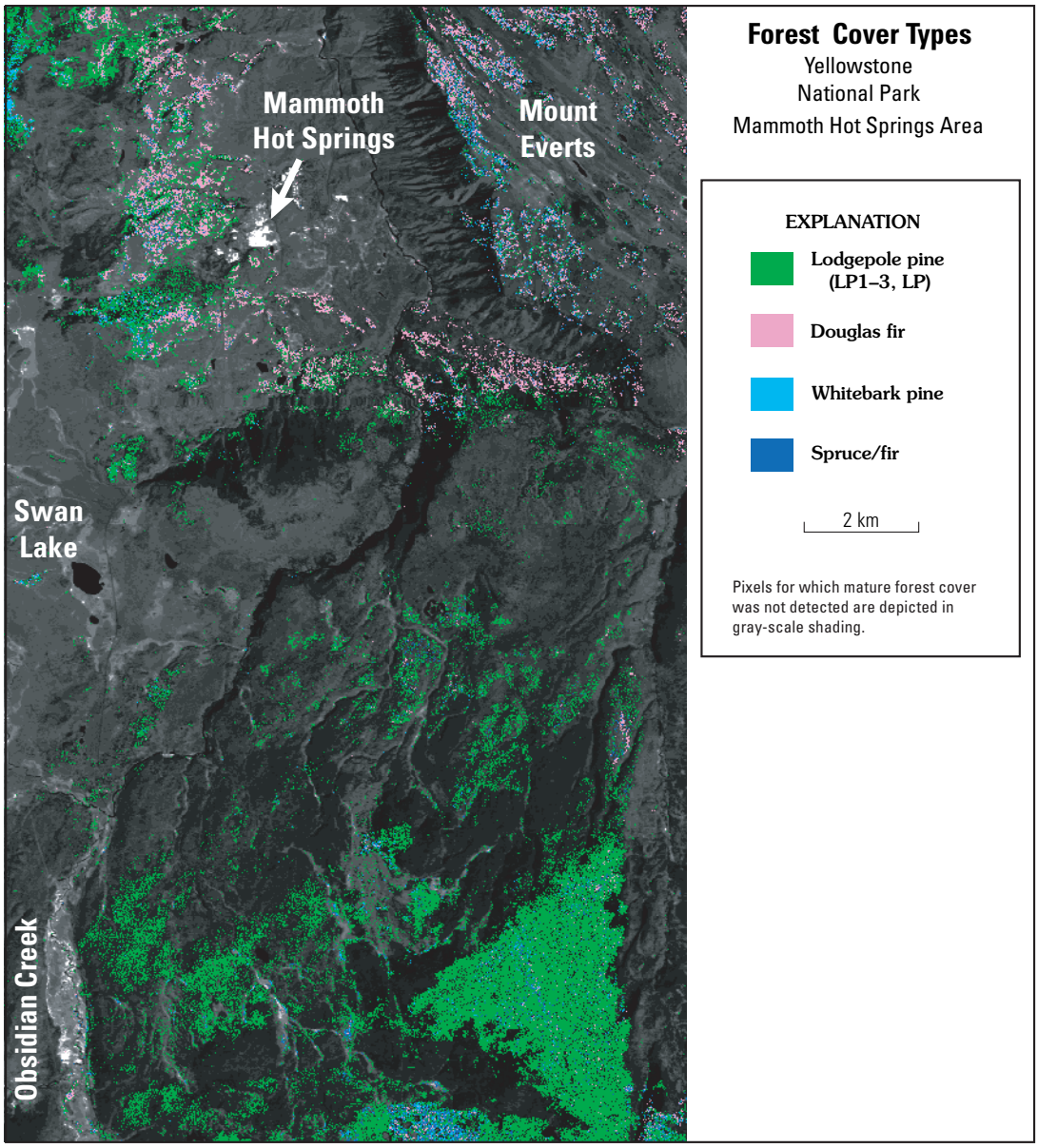

Figure 8. Map of forest cover types for the Mammoth Hot Springs area, Yellowstone National Park, derived from AVIRIS data using the USGS Tetracorder algorithm.

other grasses. Idaho fescue, Richardsons needlegrass, and bluebunch wheatgrass are mixed with the sagebrush at lower altitudes in the valley. At higher altitudes, Idaho fescue and bearded wheatgrass are prevalent. Two subcategories described by Despain (1990) of this grassland were distinguished: the drier, bearded wheatgrass phase (fescue/wheatgrass2) and the moist, sticky geranium phase (fescue/wheatgrass1). These two cover types are at higher altitudes in the scene compared to the other grasslands. These closely related cover types are near each other, but they have distinct boundaries. Possibly the undulating terrain in the valley affects the distribution of the wet phase, causing it to be present in depressions and in areas of greater snow accumulation that remain wetter throughout the year. The distribution of riparian vegetation types (willows, sedges, and wetlands) were primarily along streams and rivers, as expected. The distributions shown on the maps are reasonable, on the basis of coarse field surveys. These maps of nonforest cover types produced from AVIRIS data may be useful to assess winter-grazing resources for the large mammals in the Park, for example bison and elk. These maps, combined with other data, may contribute to a better understanding of the movements of mammal populations within and beyond Park boundaries.

Because nonforest vegetation changes drastically from season to season, the spectral signatures of the vegetation cover types derived from this specific flight do not necessarily have the same reflectance that will be recorded at different times of the year and in different years. For example, deciduous vegetation, such as willow, drops its leaves at the end of the fall and grows new ones in the spring. The number of leaves and their size and biochemical composition vary from year to year, thus altering the canopy reflectance. In addition, interannual variation in

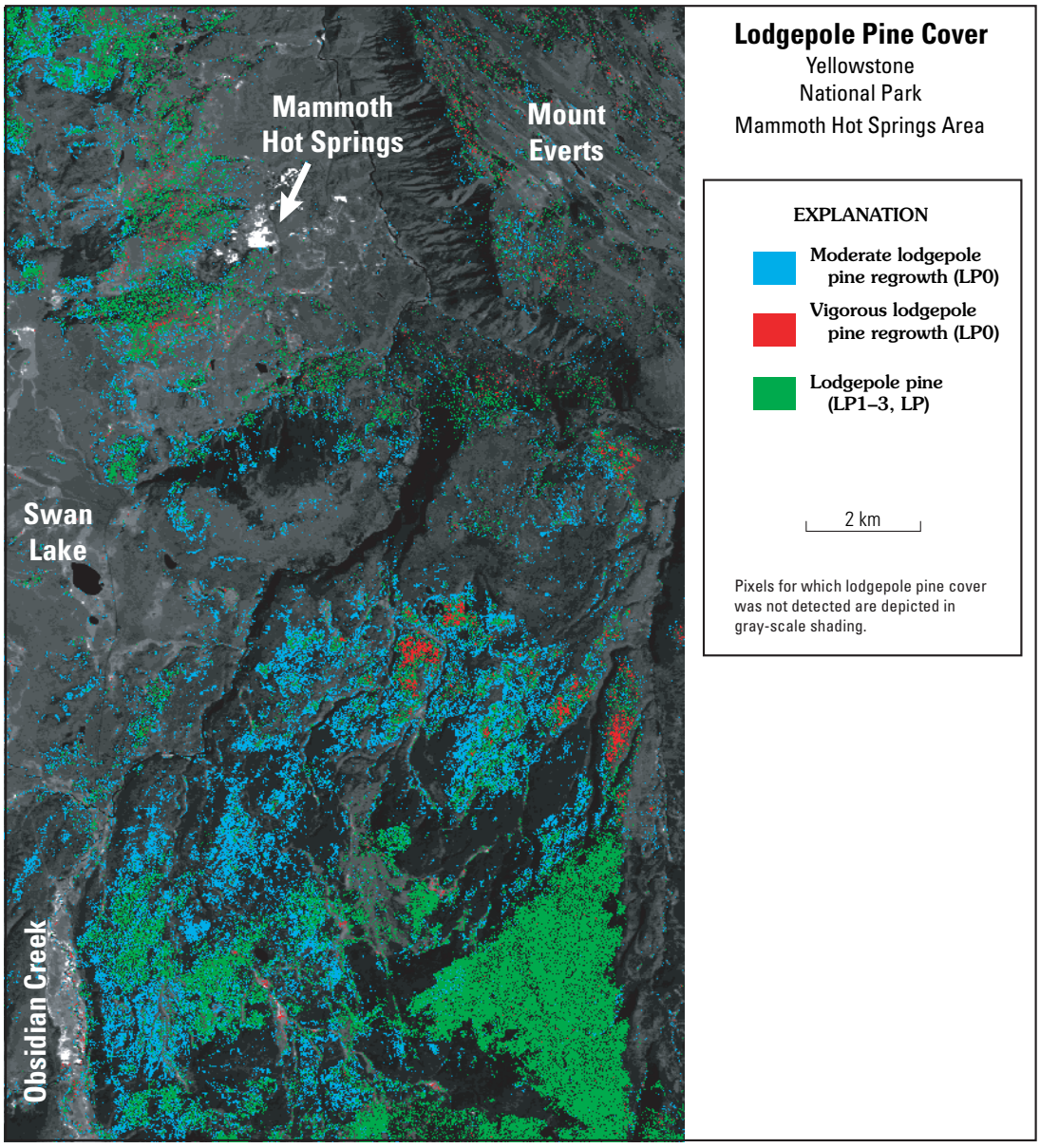

Figure 9. Map of lodgepole pine cover for the Mammoth Hot Springs area, Yellowstone National Park, derived from AVIRIS data using the USGS Tetracorder algorithm.

reflectance may result from local factors, such as precipitation or temperature, that affect the vegetation. Identification of vegetation cover types using additional AVIRIS data acquired in the future possibly will require creation of new entries in the spectral library for the nonforest areas.

The temporal changes of reflectance for evergreen conifer forests are less extreme than for other vegetation types. However, during the year, the conifers change. In the spring, reproductive bodies grow and new needles are produced (commonly a lighter shade of green). In the fall and winter, needles drop and the biochemical composition of the needles changes to produce substances that have antifreeze properties. Nonetheless, if annual flights are timed to occur at similar conditions, possibly areas derived from flights on one date will serve as a spectral library to map conifer cover types using AVIRIS data in following years.

Hot-Spring Microorganisms

The characteristic spectral signatures of hot-spring bacteria and algae in the AVIRIS remote-sensing data were used to map hot-spring microorganisms. Figure 11 shows the results for the Upper and Lower Geyser Basin areas of Yellowstone. The narrow chlorophyll-absorption and strong water-absorption features in the reflectance spectra of the hot-spring microorganisms (fig. 4) were not confused with the spectra of vegetation. For this scene, several different types of bacterial mats were used as reference entries in the spectral library that was used in the Tetracorder analysis. Most of the AVIRIS pixels that were mapped as containing hot-spring microorganisms had spectral signatures that matched a single entry in the library (see the bacteria spectrum in fig. 4). Because the conditions in which the microorganisms grow change over short lateral distances, it is likely that the 17.5-m resolution of the AVIRIS data was

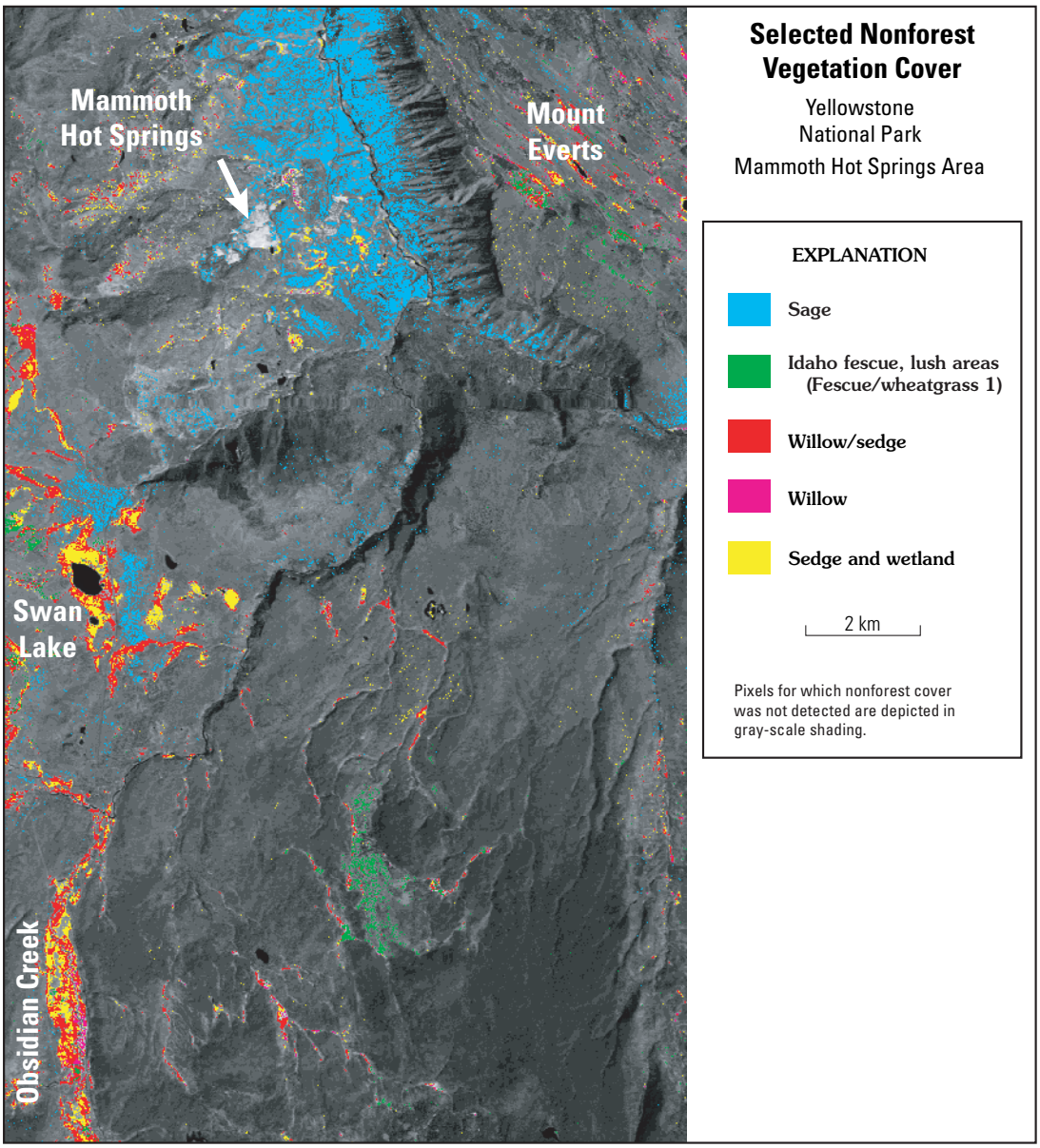

Figure 10. Map of selected nonforest cover types for the Mammoth Hot Springs area, Yellowstone National Park, derived from AVIRIS data using the USGS Tetracorder algorithm.

insufficient to resolve distinct bacterial communities. For such large pixels, each pixel potentially contains several different bacterial or algal communities, or both, in addition to surrounding vegetation and soil. Smaller pixel sizes will be more useful in identifying individual species and in defining their related environmental conditions in the hydrothermal areas.

Because each hot-spring microorganism requires specific conditions for its growing environment (for example, a narrow range of water temperature and pH; Brock, 1986), mapping the distribution of bacterial/algal mats with AVIRIS data may provide important information in the study of hydrothermal systems. Higher spatial resolution AVIRIS data (~2-m pixel size) were collected in 1998 for selected areas of the Park. These data revealed a greater diversity in reflectance signatures from microbial mats that are caused by changes in species composition (R.F. Kokaly, unpub. data). The data possibly will provide useful information for detailed study of the hot-spring bacterial and algal communities. In addition, multitemporal images could be used to study seasonal and long-term changes in the hydrothermal systems.

In Norris Geyser Basin, the maps of hot-spring microorganisms complement the information from the mineral maps made from AVIRIS (Livo and others, this volume). Maps created for both the minerals and the hot-spring microorganisms were compared. Together, these maps show the overall extent of the hydrothermal area. In some areas, the mineral signatures were weak, but the bacteria signature was very strong. Because thermophilic microorganisms live only in areas of moving hot water, we interpret those areas as having thriving microbial mats that cover the underlying material and mask the mineral signature in the reflectance spectra. Thus, use of the mineral and hot-spring-microorganisms maps in combination shows not only the overall extent of thermal areas, but also which parts had actively flowing water at the time of the AVIRIS flight.

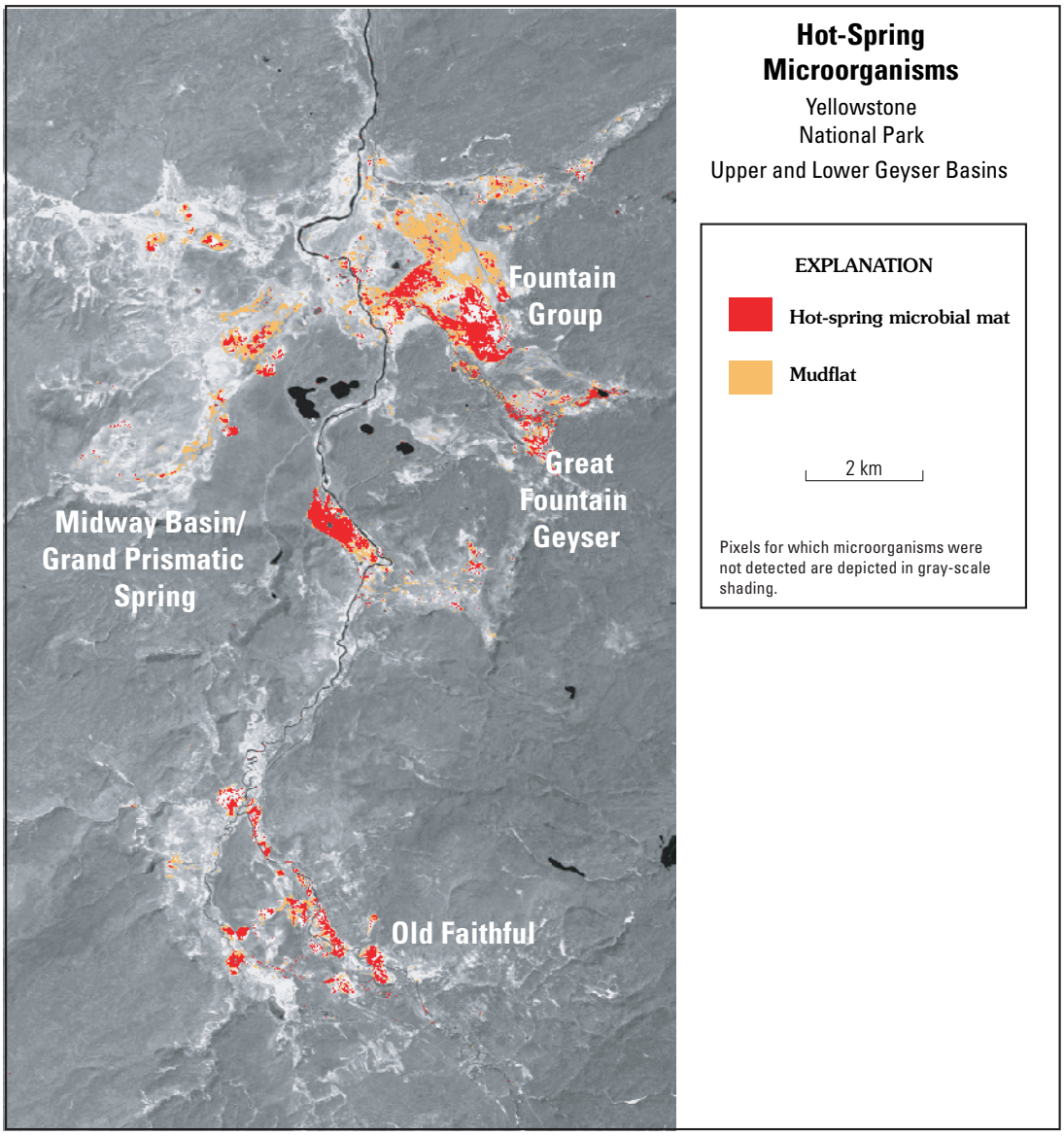

Figure 11. Map of microbial mats in the Upper and Lower Geyser Basins, Yellowstone National Park, derived from AVIRIS data using the USGS Tetracorder algorithm.

Conclusions

Airborne visible and infrared imaging spectrometer (AVIRIS) data calibrated to ground reflectance, a spectral library of vegetation reflectance, and the USGS Tetracorder system were used to produce maps of vegetation types in Yellowstone National Park. This spectroscopic approach to remote sensing included identification and mapping of forests of whitebark pine, Douglas fir, Engelmann spruce/subalpine fir, and lodgepole pine. Different age classes of lodgepole pine also were discriminated. Variations in the spectral signatures of lodgepole regrowth after the 1988 fires were observed. Representative spectra of these variations were used to differentiate and map moderate and vigorous regrowth of lodgepole pine. Nonforest vegetation types also were mapped using imaging spectroscopy, including sagebrush, wetlands, and various moisture regimes of grasslands. The chlorophyll- and water-absorption features in plant spectra were used in combination to successfully identify vegetation cover. The forest cover maps produced using Tetracorder agreed, in general, with aerial-photograph interpretations. A statistical analysis of these maps by Kokaly and others (2003) quantified the agreement at 74 percent. Field verification of vegetation cover maps also confirmed the results, including: (1) the identification of whitebark pine on the slopes of Mount Washburn, (2) mapping of Douglas fir and Engelmann spruce in the Mt. Everts area, and (3) detection of areas of vigorous lodgepole regrowth following the 1988 fires.

In this study, reflectance signatures of vegetation cover in Yellowstone National Park were created by averaging the spectra of AVIRIS pixels over known areas of vegetation. The conifers showed variation in the strengths and shapes of the pigment absorption at 0.68 μm and the leaf-water absorptions at 0.98 and 1.20 μm. The absorption strengths, as measured by

continuum-removed band depths, increased from the moderate absorption strengths in stands of lodgepole pine to the strongest absorption by Douglas fir forests. Reflectance signatures of lodgepole age classes showed variation in the near-infrared plateau region (0.7 to 1.3 μm), including increasing water absorption and decreasing continuum slope in young to middle age to old-growth stands.

Field reflectance measurements revealed a spectral signature of the hot-spring microorganisms that was distinct from the reflectance spectra of higher plants. Maps of hot-spring microorganisms were produced by comparing the field reflectance signature of bacteria to AVIRIS reflectance data. These microorganism maps complement the geologic information in mineral maps by showing areas where hot water is flowing on the surface. Future work will include efforts to discriminate and map individual species of bacteria and algae in the hydrothermal areas, in order to generate, indirectly, pH and temperature maps of hot springs. However, because bacterial and algal communities change markedly over short lateral distances, we suggest that high spatial-resolution-imaging-spectroscopy data will be even more effective for studying the hydrothermal areas.

Averaged AVIRIS spectra of vegetation canopies and field-measured-reflectance spectra of microbial mats both were compared to the spectra of AVIRIS pixels. The successful use of field spectra to map biologic materials required good calibration of AVIRIS data to surface reflectance. A combination of radiative-transfer modeling and a ground-calibration site was used. The calibrated AVIRIS data were of sufficient quality to match with laboratory measurements of minerals (Livo and others, this volume). Production of highly calibrated AVIRIS data in Yellowstone National Park in the future, during different seasons and at varying spatial resolutions, may establish the temporal consistency of canopy reflectance from conifer forest types. If the reflectance signatures of individual conifer types are consistent, the development of a set of reflectance spectra for use in mapping conifers in the northern Rocky Mountain region will be explored using the Tetracorder system and other algorithms that compare spectral shapes.

The versatility of imaging spectroscopy was demonstrated by its ability to address many issues with one data set: detection of hot-spring microorganisms, mapping of forest cover types, distinction of lodgepole pine age classes, and discrimination of nonforest vegetation types. The success of a spectral-feature-analysis approach in the remote sensing of vegetation was demonstrated. Specifically, the USGS Tetracorder system was used for normalization and comparison of spectral features. Other algorithms that focus on spectral-feature comparisons are expected to produce similar results. This analysis of AVIRIS data showed that recent advances in remote sensing, leading to the development of airborne-imaging spectrometers, have resulted in a tool applicable to the study of many parts of the Yellowstone ecosystem. In the future, additional airborne-spectrometer data should be acquired and analyzed to increase our understanding of the unique geologic features and biological systems of Yellowstone National Park.

Acknowledgments

The authors thank Ann Rodman, Ann Deutch, and the staff at Yellowstone National Park for help with research permits, field surveys, and for their enthusiastic support of our research efforts. We acknowledge Robert Green and the AVIRIS team at NASA/Jet Propulsion Laboratory for assistance in the planning and collection of AVIRIS data over Yellowstone National Park. This research was funded by the U.S. Geological Survey under the Yellowstone Project of the Mineral Resources Program.

References Cited

Adams, J.B., Smith, M.O., and Gillespie, A.R., 1993, Imaging spectroscopy—Interpretation based on spectral mixture analysis, *in* Pieters, C.M., and Englert, P.A., eds., Remote geochemical analysis—Elemental and mineralogical composition: Cambridge, Cambridge University Press, p.145–166.

Asner, G.P., and Lobell, D.B., 2000, A biogeophysical approach for automated SWIR unmixing of soils and vegetation: Remote Sensing of Environment, v. 74, p. 99–112.

Boardman, J.W., and Goetz, A.F.H., 1991, Sedimentary facies analysis using AVIRIS data—A geophysical inverse problem, *in* Green, R.O., ed., Proceedings of the third airborne visible/infrared imaging spectrometer (AVIRIS) workshop: Pasadena, NASA Jet Propulsion Laboratory Publication, v. 91-28, p. 4–14.

Brock, T.D., 1986, Thermophiles—General molecular and applied microbiology: New York, Wiley and Sons, 316 p.

Brock, T.D., 1994, Life at high temperatures—Yellowstone National Park, Wyoming: Yellowstone Association for Natural Science, History, and Education, Inc., 31 p.

Choquette, S.J., Travis, J.C., and Duewer, D.L., 1998, SRM 2035—A rare earth oxide glass for the wavelength calibration of near infrared dispersive and Fourier transform spectrometers, *in* Conference on optical diagnostic methods for inorganic transmission materials, 1998, Proceedings: Bellingham, Wash., International Society for Optical Engineering, v. 3425, p. 94–102.

Clark, R.N., 1981, Water, frost, and ice—The near-infrared spectral reflectance 0.65–2.5 μm: Journal of Geophysical Research, v. 89, p. 6,329–6,340.

Clark, R.N., 1999, Spectroscopy of rocks and minerals and principles of spectroscopy, *in* Rencz, A.N., ed., Remote sensing for the earth sciences—Manual of remote sensing (3d ed.), volume 3: New York, Wiley and Sons, p. 3–58.

Clark, R.N., Gallagher, A.J., and Swayze, G.A., 1990, Material absorption band depth mapping of imaging spectrometer data using a complete band shape least-squares fit with library reference spectra, *in* Green, R.O., ed., Proceedings of the second airborne visible/infrared imaging spectrometer (AVIRIS) workshop: Pasadena, NASA Jet Propulsion Laboratory Publication, v. 90-54, p. 176–186.

Clark, R.N., and Roush, T.L., 1984, Reflectance spectroscopy—Quantitative analysis techniques for remote sensing applications: Journal of Geophysical Research, v. 89, p. 6,329–6,340.

Clark, R.N., and Swayze, G.A., 1995, Mapping minerals, amorphous materials, environmental materials, vegetation, water, ice and snow, and other materials—The USGS Tricorder algorithm, *in* Green, R.O., ed., Summaries of the fifth annual NASA Jet Propulsion Laboratory airborne earth science workshop: Pasadena, NASA Jet Propulsion Laboratory Publication, v. 95-1, p. 39–40.

Clark, R.N., Swayze, G.A., Gallagher, A.J., Gorelick, N., and Kruse, F.A., 1991, Mapping with imaging spectrometer data using the complete band shape least-squares algorithm simultaneously fit to multiple spectral features from multiple materials, *in* Green, R.O., ed., Proceedings of the third airborne visible/infrared imaging spectrometer (AVIRIS) workshop: Pasadena, NASA Jet Propulsion Laboratory Publication, v. 91-28, p. 2–3.

Clark, R.N., Swayze, G.A., Heidebrecht, K.B., Goetz, A.F.H, and Green, R.O., 1993, Comparison of methods for calibrating AVIRIS data to ground reflectance, *in* Green, R.O., ed., Summaries of the fourth annual NASA Jet Propulsion Laboratory airborne earth science workshop: Pasadena, NASA Jet Propulsion Laboratory Publication, v. 93-26, p. 31–34.

Clark, R.N., Swayze, G.A., Livo, K.E., Kokaly, R.F., Sutley, S.J., Dalton, J.B., McDougal, R.R., and Gent, C.A., 2003, Imaging spectroscopy—Earth and planetary remote sensing with the USGS Tetracorder and expert system: Journal of Geophysical Research, v. 108 (E12), p. 5,131.

Clark, R.N., Swayze, G.A., Livo, K.E., Kokaly, R.F., King, T.V.V., Dalton, J.B., Vance, J.S., Rockwell, B.W., Hoefen, T., and McDougal, R.R., in press, Surface reflectance calibration of terrestrial imaging spectroscopy data—A tutorial using AVIRIS, *in* Green, R.O., ed., Proceedings of the 11th JPL airborne sciences workshop: Pasadena, NASA Jet Propulsion Laboratory Publication.

Despain, D.G., 1990, Yellowstone vegetation—Consequences of environment and history in a natural setting: Santa Barbara, Roberts Rinehart Publishers, 239 p.

Elvidge, D.E., 1990, Visible and near infrared reflectance characteristics of dry plant materials: Remote Sensing of Environment, v. 11, p. 1,775–1,795.

Gamon, J.A., Field, C.B., Roberts, D.A., Ustin, S.L., and Valentini, R., 1993, Functional patterns in an annual grassland during an AVIRIS overflight: Remote Sensing of Environment, v. 44, p. 239–253.

Gao, B.C., Heidebrecht, K.B., and Goetz, A.F.H., 1993, Derivation of scaled surface reflectance from AVIRIS data: Remote Sensing of Environment, v. 44, p. 165–178.

Gao, B.C., Heidebrecht, K.B., and Goetz, A.F.H., 1997, Atmosphere removal program (ATREM), Version 3.0 user's guide: Boulder, University of Colorado, Center for the Study of Earth from Space, 27 p.

Green, R.O., Eastwood, M.L., Sarture, C.M., Chrien, T.G., Aronsson, M., Chippendale, B.J., Faust, J.A., Pavri, B.E., Chovit, C.J., Solis, M., Olah, M.R., and Williams, O., 1998, Imaging spectroscopy and the airborne visible/infrared imaging spectrometer (AVIRIS): Remote Sensing of Environment, v. 65, p. 227–248.

Howard, J.A., 1991, Remote sensing of forest resources—Theory and application: New York, Chapman and Hall, 420 p.

Huete, A.F., Justice, C., and van Leeuwen, W., 1999, MODIS vegetation index (MOD 13) algorithm theoretical basis document, Version 4: NASA Goddard Space Flight Center Technical Report, available at http://eospso.gsfc.nasa.gov/atbd/modistables.html.

Ingle, J.D., 1988, Spectrochemical analysis: Engelwood Cliffs, N.J., Prentice-Hall, 590 p.

Jakubauskas, M.E., 1996, Thematic mapper characterization of lodgepole pine seral stages in Yellowstone National Park, USA: Remote Sensing of Environment, v. 56, p. 118–132.

King, T.V.V., Clark, R.N., and Swayze, G.A., 2000, Applications of imaging spectroscopy data—A case study at Summitville, Colorado, *in* Kuehn, F., King, T.V.V., Hoerig, B., and Peters, D.C., eds., Remote sensing for site characterization: New York, Springer, p. 164–185.

Kokaly, R.F., 2001, Investigating a physical basis for spectroscopic estimates of leaf nitrogen concentration: Remote Sensing of Environment, v. 75, p. 153–161.

Kokaly, R.F., and Clark, R.N., 1999, Spectroscopic determination of leaf biochemistry using band-depth analysis of absorption features and stepwise multiple linear regression: Remote Sensing of Environment, v. 67, p. 267–287.

Kokaly, R.F., Clark, R.N., and Livo, K.E., 1998, Mapping the biology and mineralogy of Yellowstone National Park using imaging spectroscopy, *in* Green, R.O., ed., Summaries of the seventh annual NASA Jet Propulsion Laboratory airborne earth science workshop: Pasadena, NASA Jet Propulsion Laboratory Publication, v. 97-21, p. 245–254.

Kokaly, R.F., Despain, D.G., Clark, R.N., and Livo, K.E., 2003, Mapping vegetation in Yellowstone National Park using spectral feature analysis of AVIRIS data: Remote Sensing of Environment, v. 84, p. 437–456.

Martin, M.E., Newman, S.D., Aber, J.D., and Congalton, R.G., 1998, Determining forest species composition using high spectral resolution remote sensing data: Remote Sensing of Environment, v. 65, p. 249–254.

Mattson, D.J., and Reinhart, D.P., 1997, Excavation of red squirrel middens by grizzly bears in the whitebark pine zone: Journal of Applied Ecology, v. 34, p. 926–940.

Mattson, D.J., Blanchard, B.M., and Knight, R.R., 1992, Yellowstone grizzly bear mortality, human habituation, and whitebark pine seed crops: Journal of Wildlife Management, v. 56, p. 432–442.

Mustard, J.F., and Pieters, C.M., 1987, Abundance and distribution of ultramafic microbreccia in Moses Rock dike—Quantitative applications of imaging spectrometer data: Journal of Geophysical Research, v. 94, p. 13,619–13,634.

Mustard, J.F., and Sunshine, J.M., 1999, Spectral analysis for earth science investigation, *in* Rencz, A.N., ed., Remote sensing for the earth sciences—Manual of remote sensing (3d ed.), volume 3: New York, Wiley and Sons, p. 251–306.

Peterson, D.L., and Hubbard, G.S., 1992, Scientific issues and potential remote sensing requirements for plant biogeochemical content: Journal of Imaging Science and Technology, v. 36, p. 445–455.

Roberts, D.A., Gardner, M., Church, R., Ustin, S., Scheer, G., and Green, R.O., 1998, Mapping chaparral in the Santa Monica Mountains using multiple endmember spectral mixture models: Remote Sensing of Environment, v. 65, p. 267–279.

Rockwell, B.W., Clark, R.N., Livo, K.E., McDougal, R.R., and Kokaly, R.F., 2002, AVIRIS data calibration information—Wasatch Mountains and Park City region, Utah: U.S. Geological Survey Open-File Report 02-199, 12 p.

Sunshine, J.M., and Pieters, C.M., 1993, Estimating modal abundance from the spectra of natural and laboratory pyroxene mixtures using the modified Gaussian model: Journal of Geophysical Research, v. 98, p. 9,075–9,087.

Sunshine, J.M., Pieters, C.M., and Pratt, S.F., 1990, Deconvolution of mineral absorption bands—An improved approach: Journal of Geophysical Research, v. 95, p. 6,955–6,966.

Swayze, G.A., Smith, K.S., Clark, R.N., Sutley, S.J., Pearson, R.M., Vance, S.J., Hageman, P.L., Briggs, P.H., Meier, A.L., Singelton, M.J., and Roth, S., 2000, Using imaging spectroscopy to map acid mine waste: Environmental Science and Technology, v. 34, p. 47–54.

Teillet, P.M., Staenz, K., and Williams, D.J., 1997, Effects of spectral, spatial, and radiometric characteristics on remote sensing vegetation indices of forested regions: Remote Sensing of Environment, v. 61, p. 139–149.

Van der Meer, F., and Bakker, W., 1997, CCSM—Cross correlogram spectral matching: International Journal of Remote Sensing, v. 18, p. 1,197–1,201.

Vane, G., Duval, J.E., and Wellman, J.B., 1993, Imaging spectroscopy of the Earth and other solar system bodies, *in* Pieters, C.M., and Englert, P.A., eds., Remote geochemical analysis—Elemental and mineralogical composition: Cambridge, Cambridge University Press, p.121–143.

Hydrothermally Altered Rock and Hot-Spring Deposits at Yellowstone National Park—Characterized Using Airborne Visible- and Infrared-Spectroscopy Data

By K. Eric Livo, Fred A. Kruse , Roger N. Clark, Raymond F. Kokaly, and W.C. Shanks, III

Chapter O *of*
Integrated Geoscience Studies in the Greater Yellowstone Area—Volcanic, Tectonic, and Hydrothermal Processes in the Yellowstone Geoecosystem
Edited by Lisa A. Morgan

Professional Paper 1717

U.S. Department of the Interior
U.S. Geological Survey

Contents

Abstract 493
Introduction 493
Methods 493
Spectral Identification of Minerals 493
    USGS Methods 494
    Analytical Imaging and Geophysics Methods 494
Geologic Structure, Volcanic History, and Geologic Setting 494
Alteration Minerals 494
Hydrothermal Waters 494
Hyperspectral Remote Sensing 495
Mapping Results 496
    Upper, Midway, and Lower Geyser Basins 497
    Norris Geyser Basin 498
    Roaring Mountain 499
    Grand Canyon of the Yellowstone River 499
    Mammoth Hot Springs 506
Conclusions 506
References Cited 506

Figures

1. Schematic cross section of USGS mineral deposit model 25b 495
2–3. Mineral spectra for:
    2. Clay minerals, calcite, alunite, and siliceous sinter 496
    3. Iron-bearing minerals 497
4. 1996 AVIRIS maps 498
5–9. Mineral maps:
    5. Upper Geyser Basin 500
    6. Lower, Midway, and Upper Geyser Basins 501
    7. Norris Geyser Basin and Roaring Mountain 502
    8. Grand Canyon of the Yellowstone River 503
    9. Mammoth Hot Springs 505

Hydrothermally Altered Rock and Hot-Spring Deposits at Yellowstone National Park—Characterized Using Airborne Visible- and Infrared-Spectroscopy Data

By K. Eric Livo,[1] Fred A. Kruse ,[2] Roger N. Clark,[1] Raymond F. Kokaly,[1] and W.C. Shanks, III[1]

Abstract

The hydrothermal system in Yellowstone National Park has created altered rock and hot-spring deposits that were mapped using AVIRIS (airborne visible and infrared imaging spectrometer) data. The mapped minerals are indicative of the geologic processes and environments that controlled their formation. Ongoing volcanic activity is expressed at the surface by geothermal features, earthquakes, and geologically recent caldera formation. Precipitated minerals such as siliceous sinter and travertine on the surface are derived from chloride-rich alkaline solutions that are leaching silica and calcite from the underlying country rock. Siliceous sinter and montmorillonite are associated with hydrothermal systems abundant in hot water, whereas kaolinite and alunite are associated with acidic-vapor-dominated hydrothermal systems.

Introduction

Remotely sensed data are used to map hydrothermally altered rock and hot-spring deposits in Yellowstone National Park (the Park). The airborne imaging-spectroscopy data contain spectra of reflected light that record absorption features that are unique to the surface materials from which sunlight is reflected. Analysis of these features permits identification of the mineralogy of some surface soils and bedrock lithologies.

Hydrothermal-water chemistry and bedrock lithologies can be inferred from the types of minerals on the land surface. Researchers have extensively studied water chemistry in Yellowstone National Park and the associated altered minerals that form within the hydrothermal cells. This report links the observed altered rock, identified from imaging-spectroscopy data, with the underlying geological processes, and it associates mineral trends with fracture systems.

[1]U.S. Geological Survey, Denver Box 25046, M.S. 973, Denver Federal Center, Denver CO 80225.

[2]Horizon GeoImaging, LLC, 4845 Pearl East Circle, Suite 101, Boulder, CO 80301.

Methods

Remotely sensed data were collected using NASA's Jet Propulsion Laboratory airborne visible and infrared imaging spectrometer (AVIRIS) in the late summer of 1996 and fall of 1998. Data were collected at a pixel-spatial resolution of 20 m in most of the Park (in 1996) and at a pixel-spatial resolution of 2×6 m at selected sites (in 1998). Both data sets have 224 continuous spectral channels ranging from 0.4 to 2.5 micrometers (μm). Minerals were spectrally identified using the U.S. Geological Survey (USGS) Tetracorder program (Clark and others, 1990, 1991, 2003; Clark, Swayze, and Gallagher, 1993; Clark and Swayze, 1995; Rockwell and others, 1999) and methods developed by Analytical Imaging and Geophysics (AIG) (Kruse and others, 1996; Boardman, 1997, 1998; Kruse, 1998, 1999). USGS processing utilized a custom goodness-of-fit spectral-analysis routine, whereas AIG processing characterized "pure" spectral end-members (Kruse and others, 1993; Kruse, 1998, 1999) using the Environment for Visualizing Images (ENVI) software (Research Systems, Inc., Boulder, Colo.). Both analysis techniques use spectral libraries for initial material identification. Hyperspectral-mapping methods were then used to determine the occurrence and abundance of specific materials. These data were then field-checked to ensure correct identification.

Spectral Identification of Minerals

Spectral identification of minerals is accomplished by using diagnostic absorption features within the measured light spectrum. Every pixel in the image has a measured spectrum that can be visually or mathematically analyzed, comparing the pixel-spectral features against known mineral-spectral features. A variety of techniques exist for this analysis. We used the USGS Tetracorder method, in which the spectral features of an image pixel are compared to data from a mineral-spectral library, and we also used the AIG ENVI end-member method to identify unique spectral end-members.

USGS Methods

AVIRIS data were converted from radiance to reflectance and then calibrated to absolute reflectance relative to ground. This two-step process is described in Clark, Swayze, Heidebrecht, and others (1993). The first step uses the atmospheric-removal algorithm (ATREM) (Gao and others, 1997) to remove atmospheric effects of solar irradiance, atmospheric absorption, and atmospheric scattering and then converts the data from radiance to reflectance. In the second step, residual atmospheric absorptions were removed by calibrating the data against field data measured with a hand-held spectrometer at a calibration site.

Spectral-feature analysis was then used to identify minerals in the image. The USGS Tetracorder program (Clark and others, 2003) was used for initial processing and identification. This program tests band-absorption features from the image-pixel spectra against known mineral-absorption features from the USGS mineral library using a goodness-of-fit algorithm. Multiple (continuum-removed) absorption features for each spectrum are used concurrently to generate a weighted average for spectral goodness-of-fit, band depth, and fit × depth. Defined thresholds for each value must be exceeded. The mineral-library spectrum with the highest goodness-of-fit value is selected for initial identification for each pixel. Image pixels containing abundant vegetation are masked. Visual analysis and iterative processes that vary internal tetracorder parameters and add new mineral spectra to the spectral library are used to create the final mineral identifications (the mineral maps).

Analytical Imaging and Geophysics Method

Spectral-feature analysis using the AIG method began with calibrated AVIRIS data derived from ATREM. Artifacts were removed using the AIG program "Effort," which performs a statistical running average. No field calibration was performed. ENVI software was used to derive end-member spectra using standard minimum-noise (statistical) derivatives. Mineral identification of the end-member spectra used mineral-library-classification routines within ENVI and visual interpretation of the end-member spectra.

Geologic Structure, Volcanic History, and Geologic Setting

The Yellowstone National Park region was the locus of three large caldera-forming volcanic eruptions during the last 2.1 million years. Widespread airborne volcanic ash and lava flows cover much of the present land surface from these and later eruptions. Volcanic activity is ongoing, and heat flow is 30 times greater than the continental average (Smith and Braile, 1993). The volcanism is associated with intensive earthquake activity (Smith and Braile, 1993) that drives the geothermal system; it continually opens and reopens radial- and concentric-fracture systems, thus maintaining local fluid pathways.

One hypothesis is that the volcanic activity is a result of the North American crustal plate overriding a hot-spot mantle plume. The volcanic lavas and ash deposits overlie crustal sedimentary, igneous, and metamorphic rocks. Two important rock types that influence the mineral-alteration assemblages in the region are the widespread quartz-rich rhyolite flows that underlie many of the geyser basins and the limestone that underlies the terraces at Mammoth Hot Springs.

Alteration Minerals

Figure 1 (from Mosier and others, 1986) shows a cross-section model (Creede system) illustrating the alteration pattern that is typical for acid-sulfate hydrothermal-vein systems such as those in Yellowstone National Park. This model illustrates the fluid channelways that allow ascending hot water to react with the wallrock, altering the existing minerals. Quartz, adularia, illite, and sulfides, with or without kaolinite, are formed at depth, whereas quartz, kaolinite, and alunite are formed near the surface. White and others (1975) drilled and cored several geyser basins and identified a similar distribution of minerals within the acid-sulfate system at Porcelain Terrace in Norris Geyser Basin. At depths of 600 to 1,000 ft, mixed-layer illite-montmorillonite with pyrite was present; from 200 to 600 ft, kaolinite, sparse montmorillonite, cristobalite, chalcedony, goethite, and sanidine were present; and from the surface to a depth of 200 ft, alunite, kaolinite, cristobalite, and sanidine were present.

Hydrothermal Waters

Water chemistry is a controlling factor in determining the species of mineral alteration. White and others (1988) extensively drilled and cored Norris, Lower, and Upper Geyser Basins. They determined water-chemistry changes with depth, and they associated mineral-alteration species with water chemistry. They identified four types of water. Type-1 water is of neutral pH and is chloride-silica rich; it has altered the mafic minerals in rhyolite country rock to goethite, hematite, and chalcedony and has changed plagioclase to siliceous sinter and montmorillonite. Type-2 water is formed from vapor-dominated gas and has less chloride than the other water types. Near the surface, type-2 water is acidified by oxidation of hydrogen sulfide; it is then recirculated and reheated within 100 ft of the surface. Type-2 water bleaches the surrounding country rock, leaches ferric oxides, and creates montmorillonite, illite, and chlorite. Type-3 water is acid-chloride-sulfate rich and

is generated by restricted flow of neutral pH, chloride-silica-rich water that combines with sulfur and rain and snowmelt surface water. Type-3 water bleaches the country rock, leaching all ferric oxides. Type-4 water is acid-sulfate rich, low in chloride, and is generated above a boiling water table where steam combines with hydrogen sulfide gas to yield restricted, hot, low-pH water. Type-4 water bleaches the country rock, leaches ferric oxides, and alters potassium feldspar and sanidine to kaolinite, opal, and cristobalite. Type-4 water forms mixed-layer clay minerals—montmorillonite is dominant at temperatures lower than 198°C; mixed-layer montmorillonite-illite is dominant between 198°C and 238°C; and illite is dominant at temperatures higher than 238°C (White and others, 1988).

Chloride-rich siliceous sinter deposited by type-1 water is widespread in Upper and Lower Geyser Basins, on the basin floor at Norris Geyser Basin, and in the Hayden River valley. Acid-sulfate deposits are common at Roaring Mountain, in the Grand Canyon of the Yellowstone River, and at higher elevations at Norris Geyser Basin. The near-surface alunite environment was characterized by White and others (1988) and Thompson (1991) as containing chalcedony and porous opaline sinter, sulfur, and cristobalite that formed from decomposed rhyolite—all associated with sulfurous gases and aqueous vapors emitted from ground fissures.

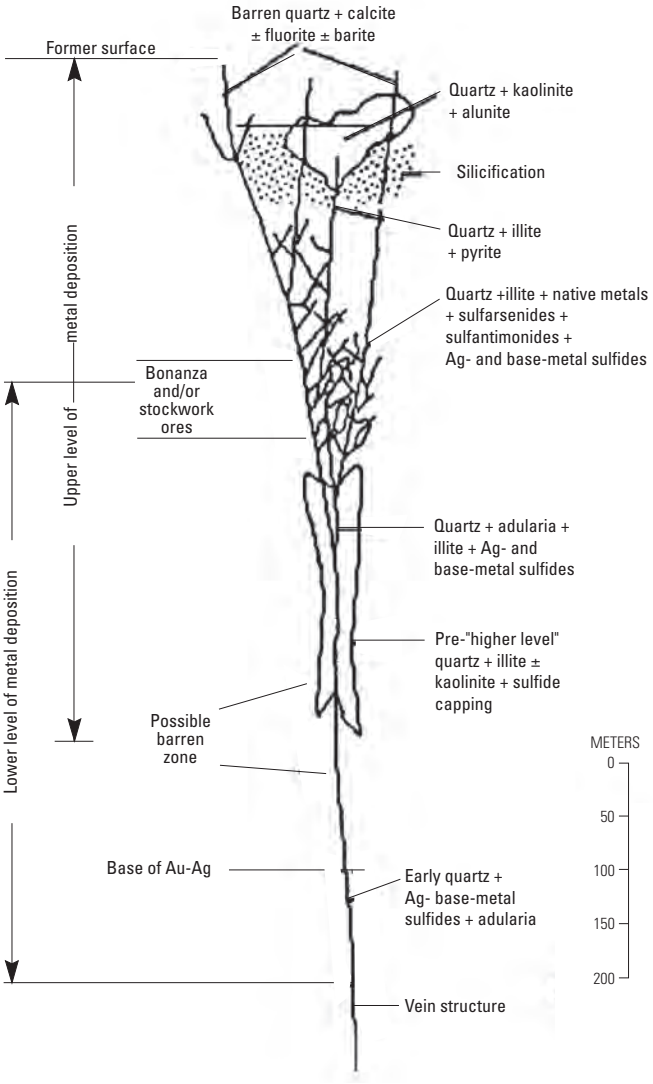

Figure 1. Schematic cross section of USGS mineral deposit model 25b. This interpretive model for the Creede caldera system exhibits the alteration pattern typical for acid-sulfate systems (from Mosier and others, 1986).

Hyperspectral Remote Sensing

The AVIRIS imaging-spectrometry data contains 224 channels measured from the edge of the ultraviolet through the visible and into the near-infrared wavelengths of light. Each data channel (wavelength interval or band) forms an image of the Earth's surface as an array of pixels, with all data channels coregistered to each other. Each pixel (geographic location in the image) contains a spectrum formed from the 224 channels of data.

Spectral identification of minerals uses diagnostic absorption features within the measured light spectrum. Absorption features have band-center wavelengths, band depths, and band shapes that can be used to characterize every mineral. When these features are unique, they identify specific minerals, such as kaolinite, montmorillonite, and alunite. When these features are shared by several minerals (as in illite, sericite, and muscovite) or mineral combinations, they differentiate a spectral group of minerals. These absorption features are the result of the way molecular bands interact with incident light within the mineral. They indicate compositional differences in the minerals, but not structural differences.

Spectral abundance of a mineral may be qualitatively characterized using the intensity of its absorption-feature band depth. Quantitative measurements require knowledge of mineral-grain sizes, exact mineral-mixture proportions, and mineral chemical compositions and ion substitutions, all of which must be characterized in the laboratory.

Examples of spectra for several minerals in the Yellowstone hot-spring environments are shown in figures 2 and 3. Figure 2 shows the spectra for clay minerals, calcite, alunite, and siliceous sinter. The unique absorption features of interest generally are in the 2.2- to 2.4-μm-wavelength region. Siliceous sinter, as used here, is a spectral group of SiO_2 minerals including opal, chalcedony, and cristobalite derived from hydrothermal fluids and (or) the decomposition of rhyolite. The identification of these minerals uses a hydration-absorption feature that is present in some silica at the 2.2- to 2.4-μm-wavelength region. Quartz does not have this absorption feature; therefore it is not readily identified within AVIRIS wavelengths. Figure 3 shows the spectra for iron oxide (hematite), iron hydroxide (goethite), and iron sulfate (jarosite). Shifts in the absorption-feature minima of these

minerals in the 0.5- to 0.6-µm region are responsible for the colors of minerals as the eye sees them—yellow (jarosite), brown (goethite), and red (hematite). Other features used for identification are in the 0.42- and 0.9-µm wavelengths.

A partial sequence of the mineralization, identified by White and others (1975) and Keith and others (1978) using drill-core and water-chemistry studies, was spatially mapped using the imaging-spectroscopy data for surface exposures along the Firehole River (Upper, Midway, and Lower Geyser Basins), at Roaring Mountain, in the Grand Canyon of the Yellowstone River, and in parts of Norris Geyser Basin. The association of mineralization, identified by White and others (1975), with spectrally mapped areas of mineralization, links the geochemistry identified in past studies with our present results. Kaolinite and alunite were mapped at the tops of active hydrothermal systems and along the canyon rim of the Yellowstone River, whereas illite and montmorillonite were mapped on the lower walls of the canyon. Iron oxides were mapped in minor amounts throughout the Park, except for the Yellowstone canyon, where they are present in massive, complex combinations of hematite and goethite in association with the iron-sulfate mineral jarosite.

Mapping Results

The mapping results were verified; limited field-checking during a 2-week field excursion indicated very good agreement between the geology and the maps. The Upper, Lower, and Norris Geyser Basins, Mammoth Hot Springs, and the west end of the rim of the Grand Canyon of the Yellowstone River were examined in the field. The canyon walls and the northeast end of the Yellowstone Grand Canyon were not examined. The field verification included examination of hand-held samples and spectral field measurements using an ASD (analytical spectral devices) field spectrometer. Several dozen samples were brought to the laboratory for further spectral characterization. Results also were checked by examining spectra from the AVIRIS data over areas of known mineralization and over mineral locations identified through our mapping algorithms.

Several mineral groups were mapped, and specific minerals were identified. Kaolinite-family clay minerals are grouped, although minor spectral differences exist. The illite/sericite/muscovite spectral group is mapped as a general clay-mineral unit whose mineral members are spectrally indistinguishable and are referred to as illite. Two types of

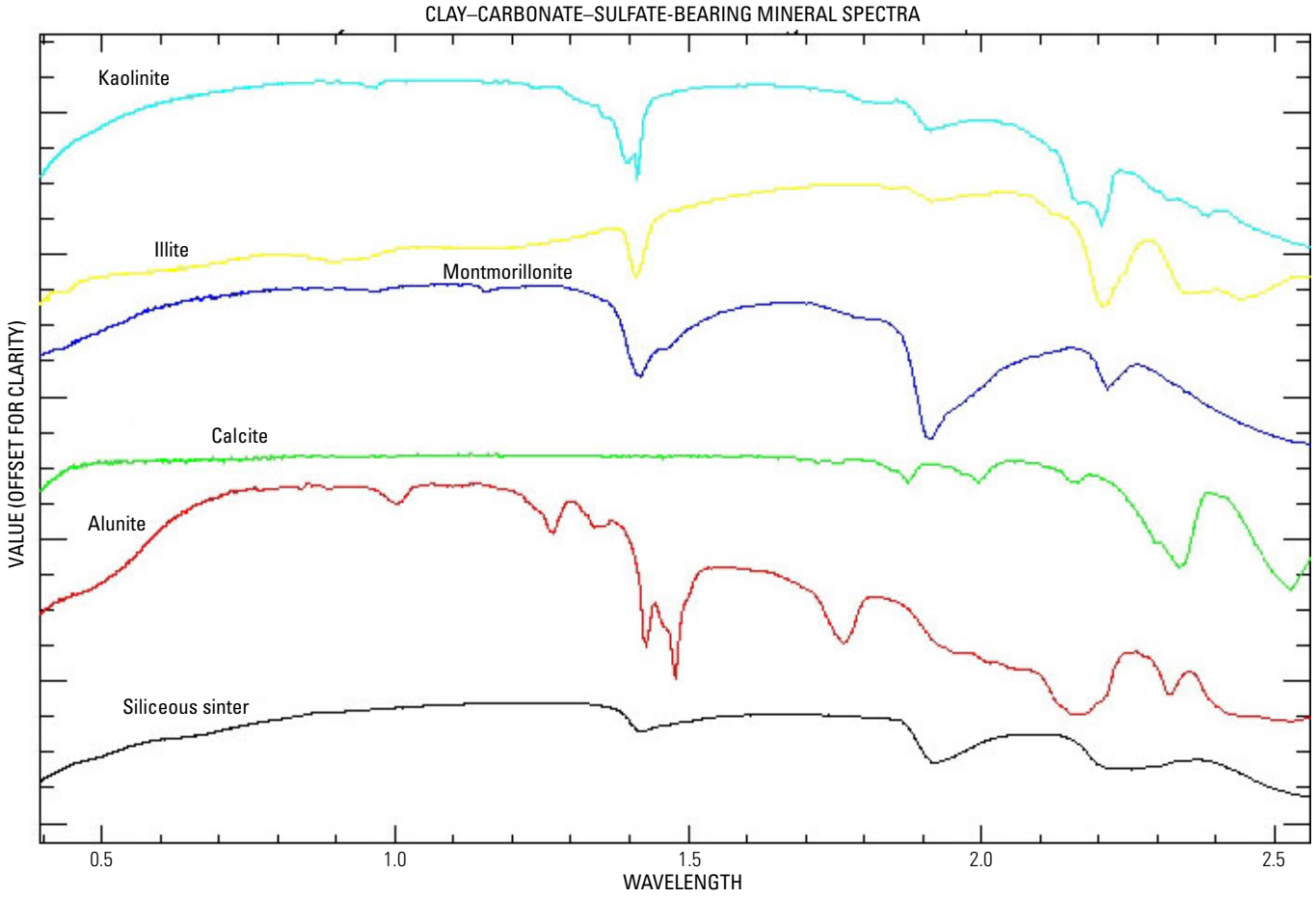

Figure 2. Mineral spectra for clay minerals, calcite, alunite, and siliceous sinter.

siliceous sinter were mapped—one is spectrally pure, and the other appears to be mixed with clay minerals. In this report, chalcedony, opaline sinter, and cristobalite are not spectrally separated; they are grouped as siliceous sinter.

Upper, Midway, and Lower Geyser Basins

Several large siliceous sinter deposits trend parallel to the Firehole River. These deposits generally are near the valley bottoms. They formed from neutral-pH chloride-rich hydrothermal fluids (White and others, 1975; Bargar and Beeson, 1985). Figures 4*A* and 4*B* provide an overview of hot-spring activity in the vicinity of the Firehole River. The deposits mapped, using the 1996, 20-m-pixel AVIRIS data, are characteristic of those in alkaline, active hot-spring environments and are consistent with the known mineralogy of the systems in Yellowstone National Park. The principal mineral adjacent to the Firehole River is hydrothermal silica, which has a characteristic spectral signature. Kaolinite, indicating more acidic water, also is present in some areas. Biological elements of the hot-spring systems also were mapped (principally, coloring of deposits and (or) thermal waters by thermophilic algae; see Kokaly and others, this volume). Chlorophyll-rich vegetation is shown in shades of red in figure 4*A* (false-color composite using AVIRIS wavelengths 0.85, 0.67, and 0.55 μm; colored red, green, and blue, respectively). In figure 4*A*, siliceous sinter deposits are colored white and dry grass and burnt areas are colored light green. Figure 4*B* (AVIRIS minerals map) provides an overview of the distribution of selected geologic materials; silica and kaolinite are colored green and red and show the locations of major geyser basins.

The Upper Geyser Basin sinter deposits (fig. 5; 1998, 6-m spatial-resolution image) are on a northwest linear trend (also seen at the bottom of fig. 6; 20-m resolution). The Midway Basin (sinter at the center of fig. 6) and Lower Geyser Basin (sinter at the top of fig. 6) sinter deposits appear to form a semicircular feature in the AVIRIS image. Generally, these deposits contain an inner zone of sinter mixed with minor amounts of clay minerals, whereas the outer regions are only sinter. Kaolinite deposits are scattered in and west of Old Faithful Geyser (bottom right sinter deposit with a semicircular boardwalk in fig. 5), east of Midway Geyser Basin (right center, fig. 6), and along a northeastward trend on the north side of Lower Geyser Basin (top, fig. 6). The presence of kaolinite, which is associated with acid-sulfate alteration, indicates the presence of local sulfur-rich fluids in basins that contain

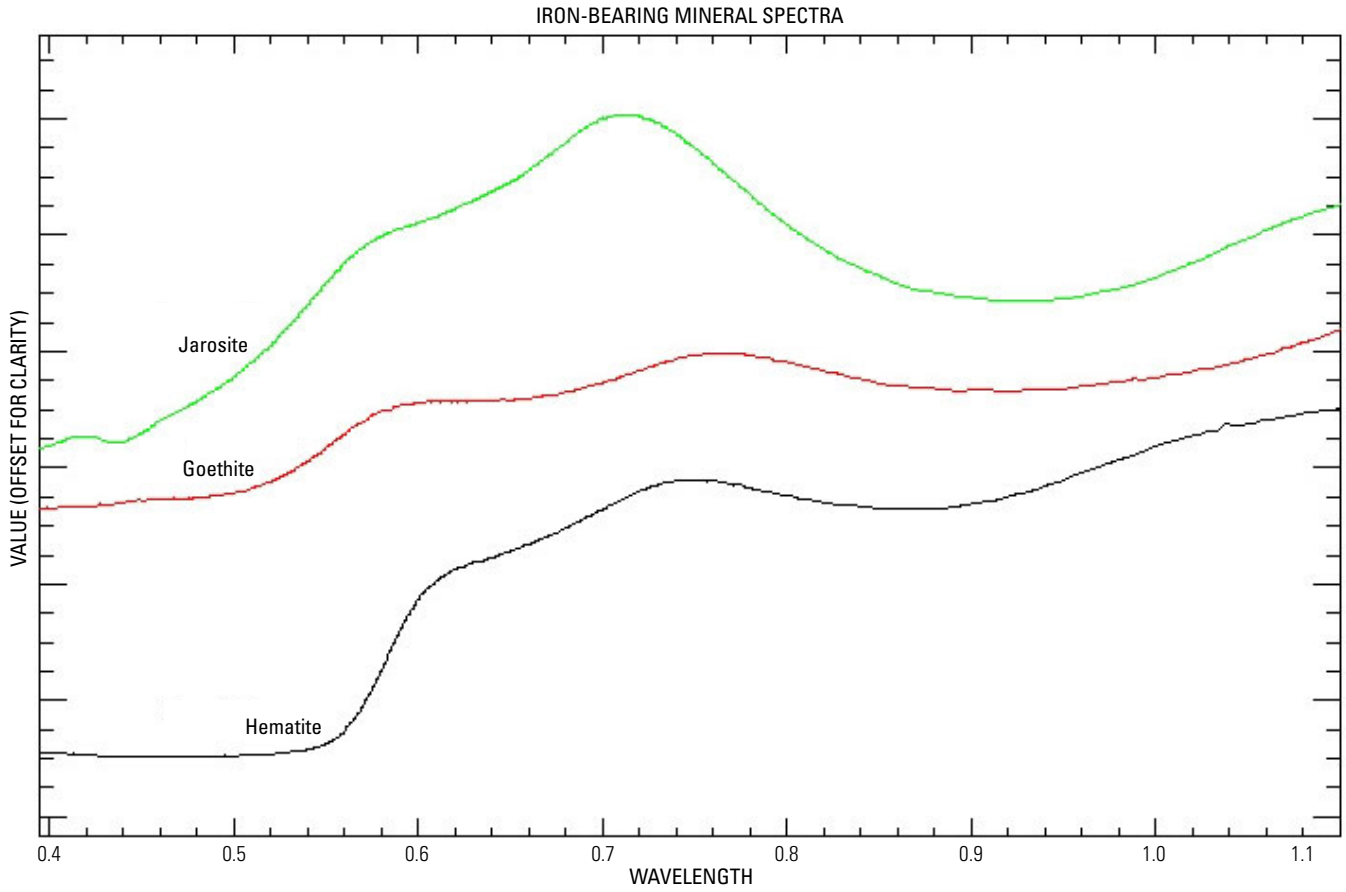

Figure 3. Mineral spectra for iron-bearing minerals.

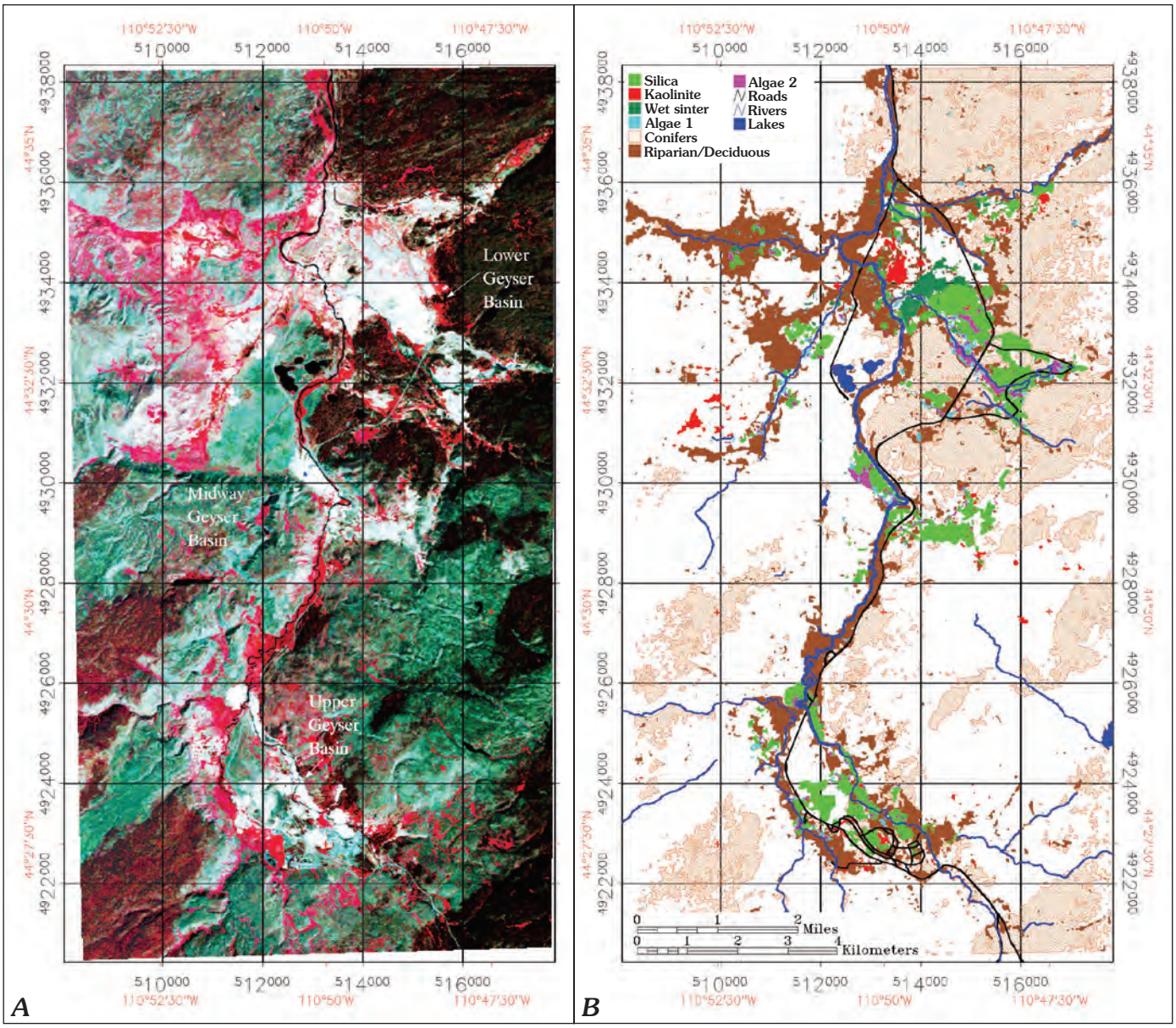

Figure 4. 1996 AVIRIS maps. *A,* false-color composite map. *B,* Derived map.

neutral-pH chloride-rich water. Wet soils are widespread in the Lower Geyser Basin; they are less common in the Upper Geyser Basin. These soils are in drainage channels that lead from hot-spring vents, as seen on the 6-m resolution (low altitude) image in figure 5. Figure 5 also shows the kaolinite in the Old Faithful Geyser sinter (noted above) very near to, or within, one of the discharge channels. A minor kaolinite anomaly also is present just west of the Old Faithful Inn in a slightly raised area at the south end of the northwestward linear trend of sinter deposits. Generally, kaolinite appears to be present in drier surroundings; it is not closely associated with wet soils.

The AIG- and USGS-derived maps (figs. 4, 5, and 6) identify and locate similar mineralogy. Although both methods use the same data, the processes are significantly different. AIG methods detect statistical spectral differences in the data, and then they identify the resulting "end-member" spectra in the entire data set. USGS Tetracorder processing is rules based and statistically identifies the mineralogy of each pixel, independent of any other pixel, using a matching mineral-spectral library.

Norris Geyser Basin

Norris Geyser Basin (lower center, fig. 7) contains a complex mix of mineral-alteration suites formed by ongoing fluctuations of the underlying hydrothermal-system water chemistry. It contains four siliceous-sinter centers in the basin lowland, an alunite center on a hill to the southwest, and kaolinite encircling the basin sides. Alunite and kaolinite

follow an apparent north-south linear trend on the west side of the basin. The large alunite center (Ragged Hills) is on the south end of this trend, and kaolinite and minor alunite are on the north end.

Stable isotopes of alunite collected at Ragged Hills and Roaring Mountain were studied by Pat Shanks (USGS) using hydroxyl and sulfate components. Sulfur-isotope values indicated that the alunite at Ragged Hills was derived from sulfate, that in turn, was derived from surficial oxidation of H_2S in steam. Alunite and kaolinite rimming the geyser basin may be indicative of changes in water chemistry from neutral-pH chloride-rich water in the basin to a low-pH vapor-dominated system on the topographically higher sides of the basin. The study concluded that, although the Norris Geyser Basin sulfur isotopes of alunite were similar to those of local geothermal H_2S, the sulfur isotopes of the Roaring Mountain alunite were significantly different. This may indicate that the Roaring Mountain alunite is much older than the Norris Geyser Basin alunite.

Roaring Mountain

Roaring Mountain (mid-upper left, fig. 7), just north of Norris Basin, is a large acid-sulfate system with a restricted, steam-heated vapor-dominated water supply. A region of alunite-rich ground mixed with kaolinite is surrounded by areas characterized by abundant kaolinite. Sparse siliceous sinter is present west of Roaring Mountain, near the road. A calcite center east of the main alunite deposit at Roaring Mountain was field-checked; the calcite is Paleozoic limestone.

Preliminary field examination in Norris Geyser Basin indicates that the siliceous sinter is in down-cut, eroded, lowland sites. Alunite-kaolinite-rich deposits are resistant to erosion and become topographic highs. An understanding of the time of formation of the alunite and kaolinite and the mineralization-formation depth is complicated by this erosional process. Siliceous sinter presently is being deposited. In the field, we observed deposition of new terrace deposits and deposition of sinter onto and around the wooden boardwalk.

Areas surrounding Norris Geyser Basin and Roaring Mountain contain significant mineral alteration. In figure 7, a large alteration center is at Elk Park. Elk Park (west of Norris Geyser Basin) contains a major center of kaolinite-alunite, which is bordered on the east by siliceous sinter.

Grand Canyon of the Yellowstone River

The Grand Canyon of the Yellowstone River allows a three-dimensional perspective of an acid-sulfate system in which sulfur-rich hydrothermal fluids have leached the surrounding country rock and converted feldspar minerals to clay minerals. The clay mineralogy is dependent on temperature and pressure (White and others, 1988); kaolinite is present near the surface, and mixed-layer illite-montmorillonite is forming at depth. Iron is leached from mafic minerals in this acidic (low pH) environment and then combines with sulfur to form pyrite. Pyrite weathers to jarosite, which has been spectrally identified in the canyon. Alunite with kaolinite forms near the surface. Adjacent to this acid-sulfate hydrothermal system, chloride-rich alkaline water deposits siliceous sinter at the surface. Figure 8*A* shows the locations of mapped clay minerals, siliceous sinter, and alunite. Figure 8*B* shows the locations of mapped iron-bearing oxide, hydroxide, and sulfate.

In the northeastern third of the canyon, alteration minerals were mapped primarily on the north side of the canyon. Kaolinite was mapped along the canyon rim and down to the canyon bottom. Alunite is present with kaolinite; alunite and kaolinite centers are near the rim top at Sulphur Creek, and small exposures are on the north wall and near the canyon bottom. Kaolinite was differentiated into two spectral types: a "spectrally pure kaolinite" (colored orange in fig. 8*A*) and mixed kaolinite with other clay minerals (probably sericite or illite) (colored magenta in fig. 8*A)*. The "spectrally pure kaolinite" and alunite are associated with goethite, whereas the mixed kaolinite is associated with jarosite and hematite (compare figs. 8*A* and 8*B*). The distributions of jarosite, hematite, and mixed kaolinite indicate the presence of strongly acidic conditions near the canyon rim (possibly quartz-sericite-pyrite alteration), whereas the distributions of goethite and alunite indicate the presence of a milder acidic environment north of the rim. Hot-spring deposits of siliceous sinter with montmorillonite are evident along Sulphur Creek, near the canyon bottom, and on the south rim at Moss Creek; montmorillonite is present on the canyon bottom extending to the northeast edge of the image.

In the southwestern third of the canyon, kaolinite was mapped along the rim and on the canyon walls. "Spectrally pure kaolinite" in figure 8*A* is along the rim and is associated with jarosite along the upper canyon slopes. Kaolinite, mixed with other clay minerals and alunite, is on the lower slopes and is associated with goethite and goethite-jarosite mixtures. Hematite is in two centers; it is associated with both spectral classes of kaolinite. Illite is present in the lower half of the canyon, and montmorillonite is at the bottom; both minerals are associated with goethite.

Hot springs just south of the canyon have formed a small alunite-kaolinite-goethite center, which is surrounded by siliceous sinter. The sinter includes kaolinite and lesser montmorillonite, indicating a change in local water composition (at least at the surface) from the water that mineralogically altered the canyon terrain. Sulphur Springs and Violet Springs, farther south in the Hayden valley, contain siliceous-sinter cores surrounded by montmorillonite and lesser kaolinite.

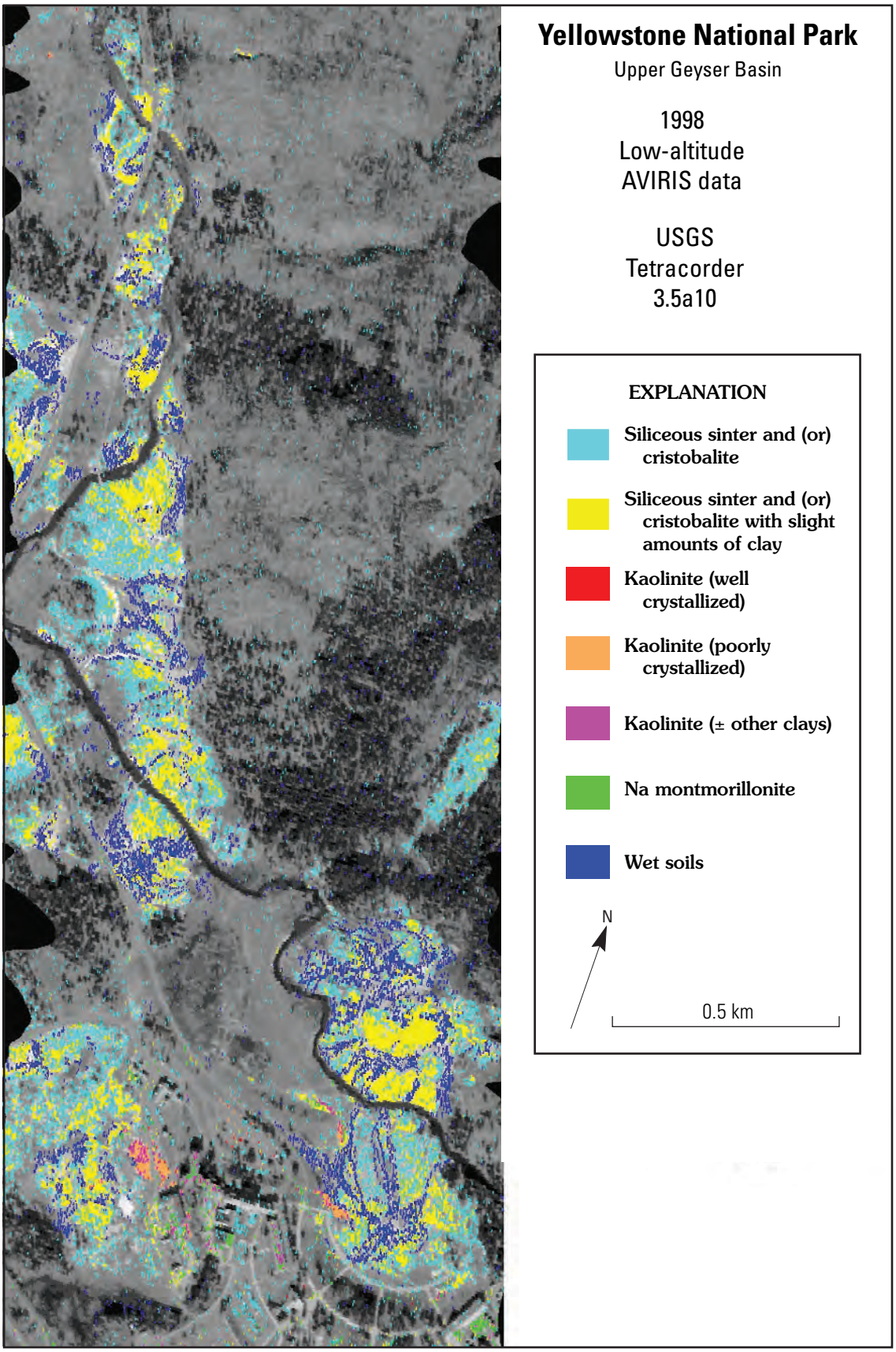

Figure 5. Mineral map of Upper Geyser Basin.

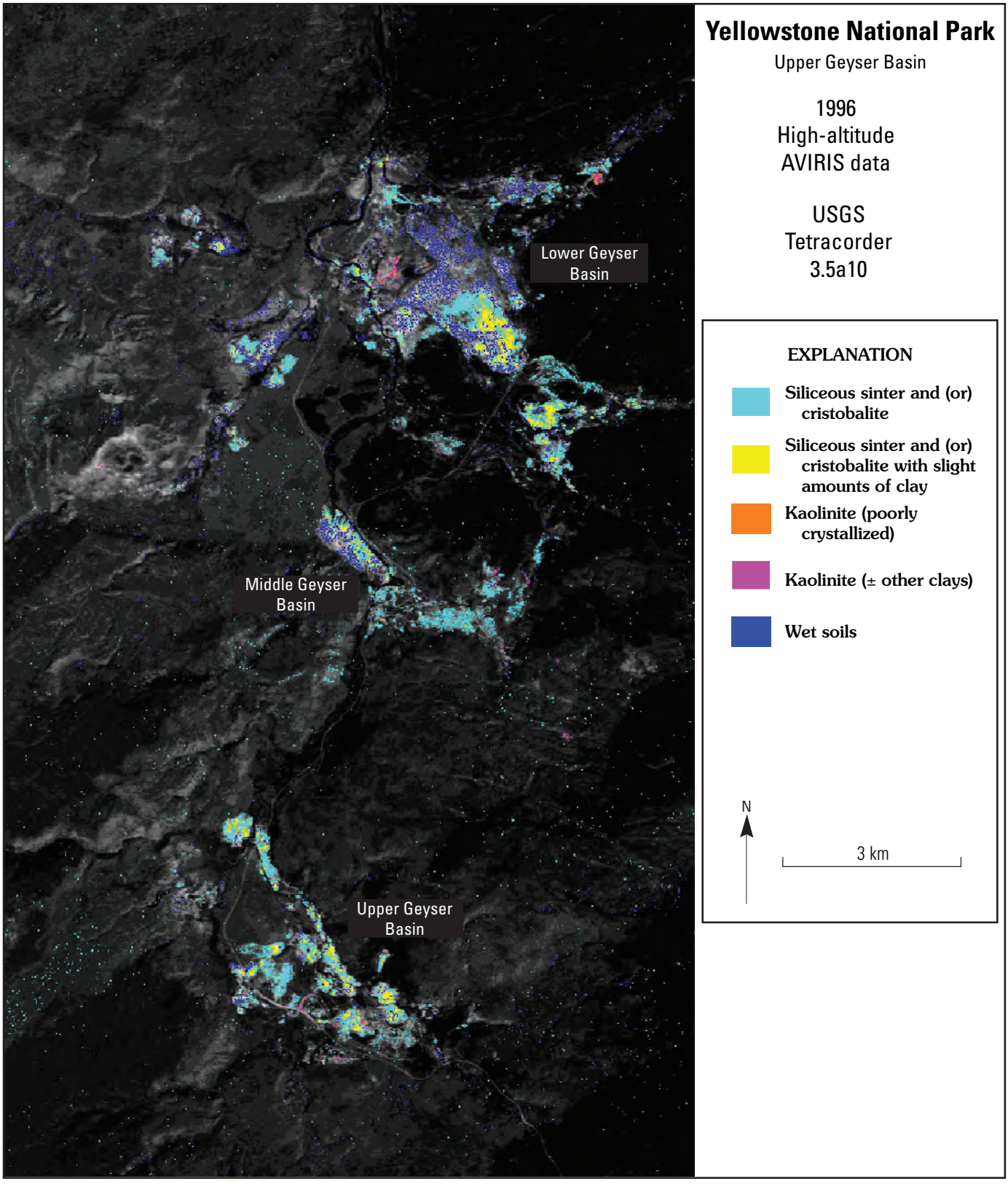

Figure 6. Mineral map of Lower, Midway, and Upper Geyser Basins.

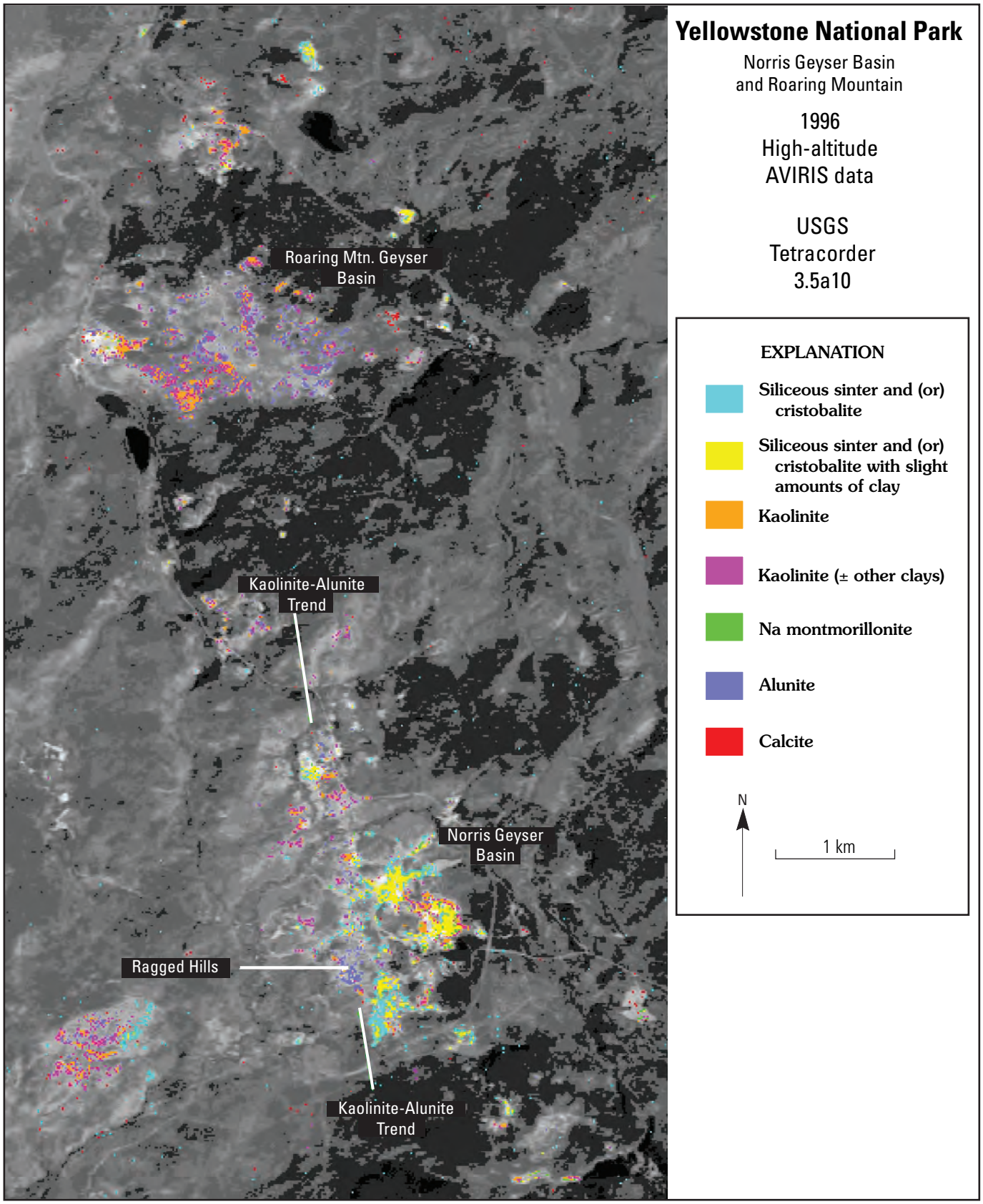

Figure 7. Mineral map of Norris Geyser Basin and Roaring Mountain.

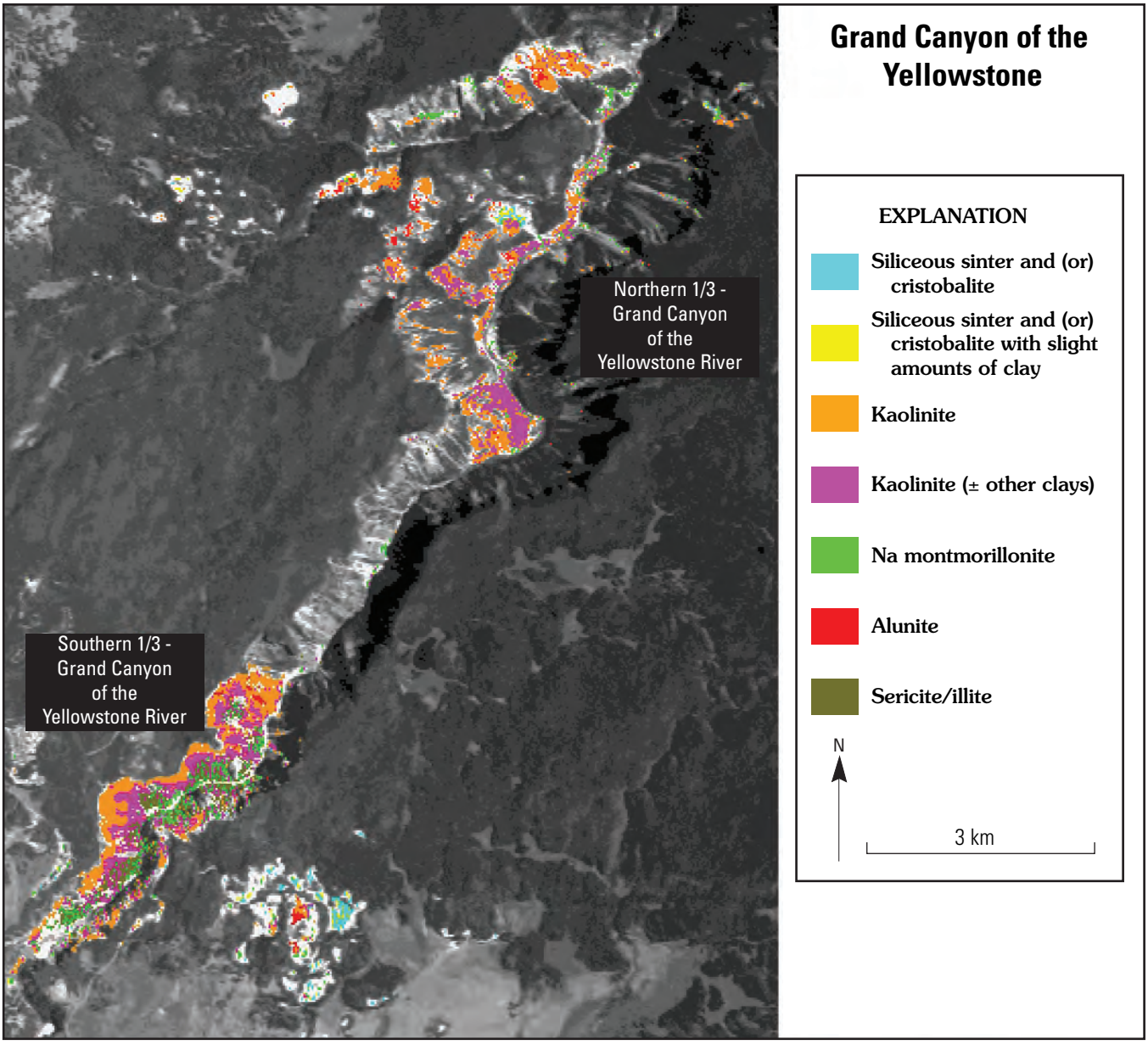

A

Figure 8*A*. Map of sinter, clay minerals, and sulfate minerals of the Grand Canyon of the Yellowstone River.

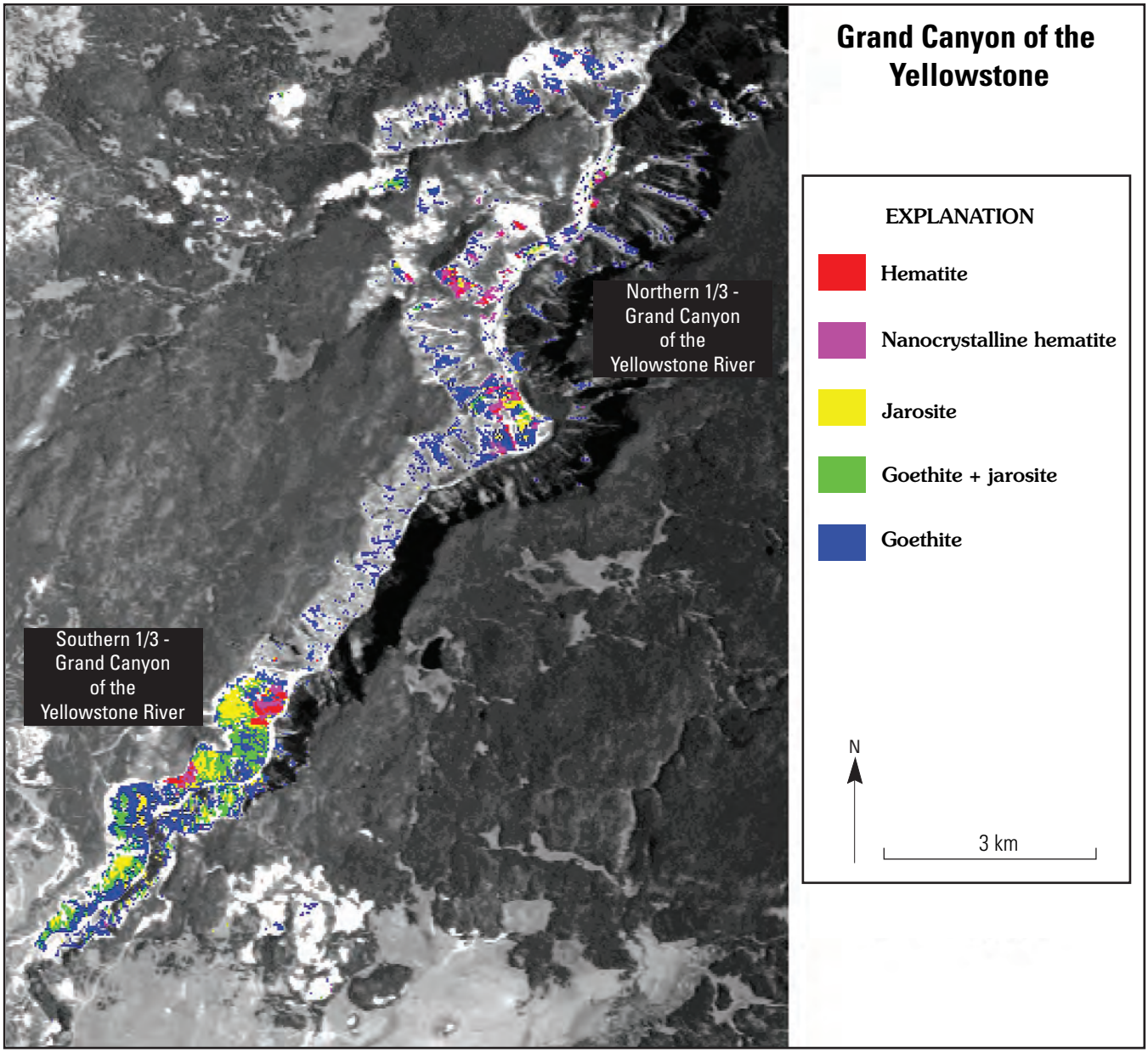

B

Figure 8*B*. Map of iron-bearing minerals of the Grand Canyon of the Yellowstone River.

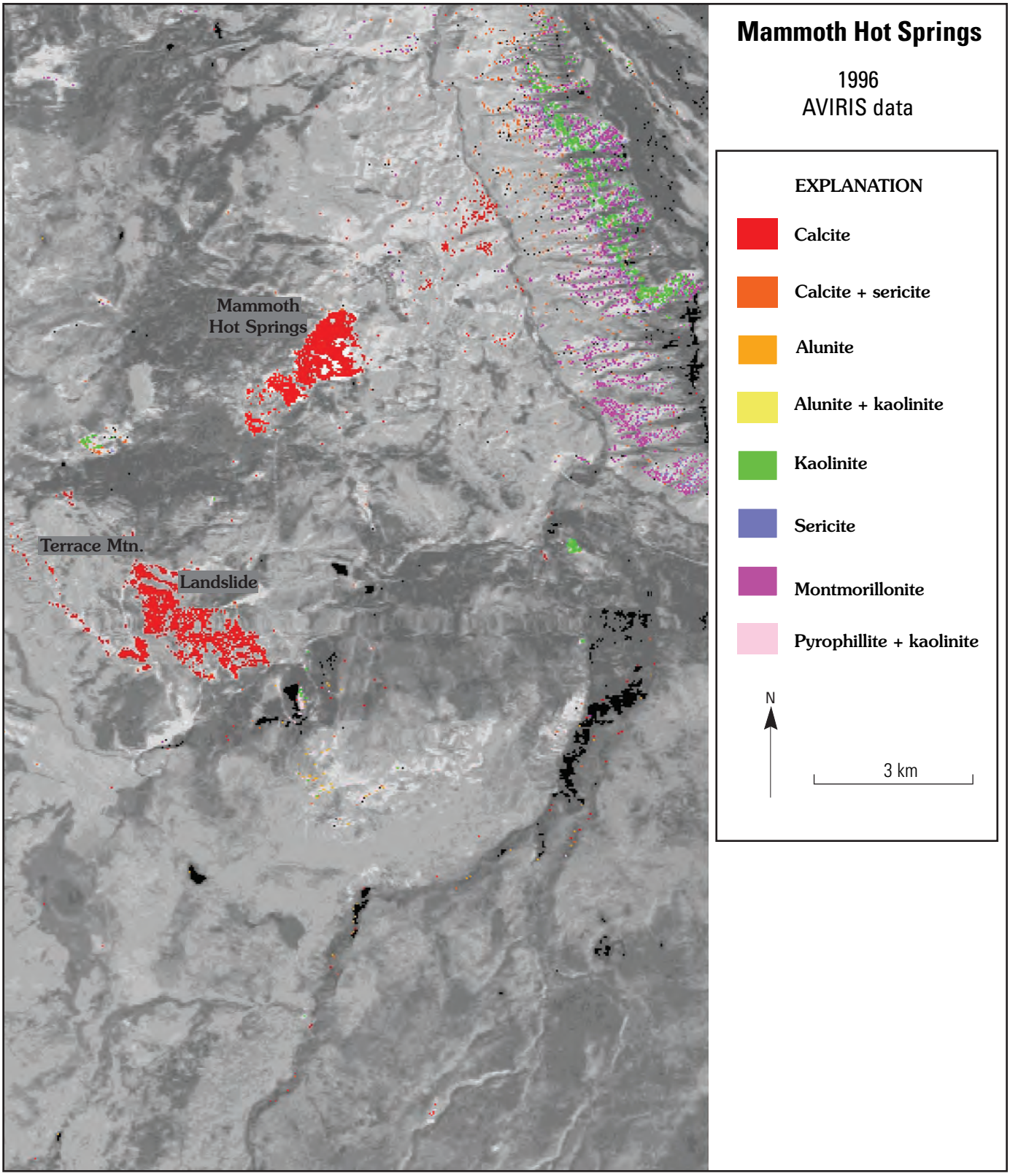

Figure 9. Mineral map of Mammoth Hot Springs.

Mammoth Hot Springs

Mammoth Hot Springs (fig. 9) is a large travertine deposit that was precipitated from water that percolated through underlying limestone bedrock. Mammoth Hot Springs and Terrace Mountain, an inactive travertine deposit to the southwest, have strong carbonate spectral features that map as calcite. Travertine has slid down the southeast side of Terrace Mountain, forming a well-exposed jumble of calcite. Of note is the clean appearance of the travertine; no clay minerals are mapped in the deposits. Kaolinite and alunite are mapped in a small region just west of Mammoth Hot Springs, whereas a variety of clay minerals are mapped across the river, to the northeast, in sedimentary terrain. Travertine deposits are also found north of the Lower Geyser Basin at Terrace Spring and north of Gardner, Mont. (neither area is shown on fig. 9).

Conclusions

Geochemical differences in the types of hydrothermal activity in Yellowstone National Park are inferred from mineral distributions that were mapped using imaging spectrometry. Two main geochemical systems in the basins examined in this study were identified and mapped: (1) abundant neutral-pH chloride-rich water and (2) restricted acid-sulfate water. Abundant neutral-pH chloride-rich water is assumed to have a meteoric (surface-derived) origin, indicated by silica and montmorillonite mapped at Lower and Upper Geyser Basins, Mammoth Hot Springs, and in parts of Norris Geyser Basin. This water is recirculated by convective heating in the geothermal source rock, and it leaches and transports silica and chloride complexes to the surface. Restricted acid-sulfate water is postulated on the basis of the presence of alunite, kaolinite, and jarosite in parts of Norris Geyser Basin, on Roaring Mountain, and in the Grand Canyon of the Yellowstone River. The water is derived mainly from the neutral-pH chloride-rich water; it is enriched in sulfates as a result of near-surface boiling that concentrates steam, H_2S, and CO_2 gases that, in turn, lower the pH of the water and form acid-sulfate minerals.

Geologic structure and wallrock lithology control fluid access to and from geothermal reservoirs and also control the fluid chemistry-wallrock reactions. Carbonate-rich bedrock lithologies yield fluids that are saturated with calcium carbonate, forming travertine terraces. Rhyolite volcanic beds yield fluids that are saturated in silica. Spectral mineral mapping can identify and distinguish both deposit types.

As fluid-channel locations change with time, blocking and unblocking passageways through fluid-leaching action and earthquakes, shifts in fluid chemistry change the compositions of alteration minerals. Overprinting of these alteration minerals is present in most of the areas mapped, suggesting that chemical-compositional changes are active within the hydrothermal systems of Yellowstone National Park.

AVIRIS data has been used to map regional hydrothermal-alteration assemblages in selected areas of Yellowstone National Park. Many of the areas are inaccessible or are in hazardous terrain, thus restricting ground access. Analysis of these data have identified structural trends, and mapped minerals may indicate underlying fluid geochemistry. This study has introduced new questions about the complex mineralogic overprinting that occurs through time.

References Cited

Bargar, K.E., and Beeson, M.H., 1985, Hydrothermal alteration in research drill hole Y-3, Lower Geyser Basin, Yellowstone National Park, Wyoming: U.S. Geological Survey Professional Paper 1054-C, 23 p.

Boardman, J.W., 1997, Mineralogic and geochemical mapping at Virginia City, Nevada, using 1995 AVIRIS data, in Proceedings of the twelfth thematic conference on geological remote sensing, Denver, Colo.: Ann Arbor, Environmental Research Institute of Michigan, p. 21–28.

Boardman, J.W., 1998, Leveraging the high dimensionality of AVIRIS data for improved sub-pixel target unmixing and rejection of false positives—Mixture tuned matched filtering, *in* Summaries of the seventh JPL airborne earth science workshop, v. 1, AVIRIS workshop: Jet Propulsion Laboratory Publication 97-21, 55 p..

Clark, R.N., Gallagher, A.J., and Swayze, G.A., 1990, Material absorption band depth mapping of imaging spectrometer data using a complete band shape least-squares fit with library reference spectra, *in* Proceedings of the second airborne visible/infrared imaging spectrometer (AVIRIS) workshop: Jet Propulsion Laboratory Publication 90-54, p. 176–186.

Clark, R.N., and Swayze, G.A., 1995, Mapping minerals, amorphous materials, environmental materials, vegetation, water, ice and snow, and other materials—The USGS Tricorder algorithm, *in* Green, R.O., ed., Summaries of the fifth annual JPL airborne earth science workshop, January 23–26: Jet Propulsion Laboratory Publication 95-1, p. 39–40.

Clark, R.N., Swayze, G.A., and Gallagher, A.J., 1993, Mapping minerals with imaging spectroscopy, chap. N *of* Scott, R.W., Jr., Detra, P.S., and Berger, B.R., eds., Advances related to United States and international mineral resources—Developing frameworks and exploration technologies: U.S. Geological Survey Bulletin 2039, p. 141–150.

Clark, R.N., Swayze, G.A., Gallagher, A.J., Gorelick, N., and Kruse, F.A., 1991, Mapping with imaging spectrometer data using the complete band shape least-squares algorithm simultaneously fit to multiple spectral features from multiple materials, *in* Proceedings of the third airborne visible/infrared imaging spectrometer (AVIRIS) workshop: Jet Propulsion Laboratory Publication 91-28, p. 2–3.

Clark, R.N., Swayze, G.A., Heidebrecht, K.B., Goetz, A.F.H., and Green, R.O., 1993, Comparison of methods for calibrating AVIRIS data to ground reflectance, *in* Summaries of the fourth annual JPL airborne geosciences workshop, Volume 1: AVIRIS Workshop, Jet Propulsion Laboratory Publication 93-26, p. 31–34.

Clark, R.N., Swayze, G.A., Livo, K.E., Kokaly, R.F., Sutley, S.J., Dalton, J.B., McDougal, R.R., and Gent, C.A., 2003, Imaging spectroscopy—Earth and planetary remote sensing with the USGS Tetracorder and expert systems: Journal of Geophysical Research, v. 108, no. E12, 5131, doi: 10.1029/2002JE001847, 44 p.

Gao, Bo-Cai, Heidebrecht, K.B., and Goetz, A.F.H., 1997, Atmosphere removal program (ATREM) Version 3.0 User's Guide: Boulder, University of Colorado, Center for the Study of Earth From Space, 27 p.

Keith, T.E.C., White, D.E., and Beeson, M.H., 1978, Hydrothermal alteration and self-sealing in Y-7 and Y-8 drill holes in northern part of Upper Geyser Basin, Yellowstone National Park, Wyoming: U.S. Geological Survey Professional Paper 1054-A, 26 p.

Kruse, F.A., 1998, Spectral identification of image end-members determined from AVIRIS data [abs.], *in* Summaries of the seventh JPL airborne earth science workshop, v. 1. AVIRIS workshop: Jet Propulsion Laboratory Publication 97-21, p. 257.

Kruse, F.A., 1999, Mapping hot spring deposits with AVIRIS at Steamboat Springs, Nevada, *in* Summaries of the eighth JPL airborne earth science workshop: Jet Propulsion Laboratory Publication 99-17, p. 239–245.

Kruse, F.A., Huntington, J.H., and Green, R.O., 1996, Results from the 1995 AVIRIS geology group shoot, *in* Proceedings, second international airborne remote sensing conference and exhibition: Ann Arbor, Environmental Research Institute of Michigan, v. I, p. I-211–I-220.

Kruse, F.A., Lefkoff, A.B., and Dietz, J.B., 1993, Expert system-based mineral mapping in northern Death Valley, California/Nevada, using the airborne visible/infrared imaging spectrometer (AVIRIS), *in* Remote Sensing of Environment, special issue on AVIRIS, May–June 1993: Elsevier, v. 44, p. 309–336.

Mosier, D.L., Sato, Takeo, Page, N.J., Singer, D.A., and Berger, B.R., 1986, Descriptive model of Creede epithermal veins, *in* Cox, D.P., and Singer, D.A., eds., Mineral deposit models: U.S. Geological Survey Bulletin 1693, p. 145–149.

Rockwell, B.W., Clark, R.N., Livo, K.E., McDougal, R.R., Kokaly, R.F., and Vance, Sam, 1999, Preliminary materials mapping in the Park City region for the Utah USGS-EPA imaging spectroscopy project using both high and low altitude AVIRIS data, *in* Green, R.O., ed., Summaries of the eighth JPL airborne earth science workshop, Jet Propulsion Laboratory Publication 99-17, p. 365–375.

Smith, R.B., and Braile, L.W., 1993, Topographic signature, space-time evolution, and physical properties of the Yellowstone-Snake River Plain volcanic system—The Yellowstone hotspot, *in* Snoke, A.W., Steidtmann, J.R., and Roberts, S.M., eds., Geology of Wyoming: Geological Survey of Wyoming Memoir 5, p. 694–754.

Thompson, A.J.B., 1991, Acid-sulfate alteration in the Marysvale-Pioche mineral belt—A guide to gold mineralization: Utah Geological and Mineral Survey Miscellaneous Publication 91-2, 29 p.

White, D.E., Fournier, R.O., Muffler, L.J.P., and Truesdell, A.H., 1975, Physical results of research drilling in thermal areas of Yellowstone National Park, Wyoming: U.S. Geological Survey Professional Paper 892, 70 p.

White, D.E., Hutchinson, R.A., and Keith, T.E.C., 1988, The geology and remarkable thermal activity of Norris Geyser Basin, Yellowstone National Park, Wyoming: U.S. Geological Survey Professional Paper 1456, 84 p.

Monitoring Changes in Geothermal Activity at Norris Geyser Basin by Satellite Telemetry, Yellowstone National Park, Wyoming

P

By Irving Friedman

Chapter P *of*
Integrated Geoscience Studies in the Greater Yellowstone Area—Volcanic, Tectonic, and Hydrothermal Processes in the Yellowstone Geoecosystem

Edited by Lisa A. Morgan

Professional Paper 1717

U.S. Department of the Interior
U.S. Geological Survey

About the Author

It is perhaps fitting that the last paper in this volume is also the last of over 200 scientific papers to be written by Irving Friedman whose scientific career began in the mid-1940s and ended with his death at the age of 85 on June 28, 2005. Irving was a member of the famed group of postdoctoral researchers in Nobel laureate Harold Urey's laboratory at the Institute for Nuclear Studies at the University of Chicago. There he built the first mass spectrometer for routine measurement of the hydrogen isotope composition of water. As a research chemist with the USGS for over 43 years, Irving pursued the understanding of every aspect of the water cycle with studies of water in oceans, rivers, lakes, glaciers, hot springs, the atmosphere, magmas, minerals, rocks, meteorites, plants, animals, and the Moon. For his contributions to our understanding of the water cycle, Irving is called the "father of isotope hydrology." Irving had a career-long interest in scientific studies at Yellowstone beginning with his first visit while an undergraduate student at Montana State University in Bozeman. He significantly advanced the scientific knowledge of the Park for decades. His work on the geochemistry of obsidian allowed huge advances in archeology and anthropology in the Park and worldwide. He was a legend in the Park for his ability to "instrument anything." His low-cost method of monitoring Yellowstone's total geothermal output that is presented in Chapter I of this volume and the satellite telemetry monitoring of Norris Geyser Basin presented in the following chapter, will be standards for many years to come. Irving received many awards and honors in his lifetime. None meant more to him than "Honorary Yellowstone Park Ranger"—complete with felt hat—that was awarded to him for his longtime contributions leading to better protection of the Park and its resources.

Contents

Abstract....513
Acknowledgments....513
Introduction....513
Precipitation....515
Observed Changes in Thermal Activity....524
    Echinus Geyser....524
    Steamboat Geyser....524
    Basin-Wide Thermal Event....525
    Diurnal Changes in Discharge....527
Water Chemistry....529
    Chloride and Sulfate Flux from Norris Geyser Basin....529
Summary and Conclusions....532
References Cited....532

Figures

1–2. Photographs of:
    1. Weir....514
    2. Interior of stilling well box....515
3–12. Plots of:
    3. Discharge of Tantalus Creek versus time from 1998 to 2003....516
    4. Instantaneous discharge measurements at Tantalus Creek weir....525
    5. Discharge of Tantalus Creek....526
    6. Discharge at Tantalus Creek weir and temperature in Echinus Geyser pool....527
    7. Discharge of Tantalus Creek showing effect of eruptions of Steamboat Geyser....528
    8. Discharge and water-temperature data during a thermal event....529
    9. Discharge and water temperature of Tantalus Creek for various dates....530
    10. Discharge versus chloride and sulfate concentrations for water samples at Tantalus Creek weir....531
    11. Discharge versus chloride and sulfate fluxes for water samples at Tantalus Creek weir....531
    12. Discharge versus chloride-sulfate ratio for water samples at Tantalus Creek weir....532

Monitoring Changes in Geothermal Activity at Norris Geyser Basin by Satellite Telemetry, Yellowstone National Park, Wyoming

By Irving Friedman[1]

Abstract

Instrumentation on a weir on Tantalus Creek, which captures 98 percent of the surface discharge of Norris Geyser Basin, Yellowstone National Park (the Park), records discharge and water temperature every 10 minutes and telemeters recorded data every hour via GOES satellite. Plots of discharge from June 1998 through mid-November 2003 record frequent—and often large—changes in discharge.

Data recorded during five eruptions of Steamboat Geyser (May 2000, April 2002, September 2002, April 2003, and October 2003) allow calculation of the time and duration of the eruptions, as well as amounts of water released by each eruption.

Water discharge at the weir also recorded the eruptions of Echinus Geyser, one of the major attractions in Norris Geyser Basin. Prior to late September 1998, Echinus erupted regularly approximately every 50 minutes. During the winter of 1998, and probably coincident with a major increase in thermal activity in the Ragged Hills area about a kilometer west of Echinus, Echinus ceased to erupt.

A basin-wide thermal event that began in April 2002 was recorded. During this event—which was not directly witnessed—the discharge from the basin increased in minutes from 5 ft^3 per second (cfs) to more than 10 cfs, while water temperature at the weir increased from 25°C to 70°C. In order to account for this temperature increase, the increased discharge from the basin would have to have been close to the boiling point. The discharge and temperature returned to normal in a day or two.

Chloride and sulfate concentrations in water samples collected from 1988 to late 2002 show that these concentrations are independent of stream discharge

This study proves the utility of satellite telemetry of hydrothermal and geochemical data from remote areas.

[1]U. S. Geological Survey.

Acknowledgments

This research could not have been carried out without the aid received from Rick Hutchinson, park geologist, who died in an avalanche in March 1997 while providing assistance to another investigator. Rick not only made the installation of the weir at Tantalus Creek possible but was instrumental in its construction, including backpacking concrete and other heavy construction materials to the site.

I wish to acknowledge the help of Park personnel attached to the firefighting group (“Fire Cache”), who took this project under its wing, provided access to the satellite platform, and also backpacked the heavy electronic equipment to the site. These include Phil Perkins, Pet Overstreet, Ashley Sipes, and Jim Kitchen. Thanks are also due to park personnel Steven Miller and Guida Veronda. Recently, the installation by Henry Heasler, park geologist, of a temperature recorder in the outflow from Steamboat Geyser has made it possible to accurately time the eruptions of this geyser. Heasler has also been responsible for the installation of a rain gage in the Norris Geyser Basin.

Daniel Norton, my collaborator in many projects within the Park, was of great help in getting this project started.

Introduction

White and others (1988) stated in their monograph that Norris Geyser Basin (NGB) is the most diverse thermal area in Yellowstone National Park (the Park). Not only does it have a greater variety of thermal features than anywhere else in the Park, but these thermal features also change rapidly with time (days to years), and the thermal waters display a wide variety of chemical compositions.

In 1988, we began to monitor the total amount of thermal water leaving Norris Geyser Basin in order to determine whether the changes in activity of the thermal features are a result of variations in thermal input to the basin or whether the changes are due to variations in the redistribution

Figure 1. *A,* Photograph of weir looking upstream. *B,* Photograph of weir looking downstream. A, The gray plastic stilling well box can be seen at the right of the weir plate. B, Confluence of Tantalus Creek and Gibbon River is just out of sight beyond the upper left side of the photograph.

Figure 2. Photograph of the interior of the stilling well box showing the float gage. A, The bottle at the left is a float that is connected to the precision wire-wound potentiometer contained in the bottle to the right. B, The shaft of the potentiometer. C, is sealed by an O-ring where it passes through the bottle cap. This seals the interior of the bottle from the atmosphere. However, over time, a small amount of water enters the bottle. This leakage is captured by silica-gel desiccant contained in a cloth bag inside the bottle. The stilling well box is covered to prevent snow buildup on the equipment.

of thermal energy among various parts of the Norris system due to changes in conduits feeding various springs within the basin. This monitoring was carried out by measuring the discharge of Tantalus Creek, which receives 98 percent of the surface water leaving the basin (a small amount bypasses Tantalus Creek and flows directly into the Gibbon River). In 1988,[1] a dam and weir were constructed on the creek at a site 100 m from the point at which Tantalus Creek discharges into the Gibbon River (fig. 1). The discharge was measured by determining the height of the water behind a 36-inch-wide Cipoletti weir using a float gage (fig. 2) and referring to standard discharge tables that relate discharge to the height of the water in the weir. The discharge was recorded every hour, but, later, the recording interval was shortened to 10 minutes.

Initially, data was telemetered by radio to Norris Museum and was accessed via modem. The telemetry equipment operated intermittently and was replaced in August 1998 by an on-site "Onset StowAway" data logger that stored readings taken every 10 minutes and had a memory of 270 days of data. Because the site was visited infrequently and because equipment failure—usually the failure of the wire-wound potentiometer that responded to changes in water level—was not detected until the next visit, we added a data-collection platform that telemetered data via GOES satellite to a receiver in Menlo Park, Calif., and then by modem to Denver, Colo., where daily inspections of the data assured that long periods of lost data did not occur.

The data are plotted as discharge in cubic feet per second (cfs) versus time. Figure 3 shows plots for every 2 months beginning in August 1998. Vertical lines in each plot separate days.

In addition to instrumental data, occasional measurements of discharge were made manually by reading a staff gage that measured the height of water behind the weir. These data are plotted in figure 4. The discharge from NGB exhibits great variability, for example, discharge was sustained at 6 cfs for several months in early 1989, and again for a short period in 1991, interspersed with flows as low as 1.5 cfs.

Precipitation

To access the effect of precipitation on the discharge of Tantalus Creek, precipitation at the two nearest weather-reporting stations (Mammoth, 32 km to the north, and Canyon, 24 km to the east) are plotted on the discharge record (fig. 3). The majority of the large, sudden increases in discharge last for a day or so and correlate with significant increases in precipitation recorded at one or both of the weather stations.

[1]The device that measured stream discharge at the Tantalus Creek weir failed in mid-January 2004. The equipment was replaced in July 2004 by an automatically operated station maintained by the U.S. Geological Survey Water Resources Division (Tantalus Creek, station no. 06036940). The station collects data on stream discharge, water temperature and precipitation every 15 minutes and transmits the data in real time via GOES satellite. Plots and tabular data can be viewed and retrieved on the internet at: http://waterdata.usgs.gov/mt/nwis/uv/?site_no=06036940&PARAmeter_cd=00060,00065,00010.

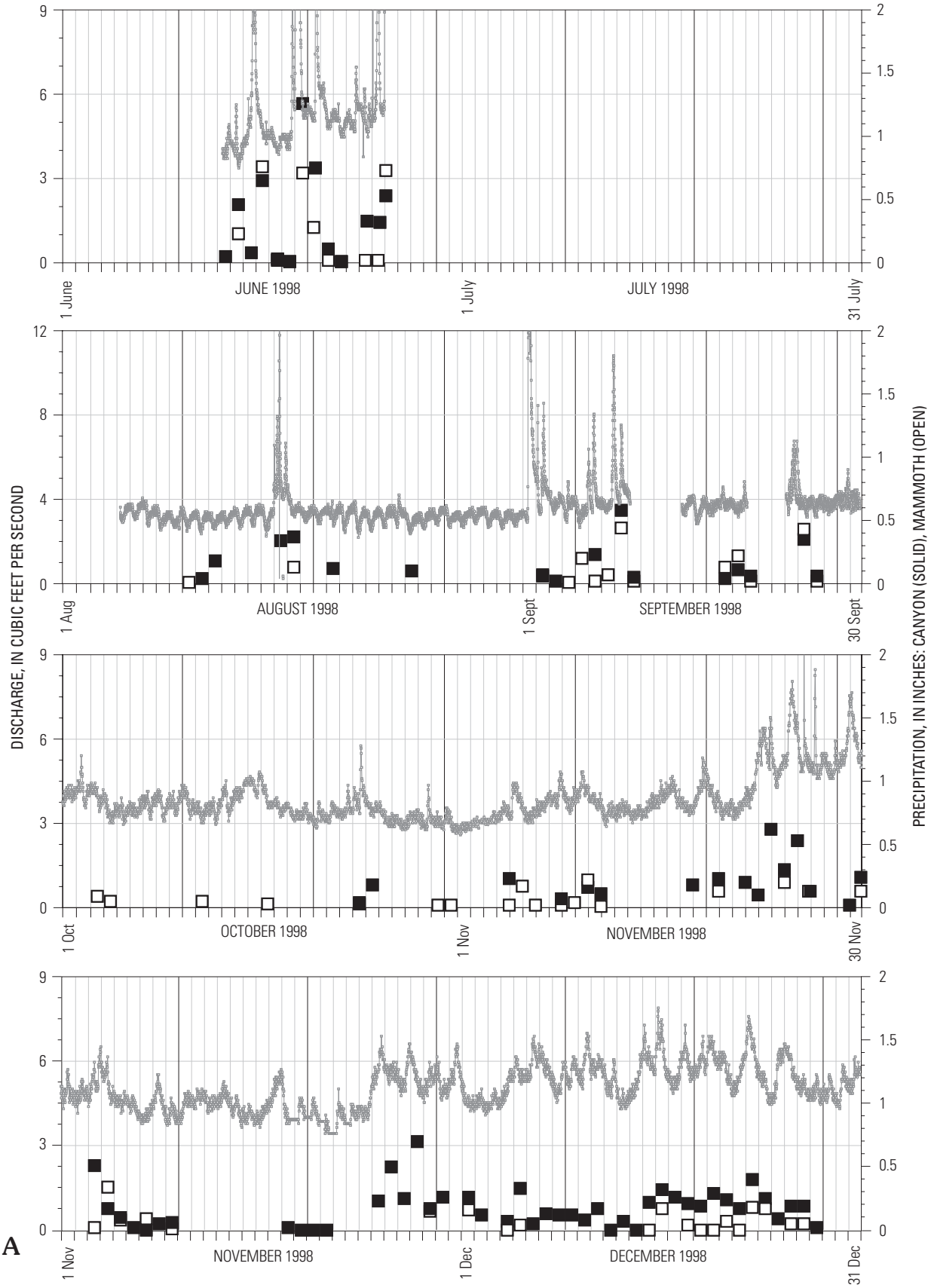

Figure 3 (above and succeeding pages). Plots of discharge of Tantalus Creek versus time from 1998 to 2003. Precipitation recorded at nearby weather stations (Canyon and Mammoth) are also plotted. Precipitation data for

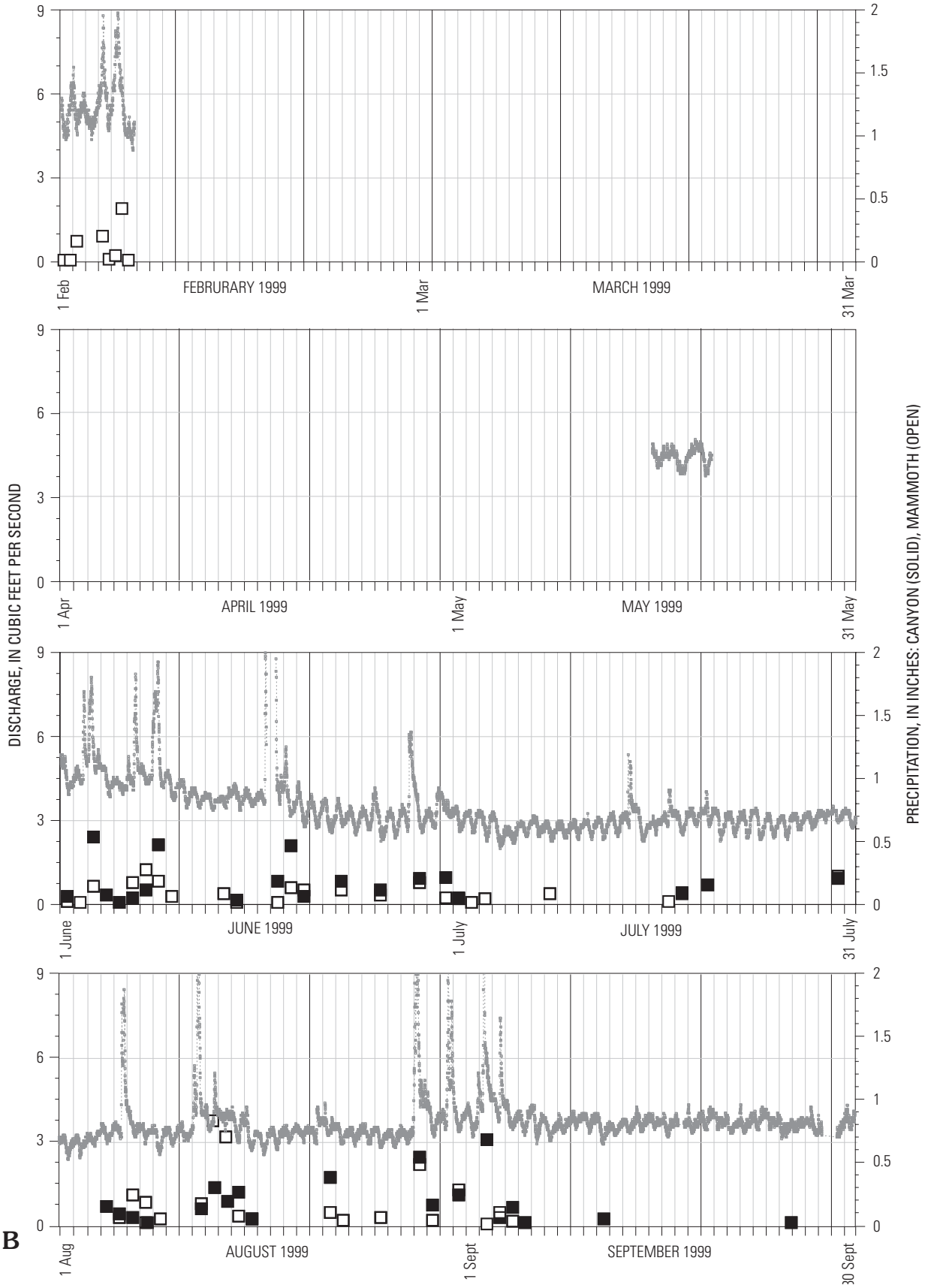

B

Canyon from October 2001 to December 2002 are not available. Precipitation in Norris Geyser Basin, recorded by a rain gage installed in mid-June 2003, is also shown.

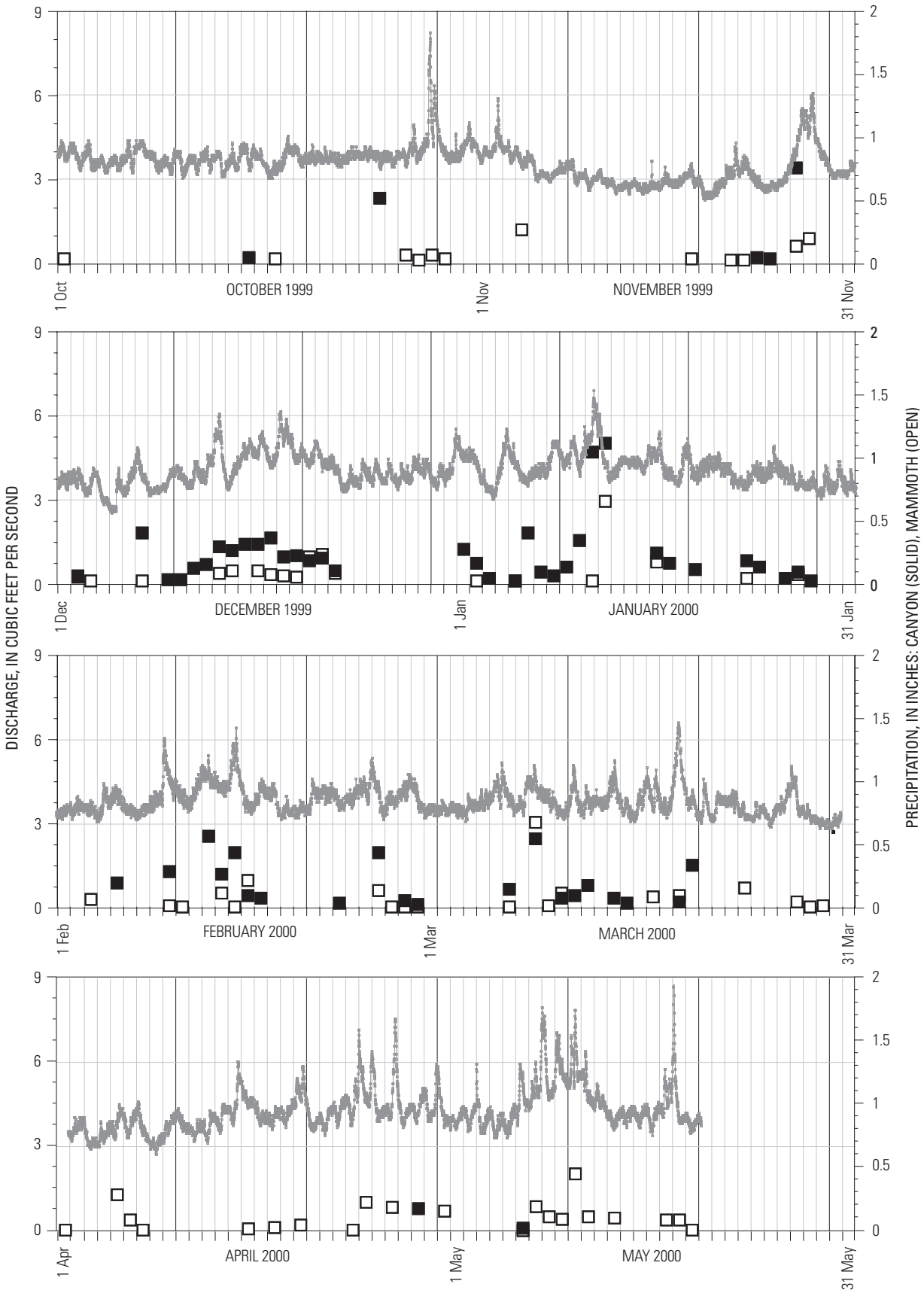
DISCHARGE, IN CUBIC FEET PER SECOND
PRECIPITATION, IN INCHES: CANYON (SOLID), MAMMOTH (OPEN)
9
6
3
0
2
1.5
1
0.5
0
1 Oct
OCTOBER 1999
1 Nov
NOVEMBER 1999
31 Nov
1 Dec
DECEMBER 1999
1 Jan
JANUARY 2000
31 Jan
1 Feb
FEBRUARY 2000
1 Mar
MARCH 2000
31 Mar
1 Apr
APRIL 2000
1 May
MAY 2000
31 May

C

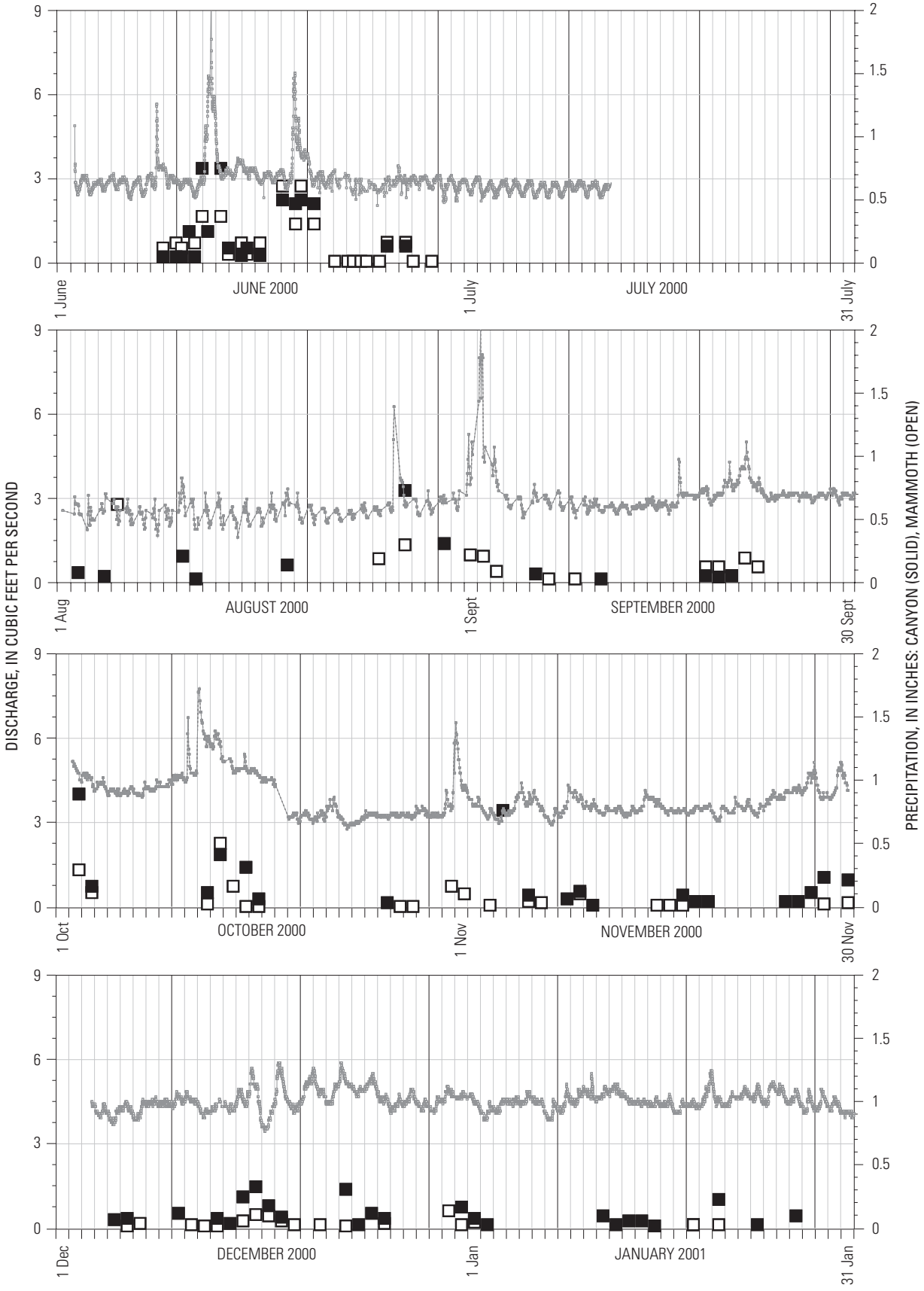
DISCHARGE, IN CUBIC FEET PER SECOND
PRECIPITATION, IN INCHES: CANYON (SOLID), MAMMOTH (OPEN)
0
3
6
9
0
0.5
1
1.5
2
1 June
JUNE 2000
1 July
JULY 2000
31 July
1 Aug
AUGUST 2000
1 Sept
SEPTEMBER 2000
30 Sept
1 Oct
OCTOBER 2000
1 Nov
NOVEMBER 2000
30 Nov
1 Dec
DECEMBER 2000
1 Jan
JANUARY 2001
31 Jan

D

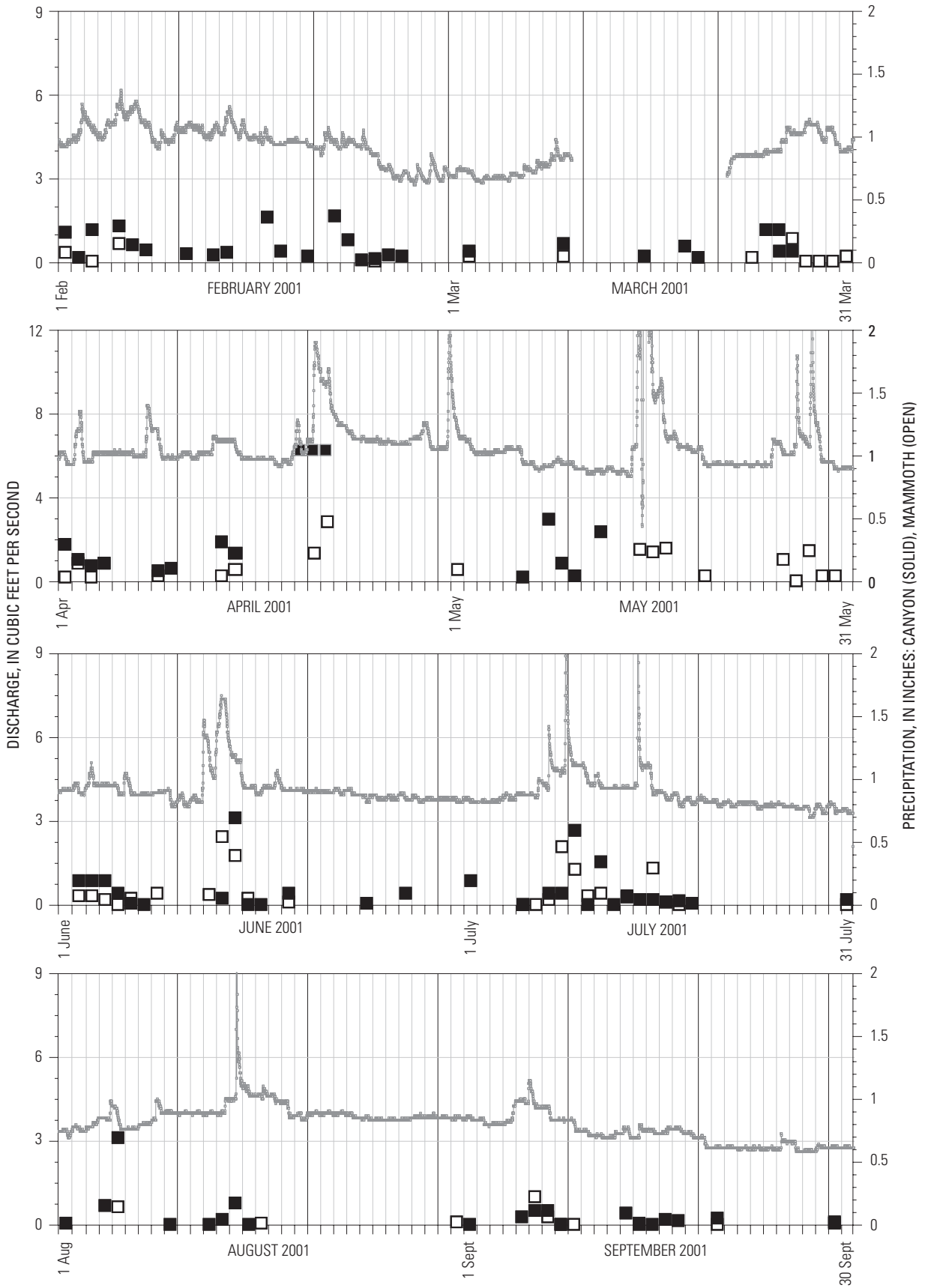
DISCHARGE, IN CUBIC FEET PER SECOND
PRECIPITATION, IN INCHES: CANYON (SOLID), MAMMOTH (OPEN)
1 Feb
FEBRUARY 2001
1 Mar
MARCH 2001
31 Mar
1 Apr
APRIL 2001
1 May
MAY 2001
31 May
1 June
JUNE 2001
1 July
JULY 2001
31 July
1 Aug
AUGUST 2001
1 Sept
SEPTEMBER 2001
30 Sept

E

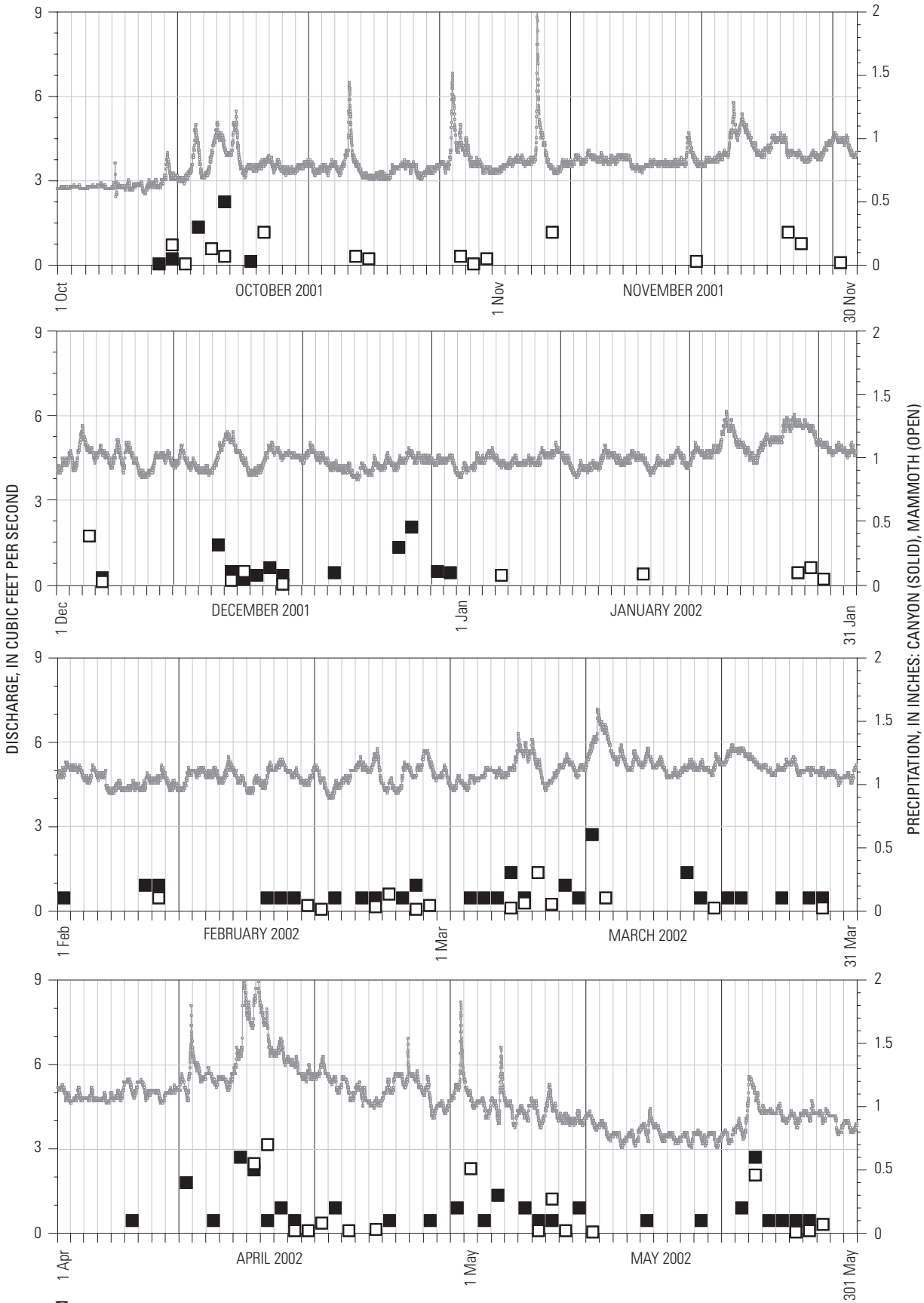
DISCHARGE, IN CUBIC FEET PER SECOND
PRECIPITATION, IN INCHES: CANYON (SOLID), MAMMOTH (OPEN)
9
6
3
0
2
1.5
1
0.5
0
1 Oct
OCTOBER 2001
1 Nov
NOVEMBER 2001
30 Nov
1 Dec
DECEMBER 2001
1 Jan
JANUARY 2002
31 Jan
1 Feb
FEBRUARY 2002
1 Mar
MARCH 2002
31 Mar
1 Apr
APRIL 2002
1 May
MAY 2002
301 May

F

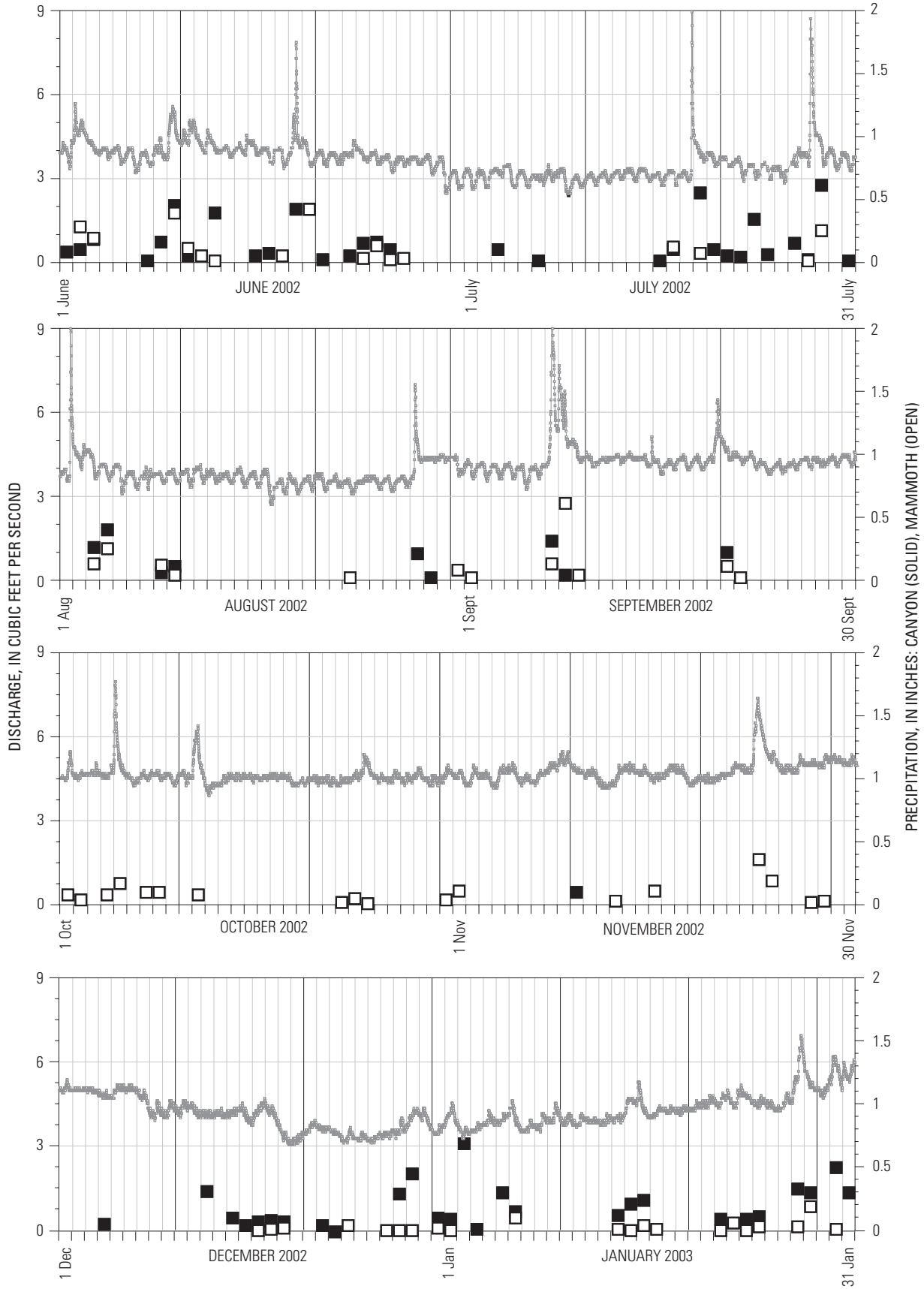
DISCHARGE, IN CUBIC FEET PER SECOND
PRECIPITATION, IN INCHES: CANYON (SOLID), MAMMOTH (OPEN)
9
6
3
0
2
1.5
1
0.5
0
1 June
JUNE 2002
1 July
JULY 2002
31 July
1 Aug
AUGUST 2002
1 Sept
SEPTEMBER 2002
30 Sept
1 Oct
OCTOBER 2002
1 Nov
NOVEMBER 2002
30 Nov
1 Dec
DECEMBER 2002
1 Jan
JANUARY 2003
31 Jan

G

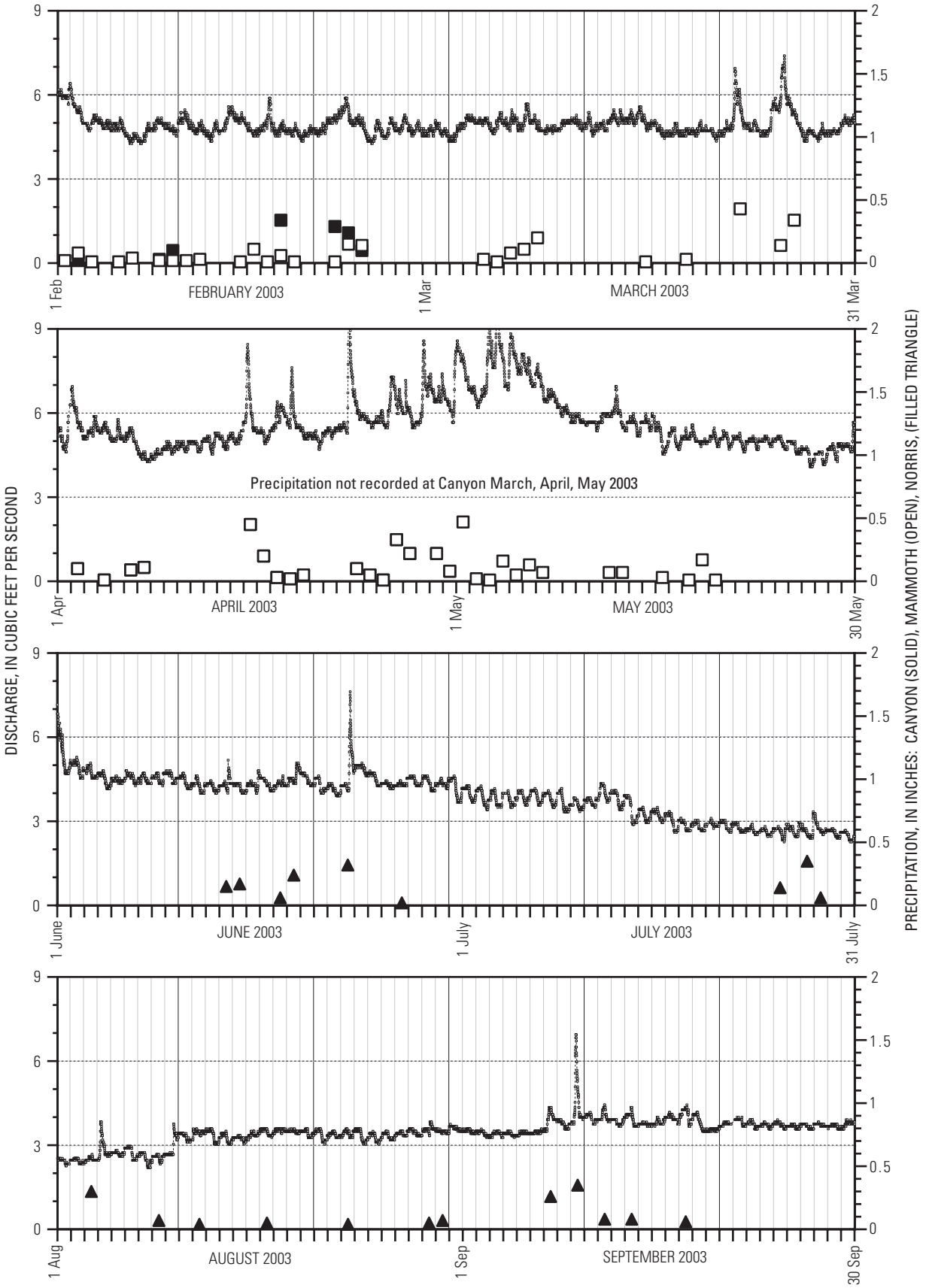
DISCHARGE, IN CUBIC FEET PER SECOND
PRECIPITATION, IN INCHES: CANYON (SOLID), MAMMOTH (OPEN), NORRIS, (FILLED TRIANGLE)
9
6
3
0
2
1.5
1
0.5
0
1 Feb
FEBRUARY 2003
1 Mar
MARCH 2003
31 Mar
Precipitation not recorded at Canyon March, April, May 2003
1 Apr
APRIL 2003
1 May
MAY 2003
30 May
1 June
JUNE 2003
1 July
JULY 2003
31 July
1 Aug
AUGUST 2003
1 Sep
SEPTEMBER 2003
30 Sep

H

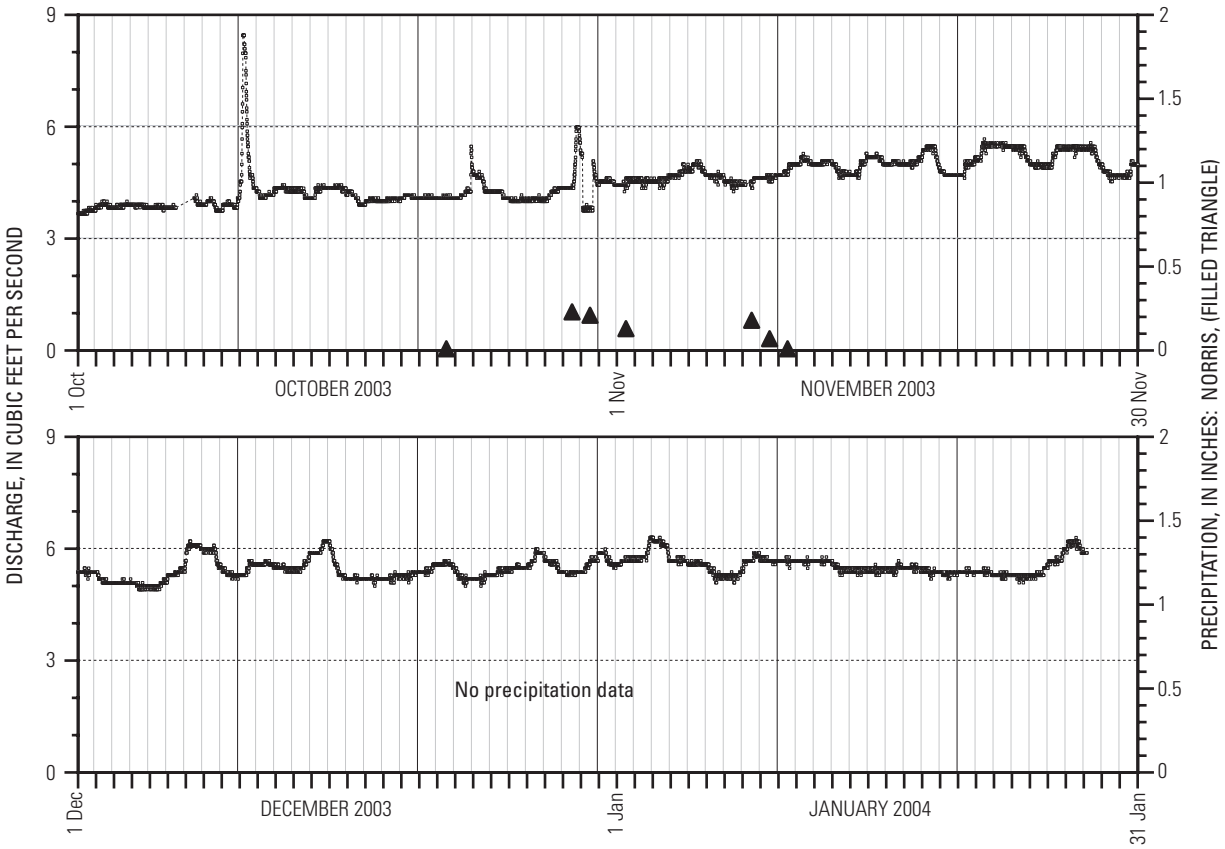

I

Observed Changes in Thermal Activity

Echinus Geyser

During the winter of 1998–1999 thermal activity greatly increased in an area about 2 km northeast of the "Hundred Springs Plain" in Norris Geyser Basin. This area, informally known as the "Ragged Hills," has now become a major contributor of thermal activity. Apparently coincident with this change of focus of activity in the NGB, the nature of the eruptions of Echinus Geyser changed. For many years, these eruptions occurred every 50–60 minutes and resulted in discharge, for 5 to 20 minutes, to heights of 10 to 20 m (fig. 5*A*). Since the outbreak of activity in the Ragged Hills area, Echinus rarely erupts, and the eruptions are much less intense than was previously the case. This change in Echinus is shown in detailed plots of the discharge of Tantalus Creek (fig. 5), where the Echinus eruptions are clearly displayed in data taken in the fall of 1998 (fig. 5*A*). Similar plots of data acquired in the late winter and spring of 1999—and in subsequent years—show very small eruptions at 2- to 5-hour intervals and no eruptions for some days (figs. 5*B*, 5*C*, 5*D*, 5*E*). It is interesting to note that a temperature recorder, placed in the Echinus pool (fig. 6), shows periodic (~hourly), short-term (few minutes) increases in water temperature in the pool, indicating that Echinus was still erupting small amounts of water every hour or so (its previous period). However, these eruptions were too small to result in a significant increase in the outflow of Tantalus Creek.

Coincident with the activity at Ragged Hills, the average flow of Tantalus Creek increased in late November 1998 from 3 to 4 cfs to approximately 4 to 5 cfs. It remained high for several months. Subsequently, Tantalus Creek exhibited periods of increased flow (for example, winter 1999 through early spring 2000). Except for these periods of high discharge, the discharge of Tantalus has returned to a flow of approximately 3 cfs. However, Echinus has not returned to its former (pre-Ragged Hills) eruptive pattern. Apparently, thermal water that previously fed Echinus has now been shunted to the Ragged Hills thermal area.

Steamboat Geyser

A description of the history of Steamboat Geyser is given in the classic publication on the Norris Geyser Basin by White and others (1988).

During the early morning of May 2, 2000, two tourists sleeping in their camper parked in the visitors center parking lot, less than 1 km from Steamboat, were awakened by noise and violent ground shaking. As they drove away, fearing that an

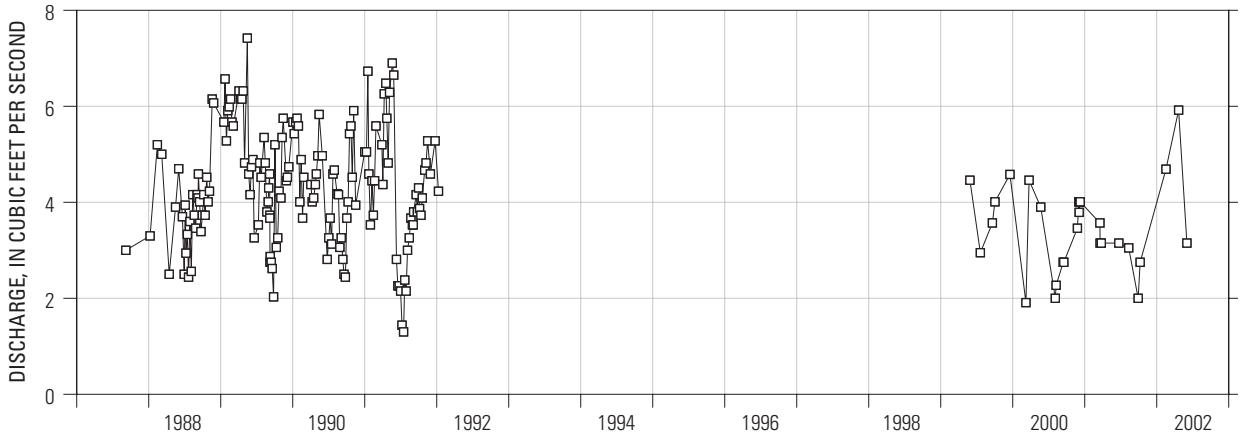

Figure 4. Plot of instantaneous discharge measurements made from a staff gage at the Tantalus Creek weir.

earthquake was occurring, they saw a large plume of steam and water from the vicinity of Steamboat and reported the eruption. Because the eruption occurred early in the morning and shortly after the opening of the park to tourists, only one other person, a park employee on his way to work, reported seeing the eruption.

The eruption was captured by the monitoring equipment in place at Tantalus Creek, as can be seen in figure 7*A*, which shows discharge data for May 1 and 2. The record for May 1 shows that the somewhat irregular eruptions of Echinus Geyser was followed in the early morning of May 2 by the eruption of Steamboat Geyser. The first arrival of the water phase of Steamboat occurred at approximately 5:20 a.m. local time. The water phase lasted 40 to 60 minutes, reaching a peak discharge rate of 1.4 ft^3/s (10.5 gal/s). The total amount of water discharged during the eruption can be calculated from the area under the curve in figure 7*A* from the assumed base flow shown on the figure to the peak of the curve and is approximately 7,600 ft^3 (57,000 gal). The water phase of the eruption was followed by the eruption of steam and a little water. In addition to the water that was measured, a large, but unknown, amount of steam escaped into the atmosphere.

In 2001 and 2002 Steamboat erupted again. Tantalus Creek discharge data for the three eruptions (May 2, 2000, April 26, 2002, and Sept. 13, 2002—figs. 7*A*, 7*B*, and 7*C*, respectively) show that the three eruptions resemble each other very closely, both in maximum water discharge and eruption duration. The total water erupted for each event is: May 2, 2000, event—7,600 ft^3; April 26, 2002, event—4,600 ft^3; Sept. 13, 2002, event—8,700 ft^3.

Two eruptions occurred during March 2003—the data are plotted in figures 7*D* and 7*E*. These two closely spaced eruptions, which occurred during March 22–23 and during March 26, lasted far longer than those that occurred in 2000 and 2002. The first of these erupted approximately 62,000 ft^3 of water, and the second 36,000 ft^3.

A temperature recorder, located in the Steamboat Geyser outflow channel, close to the geyser, recorded the first pulse of water from the eruption of April 27, 2003, at 02:53 mountain standard time (m.s.t.). The first indication of this event at the Tantalus Creek weir occurred at 04:20 (m.s.t.), which indicates a travel time of 1 hour 27 minutes.

The times recorded for the eruption of October 22, 2003, were 19:25 (m.s.t.) for the eruption and 21:00 (m.s.t.) for the first increase at the weir. The travel time of 1 hour 35 minutes agrees with the travel time calculated for the previous eruption.

Basin-Wide Thermal Event

For the past 75 years, widespread disturbances (thermal events) have been observed in Norris Geyser Basin (White and others, 1988, p. 61 and table 8). During these thermal events, increased discharge was observed to have occurred simultaneously at a large number of the thermal features in the geyser basin. These events lasted for a day or so, and the increased basin-wide activity slowly declined for several days. Thermal events were said to usually occur in the summer or early fall. The fact that they never have been observed during the winter or early spring may be because of the lack of observers during these parts of the year. During the thermal events of 1988, 1989, 1990, 1991, and 2003, the discharge of Tantalus Creek did not increase. These thermal events appear to be caused by a short-term redirection of thermal water rather than an overall increase in thermal water input to the geyser basin.

With the introduction of a water-temperature sensor to the Tantalus Creek weir station, which telemeters via GOES satellite stream discharge of the entire Norris Geyser Basin, we were able to detect and measure the results of a very large thermal event that occurred on April 14, 2002 (fig. 8). The event was initiated very suddenly when the discharge of water from Norris Geyser Basin doubled within 30 minutes. The water temperature increased from 25°C (77°F) to a maximum of 70°C (158°F). The discharge and temperature decreased to pre-eruption levels during the next 4 to 6 days. The seismic network maintained by the University of Utah did not record any seismic signal associated with this thermal event.

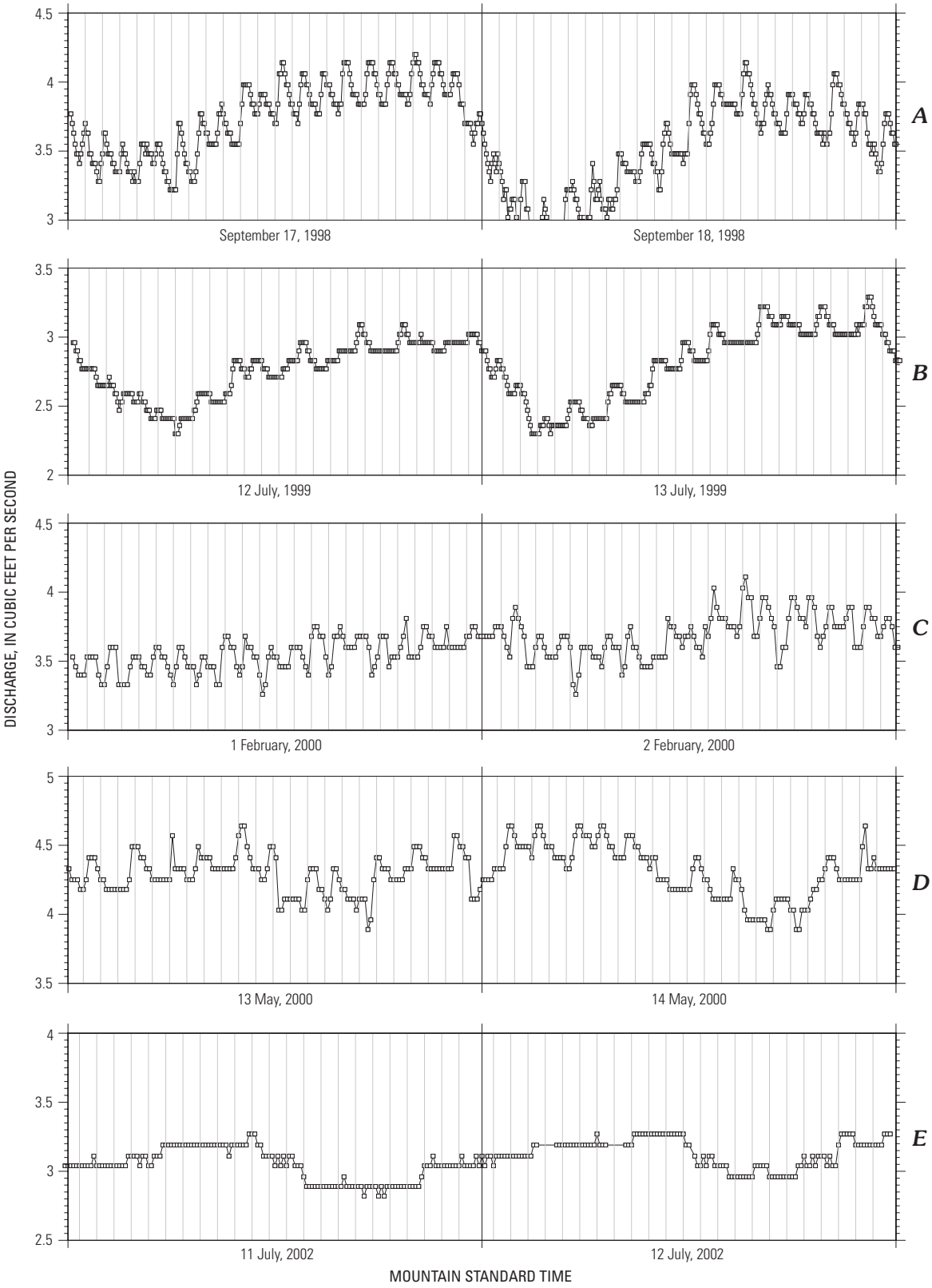

Figure 5. Plots of discharge of Tantalus Creek. *A*, Plot of the data collected September 17–18, 1998, showing the approximately hourly increase in discharge due to the eruption of Echinus Geyser before the increased thermal activity at Ragged Hills. *B*, *C*, *D*, and *E* are plots of data after the increase in activity at Ragged Hills and illustrate the decline in eruptive activity of Echinus Geyser.

The thermal event began with the sudden (within 30 minutes) increase in discharge from 6.5 cfs to 14–15 cfs (A, fig. 8). Simultaneously, the water temperature at Tantalus weir increased from 23° to 42°C. During the next 30 minutes (B, fig. 8), the discharge decreased to 9 cfs and the water temperature increased to 48°C. The temperature remained relatively stable for about 8 hours, while the discharge slowly decreased from 9 to 8 cfs (C, fig. 8). For the next 12 hours, water temperature increased to 70°C and the discharge varied from 7 to 9.3 cfs. The temperature maximum (70°C) (D, fig. 8) occurred an hour before the peak discharge of 9.3 cfs (E, fig. 8). The water temperature and discharge slowly declined for the next several days and reached steady values of 4.5 cfs and 40°C by April 29, 5 days after the beginning of the event.

The complexity of the discharge-temperature events indicates that, during the thermal event, water of different temperatures—and probably from different sources—erupted at different times.

Diurnal Changes in Discharge

A pronounced diurnal variation in discharge from NGB has been observed. This effect occurs during periods when precipitation inflow is absent. During the summer, discharge *decreases* during the daytime and *increases* at night. The onset of the decrease seems to coincide with sunrise and the decrease with sunset (fig. 9*A*). The diurnal variation in discharge is approximately 10 percent of the peak flow. When temperature data became available in early 2002, the water temperature was observed to increase during the day and decrease at night, as might be expected due to solar heating of the bed of shallow Tantalus Creek.

The diurnal oscillation in discharge is easily seen in the discharge data. For example, refer to the August 1998 and April 1999 records (fig. 3).

Two records of winter discharge (figs. 9*B* and 9*C*) also show a diurnal variation but are out of phase with the summer and spring records (figs. 9*A* and 9*D*). The reasons for these

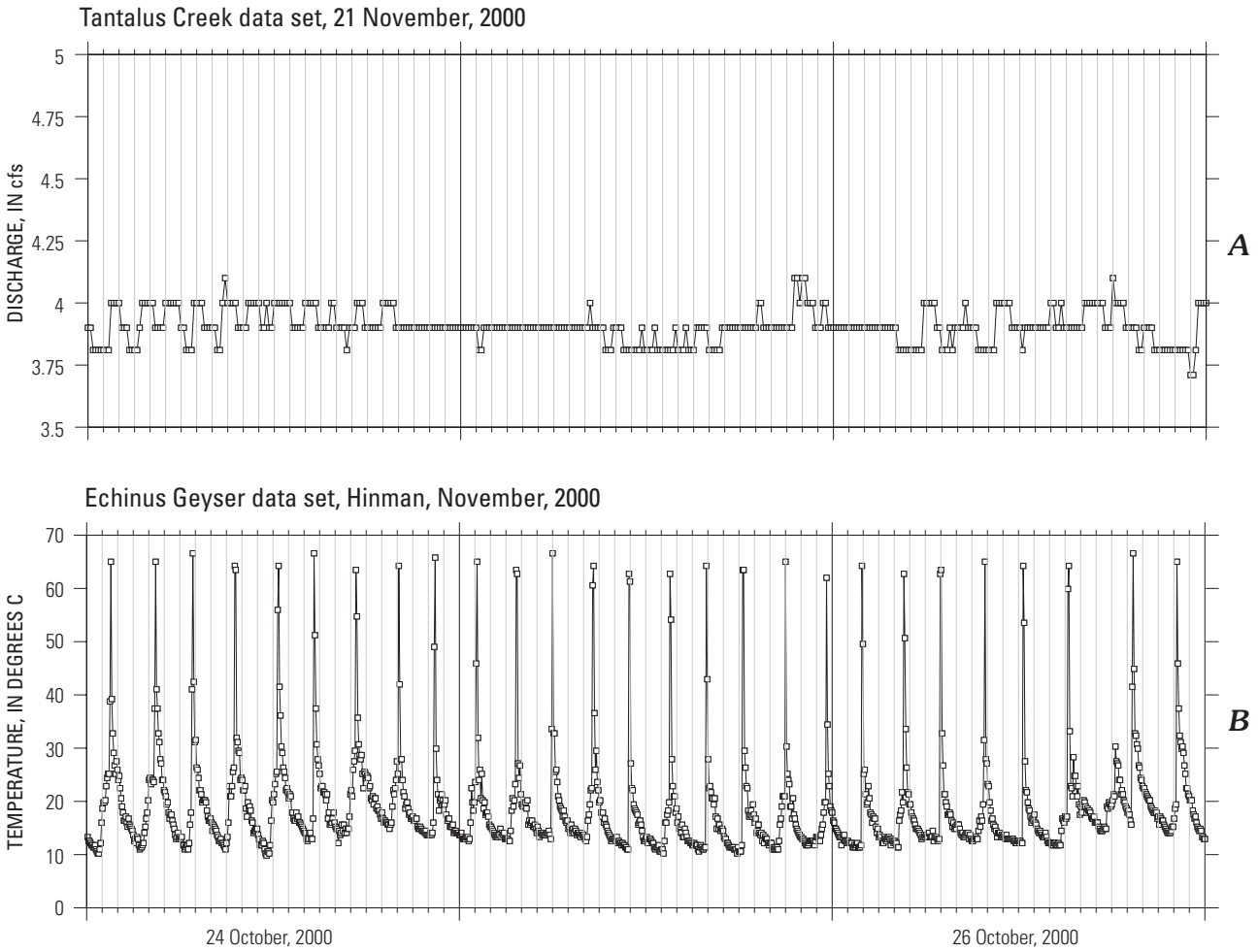

Figure 6. *A*, Plot of discharge at the Tantalus Creek weir for October 24–26 showing the absence of discharge due to eruptions of Echinus Geyser. *B*, Plot of temperature recorded in the Echinus Geyser pool that surrounds the orifice of Echinus Geyser. The temperature record clearly shows that hot water periodically (once every 2.5 hours) entered the pool. This indicated that Echinus erupted, but that it did not emit enough water to (1) produce a subaerial water jet, and (2) show as increased discharge of Tantalus Creek.

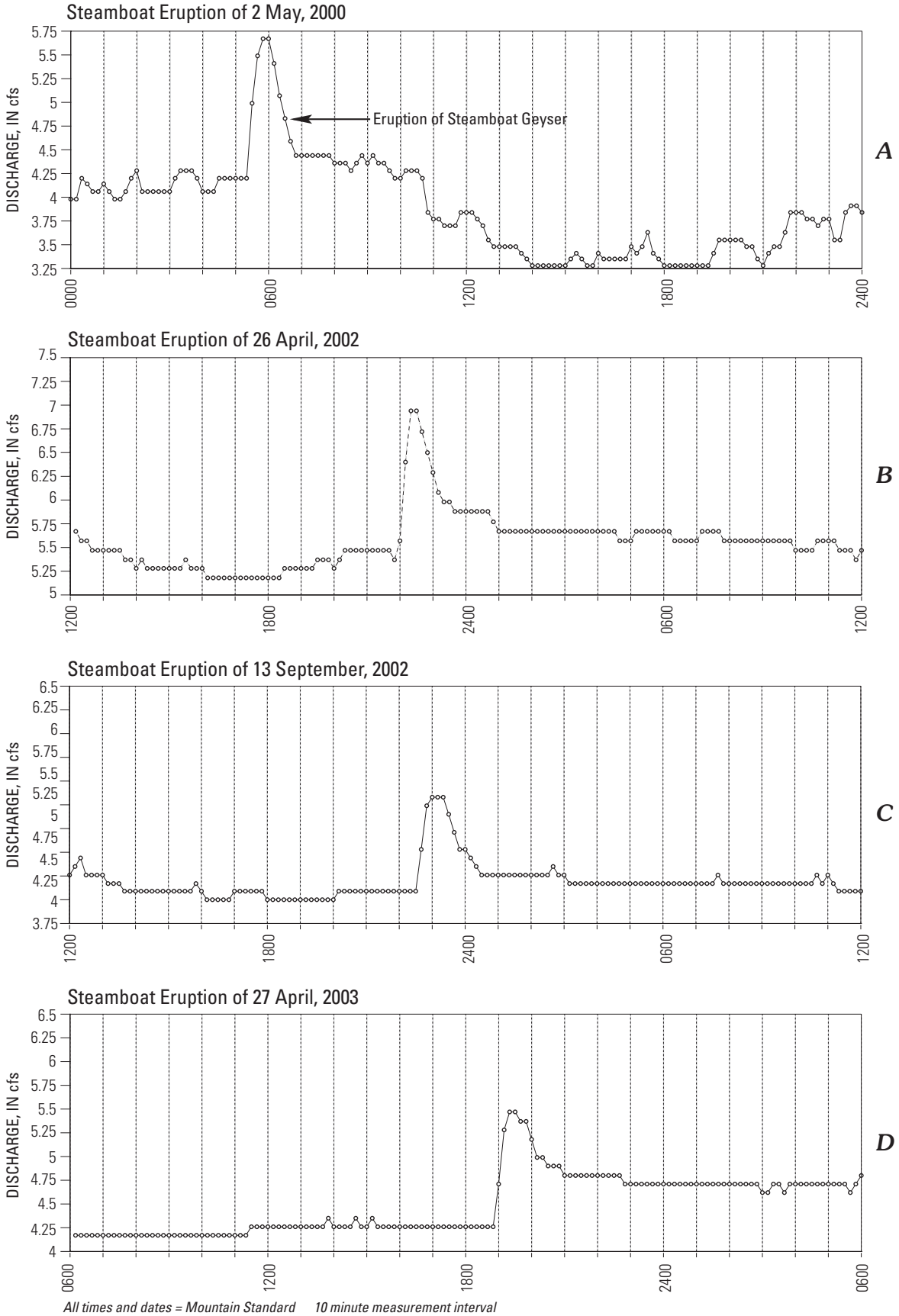
Steamboat Eruption of 2 May, 2000
DISCHARGE, IN cfs
5.75
5.5
5.25
5
4.75
4.5
4.25
4
3.75
3.5
3.25
Eruption of Steamboat Geyser
0000
0600
1200
1800
2400
A
Steamboat Eruption of 26 April, 2002
DISCHARGE, IN cfs
7.5
7.25
7
6.75
6.5
6.25
6
5.75
5.5
5.25
5
1200
1800
2400
0600
1200
B
Steamboat Eruption of 13 September, 2002
DISCHARGE, IN cfs
6.5
6.25
6
5.75
5.5
5.25
5
4.75
4.5
4.25
4
3.75
1200
1800
2400
0600
1200
C
Steamboat Eruption of 27 April, 2003
DISCHARGE, IN cfs
6.5
6.25
6
5.75
5.5
5.25
5
4.75
4.5
4.25
4
0600
1200
1800
2400
0600
D
All times and dates = Mountain Standard 10 minute measurement interval

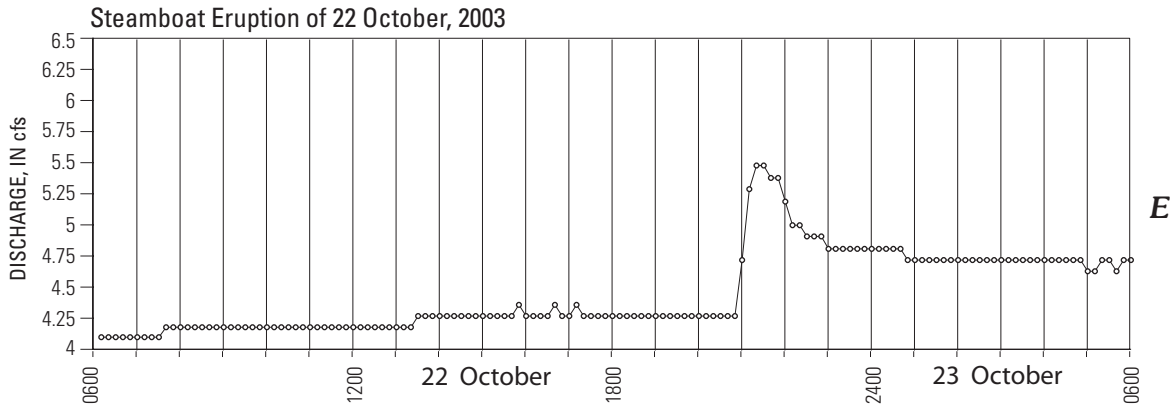

Figure 7 (above and facing page). Plots of the discharge of Tantalus Creek showing the effect of eruptions of Steamboat Geyser. *A*, Eruption of May 2, 2000. *B*, Eruption of April 26, 2002. *C*, Eruption of September 13, 2002. *D*, Eruption of April 27, 2003. *E*, Eruption of October 22, 2003.

oscillations in discharge are not apparent. The decreased flow during the day in summer might be related to increased evapotranspiration during the day. The increased flow during the day in winter might be due to increased snowmelt. However, almost all of NGB is free of snow in winter due to the warmth of the ground—therefore, snowmelt cannot explain the increase in discharge from NGB during the day in winter.

Water Chemistry

To measure chloride and sulfate fluxes exiting Norris Geyser Basin, water samples were periodically collected. These samples were analyzed by the water quality laboratory of the Water Resources Division, USGS, Denver, Colo.

Chloride and Sulfate Flux from Norris Geyser Basin

Samples for chemical analysis were collected weekly during 1989–1991. Since then, samples have been collected intermittently. All samples were filtered through a 5-µm filter during collection. The chloride concentration varies from 350 to 550 ppm; sulfate varies from 100 to 180 ppm. Although the concentration of chloride does not appear to be a function of discharge (fig. 10), the concentration of sulfate increases as discharge decreases below 2 cfs. However, both chloride and sulfate *fluxes* are linear functions of discharge (fig. 11). A similar variation of chloride flux with discharge has been observed for Mammoth Hot Springs as well as springs in the Boundary Creek drainage in the southwestern portion of the Park

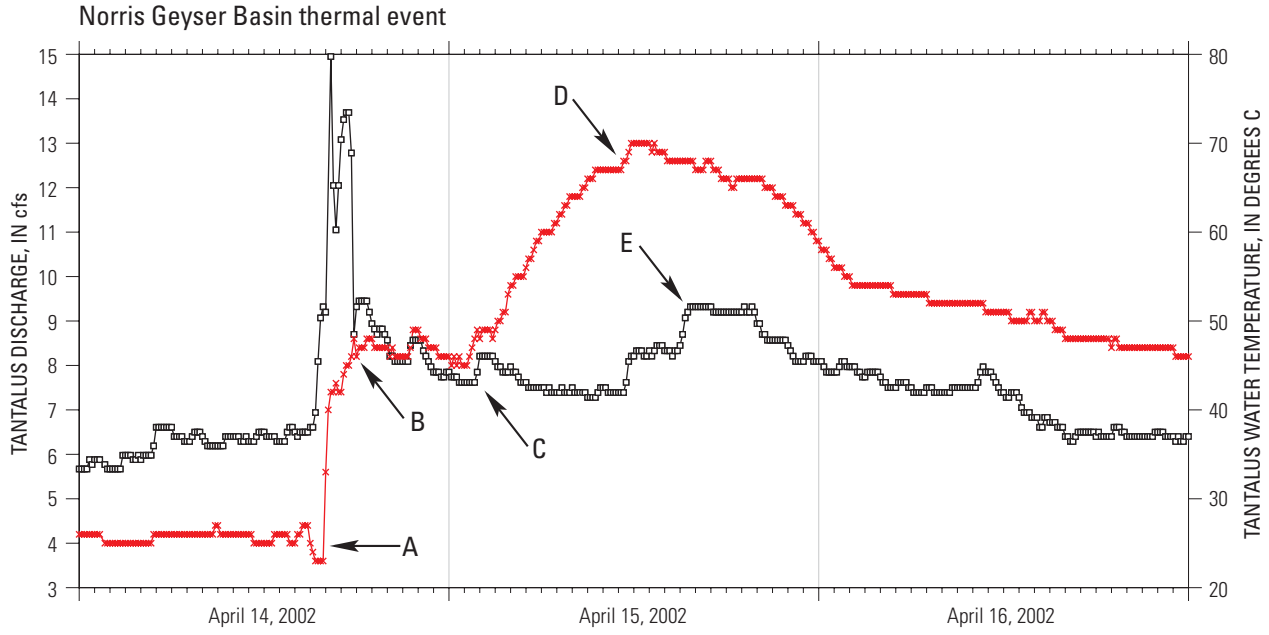

Figure 8. Plots of discharge and water-temperature data acquired during a thermal event. The temperature record is shown in red and the discharge in black.

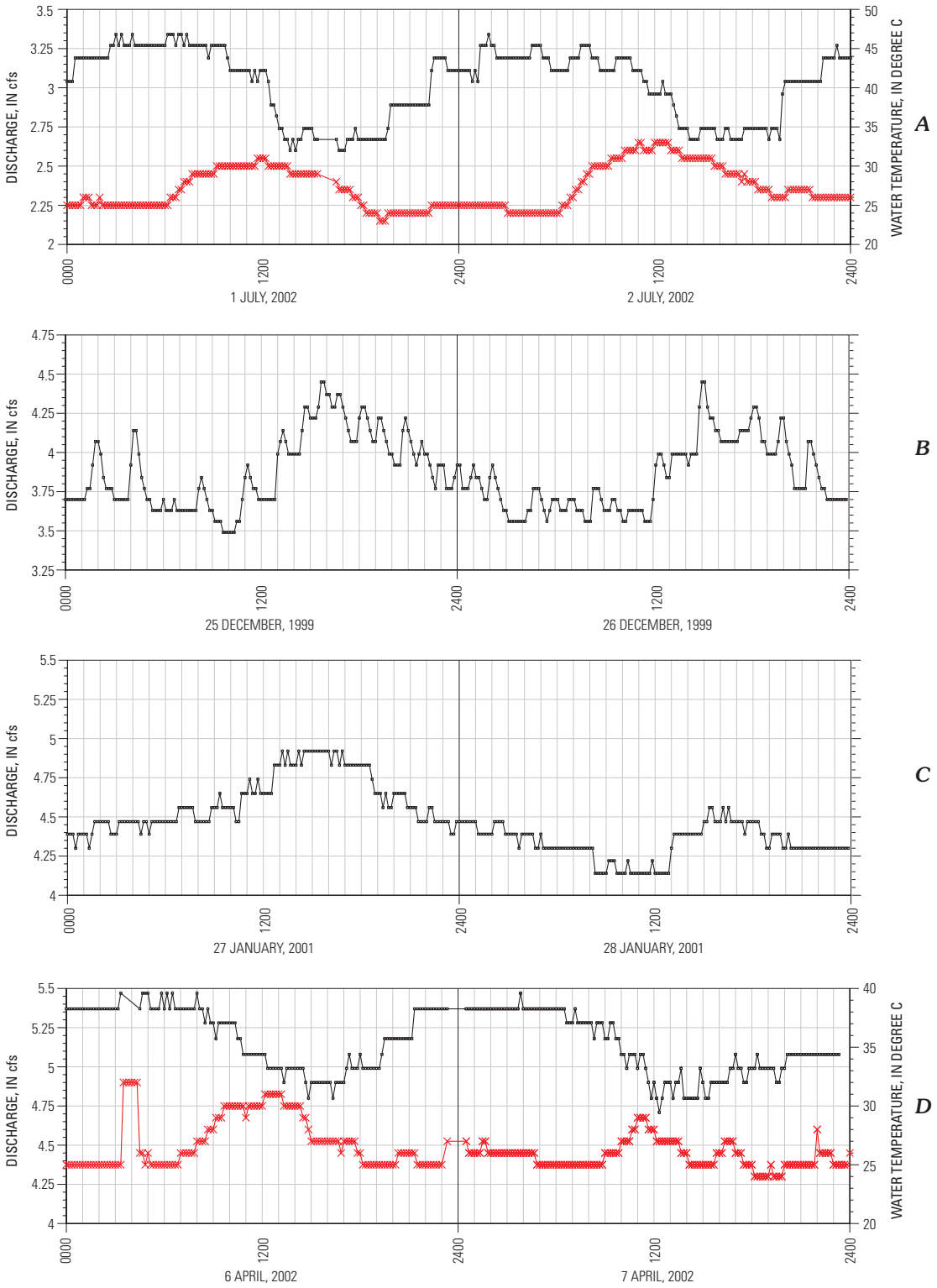

Figure 9. *A*, Plot of 2-day discharge and water temperature of Tantalus Creek for July 1–2, 2002, illustrating diurnal variation in these variables. *B*, Plot of discharge for December 25–26, 1999. *C*, Plot of data for January 27–28, 2001. *D*, Plot of data for April 6–7, 2002. The variation in discharge for the two winter plots (*B*, *C*) are not in phase with the summer data (*A*, *D*). The temperature record is shown in red and the discharge in black.

(Friedman and Norton, 1990; Friedman and Norton, this volume). The chloride versus sulfate flux did not appear to be a function of the discharge (fig. 12).

Most (94 percent) of the chloride exiting the Park is derived from the magma underneath the Park (Norton and Friedman, 1985). Sulfate is believed to be formed largely by the oxidation of reduced sulfur, present either as hydrogen sulfide or elemental sulfur, which are also products of magma. Oxidation occurs when oxygenated water from the surface interacts with the reduced sulfur species—it is unclear whether bacteria are involved with this process (Truesdell and others, 1978; Schoen and Rye, 1970).

In Norris Geyser Basin, the ratio of chloride to sulfur (Cl/S) varies from about 8 to 14 (a chloride to sulfate ratio of 2.5 to 4.5) and is not related to discharge (fig. 11).

Fournier and others (1997) observed that chloride concentration increased at Cistern Spring for several months preceding a thermal disturbance. Immediately following the onset of disturbances, decreased chloride and *increased* sulfate was found. In another example quoted—a neutral-chloride spring at Opal Terrace—the sulfate was observed to *decrease* from 133 ppm to 99 ppm in the 4 days following a disturbance.

Our sampling, although not as detailed as that of Fournier and others (1997), covered a longer time period and integrated the thermal activity of the whole basin. During the distur-

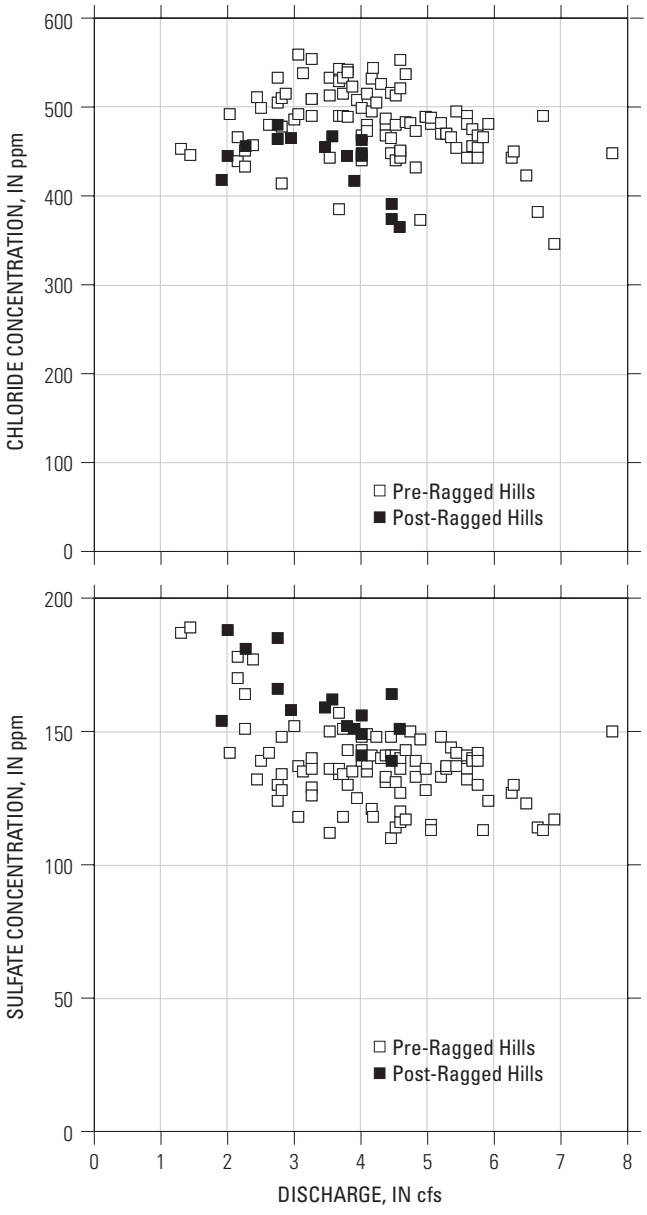

Figure 10. Plots of discharge versus chloride and sulfate concentrations, in parts per million, of water samples collected during 1988–2002 at the Tantalus Creek weir.

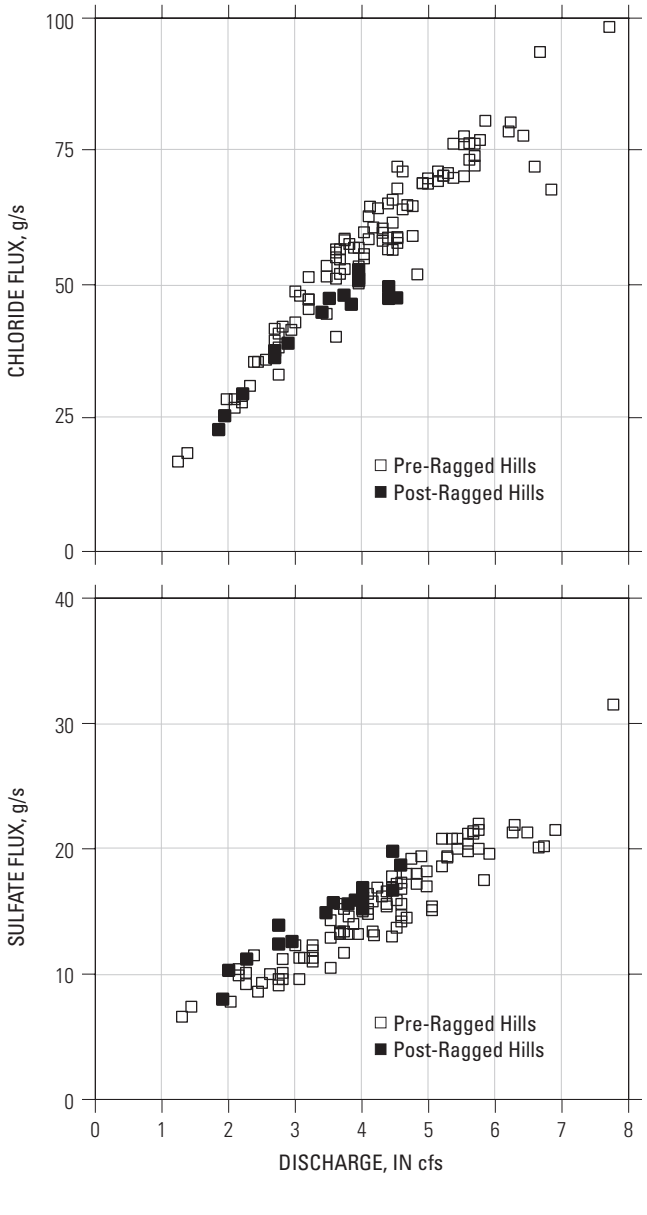

Figure 11. Plots of discharge versus chloride and sulfate fluxes, in grams per second, for water samples collected during 1988–2002 at the Tantalus Creek weir.

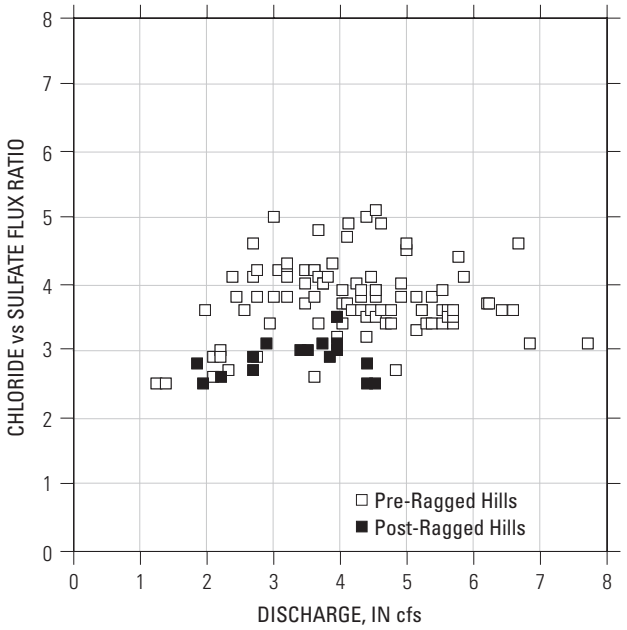

Figure 12. Plot of discharge versus chloride-sulfate ratio for water samples collected during 1988–2002 at the Tantalus Creek weir.

bances of 1988, 1989, 1990, and 1991, both discharge and chloride flux decreased and regained their former values during a period of several months. The changes in both discharge and chloride flux during the 1988, 1989, and 1991 disturbances were as large as a factor of 3, whereas the changes during the 1990 event were much smaller. The changes in sulfate flux were in the same direction as the changes in chloride flux. The ratio of chloride to sulfate flux varied from approximately 2 to 4. With the exception of the data for 1991, the ratio was independent of the discharge rate. In 1991, for discharge rates below 4 cfs, the ratio increased with discharge. At higher discharges, the changes are more random but show a tendency to decrease with increasing discharge. A factor of 4 change in chloride flux over a time interval of a month or so occurred several times in our 4-year data set

Summary and Conclusions

The data presented here illustrate the usefulness of satellite-telemetered data of thermal features that are acquired at closely spaced time intervals.

1. Although some of the variation in discharge from NGB can be related to the effect of precipitation within the basin, examples are given that relate changes in discharge to the eruption of specific thermal features such as Steamboat and Echinus Geysers. Other basin-wide changes are due to changes in thermal-water input from deep sources.
2. An important finding is the large month-to-month change in both chloride and sulfate fluxes. A change by a factor of 4 in chloride flux over a time interval of a month or so occurred several times in our 4-year data set. These measurements confirm qualitative observations made over the years of the extreme variability of thermal activity at NGB. This variability is not restricted to individual thermal features but includes the entire geyser basin
3. A daily variation in discharge occurs with a amplitude of 10 percent. Maximum discharge occurs during the night in summer and during the afternoon in winter. The mechanisms for these diurnal variations in discharge are poorly understood.

References Cited

Fournier, R.O., Janik, C.J., and Weltman, U., 1997, Chemical and isotopic changes in thermal waters during an annual hydrothermal disturbance at Norris Geyser Basin, Yellowstone National Park: Eos, Transactions, American Geophysical Union, v. 78, no. 46, (Suppl.), p. 808.

Friedman, I., and Norton, D.R., 1990, Anomalous chloride flux discharges from Yellowstone National Park: Journal of Volcanology and Geothermal Research, v. 42, p. 225–234.

Norton, D.R., and Friedman, I., 1985, Chloride flux out of Yellowstone National Park: Journal of Volcanology and Geothermal Research, v. 26, p. 231–250.

Schoen, R., and Rye, R.O., 1970, Sulfur isotope distribution in solfataras, Yellowstone National Park: Science, v. 170, p. 1,082–1,084.

Truesdell, A.H., Rye, R.O., Whelan, J.F., and Thompson, J.M., 1978, Sulfate chemical and isotopic patterns in thermal waters of Yellowstone Park, Wyoming, *in* Zartman, R.E., ed., Short papers of the Fourth International Conference, Geochronology, Cosmochronology, Isotope Geology: U.S. Geological Survey Open-File Report 78-701, p. 435–436.

White, D.S., Hutchinson, R.A., and Keith, T.E.C., 1988, The geology and remarkable thermal activity of Norris Geyser Basin, Yellowstone National Park, Wyoming: U.S. Geological Survey Professional Paper 1456, 84 p.